Dinesh Kumar Aswal *Editor*

Handbook on Radiation Environment, Volume 2

Dose Measurements

Springer

Handbook on Radiation Environment, Volume 2

Dinesh Kumar Aswal
Editor

Handbook on Radiation Environment, Volume 2

Dose Measurements

Springer

Editor
Dinesh Kumar Aswal
Health, Safety and Environment Group
Bhabha Atomic Research Centre
Mumbai, Maharashtra, India

ISBN 978-981-97-2798-8 ISBN 978-981-97-2799-5 (eBook)
https://doi.org/10.1007/978-981-97-2799-5

This Springer imprint is published by the registered company Springer Nature Singapore Pte Ltd.
The registered company address is: 152 Beach Road, #21-01/04 Gateway East, Singapore 189721, Singapore

Paper in this product is recyclable.

Dedicated to
70 Glorious Years of
Bhabha Atomic Research Center
In the Service of India

Founded: 3 January 1954

Foreword

(Source: Department of Atomic Energy)

India is one of the fastest growing nations in the world and requires significant growth to fulfil the demand in energy, food, health care and industry. Towards this, nuclear and radiation technologies stand as shining beacons. And as a means of enabling a detailed understanding on these burgeoning technologies, I introduce this Handbook on Radiation Environment with great pleasure. This handbook is indeed a timely and well-thought-out exploration into the fascinating domain of radiation that influences our everyday lives and is poised to shape the future of energy sustainability.

I understand the pivotal role that nuclear energy and radiation technologies play in our quest for a clean, efficient and sustainable power source. The global resurgence of interest in nuclear and radiation technologies highlights the importance of a nuanced understanding of radiation and its implications. This handbook, meticulously crafted by experts in the field, not only provides a comprehensive overview but also invites us to re-evaluate our existing paradigms.

Volume I of this handbook navigates through the sources, applications and policies of radiation, encompassing everything from the ubiquity of radiation to the evolution of radiation protection policies. This volume serves as a foundational resource for

both experts and enthusiasts, offering insights into the dynamic and interconnected world of radiation. On the other hand, Volume II of the handbook delves into the specifics of external and internal dosimetry. From the fundamentals of ionizing radiation to monitoring strategies and advanced techniques like Monte Carlo simulations, this volume provides a comprehensive guide for professionals in the field. For those of us engaged in the domain of atomic energy, this handbook serves as a valuable resource, offering insights that transcend traditional disciplinary boundaries. It is a testament to the collaborative efforts of scientists, researchers and policymakers who strive to strike a delicate balance between harnessing the benefits of ionizing radiation and safeguarding the well-being of our environment and its inhabitants.

As we stand at the crossroads of scientific innovation and responsible energy management, I wish for this handbook to serve as a guiding beacon. I commend the Editor and the authors for their dedication and vision in compiling this invaluable resource. May it inspire and inform, creating a collective understanding that empowers us to navigate the complexities of the radiation environment with wisdom and foresight.

Ajit Kumar Mohanty

Mumbai, India

Dr. Ajit Kumar Mohanty
Chairman, Atomic Energy Commission
Secretary, Department of Atomic Energy

Preface

Ionizing radiation comprises subatomic particles or electromagnetic waves possessing sufficient energy to ionize atoms or molecules by extracting electrons. This distinctive capability, combined with the naturally occurring and artificially generated nature of such radiations, opens up intriguing possibilities for the peaceful utilization of ionizing radiation. Its applications span a wide spectrum, encompassing activities such as improving crop production, purifying waste, treating cancer, delving into the nucleus's core, and harnessing energy through nuclear fission. However, the advantages of ionizing radiation must be judiciously evaluated in light of its potential hazards. Whether utilized for beneficial purposes or to comprehend associated risks, each application necessitates precise dose measurements, a field known as radiation dosimetry. Volume II: Dose Measurements of the Handbook on Radiation Environment aims to provide assistance to experts, policymakers, and interested readers in cultivating a comprehensive understanding of ionizing radiation dosimetry. This volume complements the preceding Volume I: Sources, Applications, and Policies.

To ensure a coherent narrative, Volume II has been organized into two parts—*External Dosimetry* and *Internal Dosimetry*—distinguishing between external and internal exposure scenarios. Part I, *External Dosimetry*, commences with Chapter "Ionizing Radiation Measurements", providing a general introduction to radiation dosimetry and establishing the context for subsequent chapters. Chapters "Radiation Processes, Radiation Quantities, and Units" to "Monitoring of External Neutron Exposures" then offer a succinct grasp of the fundamentals, encompassing the interaction of ionizing radiation with matter, various dosimetric quantities, metrology, the biological effects arising from such interactions, and the monitoring of external gamma, beta, and neutron exposures. The section then progresses to provide a detailed exploration of various environments in external dosimetry. Specific environments are addressed in subsequent chapters, starting with Chapter "Radiation Environment in Nuclear Fuel Cycle Facilities", which examines the radiation environment in nuclear fuel cycle facilities. Chapters "Radiation Environment in Industrial and Research Facilities" and "Radiation Environment in Particle Accelerator Facilities" then delve into the radiation landscape in industrial and research facilities,

as well as particle accelerator facilities, respectively. Chapter "Radiation Environment in Medical Facilities" intricately explores the radiation environment in medical facilities, discussing nuclear medicine radiation dose assessment and occupational and patient doses in medical facilities. In Chapter "Role of Bayesian Inference in TLD-Based Personnel Monitoring", the exploration of advanced subjects like the application of Bayesian inference in personnel monitoring using TLD showcases the incorporation of cutting-edge technologies into radiation safety protocols. Chapters "Retrospective Dosimetry" and "Biological Retrospective Dosimetry" subsequently introduce captivating areas of retrospective and biological retrospective dosimetry, offering insights into comprehending accidental exposures.

Part II, titled *Internal Dosimetry*, commences with Chapter "Introduction to Internal Dosimetry", providing an introduction to Internal Dosimetry and establishing the groundwork for comprehending the subsequent chapters. In Chapter "Biokinetic Models of Radionuclides", an in-depth exploration of the biokinetics of radionuclides unfolds, delving into the physiological processes that govern the movement of radioactive materials within the body. Chapter "Monte Carlo in Internal Dosimetry" introduces the integration of sophisticated simulations, such as Monte Carlo techniques, to enhance our understanding of radiation distribution within biological tissues. The significance of precision is further underscored in Chapter "Internal Dose Evaluation, Quality Assurance and Uncertainty Analysis", which delves into dose evaluation, quality assurance, and uncertainty analysis—integral components ensuring the accuracy of internal dosimetric assessments. Chapters "Direct Monitoring Method to Detect Internal Radioactive Contamination" and "In-Vitro Monitoring Techniques" meticulously explore in-vivo and in-vitro monitoring techniques, respectively, providing a detailed examination of the methods employed to measure internal radiation exposure. Chapter "Radon Inhalation Dose Monitoring" narrows its focus to radon inhalation dose monitoring, addressing a specific internal exposure scenario with unique considerations. The application of liquid scintillation counting in internal dosimetry is extensively covered in Chapter "Liquid Scintillation Based In-Vitro Analysis of Various Radionuclides in Bioassay Samples". Chapter "Radiation Dose Assessment in Nuclear Medicine" offers a comprehensive overview of the challenges and considerations associated with dose measurements in nuclear medicine followed by an exploration of internal measurement techniques during off-normal conditions in Chapter "Internal Radioactive Contamination Monitoring During Off-Normal Situations", both reflecting the adaptability of dosimetric practices in various situations. Finally, Chapter "Decorporation of Radionuclides" delves into the intricate process of decorporation of radionuclides, emphasizing the importance of mitigating internal radiation exposure through targeted interventions.

Together, these chapters strive to provide readers with a comprehensive grasp of ionizing radiation dosimetry spanning a wide array of exposure scenarios. Positioned as an advanced volume relative to Volume I, the primary audience is targeted towards radiation safety practitioners and experts. Nevertheless, my aim is to make these sophisticated concepts accessible, with the hope that this volume will also engage

university students, researchers, and individuals with a general interest in radiation measurements.

In my capacity as the Director of the Health, Safety and Environment Group at Bhabha Atomic Research Centre, I am acutely aware of the significant responsibility involved in accurately measuring doses across diverse exposure environments to ensure the safety of practitioners and users. This awareness prompted the creation of this volume, serving as a comprehensive platform for individuals involved in ionizing radiation dose measurements. The preparation of this volume was a substantial undertaking, given the rapidly advancing research in crucial chapter topics and the challenge of condensing decades of knowledge into a concise format. I extend my heartfelt gratitude to all the chapter authors for their expertise, cooperation, and dedication, as their contributions were integral to the success of this endeavor. Special appreciation goes to Dr. T. Palani Selvam, Hemant Patni, and Anirudh Chandra for their tireless efforts in coordinating the technical reviews of all chapters, ensuring their meaningful contribution to the overarching narrative.

Mumbai, Maharashtra, India Dinesh Kumar Aswal
February 2024

Contents

Editor and Contributors

About the Editor

Dr. Dinesh Kumar Aswal holds prominent roles within the Trombay Council (TC) at the Bhabha Atomic Research Center (BARC), serving as its senior member. He also assumes key positions such as Director of the Health, Safety and Environment Group (HS&EG), Associate Director of the Medical Group, and Director of the National Radiation Emergency Response under the Department of Atomic Energy, Government of India. His responsibilities encompass safeguarding nuclear and radiological safety across the entire nuclear fuel cycle. Internationally renowned for his scientific expertise, administrative prowess, and diplomatic acumen, Dr. Aswal has an extensive list of accomplishments. He has edited nine books, authored over 50 book chapters, filed nine patents, and published more than 500 journal and conference papers, with an impressive H-index of 56 and over 11800 citations. Dr. Aswal's leadership extends beyond his scientific endeavors. He has held administrative positions in prestigious national institutes, including Director of the National Physical Laboratory (CSIR-NPL) in New Delhi, Director of the Central Electronics Engineering Research Institute (CEERI) in Pilani, and Director of the National Institute of Science, Technology and Development Studies (CSIR-NISTADS) in New Delhi. He has also chaired the National Accreditation Board for Testing and Calibration Laboratories (NABL) and served as Secretary of the Atomic Energy Education Society (AEES) in Mumbai. His notable achievements include implementing the redefined International System of Units (SI) based on fundamental and atomic constants and establishing the National Atomic Clock Ensemble to generate Indian Standard Time (IST), renowned for its exceptional accuracy.

Furthermore, Dr. Aswal has contributed significantly to India's nuclear program, developing key technologies such as radiation detectors and hydrogen sensors. He has also pioneered technologies to address societal challenges, including recycling plastic waste, measuring air pollution and enhancing security features for currency notes. Internationally, he has been invited to deliver lectures and engage in collaborative research at esteemed institutions across Japan, France, Germany, Israel, the

United States, and more. He is a Fellow of the International Association of Advanced Materials (FIAAM), Sweden, and the National Academy of Sciences, India (FNASc), among other prestigious honors. Additionally, he serves as Chairman or member of various national committees of the Government of India, further cementing his impact and influence in the scientific community.

Contributors

Deepak Kumar Akar Internal Dosimetry Section, Radiation Safety Systems Division, Health, Safety and Environment Group, Bhabha Atomic Research Centre, Trombay, Mumbai, India;
Homi Bhabha National Institute, Mumbai, India

Dinesh Kumar Aswal Health, Safety and Environment Group, Bhabha Atomic Research Centre, Mumbai, India

A. K. Bakshi Radiological Physics and Advisory Division, Bhabha Atomic Research Centre, Mumbai, India

Sonali P. D. Bhade Radiation Safety Systems Division, Bhabha Atomic Research Centre, Trombay, Mumbai, India

Nagesh Bhat Radiological Physics and Advisory Division, Health, Safety and Environment Group, Bhabha Atomic Research Centre, Mumbai, India

Anirudh Chandra Health, Safety and Environment Group, Bhabha Atomic Research Centre, Mumbai, India

Arghya Chattaraj Bhabha Atomic Research Centre, Mumbai, India

Rajesh K. Chaurasia Radiological Physics and Advisory Division, Bhabha Atomic Research Centre, Mumbai, India

S. Chinnaesakki Health, Safety and Environment Group, Bhabha Atomic Research Centre, Mumbai, India

Sandipan Dawn Radiological Physics and Advisory Division, Bhabha Atomic Research Centre, Mumbai, India

Riya Dey Bhabha Atomic Research Centre, Mumbai, India

G Ganesh Health Physics Division, Bhabha Atomic Research Centre, Mumbai, India

Sushanta Halder Internal Dosimetry Section, Radiation Safety Systems Division, Health, Safety and Environment Group, Bhabha Atomic Research Centre, Trombay, Mumbai, India

G. Haridas Bhabha Atomic Research Centre, Mumbai, India

Kamaldeep Health Physics Division, Bhabha Atomic Research Center, Mumbai, India

K Kannan Health Physics Division, Bhabha Atomic Research Centre, Mumbai, India

Arshad Khan Radiological Physics and Advisory Division, Health, Safety and Environment Group, Bhabha Atomic Research Centre, Trombay, Mumbai, India

D. B. Kulkarni Radiation Safety Systems Division, Bhabha Atomic Research Centre, Mumbai, Maharashtra, India

Prakash Mandal Radiation Safety Systems Division, Bhabha Atomic Research Centre, Trombay, Mumbai, India

S. N. Menon Radiological Physics and Advisory Division, Bhabha Atomic Research Centre, Mumbai, India

Lokpati Mishra Radiation Safety Systems Division, Bhabha Atomic Research Centre, Mumbai, India

Rosaline Mishra Radiological Physics and Advisory Division, Health, Safety and Environment Group, Bhabha Atomic Research Centre, Trombay, Mumbai, India

Vijayakriti Mishra Internal Dosimetry Section, Radiation Safety Systems Division, Health, Safety and Environment Group, Bhabha Atomic Research Centre, Mumbai, India

Minal Y. Nadar Internal Dosimetry Section, Radiation Safety Systems Division, Health, Safety and Environment Group, Bhabha Atomic Research Centre, Trombay, Mumbai, India

Suma Nair Internal Dosimetry Section, Radiation Safety Systems Division, Health, Safety and Environment Group, Bhabha Atomic Research Centre, Mumbai, India

Rupali Pal Radiological Physics and Advisory Division, Bhabha Atomic Research Centre, Mumbai, India

T. Palani Selvam Radiological Physics and Advisory Division, Health, Safety and Environment Group, Bhabha Atomic Research Centre, Mumbai, India

Soumitra Panda Internal Dosimetry Section, Radiation Safety Systems Division, Health, Safety and Environment Group, Bhabha Atomic Research Centre, Trombay, Mumbai, India

J P N Pandey Health Physics Division, Bhabha Atomic Research Centre, Mumbai, India

Munir S. Pathan Radiological Physics and Advisory Division, Health, Safety and Environment Group, Bhabha Atomic Research Centre, Mumbai, India

Hemant Kumar Patni Internal Dosimetry Section, Radiation Safety Systems Division, Health, Safety and Environment Group, Bhabha Atomic Research Centre, Trombay, Mumbai, India

Supreetha Prabhu Radiation Safety Systems Division, Bhabha Atomic Research Centre, Trombay, Mumbai, India

S. M. Pradhan Radiological Physics and Advisory Division, Health, Safety and Environment Group, Bhabha Atomic Research Centre, Mumbai, India

Prathibha Pradosh Radiation Safety Systems Division, Bhabha Atomic Research Centre, Trombay, Mumbai, India

V Ramprasath Health Physics Division, Bhabha Atomic Research Centre, Mumbai, India

Nanda Raveendran Radiation Safety Systems Division, Bhabha Atomic Research Centre, Trombay, Mumbai, India

R. Ravishankar Bhabha Atomic Research Centre, Mumbai, India

Priyanka J. Reddy Radiation Safety Systems Division, Bhabha Atomic Research Centre, Trombay, Mumbai, India

Rahul Roy Internal Dosimetry Section, Radiation Safety Systems Division, Bhabha Atomic Research Centre, Trombay, Mumbai, India

Bijay Kumar Sahoo Radiological Physics and Advisory Division, Health, Safety and Environment Group, Bhabha Atomic Research Centre, Trombay, Mumbai, India

Sridhar Sahoo Radiological Physics and Advisory Division, Bhabha Atomic Research Centre, Mumbai, India

Rajesh Sankhla Radiation Safety Systems Division, Bhabha Atomic Research Centre, Trombay, Mumbai, India

B. K. Sapra Radiological Physics and Advisory Division, Health, Safety and Environment Group, Bhabha Atomic Research Centre, Trombay, Mumbai, India

Deepa Sathian Radiological Physics and Advisory Division, Bhabha Atomic Research Centre, Mumbai, India

Meghnath Sen Radiation Safety Systems Division, Bhabha Atomic Research Centre, Mumbai, Maharashtra, India

Sunil Dutt Sharma Radiological Physics and Advisory Division, Bhabha Atomic Research Centre, Mumbai, India

Vandana Shrivastava Health, Safety and Environment Group, Bhabha Atomic Research Centre, Mumbai, India

I. S. Singh Radiation Safety Systems Division, Bhabha Atomic Research Centre, Mumbai, India

Pradeep Kumar Singh Internal Dosimetry Section, Radiation Safety Systems Division, Bhabha Atomic Research Centre, Trombay, India

Sunil K. Singh Radiation Safety Systems Division, Bhabha Atomic Research Centre, Mumbai, Maharashtra, India

Usha Yadav Radiological Physics and Advisory Division, Health, Safety and Environment Group, Bhabha Atomic Research Centre, Mumbai, India

Ionizing Radiation Measurements

Dinesh Kumar Aswal and Anirudh Chandra

1 Introduction

Ionizing radiation as a phenomenon includes energetic particles and electromagnetic waves and holds a unique position in various sectors. Ionizing radiations are characterized by their ability to dislodge electrons from atoms and are comprised of X-rays, gamma rays, alpha, beta particles, etc. This form of energy is harnessed across diverse applications, ranging from medical diagnostics and cancer treatment to industrial processes and nuclear power generation. In medical contexts, ionizing radiation is instrumental in diagnostic imaging, such as X-ray radiography and computed tomography (CT) scans, providing invaluable insights into the human body's internal structures. Moreover, radiation therapy utilizes controlled doses to combat cancer cells. These crucial applications demand precise measurements to ensure effective treatment while minimizing exposure to healthy tissues. Industrial applications, especially in manufacturing and non-destructive testing, leverage ionizing radiation for material inspection and quality control. In nuclear power plants, ionizing radiation is inherent, driving the need for meticulous measurements to monitor and manage potential risks associated with nuclear processes.

Given its diverse applications, measuring ionizing radiation is important for safeguarding public health [1], occupational safety [2], process control, and environmental well-being [3]. Occupational environments, medical facilities, and public spaces are equipped with radiation detection instruments to quantify and mitigate potential risks of excessive ionizing radiation. These instruments range from Geiger-Mueller counters and scintillation detectors to advanced solid-state detectors, each tailored to specific applications. However, ionizing radiation measurements pose inherent challenges. Calibration drift, detector inefficiencies, and environmental factors can impact measurement accuracy. The diverse types of ionizing radiation

D. K. Aswal (✉) · A. Chandra
Health, Safety and Environment Group, Bhabha Atomic Research Centre, Mumbai 400085, India
e-mail: dkaswal@barc.gov.in

D. K. Aswal (ed.), *Handbook on Radiation Environment, Volume 2*,
https://doi.org/10.1007/978-981-97-2799-5_1

require specialized detectors, and discriminating between various radiation sources can be difficult. Moreover, the dynamic nature of radiation fields and the potential for high radiation doses in certain environments means that robust and reliable measurement systems are needed.

Emerging innovations in ionizing radiation measurements seek to address these challenges. Artificial intelligence (AI) is making significant strides in enhancing the accuracy and efficiency of measurements. Machine learning algorithms can analyze complex radiation data patterns, improving the ability to differentiate between background radiation and potential hazards. Additionally, advancements in sensor technologies, such as solid-state detectors with enhanced sensitivity and durability, contribute to more reliable measurements in various settings. Furthermore, miniaturization and portability are becoming key trends in radiation measurement devices [4], enabling real-time monitoring in diverse environments. Wireless connectivity and remote data access allow operators to monitor radiation levels remotely, improving safety protocols and response capabilities [5].

This introductory chapter aims to provide the reader with a gist of ionizing radiation measurements to enable a broader understanding of the rest of the volume. Section 2 discusses the importance of measuring ionizing radiation. Sections 3 and 4 briefly discuss the means and ways of measuring radiation, while Sects. 5, 6, and 7 discuss its various domain applications, challenges, and emerging technologies.

2 Importance of Measuring Ionizing Radiation

Accurate and precise measurements of any physical quantities are indispensable across various domain applications. They form the bedrock of scientific research, industrial processes, healthcare, environmental monitoring, technology, and safety compliance. The importance of measurements can be understood by looking at the consequences of improper measurements. For example, the Mars Climate Orbiter, a NASA spacecraft, was designed to study the Martian atmosphere. However, a navigation error occurred due to a mix-up between metric and imperial units in the software and inaccurate measurements of thrust led to the spacecraft burning up in the Martian atmosphere instead of entering orbit, resulting in a mission failure and a loss of $125 million [6].

In scientific research, reliable data and experimental validity hinge on precise measurements, ensuring the integrity of findings and supporting hypotheses. Industries rely on accurate measurements for quality control, process optimization, and compliance with regulatory standards, contributing to product consistency and efficiency. In healthcare, precise measurements are crucial for diagnostic accuracy and proper drug dosages, impacting patient care outcomes. Environmental sciences leverage accurate measurements for resource management, climate research, and conservation efforts. Navigation systems, communication technologies, and safety regulations all demand accurate measurements for optimal performance and compliance. Ultimately, accurate and precise measurements are foundational in advancing

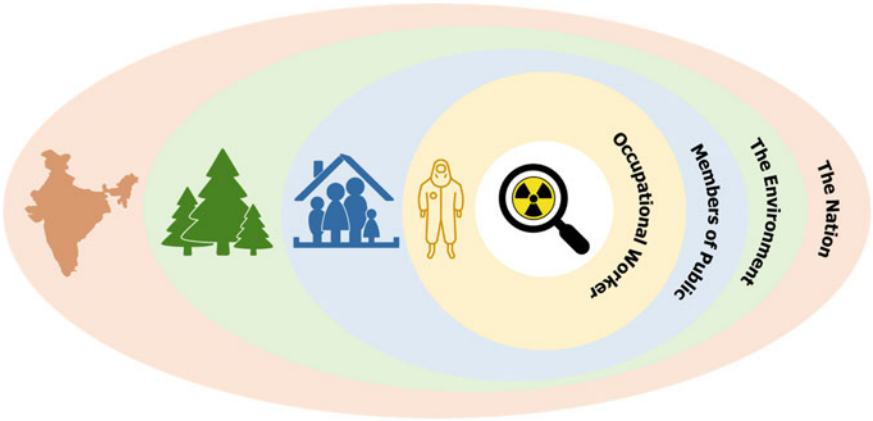

Fig. 1 Accuracy and precision in measuring ionizing radiation have implications on the protection of occupational workers, members of the public, the environment, and the nation

knowledge, innovation, and safeguarding the well-being of individuals and the environment. And these considerations directly apply to nuclear technology as well (as illustrated in Fig. 1).

In the occupational setting, workers in ionizing radiation industries such as nuclear power, healthcare, and research laboratories may be exposed to ionizing radiation as part of their daily activities. Accurate measurement of radiation levels is essential to assess and monitor the radiation dose received by these workers, ensuring that it remains within permissible limits established by regulatory authorities. Regular monitoring helps identify potential overexposure and allows for prompt corrective actions to minimize health risks. Additionally, it enables the optimization of radiation protection measures, ensuring that workers are adequately shielded and that their exposure is kept as low as reasonably achievable (ALARA) [7]. Precise measurements also help monitor the process such as neutron flux in the core of a reactor and dose delivery to target materials and patients [8].

Protecting the public from ionizing radiation is another concern, particularly in the vicinity of nuclear facilities, medical facilities, and areas with elevated sources of radiation. Continuous monitoring of radiation levels in these areas helps to assess potential risks and implement necessary protective measures. For instance, in the event of a nuclear accident or a medical radiation incident, real-time measurements guide emergency response efforts [9], allowing for the timely evacuation of affected areas and the provision of appropriate medical care.

Environmental protection is another crucial aspect of ionizing radiation measurement. Activities such as mining, nuclear testing, and nuclear accidents can lead to the release of radioactive substances into the environment. Monitoring radiation levels in air, water, soil, and biota is essential to assess the impact on ecosystems and human health [3]. Long-term environmental monitoring provides valuable data for

understanding the behavior of radionuclides in different environmental compartments, helping remediation efforts [10], and ensuring sustainable environmental management.

From a national security perspective, the measurement of ionizing radiation plays a vital role in detecting and responding to potential threats. Illicit trafficking of radioactive materials, nuclear terrorism, and the testing of nuclear weapons are significant concerns for national security. Radiation detection and measurement technologies are essential components of border security and nuclear non-proliferation efforts as well [11]. Continuous monitoring helps identify abnormal radiation signatures, facilitating the early detection of illicit activities and enhancing the ability to respond swiftly to mitigate potential risks. In a wider context, the ramifications for workers, public, and environment arising from the accurate, precise, and timely measurements in ionizing radiation applications extend to ensuring safety and optimizing processes, thereby enabling national progress.

3 Measurement Units

But to understand ionizing radiation and its effects, one must use appropriate units of measurement. The choice of units depends on the physical quantity being measured and the domain application. Incidentally, a variety of diverse, yet interconnected radiation measurement units are used in all ionizing radiation applications. Figure 2 shows a subset of these measurement scenarios, including the fuel cycle of nuclear power production as well as non-power industries. In this section, we present some simple and general information about typical measurement units encountered in ionizing radiation measurements.

In the international scientific community, radiation measurement predominantly adheres to the System Internationale (SI), a standardized system derived from the metric system. Nevertheless, certain countries, for example, the United States, continue to utilize the conventional system of measurement, adding a layer of complexity to any discussion surrounding radiation quantification. In this section, we try to include both the systems of measurement for the sake of completion.

Different aspects of ionizing radiation necessitate distinct units of measure. When gauging the radiation emitted by a radioactive material, scientists turn to the conventional unit curie (**Ci**) or the SI unit becquerel (**Bq**). The curie, paying homage to the pioneering scientist Marie Curie, expresses the amount of radioactive material (and therefore amount of emitted radiation), while the becquerel (named after Henri Becquerel) provides a modern, standardized counterpart and is related to the curie as $1\ \text{Ci} = 3.7 \times 10^{10}$ Bq. To put these units in context, a laboratory scale check source contains a few micro curie (μCi) of radioactive material, in the treatment of thyroid cancer approximately a few milli curie (mCi) of radioactive iodine is used and during the Chernobyl power plant accident, approximately a few million curie (MCi) of radioactive cesium were released into the environment [12].

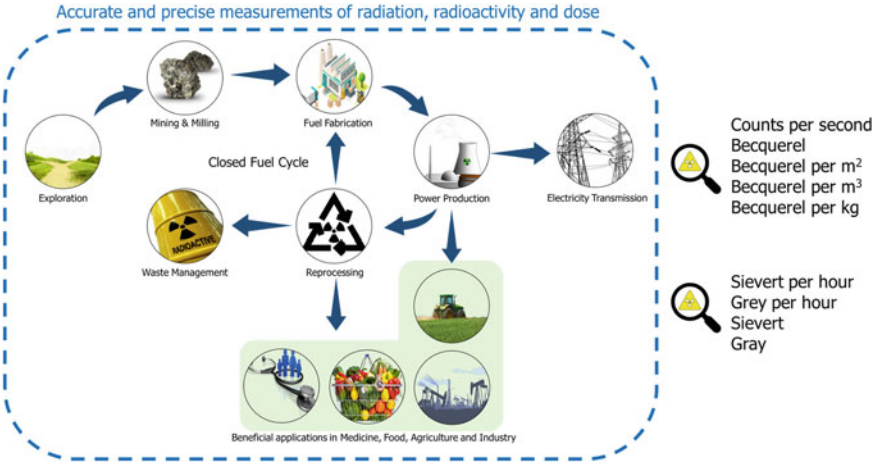

Fig. 2 Illustrating domain applications where a variety of measurement units are used. The choice of unit depends on the context, such as the use of counts per second for radiation detection, Becquerel per m^2 for radioactivity measurement on surfaces, Sievert per hour for dose rate measurements, Gray for dose measurements, etc.

Besides quantifying the amount of radiation vis-à-vis radioactivity, the amount of radiation traveling through the air is also quantified through a quantity called as exposure. This is applicable only to gamma radiation and X-rays and is typically measured by several radiation monitoring instruments used for radiation surveys. The SI unit for this quantity is **Col/kg** and its older/conventional units are roentgen (R) or roentgen per hour (**R/h**) (again, named after a famous physicist, Wilhelm Roentgen).

To measure the effects of these radiations on matter, a different set of quantities are used. Beginning with the absorbed dose or the amount of energy deposited by ionizing radiation in any matter, (concrete block or human tissue, it does not matter). This quantity is measured by the conventional unit **rad** or the SI unit **gray** (Gy) (in honor of the English physicist Louis Harold Gray). The rad, once the standard unit, has now been superseded by the Gy, with 1 Gy equivalent to 100 rad. As individuals are exposed to radiation, energy is deposited in their body tissues, making accurate measurement critical in assessing potential health impacts.

Moving beyond the absorbed dose, scientists evaluate the biological risk of ionizing radiation, which signifies the likelihood of individuals suffering health effects from radiation exposure. The conventional unit for this assessment is **rem**, or the SI unit sievert (**Sv**) (named after the famed medical physicist Rolf Sievert). The rem has been replaced by the Sv, where 1 Sv is equivalent to 100 rem, representing a standardized measure in the international scientific community.

Here two types of quantities use the same SI units of Sv, depending on their purpose. These quantities are defined for the purpose of administering protection against radiation exposure and hence they are termed as protection quantities [13].

The first is the equivalent dose (H), which is simply the absorbed dose multiplied by a weighting factor called as the radiation weighting factor (w_R). This quantity accounts for differences in the ionization potential of different radiations to capture their inherent differences in hazard. This does not account for radio-sensitivities of different human tissues/organs and is typically defined for individual organs/tissues. But to ascertain biological risk, i.e., harm to the human body, scientists use another quantity called as the effective or whole-body dose (E). This is simply the weighted sum of the equivalent dose to the various tissues and organs in the human body, weighted by a quantity that reflects their radio-sensitivity. This quantity is called the tissue weighting factor (w_T).

Together, the equivalent dose and effective dose reflect the human impact of ionizing radiation and are the basis for several regulatory limits [7] designed to administratively restrict radiation exposure in several domain applications. For example, humans receive an average annual effective dose of 2.4 mSv from naturally occurring radioactive material [14], whereas the annual effective dose limit applied to members of the public due to radiation technologies is 1 mSv, over and above the natural dose [15].

However, these protection quantities are difficult to measure operationally. They are only inferred and not technically measured. Therefore, another set of quantities that are operationally measurable and relate to the protection quantities are the personal dose equivalent (Hp) and ambient dose equivalent (H*), [13] which also use the same SI units, i.e., Sv. These quantities are very good approximations of the protection quantities and are related to them through conversion functions and theoretical models. Suffice to say that commercial radiation measuring instruments typically represent the measured dose or dose rate in these quantities.

In conclusion, the measurement of emitted radiation, dose, and biological risk indicates a rather complex process of trying to assess the impact of ionizing radiation. In fact, the transition from conventional to SI units mirrors the global effort to standardize measurements and facilitate seamless communication as well as understanding within the scientific and industrial community.

4 Measurement Techniques

The detection and measurement of nuclear radiation requires specialized instruments due to the invisible nature of these radiations. Human perception falls short in sensing their presence. Historically, ionizing radiation detection has always been intertwined with the evolution of scientific understanding and technological advancements. The fundamental principles guiding the measurement of these radiations revolve around the deployment of radiosensitive detectors and the subsequent recording of radiation-induced effects. Ionizing radiation induces electrical charges in neutral atoms or molecules and the distinction between direct ionizing effects of charged-particle radiation (such as alpha and beta) and the indirect effects of neutral radiation (such as neutron, gamma, and X-rays) lays the foundation for detection principles.

4.1 A Brief History

The journey began with Wilhelm Conrad Rontgen's discovery of X-rays in 1895, leading to the invention of the first medical X-ray photograph in December of the same year. Rontgen's work laid the groundwork for the emergence of radiation detectors, and in 1901, he was awarded the Nobel Prize in Physics for this groundbreaking discovery. Henri Becquerel's experiments in 1896 marked the serendipitous discovery of radioactivity, unveiling the emission of invisible rays from uranium compounds. Marie and Pierre Curie, in collaboration with Becquerel, furthered the field by introducing the concept of radioactivity and discovering radium and polonium. Madame Curie coined the term 'radioactivity', and their contributions earned them the Nobel Prize in Physics in 1903.

The early twentieth century saw the development of various detection instruments. The gold-leaf electroscope, thermoluminescence phenomenon, and photographic plates were employed to detect radiation effects. Rutherford's work on alpha, beta, and gamma rays, along with the invention of the spinthariscope by Crookes in 1903, allowed for the detection of individual radiation events. The cloud chamber, introduced by C.T.R. Wilson in 1911, provided a visual representation of particle tracks. The subsequent decades witnessed the rise of gas-filled detectors, including the Geiger-Muller counter in the late 1920s. These detectors enabled more efficient and practical measurement of radiation.

Photographic emulsions, scintillation detectors, and ionization chambers became integral components of radiation detection during the mid-twentieth century. The advent of semiconductor detectors, such as silicon and germanium, in the late 1950s and early 1960s, marked a significant advancement, offering improved sensitivity and compact design. The evolution continued with the development of neutron detectors, activation detectors, and scintillation materials like thallium-activated sodium iodide crystals. The introduction of thermoluminescent dosimeters (TLD) in the 1940s and the Cherenkov detector in 1937 broadened the scope of radiation detection applications. As technology progressed, amplifier circuits, photomultipliers, and transistor-based circuits replaced vacuum-tube circuits in the mid-twentieth century. The transition to microprocessor-based instruments in the 1960s further enhanced the capabilities of radiation detectors, enabling higher counting rates and portability.

4.2 Principles of Measurement

At the core of radiation monitoring devices lies a radiosensitive detector, a key component that reacts to ionizing radiation [16]. These detectors are designed to register various physical effects triggered by radiation exposure, ultimately allowing for the measurement of radiation intensity. Detection heavily relies on devices sensitive to these physical or chemical impacts of radiation, involving ionization in gases, ionization and excitation in specific solids, chemical alterations, and neutron activation.

One prominent effect harnessed in these devices is ionization. As radiation passes through a medium, it liberates charged particles, creating ion-pairs. These ion-pairs, indicative of the radiation's presence, can be collected to generate an electrical signal. The magnitude of this signal corresponds directly to the intensity of the radiation, forming the basis for quantifying its impact.

In ionizing radiation detection, the response mechanism of detectors is diverse. Some detectors manifest their reaction by emitting light pulses in response to radiation exposure—examples include scintillation detectors such as crystals (ex: NaI(Tl), CsI(Tl)), plastics (ex: anthracene), or organic liquid (ex: 2,5-diphenyloxazole). By meticulously counting these light pulses, the intensity of the radiation can be gauged. This method provides a dynamic and real-time assessment, capturing the immediate impact of ionizing radiation on the detector. Conversely, certain detectors are designed to store the effects of ionizing radiation over an extended period, deferring the assessment until a later time—examples include dosimeters such as thermoluminescent dosimeters (TLDs) and optically stimulated dosimeters (OSLDs). This delayed response enables a retrospective examination of radiation exposure, offering a unique perspective on long-term effects. These detectors, often employed in scenarios requiring cumulative radiation data, contribute to an understanding of radiation impact over time. Fundamentally, all these radiation monitoring devices share a common thread—they respond to the energy deposited in them by ionizing radiation. The energy transfer from radiation to the detector becomes the measurable parameter, offering a tangible and quantifiable basis for assessing radiation levels.

Radiation detection instruments rely on three primary detector types [8, 16]: Gas-Filled Detectors, Scintillators, and Solid-State detectors, each tailored for specific purposes. Figure 3 shows the basic working principles of these three types of detectors.

4.3 Gas-Filled Detectors

The most common type of detector is a gas-filled radiation detector which works on the principle that as the radiation passes through air or specific gas, ionization occurs in air or molecules. The ion-pairs produced are collected and measured as currents or pulses. There are three types of Gas-filled detectors, simply depending on the amount of voltage bias applied.

Ionization Chambers

These operate at low voltage, measuring absorbed dose over time. They excel in high-energy gamma ray detection without dead time issues but lack radiation discrimination for spectroscopy. Ion chambers find applications in survey meters and laboratories for reference standards.

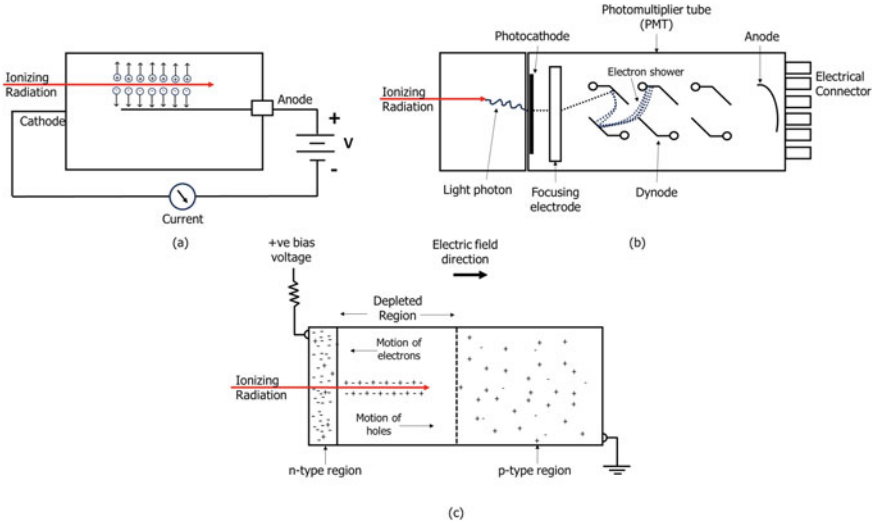

Fig. 3 Schematic of working principles of **a** Gas-filled detectors, **b** Scintillation detectors, and **c** Semiconductor detectors

Proportional Counters

Operating at a higher voltage, they drift ions toward the detector anode, undergoing gas amplification for proportional pulse strength. Ideal for spectroscopy applications, proportional counters are sensitive and effective for alpha and beta detection, serving as contamination screening detectors.

Geiger-Mueller Tubes (G-M Tubes)

Operating at high voltage, G-M tubes function as simple counting devices. Dead time challenges at higher exposure rates are managed through quenching, either electronically or chemically. While valuable for count rates and dose rates, they exhibit dead time lag, addressed through calibration or algorithmic corrections.

4.4 Scintillation Detectors

These detectors rely on materials exhibiting scintillation when exposed to radiation. Photon interaction results in flashes of light, enabling sensitive and specific spectroscopic profiling of radioactive materials. Coupled with photomultiplier tubes, scintillation detectors offer high sensitivity and are crucial in radiation security applications, distinguishing between natural, medical, and potentially hazardous sources.

4.5 Solid-State Detectors

Utilizing semiconductor materials like silicon, solid-state detectors operate similarly to ion chambers but on a smaller scale and lower voltage. Comprising n-type and p-type layers, they form a depletion zone where radiation induces re-ionization, producing electronic pulses for measurement. Solid-state detectors boast quick response times and durability against high radiation, making them ideal for electronic dosimetry in intense radiation environments.

5 Application Domains

Ionizing radiation detection has applications wherever radiation is used. The purpose of detection may vary, such as monitoring to ensure the safety of workers, or to inspect a process, or ensure optimisation of dose delivery, etc. More discussion on application domains is given below and illustrated in Fig. 4.

5.1 In Industry and Medicine

In industry, the monitoring of radiation levels is essential for ensuring occupational safety, regulatory compliance, and the prevention of potential hazards. Industries such as nuclear power generation, medical diagnostics and treatment, and industrial radiography heavily rely on sophisticated radiation detection systems.

In nuclear power generation (Fig. 4a), radiation detectors are integral components of safety measures. Continuous surveillance of radiation levels within nuclear reactors helps in the early detection of abnormalities, allowing for prompt intervention to prevent potential incidents. These detectors contribute to the maintenance of operational integrity and the protection of both workers and the surrounding environment. Measurements also play a role in ensuring the health safety of workers in the form of individual and area monitoring programs. Furthermore, in the decommissioning phase of nuclear facilities, radiation detection aids in the assessment of radioactive contamination, facilitating the safe dismantling and disposal of nuclear infrastructure.

The medical field (Fig. 4b), particularly diagnostic imaging and radiation therapy, benefits significantly from precise radiation detection. In diagnostic procedures, such as X-rays, computed tomography (CT) scans, and positron emission tomography (PET) scans, detectors ensure accurate imaging while minimizing radiation exposure to patients. Radiation therapy, used in the treatment of cancer, relies on sophisticated detectors to precisely deliver therapeutic doses to targeted tissues, maximizing treatment efficacy while minimizing damage to healthy cells.

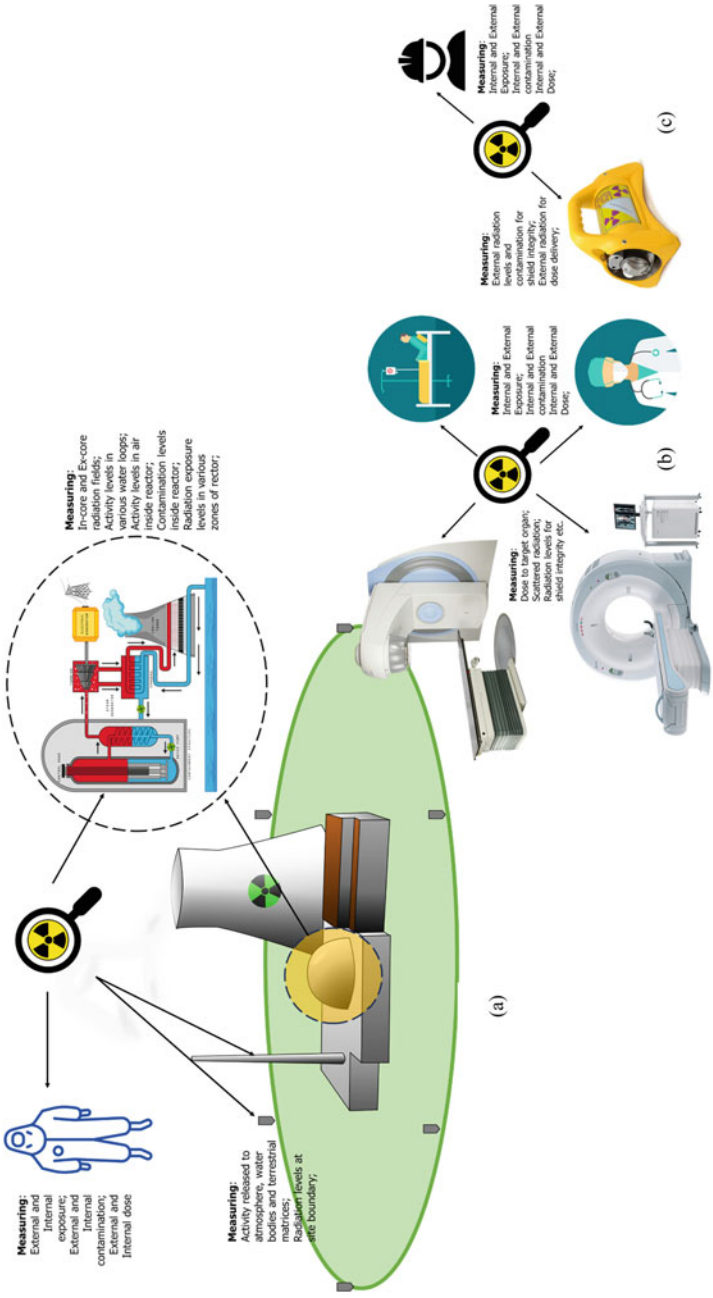

Fig. 4 Illustrating the application of ionizing radiation detection in diverse environments such as **a** nuclear power plants, **b** nuclear medicine, and **c** industrial radiography

Industrial radiography (Fig. 4c), a non-destructive testing technique widely used in manufacturing and construction, depends on radiation detection for flaw detection and quality control in materials. By utilizing radiation sources to inspect the internal structures of objects, such as welds and pipelines, industrial radiography ensures the integrity and reliability of critical components. This application is particularly prevalent in sectors like aerospace, oil and gas, and construction, where the detection of structural imperfections is vital for maintaining safety standards.

5.2 In the Environment

Radiation detection is also important in environmental applications, contributing significantly to monitoring and safeguarding ecosystems from the potential impacts of ionizing radiation. Natural and anthropogenic sources can introduce radioactive materials into the environment, necessitating vigilant surveillance to assess their levels and mitigate associated risks. Monitoring radiation in air, water, and soil helps identify potential contamination hotspots, enabling prompt interventions to protect both environmental health and public safety.

In environmental research, radiation detection plays a role in studying the impact of nuclear activities, such as nuclear power plants or historical nuclear events, on ecosystems. This data aids scientists in understanding the long-term effects of radiation exposure on flora and fauna, guiding conservation efforts, and ensuring the sustainable management of biodiversity. Additionally, radiation detection is instrumental in overseeing nuclear waste disposal sites, preventing unauthorized access, and assessing the effectiveness of containment measures.

Furthermore, in the aftermath of environmental disasters, such as nuclear accidents or radiological incidents, radiation detection becomes indispensable for assessing contamination levels and guiding cleanup efforts. For example, the international network of The International Monitoring System (IMS) of the Comprehensive Test Ban Treaty Organization (CTBTO) monitors radiation to detect potential nuclear explosions [17]. In India, the country-wide network of the Indian Environmental Radiation Monitoring Network (IERMON) of radiation detectors ensures vigilance to any unwarranted event involving ionizing radiations [18]. Rapid and accurate detection allows authorities to implement timely measures to mitigate the spread of radioactive materials, minimizing the ecological impact and facilitating the restoration of affected areas.

In essence, radiation detection in environmental applications acts as a vital tool in the ongoing commitment to preserving the delicate balance of ecosystems and safeguarding the planet's biodiversity.

6 Challenges in Radiation Detection

Like any other measurement instrument, radiation detectors often face issues of calibration and maintenance. The calibration of radiation detectors is of the utmost importance in any domain application. Here we present some important calibration and maintenance challenges with respect to the nuclear industry [19].

- **Inappropriate Calibration Frequency Extension:** In many instances in the nuclear industry, calibration frequencies for certain detector types are often extended without considering degradation and failure mechanisms, jeopardizing monitor reliability. This is in part a systemic problem as well as one of negligence. Possible solutions include implementing stringent calibration practices, emphasizing proper training for maintenance workers and adherence to recommended frequencies, and preventing unknowing degradation.
- **Expertise Drain in Radiation Detection:** A decline in radiation detection experts contributes to improper handling, calibration, and maintenance of monitors, demanding a remedy to ensure knowledgeable oversight. Solutions include reinstating expert oversight in the calibration and maintenance process and providing relevant training to maintenance personnel on radiation detection principles.
- **Technological Obsolescence:** Aging equipment and the non-existence of radiation detector suppliers pose challenges, leading to complexities and substantial replacement costs. Solutions include exploring technology upgrades and considering electronic retrofits and detector substitutions, to extend the lifetime of monitors without the need for complete replacements. Conducting independent assessments to evaluate system health and identifying suitable upgrades is also important.

In nuclear medicine, challenges are associated with both therapy and diagnostics. The challenges in radiation therapy technologies [20] involve implementing advanced techniques like small field dosimetry (SRS/SBRT), imaging dosimetry, and 4D dosimetry for moving targets. Small field dosimetry faces issues due to partial volume effects, requiring 3D dosimeters for accurate measurement. Intensity-modulated radiation therapy (IMRT) and volumetric modulated arc therapy (VMAT) demand high-resolution 3D dosimetry to handle dynamic changes and sophisticated mechanical movements. Imaging dosimetry introduces concerns about increased imaging volume and potential complications, necessitating accurate measurement of imaging dose. 4D dosimetry for moving targets is challenging due to non-uniform tissue and deformable organs, requiring precise 3D and high-resolution measurements.

In diagnostics, the progression of single photon emission computed tomography (SPECT) and positron emission tomography (PET) depends on overcoming distinct challenges in detector design and electronics [21]. Energy resolution in PET, a critical factor influencing image quality, demands innovative materials like cerium bromide (CeBr3) or a shift to direct conversion detectors such as cadmium zinc telluride (CZT) or thallium bromide (TlBr). Concurrently, intensive research targets timing

resolution enhancement, vital for signal-to-noise improvement and the implementation of time-of-flight PET. This involves novel configurations like side readouts, meta scintillators, and leveraging Cherenkov light emission, complemented by signal processing methods like convolutional neural networks (CNN). Spatial resolution, impacted by acollinearity and positron range, poses another challenge. Overcoming this necessitates tackling the inherent limitations of PET detectors, exploring unique configurations like layered scintillators, and addressing spatial constraints related to monolithic scintillators.

7 Emerging Technologies—AI

Radiation detection and measurement has a rich history that extends back several decades and development in this field follows technological developments of the time. At present, Artificial Intelligence and Machine Learning (AI/ML) are the latest emerging technologies and here we discuss some ways in which AI can play a role in ionizing radiation detection, measurement, and applications [22]. Though this is a dynamically evolving technology, here we have attempted to capture the flavor of AI-driven improvements in nuclear medicine and radiation protection in the nuclear industry, and it is by no means an exhaustive exploration.

Among the several domain applications of radiation measurement, one can argue that AI has made early contributions to nuclear medicine than industrial applications. Some of the early applications of AI in nuclear medicine included enhancing image quality, quantification accuracy, and precision. AI utilizes imaging data for disease diagnosis, prognosis, lesion classification, and imaging physics. In particular, radiomics has seen this emergence, where high-dimensional features are extracted using convolutional neural networks (CNNs) [23]. This aids in diagnosis, treatment monitoring, and correlation analyses with histopathology or gene mutations. Machine learning (ML) methods like naive Bayes and support vector machines have long been employed, but deep learning (DL) technologies, such as CNNs and artificial neural networks, are known for their superior performance.

In radiopharmaceutical therapies (RPT), AI-driven theranostic drug discovery explores molecular parameters for optimal outcomes [24]. Precision dosimetry, essential for assessing energy deposition in tissues, benefits from AI-based image reconstruction, reducing scanning time and enhancing quantification accuracy. Predictive dosimetry and digital twins allow personalized RPTs, predicting absorbed doses and optimizing therapies. AI also impacts clinical workflow by increasing efficiency in patient scheduling, predictive device maintenance, quality control monitoring, and real-time device performance evaluation. Triage of urgent findings and automation of time-consuming tasks contribute to faster report turnaround times, ensuring safer and more reliable nuclear medicine practices.

The learnings from and applications of AI in nuclear medicine have in a way contributed to its emergence in industrial applications as well. AI does hold a significant potential in enhancing radiation detection and measurement, offering improved

efficiency, accuracy, and automation in various aspects of radiation protection in the nuclear industry. Here are several ways in which AI can be applied in this field:

- **Automated Data Analysis**: AI algorithms can process and analyze vast amounts of radiation data more efficiently than traditional methods [25]. They can identify patterns, anomalies, or trends in radiation levels [26], aiding in the early detection of potential issues.
- **Image Recognition for Contamination**: AI-powered image recognition systems can be employed to identify and locate radioactive contamination. This is particularly useful in facilities handling radioactive materials where visual inspection may not be sufficient.
- **Real-time Monitoring and Alerts**: AI algorithms can continuously monitor radiation levels in real time. If abnormal readings are detected, automated alerts can be generated, allowing for prompt response and intervention to minimize potential hazards.
- **Spectroscopy and Isotope Identification**: AI can assist in the analysis of spectroscopic data, helping to identify specific isotopes and differentiate between various types of radiation. This capability [27] is valuable in scenarios where distinguishing between different radiation sources is crucial.
- **Dosimetry and Exposure Assessment**: AI can enhance the accuracy of dose calculations and exposure assessments [28, 29]. Machine learning models can predict radiation doses based on various factors, aiding in risk assessment and management.
- **Predictive Maintenance**: AI algorithms can predict equipment failures or issues in radiation detection devices, allowing for proactive maintenance. This predictive maintenance approach ensures that detection systems are operational when needed, reducing the risk of undetected radiation exposure.
- **Robotic Systems for Remote Monitoring**: AI-powered robots equipped with radiation detectors can be deployed in hazardous environments for remote monitoring [30]. These robots can navigate and collect data autonomously, reducing the need for human presence in potentially dangerous areas.
- **Data Integration and Decision Support**: AI can integrate data from multiple sources [5], including weather conditions, facility status, and historical radiation data. This holistic approach enables better decision support for managing and mitigating radiation risks.

8 Conclusion

Human inability to physically perceive ionizing radiation means that the field of ionizing radiation measurements is an important element across diverse domains. Accurate, precise, and timely measurement supports scientific research, industrial processes, healthcare, environmental monitoring, technology, and safety compliance. Industries, particularly nuclear power generation, medical diagnostics, and industrial

radiography, rely on accurate measurements for safety, quality control, and regulatory compliance. In healthcare, precise measurements are paramount for diagnostic accuracy and personalized treatment. Environmental monitoring uses measurements for resource management, climate research, and conservation efforts. The protection of occupational workers, the public, and the environment from ionizing radiation necessitates accurate measurements to assess and monitor radiation exposure. And in the path toward radiation detection development, right from Röntgen's discovery of X-rays to the development of gas-filled detectors, scintillators, and solid-state detectors, the continuous advancement of technology in this field has enabled better detectors and techniques to evolve. Principles of measurement, based on ionization effects, indicate that diverse mechanisms are often employed by detectors to register the presence of ionizing radiation. And when it comes to quantifying these measured values, a variety of different, yet interrelated units are employed. The transition from conventional to SI units also shows the global effort to standardize measurements. In conclusion, accurate and precise ionizing radiation measurements are foundational in advancing knowledge, ensuring safety, and optimizing processes across various domains while also shaping a safer, more informed, and technologically advanced future.

References

1. Wedekind L (2001) Radiation technology for public health and safety. International Atomic Energy Agency, 25 Oct 2001. [Online]. Available https://www.iaea.org/newscenter/news/radiation-technology-public-health-and-safety. Accessed 6 Jan 2024
2. International Atomic Energy Agency (2018) Occupational radiation protection. IAEA Safety Standards Series No. GSG-7, IAEA, Vienna
3. International Atomic Energy Agency (2005) Environmental and source monitoring for purposes of radiation protection. IAEA, Vienna
4. Sprint Diagnostics (2024) The future of X-ray technology: innovations and emerging trends. ," Sprint Diagnostics, [Online]. Available https://www.sprintdiagnostics.in/blog/future-x-ray-technology-innovations-emerging-trends. Accessed 7 Jan 2024
5. Ahmad MI, Ab Rahim MI, Nordin R, Mohammed F, Abu-Samah F, Abdullah NF (2021) Ionizing radiation monitoring technology at the verge of internet of things. Sensors (Basel) 21(22):7629
6. Grossman L (2010) Nov. 10, 1999: metric math mistake muffed mars meteorology mission. Wired, 10 Nov 2010. [Online]. Available https://www.wired.com/2010/11/1110mars-climate-observer-report/. Accessed 6 Jan 2024
7. International Commission on Radiological Protection (2007) ICRP publication 103: the 2007 recommendations of the international commission on radiological protection. Elsevier, New York
8. Cember H (2009) Health physics instrumentation. In: Introduction to health physics, 4th edn. McGraw Hill Medical, London, pp 427–505
9. International Atomic Energy Agency (1999) Generic procedures for monitoring in a nuclear or radiological emergency. IAEA, Vienna
10. Bao Q, Dong J, Dong Z, Yang M (2022) A review on ionizing radiation-based technologies for the remediation of contaminated groundwaters and soils. Chem Eng J 446(Part 2):136964
11. International Atomic Energy Agency (2002) Detection of radioactive materials at borders. IAEA, Vienna

12. International Atomic Energy Agency (1996) One decade after Chernobyl: summing up the consequences of the accident. IAEA, Vienna
13. International Commission on Radiological Protection (2021) Use of dose quantities in radiological protection, ICRP Publication 147. Ann ICRP 50(1)
14. Atomic Energy Regulatory Board (2020) Background natural radiation. AERB, 5 Sept 2020. [Online]. Available https://www.aerb.gov.in/english/background-natural-radiation. Accessed 6 Jan 2024
15. Atomic Energy Regulatory Board (2017) Radiological protection principles. AERB, 15 May 2017. [Online]. Available https://www.aerb.gov.in/english/radiation-protection-principle. Accessed 6 Jan 2024
16. Knoll GF (2010) Radiation detection and measurement, 4th edn. Wiley, New Jersey
17. CTBTO, The international monitoring system. CTBTO [Online]. Available https://www.ctbto.org/our-work/international-monitoring-system. Accessed 7 Jan 2024
18. BARC, BARC activities for environmental surveillance and radiation protection. BARC, [Online]. Available https://www.barc.gov.in/randd/erm.html. Accessed 7 Jan 2024
19. Cox B, Darios E (2022) Radiation monitor maintenance issues challenging our industry—Is this an unintended consequence of the maintenance rule? Nuclear News Wire, 19 Oct 2022. [Online]. Available https://www.ans.org/news/article-4329/radiation-monitor-maintenance-issues-challenging-our-industryis-this-an-unintended-consequence-of-the-maintenance-rule/. Accessed 7 Jan 2024
20. Yin FF, Oldham M, Cai J, Wu Q (2010) Dosimetry challenges for implementing emerging technologies. J Phys Conf Ser 250(1):8–11
21. Enlow E, Abbaszadeh S (2023) State-of-the-art challenges and emerging technologies in radiation detection for nuclear medicine imaging: a review. Front Phys 11
22. Andresz A, Zephir A, Bez J, Karst M, Danieli J (2022) Artificial intelligence and radiation protection. A game changer or an update? Radioprotection 57(2):157–164
23. Cheng Z, Wen J, Huang G, Yan J (2021) Applications of artificial intelligence in nuclear medicine image generation. Quant Imag Med Surg 11(6):2792–2822
24. Saboury B, Bradshaw T, Boellaard R, Buvat I, Dutta J, Hatt M, Jha AK, Li Q (2023) Artificial intelligence in nuclear medicine: opportunities, challenges, and responsibilities toward a trustworthy ecosystem. J Nucl Med 64(2):188–196
25. Science Japan (2021) sing AI to analyze radiation measurement data--New method developed by JAEA and Nagoya University. Science Japan, 6 Apr 2021. [Online]. Available https://sj.jst.go.jp/news/202104/n0406-02k.html. Accessed 6 Jan 2024
26. Chandra A, Saindane S, Murali S (2023) Process identification and discrimination in the environmental dose rate time series of a radiopharmaceutical facility using machine learning techniques. Appl Radiat Isotopes 198:110878
27. The Alan Turing Institute, "Radiation detectors and machine learning," The Alan Turing Institute, [Online]. Available: https://www.turing.ac.uk/research/research-projects/radiation-detectors-and-machine-learning. [Accessed 6 January 2024].
28. Jensen PJ, Zhang J, Koontz BF, Wu QJ (2021) A novel machine learning model for dose prediction in prostate volumetric modulated arc therapy using output initialization and optimization priorities. Front Artif Intell 4
29. van Velzen SGM, Gal R, Teske AJ, van der Leij F, van den Bongard DHJG, Viergever MA, Verkooijen HM, Išgum I (2021) AI-based radiation dose quantification for estimation of heart disease risk in breast cancer survivors after radiation therapy. Int J Radiat Oncol Biol Phys 112(3):621–632
30. Zhuang J, Zheng G (2022) An intelligent robot detection system of uncontrolled radioactive sources. In: Computational intelligence and neuroscience

External Dosimetry

Radiation Processes, Radiation Quantities, and Units

Riya Dey, S. Chinnaesakki, S. M. Pradhan, and T. Palani Selvam

1 Brief History of Radioactivity

The last five years of the nineteenth century opened up an unprecedented era of scientific discovery that re-evaluated the classical theory that governed physics. On 20th January, 1896, Professor Henri Becquerel attended a lecture by Henri Poincaré on the X-rays discovered by Wilhelm Röntgen. Inspired by this lecture, Becquerel started performing experiments with a fluorescent material, which happened to be potassium-uranyl sulfate. By the end of 1896, he published several articles on his investigations on the 'Becquerel rays' which indicated that the rays were released from the uranium present in his crystals and their intensity did not noticeably reduce even after several months. Later on, in 1898 Marie Curie and her husband Pierre Curie, who were very much intrigued by the findings of Professor Henri Becquerel, discovered two naturally occurring, strongly radioactive elements, radium and polonium. Marie Curie referred to this phenomenon as 'Radioactivity' which was earlier named as 'Becquerel rays' or 'Uranic rays'.

All these accomplishments paved the way for a new era of science and technology such as the discovery of neutrons by James Chadwick in 1932 and artificial radioactivity by Irene Curie and F. Joliot in 1934. Ernest Rutherford, while working at McGill University in Montreal, discovered that the erstwhile Becquerel rays were composed of two different components which he named as alpha and beta. It was found that a thin paper was able to stop alpha particles whereas beta rays could pass through the paper but could be stopped by sheets of metal. In 1900, Paul Villard discovered a third, even more penetrating, component of the radiation which was named as gamma rays.

Since then, many natural and artificially produced radionuclides have found several peaceful applications in medicine, agriculture, environment, industry, and

R. Dey (✉) · S. Chinnaesakki · S. M. Pradhan · T. Palani Selvam
Bhabha Atomic Research Centre, Mumbai 400085, India
e-mail: riyadey@barc.gov.in

D. K. Aswal (ed.), *Handbook on Radiation Environment, Volume 2*,
https://doi.org/10.1007/978-981-97-2799-5_2

electricity generation. This widespread use, though beneficial, also necessitates stringent regulations and therefore the precise monitoring of radiation dose received by the individuals, to enforce these regulations. To develop a basic understanding on radiation dose and its measurements as well as being an introduction to this volume, this chapter provides an overview of several radioactive processes such as decay by alpha, beta, gamma emission, internal conversion, electron capture, and spontaneous neutron fission, in addition to the various radiation quantities and their units.

To begin with, first we have to understand what is 'Radioactivity'. Radioactivity is the process of spontaneous emission of electromagnetic and/or nuclear particle radiation by the decay and transformation of unstable atomic nuclei. Through this process, the unstable atoms rearrange themselves to achieve stability via one or more successive decays. At present, there are about 3000 radionuclides and 237 stable nuclides. The guiding principles which define the stability of atoms and their decay are governed by:

(a) The neutron/proton (n/p) ratio within the nucleus.
(b) The mass–energy relationship of parent, progeny, and the emitted particles.

It is observed that stable nuclei contain a certain combination of proton and neutron numbers and they fall into a band which is referred to as the valley of stability. In either direction of the valley, lie the unstable nuclei. Now the question is why the n/p ratio is crucial for nuclear stability. The answer lies in the balance between 'Nuclear Force' among the nucleons (depends roughly on the nuclear volume and is a very strong and short-range force) and the repulsive 'Coulomb Force' between the protons in the nucleus.

Inside the nucleus, the n-p interaction is slightly stronger than the n–n or p-p reaction. Nuclei with equal numbers of neutrons and protons are more stable since the number of n-p interactions is maximized. Thus, it is seen that in many stable nuclei of low mass number, the numbers of neutrons and protons are equal or approximately so.

The plot, similar to the nuclide chart (Fig. 1), indicates the stable nuclei in black, whereas the neutron-rich nuclei and proton-rich nuclei lie above and below the zigzag line, respectively. The plot shows that for stable nuclei of lighter elements, there are approximately equal numbers of protons and neutrons, i.e., $n = Z$, e.g., ${}^{4}_{2}\mathrm{He}_2$, ${}^{10}_{5}\mathrm{B}_5$, ${}^{12}_{6}\mathrm{C}_6$, ${}^{14}_{7}\mathrm{N}_7$, ${}^{16}_{8}\mathrm{O}_8$, etc. For a heavier stable nucleus, the number of neutrons is more than the protons. In such a nucleus, the coulomb repulsion between the protons is large and extra neutrons are needed to supply additional binding energy to hold the nucleus together. Lead (${}^{208}\mathrm{Pb}$) is the heaviest stable isotope, which has 82 protons and 126 neutrons. For Caesium-137 (55 protons and 82 neutrons), the ratio of neutrons to protons is 1.49, and for Uranium-238 (92 protons and 146 neutrons), the neutron to proton ratio is 1.59, making them unstable.

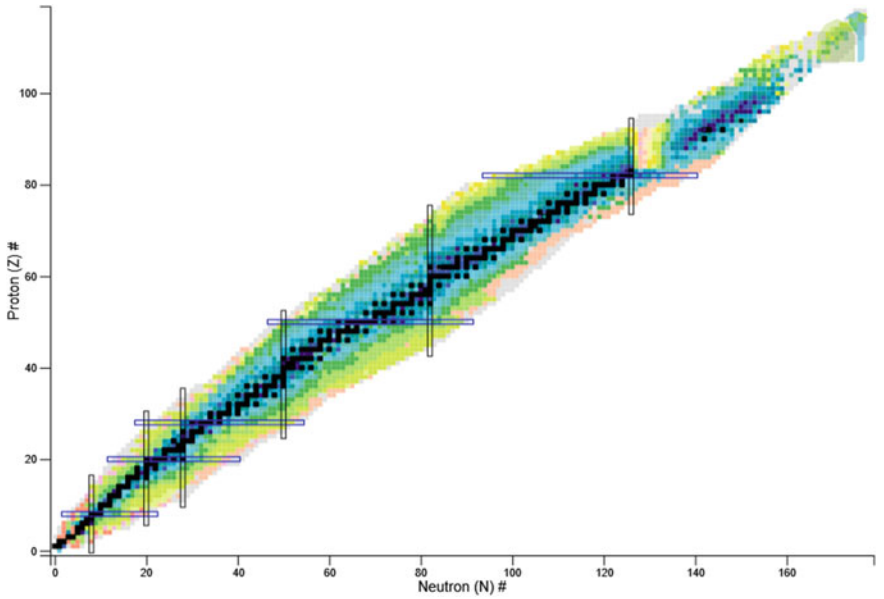

Fig. 1 Numbers of neutrons and protons in stable nuclei. The stable nuclides are indicated in black and the unstable nuclides are residing on either side of it. *Data source* National Nuclear Data Center, Brookhaven National Laboratory, Evaluated Nuclear Structure Data File (ENSDF), chart of nuclides [1])

2 Radioactive Decay

Now that we are familiar with the underlying reason why a nuclide behaves as radioactive, the next question is what happens when a radioactive nuclide decays. The term 'radioactive decay' indicates the spontaneous conversion of one radioisotope into one or more different isotopes (known as 'decay products' or 'daughter products'), accompanied by the emission in the form of alpha–beta or photons (Gamma radiation or X-rays). Radioactive half-life, $T_{1/2}$, is the time required for half of the radioactive atoms present to decay. For example, if N_0 is the number of radioactive atoms present initially at time $t = 0$, then the number of radioactive atoms present at a given time t, $N(t)$, is given by

$$N(t) = N_0 e^{-\lambda t} \tag{1}$$

where λ is the decay constant which has a unit of s^{-1}. When $t = T_{1/2}$, $N(t) = N_0/2$, Equation (1) becomes

$$\frac{N_0}{2} = N_0 e^{-\lambda T_{1/2}} \tag{2}$$

$$T_{1/2} = \frac{\ln 2}{\lambda} \tag{3}$$

Depending upon the type of radionuclide, $T_{1/2}$ may vary from a few seconds to billions of years.

The study of radioactivity and production as well as the separation of radioisotopes has led to many important discoveries in the field of atomic and nuclear physics and has offered societal benefits. The nuclear structure has been unveiled as a result of 'Nuclear Spectroscopy' which deals with the study of nuclear energy levels. The basis of all these studies is the identification and quantification of radioactivity. Therefore, it is essential to understand the types of decay, decay kinetics, and measurements of the radioactive emissions. In the following section, we will briefly describe these concepts.

2.1 Types of Radioactive Decay

As discussed previously, radioactive nuclides emit alpha or beta particles or gamma rays to reach a stable configuration. These subatomic particles (alpha and beta) and electromagnetic waves (gamma and x-rays) are referred to as ionizing radiation as they have adequate energy to ionize atoms or molecules by removing the electrons from the shell. An overview of these ionizing radiations is given below.

2.1.1 Alpha Particle Emission

Usually heavy nuclei such as Uranium, Thorium, and Radium and artificially produced nuclei such as Plutonium, Neptunium, Americium, and so forth decay by the emission of alpha particles. Alpha particle is a nucleus of a helium atom which contains two protons and two neutrons. In alpha decay, the atomic number Z of the parent nucleus decreases by two and the mass number A by 4. An example of alpha decay is given below

$$^{226}_{92}\mathrm{Ra} \rightarrow {}^{222}_{86}\mathrm{Rn} + {}^{4}_{2}\mathrm{He} + \mathrm{Q} \tag{4}$$

The energy released (Q value) in the above nuclear transformation is 4.87 MeV, which is shared by the alpha particle and radon nucleus. An alpha decay sometimes can be followed by a beta particle or gamma-ray emission or both. The alpha particles are mono-energetic in nature and their range in matter is very short (of the order of 10^{-7} m) and is approximately 0.03 mm in the body tissue.

2.1.2 β−(Electron) Decay

To attain stability, a neutron-rich nucleus decays by emission of β^- particle (electron) along with an antineutrino ($\overline{\nu}$) (an elementary subatomic particle having infinitesimal mass and no electric charge). In this case, the neutron converts into a proton and thus the unstable atom gains a more stable n/p ratio. For such kind of process to be energetically possible, the energy release or Q value must be positive. The negative beta particle thus can be emitted with variable energy from zero up to Q. The energy difference between the Q value and the β^- particle energy is carried away by $\overline{\nu}$. During beta decay, if the daughter nucleus is in the excited state, gamma emission is possible with an energy equal to the difference between the excited state and ground state of the daughter nucleus. After the β^-decay, the atomic number Z of the daughter nuclide increases by one whereas the mass number A remains the same. An example of beta decay is given below

$$^{99}_{42}\mathrm{Mo} \rightarrow {}^{99\mathrm{m}}_{43}\mathrm{Tc} + \beta^- + \overline{\upsilon} + Q \tag{5}$$

Q value in the above nuclear transformation is 1.357 MeV.

2.1.3 β + (Positron) Decay

Positron is a positively charged particle denoted by β^+. It has the same mass as an electron but an opposite charge. In positron emission (or decay), a proton in the parent nucleus decays into a neutron emitting a neutrino and a positron. In β^+ decay, the atomic number Z of the daughter nuclide decreases by one whereas the mass number remains the same. Similar to β^- decay, in β^+ decay, the positron can have a continuous energy ranging from 0 to Q whereas neutrino (ν) possesses an energy equivalent to the energy difference between the Q value and β^+ energy. In this process, the conversion of a proton into a neutron leads to the creation of a mass equivalent of two electrons (each with 0.511 MeV). Hence, β^+emission is possible when the energy difference between the parent and daughter nuclides is equal to or greater than 1.02 MeV. An example of this type of decay is given below

$$^{64}_{29}\mathrm{Cu} \rightarrow {}^{64}_{28}\mathrm{Ni} + \beta^+ + \nu + Q \tag{6}$$

with a Q value of 1.674 MeV.

2.1.4 Electron Capture

In the electron capture process, a parent nucleus captures one of its orbital electrons (usually from the k-shell; hence sometimes it is called K-capture) and combines with a proton yielding a neutron which stays inside the nucleus and a neutrino is emitted. An example of this process is given below

$$^{57}_{27}\mathrm{Co} + \beta^- \rightarrow {}^{57}_{26}\mathrm{Fe} + \nu + Q \tag{7}$$

with a Q value of 0.836 MeV.

After capturing an electron from the K-shell, a vacancy is created and it is then filled by the transition of electron from upper orbitals (e.g., L-shell or M-shell). The energy difference between these shells generates characteristic X-rays. The daughter nuclei produced via electron capture can be either in ground state or excited state. If it is in the excited state, a gamma ray is released during the de-excitation process.

2.1.5 Gamma-Ray Emission

When a radionuclide undergoes alpha or beta decay, the nucleus of the resultant radionuclide is generally left in an excited energy state which is unstable. The excited nucleus either goes to the ground state directly or in steps to the lower energy states through the emission of gamma radiation. A nuclide in an excited energy state is referred to as a nuclear isomer. The energy, E_γ, of a gamma ray may be described as the difference in energy states of the nuclear isomers:

$$E_\gamma = h\upsilon = E_1 - E_2 \tag{8}$$

where $h\upsilon$ is the energy of the electromagnetic radiation and E_1 and E_2 are the energy levels of the nuclear isomers. Thus, the energies of gamma rays are discrete in nature.

2.1.6 Internal Conversion

The common de-excitation mechanism of an excited nucleus is via the emission of a gamma ray having energy equivalent to the energy difference between excited and ground states. Another mechanism of de-excitation is via internal conversion. In this process, the nuclear excitation energy (E_{ex}) is transferred directly to one of the orbital electrons. Since this energy is more than its binding energy (E_b) at that orbital, the electron gets ejected from its orbit with an energy (E_e) equivalent to

$$E_e = E_{\mathrm{ex}} - E_b \tag{9}$$

The energy E_e being a discrete fixed value, the conversion electrons are mono-energetic in nature. Hence, they appear as line spectra superimposed on the continuous beta-particle spectra of the radionuclide. After electron ejection, a vacancy is created in that shell, and as a result, characteristic X-rays may be emitted if an electron from the upper shell fills that vacancy. There is also another competing mechanism in which the energy of a characteristic X-ray is transferred to a nearby electron which is then ejected from the atom. This electron emission process is known as Auger electron emission. An example of internal conversion is the decay of ^{137}Cs which is transformed to $^{137\mathrm{m}}$Ba (94.7%) (which is an excited metastable state of ^{137}Ba)

via beta emission. Out of this 94.7%, with a probability of 85.1%, the excited state returns to the ground state by emitting a gamma having energy 661.57 keV, while the rest 9.6% returns to stability through internal conversion.

2.1.7 Spontaneous Fission

In spontaneous fission, an unstable heavy nucleus breaks up into two lighter fragments known as fission fragments, and also more than one neutron on an average is emitted simultaneously. Spontaneous fission is observable in elements with mass number $A = 230$ or above. An example of spontaneous fission is ^{252}Cf ($T_{1/2} = 2.65$ years) which is used as a neutron source. It decays primarily through alpha emission (96.91% probability); thus, the remaining ^{252}Cf decay process occurs via spontaneous fission with a probability of 3.09% which results in emission of an average number of 3.7 neutrons per fission.

A summary of different types of radioactivity decay phenomena discussed above is summarized in Table 1.

Table 1 Summary of different types of radioactivity decay

Mode of decay	Reaction	Description
Alpha (α)	${}^{A}_{Z}X \rightarrow {}^{A-4}_{Z-2}Y + \alpha$	Proton-rich nuclides emit alpha particle, which is helium nucleus having two protons and two neutrons
Beta–negative (β^-)	${}^{A}_{Z}X \rightarrow {}^{A}_{Z+1}Y + \beta^- + \overline{\nu}$	In neutron-rich nuclides, neutron decays to proton and emits negatively charged beta particles. Anti-Neutrino is also emitted in the reaction in order to conserve energy and momentum
Beta–positive (β^+)	${}^{A}_{Z}X \rightarrow {}^{A}_{Z-1}Y + \beta^+ + \nu$	In proton-rich nuclides, proton decays to neutron and emits positively charged beta particles along with a neutrino
Electron capture	${}^{A}_{Z}X + \beta^- \rightarrow {}^{A}_{Z-1}Y^* + \nu$	An orbital electron is 'captured' by the nucleus and it combines with a proton yielding a neutron. The neutron stays inside the nucleus and a neutrino is emitted. Characteristic X-rays along with gamma emission take place
Gamma	${}^{A}_{Z}X^* \rightarrow {}^{A}_{Z}X + \gamma$	An excited nucleus emits gamma photon to reach to the ground state
Isomeric transition	${}^{A}_{Z}X^m \rightarrow {}^{A}_{Z}X + \gamma$	It occurs in the long-lived metastable states (isomers) of parent nuclei
Internal conversion	${}^{A}_{Z}X^* \rightarrow \left[{}^{A}_{Z}X\right]^+ + \beta^-$	An excited nucleus ejects electron instead of gamma emission
Spontaneous fission	${}^{A}_{Z}X \rightarrow Y_H + Y_L + n$	In this process, the heavy parent nucleus splits into lighter fragments and also several neutrons are emitted simultaneously

3 Radiological Quantities and Units

As we are now familiar with the radioactive decay processes, let us discuss how radiation is measured. The parameters associated with such field measurements are known as physical quantities. Depending on how and where they are measured, there are several physical quantities, e.g., exposure, fluence, Kerma, absorbed dose, etc., and these parameters are described [2] in these subsequent sections.

3.1 Activity

The activity, A, of a radionuclide is measured as a product of the decay constant (λ) and the number of nuclei, N, thus

$$A = N\lambda \tag{10}$$

Radioactive decay is a statistical process in which the mean (or average) number of spontaneous nuclear transformations per unit time interval is defined in terms of one Bq, which is also known as one disintegration per second. 1 Ci (curie) = 3.7×10^{10} Bq corresponds to 1 g of ^{226}Ra which has an activity of 3.7×10^{10} Bq.

3.2 Exposure

The ionizing power of electromagnetic radiation in air is known as exposure, X (SI unit = C/kg (Coulomb/kg)). It is the quotient of dQ by dm, where dQ is the absolute value of the total charge of the ions of one sign produced in air when all the electrons and positrons liberated or created by photons in air of mass dm are completely stopped in air, thus

$$X = \frac{\mathrm{d}Q}{\mathrm{d}m} \tag{11}$$

The ionization produced by auger electron is included in the dQ term; however, the ionization due to photons emitted by radiative processes (i.e., Bremsstrahlung and fluorescence photons) is not to be included in dQ. The special name of the unit is Roentgen (R). 1 R = 2.58×10^{-4} C kg^{-1}.

3.3 Exposure Rate

The exposure rate $\dot{X}$ is the quotient of dX by dt, where dX is the increment of exposure in the time interval dt, thus,

$$\dot{X} = \frac{\mathrm{d}X}{\mathrm{d}t} \tag{12}$$

The SI unit is C kg^{-1} s^{-1}. Exposure rate is used for the description of x-rays and gamma radiation in the unit of R h^{-1}.

3.4 Fluence

Fluence, Φ, is the quotient of dN by da, where dN is the number of particles incident on a sphere of cross-sectional area da, thus,

$$\Phi = \frac{\mathrm{d}N}{\mathrm{d}a} \tag{13}$$

The unit of Fluence is m^{-2}. Fluence is independent of the direction distribution of the particles entering the sphere. In radiation transport calculations, Fluence is frequently expressed in terms of the length of particle trajectories. Fluence Φ is then given by

$$\Phi = \frac{\mathrm{d}l}{\mathrm{d}V} \tag{14}$$

where dl is the sum of the particle trajectories in the volume dV.

3.5 Fluence Rate

The fluence rate (Φ_f) is the quotient of dΦ by dt, where dΦ is the increment of the fluence in the time interval dt. Its unit is m^{-2} s^{-1}.

3.6 Flux

The flux (N_f) is the quotient of dN_f by dt, where dN_f is the increment of the particle number in the time interval dt, thus

$$N_f = \frac{\mathrm{d}N_f}{\mathrm{d}t} \tag{15}$$

Its unit is s^{-1}.

3.7 Kerma

The Kerma, K, is the quotient of $\mathrm{d}E_{\mathrm{tr}}$ by $\mathrm{d}m$, where $\mathrm{d}E_{\mathrm{tr}}$ is the sum of initial kinetic energies of all charged particles liberated by uncharged particles in a mass $\mathrm{d}m$ of material, thus,

$$K = \frac{\mathrm{d}E_{tr}}{\mathrm{d}m} \tag{16}$$

The SI unit of Kerma is J kg^{-1}. The special name of the unit is Gray (Gy). The quantity $\mathrm{d}E_{\mathrm{tr}}$ includes the kinetic energy of the Auger electrons.

For a Fluence, Φ, of uncharged particles of energy, E, the Kerma, K, in a specific material is given by

$$K = \Phi E \frac{\mu_{tr}}{\rho} \tag{17}$$

$\frac{\mu_{tr}}{\rho}$ is the mass energy transfer coefficient of the material for these particles. Equality of absorbed dose and Kerma is approached to the degree that charged particle equilibrium exists, that radiative losses are negligible, and that the energy of the uncharged particles is large compared to the binding energy of the released charged particles. Charged particle equilibrium exists at a point if the distribution of the charged particle radiance with respect to energy is constant within distances equal to the maximum charged particle range. Under the conditions of charged particle equilibrium, the numerical value of collision Kerma at a point of interest equals the value of absorbed dose.

3.8 Absorbed Dose

In radiation biology, clinical radiology, and radiological protection, the absorbed dose, D, is the basic physical dose quantity, and it is used for all types of ionizing radiation and any irradiation geometry. It is defined as the quotient of $\mathrm{d}\varepsilon$ by $\mathrm{d}m$, where $\mathrm{d}\varepsilon$ is the mean energy imparted to matter of mass $\mathrm{d}m$ by ionizing radiation, thus

$$D = \frac{\mathrm{d}\varepsilon}{\mathrm{d}m} \tag{18}$$

The SI unit of the absorbed dose is J kg^{-1} and its special name is Gray (Gy).

3.9 Absorbed Dose Rate

Absorbed dose rate $\dot{D}$ is the quotient of dD by dt, where dD is the increment of absorbed dose in the time interval dt. Thus

$$\mathrm{D} = \frac{\mathrm{d}D}{\mathrm{d}t} \tag{19}$$

The SI unit is J kg^{-1} s^{-1}. The special name of the unit is Gray per second (Gy s^{-1}).

4 Quantities Used in Radiological Protection

Dosimetric quantities are required to assess radiation exposures of humans and other organisms in a quantitative way and establish principles of radiological protection, particularly the principle of dose limitation and optimisation of protection. The International Commission on Radiological Protection (ICRP) and the International Commission on Radiation Units and Measurement (ICRU) have developed different quantities for use in radiological protection. The hierarchy of quantities can be described by *primary limiting quantities* (also called as *protection quantities*) and *operational quantities* for monitoring of external exposure. The protection quantities are not measurable in the exposed individual. Therefore, operational quantities have been defined by ICRU for use in radiological protection. The operational quantities provide a conservative estimate of the protection quantities in almost all practical situations of occupational exposure. Further, the operational quantities can be realized in laboratory conditions which make them suitable for calibration and dose assessment using a monitoring system.

4.1 Limiting Quantities (Protection Quantities)

In 1977, the ICRP Report 26 [3] introduced the organ (or tissue) dose equivalent, H_{T}, and the effective dose equivalent, H_{E}. These parameters take into account the effect of tissue response due to the interaction of different types of radiation with different tissues and organs in the human body. In subsequent publications (ICRP Report 60 [4] and ICRP Report 103 [5]), some important modifications of these parameters are introduced. The present system of quantities is summarized below.

Table 2 Radiation weighting factor for different radiations

Radiation type	Radiation weighting factor, W_R
Photons	1
Electrons and muons	1
Protons and charged pions	2
Alpha particles, fission fragments, heavy ions	20
Neutrons	A continuous curve as a function of neutron energy

The data are reproduced from ICRP Report 103 [5]

4.1.1 Equivalent Dose in an Organ or Tissue

The absorbed dose at a point is generally the fundamental dose quantity which is a physical measurable quantity. However, in radiation protection, the mean dose in an organ D_{T} is used as the basic protection quantity which correlates to the exposure risk. The equivalent dose in an organ or tissue T is defined by

$$H_T = \sum_R w_R D_{T,R} \tag{20}$$

where $D_{T,R}$ is the mean organ dose deposited in the organ or tissue T by radiation of type R. The radiation weighting factor w_R characterizes the relative biological effectiveness of the specific radiation R for induction of stochastic effects at low doses relative to photons. Thus, w_R is chosen as 1 for photons. For other radiations, the values of w_R are given in Table 2. A continuous function of energy is used in the case of radiation weighting factors for neutrons (Fig. 2). These factors have replaced the mean quality factors used in the concept of organ dose equivalent of ICRP 26 [3]. The unit of equivalent dose is J kg^{-1} and has the special name Sievert (Sv).

4.1.2 Effective Dose

The effective dose, E, is the weighted sum of organ equivalent doses:

$E = \sum_T w_T \sum_R w_R D_{T,R} = \sum_T w_T H_T$ with $\sum_T w_T = 1$.

where w_T is tissue weighting factor for tissue T. w_T values are chosen to represent the contributions of individual tissues and organs to the overall radiation detriment due to stochastic effects. Table 3 shows the w_T values for various organs and tissues adopted by ICRP 103 [5]. The sum is performed over all organs and tissues of the human body considered in the definition of E. The unit of effective dose is the same as the equivalent dose, i.e., Sv.

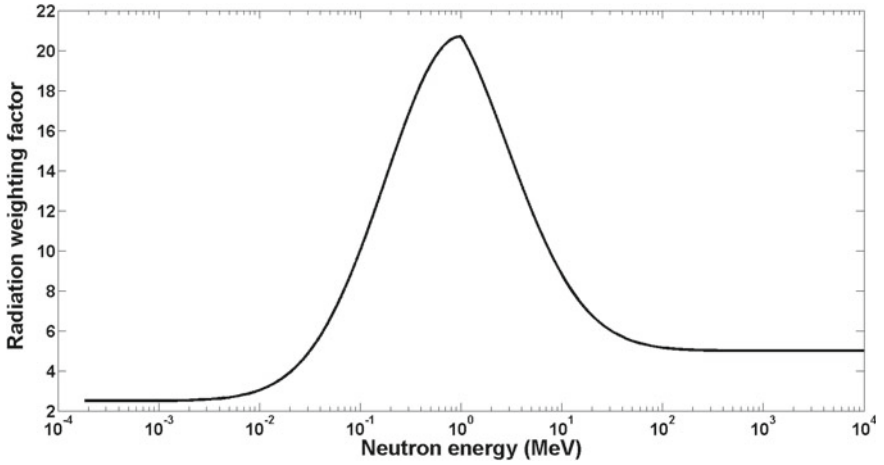

Fig. 2 Radiation weighting factor for neutron [5]

Table 3 Tissue weighting factor w_T for different organs and tissues

Tissue	Weighting factor (w_T)	$\sum w_T$
Bone-marrow (red), colon, lung, stomach, breast, remainder tissues[a]	0.12	0.72
Gonads	0.08	0.08
Bladder, esophagus, liver, thyroid	0.04	0.16
Bone surface, brain, salivary glands, skin	0.01	0.04

The data are reproduced from ICRP report 103 [5]
[a] Remainder Tissues (14 in total): Adrenals, Extra thoracic (ET) region, Gall bladder, Heart, Kidneys, Lymphatic nodes, Muscle, Oral mucosa, Pancreas, Prostate, Small intestine, Spleen, Thymus, Uterus/cervix

4.2 Operational Quantities

4.2.1 Dose Equivalent and Quality Factor

The protection quantities defined by ICRP are not measurable in practice; hence, these quantities cannot be used directly in radiation monitoring. To meet this requirement, the operational quantities defined by ICRU are intended to provide a reasonable estimate of the protection quantities due to external radiation exposure of the human body under most irradiation conditions [6–9]. The parameter dose equivalent, H, has been used in this context which is defined at a point in tissue as the product of absorbed dose (D) and quality factor (Q). Q is defined as a function of unrestricted linear energy transfer, L_∞ (often denoted as L or LET), of charged particles in water [10].

Quality factor function Q (L) is given by the following equation [5]:

$Q\,(L) = 1$ for $L < 10$ keV/μm.
$Q\,(L) = 0.32\,\mathrm{L} - 2.2$ for $10 \leq L \leq 100$ keV/μm.
$Q\,(L) = 300/\sqrt{L}$ for $L > 100$ keV/μm.
The quality factor Q at a point in tissue is given by

$$Q = \frac{1}{D} \int_0^\infty Q(L) D_L \mathrm{d}L$$

where D is the absorbed dose at that point, D_L is the distribution of D in L at the point of interest. This function is most important for neutrons because various types of secondary charged particles are produced in tissue.

Now the choice of different operational quantities depends on the type of task in radiological protection. For example, area monitoring is carried out for controlling the radiation in workplaces, and individual monitoring is required for controlling and limiting the individual exposures. For these two tasks, ICRU has defined two separate operational quantities since the monitoring process for these two types is different. In the case of area monitoring, measurements are done by area monitors (fixed/portable) in free air medium, whereas individual monitoring is carried out by personal dosimeters that are worn on the body. The presence of the body strongly influences the radiation field seen by the personal dosimeter since the radiation will be absorbed as well as backscattered by the body. Thus, in a given situation, the radiation field measured by area monitors will be different from the dose recorded in personal dosimeters. A brief summary of these parameters is given below.

4.2.2 Operational Quantities for Area Monitoring

The operational quantities for area monitoring are defined based on a dose equivalent value at a point in the ICRU sphere. It is a sphere of 30 cm diameter made of tissue-equivalent material, ICRU (soft) tissue with a density of 1 g cm^{-3}. The mass composition of the ICRU tissue is 76.2% oxygen, 11.1% carbon, 10.1% hydrogen, and 2.6% nitrogen [9]. Although such material is difficult to fabricate for practical use, it simulates the tissue compositions for theoretical calculations of absorbed dose/dose equivalent in the human body. In most cases, the ICRU sphere adequately approximates the human body taking into consideration of scattering and attenuation of the radiation field.

In general, the operational quantities are defined as a point function, i.e., their values depend on the radiation field at a point. However, the human body is exposed to a broad radiation field, and the dose at a point on the human body will comprise of total dose due to different components of the radiation field at that point. To correlate with human body exposure, the concepts of ‘expanded’ field and ‘expanded and aligned’ fields are introduced and the value of the operational quantity is given by the dose at a point at a fixed depth in the ICRU sphere.

Expanded field is a hypothetical radiation field in which spectral and angular fluence has the same value at all the points in the ICRU sphere equal to the value

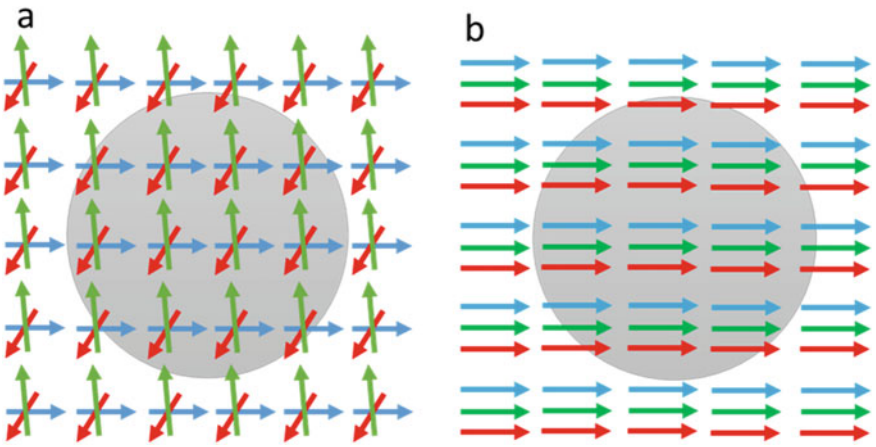

Fig. 3 Diagram of **a** an expanded and **b** an oriented radiation field

in the actual field at the point of interest. Expanded and aligned field is obtained if all radiations in the expanded field are aligned in one direction. Thus, it is the uniform, unidirectional field that has the same spectral fluence distribution as in the expanded field (see Fig. 3). Based on these two auxiliary concepts, two quantities namely Ambient Dose Equivalent, $H^*(10)$, and Directional Dose Equivalent, $H'(d, \Omega)$, are introduced.

A. **Ambient Dose Equivalent, $H^*(10)$**

The ambient dose equivalent, $H^*(10)$, at a point in a radiation field, is the dose equivalent that would be produced by the corresponding expanded and aligned field in the ICRU sphere at a depth of 10 mm on the radius vector opposing the direction of the aligned field [9]. For area monitoring, ambient dose equivalent, $H^*(10)$, is used for assessing effective dose.

B. **Directional Dose Equivalent, $H'(d, \Omega)$**

The directional dose equivalent, $H'(d, \Omega)$, at a point in a radiation field, is the dose equivalent that would be produced by the corresponding expanded field in the ICRU sphere at a depth, d, on a radius in a specified direction Ω [9]. For weakly penetrating radiation $d = 0.07$ mm, $H'(d, \Omega)$ is then written $H'(0.07, \Omega)$ and is used to assess the equivalent dose to skin, hands, and feet.

4.2.3 Operational Quantities for Individual Monitoring

Individual monitoring for external exposure is usually performed with dosemeters worn on the body, and for this purpose, the operational quantity personal dose equivalent, $H_p(d)$, has been introduced.

Table 4 List of operational quantities used for individual monitoring

Assessment parameter	Operational quantity used	Recommended depth d (mm) [9]
Effective dose	H_p (10)	10
Equivalent dose to the skin, and to the hands and feet	H_p (0.07)	0.07
Monitoring the dose to the lens of the eye	H_p (3)	3

A. The Personal Dose equivalent, H_p (d)

The personal dose equivalent, H_p (d), is the dose equivalent in ICRU (soft) tissue at an appropriate depth, d, below a specified point on the human body [9]. The specified point is usually given by the position where the individual dosimeter is worn. Such examples are given in Table 4.

Since H_p (d) values are defined for a person, in the existing radiation field, their values vary from one person to another and depend also on the location of the body where the dosimeter is worn. It is also important to wear the personal dosimeter at a position on the body that is representative of body exposure. With such precaution, an operational quantity can provide a conservative estimate of the relevant protection quantity.

5 Summary

- Activity of radioactive source is expressed in Bq, the SI unit is Ci.
- 1 Ci (curie) $= 3.7 \times 10^{10}$ Bq.
- 1 Bq $= 1$ disintegration/s.
- Proton-rich nuclides emit alpha particles, the atomic number (Z) of the parent nuclides is reduced by two and the mass number (A) by 4.
- A neutron-rich nucleus decays by a β- particle (electron) emission along with an antineutrino.
- In β^+ decay, neutrinos and positrons are emitted.
- In the Electron capture process, a parent nucleus captures one of its orbital electrons and combines with a proton yielding a neutron which stays inside the nucleus and a neutrino is emitted.
- An excited nucleus generated via any decay scheme can emit gamma radiation.
- In the internal conversion process, the energy of the excited nucleus is given to an orbital electron.
- Exposure is expressed in C kg^{-1} or R.
- Protection quantities developed by ICRP are organ absorbed dose, organ equivalent dose, and effective dose.
- Absorbed dose is expressed in J kg^{-1} or Gy.
- Equivalent dose and Effective dose are expressed in Sv.

- Radiation weighting factor, tissue weighting factor, and Quality factor have no units.
- Operational quantities developed by ICRU are ambient dose equivalent, directional dose equivalent, and personal dose equivalent.
- The unit of operational quantities is J kg^{-1} or Sv.

References

1. http://www.nndc.bnl.gov/chart. Accessed on 17 Oct 2023
2. ICRU Report 85 (2011) Fundamental quantities and units for ionizing radiation. J of the ICRU 11(1)
3. ICRP Publication 26 (1977) Recommendations of the international commission on radiological protection, (Series: ICRP, 26; Ann ICRP 1(3)). Pergamon Press, London
4. ICRP Publication 60 (1991) Recommendations of the international commission on radiological protection. Ann ICRP 21(1–3)
5. ICRP Publication 103 (2007) The 2007 recommendations of the international commission on radiological protection. Ann ICRP 37(2–4)
6. ICRU Report 39 (1985) Determination of dose equivalents resulting from external radiation sources, international commission on radiation units and measurements, (Series: ICRU Report 39), Bethesda
7. ICRU Report 43 (1988) Determination of dose equivalents from external radiation sources - part 2, international commission on radiation units and measurements, (Series: ICRU Report 43), Bethesda
8. ICRU Report 47 (1992) Measurement of dose equivalents from external photon and electron radiation, (Series: ICRU Report 47), International Commission on Radiation Units and Measurements, Bethesda
9. ICRU Report 51 (1993) Quantities and units in radiat prot dosim. International Commission on Radiation Units and Measurements, (Series: ICRU Report 51), Bethesda
10. ICRP Publication 74 (1996) Conversion coefficients for use in radiological protection against external radiation. Ann ICRP 26(3/4)

Ionizing Radiation Metrology

Sunil K. Singh, D. B. Kulkarni, and Meghnath Sen

1 Introduction

Metrology is the activity which deals with the science of measurement. It establishes a common understanding of measurement units to ensure that measurements are stable, comparable, accurate, and have a stated level of uncertainty. It has fundamental importance in areas like national/international trade, health, industry, safety, environmental monitoring, food safety, regulatory, law enforcement, and other sectors. Metrology gives sureness to measurement results so that society can enjoy the benefits of the applications with maximum reliability.

The metrological measurement results are linked to its national standard (primary/reference measurement standards) through a documented unbroken chain of calibrations, each contributing to the measurement uncertainty. The responsibility of maintaining these measurement standards and their dissemination lies with the organizations recognized by the government of that country and are termed as the National Metrology Institute (NMI) or Designated Institute (DI) of that country. Therefore, the NMI/DIs of a country have the responsibility to develop, establish, maintain, and upgrade various measurement standards and to disseminate them by means of providing the traceable calibration of measurements in the country.

NMI/DI also establish degree of equivalence with other NMIs/DIs through participation in international intercomparisons coordinated by one of the NMI/DI. In general, a country has only one NMI which has the capability in all areas but if they do not have the capability in a particular area, the same responsibility is designated to other institute(s) having the capability to develop, establish, maintain, and upgrade various measurement standards in that particular field/area. In India, the Council of Scientific and Industrial Research (CSIR)—National Physical Laboratory (NPL) is

S. K. Singh (✉) · D. B. Kulkarni · M. Sen
Radiation Safety Systems Division, Bhabha Atomic Research Centre, Mumbai, Maharashtra 400085, India
e-mail: bhusunil@barc.gov.in

D. K. Aswal (ed.), *Handbook on Radiation Environment, Volume 2*,
https://doi.org/10.1007/978-981-97-2799-5_3

the NMI catering to all metrological areas except Ionizing Radiation, for which the responsibility is designated to Bhabha Atomic Research Centre (BARC) as the DI for Ionizing Radiation (IR).

Along similar lines, the responsibility of establishing and maintaining international measurement standards and their dissemination lies with the International Bureau of Weights and Measures (BIPM) [1] which is an international organization established by the Metre Convention. BIPM is also an organization through which its Member States act together on matters related to measurement science and measurement standards. The activities of BIPM are supervised by the International Committee for Weights and Measures (CIPM) which in turn reports to the General Conference on Weights and Measures (CGPM). The structure of the global metrology system concerning ionizing radiation metrology, standards used, their details, and linkage with each other is presented in detail, later in this chapter. This chapter particularly addresses Ionizing Radiation as the area of metrology; however, other fields of measurement or metrology are also correlated in a suitable manner.

2 Evolution of Metrology

Measurement is a process of quantification of a phenomenon, in terms of assigning it a numerical value along with a physical unit. Every measurement requires the definition of the measurand, i.e. the quantity which is to be measured. The development of the initial system of measurement took place by referring to human body parts (human morphology) of prominent personnel as names of measurand units. For the purpose of measuring length, historically, body parts like hands, foot, fingers, etc. are often referred, corresponding to the length of that part of the body. This system has some discrepancies as different persons in different parts of the country or world have different lengths of the referred body part leading to non-uniform measurement system. Thus, with the growth of industry and expansion of trade, there was a growing need for synchronization of weights and measures amongst various countries. This led to the adoption of standards of measurement by assessment with standards adopted from nature instead of human morphology. One of the first such standards taken from nature was the metre, which was demarcated, in a decree by the French National Assembly, as being equal to the ten millionth part of one quarter of the terrestrial meridian but quantified by measurements taken between Dunkerque and Barcelona. Therefore, once the base unit of length is defined, the definition of other resulting units of measure like the square metre (for area) and the cubic metre (for volume) becomes easy. This also led to the definition of kilogram, as the weight of a defined volume of readily purified water.

Concerning this, in 1795, France introduced a decimal metric system via the law 'On weights and measures' which brought about a key change in the day-to-day life of the common people, promptly allowing the calculation of length, areas, volumes, density, etc. Thereafter, the first standard of distance and mass, i.e. metre and kilogram were established, and against this, all other future copies of standards were compared. Other countries too started following a similar system.

Therefore, with time, a need was felt to establish an international structure to ensure comparability and conformity between the measurement systems of various economies, which in turn brought international communities together. With multiple discussions and deliberation, a diplomatic treaty was signed in Paris on 20th May 1875 between countries which is recognized as the Metre Convention. This treaty of Metre Convention further led to the formation of various international organizations like the General Conference on Weights and Measures (CGPM), the International Committee for Weights and Measures (CIPM) along with the Bureau International des Poids et Mesures (BIPM), through which its Member States act together on matters related to measurement science and measurement standards. The signing of the Metre Convention, i.e. the date of 20th May is designated as World Metrology Day and is celebrated annually by the metrological community.

With time, trade between economies increased manifold, demanding a consistent measurement methodology with proper product quality, acceptable across all trading partners. This necessitated an open, transparent, and wide-ranging measurement scheme that was capable of providing information on the degree of equivalence of measurement services offered by a nation, which was to be considered as a technical basis concerning international trade, business, and relevant regulatory activities. To address this growing need for an accepted and coordinated worldwide activity, CIPM came up with a draft Resolution in the year 1995, which was adopted in 1999 by CGPM as CIPM Mutual Recognition Arrangement (CIPM-MRA). CIPM-MRA laid down certain conditions for establishing the degree of equivalence between national measurement standards maintained by NMIs and made an arrangement for the recognition of calibration certificates issued by them.

3 Role of CIPM-MRA in Metrology

The CIPM Mutual Recognition Arrangement [2] is the framework through which National Metrology Institutes (NMIs) demonstrate the international equivalence of their measurement standards and the calibration and measurement certificates they issue.

The main mechanisms through which the CIPM-MRA achieves these objectives are as follows:

- International comparisons of measurements, known as key comparisons.
- Regional comparisons of measurements, known as regional key comparisons.
- Supplementary comparisons.

- Open peer-review of the participants calibration and measurement capabilities, based mainly on the results of comparisons.
- Reviewed implementation of the participants quality management systems and demonstration of competence.

The outcomes of the Arrangement are the internationally recognized (peer-reviewed and approved) Calibration and Measurement Capabilities (CMCs) of the participating institutes. The recognized CMCs and supporting technical data are made publicly available in a database maintained by BIPM. This database is termed as Key Comparison Database of BIPM (KCDB). The CIPM-MRA is an important tool for helping NMIs/Designated Institutes (DIs), in the development of their country's quality of measurements pertaining to industry, health, environment, and science.

4 Global Metrology Structure: Current Status

Quality infrastructure consists of the following components—a system of metrology standards, body issuing standards, and an accreditation system. Roles, responsibilities, relevance, and interrelation of these bodies in the system are explained below.

4.1 Metrology

There are various international organizations which are involved in establishing and maintaining calibration and measurement capabilities. These organizations include CGPM, CIPM, Consultative Committees (CC), Working Groups, BIPM, JCRB, RMO, IAEA SSDL Network, and KCDB.

4.1.1 CGPM: General Conference on Weights and Measures

The CGPM is an intergovernmental organization formed primarily due to Metre Convention and is responsible for the International System (SI) of units. It has the responsibility of ensuring that the SI is widely disseminated and, if necessary, modify it so that it reflects the latest advancements in science and technology. It provides a forum for the diplomatic representatives of the member states. It is a supreme authority consisting of delegates from all the member states which have the responsibility to elect CIPM, approve major CIPM decisions, allocate funds to BIPM, promote SI Units, supervise the systems of measurement, and approve new technical

definitions considering the expert recommendations of CIPM. Usually, it meets once in 4 years. India became a Member of CGPM by signing the treaty (Metre convention) in 1957 with CSIR-NPL as its NMI.

4.1.2 CIPM: International Committee for Weights and Measures

CIPM is an advisory committee of experts/metrologists of high standing with eighteen persons as its members, each from a different nation. The primary task of CIPM is to disseminate the uniformity in measurement units, worldwide, by directly acting or through CGPM by submitting appropriate proposals. It also acts as the supervisory body for the BIPM which meets annually. Considering different fields of measurements, CIPM has set up many consultative committees (CC) to get technical assistance in its routine work. It also discusses the reports presented by respective Consultative Committees.

4.1.3 Consultative Committees (CC)

Considering the large number of measurement quantities of day-to-day interest, CIPM has formed various Consultative Committees, within the ambit of the International System of Units (SI). Each committee provides a platform where NMIs and DIs of various nations can meet and discuss the jointly identified measurement challenges, identify, and plan relevant research topics and approve the degrees of equivalence in calibration and measurement capabilities. Consultative Committees are technical committees set up by CIPM, in each area of metrology, to assist it scientifically in its work. CIPM has formed ten such committees in which the Consultative Committee of Ionizing Radiation (CCRI) is one of the Consultative Committee covering the metrological area concerning ionizing radiation. Similarly, other Consultative Committees are for length, mass, time & frequency, thermometry, units, etc. with their acronyms as CCL, CCM, CCTF, CCT, CCU, etc., respectively.

The establishment of CCRI took place in 1958 due to increased applications of ionizing radiation (e.g. radiation therapy by using Co-60-based exposure devices and linear accelerators, individual monitoring of doses for occupational workers of nuclear power plant, etc.) in public, necessitating measurement standards. Even now, the role of CCRIs continues to be crucial in formulating international equivalence of measurement standards in the field of ionizing radiation and identifying new issues that require collective redressal. Each committee has a president who is usually a CIPM member. Consultative Committee membership is reserved only for the NMI/DIs of its Member States.

The roles and responsibilities of Consultative Committees, in their respective metrological fields, are described on their dedicated webpages managed by BIPM. These Consultative Committees are also tasked with the responsibility of planning the key comparisons and their successful execution along with confirming the validity

of the intercomparison results [3]. These responsibilities are within the framework of the CIPM-MRA, and it includes the following:

(a) the identification of the key comparisons in their respective fields;
(b) initiation, organization, and execution of the identified key comparisons, with the collaboration of the BIPM, at decided intervals;
(c) reviewing the CIPM key comparison results and determination of key comparison reference values (KCRV) and the degrees of equivalence in accordance with the proposals of the relevant working groups;
(d) approval of the final CIPM key comparison report for its publication in the BIPM database (KCDB);
(e) examination and confirmation of Regional Metrology Organization (details in the coming sections) key and supplementary comparison results and its incorporation in the BIPM database (KCDB);
(f) examination and confirmation of bilateral key comparison results for its entry into the BIPM database (KCDB).

4.1.4 BIPM: International Bureau of Weights and Measures

BIPM is an international/intergovernmental organization, which acts as a central body through which the scientific community of its member states discuss and act together on any relevant matter related to science and measurement standards. It was created on 20 May 1875, as an outcome of the Metre Convention, a treaty initially signed by 17 nations. Since 1969, the site where BIPM is located (i.e. Parc de Saint-Cloud, at Sèvres, in the suburbs south-west of Paris) has been considered as an international territory, and the BIPM is accorded with all the rights and privileges of an intergovernmental organization. To support the activities of CGPM and CIPM, BIPM also acts as a secretariat which provides an appropriate platform for meetings and other laboratory facilities supporting metrology. BIPM works under the authority of CGPM and the supervision of CIPM. It coordinates international key comparisons of national measurement standards with other NMIs/DIs and directly disseminates SI units by means of providing traceable calibration services. Therefore, BIPM has also established and is maintaining appropriate measurement/reference standards for its use as the basis of international key comparisons. Regular meeting reports of the CGPM, the CIPM, and all the appointed Consultative Committees are compiled and published by the BIPM. Inter-relation between all the above-listed international agencies dealing with metrology is shown in Fig. 1.

4.1.5 National Metrology Institute/Designated Institute (NMI /DI)

BIPM being an international organization, establishes and maintains appropriate measurement standards. Scientifically, it coordinates with its member economies having similar metrological status. Thus, the government of a member state designates one institute as a metrology institute that represents and coordinates with BIPM

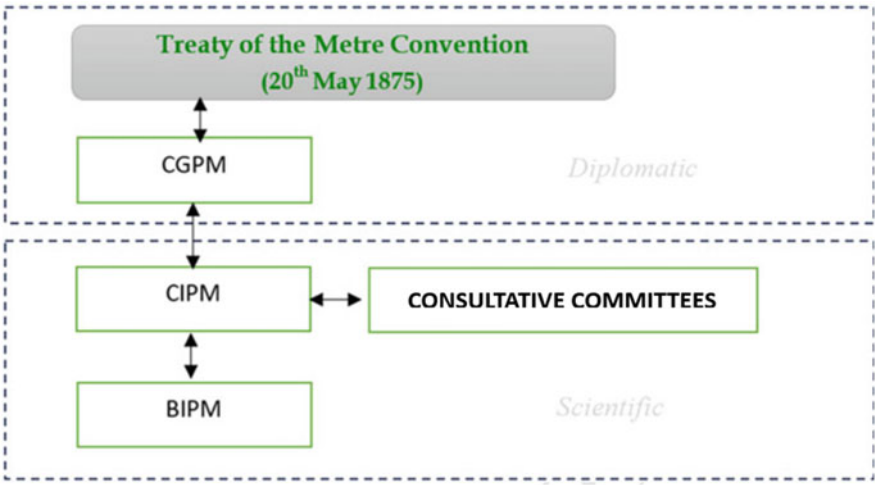

Fig. 1 Inter-relation between international agencies dealing with metrology

in the field of metrology. Such institutes are termed as National Metrology Institutes (NMIs). However, NMIs may not cover all the areas of metrology and thus NMI designates other capable institutes as metrology institutes in that area of metrology. Such designated metrology institutes are termed as Designated Institutes (DIs) for that metrological area. NMI and DIs do not have any overlapping areas of metrology. In an economy, there is only one NMI whereas there can be multiple DIs. In India, CSIR-NPL, New Delhi, is the NMI whereas BARC, Mumbai, is the DI for ionizing radiation metrology. NMI/DI of an economy/country is designated by the government of that economy which is globally recognized for its metrological activities and forms a part of the international metrology system. The measurement standards maintained by NMI/DIs are recognized as national measurement standards which facilitates the recognition of its measurement capabilities. NMI/DIs of an economy have the responsibility of developing, establishing, and maintaining national measurement standards and disseminating the international System of Units (the SI) nationally by means of providing traceable calibrations. The calibration and measurement traceability (unbroken chain) are a vertical concept (downwards and upwards respectively) as depicted in Fig. 2.

4.1.6 Regional Metrology Organizations (RMOs)

Given the large number of countries in the world, it may not be possible for BIPM to coordinate with each and every NMI/DI of its member nation. Therefore, to facilitate better coordination between its member NMIs/DIs, CIPM-MRA has recognized various regional associations of NMIs/DIs termed as Regional Metrology Organizations (RMOs). Currently, there are six RMOs namely APMP (Asia Pacific Metrology

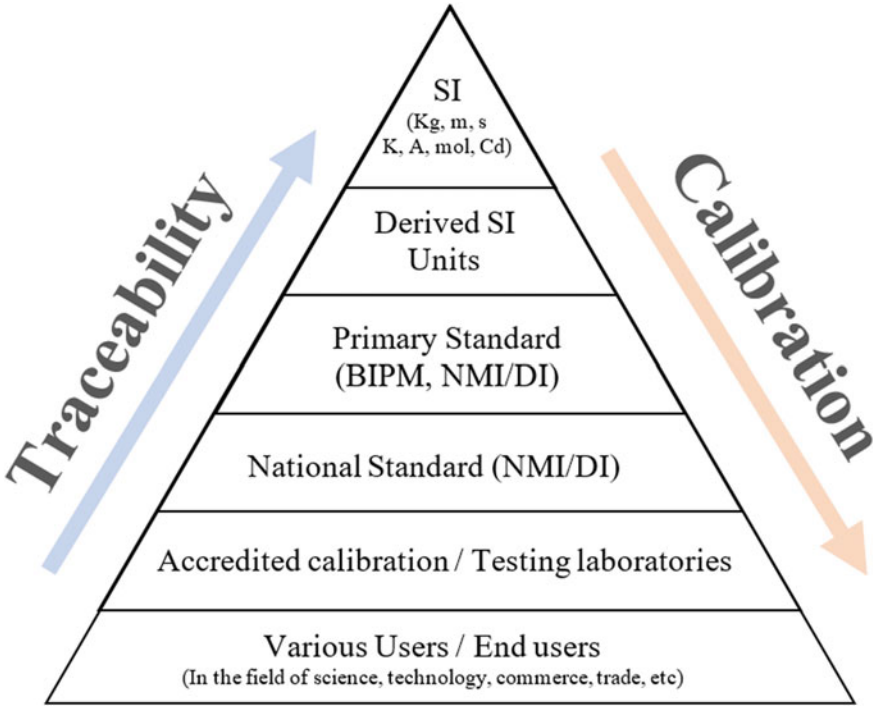

Fig. 2 Calibration and unbroken chain of measurement traceability

Programme), AFRIMETS (Intra-Africa Metrology System), COOMET (Euro-Asian Cooperation of National Metrological Institutions), EURAMET (European Association of National Metrology Institutes), GULFMET (Gulf Association for Metrology), and SIM (Inter-American Metrology System) that are recognized in the international system of metrology. India comes under APMP and is one of its founding members. These RMOs cover a wide range of activities within their region, as described on their respective websites. However, their key responsibility, within the CIPM-MRA framework, are defined by CIPM in *CIPM-MRA-P-12* document [3]. RMOs are responsible for the following:

(a) making proposals to the Consultative Committees on the requirement/choice of key comparisons;
(b) carrying out the RMO key comparisons, described in the Technical Supplement to the Arrangement, corresponding to the CIPM key comparisons;
(c) participation in the JCRB (another agency as described in the coming sections);
(d) carrying out supplementary comparisons to support mutual confidence in the validity of calibration and measurement certificates issued by participating NMIs/DIs.

The Structure of these RMOs is also in line with the CIPM structure. Therefore, similar to consultative committees formed by CIPM, RMOs too have their own technical committees (TCs). For example, considering ionizing radiation, the technical committee in the APMP is TCRI (Technical committee for ionizing radiation).

4.1.7 Joint Committee of the Regional Metrology Organizations and the BIPM (JCRB)

Coordination of inter-RMO activities is seen by a joint committee between various RMOs and the BIPM, termed as Joint Committee of the Regional metrology organizations and the BIPM (JCRB). The JCRB operates as per CIPM-MRA [3] and accommodates the representatives from all the recognized RMOs. The committee is chaired by the BIPM Director, with support from its Executive Secretary. JCRB is mainly tasked with the responsibility to

(a) coordinate various activities amongst recognized RMOs for establishing confidence needed for the recognition of NMI/DI-issued calibration certificates and measurement results,
(b) review requests from RMOs related to CIPM-MRA, and
(c) make policy suggestions to the RMOs and to the CIPM.

The detailed terms of reference of the JCRB are also described in the CIPM-MRA document, *CIPM-MRA-P-12*.

The graphical interrelationship between the various stakeholders of metrology structure is presented in Fig. 3.

4.1.8 The IAEA/WHO Network of Secondary Standards Dosimetry Laboratories (SSDL)

After Second World War, the use of ionizing radiation in industry, medicine, and scientific research increased many fold, which necessitated the need for reliable radiation dosimetric results between various users. At that time, most of the countries were not getting traceability in measurements due to the unavailability of relevant primary standards in their country or not having a good relationship with countries maintaining such primary standards. Therefore, a group of experts met in Geneva in November 1968, in coordination and collaboration between World Health Organization and IAEA, and discussed various ways of improving ionizing radiation dosimetry results especially for its application in the field of radiotherapy and radiation protection at a worldwide scale [4, 5]. In the meeting, the group recognized the urgent need for improving dosimetry in radiation medicine especially for its branches like X-ray diagnosis, radiotherapy, and nuclear medicine, even in its non-medical applications like radiation protection. As a result, in 1976, IAEA/WHO SSDL Network was established by IAEA in collaboration with WHO, to ensure the traceability of measurements, mainly for the countries that were not members of

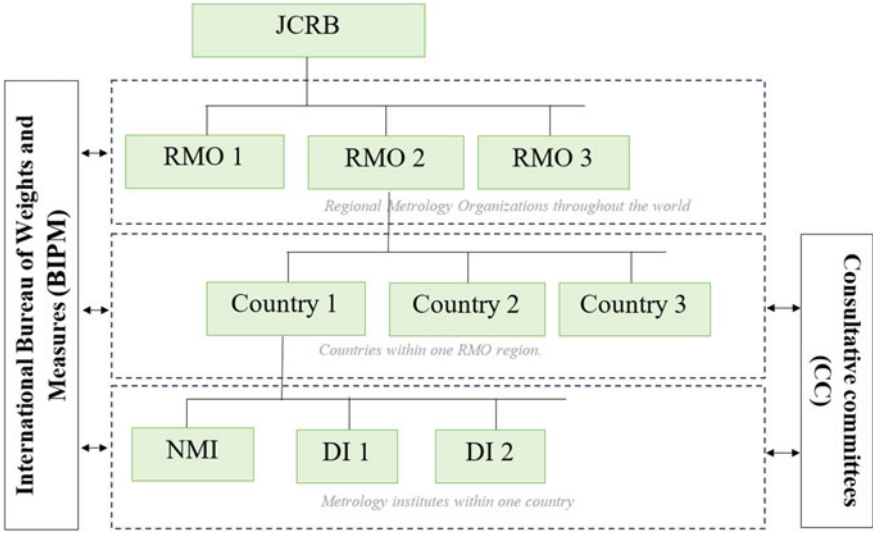

Fig. 3 Interrelationship between the various stakeholders of metrology structure

the Metre Convention or had no access to primary standard dosimetry laboratory, PSDLs [5]. Therefore, many countries joined this network of SSDL for getting better traceability.

The competent authority of the nation, that joins the SSDL network, designates one of its capable laboratory/organizations as SSDL which undertakes the duties of providing measurement traceable to SI units. The standards, maintained by SSDL, are directly or indirectly traceable to one of the primary standards maintained by NMI or DI or BIPM. If the SSDL has no access to such a standard, then the intermediate step of IAEA calibrations is used to get the required traceability to the primary standard. The IAEA maintains a calibration laboratory, which acts as a central laboratory, and provides reference irradiations, comparison programmes, and dosimetry audit services to its Member States to maintain the confidence in the dosimetry standards concerning the areas of radiation medicine and radiation protection. In general, a SSDL maintains a secondary standards dosimeter. The SSDL Network is tasked with the responsibility to provide and maintain the links between the various end users of radiation dosimeters, SSDLs, and the international measurement system. The link between the international measurement system for radiation dosimetry through IAEA SSDL network is shown in Fig. 4. Apart from this, the network also provides a forum to its member SSDLs in which they can regularly perform comparisons for strengthening the confidence in the ionizing radiation dosimetry consistently.

In the CIPM-MRA framework, IAEA is one of the first few signatories which has published its CMCs in the KCDB after a rigorous peer-review carried out by all the RMOs with JCRBs endorsement. India became a member of this network at the time of its formation, i.e. in the year 1976 itself.

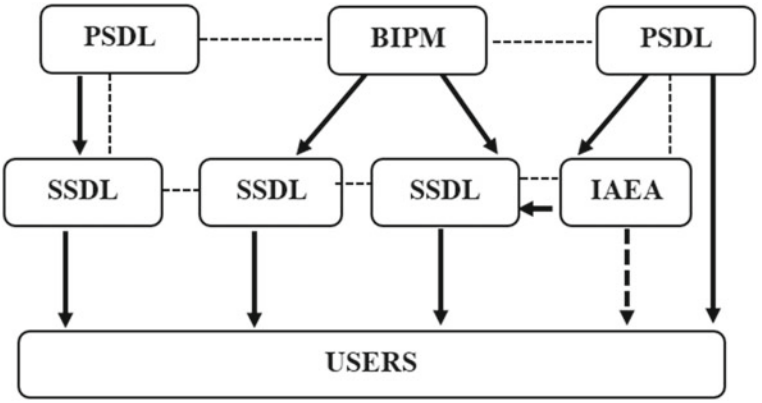

Fig. 4 Traceability to the international measurement system for radiation dosimetry through IAEA SSDL network [5]

4.1.9 Key Comparison Database of BIPM (KCDB)

KCDB is a freely available web resource [6], maintained by BIPM, which hosts the details of its member state NMIs/DIs, their internationally peer-reviewed/recognized Calibration and Measurement Capabilities (CMCs), and the results of intercomparisons supporting their CMCs. Therefore, KCDB provides a reliable quantitative database to worldwide users giving access to the comparability of national metrological services with a technical basis required for international trade, commerce, and regulatory affairs.

5 Ionizing Radiation Metrology and Measurement Standards

Accurate measurement of radiological quantities is needed in every country where ionizing radiation is used. Countries either maintain a national measurement standard for relevant quantities or make necessary arrangements for ready access to such standards established and maintained in another country. National measurement standards for a given quantity are recognized in a regulatory form by the competent authorities. Such standards are traceable to the International System of Units (SI) and may be either a primary standard maintained at an NMI or a secondary standard that is traceable to a primary standard [5]. The Metrology of ionizing radiation can be broadly categorized into three categories a) measurement of dose (kerma, dose, dose equivalent, etc.), b) measurement of intensity (fluence, emission rate, etc.), and c) measurement of radioactivity (disintegration per second).

The international system of units defines three derived SI units i.e. *Gy* (Gray), Sv (Sievert), and *Bq* (Becquerel) that is used to measure/quantify ionizing radiation.

Unit *Gy* (i.e. Joule/Kg) is used to measure dose to the medium whereas *Sv* measures dose to the human body along with the risk associated with that dose. Internationally, ionizing radiation-related activities are distributed in three sections of CCRI namely CCRI Section I (Dosimetry): X- and gamma rays, charged particles; CCRI Section II (Radioactivity measurement): Measurement of radionuclides; and CCRI Section III (Neutron): Neutron measurements.

5.1 Dosimetry: X-rays, Gamma Rays, and Charged Particles

In general, two physical quantities are used to quantify the amount of radiation in external dosimetry: kerma/rate and absorbed dose/rate [7]. Based on kerma, other quantities that are covered under this category (Dosimetry) of ionizing radiation measurement are ambient dose equivalent/rate, directional dose equivalent/rate, and personal dose equivalent/rate. This section of Ionizing radiation, i.e. Dosimetry deals with the application of ionizing radiation in scientific research (material characterization), medicine (for diagnostic radiology and treatment of cancer), radiation protection (occupational workers and public), and radiation processing (application of high doses of ionizing radiation to modify biological, physical, and chemical properties of the irradiated matter). In medicine (concerning radiotherapy and brachytherapy), accurate dosimetry is of utmost importance for the effectiveness of cancer treatment. Similarly, accuracy is also important for dosimetry of occupational workers, patients undergoing diagnostics, and in the field of radiation processing (like blood irradiation, sterilization of health care products, processing of food & agriculture products, etc.). Sources of ionizing radiation that are primarily covered under this section are X-rays (0–50 kV and 50–300 kV, Mega Volts), beta radiation, electrons, photons from radionuclide sources (^{60}Co, ^{137}Cs, ^{192}Ir, ^{125}I, etc.), protons, heavy ions, etc. A few of the primary standards that are used for the realization of external dosimetric quantities for different kinds of radiation beams are described below.

In general, a primary standard is an instrument of the highest metrological quality, for a given physical quantity, that permits determination of a unit of the quantity without reference to other standards of the same quantity [8].

5.1.1 Dosimetry in kilovoltage X-rays (Air kerma)

In medicine, the desirable quantity is absorbed dose to water, D_w, but the realization of this quantity in kilovoltage X-rays (up to 300 kV) is through the measurement of air kerma, K_a, using free air ionization chamber (FAIC) (Fig. 5).

FAIC is a device which directly realizes air kerma. It allows the entrance of radiation from the diaphragm whose aperture area is known, and the signal is collected at the collecting plate of known length (in the beam direction). Therefore, the projection of the aperture area on the collecting plate (shaded area near point p' in Fig. 5), inside the larger volume, defines the volume of air whose direct photon interaction with

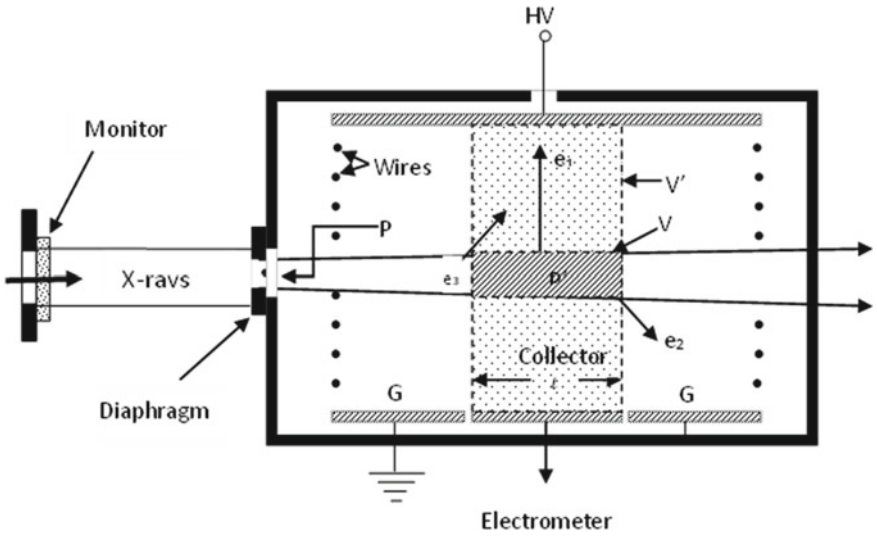

Fig. 5 Schematic of a typical free air ionization chamber. [9]

air is accounted for in the definition of measured air kerma. If the plate separation (signal and high voltage plate) is such that generated secondary electrons, within the interaction volume, do not reach the chamber walls, then the chamber is considered as 'wall-less'. Once this condition is satisfied, then the air kerma rate at the entry point (the diaphragm) is determined by the equation,

$$\dot{K}_a = \frac{I}{m_a} \frac{\left(W_a/e\right)}{(1-g)} \prod_i k_i \tag{1}$$

where

I = the ionization current measured by electrometer;

m_a = the mass of air in the defined volume (shaded area near point p' in Fig. 5);

W_a = the average energy required to create one ion pair in the dry air;

e = the charge of one electron;

g = the correction for adjusting radiative losses.

5.1.2 Air kerma from Radionuclide-Based Photon Beams (Cobalt-60/ Cs-137/Ir-192 Gamma Rays)

It is not feasible to use Free air ionization chambers at energies above 300 keV as the required plate separations will be very high and it will not be possible to apply appropriate voltage to get near 100% collection of the charges generated during interaction. Therefore, cavity ionization chambers (of various shapes and sizes) are used to realize air kerma and in turn directly can also be used to realize absorbed dose to water. For cavity ionization chambers, graphite is the obvious choice of wall material due to its radiation interaction coefficients similar to that of dry air (and also to water) [8]. The use of a cavity ionization chamber, in comparison to a free air ionization chamber, is more complex for realizing air kerma/rate as the mean ionization current, I, per unit mass of air, $m_{a,}$ measured is closely related to the mean absorbed dose rate to the air of the cavity. This ionization current is due to the interaction of radiation in the graphite wall. The wall-generated electrons deposit their energy in air cavity giving rise to the absorbed dose rate in the air cavity. Therefore, this absorbed dose rate in the air cavity is dependent on the ratio of mean mass stopping powers of carbon and air, $s_{c,a}$ and the ratio of mean mass energy absorption coefficients $(\mu_{en}/\rho)_{a,c}$. Thus, the equation for estimation of the air kerma rate, using an air-filled cavity ionization chamber, is given as

$$\dot{K}_a = \frac{I}{m_a}\frac{W_a}{e}\frac{\left(\mu_{en}/\rho\right)_{a,c}}{(1-g)}S_{c,a}\prod_i k_i \tag{2}$$

The correction factors k_i includes mainly.

(a) correction factor k_{wall}: it corrects for attenuation and scattering of photons in the chamber wall,
(b) axial non-uniformity factor k_{an} (sometimes replaced by the point source non-uniformity factor k_{pn}): it corrects for the sensitivity of the chamber response to the divergence of the beam, etc.

A design of a typical cylindrical graphite ionization chamber is shown in Fig. 6.

5.1.3 Dosimetry for Absorbed Dose to Water

For ^{60}Co gamma rays and other higher energy photons (Mega Volts x-rays), the primary standards for absorbed dose to water are basically the same. Two prominent equipment that are used as primary standards are.

(a) Cavity ionization chambers
(b) Calorimetry (mostly water or graphite based).

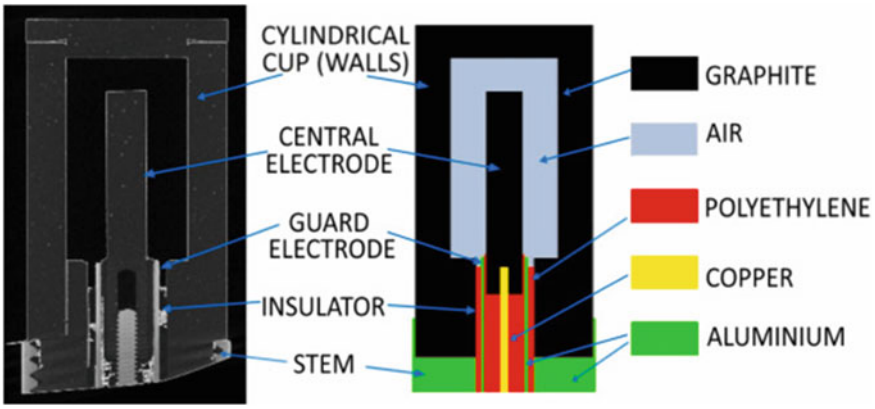

Fig. 6 Typical cylindrical graphite ionization chamber [10]

For ^{60}Co gamma rays, small volume cavity ionization chambers are used to determine the absorbed dose to water by placing them inside a water phantom (by means of waterproof sleaves). Thereafter a perturbation correction is applied, which accounts for the perturbation due to the presence of the ionization chamber inside the water phantom. The absorbed dose rate to water under this scenario is evaluated using the equation

$$\dot{D}_w = \frac{I}{m_a}\frac{W_a}{e}\Psi_{w,c}\left(\mu_{en}/\rho\right)_{w,c}\beta_{w,c}S_{c,a}\prod_i k_i \tag{3}$$

where $\Psi_{w,c}$ is the photon fluence ratios for water and graphite whereas $\beta_{w,c}$ is the ratio of absorbed dose rate to collision kerma rate ratio.

Experimental work along with theoretical evaluation is essential for the evaluation of this perturbation correction which allows for its accurate determination [11]. Based on this approach, the BIPM maintains its standard for absorbed dose to water.

Apart from the cavity ionization chamber, the most widely used technique for estimating the absorbed dose to water is based on the technique of calorimetry. Here, the concept of conversion of absorbed dose from the radiation field to heat is applied. When ionizing radiation interacts with the medium, most of the energies transferred to the medium (during interaction) are converted to heat. If the absorbed energy is completely converted into heat, then the absorbed dose, D_m (Gy or J/Kg), to material m is given by

$$D_m = C_m.\Delta T.\Pi k_i \tag{4}$$

where

C_m is the specific heat capacity of the material ($J.Kg^{-1}.K^{-1}$),

ΔT is the measured temperature rise (K), and

k_i is the correction factor.

The material-specific quantity, specific heat capacity, can be measured without referring it to a standard of absorbed dose/rate. Therefore, the measured absorbed dose by this technique is directly traceable to the SI unit of temperature. These calorimeters can be made using any material, but graphite and water are most widely used for this purpose.

Water being a liquid, its construction is highly challenging. However, several Primary Standard Dosimetry Laboratories (PSDLs) have established water calorimeter as their primary standard for absorbed dose to water [8]. On the other hand, many PSDLs also use graphite as a construction medium due to its easy handling and having its radiation interaction characteristics similar to water. However, this requires a conversion from absorbed dose to water from absorbed dose to graphite. The estimated uncertainty of the measured absorbed dose to water using both graphite and water calorimetry remains the same. A typical photograph of graphite and water calorimeter is shown in Figs. 7, 8, and 9.

5.1.4 Megavoltage X-rays and Electrons

For Megavoltage X-rays and high-energy electrons, calorimetry (as discussed in Sect. 5.1.3) is widely used for estimating absorbed dose to water.

5.1.5 Calibration Laboratories

Primary standards are sophisticated instruments/methods and cannot be used for day-to-day calibrations. Therefore, day-to-day calibration of radiation monitors (dosimeters, survey meters, pockets dosimeters, area gamma monitors, etc.) are carried out by calibration laboratories, having sufficient infrastructure, against their secondary or working standards which are calibrated against a primary standard. The infrastructure required for establishing a calibration laboratory includes a dedicated room with adequate shielding complying with regulatory norms, a secondary standard ionization chamber, a linear distancing system, a laser aligning system, a measuring scale, instruments to measure environmental conditions like temperature, pressure, and humidity, etc. Such facilities are, in general, separated from areas where other activities are carried out. Access to these areas is restricted and should have administrative control. Variations of temperature and humidity of the ambient air play an important role in such laboratories; therefore, the rooms where reference standard instrument calibration equipment and user dosimeters are stored and calibrations are carried out

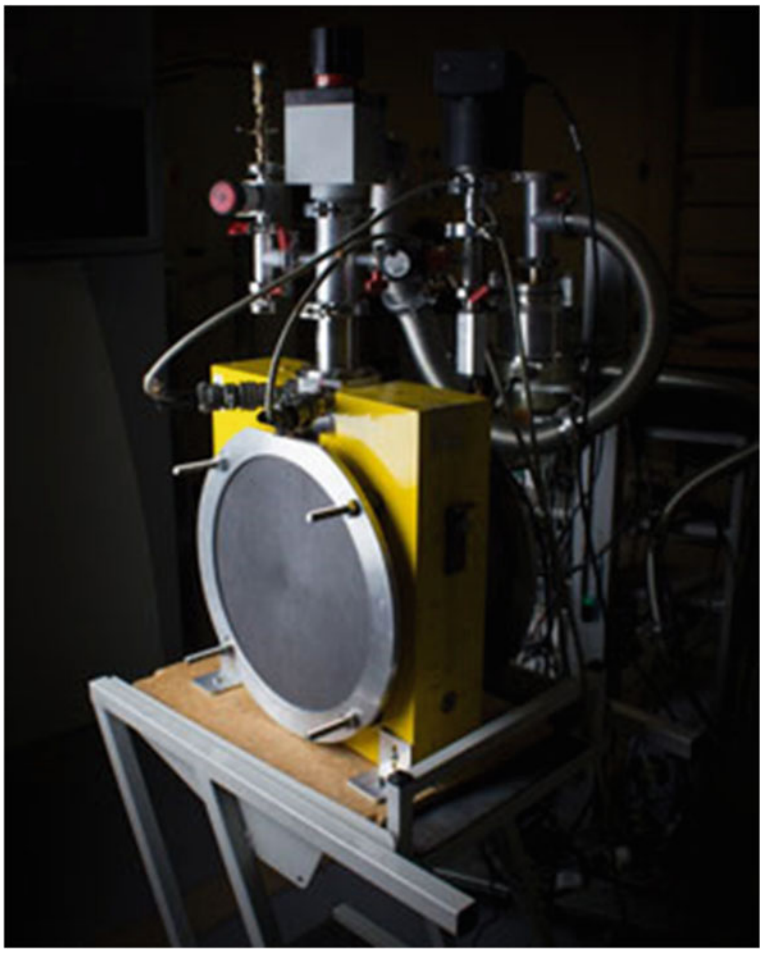

Fig. 7 Graphite calorimeter of ARPANSA [12]

should be air conditioned to minimize such effects. Even the environment conditions (temperature, pressure, humidity) of such facilities are regularly monitored and recorded. Calibrations should not be carried out when the ambient environmental conditions are beyond the requirement as it may jeopardize the calibration result. Each laboratory defines and documents the limits of these environmental conditions within which they perform the calibrations [8].

For most of the calibration activities related to X and gamma radiation, a secondary standard ionization chamber (cylindrical or spherical) of appropriate dimension is calibrated against the primary standards of air kerma and absorbed dose to water and is used for day-to-day services. Cavity chambers of various make and models are available in the market. A typical example of cylindrical and spherical chambers is shown in Fig. 10.

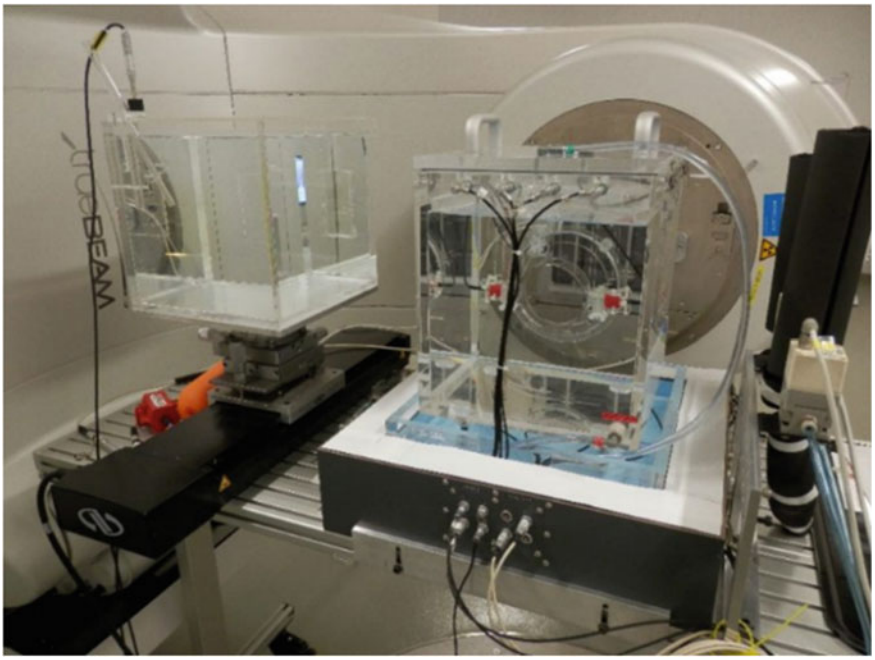

Fig. 8 Water calorimeter (LNHB) [13]

For absolute and relative electron beam dosimetry, parallel plate ionization chambers (Fig. 11) are designed and used for electron energies above 2 MeV for measuring the quantity absorbed dose to water.

5.2 Radioactivity Measurement: Measurement of Radionuclides

Radionuclides are widely used in many medical, industrial, and research applications. In medical applications, they are used for diagnostics, therapy, etc. whereas in research applications they are used as tracers, carbon dating, calibration of spectrometers, etc. Mostly the information related to radionuclides for such applications is given in the form of activity (Bq) or emission rate (particles/s).

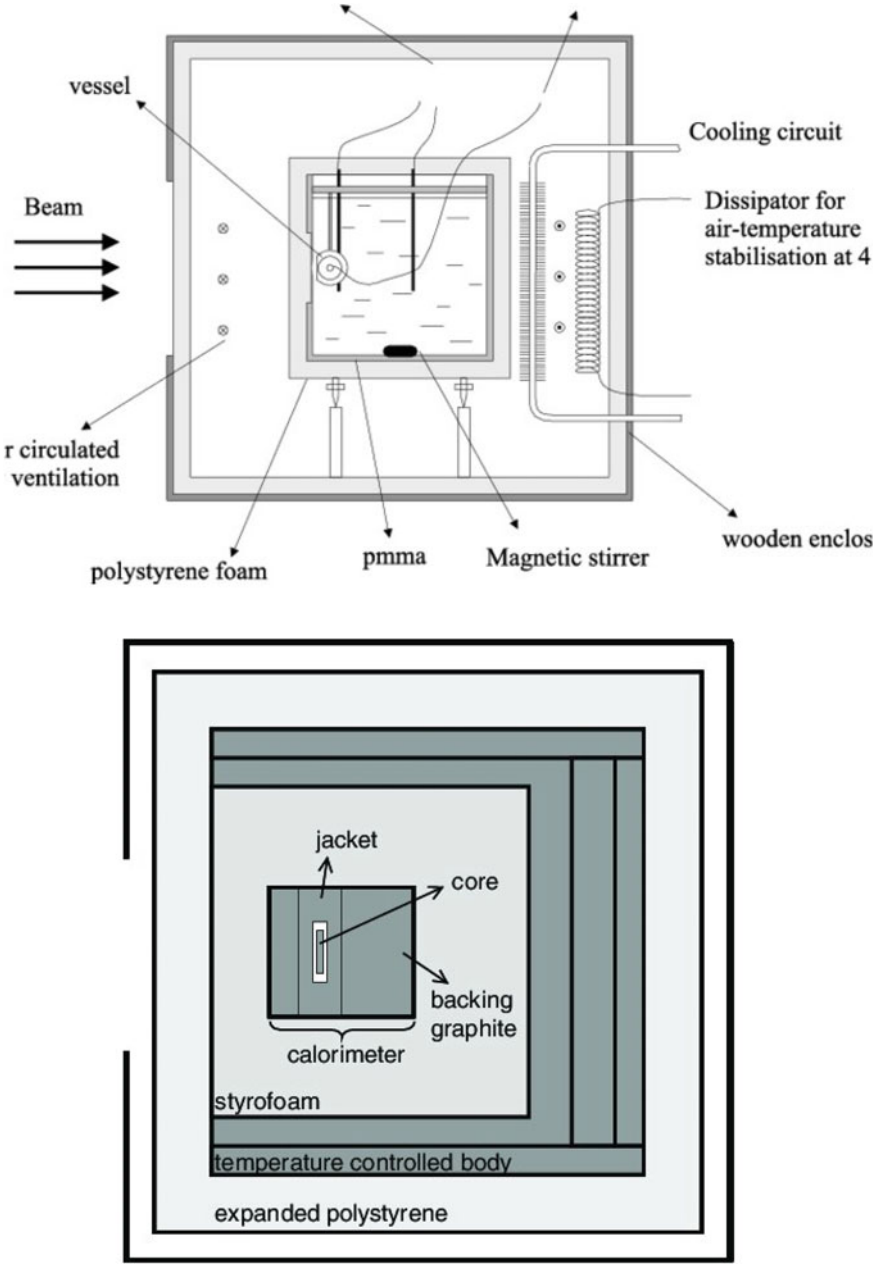

Fig. 9 Schematic drawing of the sealed water calorimeter and portable graphite calorimeter [14, 15]

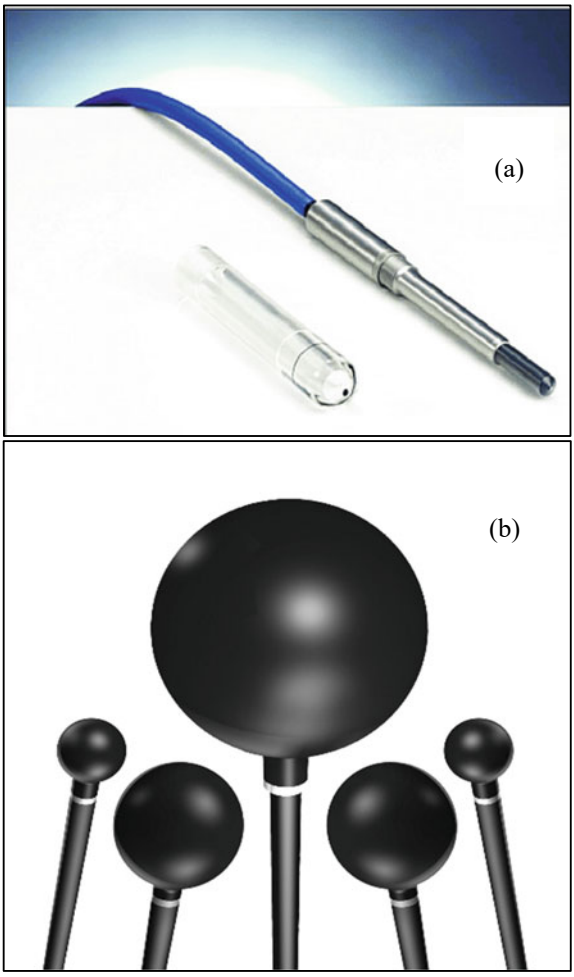

Fig. 10 **a** Farmer-type chamber (radiotherapy), **b** exradin chambers of various sizes

5.2.1 Activity Measurements: Absolute/Primary Standards

The absolute or direct methods involve measurements of activity using only count rates. Hence it involves only standard of time and is never based on any other radioactivity standard. The methods of absolute activity measurements are coincidence technique, anti-coincidence technique [17–23], CIEMAT/NSIT efficiency tracing technique [24–26], Triple to Double Coincidence ratio (TDCR) [27–29], internal gas counting, etc. Each method has its advantages and disadvantages and can be used in specific conditions. The coincidence counting is the most powerful technique and is employed by most of the international metrology institutes.

A. **Coincidence counting Technique**:

Coincidence counting is an absolute technique for activity measurement of radionuclides and has been used for over 60 years [17–23]. Coincidence technique

Fig. 11 Plane parallel ionization chamber for reference high-energy electron dosimetry [16]

with its variants allows one to measure the activity of the majority of radionuclides directly, without having to assume any particular value for source and detector efficiencies, decay scheme parameters, or branching ratios. All radionuclides that decay by simultaneously releasing two or more radiations in quick succession (prompt emission), such β-γ, α-γ, electron capture-γ, γ –γ, and γ-x, can be directly standardized by this technique. For simple two-stage beta-gamma decay of a source with a true disintegration rate (N_0) and beta and gamma detection efficiencies (ε_β, ε_γ), the count rates for β (N_β), γ (N_γ), and coincidence (N_c) would be

$$N_\beta = N_0 \varepsilon_\beta$$

$$N_\gamma = N_0 \varepsilon_\gamma$$

$$N_c = N_0 \, \varepsilon_\beta \varepsilon_\gamma$$

The value of N_0 is then simply

$$\frac{N_\beta N_\gamma}{N_c} = \frac{N_0 \varepsilon_\beta N_0 \varepsilon_\gamma}{N_0 \varepsilon_\beta \varepsilon_\gamma} = N_0 \tag{5}$$

Here no knowledge of detector efficiencies is required, but these can be calculated as

$$\varepsilon_\beta = \frac{N_c}{N_\gamma} \tag{6}$$

$$\varepsilon_\gamma = \frac{N_c}{N_\beta} \tag{7}$$

These simplified equations are useful only for radionuclides with beta-gamma emission having a simple decay scheme. There is another assumption that each detector should be sensitive to only one type of radiation. In reality, these conditions cannot be achieved and some modifications to the equations shown above have to be done. Such a method is called Efficiency Extrapolation Technique (EET) [17–19].

B. **Efficiency Extrapolation technique**:

In coincidence measurements, one of the detectors (usually the beta detector) or both the detectors are not sensitive to only a single type of radiation. Hence basic expression for the count rates in the beta detector required modification to include the gamma sensitivity of the beta detector for gamma photons and conversion electrons. The activity can be calculated using the equation

$$\frac{N_\beta N_\gamma}{N_c} = N_0\left[1 + \left(\frac{1-\varepsilon_\beta}{\varepsilon_\beta}\right)\left(\frac{\alpha\varepsilon_{\mathrm{ce}} + \varepsilon_{\beta\gamma}}{1+\alpha}\right)\right] \tag{8}$$

where

α is the conversion coefficient,

$\varepsilon_{\mathrm{ce}}$ is beta detector efficiency for conversion electrons, and

$\varepsilon_{\beta\gamma}$ is beta detector efficiency for gamma rays.

The above equation represents a straight line and N_0 reduces to $N_\beta N_\gamma / N_c$ when beta efficiency (ε_β) approaches unity.

The method cannot be used directly for pure beta emitters as there is no prompt coincidence emission of two or more particles. In that case, Efficiency Tracing Technique (ETT) is used.

C. **Efficiency Tracing Technique:**

When dealing with radionuclides that emit a single type of radiation or those whose excited state has a long half-life, such as ^{137}Cs with 133 s for a 662 keV level of $^{137\mathrm{m}}$Ba, the efficiency extrapolation technique cannot be used directly. Nonetheless, the activity of the beta emitter can be ascertained using the efficiency tracing technique (ETT) which is the variation of the coincidence technique, if a mixture consisting of a pure beta ray emitter and a suitable radionuclide that emits concurrent beta and gamma rays is created [3–5]. If we denote the pure beta emitter as Traced nuclide and beta-gamma emitting radionuclide as Tracer nuclide then $N_{\beta(\mathrm{Traced})}/M_{(\mathrm{Traced})}$ is a function of $[1 - \varepsilon_{(\mathrm{Tracer})}]$. The activity concentration of Traced nuclide is obtained by plotting $N_{\beta(\mathrm{Traced})}/M_{(\mathrm{Traced})}$ versus $[1 - \varepsilon_{(\mathrm{Tracer})}]$ and extrapolating it to zero, where $N_{\beta(\mathrm{Traced})}$ is the count rate due to traced nuclide in the beta channel, $M_{(\mathrm{Traced})}$ is the mass of traced nuclide in the source, and $\varepsilon_{(\mathrm{Tracer})}$is the detection efficiency of the tracer.

The count rate measured in the beta channel is due to both traced nuclide and tracer nuclide. The count rate due to traced nuclide only is calculated by subtracting the count rate due to tracer nuclide betas from the total count rate. The count rate due to tracer nuclide betas is calculated by multiplying the already known activity of the tracer by the beta counting efficiency of the tracer ($\varepsilon_{(\text{Tracer})}$). Traced nuclide count rate is divided by the mass of traced nuclide added in the source, decay corrected to reference date, and then plotted versus $[1 - \varepsilon_{(\text{Tracer})}]$. Thus, the coincidence technique can be used for standardization of pure beta emitters with the use of beta-gamma emitting tracer nuclide by Efficiency Tracing Technique.

The 4π β-γ coincidence method is the most effective and popular primary standardization method for measuring radioactivity. Worldwide three types of 4π β-γ coincidence systems are widely used for primary standardization of radioactive solutions of various radionuclides. These are a 4π gas flow proportional counter-based system (Fig. 12), a liquid scintillator-based system (Fig. 13), and a plastic scintillator-based coincidence system (Fig. 14).

CIEMAT/NIST efficiency tracing technique and Triple to Double Coincidence Ratio (TDCR) are also the primary methods for standardization of radionuclides and are also used in RSS.

D. **Secondary Standards for activity measurement:**

The primary standards provide the most accurate measurements with the lowest uncertainties but these are cumbersome, time-consuming, and available in limited quantities. Hence, primary standards are not used for routine measurements and calibration. For routine calibration, secondary standards which are directly calibrated against the primary standards are used. Some of the secondary standards used for radioactivity measurements are as follows:

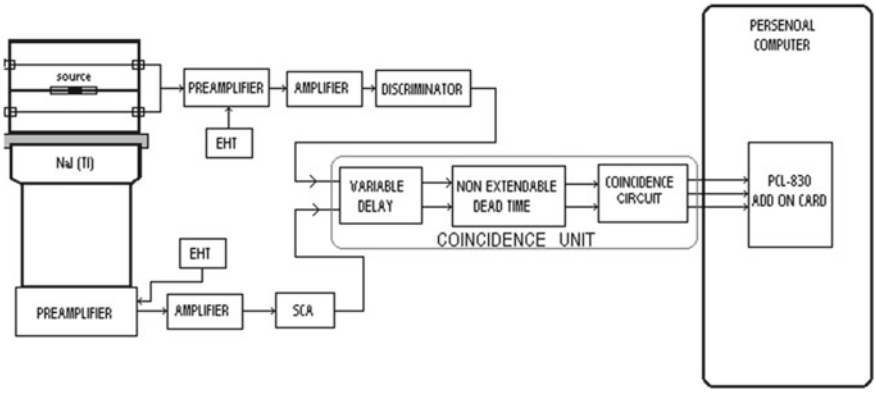

Fig. 12 Block diagram of proportional counter-based 4π β(PC)-γ coincidence counting system

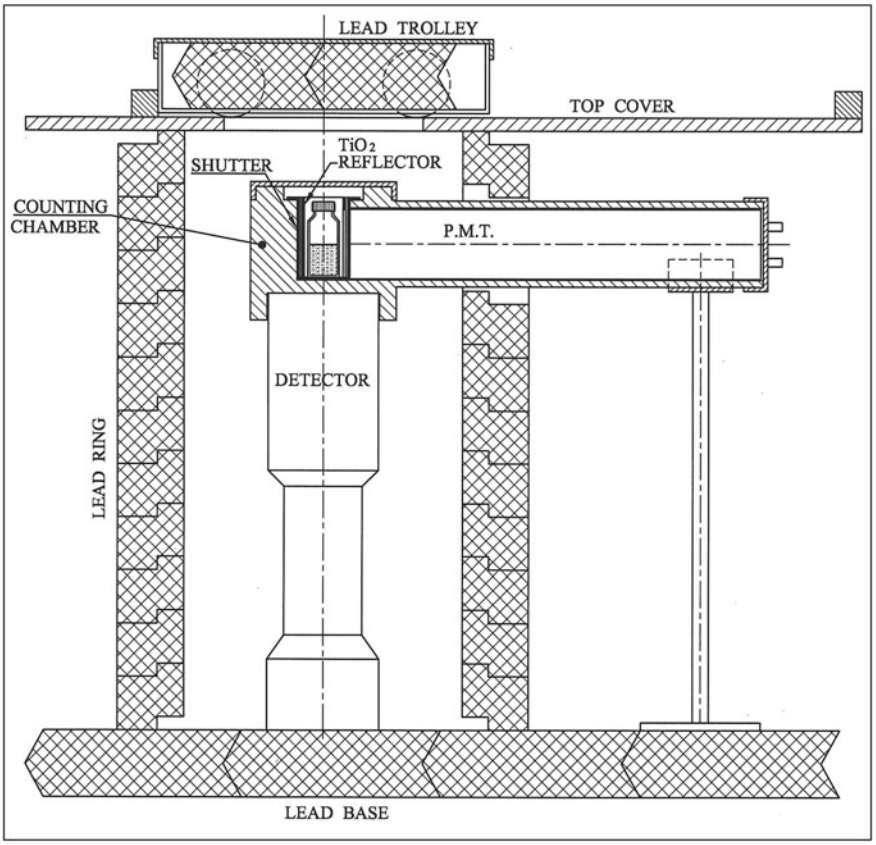

Fig. 13 Schematic of 4π β(LS)-γ coincidence counting system

(1) Re-entrant type 4π Gamma ion chamber.
(2) HPGe gamma spectrometers.

The photographs of the secondary standards are shown in Figs. 15 and 16.

5.2.2 Emission Rate Measurement

In radiation protection surveillance programmes, surface contamination monitors are widely employed to estimate surface activity levels accurately and assess related risks. Large area beta reference sources are frequently used to calibrate surface contamination monitors in terms of surface emission rates [30, 31]. Hence it is very important to know the particle emission rates from large area reference sources accurately [32, 33].

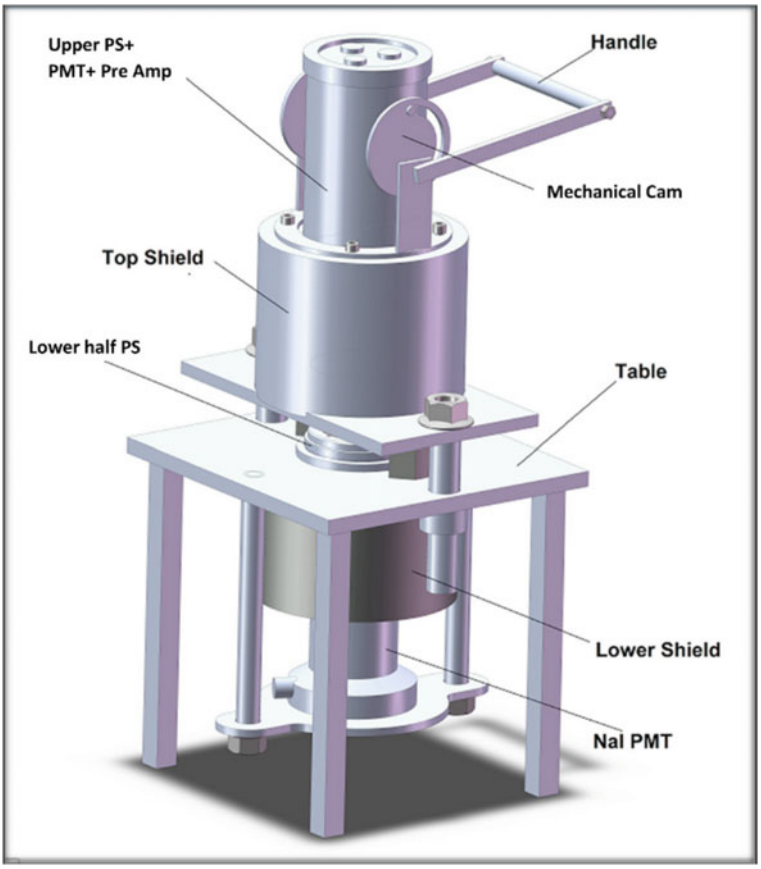

Fig. 14 3-D model of a 4π β(PS)-γ coincidence counting system

The widely accepted gas flow multi-wire proportional counter (MWPC) is utilized to measure the surface emission rate. Standard laboratories worldwide are the primary users and establish the MWPC as a primary standard for measuring the surface emission rates of large area alpha and beta sources. The schematic of the large area windowless 2π gas flow multi-wire proportional counting system is shown in Fig. 17a. Similarly, the 4π proportional counter of the Proportional counter-based 4πβ(PC)-γ coincidence counting system is used for smaller point sources of beta emitting radionuclides. The photograph of 4π proportional counter of the Proportional counter-based 4πβ(PC)-γ coincidence counting system is shown in Fig. 17b.

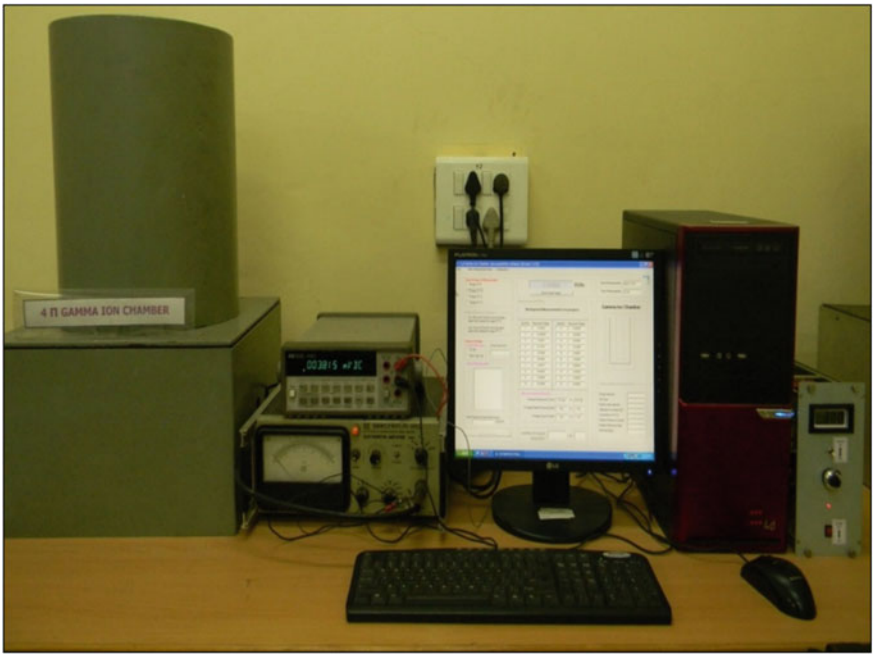

Fig. 15 4π-γ ion chamber for activity measurements of gamma emitting radionuclides

Fig. 16 HPGe gamma spectrometer for activity measurements of gamma emitting radionuclides

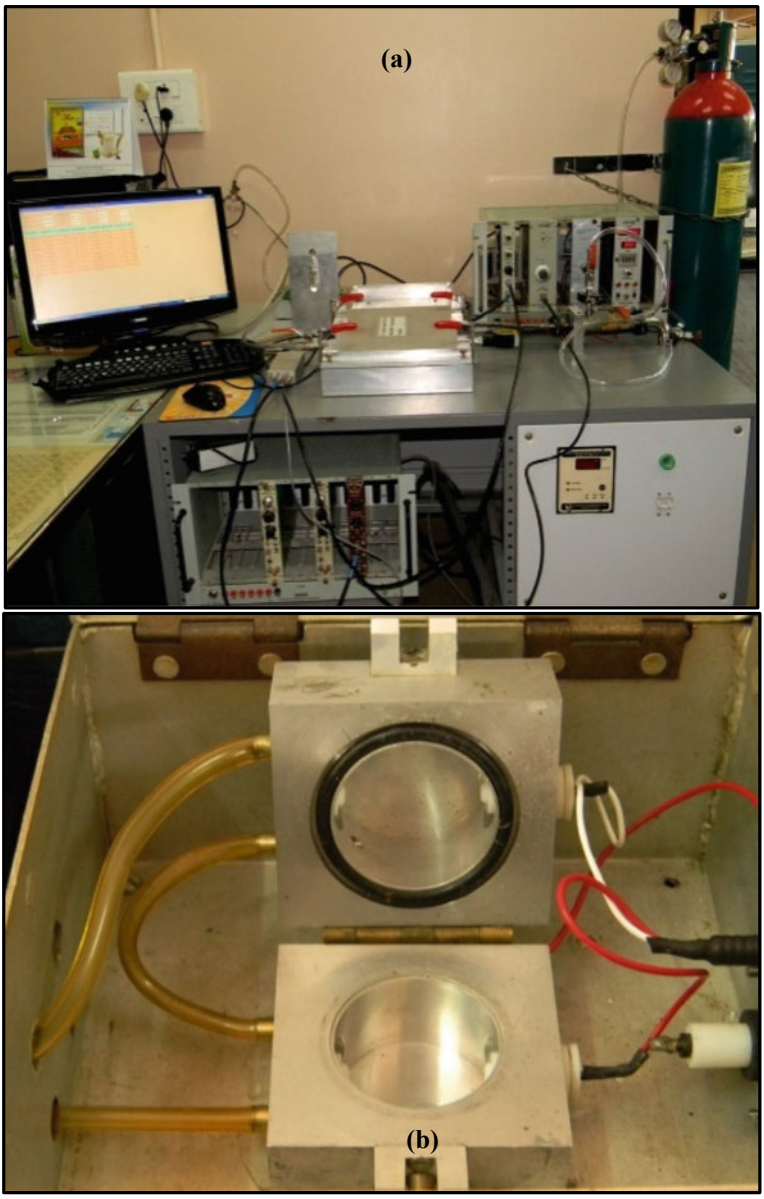

Fig. 17 **a** Large area multi-wire window less proportional counting system (for large area sources) and **b** 4π Proportional counter of $4\pi\beta$(PC)-γ coincidence counting system (for point sources) for emission rate measurements

This type of counter has the advantage of introducing the radioactive sample directly into the detector's sensitive volume. With no entrance window between the radioactive source and the counter's sensitive volume, there is no loss of detection efficiency, and all particles emitted from the source surface into the measurement volume are detected [34].

5.3 Neutron Measurements

Neutrons are encountered and utilized in diverse fields such as nuclear power plants, research reactors, cancer treatments using BNCT (Boron Neutron Capture Therapy), neutron physics experiments, cement industries, industrial radiography, imaging, calibration of neutron measuring instruments, etc. The accurate measurement of neutron exposure is based on the use of various types of neutron standards pertaining to different quantities viz. neutron yield/source strength (Q, n/s), fluence (Φ, n/cm^2)/ , fluence rate ($\Phi^{\cdot}$, n/cm^2/s), absorbed dose rate to tissue (D, Gy/h), etc. in accordance with the latest Calibration and Measurement Capability (CMC) rules governed by CCRI/BIPM [35]. Other monitoring quantities such as Ambient and Personnel dose equivalent rates [$H^*(10)$ and $H_p(10)$, Sv/h] are evaluated on the basis of the knowledge of neutron fluence rate.

For the measurement of neutron source yield (Q), the $MnSO_4$ bath system is used as the Primary standard for laboratory sources whereas for mono-energetic fast neutrons viz. D-T interaction produced 14.57 MeV neutrons, Proton Recoil Telescope (PRT) is used as a primary standard. For day-to-day use, Precision Long Counter (PLC) is used as the secondary standard for the determination of neutron yield for commonly available radionuclide neutron sources which is traceable to the $MnSO_4$ bath system. The laboratory neutron sources standardized using $MnSO_4$ bath system or PLC are then used for day-to-day R&D activities, testing and calibration of neutron monitoring devices. Standard Thermal Assembly in Graphite (STAG) facility is used as the primary standard for thermal neutron fluence rate whose output is standardized using gold foil activation technique. Neutron fluence from Thermal/ fast neutron field is also characterized by means of foil activation technique (primary method), using foils of different materials. Brief details of the primary and secondary standard systems described in this section are presented below.

5.3.1 $MnSO_4$ Bath System

$MnSO_4$ bath system is established as the primary standard towards the quantification of source yield (Q) of mainly standard neutron sources used by the majority of the NMIs. The system typically consists of a spherical tank of about 1-m diameter filled with saturated $MnSO_4$. H_2O aqueous solution and a gamma spectrometry system having NaI(Tl) detector. Apart from that, a motor and other piping systems remain there for circulation of the solutions between the main spherical tank and the shielded

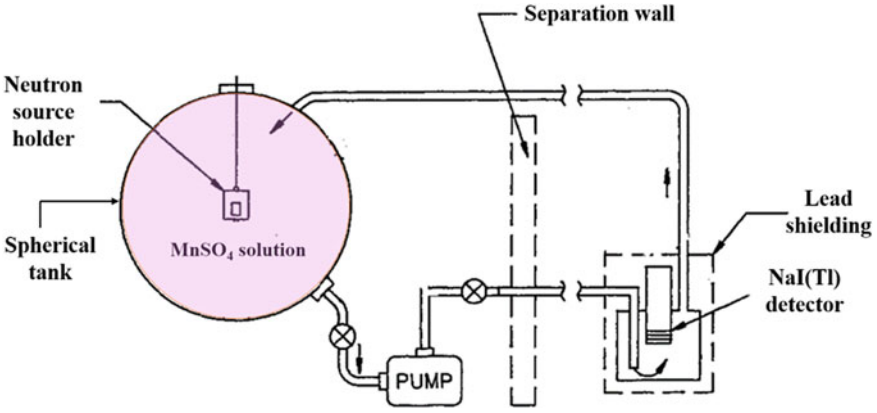

Fig. 18 Pictorial diagram of a typical $MnSO_4$ bath facility

re-entrant chamber (above which the detector is placed) which has been pictorially depicted in Fig. 18. During neutron yield measurement, the sealed neutron source is placed inside a metallic tube which places the source exactly at the centre of the tank. Fast neutrons emitted by the source get moderated by elastic collision with constituent elements of the solution (mainly H atoms) resulting in the generation of thermal neutrons. A fraction (f) of these neutrons are absorbed by the ^{55}Mn isotope resulting in the formation of ^{56}Mn as shown below:

$$^{55}_{25}\mathrm{Mn} + {}^{1}_{0}\mathrm{n} \rightarrow {}^{56}_{25}\mathrm{Mn} \rightarrow {}^{56}_{26}\mathrm{Fe} + \beta^{-} + \gamma \tag{9}$$

The fraction of neutrons absorbed is given by the following equation:

$$f = \frac{N_{\mathrm{Mn}}\sigma_{\mathrm{Mn}}}{N_{\mathrm{Mn}}\sigma_{\mathrm{Mn}} + N_{\mathrm{S}}\sigma_{\mathrm{S}} + N_{\mathrm{O}}\sigma_{\mathrm{O}} + N_{\mathrm{H}}\sigma_{\mathrm{H}}} \tag{10}$$

where $\sigma_{\mathrm{Mn}} = \sigma_o\left(1 + G\breve{r}\,s\right)$; G refers to self-shielding; and 'r' and 's' are spectral index and resonance integral, respectively. Also, N_{Mn}, N_{S}, N_{O}, and N_{H} are the respective concentrations of manganese, Sulphur, oxygen, and hydrogen per cm^3 in the solution and σ_{Mn} (13.2 b), σ_{S} (0.52 b), σ_{O} (0.0002 b), and σ_{H} (0.33 b) are the respective capture cross section of these elements for thermal neutrons. Considering the negligible value of σ_{O} and $\mathrm{N_{Mn}} = \mathrm{N_S}$, the above equation may be written as

$$\frac{1}{f} = 1 + \frac{\sigma_{\mathrm{S}}}{\sigma_{\mathrm{Mn}}} + \frac{N_{\mathrm{H}}\sigma_{\mathrm{H}}}{N_{\mathrm{Mn}}\sigma_{\mathrm{Mn}}} \tag{11}$$

On keeping the source inside the tank for at least about ten half-lives of ^{56}Mn (2.58 h), the radioactive equilibrium is reached. The energy of the most probable emitted photon from ^{56}Mn isotope is 846 keV with an abundance of 98.9%. The count rate

due to the decay of ^{56}Mn is then measured and correlated to the neutron yield using the efficiency of the $MnSO_4$ bath system with the following final equation:

$$Q = \frac{C}{\varepsilon}\left(1 + \frac{N_S\sigma_S}{N_{Mn}\sigma_{Mn}} + \frac{N_H\sigma_H}{N_{Mn}\sigma_{Mn}}\right)\left(\frac{1}{(1-L)(1-S)(1-F)}\right) \quad (12)$$

where 'ε' is the efficiency of the entire $MnSO_4$ bath system which is estimated separately using a known amount of active $MnSO_4$ solution, standardized using 4πβ-γ coincidence system [36–38]. L, S, and F are the leakage, source self-absorption, and fast neutron absorption correction factors, respectively. The system in general has the capability to measure the neutron yield from about 10^4 to 10^7 (n/s) within an uncertainty of ±3% ($k = 2$).

5.3.2 Proton Recoil Telescope

For the measurement of the neutron yield of mono-energetic fast neutrons viz., D-T interaction produced 14.57 MeV neutrons, the Proton Recoil Telescope (PRT) is used as a primary standard. It consists of a polyethylene radiator $(C_2H_4)_n$ and a charge particle detector viz. semiconductor detector or CsI(Tl) scintillation detector in an optimized geometrical arrangement kept inside a vacuum chamber made of aluminium. The typical arrangement pictorial view is shown in Fig. 19. The system works based on the principle of elastic collision of fast neutrons with the thin radiator resulting in the generation of recoil protons which after travelling through the vacuum are detected in the CsI (Tl) detector placed at a particular solid angle with respect to the radiator. Based upon the n-p double differential scattering cross section data from ENDF- VII, the efficiency (counts/neutron/steradian) of the system is analytically calculated for the specific mono-energetic neutrons [39, 40]. The neutron yield of the source is determined by using the efficiency. The system is mainly used for the measurement of the yield of 14.57 MeV neutrons produced from the accelerator-based D-T (^{2}H-^{3}H) neutron generator.

5.3.3 Precision Long Counter (PLC)

It is the secondary standard for the measurement of yield laboratory neutron sources, traceable to the $MnSO_4$ bath system. In general, it consists of a BF_3/^{3}He proportional counter which is kept at the centre of an optimized cylindrical moderating assembly made of High-Density Polyethylene (HDP). One annular absorber layer made up of 5% boron-loaded polythene is kept in between two concentric HDP cylindrical moderators. The thickness, length, and positions of different inner and outer moderators are optimized in such a way that their efficiency (counts/n/cm^2) becomes independent of neutron energy for a certain range [41]. It is a unidirectional system. The schematic layout of a typical De Pangher type long counter is given in Fig. 20**.** The standard works based on the moderation of fast neutrons by elastic

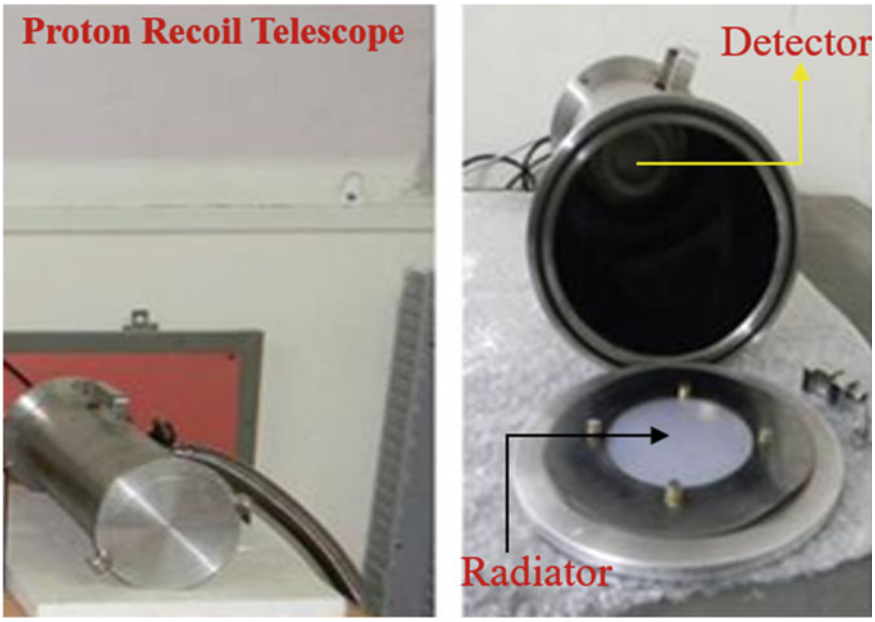

Fig. 19 Pictorial depiction of proton recoil telescope

collision with the moderating assembly to the thermal region which is detected by the thermal neutron detector giving output signal. The system is capable of calibrating commonly available neutron sources viz. ^{241}Am-Be, ^{241}Am-B, and ^{252}Cf at a lesser time in comparison with the $MnSO_4$ bath system and also sources of any shape/design.

The governing equation for the determination of neutron yield of sources is as follows:

$$Q = \frac{4\pi K}{\in f_A} \tag{13}$$

where Q is the neutron source yield (n/s) and f_A is the anisotropy factor of the source under calibrations. For standard design of the ISO-8529-1 recommended sources, the values are given whereas the same for other sources having any specific design may need to be evaluated previously. K is the response factor (cps.cm^2) or source-detector characteristic constant which can be obtained from the following equations:

$$[C_t(r) - C_i(r)]F_a(r) = \frac{K}{(r + r_0)^2} \tag{14}$$

where $C_t(r)$ and $C_i(r)$ are the measured total and in-scatter count rates for a distance 'r' in between the centre of the source to the front surface of the PLC. These are

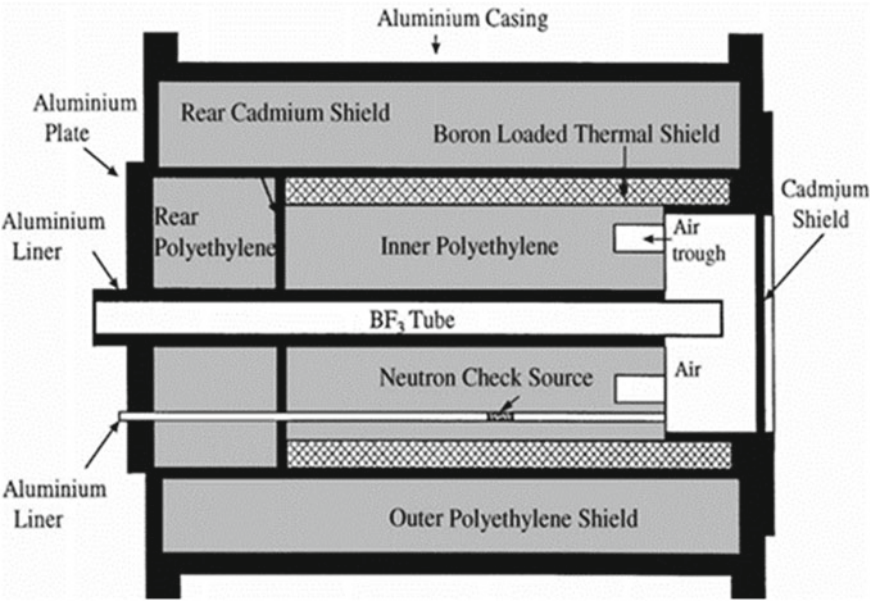

Fig. 20 Schematic layout of typical De Pangher type precision long counter

measured at the same distances in the absence and presence of the ISO-8529-2 recommended shadow cone, respectively [42]. $F_a(r)$ is the air out-scatter correction factor as mathematically given as follows:

$$F_a(r) = \exp^{\overline{\Sigma} r} \tag{15}$$

where $\overline{\Sigma}$ is the average cross section for air considering N and O as the main elements whose values are given in ISO-8529-2 and r the distance between the surface of PLC front surface and centre of the source. 'r_0' is the effective centre (distance from the inner surface of PLC to the inside of detector where it behaves as a point detector) which is obtained from the empirical equations for the PLC. In general, 'r_0' is a function of neutron energy and increases as the neutron energy increases.

It is worth mentioning that, both $MnSO_4$ bath system and PLC are typically in-house standards due to their heavy weight and bulky nature. However, in order to provide traceability in terms of neutron yield based on the request of other calibration laboratories, NMIs/DIs do develop light weight secondary standards which play an important role towards onsite calibrations of both poly-energetic as well as mono-energetic neutron sources [43, 44].

5.3.4 Standard Thermal Assembly in Graphite (STAG) Facility

It is a primary standard facility for the thermal neutron fluence rate. It consists of six ^{241}Am-Be sources placed inside a cubical assembly entirely made of graphite blocks. The entire outer surface is covered by the cadmium layer (~1 mm thick) in order to absorb the thermal neutrons. Fast neutrons emitted by the source get moderated by a graphite moderator which in turn produces thermal neutrons. In order to get a better uniformity of thermal neutron fluence rate, the sources have been in staggered positions. For practical applications, different side ports as well as central cavities [~4 cm × 4 cm × 15 cm] are kept where the exact thermal neutron fluence rates are determined by foil activation methods. The pictorial depiction of a typical STAG facility is shown in Fig. 21. The removable central channel is mainly used for irradiation of different solid-state detectors/dosimeters for different applications. In the same way, the thermal neutron fluence rates at the side ports are used for the calibration of all kinds of thermal neutron sensitive gas filled detectors which are used in nuclear reactors. Being the highest standard thermal neutron fluence rate, the degree of equivalence is established through international intercomparison using the foil activation technique as discussed in detail subsequently [45, 46].

Fig. 21 Pictorial depiction of a typical STAG facility

5.3.5 Thermal/Fast Neutron Field Characterizations: Foil Activation Technique

Determination of thermal or fast neutron fields at various installations such as reactors, accelerators, and also from a source housing facility mainly in terms of fluence rate is an extremely important and challenging task. The foil activation technique is one of the most widely used techniques by almost all NMIs to accomplish the same. Both thermal and fast neutron fluence rates with high accuracy can be measured using this method. The basic principle is as follows: Highly pure and thin (specifically for thermal neutron measurement) metallic foils with sufficient neutron activation cross section are irradiated in the respective neutron fields for the required time to get nearly saturation activity in the inactive foil. The induced radioactivity is then measured by preferably using the $4\pi\beta$-γ coincidence counter or HpGe detector and the neutron fluence rate is estimated from the activity with respect to the following general equation:

$$\dot{\Phi} = \frac{A\left(1 - \frac{1}{R_{Cd}}\right)}{N\sigma\left(1 - e^{-\lambda t_{irr}}\right)e^{-\lambda t_d}} \tag{16}$$

where $\dot{\Phi}$: thermal neutron fluence rate, A: measured radioactivity, N: Number of inactive atoms, σ: Activation cross section for thermal neutron, t_{irr}: Irradiation time, t_d: Decay time, λ: Decay constant of respective radioactive atom, and R_{Cd}: Cadmium ratio. R_{Cd} is a very important factor which allows one to correct for the estimation of pure thermal neutron fluence rate. For thermal neutrons various foils viz. ^{197}Au (n, γ) ^{198}Au, ^{115}In (n, γ) ^{116}In, ^{55}Mn (n, γ) ^{56}Mn, etc. are used whereas for fast neutrons ^{115}In (n, n') ^{115}In^{m}, $^{63/65}$Cu (n, 2n) $^{62/64}$Cu, and ^{58}Ni (n, p) ^{58}Co foils are used, respectively. Due to low activation cross sections of the foils used for fast neutron measurements, relatively thick foils are used along with longer irradiation times (~typically about 24 h) to get sufficient activity. For further details of the type of foils, their isotopic abundance, cross section, and type decay schemes, readers may refer [47]. It is important to mention here that it is a passive method and also based on cumulative exposure, therefore, cannot provide any sudden change of rate in fluence rate. However, the biggest advantage of the technique is that it can be used for the measurement of pulsed neutron fields and the measurements can be done at high temperature and pressure conditions, due to its small size and capability to withstand these extreme conditions.

5.3.6 Calibration Services of Neutron Monitoring Instruments

All the nuclear installations such as reactors and accelerators dealing with neutrons possess various neutron monitoring instruments such as fluxmeters, neutron rem counters, and electronic pocket dosimeters whose periodic calibrations are mandatory in terms of fluence rate, ambient and personnel dose equivalent rates, respectively.

NMIs/DIs do provide the calibration services of these instruments using various ISO-8529-1 (2021) recommended reference neutron sources viz. ^{241}Am-Be and ^{252}Cf. As per the latest CMS rules, all calibrations are traceable with respect to fluence rate fluence rate ($\dot{\Phi}$) only. However, the total fluence rates consist of primary as well as scattered neutrons. The % scattered contribution (due to the interaction of primary neutrons in the walls, floor, ceilings, etc.) is measured by using an ISO-8529-2 recommended shadow cone and the PLC.

6 Conclusion

The applications of ionizing radiation dosimetry and neutron measurements span scientific research, medicine, radiation protection, and radiation processing, with radionuclide metrology finding extensive use in nuclear medicine and radiation protection. This chapter highlighted the utmost significance of accurate and reliable measurements in such diverse domains. The evolution of measurement standards from human morphology to nature-based standards was discussed, reflecting a continuous process for precision. The globalization of trade prompted the establishment of international organizations under the 'Metre Convention', including CGPM, CIPM, and BIPM. The demand for quality products within a comparable system led to the formulation of the 'Mutual Recognition Arrangement' (CIPM-MRA) by CIPM, facilitating the recognition of calibration certificates across economies.

Within the field of metrology, economies are represented by their Metrology Institutes (NMI and DI), entrusted with the responsibility of maintaining national standards, providing traceable calibration, and collaborating with international organizations. Focusing specifically on ionizing radiation metrology, the formation of the Consultative Committee for Ionizing Radiation (CCRI) by CIPM highlights the intricate divisions in dosimetry, radionuclide measurements, and neutron measurements.

The chapter attempted to shed light on the pivotal role of primary measurement standards, primarily maintained by BIPM and NMIs/DIs of various countries, in ensuring the accurate realization of measurements. A brief overview of key primary standards in dosimetry, radionuclide measurements, and neutron measurements further emphasized the intricate calibration processes involved. For countries without primary standards, the maintenance of secondary standards calibrated against established primary standards ensures a harmonized approach to measurement accuracy on a global scale.

Overall, this chapter underscored the collaborative efforts and international frameworks essential for advancing ionizing radiation metrology and maintaining the integrity of measurement standards across diverse applications.

References

1. BIPM Webpage, https://www.bipm.org/en/. Last accessed on 26 Dec 2023
2. CIPM MRA-P-11, https://www.bipm.org/documents/20126/43742162/CIPM-MRA-P-11.pdf. Last accessed on 26 Dec 2023
3. CIPM MRA-P-12, https://www.bipm.org/documents/20126/43742162/CIPM-MRA-P-12.pdf. Last accessed on 26 Dec 2023
4. Subrahmanian G, IAEA Bull 21(5). The Development and Functions of the Indian Secondary Standards Dosimetry Laboratory. https://www.iaea.org/sites/default/files/21505093139.pdf. Last accessed on 26 Dec 2023
5. IAEA SSDL Charter 2 (2018) The IAEA/WHO network of secondary standards dosimetry laboratories. https://ssdl.iaea.org/Content/SSDL_Charter_2nd_Edition.pdf. Last accessed on 26 Dec 2023
6. KCDB Website, https://www.bipm.org/kcdb/. Last accessed on 26 Dec 2023
7. ICRU Report 60 (1998) Fundamental quantities and units for ionizing radiation. ICRU, Bethesda, Maryland 20814
8. IAEA TRS 469 (2009) Calibration of reference dosimeters for external beam radiotherapy. International Atomic Energy Agency, Vienna
9. Attix FH (1986) Introduction to radiological physics and radiation dosimetry. J. Wiley and Son, New York
10. Scymko MM, Szymko, Knyziak AB, Derlaciński M (2022) Graphite ionization chamber as an ionometric standard of absorbed dose to water for Co-60 gamma radiation. Measurement 194
11. Boutillon M, Perroche A, Ionometric determination of absorbed dose to water for cobalt-60 gamma rays
12. Graphite calorimeter, ARPANSA, https://www.arpansa.gov.au/our-services/testing-and-calibration/calibration/psdl/australian-primary-standards/graphite-calorimeter. Last accessed on 26 Dec 2023
13. Water calorimeter (LNHB), http://www.lnhb.fr/presentation-en/graphite-and-water-calorimeters/. Last accessed on 26 Dec 2023
14. Palmans H, Thomas R, Simon M, Duane S, Kacperek A, DuSautoy A, Verhaegen F, A small-body portable graphite calorimeter for dosimetry in low-energy clinical proton beams. Phys Med Biol 49(16)
15. Seuntjens J, Palmans H, Correction factors and performance of 4 °C sealed water calorimeter. Phys Med Biol 44(3)
16. PTW Roos chamber, https://www.ptwdosimetry.com/en/products/roos-electron-chamber. Last accessed on 26 Dec 2023
17. Baerg AP (1966) Measurement of radioactive disintegration rate by the coincidence method. Metrologia 2(23)
18. Baerg AP (1973) The efficiency extrapolation method in coincidence counting. Nucl Instrum Methods 112:143–150
19. Campion PJ (1959) The standardization of radio isotopes by the beta gamma coincidence method using high efficiency detectors. Int J Appl Radiat Isot 4:232
20. Dunworth JV (1940) The application of method of coincidence counting to experiments in nuclear physics. Rev Sci Instrum 11:167
21. Geiger H, Werner A (1924) Die Zahl der von Radium ausgesandten Teilchen. Z Phys 21:187
22. Novi H (1973) Proceedings of first international summer school on radionuclide metrology. Nucl Instrum Methods 112
23. NCRP Report 28 (1961) National council on radiation protection and measurements, a manual of radioactivity procedures. NCRP Report 28
24. NCRP Report 58 (1985) National council on radiation protection and measurements, a handbook of radioactivity measurements procedures. NCRP Report 58
25. Garcia-Toraño E, Martin Casallo MT, Rodriguez L, Grau A, Los Arcos JM (1991) On the standardization of beta-gamma emitting nuclides by liquid scintillation counting. In: Ross H, Noakes JE, Spaulding JD (eds) Liquid scintillation counting and organic scintillators. Lewis Publishers, Chelsea MI, pp 307–316

26. GrauMalonda A, Garcia-Toraño E (1982) Evaluation of counting efficiency in liquid scintillation counting of pure beta-ray emitters. Int J Appl Radiat Isot 33:249–253
27. Günther EW (1994) Standardization of 59Fe and 131I by liquid scintillation counting. Nucl Instrum Methods A 339:402
28. Cassette P, Vatin R (1992) Experimental evaluation of TDCR models for the 3-PMT liquid scintillation counter. Nucl Instrum Methods Phys Res A312:95
29. Grau MA, Coursey BM (1988) Calculation of beta-particle counting efficiency for liquid scintillation systems with three phototubes. Appl Radiat Isot 39:1191–1196
30. ISO 8769 (1988) Reference sources for the calibration of surface contamination monitors-beta–emitters (maximum beta energy greater than 0.15 MeV) and alpha–emitters, 1st edn. International Organization for Standardization, Geneva
31. Wuu J-L et al (2002)The alpha beta emitter measurement system in INER. Appl Radiat Isot56:261–264
32. King LE et al (2008) A new large-area 2π proportional counting system at NIST. Appl Radiat Isot 66:877–880
33. Mostert JC (2008) A primary standard for the measurement of alpha and beta particle surface emission rate at the National Metrology Institute of South Africa. Appl Radiat Isot 66:925–928
34. Lee KB et al (2005) Measurement of beta surface emission rate from an extended area 36 Cl source using a multiwire proportional counter. Appl Radiat Isot 63:99–105
35. CMCs (2020) Rules for ionizing radiation CMCs. www.bipm.org. Last accessed on 26 Dec 2023
36. Roberts NJ, Moiseev NN, Kralik M (2011) Radionuclide neutron source characterization techniques. Metrologia 48:S239–S253
37. Axton EJ (1986/87) Intercomparison of neutron-source emission rates (1979–1984). Metrologia 23:129–144
38. Singh Y, Ghodke S, Sen M, Sathian V, Kulkarni MS (2018) Evaluation of correction factors for Neutron source emission rate measurement using Manganese Sulphate bath system. In: Book of abstracts, IARCIC-2018, Mumbai, India
39. Ghodke S, Sathian V, Singh Y, Patel T, Santra S (2020) Absolute measurement of 14.57 MeV neutron fluence rate using proton recoil neutron telescope. Radiat Prot Dosim 190:307–319
40. Ghodke S, Sathian V, Singh Y, Santra S (2022) Efficiency calculation of proton recoil neutron telescope with relativistic correction for neutron energy 4 to 20 MeV. Appl Radiat Isot 184:110171
41. Ghodke S, Kumari S, Singh Y, Sathian V, Mahant AK, Sharma DN (2012) Standardisation of water-moderated ^{241}Am–Be neutron source using De Pangher neutron long counter: experimental and Monte Carlo modelling. Radiat Prot Dosim, 358–361
42. ISO-8529-2 (2000) Reference neutron radiations: calibration fundamentals of radiation protection devices related to the basic quantities characterizing the radiation field, Part-2
43. Sen M, Sathian V, Shobha G, Sujatha PN, Yashoda S, Kulkarni MS, Babu DAR (2015) Development of a portable transfer standard for the neutron source yield measurement using Fluka simulation. Nucl Instrum Methods Phys Res B 360:145–149
44. Sen M, Sathian V, Shobha G, Jitendra M, Tarun P, Yashoda S, Kulkarni MS (2018) Online measurement of neutron yield of D-D (^{2}H-^{2}H) neutron generator using indigenously developed light weight transfer standard. In: 33rd IARP international conference, Mumbai
45. Caswell RS, Lewis VE (1992) Neutron measurement intercomparisons sponsored by CCEMRI*, Section III (neutron measurements). Radiat Prot Dosim 44:105–110
46. Kannan A, Rao PS, Sachadev RN, Shaha VV, Sharma D, Srivastava PK, Activities of radiation standards section, BARC/I992/E/O48 https://inis.iaea.org/collection/NCLCollectionStore/_Public/24/067/24067417.pdf. Last accessed on 26 Dec 2023
47. Beckurts KH (1964) Book by K. H. Beckurts, K. Wirtz, Neutron physics. ISBN: 978-3-642-87614-1

Interaction of Ionizing Radiation with Matter

T. Palani Selvam, Vandana Shrivastava, and S. Chinnaesakki

1 Introduction

Radiation is classified into two main categories: *Nonionizing* and *Ionizing*, depending on its ability to ionize matter. The ionization potential of atoms, *i.e.* the minimum energy required for ionizing an atom, ranges from a few eV for alkali elements to 24.6 eV for helium (noble gas). Figure 1 shows the flow chart on the classification of radiation.

Ionization of any matter depends on the energy of incident radiation and the ionisation potential of the matter. Ionizing radiation can ionize matter directly as its energy is higher than the ionisation potential of the matter. Non-ionizing radiation cannot ionize matter as its energy is lower than the ionization potential of the matter. Ionizing radiation can be categorised into two categories:

(a) Directly ionizing radiation (charged particles) electrons, positrons, protons, Pions (negative π mesons), alpha particles, heavy ions (^{12}C, ^{14}N, or ^{20}Ne)
(b) Indirectly ionizing radiation (neutral particles) photons (x-rays, gamma rays), neutrons

The energy transfer mechanism of ionizing radiation plays a vital role in its detection and measurement. Hence, understanding its interaction with matter is important in radiation dosimetry. Depending upon the type of radiation the interactions may be with either nuclei or orbital electrons of the medium or both. In general, ionization or excitation is the primary mechanism resulting from the interaction. Type of interaction and its probability depend upon the radiation type, energy and medium.

T. P. Selvam (✉) · V. Shrivastava · S. Chinnaesakki
Health, Safety and Environment Group, Bhabha Atomic Research Centre, Mumbai 400085, India
e-mail: pselvam@barc.gov.in

D. K. Aswal (ed.), *Handbook on Radiation Environment, Volume 2*,
https://doi.org/10.1007/978-981-97-2799-5_4

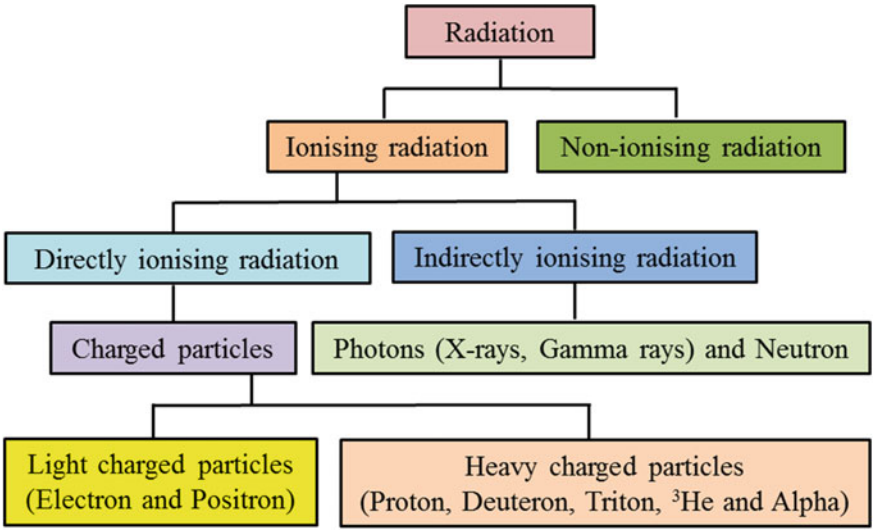

Fig. 1 Classification of radiation

Energy deposition to the medium by directly ionizing radiation is due to direct coulomb interactions between the incident direct ionizing charged particle and orbital electrons of atoms in the medium. Whereas for indirectly ionizing radiation (photons or neutrons) it is a two-step process: (a) firstly it releases a charged particle (photons release electrons or positrons, neutrons release protons or heavier ions) in the medium, and (b) these released charged particles deposit energy through coulomb interactions with orbital electrons of the atoms in the medium.

2 Interaction of Charged Particles with Matter

Charged particles are classified as below:

(a) Light charged particles (Examples: electrons and positrons)
(b) Heavy charged particles (Examples: proton, deuteron, Triton, ^{3}He, α particle, etc.)
(c) Heavier charged particles are nuclei of heavier atoms (Examples: ^{2}C, ^{14}N, ^{20}Ne, etc.)

A heavy or light charged particle has an associated coulomb electric force field and interacts with the orbital electrons of the absorber. This interaction process is called inelastic collision. During this inelastic collision, the charged particle transfers some amount of its kinetic energy to the orbital electrons. As a result of each such collision, the atomic electrons experience a transition to an excited state (*excitation*) or to an unbound state (*ionisation*).

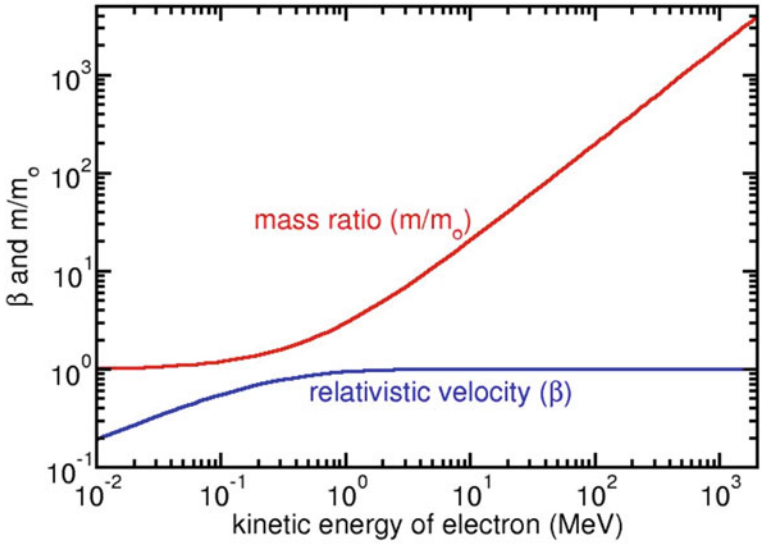

Fig. 2 Variation of relativistic velocity (β) and mass ratio (m/m_0) with kinetic energy of electron

The maximum energy transferred by a charged particle to an orbital electron in a single collision depends on the type of the charged particle and the velocity v with which it travels. For example, a classical particle travels with a velocity $v \ll c$ whereas a relativistic particle travels with a velocity $v \sim c$. When a charged particle of rest mass m_0 travels with a velocity of light c, its mass 'm' increases as given below:

$$m(v) = \frac{m_0}{\sqrt{1-\beta^2}} = \gamma\, m_0 \tag{1}$$

where $\beta = v/c$; $\gamma = 1/\sqrt{1-\beta^2}$; $\gamma = m(v)/m_0$.

Figures 2, 3 and 4 present an increase of relativistic velocity (β) and mass ratio ((m/m_0)) with kinetic energy of electron, proton and helium ion, respectively. Note that even 10 keV electron has a velocity of about 20% of the velocity of light. At this energy, mass of electron is higher by 2% as compared to its rest mass. For proton to attain 20% of velocity of light, the kinetic energy is about 20 MeV. When the kinetic energy proton is about 1 GeV, its mass increases by a factor of about 2 whereas for helium ion the mass attains a factor of 2 when the kinetic energy is about 3.75 GeV.

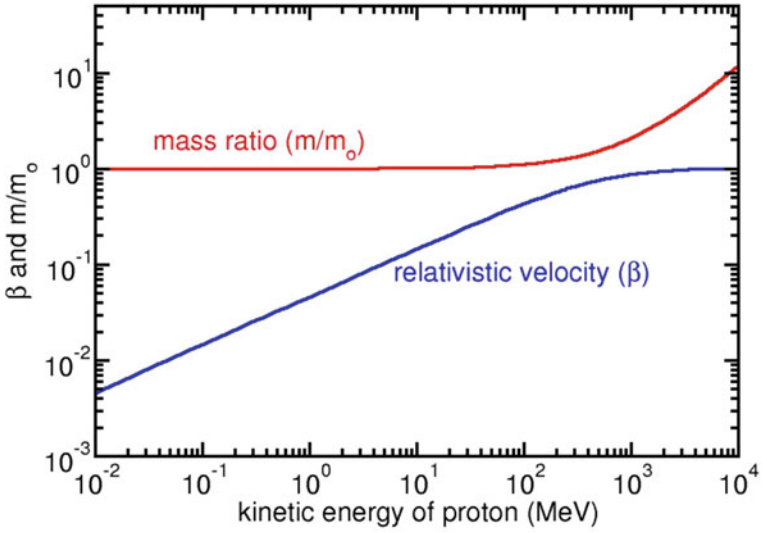

Fig. 3 Variation of relativistic velocity (β) and mass ratio (m/m_0) with kinetic energy of proton

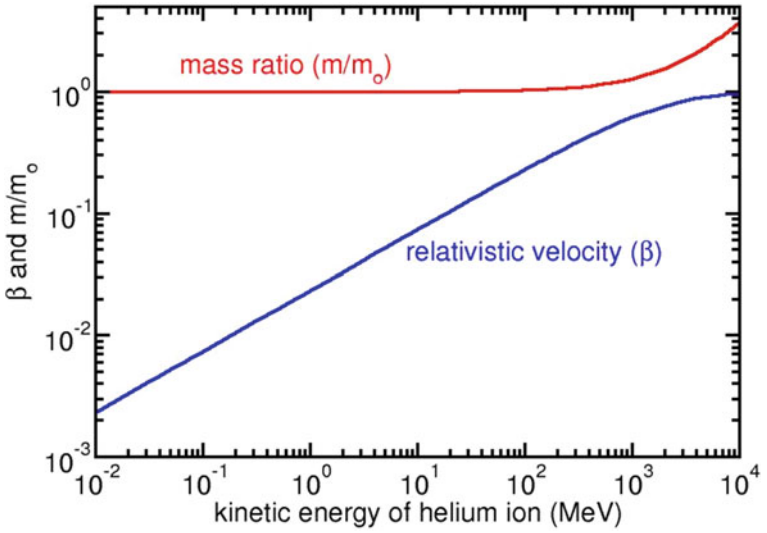

Fig. 4 Variation of relativistic velocity (β) and mass ratio (m/m_0) with kinetic energy of helium ion

2.1 Maximum Energy Transfer in a Single Collision

A classical heavy charged particle ($v \ll c$) of rest mass M having an initial kinetic energy E_i can transfer a maximum kinetic energy $\Delta E_{\max}$ to an orbital electron of mass m_e as per the following relation:

$$\Delta E_{\max} = \frac{4Mm_e}{(M + m_e)^2} E_i \tag{2}$$

In the case of heavy charged particles (example: protons and heavy ions), $M + m_e \approx M$.

$$\Delta E_{\max} = \frac{4m_e}{M} E_i \tag{3}$$

For protons ($M = 1836\ m_e$), $\Delta E_{\max} = 0.0022 E_i$ which implies that an incident proton with velocity in the classical range can transfer a maximum of 0.22% of its initial kinetic energy to orbital electron per collision.

Using $E_i = \frac{1}{2} M v^2$ in Eq. (3) gives

$$\Delta E_{\max} = 2m_e v^2 \tag{4}$$

This equation indicates that a classical heavy charged particle transfers two times of its initial velocity to the target electron, i.e. kinetic energy of the electron is $\frac{1}{2} m_e (2v)^2 = 2m_e v^2$.

When the velocity of the incident heavy charged particle gets relativistic ($\boldsymbol{\beta} \sim 1$):

$$\Delta E_{\max} = 2m_e c^2 \left(\frac{\beta^2}{1 - \beta^2} \right) \left[1 + 2(m_e/M)\left(1 - \beta^2\right)^{-1/2} + m_e/M)^2 \right]^{-1} \tag{5}$$

Note that for the relativistic heavy charged particles, the factor in the square bracket of Eq. (5) affects the maximum energy transferred to the orbital electron only by 0.23% at 1 GeV proton. At 1 GeV alpha particle, the factor affects only 0.03%. Hence, Eq. (5) can be rewritten as:

$$\Delta E_{\max} = 2m_e c^2 \left(\frac{\beta^2}{1 - \beta^2} \right) \tag{6}$$

Table 1 presents maximum kinetic energy $\Delta E_{\max}$ that can be transferred to a stationary target electron in a single collision by the incident proton and helium ion. In classical domain (Eq. (3)) there is a linear relationship between the kinetic energy of heavy charged particle $\Delta E_{\max}$ per collision. Whereas as the kinetic energy approaches relativistic, $\Delta E_{\max}$ per collision is higher when using the relativistic

relationship (Eq. 6) as compared to classical approximation (Eq. 4). For example, the difference is about 5% at 100 MeV proton and 14% at 1000 MeV helium ion (see Table 1).

Figure 5 and 6 present maximum kinetic energy transferred to the target electron in a single collision $\Delta E_{\max}$/collision. (keV/collision) for proton and helium ion, respectively, using the classical (Eq. (4)) and relativistic (Eq. (6)) relationships.

Note that when the incident charged particle is a positron, then by substituting $M = m_e$ in Eq. (3) gives $\Delta E_{\max} = E_i$ which means it can transfer its entire energy

Table 1 Maximum energy transferred to a stationary target electron per collision (in keV/collision) by the incident proton and helium ion

Kinetic energy (keV)	Proton			Helium ion		
	Relativistic velocity	Classical relationship (Eq. 4)	Relativistic Relationship (Eq. 6)	Relativistic velocity	Classical relationship (Eq. 4)	Relativistic Relationship (Eq. 6)
10^2	0.0146	0.22	0.22	0.0073	0.0548	0.0548
10^3	0.0461	2.20	2.20	0.0232	0.5483	0.5483
10^4	0.1448	21.8	21.9	0.0731	5.48	5.49
10^5	0.4282	218	229	0.2271	54.83	55.57
10^6	0.8750	2178	3340	0.6151	548	622
10^7	0.9926	2.18×10^4	1.38×10^5	0.9624	5483	12,840

The values are given using the classical and relativistic relationships

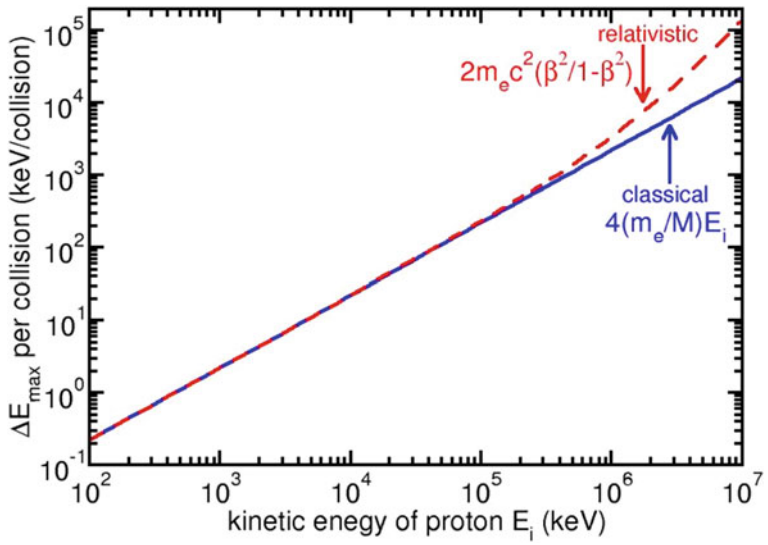

Fig. 5 Maximum kinetic energy transferred to target electron $\Delta E_{\max}$ in a single collision (keV/collision) by the incident proton of kinetic energy E_i

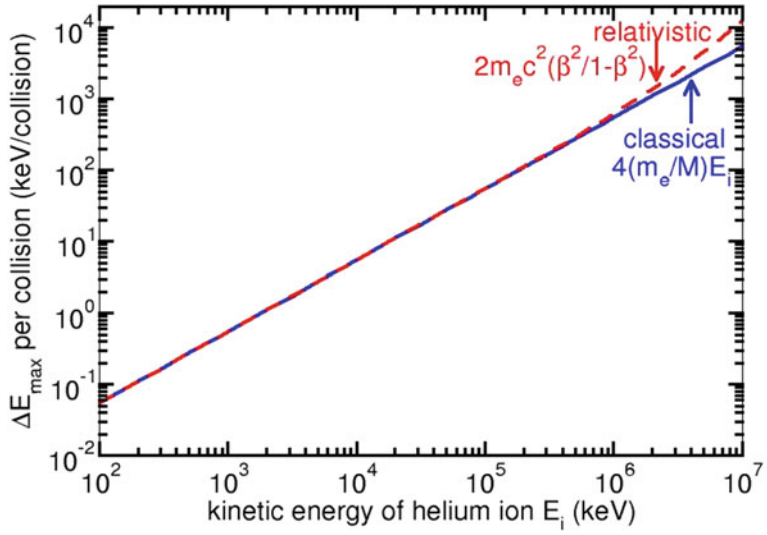

Fig. 6 Maximum kinetic energy transferred to target electron $\Delta E_{\max}$. in a single collision (keV/collision) by the incident helium ion of kinetic energy E_i.

to the orbital electron. Whereas in the case of incident electron, only half of its initial kinetic energy is transferred to the orbital electron $E_{\max} = E_i/2$, as the incident electron and the outgoing electron are indistinguishable after collision. This also implies that whichever electron carries higher energy will be treated as the primary electron. The above maximum energy transfer mechanism for incident electron or positron is applicable for both classical and relativistic cases.

3 Interaction of Light Charged Particles with Nucleus

Light charged particles (electrons and positrons) undergo the following interactions with the nucleus of the target material [1]:

(a) Elastic collision: In this collision, the incident particle deflects from its original direction after the collision by transferring fraction of its energy to the nucleus (energy transfer is negligible as the mass of the electron is negligible as compared to the nucleus). The incident electron does not radiate, nor does it excite the nucleus. The incident electron loses only the kinetic energy required for conservation of momentum between the incident electron and the nucleus.
(b) Nuclear reaction: A relativistic electron can undergo nuclear reaction when striking the nucleus with an emission of neutron or proton.
(c) Inelastic collision: In this Coulomb interaction bremsstrahlung photons are emitted when energetic electrons or positrons incident on the nucleus.

4 Interaction of Heavy Charged Particles with Nucleus

Heavy charged particles undergo the following interactions with the nucleus of the target material [1]:

(a) Elastic collision: In this collision, the incident particle deflects from its original direction after the collision by transferring a fraction of its energy to the nucleus (energy transfer is negligible when the nucleus is heavy). The incident heavy charged particle loses only the kinetic energy required for conservation of momentum between the incident electron and the nucleus. Example: Rutherford scattering of a particle with nucleus of gold.
(b) Inelastic collision: In this interaction, the nucleus is left in an excited state. The excited nucleus comes to ground state with an emission of gamma photon. This is called nuclear excitation. ${}_{Z}^{A}X\ (\alpha,\ \alpha){}_{Z}^{A}X^{*} \Rightarrow {}_{Z}^{A}X^{*} \rightarrow {}_{Z}^{A}X + \gamma$
(c) Nuclear reaction: The heavy charged particle collides with a nucleus resulting in production of two other particles.

Examples: When deuteron (d) bombards ^{14}N results in production of proton (p) and ^{15}N.

${}_{7}^{14}\mathrm{N(d, p)}{}_{7}^{15}\mathrm{N}$;

When alpha particle (α) bombards ^{239}Pu results in production of neutron (n) and ^{242}Cm.

^{239}Pu (α,n) ^{242}Cm

When proton (p) bombards^{18}O results in production of neutron (n) and ^{18}F

^{18}O (p,n) ^{18}F

In this case, ^{18}F further decays with β^{+} emission.

5 Stopping Power of Light Charged Particles

Stopping power is defined as gradual energy loss of charged particle when it travels through an absorbing medium. The stopping powers of light charged particles are categorized into two classes:

(a) Collision stopping power: It occurs when a charged particle interacts with orbital electrons of the absorber and transfers energy to the orbital electrons. Both heavy and light charged particles experience this type of interaction.
(b) Radiative stopping power: It occurs when a light charged particle interacts with nuclei of an absorber. In this interaction, light charged particles lose a significant fraction of its initial kinetic energy. This process is known as bremsstrahlung interaction.

Stopping power of a charged particle has a significant role in radiation dosimetry. It depends on the mass (M), charge (q), velocity (v) and kinetic energy (E_k) of charged particle as well as on the density (ρ) and atomic number (Z) of the absorbing medium.

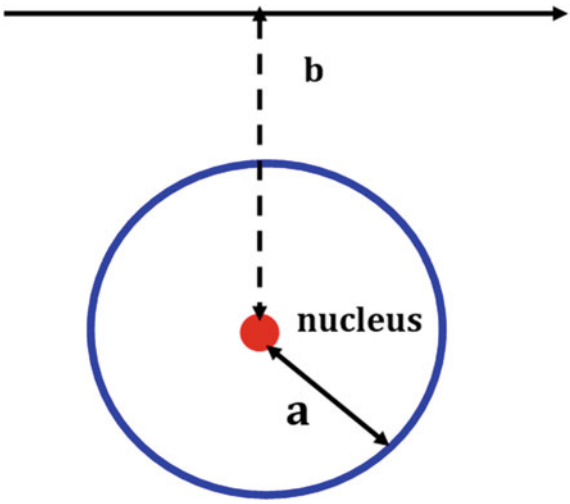

Fig. 7 Diagram depicting interaction of an electron with an atom. In the figure "a" denotes the atomic radius and "b" the impact parameter

When electrons are incident on an absorber, they lose energy through coulomb interactions with nuclei and orbital electrons of the absorber atoms (Fig. 7). The interactions are categorised into three categories that depend on the classical impact parameter b, which is defined as the perpendicular distance between the electron direction before the interaction and the atomic nucleus, compared to the classical atomic radius a:

i. For $b \gg a$, the charged particle will undergo a *soft collision* (Coulomb force interaction with orbital electron) with the whole atom and orbital electrons will receive a small amount of energy from the incident electron.
ii. For $b \approx a$, the charged particle will undergo a *hard collision* (Coulomb force interaction with orbital electron) with an orbital electron and it will receive a significant fraction of the electron's kinetic energy.
iii. For $b \ll a$, the charged particle undergoes a radiative collision with the atomic nucleus (Coulomb force interaction with external nuclear field) and the emitted bremsstrahlung photon energy may range from zero to E_k of charge particle. Note that only the electrons and positrons undergo radiative collision.

When a charged particle travels in a medium, it undergoes multiple columbic interactions before it loses its complete energy. In each *elastic* or *inelastic collision,* the charged particle's trajectory gets altered. In this interaction, the particle's kinetic energy is transferred to the medium (*collision loss*) or to photons (*radiative loss*). The rate of energy loss per unit of path length by a charged particle in a medium is called the linear *stopping power* ($\mathrm{d}E/\mathrm{d}x$), which has the unit of MeV/cm. Linear stopping power, divided by the density ρ ($\mathrm{g/cm^3}$) of the absorbing medium, is referred as mass stopping power $(S/\rho) = (1/\rho)(\mathrm{d}E/\mathrm{d}x)$. The unit of mass stopping power is

MeV-cm^2/g. The total mass stopping power $(S/\rho)_{\text{tot}}$ for a charged particle of kinetic energy E_K moving into an absorber of atomic number Z is the sum of the collision $(S/\rho)_{\text{coll}}$ and radiative $(S/\rho)_{\text{rad}}$ stopping powers.

5.1 Collision Stopping Power of Electrons and Positrons

Mass-collision stopping powers $(S/\rho)_{\text{coll}}$ of electrons or positrons are almost identical and are derived in ICRU Report 37 [2]. The final expression is given below:

$$(S/\rho)_{col} = 2\pi r_e^2 N_A \left(\frac{m_e c^2}{\beta^2}\right)\left(\frac{Z}{A}\right)\left[\ln\frac{T^2}{I^2} + \ln(1+\tau/2) + F^{\pm}(\tau) - \delta\right] \quad (7)$$

For electrons:

$$F^{-}(\tau) = \left(1-\beta^2\right)\left[1 + \tau^2/8 - (2\tau+1)\ln 2\right] \quad (8)$$

For positrons:

$$F^{+}(\tau) = 2\ln 2 - \left(\beta^2/12\right)\left[23 + 14/(\tau+2) + 10/(\tau+2)^2 + 4/(\tau+2)^3\right] \quad (9)$$

where

T	Kinetic energy of electron or positron
Z	Atomic number of the absorber
A	Atomic mass of the absorber
$m_e c^2$	Rest mass energy of electron
τ	$T/m_e c^2$ is the kinetic energy of electron/positron in units of electron rest mass energy
I	Mean excitation energy of the medium
δ	Density effect correction
$\beta = v/c$	Velocity of electron in units of velocity of light
N_A	Avogadro number
r_e	Classical radius of electron

The main factors that affect $(S/\rho)_{\text{col}}$ are:

$\frac{1}{\beta^2}$	This is the initial behavior of ionization loss, i.e. as the velocity of the electron increases stopping power decreases
$\frac{Z}{A}$	Represents electron density of the medium. For absorbers having higher electron density, stopping power will be higher
$F^{\pm}$	At relativistic energies this term results in increase in stopping power
δ	Decreases the stopping power due to polarization of medium by the electric field of incident particle.

5.2 Radiative Stopping Power of Electrons

Energy loss by electrons through radiation (bremsstrahlung) is distributed among secondary photons. The secondary photons can have energies from zero to the initial energy of the primary particle. The collision loss mechanism prevails more when the electron energy is low whereas bremsstrahlung process becomes significant at high energies. The definition of mass-radiative stopping power $(S/\rho)_{\text{rad}}$ is given by:

$$(S/\rho)_{\text{rad}} = \frac{N_A}{A} \int_0^T k \frac{\mathrm{d}\sigma_{\text{rad}}}{\mathrm{d}k} \mathrm{d}k \tag{10}$$

where $\frac{\mathrm{d}\sigma_{\text{rad}}}{\mathrm{d}k}$ is the differential radiative cross section that emits a photon energy k due to the electron interaction with the nuclear Coulomb field.

$$\mathrm{d}\sigma_{\text{rad}} = \sigma_0 B Z^2 \left(\frac{T + m_e c^2}{T} \right) \frac{\mathrm{d}k}{k} \text{ cm}^2/\text{nucleus} \tag{11}$$

T Total energy of electron (kinetic energy + rest mass energy).
Z Atomic number of the absorber

$\sigma_0 = \frac{1}{137} \left(\frac{e^2}{m_e c^2} \right)^2 = 0.58$ mb/nucleus

B in Eq. (11) is a slowly varying function of Z and T, of the order of magnitude of 10. At high energies, the electron loses large fraction of energy in the production of high-energy photons that again, may interact in the medium. Eventually, radiation losses can no longer compete with collision losses, and the energy of the primary electron is dissipated in excitation and ionization of the atoms.

For non-relativistic electrons

$$\sigma_{\text{rad}} = \frac{16}{3} \alpha r_e^2 Z^2 \tag{12}$$

For highly relativistic case:

$$\sigma_{\text{rad}} = 8\alpha r_e^2 Z^2 \left[\ln \left(\frac{T}{m_e c^2} - \frac{1}{16} \right) \right] \tag{13}$$

For extremely relativistic case:

$$\sigma_{\text{rad}} = 4\alpha r_e^2 Z^2 \left[\ln \left(\frac{183}{Z^{1/3}} + \frac{1}{8} \right) \right] \tag{14}$$

where

$\alpha = \frac{e^2}{4\pi\varepsilon_o} \frac{1}{\hbar c} = \frac{1}{137}$ (fine structure constant); $\hbar c = \frac{h}{2\pi} c \approx 200$ (MeV fm).

Thus, the expression for $(S/\rho)_{\text{rad}}$ is written as

$$(S/\rho)_{\text{rad}} = \frac{N_A}{A}\sigma_{\text{rad}} T \tag{15}$$

For electrons, the total stopping power is sum of collision and radiation stopping powers.

$$(S/\rho)_{\text{tot}} = (S/\rho)_{\text{col}} + (S/\rho)_{\text{rad}} \tag{16}$$

Figure 8a, b show collision and total stopping powers (collision + radiative) of air and water for electrons as a function of kinetic energy of electron, respectively. These data are based on ESTAR [3]. The stopping power decreases initially with increasing energy due to $1/\beta^2$ term (Eq. 7). Note that at relativistic energies, the collision stopping power increases due to the relativistic term in Eq. (7). As the energy of the electron increases there will be a contribution to stopping power due to radiative collisions. Hence, the total stopping power is higher than the collision stopping power for energy above 1 MeV and the difference increases as the energy increases. For example, the difference is about 1%, 1.5% and 2% at 10, 50 and 100 MeV respectively.

5.3 Comparison of Collision and Radiative Losses for Electrons

Bremsstrahlung yield is in proportion to Z^2 and linearly increases with electron energy. Whereas the collision stopping powers for high-energy electrons show a logarithmic increase with energy and linearly increases with Z/A. Bremsstrahlung becomes a dominant mechanism of energy loss at high energies. Therefore, as energy of electron increases, contributions of collision loss and radiative loss changes. At particular energy, the two losses are equal. This energy is called electron critical energy T_c.

The critical energy is approximated by Berger et al. [4]):

$$T_c = \frac{800}{Z + 1.2} \text{ (MeV)} \tag{17}$$

For tungsten T_c is about 10.6 MeV.

6 Radiation Length

The distance over which the kinetic energy of the incident electron is reduced by a factor of $(1/e)$ due to only radiation loss is known as radiation length and is denoted by X_0 and expressed in units of g/cm^2. As per the definition X_0 is based on energy

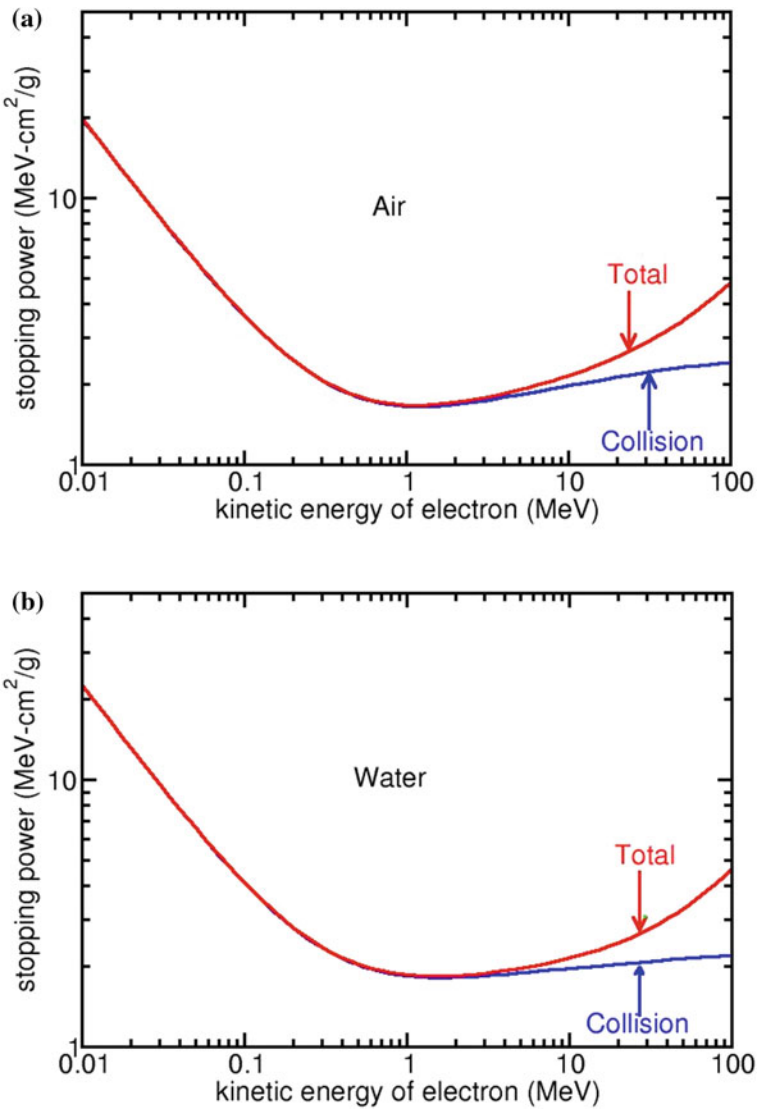

Fig. 8 Total and collision stopping power for electrons shown as a function of kinetic energy of electron: **a** air and **b** water. Data are taken from ESTAR [3]

loss due to radiation, derivation of expression for X_0 for an initial total energy of electron (T) utilizes the expression of mass-radiative stopping power of electrons corresponding to extremely relativistic case (Kenneth and Walter 1972) [5]:

$$\left(\frac{S}{\rho}\right)_{\text{rad}} = 4\alpha \frac{N_A}{A} r_e^2 Z^2 \left[\ln\left(\frac{183}{Z^{1/3}} + \frac{1}{8}\right)\right] T \tag{18}$$

Note that at the extremely relativistic case, one can assume $T = E_k + m_e c^2 \approx E_k$. Equation (18) can rewritten as

$$\left(\frac{S}{\rho}\right)_{\text{rad}} = -\frac{1}{\rho}\frac{\mathrm{d}E}{dx} = k\,E_k \tag{19}$$

where

$$k = 4\alpha\frac{N_A}{A}r_e^2 Z^2\left[\ln\left(\frac{183}{Z^{1/3}} + \frac{1}{8}\right)\right] \tag{20}$$

Here k is the constant for a given absorber whose atomic number is Z.

Equation (19) can be rewritten as

$$\frac{\mathrm{d}E}{E_k} = \frac{\mathrm{d}E}{E} = -k\,\mathrm{d}x \tag{21}$$

Here E_k is written as E and $\rho\,\mathrm{d}x$ as $\mathrm{d}x$ for convenience. Note by this approach $\boldsymbol{dx}$ has the units of g/cm^2.

Integrating Eq. (21) gives

$$\ln E = -k\,x + C \tag{22}$$

When $\boldsymbol{x} = 0$; $C = \ln E(0)$.

At depth x in the medium kinetic energy of electron is $E(x)$, i.e. $(x) < E(0)$; $E(0)$ implies kinetic energy electron at $\boldsymbol{x} = 0$ which is the initial kinetic energy of the electron.

Substituting $C = \ln E(0)$ in Eq. (22) gives

$$\ln\left[\frac{E(x)}{E(0)}\right] = -kx \tag{23}$$

Equation (23) is written as:

$$\frac{E(x)}{E(0)} = \mathrm{e}^{-kx} \tag{24}$$

As per the definition of radiation length

$$\frac{E(x)}{E(0)} = \frac{1}{e} \tag{25}$$

$$\mathrm{e}^{-kx} = \frac{1}{e} \tag{26}$$

This means $x = 1$; or $x = \frac{1}{k} = X_0 x = \frac{1}{k} = X_0$

$$\frac{1}{X_0} = \frac{N_A}{A} 4\alpha r_e^2 Z^2 \left[\ln\left(\frac{183}{Z^{1/3}} + \frac{1}{8} \right) \right] \tag{27}$$

$$X_0 = \left\{ \frac{N_A}{A} 4\alpha r_e^2 Z^2 \left[\ln\left(\frac{183}{Z^{1/3}} + \frac{1}{8} \right) \right] \right\}^{-1} \tag{28}$$

Note that in the energy region where the concept of radiation length is valid, i.e. energy loss is primarily due to radiative processes, $1/X_0$ is proportional to Z^2 (or X_0 is inversely proportional to Z^2) and is independent of kinetic energy of electron. When the effect of atomic electrons and a correction for the Born approximation [6] is included:

$$X_0 = \left\{ \frac{1 + 0.12\left(\frac{Z}{82}\right)^2}{\frac{N_A}{A} 4\alpha r_e^2 Z(Z+1)^2 \left[\ln\left(\frac{183}{Z^{1/3}} + \frac{1}{8} \right) \right]} \right\} \tag{29}$$

7 Range and Path Length

A charged particle such as an electron interacts with orbital electrons or with the nucleus of the medium that it encounters. The path of the electron is curved in nature due to extensive multiple scattering. The actual path followed by an electron in its travel through matter gives rise to the concept of pathlength, while the thickness of the material that the electron can just penetrate, gives rise to the concept of range. The distance the electron travels before being stopped is called the range. The term is not precise because, for stochastic reasons, not every electron starting with the same energy travels the same distance before stopping. As electrons slow, they experience deflections along the paths and statistical fluctuations in energy loss. Deflection of electrons is mostly due to elastic scattering with the nuclei of the absorber. Paths are not straight and for a group of particles all starting with the same energy, there are fluctuations in the total path length traveled.

Most of these interactions result in transfer of little fractions of the initial kinetic energy of the particle. This implies that the particle loses its kinetic energy gradually and continuously. This process is known as the Continuous Slowing Down Approximation (CSDA). The path length is the total distance traveled by an electron along its actual trajectory until the electron comes to rest, whatever may be its direction. The projected path range is the sum of individual path lengths projected onto the incident beam direction. The CSDA range of an electron with initial kinetic energy E_0 is obtained by integrating the reciprocal of the total stopping power $(S(E)/\rho)_{\text{tot}}$:

$$R_{\text{CSDA}} = \int_0^{E_0} \frac{\mathrm{d}E}{(S(E)/\rho)_{\text{tot}}} \tag{30}$$

Note that the CSDA range is a calculated quantity which represents the mean pathlength along the trajectory of electron, and not the depth of penetration in a defined direction.

Because of multiple scattering of electrons, there is a considerable difference in the values of pathlength and range. The difference is particularly pronounced in the case of low energy electrons and high Z materials. Figure 9 shows the typical electron track in a medium. The electron with an initial kinetic energy E_0 loses energy continuously in the medium. It produces secondary electrons which have sufficient energy, E_δ, to form its own track. These electrons are known as δ-electrons. The incident electron also produces bremsstrahlung photon of energy E_γ in the field of nucleus. Eventually, the electron comes to rest after losing its entire energy. The shortest distance traveled by the electron is known as range, R. Total curved path traveled by the electron is known as pathlength (see Fig. 9). Thus, $s > R$, always. The typical energy loss for a therapy electron beam, averaged over its entire range R, is about 2 MeV/cm in water and water-like tissues. Thus, a 2 MeV electron has a range of 1 cm in water.

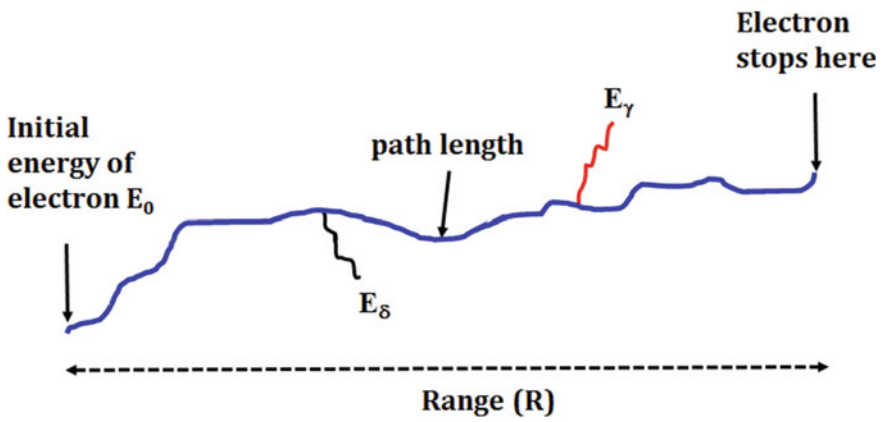

Fig. 9 Electron with an initial energy of E_0 traverses in a medium. Due to extensive multiple scattering, the pathlength is zigzag. On its track, the electron produces a secondary electron of kinetic energy E_δ and a bremsstrahlung photon of energy E_γ. The electron eventually stops after losing its entire energy. The dark thick blue line suggests that the electron loses energy continuously through ionization and secondary electrons thus produced are not able to form their own track as they are absorbed. R is the range of electron

8 Stopping Power of Heavy Charged Particle

8.1 Collision Stopping Power of Heavy Charged Particle

For a classical heavy charged particle ($\beta \ll 1$) of charge (ze) traveling through an absorber of atomic number Z and atomic weight A, the mass-collision stopping power is given by Podgorsak [1]:

$$\left(\frac{S}{\rho}\right)_{\text{col}} = \frac{(ze^2)^2 N_A}{4\pi\varepsilon_0^2 m_e v^2}\left(\frac{Z}{A}\right)\ln\left[\sqrt{\frac{2m_e v^2}{I}}\right] \tag{31}$$

where the symbols have usual meaning.

For non-realistic quantum–mechanical case [1]:

$$\left(\frac{S}{\rho}\right)_{\text{col}} = \frac{(ze^2)^2 N_A}{4\pi\varepsilon_0^2}\left(\frac{1}{m_e v^2}\right)\left(\frac{Z}{A}\right)\ln\left[\frac{2m_e v^2}{I}\right] \tag{32}$$

For realistic quantum–mechanical case [1]:

$$\left(\frac{S}{\rho}\right)_{\text{col}} = \frac{(ze^2)^2 N_A}{4\pi\varepsilon_0^2}\left(\frac{1}{m_e v^2}\right)\left(\frac{Z}{A}\right)\left[\ln\frac{2m_e v^2}{I} + \ln\beta^2 - \ln\left(1-\beta^2\right) + \beta^2\right] \tag{33}$$

By including the K-shell correction C_K/Z and the polarization correction δ into Bethe's relativistic quantum–mechanical expression results in the following relationship for the mass-collision stopping power for heavy charged particles [1]:

$$\left(\frac{S}{\rho}\right)_{\text{col}} = \frac{(ze^2)^2 N_A}{4\pi\varepsilon_0^2}\left(\frac{1}{m_e v^2}\right)\left(\frac{Z}{A}\right)\left[\ln\frac{2m_e v^2}{I} + \ln\beta^2 - \ln\left(1-\beta^2\right) + \beta^2 + C_k/Z - \delta\right] \tag{34}$$

In Eq. (34), the following processes lower the collision stopping power:

(a) C_K/Z accounts for non-participation of bound K-shell electrons in the ionization loss process which results in lowering the ionization loss. It is effective only at low kinetic energies of the charged particle.

(b) Polarization (density effect) correction δ which is applicable only to condensed media such as solids and liquids. A charged particle's traversal in condensed media results in the dipole distortion of the atoms near the track of the charged particle which weakens the Coulomb force field that would be experienced by the distant atoms. This phenomenon decreases its participation in the ionization loss process and results lowering of collision stopping power. Note that the polarization correction does not apply for gases, because in gases, the atoms are sparsely distributed. Density correction is also negligible for heavy charged

particles at energies of interest in medical physics, but is significant for light charged particles such as electrons and positrons [1].

The expression for mass-collision stopping power $(S/\rho)_{\text{col}}$ of heavy charged particle does not depend on mass of the particle. It depends on:

(a) atomic number Z and atomic mass A of the absorber in the form of (Z/A)
(b) mean ionization-excitation potential I of the absorber in the form of $(-\ln I)$
(c) particle velocity v: $(S/\rho)_{\text{col}}$ initially increases with velocity at non-relativistic velocity region, reaches a maximum value, then decreases as $1/v^2$, reaches a broad minimum (kinetic energy is around $3M_{\text{abs}}c^2$; where M_{abs} is rest mass of the absorber) and slowly increases as the velocity approaches velocity of light c (due to the relativistic term $\ln \beta^2 - \ln(1-\beta^2) + \beta^2$).

The kinetic energy of the heavy charged particle at which $(S/\rho)_{\text{col}}$ attains a maximum value can be obtained by differentiating the non-relativistic equation for $(S/\rho)_{\text{col}}$ with respect to kinetic energy of the heavy charged particle and setting it to zero. Thus, the kinetic energy of heavy charged particle at which $(S/\rho)_{\text{col}}$ attains a maximum value is given by Podgorsak [1]:

$$(E_k)_{\max} = \left(\frac{M\,I}{4\,m_e}\right)e \tag{35}$$

where M is the rest mass of the heavy charged particle, I is the mean ionization potential of the absorber, is rest mass of electron and $e = 2.78$. By using $= M_p\,A$, where M_p the mass of proton and A atomic mass number of the absorber, and setting $M_p/m_e \approx 2000$ and $e \approx 3$ [1]:

$$(E_k)_{\max} = 1500AI \tag{36}$$

Figure 10 presents mass-collision stopping power in water versus kinetic energy proton. These data are based on PSTAR [7]. In the low energy region mass-collision stopping power increases initially with energy and reaches a maximum value at about 100 keV. This trend is due to the reduced charge effect of the incident particle. Thereafter, it decreases due to $1/v^2$ effect. At higher energy (above 1 GeV), it gradually increases with kinetic energy due to relativistic effect.

8.2 Nuclear Stopping Power of Heavy Charged Particles

When a heavy charged particle travels in a medium, it will also lose energy by means of elastic collision with atomic nuclei. After this elastic collision, the nucleus recoils

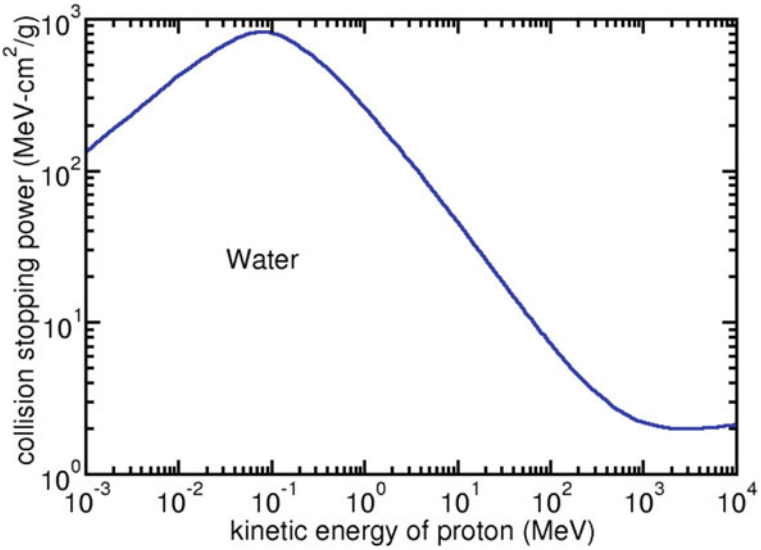

Fig. 10 Variation of mass-collision stopping power in water with kinetic energy proton. Data are taken from PSTAR [7]

and the recoil energy of the nucleus can be derived from the kinematics. Energy lost per unit path length due to this mechanism is called mass nuclear stopping power of heavy charged particles. Consider a heavy charged particle of mass M moving with kinetic energy E undergoes an elastic collision with the target nucleus of the atom of mass M_t. After the collision, the target nucleus scatters through an angle $\boldsymbol{\theta}$ with respect to the incident direction of the heavy charged particle. The nuclear stopping power is expressed as [8]:

$$\left(\frac{S}{\rho}\right)_{\text{nuc}} = \frac{2\pi N_A}{A} \int_0^{\pi} \frac{\mathrm{d}\sigma_{\text{el}}}{\mathrm{d}\Omega} W(\theta, E) \sin\theta \mathrm{d}\theta \tag{37}$$

where

$W(\theta, E)$ is the recoil energy of the target nucleus which depends on scattering angle $\boldsymbol{\theta}$ and $\boldsymbol{E}$. $W(\theta, T)$ is given by:

$$W(\theta, E) = \frac{4\, M\, M_t}{(M + M_t)^2} E \sin^2 \frac{\theta}{2} \tag{38}$$

The Rutherford cross section for elastic scattering for a high-energy region is described by:

$$\frac{\mathrm{d}\sigma_{\text{el}}}{\mathrm{d}\Omega} = \frac{N_A Z^2 z^2 r_e^2}{4A} \frac{m_e c^2}{pc\beta} \frac{1}{\sin^4(\theta/2)} \ (\text{MeV}^2\,\text{cm}^{-1}\,\text{sr}^{-1}) \tag{39}$$

where

z is charge of the incident heavy charged particle

p is relativistic momentum of the heavy charged particle and is given by

$$p = \frac{1}{c}\sqrt{\left(E + Mc^2\right)^2 - \left(Mc^2\right)^2} \tag{40}$$

As the radiative stopping power for heavy charged particles is negligible, the total stopping power is given by:

$$\left(\frac{S}{\rho}\right)_{\text{tot}} = \left(\frac{S}{\rho}\right)_{\text{col}} + \left(\frac{S}{\rho}\right)_{\text{nuc}} \tag{41}$$

Figure 11 presents nuclear stopping power of protons versus kinetic energy of protons for lead and water. This plot is based on PSTAR [7].

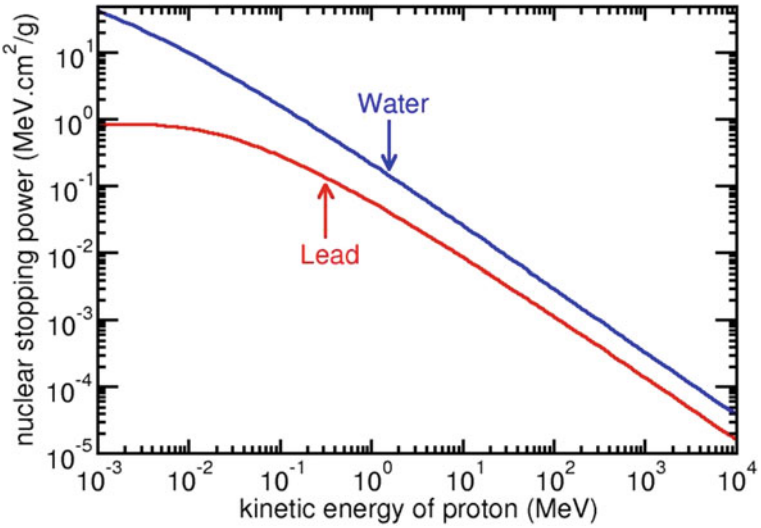

Fig. 11 Nuclear mass stopping power of protons versus kinetic energy of protons for lead and water. Data are based on PSTAR [7]

9 Scaling Relationships for Mass-Collision Stopping Power

Case 1: Same charged particle with same velocity v moving in two different media, i.e. medium m_1 and medium m_2. Electron densities of m_1 and m_2 are $(Z/A)_{m_1}$ and $(Z/A)_{m_2}$, respectively. The mass-collision stopping powers the charged particle for m_1 and m_2 are $(S/\rho)_{m_1}$ and $(S/\rho)_{m_2}$, respectively.

The mass-collision stopping powers of Medium 1 and Medium 2 are related by:

$$\frac{(S/\rho)_{m_1}}{(S/\rho)_{m_2}} = \frac{(Z/A)_{m_1}}{(Z/A)_{m_2}} \tag{42}$$

Assume m_1 and m_2 represent water and air, respectively. For water and air, the values of $\boldsymbol{Z/A}$ are 0.555 and 0.599, respectively. Hence, for any charged particle for a given velocity v the mass-collision stopping power of water will be about 11% higher than that of air considering that corrections for density mean ionization potential of water and air are negligible.

Case 2: Two different charged particles (say alpha particle and proton) of charges z_1 and z_2 (suffix on z represents particle type) both moving with the same velocity v in the same medium. The mass-collision stopping powers of these two charged particles are represented by $(S/\rho)_1$ and $(S/\rho)_2$, respectively (suffix on (S/ρ) represents particle type).

As the velocity and medium are the same, the ratio of mass-collision stopping powers will only depend on charges of the particles. Hence, we have the following relationships:

$(S/\rho)_1 \propto z_1^2$; $(S/\rho)_2 \propto z_2^2$.

The mass-collision stopping powers of the two charged particles are related by:

$$\frac{(S/\rho)_1}{(S/\rho)_2} = \frac{z_1^2}{z_2^2} \tag{43}$$

$z_1 = 2$ for alpha particle and $z_2 = 1$ for proton.

$$\frac{(S/\rho)_1}{(S/\rho)_2} = \frac{2^2}{1^2} = 4 \tag{44}$$

Thus, mass-collision stopping power of an alpha particle is four times higher than that of proton (or electron) when they travel with the same velocity while the medium is same.

Case 3: Same as Case 2, but particle of charge z_1 travels in medium m_1 and particle of charge z_2 travels in medium m_2, while the velocity v of the two charged particle is same. Suffix on (S/ρ) represents particle type.

$$\frac{(S/\rho)_1}{(S/\rho)_2} = \left(\frac{z_1^2}{z_2^2}\right)\frac{(Z/A)_{m_1}}{(Z/A)_{m_2}} \tag{45}$$

Case 4: Same as Case 2, but two different charged particles of charges z_1 and z_2 are traveling with velocity v_1 and v_2, respectively. Suffix on (S/ρ) represents particle type.

$$\frac{(S/\rho)_1}{(S/\rho)_2} = \frac{z_1^2}{z_2^2}\frac{v_2^2}{v_1^2} \tag{46}$$

Case 5: Same as Case 4, but two different media.$(S/\rho)_1^{m_1}$ and $(S/\rho)_2^{m_2}$ are mass-collision stopping powers of charged particle of charge z_1 for medium m_1 and charged particle of charge z_2 for medium m_2, respectively.

$$\frac{(S/\rho)_1^{m_1}}{(S/\rho)_2^{m_2}} = \frac{z_1^2}{z_2^2}\frac{v_2^2}{v_1^2}\frac{(Z/A)_{m_1}}{(Z/A)_{m_2}} \tag{47}$$

10 Scaling Relationships for Range of Charged Particles

Case 1: Two similar charged particles traveling in two different media, i.e. m_1 and m_2. Assume the particle has the same velocity in both m_1 and m_2. Mass densities of m_1 and m_2 are ρ_{m_1} and ρ_{m_2}, respectively. The electron densities of m_1 and m_2 are $(Z/A)_{m_1}$ and $(Z/A)_{m_2}$, respectively.

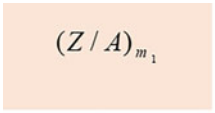

Medium $m_1; \rho_{m_1}$

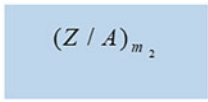

Medium $m_2; \rho_{m_2}$

Ranges of the charged particle in the two media are given by:

$$R_1 \propto \frac{1}{(Z/A)_{m1}} \frac{1}{\rho_{m1}} \tag{48}$$

$$R_2 \propto \frac{1}{(Z/A)_{m2}} \frac{1}{\rho_{m2}} \tag{49}$$

$$\frac{R_1}{R_2} = \frac{(Z/A)_{m2}}{(Z/A)_{m1}} \frac{\rho_{m2}}{\rho_{m1}} \tag{50}$$

For varieties of materials $\frac{Z}{A} \approx \frac{1}{2}$

Hence, it is reasonable to write

$$\frac{R_1}{R_2} \approx \frac{\rho_{m_2}}{\rho_{m_1}} \tag{51}$$

Case 2: Two different charged particles (say alpha particle and proton) of charges z_1 and z_2 (suffix on z represents particle type) both moving with the same velocity v in the same medium. The mass-collision stopping powers of these two charged particles are represented by $(S/\rho)_1$ and $(S/\rho)_2$, respectively (suffix on (S/ρ) represents particle type).

Charge z_1 **and velocity** v

Charge z_2 **and velocity** v

We know that Range R (in cm) of a charged particle whose initial kinetic energy E_0 and velocity β_0 is given by:

$$R = \int_{E_0}^{0} \frac{\mathrm{d}E}{-\frac{\mathrm{d}E}{\mathrm{d}x}} \tag{52}$$

$$R \propto \frac{1}{-\frac{dE}{dx}} \tag{53}$$

Therefore

$$R \propto \frac{1}{z^2}; R \propto \frac{1}{(Z/A)}; R \propto \frac{1}{\rho} \text{ as } -\frac{dE}{dx} \propto \rho; R \propto \beta^2.$$

Kinetic energy of the charged particle E is given by a relativistic relationship

$$E = (\gamma - 1)M_0c^2 \tag{54}$$

where M_0 is the rest mass of the charged particle and $\gamma = \frac{1}{\sqrt{1-\beta^2}}$.

Differentiating Eq. (54) with respect to β gives:

$$dE = -\frac{M_0c^2}{\sqrt{(1-\beta^2)^{3/2}}} 2\beta d\beta \tag{55}$$

$$R = \int_{E_0}^{0} \frac{dE}{-\frac{dE}{dx}} \tag{56}$$

$$R = \frac{1}{(Z/A)} \frac{1}{\rho} \frac{1}{z^2} \int_0^{\beta_0} \frac{\beta^2}{\ln\left\{\frac{2m_ec^2\beta^2}{I(1-\beta^2)}\right\} - \beta^2} M_0c^2 \frac{\beta d\beta}{(1-\beta^2)^{3/2}} \tag{57}$$

Thus in general

$$R \rightarrow f[M, z, (Z/A), \rho, \beta] \tag{58}$$

$$R \propto \frac{1}{(Z/A)} \frac{1}{\rho} \frac{1}{z^2} M_0 F(\beta_0, I) \tag{59}$$

where I is mean ionization potential.

For charged particle of charge z_1 and rest mass M_1:

$$R_1 \propto \frac{1}{(Z/A)} \frac{1}{\rho} \frac{1}{z_1^2} M_1 \tag{60}$$

For charged particle of charge z_2 and rest mass M_2:

$$R_2 \propto \frac{1}{(Z/A)} \frac{1}{\rho} \frac{1}{z_2^2} M_2 \tag{61}$$

For two different particles of charges z_1 and z_2 traveling with the same velocity in a given medium, R_1/R_2 is given by:

$$\frac{R_1}{R_2} = \frac{M_1}{M_2}\frac{z_2^2}{z_1^2} \tag{62}$$

11 Čeronkov Radiation

It is known that:

(a) A charged particle radiates energy in free space in the form of photon radiation only if accelerated or decelerated
(b) A charged particle in rectilinear uniform velocity motion in free space does not lose its kinetic energy in the form of photon radiation

However, if a charged particle moves with uniform rectilinear motion through a transparent dielectric material, part of its kinetic energy is radiated in the form of electromagnetic radiation. This happens when the velocity of the charged particle v exceeds phase velocity of light in a particular medium c_n:

$$v \gg c_n = \frac{c}{n} \tag{63}$$

where n is the index of light in the particular medium and c is the velocity of light in vacuum. This phenomenon of emission of light in the visible region is known as Čeronkov radiation. Čeronkov radiation is bluish in color

The principle of emission of Čeronkov radiation is shown in Fig. 12. A charged particle of velocity v travels from A to C and $\triangle t$ is the time taken to cover this distance $AC\ (= v\triangle t)$ [8]. The electromagnetic radiation emitted from A reaches C in time $\triangle t$. So $AB = (c_n/\triangle t)$. Note that the wavefronts propagate slower than the particle itself, therefore the radiation will always be confined to a cone behind the particle [9]. The radiation moves outward perpendicular to the walls of the cone, at an angle θ relative to the direction of the particle. This angle is fixed by the cone's geometry which can be obtained by comparing the distance traveled by the wavefronts and particle [9]. As the light wave is emitted in a conical fashion with a polar angel of θ which satisfies [8]:

$$\text{Cos}\theta = \frac{AB}{AC} = \frac{(c_n/t)}{v\triangle t} = \frac{(c/n)\triangle t}{\beta c\triangle t} = \frac{1}{\beta n} < 1 \tag{64}$$

The emission of Čeronkov radiation involves a large number of atoms of the dielectric medium which are polarized by the fast charged particles moving with uniform velocity through the medium [1]. The orbital electrons of the polarized atoms

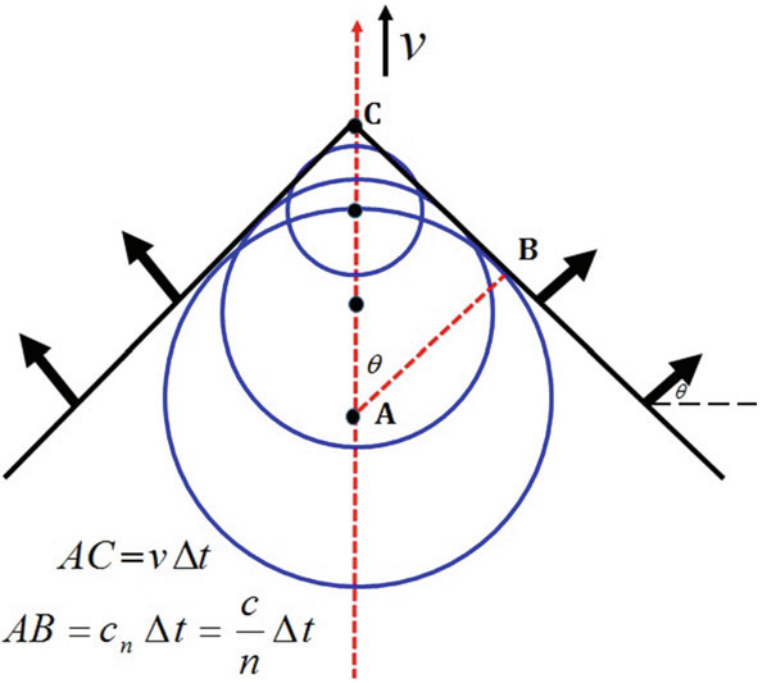

Fig. 12 Illustration of emission of Čeronkov radiation [9]

are accelerated by the fields of the charged particle and emit radiation coherently when $v \gg c_n = c/n$. Thus, the emission of these light photons does not come directly from the charged particle.

Some features of Čeronkov radiation are described below [1]:

(a) Čeronkov radiation is emitted along the surface of a forward directed cone centered on the charged particle direction of motion. The cone is specified as:

$$\text{Cos}\,\theta_{\text{cer}} = \frac{c_n}{v} = \frac{c}{nv} = \frac{1}{\beta n} \tag{65}$$

where θ_{cer} is the Čeronkov angle defined as the angle between the direction of motion of charged particle and the envelope of the cone.

(b) Equation (65) suggests that for a given charged particle and dielectric medium there is a threshold velocity v_{th} below which emission of Čeronkov radiation is not possible.

$$v_{\text{th}} = \frac{c}{n};\ \ \beta_{\text{th}} c = \frac{c}{n}\ ;\ \beta_{\text{th}} = \frac{1}{n}$$

- When $v > v_{\text{th}}$ Čeronkov radiation is emitted with Čeronkov angle θ_{cer}
- When $v < v_{\text{th}}$ Čeronkov is radiation not emitted
- For water, $n = 1.33$; $v_{\text{th}} = \frac{c}{n} = \frac{c}{1.33} = 0.75\,c$. This velocity threshold corresponds to energy threshold of Čeronkov radiation

$$(E_k)_{\text{th}} = \frac{m_e c^2}{\left(\sqrt{1-\beta_{\text{th}}^2}\right)} = \frac{n \times 0.511}{\sqrt{n^2-1}} = 0.775 \text{ MeV} \tag{66}$$

(c) Total energy appearing as Čeronkov radiation is negligible when compared to the total energy loss by a charged particle through collision and radiative losses. For example, electrons lose about 2 MeV/(g/cm^2) in water through collision and radiative losses and only about 400 keV/(g/cm^2) through Čeronkov losses.

(d) Equation (65) shows that a maximum angle of emission $(\theta_{\text{cer}})_{\max} = \arccos(1/n)$. For relativistic electrons ($\beta \to 1$) in water ($n = 1.33$), $(\theta_{\text{cer}})_{\max} = 41.2^\circ$

(e) Frequencies of Čeronkov radiation appear in the high frequency region of visible light of electromagnetic spectrum, but do not extend to the x-ray region because for x-rays $n < 1$.

12 Interaction of Photons with Matter

For x and gamma photons, in terms of energy loss, there are three important processes such as photoelectric effect, Compton effect and pair production.

12.1 Thompson Scattering

The scattering of photons by free electrons is known as Thomson scattering. Such scattering is possible when the incident photon energy is small, i.e. $h\nu \ll m_e c^2$. The differential Thomson electronic cross section per unit solid angle [mb/(electron-steradian)] is given by:

$$\left(\frac{\mathrm{d}\sigma_e}{\mathrm{d}\Omega}\right)_{Th} == \frac{r_e^2}{2}\left(1+\cos^2\theta\right) \tag{67}$$

Here θ is angle of scattering ($\theta = 0^\circ$ to π). Figure 13 shows the plot of $\left(\frac{\mathrm{d}\sigma_e}{\mathrm{d}\Omega}\right)_{\text{Th}}$ versus θ.The plot shows that at $\theta = \pi/2$, the value of $\left(\frac{\mathrm{d}\sigma_e}{\mathrm{d}\Omega}\right)_{\text{Th}} = 39.8$ mb/(electron-steradian) at $\theta = 0$ and $\theta = \pi$, the values is 79.5 mb/(electron-steradian).

The differential Thomson electronic cross section per unit polar angle, i.e. fraction of incident energy scattered into a cone of angle between θ and $\theta + d\theta$ is given by:

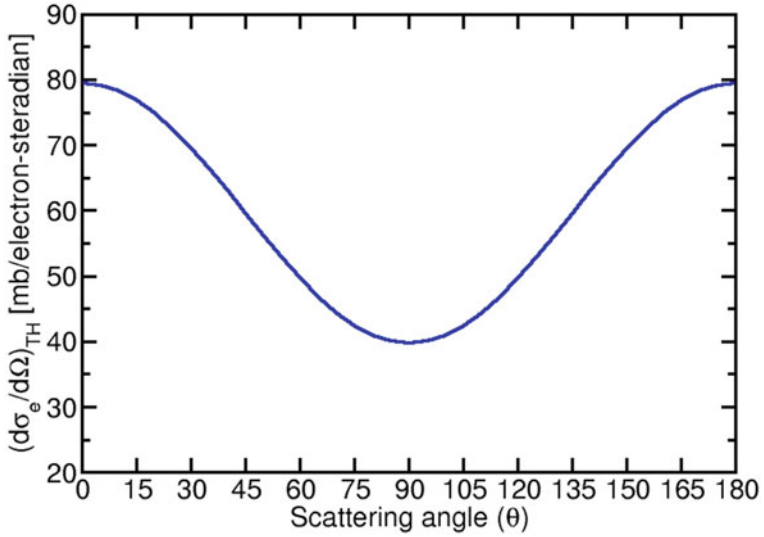

Fig. 13 Plot of differential Thomson electronic cross section per unit solid angle versus polar angle. Figure adapted from [2]

$$\left(\frac{\mathrm{d}\sigma_e}{\mathrm{d}\theta}\right)_{\mathrm{Th}} = \left(\frac{\mathrm{d}\sigma_e}{\mathrm{d}\Omega}\right)_{\mathrm{Th}} \frac{\mathrm{d}\Omega}{\mathrm{d}\theta} = 2\pi \sin\theta \frac{r_e^2}{2}\left(1+\cos^2\theta\right)^2 = \pi r_e^2 \sin\theta \left(1+\cos^2\theta\right) \tag{68}$$

Figure 14 presents $\left(\frac{\mathrm{d}\sigma_e}{\mathrm{d}\theta}\right)_{\mathrm{Th}}$ versus θ. The figure shows that $\left(\frac{\mathrm{d}\sigma_e}{\mathrm{d}\theta}\right)_{\mathrm{Th}} = 0$ at $\theta = 0$ and $= 180°$, reaches maxima at $\theta = 55°$ and $\theta = 125°$ and attains a minimum at $\theta = 90°$.

The total Thomson electronic cross section is obtained by integrating Eq. (67) overall scattering angles
($\theta = 0°$ to π):

$$\sigma_{e,\mathrm{Th}} = \int \left(\frac{\mathrm{d}\sigma_e}{\mathrm{d}\Omega}\right)_{\mathrm{Th}} \mathrm{d}\Omega = 2\pi \int_0^{\pi} \left(\frac{\mathrm{d}\sigma_e}{\mathrm{d}\Omega}\right)_{\mathrm{Th}} \sin\theta \mathrm{d}\theta = 2\pi r_e^2 \int_0^{\pi} \left(1+\cos^2\theta\right)\mathrm{d}\theta \tag{69}$$

$$\sigma_{e,\mathrm{Th}} = \frac{8\pi}{3} r_e^2 = 0.665\, b \tag{70}$$

Note that this is an important relation and does not contain any photon energy term, thus the value $\sigma_{e,\mathrm{Th}} = 0.665\, b$ is independent of photon energy.

The total atomic Thomson cross section is given by:

$$\sigma_{a,\mathrm{Th}} = Z\, \sigma_{e,\mathrm{Th}} \tag{71}$$

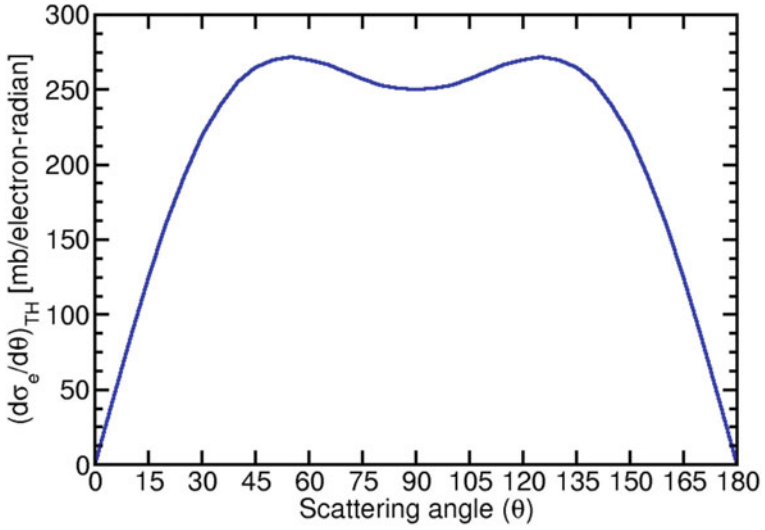

Fig. 14 Plot of differential Thomson electronic cross section per unit polar angle versus polar angle. Figure adapted from [2]

Thus, $\sigma_{a,Th}$ linearly depends on atomic number Z of the absorber. For incident photon energy larger than the binding energy of electron E_B but smaller than $m_e c^2$, i.e. $E_B \ll h\nu \ll m_e c^2$, Eq. (67) is valid. However, at larger θ and larger photon energies, i.e. $h\nu \rightarrow m_e c^2$, Thomson coherent scattering with free electron diminishes in favor of incoherent Compton scattering.

12.2 Rayleigh Scattering

Rayleigh scattering is a process in which the incident photons are scattered by the bound atomic electrons of the absorber. In this process, the atom is neither excited nor ionized. The atom as a whole absorbs the momentum transferred by the photons. The incident photon is then scattered through an angle θ (Fig. 15). As the energy of recoil atom is very small, there is no change in the energy of incident photon after Rayleigh scattering. The scattering angles are relatively small because the recoil atom does not produce atomic excitation or ionization and the bound electrons of the absorber revert to their original state.

The differential Rayleigh atomic cross section per unit solid angle in terms of Thomson electronic scattering cross section $\left(\frac{d\sigma_e}{d\Omega}\right)_{Th}$ is given by:

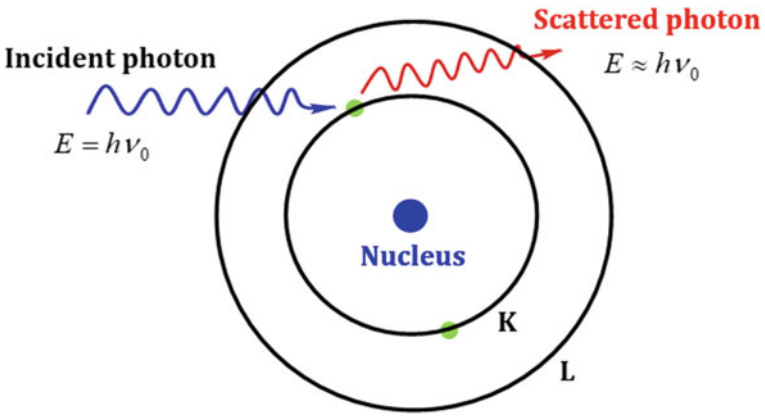

Fig. 15 Pictorial representation of Rayleigh scattering. The incoming photon undergoes a collision with the atomic electron which transfers negligible energy to the atom. The photon is deviated from its original direction without losing energy

$$\left(\frac{d\sigma_a}{d\Omega}\right)_R = \left(\frac{d\sigma_e}{d\Omega}\right)_{Th} [F(x,z)]^2 = \frac{r_e^2}{2}\left(1+\cos^2\theta\right)[F(x,z)]^2 \tag{72}$$

where

$\left(\frac{d\sigma_e}{d\Omega}\right)_{\text{Th}}$ is Thomson electronic scattering cross section [barn/(electron-steradian].

$[F(x,z)]$ is atomic form factor which depends on atomic number Z of the absorber and momentum transfer variable $x = \sin(\theta/2)/\lambda$; with $\boldsymbol{\lambda}$ being the wavelength of incident photon.

The differential Rayleigh atomic cross section per unit polar angle [barn/(atom-radian)] is given by:

$$\begin{aligned}\left(\frac{d\sigma_a}{d\theta}\right)_R &= \left(\frac{d\sigma_a}{d\Omega}\right)_R \frac{d\Omega}{d\theta} = \left(\frac{d\sigma_e}{d\Omega}\right)_{\text{Th}} 2\pi \sin\theta [F(x,z)]^2 \\ &= \pi r_e^2 \sin\theta\left(1+\cos^2\theta\right)[F(x,z)]^2\end{aligned} \tag{73}$$

12.3 Photoelectric Effect

Photoelectric effect is predominant with low energy photons and high atomic number of the absorber. In this process, the photon interacts with an absorber atom and gets absorbed completely. The incoming photon disappears and as a result, an electron (photoelectron) is ejected from one of the bound shells of the atom (Fig. 16). The most probable origin of the photoelectron is the most tightly bound or *K*-shell of the atom. The photon energy $h\nu_0$, the kinetic energy of the photoelectron E_{pe} are related

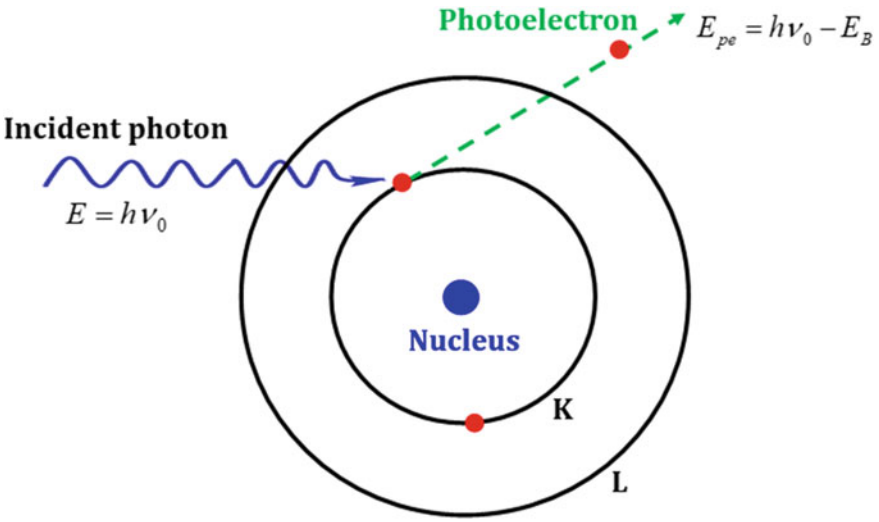

Fig. 16 Schematic diagram of photoelectric effect. The incident photon with energy $h\upsilon_0$ is absorbed and knocks out the K-shell electron having binding energy E_B. The ejected photoelectron moves with a kinetic energy of $E_{\text{pe}} = h\upsilon_0 - E_B$

by:

$$E_{\text{pe}} = h\upsilon_0 - E_B \tag{74}$$

Here, E_B is the binding energy of the photoelectron usually the K-shell.

On ejection of an electron from a shell, a vacancy is created in the atom which results in the atom to become excited. There are two probable phenomena by which an excited atom gets equilibrium: (a) ejection of mono-energetic Auger electrons from the atom by redistributing excess energy to the available electrons or (b) an electron from another higher energy shell would fall into the vacancy created and as associated characteristic X-ray is emitted. The emitted X-ray may again undergo photoelectric absorption process and produce the X-ray. This process may continue until all the energy of photon is absorbed. To conserve momentum in this process, the recoiling atom retains a very small amount of energy upon ejection of an electron which is generally ignored for all practical purposes.

The probability of photoelectric absorption per atom, τ with photon energy E and atomic number of absorber Z is approximated as

$$\tau \cong c \times \frac{Z^n}{E^{3.5}} \tag{75}$$

Depending upon the value of E the exponent n varies between 4 and 5.

12.4 Compton Scattering

In Compton Scattering, the incident photon with initial energy $h\nu_0$ and momentum $h\nu_0/c$ interacts with an orbital electron which is either at rest or loosely bound. After the collision, the incident photon is scattered through an angle θ with a reduction in energy ($h\nu'$) and momentum ($h\nu'/c$). The orbital electron scatters through an angle $\boldsymbol{\varphi}$ with kinetic energy E_e and momentum p_e (Fig. 17). Depending upon angle of scattering of photon, the orbital electron may receive kinetic energy from zero to a large fraction of energy of photon. The Compton scattering process is illustrated in Fig. 17.

Using the following three relativistic relationships for conservation of total energy and momentum an expression for $h\nu'$ and E_e can be derived.

$$h\nu' = \frac{h\nu_0}{1 + \alpha(1 - \cos\theta)} \tag{76}$$

where $\alpha = h\nu_0/m_e c^2$

Kinetic energy of Compton electron E_e is given by:

$$E_e = h\nu_0 - h\nu' \tag{77}$$

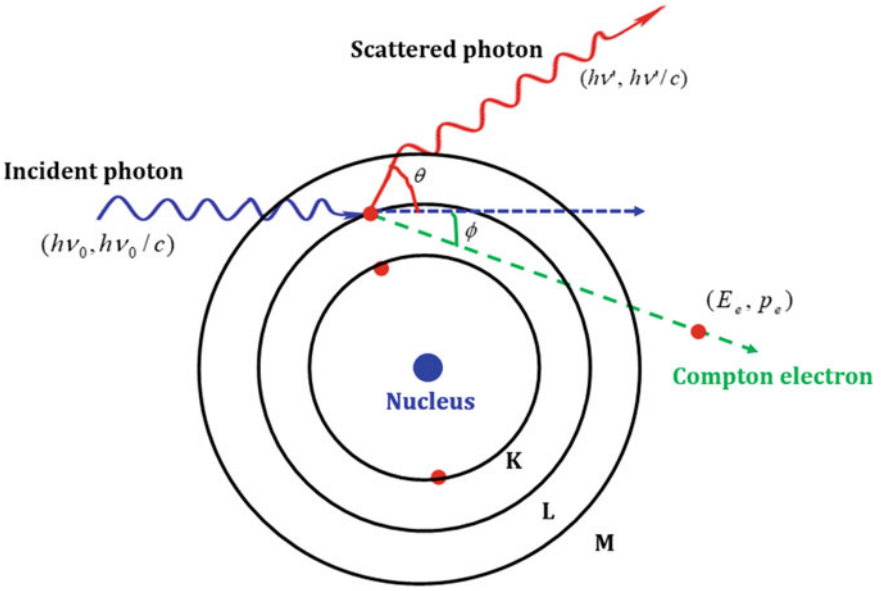

Fig. 17 Illustration of Compton scattering. The photon with initial energy $h\nu_0$ and momentum $h\nu_0/c$ moving in x direction undergoes a scattering with an orbital electron. After the collision, the photon scatters through an angle θ with energy of $h\nu'$ and momentum $h\nu'/c$. The electron recoils through an angle φ with kinetic energy of E_e and momentum p_e

$$E_e = \frac{\alpha h\nu_0(1-\cos\theta)}{1+\alpha(1-\cos\theta)} \tag{78}$$

At $\theta = 0°$, $h\nu' = h\nu_0$ (there is no energy loss) and the kinetic energy of Compton electron $E_e = 0$.

At $\theta = \pi$, $(1-\cos\theta) = 2$.

$$h\nu' = \frac{h\nu_0}{1+2\alpha} \tag{79}$$

$$E_e = \frac{2\alpha h\nu_0}{[1+2\alpha]} \tag{80}$$

Following are the important inferences that can be made from Compton scattering:

(a) When $\theta = 0°$, the energy of the scattered photon $h\nu' = h\nu_0$, independent of $h\nu_0$ and the kinetic energy of Compton electron $E_e = 0$.
(b) When $\theta = \pi$, $(1-\cos\theta) = 2$; $h\nu' = \frac{h\nu_0}{1+2\alpha}$; $E_e = \frac{2\alpha h\nu_0}{[1+2\alpha]}$
(c) The maximum fractional energy transferred to the electron is given by $\frac{(E_e)_{\max}}{h\nu_0} = \frac{2\alpha}{1+2\alpha}$
(d) When the scattering angle θ is larger than the scattered photon energy cannot exceed
(e) 0.511 MeV whatever may be the energy of incident photon.

Table 2 presents kinetic energy transferred to the orbital electron as a function of photon energy for the angle of scattering $\theta = \pi$. As the energy of photon increases from 0.025 to 50 MeV, the percentage maximum energy transferred to electron increases from 9 to 99.7%.

12.5 Pair Production

When the incident photon energy $E = h\nu_0$ is above twice the rest of the mass energy of electron, i.e. $2m_ec^2 = 1.022$ MeV, it produces an electron–positron pair upon interaction with the nuclear field of an absorbing medium and the photon gets absorbed completely (Fig. 18). The condition required for the effect to take place is that the energy, charge and momentum must be conserved. This effect is not possible in free space even if $h\nu_0 > 2m_ec^2$ because in free space energy and charge only can be conserved not the linear momentum. Therefore, to conserve the linear momentum, it only occurs in the coulomb field of either atomic nucleus or orbital electron so that a suitable fraction of the momentum carried by the photon is taken up by them. The kinetic energy of the electron (E_{e^-}) and positron (E_{e^+}) pair produced will be the difference between the energy of the incoming photon and the energy equivalent of two electron masses ($2m_ec^2 = 1.022$ MeV). The probability of pair production in the field of nucleus σ_{PP} with photon energy $\boldsymbol{E_\gamma}$ and atomic number of absorber Z can

Table 2 Scattered photon energy, maximum energy transferred to electron and maximum fractional energy transferred to electron by Compton scattering process when angle of scattering $\theta = \pi$

Photon energy, $h\nu_0$(MeV)	α	$h\nu'$ (MeV)	$(E_e)_{\max}$(MeV)	$\frac{(E_e)_{\max}}{h\nu_0}$
0.025	0.049	0.023	0.002	0.089
0.05	0.098	0.042	0.008	0.164
0.100	0.196	0.072	0.028	0.280
0.250	0.489	0.126	0.124	0.495
0.500	0.978	0.169	0.331	0.662
1	1.957	0.203	0.796	0.796
2	3.914	0.227	1.773	0.887
5	9.785	0.243	4.757	0.951
10	19.569	0.249	9.751	0.975
20	39.139	0.252	19.748	0.987
50	97.847	0.254	49.746	0.995
100	195.695	0.255	99.745	0.997

be approximated as $\sigma_{PP} \propto Z^2 \ln(E_\gamma)$. Pair production can also occur in the field of electron. However, the threshold energy of photon for this to happen is $4m_e c^2 = 2.044$ MeV.

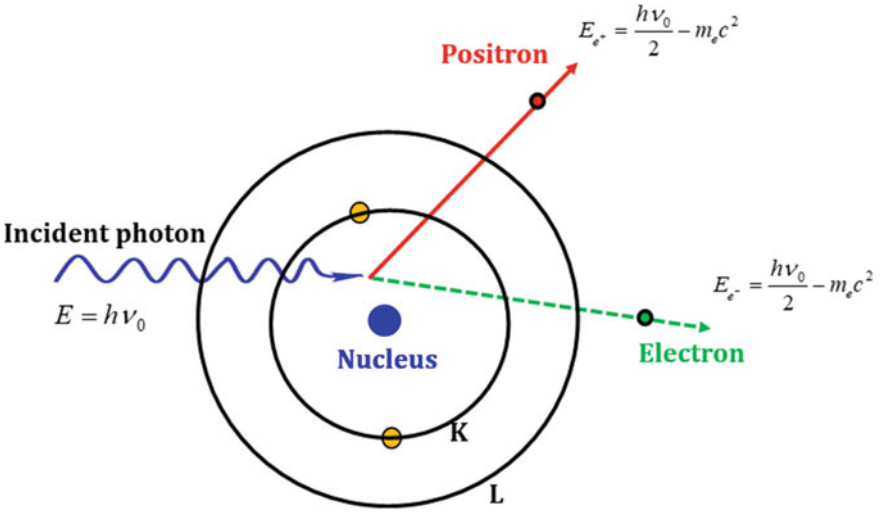

Fig. 18 Depiction of pair production in the field of nucleus of an absorbing medium

The electron–positron pair formed in the pair production process loses their energy in their usual way, i.e. through collisional and radiative losses. The positron annihilates with an electron at the end of its track. As a result, two 0.511 MeV gamma ray photons will be produced and emitted in opposite directions.

12.6 Photonuclear Reactions

Photonuclear reaction or photodisintegration is the process in which the photon is absorbed by the nucleus and nucleons are ejected from nucleus. The probability of a photonuclear reaction is much smaller in comparison with a photoelectric effect, Compton scattering, and pair creation. However, this reaction is important from the viewpoint of radiation protection because neutrons are also ejected from the nucleus. In addition, the residual nucleus after the reaction frequently becomes radioactive. Photonuclear reactions occur when the incident photon energy is greater than the threshold energy of the photonuclear reaction. The photodisintegration process can lead to the production of: (a) neutrons (γ,n), (γ,2n), (γ, 3n), (b) protons (γ,p), (c) alpha particles (γ,α), (d) tritium (γ,t), (e) ^{3}He (γ,^{3}He), and (f) combination of these (γ,np), (γ,nα). Thresholds are unique to each element and are calculated from the Q-value of the photonuclear reaction. Table 3 presents threshold energies (in MeV) for various photonuclear production of elements. These data are taken from IAEA handbook [10].

13 Interaction of Neutrons with Matter

13.1 Classification of Neutrons

In terms of their kinetic energy E_n, neutrons are classified into several categories (Podgorsak [1]):

(a) Ultracold neutrons ($E_n < 2 \times 10^{-7}$ eV)
(b) Very cold neutrons (2×10^{-7} eV $\leq E_n \leq 5 \times 10^{-5}$ eV)
(c) Cold neutrons (5×10^{-5} eV $\leq E_n \leq 0.025$ eV)
(d) Thermal neutrons ($E_k \approx 0.025$ eV)
(e) Epithermal neutrons (1 eV $< E_n <$ 1 keV)
(f) Intermediate neutrons (1 keV $< E_n <$ 0.1 MeV)
(g) Fast neutrons ($E_n >$ 0.1 MeV)

Note that the velocities of an ultracold neutron ($E_k = 2 \times 10^{-7}$ eV), thermal neutron ($E_k = 0.025$ eV) and fast neutron ($E_k = 2.5$ MeV) are ~ 6 m/s ($v/c \approx 2 \times 10^{-8}$), ~ 2200 m/s ($v/c \approx 7 \times 10^{-6}$) and ~ 1.4×10^7 m/s ($v/c \approx 0.05$), respectively [1].

Table 3 Photonuclear threshold energies of different target materials (IAEA [10])

Photodisintegration with target material	Photonuclear threshold Energies (MeV)									
	(γ, n + 2α)	(γ,n)	(γ,p)	(γ,t)	(γ,^{3}He)	(γ,α)	(γ,2n)	(γ,np)	(γ,2p)	(γ,3n)
γ + ^{2}H	–	2.22	–	–	–	–	–	–	–	–
γ + ^{9}Be	1.67	–	16.89	17.69	21.18	–	20.56	18.92	29.34	31.24
γ + ^{12}C	–	18.72	15.96	27.37	26.28	7.37	31.84	27.41	27.19	53.13
γ + ^{14}N	–	10.55	7.55	22.74	20.74	11.61	30.62	12.50	25.08	46.24
γ + ^{16}O	–	15.66	12.13	25.03	22.79	7.16	28.89	22.96	22.34	52.06
γ + ^{23}Na	–	12.42	8.79	17.43	24.45	10.47	23.49	19.16	24.06	40.59
γ + ^{24}Mg	–	16.53	11.69	26.69	23.13	9.31	29.68	24.11	20.48	49.06
γ + ^{27}Al	–	13.06	8.27	18.21	23.71	10.09	24.42	19.36	22.41	41.36
γ + ^{28}Si	–	17.18	11.58	27.53	23.23	9.98	30.49	24.64	19.86	49.53
γ + ^{32}S	–	15.04	8.86	24.01	19.05	6.95	28.10	21.18	16.16	47.07
γ + ^{35}Cl	–	12.65	6.37	17.95	19.64	7.00	24.15	17.79	17.25	39.90
γ + ^{52}Cr	–	12.04	10.50	22.41	21.79	9.35	21.30	21.56	18.57	34.30
γ + ^{56}Fe	–	11.20	10.18	20.87	20.25	7.61	20.50	20.41	18.25	33.87
γ + ^{58}Ni	–	12.22	8.17	21.15	17.68	6.40	22.47	19.55	14.20	39.11
γ + ^{59}Co		10.45	7.36	16.57	20.25	6.94	19.03	17.41	19.32	30.40
γ + ^{63}Cu	–	10.85	6.12	16.06	18.86	5.78	19.74	16.72	17.26	31.46
γ + ^{88}Sr	–	11.11	10.61	20.70	21.37	7.91	19.54	20.53	19.23	31.03
γ + ^{90}Zr	–	11.97	8.36	20.71	18.83	6.68	21.29	19.84	15.43	33.64
γ + ^{93}Nb	–	8.83	6.04	13.39	15.65	1.93	16.71	14.68	15.44	28.77
γ + ^{107}Ag	–	9.54	5.79	13.96	16.39	2.81	17.47	15.35	15.14	27.51
γ + ^{114}Cd	–	9.04	10.27	16.75	18.92	4.10	15.58	18.76	18.27	24.98
γ + ^{120}Sn	–	9.11	10.66	17.11	19.62	4.81	15.59	19.23	18.97	24.92
γ + ^{120}Sb	–	9.24	5.78	12.89	17.29	3.07	16.26	14.88	16.44	25.81
γ + ^{127}I	–	9.14	6.20	13.41	16.29	2.18	16.28	15.32	15.30	25.83
γ + ^{133}Cs	–	8.99	6.08	13.15	16.12	2.00	16.15	15.02	15.21	25.45
γ + ^{141}Pr	–	9.40	5.23	13.40	14.43	1.32	17.32	14.41	13.37	27.10
γ + ^{159}Tb	–	8.13	6.13	11.95	14.38	0.14	14.91	14.07	14.65	23.65
γ + ^{165}Ho	–	7.99	6.22	11.67	14.16	−0.14	14.66	13.88	14.79	23.07
γ + ^{181}Ta	–	7.58	5.94	10.95	13.04	−1.53	14.22	13.33	13.91	22.13
γ + ^{184}W	–	7.41	7.70	12.22	13.22	−1.66	13.60	14.63	14.23	21.67
γ + ^{197}Au	–	8.07	5.78	11.33	13.56	−0.95	14.71	13.70	14.04	23.08
γ + ^{208}Pb	–	7.37	8.01	12.88	14.39	−0.52	14.11	14.85	15.38	22.19
γ + ^{209}Bi	–	7.46	3.80	9.42	10.94	−3.14	14.35	11.17	11.81	22.44
γ + ^{232}Th	–	6.44	7.75	10.41	12.15	−4.08	11.56	13.31	13.25	18.35
γ + ^{238}U	–	6.15	7.62	9.97	11.88	−4.27	11.28	13.39	13.01	17.82

13.2 Neutron Interactions with Nuclei of Absorber

The neutrons interact with the nuclei of the absorber by the following processes:

(a) Elastic scattering, (b) Inelastic scattering, (c) Non-elastic scattering, (d) Neutron capture, (e) Spallation, and (f) fission.

13.2.1 Elastic Scattering

In elastic scattering, a neutron of mass m_n with kinetic energy E_n collides with a nucleus of mass M. After the collision, the nucleus recoils with an angle ϕ with respect to the initial direction of neutron. The kinetic energy transferred to the target nucleus of mass M is given by:

$$\Delta E_n = \frac{4m_n M}{(m_n + M)^2} E_n \mathrm{Cos}^2\phi \tag{81}$$

Maximum kinetic energy transferred to the target nucleus during a head-on collision ($\phi = 0$) is given by:

$$(\Delta E_n)_{\max} = \frac{4m_n M}{(m_n + M)^2} E_n \tag{82}$$

The kinetic energy of the scattered neutron after a head-on collision is given by:

$$\begin{aligned} E_n' &= E_n - (\Delta E_n)_{\max} = E_n - \frac{4m_n M}{(m_n + M)^2} E_n \\ &= E_n\left(1 - \frac{4m_n M}{(m_n + M)^2}\right) = E_n\left[\frac{(m_n - M)}{(m_n + M)}\right]^2 \end{aligned}$$

If the target is a proton, i.e. $m_n \approx m_p = M$, $E_n' = 0$ which implies the incident neutron can transfer its full energy to the proton in a head-on collision. Table 4 provides fractional kinetic energy that will be transferred to different target elements. Also included in the table is fractional kinetic energy retained by scattered neutron.

The average kinetic energy transferred to the recoil nucleus in a single collision is given by

$$(\Delta E_n)_{\mathrm{avg}} = \frac{4m_n M}{(m_n + M)^2}\frac{1}{2} E_n = \frac{2m_n M}{(m_n + M)^2} E_n \tag{83}$$

When the neutron interacts with hydrogen nucleus (i.e. a proton with mass m_p), then $M = m_n \approx m_p$. In this scenario, it will transfer on an average of 50% of its initial E_n to the proton in a head-on collision [see Eq. (83)]. In a head-on collision, the maximum transferable energy to the proton equals to the initial neutron energy

Table 4 Maximum fractional energy transferred to target nucleus by a neutron of kinetic energy E_n in a single elastic collision with the target nucleus $(\Delta E_n)_{max}/E_n$, fractional energy carried by the scattered neutron E_n'/E_n in a head-on collision with target nucleus and average energy transferred to the target nucleus $2m_n\, M/(m_n + M)^2$

Target nucleus	$(\Delta E_n)_{max}/E_n$	E_n'/E_n	$2m_n\, M/(m_n + M)^2$
${}^{1}_{1}H$	1.000	0	0.500
${}^{2}_{1}H$	0.899	0.101	0.444
${}^{4}_{2}He$	0.640	0.360	0.320
${}^{9}_{4}Be$	0.360	0.640	0.180
${}^{12}_{6}C$	0.284	0.716	0.142
${}^{16}_{8}O$	0.221	0.779	0.111
${}^{56}_{26}Fe$	0.069	0.931	0.034
${}^{118}_{50}Sn$	0.033	0.967	0.017
${}^{238}_{92}U$	0.017	0.983	0.008

E_n [see Eq. (82)]. The recoil proton then transfers its kinetic energy through coulomb interactions with the nuclei and orbital electrons in the medium. When $M >> m_n$, the energy transfer from the neutron to the medium is less efficient (see Eq. (82)).

Following may be noted in elastic scattering of neutrons:

(a) Conservation of total kinetic energy
(b) Conservation of momentum
(c) Recoiling particle receives energy lost by the neutron
(d) Head-on collision leads to maximum energy transfer
(e) Elastic scatter cross sections depend on energy and material.

13.2.2 Inelastic Scattering

In inelastic scattering, the target nucleus first absorbs the incident neutron and then re-emits it in a different direction with a lower energy. In this process, the nucleus becomes excited and achieves stability by emitting high-energy gamma rays. This process is illustrated by the following relationship:

$$ {}^{1}_{0}\boldsymbol{n} + {}^{A}_{Z}\boldsymbol{X} \rightarrow {}^{A+1}_{Z}\boldsymbol{Y^*} \rightarrow {}^{A}_{Z}\boldsymbol{X^*} + {}^{1}_{0}\boldsymbol{n} \rightarrow {}^{A}_{Z}\boldsymbol{X} + {}^{1}_{0}\boldsymbol{n} + \boldsymbol{\gamma} $$

${}^{A}_{Z}\boldsymbol{X}$ is the stable target nucleus, ${}^{A+1}_{Z}\boldsymbol{Y^*}$ is the unstable compound nucleus, ${}^{A}_{Z}\boldsymbol{X^*}$ is the excited target nucleus.

Thus in the case of inelastic scattering, neutron is absorbed and then re-emitted and the nucleus absorbs some energy internally and is left in an excited state.

Example: ^{14}N(n, n')^{14}N; $E_\gamma = \sim 10$ MeV.

13.2.3 Non-elastic Scattering

Differs from inelastic scattering in that a secondary particle that is not a neutron is emitted after the capture of the initial neutron.

Example: ^{12}C(n, α)^{9}Be; $E_\gamma = 1.75$ MeV.

13.2.4 Neutron Capture

Neutron capture occurs when an incident thermal neutron is interacting with a nucleus which results in the emission of a proton or gamma ray. There are two very important reactions that are relevant in tissue: ^{14}N(n, p)^{14}C and ^{1}H(n, γ)^{2}H whereas ^{113}Cd(n, γ)^{114}Cd is important in shielding against thermal neutrons. If 1 mm thick cadmium plate is used it will absorb essentially all incident thermal neutrons less than 0.5 eV, but readily transmits neutrons having energies above 0.5 eV. A broad resonance with a peak at 0.178 eV is observed when the neutron capture cross section is plotted as a function of neutron kinetic energy. For natural Cd (12% abundance of ^{113}Cd), neutron capture cross section is 7800 b at resonance peak energy whereas it is ~ 64 × 10^3 b for pure ^{113}Cd. The stable target bombardment with neutrons is often carried out in a nuclear reactor to produce a radioactive isotope for industrial or medical purposes.

Thus neutron capture:

(a) is same as inelastic scattering, but by definition, neutron capture occurs only at low neutron energies (thermal energy range is < 0.025 eV)
(b) leads to the disappearance of the neutron
(c) accounts for a significant fraction of the energy transferred to tissue by neutrons in the low energy ranges.

Examples:

$$^{14}_{7}\mathrm{N(n,\,p)}^{14}_{6}\mathrm{C} + Q(0.626\,\mathrm{MeV}),\ E_p = 0.58\,\mathrm{MeV(kinetic\ \ energy\ \ of\ \ proton)}$$

$$^{1}_{1}\mathrm{H}(n, \gamma)^{2}_{1}\mathrm{H} + Q(2.22\,\mathrm{MeV}),\ E_\gamma = 2.22\,\mathrm{MeV}$$

$$^{10}_{5}\mathrm{B} + ^{1}_{0}\mathrm{n} \rightarrow ^{7}_{3}\mathrm{Li} + ^{4}_{2}\mathrm{He} + Q(2.3\,\mathrm{keV})$$

$$^{6}_{3}\mathrm{Li} + ^{1}_{0}\mathrm{n} \rightarrow ^{3}_{1}\mathrm{H} + ^{4}_{2}\mathrm{He} + Q(4.8\ \ \mathrm{MeV})$$

$$^{3}_{2}\mathrm{He} + ^{1}_{0}\mathrm{n} \rightarrow ^{3}_{1}\mathrm{H} + ^{1}_{1}\mathrm{p} + Q(0.765\,\mathrm{MeV})$$

The dose to tissue from thermal neutrons is due to the hydrogen capture reaction and the gamma emitted in this reaction is fairly energetic. The tissue dose depends on the volume of tissue irradiated.

13.2.5 Spallation

In this process, the nucleus captures the incident fast neutron and splits into fragments and it is important at higher neutron energies (in excess of 100 MeV). The cross sections are higher at 400–500 MeV. The tissue receives a dose maximum due to the several neutrons and de-excitation gamma rays, which are emitted.

When an incident fast neutron penetrates the nucleus and is captured by it then the nucleus energy increases sufficiently that leads to the disintegration of nucleus into many small residual components (such as α particles and protons p). This process is known as spallation.

Example: ${}_0^1\boldsymbol{n} + {}_8^{16}\boldsymbol{O} \rightarrow 3{}_2^4\boldsymbol{\alpha} + 2{}_1^1\boldsymbol{p} + 3{}_0^1\boldsymbol{n}$

The energy released in the spallation process is carried away generally by heavier fragments that deposit their energy in the absorber locally.

13.2.6 Fission Induced by Neutron Bombardment

Fission process occurs when thermal neutron is bombarded on high atomic number nuclei. In this process, the product nuclei of lower atomic numbers along with more than one fast neutron are produced and a huge amount of energy is also released. Materials that undergo fission directly are called fissile or fissionable materials and the most important fissionable materials are listed below:

^{235}U (0.7% of natural uranium).

^{239}Pu produced from ^{238}U.

^{233}U produced from ^{232}Th.

^{238}U and ^{232}Th do not undergo fission themselves and are called fertile because it can be converted as fissionable nuclides upon irradiation with fast neutrons in a nuclear reactor.

The fissionable nuclides undergo fission and break into nuclides with low atomic numbers and are called fission fragments. The fission fragments are generally radioactive and subsequently undergo radioactive decay. A general equation for fission of ^{235}U by thermal neutrons is as follows:

$$ {}_0^1\mathrm{n} + {}_{92}^{235}\mathrm{U} \rightarrow {}_{92}^{236}\mathrm{U} \rightarrow {}_a^bX + {}_d^cY + f{}_0^1\mathrm{n} $$

where the incident thermal neutron is absorbed by a nucleus $({}_{92}^{235}U)$ a compound nucleus ${}_{92}^{236}$U is formed which is unstable. To get the stability it undergoes fission and produces generally two unstable nuclei of smaller atomic number and atomic mass number ($a + d = 92$ and $b + c + f = 236$, where f is the number of fast neutrons produced by the fission process). In this process, a huge amount of energy is released; on an average about 200 MeV energy per fission of ${}_{92}^{235}$U is released and on an average, 2.5 new neutrons per fission are also produced.

Examples for fission:

$$^{1}_{0}\mathrm{n} + ^{235}_{92}\mathrm{U} \rightarrow ^{236}_{92}\mathrm{U} \rightarrow ^{147}_{57}\mathrm{La} + ^{87}_{35}\mathrm{Br} + 2^{1}_{0}\mathrm{n} + Q$$

$$^{1}_{0}\mathrm{n} + ^{235}_{92}\mathrm{U} \rightarrow ^{236}_{92}\mathrm{U} \rightarrow ^{144}_{56}\mathrm{Ba} + ^{89}_{36}\mathrm{Br} + 3^{1}_{0}\mathrm{n} + Q$$

$$^{1}_{0}\mathrm{n} + ^{235}_{92}\mathrm{U} \rightarrow ^{236}_{92}\mathrm{U} \rightarrow ^{133}_{51}\mathrm{Sb} + ^{99}_{41}\mathrm{Nb} + 4^{1}_{0}n + Q$$

$$^{1}_{0}\mathrm{n} + ^{235}_{92}\mathrm{U} \rightarrow ^{236}_{92}\mathrm{U} \rightarrow ^{140}_{54}\mathrm{Xe} + ^{94}_{38}\mathrm{Sr} + 2^{1}_{0}\mathrm{n} + Q$$

where $Q = 195$ MeV.

14 Summary

(a) Photons and neutrons are classified as indirectly ionizing radiations.
(b) Charged particles are classified as directly ionizing radiations.
(c) In photoelectric effect, entire energy of photon is transferred to the bound electron. Photoelectric effect is predominant when the incident photon energy is smaller and the atomic number of the medium is high.
(d) In Compton scattering fraction of photon energy is transferred to the orbital electrons.
(e) Threshold energy for pair production is 1.02 MeV. In pair production, electron–positron pair is created.
(f) Electron with 10 keV kinetic energy has 20% of velocity of light. Whereas proton with 20 MeV kinetic energy and helium ion with 80 MeV will travel with 20% of velocity of light.
(g) In a head-on collision:

- Electron will transfer only half of its initial kinetic energy to a target electron in a single collision. Because of same charge, the electron that carries the highest energy after the collision is identified as primary.
- Positron will transfer its full kinetic energy to a target electron in a single collision.

(h) Electrons and positrons lose kinetic energy through ionization and bremsstrahlung production.
(i) Total stopping power of light charged particles (electrons/positrons) is the sum of collision stopping power and radiative stopping power. Nuclear stopping power is not applicable to light charged particles.
(j) Total stopping power of heavy charged particles is the sum of collision stopping power and nuclear stopping power. Heavy charged particles do not lose energy through radiative process.

(k) For heavy charged particles with a velocity above 40% of the velocity of light, it is important to use relativistic relationship for calculating maximum energy transfer to the target electron in a single collision.
(l) Main influencing factors of stopping power of charged particle are electron density of the medium in which it traverses and the velocity of the charged particle.
(m) The path length of an electron is the total distance traveled along its actual trajectory until it comes to rest, whatever may be its direction.
(n) CSDA range is a calculated quantity which represents the mean path length along the trajectory of electron, and not the depth of penetration in a defined direction.
(o) Radiation length is the distance over which the kinetic energy of the incident electron is reduced by a factor of $(1/e)$ due to only radiation loss.
(p) A charged particle radiates energy in free space in the form of photon radiation only if accelerated or decelerated.
(q) A charged particle in rectilinear uniform velocity motion in free space does not lose its kinetic energy in the form of photon radiation.
(r) When the velocity of the charged particle exceeds phase velocity of light in a transparent dielectric material, part of its kinetic energy is radiated in the form of Čeronkov radiation.
(s) Elastic scattering of neutrons with atomic nuclei leads to maximum energy transfer to the target nuclei in a head-on collision.

References

1. Podgorsak EB (2010) Radiation physics for medical physicists. Springer
2. Stopping Powers for Electrons and Positrons, ICRU Report 37 (1982)
3. ESTAR: Stopping Power and Range Tables for Electrons. http://physics.nist.gov/PhysRefData/Star/Text/ESTAR.html. Accessed on 12 Dec 2023
4. Berger MJ, Seltzer SM (1964) Tables of energy losses and ranges of electrons and positrons. National Aeronautics and Space Administration, Washington, DC, NASA-SP-3012
5. Kenneth RK, Walter RN (1972) Concepts of radiation dosimetry. SLAC-153
6. Rossi B (1952) High energy particles. Prentice Hall Inc., Englewood Cliffs, New Jersey
7. PSTAR: Stopping Power and Range Tables for Protons, https://physics.nist.gov/PhysRefData/Star/Text/PSTAR.html. Accessed on 12 Dec 2023
8. Hooshang N, Shuzo U, Dimitris E (2012) Interaction of radiation with matter. CRC Press, New York
9. Handbook on photonuclear data for applications (2000) IAEA-TECDOC-Draft No. 3
10. https://casper.astro.berkeley.edu/astrobaki/index.php/Cherenkov_Radiation. Accessed on 20 Dec 2023

Biological Effects of Radiation

Nagesh Bhat, Usha Yadav, and Rajesh K. Chaurasia

1 Introduction

Cells are considered as fundamental units of life of all living organisms and the human system has nearly 10^{14} cells of different types. Constituents of a cell can be visualized as different organelles, viz., nucleus, cytoplasm enclosed in an envelope called the cell membrane. The nucleus in a cell is an information center that contains Deoxyribonucleic Acid (DNA) and histone proteins arranged in a structured manner called chromosomes. DNA molecules are the genetic material of the cell and are the most important targets for the induction of radiation damage in cells, either by radiation or by any other mutagens including those that exist in nature as well as those due to many lifestyle factors.

The tissues in an organ or system are made up of different types of cells. In some tissues, cells may continuously divide, undergo a series of modifications and maturation processes (differentiation) and then give rise to cells which are functional in nature, while in other tissues the division may be regulated or may not divide at all. Examples of organs with constituent cells having faster division rates are bone marrow, epithelial cells, epidermis, crypt cells lining the intestines, etc. Cells lining the intestines are also dividing in nature in order to dynamically maintain the food-body barrier. Reproductory systems in males and females are also known to contain dividing cells—Spermatogonia and oocytes cells in testis and ovaries divide and yield matured sperm cells ova. In some organs, cells divide very slowly as in kidney, liver, connective tissues, etc. Some tissues such as muscle and nerve cells are differentiated. These slow or non-dividing cells are generally known for their functional capabilities. Besides the type of cells that constitute the tissues, some tissues are considered vital such as lungs, heart, kidney, liver, brain and many glandular systems while few

N. Bhat (✉) · U. Yadav · R. K. Chaurasia
Radiological Physics and Advisory Division, Health, Safety and Environment Group, Bhabha Atomic Research Centre, Mumbai 400085, India
e-mail: nageshnb@barc.gov.in

D. K. Aswal (ed.), *Handbook on Radiation Environment, Volume 2*,
https://doi.org/10.1007/978-981-97-2799-5_5

peripheral organs such as limbs may not play vital roles for the survival although they may be indispensable for day to day activities. For radiation damage, these vital organs/systems, which may be also sensitive, are considered as target organs/systems.

2 Dependence of Biological Damage on Mode of Exposures

Induction of damage and its progression by radiation can be visualized on the basis of damage and the chronology of events. Some initial processes, such as physical and chemical processes, are extremely fast, leading to primary lesions, deposition of additional energy and creation of an unstable environment and reactivity. These effects may eventually translate into biological effects with longer time scales. Development of primary lesions into biological steps involves many complex biophysical, biochemical and biological interactions. During these processes, cells can sense the damage, react to them through repair processes or may even undergo death.

Changes in macromolecules, their functional impairment in cells or complete inactivation can further hamper the function of cells. Since these processes involve the action of life of cells, it is safe to assume that cells are interacting with radiation damage rather than radiation interacting with cells. With the reversal of process steps, interaction processes become very slow leading to very large time scales, extending to years to decades for the final manifestation of clinically observable biological effects. The events are listed in Table 1 chronologically, with their relevance from various fields of studies.

2.1 External Exposure

The understanding of external exposure is fairly simple. External exposures can happen due to isotopes that are present outside the body at a distance. Radiation emitted by such isotopes can penetrate the tissues and deliver doses. Highly penetrating radiation such as gamma and high energy X-rays can deliver a dose to whole body while less penetrating ones can deliver a dose to skin and extremities. Densely ionizing radiation such as alpha particles may not pose any threat from external exposure as they can be easily be stopped by biologically inactive layers of skin or even the air when the sources are at a distance.

2.2 Internal Exposure

Inhalation or ingestion of radioisotopes can lead to internal exposure to cells. Volatile isotopes such as radioactive iodine, tritium in either gas form or water vapors and

Table 1 Radiation interactions and time scales

Phase	Events and processes	Time scale (s)	Modifying factors
Physical	Energy absorption, ionizations and excitation	10^{-18}–10^{-15}	Dose distribution, let, dose rate
Physico chemical	Rearrangement of excited ionized molecules, formation of diffusible radicals such as H^o, OH^o, e-aq	10^{-15}–10^{-8}	Oxygen effect, properties of media, aqueous or dry conditions, frozen condition, temperature of media
Chemical	Formation of primary lesions, bioradicals, molecular alterations, indirect actions, long lived lesions in macromolecules, fixed damages to macromolecules	10^{-8}–10^{-3}	Radioprotectors, radiosensitizers
Bio-chemical	Enzymatic reactions, recognition of lesions, activation of repair processes, fixation of damage through repair pathways, observable DNA aberrations	10^{-3}–10^{4}	Repair inhibitors, energy metabolism
Cellular level	Cell death, cell loss, division kinetics, mutations, observable chromosomal aberrations	10^{4}–10^{7}	Modifiers of cellular repairs
Systemic (multicel-lular organisms)	Immune reactions, functional damages, adoptive responses, carcinogenesis, hereditary effects, aging, death	10^{8}–10^{10}	Tissue regeneration, infections, medical management, rehabilitation

many other isotopes as part of aerosols may get internalized by inhalation. Isotopes like ^{3}H as part of moisture, if comes in direct contact, can lead to direct absorption through pores of skin. Specific isotopes may have a tendency to get accumulated in particular tissues.

To safeguard radiation workers, radionuclide specific limits for intake are defined. These units are based on the ability of radionuclides to deliver dose per unit activity of intake, their biological hazard. These hazard values are indicated in terms of annual limit of intake (ALI) values. One ALI of intake, through any route or combined routes such as inhalation, ingestion or through the skin absorption in a year by the reference man is estimated to result in a committed dose equivalent corresponding to the allowed annual dose limit (20 mSv).

Assessment of internal exposures is done by internal dosimetry methods. Whole body gamma counting for photon emitting isotopes, urine blood and other body fluids by liquid scintillation method, contamination detection by swipe samples and many more such methods are adopted for assessment of internal exposures. The latter technique is highly sensitive and can measure very low levels of exposure which are relevant for regulatory measures. In the work environment, it is possible to restrict inhalation doses by constant monitoring and control. For mitigation of such

air borne volatile radionuclides, proper ventilation, handling devices such as fume hoods, glove boxes and personnel protective gears are used. External contamination can be monitored/detected by contamination monitors.

Biologically incorporated radionuclides pose a stronger risk as they are difficult to biologically eliminate from the tissues. To accelerate the removal, many interventional measures known as decontamination and decorporation methods are used based on biochemistry of the particular radionuclide.

3 Radiation Effects at Sub-Cellular Levels

DNA being the information bank of life in a cell, is considered as the most radiosensitive molecule. Damage induction in cells can be either by direct ionization in the DNA molecules or through indirect mechanism through the production of radiolytic products of water such as free radicals and reactive oxygen species. This can trigger a chain of chemical events with biomolecules leading to structural changes of these critical molecules and may lead to observable biological outcome. There are numerous possibilities of DNA damage by radiation. However, cells are well-equipped to address such damages very effectively. In fact, most of these damages are repairable and do not pose any threat to either the function or life of the cells. Nonetheless, with non-zero probability, sometimes cells may end up introducing some errors when the damages involved are very serious in nature. In particular, double strand breaks (DSB) and cluster damages, which are typically found in radiation exposures, are known to pose such challenges to cells. An estimate shows, 1 Gy of gamma irradiation can yield about 30–40 DSBs, about 1000 single strand breaks (SSB) and equal number of base damages. Although DSBs are considered as serious in nature, more than 98–99% of these are properly repaired leading to complete normalcy of life of cell. Besides SSB and DSB, numerous other effects involving crosslinking of various non-DNA molecules with DNA are possible [1]. Various types of damage are visually represented in Fig. 1. Nonetheless, cells can easily address such minor damages through effective repair pathways.

4 Effects at Cellular Level

Cell being the basic fundamental and live functional unit in an organ or tissue may see deleterious effects upon damage to its constituting molecules. Macromolecules like proteins, lipids and carbohydrates have high turnover rates in cells and can be recreated by cells when damaged. They are synthesized, activated or degraded as per the need. There are certain cells where structural proteins last for years to decades and damage to these may result in tissue damage such as collagen, elastin of muscles and connective tissues and crystalline proteins of eye lenses. DNA is thought to be the most important target as it holds all the information for cells survival and

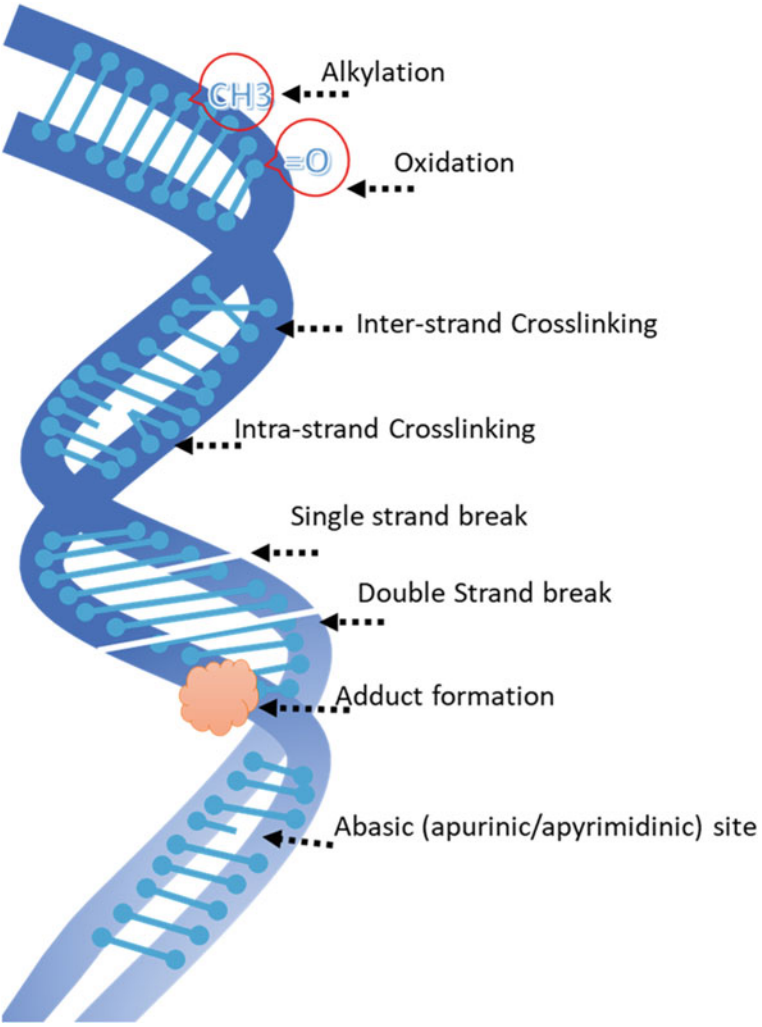

Fig. 1 Different types of DNA damages caused by chemical or radiation as mutagen

reproduction. DNA is synthesized once and stays there lifelong in the cells. The after effect of molecular damage can be of multiple types (Fig. 2). If cells are able to repair the damage the repair it does not lead to any effect on the cell functionality. Cells with mis-repaired DNA damage may acquire mutations or structural chromosomal aberrations leading to altered cell function (cell modification) or cell death.

While small amount of cell death at low doses < 1 Gy acute does not lead to significant differences in the organ function, considerable cell killings after a threshold dose results in deterministic type of health effect. Threshold dose for different cell/tissue kinds can be different as per their sensitivity to radiation. Hence, there are

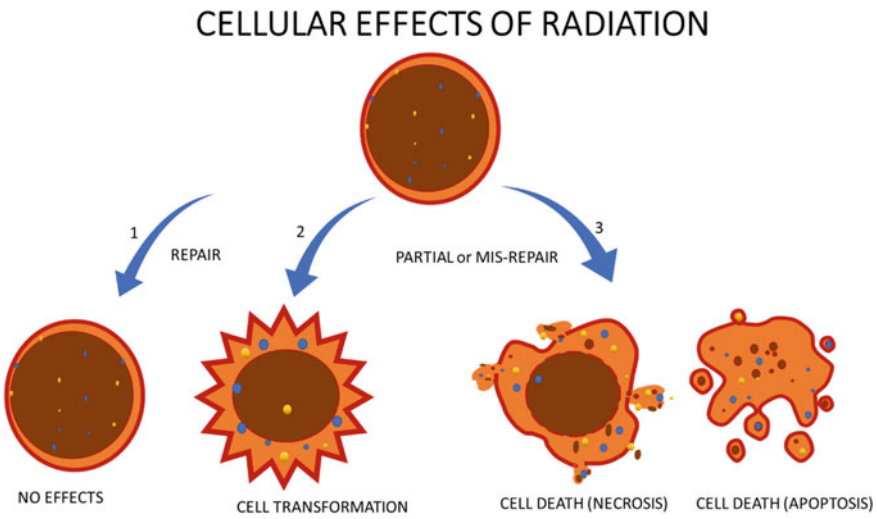

Fig. 2 Cellular effects after radiation exposure include cell transformation and cell death. There are additional effects such as cell division delay and arrest and cell senescence

different thresholds for different organ systems. For mutations, they are rare probabilistic events. Majority of DNA in our cells is non-coding, hence the alteration in these sequences will not pose a risk of mutation in the cells. However, once arisen, mutations have the ability to pass on from one generation to next generation of the cell. If the cell is a germ cell then the mutation can be passed on to the progeny of the individual with mutation. Mutations in genes controlling the cell division may lead to uncontrolled cell growth, i.e., tumor/cancer. Cancer and genetic effects are mutation probability dependent effects, hence stochastic in nature. Radiation has also been observed to accelerate cell senescence (loss of function with age). Differentiated cells such as neurons and muscle cells do not divide and hence may live and keep functioning for years with unrepaired or mis-repaired damage before showing symptoms of aging. Long-term deterministic effects on tissues such as cardiovascular damage usually appear due to accelerated cell senescence.

5 Factors Modifying the Damage at Molecular/Cellular Levels

5.1 Dose and Dose Rate Effect

Cell death occurs as a direct function of radiation dose. It follows a linear quadratic radiation response for acute low linear energy transfer (**LET**) radiation exposures. Same radiation dose may be delivered in different time durations resulting in different

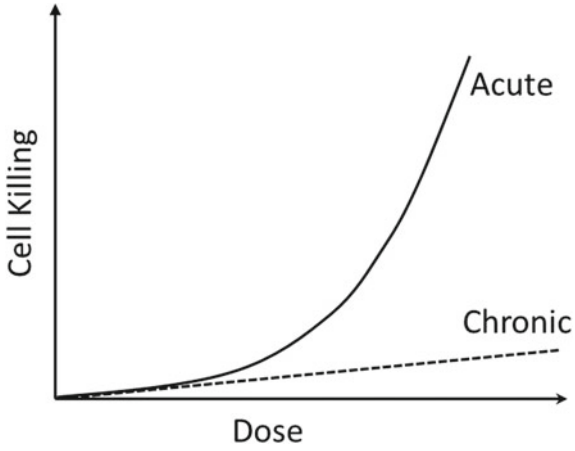

Fig. 3 Radiation response of cell death with acute and chronic radiations

levels of biological effects which is termed as dose rate effect. Dose rate effects, especially for exposure with X-rays, gamma rays like radiations are distinctly observed. With such low LET radiations, the ionization is sparsely distributed and hence, single track rarely creates lethal damage. This is because at low doses and/or low dose rates (0.2 Gy and/or 0.5 Gy/h) damages are separated by space or time giving very less chance of mis-repair to the cell. However, with acute high doses (few Grays in few minutes) multiple tracks create ionizations together and result in increased mis-repair of the molecules which leads to lethal effect on a cell. Hence, chronic exposures are relatively less lethal compared to acute exposures (Fig. 3). Similarly, protracted exposures (several grays in several hours to days) are less damaging than acute but more than chronic. Animal model experiments have shown that the total induction of mutation is much lower, at least by a factor of two when dose and dose rates are low. Hence, while calculating risk for chronic exposure induced risk for long-term effects, a dose and dose rate effectiveness factor (**DDREF**) of two is applied to reduce the risk by half of what occurs in acute exposures.

5.2 Quality of Radiation

Same dose of different radiation may produce different levels of effect. It depends on the LET capacity of the radiation. High LET radiations such as alpha and neutrons are more effective in cell killing compared to low LET radiations like gamma and x-rays. High LET radiations such as neutrons and alpha produce linear radiation response for cellular effects while Low LET radiations have lower response but linear quadratic in nature (Fig. 4a). This is because majority of the lethal damages in case of low LET radiations are formed by interaction of two track events for which probability increases exponentially with dose. Whereas, high LET radiation tracks are dense enough to create lethal damages with single track events and hence effectiveness

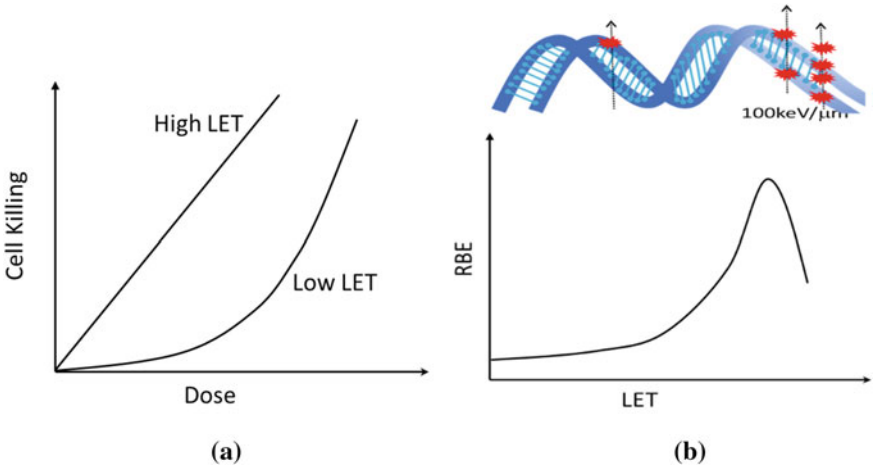

Fig. 4 Effect of LET on biological effectiveness **a** linear versus quadratic radiation response of high and low LET radiations respectively, **b** correlation between LET and relative biological effectiveness of radiations

increases linearly with dose. In case of low LET radiations if dose or dose rates are small enough to minimize interaction of two or more tracks the response becomes linear, whereas there is small to no effect of dose rate in case of high LET radiation.

Relative biological effectiveness (**RBE**) of a radiation is a measure of effectiveness with respect to gamma radiation. It is measured as the ratio of doses required by Co-60 Gamma radiation to the test radiation to produce the same effect. RBE of radiations increases with increasing LET up to ~ 100 keV/μm followed by reduction in RBE due to overkill (Fig. 4b). Cell death fraction increases with high LET causing higher ionizations, however, excess energy transfer than required to kill a cell will not increase the outcome much further and this is termed as overkill effect. It is also found that, at 100 keV/μm, the approximate gap between two different ionizations is same as the diameter of a DNA molecule. Hence, more effective to create DNA double strand breaks and the most lethal DNA damage [1].

5.3 Cell/Tissue Sensitivity

Different tissue types vary in their radio-sensitivities. Bergonie and Tribondeau law of radio sensitivity predicts three features responsible for the radiation sensitivity, (i) mitotic rate or cell division rate (ii) mitotic future or inherent ability to divide upon demand and (iii) differentiation status, i.e., primitive stem cells or differentiated functional cells [2]. It states that dividing cells are more radio sensitive in comparison to non-dividing cells and stem cells are more sensitive compared to fully differentiated cells. The most radiosensitive, dividing subset of cells in human body include; bone

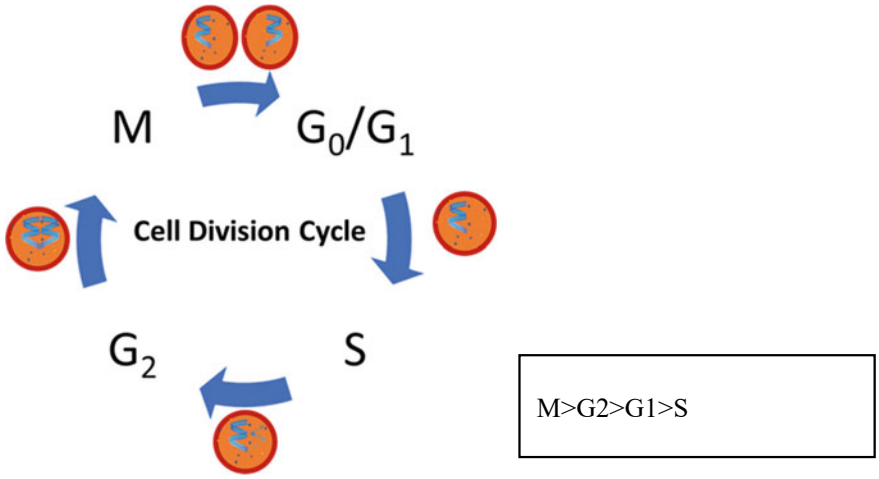

Fig. 5 Cell division phases and decreasing order of their radio-sensitivities

marrow stem cells, GI tract stem cells, lung epithelium, etc. whereas fully differentiated, non-dividing cells are represented by nerve cells, muscle cells and bone cells. Among the dividing cells, those in M phase are most sensitive whereas cells in S phase are most radioresistant. This is attributed to differential expression of DNA repair proteins during these phases. Radio-sensitivity of different stages is depicted in (Fig. 5).

5.4 Presence or Absence of Radiation Modifier

Certain chemicals can enhance or reduce the effectiveness of radiation. Agents which reduce the effect of radiation are known as radioprotector and the ones which enhance the effect are known as radiosensitizers. Radioprotectors can reduce the damage by scavenging radiation induced free radicals and reactive oxygen species. Some agents can enhance cell survival by enhancing the expression of pro-survival genes and antioxidant enzymes. There are several plant extracts reported to work as radioprotectors in-vitro experiments. *Amifostine* is one approved drug used for radiation protection of normal tissues during radiotherapy of cancers. Radiosensitizers, enhance free radical formation, or impair DNA repair. *Gemcitabine*, *5 bromo uracil*, *Cisplatin*, *Docetaxel,* etc. are well known radiosensitizers used in radiotherapy. Oxygen is also known as the most potent radiosensitizers. Tumor cells in the hypoxic region are 2–3 times resistant to radiation than the well oxygenated cells. Radiosensitizers or radioprotectors used in therapy have a differential effect on normal and tumor cells. Both types of agents are chosen such that they have the best normal cell protection

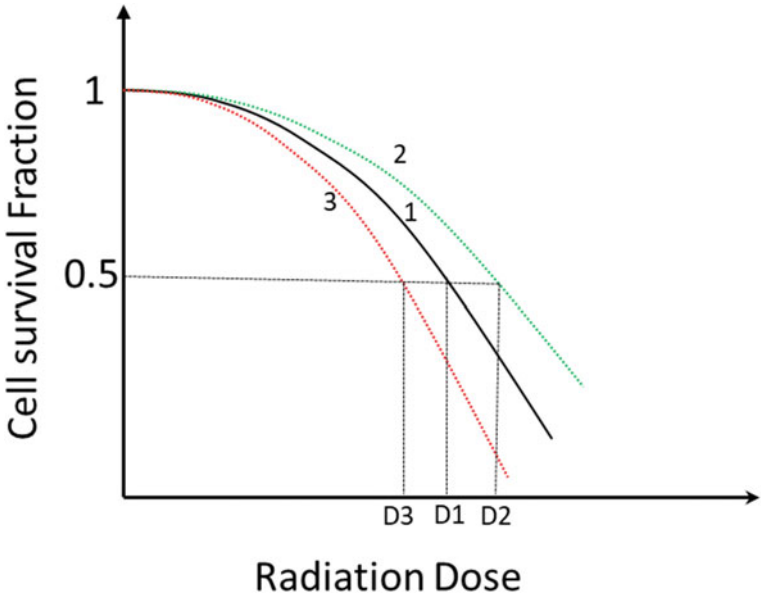

Fig. 6 Survival fraction of cells with increasing radiation dose. Curves 1, 2 and 3 represent typic curve without any modifier, with a radioprotector and with a radiosensitizer respectively. Radiation effectiveness changes in the presence of a modifier. To produce certain effect, it requires higher (D1) or lower dose in the presence of protector or a sensitizer respectively

and highest tumor cell sensitization for radiation. Figure 6 demonstrates how radiation response for cell survival is enhanced in the presence of a radioprotector and reduced in the presence of a radiosensitizer.

6 Classification of Radiation Effects

Based on the mechanism of damage induction, effects can be broadly classified into two categories; tissue reactions and stochastic effects. Tissue reactions are also known as deterministic effects. At cellular level, two major types of effects, i.e., either cell death or cell modification. All the tissues are dynamically maintained and hence, death of small percentage of cells which are killed go unnoticed by tissues and recovery takes place without any clinical expressions. Hence, when the fraction of cells killed in a tissue is not very significant, those tissues do not show any clinically observable symptoms. However, when fraction of cells killed becomes very significant, it can lead to functional impairment as well as the expression of stress in the form of clinically observable symptoms. These symptoms are known as tissue reactions or deterministic effects. These effects cannot occur at smaller doses. The doses at which such symptoms start appearing are known as threshold doses.

Threshold doses for a given deterministic effect depend on the sensitivity of the tissue. With increasing dose beyond threshold doses, the severity of effect is bound to increase.

Examples for deterministic effects are; NVD syndrome or radiation sickness, Haematopoietic or bone marrow syndrome, gastrointestinal (GI) syndrome and central nervous system (CNS) syndrome. In addition, individual organs can show functional impairments—Lungs exposure can lead to pneumonitis; Large eye lens exposure can lead to radiation induced cataract; Temporary and permanent sterility can be observed in both males and females due to gonadal exposures; Skin erythema, skin burns, blister formation and necrosis can occur due to skin exposure.

Deterministic effects appear within few days to weeks in most cases. The manifestation of symptoms depends on organs involved, their functions and also the sensitivity of cells they are made up of.

Non-lethal genetic alterations such as point mutations and translocations are considered as mutations at cellular level. Such mutations may not lead to cell death but may lead to changes in genetic pool. Such changes in genetic information on somatic cells are thought to be responsible for effects such as radiation induced carcinogenesis. If mutations occur in germ cells, possible consequences are heritable effects in the progeny generations. Induction of mutation is stochastic in nature. Most of the mutations are harmless in nature and eventually lead to inactive cells which may get eliminated over time. Induction of such stochastic effects by radiation is a very rare event at cellular levels. At low doses (< 200 mSv), there is no conclusive human data to demonstrate the carcinogenesis risk. For heritable risk, even at high doses, there is no conclusive data though extensive epidemiological studies were conducted over several decades with high dose exposed populations such as Atomic Bomb Survivor (ABS) cohort, people living in high background areas and also low dose exposed cohort such as radiation workers. Though stochastic effects are considered as key factors while defining dose limits, human evidence for the same at low doses is not available. All the risk estimates are based on past acute high dose exposures.

7 High Dose Effects—Tissue Reactions

7.1 NVD Syndrome

Severe acute exposures to doses exceeding 1 Gy, whole body, can result in symptoms of sickness known as radiation sickness. Typical symptoms of sickness are; nausea, vomiting and diarrhea. Besides, minor symptoms such as fatigue, fever, apathy, shock, agitation, ataxia, agitation and ileus can set in too. These are prodromal manifestations and are known to originate from brain as part of defense mechanism after sensing the damage in body and hence are also known as neuro-vegetative syndrome referring to a combination of responses from nervous system and body.

Table 2 Prognostic expectation of symptoms at different dose levels [3]

Symptom	Dose (Gy)	Suggested actions
Nausea but no vomiting	< 1	Outpatient with 5-weeks surveillance period
Vomiting in 2–3 h after exposure	1–2	Surveillance in a site hospital (or outpatient for 3 weeks followed by hospitalization, if necessary)
Vomiting in 1–2 h after exposure	2–4	Hospitalization in a haematological or surgical (burns) department of a site hospital
Vomiting earlier than 1 h after exposure and/or other severe symptoms	> 4	Hospitalization in a well-equipped haematological or surgical department of a site hospital OR transfer to a specialized hospital for handling radiation injuries

In the past, such symptoms were effectively used as a prognostic indicator of radiation exposures when a large number of individuals were exposed for the purpose of medical triage. Table 2 is a prognostic expectation of symptoms at different dose levels.

A Triage Score − "*T*" is assigned as follows:

$$T = (N/L) + E$$

Where $E = 0$ if no emesis, $E = 2$ if emesis.

In a normal healthy human population, *N*/*L* ratio from a complete blood count (CBC) with differential has been found to be approximately 2.1. A value exceeding 3.7 is usually called for medical attention.

7.2 Haematopoietic Syndrome

Ensemble of blood forming organs composed of white pulp of spleen, lymphatic tissues; lymph nodes and thymus is known as haematopoietic system. This system is biologically very active, producing all blood cells such as leukocytes, i.e., lymphocytes and monocytes, red blood cells, granulocytes and platelets. Majority of these cells are produced in red bone marrow. Though not dividing, lymphocytes are highly radiosensitive cells. About 2–3 Gy of acute exposure can kill 50–75% of lymphocytes in about 4–7 days [4]. Majority of lymphocytes are in lymph circulation while only about 2–3% are in peripheral blood. Torso region of the human with flat bone and the ends of long bones is known to contain majority of bone marrow. Recovery from bone marrow depletion is possible with specialized medical care. Stem cell migration and repopulation are known to help regeneration of bone marrow up to 8–10 Gy. Doses beyond 20–30 Gy not only impair the regeneration process but are also known to fail the stem cell migration. Such exposures also may be the cause of failed stem cell transplants due to stromal injury.

Reduced leucocytes can lead to compromised immune system leading to vulnerability to infection. Besides, reduced platelet counts can lead to internal hemorrhage and further loss of blood cells. Tissue hypoxia can result due to acute depletion of red blood cells. Fever, anorexia, anaemia, breathlessness, fatigue and chills can be symptomatic observations. Systemic infection can also lead to multiple organ failures in due course during 3–8 weeks after exposure. In the dose range of 3–5 Gy, 50% fatality is observed in a time span of 1–2 months among individuals exposed. These observations were when no medical intervention was possible. This dose is also known as $LD_{50}(60)$ referring to 50% fatality in 60 days [5]. With medical interventions and support, it is possible to drastically reduce the fatality. Administration of bone marrow colony stimulants or colony growth factors (CGFs) can help regeneration of bone marrow. Antibiotics, aseptic conditions, reverse isolation and medical care help to avoid external infection and further support the recovery.

7.3 Gastrointestinal Tract Damage

Digestive system or gastrointestinal (GI) tract has a food-body barrier. The barrier is dynamic in nature. Small intestine is the most sensitive in GI for tissue reactions. Resistance is progressive in the order; mouth, pharynx, stomach, colon, rectum and oesophagus. Epithelial cell layer of intestine gets replaced with a span of 3–6 days. When the replacement is hampered, functional as well as structural damage can be observed within the same span of time. Crypt of lieberkuhn, which are stem cells, and hence show higher radiation sensitivity, show severe functional impairment upon exposure to 5 Gy. Symptoms associated with GI damage are anorexia, nausea, vomiting and diarrhea. Usually, GI damage with whole body doses exceeding 8 Gy is considered fatal with death occurring within the second week after exposure. Electrolyte imbalance, dehydration, systemic infection leading to sepsis, loss of food absorption capacity, structural damage to villi and circulatory collapse. Recovery may be possible if the exposure is limited only to GI as in internal exposure. Systemic exposure can lead to further complications and immune-suppressed conditions leading to sepsis.

7.4 Damage to Nervous System and Vasculatory Tissues

Vasculatory and nervous systems are classical examples of ensemble of high resistant tissues. However, these tissues pose extremely dangerous situations if damaged. World-wide, there are very few examples where exposures relevant to CNS damage have occurred. Doses in the range of exceeding 15–25 Gy, prodromal syndromes like agitation, apathy, convulsions, ataxia and coma can appear within few hours. Such exposures usually result in death in a span of hours to about two to three days. Severe

headache within 3–4 h followed by drifting coma can occur. In most cases leading to CNS damage, lethality occurred within 100 h post-exposure.

Such exposures are of high relevance in radiation therapy when such systems are involved in the field of treatment. Radiotherapy has shown that CNS can tolerate a dose of 55 Gy delivered over a period of 5–6 weeks. Doses beyond 70 Gy, even when fractionated can cause severe necrosis in the brain.

7.5 Damage to Individual Organs

Besides vital tissues, peripheral organs or tissues play a major role in radiation protection. In particular, skin, limbs (hands and feet) and lens of the eye need special attention as these organs are likely to be exposed more to radiation while performing certain specialized tasks such as source fabrication, handling of open isotopes and many interventional radiology procedures. Typically, these organs are least sensitive and are assigned minimal or no tissue weighting factors. These tissue weighting factors are based on stochastic effects. If we account for exclusive exposures to these peripheral organs, there are possibilities of exceeding threshold doses of deterministic effects. To avoid such serious exposures, separate limits are imposed on these organs. In therapeutic applications, certain vital organs need to be taken care due to their sensitivity towards deterministic effects. Both early effects such as clinical symptoms and late effects such as fibrosis and functional impairment are the limiting factors leading to early and late normal tissue complications respectively.

7.6 Peripheral Limbs and Skin

Basal layer of epidermis, which is rich in epithelial cells is the most radiosensitive. The layer is at a depth of 70–120 μm. Less penetrating high LET radiation such as α and very low energy protons cannot penetrate the upper inactive layer and hence, do not pose much risk or damage when exposed. Peripheral limbs, i.e., hands and feet are likely to come in contact with intense radiation while working due to contact exposures. Skin from other body parts also can get high doses during occupation due to localized contaminations. In particular, β emitters can deliver large doses to skin if such sources come in contact with skin. Many encapsulated sources, which use high density steel as encapsulation material, emit a lot of secondary electrons from their sources. Such sources if held by bare hands, can not only deliver large doses due to secondary electrons but also due to intense primary gamma rays. Intensity of radiation increases with inverse of square of the distance (inverse square law) due to isotropic emission and solid angles involved. Doses exceeding 3 Gy can result in transient erythema.

The redness due to transient erythema appears within a few hours and disappears in a day or two. Temporary depilation or loss of hair can be observed in the dose range of 3–5 Gy. Depilation generally occurs during 14–18 days post-exposure [6].

Exposure to X-ray doses up to 6–8 Gy results in fixed erythema. It is usually considered as deep tissue damage. Fixed erythema will get manifested in 2–3 weeks after exposure. For high LET radiation, threshold doses are much lesser. For example, for fast neutrons, it is 2 Gy.

At higher doses exceeding 5 Gy, falling off of the top layers of skin leading to exposed dermis is seen, which is known as dry desquamation. Dose range of 15–20 Gy will result in wet desquamation with symptoms of exudation of fluids from the exposed dermis. 15–25 Gy will lead to blisters formation in about 15–25 days. Above 25 Gy can lead to necrosis in about 21 days. Skin can tolerate doses up to 60 Gy when delivered in fractions for therapeutic reasons. In radiotherapy, changing the direction or rotating gantry treatment will also help to reduce skin dose by distributing the dose to different areas of skin. For high energy therapeutic X-rays, skin sparing can happen due to lesser skin dose due to build up effect leading to higher doses at deeper depths [7–9].

Late effects on skin such as atrophy of skin, loss of elasticity, non-functioning of sweat glands, permanent epilation resulting from total destruction of hair follicles and extensive dermal fibrosis are some of the limiting factors. Such effects are common when larger dose per fraction are delivered.

7.7 Reproductory System

Till recent past, too much importance was given to gonadal exposures due to incomplete information on heritable effects. With present knowledge, heritable effects are of least importance. Deterministic effects such as temporary and permanent sterility can be observed. In males, the spermatogonia cells which divide and mature to form sperms in the testis are considered the most radiosensitive cells as they are the least differentiated cells. Threshold dose for temporary sterility is 0.15 Gy. However, this effect is not considered as a serious effect as no morbidity is involved. Permanent sterility can be observed in the dose range of 5–6 Gy. Maturing oocytes in females are the most radiosensitive germ cells. Number of oocytes are fixed in females at the time of birth. With the increase in age, the dose required to observe sterility decreases. Temporary sterility lasting for a few months can be observed at a dose of 1 Gy in females. In both males and females, both temporary and permanent sterility are important only in therapeutic procedures where reproductory systems are likely to receive large dose.

7.8 Eye Lens

Eye is a sensory organ, constitutes many highly sensitive as well as highly resistant tissues to radiation damage. Cornea and conjunctiva are known to be sensitive to radiation exposure. Retina and the optic nerve are quite radio resistant as observed in patients undergoing therapeutic procedures. Anterior epithelial cells which possess the proliferation ability through the lifetime are very sensitive. When these cells are damaged, it can lead to cell derbies and breakdown products which eventually migrate into posterior pole of eye lens. Typical morphology of cataract due to radiation exposure differs from that of naturally occurring cataract due to this reason. Since causal relation is established, though the effect may not appear in every individual, this effect is still classified under deterministic effects. Recent information shows 1% incidence of cataract when lifetime equivalent dose to eye lens is 1 Sv. New recommendations of dose limits to eye lens, i.e., 20 mSv/year are based on this threshold dose distributed over 50 years of occupation. It is also noteworthy that simple protective devices such as lead glass protective screen and goggles reduce the eye lens doses by several order, which are easily achievable. Besides, cataract can be surgically correctable and hence, cannot be considered as highly morbid. Highly skilled radiation workers such as interventional radiologists performing cardiac procedures, orthopedic surgeons and fluoroscopy technicians are the ones who are prone to high doses to eye lens.

7.9 Vital Tissues

Many vital tissues such as lungs, heart, kidney and endocrine glandular systems can also show serious damage when exposed to large doses. However, such damages are of relevance in therapeutic procedures when in the field of treatment. Acute 10 Gy lung dose can result in acute radiation pneumonitis known as ARP-inflammation leading to 50% mortality. Fibrosis of alveolar walls leading to impaired oxygen exchange and loss of fine vasculature are examples of late effects among patients exposed to lung doses. Such damages can make the lungs predisposed to infections and pneumonias. Among glandular systems, thyroid glands are relatively more radiosensitive. Also, glands in children show higher sensitivity compared to adults.

8 In-Utero Effects of Radiation

Effects of radiation due to exposure during embryonic or fetal stage are termed as in-utero effect. It is not being transferred from the parent to the embryo/child hence different from the genetic or hereditary effect. Further, the effect depends mostly on gestational age and the absorbed dose to the fetus. Embryonic development can be

Table 3 Threshold dose required for mental retardation and lethal effect to the embryo [10, 11]

Age (days)	Threshold for lethal effects (mGy)	Threshold for malformations (mGy)
1	100	No effect
14	250	–
18	500	250
20	> 500	250
50	> 1000	500

divided into three stages, pre-implantation stage 0–10 days up to 8 weeks embryonic stage and 9–38 weeks fetal period. Major organogenesis takes place during the embryonic stage and some during fetal stage. By 6-week embryo has heartbeat and little limbs too. Major part of brain development takes place between 8 and 15 weeks but extends from 3 to 25 weeks. By 8 weeks the embryo looks like a tiny human it is now to be called as fetus. Effects of radiation during pre-implantation stage are lethal effects 'all or none'. Embryo contains only few cells which are not specialized. If only few killed-remaining pluripotent cells replace the cells loss within few cell divisions and if too many cells are damaged, the embryo is resorbed. In the organogenesis stage, if significant dose is absorbed, it may result in major developmental abnormalities in the fetus and resulting baby. These include mental retardation and organ malformations in addition to lethal effects. 8–15-week developmental period is highly sensitive for radiation induced reduction in intelligence quotient Further, the fetal stage is relatively resistant compared to younger embryonic stage and has higher threshold for lethal effects and malformations. A threshold dose required for mental retardation and lethal effect to the embryo is given in Table 3.

9 Stochastic Effects of Radiation

Cancer and hereditary diseases are well known examples of stochastic effects of radiation. These effects are induced by the induction of mutation in some crucial genes (e.g. cell cycle regulator genes, etc.) of the cells. Radiation is known to induce mutation in the genome, randomly. Unfortunately, if mutation happens to one or few sets of these crucial genes, it may lead to the transformation of a normal cell to a cancer cell. One or a few transformed cells may cause the development of cancer. Majority of damaged DNA gets repaired hence transformation is a rare phenomenon. Further, majority of transformed cells are being targeted by immune cells and eliminated from the body. Transformed cells escape from immune system, persist for longer periods (years to decades) in dormant conditions (latency period) and may develop tumor, later. Latency period for the appearance of cancer is in decades except for leukemia (3–5 yearss). Due to the involvement of these uncertainties, stochastic effects are probabilistic in nature.

It is observed that stochastic effect increases linearly with the increasing dose, in the higher dose range (above 100 mSv, based on human data of atomic bomb survivors, as shown in Fig. 7. Human data is not conclusive in the lower dose range, below 100 mSv. In the lower dose range (i.e., below 100 mSv), it is very challenging to epidemiologically detect/quantify stochastic effects of radiation (cancer and hereditary diseases), due to high background levels and inherent variations within the population caused by various carcinogens/mutagens (cigarette smoking, pesticides, etc.), which are commonly used by the common public in the society. Correlation of stochastic effect with the dose, below 100 mSv is not clear. Still, it is an open area of research/investigation. For the sake of radiation protection in such lower dose ranges, ICRP has, defined standards, assuming, stochastic effects will appear linearly with the increasing dose (ICRP-107, BEIR VII). This is known as Linear No Threshold (LNT) hypothesis.

Probability of occurrence of stochastic effect increases with the increasing dose, though severity of effect (cancer and hereditary disease) is independent of the dose (don't increase with the increasing dose). Severity of the stochastic effect depends on latency period of that stochastic effect.

Certain key features for stochastic effects, to remember:

- Occurs due to cell transformation (mutation/chromosomal aberration, etc.)
- There is no threshold dose below which stochastic effect cannot occur (every possible dose has a certain probability of inducing stochastic effect)

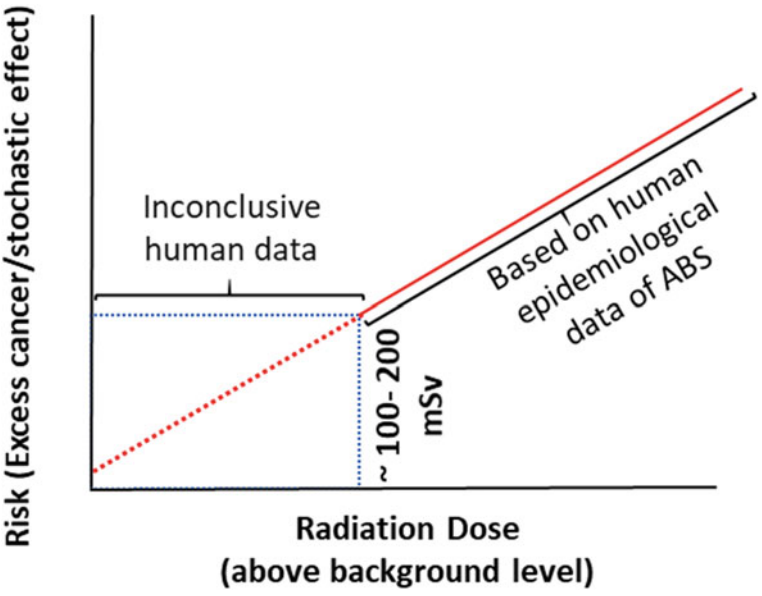

Fig. 7 Schematic illustration of incidence of effect (cancer and hereditary diseases) with the increasing dose, linearly, following Linear No Threshold (LNT) hypothesis

- Probabilistic in nature (occurs by chance in some individuals)
- Probability/risk or chance of occurrence increases with dose (chances of occurrence increase linearly with increasing dose)
- Severity of the effect is independent of dose
- E.g. Cancer and hereditary diseases.

Types of stochastic effects:

1. Somatic stochastic effect
2. Genetic or hereditary stochastic effect.

Somatic stochastic effect occurs due to mutation/transformation of somatic/vegetative/body cells, like, lung cell, liver cell, kidney cell or any other body cell expect germ cells (Fig. 8). Since transformation is there in the somatic cell, the effect will occur in the body of the same individual in the same generation. Next generation will not be affected.

Genetic or hereditary stochastic effect occurs due to mutation/transformation in germ cells. Since germ cells contribute in the formation of next generations (offspring), the effect will occur in the next generation. Current/existing generation will not be affected [12].

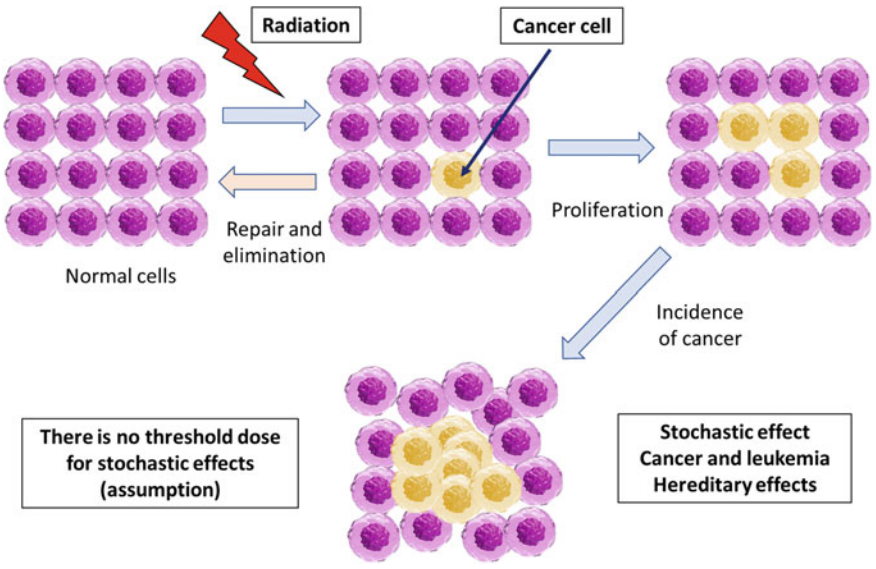

Fig. 8 Schematic illustration of mechanism of radiation induced transformation of a normal cell to the cancer cell and development/progression of cancer

9.1 Radiation Induced Carcinogenesis

Over the decades, a major source of human data made available is derived from atomic bomb survivors of Hiroshima and Nagasaki. About 100,000 enrolled ABS cohort was followed up for decades to observe a possible increase in cancer induction compared to past data and prospective data of matched controls who are not exposed. Besides, many patient data wherein large doses were involved, small scale radiological incidents and industrial accidents involving radioactive sources have also provided human data. Site specific information for tissues such as bone marrow, breast, lungs, thyroid, etc. is derived to estimate detriment which eventually leads to assignment of tissue weighing factor known as W_T which is used in estimation of equivalent dose.

Induction of cancer is a multi-step process. Increase in incidences were not observed immediately after the exposures. The gap between exposure and expression of excess risk is known as latent period. This will depend on the type of cancer too. Leukaemia begin to appear within 3–5 years with most of them appearing between 5 and 7 years while some solid tumors show a latent period ranging from 10 years to in excess of 30–40 years. Young children are known to be sensitive to radiation exposure, in particular to acute lymphocytic leukemia as well as thyroid cancers. Certain cancers are gender specific, females are found to be sensitive to breast carcinoma. With the increase in age at exposure, risk decreases. Children have shown at least 2.5 times incidences of cancers compared to adults in the age range of 50–60 years. Females always have a higher risk compared to males (due to breast and thyroid).

At low doses below 200 mSv, no concrete human data exists. Even at acute exposures, no conclusive evidence were drawn. Exact shape of response to radiation exposure at low doses is uncertain and not known. In the absence of robust data on response at low doses, linear non-threshold type response models (LNT) with correction for DDREF are adopted and this approach is known as LNT-DRF model. As per International Commission of Radiological Protection (ICRP) estimations, the suggested risk values with weighting for mortality, curability and relative length of life lost, which account for the overall morbidity is 5.5% Sv^{-1} for general public and 4.1% Sv^{-1} for occupational workers. The estimated risks are lower for occupational worker cohort due to age truncated nature, which excludes children.

9.2 Genetic Risk Estimation

There is no human evidence of radiation induced genetic effects. The initial fear of heritable effects due to radiation exposure is proven to be unwarranted. In the absence of human data, the risk evaluation is done by animal experiments through mice model. Doubling dose projection model is used to estimate and project the risk from mice model to human population.

$$\text{Risk} = P \times \text{DD} \times \text{MC} \times \text{PRCF}$$

From mice models, doubling dose (DD) is estimated to be 1 Gy, which doubled the incidence of mutation rate. *P* is the prevalence for the given set of loci of genes studied. Genetic disorders which are observable in mice such as skeletal abnormalities, change in color coat, shape of ear, etc., are evaluated. Since many disorders are recessive and multigenic in nature, correction factor Mutation Component (MC) is introduced which predicts the turn of events in population upon increased rate of induction of mutation in these genes. Besides, radiation induced damages are usually serious in nature, leading to incompatibility with live birth or progression of pregnancy leading to terminations. Majority of natural terminations of pregnancies are due to one or the other serious chromosomal anomalies which can be observed. However, this selection is not strong in lower organisms such as mice. To account for this Potential Recoverability Correction Factor (PRCF) is used. Despite these correction factors, it appears that the overall risk estimates are conservative towards higher sides. The estimates are 0.2 and 0.1% Sv^{-1} for general public and occupational workers. The risk is lower for occupational workers due to higher fraction population in non-reproductory age compared to public cohort.

9.3 Low Dose Effects

There is no human evidence of the effects of radiation at low doses below 200 mSv of acute exposure and up to about 1000 mSv of chronic exposure. It is assumed that at low doses, risks are similar to that of high doses [13]. The only information that is systematically documented is from atomic bomb survivors' studies. Even in these studies, risk estimations below 200 mSv is not only inconclusive but also questioned by the scientific community [14, 15]. Various factors such as uncertainties in dose estimation, inter-individual response, lifestyle factors, sensitivity of study population, background incidence of cancer and age group matching of control population for comparison have added the complications. Over the years, many confounders were identified but could not be eliminated completely due to inherent complexities of epidemiological data.

In the absence of human data, experimental evidence were gathered using cellular and animal models. Nonetheless, the question of validation of these models used for projecting the risk on human beings prevailed. It is known that experimental animal models are prone to genetic instabilities, weaker natural selection and inherently possess poor immune systems. It is also known that heritable abnormalities are more pronounced in such model systems upon exposure to challenges such as radiation and mutagenic agents. In the past, estimation of genetic risk was grossly over estimated owing to this fact and projected directly on human population leading to erroneous conclusions.

Large uncertainties are expected out of both experimental and epidemiological studies at low doses. Most of these observations are inconclusive due to statistical

reasons. It is generally accepted by the guideline makers that if at all any countering effects exist, it is all part of the observation in both experimental and epidemiological studies, and hence, there is no need to emphasize on the same as it is likely to undermine the importance of harmful risks. However, many epigenetic observations, reports on hormesis predicting possible beneficial effects of low levels of radiation exposure, immune-modulations, adoptive response and bystander effects have contributed and questioned the effects of radiation at low doses.

The biggest challenge of projecting the risk onto the study population in an epidemiological study is to complete the task of lifetime risk estimates in the reference population, which will take several decades to conclude. Besides, inherent variations within reference population, loss to follow up subjects, lack of matched control or unexposed cohort, very low probability of incidences, large variation of background and many such epidemiological parameters lead to the observations not only inconclusive but also erroneous if not interpreted appropriately.

Currently, it is accepted that the risk estimates at low doses are done only for the purpose of defining operational parameters such as dose limits and constraints. The line of approach is always done in a conservative manner, which has led to many unwarranted operational constraints, expenses, misconceptions and also undue fear. The guidelines clearly suggest not to estimate individual risks due to such low doses, and predict risks due to medical and diagnostic exposures.

9.4 Observations from High Background Area

There are many pockets of high background radiation areas around the world with doses ranging from 5 mSv to as high as 100 mSv per year. Many of these belts are well occupied, with generations who have lived there. Major fraction of the dose is delivered by external origin and also through inhalation due to radon and thoron progenies. Many countries have studied these populations with a systematic approach for establishing possible outcomes. The most important emphasis is to observe heritable effects and changes in cancer incidences among these. The studies have also tried to mechanistically establish possible molecular and cytogenetic effects.

Some studies have indicated marginal changes in chromosomal aberrations while most others have drawn null conclusions. No evidence of heritable effects is reported in any of these populations, which is considered as a major outcome of these studies as initially it was thought that radiation can have serious heritable effects. Later, it was hypothesized that the serious nature of cellular level changes due to radiation damage, which is not viable with progression of the cell cycle and likely early termination is responsible for such results. A correction factor for Potential Recoverability Correction Factor (PRCF) is introduced to correct the risk estimations from the doubling dose model.

No increase in cancer incidences was observed in these high background areas. Many studies have explored mechanistic possibilities such as hormesis, adaptive responses, bystander effects and low dose immune-modulations. The expected

number of excess is within the statistical uncertainties and hence, all these models are inconclusive.

10 Conclusion

Radiation effects on humans are trivial at low doses. No conclusive human data exists below 200 mSv even from atomic bomb survivors. No human data is available for genetic effects. Risk analysis of stochastic effects at low doses is only limited to define dose limits. These risk figures should not be considered for risk estimation of low doses. Information on observed effects is derived from past radiological incidents and the largest cohort of atomic bombing survivors. Radiation has the ability to render serious deleterious deterministic effects when exposed to high doses, acutely, over medically significant doses, i.e., exceeding 1 Gy. Mechanistic knowledge on biological effects of such high doses has helped to avoid, mitigate and manage such incidents.

References

1. Hall EJ, Giaccia AJ (2018) Radiobiology for the radiologist, 8th edn. Lippincott Williams & Wilkins
2. Vogin G, Foray N (2013) The law of Bergonié and Tribondeau: a nice formula for a first approximation. Int J Radiat Biol 89(1):2–8. https://doi.org/10.3109/09553002.2012.717732
3. International Atomic Energy Agency (2005) Generic procedures for a medical response during a nuclear or radiological emergency. EPR-Medical-2005
4. Andrews GA, Auxier JA, Lushbaugh CC (1965) The importance of dosimetry to the medical management of persons accidentally exposed to high levels of radiation. No. ORNL-P-1446; CONF-650302-22. Oak Ridge National Lab.(ORNL), Oak Ridge, TN (United States)
5. CDC radiation emergencies \textbar acute radiation syndrome: a fact sheet for physicians, Apr 2022. Accessed 13 June 2023 [online]. Available https://www.cdc.gov/nceh/radiation/emergencies/arsphysicianfactsheet.htm
6. I. and WHO. How to recognize and initially respond to an accidental radiation injury [online]. Available https://www.who.int/ionizing_radiation/a_e/IAEA-WHO-Leaflet-Eng%20blue.pdf
7. Hopewell JW (1990) The skin: its structure and response to ionizing radiation. Int J Radiat Biol 57(4):751–773. https://doi.org/10.1080/09553009014550911
8. Kemerink GJ, van Engelshoven JMA, Simon KJ, Kütterer G, Wildberger JE (2016) Early X-ray workers: an effort to assess their numbers, risk, and most common (skin) affliction. Insights Imaging 7(2):275–282. https://doi.org/10.1007/s13244-015-0457-2
9. Balter S, Hopewell JW, Miller DL, Wagner LK, Zelefsky MJ (2023) Fluoroscopically guided interventional procedures: a review of radiation effects on patients' skin and hair \textbar radiology. Radiology 254(2). Accessed 13 June 2023 [online]. Available https://doi.org/10.1148/radiol.2542082312
10. Amin AAE (2020) Radiation protection course for radiologists L4, radiation effects on embryonic development and foetal life, 28 Aug 2020 [online]. Available https://www.slideshare.net/AminAmin/radiation-protection-course-for-radiologists-l4
11. ICRP (2003) Biological effects after prenatal irradiation (embryo and fetus). ICRP Publication, 90

12. Nakamura N, Yoshida N, Suwa T (2023) Three major reasons why transgenerational effects of radiation are difficult to detect in humans. Int J Radiat Biol:1–15. https://doi.org/10.1080/09553002.2023.2187478
13. P. 2 BEIR VII (2006) Health risks from exposure to low levels of ionizing radiation: in national research council 2006. The National Academies Press, Washington, DC [online]. Available https://doi.org/10.17226/11340
14. Calabrese EJ (2015) On the origins of the linear no-threshold (LNT) dogma by means of untruths, artful dodges and blind faith. Environ Res 142:432–442. https://doi.org/10.1016/j.envres.2015.07.011
15. Calabrese EJ (2019) The linear no-threshold (LNT) dose response model: a comprehensive assessment of its historical and scientific foundations. Chem Biol Interact 301:6–25. https://doi.org/10.1016/j.cbi.2018.11.020

Monitoring of External Gamma and Beta Exposures

S. M. Pradhan, Munir S. Pathan, and T. Palani Selvam

1 Introduction

Individual exposure to external ionizing radiation occurs in almost all radiation facilities involved in handling of radioactivity and radiations for various purposes. The exceptions could be the facilities where weakly penetrating (non-penetrating) radiation such as photons of less than a few keV, betas of less than 65 keV and alpha radiations are only used. The external exposure also occurs in practices such as operation of jet aircraft (aviation industry), space flights (space exploration), operations with and storage of materials not usually regarded as radioactive, but which contain significant traces of natural radionuclides, etc. due to naturally occurring radioactive materials (NORM). The weakly penetrating radiations mentioned above though irrelevant for external exposure monitoring are very important for internal exposure monitoring when open radionuclides enter the body through various routes. Three broad classes of human exposure to ionizing radiation are occupational exposure, medical exposure and public exposure. Exposure at work due to the activities carried out to accomplish the work is treated as occupational exposure. Medical exposure pertains to the exposure of patients as part of diagnosis or treatment. Public exposure is defined to comprise all other exposures (other than occupational and medical exposure). Dose limits are specified for control of occupational exposure and public exposure. It is a legal requirement to demonstrate compliance with the dose limits. Hence monitoring and assessment of doses to occupational workers and members of public is carried out thereby ensuring radiological safety. The method of monitoring is different for the two types of exposure. In case of external exposure, individual occupational doses generally are measured directly by a dosimeter worn by the

S. M. Pradhan (✉) · M. S. Pathan · T. Palani Selvam
Radiological Physics and Advisory Division, Health, Safety and Environment Group, Bhabha Atomic Research Centre, Mumbai 400085, India
e-mail: smppms@barc.gov.in

D. K. Aswal (ed.), *Handbook on Radiation Environment, Volume 2*,
https://doi.org/10.1007/978-981-97-2799-5_6

person during the course of work. Public exposures are assessed through indirect measurements and calculations.

The radiations causing external exposure are mainly photons (gamma and X-rays), beta and neutrons. The external exposure due to energetic particles such as protons, muons and pions is not very common and is restricted to cosmic radiation and small component of radiation field outside the shielding of high energy particle accelerators. This chapter deals with the monitoring of external photon and beta exposures along with associated general monitoring principles. The relevance of monitoring of occupational exposure, different quantities used for radiation protection, calibration of personal dosimeters, design of monitoring program along with an example of $CaSO_4$:Dy based personnel monitoring system is described in the chapter. The chapter ends with description of recent advances in the field of external radiation personal dosimetry.

2 Relevance of Individual Dose Monitoring in Radiological Protection

Ionizing radiation and radioactive materials have various beneficial uses, but some processes, like nuclear power production, generate them as unwanted by-products. Exposure to ionizing radiation can pose health risks. Therefore, there are both benefits and risks associated with activities involving ionizing radiation. Radiological protection aims to safeguard humans from the harmful effects of ionizing radiation without overly restricting beneficial practices that involve radiation exposure. This is done by preventing deterministic effects and minimizing the risk of stochastic effects to an acceptable level. The system of radiological protection for proposed and ongoing practices is based on three general principles [1–4]:

1. Principle of justification of practice
2. Principle of optimization of protection
3. Principle of dose limits.

The principle of justification requires that any activity involving radiation must offer a clear benefit that outweighs the potential harm from radiation exposure. This harm can manifest as radiation detriment which is reflected in both individual and collective doses resulting from a practise. Optimization, the second principle, stresses that within justified practises, efforts should be made to minimize individual radiation doses, reduce the number of exposed individuals and prevent potential exposures. These exposures are expected to be kept as low as reasonably achievable (ALARA) with due consideration of economic and social factors in making decisions about radiation protection levels. The third principle establishes dose limits for individuals, setting clear boundaries for acceptable levels of exposure for both workers and the public. International organizations like the ICRP and IAEA provide recommendations on these limits, which are often adopted as legally binding standards by national regulatory bodies. To ensure the continuation of such practises, it's crucial to

monitor individual doses from relevant exposure pathways accurately. This highlights the importance of individual monitoring for external gamma and beta radiation.

The assessment and control of external and internal exposures is the primary objective of the monitoring. This is done out by carrying out measurements in the workplaces and associated areas for deriving information on the status of radiological conditions including doses incurred. The level of protection which may be quantified in terms of values of protection quantities can be achieved and demonstrated based on the monitoring program. Satisfactory monitoring results provide reassurance of the safety status. Further, monitoring data may be used for reviewing optimization programmes.

Types of Monitoring

There are several ways in which monitoring programmes can be subdivided. Depending on the subjects to be monitored, the program can be categorized into the following two types.

1. Environmental/public
2. Occupational.

Environmental/public monitoring program: The objective of this program is to protect public and environment due to operation of practices. The monitoring program includes monitoring discharges from the practices, assessment of exposure or potential exposure of population, and verifying adequacy of controls on discharges from the practice.

Occupational monitoring program: Occupational monitoring program is directed towards radiological protection of radiation workers and the workplaces. The monitoring program includes assessment exposure of workers, determination of status of radiological conditions, evaluation and improvement of operating procedures, provision of dose information in case of accidental exposures, etc.

The occupational monitoring program comprises two main components: workplace monitoring and individual monitoring. Workplace monitoring involves measurements taken within the working environment, while individual monitoring entails measurements conducted on workers themselves or of radioactivity present on their bodies, followed by the interpretation of these measurements. Workplace monitoring can be divided into three categories: monitoring for external radiation, air contamination and surface contamination. On the other hand, individual monitoring can be subdivided into three categories as well: monitoring for external exposure, internal exposure and skin contamination. This chapter covers individual monitoring for external exposure in greater detail.

3 Quantities Used in Radiological Protection and Their Interrelationship

The quantities used in radiological protection are described in a separate chapter. The three classes of the quantities are limiting quantities or protection quantities, operational quantities and physical quantities. The protection (limiting) quantities [1, 2, 4] are defined in an organ or tissue (Equivalent dose) and whole body (Effective dose) and are used to specify the dose limits. The protection quantities are defined for both external and internal radiation exposure of human body. As the protection quantities are not practically measurable, operational quantities are defined by ICRU [5–8] for assessment of the protection quantities. The operational quantities can be realized in the laboratory and used for calibrating the measuring devices and instruments. For monitoring the external exposure, separate operational quantities are specified for area monitoring [Ambient dose equivalent $H^*(d)$ and Directional dose equivalent $H'(d, \Omega)$] and individual monitoring [Personal dose equivalent $H_p(d)$].

Protection quantities and operational quantities are connected to 'basic physical quantities' widely used in radiation metrology, particularly in dosimetry. These physical quantities are defined regardless of any specific aspect of radiological protection. They are directly measured through primary standards at national laboratories and encompass neutron fluence, photon exposure (or air kerma), and absorbed dose from beta radiation, among others. Additionally, these quantities are point-specific, meaning they are defined at any location within a radiation field. As previously noted, protection quantities such as equivalent dose and effective dose cannot be directly measured. Operational quantities, however, are formulated to offer a practical estimation of the corresponding protection quantity in typical working scenarios. Ensuring that the operational quantity (denoted as H_{op}) provides a conservative estimate of the appropriate protection quantity (denoted as H_{prot}) is crucial. This verification involves confirming that the ratio $H_{\text{prot}}/H_{\text{op}}$ remains at or below unity. Hence, establishing a relationship between these two types of quantities becomes imperative. When irradiation conditions are known, the values of both quantities can, in principle, be calculated based on physical parameters such as particle fluence (ϕ), air kerma free in air (K_a) and tissue absorbed dose (D) [7]. Figure 1 illustrates the interconnection among physical, protection and operational quantities, while Table 1 [9] offers insights into the application of these quantities.

3.1 Conversion Coefficients for External Exposure

Conversion coefficients relate operational quantities and protection quantities to physical quantities. These are calculated using radiation transport codes, and the appropriate models or phantoms corresponding to the quantity. These coefficients undergo cross-validation or comparison to ensure that operational quantities provide conservative estimates of protection quantities. Furthermore, conversion coefficients

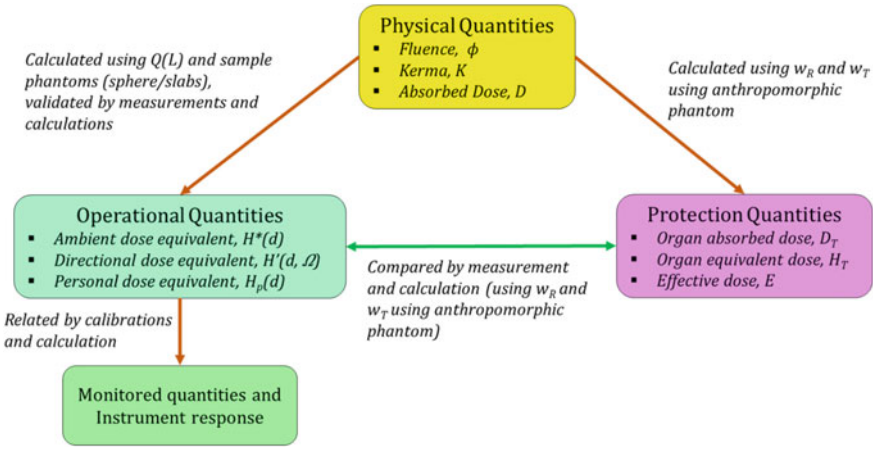

Fig. 1 Relationship of quantities for radiological protection monitoring purposes (adapted from [10] with permission from International Commission on Radiological Protection)

Table 1 Application of the protection quantities (ICRP 103 [4]) and the ICRU Report 39/51 [5, 8] operational quantities (existing operational quantities)

	Whole body	Lens of the eye	Local skin
Protection quantity	Effective dose E	Equivalent dose to the lens of the eye H_T lens	Equivalent dose to local skin H_T local skin
Operational quantity			
Area monitoring	Ambient dose equivalent $H^*(10)$	Directional dose equivalent $H'(3, \Omega)$	Directional dose equivalent $H'(0.07, \Omega)$
Individual monitoring	Personal dose equivalent $H_p(10)$	Personal dose equivalent $H_p(3)$	Personal dose equivalent $H_p(0.07)$

enable the translation of operational quantities into practical applications, such as calibrating dosimeters, assessing performance, conducting type testing and other essential tasks related to dosimetry and survey instruments.

3.1.1 Conversion Coefficient for Protection Quantities

Conversion coefficients linking physical quantities to dose quantities within the human body for external exposure to photons, neutrons or electrons have been computed for monoenergetic radiation. These calculations have been carried out through Monte Carlo simulations by various research groups employing geometrically defined anthropomorphic phantoms, such as the hermaphrodite or ADAM and EVA models [10–12]. An extensive dataset of evaluated coefficients for these three

types of radiation was meticulously compiled by an international committee from the ICRU/ICRP, subsequently published by the ICRP [10], and is now recommended for general application.

In line with the 2007 recommendations of ICRP Publication 103, conversion coefficients for protection quantities have been developed by the ICRP in their publication 116 (2010) [13]. These conversion coefficients are derived from mathematical reference phantoms [14], representing both reference male and reference female anatomies [15], across eight standard geometrical orientations of the incoming radiation field. The reference computational models are constructed from computed tomographic data of actual individuals, resulting in digital three-dimensional representations of human anatomy. ICRP 116 includes conversion coefficients for a broad spectrum of particle types and energies, encompassing those present in cosmic radiation and particle accelerators, with energy ranges extending, in some instances, up to 200 GeV.

3.1.2 Conversion Coefficient for Operational Quantities

As previously noted, conversion coefficients are indispensable for calibrating measurement devices across various radiation types and quantities of interest. While conversion coefficients for ambient and directional dose equivalents have been determined using the ICRU sphere phantom, those for personal dose equivalent quantities are specified for the ICRU slab phantom [pertaining to $H_p(10)$ and $H_p(0.07)$] as well as wrist and finger phantoms [solely for $H_p(0.07)$. Evaluated and recommended data for photons, neutrons and beta radiation can be found in ICRP 74 [10], ICRU 57 [16], and certain pertinent ISO/IEC standards [17, 18]. Additionally, the conversion coefficients for $H_p(3)$ calculated for the cylinder phantom of ICRU tissue [19] are also outlined in the aforementioned ISO/IEC standards.

4 Calibration of Personal Dosimeters

Calibration is the process to establish the relationships between values indicated by a measuring instrument/measuring system, and the corresponding known values of a measurand under specified conditions [20, 21]. In other words, the indication given by a radiation measuring instrument is quantitatively determined as a function of values of the measurand under standard conditions during calibration. Depending on the extent of information is required, the calibration procedure for personal dosimetry system can be categorized into following two categories.

(a) Type tests: These tests are carried out to determine the characteristics of a particular type or model of a production instrument/dosimetry system. These involve extensive testing over a wide range of the influence quantities such as energy,

angle of incidence, dose or dose rate and radiation type, a variety of environmental conditions. Specific performance requirements for radiation monitoring equipment are specified in various national and international standards such as the International Electrotechnical Commission (IEC).

(b) Routine calibration: This is carried out to determine a calibration factor for routine application of the dosimeter and dosimetry system. Routine calibration of personal dosimeters can be done free in air or on a PMMA phantom, and even with a type of radiation different than that the system is intended to measure. Such simplifications are justified when routine calibration method is finalized during the type test of the dosimetry system. The correspondence between the response of dosimeters per unit time (or exposure/air kerma) in the test (routine calibration) field and the dosimeter response per unit $H_p(d)$ under type test conditions is established.

4.1 Quantities, Phantom and Radiation Beams for Calibration of Personal Dosimeters

The personal dosimeters should be calibrated in terms of operational quantities for individual monitoring of external exposure, i.e. the personal dose equivalent $H_p(d)$ with the recommended depth $d = 10$ mm to estimate effective dose and $d = 0.07$ mm to estimate equivalent dose to skin and $d = 3$ mm for estimating dose to the lens of the eye. Though the operational quantities for individual monitoring are defined in human body, their definition is extended to ICRU tissue phantoms [6] of appropriate shape and size to provide an approximation of the absorption and backscatter conditions of the human body. Three types of phantoms, all composed of ICRU soft tissue, are recommended for calibration of whole-body dosimeters, wrist or ankle dosimeters and finger dosimeters. These are a slab phantom to represent a human torso, a pillar phantom for wrist or ankle dosimeters and a rod phantom for finger dosimeters. For $H_p(3)$ the proposed phantom is the cylinder phantom defined by Bordy et al. [19] as a cylinder of 20 cm length and 20 cm diameter made of ICRU tissue. Conversion coefficients relating the air kerma free in air with the $H_p(d)$ are published in literature [10, 16, 17] for various phantoms, radiation beam qualities and angle of incidences.

ICRU tissue phantoms are not generally available for practical measurement due to difficulty in fabrication of ICRU tissue material. To tide over the situation, ISO has recommended surrogate practical phantoms for experimental measurements of the response as a function of radiation energy and direction of radiation incidence and calibrations of personal dosemeters. The different specified phantoms are the ISO slab phantom for whole body dosemeters worn on the body, the ISO pillar phantom for dosimeters worn on the wrist or the ankle, the ISO rod phantom for dosimeters worn on the fingers and the cylinder phantom for the eye dosimeters (Fig. 2). The ISO slab phantom is water filled hollow slab with PMMA walls (front wall 2.5 mm thick, other walls 10 mm thick) and of outer dimensions 30 cm × 30 cm × 15 cm. The ISO pillar phantom is a water filled hollow cylinder with PMMA walls and an

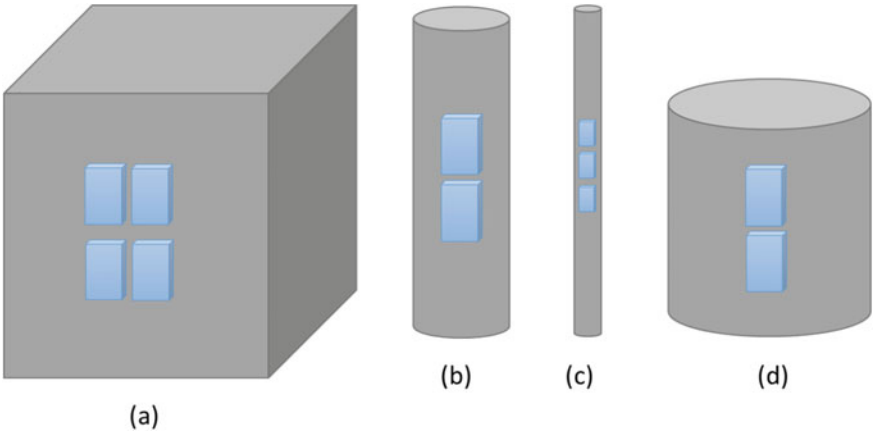

Fig. 2 Phantoms used for calibration of personnel dosimeters (**a** ISO slab phantom, **b** ISO pillar phantom, **c** ISO rod phantom and **d** cylinder phantom)

outer diameter of 73 mm and a length of 300 mm. The cylinder walls have a thickness of 2.5 mm and the end faces of 10 mm. ISO rod phantom is a PMMA cylinder of 19 mm diameter and a length of 300 mm. The cylinder phantom is a water filled hollow cylinder with PMMA walls and an outer diameter of 200 mm and a length of 200 mm. The cylinder walls and the end faces have a thickness of 5 mm. These ISO phantoms are designed to provide the same backscatter as phantoms made of ICRU tissue. When these phantoms are employed as described above, no correction factors are required to be applied to the reading of the instrument under test due to possible differences in backscatter factor or properties between these phantoms and those made of ICRU tissue.

In case of irradiation with reference radiations of a mean energy equal to or above that of the radionuclide ^{137}Cs, electron equilibrium may not be established at the phantom surface where dosimeters are located. Hence, to establish the required equilibrium, a solid PMMA slab of appropriate thickness and outer dimensions equal to that of the phantom is positioned as close as possible in front of the dosimeters. The influence of the PMMA plate on the photon field by scattering and attenuation is taken into account by a correction factor k_{PMMA}. The values of required thickness of the PMMA slab and the correction factor k_{PMMA} are specified in ISO standard [17]. When several personal dosemeters are irradiated simultaneously on the front face of the slab phantom, radiation beam intensity reaching the interior of the phantom may diminish considerably depending on the quality of incident radiation. Accordingly, the amount of back scatter reaching the dosimeters from the phantom will also get affected. In addition, possible non-uniformity of incident beam intensity across phantom may cause uneven irradiation. Therefore, to minimize the above effects, number of dosimeters for simultaneous irradiation are limited. This is achieved by requiring that the dosimeters are located within a circle with a diameter, d_F, given by the approximate locus of the 98% isodose contour with respect to the dose in the

centre of the phantom front face. The values of d_F depend on the radiation quality and they are given for every reference radiation in the above ISO standard.

Photon reference fields for calibration of personal dosimeters are described in ISO standard ISO 4037-1 [22]. Four series of continuous reference filtered X radiation, each series being characterized by the resolution of the spectrum are specified. The four series are in order of increasing filtration:

(a) The high air kerma rate series: H-series;
(b) The wide-spectrum series: W-series;
(c) The narrow-spectrum series: N-series and
(d) The low air kerma rate series: L-series.

The convention for naming the reference filtered X radiation is that the letter L, N, W or H indicating the radiation quality is followed by the generating potential in kilo-electron-volt. Reference radiations produced by using radioactive sources are denoted by the letter S combined with the chemical symbol of the radionuclide (Ex. S-Cs, S-Co); reference radiations produced by nuclear reactions are denoted by the letter R followed by the chemical symbol of the element of the target responsible (Ex. R-C, R-F) for the emission of the radiation and fluorescence radiation are denoted by the letter F combined with the chemical symbol of the element of the fluorescence target responsible for the emission of the radiation (Ex. F-Sn, F-Cd).

Calibration of personal dosimeters in terms of $H_p(d)$ for photon beams involves three steps:

(a) Air kerma free in air (K_{air}) is measured in a reference field, using a reference ionization chamber calibrated by a standards laboratory.
(b) Using the conversion coefficients specified in the ISO standard, $H_p(d)$ is obtained from K_{air} for the desired phantom.
(c) The dosimeter badge being calibrated is then placed at the calibration point on a phantom and its reading M is determined. $N_{H_p} = H_p(d)/M$ gives the calibration factor in terms of the personal dose equivalent for the dosimeter badge.

To calibrate personal dosimeters and determine their response as a function of beta energy, ISO 6980 standard specifies the production, calibration and use of beta-particle reference radiation fields for the calibration of dosemeters and dose rate meters for protection purposes. The methods of production and characterization of the reference radiation are described in ISO 6980-1 [23], determination of absorbed dose rate to a reference depth of tissue from beta particle reference radiation fields is provided in ISO 6980-2 [24] and ISO 6980-3 [25] describes procedures for the calibration of dosemeters and dose rate meters.

5 Design of Monitoring Program

Personnel (individual) monitoring is used to estimate doses received by workers from external exposure in most of the circumstances. In situations where radiation field remains almost constant or individual monitoring is difficult to perform, individual doses may also be assessed from the results of workplace monitoring. In case of systematic individual monitoring, each radiation worker is issued an integrating personal dosimeter. The agency providing personnel monitoring service should be approved by the regulatory body. The individual monitoring service should operate under a quality management system (QMS) which is established as per the international standard such as ISO 17025 for testing and calibration laboratories. The QMS should include several provisions that include general requirements on impartiality of laboratory operation and confidentiality of information obtained or created, laboratory structure requirements, resource requirements, process requirements and management system requirements. Further, the service should evaluate and report the personnel doses in terms of the operational quantities, personal dose equivalent, $H_p(d)$ with adequate accuracy for all relevant types of radiation. The operational quantities are still not implemented in some individual monitoring services. In case of $CaSO_4$:Dy based personnel monitoring system in India, individual doses are presently reported in terms of whole-body dose and skin dose. These quantities are being replaced with the internationally recommended personal dose equivalent, $H_p(d)$.

5.1 Who Should Be Monitored?

Generally, operating management of a radiation facility takes decision on providing individual monitoring for a group of workers. Such decisions are reviewed by regulatory body. The above decision mainly depends on factors which are technical in nature or concerned more with industrial relations. Considerations of expected dose levels vis-a-vis relevant dose limits, the likely variations in the dose, and the complexity of the measurement and interpretation procedures are included to arrive at the decision. Individual monitoring for external radiation being simple and cheaper is used for all those who are occupationally exposed. In situations as that of air crew where circumstances prevent the doses from exceeding an identified level or the circumstances where incurred doses are consistently low, the need of personnel monitoring may not arise.

ICRP 75 recommends that groups in which the annual effective dose to some individuals is liable to exceed a selected value between 5 and 10 mSv should certainly be monitored. Groups in which all members are likely to receive an annual effective dose of less than 1 mSv will not need monitoring. The monitoring of intermediate group is desirable. The values of dose relate to the doses liable to be received, not those currently received.

5.2 Monitoring Period

The monitoring period or the period of deployment of the dosimeter is generally decided based on the type of radiation facility, nature of radiation field whether dynamic or almost uniform, the expected levels of incurred dose associated with the work, any limitations of the dosimeters such as fading properties, detection limit of the dosimetry system and any additional requirements by the regulatory body. Longer monitoring period may hamper proper investigation of unusual exposures and timely discovery of any abnormal exposure situations. In India, monitoring frequency of monthly and quarterly are generally used for monitoring of external exposure.

5.3 Considerations for Use of Skin, Extremity and the Eye Lens Personal Dosimeters

A single whole-body dosimeter worn on the trunk in the position of the highest exposure at the surface of the trunk is suitable for monitoring of most of the radiation fields encountered in occupational dosimetry. When lead apron is used in medical uses of radiation, the whole-body dosimeter should be used under the lead apron. For such applications studies also suggest use of two dosimeters one under protective clothing and the other on unshielded part of the body to obtain better assessment of effective dose. In case of non-homogeneous exposure conditions, the organs or tissues such as the skin, extremities or lens of the eye are liable to receive significant exposures which may not be estimated adequately by whole body dosimeter. Monitoring of the concerned organ/tissue by suitable dosimeters is required when equivalent dose received is sizable fraction of the dose limit. Extremity dosimeters are worn in positions that will measure the dose to the areas of the body expected to receive the highest dose. If such position is not known in advance or it is impractical to wear at these locations, a correction factor is used to estimate the maximum dose. The dosimeters to monitor dose to the lens of the eye are worn near to the eye receiving maximum dose.

5.4 Issue of DRDs

Supplementary dosimeters of direct reading type (i.e. active dosimeters) are used for controlling individual exposure on a day to day basis, or during a particular task. Such dosimeters could be required when radiation field intensity may vary significantly during the course of work. Most of DRDs are equipped with programmable dose/dose rate alarms to alert the user. Further as the dose estimates are obtained immediately, dose control is possible with the DRDs. With prior approval by the regulatory body, active dosimeter can also be used as a replacement for the dosimeter

of record (official dosimeter). For this the active dosimeter should be of a suitable design and having appropriate performance characteristics for parameters such as sensitivity, precision, reliability, linearity, energy and angular response, response to pulsed radiation, electromagnetic interference, effect of environmental conditions.

5.5 Recording and Investigation Levels

The recording level and investigation level are used in the individual monitoring with specific purpose. The recording level provides a level of effective (or equivalent) dose above which a result from a monitoring programme is included in a dose record. The requirement of recording level is to eliminate recording trivial doses from dose record as there is large uncertainty in dose and effect relationship at such dose levels. ICRP [3] has recommended that the recording level for individual monitoring should be derived from the duration of the monitoring period and an annual effective dose no lower than 1 mSv or an annual equivalent dose of about 10% of the relevant dose limit. In rare cases when external and internal exposures contribute significantly to the total dose, lower recording levels for each component may be derived. In case of individual monitoring for external exposure, generally the measured dose is usually entered directly as a measure of the effective dose. This implies that the minimum detection level (MDL) of the system is used as the recording level with results below that level being deemed to be zero. When control dosimeters are used for estimation of zero dose signals and contribution of background radiation exposure to evaluate personal dose from individual dosimeter, variations associated with the control reading influences strongly the minimum detection level [26, 27]. For $CaSO_4$:Dy based TLD badge system, the MDL was found to depend on duration of monitoring period [28]. Further, it was observed that MDL derived from freshly annealed dosimeters at laboratory generally does not represent the situation for service dosimeters. Based on the statistical analysis of readings of control cards issued to institutions, recording level 0.10 mSv and 0.20 mSv has been evaluated for monthly and quarterly monitoring respectively for the above monitoring system.

Investigation level (IL) is defined as the level of measured quantity, above which the cause or the implications of the result is examined. This is set by operating management and applies for occupational exposure. IL initiates a review of the protection arrangements and address how a particular value above the investigation level was received. The purpose of the review of cases exceeding the investigation limit is to learn from the experience gained and apply that experience to any future operations of a similar nature. In Indian personnel monitoring programme for external exposure, whole body dose equal to or greater than 10 mSv and skin/extremity dose equal to or greater than 250 mSv in a monitoring period is followed for regulatory review of exposure cases.

6 Accuracy Requirements and Periodic Performance Evaluation of Individual Monitoring

The main objective of individual monitoring is to provide a reliable measurement of the operational quantities $H_p(d)$, for almost all practical exposure situations with a prescribed overall accuracy. Accuracy requirements for monitoring individual exposure given by ICRP in its publication ICRP 75 are (i) 10% accuracy at 95% confidence level (i.e. $1\sigma = 5\%$) for measurement of radiation field in good laboratory conditions. (ii) an uncertainty of a factor of 1.5 at the 95% confidence level in the estimation of Effective Dose around the relevant dose limit due to photons in the workplace radiation fields. (iii) The uncertainty factor greater than 1.5 in case of neutrons and electrons. (iv) Greater uncertainties at low levels of effective doses for all qualities of radiation. The uncertainties are specified for estimation of effective dose. As $H_p(d)$ is reasonable and adequate estimate of the corresponding protection quantities (Effective dose and Equivalent dose), the above requirements are also applicable to measurement of $H_p(d)$, for doses below the relevant annual dose limit. Radiation field in good laboratory conditions implies knowledge about radiation source, irradiation geometry, irradiation time, environmental conditions, etc. Workplace radiation field generally involve unknown energy spectrum and orientation of the radiation field. Hence, the uncertainties in a measurement made with an individual dosemeter are expected to be significantly greater for the workplace fields. Further, non-uniformity and uncertain orientation of the radiation field relative to individual body lead to errors in standard model based calculation of Effective dose.

It is important to verify that the performance of a personal dosimetry system satisfies the ICRP accuracy requirement. The accuracy requirements concerning the workplace fields have been converted into the form of Trumpet curve for practical application. ISO 14146 (2018) [29] specifies criteria and the test procedures for periodic evaluation of dosimetry services. The criteria of the standard are based on the trumpet curve. The trumpet curve represents pictorially accuracy intervals as a function of true dose. The response (ratios of measured dose to true dose) data of a given performance test are plotted on the trumpet curve. 90% of the points should lie within the limits of the curve for satisfactory performance. For photon radiation with a mean energy of $E_{\text{ph}} > 10$ keV and for beta radiation with a mean energy of $E_{\text{beta}} > 0.2$ meV, Upper limit H_{ul} and Lower limit H_{ll} of the curve are given as under.

$$H_{\text{ul}} = 1.67\left(1 + \frac{H_o}{4H_o + H_{\text{ref}}}\right) \tag{1}$$

$$H_{\text{ll}} = 0.71\left(1 - \frac{2H_o/1.33}{H_o/1.33 + H_{\text{ref}}}\right) \tag{2}$$

For photon radiation with a mean energy of $E_{\text{ph}} \leq 10$ keV, and for beta radiation with a mean energy of $E_{\text{beta}} \leq 0.2$ meV, the above limits are as under.

$$H_{\text{ul}} = 2 \tag{3}$$

$$H_{\text{ll}} = 0.5(1 - \frac{2H_o/1.5}{H_o/1.5 + H_{\text{ref}}}) \tag{4}$$

H_o is lower dose limit and H_{ref} is conventional quantity value of the delivered dose.

The factors 0.71 and 1.67 are similar to the corresponding factors in ICRP 75, i.e. $1/1.5 = 0.67$ and 1.5.

American National Standard—American National Standard for Dosimetry—Personnel Dosimetry Performance—Criteria for Testing American ANSI/HPS N13.11-2009 [30] provides a method of performance evaluation of in terms of performance quotients (P_i), i.e. relative difference between measured dose and true dose. Bias (B) calculated as absolute value of average of P_i is added in quadrature with Standard deviation (S) of P_i to obtain Tolerance level (L). Acceptance criteria are expressed in terms of L value. Though ANSI method is not directly based on the ICRP approach, limits are expressed on total uncertainty in the measurement of personal dose.

The performance limits on energy and angular response, coefficient of variation, linearity, response to mixed radiation, fading, etc. specified in standards for type testing of individual monitoring system such as IEC 62387 [18] are also intended to satisfy the overall accuracy requirements.

7 Description of Indian Personnel Monitoring System for *X*, Gamma and Beta Monitoring

In India, the centralized official Personnel Monitoring Service (PMS) was started in 1952 by Bhabha Atomic Research Centre (BARC) using the Film Badge. With the indigenous development of $CaSO_4$:Dy based TLD monitoring system, replacement of Film Badge by TLD Badge was initiated in 1975 in a phased manner to monitor doses from X, gamma and beta radiation. With this advent, decentralization of PMS became feasible and the first outstation TLD Laboratory was set up by BARC at TAPS, Tarapur in 1978. Subsequently TLD Laboratories were set up at the remaining nuclear power stations to provide in-house PMS to radiation workers of NPCIL. TLD and film badge services coexisted until 2003, after which film badge-based monitoring was phased down. To meet the largescale requirement of dosimetry system and to disseminate technical know-how developed over the years, the technology to manufacture TL Phosphor, TLD Cards and TLD Badge Reader was transferred to Private Institutions. To cater to the increased demand for PMS, three Private Laboratories were accredited by BARC to cover non-DAE Institutions. At present about 250,000 radiation workers from different radiation facilities in the country such as DAE (Department of Atomic Energy) facilities, industry establishments, medical hospitals and research institutions are being monitored.

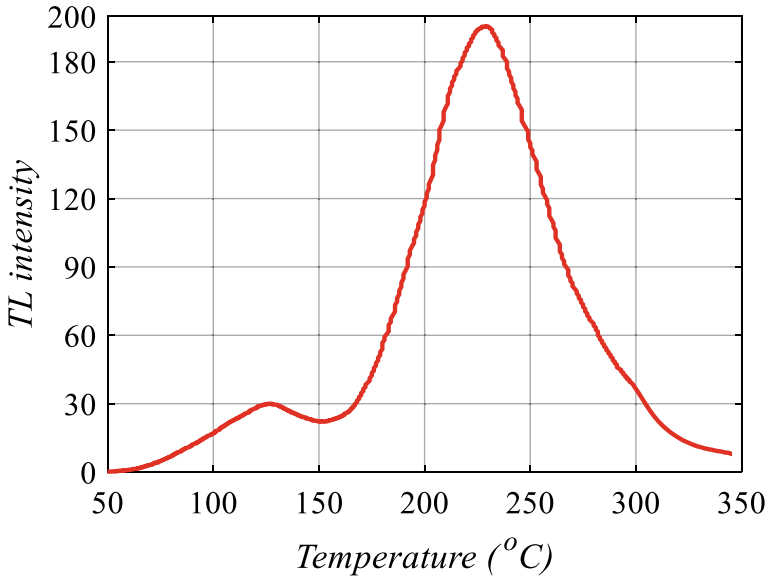

Fig. 3 Typical glow curve of $CaSO_4$:Dy

7.1 TLD Personnel Monitoring System

7.1.1 TL Phosphor

TLD personnel dosimeter utilizes $CaSO_4$:Dy TL phosphor as a radiation detector [31]. The concentration of dopant Dy is optimized to 500 ppm in $CaSO_4$ such that a highly sensitive TL phosphor (i.e. approximately 30 times the sensitivity of LiF: Mg, Ti) with negligible neutron sensitivity (3.8 mGy equivalent ^{60}Co gamma-ray response per 10^{10} thermal neutron/cm^2) is achieved [32]. That makes the phosphor effectively useful in external monitoring of *X*, gamma and beta radiation even in presence of neutron radiation.

The phosphor has a primary TL glow peak at 220 °C (for $CaSO_4$:Dy Teflon Disc, TL peak is around 230 °C). Typical glow curve (GC) of $CaSO_4$:Dy is shown in Fig. 3. For both low and high LET (Linear Energy Transfer) radiations in the dose range of concern in radiation protection, the TL response is linear, and the GC shape stays stable.

7.1.2 TLD Card and TLD Badge

$CaSO_4$:Dy exhibits energy-dependent response for photons owing to its effective atomic number Z_{eff} (15.3) higher than that of tissue. Therefore, multi-element dosimeters based on this phosphor with appropriate filtration are designed to achieve

compensation for energy dependent response. Such arrangement also helps in approximate identification of type and energy of radiation. TLD card used in the monitoring system consists of nickel platted aluminium plate/card (Fig. 4) in which three Teflon TLD Discs (13.3 mm dia. and 0.8 mm thick) are clipped onto circular holes (12 mm diameter). TLD Discs are made by cold pressing homogenous mixture of $CaSO_4$:Dy phosphor and Polytetrafluoroethylene (PTFE) in weight ratio of 1:3 mixed at liquid nitrogen temperature. Subsequently the discs are subjected to heat treatment at 400 °C to impart the strength and flexibility. The procedures have been standardized to get a large number of TLD discs with sensitivity variation within ± 7%. PTFE is a poly-tetrafluoroethylene (fluoropolymer) that serves as a binder for TLD discs. It also endures the temperatures required for TL reading and annealing for repeated use, resulting in a durable and convenient dosimeter for field application.

A TLD Card enclosed in paper wrapper and sealed in polythene is inserted into a plastic cassette/holder to make up the TLD Badge. The aluminium card has an asymmetric '*V*' cut to ensure that it is oriented correctly in the TLD cassette. The cassette has 3 filter regions corresponding to the 3 discs. Schematic of TLD card is shown in Fig. 4, and TLD badge with filter arrangement is shown in Fig. 5.

The filter composition for the three discs is as follows:

(a) Disc *D*1: Sandwiched between a pair of 1.0 mm thick Al and 1.0 mm thick Cu filters (0.6 mm Al in modified Cassette) (Copper filter nearer to the Disc),
(b) Disc *D*2 is sandwiched between two 1.6 mm thick (180 mg/cm^2) plastic filters and

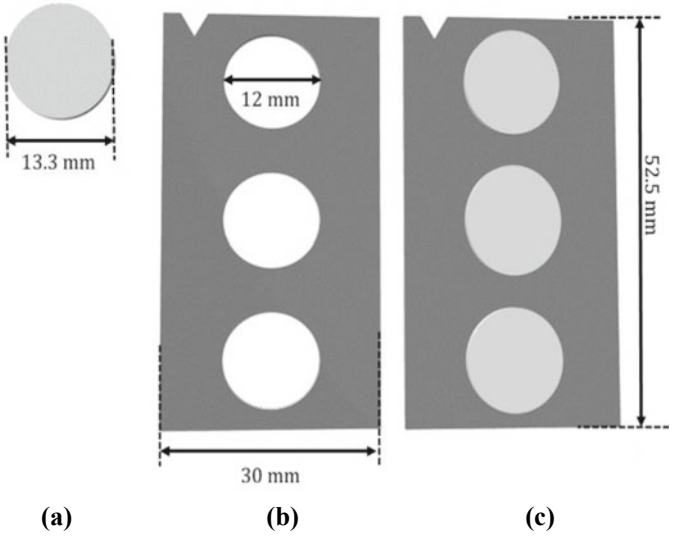

Fig. 4 Schematic of TLD card, **a** TL element (disc), **b** TLD card without disc and **c** TLD card with disc

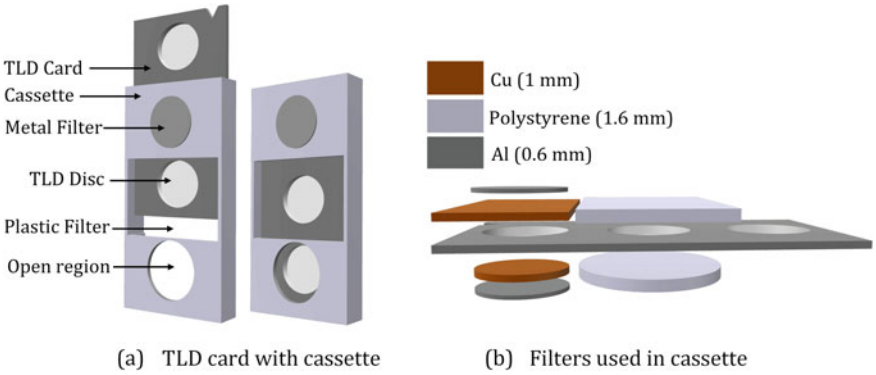

Fig. 5 TLD badge and filter arrangement (clip for fixing is not shown)

(c) Disc *D*3 is placed under a circular open window (identification paper wrapper and polythene pouch amounts to 12–14 mg/cm^2).

TLD Badges/Cassettes are divided into three categories: (a) chest badges, (b) wrist badges and (c) head badges. Though all three types of TLD Badges have the same dosimeter and design, they have different attachments (clip/strap) for wearing purposes depending on their use.

7.1.3 TLD Badge Reader

The TLD Badge Reader is a very important component of the Personnel Monitoring system. Readout of TLD cards is carried out in the badge reader to obtain dose information. The Readers are designed to apply a pre-programmed heating cycle to the TL dosimeter, detect the dosimeter's instantaneous light (GC signal) and display the total integrated light in μSv equivalent counts. In India, several versions of the TLD Badge Reader have been used in the monitoring program. All these versions rely on the reproducible, non-linear clamped heating profile to heat the dosimeter discs and the integral method of TL measurement. The integral method has less stringent requirements on heating rate compared to peak height determination for TL measurement. Initially, manual TLD Badge Readers (model BR-3A) based on contact heating were used for TLD readout. The semiautomatic TLD Badge Readers (model TLDBR-7B) [33, 34] based on N_2 Gas heating introduced during 1996–97 are currently in use for Personnel Monitoring. Most of the constraints of the manual Badge Reader have been overcome in the semiautomatic readers leading to transformation of the personnel monitoring. The operation of the reader is software controlled, and 50 TLD Cards are read in 100 min automatically.

The semiautomatic TLD Badge reader comprises microprocessor-based electronic control circuits, the PMT housing, a card transport system, a gas heater and temperature control unit, cooling fans, and a solenoid that switches the gas flow 'ON/

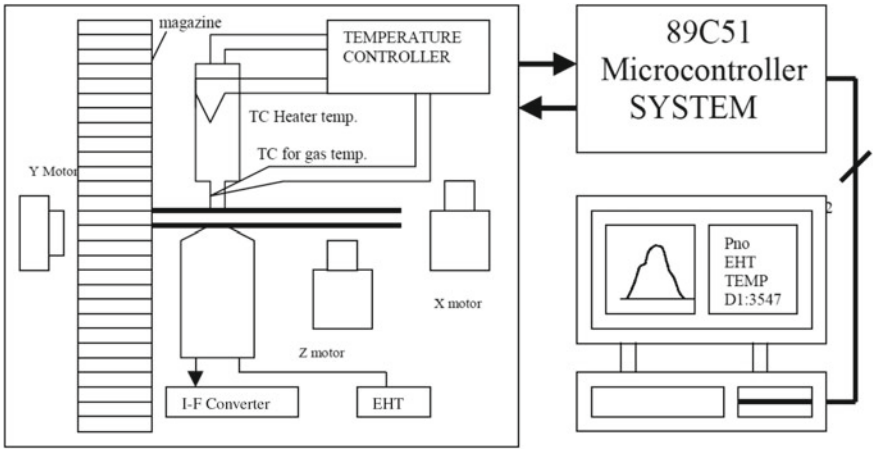

Fig. 6 Block diagram of semiautomatic TLD badge reader

OFF'. The dosimeter (TLD Card) is moved and positioned in the heating chamber so that the dosimeter Discs are sequentially located between the heater nozzle and the PMT. The Discs are heated for about 30 s each with a non-linear clamped profile of hot N_2 gas jet, and the PMT detects the TL emitted during the heating. The PMT anode current is digitized using a wide range I-F converter and then processed digitally along with other parameters such as gas temperature, EHT and so on for display storage, and recall of the GCs. The block diagram of semiautomatic TLD badge reader is shown in Fig. 6 [33, 34].

7.2 Dosimetric Characteristics of TLD Badge

As has been mentioned earlier, 3 discs filtered by different filter materials are used for compensating the photon energy dependent response. Figure 7 depicts the response of TLD badge as a function of photon energy for Disc *D*1 (filtered by composite metal filter) and Disc *D*3 (open) [32].

The response of different discs has been evaluated in terms of whole-body dose, the quantity being used presently for dose reporting. It is observed that the relative response of the bare disc (blue curve) starts increasing as photon energy decreases below ~ 200 keV and reaches to about 10 at about 30 keV. Such a large variation is attributed to significant increase in photoelectric absorption probability for the detector at lower photon energy compared to air or tissue. However, the disc sandwiched between composite metal filters (red curve) shows a modified response where the large variation is reduced to a narrow band of response values between 1.65 and 0.75. The modified response is the result of competition between photoelectric absorption by the detector and attenuation caused by the metal filters at lower photon

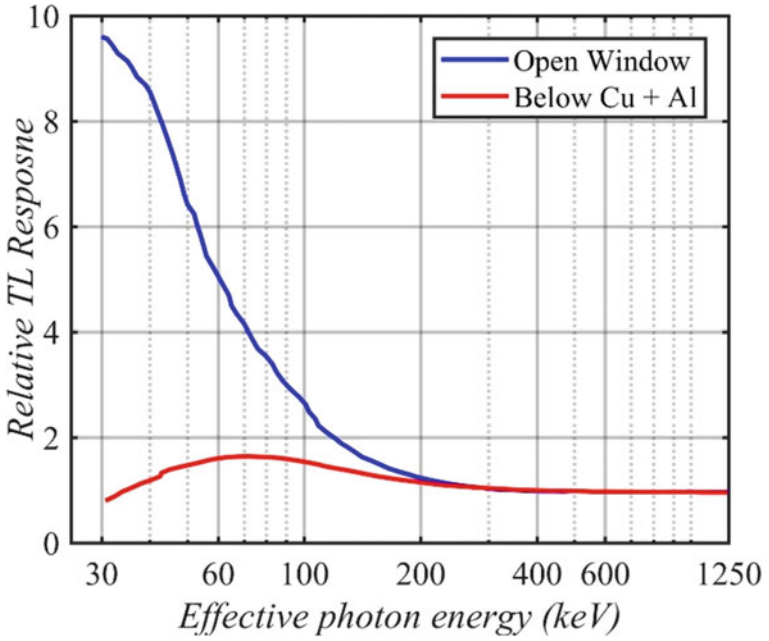

Fig. 7 Photon energy dependence of TLD badge [32]

energy. The arrangement of copper and aluminium filter (copper filter located near to the disc) in the composite metal filter minimizes production of bremsstrahlung radiation due to high energy beta radiation. From the energy response curve, it can be observed that the approximate photon energy ranges may be identified based on the ratio of readings of unfiltered and filtered discs. The photon energy response of disc *D*2 filtered with plastic filter is not significantly different than that of disc *D*3 in the indicated energy range. In fact, equality of *D*2 and *D*3 readings within few percent is used for identifying the exposure to photon radiation. Disc *D*2 plays important role for identifying and measuring the beta radiation.

The relative response of the $CaSO_4$:Dy-based TLD badge with respect to the angle of incidence studied by Vohra et al. [31] at 250 kVp X-rays (Thoraeus filter) indicates almost constant value for filtered element (*D*1) till 15° angle to plane of the badge. Whereas for the open element (*D*3), the response decreases by about 25% at the above angle. It appears that at this energy there is not significant angular dependence, however for lower energy beams significant angular dependence of *D*1 is expected due to the greater thickness of the filter traversed by the radiation at the smaller angles to plane of the badge.

The $CaSO_4$:Dy shows quite satisfactory characteristics towards environmental conditions and exhibits less than 5% fading over a period of six months for dosimetric peak/main peak. $CaSO_4$:Dy phosphor exhibit the linear response for few μGy to 30 Gy of Co-60 dose. However, in case of the personnel dosimetry system the dose

range from tens of μSv to few Sv is considered satisfactory. The $CaSO_4$:Dy based personnel monitoring system shows the linear response from 100 μSv to 1 Sv. The lower limit of measurement range generally depends upon the inherent noise from the personnel monitoring system contributed by both dosimeter and TLD reader and variations associated with ambient background dose deposition.

7.3 Calibration and Dose Estimation

7.3.1 Calibration of the Personnel Monitoring System

Calibration of the dosimetry system is based on the quantity called as whole-body dose (WBD) which is identical to air kerma on the front surface of a person also referred as photon dose equivalent [35]. The calibration of the system has been carried out by realizing WBD in terms of air kerma measured using the reference chamber on the surface of the water phantom for irradiation to different energy collimated photon beams. Subsequently the dosimeters were irradiated on the surface of the water phantom using the above photon beams. The response of the dosimeters to the different photon beams relative to reference beam of ^{137}Cs has been analysed and an algorithm [32] standardised to evaluate the personal dose in terms of whole body dose. A routine for evaluation of beta dose developed on the basis of the relative response to different beta sources has been included in the algorithm. This algorithm forms the basis of calibration for evaluating personal dose from the service dosimeters. To ensure the validity of the algorithm, Reader Calibration Factor (RCF) evaluated using the dosimeters exposed to ^{137}Cs on the surface of the phantom is required. However, on-phantom irradiation has limitations for routine monitoring where large number of dosimeters are required to be irradiated. Therefore, a correspondence of the above irradiation with free-in-air irradiation in panoramic geometry to ^{137}Cs has been utilized. Towards this, the response of TLD readers is configured to read 1.14mSv WBD per mGy of air kerma free in air (or 10 mSv per *R*) for dosimeters exposed free-in-air to ^{137}Cs. With this relation for assigning the photon dose equivalent (whole body dose), free-in-air irradiation to calibrated ^{137}Cs source in panoramic geometry is used to irradiate dosimeters to known whole body/photon dose equivalent. This method serves as derived/routine calibration method for personnel monitoring.

The personal dose is reported in terms whole body dose and skin dose (addition of whole body dose and beta dose). Whole body dose serves as an estimate of effective dose and skin dose estimates equivalent dose to the skin.

7.3.2 Dose Evaluation

The $CaSO_4$:Dy TLD badge is used to measure X, β and γ dose. The pattern of the disc readings for discs $D1$, $D2$ and $D3$ provide information about the type and approximate energy of radiation. Therefore, dose evaluation algorithm basically analyses ratios

of different disc readings to obtain probable type and energy of radiation the badge might have been exposed. As described under dosimetric characteristics of TLD badge, discs $D2$ and $D3$ readings are statistically identical for photon exposure. In such cases, ratio of $D2$ and $D1$ readings is used to identify the effective photon energy in three different ranges, namely, greater than ~ 200 keV, between 40 and 200 keV and less than ~ 40 keV. Exposure to the mixed gamma-beta fields is identified by the ratio $D3/D2$. In such cases estimation of approximate beta energy is accomplished using the ratio of disc readings ($D3$ and $D2$) after subtracting gamma component. A detailed dose evaluation algorithm is as follows:

A. **Identification of Radiation Pattern**

1. Calculate average control reading (C).
2. Subtract C from $D1$, $D2$ and $D3$ and calculate ND1, ND2 and ND3 respectively.
3. If ND1, ND2 or ND3 is < 100 μSv then set it to 100 μSv.
4. Evaluate ND3/ND2, ND2/ND1, ND3/ND1 and ND1/ND3 as $R32$, $R21$, $R31$ and $R13$, respectively.
5. If ND2 and ND3 are within 20% with respect to the higher of the two (i.e. $0.80 \leq R32 \leq 1.25$) AND $R31 \geq 0.80$ then the following cases are possible:
   (a) $R21 < 1.25$ and $R21 \geq 0.80$; labelled as Photon—Category 1, i.e. Effective photon energy greater than ~ 200 keV;
   (b) $5 > R21 \geq 1.25$; labelled as Photon—Category 2, i.e. Effective photon energy greater than ~ 40keV and less than ~ 200 keV 106;
   (c) $R21 \geq 5$; labelled as Photon—Category 3, i.e. Effective photon energy less than ~ 40 keV.
6. If ND2 and ND3 are not within 20% of each other, then the following conditions should be checked:
   (a) $R32 > 1.25$, $R31 \geq 1.5$ and $D1 \geq$ Control + 100 (μSv). This is labelled 'Beta-Photon Category'.
   (b) $R32 > 1.25$, $R31 \geq 1.5$ and $D1 <$ Control + 100 (μSv). This is labelled 'Beta Category'.

B. **Dose estimation**

1. Photon-Category 1: Effective photon energy greater than ~ 200 keV.
   (a) ND1, ND2 and ND3 are re-evaluated from original input of $D1$, $D2$, $D3$ and C.
   (b) If ND1 < 100 μSv, it is set to 0.
   (c) Dose = ND1.
2. Photon-Category 2: Effective photon energy greater than ~ 40 keV and less than ~ 200 keV
   (a) ND1, ND2 and ND3 shall be re-evaluated from original input of $D1$, $D2$, $D3$ and C.
   (b) If ND1, ND2 or ND3 evaluate to < 50 μSv, it is set to 50 μSv.
   (c) $R12$ is evaluated as $R12 =$ ND1/ND2
   (d) Dose is evaluated as

i. Dose = ND1 × [(2.6017) − (15.8861 × $R12$) + (45.5412 × $R12^2$) − (53.2834 × $R12^3$) + (22.5612 × $R12^4$)]

(e) If Dose < 100 μSv, it is set = 0.

3. Photon-Category 3: Effective photon energy less than ~ 40 keV
   (a) ND1, ND2 and ND3 shall be re-evaluated from original input of $D1$, $D2$, $D3$ and C.
   (b) If ND1, ND2 or ND3 evaluate to < 50 μSv, it is set to 50 μSv.
   (c) Dose = (ND2 + ND3)/20.
   (d) If Dose < 50 μSv, it is set to 0.
4. Beta-Photon Category and Beta Category:
   (a) ND1, ND2 and ND3 are re-evaluated from original input of $D1$, $D2$, $D3$ and C.
   (b) If ND1 < 0, it is set to 0.If ND2 and ND3 ≤ 50 μSv, it is set to 50 μSv.
   (c) Calculate RL32 as
      i. If (ND2 − 1.05 × ND1) ≥ 50 μSv, then RL32 = (ND3 − 1.1 × ND1)/(ND2 − 1.05 × ND1), else, RL32 = (ND3 − 1.1 × ND1)/50.
      ii. If RL32 < 1.00, set RL32 = 1.00
   (d) Calculate BMF as
      i. BMF = 0.35 × RL32 + 0.4, If 1.00 ≤ RL32 < 5.0
      ii. BMF = 3.5, If RL32 ≥ 5.0
   (e) Based on the value of ND3, beta dose is evaluated as
      i. Beta dose = BMF × (ND3 − 1.1 × ND1)
      ii. If Beta dose < 1000 μSv, then it is set to 0.
   (f) Photon dose = ND1.
      i. If Photon dose < 100 μSv, it is set to 0.

7.4 *Studies for Improvement in TLD Badge-Based Personnel Monitoring System*

Several developments and improvements have taken place in the TLD badge-based personnel monitoring system since its introduction in 1975. The development which has completely changed the way the dosemeters are processed is the introduction of semiautomatic hot N_2 gas based TLD badge reader during 1996–97 [33, 34]. This has not only brought automation in the TLD readout but also improved efficiency and dosimetric quality of the evaluated doses. The accompanying improvements in dosimetric performance include lowering of the minimum detection level, reduction in coefficient of variation, increase in shelf life of dosimeters, in-built facility of glow curve storage and recall for ascertaining genuineness of TL counts, etc. Towards dosimeter, developments include establishing parameters of large scale production of phosphor batches [36], study of thermal history and reusability of $CaSO_4$:Dy Teflon TLD Discs [37], study of annealing and repeated Readout of TLD Cards based on $CaSO_4$:Dy Teflon Discs, study of TLD badge response to high energy

photon radiation [38, 39] and several other improvements. Some of the latest studies on TLD badge system are described in the following sections. Various documents on the system such as handbook on the use of TLD badge based on $CaSO_4$:Dy Teflon discs for individual monitoring [40], revision of the above document as handbook on TLD-based personnel monitoring [32] and requisite booklets for accreditation of personnel monitoring laboratories were prepared.

7.4.1 Evaluation of Response and Development of Algorithms for Operational Quantities

With the introduction of the operational quantities for personnel monitoring, i.e. personal dose equivalent $H_p(d)$, studies have been carried out for the to correlate whole body dose with $H_p(10)/H_p(0.07)$. The whole body dose realized as air kerma measured on slab/water phantom surface closely approximates $H_p(0.07)$ [41]. Quantitative agreement within $\pm$ 10% between the quantity whole body dose and $H_p(0.07)$ for photons in 30 keV–1.25 MeV has been reported [42]. Even for low energy (15–30 keV) photons reported overestimation of $H_p(0.07)$ by whole body dose do not exceed 30%. Towards correlation with $H_p(10)$, it has been reported [41, 42] that the whole body dose is conservatively close to $H_p(10)$ at higher photon energies (> 40 keV); whereas it overestimates the $H_p(10)$ in diagnostic X-rays (15–40 keV). A few dose evaluation algorithms [43, 44] to calculate dose from TLD badge in terms of personal dose equivalent are reported in the literature. These algorithms are developed by mapping the angle averaged response of TL elements to the dose equivalent using linear equation or polynomial functions.

An algorithm for estimation of $H_p(10)$ using 5th order polynomial was proposed by Bakshi et al. [43] is as follows:

$$H_p(10) = N1(A_1 - A_2R12 + A_3R12^2 - A_4R12^3 + A_5R12^4 - A_6R12^5)$$

where $A_1 = 2.57535$, $A_2 = 21.83062$, $A_3 = 98.77398$, $A_4 = 202.99463$, $A_5 = 190.32674$ and $A_6 = 65.86964$ are constants.

The linear combination (LC) based algorithm for $H_p(10)$ and quadratic equation based expression for $H_p(0.07)$ proposed by Pradhan et al. [44] are as follows:

- If $r_{12} < 0.7$, $H_p(10) = 0.676 \times N1 + 0.038 \times N23$, else $H_p(10) = N1$
- $H_p(0.07) = N23(0.106 - 0.175 \times r_{12} + r_{12}^2)$

where $N23$ is average of net TL counts from $D2$ and $D3$, $N1$ is net TL counts from $D1$, $N1$, $N2$ and $N3$ are net TL counts from disc $D1$, $D2$ and $D3$ respectively, $R12 = N1/N2$ and $r_{12} = N1/N23$.

A task group in Radiological Physics and Advisory Division for implementation of operational quantities in TLD-based personnel monitoring reviewed different algorithms for operational quantities. Based on the performance evaluation of the algorithms on larger volume of dataset and review of the calibration method for LC algorithm, the values of coefficient were refined by the task group. The task group

also reviewed the algorithm for wrist badge to evaluate $H_p(0.07)$ [45]. The revised algorithms by task group for estimation of personal dose equivalent using TLD badge worn at chest and wrist position are as follows:

- Chest badge
  $H_p(10)$
  - If $r_{12} < 0.8$, $H_p(10) = 0.638 \times N1 + 0.042 \times N23$, else $H_p(10) = N1$
- **$H_p(0.07)$ due to photon**
  - If $r_{21} > 80$, $H_p(0.07) = 0.15 \times N3$
  - If $1.25 \leq r_{21} \leq 80$, $H_p(0.07) = N3 \times (0.0942{r_{31}}^2 + 0.06r_{31} + 0.084)$
  - Else $H_p(0.07) = N1$
- Wrist badge
  $H_p(0.07)$ due to photon
  - If $0.007 < r_{12} \leq 0.8$ and $r_{32} \leq 1.25$, $H_p(0.07) = N23/\left(7.099R12^2 - 14.49R12 + 8.468\right)$
  - If $r_{12} > 0.8$ $H_p(0.07) = N23$
  - If $r_{32} \leq 1.25$ and $r_{12} \leq 0.007$, $H_p(0.07) = 0.18 \times N3$
    where $r_{21} = N2/N$, $r_{31} = N3/N1$ and $r_{32} = N3/N2$.

The calculation of $H_p(0.07)$ due to beta radiation for both Chest and Wrist badges is kept the same as the evaluation beta dose using whole body dose algorithm.

A method for routine calibration involving free-in air exposure of TLD badges in panoramic geometry has been standardized. Towards this, correspondence between responses of the badge for on-phantom (ISO slab phantom) exposure to collimated S-Cs beam and the above test (routine) exposure is established. It has been found that 10 mSv of $H_p(10)$ is equivalent to $1R$ exposure in routine setup for Chest badges. The same relation holds good for $H_p(0.07)$ on ISO slab phantom. This relation is the same as that being used for present quantity, i.e. whole body dose. However, for wrist badges, the equivalence is 10.4 mSv of $H_p(0.07)$ on ISO pillar phantom $= 1R$ exposure in routine setup. If single reader calibration factor (RCF) derived for $H_p(10)/H_p(0.07)$ (ISO slab phantom) is applied while readout of service badges, then additional correction factor of 1.04 is required for the TL counts of wrist badge.

7.4.2 Some Factors Affecting Shape of Glow Curves

The accuracy of estimating dose is influenced by various parameters, which can be categorized as either field-related or dosimetry system-related. Some parameters, particularly those associated with field conditions and the use of personnel dosimeters, may not exhibit consistent behaviour and therefore cannot be effectively modelled. However, certain parameters, such as variations in temperature profiles, impurities in the nitrogen gas (use of different gas) used for heating and the effect of readout sequences, can be investigated through experiments and simulations.

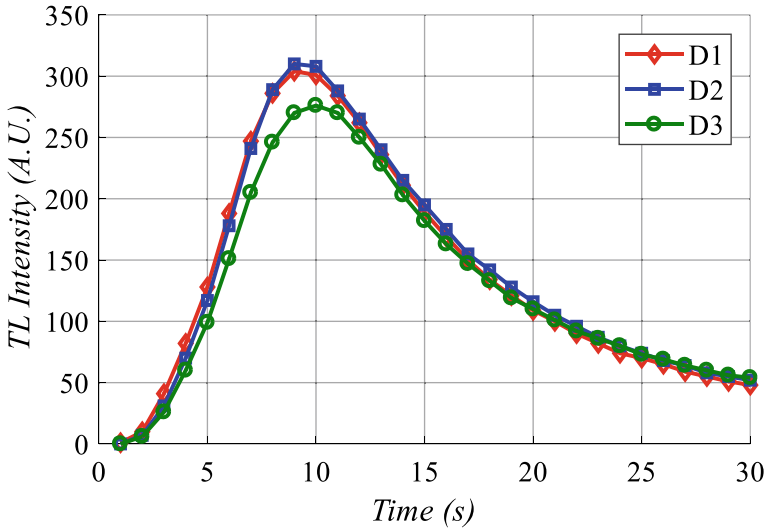

Fig. 8 Effect of surrounding temperature on GC (adopted from [47] with permission from Oxford University Press)

In a study conducted by Kumar et al. [46], the impact of different gases used for heating the dosimeter discs is analysed. The results of the study clearly indicate that a reasonably inert gas with a higher heat capacity, such as Nitrogen gas, is more efficient in stimulating TL (thermoluminescence) emission.

A study conducted to investigate the impact of sequential heating of TL elements on the GC shape and total TL counts [47] has elucidated the underlying reasons for the observed patterns in TL counts of 3 elements. The experimental results, depicted in Fig. 8, demonstrated an early occurrence of the glow peak and higher TL counts for the discs that were read or heated at the end of the reading sequence. To explain this phenomenon, a simulation was performed, considering the heating of neighbouring components within the heating chamber and the partial heating of adjacent unread discs. The convective heat exchange between the surrounding and TL element and slightly elevated starting temperature of TL element which is read later in the reading sequence lead to an excess heat delivered to the TL element. Consequently, the GC peak arrives early and the total TL counts are also marginally more than that of the TL elements read earlier in the sequence.

7.4.3 Automatic Screening of Glow Curves in Personnel Monitoring

The preceding discussion suggests that the shape of the GC can be influenced by various factors. A well-defined GC shape indicates the authenticity of radiation exposure recorded by a TLD badge and ensures accurate dose estimation. Deviations or anomalies in the GC shape may occur due to factors related to the handling and

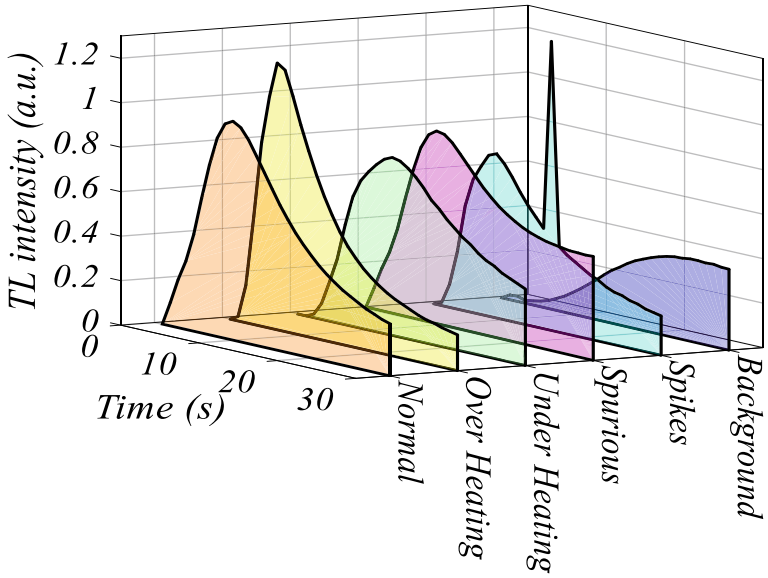

Fig. 9 Normal glow curve and various types of abnormalities in glow curve

processing of dosimeters. Figure 9 provides examples of both normal and improper GCs. To ensure precise dose estimation and avoid errors, it is important to identify anomalous curves. One approach involves defining the normal GC shape using analytically derived rules, as illustrated in Fig. 10 [48]. By employing a computer program, GCs that do not conform to the defined criteria/rules can be automatically identified, and corrective measures can be implemented to achieve accurate dose estimation. Additionally, machine learning techniques have also been employed for detecting anomalous GCs [49].

7.4.4 Improving Reproducibility of Doses in Low Dose Region

Certain variations in the total TL signal are inevitable despite control measures. These variations can be attributed to factors such as the stochastic nature of the zero dose signal. Generally, the coefficient of variation of TL counts tends to increase as the dose decreases. This occurs because the contribution of the zero-dose background, which includes inherent noise from the dosimeter and reader, becomes comparable or significant in relation to the radiation-induced signal at lower doses. The zero dose background consists of several components, such as black body radiation, dark current, disc coloration and previous dose history. To enhance the precision of dosimetry in the low dose region, a method was developed by Pradhan et al. [50]. It effectively separates the non-radiation-induced components of the TL signal from

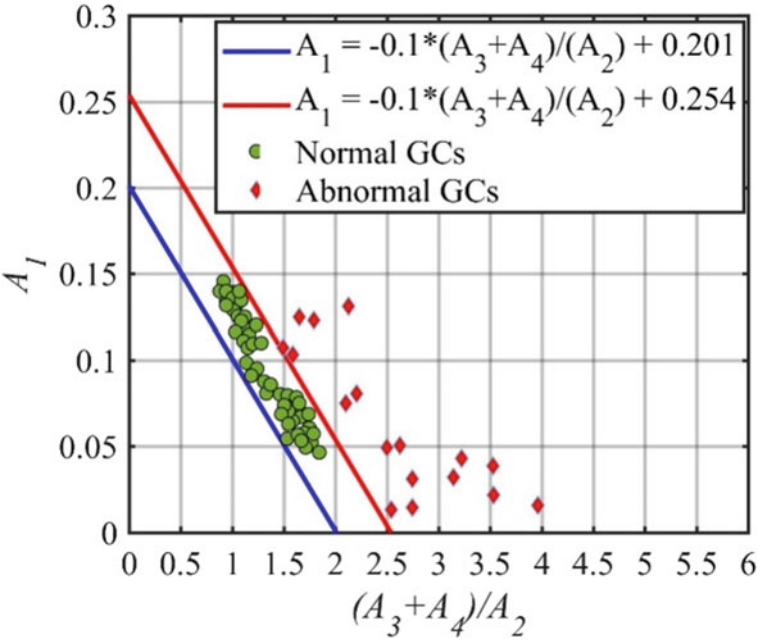

Fig. 10 Analytically defined boundary conditions for identification of abnormal GC (A_1, A_2, A_3 and A_4 are area under the normalized GC segments) (adopted from [48] with permission from Oxford University Press)

the composite signal. By segregating the real-time background signal from the total TL signal, this technique improves the precision of dosimetry at lower dose levels.

7.4.5 Estimation of Uncertainty in Measurement of Dose Equivalent at Laboratory Level

A novel technique based on random effects one way analysis of variance (ANOVA) model has been studied for estimation of uncertainty in the measurement of dose equivalent by TLD badge at laboratory level [51]. The model enables estimation of the overall variance of the performance of the sampled population. The measured dose equivalents by different laboratories of the TLD badges irradiated to a specific dose equivalent and radiation quality constituted the population. By including the results of different monitoring laboratories, variability in the system components such as dosemeter batches, TLD badge readers, dosemeter preparation and handling methods, ambient environmental conditions in the laboratory, reader calibration procedures has been introduced. The resultant estimation of the variance (uncertainty) can be thought to be representative of the monitoring system as a whole and lead to robust estimate of the uncertainty. Based on the above analysis, coefficient of variation of 6.6% and 7.4% has been estimated in the measurement of $H_p(10)$ and

whole body dose respectively at doses more than 1 mSv. Further the relative response of the monitoring system has been found to be satisfactory. The ANOVA model also helps to partition the observed variability between different components (factors among the laboratories and factors between the laboratories). This information can be used to identify the specific factors to further improve system performance.

8 Recent Developments in Individual Monitoring for External Exposure

8.1 Recommendations of New Operational Quantities

8.1.1 Limitations of Existing Operational Quantities of ICRU 39/ICRU 51

Some limitations of the operational quantities of ICRU 39/ICRU 51 have been identified in terms of their definition, discrepancies in the estimate of protection quantities, and limited range of energy and particle type. These are described below.

a. The phantoms used to calculate the protection quantities and operational quantities due to radiation field are different. The ICRU sphere phantom is used for ambient dose equivalent and the ICRU slab phantom (with dimensions 300 mm $\times$ 300 mm $\times$ 150 mm) for personal dose equivalent, whereas the protection quantities are determined in the anthropomorphic phantoms or the more recent ICRP/ICRU reference adult phantoms ICRP 110 [14]. It is obvious that the structure and geometry of phantom for protection quantities cannot be matched by phantom for operational quantities. This leads to inherent inadequacy of the operational quantities to estimate of the protection quantities.
b. ICRU 4-element tissue (a composition by mass of 76.2% oxygen, 11.1% carbon, 10.1% hydrogen, 2.6% nitrogen) considered for the definition of the operational quantities cannot be fabricated.
c. The definition of dose equivalent as the product of Q and D at a point in tissue can never be realized experimentally. It can only be calculated based on knowledge of the radiation field of secondary charged particles at the point of interest.
d. It has been observed that using either kerma approximation or full electron transport for calculating the conversion coefficients for the operational quantities does not lead to closely matching estimates of protection quantities for certain photon energy ranges.
e. Further, the use of a depth of 10 mm for $H_p(10)$ and $H^*(10)$ leads to overestimation of the effective dose by the operational quantities for low energy photons (Ep < 70 keV) due to limited penetration.

8.1.2 Basis of New Operational Quantities

In view of the conceptual inconsistencies and discrepancies associated with the existing operational quantities, new operational quantities are defined by ICRU/ICRP and published in ICRU Publication 95 (2020) [52]. The new definition of the operational quantities is based on the products of radiometric or dosimetric quantities at a point in space or on the surface of the body and conversion coefficients related to values of protection quantities [52, 53]. It involves a paradigm change by including the conversion coefficient for protection quantities in the definition of operational quantities. The new definition can be practically realized due to availability of internationally agreed phantom [14] as well as the conversion coefficients for the protection quantities based on the above phantom. The recommended operational quantities simplify the systems of protection and operational quantities and assist in the comprehension of radiological protection quantities by users.

The new operational quantities are defined for both area monitoring and individual monitoring. As mentioned earlier, the definitions include conversion coefficient for protection quantities evaluated in the whole-body ICRP/ICRU adult reference phantoms. This implies that new operational quantities are based on the same phantoms, weighting factors and calculation models as that for protection quantities. This ensures coherence of the quantities and close approximation of their numerical values for specific radiation type, energy and direction of incidence.

The new operational quantities for individual monitoring are described below.

8.1.3 Personal Dose

The personal dose, H_p, at a point on the body is the product of the particle fluence incident at that point, Φ, and the conversion coefficient, h_p, relating particle fluence to the value of effective dose, E.

$$H_p = \int h_p(E)\Phi(E)\mathrm{d}E$$

where h_p(E) is the conversion coefficient for effective dose calculated ICRP/ICRU adult reference phantoms.

The unit of personal dose is J kg^{-1}. The special name for the unit of personal dose is sievert (Sv).

8.1.4 Personal Absorbed Dose in the Lens of the Eye

The personal absorbed dose in the lens of the eye, D_p lens, at a point on the head or body is the product of the particle fluence incident at that point, Φ, and the conversion coefficient, $d_{p\,\mathrm{lens}}$, relating particle fluence to the value of absorbed dose in the lens of the eye.

$$D_{p\,\text{lens}} = \int d_{p,\text{lens}}(E)\Phi(E)\mathrm{d}E$$

where $d_{p\,\text{lens}}$ is the conversion coefficient for absorbed dose to the lens of the eye calculated using the eye model of Behrens.

The unit of personal absorbed dose in the lens of the eye is Jkg^{-1}. The special name for the unit of personal absorbed dose in the lens of the eye is gray (Gy).

8.1.5 Personal Absorbed Dose in Local Skin

The personal absorbed dose in local skin, $D_{p\,\text{local skin}}$, is the product of the particle fluence incident on the body or extremities, Φ, and the conversion coefficient, $d_{\text{plocal skin}}$, relating particle fluence to the value of absorbed dose in local skin.

$$D_{p\,\text{local skin}} = \int d_{p,\text{local skin}}(E)\Phi(E)\mathrm{d}E$$

where $d_{p,\text{local skin}}$ is the conversion coefficient for absorbed dose to the skin calculated using ICRU tissue covered with skin layer.

The unit of personal absorbed dose in local skin is J kg^{-1}. The special name for the unit of personal absorbed dose in local skin is gray (Gy).

Note: Personal dosimeters worn on the body are irradiated with radiations incident on various directions, hence the above conversion coefficients are calculated for various incident angels.

8.2 Personal Online Dosimetry Using Computational Methods

The implementation of individual radiation worker monitoring is important for ensuring compliance with regulatory dose limits and maintaining doses as low as reasonably achievable. However, the field of personal dosimetry still faces significant uncertainties, including issues related to compliance and improper usage of dosimeters. Workers do not like to wear dosimeter especially when more than one dosimeter is involved. Forgetting the dosimeter/storing dosimeter in wrong place also can happen. There are uncertainties in estimating Effective Dose/Equivalent Dose based on the operational quantities. Further, there are uncertainties in measurement of $H_p(10)$ due to energy and angular dependence, non-linearity, fading, etc. as no dosimeter is perfect. When personal dosimeter is lost, no dosimetric data is available. If personal dosimetry is carried out without a physical dosimeter, all the above issues may be overcome. PODIUM (Personal Online Dosimetry Using Computational Methods) project [54] is an innovative approach for personal dosimetry. This approach involves the development of an online dosimetry application based on computer simulations, eliminating the need for physical dosimeters. To achieve

this, it was proposed to perform the calculation of occupational doses using camera tracking devices, customized virtual human models and information obtained from the radiation source. By utilizing fast Monte Carlo simulation codes, the goal was to enable real-time personal dosimetry.

O'Connor et al. [55] demonstrated the feasibility of the PODIUM project on assessing and validating dosimetry of interventional radiology workplaces, where improvements in dosimetry are particularly necessary. In their study, they have demonstrated the feasibility of a real-time occupational dose application for clinical use in the context of Endovascular and Interventional Cardiology. Through live cases in a complex clinical setting, they evaluated a new method that successfully tracked staff and generated dose estimates. The dose received by the primary operator was measured using an active personal dosimeter (APD) and compared with the dose simulated using three Monte Carlo (MC) codes. The initial validation results were quite promising.

9 Conclusion

This chapter explores the domain of monitoring of radiation exposure from external source of radiation highlighting on its scientific basis and operational aspects. It commences by elucidating the principles of radiological protection, placing a distinct emphasis on the role of personnel monitoring to uphold not only occupational and institutional safety but also regulatory requisites.

Exploring deeper, the chapter explains the interrelationships existing among physical quantities, protection quantities and operational quantities. The chapter also describes different operational aspects of individual monitoring of external radiations such as requirements of calibration, design of monitoring program, guidelines on who should be monitored and length of monitoring period, considerations for skin, extremity and eye lens monitoring, recording and investigation levels, accuracy requirements and periodic performance evaluation of the monitoring system. Notably, the chapter dedicates a comprehensive segment to elucidate the intricacies of the Indian personnel monitoring program. This in-depth explanation encompasses the details of Thermoluminescent dosimetry techniques, the calibration methodologies employed, and the algorithms instrumental in accurate dose estimation in terms of operational quantities and different studies carried out for the system for improving the accuracy of dose estimates.

In closing, the chapter casts a spotlight on recent breakthroughs in the domain of monitoring external exposures. Emerging dosimetry technologies, exemplified by the innovative Personal Online Dosimetry Using computational Methods (PODIUM), along with new operational quantities defined by ICRU are thoughtfully explored for the profound potential they hold in elevating the precision and efficacy of radiation protection strategies. This chapter, therefore, serves as an essential resource for comprehending the intricate landscape of TLD personnel monitoring, from its foundational aspects to the recent advancements.

References

1. ICRP Publication 26 (1977) Recommendations of the International Commission on Radiological Protection, (Series: ICRP, 26; Annals of the ICRP, 1(3), 1977). Pergamon Press, London
2. ICRP Publication 60 (1990) Recommendations of the International Commission on Radiological Protection, (Series: ICRP, 60; Annals of the ICRP, 21(1–3), 1991). Pergamon Press, London
3. ICRP Publication 75 (1997) General principles for the radiation protection of the workers. Ann ICRP 27
4. ICRP Publication 103 (2007) The 2007 recommendations of the international commission on radiological protection, (Series: ICRP, 103; Annals of the ICRP, 37(2–4), 2007). Pergamon Press, London
5. ICRU Report 39 (1985) Determination of dose equivalents resulting from external radiation sources. International Commission on Radiation Units and Measurements, (Series: ICRU Report 39), Bethesda
6. ICRU Report 43 (1988) Determination of dose equivalents from external radiation sources—part 2. International Commission on Radiation Units and Measurements, (Series: ICRU Report 43), Bethesda
7. ICRU Report 47 (1992) Measurement of dose equivalents from external photon and electron radiation, (Series: ICRU Report 47). International Commission on Radiation Units and Measurements, Bethesda
8. ICRU Report 51 (1993) Quantities and units in radiation protection dosimetry. International Commission on Radiation Units and Measurements, (Series: ICRU Report 51), Bethesda
9. Otto T et al (2018) Proposal for new operational quantities for external radiation. Radiat Prot Dosim 180(1–4):10–16
10. ICRP Publication 74 (1994) Conversion coefficients for use in radiological protection against external radiation. Ann ICRP 26(3–4)
11. Snyder W (1978) Estimates of specific absorbed fractions for monoenergetic photon sources uniformly distributed in various organs of a heterogeneous phantom. MIRD Pamphlet 5
12. Kramer R, Drexler G (1982) On the calculation of the effective dose equivalent. Radiat Prot Dosim 3(1–2):13–24
13. ICRP Publication 116 (2010) Conversion coefficients for radiological protection for external radiation exposures. Ann ICRP 40(2–5)
14. ICRP Publication110 (2009) Adult reference computational phantoms. Ann ICRP 38(2)
15. ICRP Publication 89 (2002) Basic anatomical and physiological data for use in radiological protection. Ann ICRP 32(3–4)
16. Conversion coefficients for use in radiological protection against external radiation. International Commission on Radiation Units and Measurements. ICRU Report 57. Bethesda, MD (1998)
17. International Organization for Standardization (2019) ISO 4037-3:2019, Radiological protection—X and gamma reference radiation for calibrating dosemeters and dose rate meters and for determining their response as a function of photon energy—part 3: calibration of area and personal dosemeters and the measurement of their response as a function of energy and angle of incidence. ISO, Geneva
18. International Electrotechnical Commission (2020) Radiation protection instrumentation—dosimetry systems with integrating passive detectors for individual, workplace and environmental monitoring of photon and beta radiation, IEC 62387 Edition 2. IEC, Geneva
19. Bordy J et al (2011) Principles for the design and calibration of radiation protection dosemeters for operational and protection quantities for eye lens dosimetry. Radiat Prot Dosim 144(1–4):257–261
20. Bartlett D (1993) Personal dosemeter calibration requirements: are they reasonable? J Radiol Prot 13(3):199

21. IAEA Safety Report Series No. 16 (2000) Calibration of radiation protection monitoring instruments IAEA, Vienna
22. International Organization for Standardization (2019) ISO 4037-1:2019, Radiological protection—X and gamma reference radiation for calibrating dosemeters and dose rate meters and for determining their response as a function of photon energy—part 1: radiation characteristics and production methods. ISO, Geneva
23. International Organization for Standardization (2006) ISO 6980-1:2006, nuclear energy—reference beta-particle radiation—part 1: methods of production. ISO, Geneva
24. International Organization for Standardization (2006) ISO 6980-2:2006, nuclear energy—reference beta-particle radiation—part 2: calibration fundamentals related to basic quantities characterizing the radiation field. ISO, Geneva
25. International Organization for Standardization (2006) ISO 6980-3:2006, nuclear energy—reference beta-particle radiation—part 3: calibration of area and personal dosemeters and the determination of their response as a function of beta radiation energy and angle of incidence. ISO, Geneva
26. Hirning CR (1992) Detection and determination limits for thermoluminescence dosimetry. Health Phys 62(3):223–227
27. Roberson P, Carlson RD (1992) Determining the lower limit of detection for personnel dosimetry systems. Health Phys 62(1):2–9
28. Sneha C, Pradhan SM, Adtani MM (2010) Study of minimum detection limit of TLD personnel monitoring system in India. Radiat Prot Dosim 141(2):168–172
29. International Organisation for Standardisation (2018) ISO-14146:2018. Radiological protection—criteria and performance limits for the periodic evaluation of dosimetry services. ISO, Geneva
30. ANSI/HPS N13.11-2009 (2009) Personnel dosimetry performance—criteria for testing. American National Standards
31. Vohra K et al (1980) A personnel dosimeter TLD badge based on $CaSO_4$:Dy Teflon TLD discs. Health Phys 38(2):193–197
32. Datta D et al (2018) Handbook on TLD-based personnel monitoring (rev. 1-2018). In: BARC report. Bhabha Atomic Research Centre, BARC Press, Mumbai
33. Kannan S, Kulkarni MS, Ratna P, Lalsare MD (1997) An automated TLD badge reader for large scale personnel monitoring. In: Proceedings of 23rd IARP conference on recent advances in radiation protection held at Guru Nanak Dev University Amritsar, India, 19–21 Feb (1997)
34. Kulkarni MP, Ratna P, Kannan S (2000) A new PC based semi-automatic TLD badge reader system for personnel monitoring. In: Proceedings of international radiation protection association conference, Hiroshima, Japan
35. IAEA (1999) Intercomparison for individual monitoring of external exposure from photon radiation. Results of co-ordinated research project 1996–1998, IAEA-TECDOC-1126, IAEA, Vienna
36. Pradhan AS, Bakshi AK, Srivastava K, Bihari RR (1999) Parameters of large scale production of personnel monitoring TLD cards based on $CaSO_4$:Dy. Radiat Prot Dosim 85(1–4):67–70
37. Lakshmanan AR, Popli KL, Bhatt RC (1979) Thermal history and reusability of $CaSO_4$:Dy Teflon TLD discs. Phys Med Biol 24(5):999
38. Pradhan AS, Bakshi AK (2002) Calibration of TLD badges for photons of energy above 6 MeV and dosimetric intricacies in high energy gamma ray fields encountered in nuclear power plants. Radiat Prot Dosim 98(3):283–290
39. Kumar M, Kher RK, Sahni G, Chhokra K (2008) Studies on the response of the TLD badge for high-energy photons. Radiat Protect Dosim 128(3):266–273
40. Pradhan AS, Adtani MM, Varadharajan G, Bakshi AK, Srivastava K, Bihari RR (2002) Hand book on the use of TLD badge based on $CaSO_4$:Dy Teflon TLD discs for individual monitoring (No. BARC-2002/E/025). Bhabha Atomic Research Centre
41. Pradhan AS (1992) Individual monitoring dose records-correlation of whole-body doses to the new operational quantities. Radiat Prot Dosim 42(2)

42. Lakshmanan AR (1991) How to measure the new ICRU operational quantities with individual dosemeters. Radiat Prot Dosim 35(4):253–259
43. Bakshi AK et al (2007) Development of an algorithm for TLD badge system for dosimetry in the field of X and gamma radiation in terms of $H_p(10)$. Radiat Prot Dosim 123(2):148–155
44. Pradhan SM et al (2009) Development of an algorithm for evaluating personal doses due to photon fields in terms of operational quantities for TLD badge system in India. Radiat Prot Dosim 136(3):176–184
45. Bhattacharya M et al (2022) Estimation of personal dose equivalent H_p (0.07) using $CaSO_4$:Dy Teflon disc-based extremity dosemeter. Radiat Prot Dosim 198(20):1546–1556
46. Kumar M et al (2005) Studies on automatic hot gas reader used in the countrywide personnel monitoring programme. Radiat Prot Dosim 113(4):366–373
47. Pathan MS et al (2019) Study of effect of consecutive heating on thermoluminescence GCs of multi-element TL dosemeter in hot gas-based reader system. Radiat Prot Dosim 187(4):509–517
48. Pradhan SM, Sneha C, Adtani MM (2011) A method of identification of abnormal GCs in individual monitoring using $CaSO_4$:Dy Teflon TLD and hot gas reader. Radiat Prot Dosim 144(1–4):195–198
49. Pathan MS, Pradhan SM, Selvam TP (2020) Machine learning algorithms for identification of abnormal GCs and associated abnormality in $Caso_4$:Dy-based personnel monitoring dosimeters. Radiat Prot Dosim 190(3):342–351
50. Pradhan SM et al (2015) Development of a technique for improving coefficient of variation of $CaSO_4$:Dy Teflon-based TLD personnel monitoring system in low-dose region. Radiat Prot Dosim 167(4):429–436
51. Pradhan SM, Datta D, Pathan MS, Srivastava K, Selvam TP (2020) Estimation of uncertainty in measurement of dose equivalent at laboratory level using $CaSO_4$:Dy-based TLD badge system in India. Radiat Prot Dosim 188(2):135–147
52. Operational quantities for external radiation exposure. International Commission on Radiation Units and Measurements. ICRU Report 95. Bethesda, MD (2020)
53. Endo A (2016) On behalf of ICRU Report Committee 26 on operational radiation protection quantities for external radiation, operational quantities and new approach by ICRU. Ann ICRP 45(1_suppl):178–187
54. Vanhavere F, Van Hoey O (2022) Advances in personal dosimetry towards real-time dosimetry. Radiat Meas 158:106862
55. O'Connor U, Walsh C, Gorman D, O'Reilly G, Martin Z, Madhavan P, Murphy RT, Szirt R, Almén A, Andersson M, Camp A (2022) Feasibility study of computational occupational dosimetry: evaluating a proof-of-concept in an endovascular and interventional cardiology setting. J Radiol Prot 42(4):041501

Monitoring of External Neutron Exposures

A. K. Bakshi, Rupali Pal, Deepa Sathian, and Sandipan Dawn

1 Introduction

Neutron dosimetry is an important part of radiation protection programme for all facilities that handle neutron radiation, be it nuclear reactor, high energy particle accelerator, radionuclide-based neutron source, etc. Neutron being a high LET particle produces higher health hazards with respect to gamma and hence monitoring, especially of reactor personnel, of neutrons (up to 20 MeV) is considered important. Further, considering the criticality accidents involving nuclear reactors [1], neutron monitoring is considered to be a necessity. As neutron energy range varies from thermal to 20 MeV (almost 9–10 orders) for all practical purposes, it has variable radiation weighting factors for calculation of effective dose or quality factors for dose equivalent. Although considerable progress has been made in neutron dosimetry, there is no single neutron dosemeter which takes care of estimation of neutron doses in the wide neutron energy spectrum, with adequate accuracy. The neutron monitoring till date is considered to be a challenging task in the field of radiation protection, as no single method provides the combination of energy and angular response and adequate accuracy necessary to comply with the international standards. Determination of the 'dose equivalent' is considered to be the most important concept in neutron dosimetry as it accounts for the 'quality factor' of neutrons, which depends on the energy of neutron. The quality factor for fast neutrons varies in the range of 2.5–20, depending on the energy [2]. The unit of dose equivalent is Sievert. Dose equivalent is defined in the following equation

$$\text{Dose equivalent} = \text{absorbed dose(Gy)} \times \text{Quality factor} \tag{1}$$

A. K. Bakshi (✉) · R. Pal · D. Sathian · S. Dawn
Radiological Physics and Advisory Division, Bhabha Atomic Research Centre, Mumbai 400085, India
e-mail: akbakshi@barc.gov.in

D. K. Aswal (ed.), *Handbook on Radiation Environment, Volume 2*,
https://doi.org/10.1007/978-981-97-2799-5_7

It may be noted that the unit of absorbed dose is Gy.

Dedicated neutron sources like research reactors, accelerators and spallation sources produce free neutrons for use in material science and neutron scattering experiments. Mono-energetic neutrons, which are produced in neutron generators/accelerators, are used in nuclear physics studies, development of spectrometers, metrology, material damage test, activation analysis, radiography, cancer therapy, etc. Neutron individual monitoring is essential to determine the adequacy of radiation safety measures during operations of reactors, accelerators, spent fuel processing plants, nuclear fuel cycle operations and other industries involving neutron source. Individual neutron monitoring program for external radiation exposure is intended to provide information for the optimization of protection and to demonstrate that the radiation dose received by the workers does not exceed the prescribed dose limits recommended by the regulatory authority. It gives information about safe work practices and verifies the shielding adequacy of work place monitoring [3]. This chapter has been divided into two parts, viz. (i) neutron dosimetry techniques related individual monitoring including performance test criteria, calibration methodologies, etc. and (ii) criticality accident dosimetry.

2 Characteristics of a Good Individual Neutron Dosimeter

i. It should record neutron dose equivalent from a fraction to multiples of maximum permissible dose equivalent limits.
ii. Its neutron energy response should be proportional to dose equivalent response.
iii. It should be insensitive to beta, X-rays and gamma rays in particular, which normally accompanies neutrons.
iv. It should have a good signal stability with little fading due to variations in temperature and humidity conditions in the ambient.
v. It should not be toxic to the wearer.
vi. It should be rugged, light weight, easy to handle for a large scale of monitoring purpose and be reasonably inexpensive.

3 Techniques for Neutron Monitoring

3.1 Nuclear Emulsion

In neutron monitoring, the Kodak film (known as NTA) is most commonly used to measure the dose equivalent of fast neutrons [4]. In nuclear emulsions, recoil protons are produced by the elastic scattering of hydrogen atoms by neutrons in the emulsion and the surrounding hydrogenous material, e.g. backing, radiators, etc. For mono-energetic neutrons incident on the emulsion, the protons have a uniform

energy distribution up to E_n (the incident energy) [5]. Recoil protons produce ionization along the track length, and a latent image is formed by the interaction with silver halide grains. After chemical processing, the tracks become visible under the microscope when a magnification of about 500× is used. The shortest identifiable track is about 5 μm in length and consists of four developed silver grains, which correspond to proton energy of about 0.7 MeV. Track densities are determined by manually counting the tracks in a given area. In the energy range 0.7–14 MeV, there is an energy dependence of the order of ± 50% [6] for the measurement of the dose equivalent (Fig. 1). Because of different radiators inside the packed film or inside the film badge, the response varies according to whether the radiation is from the front or rear. This characteristic changes for exposure in individual monitoring owing to back scattering and absorption of neutrons from the body [6]. The main disadvantage of NTA emulsion film is post-irradiation fading of proton tracks with temperature and humidity. Extensive studies have been done to minimize the fading by doubly sealing the films in polyethylene pouches with a small amount of calcium chloride as desiccant in between two layers of polyethylene [7]. Although all measures were taken to minimize fading of NTA film, fading corrections were applied for evaluation of the neutron dose. The other method to minimize the fading of recoil proton tracks in the nuclear emulsion is sealing the NTA film in presence of dry nitrogen medium in a glove box. The films can generally be used for a period of 2 months. It may be noted that NTA film is also sensitive to gamma rays, and the evaluation of dose by counting proton tracks on the film using microscope is tedious.

In India, in the past, neutron monitoring was carried out using Kodak NTA film, which is a 30 μm thick emulsion coated on one side of the cellulose tri-acetate base and fine grain of 0.3 μm size [8]. Recoil proton tracks are produced and recorded as photographic tracks in the film due to elastic collision of fast neutrons with hydrogenous material. The films are processed using standard procedures and the tracks are counted using optical microscope. Track density are counted and the corresponding neutron dose equivalent is evaluated. A plastic holder having cadmium filter in front and back is used to absorb thermal neutrons to avoid protons of energy 0.66 MeV arising from $^{14}N(n; p)^{14}C$ reaction. On the basis of calibration with an ^{241}Am-Be source, the number of tracks/cm^2 (track density) is correlated to neutron dose equivalent, taking into account the corresponding fluence-to-dose equivalent conversion factor. The dose-equivalent range of the Kodak NTA film is between 200 μSv and 0.5 Sv, but it is dependent on neutron energy and the gamma-ray dose contribution. The lower detection limit depends on the number of areas counted. For a dose equivalent of 0.2 mSv, there would be 0.4 tracks per area of 11.4×10^{-4} cm^2 (magnification 600 times) resulting in a relative standard deviation of about 16% for the counting of 100 areas.

Disadvantages of Kodak NTA film as neutron detector are as follows:

- the effective detector energy threshold of 0.7 MeV,
- background is normally high and hence signal-to-noise ratio is poor,
- the darkening of the emulsion due to gamma rays and
- the fading of the latent image as a function of temperature and humidity.

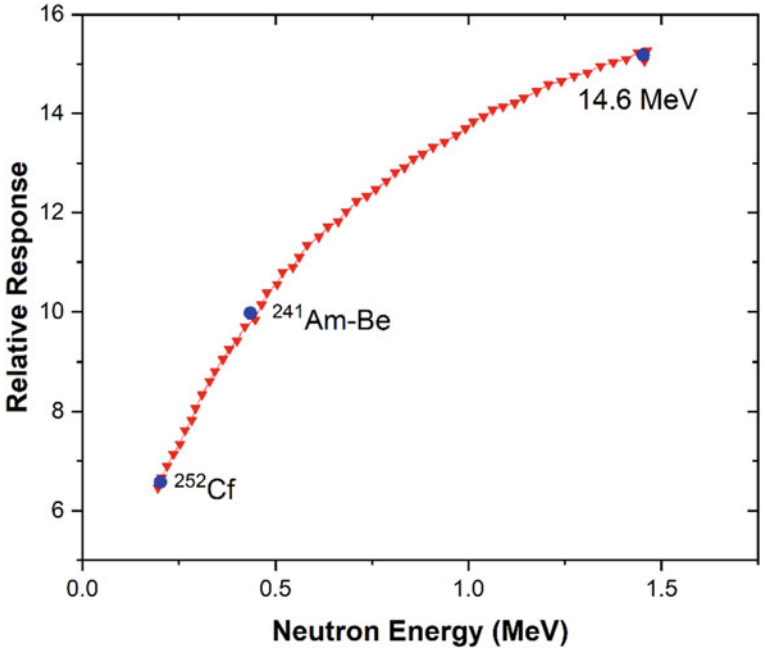

Fig. 1 Normalized dose equivalent response of NTA emulsion as a function of neutron energy in MeV (reproduced from [6] © 2022 The International Journal of Applied Radiation and Isotopes with permission from Elsevier)

However, the positive aspect of this film was that it can be used for thermal neutron detection/monitoring via the $^{14}N(n,p)^{14}C$ reaction due to the presence of nitrogen in the emulsion. The thermal neutron response of the Kodak NTA film is 1.45 times higher than that of ^{241}Am-Be source neutrons [5].

3.2 Solid State Nuclear Track Detector

Solid State Nuclear Track Detection (SSNTD) is a technique of recording tracks of ionizing particles in insulating solids and was discovered by Young in 1958 [9] and popularized by Fleischer [10]. Since then, many insulating materials have been tested and CR-39 a special type of plastic was found to be most useful for nuclear track detection. The chemical name for CR-39 is poly-allyl-diglycol carbonate (PADC) with chemical formula $C_{12}H_{18}O_7$. CR-39 stands for Columbia Resin (trade name). It is an optically clear plastic and also finds great application as a major component in copolymers used for lenses in spectacles. It is a track detector where tracks are formed due to the interaction of charged particles like protons, alpha and heavy ions with the polymer bonds of PADC. The energy deposited by protons creates damage

(breakage of bonds in the polymer) in this detector. These damages are enlarged and appear as tracks if subjected to etching and are viewed through an optical imaging system [11]. CR-39 gained widespread acceptance for personnel neutron monitoring in 1980s after the studies of Tommasino et al., Hankins et al., and Griffith et al. [12–14] on CR-39 detectors. CR-39 detectors have neutron energy threshold at 100 keV with relatively a flat energy response in the energy range 500 keV–10 MeV. It is insensitive to beta and gamma radiations. There is no post-irradiation fading of damaged tracks due to environmental conditions. The neutron energy threshold 100 keV makes it most suitable for neutron monitoring in reactor environments and fuel reprocessing facilities. The properties of CR-39 mentioned above are exploited to assemble it, as a neutron detector. Table 1 shows comparison between Kodak NTA and CR-39 SSNTD neutron dosimeters [7].

A crucial characteristic of CR-39 detectors is the background track density. This background can be attributed to (i) alpha exposure from radon during the storage of the detector (ii) cosmic radiations and (iii) surface defects and contaminants introduced during the manufacturing process. There is a considerable increase in background of CR-39 with time (ageing) due to environmental conditions that prevail during storage of these detectors from the time of manufacturing to the time of processing of the detectors, if it is not properly stored. In order to reduce the background tracks due to environmental conditions, CR-39 detectors are stored in a refrigerator and covered with thick black polythene at our laboratory.

Table 1 Comparison between Kodak NTA and CR-39 SSNTD neutron dosimeters

Dosimeter	Kodak NTA	CR-39 SSNTD
Threshold energy	500 keV	100 keV
Energy response	Energy dependent	Flat response
Post-irradiation fading	Severe	Very little fading
Response to beta and gamma	Considerable	None
Inherent background	Not much	Considerable
Minimum dose recorded	0.05 mSv	0.20 mSv
Despatch	Tedious, double sealing in dry nitrogen atmosphere	Brittle foil, simple sealing Cutting needs skill
Processing	Large scale (at a time max 200 films)	Small number (at a time max. 16 foils)
Evaluation	Tedious (on a microscope)	Easy (microfiche reader, automation)
Magnification	×750	×42
Shelf life	3–4 years	1–2 years
Availability	Imported (Kodak)	Imported (M/s Track Analysis System Limited, UK)

(reproduced from [7] © 2023 with permission from Elsevier)

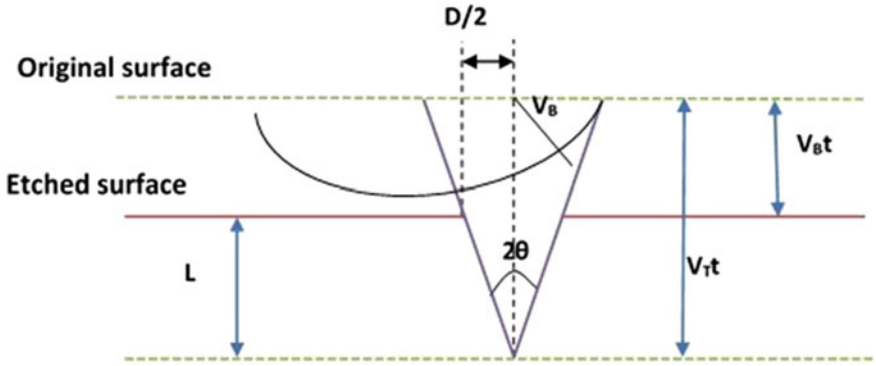

Fig. 2 Track etch geometry for a normally incident particle

3.2.1 Mechanism of Track Formation

When fast neutrons impinge on the CR-39 detector, the neutron energy is transferred which makes the chemical bonds loosen and become penetrable by any alkaline solution. When these detectors are etched in alkaline solution like 7 N KOH, the alkali penetrates faster at these damage sites than rest of the material. These damage sites are known as tracks, the size of which depends upon the incident neutron energy, i.e. smaller the energy smaller will be the diameter of the track or vice versa. For track formation, V_T/V_B has to be always greater than 1. If $V_T/V_B = 1$ no damage track is formed. Etching is a process by which tracks are magnified using alkaline solution. A track is enlarged only if the rate of etching along the track V_T exceeds the rate at which the surface is etched $V_B(V_T/V_B > 1)$. The track formation model has been explained by Tommasino et al. [15]. The track etching rate V_T is assumed to be constant and the surface etching rate V_B is isotropic. The track diameter D and the length of the track L depend essentially on the competitive effects of V_T and V_B. Duration of etching is denoted by 't'. A schematic diagram of the track formation in CR-39 detector with different track parameters is shown in Fig. 2.

3.2.2 Details of Neutron Badge Used in India

The SSNTD-based individual monitoring system was first started in 1991 for DAE units. Kodak NTA films were gradually phased out. Since 1999, CR-39 detectors-based neutron dosimeter are used for country wide fast neutron monitoring programme [16]. The neutron badge used for individual neutron monitoring comprises a CR-39 detector of dimensions 3 cm × 3 cm × 0.0750 cm, with a 1 mm thick polyethylene radiator of similar dimension in the front, sealed together in an air-tight triple laminated aluminized pouch [7]. The polyethylene radiator in the badge provides enhanced sensitivity for track detection due to recoil protons produced by the interaction of neutron with radiator. The aluminized pouch protects the detector

from ambient conditions, makes the detector dust free during handling and prevents entry of atmospheric radon/alpha particles which may produce tracks in the detector. The sealed pouch is further loaded in a plastic holder having a clip for the wearer. The frequency of monitoring service is quarterly for personnel working in neutron fields.

3.2.3 Processing of CR-39 Detector

The neutron dosemeter systems used at different laboratories for neutron individual monitoring employing SSNTD are diverse, with a wide variety of etching process, read out systems and holder designs [17]. There are several etching techniques such as chemical etching (CE), electro-chemical etching (ECE) and combination of these techniques for the processing of the detector. These techniques can be used for enhancing the damaged tracks and counted with appropriate imaging system. To cover the wide dose range, two etching techniques are adopted: (i) ECE and (ii) CE. ECE is a two step etching process for neutron dose equivalents up to 10 mSv, whereas CE is a single step process to cover the neutron dose equivalents in the range of 0.2–100 mSv.

3.2.4 Electro Chemical Etching (ECE) Technique

ECE method is developed by Tomasino [18] and Zapparoli [19]. Tracks of varying depths are produced depending upon the recoil proton energy. Application of electric field to chemical etching enlarges tracks even at small depths and makes it visible for counting at low magnification.

The ECE process is carried in two steps as follows:

Step 1: Etching at low frequency of 100 Hz for 4 h at 1500 V peak to peak constant potential. In this stage the damage tracks are marked.

Step 2: Etching at high frequency of 3.5 kHz at 1500 V for 40 min duration. In this step, the electrical stresses enlarge the tracks marked during low frequency. This initiates localized break downs at the track's tip and the resulting tracks look like trees and are large enough to be viewed easily with an imaging system.

3.2.5 Chemical Etching (CE) Technique

In normal condition, in case, neutron dose is suspected to be in excess of 10 mSv, ECE cannot be used due to higher track density which could not be counted by image analyzer. In such situation, chemical etching (CE) method is used [20]. The CR-39 detectors are subjected to chemical etching in 7 N KOH solution at 60 °C for 7 h [21]. However, there are chemical etching based processing technique with

appropriate microscope based imaging system, which can cover the dose range from 0.2 to 100 mSv or higher.

3.2.6 Track Counting

For electrochemically etched detectors, track counting is done on a PC-based automatic image analysis system [22]. The details in system are given in literature [3]. The tracks etched by chemical etching method are counted using a high magnification (20× magnification) optical microscope. With this magnification, the counting field of area 0.005 cm^2 of the detector can be covered. The diameters of the etched tracks produced by recoiled proton are in the range of 3–10 μm. Tracks are counted manually for 50 different fields around the centre of the detector. This process of counting is followed for both un-irradiated and irradiated detector and used for the assessment of track density [21]. For thermal neutrons monitoring, neutron detectors such as CR-39, LR 115, CN 85 or CR-39 are used along with converter (on the front side) containing compounds of boron and/or lithium.

3.3 Neutron Thermoluminescent Dosimeter

Albedo neutron dosimetry is based on the effect of moderation and backscattering of neutrons by the human body. Moderation and backscattering of incident neutrons by the human body moderates neutron fluence spectrum in the thermal and intermediate energy range. These backscattered neutrons (albedo neutrons) are detected by a dosimeter (usually a ^{6}LiF based thermoluminescent chip), worn on body for dosimetry of thermal neutron. The most commonly used individual neutron dosimeters for radiation protection purposes are thermoluminescent dosimeters [23, 24]. Lithium fluoride (^{6}LiF:Mg,Ti) is used as detector material in albedo dosimeter. It is almost a tissue-equivalent dosimeter.

Table 2 gives the details of TLDs used for as albedo neutron dosimeter [25]. In order to detect thermal neutrons, a pair of ^{6}LiF:Mg,Ti (TLD-600) and ^{7}LiF:Mg,Ti (TLD-700) are used in the dosimeter. The cumulative dose from TLD-700 is subtracted from TLD-600 to get thermal neutron dose [26–28].

Table 2 Comparison of gamma ray and thermal neutron sensitivities of LiF TLD

TLD material	% ^{6}Li	% ^{7}Li	Relative gamma sensitivity	Thermal neutron response relative to ^{60}Co equivalent Gy/10^{10} n cm^{-2}
^{6}LiF (TLD-600)	95.620	4.380	1.06	15.2
^{7}LiF (TLD-700)	0.007	99.993	0.86	1.1×10^{-2}

(reproduced from [25] © with permission from Elsevier)

Factors Influencing the Response of TL Materials

- Neutron cross-section of TL materials
- Luminescence spectra of TL materials
- The effect of the heating cycle
- Supralinearity and sensitization
- Self-shielding
- Composition of the TL material
- Environmental effects.

The albedo dosimeter which relies upon neutrons reflected from the body of the wearer was the first major development in neutron dosimetry after the nuclear emulsion. The reflected or albedo neutrons have energies from thermal up to the incident energy and by using a $1/v$ response of the detector and if shielded from the direct radiation, it is possible to have a response which is approximately proportional to the incident fluence. This means that the albedo dosimeter measures the dose equivalent up to 10 keV and has a rapidly decreasing response beyond this. Cadmium or boron absorbers are used to separate albedo neutrons from field neutrons as well as to analyse the neutron stray-radiation field. An additional moderator incorporated in the dosimeter increases the albedo detector response due to moderated incident neutrons. Various albedo dosimeter types have been developed in the past in order to improve the dosimetric properties; especially the energy response function and energy response for some of them is shown in Fig. 3.

(i) The non-discriminating type detects equally the incident and the backscattered neutrons with a single detector without the use of an asymmetrical neutron shield on one part of the capsule;
(ii) The discriminating type detects mainly backscattered neutrons by using a single detector inside a neutron shield in front of the dosimeter which is open on the side facing the body;
(iii) The discriminating analyser type detects incident as well as albedo neutrons by using at least two detectors, one of which is positioned inside and the other outside a neutron shield so as to obtain additional information on the incident neutron field.

The cadmium shielded dosimeter developed by Hankins [30] uses a polyethylene moderator which increases the epithermal neutron albedo response of ^{6}LiF in the centre. The dosimeter was designed to give a response to thermal neutrons equal to the albedo response to fast neutrons of 1 MeV. The response to fast neutrons at 1 MeV is only about 1.5% of that at energies below 10 keV.

The albedo dosimeter developed by Hoy [31] makes use of a cadmium shield, an incorporated moderator and two pairs of ^{6}LiF and ^{7}LiF TLDs. The contribution of field thermal neutrons measured outside the cadmium shield will be subtracted from the albedo reading of the detector facing the body. This dosimeter is fixed on a belt. A two-component albedo dosimeter has recently been developed by Piesch and Burgkhardt for commercial TLD systems with automatic readout [32] from

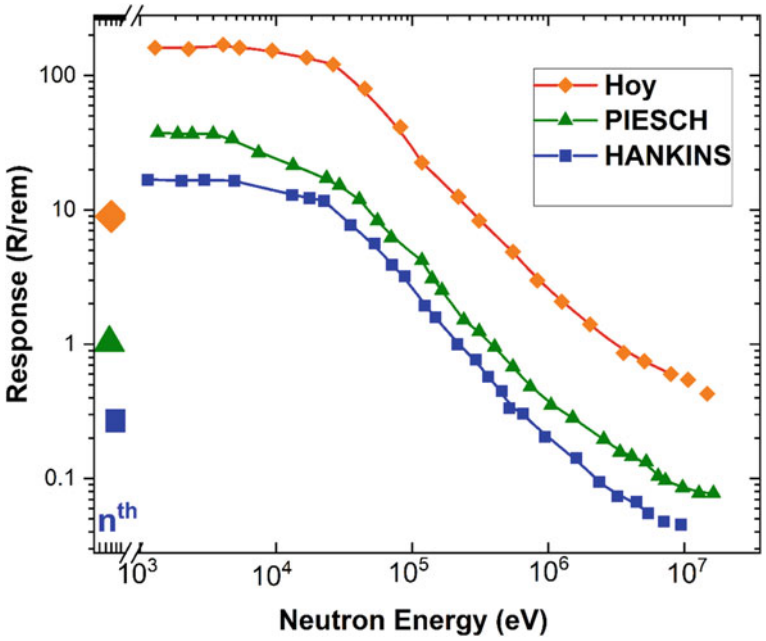

Fig. 3 Energy dependence of various albedo dosimeters (reproduced from [29] © 2023 with permission from Elsevier)

the manufacturer Alnor, Harshaw, Panasonic, Teledyne, Vinten. The boron-loaded encapsulation of the albedo dosimeter makes use of detector pairs behind a 'β-window' on the side facing the source to detect mainly thermal neutrons and behind a collimated 'albedo neutron window' on the side facing the body to detect albedo thermal neutrons. An additional advantage of the universal $\beta/\gamma/n$ dosimeters is the low effect of body-to-dosimeter distance [29]. The thermal response is equal to the albedo response to neutrons of 100 keV and to that found in the stray-radiation field of nuclear power plants.

In India, Bakshi et al. developed thermal neutron sensitive TLD-based on enriched ^{6}LiF, $CaSO_4$:Dy powder and Teflon (binder material) mixing in the weight ratio of 1:1:2 [33]. The response of this thermal neutron sensitive TLD with respect to TLD 600 and gamma sensitive TLD ($CaSO_4$:Dy + Teflon disc) is given in Table 3 for different neutron sources. It is 3 times less sensitive than TLD 600. Further details of this neutron sensitive dosimeter are available in the literature [33]. Table 3 gives the response of thermal neutron sensitive TLD for various ISO-recommended sources developed Bakshi et al. [33].

The energy response of $CaSO_4$:Dy based neutron sensitive disc irradiated on water slab phantom of size 30 × 30 × 15 cm^3 along with TLD 600 is shown in Fig. 4. It is seen that the energy response follows the same trend as that of TLD 600. This neutron sensitive TLD can be used along with CR-39 based dosimeter to cover the

Table 3 Relative response of $CaSO_4$:Dy based neutron and gamma sensitive TLD discs, and TLD 600, exposed to gamma and neutron fields under different irradiation conditions

Radiation source	Irradiation condition	Response (mSv)		
		Gamma sensitive disc	Neutron sensitive disc	TLD-600
^{137}Cs gamma	In air	1.00	–	–
Thermal neutron (graphite-moderated ^{241}Am Be))	In air	0.533	22.340	72.10
	On phantom	1.000	84.320	231
	On phantom with 1 mm Cd in front	5.210	13.200	39.62
^{241}Am-Be (fast neutron source)	In air	0.027	0.031	0.080
	On phantom	0.031	0.085	0.253
Bare ^{252}Cf	In air	0.060	0.080	0.210
	On phantom	0.065	0.240	0.760
D_2O-moderated ^{252}Cf	In air	0.220	0.420	1.790
	On phantom	0.250	2.130	7.870

The response is normalized to ^{137}Cs exposure (reproduced from [33] © 2022 Radiation Protection Dosimetry with permission from Oxford University Press)

entire energy range from thermal to 14 MeV in the countrywide neutron monitoring programme.

3.4 Radiophotoluminescent Glass Detectors

Compared to other methods of radiation detection (emulsions, track detectors, photo stimulable imaging plates, thermoluminescence, and others), radiophosphtoluminescent (RPL) detectors offer a unique combination of advantages that include rapid exploitation, reusability, insensitivity to light, temperature and humidity, and stability to fading [34, 35]. In phosphate glass dosimetry, three main techniques are used to detect neutrons:

(i) The direct interaction of neutrons with glass compounds providing additional RPL centres which are measured together with the gamma ray dose component;
(ii) Because of the production of radioactive isotopes, the glass dosimeter may serve as an activation detector for thermal and fast neutrons;
(iii) Glass dosimeters can be applied as neutron track-etch detectors by using glass types with an additional content of fissile materials (U, Th, Np) or by sandwiching them between converter foils [36].

In direct interactions, the neutron sensitivity of silver phosphate glasses is mainly based on the production of RPL centres caused by the (n, α) reactions in lithium and boron, and by lithium and oxygen recoil nuclei due to elastic scattering in the

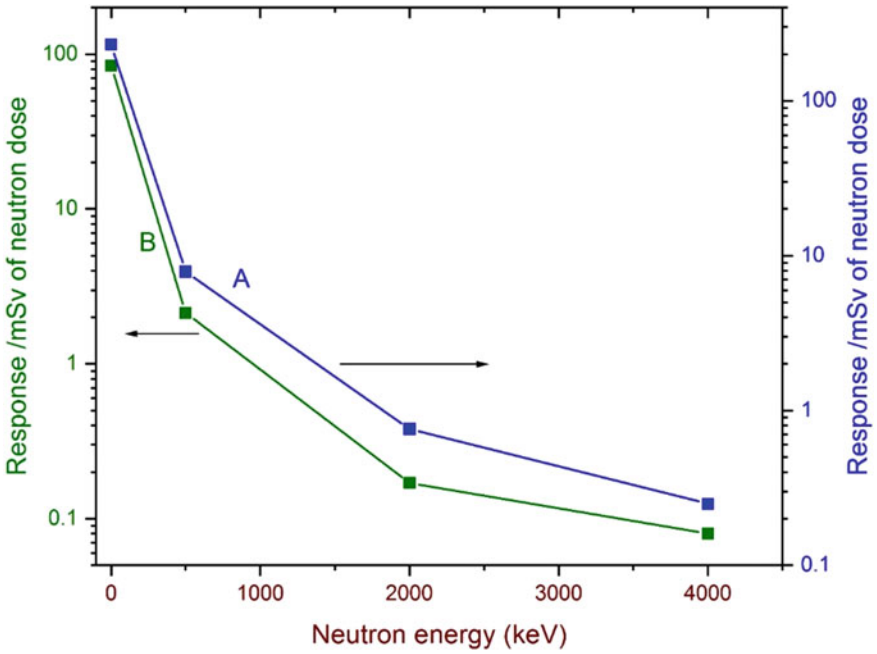

Fig. 4 Energy response of $CaSO_4$:Dy-based thermal neutron TLD (blue) and TLD 600 (DARK GREEN) (reproduced from [33] © 2023 Radiation Protection Dosimetry with permission from Oxford University Press)

fast-neutron range. The neutron response of the phosphate glass routinely applied in gamma ray dosimetry is presented in Fig. 5 as a function of neutron energy [37].

The data on experimental neutron sensitivity for different types of RPL at a fluence of 10^{10} n-cm^{-2} in terms of a ^{60}Co gamma-ray equivalent exposure are given in literature [38].

The neutron response depends mainly on the isotopic content, the thickness, size and encapsulation of the glass, and the irradiation conditions. A shielding of 1 mm Cd or the boron plastic in perforated tin spheres gives an approximate dose-equivalent reading of the FD-1 glass for both thermal neutrons and gamma rays.

In normal phosphate glass dosimeters (size $8 \times 8 \times 4.7$ mm), the reactions ^{31}P(n, p)^{31}Si ($T_{1/2} = 2.6$ h) and ^{31}P(n, γ)^{32}P ($T_{1/2} = 14$ days) are used by making measurements at two times after irradiation to separate the activation from fast neutrons and thermal and intermediate neutrons [39]. The neutron activation is preferably measured in a liquid scintillation counter by means of the Cherenkov radiation produced by the β-particle interaction directly in the transparent glass. This technique provides high efficiency (~ 50%), discrimination against both background radiation and β-particles below 1 MeV and a dose range above 5 mGy for thermal and fast neutrons.

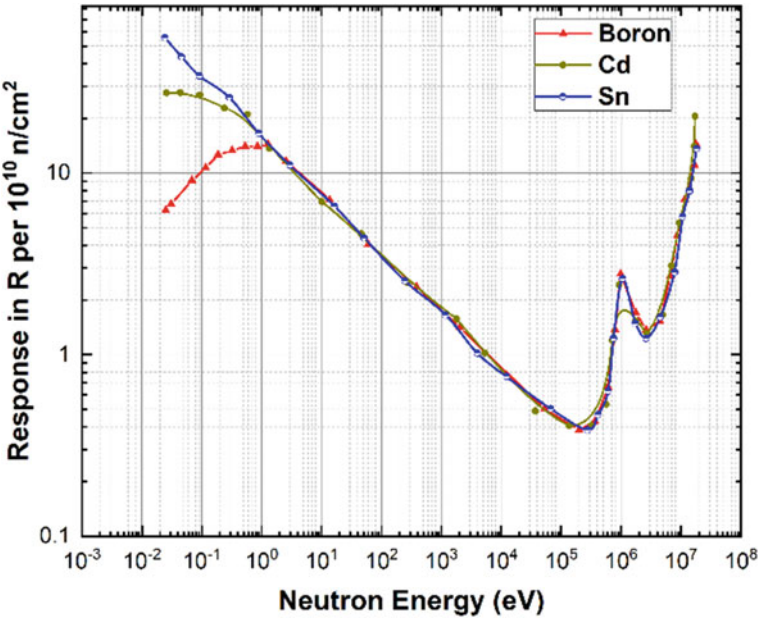

Fig. 5 Neutron energy dependence of phosphate glass dosimeters along with Boron, Cadmium and Tin activation foils [37]

A special arsenic-phosphate glass makes use of the reaction $^{75}\mathrm{As}(n, \gamma)^{76}\mathrm{As}$ ($T_{1/2}$ = 26 h) resulting in a dose reading above 1 mGy for neutron spectra with effective energies from about 0.1 to several MeV if the measurement is performed within eight hours after high-level short exposures. The activation of silver in the glass as well as of tin or cadmium in the dosimeter capsule can be used for the detection of slow neutrons above 0.1 Gy. New types of RPL detectors have properties suitable for measuring gamma-ray doses; they are superior to many other common detectors and should not be overlooked as a component of a modern personnel dosimeter. Table 4 gives the details of the activation foils used in RPL for the measurement of neutron dose of in wide range of neutron energies.

The RPL glass employed is a rigid detector consisting of a plate of silver-doped phosphate glass (35 × 7 × 1.5 mm^3) containing by weight: 48.33% O, 13.24% Na, 6.18% Al, 31.53% P and 0.72% Ag with a 2.6 g cm^{-3} density. During an irradiation, luminescence centres in the glass are activated. Before reading a detector, the centres must undergo a stabilizing heat treatment ('preheating') at 100 ºC for 1 h [34]. When illuminated under the UV laser beam of the FGD-660 readout module, de-excitation of the centres is accompanied by an orange luminescence with an intensity proportional to the number of trapped which allows rereading a detector. Upon heating to 400 ºC for 1 h, residual signal in the detector is erased and can be reused.

Table 4 Detection of neutrons by activation of phosphate glass dosimeters [39]

Nuclear reaction	Isotope fraction (%)	Resonance energy[a]	Half-life	Energy (MeV)		Emission per decay (%)
$^{31}P(n, p)^{31}Si$	100	Threshold > 2.5 MeV	2.6 h	β^-	1.48	100
$^{31}P(n, \gamma)^{32}P$	100	Epithermal (similar to Ag)	14.3 days	β^-	1.71	100
$^{109}Ag(n, \gamma)^{110m}Ag$	48.65	5.2–200 eV	253 days	γ	0.656	96
				γ	0.884	72
$^{112}Sn(n, \gamma)^{113}Sn$	0.95	20 eV–1 keV	119 days	γ	0.393	73
$^{116}Sn(n, \gamma)^{117m}Sn$	14.24		14 days	γ	0.162	91
				γ	0.159	100
$^{114}Cd(n, \gamma)^{115}Cd$	28.86	0.5 eV and (20 eV–1 keV)	53 days	γ	0.335	100
				γ	0.523	24.8
$^{63}Cu(n, \gamma)^{64}Cu$[b]	69.09	580 eV	12.8 h	γ	0.51	38
$^{23}Na(n, \gamma)^{24}Na$	100	2.850 and 30 keV	15.30 h	β^-	1.39	100
$^{75}As(n, \gamma)^{76}As$	100	47 eV–3 keV	26.5 h	β^-	3.0	100
$^{107}Ag(\gamma, n)^{106}Ag$	51.53	Threshold 10 MeV	26 min	γ	0.51	126
$^{107}Ag(n, 2n)^{106}Ag$	51.53		26 min	γ	0.19	100

[a] Neutron sensitivity in the range of epithermal neutrons in addition to the high sensitivity for thermal neutrons < 0.5 eV

[b] Low content of Copper in Tin

3.4.1 RPL Dosimeter Configuration

Figure 6 shows the configurations adopted for the fast and thermal neutron dosimeters in a mixed *n*-γ field. It consists of an assembly of RPL detectors (1.5 mm thick), (CH_2)n converter (1 mm thick in which proton equilibrium is reached for (n,p) reactions with ^{241}Am-Be neutrons, Cd converter (0.5 mm thick), Al screen (11 mm thick) and ^{10}B absorber (40 mm thick). The ^{10}B absorber serves to eliminate the thermal neutron component in order to avoid RPL glass activation. Fast neutrons are detected by their (n, p) collisions in the hydrogen-rich converter. The RPL detector downstream of the (CH_2)n detects protons from the converter plus gamma rays of mixed field. The RPL detector without converter registers the same gamma rays. Fast neutron dose is taken to be the difference between the two RPL readings. Thermal neutrons are detected by their (n, γ) reactions in the Cd converter. The RPL preceded by Cd detects gamma rays from the $^{113}Cd(n, \boldsymbol{\gamma})^{114}Cd$ reaction plus gamma rays of the mixed field. The RPL detector preceded by Al and ^{10}B registers only gamma rays incident from the mixed field. The Al is used to stop the products from the $^{10}B(n, \alpha)^{7}Li$ reaction. The dosimeter response to thermal neutrons is obtained by subtraction of the responses of the two RPL detectors [40].

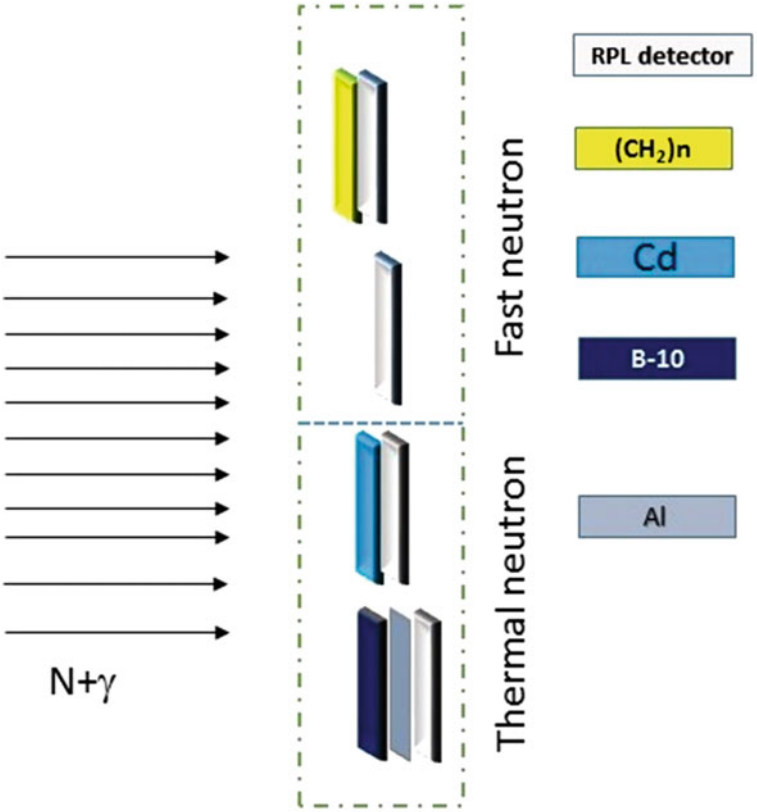

Fig. 6 Structure of dosimeters incorporating RPL detectors for measuring fast and thermal neutrons in a mixed *n-g* field (reproduced from [40] © 2023 with permission from Elsevier)

3.5 Bubble Detectors

A new type of direct-reading neutron dosimeter has been developed at the Chalk River Nuclear Laboratories [41]. This detector is prepared by suspending superheated droplets and can be triggered by neutrons giving rise to visible vapour bubbles which are trapped at the sites of formation and then counted to give a measure of the neutron dose [42].

The bubble detector consists of tiny superheated liquid droplets dispersed throughout in a firm elastic polymer (polyacrlamide) [43]. The polymer is contained in a small capped and sealed plastic (plastic detector) test tube. A low boiling point liquid floating above the polymer exerts adequate pressure on it so as to keep it in a radiation insensitive state. The detector is sensitized by removing the cap and discarding the liquid. Upon neutron irradiation visible bubbles are formed in the detector, the number of bubbles being a measure of the neutron dose equivalent. This dosimeter has built-in compensation for temperature effects on the superheated

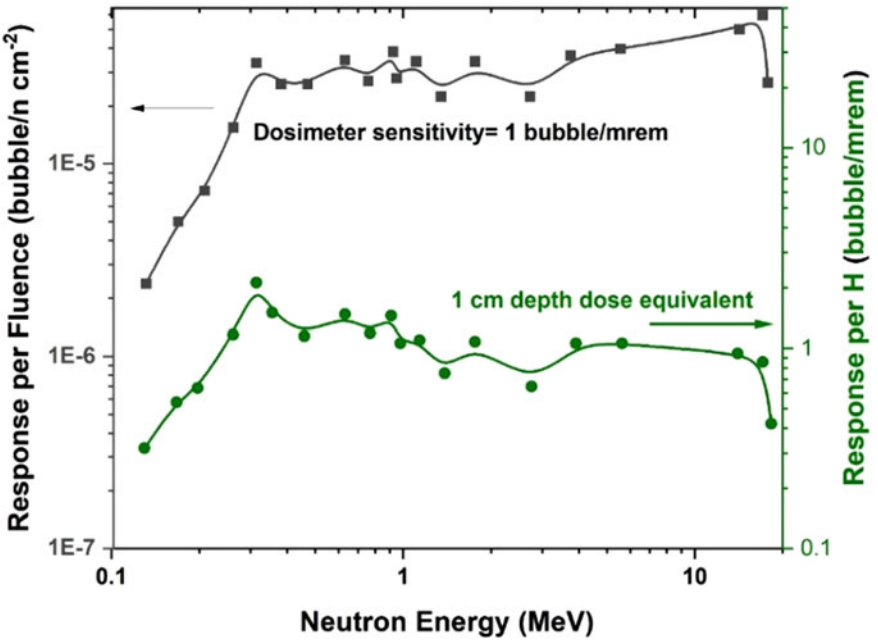

Fig. 7 BD-PND normalized response per unit fluence (closed diamonds) and response per unit dose equivalent (closed circles). Conversion from fluence to dose equivalent based on NCRP Report No. 38 [44]

droplets. This bubble detector responds to fast neutron in the energy region from 100 keV to 15 MeV. Response depends strongly on the degree of superheat. Figure 7 shows the energy response of bubble detector in terms of neutron fluence and dose equivalent [44].

3.5.1 Features of Bubble Detectors

- Direct reading neutron dosimeter which is energy dependent.
- Prepared by suspending super-heated liquid of a mixture of Freon and iso-butane in an elastic polymer gel of glycerol and polyacrylamide.
- Linear dose equivalent response.
- Droplets are triggered by neutrons induced protons giving rise to vapour bubbles which are trapped at the site of formation.
- The bubbles can be counted by naked eye or by capturing the image in a monitor.
- The sensitivity is greater than 10 bubbles per μSv.
- Compact, reusable, zero background and requires no power supply.
- Consists of minute droplets of a superheated liquid dispersed throughout an elastic polymer.

Neutrons strike droplets producing secondary charged particles. Charged particles cause droplets to vapourize, producing bubbles. Bubbles remain fixed in a polymer. Bubbles can be counted by eye or in automatic reader. Dose is proportional to the number of bubbles.

In India, Vaijapurkar and Ponraju developed superheated drop detector/bubble detectors for neutron detection [45, 46]. Ponraju et al. [46] used an aqueous solution of acrylamide (12%), polyacrylamide gel (27%) and glycerol (38%) for bubble detector. After degassing, the solution was maintained at 273 K. This solution was used as host medium for the homogenous mixture. Fifty ml of the host medium was taken in a stainless steel pressure chamber and the homogenous mixture was injected into it at 273 K. The homogenous mixture was dispersed uniformly as fine droplets in the host medium using mechanical stirring for about 20 min. Then the emulsion was poured into a glass vial (100 ml capacity) and irradiated in a gamma chamber for a total dose of 200 Gy to increase the viscosity of the host medium. After completion of the in situ polymerization, the vial was placed in a stainless steel pressure chamber and pressurized to 10 atmosphere using argon gas.

Vaijapurkar [45] made a host medium, i.e. the polymer matrix, consisting of polyacrylamide with salt additives. An uniform solution is made by constant stirring. The mixture is then subjected to heat cycles until the desired degree of polymerization is achieved. The polymer is then allowed to cool to room temperature. The low boiling point liquid, i.e. CCI_2F_2, is then dispersed uniformly in the matrix. This process is carried out in a pressure chamber so as to preserve the superheated state of the low boiling point liquid. It is then transferred to suitable glass vials of 15 ml capacity. The vials are stored for 24 h at 10 °C before further use. Vaijapurkar [45] employed an acoustic technique to ensure accurate measurement of the number of bubbles formed due to neutron interaction. The glass vials used had a flat base which offered more area of contact between the vial and the acoustic transducer. An acoustic coupling liquid was introduced between the base of the vial and the acoustic transducer to ensure proper acoustic coupling. The ultrasonic transducer having a resonant frequency of 200 kHz was used along with the necessary signal conditioning network and counter.

Table 5 presents variation of sensitivity of bubble detectors with temperature at a given exposure of 10 μSv. It is evident from Table 5 that the sensitivity of the detector exhibits a temperature coefficient of 0.87%/°C. The sensitivity sharply rises at about 35 °C. This may be attributed to a part of the superheated droplets becoming quasi-stable at this temperature. The variation in sensitivity for the temperature range 10 to 35 °C is about 20%. Statistical variation in readings is also of the same order but the trend of rise in sensitivity is very evident. The detector stored at temperatures between 5 and 25 °C retained the uniform suspension of droplets and sensitivity of 15 ± 2 bubbles/10 μSv up to an observed time of one week. The sensitivity of the detector in each vial was measured at different intervals by exposing the sensor to a neutron dose of 10 μSv.

Ponraju et al. [46] also developed an ultrasonic bubble counting method for measuring the neutron dose. The attenuation of ultrasound has good correlation with the bubble population when the sound wave passes through the bubbles. Hence by measuring ultrasonic attenuation, it is possible to measure the neutron dose. The

Table 5 Sensitivity of bubble detector at different temperature developed by Vaijapurkar et al. [45] (reproduced from [45] © 2023 with permission from Elsevier)

S. No.	Temperature °C	Sensitivity bubbles/10 μSv
1	10	15.00 ± 2.35
2	15	16.00 ± 2.35
3	21	16.67 ± 0.71
4	22	17.00 ± 0.25
5	25	16.60 ± 1.55
6	30	18.00 ± 1.32
7	33	18.50 ± 1.42
8	35	26.00 ± 4.36

accuracy of bubble counting and the neutron dose measurements in this method is within acceptable limit (10%). It is observed that ultrasonic attenuation increases linearly with number of bubbles and hence the measured ultrasonic attenuation can be directly correlated with the neutron dose.

3.6 Fluorescence Nuclear Track Detector (FNTD)

Novel Al_2O_3:C,Mg fluorescent nuclear track detectors (FNTDs), recently developed by Landauer, Inc. [47, 48] have demonstrated a promising performance for dosimetry of neutrons, protons and other heavy charged particles. FNTD technology is based on a single crystal of aluminium oxide doped with carbon and magnesium (Al_2O_3:C,Mg), and has aggregate oxygen vacancy defects. Major advantages of Al_2O_3:C,Mg FNTD over conventionally processed CR-39 SSNTD include superior spatial imaging resolution, a wider range of LET sensitivity, no need for post-irradiation chemical processing of the detector, and the capability to anneal and reuse the detector. FNTDs show a low-LET threshold at 0.4 keV/μm, do not saturate at LET in water as high as 1800 keV/μm, and are capable of counting track density with irradiation to fluences in excess of 10^6 cm^{-2} without saturation. It is noted that the dynamic range of measured dose and LETs of SSNTD can be extended by using other readout technique like optical densitometry and atomic force microscopy. Aluminium-oxide single crystals doped with carbon and magnesium (Al_2O_3:C,Mg) exhibit a high concentration of complex $F_2{}^{2+}$ (2 Mg) colour centres that undergo radiochromatic transformation into F^{2+}(2 Mg) centres when exposed to ionizing radiation. The number of centres transformed depends on the local energy deposition and the centres available. The F^{2+} (2 Mg) centres show high quantum-yield intra-centre fluorescence at 750 nm when excited around 620 nm with a short life-time of 75 ± 5 ns. This allows the detector to be imaged with confocal laser scanning microscopy to assess 3D energy deposition patterns with μm-resolution and reconstruction of single ion tracks and their energy loss [49, 50].

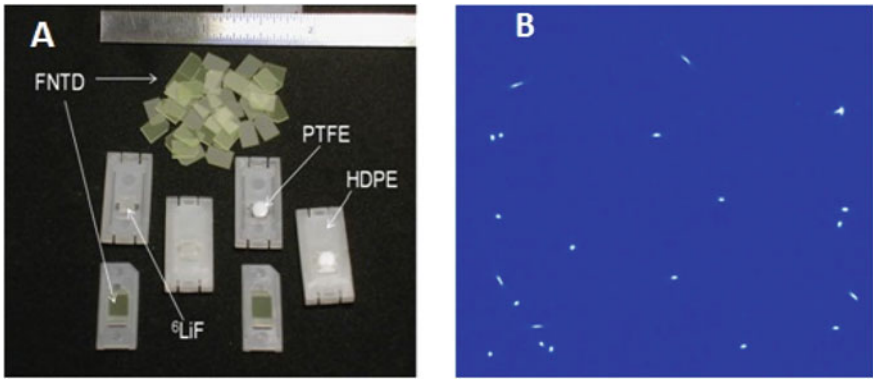

Fig. 8 (A) FNTDs and the PE converter cases with ^{6}LiF and PTFE chips. FNTDs were cut in the form of $6 \times 4 \times 0.5$ mm^3 rectangular plates with the long side aligned along the optical *c*-axis of the crystal. One side of the FNTD was polished, (B) fluorescent image with recoil proton tracks. FNTD was irradiated with ^{241}Am-Be neutrons behind a polyethylene converter (reproduced from [49] © 2023 with permission from Elsevier)

Track detectors, including FNTDs, have traditionally measured neutron dose by relating track density of nuclear reaction products to the incident neutron fluence. For thermal neutron detection, converters containing isotopes such as ^{6}Li or ^{10}B with a high capture cross-section are widely used. For fast neutron detection, hydrogen, having the same mass as neutron, is the best convertor atom for the efficient energy transfer. For practical neutron dosimetry, an FNTD crystal is covered by ^{6}LiF and/or polyethylene (PE) converters (Fig. 8a). The reaction products such as alpha particles, tritium ions or recoil protons produce ionization of Al_2O_3:C,Mg within the track volume and are imaged in fluorescent contrast as bright features on a dark background (Fig. 8b). At low doses, and in the absence of high photon dose, track recognition and track counting produces the best result and high sensitivity for neutron dose measurements [47, 49, 51–53].

The non-destructive readout of the FNTD is performed using a confocal laser scanning fluorescent microscopy technique. Scanning of the three-dimensional spatial distribution of fluorescence intensity along the track of a heavy charged particle (HCP) permits reconstruction of particle trajectories through the crystal. During readout, FNTDs are first scanned in *Z* direction with the laser beam perpendicular to the detector surface to determine the surface position with an accuracy of 0.1 mm. After the axial surface position is found, the detectors are scanned in a plane parallel to their surface at a depth of 3.5 mm below the surface of the crystal. Single images have dimensions of 100×100 μm^2 and the number of acquired images depends on the measured dose and is adaptively varied between 25 and 100 for each of the converter areas. Determining the dose of neutrons in counting mode is relatively simple. The readout system acquires a predetermined number of images, image processing recognizes and counts fluorescent tracks and rejects any artefacts related to crystal defects and surface contaminations. The neutron dose is proportional to the

density of tracks per unit area, and the calibration coefficient in tracks/(mm^2-mSv) is determined during calibration of the dosimetry system using standard neutron fields. It has dose linearity from 0.1 to 500 mSv.

3.7 Advantages of FNTD Over SSNTD

FNTD imaging plates are reusable after thermal annealing or optical bleaching. The FNTD readout process is completely optical and non-destructive with no chemical etching or other detector preparation. Software has been developed and implemented for fast automatic scanning, image processing and track counting. Separation of fast and moderated neutron doses as well as neutrons and photons has been achieved through the use of three different converters and novel image processing techniques.

FNTD technology allows for fast and inexpensive assessment of average neutron energies in facilities by using depth profile or the ratio of track densities behind two converters. Neutron detection efficiency of FNTDs is comparable with CR-39. At the same time, FNTDs are sensitive to high energy neutrons (20–100 MeV) where CR-39 detectors lose their response because of low sensitivity to high energy recoil protons with LET less than 5 keV/μm. The lower limit of detection in track counting mode for fast neutrons was estimated at around 0.2 mSv and the saturation of the dose dependence in Power Spectrum Integral mode was not observed up to 200 Sv. For gamma photons, the lower limit of detection is currently at 5 mGy with good potential for improvement.

3.8 Diode Based Electronic Neutron Pocket Dosimeter

Real-time personal neutron dosimeters are required for occupational radiation protection at nuclear power stations, nuclear fuel reprocessing facilities, high energy accelerators and neutron handling laboratories [54]. Work in controlled areas at elevated dose rate levels shows the necessity of carrying out real-time measurements to warn people when a certain level of personal dose equivalent is exceeded. Electronic devices are able to fulfil this requirement. Personal dosimeters using active electronic detectors such as silicon diodes or other semiconductors have also been available for quite some time, but in the past, they were most often used as entry-control dosimeters that would provide an alarm when a pre-set level of dose equivalent or dose equivalent rate was encountered. With the development of improved, multi-detector, electronic personal dosimeters (EPD), it became possible to consider using these devices as workplace dosimeters that would function in the same way as passive dosimeters. The versatility and additional features available in EPDs make them good candidates for serving as routine workplace monitoring. In radiation areas, where there is potential radiation exposure from neutron, it is required to use additional active dosimeter (pocket dosimeter) along with passive dosimeter to know the

neutron dose equivalent instantly for better dose management. Pocket dosemeters consist of highly sensitive and small-sized neutron detector using a low-cost silicon PIN photodiode and polyethylene convertor as a neutron converter [55].

PIN silicon diodes are used to detect visible light but they can also be used to detect charged and uncharged radiation when reversed bias is applied. These generally have low cost, very good quantum efficiency and energy resolution. They can work with a few volts bias voltage and have a dead entrance layer of several tens of nanometres. The thin depletion layer (200–500 nm) gives them a low sensitivity for gamma rays but it is thick enough for full collection of the electron–hole pairs generated by charged particles. The pocket dosimeters can be shielded with a metallic box connected to the ground of the associated electronics to shield from electromagnetic radiation [56].

These devices have combination of converters such as $^{6}Li/^{10}B$ and polyethylene radiators over semiconductor diodes to make them sensitive to neutrons of energy thermal to 15 MeV. Incident neutrons interact with the converter or detector nuclei and produce charged particles that can deposit energy in the semiconductor and produce signal. Active detectors based on silicon PIN diodes have been developed for individual radiation protection purposes in mixed neutron and photon fields. The measured pulse height distributions reflect the energy depositions in the active part of the detector. Such neutron sensitive instruments contain two detectors to correct for the sensitivity to photons or for the lack of sensitivity for neutron energies under 500 keV. Broadly it can be said that two methods are applied. In the first one [57], a silicon diode covered with a boron-loaded polyethylene converter measures neutrons and photons, whereas the second silicon diode is bare and measures only photons. Neutron information is derived from the difference between the two diode signals. This method needs two identical silicon diodes which are not easily available. This dosemeter has a low sensitivity for low-energy neutrons and a high sensitivity for photons. The lower energy threshold of such dosemeters for fast neutrons in realistic conditions is estimated to be about 500 keV [57]. To overcome its response for thermal and low-energy neutron, the detector consists of a ^{10}B silicon junction with polyethylene converter and moderator while the other silicon diode is meant to detect fast neutrons and is covered only by a polyethylene radiator. An electronic threshold on the pulse height suppresses the photon pulses. There are two features inherent to this second method: a dip in sensitivity at neutron energies around 1 MeV and an increase for low-energy neutrons around a few keV [58]. This example shows the interdependence of microelectronics and dosimetric investigations. However, the cost of commercial dosemeters is an important parameter for routine implementation.

4 Calibration of Neutron Dosimeters

4.1 International Recommendation

ISO 8529-1:2021 [59] specifies the reference neutron radiations, in the energy range from thermal up to 20 MeV, for calibrating neutron-measuring devices used for radiation protection purposes and for determining their response as a function of neutron energy. Reference radiations are recommended for neutron fluence rates of up to 1×10^9 m^{-2} s^{-1}, corresponding to dose-equivalent rates of up to 100 mSv h^{-1} for neutron energy of 1 MeV.

The shape of the source should be spherical or cylindrical and, in the later case, it is preferable that the diameter and length are approximately the same. The thickness of the encapsulation should be uniform and small compared to the external diameter. The ^{241}Am-Be(α, n) source may be wrapped in a 1-mm-thick lead shield. This reduces the photon dose-equivalent rate to less than 5% of the neutron dose-equivalent rate. The lead shield produces a negligible change (less than 1%) in the neutron dose-equivalent rate. In the absence of the lead shield, the photon dose-equivalent rate (mainly from gamma rays having an energy of 59.5 keV) will depend upon the source construction, and may be comparable with the neutron dose-equivalent rate.

Preferably ^{241}Am-Be(α, n) and/or ^{252}Cf spontaneous fission sources should be used for routine calibration (see ISO 8529-3, 1998) [60]. ^{252}Cf sources generally have high specific source strength and are therefore small. Because of their half-life of 2.65 years, they need occasional replacement. The ^{241}Am-Be-based neutron source shall consist of an americium alloy or a homogeneous, compressed mixture of americium oxide and beryllium or boron as appropriate. Americium alloys may also be used.

4.2 Performance Tests

ISO 21909-I:2021 [61] provides the guidelines on the performance of the passive neutron dosimetry systems. This document provides performance and test requirements for determining the acceptability of neutron dosimetry systems to be used for the measurement of personal dose equivalent, $H_p(10)$, for neutrons (thermal to 20 MeV).

For the performance test of the dosimetry system, it recommends to use the reference radiation fields defined in ISO 8529-1: 2021 [59]. The tests shall be performed for the following neutron energies:

(a) thermal beam as described in ISO 8529-1:2021 [59];
(b) mono-energetic beams at 144; 250; 565 keV; 1.2; 14.8; 19 MeV described in ISO 8529-1:2021 [59];
(c) The moderated ^{252}Cf neutron source described in ISO 8529-1:2021;

(d) ^{241}Am-Be or ^{252}Cf neutron sources.

During the tests, dosimetry systems shall be irradiated on the ISO water slab phantom and under the conditions described in ISO 8529-3:1998 [60] and in ISO 29661:2012 [62].

The performance tests to be conducted for the dosimetry system are (i) coefficient of variation, (ii) linearity of dose, (iii) energy dependence and (iv) angular dependence of the response for the standard ISO-recommended neutron sources such as ^{241}Am-Be or ^{252}Cf, mono-energetic fields at different energies. One well-characterized neutron field (e.g. ^{241}Am-Be or ^{252}Cf) is sufficient to assess changes to the characteristics of a dosimetry system due to internal or external conditions such as fading, influence of photons, etc. Details of the test parameters for Coefficient of variation, linearity, energy and angular response of the dosimeter system are given in ISO 29661:2012 [62].

5 Criticality Accident Dosimetry

5.1 Requirement of Criticality Accident Dosimeter

Criticality accident dosimetry is required [63] in environments where there is a risk that persons may be exposed to a high dose of ionizing radiation from a critical assembly. The lower incidence of criticality accidents has resulted in a reduction of expertise in the area of Criticality Accident Dosimetry (CAD) over the past decades. New technologies and methodologies, and renewed regulatory interest in the area of criticality accidents, have highlighted a need to modernize CAD systems and the techniques used in dose assessment [64]. The incidents at Sarov in 1997 [65] and Tokaimura in 1999 [66] demonstrate that a fatal accident can occur even in a mature nuclear infrastructure with well-defined safety parameters [67]. This part of the chapter discusses the lessons learned from the history of criticality accidents and the philosophy and development of criticality accident dosimetry in different nations including India.

5.2 Criticality Accidents and Critical Systems

Criticality accidents are characterized by a very short, very intense pulse of radiation. The normal range for the yield from a criticality accident is between 10^{15} and 10^{20} fissions, with 10^{17} fissions as a nominal mean value. The initial pulse is generally over within a second, and cannot be anticipated. There are four types of criticality accidents based on four different critical assemblies. They are as follows: Type-A: Material test critical assemblies in air, Type-B: Water solutions of ^{235}U and ^{239}Pu,

Type-C: Water moderated critical test assemblies and reactors, Type-D: Miscellaneous assemblies. Depending on the situation, there is a potential for significant localized contamination, and some possibility of environmental releases of radioactive materials. For personnel in the vicinity of criticality accident, there is no way to avoid the initial exposure from the neutron and gamma. The time duration of radiation from criticality may vary from less than 50 μs to many minutes. The pulse triggers Criticality Accident Area Monitors, which alarm [67] and initiate an immediate evacuation of a facility [68]. The rapid evacuation of personnel reduces the risk of over exposure to ionizing radiation; however, the initial pulse alone generally involves ~ 10^{15}–10^{16} fissions. The ionizing radiation field generated by the assembly in this initial pulse is capable of delivering an absorbed dose in body tissue of tens of Gy before the radiation workers are able to reach a safe distance. An exposed individual will receive dose from neutrons of all energies, from thermal to over 10 MeV and gamma rays up to 7 MeV. Absorbed dose ranges from 100 mGy to 100 Gy and dose rates up to 10^5 Gy/s. A 93.2% enriched sphere of uranium metal can yield a dose of about 24 Gy at 1 m. History has shown that any radiation worker within the immediate vicinity of a criticality accident is likely to be severely over exposed, and fatalities arising from these incidents are not uncommon.

5.3 Criticality Accidents in the World

Table 6 gives the details of criticality accidents occurred worldwide with serious exposure to individuals. In terms of dose received by individual and fatality, accident at Rhode Islands, USA (1964), Mayak, Russia (1958), Kurchatov, Russia and Tokaimura Japan considered to be the most serious accidents.

5.4 The Criticality Accident Dosimetry System

The criticality accident dosimetry system is based on the use of activation foils for neutron fluence measurements coupled with a standard TLD for γ-ray dose determination. Sulphur, gold, copper and indium are used to measure the neutron field through multiple capture and scattering processes. The activation products resulting from these reactions are β and/or γ emitters, with half-lives sufficiently long to enable measurement of their activities following the post-incident recovery of the dosemeters. Sulphur and indium have threshold reactions because under certain energies the cross-section for the reaction with neutrons is negligible. Analysis of these materials allows determination of the fast component of the neutron field. Bare and cadmium covered gold and copper foils are used to estimate the thermal and epithermal components of the neutron field. The activation of indium is analysed using high-resolution γ spectrometry. In contrast, the β emission from the sulphur is counted using plastic scintillator-based beta detectors in large lead shields. The

Table 6 Details of criticality accidents occurred worldwide [69]

Accident	Date	No of persons injured	Estimated average whole body dose to victims	Fatalities
Los Alamos, New Mexico, U.S.A.	August 1945	1	2 Gy neutron and 0.1 Gy gamma	1 (day 24)
Los Alamos, New Mexico, U.S.A.	May 1946	8	21, 3.6, 2.5, 1.6, 1.1, 0.65, 0.47, 0.37 Sv	1 (day 9)
Argonne, Illinois, U.S.A.	June 1952	3	1.59, 1.26, 0.61 Gy	0
Mayak, Russia	March 1953	2	10, 1 Gy	0
Mayak, Russia	April 1957	6	30 Gy and five workers with 3 + Gy	1 (day 12)
Mayak, Russia	January 1958	4	60 Gy for three workers and 6 Gy for fourth	3 (days 5–6)
Oak Ridge, Tennessee, U.S.A.	June 1958	7	3.65, 3.39, 3.27, 2.70, 2.36, 0.69, 0.69 Gy	0
Vinca, Yugoslavia	October 1958	6	4.36, 4.26, 4.19, 4.14, 3.23, 2.07 Gy	1 (day 32)
Los Alamos, New Mexico, U.S.A.	December 1958	3	45, 1.35, 0.5 Gy	1 (35 h)
Idaho, U.S.A	October 1959	2	0.5, 0.3 Sv	0
Siberia, Russia	July 1961	1	2 Gy	0
Hanford, Washington, U.S.A.	April 1962	2	1.1, 0.43 Sv	0
Sarov, Russia	March 1963	2	5.5, 3.7 Gy	0
Rhode Island, U.S.A.	July 1964	3	100, 1, 0.6 Gy	1 (49 h)
Mol, Belgium	December 1965	1	5 Gy	0
Chelyabinsk	April 1968	2	5–10, 20–60 Gy	2
Mayak, Russia	December 1968	2	24.5, 7 Gy	1 (about day 30)
Kurchatov, Moscow, Russia	February 1971	2		0
Kurchatov, Moscow, Russia	May 1971	4	60, 20, 9, 9 Gy	2 (24 h and 2 weeks)
Siberia, Russia	December 1978	1	2.5 Gy and seven other workers with 0.05–0.5 Gy	0

(continued)

Table 6 (continued)

Accident	Date	No of persons injured	Estimated average whole body dose to victims	Fatalities
Constituyentes, Argentina	September 1983	3	23 Gy gamma and 17 Gy neutron and two others with 0.2 Gy gamma and 0.15 Gy neutron	1 (48 h)
Sarov, Russia	June 1997	1	45 Gy neutron and 3.5 Gy gamma	1 (66 h)
Tokaimura, Japan	September 1999	3	17, 8, 1–2 Gy	2 (day 83 and 211)

dose from photons is measured with a standard TLD and reader, which is capable of responding linearly to dose up to 10 Gy and supra-linear corrections can be made beyond this dose. These systems are well maintained and calibrated for use in any unusual criticality event. The dosimetry systems use analytical techniques to derive the neutron fluence based on the integral cross sections of reactions in different materials. The results from all components of the criticality dosimetry system are analysed to determine the dose to individuals based on the derived radiation quality. These criticality accident dosimetry techniques, which differ markedly from those used in the routine radiological protection, are as follows:

(i) Quick sorting of exposed people is required through the measurement of induced activities of Indium foil included in dosemeter or sodium activation in the body.
(ii) Maximum absorbed doses of neutron and gamma in the body have to be evaluated. For neutrons the dose is due to heavy charged particles, protons from $^{14}N(n, p)^{14}C$ reaction and gamma rays from $^{1}H(n, \gamma)^{2}D$ reaction.
(iii) The orientation of the irradiated person with respect to the direction of the source is needed.
(iv) The doses to be measured may vary within a large range from some mGy up to l0 Gy and even more.
(v) The dosimetry system used must be capable of giving separately the neutron and the gamma components of the dose with an uncertainty of < 50% within 48 h and 25% 4 days later.
(vi) Knowledge of the neutron spectrum may be of great help for accurate dose assessment.
(vii) The estimation of the dose has to be achieved even if no personal dosemeter is worn.

In addition, the assessment of the gamma dose may be complicated by the response of gamma dosemeters to neutrons. There are various other methods used for accidental dosimetry. One such neutron dosemeter is a silicon diode, the forward voltage of which is increased if exposed to neutrons due to the displacement of silicon atoms from their lattice sites, which increases electrical resistance across the diode and this device is easily and rapidly processed on a PIN diode reader manufactured for

Table 7 Characteristics of activation foils used in the criticality accident dosimeter

Activation foils	Nuclear reaction	Half-life	Neutron energy interval
Gold	^{197}Au $(n, \gamma)^{198}$ Au	2.7 days	Thermal neutrons (< 0.4 eV)
Copper	^{63}Cu $(n, \gamma)^{64}$Cu	12.7 h	
Indium	^{115}In$(n, \gamma)^{116}$In	54 min	
Gold (Cd)	^{197}Au $(n, \gamma)^{198}$ Au	2.7 days	Intermediate neutrons (0.4 eV – 100 keV)
Copper (Cd)	^{63}Cu $(n, \gamma)^{64}$Cu	12.7 h	
Indium (Cd)	^{115}In$(n, \gamma)^{116}$In	54 min	
Indium	^{115}In$(n, n')^{115m}$In	4.5 h	Fast neutrons > 1.2 MeV
Iron	^{54}Fe$(n, p)^{54}$Mn	312.13 days	Fast neutrons > 2.2 MeV
Sulphur	^{32}S$(n, p)^{32}$P	14.3 days	Fast neutrons > 2.9 MeV
Nickel	^{58}Ni$(n, p)^{58m}$Co	71 days	Fast neutrons > 3.8 MeV
Magnesium	^{24} Mg$(n, p)^{24}$Na	15 h	Fast neutrons > 7 MeV
Aluminium	^{27}Al$(n, \alpha)^{24}$Na	15 h	Fast neutrons > 8 MeV
Copper	^{63}Cu$(n, 2n)^{62}$Cu	9.78 min	Fast neutrons > 12 MeV

the assessment of the fast neutron dose. However there are no suppliers for new diodes since the commercial requirement has become too limited to support a manufacturing line. The results from a criticality dosemeter can also be compared with biological assessments of dose, such as body sodium activation, activation of body hair and clothing. In the absence dosemeter on the body of radiation worker, the body sodium activation through ^{23}Na$(n,\gamma)^{24}$Na reaction may give a rough estimation of the dose received by individuals even if the relationship between the measured specific activity of ^{24}Na and the neutron dose vary with the shape of the neutron spectrum. The commonly used activation foils in a criticality accident dosimeter, their decay mode, half-life and type of radiation emitted are given in Table 7.

5.5 Criticality Accident Dosimetry Systems Used in Various Countries

Table 8 gives the details of the activation foils used in criticality accident dosimetry system used in several countries including India. The criticality accident dosimeter of Pacific North West National Laboratory, PNAD, is shown in Fig. 9 and associated components are given in Table 9 [70].

Table 8 Details of activation foils used in criticality accident dosimeter in different countries including India

Country	Activation foils in criticality accident dosimeter
U.K.	Au, Au(Cd), Cu, Cu(Cd), In, S, TLD($CaSO_4$:Dy) (gamma)
Canada	In, S, Rh and fission track detectors
Germany	Cu, Sn, Rh, Al, S, and Au
Yugoslavia	In, In(Cd), Cu, S and Mg
Japan	In, S, Al, Mg and Fe
Japan Atomic Energy Research Institute (JAERI)	Thorium doped fission-track detector (neutron), glass dosimeter (gamma)
Poland	Threshold detectors, film badge (gamma)
European Nuclear Energy Agency (ENEA)	Au, Au(cd), Cu(cd), S, In
Pacific Northwest National Laboratory, USA	In(cd), In, Cu, Cu(cd), S
India	Au, Au(cd), Cu(cd), In, In (Cd), Rh, S, Ni, Mg, Al, TLD 600 and TLD 700

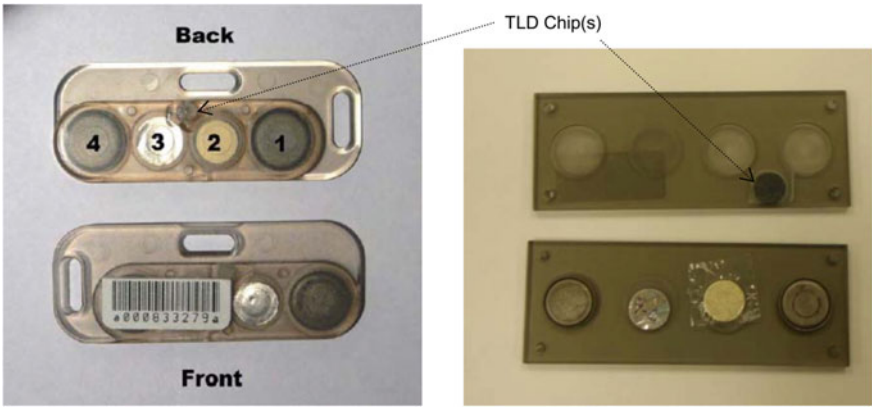

Fig. 9 Photograph of Hanford PNAD criticality dosimeter with different components [70]

Table 9 Materials and approximate dimension of PNAD components [70]

Position in PNAD	Description	Diameter (cm)	Thickness (cm)
1	Indium (Cd covered)	1.27	0.0127
2	Sulphur pellet	1.27	0.292
3	Indium (bare)	1.14	0.0127
4	Copper (Cd covered)	1.27	0.0127
5	TLD 700 chip	0.32 × 0.32	0.089

5.6 The Criticality Accident Dosimeter (CAD) Badge in India

A criticality accident dosimetry (CAD) badge designed and developed by Bhabha Atomic Research Centre (BARC) consists of activation foils such as gold, copper, indium, iron, sulphur, nickel, magnesium and aluminium for neutron dose estimation and ^{7}LiF:Mg:Ti (TLD-700), ^{6}LiF:Mg:Ti (TLD-600) discs for gamma-neutron dose measurements [71]. Bare and Cd covered gold, copper and indium foils are used for thermal, epithermal and intermediate energy neutrons [72]. Indium is used as exposure indicator and along with iron, sulphur, nickel, magnesium and aluminium are used for fast neutron spectrum and dose measurements. The foils are permanently sealed in a plastic badge holder of dimensions 8 cm x 5 cm × 0.8 cm. Each dosimeter badge has an identification number printed on it. The CAD badge is being used at various nuclear facilities of DAE and an annual service for the badges has been provided for replacement with fresh badges for neutron-gamma dose evaluation.

5.7 Details of the Processing of CAD Badge

During the unusual event of a criticality accident involving fissile materials such as $_{92}U^{235}$, $_{94}Pu^{239}$, the foil detectors in the CAD badge, viz.: ^{197}Au, ^{63}Cu, ^{115}In, ^{54}Fe, ^{32}S, ^{58}Ni, ^{24} Mg, ^{27}Al will get activated by fission neutrons and undergo the various nuclear reactions: ^{197}Au$(n,\ \gamma)^{198}$Au, ^{63}Cu$(n,\ \gamma)^{64}$Cu, ^{63}Cu$(n,\ 2n)^{62}$Cu, ^{115}In$(n,\ \gamma)^{116m}$In, ^{115}In$(n, n')^{115m}$In, ^{103}Rh$(n, n'\gamma)^{103m}$Rh, ^{54}Fe$(n, p)^{54}$Mn, ^{32}S$(n, p)^{32}$P, ^{58}Ni$(n, p)^{58m}$Co, ^{24} Mg$(n, p)^{24}$Na and ^{27}Al$(n, \alpha)^{24}$Na. All the product nuclides are radioactive and emit beta-gamma radiations with their characteristic half-lives. The activities of ^{198}Au, ^{64}Cu, ^{62}Cu, ^{116m}In, ^{115m}In, and ^{54}Mn are measured using HPGe gamma ray spectrometer. The ^{198}Au activity is measured by counting 0.412 MeV gamma rays. The ^{64}Cu activity is measured by counting 0.511 MeV annihilation radiations. Activity of ^{116m}In produced due to thermal neutron is measured by counting 0.417 MeV gamma ray and fast neutron induced activity of ^{115m}In is measured by counting 0.336 MeV gamma rays. The ^{54}Mn activity is measured by counting 0.835 MeV gamma rays. For gamma activity measurement, the area under the photo-peak of the respective gamma lines (after subtraction of the background) gives the net counts per second (CPS). Activity is calculated using the corresponding efficiency of the detector with respect to the photo-peak energy. The ^{32}P beta activity induced in sulphur is counted using a beta counting system with plastic scintillator as a beta detector. Gamma spectrometer is calibrated using standard beta-gamma sources such as ^{137}Cs, ^{60}Co, ^{152}Eu, ^{22}Na, ^{133}Ba, whereas beta counting system is calibrated with a ^{32}P beta source.

After irradiating the CAD badges in the neutron field, the foil detectors are counted in the counting set up. The measured count rate is related to the neutron fluence by the equation

$$A_i = N_i \varepsilon_1 \varepsilon_2 \varepsilon_3 \left[(1 - e^{-\lambda t}) e^{-\lambda T} f_s f_d \int \sigma_i(E) \phi(E) \mathrm{d}E \right] \quad (2)$$

where A_i is the count rate of ith detector in the counting set up, N_i is the number of the atoms, ε_1 is the isotopic abundance, ε_2 is the abundance of the radiation counted, ε_3 is the efficiency, f_s is the self-shielding factor for the foil, f_d is the flux depression factor of the foil for that medium, $\sigma_i(E)$ is the activation cross section at the energy E, $\phi(E)$ is the neutron fluence rate of energy E, t is the irradiation time, T is the decay time. The data obtained from the activation detectors are interpreted in terms of a spectral model which assumes thermal neutrons up to 0.4 eV, a slowing down spectrum in the intermediate range from 0.4 eV to 1 MeV and a Maxwellian fission spectrum from 100 keV to 10 MeV. The neutron dose can be derived using appropriate fluence to dose conversion factors.

6 Conclusion

Neutron monitoring of radiation workers is an integral part of the radiation protection programme. Working principles of some active detectors such as neutron electronic pocket dosimeters, bubble detectors are discussed in the chapter. Further, passive dosimeters such as CR-39 based SSNTD, TLD 600/TLD 700 pair and FNTD are also discussed. Neutron personal dosimeter used in India, it's processing technique and dose evaluation procedures are elaborated in the chapter. The calibration procedures of the detectors as per the guidelines of international standards has been discussed briefly. In the later part of the chapter, working principle of criticality dosimeters used in fuel reprocessing facilities during commissioning of the nuclear reactor accelerator in different countries including that used in India is discussed.

References

1. Ilić R, Durrani Saeed A (2003) Handbook of radioactivity analysis, solid state nuclear track detectors. In: L'Annunziata MF (ed). Academic Press, 179–237
2. Dorshel B, Schuricht V, Stener J (1996) The physics of radiation protection. Nucl. Techn. Publ, Ashford, p 309
3. Rupali P, Deepa S, Kumar V, Babu Rajesh Jayalakshmi, Bakshi AK, Chougaonkar MP, Kar S, Mayya YS, Joshi VM (2011) Present status of fast neutron personnel dosimetry system based on CR-39 solid state nuclear track detectors; BARC Report, BARC Report No. BARC/2011/E/015
4. Höfert M, Piesch E (1985) Neutron dosimetry with nuclear emulsions. Radiat Prot Dosim 10(1–4):189–195
5. Bartlett DT, Bird TV, Miles JCH (1980) The NRPB nuclear emulsion dosemeter, NRPB Report No. 99
6. Massand OP, Singh D, Kundu HK, Marathe PK (1979) Energy dependence of Kodak NTA neutron personnel monitoring film. Int J Appl Radiat Isot 30(4):249

7. Dhairyawan MP, Marathe PK, Massand OP (2003) Use of CR-39 solid state nuclear track detectors in neutron personnel monitoring. Radiat Meas 36(1–6):435–438
8. Massand OP, Singh D (1982) Computed response of Kodak NTA dosimeter for moderated neutron spectra. Health Phys 42(2):226–230
9. Young DA (1958) Etching of radiation damage in lithium fluoride. Nature 182:365–367
10. Fleischer RL, Buford Price P, Walker Robert M (1975) Nuclear tracks in solids. University of California Press, Berkley
11. Azimi-garakani D, Tommasino L, Torri G (1988) Further investigation on electrochemically etched CR-39 neutron detectors. Nuclear Tracks Radiat Meas 15(1–4):309–312
12. Tommasino L, Zapparoli G, Griffith RV (1981) Electrochemical etching mechanisms. Nucl Tracks 4:191–196
13. Hankins DE, Westermark J (1987) Preliminary study on the use of track size distribution on electrochemically etched CR-39 foils to infer neutron spectra. Radiat Prot Dosim 20:109–112
14. Griffith RV, Thorn Gate JH, Davidson KJ, Rueppel DW, Fisher JC (1981) Mono energetic neutron response of selected etched plastics for personnel neutron dosimetry. Radiat Prot Dosim 1(1):61–71
15. Tommasino L, Harrison KG (1985) Damage track detectors for neutron dosimetry: I. Registration and counting methods. Radiat Prot Dosim 10(1–4):207–217
16. Massand OP, Kundu HK, Marathe PK, Supe SJ (1990) Development of neutron personnel monitoring system based on CR-39 solid state nuclear track detector. BARC Report No. 1528
17. Tanner RJ, Bartlett DT, Hager LG (2005) Operational and dosimetric characteristics of etched–track neutron detectors in routine neutron radiation protection dosimetry. Radait Meas 40:549–559
18. Tommmasino L (1980) Solid di-electric detectors with breakdown phenomena and their applications in radioprotection. Nuclear Instrum Methods 173:73–83
19. Zapparoli G, Tommasino L, Djeffal S, Maiorana A (1986) Additional results with electrochemically etched CR-39 neutron dosemeters. Nucl Tracks 12(1–6):675–678
20. Sathian D, Rupali R, Jayalakshmi V, Sarala N, Marathe PK, Kolekar RV, Chourasiya G, Kannan S (2009) Use of chemical etching of CR-39 foils at elevated temperature for fast neutron personnel monitoring in India. Ind J Phys 83(6):863–869
21. Rupali P, Jayalakshmi V, Deepa S, Chaurasiya G (2009) Dosimetric systems and characteristics of CR-39 for use in individual neutron monitoring. IEEE Trans Nucl Sci 56(6), Part: 2:3774–3778
22. Pal RR, Jayalakshmi V, Sathian D, Chaurasiya G, Mayya YS, Kumar V, Babu R, Joshi DG, Chadda VK (2008) Influence of automated image analysis system on the dosimetric characteristics of CR-39. J Radiat Protect Environ 31(1–4):362–364
23. Mckinlay AF (1981) Thermoluminescence dosimetry. Med. Phys. Handbooks, 5. Adam Hilger Ltd., Bristol
24. Oberhofer M, Scharmann A (eds) (1981) Applied thermoluminescence dosimetry. Adam Hilger Ltd., Bristo
25. Ayyangar K, Lakshmanan AR, Chandra B, Ramadas K (1974) A comparison of thermal neutron and gamma ray sensitivities of common TLD phosphors. Phys Med Biol 19:665–676
26. Marshall M, Douglas JA, Budd T, Churchill WL (1977) A two temperature readout of thermoluminescent LiF, its properties and its uses for personnel dosimetry. Proc Conf Int Radiat Prot Assoc 4:1257–1260
27. Johnson TL, Luersen RB (1980) Fading of un-annealed LiF (TLD-600) for thermal neutrons and gamma rays. Health Phys 38:853–856
28. Nash AE, Johnson TL (1977) LiF (TLD-600) thermoluminescence detectors for mixed thermal neutron and gamma dosimetry, luminescence dosimetry. In: Proceedings of 5th international conference. Sao Paulo, Brazil, 14–17 Feb 1977, 393–403
29. Piesch E (1982) Albedo neutron dosimetry. Int J Appl Radiat Isot 33:1061–1076
30. Hankins DE (1975) The effect of energy dependence on the evaluation of albedo neutron dosimeters. In: Proceedings of 9th mid-year topical symposium. Health Physics Society, Denver, CO

31. Hoy JE (1972) Personnel albedo neutron dosimeter with thermoluminescent ^{6}LiF and ^{7}LiF, Savannah River Lab., DuPont de Nemours (E.I.) and Co., Aiken, SC, Rep. DP-1277
32. Piesch E, Burgkhardt B (1984) A universal beta/gamma/neutron albedo dosemeter for personnel monitoring. Radiat Prot Dosim 6:281
33. Bakshi AK, Pradhan AS, Kher RK, Srivastava K, Varadharajan G, Chatterjee S, Sathian V (2009) Study on the response of indigenously developed $CaSO_4$:Dy phosphor-based neutron dosemeter. Radiat Prot Dosim 133(2):73–80
34. Chiyoda Techno Glass Corporation (2008) User's manual for reading module FGD-660 (ref: AS-04-21-0010-R0)
35. Croft S, Weaver D (1986) The application of radiophotoluminescent glass to gamma dosimetry in mixed n-g fields. Radiat Prot Dosim 17:67–70
36. Becker K (1965) Nuclear track registration in dosimeter glasses for neutron dosimetry in mixed radiation fields. U.S. Naval Radiological Defence Laboratory, San Francisco, Rep. USNRDL-TR-904
37. Piesch E, Burgkhardt B, Hofmann I (1979) Calibration of neutron detectors in radiation protection, a report on the Karlsruhe results of the European Neutron Dosimetry Intercomparison Program 1977/78, Report No. KFK-2847
38. EURATOM (1977) Technical recommendations for the use of radiophoto-luminescence dosimetry for individual monitoring. Commission of the European Communities, Luxembourg, Rep. EUR-5655
39. Piesch E (1972) Developments in radiophotoluminescence dosimetry. Topics in radiation dosimetry. In: Attix FH (ed), 461
40. Nourreddine A, Salem YO, Nachab A, Roy C (2015) Study of a new neutron dosimeter incorporating RPL detectors. Radiat Meas 83:47–50
41. Ing H, Birnboim HC (1984) A bubble-damage polymer detector for neutrons. Nucl Tracks 8(1–4):285
42. Apfel RE, Roy SC (1985) Superheated drop detector: a possible alternative for neutron dosimetry. Neutron Dosimetry Radiat Prot Spec Issue Radiat Prot Dosim 10(1–4):327
43. Ing H, Noulty RA, Mclean TD (1997) Bubble detectors—a maturing technology. Radait Meas 27(1):1–11
44. Lewis BJ, Smith MB, Ing H, Andrews HR, Machrafi R, Tomi L, Matthews TJ, Veloce L, Shurshakov V, Tchernykh I, Khoshooniy N (2012) Review of bubble detector response characteristics and results from space. Radiat Prot Dosim 150(1):1–2
45. Vaijapurkar S, Paturkar R (1995) Superheated liquid neutron sensor based on polymer matrix. Radiat Meas 24:309–313
46. Ponraju D, Subramanian CV, Ramesh AS, Sebastian L, Viswanathan S (1999) Ultrasonic bubble counting technique for neutron dose measurements in bubble damage detectors. Radait Meas 30:471–475
47. Akselrod GM, Akselrod MS, Benton ER, Yasuda N (2006) A novel Al_2O_3 fluorescent nuclear track detector for heavy charged particles and neutrons. Nucl Instr Meth B 247:296–306
48. Akselrod MS, Yoder RC, Akselrod GM (2006) Confocal fluorescent imaging of tracks from heavy charged particles utilizing new Al_2O_3:C, Mg crystals. Radiat Prot Dosim 119(1–4):357–362
49. Akselrod MS, Sykora GJ (2011) Fluorescent nuclear track detector technology—a new way to do passive solid state dosimetry. Radiat Meas 46:1671–1679
50. Klimpki G, Mescher H, Akselrod MS, Jäkel O, Greilich S (2016) Fluence-based dosimetry of proton and heavier ion beams using single track detectors. Phys Med Biol 61:1021–1040
51. Sykora GJ, Akselrod MS, Salasky M, Marino SA (2007) Al_2O_3:C, Mg fluorescence nuclear track detectors for passive neutron dosimetry. Radiat Prot Dosim 126:278–283
52. Sykora GJ, Salasky M, Akselrod MS (2008) Properties of novel fluorescent nuclear track detectors for use in passive neutron dosimetry. Radait Meas 43:1017–1023
53. Sykora GJ, Akselrod MS, Vanhavere F (2009) Performance of fluorescence nuclear track detectors in monoenergetic and broad spectrum neutron fields. Radait Meas 44:988–991

54. Aoyama T, Oka Y, Honda K, Mori C (1992) A neutron detector using silicon PIN photodiodes for personal neutron dosimetry. Nucl Instrum Methods Phys Res A314:590–594
55. Rupali P, Singh A, Topkar A, Bakshi AK, Chougaonkar MP, Babu DAR (2013) Development and dosimetric studies of neutron pocket dosimeter in the energy range from thermal to fast. In: Proceedings of the national symposium on nuclear instrumentation, 1–4
56. Barelau DB, Paul D, Dubarr YB, Makovicka L, Decossas JL, Vareille JC (1992) Principles of an electronic neutron dosemeter using a PIPS detector. Radiat Prot Dosim 44:363–366
57. Barthe J, Bord YJM, Mourgues M, Lahay ET, Boutruche B, Segur P (1994) New devices for individual neutron dosimetry. Int Works Ind Monit Villigen Radiat Prot Dosim 54:365–368
58. Alberts WG, Dietz E, Guldbakke S, Kluge H (1994) Response of an electronic personal neutron dosemeter. Radiat Prot Dosim 57:207–210
59. International Organization for Standardization (ISO) (2021) Reference neutron radiations—part 1: characteristics and methods of production. ISO 8529-1
60. International Organization for Standardization (ISO) (1998) Reference neutron radiations -Part 3: calibration of area and personal dosimeters and determination of their response as a function of neutron energy and angle of incidence. ISO 8529-3
61. International Organization for Standardization (ISO) (2021) Passive neutron dosimetry systems—part 1: performance and test requirements for personal dosimetry. ISO 21909-I
62. International Organization for Standardization (ISO) (2012) Reference radiation fields for radiation protection—definitions and fundamental concepts. ISO 29661
63. https://www.legislation.gov.uk/uksi/1999/3232/made/data.pdf. Accessed on 30 Nov 2023
64. Asselineau B, Trompier F, Texier C, Itié C, Médioni R, Tikunov D, Muller H, Pelcot G (2004) Reference dosimetry measurements for the international intercomparison of criticality accident dosimetry. Radiat Prot Dosim 110(l–4):459–464
65. International Atomic Energy Agency (2001) The criticality accident in Sarov–Vienna. Publication STI/PUB/1106
66. Endo A (2010) Dose assessment in the criticality accident in Tokai-mura. Radiat Meas 45:1484–1489
67. International Electrotechnical Commission (IEC) (2014) Radiation protection instrumentation—warning equipment for criticality accidents, 60860
68. American National Standard Institute (ANSI) (2017) Report No. ANSI/ANS-8.3-1997; R2003; R2012; R2017: "criticality accident alarm system"
69. https://en.wikipedia.org/wiki/Criticality_accident. Accessed on 30 Nov 2023
70. Hill RL, Conrady MM (2010) PNNL results from 2009 silene criticality accident dosimeter intercomparison exercise, PNNL-19503
71. Bricka M, Médioni R (l982) Measurement of neutron and gamma radiation. IAEA Technical Reports Series No. 2ll. STI/DOC/l0/2ll. IAEA, Vienna, 57–82
72. Adams N, Dennis JA (1963) A new method of using gold foils for the investigation of the leakage spectra from critical assemblies. IAEA, Vienna

Radiation Environment in Nuclear Fuel Cycle Facilities

V Ramprasath, K Kannan, J P N Pandey, and G Ganesh

1 Introduction

The demand for energy worldwide is rising swiftly, prompting many countries to consider nuclear energy as a viable alternative to meet this demand sustainably. There's also a pressing global imperative to adopt non-fossil fuel sources to curb carbon dioxide emissions. As a way to resolve these demands, generating electricity via nuclear reactors offers a sustainable, environmentally friendly energy solution. However, the long-term operation of nuclear reactors presents two fuel cycle choices: either a one-time use cycle with spent fuel disposal or a closed cycle involving reprocessing and recycling of fissile materials. Both options necessitate effective and secure waste management strategies.

Nuclear fuel cycle facilities discussed in this chapter are as follows: uranium mining, uranium based fuel fabrication, spent fuel reprocessing, fabrication of mixed oxide (MOX) fuel (using plutonium and uranium) and management of liquid and solid wastes arising from reprocessing and fuel fabrication operations. Nuclear Fuel Cycle facilities have several engineering safety features such as shielding, ventilation, containment and remote operation. These features aim at reducing exposure to plant personnel and keeping the release of radioactive materials to environment below the limits stipulated by the regulatory authorities. Radiological surveillance and monitoring in nuclear facilities are carried out by professionally trained operational health physicists to ensure radiation protection for workers and the environment from potential radiation hazards and to comply with regulatory safety aspects and limits. All nuclear facilities are designed and operated to ensure minimal exposure

V. Ramprasath (✉) · K. Kannan · J. P. N. Pandey · G. Ganesh
Health Physics Division, Bhabha Atomic Research Centre, Mumbai 400085, India
e-mail: vrprasad@igcar.gov.in

D. K. Aswal (ed.), *Handbook on Radiation Environment, Volume 2*,
https://doi.org/10.1007/978-981-97-2799-5_8

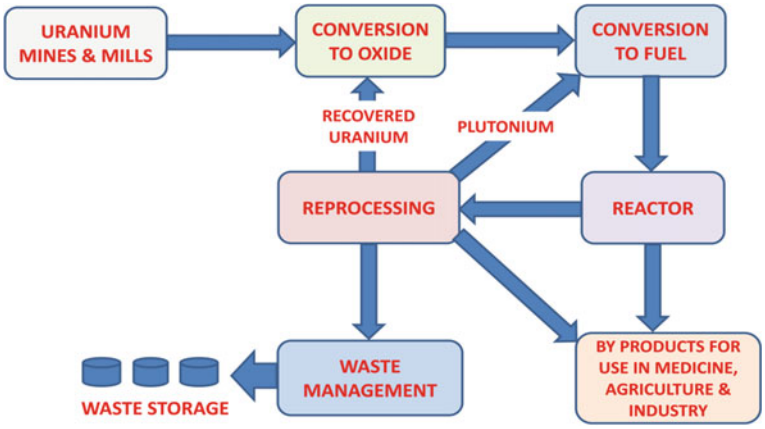

Fig. 1 Block diagram of closed nuclear fuel cycle

to workers, the environment, and the public, both in routine operations and in the event of accidents.

2 Nuclear Fuel Cycle

The nuclear fuel cycle is a process involving various steps to produce nuclear materials for useful extraction of electricity from uranium and other fissile materials in nuclear reactors. It also involves management of wastes generated during process operations in the facilities. Nuclear fuel cycle involves uranium mining and milling operations, nuclear fuel fabrication, spent fuel reprocessing and nuclear waste management. The fuel cycle starts with mining of uranium and ends with the disposal/management of nuclear waste. Figure 1 depicts the various activities covered in Nuclear Fuel Cycle.

3 Uranium Mining and Milling

Uranium mining involves three main processes: extracting ore, milling it to extract uranium, and managing resulting uranium compounds and tailings. The mechanized cut-and-fill method is now widely used for efficient ore recovery, with automated loading and transportation to eliminate direct handling. Mining operations are fully automated using large trackless equipment like drill jumbos and scissor lifts, which eliminates the direct ore handling. Uranium is typically extracted through hydrometallurgical route by acid leaching or alkali leaching, depending on the ore characteristics, followed by crushing and wet grinding. The ground ore is then thickened

and leached in controlled conditions before undergoing filtration and ion exchange to absorb uranyl ions in the ion exchange resin. Further treatment with magnesia yields Magnesium di-uranate (MDU) or yellow Cake. The coarse fraction is sent to the mine for backfilling and the fine portion is neutralised to precipitate the dissolved activities and is then discharged into a tailings pond. The bulk of solids are retained in the tailings pond. Almost the entire mass of ore mined comes out as waste after recovery of the small amounts of uranium. The Yellow Cake is dried and packed for processing into nuclear-grade uranium fuel. This comprehensive process ensures efficient extraction and processing while minimizing human involvement in ore handling.

3.1 Radiation Hazards During Uranium Mining and Milling Operations

Uranium-238 (^{238}U) occurs in ores (typically as Pitchblende). Natural uranium is made up of 99.28% of ^{238}U, 0.7% of ^{235}U and 0.005% of ^{234}U. Contribution from the members of the ^{235}U decay chain to radiation hazards is usually negligible in low grade uranium mines. The beta and gamma radiations emitted by the daughter elements of ^{238}U present in the ore constitute the external radiation hazards.

As the miners work in tunnel-like structures, they are always surrounded by the ore body and are thus continuously exposed to external radiation. In this situation, the exposure is truly whole body irradiation. The internal radiation hazard to miners is mainly due to inhalation of airborne radioactivity. Due to radiological decay chain of uranium, the concentration of radon (^{222}Rn) in the air of the mines will be relatively high. ^{222}Rn and its short-lived daughters ^{218}Po, ^{214}Pb, ^{214}Bi, ^{214}Po, ^{210}Pb are the principle sources of internal exposure. Being a noble gas, radon is highly mobile. It enters the mine atmosphere by emanation from the ore body. The radon exhalation rate in underground uranium mines is influenced by various factors such as ore grade, porosity, surface area, barometric pressure, and temperature. The ground water flowing through mineralized rock strata and seeping into the mine galleries is yet another source of radon. Owing to its comparatively short half-life, radon builds up rapidly in poorly ventilated working areas in mines. Even in ventilated areas, radon is often found in appreciable concentrations.

The daughter products of ^{222}Rn cling to the dust produced during mining tasks like drilling, blasting, and hauling, exposing workers to potentially radioactive particles they may inhale and deposit in their respiratory systems. Due to the substantial volume (of the order of tons) of ore processed to obtain uranium, the mining process yields significant amounts of tailings and chemical wastes containing nitrates, sulfates, nickel, and arsenic. These wastes not only retain traces of uranium but also harbor its radioactive derivatives, notably ^{226}Ra, posing a major concern. Uranium ore typically contains various radioisotopes from its decay series, which can become

significant throughout mining operations. Miners are equipped with passive dosimeters to monitor individual exposure to alpha and gamma radiation, alongside modern protective gear like respirators, ear-muffs, gumboots, safety helmets, and safety goggles to mitigate risks. Engineering controls are implemented to reduce noise levels from heavy machinery underground, with regular monitoring of noise, air quality, radiation levels, and surface contamination conducted using advanced instruments to ensure compliance with conventional and radiological safety standards. Ventilation systems in underground uranium mines are specially designed to address radon emissions, providing ample fresh air intake. As mines deepen, maintaining strata stability becomes a critical concern, leading to the implementation of safety parameters in mine design. Excavated ore voids are systematically filled with mill tailings to manage the mine's structural integrity. During refining and conversion, it's crucial to control dust and ensure good ventilation to reduce the risk of inhaling uranium. Controlling contamination is also essential to prevent uranium intake through ingestion, as it can harm the kidneys. Additionally, efforts should be made to limit the release of uranium into the environment from ventilation systems.

To mitigate radon levels in mines, several measures can be implemented:

(a) Reduction of dust concentrations in the air, such as through the use of water sprays.
(b) Installation of efficient, high-capacity ventilation systems to effectively purge radon.
(c) Closure and blocking off of side tunnels that are no longer in use.
(d) Application of materials on walls and surfaces within the mines to decrease radon diffusion.

Furthermore, tailings resulting from ore processing are typically contained in engineered ponds to prevent the dispersion of radium and other isotopes into groundwater, lakes, streams, and rivers. The yellowcake, while having low radioactivity initially as it no longer contains radioactive decay products, may see an increase in radioactivity due to the growth of ^{234}Th and ^{234}Pa daughters, with half-lives of 24 days and 1.1 minute respectively. This may lead to some external exposure in later processing due to associated beta and gamma radiations.

4 Uranium Based Fuel Fabrication

In uranium fuel fabrication facility, the raw Magnesium di Uranate (MDU) obtained from mining and milling is dissolved in nitric acid, which is further purified by solvent extraction method. When Uranyl nitrate solution is treated with mixture of kerosene (n-Dodecane) and TBP (Tri Butyl Phosphate), uranium gets loaded into organic medium. It is then stripped and transferred to aqueous phase. Purified uranium solution is treated with ammonia to get Ammonium di-Uranate (ADU). ADU is then

calcined (i.e., heated) and reduced in cracked ammonia atmosphere. It is further stabilized in controlled conditions to produce stable UO_2 powder. UO_2 powder is pre-compacted in roll compaction press. The pre-compacted powder is mixed with zinc stearate as a lubricating medium and then compacted into green pellets. These green pellets are sintered in cracked ammonia atmosphere in sintering furnace. After the centerless grinding of sintered pellets to get uniform diameter, they are filled in zircoloy (Zirconium alloy) tubes which form the fuel for the nuclear reactor.

4.1 Radiation Environment in Uranium Fuel Fabrication Facility

In uranium handling facilities, uranium and its immediate daughter products are the main sources of radiation exposures. Naturally occurring uranium consists of a mixture of ^{238}U, ^{235}U and ^{234}U isotopes with an isotopic abundance of 99.285%, 0.72% and 0.005% respectively. All these uranium isotopes are long-lived alpha emitters with alpha energy ranges from 4.15 to 4.8 MeV. Beta and gamma activities due to build-up of the daughter products ^{234}Th, ^{234}Pa, and ^{231}Th are also invariably present along with uranium isotopes. List of uranium series isotopes and their immediate daughter products with their alpha, beta, and gamma emission details are given in Table 1 [1].

4.2 Radiological Hazards in Uranium Handling

The potential hazards met during production of $U0_2$ are as follows: (i) chemical and radiotoxicity of uranium, (ii) criticality hazards from enriched uranium, (iii) chemical toxicity of various chemicals used in the process. ^{238}U being an alpha emitter, freshly prepared uranium will not cause any external radiation hazard. Though the criticality hazard is low at the enrichments used for thermal power reactor fuels, safety considerations look for built-in control based on safe geometry and inventory. As the uranium is getting aged, build-up of beta-gamma emitting daughter products is the source of external exposure. There exists a secular equilibrium between the parent uranium and daughters and hence the beta activity will be either equal to or less than alpha activity. But in some special operational situations, external exposure will be significant due to the selective accumulation of these beta gamma emitting daughters. However, this excess activity will be decayed with the half-life of the longest-lived daughter. Uranium isotopes are more hazardous once they are deposited internally as they emit alpha particles. The control of in-plant hazards arising out of inhalation/ingestion is the chief consideration for the adoption of safety measures it the design of fuel fabrication facility.

Table 1 Radioactive properties of uranium series isotopes

Isotope	Half-life	Alpha energy (MeV)	Beta (maximum energy) (MeV)	Gamma energy (keV)
^{238}U				
^{238}U	4.47×10^9 years	4.15 (22.3%) 4.20 (77.5%)		49.55 (0.0697%) 113.5 (0.0174%)
^{234}Th	24.10 days		0.08 (1.6%) 0.10 (6.5%) 0.11 (14.1%) 0.20 (77.8%)	63.30 (3.8%) 92.38 (2.18%) 92.80 (2.15%)
^{234m}Pa	1.159 minutes		1.22 (1.0%) 2.27 (97.6%)	258.23 (0.074%) 742.81 (0.094%) 766.36 (0.323%) 1001.03 (0.847%)
^{234}U	2.455×10^5 years	4.72 (28.4%) 4.78 (71.4%)		
^{235}U				
^{235}U	7.04×10^8 years	4.21 (5.95%) 4.32 (3.3%) 4.37 (18.8%) 4.40 (57.2%) 4.41 (3.0%) 4.50 (1.3%) 4.56 (3.8%) 4.60 (4.74%)		109.2 (1.66%) 143.77 (10.94%) 163.36 (5.08%) 185.72 (57.0%) 202.12 (1.08%) 205.32 (5.02%)
^{231}Th	25.52 hours		0.14 (2.7%) 0.21 (12.2%) 0.289 (13%) 0.290 (41%) 0.31 (29%)	25.6 (13.9%) 84.2 (6.7%)
^{231}Pa	3.27×10^4 years	4.74 (8.4%) 4.94 (2.9%) 4.95 (22.5%) 5.01 (25.3%) 5.031 (20%) 5.034 (2.8%) 5.06 (11.7%)		27.4 (10.8%) 283.69 (1.7%) 300.06 (2.4%) 302.67 (2.3%) 330.04 (1.4%)
^{232}U				
^{232}U	70.6 years	5.14 (0.325%) 5.26 (30.6%) 5.32 (69.1%)		
^{228}Th	1.9 years	5.34 (26.0%) 5.42 (73.4%)		84.4 (1.19%)
^{224}Ra	3.6 days	5.45 (5.25%) 5.69 (94.7%)		240.99 (4.1%)
^{220}Rn	55.8 sec	6.29 (99.9%)		

(continued)

Table 1 (continued)

Isotope	Half-life	Alpha energy (MeV)	Beta (maximum energy) (MeV)	Gamma energy (keV)
^{216}Po	148 msec	6.79 (100%)		
^{212}Pb	10.64 hours		0.16 (5.0%) 0.33 (81.7%) 0.57 (13.3%)	238.63 (43.6%) 300.09 (3.18%)
^{212}Bi	60.54 minutes	6.05 (25.1%) 6.09 (9.7%)	0.63 (1.9%) 0.74 (1.4%) 1.52 (4.5%) 2.25 (55.3%)	39.86 (1.1%) 727.33 (6.65%) 785.37 (1.11%) 1620.74 (1.51%)
^{208}Tl	3.058 minutes		1.04 (3.2%) 1.29 (24.1%) 1.52 (22.1%) 1.80 (49.2%)	277.37 (6.6%) 510.7 (22.5%) 583.19 (85.0%) 763.45 (1.8%) 860.53 (12.4%) 2614.51 (99.8%)
^{208}Pb	Stable			

4.2.1 External Exposure Hazards

As freshly separated uranium does not contain daughter products and since uranium is an alpha emitter, freshly prepared uranium will not cause any external radiation hazard. However, beta and gamma activity builds up with time due to ^{234}Th ($T_{1/2}$ 24.1 days) and ^{234} Pa ($T_{1/2}$ 1.18 min) from ^{238}U and ^{231}Th ($T_{1/2}$ 25.1 hours) from ^{235}U. As the daughter products build up, external radiation hazard increases with time till equilibrium is established. ^{238}U daughter products, ^{234}Th and ^{234m}Pa having beta energy 0.2 MeV and 2.29 MeV respectively, contribute to beta dose of workers handling uranium compounds in open form. 1.001 MeV gamma from ^{234m}Pa is a significant contributor to external gamma dose. Interaction of alpha particles from uranium with nuclei of low-Z atoms generates neutrons. The magnitude of neutron flux depends on the activity of uranium which is a function of enrichment. Spontaneous fission of ^{238}U, (α, n) reaction between alpha particle from uranium isotopes and ^{19}F nuclei are the sources of neutron exposure.

Uranium recovered from spent fuel (Depleted Uranium-DU) requires additional considerations. The utilization of uranium fuel in reactors results in the formation of fission products, isotopes of transuranic elements neptunium and plutonium, and artificial isotopes of uranium ^{232}U, ^{233}U, and ^{236}U. The main contributor to the external dose from DU is ^{208}Tl (daughter product of ^{232}U) which emits 2.61 MeV gamma ray. Bremsstrahlung radiation produced by deceleration of beta particles in surrounding uranium material and container walls can also contribute to external exposure.

4.2.2 Internal Exposure Hazards

Chemical toxicity as well as radiological toxicity of uranium is considered while establishing control limits. Based on enrichment, mode of entry, solubility/transportability of the material, it can be determined whether the chemical or radiological hazard is controlling.

American Conference of Governmental Industrial Hygienists (ACGIH) has recommended TLV-TWA (Threshold Limit Value-Time Weighted Average) value of 0.2 mg/m^3 and TLV-STEL (Short-Term Exposure Limit) value of 0.6 mg/m^3 [2]. OSHA (Occupational Safety and Health Administration, Department of Labour, USA) has set Permissible Exposure Limit (PEL) 8-h TWA concentration of 0.05 mg/m^3 [3] for soluble compounds of inhaled uranium and 0.25 mg/m^3 for insoluble compounds of inhaled uranium. Chronic exposure occupational limit (TWA) given by National Institute for Occupational Safety and Health (NIOSH) for insoluble uranium compounds is 0.2 mg/m^3 and for soluble compounds it is 0.05 mg/m^3 [4]. NIOSH has also recommended Immediately Dangerous to Life or Health (IDLH) value of 10 mg/m^3 for uranium compounds.

Different chemical forms of uranium present in the workplace play a key role in appraising the internal radiation hazard. Solubility class of uranium compounds encountered in fuel fabrication facilities and respective Derived Air Concentration (DAC) values (for 5 μm size aerosols) based on revised committed effective coefficients by ICRP publication 137 [5] are given in Table 2. Materials have been classified into F, M, S types based on the absorption rates of the materials from lung into the body fluids. For all isotopic compositions of uranium compounds of Type S (insoluble) and intermediate Type M/S, radiological toxicity is more than chemical toxicity and the DAC is fixed based on radiological toxicity. Type F (soluble), Type M (moderately soluble) and intermediate Type F/M compounds are chemically toxic and hence the occupational intakes are limited by chemical toxicity considerations.

Table 2 Classification of uranium compounds as per ICRP Report 137

Chemical compound	Absorption type	[b]DAC (Bq/m^3)
U_3O_8, UO_2	M/S	1.6
Unspecified form, UF_4, vaporized uranium metal, uranyl acetylacetonate, depleted uranium, uranium ore dust, irradiated fuel fragments	M	[a]5.0
$UO_2(NO_3)_2$, ADU, UO_3, uranium peroxide hydrate	F/M	
Uranyl tributyl phosphate, UF_6, UO_2F_2	F	

[a] Based on chemical toxicity limit of 0.2 mg/m^3

[b] DAC is calculated from the composite ALI values for Natural Uranium

In operations involving handling of uranium compounds in powder form in open system, main hazard is due to inhalation of uranium bearing compounds suspended in air. Particle size of the airborne uranium decides the deposition of the inhaled particles in different regions of lung. The ICRP Publication 137 (2017) provides the necessary data of effective dose coefficients (Sv/Bq intake) for all the absorption types and for particle sizes of 5μm and for 1 μm AMAD for most common uranium isotopes. Once the intake (Bq) is assessed by workplace monitoring or bioassay, the internal dose assessment for the occupational worker can be made for intake of uranium through inhalation and ingestion routes. Typically, for inhalation of F type of ^{238}U isotope (Ex. UF6) of 5 μm particle size, the effective dose coefficient works out to be 2.2×10^{-7} Sv/Bq, while for intermediate Type M/S compound of ^{238}U isotope (Ex. UO2), the value is 4.8×10^{-6} Sv/Bq.

In wet (uranium handled in solution) section of fuel fabrication process, ventilation is maintained at about ten air changes per hour. Filtered and washed air supply is provided to all sections in dry area to give about fifteen air changes per hour. In order to contain the release of uranium, all the equipments which generate uranium dust are enclosed and kept at negative pressure with respect to surroundings by local exhausts. When uranium compounds are handled in powder form, potential for surface and personnel contamination exists. Eating with contaminated hands may lead to ingestion of radioactive material. Body movements may dust off contamination on personnel causing airborne activity which can enter body through inhalation. Surface contamination can also become airborne through re-suspension of uranium compounds as a result of air movements potentially resulting in internal exposure. Exposure to uranium dust is prevented using appropriate PPE (Personal Protective Equipment) such as dust respirators.

5 Reprocessing of Spent Fuel

In a reprocessing plant using PUREX (Pu, U recovery by extraction) process, spent fuel is chopped and dissolved in nitric acid, plutonium and uranium are separated from fission products, purified and converted to respective oxide forms. Depleted Uranium (about 98%) is stored for recycling in fast breeder reactor. ^{239}Pu (about 0.4%) is formed when neutrons are absorbed in atoms of non-fissionable uranium (^{238}U) in reactor. This is very valuable and is used as fuel for fast reactors. Mixed long-lived radioactive fission products (about 1%) are stored in stainless steel tanks in liquid form before vitrified.

All the operations in reprocessing facilities are carried out remotely in process cells and hot cells having concrete shielding of about one to two meter thickness. Reprocessing of spent fuel poses challenge in radiation protection due to handling of plutonium, uranium and fission products in various forms in large quantities during

various stages of operations. Important process steps in reprocessing are as given below.

(a) Head-end treatment involving mechanical de-cladding followed by dissolution of fuel in nitric acid, feed clarification and adjustment of chemical conditions of the solution for solvent extraction
(b) Co-decontamination involving extraction of uranium and plutonium in 30% TBP(n-dodecane) leaving bulk of the fission products in aqueous phase which goes as high active waste
(c) Washing/scrubbing of organic stream with nitric acid to backwash fission products co-extracted with uranium and plutonium
(d) Partitioning of uranium and plutonium by selective reduction of Pu(IV) in the organic phase to Pu(III) which goes to the aqueous phase, and back extraction of U(VI) with 0.01 M dilute nitric acid
(e) Further purification of uranium and plutonium streams to obtain uranium and plutonium of desired purity
(f) Waste management.

5.1 Radiological Hazards and Radiation Environment in Reprocessing

5.1.1 Safety in Fuel Storage

In the fuel storage ponds where fuels are stored for reprocessing, several meters of water are used for shielding and for heat removal purposes. The heat removal and water clean-up system consists of circulating pond water through heat exchangers, filter, and ion exchange beds. This will help (i) in ensuring very minimum activity in pool water (ii) in preventing the contamination of the area and (iii) in preventing air borne radioactivity due to re-suspension of contamination. It is advantageous to clean the bottom of the fuel pool occasionally and thus keep the accumulated amounts of powdered fuel sludge low.

5.1.2 Containment and Confinement

As the radioactive material is in a highly dispersible solution form and operations like boiling, transferring and agitating liquids are the part and parcel of the process, it is necessary to achieve high degree of containment to ensure safety for personnel and environment. All the equipments are fabricated out of corrosion resistance stainless steel with tungsten inert gas welding technique to provide long life and to guard against weld failures.

The reprocessing process flow sheet involving dissolution, liquid transfers, chemical separation, processing, and storage has high potential for leakage and spilling. Such leakages and spillages can result in high levels of contamination, and result in external and internal to the occupational workers. All chemical operations are done in adequately shielded process cells remotely. The process ventilation system treats the radiolnuclides generated by the processes and equipment such as off-gas from process tanks, storage tanks, fume hoods, glove boxes, and process cells.

The standard scheme of dividing the plant into the well-known radiation zones for confinement of contamination and control of air borne radioactivity by isolating the sources in glove boxes, vessels, etc., coupled with a well-balanced ventilation system form part and parcel of reprocessing facilities.

5.1.3 Safety in Evaporation

A number of evaporators are used in reprocessing facilities to achieve desired feed concentration or to reduce waste volumes in order to economize on precious tankage. The evaporators have heating/cooling jackets. The following important safety issues are related with these evaporators:

a. Failures of coils due to variety of reasons leading to contamination of inactive steam, steam condensates, or process cooling water.
b. Small amounts of organic may escape into the aqueous streams and may undergo nitration leading to explosive reaction under some conditions of temperature and pressure. TBP/HNO_3/Uranyl nitrate solution forms a mixture called red oil which reacts violently above 135 °C. Hence, low pressure steam below 2 kg/cm^2 is normally used for evaporation purpose to ensure that the solution temperature is always below 135 °C. Control on supply steam pressure and suitable cut off interlocks on temperature and pressure settings ensure safety against these incidents.
c. Destruction of acid, called acid killing, using formaldehyde (HCHO) is regularly carried out in waste evaporators. This reaction of HCHO-HNO_3 is exothermic and produces large amount of non-condensable. The reaction is slow at temperatures below 90 °C and can lead to accumulation of un-reacted HCHO. On initiation of the reaction, the un-reacted HCHO could lead to release of large quantity of heat and non-condensables, resulting in system pressurization and possible blow-back of activity to the working areas. To ensure that acid killing operation using formaldehyde (HCHO) is carried out smoothly without loss of negative pressure in the system, suitable interlocks are provided i) for closure of LP steam supply with negative pressure observation in evaporator, ii) for formaldehyde pump cut off when the temperature of the evaporator falls below 95 °C and/or the negative pressure in the corresponding evaporator falls below prescribed limit for the process.

5.1.4 Sources of Potential Exposures

Some of the typical incidents with potential for contamination, external and internal exposures in reprocessing facilities are leakages from the pumps used for transferring radioactive liquids, over-flow from the receiving tanks, blow-back due to vacuum created in the steam transfer lines due to condensation, pipelines leakage at joints due to corrosion, pressurization of process vessels leading air activity release through process instrumentation probe lines, etc. In the reprocessing facility, the main radiological risk is criticality accident resulting in loss of confinement/containment and which can also result in huge radiation exposures of personnel. Criticality safety is ensured through use of geometrically safe equipments for handling solutions containing plutonium, control on total mass in glove boxes/fume hoods, control on concentration of fissile material. Administrative control on the process parameters is also exercised to avoid accumulation of plutonium in equipments/tanks/pipes/glove boxes [6].

It's important to highlight that, compared to nuclear power reactors, reprocessing facilities are generally safer due to several factors. These include lower potential energy for spreading radioactive materials, the absence of volatile or gaseous fission products like ^{131}I and short-lived fission gases, and longer time constants for energy transients. Reprocessing plants also operate at lower process temperatures and process pressures, often under negative pressure. However, they handle highly reactive and corrosive solutions with high specific activity, posing unique containment challenges as compared to nuclear reactors. Despite this, they adhere to the principles of defense in depth and multiple barriers for safety.

5.2 Radiological Hazards in Reprocessing Facilities

There are various radiological hazards associated with handling of plutonium in back-end nuclear fuel cycle facilities and also in plutonium based fuel fabrication. Plutonium obtained from spent fuel reprocessing operations contains isotopes of ^{238}Pu, ^{239}Pu, ^{240}Pu, ^{241}Pu, ^{242}Pu, and also ^{241}Am which is formed from the decay of ^{241}Pu. ^{239}Pu is the major component ($\approx$70 to 90 wt. %) with the half-life of 2.41×10^4 years. It emits alpha particles of energy 5.15 MeV. ^{239}Pu is highly radiotoxic due to its emission of high LET radiation, high specific activity, and high biological half-life. ^{238}Pu with the half-life of 87.7 years emits alpha particles of energy 5.499 MeV.

Principal hazards in handling plutonium are contamination, radiation dose, fire, and criticality accidents. Isotopes of internal hazard concern in a reprocessing plant are ^{239}Pu, ^{241}Am, and ^{238}U. Since the Annual Limit of Intake (ALI) of $PuNO_3$ (Type M compound) is just 625 Bq (for 5 μm particle size with DCF of 3.2×10^{-5} Sv/Bq) and has high effective half-life, it is considered to be the most hazardous nuclide in reprocessing plants. About 10–70% of deposited Type M compound of plutonium ($PuNO_3$) in lung compartments is absorbed in body fluids with clearance half-life of 140 days whereas 1–10% of deposited Type S compound of plutonium (PuO_2) is

absorbed in body fluids with a lung clearance half-life of 6000–7000 days. Hence, Annual Limit on Intake is more restrictive for Type M compounds of plutonium than for Type S compounds.

Inhalation of significant quantities of plutonium can occur inadvertently in a matter of moments usually due to a breach of containment or loss of ventilation control resulting in transient but high airborne concentrations of plutonium. However, measurement of air borne activity due to ^{239}Pu is a difficult task using conventional continuous air monitors because of interference from radon-thoron daughter product concentration (alpha energy > 6 MeV) and low DAC value. Typical radon and thoron background alpha activity in ventilated room is a few Bq/m^3, but the DAC of ^{239}Pu oxide is about 1 Bq/m^3 only. In order to overcome this difficulty, detection of ^{239}Pu air activity is carried out using a solid-state semiconductor Passivated Ion Implanted Silicon detector (PIPS) detector connected to a charge sensitive pre-amplifier and a multi-channel analyzer.

Any chelating agent, for decorporation of plutonium from the body fluids, should form a more stable chelate which would not hydrolyze under physiological pH conditions. For soluble plutonium compounds such as $PuNO_3$, the chelating agent Ca-DTPA (trisodium calcium diethylene triamine pentaacetate, also known as Pentetate calcium trisodium) enhances excretion. Ca-DTPA should be administered as early as possible before plutonium gets metabolized in the body fluid. Administration of Ca-DTPA (to dogs) one hour after exposure and continued up to 64 days has shown that the initial pulmonary plutonium burden came down by 85% at the end of 64 days. Chelation therapy is not amenable for the removal of highly insoluble plutonium compounds such as PuO_2.

Fission products are major components in the contribution of external exposure in reprocessing facilities. ^{137}Cs and ^{90}Sr with the half-lives of 30.2 years and 28.8 years respectively are major contributors to external exposure in back-end fuel cycle facilities. ^{137}Cs with the gamma emission of 661.6 keV contributes to external exposure while beta emitters ^{90}Sr ($T_{1/2} = 28$ years, 0.546 MeV) in secular equilibrium with ^{90}Y ($T_{1/2} = 64$ h, 2.28 MeV) contribute to skin dose and dose to extremities. ^{106}Ru with the half-life of 367 days (512 keV gamma) is also considered significant due to its high volatility which may result in high gamma dose rates in pipes, equipment, etc. Spontaneous fission of plutonium isotopes (primarily from ^{240}Pu to ^{242}Pu) and (α, n) reaction with impurities are sources of very small neutron exposures to the lab personnel involved in plutonium reconversion operations.

^{241}Pu decays with beta emission to ^{241}Am ($T_{1/2} = 433$ years) which contributes significantly to external exposure because of its gamma emission of 60 keV. Also,^{239}Pu emits gamma rays of energies 207, 380, and 420 keV in addition to 17–20.5 keV X-rays which contribute significantly to external exposures while handling large quantity of plutonium. Significant growth of ^{241}Am will increase gamma dose in plutonium products stored for longer period. ^{237}Np formed by decay of ^{241}Am (and also by beta decay of ^{237}U) is also an alpha emitter with a half-life of 2.14×10^6 years. In purified form, it requires conventional alpha containment. However, some gamma shielding will be required when handling kilogram quantities on account of the presence of ^{233}Pa ($T_{1/2} = 27$ days) which is the daughter product of ^{237}Np. At secular

equilibrium, 0.7 mCi of ^{233}Pa is present in a gram of ^{237}Np. One half of the equilibrium quantity is present in twenty seven days after separation of ^{237}Np. The main penetrating radiation from ^{233}Pa is 0.31 MeV gamma rays with an abundance of 44%. While the growth of ^{233}Pa is not significant in the short time it takes for the material to be processed in the laboratory, the growth of ^{233}Pa during long-term storage of plutonium will pose external radiation exposure potential.

The possibility of a fire or explosion is a serious threat because the consequences of a fire could lead to loss of containment and subsequent dispersal of highly mobile plutonium particulates. Fire fighting with water to maintain containment could create the potential for a criticality accident and/or loss of containment in the immediate vicinity.

Primary approach to safe handling of plutonium involves planning, engineered controls, such as the use of glove boxes, remote handling systems, geometrically safe containers, HEPA filtration, and dynamic ventilation systems. Further safety considerations include administrative controls such as mass/concentration limits to avoid criticality, training, standard operating procedures, personnel and area radiation monitoring and emergency response system.

5.3 Monitoring of Gaseous Effluents

The containment of vapors in vessels/tanks is achieved by keeping them under negative pressure with the help of blowers and exhaust fans. The aerosol clean-up systems like condensers, scrubbers, cyclone/mist separators form part of the off-gas cleaning equipment. The off-gases from vessels, hot cells, and glove boxes are filtered through special filters before being sent to the main HEPA filter banks where they mix with plant ventilation air. Gaseous effluents generated are discharged into the environment through a tall stack after monitoring activities of gross alpha, gross beta, tritium, carbon-14, ^{129}I, and gaseous isotope ^{85}Kr.

Krypton-85 (^{85}Kr) is one of the fission products formed during fission and is chemically an inert radioactive gas with a half-life of 10.7 years. It decays to ^{85}Rb emitting a beta of maximum energy 0.687 MeV (E_{max}). It also emits a gamma of energy 0.514 MeV with an abundance of 0.4%. It has a fission yield of 0.3%. Krypton-85 is produced in small quantities by the interaction of cosmic rays with stable krypton-84 in the atmosphere. Natural sources maintain an equilibrium inventory of about 0.09 PBq in the atmosphere. The long half-life of the gas allows the gas to mix thoroughly in the atmosphere. As a noble gas, krypton does not generally participate in any biological processes. After being taken into the body, a very small amount can be dissolved in the bloodstream and distributed to organs and tissues throughout the body. Nevertheless, the tissue of most concern from exposure to a cloud of krypton-85 gas is generally the skin, with most of the dose resulting from the beta particles associated with its radioactive decay.

Tritium, a radioactive isotope of hydrogen, has a half-life of 12.3 years. It decays into ^{3}He by emitting low-energy beta radiation, with an average energy of 5.7 keV

and a maximum energy of 18.6 keV. ^{14}C, a radioactive isotope of carbon, has a half-life of 5730 years and decays into ^{14}N by emitting low-energy beta radiation, with an average energy of 49.5 keV and a maximum energy of 156 keV. These isotopes occur naturally in the atmosphere due to interactions with cosmic rays and are also produced in nuclear reactors. Tritium is primarily generated in nuclear fuel through ternary fission, occurring approximately once for every 10,000 fissions. ^{14}C is produced during reactor operations as a neutron activation product from carbon, nitrogen, and oxygen present in the fuel (^{14}N$(n, p)^{14}$C; ^{17}O$(n, \alpha)^{14}$C). Despite their long half-lives and widespread distribution, they pose minimal external radiation risk and are mainly of interest for internal dose assessment due to their role in biological metabolism.

^{129}I, with a half-life of 17 million years, is a byproduct of nuclear fission, originating from the decay of ^{129}Te. It undergoes beta decay to ^{129}Xe, emitting a beta particle with a maximum energy of 154 keV. Additionally, it emits gamma radiation with an energy of 39.6 keV (abundance of 0.7%), along with internal conversion electrons and X-rays with various energies (29.46, 29.78, 33.52, 33.56, and 34.4 keV). A small amount of ^{129}I is naturally produced in the upper atmosphere through interactions with xenon. However, the discharge of ^{129}I from nuclear industry operations is concerning due to its long half-life and its potential to enter the food chain, concentrating in the human thyroid. While most fission products remain within fuel cladding, fuel reprocessing plants are the main source of emissions of ^{85}Kr and ^{129}I in the nuclear fuel cycle. However, ^{14}C and ^{3}H may be emitted from both reactors and reprocessing plants.

A comprehensive sampling system is used in reprocessing plants for the measurement of ^{3}H, ^{14}C, and ^{129}I released as gaseous effluents through stack. This sampling system facilitates continuous sampling of these radionuclides released through the off-gas stream and the quantification is carried out offline. Suitable radiometric methods such as gross α/β air monitors for online sampling and monitoring of particulate activities and GM tube/plastic scintillator based ^{85}Kr monitoring system (online) are adopted in the gaseous effluent monitoring system. The monitoring of ^{14}C involves online sampling and absorption of ^{14}C in the form of carbonate followed by assimilation in the absorbent mixture of ethanol amine and methanol which is subjected to liquid scintillation counting for estimation of ^{14}C. The monitoring of ^{3}H is done through absorption of ^{3}H in water as HTO in bubblers followed by liquid scintillation counting. Online sampling of ^{129}I is carried out using activated charcoal filter cartridge impregnated with silver nitrate for elemental and molecular iodine followed by gamma spectrometry using High Purity Germanium (HPGe) detector for the measurement of gamma energy of ^{129}I (γ-39 keV).

6 Safety Aspects of MOX Fuel

The fabrication of MOX fuel pins involves various metallurgical operations such as mixing, milling, pre-compaction, granulation of pre-compacts, final compaction of granules, sintering of pellets followed by fuel pin fabrication. The whole operation, which is undertaken in a chain of glove boxes, requires extensive on-the-spot health physics surveillance and supervision at every stage of the operation. The MOX fuel fabrication poses challenge in minimizing external exposure and preventing internal exposure due to high radiotoxicity associated with plutonium and the presence of ^{241}Am in it. Plutonium obtained from reprocessing of irradiated spent fuel containing ^{238}Pu, ^{239}Pu,^{240}Pu, and ^{242}Pu isotopes is a source of neutrons due to spontaneous fission as well as (α, n) reaction with the impurities. It is handled in various forms such as powder, granules, pellets, and pellets encapsulated in pins during these operations. The fuel pins contain annular mixed oxide pellets consisting of depleted UO_2 and PuO_2. Radiological measurements such as radiation survey for gamma and neutron, air activity concentration and contamination levels are carried out at every stage of operation to assess overall radiological safety.

6.1 Radiation Environment in MOX Fuel Fabrication

Handling plutonium in large quantities requires compliance with stringent safety requirements such as criticality control, control on external exposure and prevention of internal exposure due to plutonium. Nuclear properties of plutonium isotopes are given in Table 3 [7]. External radiation hazards exist for personnel during the handling of plutonium because the radioactive decay of commonly encountered Pu-isotopes produces γ rays and X-rays. Low and medium energy γ rays, mainly from ^{241}Pudecay product (primarily ^{241}Am), are the major contributors to the external radiation exposure of personnel handling plutonium.

Isotope of plutonium, ^{241}Pu ($T_{1/2}$ = 14.4 years) β^- decays to ^{241}Am ($T_{1/2}$ = 432.2 years), which α-decays with emission of 59.6 keV gamma radiations to ^{237}Np daughter. Consequently, gamma radioactivity resulting from ^{241}Am increases over the time since reprocessing. Therefore, special attention has to be given to the ingrowth of ^{241}Am. The γ emission from other Pu-decay products also contributes to the external exposure. Exposure due to neutron from spontaneous fission of ^{238}Pu, ^{240}Pu, and ^{242}Pu is also significant contributor to the external exposure while handling plutonium. Additional neutron radiation arises from (α, n) reaction with oxygen. The neutron has wide energy distribution with a maximum of 13 MeV and mean energies of 1–5MeV (depending on nuclei involved). It may be noted that neutron dose rate is proportional to quantity of plutonium (because number of neutrons emitted per gram depends on wt%), whereas gamma dose rate is proportional to area of the source as much of the gamma photons are attenuated in the matrix itself.

Table 3 Nuclear properties of plutonium and related isotopes

Isotope	Half-life (years)	Decay mode	Energy (α) MeV	Specific activity (Bq/g)	Neutron emission rate (n/s/g)	
					Spontaneous fission	(α, n) for oxide
^{236}Pu	2.85	α	5.763	1.86×10^{13}	3.7×10^{4}	4.3×10^{5}
^{238}Pu	87.7	α	5.495	6.0×10^{11}	2.62×10^{3}	1.4×10^{4}
^{239}Pu	2.41×10^{4}	α	5.147	2.0×10^{9}	0.03	45
^{240}Pu	6.54×10^{3}	α	5.162	8.0×10^{9}	1.02×10^{3}	170
^{241}Pu	14.4	β	0.021 (β)-99.997%	3.7×10^{12}	–	–
^{241}Pu	7.2×10^{5}	α	4.89 (α)-0.002%	0.07×10^{9}	8.8×10^{2}	–
^{242}Pu	3.76×10^{5}	α	4.898	1.0×10^{8}	1.7×10^{3}	2.7
^{241}Am	4.32×10^{2}	α	5.477	1.2×10^{11}	1.1	2600

6.2 Potential for Exposures

Radiation exposures of personnel are kept well below the limits defined by regulation. In compliance with "ALALRA" concept, measures are taken to minimize the exposure. The assessment of dose from external radiation sources is performed by individual monitoring using personnel monitoring devices like TLDs and neutron badges. Important measures such as local shielding around storage containers and hoppers, composite radiation shielding for glove boxes, use of lead impregnated aprons and hand gloves, automation & remotization of operations, periodic decontamination of glove boxes and use of digital dosimeters are implemented for personal exposure control.

Internal exposure can occur when radionuclides are inhaled, ingested, or otherwise taken into body through wounds. In the facility potential internal exposure results primarily for alpha activity of plutonium deposited in the body by inhalation, ingestion, or wounds. Plutonium and/or their daughter radionuclides decay mainly through alpha decay process. Therefore, containment of plutonium is essential to avoid internal contamination of personnel. Plutonium is handled in leak-tight glove boxes. These glove boxes are kept under negative pressure with respect to the atmosphere outside the glove boxes. Work with plutonium requires glove boxes of high integrity, i.e., leakage rates less than 0.05% box volume per hour. This is achieved by a well-defined ventilation system which ensures no release of the radioactivity to the work environment. Individual monitoring for internal dose assessment is carried out using in vivo and in vitro measurements. The glove forms the most vulnerable component of a glove box (glove box "O" rings), especially in a fire or explosion, because they are most susceptible to damage. The gloves should have long life and

highly polished surface with very low permeability rates. Further they should be checked at regular intervals for their integrity like the presence of pin-holes to avoid the spread of contamination.

Installation of equipments in glove boxes is as much of an art as science and requires lot of foresight. Each equipment is to be viewed as consisting of two parts—one which will come in direct contact with radioactive materials and must therefore be contained inside the glove box; the second part, which concerns itself with the driving mechanism of the equipment, can be located outside in the immediate vicinity of the glove box. The two parts are connected through seals of various kinds located on the walls of the glove box, e.g., shaft seals, low speed seals, etc. This type of delineation becomes very important when equipment dimensions exceed the dimensions of the glove box. When maintenance jobs are to be done in a glove box which is part of train of glove boxes, the whole train needs to be thoroughly decontaminated before the job begins.

6.3 Criticality Safety

Criticality can be defined as any fissile material system attaining self-sustained nuclear chain reaction under certain physical conditions. Fissile material handled outside the reactor such as in reprocessing facilities or fuel fabrication facilities can result in a potential criticality accident if the chain reaction is uncontrolled. The hazard is due to accompanying radiation which can deliver lethal doses to workers in the neighborhood of the criticality accident. The fissile materials such as ^{239}Pu, ^{235}U, and ^{233}U are mainly handled in Nuclear Fuel Cycle Facilities. In these facilities, there is a potential for inadvertent criticality. Hence these facilities require criticality safety compliance at each and every stage of the operation and also during the storage of the fissile materials to prevent any inadvertent criticality excursion. To ensure systems with fissile material remain subcritical, safety measures are based on defense-in-depth. This involves designing systems with fail-safes to prevent criticality accidents caused by single failures like component malfunctions or human errors. The double contingency principle is preferred for criticality safety, requiring protection against multiple changes by providing different levels of protection. According to this principle, if a criticality accident could occur due to two simultaneous changes in process conditions, it must be demonstrated that these changes are independent and have a low probability of occurring.

Criticality Accident Alarm System (CAAS) is used to detect the criticality accident and warn the personnel for quick evacuation from the laboratories in fuel fabrication and reprocessing facilities. CAAS responds immediately to the Minimum Accident of Concern (MAC), which is assumed to deliver the equivalent of an absorbed dose rate in free air of 0.2 Gy/min at 2 m from the reacting material. Based on this MAC, the detection criterion for CAAS translates to approximately 0.04 Gy/h (gamma dose rate) and integrated gamma dose rate as 3.0 mrad in 500 ms, at a distance of 10 m from the surface of the reacting material. System Criticality Alarm (SCA)

module generates alarm when two out of three channels exceed these limits. The placement of a CAAS is evaluated so as to ensure that the system will respond to the above criteria. To protect for slow quasistatic accidents (wherein a slow increase in reactivity could occur leading from sub-criticality to super criticality to self-shutdown without setting off emplaced criticality alarm), CAAS is supplemented by warning devices such as wide range area gamma monitors.

The sub-criticality of the system is demonstrated by calculating k_{eff} (Multiplication factor) and controlled by limiting one or more process parameters. The control parameters that may be considered for ensuring sub-criticality are (i) Mass control (ii) Volume control (iii) Concentration control (iv) Geometry control (v) Nuclear poison control (vi) Spacing control between the systems, i.e., separation distance between the systems and (vii) Administrative Control.

7 Review of Criticality Accidents

An effective nuclear power program depends on recovery of fissile material from spent fuel and recycling it back into reactors. Hence, large-scale chemical processing is inevitable. Especial care is needed to avoid a criticality incident and the possible severe exposures to personnel or contamination of plant areas. In this context, there is much to be learnt from experience of facilities where criticality accidents occurred. In this section, the incidents outside reactors and critical experiment facilities are focused. During the fifteen year period between 1951 and 1965, there was one criticality incident each year. In 1951 alone, there were four criticality incidents. As of the year 2000, there have been total of 22 major process related criticality incidents in the world [8]. Figure 2 shows the chronology of these 22 accidents.

These accidents can be summarized as follows:

- 21 of 22 excursions occurred in solution or slurries.
- 18 accidents occurred in manned and unshielded facilities.
- Nine fatalities resulted from these accidents.
- No equipments were damaged in these accidents.

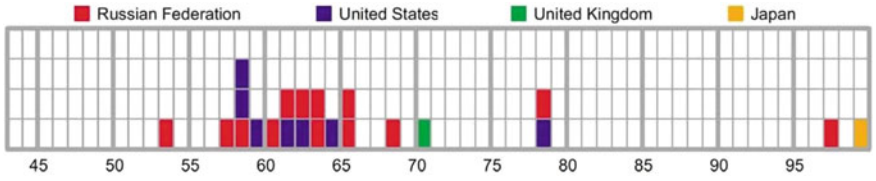

Fig. 2 Chronology of process criticality accidents. Plot shows number and location of accidents by year from 1945 to 2000 (reproduced from [8] @ LA-13638, LANL with permission from OSTI, DOE, US)

- One accident resulted in measurable fission product contamination beyond the plant boundary and in measurable exposure to the public at Tokai fuel fabrication plant.

Among these incidents, one is related to metal ingots which are not included in further discussions. Additionally, not included in further discussion are process accidents related enrichment and uranium hexafluoride such as

1. Electrostal machine building plant November 3, 1965—accident related to conversion of UF_6 to UO_2
2. Siberian chemical combine December 13, 1978—accident related to Pu metal ingots in storage containers
3. Novosibirsk chemical concentration plant May 15, 1997—accident related to chemical etching process in the fuel rod production

Table 4 provides the remaining criticality accidents that can be related to fuel reprocessing facilities. The location of the accidents, cause, accident description, and total fission of the accidents are described in the table.

Based on these process accidents, the following lessons have been identified:

1. Vessels with geometries that favor criticality should be avoided, particularly when high concentration solutions might be present.
2. No verbal procedures should be used. Instead, documented procedures should be used.
3. Operators should be aware of any abnormal conditions of the processes.
4. Fissile material accountability must consider criticality control when tracking material accumulations in the equipment.
5. Operators should be trained to respond to potential equipment failure or human errors.
6. Operators should be trained to deal with possible off-normal conditions for the processes involving both organic and aqueous solutions.
7. Operators should be trained to follow procedures.

8 Radioactive Waste Management

Waste management facilities are tasked with handling, treating, and storing various liquid and solid wastes produced by nuclear fuel cycle facilities. Managing wastes from reprocessing plants poses challenges, which are explored in detail in this manuscript. Different types of solid wastes are disposed safely in underground structures based on their classification. Liquid waste streams generated by reprocessing plants include High Level (HL), Intermediate Level (IL), and Low Level (LL) wastes, which are transferred to Waste Management Facilities. LL liquid wastes are released into the environment through approved aquatic routes after ensuring their activity levels comply with regulatory limits. Other waste streams are transported via shielded concrete trenches to treatment facilities for further management. To

Table 4 A summary of solution criticality incidents (reproduced from [9] @ 2017 NUREG/CR-7232 with permission from LANL)

(#) Accident	Operation cause	Description	Total fission
(1) 3/15/1953, Mayak Production Association, Russia	Pu purification [operator error/ procedural error]	There were 18 vessels containing plutonium nitrate solution in a staging area where operations of mixing, dilution, volume measurement, sampling, and interim storage were done. Each vessel had a 500 g plutonium mass limit. An excursion occurred in Vessel 18 (originally contained 26 L), which contained 848 ± 45 g of plutonium in 31 L at the time of the accident. The cause of this excursion was due to unrecorded transfer of 5 L of solution from Vessel 1 to Vessel 18	2×10^{17} fissions. This was based on a temperature rise of 60 °C in 31 L of the solution
(2) 4/21/1957, Mayak Production Association, Russia	Uranium purification [equipment failure—defect in the filter fabric]	Impure uranyl nitrate (90% enriched uranium) and oxalic acid solution were mixed in a vessel to precipitate the uranyl oxalate trihydrate, which was done within a glovebox. This precipitate slurry was then vacuumed to a holding tank from which it was drained into a filter vessel. The precipitate containing uranium was collected on the filter fabric, and the filtrate was pulled through by vacuum and collected in a filtrate receiving vessel. An excursion occurred in this vessel that caused the filter vessel to bulge upward, followed by a violent release of gas and ejection of some of the precipitate out of the filter vessel and onto the glove box floor	A fission yield of 1×10^{17} fissions. This yield was based on the measurement in the room and the concentration of ^{24}Na in the operator's blood (17 h after the accident, the dose was 245 Bq/cc)
(3) 1/2/1958,Mayak, Production Association, Russia	Solution critical experiment [operator error]	Based on the 4/21/1957 accident, a solution criticality experiment was conducted using highly enriched uranyl nitrate solution (90% enriched). The experiment was conducted in a cylindrical vessel that could hold an excess of 400 L of solution to measure a wide range of critical states. Typically after each experiment, the solution must be drained to a smaller vessel which was criticality-safe. Experimenters decided one day to circumvent the routine by manually pouring the solution out of the experiment vessel. This routine created an excursion because human bodies provided additional reflection of the neutrons, which created a criticality-unsafe configuration	Based on fission product activity in the solution, a single pulse event was about 2×10^{17} fissions

(continued)

Table 4 (continued)

(#) Accident	Operation cause	Description	Total fission
(4) 6/16/1958 Y-12 Plant, Oak Ridge, TN, U.S.	Uranium recovery [equipment failure]	Solid wastes with highly enriched uranium (93% enriched) were dissolved in nitric acid, purified, concentrated and then converted to uranium tetrafluoride. A 55-gallon drum served as a residue collection tank. Because there were apparent leaks in the system, liquid accumulated in the drum to about ~ 56 L with 2.1 kg of ^{235}U mass. This condition yielded excursions that lasted for about 20 min	Based on the instruments at the site and detectors nearby, the first spike was about 6×10^{16} fissions, with a total of 1.3×10^{18} fissions
(5) 12/30/1958 Los Almos, NM, U.S	Plutonium recovery [equipment design]	An organic treatment tank, which typically contained solutions < 0.1 g Pu/liter and traces of americium. This tank was made of stainless steel and had a volume of 1000 L. Before the accident, tank contained an aqueous layer of 330 L with 60 g of Pu, and an organic layer of 160 L with 3.1 kg of Pu. Aqueous layer was located at the bottom of the tank. This configuration was subcritical. When the stirrer was started, the motion altered the reactivity of tank, and an excursion occurred in about 3 s. The excursion was terminated by the stirring action. After this accident, a criticality-safe tank was used	Based on the reactivity of the system, the excursion yielded 1.5×10^{17} fissions
6) 10/16/1959, ldaho Chemical Processing Plant, lD, U.S.	Uranium extraction [operator error, Equipment failure]	The impurity extraction process occurs in three pulse columns. Intermediate between the first and second cycle extraction, the uranyl nitrate solution (91% enriched uranium) was stored in two banks of long pipes (referred to as pencil tanks). There was a line leading from the interconnected pipes to the 18,900 L waste receiving tank. As required, operators needed to conduct analysis by collecting samples using a sparging operation. Because the air sparging was so forceful, and the pressure gage of the other pipe was functioning improperly, the liquid in the pipes was forced to the top of the loop that drained into the receiving tank. Excursions boiled away half of the 800 L solution volume that terminated the criticality	Based on the strip chart recordings from the continuous air monitors at various locations, the initial spike of at least 10^{17} fissions, followed by boiling of 15–20 min to yield a total of 4×10^{19} fissions

(continued)

Table 4 (continued)

(#) Accident	Operation cause	Description	Total fission
(7) 12/5/1960, Mayak Production Association, Russia	Plutonium recovery [operator error]	The accident occurred in the waste solution process to recover plutonium. A total of 4 purification vessels were used in the process. All vessels were contained in glove boxes. A holding tank was used to keep solutions for various stages of the purification process. Because of overloading, the mass limit in the initial purification process was passed, and subsequent purification process resulted in a criticality accident. Excursions occurred in the holding tank, which contained 894 g of plutonium. 180 g of Pu was flushed out of the holding tank during the accident	The excursions yielded a total of 2.5×10^{17} fissions
(8) 1/25/1961, ldaho Chemical Processing Plant, lD, U.S.	Uranium purification [operator error, equipment design]	The accident occurred in the upper disengagement head of the H-110 product evaporator. Because the disengagement head was not a favorable geometry, any solution that reached this section may yield criticality. Despite an overflow line to prevent a significant amount of solution reaching this section, 200 g of uranyl nitrate solution with 90% enrichment per liter was apparently rapidly ejected up into this section causing excursions. This action was due to operators attempting to clear the plugged line with air. The cause of the ejection of the solution upward was due to the high air pressure which forced the solutions in the favorable geometry section to move upward into the disengagement head	Because of no instrument read out of the event, it was calculated to be 6×10^{17} fissions
(9) 7/14/1962, Siberian Chemical Combine, Russia	Uranium enrichment plant [equipment failure and operator error]	The accident was caused by the accumulation of high concentration of UF_6 in the vacuum pump oil reservoir. Four days before the accident, there was a sudden flow rate increase of UF_6 into the reservoir. The operator turned on the vacuum pump and approached the equipment (~ 0.5 m) to open a valve between pump and holding vessels. This resulted in a criticality event	The total number of fissions for both excursions was estimated by fission product analysis to be about 1.2×10^{15}

(continued)

Table 4 (continued)

(#) Accident	Operation cause	Description	Total fission
(9) 4/7/1962 Hanford Works, U.S.	Plutonium recovery [operator error]	The transfer tank with a capacity of 69 L received solution containing 45 g Pu per liter and later additions of other diluted solutions which caused an excursion that lasted for 37.5 h. The shutdown mechanism for the accident was due to a central pipe that entered the bottom of the vessel. Fission reactions might have driven off CCl_4 and converted most of the remaining organic to dibutyl phosphate. This phosphate, with extracted plutonium, may have gone to the bottom of the vessel and into the pipe to stop the excursion	An initial spike estimated to be no more than 10^{16} fissions, and lasted for 37.5 h to total fission of 8×10^{17}
(10) 9/7/1962, Mayak Production Association, Russia	Plutonium recovery [operator error and equipment design]	Dissolution vessels were used to dissolve solid Pu residue to further purify plutonium. Due to the unfavorable geometry of the vessels and undetermined plutonium concentration, excursions occurred in the vessels	A total of three excursions were detected and estimated to have total of 2×10^{17} fissions
(11) 1/30/1963. Siberian Chemical Combine (Tomsk), Russia	Uranium recovery [operator error]	The recovery process required that dry precipitate of uranium (90% enriched) be placed into concentrated nitric acid for the dissolution process. The criticality control was based on the total fissile mass and fissile concentration. Because the operator recorded the concentration of the uranium precipitate incorrectly, this action led to the first excursion in a large diameter collection vessel. For next 10 h, eight additional excursions occurred	The total fissions was estimated to be 7.9×10^{17}
(12) 12/2/1963, Siberian Chemical Combine (Tomsk), Russia	Uranium purification [equipment design]	A number of process vessels containing both aqueous and organic solutions of uranium (90% enriched) were used for the purification process. In each vessel, a level indicator showed the level of the solution. However, this indicator worked well with aqueous solutions, but not with organic solutions. Since the organic solution is less dense than an aqueous solution, the organic solution was transferred to other vessel via the vacuum system. Over time, a final vessel accumulated excessive organic solution which led to excursions, which lasted for hours	Based on the ^{140}La fission product analysis, the total fissions were about 6×10^{16}

(continued)

Table 4 (continued)

(#) Accident	Operation cause	Description	Total fission
(13) 7/24/1964, United Nuclear Fuel Recovery Plant (Wood River), U.S.	Uranium recovery [operator error]	An operator mistook a highly concentrated uranyl (93% enriched uranium) nitrate solution as trichloroethane as the washing fluid for the solvent extraction columns. The operator pulled this solution into a vessel containing a large quantity (41 L) of sodium carbonate solution. A series of excursions occurred after the combined solution (about 51 L) was stirred automatically	The first excursion was estimated as 1.0×10^{17} to 1.1×10^{7}, with 20% of the combined solution ejected. The total fissions for the entire event were about 1.30×10^{17} to 1.55×10^{17}
(14) 12/16/1965, Mayak Production Association, Russia	Uranium recovery [equipment design]	The residues (90% enriched uranium) being recovered were produced from dissolution, precipitation, and reduction processes. The accident occurred in a dissolution vessel or holding vessel. A total of 11 excursions occurred. The cause of the accident was probably due to unfavorable critical configurations of the vessels	The total fissions for the accident were about 5.5×10^{17}
(15) 12/10/1968, Mayak Production Association, Russia	Plutonium processing [equipment design and operator error]	An unfavorable vessel geometry was used to store a plutonium organic solution. The operator was instructed to pour 35 L of plutonium organic and aqueous solutions into a 60 L vessel. First excursion occurred with 16 L containing 880 g of plutonium ejected. The remaining plutonium in the vessel was about 709 g	The total fissions were about 1.3×10^{17} with the first excursion of about 3×10^{16}
(16) 8/24/1970, Windscale Works, United Kingdom	Plutonium recovery [equipment design]	The plutonium recovery was done using a dissolver, conditioner, and transfer vessel. The criticality accident occurred in the transfer vessel, where excess plutonium solution accumulated, and was well above the criticality limit. A large mass of plutonium accumulated in the vessel over a period of 2 years	The total fissions were about 10^{15}. It lasted for less than 10 s

(continued)

Table 4 (continued)

(#) Accident	Operation cause	Description	Total fission
(17) 10/17/1978, ldaho Chemical Processing Plant, U.S.	Uranium extraction [equipment failure and operator error]	A pulsed column with larger diameter regions at top and bottom of column is used in the uranium solvent extraction phase. Two streams of organics (with a density lighter than aqueous solutions), and the aqueous solutions were flowing in the column. The organic solution containing uranium was extracted in the column. The first cause of accident was the leaking water valve on the make-up tank. The chart recorder had run out of paper and procedures were not followed. The event was caused by the accumulation of the solution over time (~ 1 month)	Total fissions were about 2.7×10^{18}
(18) 9/30/1999, JCO Fuel Fabrication Plant, Japan	Uranium processing [operator error]	A special request to process uranyl nitrate solution at 18.8% enrichment of uranium was done for this operation. The operation had been done routinely for uranium enrichment of up to 6%. Manual pouring of the solution from one vessel to another vessel was performed in the operation. To save time for dissolution, the operators did not follow the procedure, and poured the bucket of solutions to a precipitation vessel with an unfavorable geometry. Eventually excursions occurred	Total fissions were about 2.5×10^{18}

detect radioactivity leakage from primary waste transfer lines into secondary lines, annulus air sampling between the two pipes is conducted. Annulus Sampling Systems are employed for this purpose along waste transfer trenches. Additionally, borehole monitoring is conducted periodically around these facilities to monitor any migration of radionuclides into the environment.

8.1 Radiation Sources and Hazards Associated with Radioactive Waste Management

Waste management facilities designed for the safe handling of radioactive waste adhere to several key principles: delaying and allowing for natural decay; diluting and spreading out waste; recycling and reusing materials where possible; and concentrating and containing waste when necessary. The central goals of radioactive waste management have always been to minimize waste volume and achieve near-zero discharge of radioactivity. The primary objective is to safeguard both present and future generations, as well as the environment, from potential hazards associated with radioactive waste. Effective management involves the regulated application of technology and resources to ensure the protection of the public, workers, and the environment from the harmful effects of radiation. Recent developments, such as the implementation of the "wealth from waste" concept and the separation of actinides to reduce nuclear waste's radiotoxicity, have shifted the focus of radiation protection in waste management. This now includes controlling neutron exposure and internal exposure from actinides, in addition to existing concerns about external exposure from beta and gamma radiation.

General Principles for treatment and disposal of wastes are categorized as given below:

(a) Dilute and Disperse for Low-level Effluents.
(b) Concentrate and store for Medium and High-level waste and
(c) Delay and decay for ^{131}I, ^{135}Xe bearing waste streams.

The major components of High-Level Waste (HLW) are as follows:

(a) Fission product such as ^{90}Sr, ^{106}Ru, ^{137}Cs, ^{144}Ce, ^{147}Pm.
(b) Actinides such as ^{241}Am, ^{244}Cm, un-recovered uranium and plutonium.
(c) Chemicals introduced in reprocessing plant like HNO_3, traces of tri-butyl phosphate, and degraded products.

The wastes originating from reprocessing plants contain activation products such as ^{60}Co, ^{54}Mn, ^{3}H, ^{14}C apart from fission products such as ^{137}Cs, ^{90}Sr. High-level acidic wastes have activity level in the order of 100 Ci/liter, medium-level alkaline waste have activity in the range of 1 Ci/liter and low-level liquid waste have activity in the range of 1 mCi/liter. Major solid wastes handled are hull pieces (left out

cladding material, Zirconium alloy, after dissolution of spent fuel in reprocessing facilities), feed clarification filter bags used for filtration of zirconium fine particles in reprocessing facilities, spent ion exchange resins, off-gas deep-bed filters, and HEPA filters.

8.2 Management of Solid Waste

Radioactive solid waste generated throughout various stages of the nuclear fuel cycle varies widely in materials, sizes, shapes, and degrees of contamination. These wastes are classified based on factors such as radiation intensity, concentration, and type of radioactivity. They are further sorted into categories such as compressible or non-compressible, and combustible or non-combustible. A significant portion of the total solid waste consists of low-activity materials, which are typically either combustible or compressible. Specially designed incinerators are utilized to burn combustible waste, resulting in a volume reduction of approximately 50. Additionally, hydraulically operated baling presses are employed to compress low-activity non-combustible waste, effectively reducing its volume.

The solid wastes are segregated, tagged, and disposed appropriately as per the waste categorization procedures. Typical description of shallow land disposal structures is as given below

- Brick walled trenches: It has typical dimensions of about 20 m $\times$ 10 m at top and 15 m $\times$ 5 m at the bottom and about 3 m deep. Solid wastes with dose rate of up to 0.2 mGy/h are normally disposed in such trenches.
- RCC Trench: It is an engineered disposal facility built underground or above ground with thick RCC side walls and bottom. It has typical dimensions of about 15 m (L) $\times$ 2 m (W) $\times$ 2.0 m (depth). These trenches are covered with RCC slabs so that radiation dose on contact is less than 10 μGy/h. Finally waterproofing of the top and sides are provided to avoid ingress of rainwater. Solid wastes with dose rate up to 0.5 Gy/h are normally disposed in these trenches.
- Tile Hole: Tile hole is a cylindrical concrete lined steel container with top open and located totally below ground level. Typical dimensions are depth of about 5 m and internal diameter of about 1 m. Solid wastes with dose rate above 0.5 Gy/h are disposed in these trenches. Generally, high-level solid waste like hulls removed after dissolution in a reprocessing facility which are also highly contaminated with alpha emitters are stored in tile holes for extended storage.

8.3 Management of Liquid Waste

In a reprocessing plant using PUREX process, spent fuel is chopped and dissolved in nitric acid. Plutonium and uranium are separated from fission products, purified, and then converted to respective oxide forms. High-level Liquid Wastes generated

at reprocessing plants from first cycle raffinate contain almost 99.9% of the entire radioactivity originally associated with the spent fuel. These streams are acidic in nature with 3–4 M nitric acid and having gross beta-gamma activity in the order of 100–200 Ci/liter. High-level liquid wastes are stored in stainless steel tanks in liquid form before sending for vitrification for converting to vitrified glass product for long-term storage in Advance Vitrification System (AVS). An Advanced Vitrification System (AVS) handles million curies of fission products remotely in hot cells in order to obtain vitrified waste in canisters which are packed in over packs for long-term storage. In AVS, Joule Heated Ceramic Melter (JHCM) is used for glass formation at high temperature using glass frits for vitrification of this high-level radioactive liquid waste. AVS has several engineered safety features such as shielding, ventilation, containment, and remote operations. These features aim at reducing exposure to plant personnel and keeping the release of radioactive materials to environment below the limits prescribed by the regulatory authority. The vitrified waste canisters containing vitrified waste in glass form (of activity of the order of few lakh curies) are safely stored in underground shielded vaults.

Intermediate-level Liquid Wastes generated at reprocessing plants are evaporator concentrates, solvent washes, and rinses. The wastes are alkaline in nature and have considerable salt loading. These wastes have Gross Beta-Gamma activity up to 100 mCi/liter and the associated alpha activity (^{239}Pu). The process consists of a batch pre-treatment step of plutonium-precipitation followed by continuous Ion Exchange treatment for removing ^{137}Cs and ^{90}Sr isotopes. The high active elute which is expected to be around 8% of the ILW treated is sent to HLW treatment system. The sludge from the pre-treatment step after dissolution is recycled back to reprocessing plant for recovery of heavy metals. The acidic wastes from reprocessing plants will be neutralized and directly put in the IX Treatment system.

Low-Level Liquid Wastes (LLLW) generated at reprocessing plants and from other nuclear facilities are discharged into the environment through authorized aquatic route. Major sources of Low-Level Liquid waste are the condensates from waste evaporation cycle, potential active drains, and washings which are collected in delay tanks and further diluted before discharged into the environment. ^{238}U and ^{239}Pu contribute alpha activity, whereas gross beta activity is mainly due to presence of ^{137}Cs, ^{90}Sr/^{90}Y, ^{106}Ru, and traces of other fission products including ^{99}Tc which even in LLLW of a reprocessing plant is required to be quantified. As ^{99}Tc is a beta emitting long-lived fission product ($T_{1/2} = 2.13 \times 10^5$ years) with E_{max} = 293 keV and due to its anionic behavior and high mobility, it is considered as one of the most important radionuclides from waste management point of view-considering environmental impact. ^{99}Tc is estimated using either solvent extraction method using Tetra phenyl arsonium chloride (TPAC) as a solvent to extract ^{99}Tc followed by Liquid Scintillation Counting or by co-precipitation method followed by beta counting. Liquid wastes with low levels of activity containing ^{90}Sr and ^{137}Cs as major radionuclides are treated by co-precipitation using chemicals like barium chloride, sodium sulfate, potassium ferrocyanide, copper sulfate, etc. Subsequent to precipitation, the resultant sludge from clarifloculator is further concentrated by decantation, filtration, and centrifugation. The resulting solids containing bulk of the

radioactivity originally present in the liquid waste are immobilized in cement matrix before disposal. The low-level liquid effluents are released to the environment after ensuring that activity levels are well below the authorized discharge levels by the regulatory authority.

9 Conclusion

The radiological exposures in nuclear fuel cycle facilities differ from one facility to another, depending on the type of radioactive material being handled and its various forms during different operations. It is crucial to thoroughly study and implement the specific operational health physics aspects of each facility in order to achieve excellence in radiation protection. In this manuscript the radiological safety aspects of nuclear fuel cycle facilities have been highlighted with the objective of not only controlling personnel exposures according to the ALARA principle but also minimizing the environmental impact as much as possible. Additionally, a review of several criticality accidents that have occurred in reprocessing facilities is done to emphasize the importance of providing adequate training to radiation workers regarding the potential radiological exposures associated with each stage of operation in nuclear facilities.

References

1. Table of Radionuclides, Monographie BIPM-5, vols 1–6 (2004–2011)
2. American Conference of Governmental Industrial Hygienists (ACGIH) (2021) Documentation of the threshold limit values (TLVs) and biological exposure indices (BEIs)
3. Occupational Safety and Health Administration (OSHA) (2023) Occupational chemical database. Department of Labor, United States. https://www.osha.gov/chemicaldata/ (2019). Accessed on 12 Dec 2023
4. Barsan ME (2007) NIOSH pocket guide to chemical hazards
5. Occupational intakes of radionuclides. ICRP Publication 137, Part 3, vol 46 (2017)
6. Pushparaja (2019) Radiological protection and safety—a practioner's guide. Notion Press, Chennai, India
7. Safe handling and storage of plutonium, safety reports series no. 9. International Atomic Energy Agency Vienna (1998)
8. McLaughlin TP, Monahan SP, Pruvost NL, Frolov VV, Ryazanov BG, Sviridov VI (2023) A review of criticality accidents 2000 revision. United States. https://doi.org/10.2172/758324. Accessed on 12 Dec 2023
9. Bixler NE et al (2017) Review of spent fuel reprocessing and associated accidental phenomena. U.S. Nuclear Regulatory Commission, NUREG/CR-7232

Radiation Environment in Industrial and Research Facilities

Sridhar Sahoo and T. Palani Selvam

1 Introduction

Ionising radiation has registered a phenomenal growth all over the world for a wide variety of peaceful purposes in industry, medicine, agriculture and research. Radioisotopes and radiation technology contribute significantly to the growth in industry. The industrial applications include finding defects in radiography testing, determination of process parameters using nucleonic gauges, X-ray baggage scanning systems at sea ports, land ports and airports, scanning cargo, irradiation of food and other allied products, etc. Radioisotopes have a wide spectrum of applications in research studies, especially in physio-chemical, bio-medical, agricultural, veterinary sciences, pharmaceuticals and industrial research. Unsealed radiation sources of different strengths and physical forms are handled in such studies in open fields as well as in laboratories. This could cause radiation incidents/accidents like surface contamination and air-borne contamination. Apart from these probable incidents, research activities in these fields generate radioactive wastes of different magnitudes, from simple laboratory swipes to animal carcasses. Hence, handling of radiation sources in such applications necessitates supervision from a radiological safety standpoint. Different types of radiation sources with activity ranging from several kBq to few MBq are being used in research applications. These include mainly ^{3}H, ^{14}C, ^{35}S, ^{32}P, ^{125}I, etc. Although the activity of sources used in research applications is very small, these sources will still have the potential to cause significant radiological hazards and contamination, if they are not handled safely. In this Chapter, applications of ionising radiations in the above-mentioned industrial applications and research areas where the radiation sources are used, are discussed.

S. Sahoo (✉) · T. Palani Selvam
Radiological Physics and Advisory Division, Bhabha Atomic Research Centre, Mumbai 400085, India
e-mail: ssridhar@barc.gov.in

D. K. Aswal (ed.), *Handbook on Radiation Environment, Volume 2*,
https://doi.org/10.1007/978-981-97-2799-5_9

2 Industrial Radiography

The industrial radiography is an indispensable, versatile and well-established non-destructive testing (NDT) technique for quality assurance in all types of industries. Varieties of industrial gamma radiography exposure devices (IGREDs), commonly known as radiography camera, are being deployed for carrying out radiography work. These devices shall incorporate built-in-design safety features, interlocks and effective locking mechanisms to ensure that the operation, servicing and maintenance meet acceptable standards of safety. NDT can help to prevent the failures of engineering structures that could have an adverse impact on safety and reliability in industries as well as the environment. Industrial radiography testing is an important non-destructive testing technique and it is widely used in industry for inspection of welds, castings and assemblies. Industrial radiography uses ionising radiation (X-rays, gamma rays or neutron sources) to locate defects such as cracks, flaws, etc. (Fig. 1). Radiography ensures the structural integrity, quality of equipment and structures such as vessels, pipes, welded joints, castings, etc.

Exposure devices are classified according to the location of the source assembly when the device is in the working position (working position means the condition of the source assembly in the industrial gamma radiography exposure device at the position intended for the performance of industrial gamma radiography [1].

Category I

The exposure device which does not allow the source assembly to be moved out of the source housing, but causes exposure by opening a shutter and/or by moving the source assembly within the device.

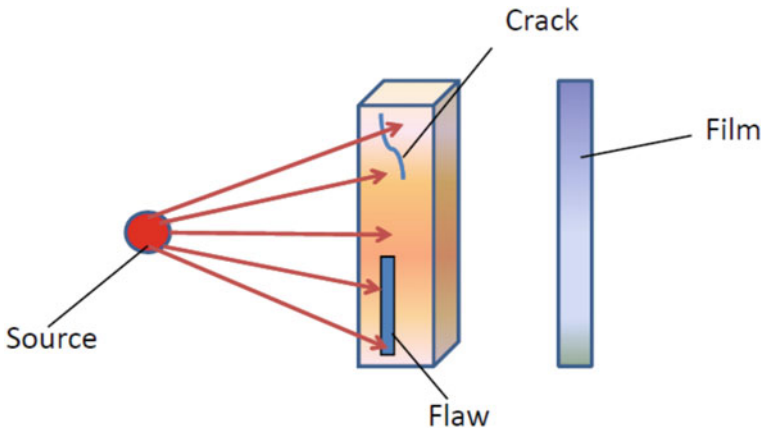

Fig. 1 A schematic diagram of radiography testing

Category II

The exposure device in which the source assembly is driven out of its secured position in the source housing to an essentially unshielded position at its working position for radiography exposure, either mechanically, electrically, pneumatically or by other means by an operator at a distance away from the source housing. This type of exposure device using a remote control (remote control means a device enabling the source assembly to be moved to and from the exposure device to the working position by operation from a distance away from the exposure device) mechanism shall also require a source guide tube.

Category-X

Exposure devices for gamma radiography are designed for special applications where the unique nature of the application precludes full compliance with this standard. These are self-propelled intra-tubular gamma radiography exposure devices such as pipeline crawler and gamma radiography exposure devices for underwater use.

Depending upon mobility, the exposure devices are classified as below [1]:

Class P: Portable source housing designed to be carried by one person only. The gross weight of a portable exposure device shall not exceed 30 kg.

Class M: Mobile, but not portable, source housing designed to be moved easily by suitable means, such as caster wheels or a trolley provided for the purpose, but does not qualify for portable category.

Class F: The exposure device designed for installation in a fixed location or with mobility restricted to the confines of a particular working area.

Radiography technique utilises sealed gamma sources such as ^{192}Ir, ^{60}Co, ^{75}Se and ^{169}Yb contained in IGRED and X-rays as source. These artificially produced gamma sources have many advantages over X-ray machines since they are compact, rugged, and ideal for field work and doesn't need electricity. These ^{192}Ir and ^{60}Co source-based IGREDs are the backbone of radiography practise and cover inspection of a range of 15–175 mm of steel equivalents [2]. Recently ^{75}Se source has been widely used for radiography of low thickness jobs (4–30 mm of steel) due to better image quality, little longer half-life in comparison to ^{192}Ir, lower exposure rate constant which requires lesser cordon area and more operator safety. Figure 2 presents the schematic diagram of an industrial radiography camera and accessories. Table 1 presents the commonly used sources in radiography and their properties [3].

Radiography can be carried out using X-rays from industrial X-ray units or from high-energy linear accelerators. Industrial X-ray machines in the range of 50–400 kV are used for inspection of metal thicknesses up to 7.5 cm steel equivalents. Electron linear accelerators up to 30 MV are used for radiography of thick concrete or composite materials made of concrete, lead and steel [2].

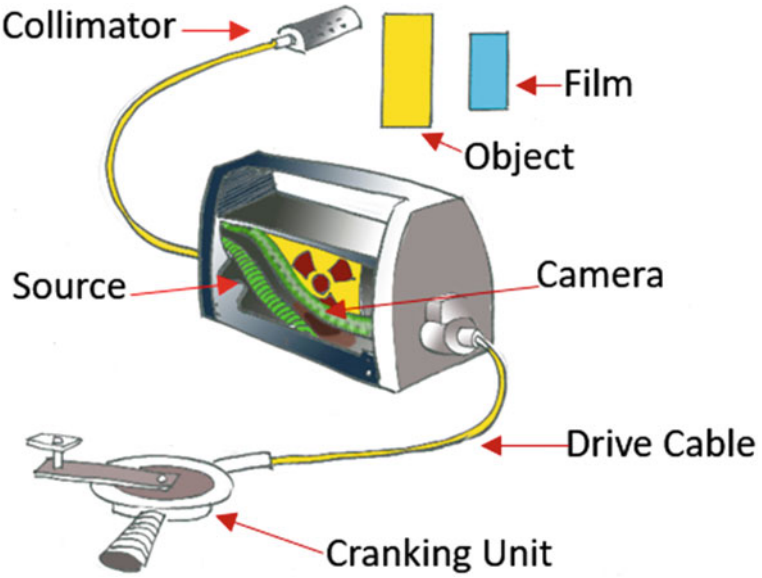

Fig. 2 Schematic diagram of an industrial radiography camera with accessories

Table 1 Commonly sources used in radiography and their properties [3]

Source	Half-life	Exposure rate constant (R/h/Ci at 1 m)	Inspection range in steel (mm)	Energy of gamma rays (keV)
^{60}Co	5.25 years	1.33	40–200	1170 and 1330
^{192}Ir	74.8 days	0.48	20–70	200–800
^{75}Se	120 days	0.215	4–30	9–400
^{170}Tm	128 days	0.003	2–12	50–90
^{169}Yb	32 days	0.125	2–10	60–300

2.1 Radiography Exposure Devices Used Worldwide

Table 2 presents the parameters/specifications of a few radiography cameras used across the world for industrial radiography purposes. These camera models use either ^{192}Ir, ^{60}Co or ^{75}Se source and are designed and developed as per various international standards. These exposure devices use mainly high atomic number materials or a combination of materials such as stainless steel (SS), lead, depleted uranium (DU) and tungsten as shielding materials. These radiography equipment/cameras satisfy the safety requirements mentioned in various international and national documents [4–8].

Table 2 The radiography camera models available worldwide

Specifications/ parameters	ROLI-2	INC IR-100	Sentinel SCARPro	COCAM-120	SPEC-300	Sentinel delta-880
Isotope	^{192}Ir	^{192}Ir/^{75}Se	^{75}Se	^{60}Co	^{60}Co	^{192}Ir/^{75}Se/ ^{169}Yb
Maximum capacity	2.4 TBq (65 Ci)	4.44 TBq (120 Ci)	3 TBq (81 Ci)	4.4 TBq (120 Ci)	11.1 TBq (300 Ci)	150/150/ 108 (Ci)
Shielding material	Lead and heavy alloy	DU	Tungsten and SS	DU, tungsten and lead	DU	DU
Package	Type B(U)	Type B	Type A	Type B(U)	Type B(U)	Type B(U)
Weight (kg)	38	24.1	16.8	316	354	23.6
Category	Mobile	Portable	Portable	Mobile	Mobile	Portable
Country of origin	India	USA	USA	India	USA	USA

2.2 Neutron Sources

Radiography carried out with the help of neutrons is called neutron radiography or neutron imaging. Neutron radiography is widely used in the inspection of nuclear fuel elements, aerospace industry, space programmes, inspection of ordnance and explosives, etc. The unique advantage is its ability to reveal light elements. Neutron radiography provides different images than X-rays or gamma rays. This is due to different types of interactions in materials, i.e. neutron interacts directly with the nucleus whereas X-rays and gamma rays interact with orbital electrons. Neutron attenuation is generally higher in low Z materials and hence it is absorbed by hydrogenous materials such as plastics, water and oils. Many metals such as lead and steel allow most neutrons to pass through them.

Neutron sources used in neutron radiography are ^{241}Am-Be, ^{252}Cf, electrically driven D-T reactions in vacuum tubes and thermal neutron beams from nuclear reactor. Alpha particles emitted from ^{241}Am interact with beryllium (^{9}Be) nuclei and produce neutrons with an average energy of 4.3 meV ($E_{\max} = 11$ meV). In ^{252}Cf source, neutrons with an average energy of 2.1 meV are produced by spontaneous fission. In D-T fusion reaction (equation given below), neutrons of energy 14.06 meV neutrons are produced, when high-energy deuterium ions from accelerators are bombarding tritium target.

$$ {}_{1}^{2}H + {}_{1}^{3}H \rightarrow {}_{2}^{4}He(3.52\,\text{MeV}) + {}_{0}^{1}n(14.06\,\text{MeV}) \quad (1) $$

3 Nucleonic Gauges

In industry, a number of physical parameters are determined by using nucleonic gauges also known as ionising radiation gauging devices containing sources of ionising radiation, i.e. charged particles (alpha and beta rays); gamma rays, X-rays, and neutrons. Nucleonic gauges are used for online industrial process control and quality control parameters. These include measurement of the level of product in huge silos, tanks, density measurement, moisture content of soil, thickness measurement of steel plate, paper, film, concentration of hydrocarbons, ash content in coals, exploration of coal and oil and so on. Different types of radiation sources with activity ranging from several MBq to a few GBq are being used for this purpose depending on the applications and characteristics of sources. These include mainly ^{241}Am, ^{85}Kr, ^{90}Sr, ^{147}Pm, ^{55}Fe, ^{109}Cd, ^{60}Co, ^{137}Cs, ^{241}Am-Be, ^{252}Cf, etc. Although the activity of sources used in nucleonic gauges is very small, they have a reasonably long half-life, and therefore the sources would still have the potential to cause significant radiological hazards, if they are not handled safely and not provided adequate physical security during their use, transport and storage. Nucleonic gauges are ideal instruments designed for adverse industrial environments, including high-temperature and high-pressure conditions. Table 3 presents common radiation sources used in nucleonic gauges and their uses. As these systems contain radioactive material, the use and possession of the nucleonic gauges need to be regulated by regulatory authorities.

3.1 Principle of a Nucleonic Gauge

The basic principle of nucleonic gauge depends on the interaction of radiation with matter such as radiation is attenuated, absorbed, or back scattered when it travels through material. A nucleonic gauge consists of a suitable source (gamma, beta, alpha, neutron, bremsstrahlung radiation), selected based on the parameters to be measured such as range, density of the material, sensitivity, etc.

Detectors such as ionisation chamber, scintillation counter, G. M. counter and semiconductor detector are selected based on the source used in the nucleonic gauge. Scintillation counter or semiconductor detector is used when spectrometry is necessary. For accurate measurement with quick response, an ionisation chamber or a scintillation counter is used. For fixed gauges, when accuracy is not required, a G. M. counter is used. Different types of gauges, sources used and their principle of working are described below.

Table 3 Commonly used radiation sources in nucleonic gauges, their physical properties and uses

Isotopes	Half-Life	Energy (MeV)	Uses
Gamma sources			
^{60}Co	5.27 years	1.33, 1.17 meV	Measurement of level of process vessels, thickness of metal plates, density of road, ores and rocks
^{137}Cs	30 years	0.662 meV	
^{241}Am	458 years	60 keV	
^{133}Ba	10 years	0.357, 0.3, 0.082 meV	
^{124}Sb	0.16 years	2.1, 1.7, 0.65, 0.61 meV	
Beta sources			
^{147}Pm	2.6 years	$E_{max} = 0.230$	Thickness of thin sheets, light paper and plastic, heavy paper, thin metal, rubber, coating thickness on metal
^{204}Tl	3.76 years	$E_{max} = 0.77$	
^{85}Kr	10.6 years	$E_{max} = 0.67$	
^{90}Sr/^{90}Y	28 years	$E_{max} = 2.27$	

Source and target	Half-life	Predominant energy	Uses
Bremsstrahlung sources			
$^{3}{}_{1}$H-$_{40}$Zr	12.2 years	4–8	Measurement of thickness, density of aluminium and iron sheets
^{147}Pm-$_{13}$Al	2.6 years	12–40	
^{85}Kr-$_{6}$C	10.6 years	20–80	
^{90}Sr-Y/$_{82}$Pb	28 years	40–140	

Source	Half-life	Dominant X-ray or gamma energy (keV)	Uses
Isotopes used for XRF gauging			
^{55}Fe	2.6 years	5.9 keV	Analysis of minerals, ores and alloys, determination of coating thickness on metal sheets, sulphur, lead content in hydrocarbon
^{109}Cd	1.3 years	22 keV	
^{125}I	57.4 days	27 keV	
^{153}Gd	236 daya	41 keV	

Isotopes	Half-life	Energy	Uses
Isotopes used for alpha gauging			
^{210}Po	138 days	5.3 meV	Measure thickness of thin film, composition of ammonia in an ammonia plant, methane content in a coal mine and elimination of static charge in silk yarn
^{239}Pu	24,300 years	5.15 meV, 5.13 meV, 5.10 meV	
^{241}Am	458 years	5.48 meV, 5.44 meV, 5.38 meV	

Source	Half-life	Yield (n/s/Ci)	Uses
Neutron isotopic sources used for gauging			
^{210}Po-Be	0.379 years	3×10^6 n/s/Ci	Moisture measurement and oil to water content in well logging
^{239}Pu-Be	24,300 years	1.6×10^6 n/s/Ci	
^{226}Ra-Be	16,200 years	1.7×10^7 n/s/Ci	
^{241}Am-Be	458 years	2.7×10^6 n/s/Ci	
^{124}Sb-Be	0.164 years	1.0×10^6 n/s/Ci	
^{252}Cf (fission source)	2.65 years	2.3×10^9 n/s/mg (531 Ci/g)	

3.2 *Classification of Nucleonic Gauges*

The nuclear gauges are classified as continuous gauges (to monitor the product online) and static gauges. Static gauges are (a) Fixed gauge used in an industry to measure the thickness of a sheet and (b) Portable gauge used in construction industries to measure the moisture and the density using suitable gamma and neutron emitters.

3.2.1 Gamma Gauges

Gamma gauges are used to measure thickness of steel sheets and plates in industries during the manufacturing process. It is also used to monitor fluid levels in large process storage tanks, individual cans in assembly line, continuous monitoring of the fuel level in rockets and monitoring of level in molten glass in glass and ceramic industries. Gamma gauges are used to measure the density of solid or liquid material flowing inside a pipe. A schematic diagram of gamma gauges using transmission principle is presented in Fig. 3.

Gamma back-scattering gauges are also used to determine the wall thickness of a boiler, density of soil, metal sheet thickness (up to 12 mm of steel) and coating thickness of one material on the other (Fig. 4). Since gamma radiation has more penetrating power than the alpha and beta, more thickness and higher density material can be checked with gamma gauges. ^{60}Co, ^{137}Cs and ^{241}Am sources are widely used in gamma gauges.

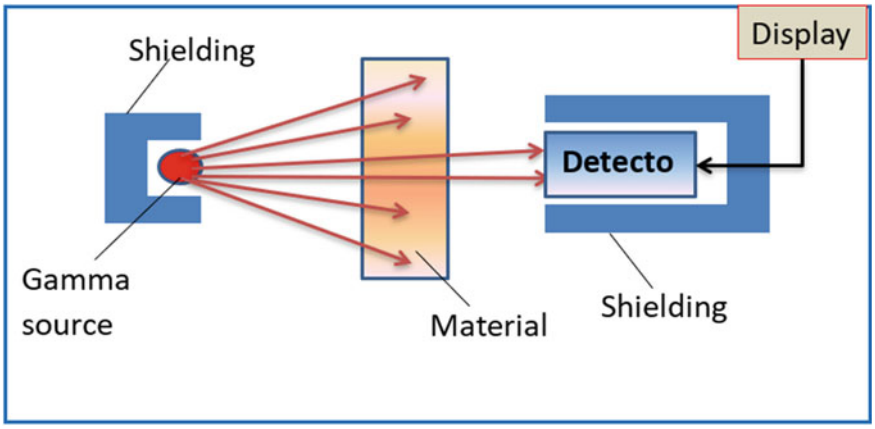

Fig. 3 Gamma gauges using transmission principle

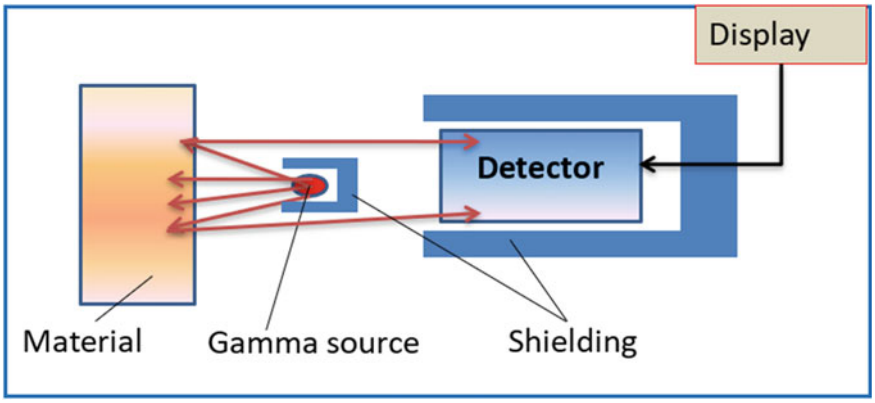

Fig. 4 Gamma gauges using back-scattering principle

3.2.2 Beta Gauges

Beta gauges are widely used in gauging application for measurement of density thickness in the range of 0–1300 mg/cm^2. Beta transmission gauges are used to measure the thickness of paper, plastic and metal foil, plastic films, measurement of density of solid or liquid, hydrogen content in hydrocarbon liquids, etc. A schematic diagram of beta gauges using transmission principle is presented in Fig. 5.

Beta back-scattering gauges are used to determine the coating thickness of one material on another, such as zinc coating in the galvanising sheet, determining the composition in the bi-metal alloys, etc. The beta source should be a pure beta emitter with long half-life and high specific activity. The sources preferred in beta gauges are ^{85}Kr, ^{147}Pm, ^{204}Tl and ^{90}Sr-^{90}Y.

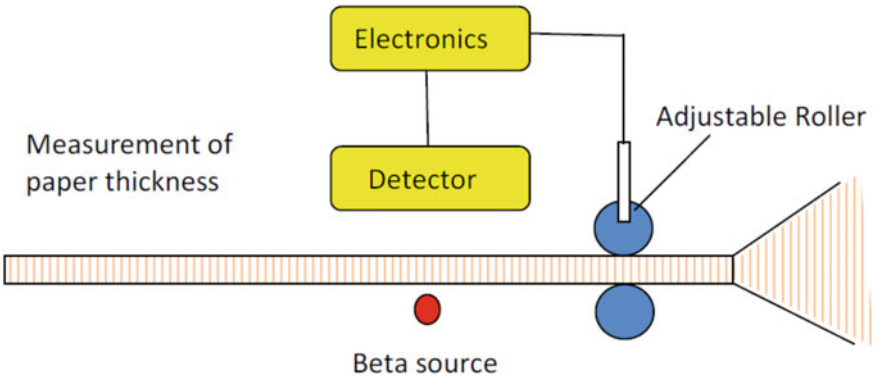

Fig. 5 Beta gauges using transmission principle

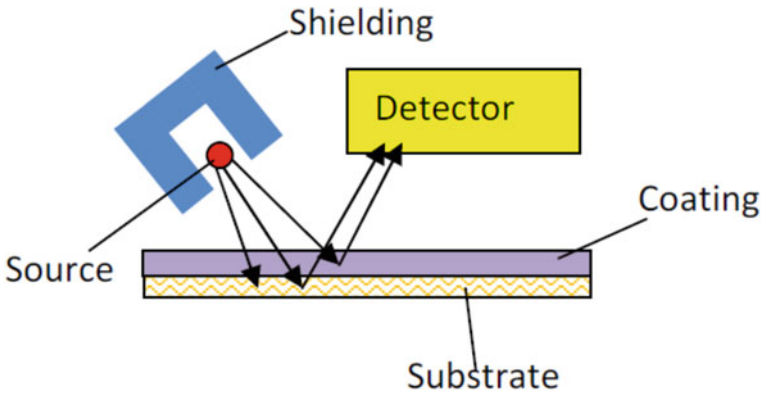

Fig. 6 Coating thickness measurement by XRF method

3.2.3 Bremsstrahlung Gauges

Bremsstrahlung gauges uses beta sources and suitable target (^{3}H-$_{40}Zr$, ^{147}Pm-$_{13}Al$, ^{90}Sr-Y-$_{82}Pb$, etc.) to produce bremsstrahlung radiations. These gauges are similar to beta gauges and are used for determination of thickness and density of aluminium and iron sheets in the industry.

3.2.4 X-ray Fluroscence (XRF) Gauges

XRF gauges use low energy X-rays or gamma sources such as ^{55}Fe, ^{109}Cd, ^{125}I and ^{153}Gd for analysis qualitative or quantitative analysis of the element (Fig. 6). These X-rays or gamma rays knock down orbital electron of the element to be analysed and characteristic X-rays are produced which are unique to that element. XRF gauges are used for (a) analysis of minerals, ores and alloys, (b) determination of coating thickness, (c) sulphur and lead content in hydrocarbon, (d) positive material identification (PMI) testing.

3.2.5 Alpha Gauges

In alpha gauges, alpha sources (^{210}Po, ^{241}Am) are (i) used to measure thin film thickness, (ii) composition of ammonia in an ammonia plant, (iii) to monitor the methane content in a coal mine and (iv) used for elimination of static charge in silk yarn production industries or explosive industries. The decrease in energy of alpha particles in matter, through which it passses, is a measure of thickness and is measured with the help of an ionisation chamber.

3.2.6 Neutron Gauges

Neutron gauges are widely used in moisture measurement in soil, rock, well logging and exploration of minerals and ores (Fig. 7). Neutrons from ^{241}Am-Be source, ^{252}Cf, 14.1 meV neutrons from D-T accelerators are generally used in neutron gauges and various useful parameters are measured through moderation, transmission and activation of neutrons.

In neutron-neutron logging, the neutrons from ^{241}Am-Be source are slowed down in the surrounding media and the thermal neutrons are detected by BF_3 counter. The neutron-neutron logging technique is used for (a) determination of moisture content and porosities of soil and elemental analysis in rocks, (b) Assaying of high thermal neutron capture cross-section elements such as B, Li, Cd rare earths, etc.

In neutron-gamma logging, high-energy gamma rays from neutron capture in the surrounding media (chlorine in water) are emitted, is used to locate the oil–water interface. The gamma spectrometry through integral n-γ logging is used to find the elements such as Al, Cl, Mn, Fe and Ni present in oils. 14.1 MeV neutron generators (D-T) are used for the determination of carbon to oxygen ratio, i.e. oil to water content in well logging applications. A list of application is presented in Table 3.

3.3 Radiation Safety in Nucleonic Gauges

The activities involved in the nucleonic gauges are in the range of few μCi to Ci and they are self-shielded, and provided with maximum built-in safety features. It is also mandatory that the nucleonic gauges must comply with the requirements of relevant International Standards and types approved by regulatory authority of the user country [9–11]. The radiation source and source housing must satisfy various types of tests to withstand during normal use and accidental conditions [11]. The

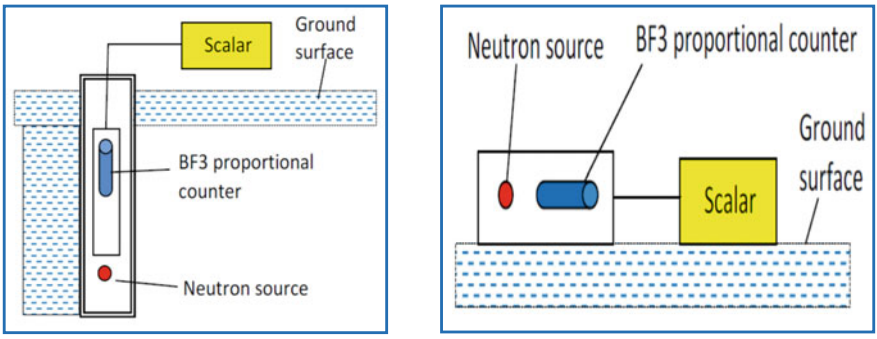

(a) **(b)**

Fig. 7 **(a)** Sub-surface and **(b)** surface neutron gauges for measurement of moisture content of soil

user must provide adequate physical protection to nucleonic gauges, by preventing unauthorised access, periodic maintenance and quality assurance by trained and authorised individuals. In addition to these, comprehensive radiation protection programmes such as availability of a qualified Radiological Safety Officer and radiation monitoring instruments must be provided by the user.

4 Radiation Processing of Food and Allied Products

Radiation processing is one of the technologies that are useful to preserve food and to make it safe for human consumption. Radiation processing of food involves controlled irradiation of food products from gamma rays (^{60}Co or ^{137}Cs), electron beam up to 10 meV energy and X-rays up to 7.5 MV [12–15].

The energy from ionising radiation is absorbed by food and microorganisms which leads to ionisation of the water and other biologically important molecules. The damage to DNA is mainly responsible for death of microorganisms which results in extension of shelf life of foods as well as ensures its safety from pathogens. It also results in death of insects thus achieving disinfestations. By treating various foods with different doses ranging from as low as 100 Gy to as high as 10 kGy, radiation processing can achieve sprout inhibition in tubers, bulbs and rhizomes, disinfestation of cereals, pulses, dry fruits and dried fish, disinfestation of fruits and vegetables for quarantine, shelf life extension of perishable products like fish and meat, elimination of parasites and pathogens in food and decontamination of spices and herbal products [16].

Radiation processing is used to preserve food without causing perceptible changes in the quality of food. Extensive studies have established the toxicological, microbiological and nutritional safety of radiation processed foods [13]. This processed food is checked for any induced radioactivity, presence of any pathogens or their toxins, mutagenic or carcinogenic radiolytic products and nutritive.

4.1 Sources Used in Radiation Processing of Food and Allied Products

^{60}Co and ^{137}Cs gamma sources meet the requirements for radiation processing of food and allied products.^{137}Cs is not used in industrial processing due to its many disadvantages such as caesium chloride is highly dispersible, water soluble and extremely toxic in nature and has a half-life of 30 years.

^{60}Co source is widely used in radiation processing industry due to the ease of production in nuclear reactors. The gamma rays (photons) are able to penetrate deeper into materials since they have no mass. The gamma rays from ^{60}Co source are also used for sterilisation of medical products and hygienisation of dry sewage sludge.

As a result, gamma radiation is suitable for irradiation of non-uniform and high density (thicker) materials. Bremsstrahlung X-rays generated from X-ray machines with energy up to 7.5 MeV are also used in radiation processing.

Cross-linking of wires, cables and rubbers and colouration of diamonds and precious stones are also possible using 2 MeV electron beam [17–19]. Electron beams up to 10 MeV energy from linear accelerators, to eliminate the risk of inducing radioactivity, are also used for irradiation of different food and medical products. The disadvantage of electron beam is the penetration limit, as mass of electron is very small. The range of 10 MeV electron in a unit density material is approximately 38 mm whereas the range of gamma rays from ^{60}Co source is approximately 300 mm. Electron beam is best suited for low density, uniformly packaged products.

4.1.1 Gamma Irradiator Types

Gamma irradiators are divided into two types based on the shielding cover provided to the source when in use and when not in use: (a) Self-contained irradiators (category I &III), and (b) Panoramic irradiators (category II and IV).

4.1.2 Self-contained Irradiator (Category I and III)

In Self-contained dry source storage, gamma irradiators (**Category I**) are specially designed for radiation research and hospitals/blood banks. These irradiators are commercially known as Gamma Irradiation Chambers (GIC) /Gamma Chambers/ Blood Irradiators and mainly house either ^{60}Co or ^{137}Cs radiation sources of activity in the range from tens to hundreds of TBq. Blood Irradiators are used for irradiation of blood and blood products/components in hospitals and blood banks for clinical and research purposes. The source is always enclosed in a dry container and is shielded at all times and can be installed in an existing laboratory. Human access to the sealed source and the volume undergoing irradiation is not physically possible in the designed configuration. In category III wet source storage irradiator, the sealed source is contained in water filled storage pool and is shielded at all times. Human access to the sealed source and the volume undergoing irradiation is physically restricted in the designed configuration and proper mode of use.

4.1.3 Panoramic Irradiator (Category II and IV)

In Panoramic, category II dry source storage irradiator, the sealed source constructed of solid materials is enclosed in a dry container, is fully shielded when not in use and is exposed within a radiation volume for use. Human access to the radiation volume is maintained inaccessible during use by an entry control system. In category IV Panoramic, wet source storage irradiator, the sealed source is contained in water filled storage pool and is fully shielded when not in use and is exposed within a

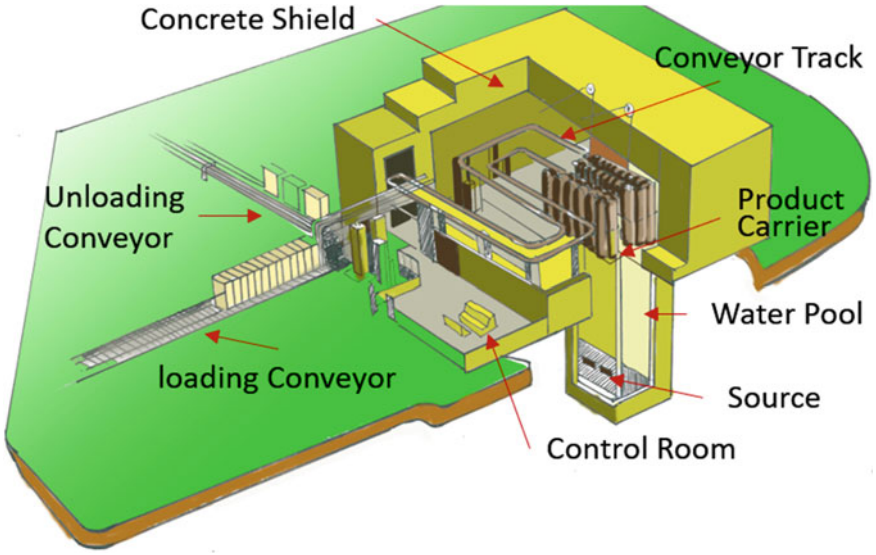

Fig. 8 Panoramic category IV wet source storage irradiator

radiation volume for use [20]. Human access to the radiation volume is maintained inaccessible during use by an entry control system.

Panoramic irradiators are more suitable for pilot-scale and full commercial-scale operations. The source is in the form of a rack or cylinder and consists of several ^{60}Co pencils. The source pencils are surrounded by several product containers irradiated simultaneously (Fig. 8).

4.2 Radiation Safety in Radiation Processing Facility

The activities of the sources used in processing facilities are in the order of PBq and the power of beam in electron accelerators is in the order of kW. Any type of accident/exposure will lead to serious health consequences/death to the exposed person. Hence, there is a necessity of stringent regulations in RPFs. It is necessary that the plants shall be designed, constructed and commissioned in line with mandatory safety requirements mentioned in international safety codes and standards [20–23]. It is the utmost duty of the owner to ensure a high standard of safety and reliability in the operation and maintenance of facilities, radiation monitoring instruments, employing qualified manpower such as RSO, operators for safe operation of plant, emergency response plans and preparedness, etc.

5 Container Scanning Facilities

Ionising radiations (X-rays and gamma rays) are widely used for scanning purposes which includes scanning of consignments, baggage, whole cargo, etc. X-ray baggage scanning is the investigation system regularly utilied for security screening of small baggages at airports, railway stations, shopping malls, etc.

The cargo imaging inspection systems are aimed at finding illegal goods, such as weapons, explosives, drugs, smuggled goods, etc. through the imaging of large cargo containers. The cargo scanning in the sea ports increases revenue collection for Customs. The scanning systems installed in the border increase the security and protection of the country.

Cargo scanning system utilises 6–9 MV X-rays from linear accelerator (LINAC) and ^{60}Co radioactive source for scanning of cargo containers. The scanned image is presented in Fig. 9. The scanning may be accomplished by moving the cargo vehicle in between the fixed X-ray source and detector array or vice-versa. Table 4 presents typical energy and radiation source used for various scanning systems.

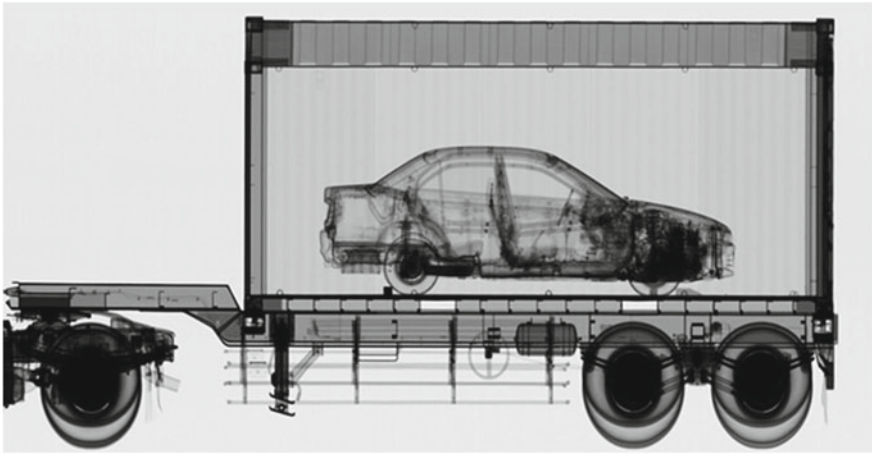

Fig. 9 Scanning image of a Cargo [24]

Table 4 Typical energy and radiation source used for various scanning systems

S. No.	System type	Energy and source used
1	Postal parcel inspection system	60–80 kV X-rays
2	Small and medium baggage inspection systems	110–160 kV X-rays
3	Large cargo consignment inspection systems	160–220 kV X-rays
4	Container scanners	6–9 MV X-rays and ^{60}Co

Fig. 10 Gamma-ray image of a truck showing goods inside a shipping container [25]

5.1 Classification of Container Scanners

Container scanners are basically classified according to the use of the energy source (isotope or X-ray based). The classification is also done on the basis of operation (drive by and drive through) and mobility of the scanning system.

5.1.1 Radioisotope Based Scanning Systems

Radioisotope based scanning systems generally uses ^{60}Co radioactive source of activity 37 GBq–1.1 TBq and a vertical tower of gamma detectors. The photons from ^{60}Co source are able to penetrate up to 15–18 cm of steel and these systems provide good quality images which can be used for identifying cargo and detecting anomalies (Fig. 10). These scanners are used by customs officials at borders and sea ports.

5.1.2 X-ray Based Scanning Systems

LINAC-based Vehicle Scanners: LINAC-based scanning systems use a high-energy bremsstrahlung spectrum (X-rays) having energy in the 4–9 MV range produced in a linear accelerator (LINAC). These high-energy X-rays can penetrate up to 30–40 cm of steel in vehicles moving with velocities up to 13 km/h. Such systems are available in various modalities like fixed, mounted on road vehicles or rails. This system is more suitable for the detection of special nuclear materials.

X-ray tube-based vehicle scanners: X-ray tube-based vehicle scanners generally consists of one X-ray tube, normally operated at a potential of 150–250 kV and 15 mA tube current, works on back-scattering principle (tube and detectors are installed on the same side) for imaging of suspicious vehicles, passenger vehicles, etc. These types of scanners are mounted on a road vehicle and scan the stationary suspicious vehicle /object.

The scanners are also classified as drive by and drive through from an operation point of view. In drive by mode, the crew members of the vehicle have to get down and wait in a designated area till the scanning process is completed. In this case, the crew members get negligible dose due to the scanning process. In drive through scanning mode, the crew members of the vehicle remain in the cabin and are exposed to few μSv of dose because of primary radiation. These systems have advantage of high throughputs. One more drive through scanning system is available, where exposure/radiation beam starts only when scanning container comes in front of the collimator of the scanning device. Here the crew members are exposed to the scattered radiation only. Various safety systems such as infrared systems and sensors are in place to prevent any accidental exposure to the operator.

5.2 Classification on the Basis of Mobility

LINAC-based Mobile Scanner: LINAC-based mobile (**or boom type**) scanner system is housed in the vehicle and an array of detectors are mounted on a boom. A fan shape beam is produced by the 5 MV accelerators, used for scanning up to 250 mm of steel. It is operated in an open space with appropriate safety arrangements like cordoning off, fencing, etc. The electrical generator incorporated into the system allows its use without the need for a local power supply. These high-energy scanners are used for inspection and identification of the cargo and detection of contraband, illegal drugs, weapons and other dangerous objects.

LINAC-based rail scanner: LINAC-based rail scanner is used for scanning the materials in a moving goods train. The LINAC is housed in a room having concrete walls about 0.5 m thickness and an array of detectors is mounted in the opposite direction of the LINAC in the room. These are transmission type scanners. Scanning is possible for trains carrying the containers, moving with a velocity of 60 km/h. These systems are used by customs at the borders.

5.3 Radiation Safety in Scanning Facilities

Radiation safety in the operation of the scanning facility is crucial considering factors such as movement of non-radiation workers, operation of mobile scanners and dose received by the drivers in "drive through" mode. The scanning system (LINAC-based or ^{60}Co-based) produces considerably high dose rates due to high thickness penetration requirements. For example, the typical dose rate from a dual energy accelerator (4 and 6 MV) is of the order of 50 Gy/h at 1 m (this may vary from one make/model to another make/model) [26]. Hence, such scanners should have inbuilt multiple safety systems to prevent any potential exposure to the operators or drivers carrying containers. Performance testing/type approval tests of the scanning systems

are carried out to ensure the inbuilt safety associated with the system. Based on the functional performance of the safety system type approval for a particular model is issued by Regulatory Body. The housing for ^{60}Co source or X-ray source should incorporate adequate shielding so that the radiation level outside the system does not exceed the leakage limits specified by the Regulatory Body.

The dose received by the driver carrying containers is the main safety concern for drive through systems. It is observed that the dose received by the driver during scanning is well within the international recommended limit of 0.25 μSv per scan, which is 4000 times less than the annual effective dose limit for the member of the public [27].

In LINAC-based container scanners, the enclosed installation is constructed with concrete walls of sufficient thickness to reduce the primary, leakage and scattered dose below the acceptable limits. For example, the primary concrete wall at 5 m from the focal spot of a 6 MV accelerator having an output of 50 Gy/h at 1 m is about 1.5 m [26]. However, the exact wall thickness depends on workload, occupancy, distance factor, contribution of scattering and leakage, etc. The recommended dose limit for the public in planned exposure situations is 1 mSv in a year [28]. Considering workload of 2000 h in a year (8 h/day × 5 days/week × 50 weeks/years), the radiation levels outside the facility should not exceed 0.5 μSv/h. In case of mobile vehicle mounted scanner, the radiation safety is achieved by cordoning off the required area. Emergency push buttons are provided at suitable locations of the vehicle carrying scanner, which is easily accessible during an emergency and can turn off the exposure.

6 Radiotracer Applications in Industries

Radiotracer techniques are widely used in industries for process optimisation, measuring fluid dynamics parameters and troubleshooting investigations [29]. Radioisotopes are added to the industrial systems/vessels/pipes to find out (i) blockage and leak detection and location in buried pipelines, (ii) flow rate measurement, (iii) sediment transport and effluent dispersion in ports, (iv) wear and corrosion rate monitoring and (v) effective management of oil field, etc. The radiotracers have several advantages such as (i) high detection sensitivity, (ii) online detection and quick analysis of results, and (iii) can be used in harsh climatic conditions. Commonly gamma and beta emitting isotopes used in the tracer studies are ^{3}H, ^{24}Na, ^{82}Br, ^{46}Sc, ^{131}I, etc. [29].

^{82}Br is used as a radiotracer to locate blockage/leakage in heat exchangers/pipes. Valuable information about the effectiveness and economics of wells is obtained using tritiated water (^{3}H) as a tracer in oil industry. Discharge rate/flow rate measurement at pumping stations in canal is possible using radiotracers such as aqueous solution of ^{131}I. ^{46}Sc labeled glass as a tracer is widely used in sea ports to study the dynamic behaviour of sediment, and monitor the movement of dredged material and navigation channels in harbours.

7 Research Applications of Ionising Radiation

Radioisotopes are used in medicine, agriculture, and research applications for societal benefit. A variety of isotopes are used to help researchers to create technologies and test new medicines, to label/tagged specific biological molecules or compounds and procedures that benefit plants, animals and people. Radionuclides such as ^{3}H, ^{14}C, ^{35}S, ^{32}P, ^{33}P and ^{125}I in unsealed form are extensively used in research applications (Table 5). Decay scheme and half-life of some radionuclides are given in Table 6.

Table 5 Radionuclides and their uses of unsealed radionuclides for research

Radionuclide	Typical use
^{3}H	Cell proliferation assays (^{3}H-thymidine); tagging cellular proteins (^{3}H-amino acids)
^{14}C	Tagging cellular proteins (^{14}C-amino acids)
^{32}P	Probes for northern and Southern blots (α-dNTPs); invitro kinase reactions (γ-ATP); metabolic labeling of cellular proteins (ortho-^{32}P)
^{33}P	Probes for northern and Southern blots (α-dNTPs)
^{35}S	Metabolic labeling of cellular proteins or in vitro translations (^{35}S-methionine/cysteine)
^{125}I	Labeling of cellular surface proteins or of purified proteins in vitro (free ^{125}I); immunoblot detection reagent (^{125}I-Protein A)

^{3}H: Tritium labeled compounds are used as radiotracers in biochemistry, enzyme mechanisms, and in environmental sciences for the development of crop protection agents
^{14}C: Carbon-14 labeled compounds are indispensable tools in the assessment of novel pharmaceuticals using absorption, distribution, metabolism and excretion (ADME) studies in living beings and in enzymatic and sub-cellular in vitro research applications

Table 6 Decay scheme and half-life of some radionuclides.“
In the table, the energy of beta particles is the maximum energy (Emax) emitted

Name	Symbol	Type of decay and energy (MeV)	Half-life
Tritium-3	^{3}H	β^{-} (0.019)	12.26 years
Carbon-14	^{14}C	β^{-} (0.155)	5730 years
Phosphorous-32	^{32}P	β^{-} (1.71)	14 days
Sulphur-35	^{35}S	β^{-} (0.167)	87.2 days

^{35}S: Sulphur-35 radiolabeled amino acids are widely used as radiotracers studies including protein synthesis, protein metabolic labeling, cell labeling, protein degradation and pulse-chase analysis
^{32}P: Radioisotopes are now a day’s extensively used in agricultural research to understand chemical and biological processes in plants. For example, to study the fertiliser uptake in plants, phosphate solution (^{31}P) mixed with radioactive ^{32}P is injected into the root system (Fig. 11). Plants use both ^{32}P and ^{31}P in a similar manner. The movement of radioactive ^{32}P throughout the plant can be monitored with the help of a Geiger Muller counter and the fertiliser uptake can be estimated

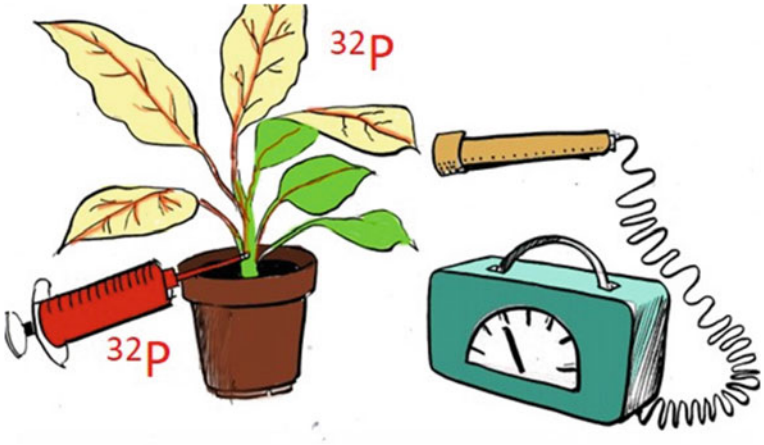

Fig. 11 Application of ^{32}P in agriculture for fertiliser uptake

8 Consumer Products and Equipment

Consumer products are devices or equipment that contain a very small activity of radioactive sources or very low energy of X-rays. The consumer products are a *device or manufactured item into which radionuclides have deliberately been incorporated or produced by activation, or which generate ionising radiation, and which can be sold or made available to members of the public without special surveillance or regulatory control after sale* [30].

Examples of consumer products are smoke detectors; explosive/narcotic detectors; radio-luminous products using tritium light sources; thorium and ^{85}Kr used in the lamp industry; incandescent gas mantles; and glassware that may contain uranium compounds (Fig. 12). Tritium Filled Sources (TFS) are non-electrical light sources used for night-illumination of various military gadgets, commercial and industrial buildings as warning signs. TFS are sealed glass tubes filled with tritium gas and coated internally with suitable phosphor material.

In addition, equipment such as baggage scanning systems, X-ray fluoresce equipment (XRF), X-ray diffractometer (XRD), self-shielded X-ray equipment for NDT/PCB analysers, etc. are widely used in the public domain. These equipment's houses a low energy X-ray unit, and is used for security or qualitative /quantitative element analysis purposes. The analytical equipment uses low energy X-rays, so the hazard potential is low. However, these equipment are not consumer products and need to be regulated by the regulatory body.

The users are not aware about the presence of radioactivity in these products and the potential harm due to the result of radiation exposure in case of improper use. The consumer's products containing radioactive substances are designed, constructed, tested and demonstrated the necessary regulatory compliance in accordance with national and international standards. These products are designed in such a way that

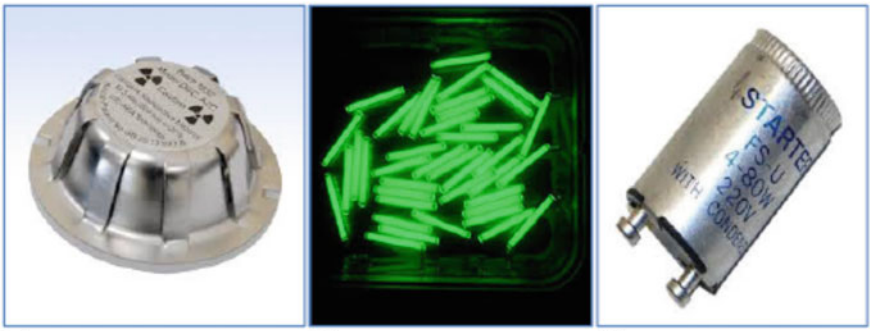

Fig. 12 **(a)** Smoke detectors, **(b)** tritium light sources, **(c)** fluorescent lamp starters

they will not give unacceptable radiation doses to individual members of the public and the population. The effective dose to an individual member of the public will not exceed 1.0 mSv in a year even in a low probability (accident) scenario and 10 μSv in a year under normal circumstances [30]. Hence, the end users of these products need not be regulated. However, the manufacturer and suppliers who are handling these products in bulk are being regulated in accordance with the applicable rules and regulatory framework.

9 Conclusion

Radiation technology using radioisotopes and radiation generating equipment is being extensively used in the world in the fields of healthcare, industry, agriculture and research. With technological advancement, new equipment fitted with radiation sources has become available for various industrial applications. To avoid hazards to the worker, public and environment, radiation sources/ionising radiation should be handled carefully as per the safe operating procedure/safety manual, in the presence of safety infrastructure, trained and certified manpower, monitoring instruments, etc. as instructed by regulating authority.

References

1. AERB Safety Standard No. AERB/RF-IR/SS-1 (Rev. 1) (2007) Industrial gamma radiography exposure devices and source changers
2. Kumar U (2021) Industrial gamma radiometry and imaging applications using sealed radioisotope sources and radiation. Non-power applications of nuclear technologies. ISBN: 978-81-954733-2-8
3. NAARI Bulletin (2005) Radiation in non-destructive testing, vol XII

4. AERB/RF-IR/SC-1 (Rev. 1) (2016) AERB safety code industrial radiography
5. ISO 3999 (2004) Radiation protection—apparatus for industrial gamma radiography—specifications for performance, design and tests
6. ANSI N432 (1980) Radiological safety for the design and construction of apparatus for gamma radiography
7. AERB/SS/3-Rev-1 (2001) Safety standard on testing and classification of sealed radioactive sources
8. IAEA TS-R-1 (2004) Regulations for the safe transport of radioactive material
9. IAEA Tecdoc-1459 (2005) Technical data on nucleonic gauges. IAEA
10. IEC 62598 (2011) Nuclear instrumentation-constructional requirements and classification of radiometric gauges
11. AERB/SS/2-Rev-1 (2001) Safety standard on design and construction of industrial radiation gauging devices
12. US Food and Drug Administration (2022). https://www.fda.gov/food/buy-store-serve-safe-food/food-irradiation-what-you-need-know. Accessed on 07 Oct 2022
13. WHO (1988) Food irradiation: a technique for preserving and improving the safety of food. World Health Organization. https://apps.who.int/iris/handle/10665/38544
14. IAEA Technical reports series no. 481 (2015) Manual of good practice in food irradiation: sanitary, phytosanitary and other applications. International Atomic Energy Agency, Vienna
15. Saravanan T, Tyagi AK, Singh R (2021) Gamma irradiation for preservation of food and allied products. Non-power applications of nuclear technologies. ISBN: 978-81-954733-2-8
16. World Health Organization (1999) High-dose irradiation: wholesomeness of food irradiated with doses above 10 kGy report of a joint FAO/IAEA/WHO Study Group, WHO Technical Report Series No. 890
17. Pant HJ, Bhardwaj TK, Kumar U, Pujari PK (2022) Applications of radioisotopes and radiation technology in industry: current status and prospects. Curr Sci 123(3):377–387
18. Sarma KSS, Rawat KP, Benny PG, Khader SA (2011) Developments in electron beam processing technology. BARC Newsl 323:38–41
19. Aswal DK, Nakhe SV, Shukla P, Chaudhary N, Ganguli T, Upadhyay BN (2022) An overview of key enabling technologies for DAE's nuclear programme. Curr Sci 123(3):353–360
20. ANSI-N43.10 (1984) Safe design and use of panoramic, wet source storage irradiators (category IV)
21. IAEA Specific Safety Guide No. SSG-8 (2010) Radiation safety of gamma, electron and X-ray irradiation facilities. https://www.iaea.org/publications/8401/radiation-safety-of-gamma-electron-and-x-ray-irradiation-facilities
22. IAEA Safety Series No. 107 (1992) Radiation safety of gamma and electron irradiation facilities
23. AERB SS NO. AERB/RF-IRRAD/SS-6 (Rev-1) (2007) Land based stationary gamma irradiators. https://www.aerb.gov.in/storage/uploads/documents/regdoc1eTGz.pdf
24. https://www.symmetrymagazine.org/article/august-2010/accelerator-apps-cargo-scanning. Accessed on 20 Dec 2022
25. https://www.wikiwand.com/en/Cargo_scanning. Accessed on 20 Dec 2022
26. Alok P, Sunil Kumar JVK (2018) Radiation safety aspects in high energy accelerator based container scanners. e-J Nondestr Test (eJNDT) 04:1435–4934
27. ANSI N43.17 (2009) Radiation safety for personnel security screening systems using X-ray or gamma radiation
28. ICRP Publication 103 (2007) Recommendations of the international commission on radiological protection
29. Pant HJ (2022) Applications of the radiotracers in the industry: a review. Appl Radiat Isot 182:110076. https://doi.org/10.1016/j.apradiso
30. IAEA Safety Standards Series No. SSG-36 (2016) Radiation safety for consumer products. https://www.iaea.org/publications/10716/radiation-safety-for-consumer-products

Radiation Environment in Particle Accelerator Facilities

G. Haridas, R. Ravishankar, Arghya Chattaraj, and T. Palani Selvam

1 Introduction

There is a large demand for accelerators today for various applications in applied research, industry, and medicine. Besides, accelerators are also widely used for basic research. A large number of accelerators worldwide are used for such applications (www.acceleratorsamerica.org). The energy of electrons is usually less than 10 MeV for medicine, industry, and food processing [1], whereas the energy required for research applications may go to very high energies, of the order of TeV (www.home.web.cern.ch). The famous "Livingston plot", (Fig. 1) predicts a ten-fold increase in the particle energy after every seven years [2]. The use of such accelerators with high energy and pulsed nature causes several challenges in ensuring radiation safety [3]. For example, when high energy charged particles (as in synchrotron radiation sources, high energy linacs, and colliders) interact with structural materials generate a cascade of secondary particles, whose energy ranges up to several hundreds of MeV or GeV. Moreover, they are intense and highly directional. Besides, research and development are in progress for the use of high-energy and high-intensity proton accelerators for nuclear waste transmutation, fissile material breeding, and power production. High-intensity accelerators are also being used for generating Radioactive Ion Beams for nuclear physics research of exotic radionuclides.

The secondary particles/radiation generated in high-energy accelerators are bremsstrahlung X-rays, neutrons, pions, muons, gamma rays, and annihilation photons. This mixed field increases the challenge in the radiation protection program of such facilities. Radiation safety issues during the operation of electron accelerators are elaborated in IAEA Tech. rep. series 188 [4] and that of proton accelerators are described in IAEA Tech. rep. series 283 [5]. NCRP Report No. 51 [6] provides

G. Haridas (✉) · R. Ravishankar · A. Chattaraj · T. Palani Selvam
Bhabha Atomic Research Centre, Mumbai 400094, India
e-mail: haridas@rrcat.gov.in

D. K. Aswal (ed.), *Handbook on Radiation Environment, Volume 2*,
https://doi.org/10.1007/978-981-97-2799-5_10

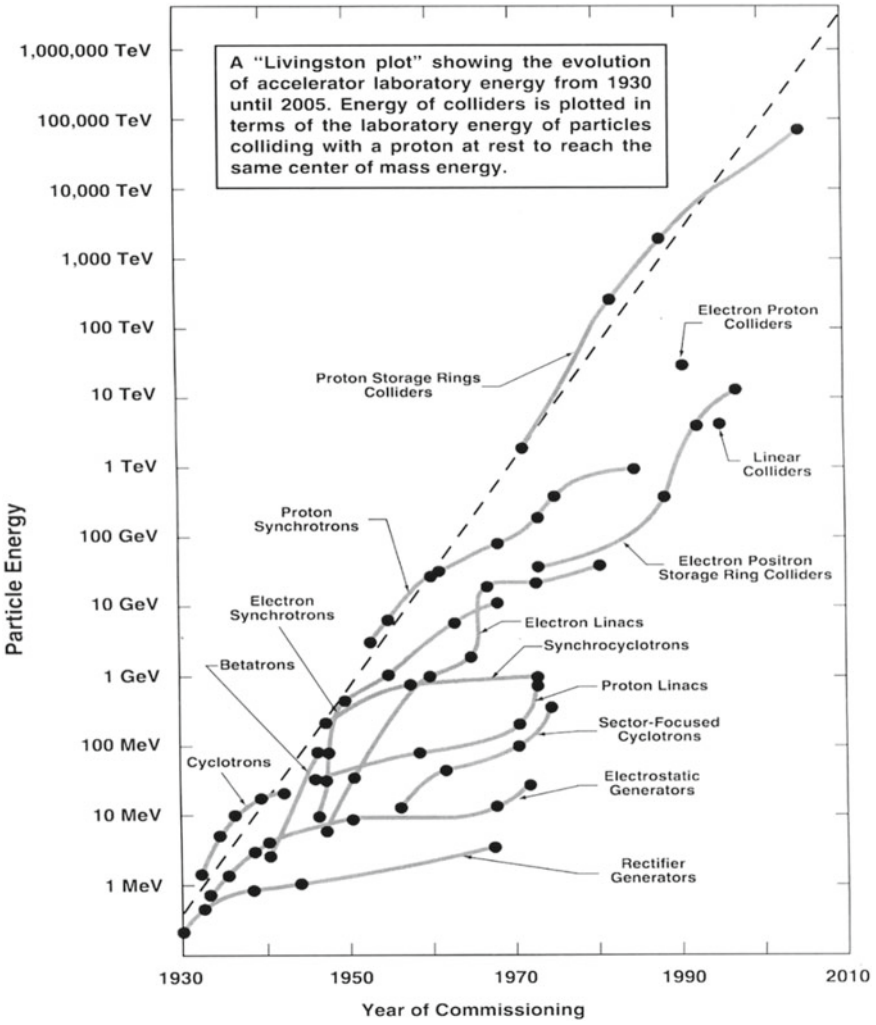

Fig. 1 Livingston plot. The envelope of the curves (dashed line) indicates an increase in energy by a factor of 10 about every seven years (reproduced from [2] with permission of Alexander Chao for reproducing from SLAC-PUB-9483)

very useful information about the radiation environment of both types of accelerators, especially in the energy region, less than 100 MeV. Radiation safety at high energy particle accelerators is described in the literature [7–11]. Specific radiation safety issues related to electron synchrotron radiation sources can be obtained from the literature [12–14].

The radiation environment in particle accelerator facilities forms the core of radiation protection concern in any particle accelerator facility. It is a strong belief that radiological protection started with particle accelerators [5] and gradually developed

into a vast subject with enormous potential for research and specialized courses. Much attention was not devoted to radiation protection until the invention of Cyclotrons (in 1932), particularly during World War II with the application of accelerators to the Manhattan Project. The cataract cases of those involved in visually aligning the accelerator beams during the late 1940s brought the field of radiation protection into the limelight. The radiological safety aspects of accelerators required an orderly investigation of the radiations produced and needed a generalized approach in arriving at solutions pertaining to radiation protection. There are problems pertaining to accelerators (unlike conventional radiation safety problems) such as detection and measurement of mixed radiation, pulsed radiation, high and low energy radiation, and Radio-Frequency (RF) and magnetic field interferences.

The knowledge base on accelerator radiation protection spread its wings for detection and measurements of radiation levels (even very high levels), radiation shielding, development of radiation dosimetry and its techniques, estimation of induced activity, ventilation designs (to prevent or minimize the hazards from radioactive gases produced), environmental impact, waste disposal, legislative and regulatory aspects.

Particle accelerators are not often thought of as potential polluters of the environment. However, sometimes the accelerator needs to be sited in densely populated areas like hospitals, universities, or in close proximity to residential areas. In this chapter, the radiation environment and radiological safety aspects of the operation of particle accelerators are described.

2 Radiation Environment of Electron Accelerators

2.1 Theoretical Aspects

The radiation environment in electron accelerators depends on the type of interaction the electrons make with the target materials or accelerator structures. At low energies, below an energy called critical energy, mainly the electron interacts through collision loss, which is due to ionization and excitation. Once the energy exceeds the critical energy, the electron mainly loses its energy by radiation emission where bremsstrahlung X-rays are emitted [6]. As the energy loss of electrons is by collision and radiation emission, the total linear stopping power of the medium is the sum of collision stopping power and radiative stopping power as given in Eq. (1)

$$(\mathrm{d}E/\mathrm{d}x)_t = (\mathrm{d}E/\mathrm{d}x)_c + (\mathrm{d}E/\mathrm{d}x)_r \tag{1}$$

where $(\mathrm{d}E/\mathrm{d}x)_c$ is the collision stopping power, $(\mathrm{d}E/\mathrm{d}x)_r$ is the radiative stopping power, and $(\mathrm{d}E/\mathrm{d}x)_t$ is the total linear stopping power.

The two stopping powers become equal at the critical energy, E_c, given empirically as

$$E_c(\text{MeV}) = \frac{800}{Z + 1.2} \tag{2}$$

where Z is the atomic number of the interacting medium. E_c decreases when Z increases. For example, the atomic number for water is 103 MeV, whereas for lead, it is 9.6 MeV (Z_{eff} of water is 6.6 whereas Z of lead is 82). This indicates that the dominance of radiation emission starts at much low energies for high Z materials in comparison with low Z materials.

2.2 Bremsstrahlung X-rays

The radiation emitted from the interaction of electrons with materials is called bremsstrahlung X-rays. The important characteristics of bremsstrahlung photons are their broad spectrum of energies (continuous spectrum) extending to the energy of the interacting electron and high angular dependence. In the direction of incidence of electron, the intensity of bremsstrahlung photon is the maximum and reduces at wider angles. The hardest (highest energy) photon arising from the interaction is emitted in the forward direction (0°), i.e., in the direction of the incident electron, and becomes softer (low energy) at wider angles. Calculations for the electron energies varying from 50 MeV to 10 GeV, reported by Vylet et al. [10] show that 99.9% of photons at 90° have energies below 10 MeV.

The forward peaking of bremsstrahlung X-rays is described by Eq. (3) [4]

$$\theta_{1/2} = \frac{100}{E_0} \tag{3}$$

where $\theta_{1/2}$ is the angle in degrees at which the intensity drops to one half of that at 0° and E_0 is the energy of incident electrons in MeV.

Moreover, the emergent bremsstrahlung spectra from an absorber medium depend highly on the absorber thickness and are of great importance in radiation shielding applications at high energy electron accelerators. Figure 2 shows forward bremsstrahlung spectra from a copper target of different thicknesses on incidence of 450 MeV electrons [15]. It can be seen that the photons from a thin target have higher energy, whereas for thick targets, the low energy contribution dominates over the thin target case.

2.3 Electromagnetic Cascade or Shower

It is clear from the above discussion that, radiation loss is the major mechanism by which an electron loses its energy for electron energies greater than the critical energy (E_c) when it interacts with an absorber medium. An electron generates a photon after

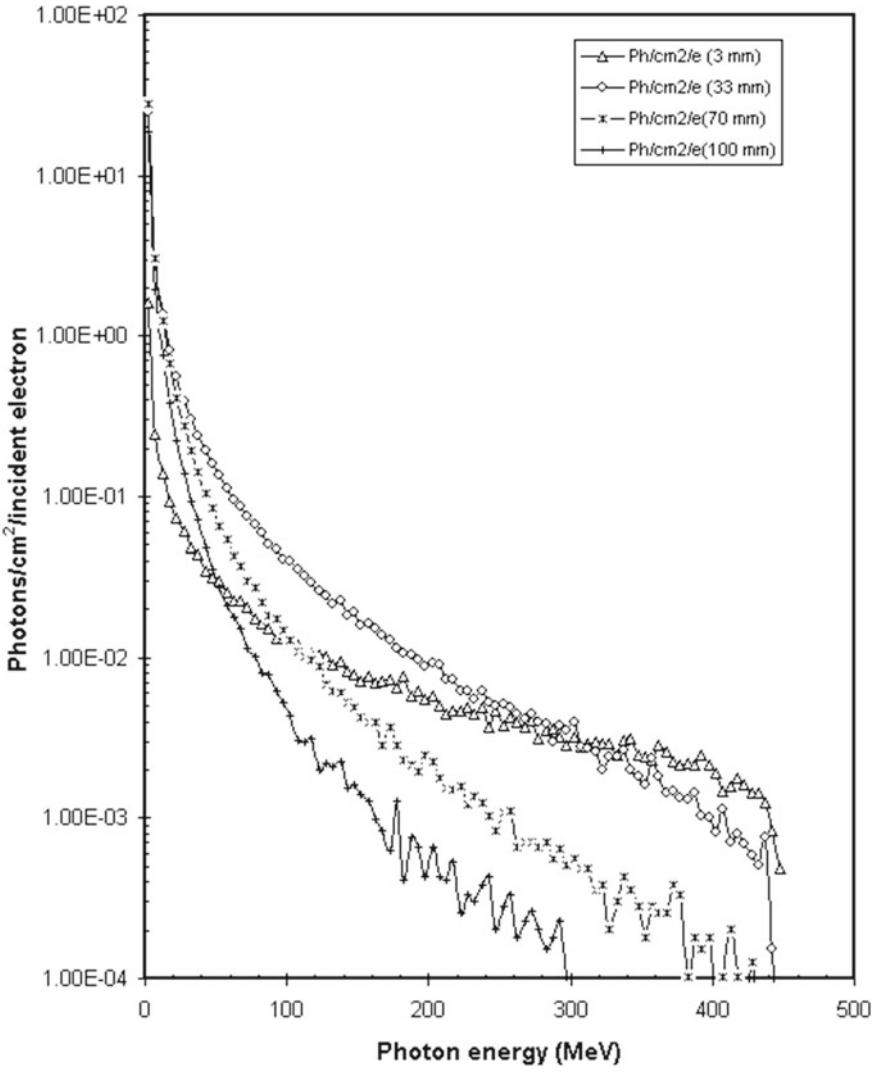

Fig. 2 Forward bremsstrahlung spectra from different copper target thicknesses on 450 MeV electron incidence (reproduced from [15] with permission from Oxford University Press])

traversing an average distance, approximately one radiation length (X_0), losing its energy by a factor of e, i.e., 63% of its initial energy [Radiation length is the thickness by which a relativistic electron loses its energy by one-third of its initial value] High energy photons in the bremsstrahlung spectrum will interact by pair production. The interacting photon will produce an electron–positron (e^+, e^-) pair after traveling an average distance of $9/7X_0$ [4]. Both the electron and positron generate bremsstrahlung photons again (as it traverses through the medium) which in turn produce (e^+, e^-)

pairs. The process of bremsstrahlung photon generation and pair production continue to take place and a cascade of positrons, electrons, and photons develop within the interacting medium. In the 1930s, this cascade was called an "electron cascade" by Homi Bhabha. He has theoretically calculated the number of electron pairs generated when a 100 GeV electron is incident on a lead plate of thickness 5 cm to be about 1000 [16]. The number of particles in the cascade approximately doubles in each step till the electron energy falls and degrades below the critical energy, E_c, beyond which the electrons undergo mostly collision, and the photons interact through Compton scattering and photoelectric absorption. The generation of an electromagnetic shower is schematically shown in Fig. 3.

When the energy of bremsstrahlung photons within the cascade reduces to a low value where the cross-section for pair production is comparable with that of Compton scattering, it causes a reduction in photon as well as the electron intensity with the result that the shower development stops and the particles exponentially attenuate due to Compton scattering and photoelectric absorption. This results in a transition curve as shown in Fig. 4, where the fraction of energy deposited during shower propagation in a medium is shown as a function of the depth of the medium expressed in terms of λ_l, where $\lambda_l = 325\ (\ln Z)^{-1.73} \times (\ln E_0)$ [3]. Electromagnetic shower in copper

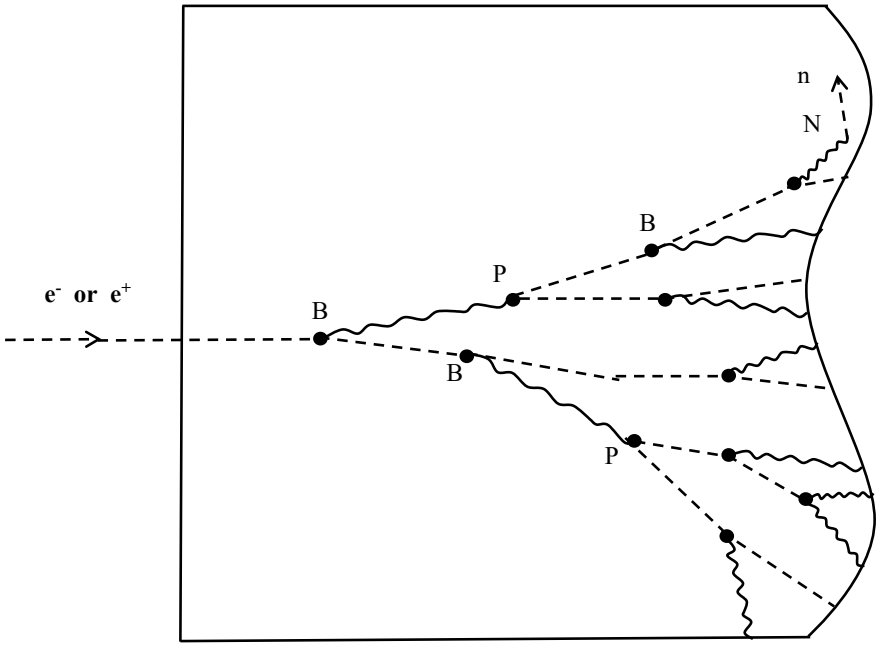

Fig. 3 Schematic diagram of electromagnetic cascade (reproduced from [4] with permission from IAEA) (*B* bremsstrahlung, *p* pair production, *N* Nuclear reaction, *n* neutron)

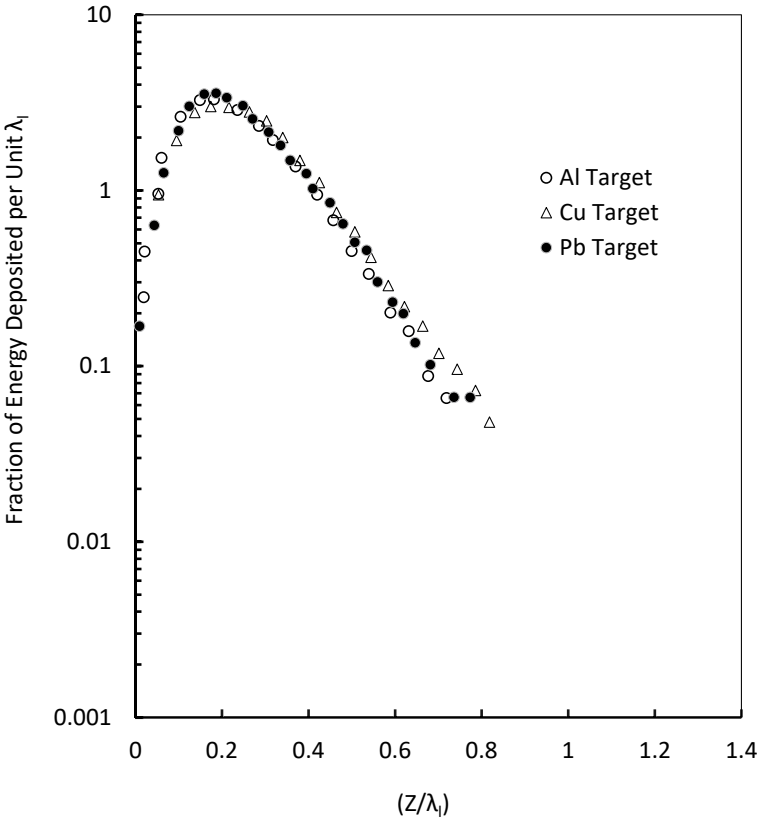

Fig. 4 Universal transition curve for the energy deposition in shower generation in a medium (adapted from [3])

and lead generated by 1 GeV electrons was experimentally studied by Nelson et al. [17], where they measured the energy absorption in thin absorbers using LiF TLDs and also calculated the energy absorbing from them.

2.4 Effect of Shower Generation on Absorbed Dose

In the forward direction (in the direction of the electron beam) generation of electromagnetic shower due to the incidence of high energy electrons or photons, the absorbed dose in the exposed material increases initially up to a certain depth, mainly in the forward direction, and then decreases. In case of a human body too, the same effect occurs and hence the dose recorded by personnel dose monitoring devices (which is worn usually on the surface of the body) underestimates the dose

by several factors [18] depending upon the energy of the incident electron or the incident bremsstrahlung spectrum. Similarly, equipment and sensitive electronic devices kept in metallic enclosures in the forward direction are likely to get damaged faster in comparison with the equipment kept without any enclosure. A methodology for deducing the conservative correction factor to correct the dose underestimation for use in personnel radiation protection was described by Haridas et al. [19] based on absorbed dose measurements in a water phantom in the bremsstrahlung X-ray environment emitted from the 450 MeV electron synchrotron, Indus-1. The equivalent thickness of different materials corresponding to water phantom for online absorbed dose measurement also was determined and described in the literature [19].

Outside the shield around high energy electron accelerators, the energy may be degraded to a large extent, and hence the underestimation factor may not be applicable [19, 20]. However, streaming of radiation may take place through the shield joints and penetrations, where the underestimation of dose may occur and hence care has to be taken. Electron accelerators operating at energies less than about 10 MeV need not consider the dose build-up as it is not significant.

In the lateral direction (90° w.r.t the beam direction), the emitted bremsstrahlung photons are softer in nature due to the low energy nature of the secondary electrons set in motion laterally, and hence no dose build-up takes place [17]. The absorbed dose per unit beam power from high Z thick targets in the forward and lateral direction as a function of electron energy is shown in Fig. 5 [4]. The absorbed dose rate beyond 100 MeV is suggested to be a linear function of energy.

2.5 *Bremsstrahlung Source Terms*

Presently, bremsstrahlung source terms for electron accelerators are calculated using the empirical relations suggested by Swanson [4] based on the curve presented in Fig. 5. In the forward direction (0°), empirical relation (Eqs. 4 and 5) for the source term normalized to electron beam power as a function of electron energy in MeV is given as

$$D = 20E^2 Gy/h - kW \quad \text{for } E < 20\,\text{MeV}(0^\circ) \tag{4}$$

$$D = 300E^2 Gy/h - kW \quad \text{for } E < 20\,\text{MeV}(0^\circ) \tag{5}$$

For the sideward direction (90°), the source term beyond 100 MeV is assumed to be proportional to the power, independent of the energy, given in Eq. (6)

$$D = 50\,Gy/h - kW(90^\circ) \tag{6}$$

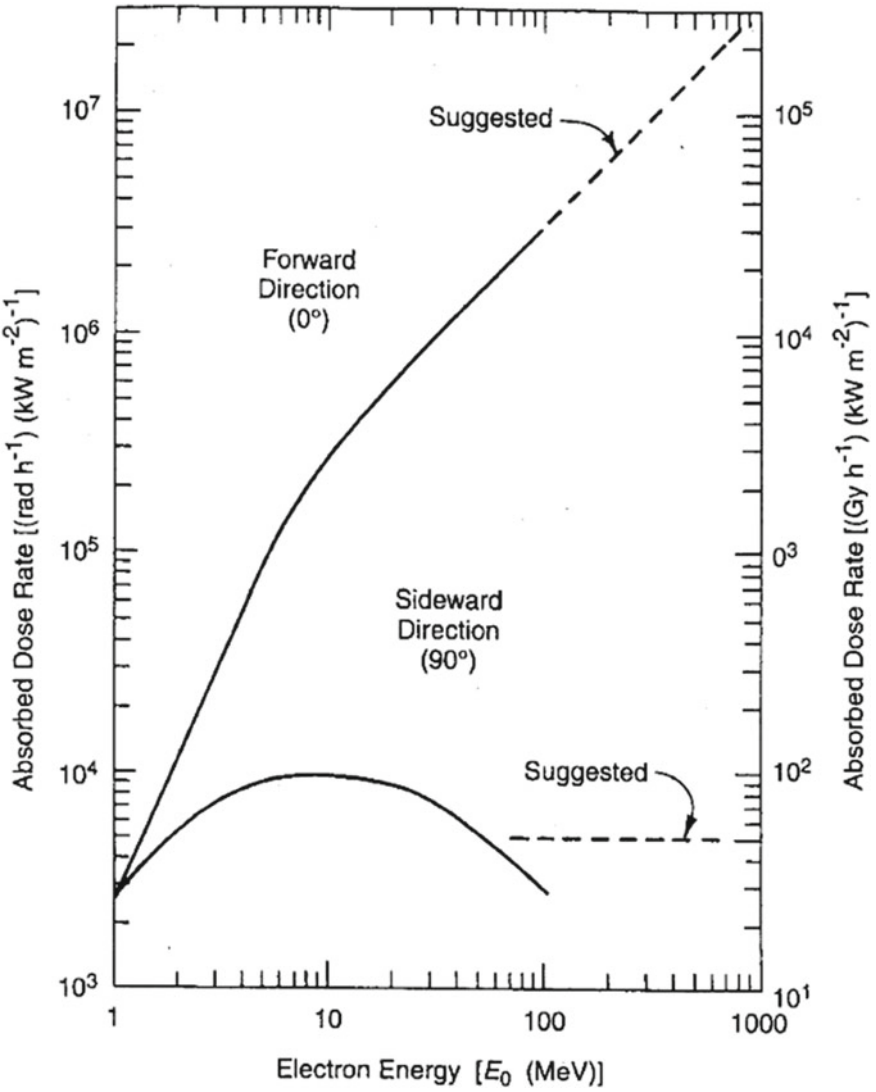

Fig. 5 Absorbed dose rate due to high *Z* thick-target bremsstrahlung in the forward and sideward direction (reproduced from [4] with permission of IAEA)

The dose rate normalized to beam power at 90° has been studied by A Ferrari et al. [21], where the authors have calculated the source term using FLUKA for electrons in the energy range 100–1000 MeV and found it to match very well with the suggested empirical relation by Swanson [4]. The same authors investigated the dose rates in the forward direction and found that the dose rate is higher by 7 times at 100 MeV and 22 times at 1000 MeV.

The forward direction source term is experimentally determined for 450 MeV and 550 MeV for a lead target thickness of 1 CSDA (Continuous Slowing Down Approximation) range (~ 26 mm) and found to be less by 28% [22] than that suggested by the empirical relation by Swanson [4]. This experimental data is simulated using EGSnrc code and found to be in excellent agreement.

The source terms by Swanson [4] which are widely used are based on experimental data obtained from absorbed dose rates in 30 cm tissue equivalent spherical phantom obtained from thick high Z materials. However, in practice, accelerated electron beam moving or circulating in a vacuum envelope, if lost, encounters a thin target of a few millimeters thick and the generated bremsstrahlung photons in the forward direction are of high energy compared with photons emitted from a thick target [23]. Moreover, as the thickness of the vacuum chamber is less, substantial electrons also will be transmitted along with bremsstrahlung photons and the source term will be different than that obtained from the empirical relations mentioned above [23]. This suggests that for forward shielding, source terms from relatively thin targets, and for lateral shielding, source terms from thick targets must be used. Monte Carlo calculations performed using EGS code for energies from 100 MeV up to 10 GeV by Tromba et al. [24] suggest that the probable locations of beam loss in the accelerator sections may be made thick enough so that the electromagnetic shower develops fully in the material and further shielding calculation can be performed by using simple exponential attenuation method. Dinter et al. [25] have calculated the dose behind various shield materials like sand, concrete, lead, etc., for electron energies ranging from 0.15 to 50 GeV and estimated the attenuation coefficient for use in radiation shielding applications.

2.6 Photo-Neutrons

The second major contributor to the radiation environment in electron accelerators is photo-neutrons. A detailed discussion of the neutron production mechanism is given by Swanson [26]. Photo-neutrons are produced as a result of the interaction of high energy photons (bremsstrahlung X-rays) with accelerator structures when the beam is striking a target or vacuum envelopes during a beam loss. In the process of electromagnetic cascade generation and its subsequent propagation through the medium, photo-neutrons are generated as bremsstrahlung photons have energy well above the neutron production threshold. It is well known that the average binding energy per nucleon is only about 8.5 MeV, whereas bremsstrahlung photons are of energy as high as hundreds of MeV or GeV (depending upon the electron energy) which are above the binding energy of nucleons and produce (x, n), (x, 2n), and (x, np) reactions. The general expression, Eq. 7 for the yield of photo-neutrons per incident electrons can be represented in terms of photon differential track length given by [26],

$$Y(E_0) = \frac{N_0 \rho}{A} \int_{k_{th}}^{E_0} \sigma_n(k) \frac{\mathrm{d}L}{\mathrm{d}k}(E_0, k)\mathrm{d}k \tag{7}$$

$\sigma_n(k)$ is the photo-neutron cross-section from (x, n), $(x, 2n)$, and (x, np) reactions and $\frac{\mathrm{d}L}{\mathrm{d}k}$ is the photon differential track length distribution representing the total track length of all photons having an energy in the interval k and $k + \mathrm{d}k$. Expressions for track length distribution can be obtained from the literature [26]. N_0, ρ, and A are the Avogadro number, medium density, and atomic weight, respectively.

There are three main photo-neutron production mechanisms decided by the photon energy regime. They are: Giant resonance mechanism, Quasi-deuteron effect, and Pion decay. The processes are briefly described below.

2.6.1 Giant Resonance Mechanism

Up to 30 MeV of photon energy, neutrons are produced through this process. During this process, a photon transfers its energy to the nucleus in which the protons as a group move away from the neutrons which appears like a dipole formation. This process has maximum cross-section at photon energies ~ 20–23 MeV for light nuclei and 13–18 MeV for medium and heavy nuclei. For a mass number higher than 40, the width of the resonance peak is approximately given as

$$k_0 = 80A^{-1/3}\mathrm{MeV} \tag{8}$$

The integrated cross-section over the photon energies from the production threshold to 30 MeV [27] is expressed as

$$\sigma = \int_{E_{\mathrm{th}}}^{30\ \mathrm{MeV}} \sigma_n(k)\mathrm{d}k \sim \frac{NZ}{A} \tag{9}$$

where $\sigma_n(k)$ is the photo-neutron cross-section and $N = A - Z$.

The neutron spectrum from the giant resonance process has two components. The first one is a standard evaporation spectrum from a compound nucleus formed by the absorption of photons and the absorber nucleus, which is described as

$$\frac{\mathrm{d}N}{\mathrm{d}E_n} = \frac{E_n}{T^2} e^{-(E_n/T)} \tag{10}$$

where $\frac{dN}{dE_n}$ is the number of neutrons per unit energy interval, T is the nuclear temperature, characteristic of the excitation of the target nucleus. The most probable neutron energy in this distribution is $E_n = T$ and the average neutron energy is *2 T*. T has a value in the range of 0.5 to 1.0 MeV for excitations produced in heavy nuclei by giant resonance effect. Thus, the average neutron energy produced from this effect is ~ 1 to 2 MeV.

The second component of the spectra is the direct emission spectrum. Neutron energies above 3–4 MeV in this spectrum are by direct neutron emission. Studies have shown that direct emission accounts for about 14% of the neutrons emitted by the giant resonance process, the remaining 86% is the evaporation neutrons for medium to high Z materials. Neutron spectra obtained from Ta and Be targets of different thicknesses on 150 MeV electron beam incidence are reproduced in Fig. 6 [4]. From the spectrum, it is seen that the maximum flux is obtained in the energy region ~ 0.1 to 1 MeV in the case of tantalum, and in the case of beryllium, it is shifted slightly to the high energy side.

Swanson [4] estimated low energy neutron yield based on photon differential track length distribution, which is in turn based on approximation B of analytical theory for selected materials ranging from Carbon to Uranium and for electron energies up to 100 MeV, as reproduced in Fig. 7.

2.6.2 Quasi-deuteron Effect

For photon energies above 30 MeV, photo-neutrons are generated by quasi-deuteron effect. Here the photon interacts with a neutron proton pair within the nucleus rather than interacting with the entire nucleus. The fundamental process is described by Swanson [4] and by Levinger [28]. The cross-section for this process is an order of magnitude less than the giant resonance process. The QD effect adds a high energy tail to the giant resonance spectrum. Results at 100 MeV suggest that the additional yield of neutrons released by photons above 30 MeV is about $10 \pm 5\%$ of the giant resonance yield. In the Quasi-deuteron effect, the neutron energy may go up to half of the incident electron energy, above which only negligible neutrons may be present.

2.7 Neutron Through Photo-Pion Production

The cross-section for the quasi-deuteron effect reduces with photon energy. As the photon energy is greater than 140 MeV (rest mass of pion), photo-pions are produced [4] due to the interaction to the interaction of the photons with nucleons. The cross-section for this process has a number of resonance peaks and the highest peak is centered around 300 MeV with a width of ~ 110 MeV [4] (reproduced with permission from IAEA). Above 300 MeV the cross-section reduces at a slower rate and reaches a value close to 100 μb. The cross-section for neutron generation through photo-pion production (Eq. 12) is only a fraction of the giant resonance cross-section. However,

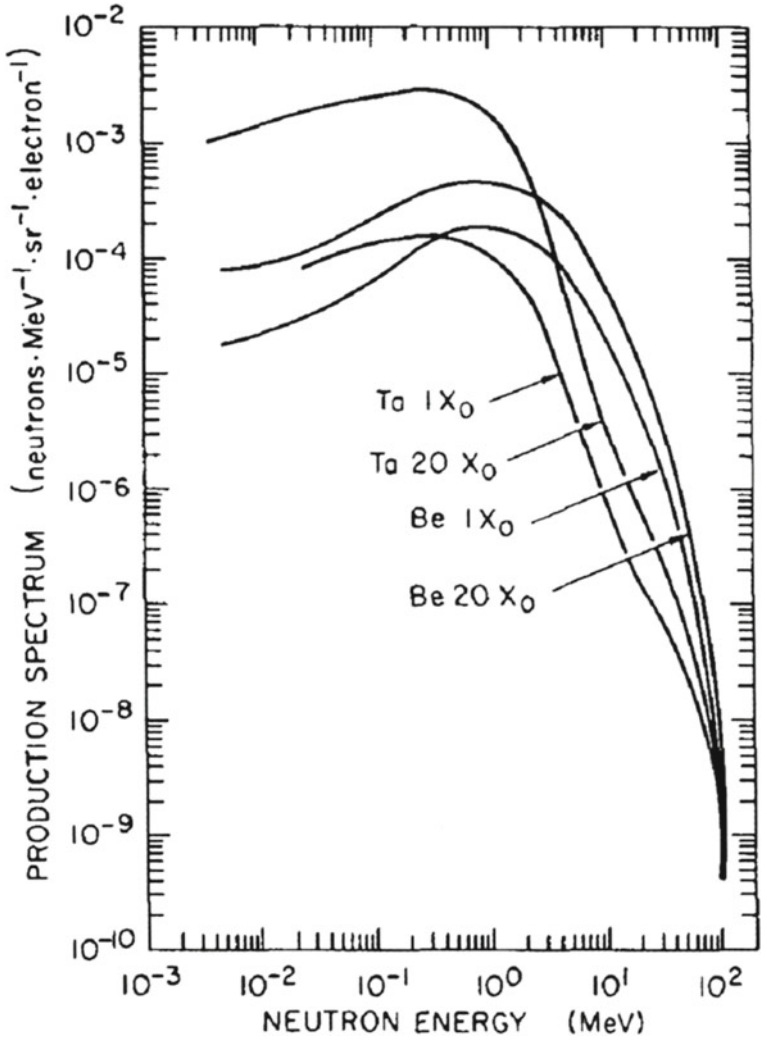

Fig. 6 Neutron spectrum from beryllium and tungsten targets of different thicknesses on 150 MeV electron incidence (reproduced from [4] with permission from IAEA)

the neutrons produced from photo-pion reaction are more penetrating than giant resonance neutrons [4]. At high energy accelerators, these penetrating neutrons contribute more to the dose rate outside the radiation shielding, whereas bremsstrahlung and giant resonance neutrons dominate within the shield.

The gamma-nucleon reaction responsible for the pion production is [7]:

$$\gamma + p \rightarrow p + \pi^0 \quad (E_{\text{th}} = 135\,\text{MeV}) \tag{11}$$

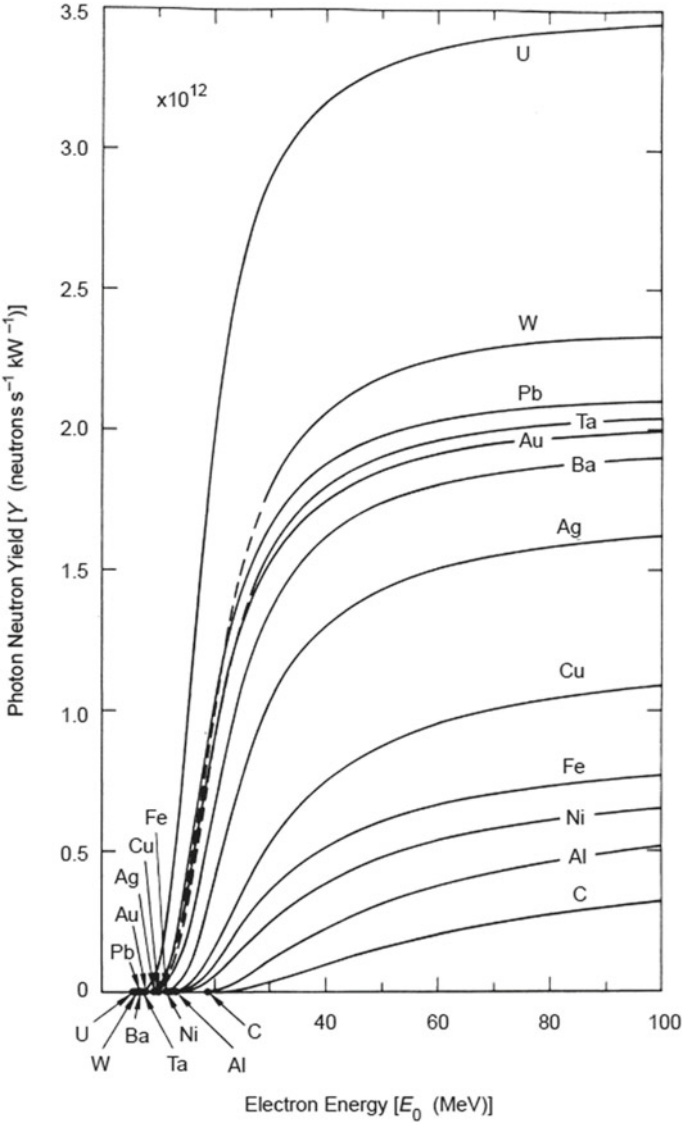

Fig. 7 Total yield of photo-neutrons from infinitely thick targets of different materials as a function of electron energy (reproduced from [4] with permission of IAEA)

$$\gamma + p \rightarrow n + \pi^{+} \quad (E_{\text{th}} = 140\,\text{MeV}) \tag{12}$$

$$\gamma + n \rightarrow p + \pi^{-} \quad (E_{\text{th}} = 140\,\text{MeV}) \tag{13}$$

Far above the energy threshold mentioned above the square of the average momentum transferred to the nucleus tends to a constant value, $q^2 = 400\,(\mathrm{MeV}/c)^2$, independent of the neutron energy. The corresponding kinetic energy of neutrons works out to be $q^2/2\,m \cong 200$ MeV [4]. The pions produced by π^+, π^- decay immediately to muons through the following decay scheme:

$$\pi^+ \rightarrow \mu^+ + \overline{\nu} \tag{14}$$

$$\pi^- \rightarrow \mu^- + \nu \tag{15}$$

where ν, $\overline{\nu}$ are the neutrino and anti-neutrino, respectively.

Also, two neutral pions annihilate to produce high energy gammas. These gammas produced further give rise to an electromagnetic cascade within the absorbers which complicates the radiation environment in such high energy accelerators. The source term for high energy neutrons in the range of 25 MeV to 100 MeV and beyond 100 MeV from a copper target as a function of electron energy is reported by Sullivan [9]. This data is useful for neutron shielding at high energy electron accelerators beyond 100 MeV.

2.8 Muons

At high energy electron accelerators, operating above hundreds of MeV, similar to (e^+, e^-) pair production, high energy bremsstrahlung photons above a threshold of 211 MeV produce (μ^+, μ^-) pairs [3]. However, the cross-section for the process is smaller approximately by $(m_\mu/m_e)^2 = 40{,}000$, where m_μ and m_e are the muon and electron rest masses, respectively. Another production mechanism of muons is the decay of pions. Charged pions are produced through photo-nuclear reactions, above a threshold of 140 MeV and then they decay to muons as described in the above section. The fluence of muons from $\pi^\pm$ decay is relatively small compared to the direct muon pair production.

The muons produced by both processes are highly forward peaked. This is because, in muon pair production and in nuclear pion production, the transverse momenta are small. As an example, the characteristic angle by which the intensity drops to $1/e$ for the production of 10 GeV muons is 10 mrad or 0.5 degree. Therefore, muons are not a problem for transverse shielding [29] but a major problem in the forward direction is due to its weakly interacting nature. Due to the larger mass of muons, they do not lose energy by radiation like electrons, and hence do not participate in electromagnetic cascade. The only mechanism by which they lose energy is by ionization.

3 Induced Radioactivity at Electron Accelerators

Due to the interaction of primary accelerated particles or secondary radiations produced in electron accelerators, if neutron emission takes place from any of the accelerator structures, it becomes activated. Generally, accelerators operating with energies less than 10 MeV are not likely to produce induced activity of any significance. In high energy accelerators, activity can be produced in shielding structures, cooling water, air, and soil. Usually, the induced activity problem is less severe in electron accelerators when compared to proton accelerators operated at the same power. The activity induced in accelerator components restricts the maintenance immediately after shutdown, whereas the activity in the air, if produced in excess, restricts the entry to the accelerator hall after prolonged operation. The half-life of the radionuclides varies from a few seconds to years. A detailed summary of radionuclides likely to be produced in electron accelerators from various materials is compiled by Swanson [4]. A brief summary of radionuclides identified in commonly used solid materials in electron accelerators is given in Table 1.

Commonly produced radionuclides in water that may be hazardous are ^{15}O, ^{13}N, ^{11}C, ^{3}H, and ^{7}Be. They are produced mainly by spallation reactions in water. They are common for both electron and proton accelerators. ^{15}O, ^{13}N, and ^{11}C are positron emitters with no accompanying gamma rays. They are short-lived but annihilation radiation can produce radiation levels around cooling water systems. ^{7}Be is long-lived (53.3 d) and trapped by ion exchange resin beds in the cooling water system, and can be hazardous. ^{3}H is the only long-lived (12.2 y) radio nuclide produced in water that cannot be trapped by ion exchange resins. Therefore, ^{3}H concentration may build up in cooling water systems and it may be desirable to dispose of the water before the concentration becomes too high.

Two radionuclides with long half-lives that are produced in soil are ^{3}H (12.2 y) and ^{22}Na (2.6 y) and can move along with groundwater through the soil. ^{3}H is produced either due to spallation reaction [8] or due to absorption of thermal neutrons by lithium-6 (8% isotopic composition) in soil, for which the cross-section is very high. On average, lithium content on Earth is of 26 mg/kg of soil [30] approximately. Activities expected from all the components are to be quantified. Radio-activation of accelerator structures/components is fixed, and therefore, proper detection/monitoring of the hot spots with subsequent local shielding, if needed, minimize the exposure rate to maintenance personnel. Production of radio-activation is not an issue of safety concern at low energy electron accelerators, operating below about 10 MeV.

Table 1 Radionuclides produced from common materials used in electron accelerators

Material	Radionuclide	Half-life	Decay mode	Gamma energy MeV	Parent isotope	Reaction type	$E_{th\ (MeV)}$
Copper	^{60}Co	5.26y	β −	1.17, 1.33	^{63}Cu	γ, n2p	18.86
	^{62}Cu	10 min	EC, β +	–	^{63}Cu	γ, n	10.84
	^{64}Cu	13 h	EC, β +, β −	–	^{65}Cu	γ, n	9.91
	^{58}Co	71 d	EC, β +	0.811	^{63}Cu	γ, sp	41.75
Stainless steel (containing Iron and Nickel), mild steel	^{56}Mn	2.58 h	β −	0.847, 1.81	^{57}Fe	γ, p	10.57
	^{51}Cr	27.8 d	EC	0.320	^{54}Fe	γ, sp	19.74
	^{52}Mn	5.6 d	EC, β +	0.74, 0.94, 1.43	^{54}Fe	γ, np	20.89
	^{54}Mn	303 d	EC	0.835	^{56}Fe	γ, np	20.42
	^{48} V	16 d	β +, EC	0.984, 1.31	^{54}Fe	γ, sp	25.86
	^{46}Sc	84 d	β −	0.889,1.12	^{54}Fe	γ, sp	37.41
	^{56}Co	78 d	EC, β +	0.847, 1.24	^{58}Ni	γ, 2n	22.45
	^{57}Co	270 d	EC	0.122, 0.136	^{58}Ni	γ, p	12.19
	^{58}Co	71 d	EC, β +	0.811	–	–	–
	^{60}Co	5.26 y	β −	1.17, 1.33	^{61}Ni	γ, p	9.86
	^{55}Fe	2.6 y	EC	0.006	^{56}Fe	γ, n	11.21
Aluminum	^{22}Na	2.6 y	β +, EC	1.27	^{27}Al	γ, 3n2p	22.51
	^{26}Al	7.4e5 y	β +, EC	1.13, 1.81	^{27}Al	γ, n	13.03
Concrete	^{15}O	2.1 min	β +	–	^{16}O	γ, n	15.67
	^{22}Na	2.6 y	β +, EC	1.27	^{23}Na	γ, n	12.44
	^{27}Si	4.14 s	β +	–	^{28}Si	γ, n	17.18
	^{26m}Al	6.37 s	β +	–	^{27}Al	γ, n	13.03

4 Radiation Environment of Proton/Heavy Ion Accelerators

Proton accelerators are potential tools for application in diversified fields like ion implantation, radio-isotope production, nuclear structure studies, solid-state physics, radiation damage, etc. Increased use of proton or ion accelerators is used in radiotherapy due to the superior quality of dose delivery to the malignant tissue without significantly affecting the nearby tissues. In the field of isotope production for medical applications like PET (Positron Emission Tomography) isotopes, proton cyclotrons are widely used across the world. These isotopes are used for obtaining good-quality images of body organs and also for treatment. Various isotopes for use in nuclear medicines are also produced with the help of protons. Presently, about 18 medical cyclotrons are operating in India for the production of Positron Emission Tomography (PET) isotopes apart from research accelerators. It is also important to note that high energy and high intensity proton accelerators are emerging to find application in the generation of intense spallation neutrons, and the transmutation of long-lived radioactive waste to short-lived, thereby reducing the radio-toxicity and generation of radioactive ion beams. Around such proton/HI accelerators, significant quantities of secondary radiation are generated as a result of interactions of accelerated charged particles with accelerator components and shielding materials. In such radiation environments, energetic neutrons dominate, with their spectrum ranging from thermal energies to TeV levels, and pose a radiation risk in the surrounding area of the public domain. In designing a proton/HI accelerator facility either for fundamental/advanced research or for other industrial/medical applications, quantification of the radiation hazards from the facility and limitation of radiation exposure through various radiation safety systems are important tasks. The following sections describe the radiation environment of proton/HI accelerators and the safety aspects.

4.1 Prompt Radiation at Proton Accelerators

At particle accelerator facilities both prompt and residual radiation are present. Prompt radiations are the radiations emitted during the beam-ON conditions. Estimation of type, energy, and quantity of radiation sources in an accelerator facility is of prime importance in evaluating the complete radiation environment. Radiation is produced by interactions of accelerated beam particles with the material it strikes (accelerator components: Dee, deflector, beam focusing and steering components, vacuum chambers, beam defining slits, collimators, experimental targets, etc.). The higher the kinetic energy of the beam particles, the greater the intensity and type of secondary radiations produced. Beam particles that are intentionally produced are called primary radiations, and all other radiations (no matter how they are produced) are termed secondary radiations.

In electron accelerator facilities, photons (bremsstrahlung) dominate [4] the radiation field followed by photo-neutrons, whereas in positive ion/proton accelerator facilities, neutron dominates the radiation field followed by gamma photons. At high energy accelerator facilities, however, shielding and other radiological safety considerations should be based on the secondary radiation yield (neutron, photons, and other particles) prevailing.

4.1.1 Secondary Radiation Yield

The details of angular and energy distributions of total secondary particle yield (both neutron and photons) from the thin targets (only a fraction of the beam interacts and ionization losses are relatively small) are significant in the study of radiation environments in a particle accelerator facility. But for practical situations related to radiation protection issues, the "thick-target situations" are of real concern. The primary accelerated proton interacting with beamlines, beam dumps, Faraday cups, vacuum chambers, etc., are thick-target conditions where the primary beam is fully absorbed or significantly degraded and secondary particles are generated. The physical process and the secondary particles generated during an interaction with target nuclei are pictorially represented in Fig. 8. Angular distributions of energy spectra in units of secondary particles (per MeV. steradian. incident primary particle) are usually evaluated to quantify the radiation environment.

Angular distributions of secondary radiation yield "dY/dΩ" and total flux, $\emptyset(\theta)$ [secondary particles/cm^2 incident primary particle] are related as given in Eq. (16):

$$\emptyset(\theta) = \frac{1}{r^2}\frac{\mathrm{d}Y(\theta)}{\mathrm{d}\Omega} \tag{16}$$

where r is the distance of the observation point from the primary particle interaction point at a specified angle, θ. The differential flux [secondary particles/cm^2. MeV incident primary particle] is given by Eq. (17):

$$\frac{\mathrm{d}\phi(\theta, E)}{\mathrm{d}E} = \frac{1}{r^2} \cdot \frac{\mathrm{d}Y(\theta, E)}{\mathrm{d}E\mathrm{d}\Omega} \tag{17}$$

NCRP Report 144 [8] gives compiled data on the angular distribution of secondary particle production for thin and thick targets.

4.1.2 Theoretical Considerations

Low/medium energy protons interact through ionization when it interacts with a medium whereas high energy protons interact through nuclear reactions and generate secondary particles. The ionization range of protons increases with their kinetic energy and the mean free path will tend to become constant at higher energies.

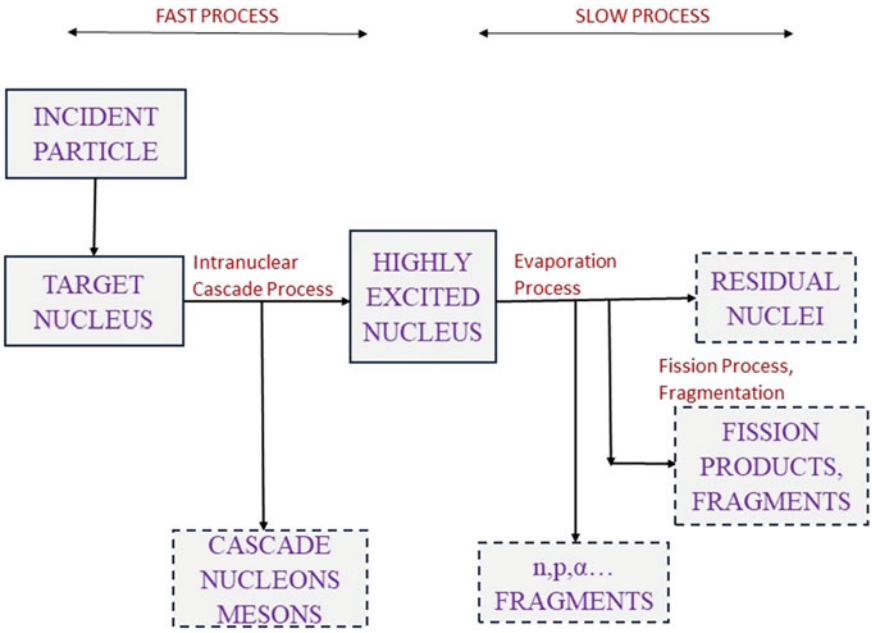

Fig. 8 The physical processes and secondary particles produced when an accelerated proton is incident on a target nucleus

However, very high energy protons undergo cascade processes (as explained in the above section) and produce a wide variety of secondary particles. Thick target yields of secondary particles from the interaction mechanisms are required for quantifying the radiation environment. Such yields can be measured directly by experimental methods or can be determined from thin target cross-section data by integrating over the range of the incident particle (proton). The yield of secondary neutrons is generally high at proton accelerators having energies approximately above 10 MeV and is of great safety concern. The total dose rate considered for radiation protection in such facilities is dominated by neutrons. At proton accelerators of all intermediate and high energies, it is vital to understand the mechanism of production and yields of neutrons.

A. **Low and intermediate energy beams below 1 GeV**

In such facilities, reactions like (p, n) generate neutrons with energies up to or close to the bombarding energy. Between 50 and 500 MeV, the neutron yield increases approximately as E_p^2, and for proton energies above 1 GeV, it is approximately proportional to E_p, where E_p is the proton energy. The angular distribution of the yield depends on the target material, thickness, and geometry due to build-up, self-absorption, and other factors.

B. Energies above 1 GeV

The estimations and measurements of neutron yields, their angular distributions, and spectral distributions are extremely complex due to the increased number of possible nuclear interactions and hence handled with Monte Carlo codes. The approximate neutron yield per μA for different primary energies and different target materials is reported by Rindi [31] for practical purposes.

The knowledge of attenuation lengths of protons in commonly used materials is important. The attenuation length or removal mean free path λ_{removal}, for protons are approximately equal to that of neutrons [5]. This becomes independent of energy above a few hundred MeV (for a given material). Removal mean free paths for common materials are given in Table 2.

Empirical formulations are available to estimate the total hadron flux emitted. As per Thomas [5], the angular fluence of hadrons in cm^{-2}, per interacting proton (in the energy region of 5 $<E_p>$ 500 GeV) at 1 m from a copper target at 1 m is approximately given as

$$\phi(\theta) = \frac{1}{2\left(\theta + 35\sqrt{E}\right)^2} \tag{18}$$

For dosimetry, knowledge of the neutron energy spectrum is very vital. More than just neutron fluence, protection quantities like dose equivalent and effective dose are also

Table 2 Proton removal mean free paths for common accelerator materials [5]

Material	Density (g/cm^3)	λ_{removal} (g/cm^{-3})	λ_{removal} (cm)
H_2	9.0E−5	43.3	4.8E+5
Be	1.85	55.5	30.03
Al	2.70	70.6	26.15
Fe	7.87	82.8	10.52
Cu	8.96	85.6	9.55
Pb	11.35	116.2	10.24
U	18.95	117.0	6.17
Air	1.29E−3	62.0	4.81E+4
H_2O	1.00	60.1	60.1
Concrete	2.50	67.4	26.96
SiO_2	2.64	67.0	25.38
Polyethylene	0.93	56.9	61.51

necessary. The protection quantities may be obtained by use of proper conversion coefficients, $g(E)$, the neutron fluence to effective dose conversion coefficient [32].

The effective dose E may be estimated from differential neutron spectrum as

$$E = \int_{E_{\min}}^{E_{\max}} g(E) \frac{\mathrm{d}\phi}{\mathrm{d}E} \mathrm{d}E \tag{19}$$

where $\frac{\mathrm{d}\phi}{\mathrm{d}E}$ denotes the differential neutron yield.

It is observed for neutrons that the spectrum averaged conversion coefficients are not that strongly spectrum dependent and simple semi-empirical relations are available in the literature wherein one can estimate approximate neutron dose equivalent for wide ranges of neutron energies using the gross neutron fluence rates. In practical cases, for a typical intermediate energy accelerator neutron spectrum, a flux of 1 n cm^2 s^{-1} produces roughly a dose equivalent of 0.5 μSv/h [33].

Nuclear Cascades

At high energy proton accelerators with high intensities of beams, nuclear cascade occurs (similar to electromagnetic cascade in case of electron accelerators). The collision of high energy nucleons with a nucleus produces a large number of particles, mostly nucleons, pions, and kaons. The major method of energy transfer and propagation of the cascade is by the interaction of high energy nucleons with energy of more than 150 MeV due to inelastic cross-sections. But practically above 450 MeV, cascade propagation due to ionization energy losses is significant, and very thick shields are required to control the dose rates (produced by cascade particles) outside.

Muons

Muon production is possible at proton accelerators at above 150 MeV, but radiation safety concerns due to muons are significant only when proton energy is above 10 GeV. Muons generally dominate in longitudinal shielding at proton energies above 20 GeV. High energy muons undergo ionization loses and multiple scattering. As the range of muons is large, earth shielding is utilized considering the economic aspects and effectiveness. Monte Carlo codes are used for estimating radiation environment due to muons. For radiation protection purpose, the fluence to dose conversion coefficients for muons can be taken approximately as 40 f Sv-m^2 for a muon energy range of 100 MeV to 100 GeV.

4.2 Radiation Environment Due to Heavy Ion Interactions

Heavy ion beams of various species are nowadays available at high energies and intensities for various research applications. Secondary particle yields from light ion and heavy ion interactions differ systematically. The nuclear reactions, (p, n), (α, n), and (d, n) are common interactions for light ions and sufficient data on neutron

yield are available whereas for heavy ions data are sparse. Ar, Ne, N, O, S, and other ion beams for different charged states with energies more than 18 MeV/amu have been made available at the Variable Energy Cyclotron Centre (DAE), Kolkata. Approximate yield measurements show neutron yields are nearly independent of a mass number of both target and projectile nuclei. For energies up to 10 MeV/amu, the approximate yield is about 2×10^{-3} neutrons per incident ion. Clapier et al. [34] in their study summarized the neutron yield (neutron/ion) from various heavy ions in the energy region ~ 3–100 MeV/amu and the total neutron yield as a function of the specific energy W [MeV/amu] is given as

$$Y(W, Z) = \frac{1.95 \times 10^{-4}}{Z^{2.75}} e^{-[0.475(\ln Z)^2]W^{1.22\sqrt{Z}}} \tag{20}$$

Also, the normalized angular distributions of either dose equivalent or neutron fluence can be expressed approximately as

$$f(\theta, \xi) = \frac{1}{4\pi}\left[\frac{1}{\log\left(1+\frac{1}{\xi}\right)}\right]\left[\frac{1}{\xi + \sin^2\left(\frac{\theta}{2}\right)}\right] \tag{21}$$

With the parameter ξ defined as

$$\xi = \frac{\phi(90^\circ)}{\phi(0^\circ) - \phi(90^\circ)} \tag{22}$$

where $\phi(\theta)$ is the fluence (or dose equivalent) at θ. For example, for intermediate energy accelerator facilities $\xi = 0.025$ for neutrons of energy below 20 MeV, produced by 86 MeV/amu C^{12} ion beam on iron whereas for neutrons of energy above 20 MeV, $\xi = 0.0003$.

4.3 Induced Radioactivity

All accelerators that can produce charged particles in excess of about 10 MeV/amu can induce radioactivity on the accelerator components (beamlines, Dee, deflector systems, slits, collimators, flanges, and other components like beam dumps.) either by primary beam or by secondary radiations like neutrons. Secondary radiations can induce radioactivity in the air [35] present in the accelerator halls/bunkers and experimental caves.

4.3.1 Induced Activity in the Air

When positive ion accelerators are operated at high energy and with high beam intensities, activation of air occurs around the accelerator which may cause serious inhalation hazards for personnel entering these areas after beam shutdown. The concentration of radionuclides in the air depends on beam parameters, target, building dimensions, and ventilation rate. According to regulatory guidelines, the design of the ventilation system should ensure that the air activity levels are well below the Derived Air Concentration (DAC) values for the radionuclides of concern.

Secondary neutrons and gamma photons produced due to the interaction of accelerated proton or ion beam interact with air nuclei producing radionuclides like ^{3}H, ^{12}B, ^{14}C, ^{13}N, ^{16}N, ^{15}O, ^{37}S, ^{37}Ar, and ^{41}Ar. Out of these radioisotopes, important radioisotopes from the radiation safety point of view are ^{11}C, ^{13}N, ^{15}O, and ^{41}Ar as their concentration can exceed DAC levels and they have sufficiently short half-life. Table 3 lists the important properties of the radionuclides produced in air in accelerator environments.

For a mixture of radionuclides, the sum of the ratio of the concentration of the radionuclides to the DAC value of the radionuclides has to be less than 1. Out of the DAC values in Table 3, ^{11}C has the most restrictive DAC value. If the total activity concentration of all the radionuclides is less than the DAC value of ^{11}C, then safety from the inhalation hazard from the listed radionuclides in the air will be taken care of.

Air activity concentration during operation and after shutdown can be estimated using Monte Carlo Codes like FLUKA [36]. During operation, the concentration of radionuclides increases and reaches a saturation activity concentration (A_{sat}). Practically for different ventilation rates, air activity concentration is calculated as follows.

For different ventilation rates V, built up of radionuclide activity concentration, $A(t)$ of a radionuclide with decay constant λ in a room of volume B, with time t during operation and after shutdown is given by the Eqs. (3) and 4, respectively [37].

During operation:

Table 3 Important radionuclides generated in air in accelerator halls and their properties

Radio-isotope	Half-life (min)	Production mode	DAC (Bq/m^3)
^{41}Ar	109.8	^{40}Ar(n, γ)^{41}Ar	4.84×10^4
^{15}O	2.03	^{16}O(n, 2n)^{15}O ^{16}O(γ, n)^{15}O	5.92×10^4
^{13}N	9.96	^{14}N(n, 2n)^{13}N ^{14}N(γ, n)^{13}N	5.92×10^4
^{11}C	20.36	^{12}C(n, 2n)^{11}C ^{12}C(γ, n)^{11}C	2.96×10^4

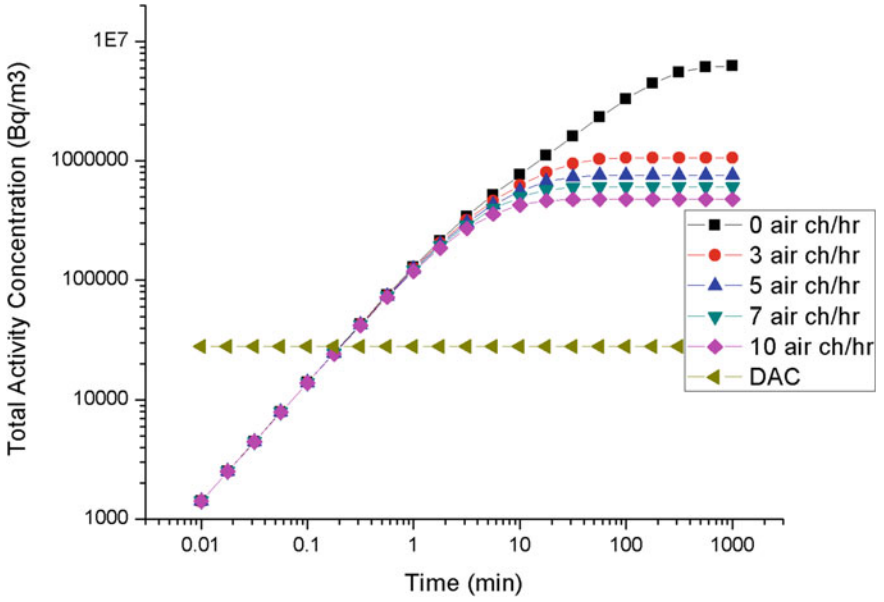

Fig. 9 Typical total air activity concentration during operation in an accelerator hall (adapted from [37])

$$A(t) = \frac{\lambda A_{\text{sat}}}{\lambda + \frac{V}{B}}\left(1 - e^{-(\lambda + \frac{V}{B})t}\right) \tag{23}$$

After shutdown:

$$A(t) = \frac{\lambda A_{\text{sh}}}{\lambda + \frac{V}{B}}\left(e^{-(\lambda + \frac{V}{B})t}\right) \tag{24}$$

A typical activity build-up in air (inside the accelerator hall) during accelerator operation and its decay after shutdown for different ventilation rates (along with DAC values) are shown in Figs. 9 and 10, respectively. These are for a 50 MeV proton beam of 10 kW dumped on a thick tantalum target inside a typical accelerator hall.

4.3.2 Induced Activity on Components

For residual activities on accelerator components, especially for commonly used materials, about 50% of the nuclear interactions produce radionuclides with a half-life longer than a few minutes; of which roughly 50% may have a half-life longer than one day [35]. To illustrate an example of activity generation on solid components, Fig. 11 depicts the formation of ^{60}Co from stable ^{59}Co. ^{60}Co is radioactive with the emission of two gamma rays of 1.17 and 1.32 MeV and has a half-life of 5.2 y.

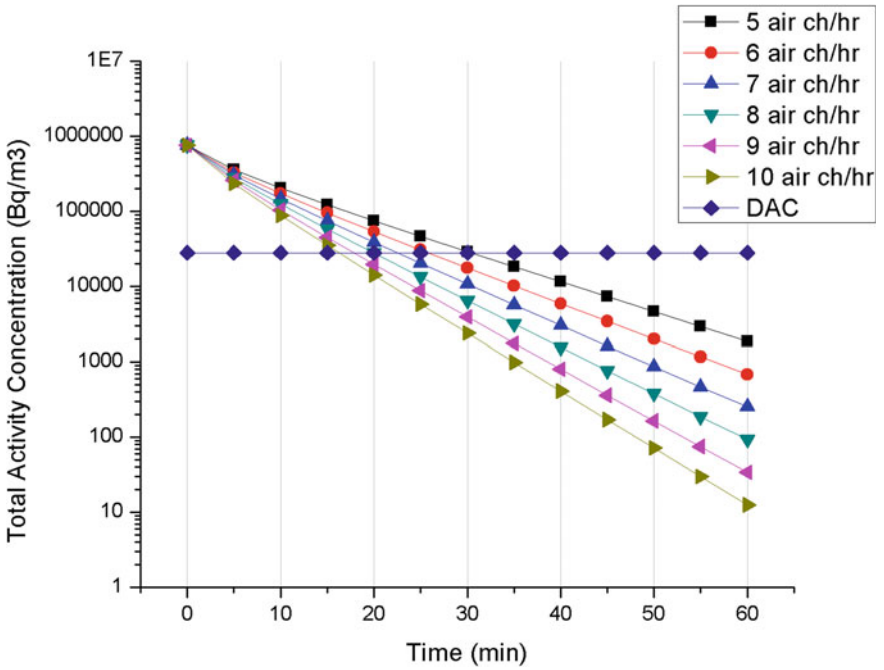

Fig. 10 Typical air activity decay pattern in an accelerator hall after the accelerator is put off (adapted from [37])

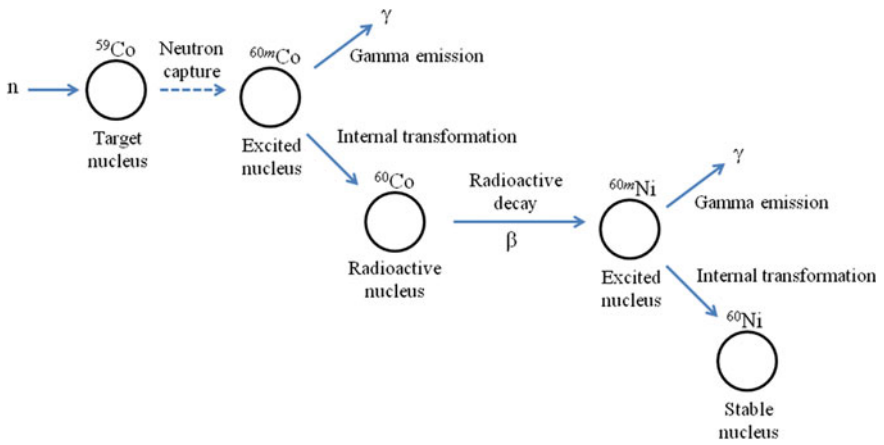

Fig. 11 Illustration of generation of induced activity on a stable metal due to capture of neutrons and the decay scheme (adapted from [37])

Table 4 Radio-isotopes of concern at positive ion accelerators

Radio-isotope	Half-life	Gamma energy (MeV)
^{56}Co	77.3 y	0.85, 1.24
^{57}Co	272 d	0.122, 0.137
^{58}Co	71 d	0.81
^{60}Co	5.24 y	1.32, 1.17
^{65}Zn	243 d	1.12
^{185}Os	94 d	0.65, 0.88, 0.87
^{183}Re	70 d	0.162, 0.053
^{182}Ta	115 d	1.22, 1.12, 1.19

There are several radioisotopes generated due to the direct interaction of protons or ions from commonly used structural materials or due to the interaction of secondary radiation with the materials. A detailed treatment of induced radioactivity in proton/ion accelerator is given in IAEA technical series report 283 [5] which can be used for the estimation of dose rate from induced radioactivity. The list of induced radioisotopes with gamma energies and half-lives on a typical positive ion accelerator is given in Table 4.

The typical remnant gross beta-gamma radiation levels of cyclotron inner components can be a few Sv/h (contact dose rate) with contamination levels as high as 10^7 cpm/cm^2.

4.3.3 Radioactivity Produced in Earth Shielding (Below Accelerator Building) and Ground Water

Earth is often used as a shielding material in large accelerator facilities as it is cost-effective. Radioactivity may be induced in earth shielding and may even migrate to the groundwater table. This may cause radioactivity to enter public water distribution lines. Practically, for low and intermediate energy accelerators below 1 GeV, no significant contamination was observed. For high energy accelerator facilities care should be taken to minimize the activation of earth material and migration of contamination to water table to be prevented. An appropriate analysis should be done in the design stage (while preparing design basis safety report) which would include: (i) identification of radionuclides that could be produced possibly in earth and ground water for that accelerator facility, (ii) estimation of the total concentration of each radionuclide, and (iii) determination of the rate of migration of such radionuclides in groundwater. Following are some important radionuclides that may be present in earth shields of accelerator facilities [38] ^{3}H, ^{7}Be, ^{22}Na, ^{32}P, ^{43}K, ^{45}Ca, ^{47}Ca, ^{46}Sc, ^{47}Sc, ^{51}Cr, ^{54}Mn, ^{55}Fe, ^{59}Fe, ^{58}Co, and ^{60}Co.

4.4 Skyshine Radiation

The prompt radiation field at a distance greater than a few hundred meters from the accelerator has direct and scattered components. The term "Skyshine" refers to radiation from a facility, scattered by air and reaching far away distances, and may lead to exposure to the public. Exposure to the public from skyshine can be prevented or minimized by proper roof shielding. Photon skyshine is rarely a problem if sufficient shielding is provided. Neutron skyshine results from the scattering process and it is largely due to neutrons having energy greater than 20 MeV that are scattered from air and reach the ground. The dose equivalent due to neutron skyshine can be estimated by using the empirical relation (Eq. 25) given below [39]:

$$H(r) = g\phi(r) = a\frac{Q}{r^2}e^{\left(\frac{-r}{\lambda}\right)}, \quad r \geqq 200\,\mathrm{m} \tag{25}$$

where $H(r)$ is the dose equivalent, $\phi(r)$ is the neutron fluence, a is the empirical constant, Q is the leakage neutron source strength (number of neutrons entering the sky), r is the distance from the accelerator source, λ is the effective attenuation of skyshine energy range neutrons in air, and g is the fluence to dose conversion coefficient.

5 Radiation Streaming Through Ducts, Labyrinths, and Tunnels

Access to the accelerated beam hall from outside is essential for routing control cables, power cables, cooling water pipes, ventilation ducts, and air conditioning ducts. Such penetrations compromise shielding integrity and should be properly designed to minimize the streaming radiations through such ducts during the operation of the accelerator [38]. S bends and multiple-legged ducts generally are designed in such a way that the dose rates at the exit of such penetrations should not exceed the regulatory limits. Normally, the duct exits are placed above the man's height [40]. Universal transmission curves of NCRP Report144 [8] can be used to estimate the dose attenuations at different legs of the duct to get the final dose rate at the exit of the duct.

6 Radiation Environment at Antiproton Accelerator Facility

6.1 About Antiprotons

The **antiproton**, ($\overline{p}$), is a member of the hadron family. It is an antiparticle of the proton and made of two up and one down antiquarks. All the measured properties of antiproton match the corresponding properties of proton. However, the electric charge, Isospin, and magnetic moment of antiproton are opposite to those of proton. The antiproton can undergo all four fundamental interactions such as strong, weak, gravity, and electromagnetism. Antiprotons are generally stable. However, these particles are typically short-lived as any interaction with a proton results in the annihilation of both particles, releasing a burst of energy. The existence of antiproton was predicted by Paul Dirac in 1933 [41]. In 1955, physicists Emilio Segrè and Owen Chamberlain achieved the first experimental confirmation of the antiproton at the Bevatron particle accelerator, located at the University of California, Berkeley. Their ground-breaking work on antiproton earned them the Nobel Prize in physics in 1959.

6.2 Production Threshold Energy of Antiprotons

Experimental observations indicate that the production of an antiproton is consistently accompanied by the creation of a new proton.

$$p + p \rightarrow p + p + p + \overline{p} \tag{26}$$

The possible alternative reaction in which electric charge can be conserved with less energy is

$$p + p \rightarrow p + p + \pi^{+} + \overline{p} \tag{27}$$

However, the conservation of energy, momentum, and charge are not the only constraints in creating new particles. Additionally, angular momentum should also be conserved. Hence, Eq. (27) does not happen. In this case, the conservation of baryon number is generalized at high energies for including antiparticles having negative baryon number (-1 for the antiproton). Therefore, the conservation of the baryon number becomes parallel to the conservation of electric charge. Creation of new antiparticles at sufficiently high energies is always possible provided that the total of new charge and total of new baryon number remain zero. It is important to emphasize that these observations are derived from experimental results obtained through the analysis of millions of collisions between relativistic particles.

In the fifties, a modern accelerator was specially designed at Berkeley for the production of antiproton. Therefore, it was important to calculate the production

threshold energy of antiproton accurately. We know that the Lorentz equations are linear, and hence, if we have a system of particles with total energy E and total momentum p in one frame, and E' and p', respectively, in another frame, then we can write

$$E^2 - c^2\vec{p}^2 = E'^2 - c^2\vec{p}'^2 \tag{28}$$

Using Eq. (28), lab frame information can be obtained from the center of the mass frame. Note that in the center of mass (CM) frame, two protons (projectile and target) move toward each other with equal and opposite velocities, and hence the total momentum is zero. In the lab frame, the target proton is at rest and the incoming proton (projectile) moves toward the target and collides. Hence, in the lab frame, the entire momentum is carried by the incoming proton.

Thus, Eq. (28) can be rewritten as

$$E_{\mathrm{CM}}^2 = \left((m_{\mathrm{in}} + m_0)c^2\right)^2 - c^2 p_{\mathrm{in}}^2 \tag{29}$$

where m_0 is the rest mass of the proton and m_{in} represents the relativistic mass of the incoming proton.

$$m_{\mathrm{in}} = \frac{m_0}{\sqrt{1 - v_{\mathrm{in\,LAB}}^2/c^2}} \tag{30}$$

From the final products of Eq. (26), at the antiproton production threshold, $E_{\mathrm{CM}} = 4m_0c^2$.

From Eq. (29), we get

$$16m_0^2c^4 = m_{\mathrm{in}}^2c^4 + m_0^2c^4 + 2m_{\mathrm{in}}m_0c^4 - c^2p_{\mathrm{in}}^2 \tag{31}$$

From Eq. (30), we can get

$$m_{\mathrm{in}}^2c^4 - c^2p_{\mathrm{in}}^2 = m_0^2c^4 \tag{32}$$

From Eqs. (31) and (32)

$$m_{\mathrm{in}}c^2 = 7m_0c^2 \tag{33}$$

Therefore, to create two extra particles [$p + \overline{p}$ in Eq. (26)] with a total rest mass energy of $2m_0c^2$, it is necessary for the incoming proton to have a total energy of $7m_0c^2$. Therefore, the kinetic energy of the incoming proton must be at least $6m_0c^2$ for the production of a proton–antiproton pair. In the case of a proton, $6m_0c^2 \approx 5.6\,\mathrm{GeV}$.

6.3 Production of Antiprotons

Antiprotons are mainly produced in collisions of cosmic ray protons with atomic nuclei in the interstellar medium. Currently, few laboratories in the world, such as CERN at Geneva and Fermi National Accelerator Laboratory, produce antiprotons [42, 43]. The collisions between protons and antiprotons reproduced conditions in the early universe and probed the structure of matter at a very small scale. The schematic diagram of FERMILAB's accelerator chain where such collisions are experimented is shown in Fig. 12.

Scientists at Fermilab created proton beams starting with hydrogen gas. They redirected a fraction of these proton beams to generate antiprotons. Antiprotons were produced by steering the proton beams onto a nickel target. These collisions result in the production of a wide range of secondary particles including many antiprotons. These antiprotons were allowed to enter a beamline, where beam operators captured and focused them prior to their injection into a storage ring. The antiprotons were accumulated and cooled within the storage ring. Cooling of the antiproton beam

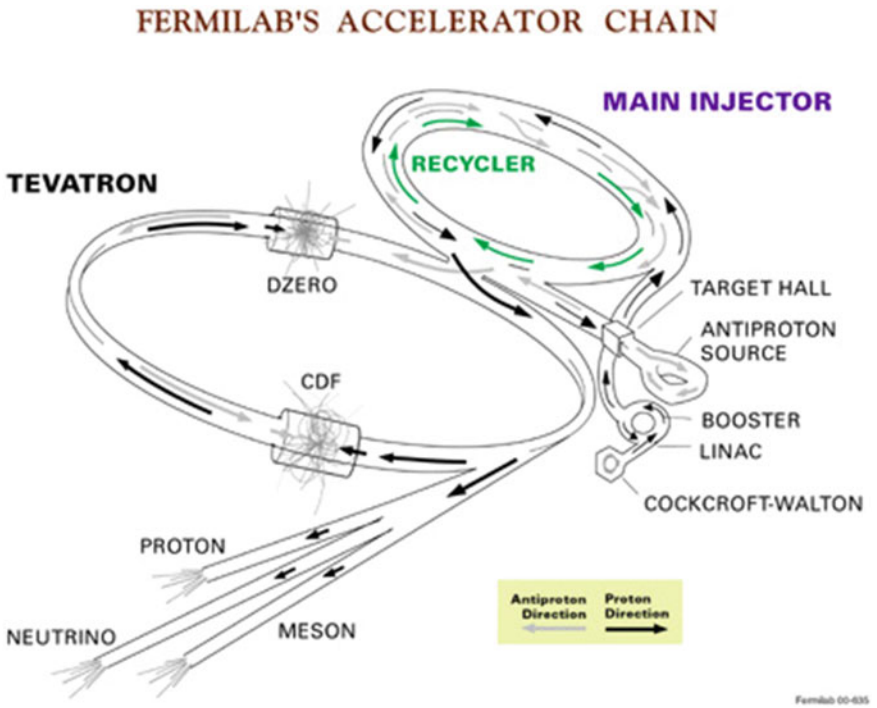

Fig. 12 The schematic diagram of FERMILAB's accelerator chain is shown. The image is taken from CERN official website (https://www.fnal.gov/pub/tevatron/tevatron-accelerator.html)

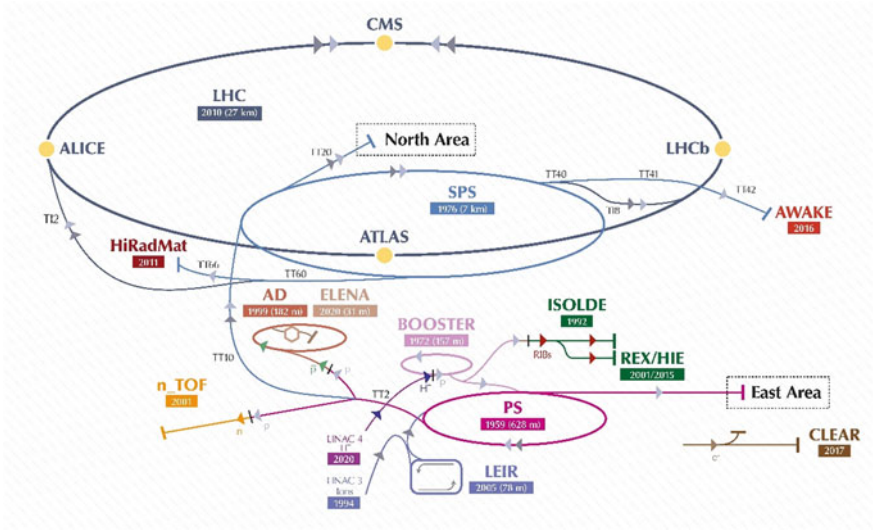

Fig. 13 CERN accelerator complex. Image is taken from CERN official website (https://en.wikipedia.org/wiki/Antiproton_Decelerator#/media/File:CERN_accelerator_complex_(cropped_2).jpeg)

reduced its size and enhanced its brightness significantly. After the accumulation of a sufficient number of antiprotons, beam operators directed them to the Recycler for further cooling and accumulation before initiating their injection into the Tevatron.

The Low Energy Antiproton Ring (LEAR) at CERN was a particle accelerator designed to decelerate and store antiprotons from 1982–1996. In 1996, LEAR was converted to Low Energy Ion Ring. CERN produces antiprotons with kinetic energies 47 and 126 MeV which are relevant to clinical applications. The schematic diagram of the CERN's accelerator complex is depicted in Fig. 13.

The Antiproton Decelerator (AD) facility at CERN produces low energy antiprotons which facilitate studies on antimatter and the creation of antiatoms. The AD ring is constructed with bending and focusing magnets which are designed to keep the antiprotons on the same trajectory as they slowed down in strong electric fields. A technique known as "cooling" is employed to minimize both the energy spread and deviation from their trajectories. Antiprotons undergo multiple cycles of cooling and deceleration until their speed is reduced to approximately a tenth of the speed of light ($0.1c$). Formation of antiprotons necessitates energy equivalent to a temperature of 10^{13}K, an occurrence that does not typically happen naturally. At CERN, a 26 GeV proton beam from Proton Synchrotron is directed into a block of metal. The commonly used target for the production of antiprotons is a thin, highly dense rod of Iridium metal, measuring 3 mm in diameter and 55 cm in length. This rod is embedded in Graphite and enclosed within a sealed water-cool titanium case. These collisions generate numerous secondary particles, including antiprotons with varying energies, some of which are very high. These antiprotons exhibit diverse energy levels and

move in random directions. The peak production is observed at an antiproton energy of 3.6 GeV. The antiprotons that emerged from the target block with diverging angles are focused before they reach the AD. Only a fraction of these antiprotons possess the appropriate energy to be injected into and stored in the AD. The AD facility at CERN effectively transforms these unruly particles into a controlled, low energy beam and makes them suitable for the production of anti-matters. These antiprotons undergo the following steps: (a) they are collected at the production energy in the AD ring, (b) decelerated to lower energies, and (c) subjected to cooling processes, including stochastic cooling and electron cooling, to reduce beam emittance. These antiprotons are then expelled from the accelerator vacuum through a 15 μm titanium window and pass several non-destructive beam monitors before reaching the biological target. The total charge extracted from the accelerator is measurable using a fast current transformer. Depending on experimental needs, the focus of the antiproton beam can be adjusted within the range of $r = 4$–15 mm. Presently, a more recent deceleration ring known as ELENA (Extra Low ENergy Antiproton) is integrated with the AD. With a circumference of 30 m, this synchrotron further decelerates the antiprotons, reducing their kinetic energy by a factor of about 50 (from 5.3 MeV to just 0.1 MeV). The electron cooling system also increases the beam density. With ELENA, the trapping efficiency (the number of antiprotons that can be trapped) of antiprotons is increased by a factor of about 10–100. As of the current status, the CERN Antiproton Decelerator [44] is the only facility capable of producing slow and stopped antiprotons. The design is capable of producing 6×10^8 antiprotons/h and with an anticipated operational schedule of 3000 h/year, it generates a sufficient quantity of antiprotons for proof-of-principle experiments required before the commercialization of any proposed antiproton application. The Antiproton Source at Fermilab [45] has showcased the capability to produce 1×10^{11} antiprotons/h and it has an average operational schedule of 4500 h/year. The Fermilab's production of antiprotons surpasses that of the CERN AD by a factor of 250 in annual quantity. While the CERN AD can decelerate antiprotons down to 100 MeV/c, Fermilab operationally produces and accelerates antiprotons starting from 8.9 GeV/c.

6.4 Transportation of Antiprotons

Over the past decade, Penning traps have been developed to confine antimatter [46, 47]. The experimental demonstration of holding antiprotons in Penning traps has been successfully conducted at CERN. Gabrielse et al. [46] successfully trapped and held 100 antiprotons for several months in the year 1991, and Holzscheiter et al. [47] has trapped 10^6 antiprotons in the year 1994. In the year 1998, NASA supported Smith et al. [48] at Pennsylvania State University (PSU) to build a trap that can hold 10^8–10^{10} antiprotons. The weight of the trap designed at PSU is approximately 200 pounds, making it easily transportable to any desired location. In the year 1999, James Martin at the NASA Marshall Space Flight Center designed the High-Performance Antimatter Trap (HiPAT), a facility capable of holding 10^{12} antiprotons for several

weeks. In most of the medical applications involving antiprotons, it is estimated that approximately 10^{10} antiprotons may be required per patient. Consequently, for treating 20 patients per day and 5 days a week, approximately 10^{12} antiprotons would need to be trapped and transported to hospitals for a one-week treatment period [49]. The U.S. Department of Transportation regulations of the United States are being negotiated to handle the transportation of antiprotons on specially built trucks or aircraft. Antiproton is not a typical radioactive source under normal conditions as there is very little radiation [49]. However, accidental mass-annihilation of the antiprotons results in the emission of radiation exceeding approximately 1 Rad.

6.5 Interaction of Antiprotons with Matter

At high velocities, both antiprotons and protons exhibit similar behavior. However, unlike protons, when antiprotons are slowed down in target material, they are captured by a nucleus and undergo annihilation on its surface [50]. For a given energy, the electronic stopping power of a proton and an antiproton in a material is the same [51]. At high velocity, the main interactions experienced by antiprotons include elastic and inelastic Coulomb collisions with atomic nuclei and atomic electrons, along with elastic and inelastic nuclear reactions with the interacting medium. The annihilation physics of antiprotons is detailed in works by Inokuti et al. [51], Lewis et al. [52], and Bassler et al. [50]. Among the products of all annihilations, seventeen strange particles have been identified [52]. Lewis et al. [52] discussed interesting properties of antiprotons, highlighting: (a) large cross-sections for scattering and annihilation, (b) high multiplicity of about 5 Pions in antiproton–nucleon annihilation near rest, and (c) rare production of K-meson in antiproton–nucleon annihilation. The antiproton is captured by a high Z nucleus when it comes to rest [53] and the antiproton will immediately spiral toward the nucleus and annihilate at its surface. Figure 14 represents annihilation event experienced by an antiproton while stopping in matter.

In the process of annihilation, 1.88 GeV energy (twice the rest mass energy of proton) is released and converted, on average, into 4 or 5 pions (π^+, π^- and π°) [51, 52]. The average kinetic energy of each Pion is approximately 300 MeV and a charged Pion with this energy level has a range of many tens of centimeters in water and human tissue equivalent media [51]. The π° mesons are highly unstable, undergoing instantaneous decay into high energy gamma rays typically ranging from 70 to 300 MeV [52]. Additionally, the antiproton can annihilate by combining with a neutron in the nucleus, leading to the production of mostly high energy pions as decay products [51]. The energy resulting from the annihilation of antiproton is deposited over a broad region [51]. Due to the solid angle covered by the nucleus, usually 1 or 2 charged pions penetrate the nucleus and induce an intra-nucleus cascade [55]. The charged fragments resulting from intra-nuclear cascade-type reactions have a very short range in the target materials, depositing their kinetic energy in the immediate vicinity of the annihilation vertex. Antiprotons annihilating on particles heavier than

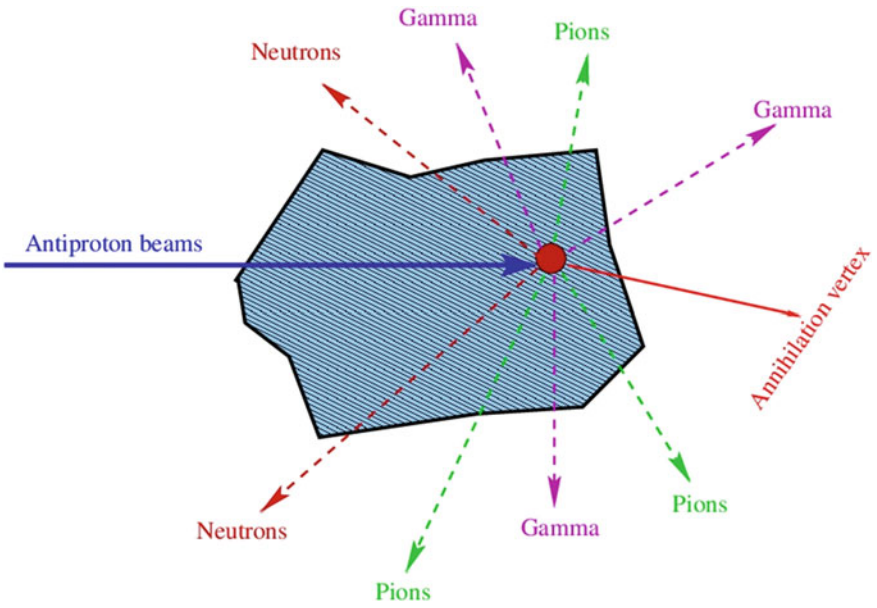

Fig. 14 Annihilation event produced by an antiproton stopping in matter. Adapted from [54]

protons will also produce neutrons which have a larger range and contribute to a certain level of background radiation [56]. Chattaraj and Selvam [57] have presented fluence spectra of protons, π^+ and π^-, as well as secondary neutrons at depths of 2 and 11.5 cm in water resulting from the interaction of 126 MeV antiprotons (see Figs. 15 and 16).

Table 5 shows the calculated FLUKA-based fluence (cm^{-2}/primary) of various annihilation products from 126 MeV antiprotons and secondary products at 2 and 11.5 cm depth [57]. Although the position of the Bragg-peak for antiproton and

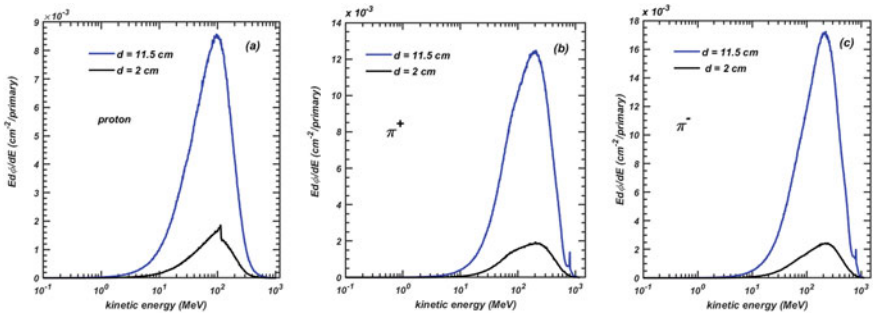

Fig. 15 On-axis fluence spectra of secondary particles such as proton, π^+ and π^- at depths $d =$ 2 and 11.5 cm in water produced by antiprotons: **a** proton, **b** π^+ and **c** π^-. Figures are taken from Chattaraj and Selvam [57]

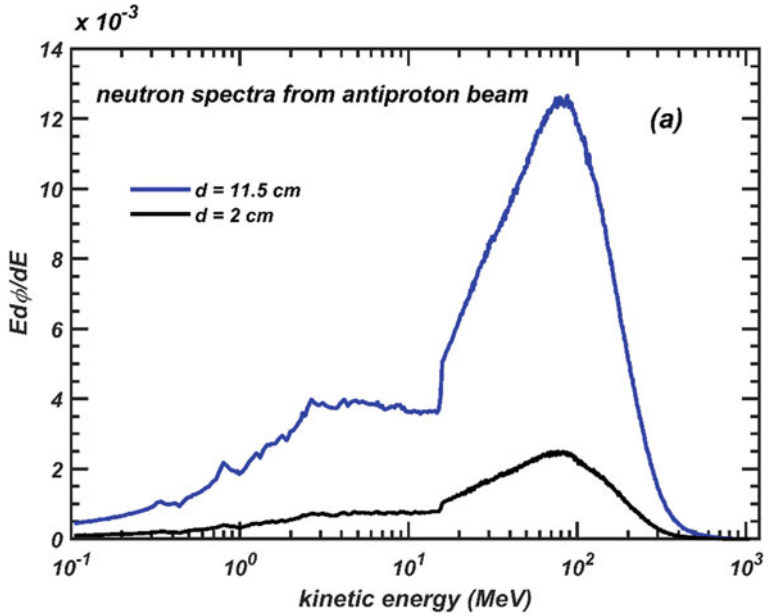

Fig. 16 On-axis fluence spectra of secondary neutrons at $d = 2$ and 11.5 cm in water: **a** antiproton. The figure is taken from Chattaraj and Selvam [57]

proton (both having equal energy) is the same, due to the annihilation of antiprotons, it deposits a higher dose as compared to protons at the Bragg-peak. For example, Chattaraj and Selvam [57] showed that at the Bragg-peak, 126 MeV antiprotons deposits 2.6 times higher dose as compared to protons (see Fig. 17).

Table 5 FLUKA-calculated fluence (cm^{-2}/primary) of various annihilation products from 126 MeV antiprotons and secondary products at 2 and 11.5 cm depth in water

Particle	Depth in water = 2 cm	Depth in water = 11.5 cm
n	7.248E−03	3.712E−02
π^+	4.169E−03	2.656E−02
π^-	5.063E−03	3.443E−02
π°	6.493E−12	3.726E−11
Photon	1.704E−02	9.315E−02
Kaons	3.037E−05	2.234E−04
Muons	3.756E−05	1.691E−04
Proton	2.993E−03	1.722E−02
Antiproton	3.840E−02	2.996E−02

Data are taken from Chattaraj and Selvam [57].

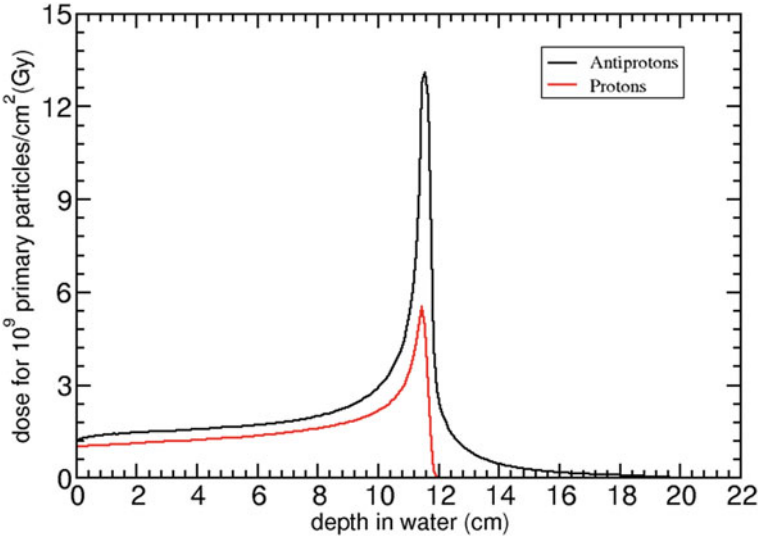

Fig. 17 FLUKA-calculated central axis depth–dose profiles in water for antiproton and proton beams. Figure is taken from Chattaraj and Selvam [57]

7 Summary

Accelerators are potential tools for scientific investigations in basic and applied physics and for societal applications. Radiation safety point of view, they are classified as either electron or proton/heavy ion accelerators. During their operation, secondary radiations are produced due to the interaction of the primary charged particles with either target materials or structural materials of the vacuum chamber. In the case of electron accelerators, bremsstrahlung X-rays is the major secondary radiation of concern, followed by photo-neutrons. In terms of dose equivalent, the photo-neutron dose equivalent of 2–3 order less than that of the bremsstrahlung X-rays due to the low photo-neutron production cross-section (few mb/nucleon). The bremsstrahlung X-rays are of broad energy and highly angular, both depend on the energy of the primary interacting electrons. Thus, in high energy accelerators, the energy of bremsstrahlung X-rays also extends up to GeV and is highly angular (γ^{-1}, where $\gamma = E/E_0$, E is the total energy of electron and E_0 is the electron rest mass energy), and hence radiation detection and subsequent protection in such facilities are very challenging. At electron accelerators where the electron energy is far above the critical energy, the radiation environment is the manifestation of electromagnetic cascade where a large number of secondary particles like electrons, positrons, bremsstrahlung X-rays, pions, muons, etc., are generated.

In proton or heavy ion accelerators, during the interaction of the energetic protons or heavy ions (whose energy is above the coulomb barrier) with targets or vacuum

chambers, slits, etc., generate neutrons which constitute the prompt radiation environment. Particles with energy below the coulomb barrier interact through collision (ionization and excitation), where nuclear phenomenon is not involved. High energy proton accelerators, operating above ~ 100 MeV generate a hadronic cascade, and a large number of secondary particles are generated such as pions, muons, high energy gamma rays, neutrons, etc. As a result of this nuclear cascade, the structural material with which primary protons interact becomes highly activated and poses severe radiation protection problems during shutdown maintenance activities, close to accelerator structural materials. Additionally, the air in the accelerator vault/area, concrete, soil, etc., also gets activated due to the interaction of secondary neutrons with them. This issue calls for proper selection of structural materials, radiation hazard assessment in the design stage (shielding and ventilation), and strict radiation hazard control measures during operation. The problem of radioactivity generation is relatively very less in electron accelerators due to the low photo-neutron generation as already described. Besides, special problems of radiation streaming through ducts, penetration, entry to shielded vaults, and noxious gas generation (e.g. ozone) are very important and adequately addressed to ensure the safety of working personnel. In the case of antiprotons, secondary radiations that would be generated are gamma, neutrons, mesons, and high LET nuclear fragments.

References

1. Milo CE (1994) High intensity accelerator for wide range of applications. Nucl Inst Methods A 353:1–5
2. Chao et al (2002) 2001 Snowmass accelerator R&D report. SLAC-PUB-9483 Stanford University, Stanford, CA
3. Swanson WP, Thomas RH (1990) Dosimetry for radiological protection at high energy particle accelerators. In: Kase KR, Bjaerngard BE, Attix FH (eds) The dosimetry of ionizing radiation, vol III. Academic press, UK
4. Swanson WP (1979) Radiological safety aspect of the operation of electron linear accelerators. Technical reports series no. 188, International Atomic Energy Agency, Vienna
5. Thomas RH, Stevenson GR (1988) Radiological safety aspects of the operation of proton accelerators. Technical report series no. 283, International Atomic Energy Agency (IAEA), Vienna
6. NCRP Report No. 51 (1979) Radiation protection design guidelines for 0.1–100 MeV particle accelerator facilities. National Council on Radiation Protection and Measurements, Washington, DC
7. ICRU Report 28 (1978) Basic aspects of high energy particle interactions and radiation dosimetry. International Commission on Radiation Quantities and Units, Bethesda
8. NCRP Report No. 144 (2003) Radiation protection for particle accelerator facilities. National Council on Radiation Protection and Measurements, Washington, DC
9. Sullivan AH (1992) A guide to radiation and radioactivity levels near high energy particle accelerators. Book published by Nuclear Technology Publishing, England
10. Vylet V, Liu JC (2001) Radiation protection at high energy electron accelerators. Radiat Prot Dosimetry 96(4):333–343
11. Fasso A, Hofert M, AIoannidou (1991) On the shielding of electron accelerators in the GeV energy range. Radiat Protect Dosim 38(4):301–305

12. Liu JC, Vylet V (2001) Radiation protection at synchrotron radiation facilities. Radiat Prot Dosimetry 96(4):345–357
13. Liu JC, Rokni SH, Asano Y, Casey WR, Donahue RJ, Job PK (2006) Comparison of design and practices for radiation safety among five synchrotron radiation facilities. Radiat Meas 41:206–220
14. Asano Y, Job PK, Berkvens P (2006) Third international workshop on radiation safety at synchrotron sources. Radiat Meas 41(2)
15. Haridas G, Nayak MK, Dev V, Thakkar KK, Sarkar PK, Sharma DN (2006) Dose buildup correction for radiation monitors in high energy photon radiation fields. Radiat Prot Dosimetry 118(3):233–237
16. Bhabha HJ, Heitler W (1937) Proc R Soc Lond Ser A 159:432–458
17. Nelson WR, Jenkins TM, McCall RC, Cobb JK (1966) Electron induced cascade showers. Phys Rev 149(1)
18. Haridas G, Thakker KK, Nayak MK, Pradhan SD, Nayak AR, Bhagwat AM (2000) Response of monitoring instruments to high energy photon radiation. Nucl Instrum Methods A 449:624–628
19. Haridas G, Dev V, Nayak MK, Thakker KK, Sarkar PK, Sharma DN (2006) Determination of dose buildup thickness for absorbed dose measurements in high energy electron photon radiation from electron storage rings. Radiat Prot Dosimetry 121(2):92–93
20. Bakshi AK, Nayak MK, Haridas G, Chatterjee S, Kher RK (2008) Estimation of bremsstrahlung photon energy in the environment of high energy electron accelerator using CaSO4:DY based TL dosimeter. Radiat Prot Dosimetry 128(1):43–48
21. Ferrari A, Pelliccioni M, Sala PR (1993) Bremsstrahlung source terms for intermediate energy electron accelerators. Nucl Instrum Methods B 82(1):32–38
22. Nayak MK, Haridas G, Sahu TK, Dashora S, Nandedkar RV, Sarkar PK (2012) Bremsstrahlung source term determination for 450 MeV electrons. Indian J Pure Appl Phys 50:494–497
23. Nayak MK, Sahu TK, Haridas G, Nandedkar RV, Bandyopadhyay T, Tripathy RM, Hannurkar PR, Sharma DN (2015) Bremsstrahlung source term estimation for high energy electron accelerators. Radiat Phys Chem 113:1–5
24. Tromba G, Rindi A, Fabretto M (1990) The shielding of electron accelerators: Monte Carlo evaluation of gamma source terms. In: Proceedings of European particle accelerator conference, France, pp 1389–1391
25. Dinter H, Pang J, Tesh K (1989) Calculation of electron-photon doses behind beam absorbers at High energy electron accelerators. Radiat Prot Dosimetry 28(3):207–210
26. Swanson WP (1979) Improved calculation of photo-neutron yields. Health Phys 37:347–358
27. Snower KA (1986) Giant resonances in excited nuclei. Annu Rev Nucl Part Sci 36:545–603
28. Levinger JS (1951) The high energy photo-effect. Phys Rev 84:43–51
29. Nelson WR, Kase KR, Sevensson JK (1974) Muon shielding around high energy electron accelerators. Nucl Inst Methods 120:401–411
30. Stewart BA (1987) Advances in soil science, vol 6. Springer, New York, NY, pp 101–147
31. Rindi A (1975) Neutron production from heavy ion interaction: some very empirical considerations. Lawrence Berkeley Laboratory Report (LBL-4212), University of California
32. ICRP Pub. 74 (1996) Ann ICRP 26 (Pergamon Press)
33. Patterson HW, Thomas RH (1994) A history of accelerator radiation protection-personal and professional memoirs. N T Publishing, UK
34. Clapier F, Zaidins CS (1983) Neutron dose equivalent rates due to heavy ion beams. Nucl Inst Methods 217:489–494
35. Barbier M (1969) Induced radioactivity. North Holland Publishing Company, Amsterdam
36. Fasso A, Ferrari A et al (2003) The FLUKA code: present applications and future developments: computational physics
37. Ravishankar R (2013) Computational and experimental radiation dosimetry in particle accelerators. Ph.D. Thesis, University of Mumbai, India
38. Patterson HW, Thomas RH (1973) Accelerator health physics. Academic Press
39. Thomas RH, Rindi A (1979) CRC Crit Rev Environ Control 9(1):51

40. Goebel K, Stevenson GR, Routti JT, Vogt HG (1975) Evaluating dose rates due to neutron leakage through the access tunnels of the SPS. CERN Lab II-RA/Note/75-10
41. Dirac PAM (1933) Theory of electrons and positrons. Proc R Soc A Math Phys Eng Sci 126(801):360–365
42. Bassler N, Alsner J, Beyer G et al (2008) Antiproton radiotherapy. Radiother Oncol 86(1):14–19
43. Jackson GP (2003) Practical uses of antiprotons. Hyperfine Interact 146(147):319–323
44. Belochitskii P et al (2001) Commissioning and first operation of the antiproton decelerator (AD). In: Proceedings of particle accelerator conference, pp 580–584
45. Church MD, Marriner JP (1993) The antiproton sources: design and operation. Ann Rev Nucl Part Sci 43:253–295
46. Gabrielse G (1992) Extremely cold antiprotons. Sci Am 267(6):78–89
47. Holzscheiter MH et al (1993) Trapping of antiprotons in a large penning trap- progress toward a measurement of the gravitational acceleration of the antiproton. In: Proceedings of the second Biennial conference on low energy antiproton physics (LEAP 92), pp 709c–718c
48. Smith GA (1993) Applications of trapped antiprotons. Workshop on Traps for Antimatter and Radioactive Nuclei, Vancouver, BC
49. Jackson G (2002) Commercial production and use of antiprotons. In: Proceedings of EPAC, pp 119–123
50. Bassler N, Holzscheiter MH, Jakel O, Knudsen HV, Kovacevic S (2008) The antiproton depth-dose curve in water. Phys Med Biol 53:793–805
51. Inokuti M (1989) Interactions of antiprotons with atoms and molecules. Nucl Tracks Radiat Meas 16:115–123
52. Lewis RA, Smith GA, Howe SD (1997) Antiproton portable traps and medical applications. Hyperfine Interact 107:155–164
53. Ponomarev LI (1973) Molecular structure effects on atomic and nuclear capture of mesons. Annu Rev Nucl Sci 395–430
54. Hall EJ (2006) Antiprotons for radiotherapy? Radiother Oncol 81:231–232
55. Markiel W, Daniel H, von Egidy T, Hartmann FJ, Hofmann P, Kanert W et al (1988) Emission of helium ions after antiproton annihilation in nuclei. Nucl Phys A 485:445–460
56. Fippel M, Soukup M (2004) A Monte Carlo dose calculation algorithm for proton therapy. Med Phys 31(8):2263–2273
57. Chattaraj A, Selvam TP (2022) Comparison of 126 MeV antiproton and proton—a FLUKA-based microdosimetric approach. Phys Med Biol 67:185014

Radiation Environment in Medical Facilities

Sunil Dutt Sharma

1 Introduction

The medical uses of ionizing radiation started way back in 1895 immediately after the discovery of X-rays by Wilhelm Conrad Roentgen. The very purpose of using ionizing radiation in medicine was the welfare of mankind. In general, we have a fear in mind that exposure to ionizing radiation is harmful. However, the medical application of ionizing radiation is unique in the sense that one offers himself or herself to receive the radiation exposure either for the diagnosis or therapy of diseases. The ionizing radiations (X-rays, gamma rays, electrons, positrons, protons, neutrons, heavy ions and alpha rays) are now routinely used in human healthcare programmes and are thought to be a basic need of almost all patients. Nowadays, it is difficult to imagine a human healthcare system without ionizing radiation-based imaging and therapeutic procedures. The medical uses of ionizing radiation can broadly be grouped into two categories as (a) diagnostic applications and (b) therapeutic applications. In recent times, the ionizing radiation-based diagnosis has become a mainstay of all diagnostic procedures. Similarly, in some cases, especially in the case of the management of cancer, ionizing radiation-based therapy has become a mainstay therapeutic procedure. Figure 1 presents the elaborate categorization of the medical uses of ionizing radiation.

The medical imaging systems/facilities can broadly be classified as transmission imaging systems (also called X-ray imaging or structural imaging or anatomic imaging systems) and emission imaging systems (also called nuclear medicine imaging systems or molecular/biologic/functional imaging systems). In the case of X-ray imaging, the medical system can broadly be classified as a planar imaging system and a volumetric imaging system. Planar imaging system provides 2-dimensional

S. D. Sharma (✉)
Radiological Physics and Advisory Division, Bhabha Atomic Research Centre, Mumbai 400 085, India
e-mail: sdsharma@barc.gov.in

D. K. Aswal (ed.), *Handbook on Radiation Environment, Volume 2*,
https://doi.org/10.1007/978-981-97-2799-5_11

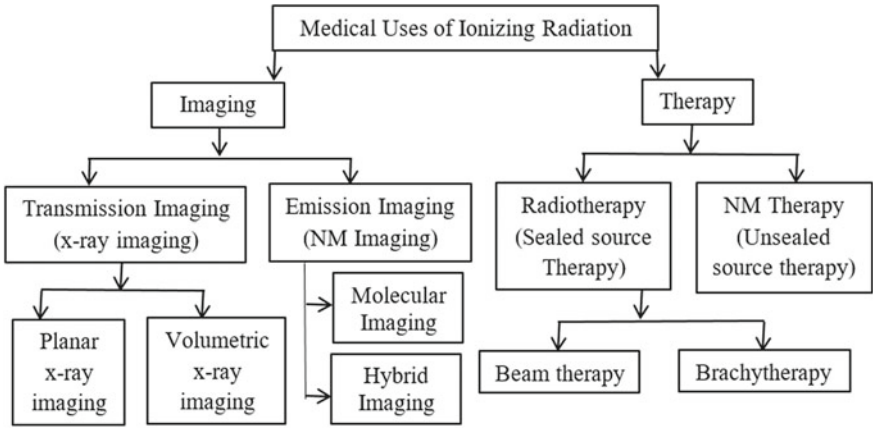

Fig. 1 Categories of ionizing radiation-based diagnostic and therapeutic medical procedures (NM: nuclear medicine)

(2D) images whereas volumetric imaging systems provide 3-dimensional (3D) images. In the case of emission imaging systems, there are two types of systems, namely molecular imaging systems and hybrid imaging systems. The basic difference between transmission and emission imaging is the source of radiation. X-rays need to be generated for imaging the patient in case of transmission imaging, whereas the patient is the source of radiation in case of emission imaging.

The therapeutic application of radiation is broadly classified as radiotherapy and nuclear medicine therapy. Radiotherapy uses either sealed radioactive sources or accelerated particles, whereas nuclear medicine therapy uses unsealed radioisotopes. Radiotherapy involves the treatment either by a radiation generator away from the patient's body (external beam therapy) or a radioactive source inside the patient's body (brachytherapy). A variety of external beam therapy systems such as standard and specialized telecobalt machines, standard and specialized medical electron accelerators, proton beam therapy systems, neutron beam therapy systems and ion beam therapy systems are available. Brachytherapy uses a remote operating device for implanting the miniature radioactive sources (e.g. ^{192}Ir, ^{60}Co) at a predefined location inside the patient's body. Manual implantation of specially prepared sources is also done in brachytherapy. In the case of nuclear medicine therapy, a variety of radiopharmaceuticals are used to relieve patients from a variety of ailments.

2 Transmission Imaging Systems and Facilities

Transmission imaging systems contain an X-ray source (X-ray tube) and a suitable radiation detector system (also called image receptor) (Fig. 2). The X-ray tube consists of a source of electrons (filament) and a target material in addition to other

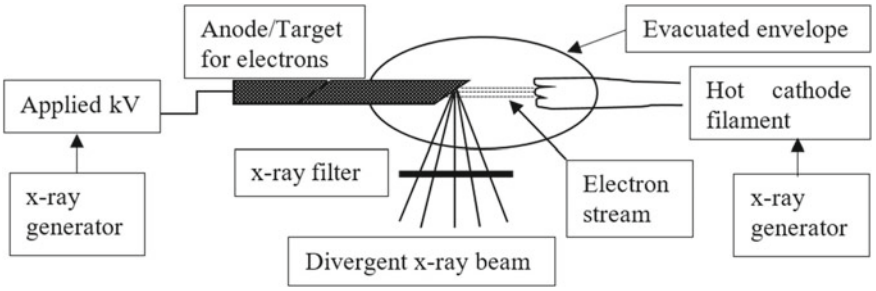

Fig. 2 Schematic cross-sectional view of an X-ray tube

components. X-rays required for imaging are produced when a stream of high-speed electrons (also called projectile or incident electrons) generated by the filament (made up of high atomic number material, e.g. tungsten) collide with atoms of the target material. The high-speed electrons interact with atoms of target materials (generally high atomic number material, e.g. tungsten) in two different ways (collision with atomic electrons and radiative interaction with the nucleus of the atom) which results in the production of characteristics and bremsstrahlung X-rays. Therefore, important components of X-ray equipment are (i) the filament circuit through which the filament is heated and the electron emission is controlled, and (ii) the high voltage source by means of which the electrons are provided energy to move across the X-ray tube. Further, a very small fraction (about 1%) of the energy of high-speed electrons is used in the production of X-rays and the remaining energy (about 99%) is dissipated in heating the target. Hence, an efficient cooling system is required for the smooth operation of the X-ray tube. A radioprotective cover (popularly called tube housing) is also provided over the X-ray tube to minimize the radiation leakage.

The type and energy of the X-ray tube and the type of radiation detector system (image receptor) and their mechanical arrangement with respect to the X-ray source depend on the technique of X-ray imaging. The X-ray energy used in various techniques of transmission imaging ranges from 20 to 150 kV. Further, X-ray beam characteristics (penetration power and nature of spectrum) required for various imaging techniques are also different from one another due to differences in the design/size of filament, X-ray target and filtration (absorber in the path of X-ray beam) used. The penetration power of the X-ray beam is varied principally by changing the high voltage (kV) across the X-ray tube. Raising the kV makes the electrons travel faster across the X-ray tube and the X-rays thus produced are more penetrating, whereas lowering the kV produces the opposite effect. Kilovoltage also alters the intensity of the X-ray beam.

The intensity of the X-ray beam is an important parameter which affects the quality of the image acquired. However, the intensity of the X-ray beam required for a particular technique depends on the type of image receptor. Control over the X-ray intensity is primarily achieved by altering the number of electrons, which are emitted from the heated filament of the X-ray tube. Making the filament hotter causes it to

emit more electrons and conversely making it cooler results in the emission of fewer electrons. These electrons constitute an electric current flowing through the X-ray tube during the exposure. This current is called tube current and is usually expressed in milliampere (mA). The intensity of the X-ray beam is directly proportional to the tube current thus doubling the mA results in doubling the X-ray beam intensity/output.

Exposure time is also an important factor in X-ray imaging. The length of time during which the X-ray tube is energized and the X-ray beam is directed towards the image receptor through the patient is exposure time, and it is more generally expressed in millisecond (ms). The timer of the X-ray equipment is connected to a switch which acts to start and stop the flow of current through the X-ray tube. In addition, filtration (inherent as well as added filters) and collimator are other important components of medical X-ray tube assembly. Filtration helps in removing the low energy components (not contributing to image formation but rather adding unwanted dose to patient skin) of the X-ray spectrum, and collimation helps in shaping the X-ray beam aperture and limiting the exposed area of the patient body.

This section provides details of technique-specific X-ray imaging systems and associated radiation environments.

2.1 X-ray Radiography Equipment

The X-ray radiography is the most important and oldest radiologic imaging technique. In an X-ray diagnostic department, different types of subjects and different body parts are presented for radiographic examinations. It is required to acquire static 2D images with practically the least motion of the object. Considering the type of clinical cases, the penetrating power of the beam, the intensity of the beam and the length of time for which it is directed at the detector through the patient are important factors in the production of a radiographic image. The X-ray radiography system must be able to vary these factors in a wide range of radiographic techniques. The typical X-ray beam energy used in radiography ranges 50–110 kV (e.g. 60–70 kV for hands and feet and 80–90 kV for skull and chest and 100 kV or more for abdomen). Similarly, mA and ms settings of the X-ray tube also depend on the part of the body to be examined and type of the image receptor available. The radiographic X-ray tubes and generators are of high power having typical values in the range of 50–120 kW. Further, a variety of X-ray generators are used with X-ray radiography machines. However, high-frequency generators are now popularly used with radiography systems. An adjustable collimator system is also available with the X-ray tube which defines 5 cm $\times$ 5 cm to 42 cm $\times$ 42 cm fields at 100 cm SID. Figure 3 presents a schematic diagram of the X-ray radiography procedure. In this technique, the body part to be examined is positioned as close to the image receptor as possible which helps in minimizing the magnification.

Both filaments and X-ray targets are made up of tungsten. The X-ray target is a rotating tungsten anode. Nowadays, almost all X-ray radiography machines use

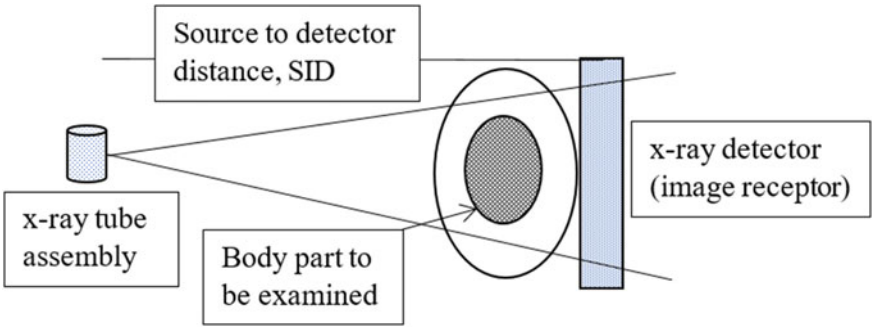

Fig. 3 Schematic representation of X-ray radiography procedure

two focal spots (area of the target from where X-rays are emerging), a small focal spot of size 0.4–0.6 mm and a large focal spot of size about 1.0–1.4 mm. Small focal spot size is required for acquiring images with high spatial resolution. The total filtration depends on the energy of the X-ray beam and it ranges from 1.5 to 2.5 mm Al equivalent [1–3]. The heat capacity of the anode is of the order of 600 kilo heat unit (kHU). In addition, the X-ray tube is mounted in a specially designed tube housing with adequate shielding so that the *Air Kerma* due to leakage radiation at one meter from the focal spot shall not exceed 1 mGy in 1 h [1–3].

As far as image receptors are concerned, screen-film systems were the most common image receptors about a decade ago. However, digital image receptors, introduced in the late 1980s, have now become a common choice because they have provided significant potential for improved effectiveness of radiography in clinical practice. Specifically, digital image receptors have several advantages over screen-film systems including wider dynamic range, rapid image acquisition and adjustable image processing (or enhancement). In the case of digital image receptors, the process of image acquisition, image rendition and image display are fully separated, and hence each component can be optimized individually. However, the use of this technology has shown large variations in image quality and patient doses as it utilizes different digital detectors and post-processing techniques [4].

Figure 4 shows the photograph of digital radiography equipment. This equipment contains a digital image receptor and an automatic exposure control (AEC) device in addition to an X-ray generator, X-ray tube assembly, collimator and X-ray tube housing as described earlier in this section. AEC device is used to maintain a suitably adequate level of image quality consistent with the level of exposure to the detector. The detectors used in AEC systems include fluorescent screens with photomultiplier tubes/photodiodes, ionization chambers and solid-state detectors.

In digital X-ray radiography, the images are recorded directly onto a pixelized imaging device through the use of a scintillator or photoconductor which captures the X-ray pattern [5]. Thin-film transistor (TFT) arrays (also called flat-panel arrays), composed of a matrix of discrete detector elements (dels) each of which contains a transistor, are used as a readout system in flat-panel detector technology. The

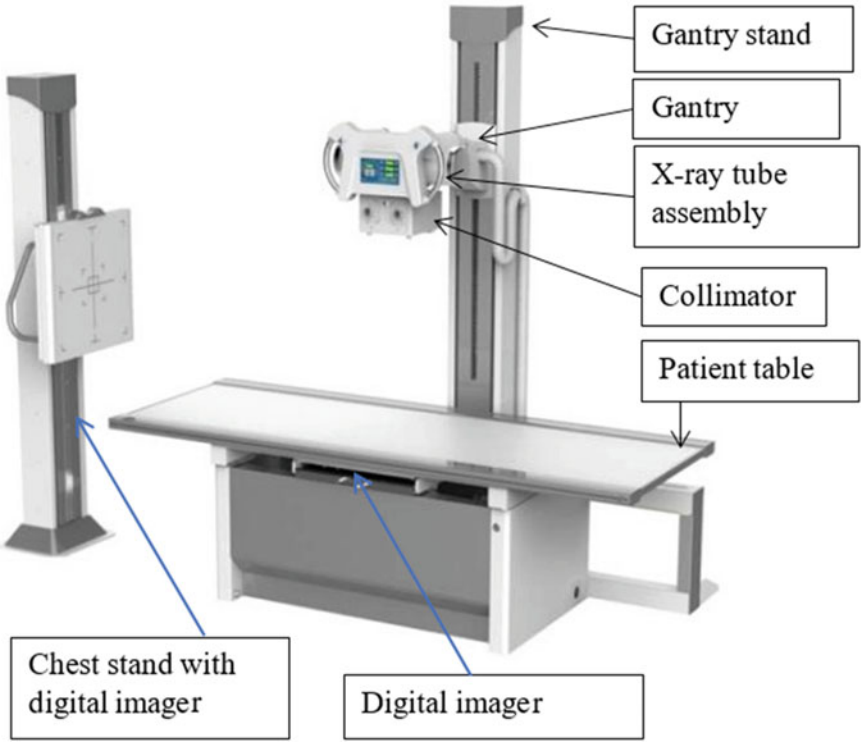

Fig. 4 Photograph of a digital X-ray radiography system with flat panel detector. *Source* https://technohealth.com.bd/product/high-frequency-50kw-630ma-digital-x-ray-machine

digital image recording systems are either indirect image recording device which uses CsI(Tl)/Gd_2O_2S and amorphous silicon (a-Si) or direct digital image recording devices which use amorphous selenium (a-Se) [5].

Figure 5 shows the schematic pattern of scattered radiation generated from the patient in the X-ray radiography room. The technologist available at the control panel may receive exposure mainly from the scattered radiation and the leakage radiation from the X-ray tube housing. To minimize the exposure to the operator, a lead glass shielded operating station is provided. In addition, radioprotective devices/garments (e.g. protective apron) are also provided both for the operator as well as for the patients or comforters (a person who assists the patient in the imaging room for undergoing X-ray imaging process in special circumstances).

A typical layout of the X-ray radiography facility is shown in Fig. 6. The size of the imaging room is typically 4.5 m by 4 m, and the thickness of the walls is typically 23 cm brick or 15 cm concrete. The thickness of the ceiling is typically 15 cm concrete. The X-ray electronics is protected from radiation exposure by using 2 mm lead equivalent glass. The control panel/operator panel is located inside the imaging

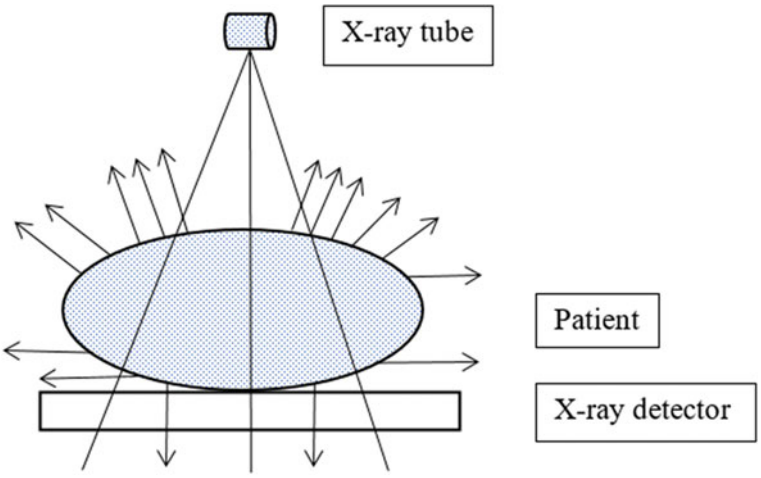

Fig. 5 Illustration of scattered (back scatter and lateral scatter) radiation generated from the patient's body along with transmitted radiation

room but with proper separation using sufficient radiation shielding (typically 1.7–2.0 mm lead equivalent glass) to keep occupational doses within control so that they can be well below the prescribed dose limits. Further, the entrance door to the imaging room is also lead lined (typically 2 mm lead equivalent) to minimize the radiation level in the location of public occupancy.

2.2 Computed Tomography Scanner

2.2.1 Brief History and Generations of CT Scanner

The advent of computed tomography (CT) as a medical imaging modality was a major breakthrough in the history of diagnostic radiology. The first clinical CT scan took place on 1 October 1971 at Atkinson Morley's Hospital, London, England. A patient with a suspected frontal lobe tumour was scanned with a prototype scanner developed by Godfrey Hounsfield and his team at EMI Central Research Laboratories in Hayes, West London [6]. The potential of CT images in medical diagnosis was very evident in the first clinical examination itself which led to enormous research and development in CT technology.

The mathematical principles of CT were developed way back in 1917 by Johann Radon whose theory demonstrated that the image of a 3D object can be reconstructed from an infinite number of 2D projections of the object. Computed tomography was made possible by developments in two fields, viz., X-ray imaging and computing. By the 1930s, conventional or geometric tomography was developed enabling the visualization of sections through a body. The radiological contrast obtained through

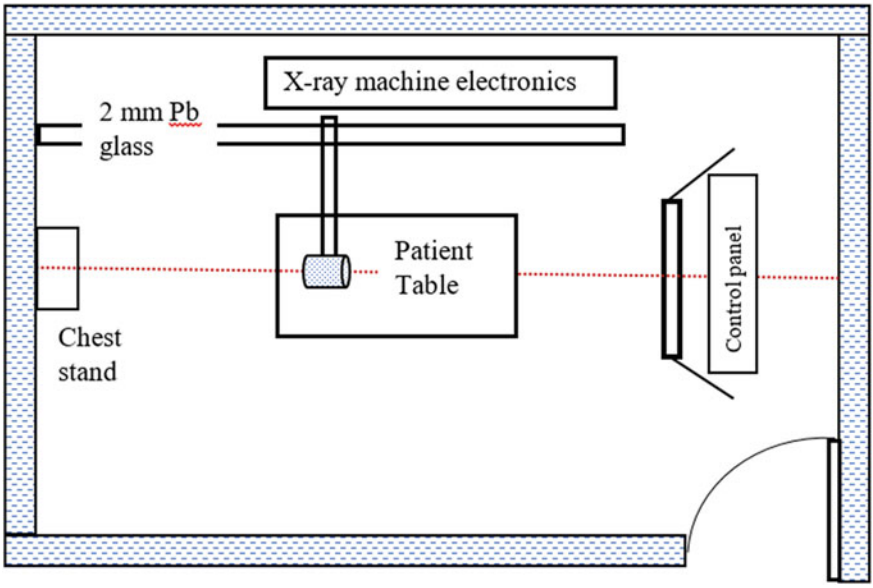

Fig. 6 A schematic layout of a typical X-ray radiography facility along with control panel

conventional tomographic techniques was poor which led to further research in the field of cross-sectional imaging culminating in Hounsfield's work at EMI developing the first computed tomography scanner. This device called EMI Mark I used a 3 mm $\times$ 13 mm wide X-ray beam and two NaI detectors rigidly coupled to the X-ray tube which acquired transmission data while translating across the field of view (FOV) of the patient [7]. After a set of translation data was acquired for that particular angle, the entire tube detector system rotated by a degree to acquire the next set of data. The translate-rotate movement and data acquisition continued for 180 projections. Hounsfield's scanner relied on the reconstruction of imaging data acquired from multiple X-ray transmissions through the object under investigation, by a computer. EMI Mark I produced images with 80 $\times$ 80 pixel resolution (3 mm pixels), and each pair of slices required approximately 4.5 min of scan time and 1.5 min of reconstruction time [8]. Second generation CT scanners replaced single detectors with an array of detectors and used a narrow fan beam to acquire more data in less duration. Movement of an X-ray tube and detector array in second generation CT scanners was also based on rotate-translate though scanning times could be reduced in comparison to first generation scanners.

In third generation CT scanners, the detector array and X-ray fan beam were designed wide enough to encompass the entire patient thickness so that translatory motion of the X-ray tube-detector system could be eliminated which led to faster acquisition times. The fixed alignment of an X-ray tube and detectors in third generation scanners resulted in ring artefacts in images. Real-time calibration of all detectors was not possible in this geometry as some detectors would always be

receiving attenuated X-ray beams through the patient. The fourth generation of CT scanners use stationary ring geometry of fixed detectors completely surrounding the patient. The X-ray tube rotates inside the detector ring through full 360° with a wide fan beam acquiring an image. Since every detector at some point of time during the scan samples receives an unattenuated X-ray beam in this geometry, real-time calibration of detectors could be performed. The number of detectors in the fourth generation (360 ring) CT scanners would be approximately sixfold compared to the third generation (60° fan angle), thus increasing the cost enormously.

Another major impediment to fast scanning then was that after each rotation the gantry had to be stopped and the connecting electrical cables rolled back into the spool before the next rotation could begin. With the introduction of slip-ring technology, inter-scan delay required to unwind cables between successive rotations of the gantry was eliminated.

Slip-ring technology enabled the continuous gantry rotation and patient-table motion which gave rise to a faster scanning technique called helical CT as the path of the X-ray tube detector system around the patient was helical in this arrangement. Now, almost all clinical CT scanners use third-generation geometry with a multi-detector array (MDA) system and X-ray fan angle of about 60° and are capable of completing an entire scan sequence within a single breath hold of the patient. The availability of improvised, stable detectors and algorithms to monitor and correct for any fluctuations in detector gain has minimized the ring artefact problem associated with third generation design. Figure 7 is the schematic representations of first, second, third and fourth generation CT scanners.

The technological innovations in CT scanner hardware and software have led to the introduction of many new clinical applications of CT in diagnosis and therapy (CT-guided interventions), making CT examinations as the largest contributor to population dose among all medical X-ray examinations [9].

2.2.2 Major Components of a CT Scanner

The major components of a computed tomography scanner are a gantry, X-ray generator, X-ray tube, patient table (couch), detectors and computer. The CT gantry is a donut-shaped structure in which X-ray tubes, detectors, high voltage generators, collimators, beam filters, data acquisition systems and other components are mounted. The patient couch is translated through the gantry aperture during the scan. Typical gantry apertures (bore diameter) of the CT scanners range from 65 to 85 cm. Figure 8 shows various components of a CT scanner and their movement directions.

The X-ray generators are an integral part of the CT system and are specially designed to be small enough to fit within the gantry. Present-day CT scanners use high-frequency X-ray generators. The high voltage produced by the generator is transmitted to the X-ray tube. The power capacity of the generator determines the range of kilovoltage (kV) and milliampere (mA) tube current settings, which are available on a particular system. The anode input power of the X-ray generator ranges from 24 to 120 kW. Since the CT scanner is designed to detect linear attenuation

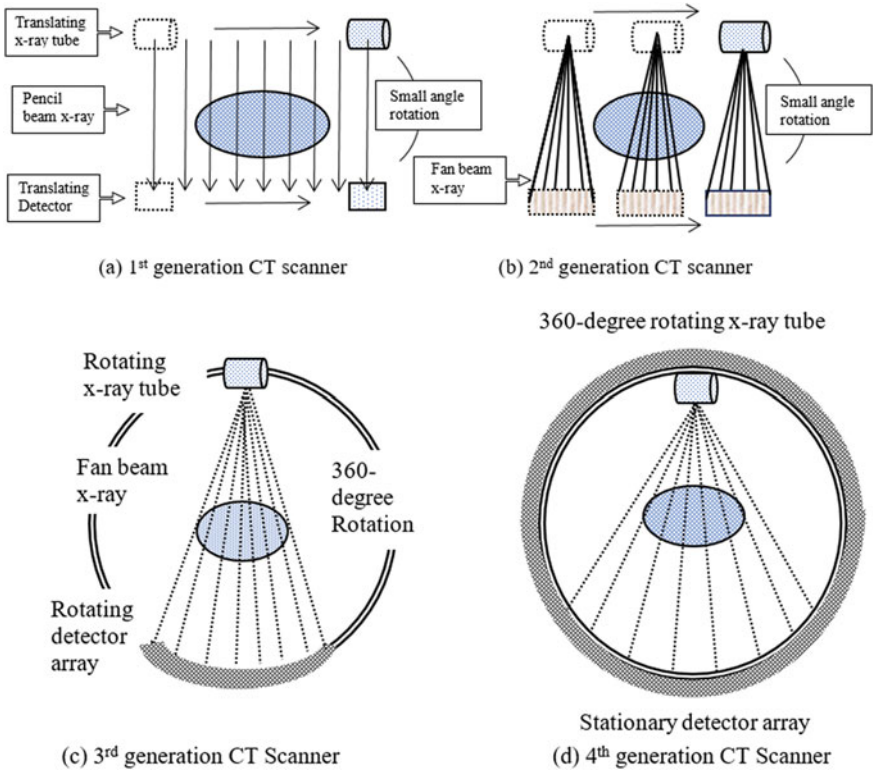

Fig. 7 Schematic representations of 1st, 2nd, 3rd and 4th generations CT Scanners

coefficient differences as low as 0.5%, it is essential that the X-ray tube voltage is highly stable. The requirement for an extremely stable power supply is one of the main cost factors for a CT scanner.

In early generations of CT scanners, stationary anode X-ray tubes were used. The limited output of stationary anode X-ray tubes necessitated a longer sampling time for each measurement of X-ray transmission. This sampling time together with the time required for rotate-translate movements of the X-ray tube and detector limited the data acquisition speed in first- and second-generation scanners. Currently, all CT scanners use rotating anode X-ray tubes, and X-rays are produced continuously (not pulsed). The X-ray tube contains two focal spots, a fine focus of about 0.5–1.0 mm and a broad focus of 1.0–2.0 mm. The ranges of kV and mA of X-ray tubes used in CT scanners are 70–140 kV and 200–1000 mA. The total filtration is of the order of 6–10 mm Al equivalent. The X-ray tubes used in CT scanners have high heat loading and fast heat dissipation capabilities. Anode heat capabilities as high as 8 MHU (Mega Heat Units) are available in current-day CT scanners.

The patient table in a CT scanner unit is an automated device linked to the computer and gantry. The table is designed to move in increments after every scan according to

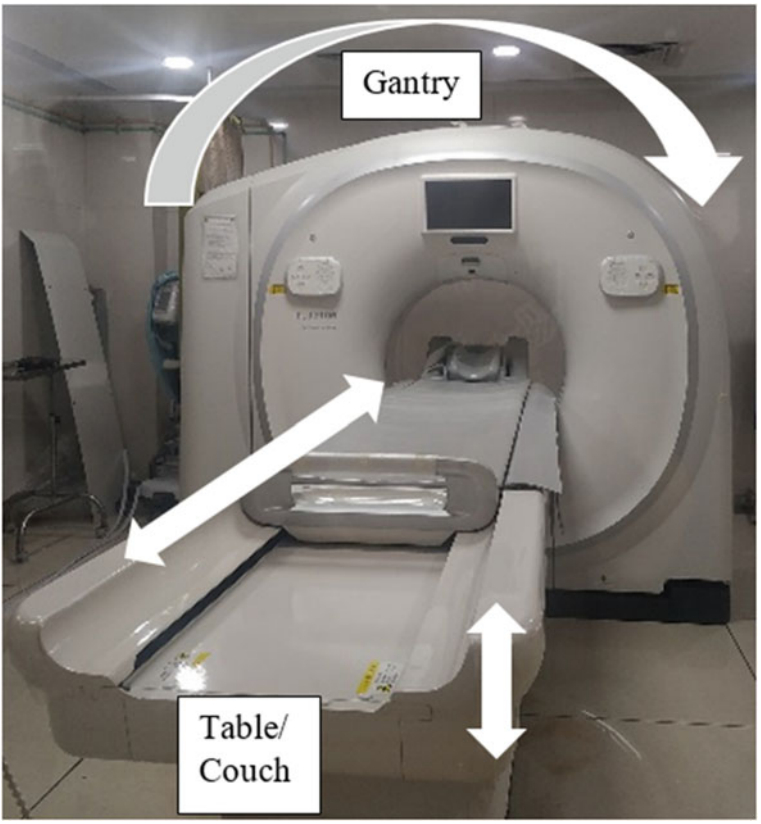

Fig. 8 Photograph of a computed tomography scanner. The arrows and arch show the movement directions. (Courtesy: MGM Hospital, Vashi, Navi Mumbai)

the scan protocol. Accurate and reproducible table movement is vital to image quality and accuracy of diagnostic information. Carbon fibre is the preferred material for the patient table due to its low X-ray attenuation properties and sturdiness.

Most of the present-day CT scanners employ similar detector designs consisting of scintillators coupled to photodiodes. The scintillators used in CT detectors should have high light output, high X-ray stopping power, good spectral match with the photo-detector, short primary decay time, low afterglow, radiation damage resistance, light-output stability, compact packaging and easy machining [10]. These demanding CT requirements make single crystals and polycrystalline ceramics the most suitable types of scintillators. Commonly used scintillators are $CdWO_4$, BGO, Gd_2O_2S:Pr, Ce (GOS), $(Y,Gd)_2O_3$:Eu and the GE Gemstone™ [10]. The scintillators for multi-detector CT (MDCT) scanners are made in 2D arrays with typical dimensions of 1 mm × 1 mm.

The computer is an integral part of the CT imaging system as image reconstruction in CT involves enormous mathematical computations. Major functions of computers

in CT systems involve the acquisition of image data, reconstruction of images, display and archival of images. Computer in CT also takes care of monitoring of kV, mA and heat loading on X-ray tubes, performing corrections to compensate for hardware artefacts and also providing various graphic options for image analysis.

Figure 9 shows a model layout plan of a CT scanner facility. CT machine is a partially self-shielded machine. The *workload* (expressed in mA-min/week) of the CT machine is a few fold higher than the X-ray radiography machine. But the wall thickness of these two facilities is approximately the same because of the partial self-shielding of the X-ray beam in CT scanners. However, it generates a lot of scattered radiation in the examination room. The radiation environment in the examination room contains mainly scattered radiation and radiation leakage from the X-ray tube. The entrance door to the examination room is lead-lined giving due consideration to the radiation safety of the general public. The entrance to the examination room from the control station and viewing window of the control station are lead-lined giving due consideration to the radiation safety of occupational workers.

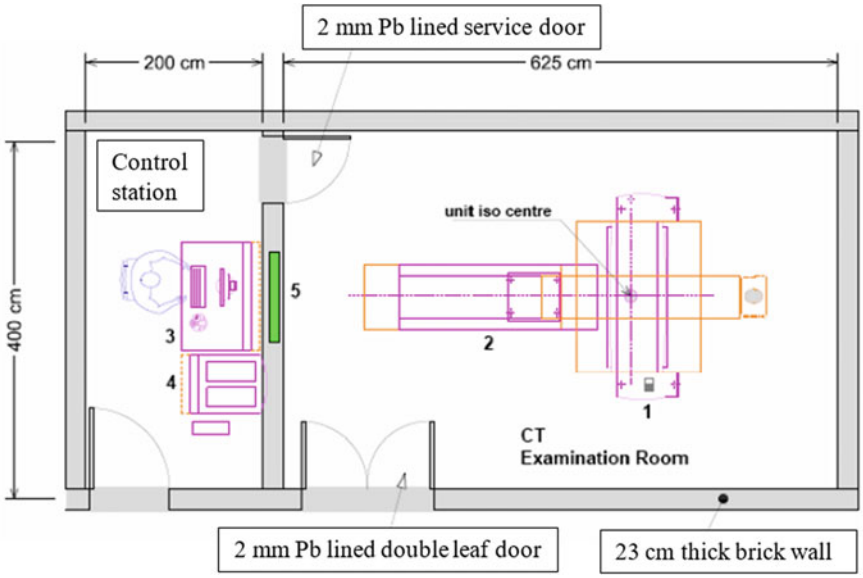

Fig. 9 A typical layout plan of a computed tomography scanner facility. *Source* https://www.aerb.gov.in/images/PDF/DiagnosticRadiology/Model-Layout-CT-Scan.pdf. (1) gantry, (2) table, (3) control panel, (4) electronics and (5) viewing lead glass window having 2 mm lead equivalent thickness

2.3 Fluoroscopy Systems

Fluoroscopy, an important real-time imaging technique, serves as a valuable tool in guiding a wide range of diagnostic and interventional procedures. It facilitates the capture of patient images, such as in angiography, and provides precise imaging guidance during interventions, like angioplasty. By generating a continuous stream of images at a rapid rate of 25–30 frames per second, fluoroscopy creates the illusion of seamless motion, allowing for enhanced visualization and accuracy in medical procedures.

Fluoroscopy imaging has progressed significantly from its humble beginnings as a basic non-invasive imaging technique to a sophisticated method with 3D capabilities. This advancement enables the guidance of life-saving interventional procedures while minimizing patient discomfort. Moreover, fluoroscopy-guided minimally invasive procedures have supplanted more invasive surgeries like open heart surgery. Recent technological strides have even made it possible to visualize smaller vessels in real time with low radiation doses to patients [11, 12].

There are five configurations of fluoroscopy systems: Gastrointestinal/genitourinary (GI/GU) systems, which position the X-ray tube under the patient table; remote systems, with the X-ray tube placed over the table; interventional vascular systems used in vascular surgery and radiology; cardiology and interventional electrophysiology systems; and mobile C-arm configurations for surgery and pain medicine. Despite their differences, all these systems share the same basic components [8].

Most fluoroscopy devices have more than one image acquisition mode of operation. For example, cardiac systems have fluoroscopy and cine acquisition modes of operation, and vascular systems have fluoroscopy and digital subtraction angiography modes of operation. Continuous fluoroscopy employs a steady X-ray beam, typically using a tube current ranging from 0.5 to 6 mA. Conversely, variable frame rate pulsed fluoroscopy, also known as pulsed fluoroscopy, involves the X-ray generator emitting a series of brief X-ray pulses with exposure times ranging from approximately 3–10 ms, as opposed to the usual 33 ms. This method helps mitigate image blurring caused by patient motion, such as pulsatile vessels or cardiac motion. Particularly in scenarios with heightened object motion, such as when positioning catheters in highly pulsatile vessels, pulsed fluoroscopy provides improved image quality at the same average dose rate [13].

The technical configurations of fluoroscopic imaging equipment are similar to that of radiographic equipment. However, depending on the type of use, there are some modifications and additions in comparison to radiography equipment. For example, high-power generator and a high heat capacity X-ray tube are generally used in a fluoroscopic system. The major difference between fluoroscopic and radiographic equipment is the image receptor. Fluorescent screens, similar to the intensifying screens used in radiographic screen-film systems, were used with fluoroscopic imaging in its early days. The dim image produced by the intensifying screen was the main disadvantage of this direct viewing system because it required the dark adaptation to the

radiologist's eye. Relatively high doses to both patient and radiologist were another disadvantage. In modern fluoroscopic systems, the fluorescent screen is coupled to an electronic device that amplifies and transforms the glowing light into a video signal suitable for presentation on an electronic display. This device is popularly known as X-ray image intensifier (XRII). Because of several advantages over XRII, recent day fluoroscopic system uses flat panel image receptors. The addition of a flat panel detector has made it possible to use the modern fluoroscopic system for a variety of medical applications such as rotational angiography and cone beam CT [13].

The oil-cooled rotating 12° angulated anode X-ray tube is used in the fluoroscopy machine. The radiation output can either be continuous or pulsed, with pulsed being more common in modern systems. The fluoroscopy equipment are operated in the voltage range of 40–125 kV, tube current in the range of 0.3–1000 mA and focal spot in the range of 0.3–1.2 mm. The total filtration is up to 1 mm Cu, and variable spectral shaping filters are also included to maximize iodine contrast. The nominal power of the X-ray generator is of the order of 100 kW and the maximum anode heat capacity is up to 6.4 MHU. The size of the image receptor ranges from 20 cm $\times$ 20 cm to 30 cm $\times$ 40 cm.

The automatic exposure control (AEC) of the fluoroscopic system controls the *Incident Air Kerma Rate* (IAKR) to the detector to prevent fluctuation in image brightness. Further, subject contrast is poor in fluoroscopic imaging which is improved through the use of radiopaque markers and through the use of exogenous contrast agents. Iodine and Barium, having K-edges of 33 and 37 keV respectively, are commonly used as contrast agents in fluoroscopic imaging. In case of contraindications due to allergy or impaired renal function, Gadolinium or carbon dioxide can be used as a contrast agent. Spectral shaping of the X-ray beam is now possible due to high heat capacity and increased current range of fluoroscopic equipment for enhancing the Iodine contrast [13].

Figure 10 shows the photograph of a C-arm fluoroscopic imaging equipment which is used for vascular and interventional procedures. Within the C-arm fluoroscopic machine, there is a mechanically linked X-ray tube and image receptor. Both components revolve together around the isocentre, which is located at the centre of the C-arm. As the C-arm rotates, the isocentre remains positioned at the centre of the field of view (FOV). Typically, the table is designed to be cantilevered, allowing for seamless and unobstructed rotation of the C-arm around the patient throughout the procedure.

Fluoroscopy-guided vascular and interventional procedures are commonly conducted in specialized rooms known as angiographic suites. A typical arrangement of such a suite is illustrated in Fig. 11. In interventional cardiology suites, C-arm fluoroscopic systems are commonly employed due to their flexibility in positioning around the patient at various angles. These suites may accommodate either single-plane or biplane systems. Biplane systems incorporate two C-arms that can be manoeuvered independently around the patient, allowing for simultaneous digital imaging during a single contrast injection. This feature is crucial as iodinated contrast, commonly used in these procedures, can be harmful to the kidneys, and the amount administered is limited by the patient's body mass.

Fig. 10 Photograph of a C-arm fluoroscopy imaging equipment used for vascular and interventional procedures (Courtesy: Jupiter Hospital, Thane, Maharashtra, India)

The total dose to the patient as well as occupational worker is relatively high in fluoroscopic imaging procedures in general and fluoroscopically guided procedures in particular. In some cases, the patient dose is higher than the threshold for the deterministic effects [11]. There are regulatory limits on the minimum distance between focus to table top distance (shall be $\geq$ 30 cm), table top dose rate at minimum focus to table top distance (Air Kerma Rate at tabletop for the minimum focus-to-tabletop distance shall be as low as possible, and in any case shall not exceed 5 cGy per minute for conventional fluoroscopy and 10 cGy per minute for pulsed fluoroscopy) and maximum range of the cumulative timer (maximum range shall be $\leq$ 5 min) for fluoroscopic imaging systems [1]. These regulatory limits are directly linked with the safety of the patients. For occupational workers, use of radioprotective aprons, thyroid shields, gonad shields and radioprotective goggles is highly recommended.

2.4 Mammography Equipment

Mammography is a breast imaging technique using low-energy X-rays. The primary aim of mammography is to examine the female breast to distinguish the existence of tumours, cysts, calcifications or any other abnormalities. Mammography equipment is designed to demonstrate low subject contrast and fine detail of the breast tissues which have small differences in X-ray attenuation. Considering the radiation risks,

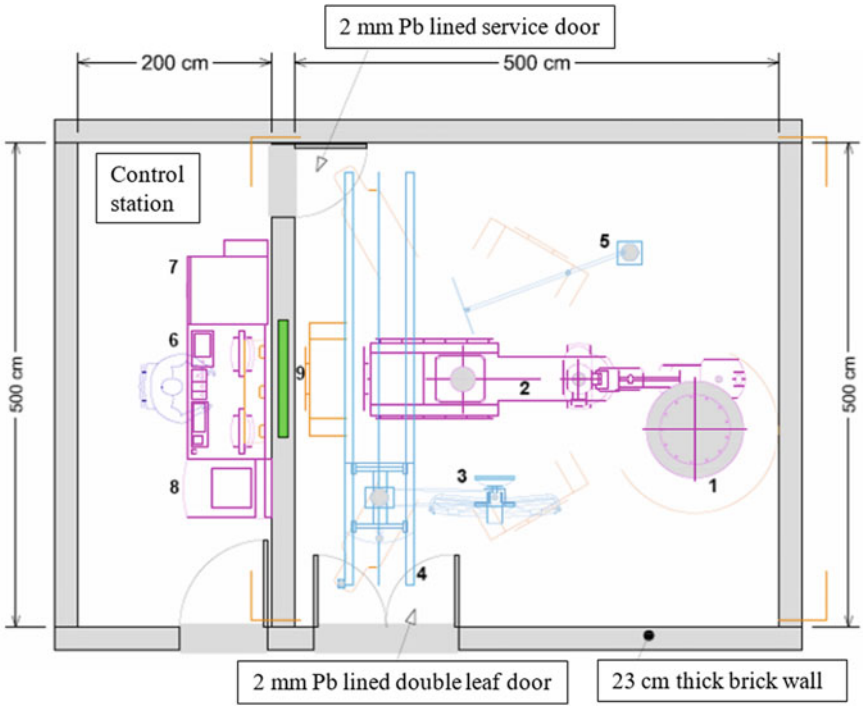

Fig. 11 Layout of a typical suite used for fluoroscopy guided vascular and interventional procedures. *Source* https://aerb.gov.in/images/PDF/DiagnosticRadiology/Model-Layout---Interventional-Radiology-Installation.pdf. (1) C-arm, (2) examination table, (3) monitor trolley, (4) overhead rails, (5) fixed radiation shield, (6) control unit, (7) electronics, (8) additional electronics and (9) viewing lead glass window having 2 mm Pb equivalence and size about 120 cm × 100 cm

optimization of techniques to achieve good image quality with minimum dose is very important. Mammography equipment comprises a high-voltage generator, a very small focus X-ray tube, a filter, a collimator, a compression system, an image receptor plate and an automatic exposure control (AEC) system as shown in Fig. 12. The X-ray tube and the image receptor are mounted on opposite sides of a mechanical assembly.

The mechanical assembly can be adjusted vertically and can rotate about a horizontal axis to accommodate patients of different heights and acquire the image from different aspects of the breast. The X-ray beam passes through a metallic spectral-shaping filter, a beam-defining aperture and the compression plate before reaching the breast of the patient. The differentially attenuated X-ray is recorded to form an image after passing through the anti-scatter grid (scatter rejection device) which is positioned between the breast supporting system and the image receptor.

The mammography X-ray machine uses a high-frequency generator and is operated typically in the range of 20 to 40 kV.The X-ray targets are molybdenum (Mo), rhodium (Rh) and tungsten (W), and spectral characteristics of the X-rays are decided

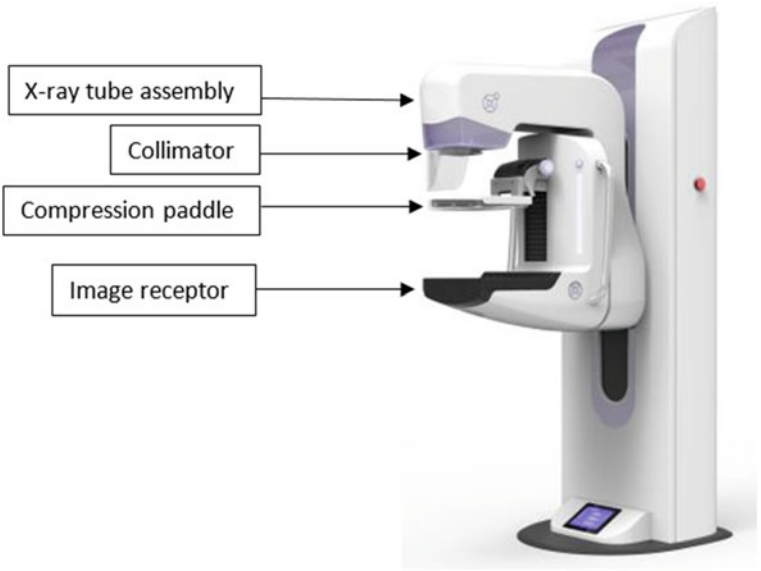

Fig. 12 Photograph of a mammography X-ray machine

by the use of different target/filter (T/F) combinations. The anode is a rotating anode and has a bevelled edge, which is at a steep angle to the direction of the electron beam. Focal spots ranging from 0.3 to 0.4 mm (contact imaging) and 0.1–0.15 mm (magnification imaging) are used to obtain high spatial resolution and optimal image quality. The X-ray window is made up of beryllium (Be) which has a low atomic number and high Young's modulus. Collimation of the X-ray beam is achieved using metal diaphragm collimators. The size of the image receptor is typically 18 cm × 24 cm or 24 cm × 30 cm.

An automatic exposure control (AEC) system is used to provide consistent signals as X-ray tube potential is varied over the varying breast thickness [14]. In the AEC system, an ionization chamber or a solid-state detector is located behind the image receptor. Present-day AEC system compensates for variation in the selected operating potential and breast thickness and density.

The quality of mammography images and the efficiency of dose are highly influenced by the characteristics of the X-ray spectrum. These X-ray spectrum shapes are determined by factors such as the material of the anode, the voltage applied to the X-ray tube, and the type and thickness of additional filtration. Prior to actual image acquisition, a short test pulse is often conducted to optimize the X-ray exposure to the patient. This optimization process may involve identifying the minimum signal from the most attenuating area of the breast. Determining the ideal X-ray spectrum for mammography requires striking a balance between image contrast, radiation dose and the level of statistical noise in the image.

Compression is vital for reducing the thickness of the breast, which is necessary to decrease the glandular dose. By reducing breast thickness through compression, the generation of scatter components is minimized, thereby enhancing image contrast. It's crucial that the compression plate allows for parallel compression of the breast to the image receptor, and that the plate's edge at the chest wall is aligned with both the focal spot and image receptor to maximize breast tissue inclusion in the image. Compression spreads out different tissues, reducing superposition from various planes and improving the visibility of structures. The use of compression reduces geometric blurring, breast dose and the ratio of scattered to directly transmitted radiation reaching the image receptor.

The technology of image receptors has improved a lot in the recent past. In its early days, X-ray mammograms were directly recorded on medical imaging film which has produced low contrast at higher radiation doses to patients. Accordingly, mammography screening in the 1950s and 1960s did not provide any useful benefits for the early detection of breast cancer [8]. Continuous developments in imaging technology have improved mammography over the last 40 years starting from screen-film to digital imaging [8]. Digital mammography technology offers simplified archival, retrieval and transmission of images, reduction in mean glandular dose (MGD), higher patient workflow and improved diagnostic accuracy [4, 15]. Gradually screen-film systems are replaced by digital imaging systems.

Regulatory limits have been prescribed for mammography X-ray imaging systems as well [1]. These limits are as follows: (i) the X-ray tube housing shall be so constructed that leakage radiation at 5 cm from any point on its external surface shall not exceed 0.02 mGy in one hour, (ii) the total filtration in mammography equipment with Mo-Mo target filter combination shall not be less than 0.03 mm Mo and for any other target filter combination, the total filtration shall be greater than or equal to 0.3 mm Al for 30 kV, 0.4 mm Al for 40 kV and 0.5 mm Al for 50 kV.

3 Emission Imaging Systems and Facilities

Emission imaging or nuclear medicine imaging procedure includes the administration of a gamma-emitting or positron-emitting radiopharmaceutical (also called a radiotracer) which gets redistributed physiologically within the patient. The subsequent decays of the radiopharmaceutical led to the emission of gamma rays or high-energy photons with enough energy such that a significant fraction of these emissions escape from the body. These escaped photons are detected using the radiation detector or camera, which can be used to localize the distribution of activity within the body. Thus, emission imaging makes use of the ionizing radiation emitted by the radionuclide administered to the patient (orally, by injection or by inhalation) in the form of radiopharmaceutical for obtaining information related to the physiological functions of the patient body. The distribution of the radiotracer in the patient is measured with a dedicated imager. The imager may be either a molecular imaging system [a gamma camera, a single photon emission computed tomography (SPECT)

or a positron emission tomography (PET) unit] or a hybrid imaging system (molecular plus structural imaging system) such as SPECT-CT, PET-CT and MR-PET. Nowadays, hybrid imaging systems are popularly being used in diagnostic nuclear medicine procedures. Details of these systems are provided in this section.

Medical cyclotron is thought to be an integral part of the nuclear medicine facility as it provides a number of radionuclides for use in the current practice of nuclear medicine. This section also contains a brief description about the construction and working of a medical cyclotron facility. Further, non-imaging studies are also very useful in examining the functionality of certain parts of the human body. For a shake of completeness, a brief detail has been included about the technicalities of thyroid uptake studies.

3.1 Gamma Camera

Gamma camera (also referred to as the Anger scintillation camera after the name of its inventor Hal Anger) is one of the most widely used emission imaging devices in the nuclear medicine department (illustrated in Fig. 13). A gamma camera utilizes a single large area NaI(Tl) crystal which is optically coupled to a large number of photomultiplier tubes (PMTs). Due to this arrangement, a gamma camera, as compared to its predecessor, i.e. rectilinear camera, can simultaneously acquire data over a much wider area of the patient and thus can accomplish rapid image acquisition as compared to the latter. Gamma cameras can either be used in the *static mode* in which a single integrated image is obtained over an extended time period or in *dynamic mode* in which many frames per second are obtained to observe the temporal distribution of activity in the region of interest which provides the physiologic information about the subject. In some cases, synchronization of these images with an electrocardiogram is also done to carry out cardiac function studies.

A collimator, usually made up of lead bar which contains a large number of holes, is placed in front of the scintillation crystal. The collimator allows the photons travelling in a particular trajectory to reach the scintillator while absorbing the rest of the photons emitted from the patient. Without a collimator, the origin of photons cannot be determined which results in the loss of spatial information about the activity distribution within the patient. By selectively transmitting the photons, the collimator led to the formation of a projected 2D image of the 3D radioisotope distribution on the surface of the scintillator crystal.

The photons coming through the collimator are absorbed in the scintillation crystal which results in the emission of secondary photons (visible or ultraviolet). These secondary photons in turn get converted into photo-electrons and further get amplified inside the PMTs. The amplitude of the electrical signal from each PMT is proportional to the amount of light generated in the crystal corresponding to its position. The electrical signal from PMT is further processed and amplified using preamplifiers. The position of each scintillation is determined by the weighted average of the signals from the PMTs, while its energy information is deduced by integrating

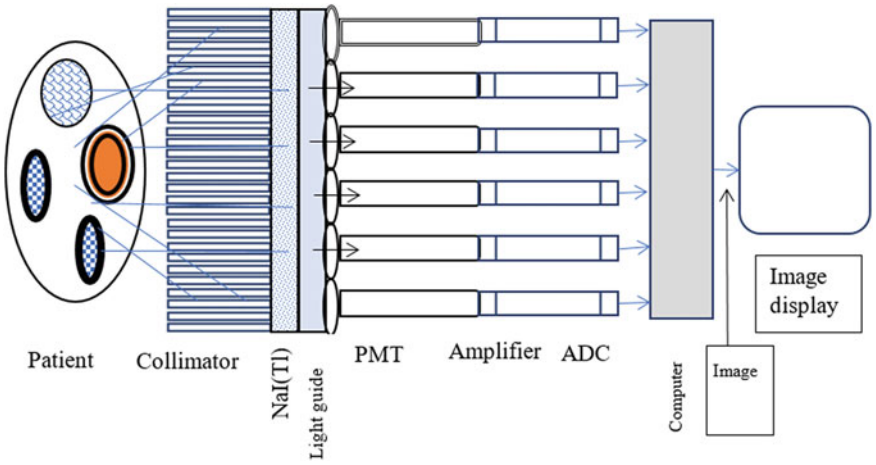

Fig. 13 Basic principles and components of a modern gamma camera

the signals from all the associated PMTs. An analog-to-digital converter (ADC) is used to digitize the output of each PMT. Signals corresponding to only those events, whose pulse amplitude falls within the selected energy band, are accepted and binned into the location (known as a pixel) corresponding to the scintillation event in the 2D image matrix.

Collimators in the gamma camera act as the *mechanical lens* as they permit only those photons that are approaching the camera from certain directions to reach the crystal and thus contribute to image formation while absorbing all other photons. There are basically four types of collimators that are used with gamma cameras: parallel hole, converging, diverging and pinhole.

Parallel hole collimator (also dubbed a "workhorse" collimator) is the most commonly used collimator in the nuclear medicine department. This collimator consists of thousands of parallel holes which lead to the formation of a projection image without any magnification or minification of the region of interest (in which activity is distributed). Parallel hole collimators are available in different variants to meet the requirements of varying gamma energy of the radionuclide to be used and sensitivity requirements of imaging. Some of the variants of parallel hole collimators are (i) low-energy, high-sensitivity, (ii) low-energy, all-purpose (LEAP), (iii) low-energy, high-resolution, (iv) medium-energy, (v) high-energy and (vi) ultra-high-energy.

Pin hole collimator is commonly used for obtaining magnified images of the small organs such as thyroid glands and the heart. It consists of a small pinhole in the conical high atomic number (Z) material assembly. The projected image formed using this collimator is inverted and either magnified if the distance between the source and the pinhole is smaller than the collimator length or minified if the distance between the two is more than the collimator length. This variation in the magnification with the distance leads to a somewhat distorted projected image of 3D objects.

A *converging collimator* is used to obtain magnified images. It has many holes which are aimed to be converging in front of the collimator. *Diverging collimators* on the other hand are used to obtain minified images. Such collimators are very handy in large field of view (FOV) requirements. In this type of collimator, holes are aimed to be converging behind the camera. Some vendors provide a single invertible converging collimator which can be used as a diverging collimator just by flipping its face. A hybrid of parallel hole and converging collimator, known as a *fan beam collimator,* is also used widely, especially in SPECT applications.

Different types of gamma cameras are available commercially. The single-headed gamma camera is the most commonly used gamma camera in clinical nuclear medicine imaging. Due to its positioning flexibility, it can obtain projection images almost at any angle. This capability of the gamma camera to take multiple views around the patient makes it capable of generating tomographic images. Another version, which is rapidly becoming popular across nuclear medicine departments, is dual-headed gamma camera (shown in Fig. 14). The two heads of such systems can be stationed in different combinations thus allowing the simultaneous acquisition of images in two different orientations.

Planar imaging is still the standard for many nuclear medicine examinations such as whole-body bone scans and hepatobiliary thyroid, and renal and pulmonary studies. The images acquired using the scintillation camera fulfils the purpose of imaging such as finding out metastatic lesions in different body parts in the case of a whole body scan.

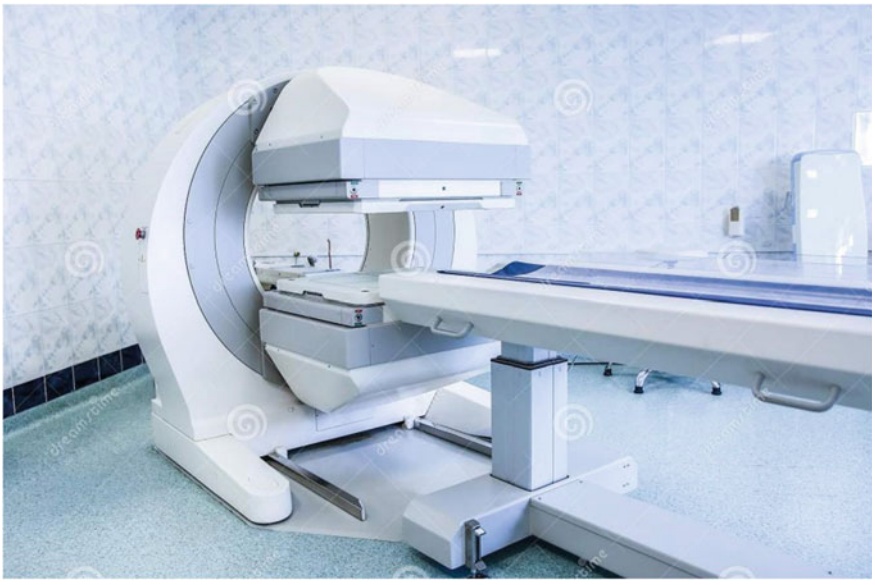

Fig. 14 Photograph of a dual-head gamma camera

3.2 SPECT Imaging System

If the gamma camera head is allowed to rotate around the patient and acquire the images at different angles with respect to its reference position, then the images obtained at different orientations can be used to generate the transverse images. This approach of reconstructing the transverse images (computed tomography) which reveal the distribution of activity within the patient is known as *Single Photon Emission Computed Tomography***.** In the SPECT system, the gamma camera head rotates about the long axis of the patient and acquires the images at equally spaced angular positions in step-and-shoot mode. The 2D projection images obtained in this way are used as 1D projection data to reconstruct transverse images using reconstruction algorithms.

Traditionally, the gamma camera head revolves around the patients in the circular orbits, but many advanced SPECT systems also provide an option of elliptical trajectory for camera head movement. Some systems even allow the camera head to trace out the patient's contour. The non-circular orbits minimize the distances between the patient and the collimator, which in turn leads to significant improvement in spatial resolution.

The reconstruction of axial or transverse images from the set of projection images is a complex and computationally intensive process. Therefore, any gamma camera, which has mechanical capabilities to acquire projection images for tomographic reconstruction, must be supplemented with adequate computation resources and software for image reconstruction, attenuation and scatter corrections, and for display and analysis of 3D image volumes in order to make it a complete SPECT system.

3.3 PET Imaging System

The positron emission tomography system (shown in Fig. 15) utilizes the detection of two simultaneously emitted annihilation photons. Positron-emitting radioisotopes are tagged into the metabolically relevant compounds, such as ^{18}F-fluorodeoxyglucose (^{18}FDG), which localize in the body after administration. The emitted positron is annihilated by combining with an electron from the surrounding tissue, and subsequently results in the production of two annihilation photons which are emitted simultaneously in almost exactly opposite directions (almost 180° apart).

The detector system of the PET scanner consists of rings of detectors which surrounds the patient. Each detector is connected with its opposite detector through a special circuitry known as a coincidence logic circuit due to which they are capable of identifying the photon pairs produced during annihilation. When a photon pair is detected by such a pair of two detectors, it is assumed that the annihilation event took place somewhere along a straight line joining these two detectors. This near-simultaneous detection of the two annihilation photons by the PET system to localize the event origin without using an absorptive collimator is known as annihilation

Fig. 15 Photograph of a positron emission tomography system

coincidence detection. Since the collimation in PET systems is carried out using electronic circuits rather than mechanical collimators, such a type of collimation is also referred to as *Electronic collimation.*

Just like SPECT systems, the data acquired is used to reconstruct the tomographic images using image reconstructing algorithms. The PET systems are widely used in oncology for detection and staging of tumours. The PET detector system offers higher sensitivity in comparison to the SPECT system, and therefore can detect even very subtle radioactive tracer uptake and thus lesions. Since many positron emitters (carbon, oxygen, fluorine) are quite physiologically relevant (fluorine is a good substitute for a hydroxyl group), therefore, they can be tagged into a large number of biochemical. The most important among these is ^{18}F-FDG. The ^{18}F-FDG is used as the substitute for glucose in such studies. Since primary tumours and their metastases have a high uptake of glucose as compared to normal tissues, the ^{18}F-FDG gets concentrated in such sites and hence reveals their locations. Due to this physiological advantage, PET scans of cancer patients have the ability to provide accurate information about the extent of the disease, which may be underestimated by CT alone. Hence, PET systems are widely used in oncology for the detection and staging of tumours.

3.4 Hybrid Imaging Systems

Nuclear medicine imaging systems have the ability to provide exquisitely sensitive measures of a wide range of biological processes due to which they stand out from other contemporary imaging modalities. However, they are poor in providing acceptable anatomic details, which are prerequisites for the identification of organs and tissues. Other imaging modalities such as magnetic resonance imaging (MRI) and X-ray-based computed tomography (CT), although provide excellent anatomical images, are limited in their ability to provide functional or physiological information. In order to take the best advantage of both of these technologies, the integration of these modalities was highly desired.

The major developments in the field of nuclear medicine imaging in the last two decades is birth of the multimodality systems. The introduction of multimodality systems in which a SPECT or PET scanner is integrated with a CT scanner or MRI system has revolutionized the domain of medical imaging. The composite units SPECT-CT, PET-CT (Fig. 16) and PET-MRI offer the fusion of diagnostic images from two complementary imaging modalities and represent one of the most sophisticated and powerful ways to visualize physiology in correlation with the anatomy of the body. The integration of CT or MRI not only provides the much-desired anatomic information but also helps in the correction of emission images for attenuation.

The combined modality of PET-CT has extensive applications in oncology, cardiology, neurology and other psychological studies. Moreover, it has become a standard

Fig. 16 Photograph of a positron emission tomography (PET) and computed tomography (CT) system. *Source* https://www.templehealth.org/services/pet-ct-scan

diagnostic tool for the staging of cancer. Its crucial role in the early assessment of cancer aids oncologists in making course corrections or altering treatment in case of ineffective therapy.

3.5 Medical Cyclotron Facility

The essence of nuclear medicine imaging are radionuclides, but most of the naturally occurring radionuclides are very heavy elements with very long half-lives. Moreover, they rarely get involved in metabolic or physiologic processes of interest, and hence they are not very useful from the radiopharmaceutical perspective. Most of the radionuclides, which can be useful for nuclear medicine imaging, have to be manufactured artificially. Such radionuclides are developed by bombarding the stable nuclei with subatomic particles (such as neutrons and protons) or ions. The bombardment of subatomic particles on these stable nuclei initiates nuclear reactions resulting in the conversion of a stable nucleus into an unstable one. The projectile charged particles (protons and ions) face the Coulombic barrier when they approach stable nuclei targets, and therefore such reactions are not possible in ordinary laboratory conditions. In order to carry out such nuclear reactions, charged particles have to be supplied with enough kinetic energy by acceleration so that they can overcome the potential barrier and subsequently penetrate into the target nuclei. Such acceleration of charge particles is possible in cyclotrons and other charged-particle accelerators.

The cyclotron was invented by E. O. Lawrence in 1931 at Berkeley, California. It consists of a vacuum chamber between the poles of an electromagnet (illustrated in Fig. 17). Two D-shaped semi-circular electrodes (known as "dees") are positioned within the vacuum chamber. There is a small gap between the two dees. A small ion source is usually placed in the centre of this gap. The dees are hollow so that the ion to be accelerated can move freely inside these electrodes. An alternating high voltage is applied across the dees. Initially, the polarity of the electrodes is set in such a way that the injected ions at the centre of the cyclotron get accelerated towards the edge of the dee. The ions moved in the circular path within the dee due to the magnetic field. When the ions approach the gap between the dees, there is a flip in the polarity of the electrical field between the two dees. Due to this polarity reversal, the ions remain continuously accelerated when crossing the gap between the dees. The continuous acceleration results in continuous increases in the radius of the circular orbit of the ions. The repetitions of this process lead to the outward spiralling trajectory of the ions. Since the increasing speed compensates increasing length of the path, therefore, ions continue to arrive in the gap exactly in phase with AC voltage. As the acceleration of ions is accomplished over many rounds in cyclic order, this accelerator is called Cyclotron.

The acceleration process described above is continued till the ions acquire the maximum possible kinetic energy which depends on the type of particles/ions to be accelerated, the diameter of the dees and the strength of the static magnetic field.

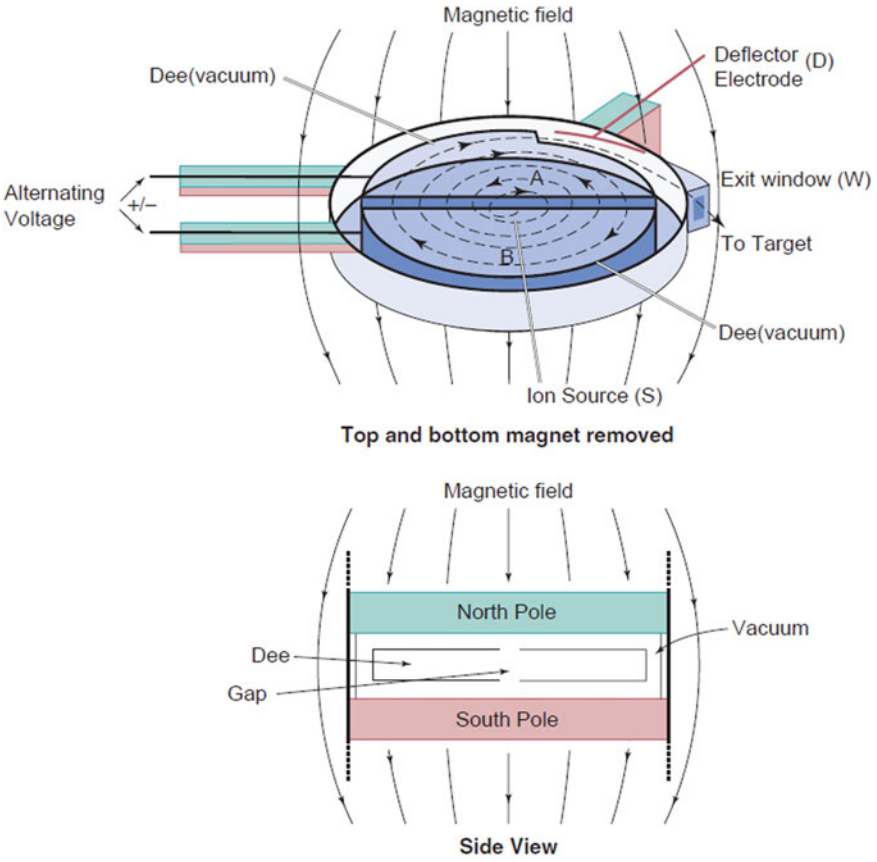

Fig. 17 Schematic diagram presenting working principle of a cyclotron

When the desired kinetic energy is achieved, the ions are extracted from their circular path and directed towards the external target.

Commercial cyclotron, which produces a large amount of clinically relevant activity, has very high setup and operational costs due to which cyclotron-produced radionuclides are more expensive than those produced by other methods. Alternately, much smaller and highly specialized cyclotrons are also available commercially which can be installed in the hospitals. These cyclotrons specifically produce positron-emitting radionuclides for positron emission tomography (PET). Medical cyclotrons offer many advantages over industrial cyclotrons and are comparatively simpler to operate.

Figure 18 shows the photograph of a self-shielded compact medical cyclotron. The beam energy of these medical cyclotrons is in the range of 10–30 MeV; apart from the production of desired positron-emitting radionuclides, neutrons and gamma radiation are also produced. Therefore, radiation shielding remains a major consideration in the design of medical cyclotron facilities. Many manufacturers use boron and

Fig. 18 Commercial self-shielded cyclotron for radionuclide production. Proton beam energy of 11 MeV and beam current 60 μA. **B:** Power supply and control cabinet, **C:** Cyclotron assembly, **D:** Retractable radiation shielding and **E:** Cyclotron assembly

polyethylene sheets to control the neutron dose level around the unit. The shielding of this cyclotron is designed in such a way that radiation workers can operate it through a control console without exceeding their acceptable dose limits.

Radiation levels in medical cyclotrons is also reduced by accelerating negative ions in place of positive ions. The acceleration of negative ions substantially reduces the production of by-product radioactivity which subsequently reduces the radiation level in the vicinity.

3.6 Typical Layout of a Nuclear Medicine Imaging Facility

Figure 19 shows a typical layout plan of a nuclear medicine imaging facility comprising a gamma camera (or SPECT or SPECT-CT) and PET (or PET-CT). The thickness of all the walls is typically 23 cm brick or 15 cm normal concrete. However, the walls of the PET/PET-CT facility are constructed from concrete using the wall thickness calculated from the workload.

The radiation environment of the nuclear medicine imaging facility mainly contains gamma rays either from ^{99m}Tc-based radiopharmaceuticals or annihilation gamma rays from positron-emitting radioisotope (e.g. ^{18}F). The facility layout and shielding thickness are worked out considering occupational and public safety. Patient safety is not a point to be considered during normal working conditions as the patient willingly receives a prescribed quantity of radiation dose. However, in abnormal situations arising from either misadministration or contamination, all available including patients should be given due consideration while designing the radiation safety programme. In case of a medical cyclotron facility, the radiation environment includes neutrons and gamma rays. The facility design and radiation safety programme should give due consideration to the presence of these radiations.

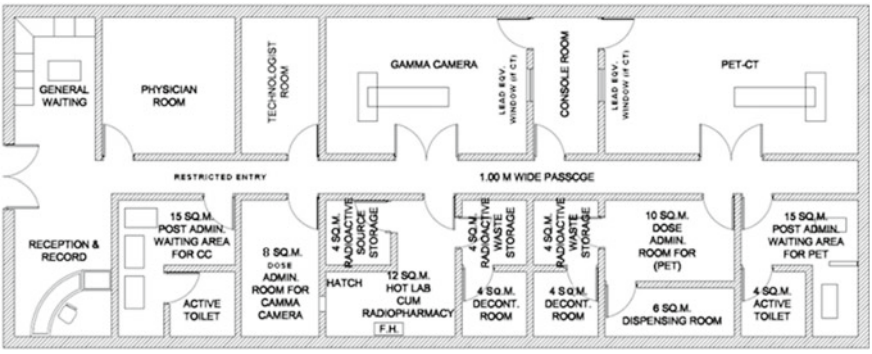

Fig. 19 Typical layout of a nuclear medicine imaging facility having gamma camera/SPECT (or SPECT-CT) and positron emission tomography (PET) or PET-CT. All the walls should be 23 cm brick or 15 cm concrete except PET/PET-CT imaging room which should be made from concrete only using the wall thickness calculated from the workload (F.H. = Fume Hood). *Source* https://www.aerb.gov.in/images/PDF/NuclearMedicine/3.6.6-Typical-layout-diagram-for-Nuclear-Medicine-Facility.pdf

Finally, the monitoring activity should include measurement of contamination and preparedness of decontamination in addition to measuring the radiation levels at important locations.

3.7 Non-imagining Diagnostic Nuclear Medicine Procedure: Thyroid Uptake Measurements

Thyroid uptake measurements are usually carried out to assess the shape, size and functioning of the thyroid gland. A thyroid uptake probe consists of a wide aperture diverging collimator followed by a cylindrical NaI(Tl) scintillation crystal (Fig. 20). A preamplifier, an amplifier and an energy discriminator follow the crystal in serial configuration. ^{123}I or ^{131}I as sodium iodide capsules are used for this type of measurement. Thyroid uptake measurements can be carried out either using a two-capsule method or a one-capsule method. In two-capsule methods, both the radionuclides containing capsules have the same activity.

Initially, both capsules are kept in the neck phantom one by one, and their respective counts are recorded. A neck phantom is a cylindrical PMMA phantom, which simulates the human neck. It is provided with a cylindrical cavity in which the capsule can be inserted. After the initial measurements, one of these capsules is administered to the patient orally while the other capsule is inserted in the neck phantom. The capsule, which is kept in neck phantom during study, is known as standard. After administration, the count rate from the patient neck is measured, initially after 4–6 h post administration and later after 24 h post administration. For background correction, the count rate from the patient thigh is also recorded during the above

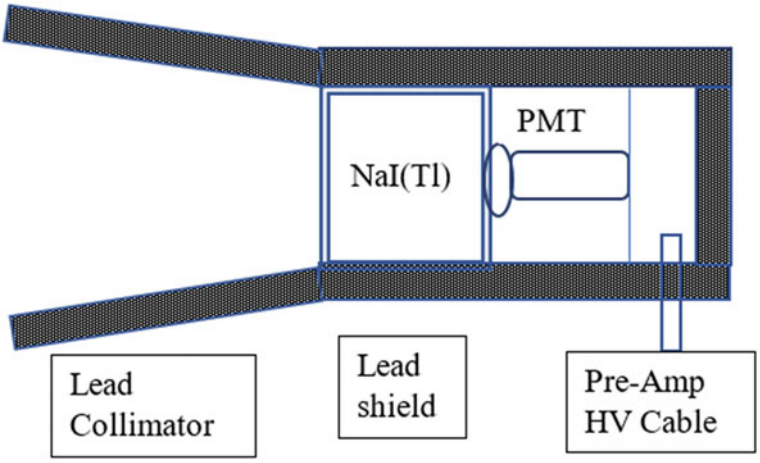

Fig. 20 A schematic cross-sectional view of a thyroid uptake probe

measurements. The count rate of the standard capsule (which is kept in the neck phantom) and ambient or room count rate (for background correction in standard) is also recorded during the above course of measurements. The distance between the detector and the object whose count rate has to be measured is kept around 30 cm. Although this arrangement reduces the sensitivity of the study, it makes the measurements relatively independent of the size, shape, position of the thyroid and the radioisotope distribution within the gland. The thyroid uptake can be calculated using the following formula:

$$\text{uptake}(\%) = \frac{C_{\text{neck}}/t_{\text{neck}} - C_{\text{thigh}}/t_{\text{thigh}}}{C_{\text{standard}}/t_{\text{standard}} - C_{\text{room}}/t_{\text{room}}} \times F \times 100\% \tag{1}$$

where

c is the total number of counts,

t is the measurement time and

F is the fraction of the administered activity in the phantom.

The two-capsule method takes into account of any day-to-day variation in the system sensitivity and corrections for radioactive decay.

Alternatively, the standard is not used in the "one-capsule method". In this method, initially after measuring the counts of the capsule in the neck "phantom" and correcting it for background using ambient or "room" counts, the capsule is administered to the patient, and the count rate around the patient's "neck" and "thigh" is recorded firstly, after 4–6 h and then again after 24 h of administration. The thyroid uptake in this case is obtained as

$$\text{uptake}(\%) = \frac{C_{\text{neck}}/t_{\text{neck}} - C_{\text{thigh}}/t_{\text{thigh}}}{C_{\text{phantomn}}/t_{\text{phantom}} - C_{\text{room}}/t_{\text{room}}} \text{Xe}^{-0.6932t/T_{1/2}} \tag{2}$$

where $T_{1/2}$ is the physical half-life of the radionuclide, and t is the time duration between phantom measurement and neck measurements.

4 Radiotherapy Systems and Facilities

Radiotherapy, an important technique for cancer treatment, traces its roots to Roentgen's discovery of X-rays in 1895, evolving continuously since then with new skills and approaches. Approximately 60% of cancer patients undergo radiotherapy, whether as primary treatment, for recurrences, or palliation. Nowadays, radiotherapy, alone or combined with surgery or chemotherapy, stands as a principal modality for various cancer cases. The goal is to deliver a high, homogenous dose to diseased tissue while minimizing unwanted side effects, and prioritizing the patient's quality of life. The aim extends beyond tumour cell destruction to enhancing patient well-being. This section provides a brief overview of radiotherapy systems, facilities and the associated radiation environment.

4.1 External Beam Therapy Systems and Facilities

External beam therapy, also known as Beam therapy, is a common radiotherapy method where the radiation source is positioned at a distance from the patient's body. Typically employing gamma rays and X-rays, it can also utilize electrons, protons, neutrons and ion beams. Beam therapy is categorized as conventional or conformal based on the treatment field size and its conformity to the tumour geometry in the given plane or volume. Conventional beam therapy uses square/rectangular or partially irregular treatment fields, while conformal beam therapy creates regular or irregular treatment field geometries to match the tumour's shape in 2D or 3D. The objective of conforming the high dose volume to the diseased tissue volume is to spare surrounding normal tissues and organs at risk, a principle known as conformal avoidance. This maximizes the avoidance of high doses to normal tissues at the risk of compromising the dose to the tumour volume. Evidence suggests that improved conformation enhances tumour control and reduces side effects. Consequently, 3D conformal therapy, including adaptation for internal organ movement, is increasingly feasible in this era. While these advanced techniques are more costly than conventional methods, it's crucial to recognize that failed conventional treatment, even if less expensive, is a waste of resources.

Nowadays, advance forms of 3D conformal radiotherapy techniques such as intensity-modulated radiotherapy (IMRT), image-guided radiotherapy (IGRT), volumetric modulated arc therapy (VMAT) and stereotactic body radiotherapy (SBRT) are very popular and are used by clinicians for managing a variety of cancer cases. Treatment using these advanced techniques is generally delivered by multimodality technologically advanced high-energy medical electron linear accelerators (LINACs)

with specialized hi-tech multileaf collimators (MLCs) and narrow cylindrical cones. Narrow converging ^{60}Co gamma-ray beams from a specialized treatment unit called Gamma Knife are used for stereotactic radiosurgery which is a form of high-precision conformal radiotherapy.

Beam therapy delivery devices are complex radiation generators. Different types of radiation generators such as low-energy X-ray machines, telegamma therapy machines, electron linear accelerators, betatron, protons accelerators and ion accelerators are used for radiation beam therapy. Among the different available radiation generators, telecobalt machines (standard and specialized) and electron linear accelerators (standard and specialized) are popularly used worldwide. Computer-controlled complex radiation delivery systems and associated hi-tech accessories employing circular treatment fields of diameter as small as 0.4 cm and square treatment fields of size as large as 40 cm × 40 cm are used in beam therapy. This section provides a brief detail about the commonly used beam therapy equipment.

4.1.1 Telecobalt Machine

The telecobalt unit was invented in the early 1950s and was deemed to be a compact beam delivery system that produces radiation adequate for most tumours. It is a simple electrotechnical device which houses a high activity (~444 TBq = 12,000 Ci) encapsulated ^{60}Co source to generate high-intensity gamma ray beams (average energy 1.25 MeV) for the treatment of different types of cancer cases. Figure 21 shows the photograph of a modern telecobalt machine, its control system, gantry and a magnified cross-sectional view of the source head.

Major components of telecobalt machine is gantry, gantry stand, source head, fixed primary collimator, moveable secondary collimator, optical system for displaying the field size and distance measurement, and a treatment table. Some of the telecobalt machines are also equipped with a multileaf collimator. The source head is typically a cast iron shell filled with lead or a mixture of lead and tungsten so that the head leakage shall comply with the requirements of standards and regulatory systems. The centre of the source head contains a cylindrical lumen which is the path for movement of a cylindrical source drawer. The source drawer contains a doubly encapsulated cylindrical ^{60}Co source (diameter = 1.5 or 2.0 cm and height = 2.5 cm and higher). The source drawer is connected to a pneumatic drive system which is used for moving the source from its resting position (OFF condition) to treatment (ON) condition and vice versa. Typically, the source head is designed for housing a ^{60}Co source of activity about 555 TBq (15,000 Ci), but the loaded activity is generally about 444 TBq (12,000 Ci). The lower part of the source head contains a fixed primary collimator and a moveable beam limiting device.

The telecobalt machine contains a rotating gantry (rotation through 360°) which maintains a constant distance from a point in space (isocentric mounting). The isocentric distance or normal treatment distance of this machine is typically 80 cm. However, 100 cm isocentric machines are also available. Depending on the technology of the manufacturer, the moveable beam limiting device (secondary collimator system) is

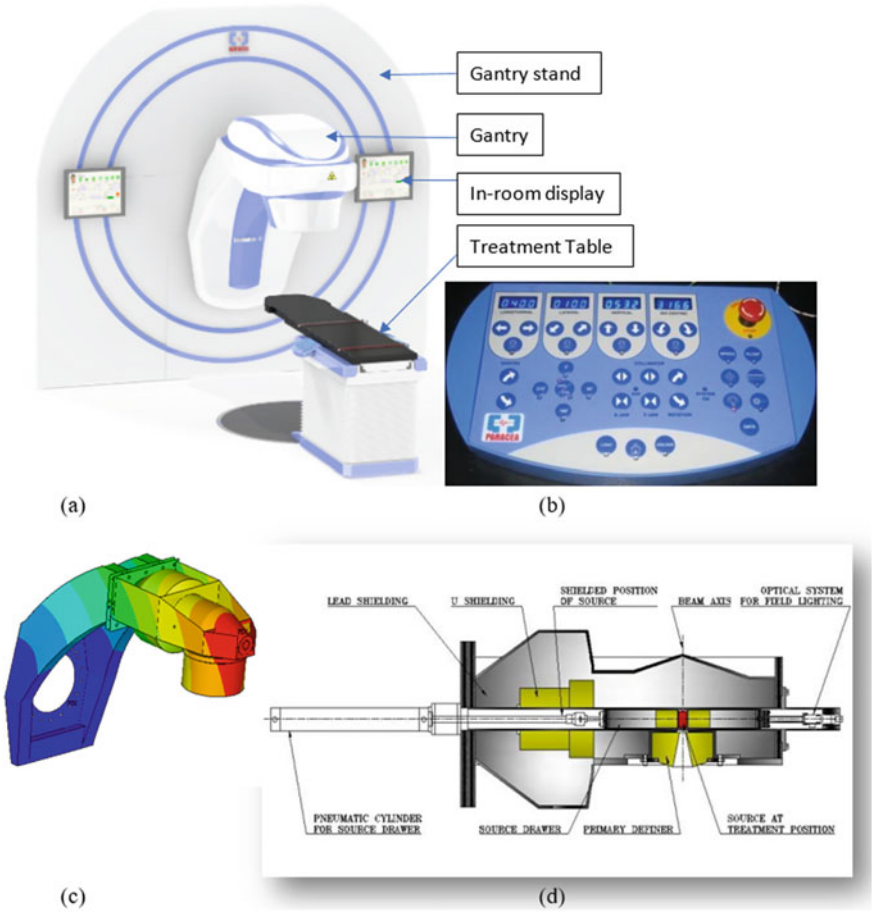

Fig. 21 Details of telecobalt machine: **a** photograph of an isocentric telecobalt machine, **b** control unit, **c** gantry and **d** magnified cross-sectional view of the source head

either jaw type or multivane type. In case of jaw type collimator, it is possible to define very small field (sub-millimeter dimension), but in case of multivane type collimator the minimum treatment field size is about 4.5 cm × 4.5 cm. The maximum field size which the collimator system can define is of the order of 35 cm × 35 cm. The collimator system is also provided with rotational capability. The source to diaphragm (or collimator end) distance is typically 45 cm. To minimize the penumbra (high dose gradient) at the field edges, penumbra trimmers are also used. To measure the distance from the source, an optical distance indicator is also mounted on the external part of the collimator. The optical system provided in the head of the telecobalt machine helps in visualizing the beam aperture to be used for the treatment and also in positioning the patient for the treatment.

The treatment table is used for positioning the patient under the ^{60}Co beam. It has three linear movements (transverse, longitudinal and lateral) as well as rotational capabilities. Linear and rotational movements of the table help in precise patient positioning. The tabletop is carbon fibre which allows maximum transmission. The control console of the machine contains many options and safety systems. Some of the movements of the telecobalt machines and its treatment tables can be controlled remotely as well. The control system is fully graphical user interface-based software control.

Standards on performance and safe use of telecobalt machines are available [2, 3, 16] which provides sufficient information for manufacturer and users of this machine. This machine is installed in a specially designed housing in line with regulatory codes and guides to provide adequate safety to occupational workers and the public. The limits on leakage radiations are provided considering the safety of patients and the radiation workers (OFF condition leakage at 5 cm from surface of the source head shall not exceed 200 μSv and at 100 cm from the source shall not exceed 20 μSv; average and maximum ON condition leakage from the source head shall not exceed 0.1 and 0.2% of the reference dose rate). The radiation environment in the treatment room contains primary, scattered and leaked photons, whereas radiation environment in control console and public waiting area is scattered and leaked photons.

Because of relatively lower energy than required to treat deep seated tumours and a large penumbra (high dose gradient region at treatment field boundary), telecobalt units were susceptible to replacement.

4.1.2 Medical Electron Linear Accelerators

The early development of microwave sources (~3000 MHz) gave a large impetus to the development of medical electron linear accelerators (LINACs), which have now become the most versatile and widely used radiotherapy equipment. Medical LINACs produce high-energy electron beams (typically 4–25 MeV) which can directly be used to deliver the dose to the tumour or can be allowed to generate high-energy bremsstrahlung X-rays (4–25 MV) to treat the deep seated tumours. Medical electron linear accelerator technology has now moved through several generations of increasing sophistication. The new LINACs are compact and offer excellent versatility in treating tumours with great precision and conformity. LINAC is a treatment device which accelerates electrons to very high energy using high-frequency electromagnetic waves. As the electron trajectories are linear in the accelerator tube, hence the name linear electron accelerator.

The main components of a medical LINAC are an electron gun, microwave generator, modulator and pulse forming network, accelerating waveguide, vacuum system, travelling waveguide and circulator, beam transport system, X-ray target, primary collimator, flattening filter, monitor chamber, moveable collimators (secondary or tertiary and jaws or multileaf collimators or both), auxiliary system, safety interlocks and control console (computer-controlled) as shown in Fig. 22. The electron gun emits electrons through the process of thermionic emission, and these electrons

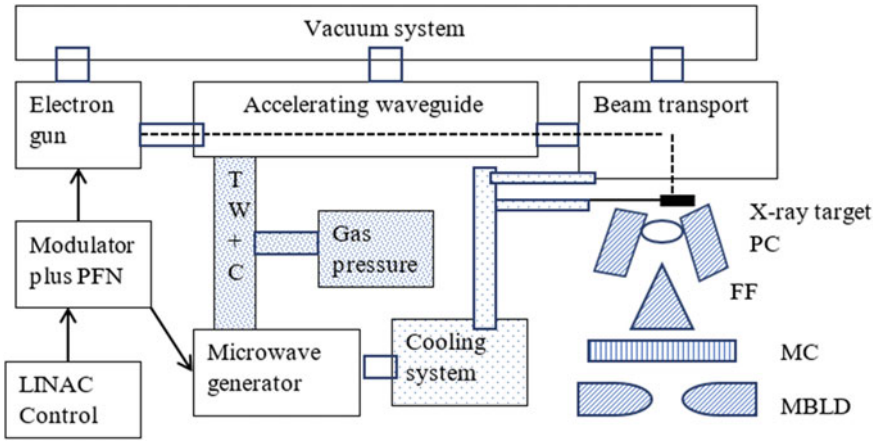

Fig. 22 Schematic cross-section of a medical electron linear accelerator showing its major systems and sub-systems. PFN: pulse forming network; TW + C: travelling wave plus circulator; PC: primary collimator; FF: flattening filter; MC: monitor chamber; MBLD: moveable beam limiting device (jaws or MLC or both)

are injected to accelerating waveguide. It is essential to digitally control the current through gun filament for dynamic beam delivery. The microwave generator (Klystron or Magnetron) provides high-wattage microwave (~3000 MHz) for the acceleration of electrons. Both the electron gun and microwave source are fed high voltage and short duration pulses in synchrony from a modulated power supply system. The typical high-voltage pulse is a few microseconds long and is repeated a few hundred times per second. The pulse repetition frequency (PRF) or pulse per second (PPS) is variable on most accelerators, but the pulse width is always constant. The PRF/PPS determines the dose rate from a LINAC.

The beam transport system deals with transporting the electron beam in vacuum from the gun to the target/exit window. The accelerating waveguide is either a standing waveguide or a travelling waveguide. This terminology refers to the type of electric field produced by the propagation of microwaves in the accelerating structure. Both types of structures incorporate magnetic steering and focusing devices. The standing wave structure helps in reducing the accelerating waveguide length due to the option of side coupling cavities while the travelling wave structure requires a relatively longer accelerating waveguide. The beam monitoring system comprises multi-segment ionization chambers that shape, manipulate and monitor the X-ray or electron beam coming out of the machine. The auxiliary systems consist of vacuum pumps, circulating cooling water, RF frequency tuner, pressurized dielectric gas for RF transmission, RF isolator and electronic timer (thyratron).

Electrons are injected into the accelerating waveguide where they absorb energy from radiofrequency (RF) fields generated by microwaves, typically at a frequency of 3000 MHz (with a 100 mm wavelength in free space). The microwave radiation

is delivered in brief pulses lasting a few microseconds, achieved by applying high-voltage pulses of around 50 kV from the pulse modulator to the microwave generator. Both the electron gun and microwave source are pulsed, ensuring that high-velocity electrons enter the accelerating waveguide simultaneously as it is energized by the microwaves. To facilitate this process, the electron gun and accelerating waveguide system must be evacuated to a low pressure, ensuring that the mean free path of free electrons between atomic collisions is significantly longer than the electron path through the system. The amount of energy an electron can absorb from the microwave frequency field in the waveguide depends on the amplitude of the electric field, which, in turn, is contingent upon the instantaneous microwave power. Even for low-energy accelerators, the power required is several megawatts but, as a result of thermal and other constraints, available microwave power sources cannot be operated at these power levels continuously nor could the cooling system for the waveguide dissipate the power losses. However, if they are pulsed at high power levels, with a duty cycle of around 0.1%, acceptable mean power can be delivered to pulses of electrons which can then be accelerated up to the necessary high energies. Pulses are typically of 4 μs duration and are delivered typically at a PRF of 250 Hz.

The electrons being accelerated tend to spread out, partly due to mutual Coulomb repulsion and mainly because the electric fields in the waveguide structure have a radial component. However, this spread can be controlled, and the electrons can be refocused onto their original trajectory by employing a coaxial magnetic focusing field. This field is generated by coils that are aligned coaxially with the accelerating waveguide. Additionally, there are steering coils that can adjust the electron beam, ensuring it exits the accelerator structure at the desired position and angle. The electron accelerator emits pulses of high-energy electrons into the treatment head, where the useful radiation beam is generated.

When the machine is being used as an X-ray generator, the electron beam is directed onto an X-ray target where it is stopped with the emission of X-rays by bremsstrahlung. The target is therefore the primary source of X-rays, which are then modified by other components in the treatment head including filters (flattening filter, FF) to control beam uniformity and the beam defining system to control the dimensions normal to the beam direction. Nowadays, LINACs have been provided options for generating unflat (or flattening filter-free) photon beams which are very popularly used for a variety of cancer cases. The intensity (or dose rate) of FFF beams is a few fold higher than flattened (FF) beams. The treatment head also contains a beam monitor consisting of detectors used both to measure the dose delivered and also to provide control signals for safety interlocks and feedback systems to the accelerator and its associated systems.

The photon collimator consists of two pairs of jaws (one pair for defining the field in the x-direction and the other pair for defining the field in the y-direction) or one pair of jaw collimator and one pair of multileaf collimator (MLC). The collimator system provides a photon or electron beam of a given dimension in a direction of our choice.

When the electron beam is to be used for treatment, it is extracted from the vacuum system through a thin window into the treatment head where it is scattered

by a scattering foil system (specific to the beam energy beam) into a broad beam. This is necessary as the electron beam diameter is only a few millimeters (about 5 mm) as it emerges from the vacuum system. The electron beam is monitored in the same way as the X-ray beam, but in this case particular attention is paid to the detection of abnormally and dangerously high dose rates which could occur in certain fault conditions. For electron beam therapy, the final beam collimation is carried out with an electron beam applicator (also called electron cone or electron applicator) which is mounted externally on the treatment head.

The treatment head also provides housing for an optical system [optical field and optical distance indicator (ODI)] simulating the treatment beams and mounting points for accessories including beam direction indication devices such as mechanical pointers which will allow precise alignment and direction of the treatment beams in relation to the patient.

Some machines are designed specifically as X-ray generators but many are dual-purpose with treatment heads capable of handling both X-rays and electrons. In this case, elaborate mechanical and electrical arrangements are required to allow the changeover from one mode of treatment to the other. For instance, it will be necessary to have an arrangement for retracting the X-ray target and filter, inserting appropriate electron scattering foils, and to have an interlock system to verify that this has been done correctly before an electron treatment can start. For each photon beam energy, a specific target and a specific flattening filter is required. Accordingly, more than one photon target and FF is available in the head of the accelerator. Scattering foils, targets and flattening filters of multi-energy medical LINAC are stored in a storage system available in the head of the accelerator which is called carousel. The carousel brings the exact combination of target/FF or scattering foil on receiving the command from the control system of the accelerator.

The temperature of certain components in the system is critical for efficient operation. In particular, the temperature of the accelerating waveguide structure and the microwave valve has to be controlled because dimensional changes associated with thermal expansions will significantly change their frequency characteristics. The X-ray target also needs to be cooled. Cooling is achieved by circulating water through the critical components and remote water to air (or in some cases water to waste water) heat exchanger. In either case, thermostatic control is necessary to maintain the operating temperature within a few degrees centigrade.

The safety interlock system guards against unsafe delivery of radiation. The safety interlocks include both hardware and software interlocks that continuously monitor the status of the machine during its operation. The functional parameters for safety interlocks and operation of the machine are computer-controlled by a feedback system that receives its commands from the monitor chamber, hardware position encoders and limit micro switches. The feedback system is key to the computer control of a LINAC. A beam collimator is required to shape the desired X-ray treatment beams while applicators are used to focus and shape electron beams. Conventional jaw collimators, MLC, micro multileaf collimators (mMLC) and special collimators (such as stereotactic radiosurgery cones) are available for shaping the X-ray beams.

A medical LINAC has three main mechanical systems, namely gantry, collimator and patient support assembly (PSA) [also called couch and treatment table]. The gantry rotates about a horizontal axis while the collimator and couch rotate about a vertical axis. The point of intersection of the collimator and gantry axes of rotation in space is called *isocentre* of the machine. Most of the medical LINACs have a 100 cm target to isocentre distance which is called normal treatment distance (NTD). In addition, the couch has three linear movements, transverse, lateral and longitudinal. The couch is also provided rotational capabilities. Nowadays 6D couch is also supplied along with the LINACs.

The treatment head of a LINAC contains proper shielding to limit the transmission of X-rays, electrons and photo-neutrons (e.g. for photon beam—in the patient plane: average and maximum leakage dose shall not exceed 0.1 and 0.2%, respectively, of the reference beam output). The head shielding and other design aspects of the LINAC shall conform to prescribed standards and regulatory specifications [16–21].

Commercially, computer-controlled LINACs with different attributes and accessories are available for various types of applications. These LINACs can be grouped into two categories, Standard (or C-arm) LINAC and Specialized (O-ring or ring gantry) LINAC. Figure 23 is the photograph of a multimodality multi-energy standard LINAC. It contains both kV and MV imaging systems. The kV imaging system is generally used in IGRT and adaptive radiotherapy, whereas MV imaging is generally used for verification of the geographical region of a patient through anatomical landmarks. As stated earlier, this LINAC is capable of generating 6 and 10 MV FFF photon beams in addition to three flattened photon beams and multiple energy electron beams.

The maximum operating dose rate for FF beam is typically 500 cGy/min, whereas it goes up to 2000 cGy/min in case of FFF beams (10 MV FFF). Very recently, MRI-LINAC has also been introduced in clinical practice. As MRI provides better soft tissue contrast, the MRI-LINAC will be very useful in those situations where very soft tissue contrast is of paramount importance.

Various versions of specialized LINACs (helical tomotherapy, robotic radiosurgery, O-ring) are available commercially. Helical tomotherapy machines have been modified to deliver other types of treatments as well. The robotic radiosurgery device (also called Cyber-knife) is thought to be very useful in many situations and in fact it is a frameless radiosurgery device. O-ring LINACs (commercially known as Halcyon and Ethos) is single energy, but it is declared as a versatile treatment machine. The recently introduced model of this LINAC also incorporates artificial intelligence-based operation.

As far as the radiation environment in the medical electron LINAC facility is concerned, photons and neutrons are available in the high-energy accelerator facility (Beam energy of 10 MV or more). These treatment units are housed in specially designed and constructed bunkers which meet the requirements of standard specifications as well as regulatory prescriptions. The shielding thickness of various walls and ceilings of the LINACs is calculated using the weekly workload (expressed in the unit of Gy/week at a 1-m distance from the X-ray target). Specialized LINAC

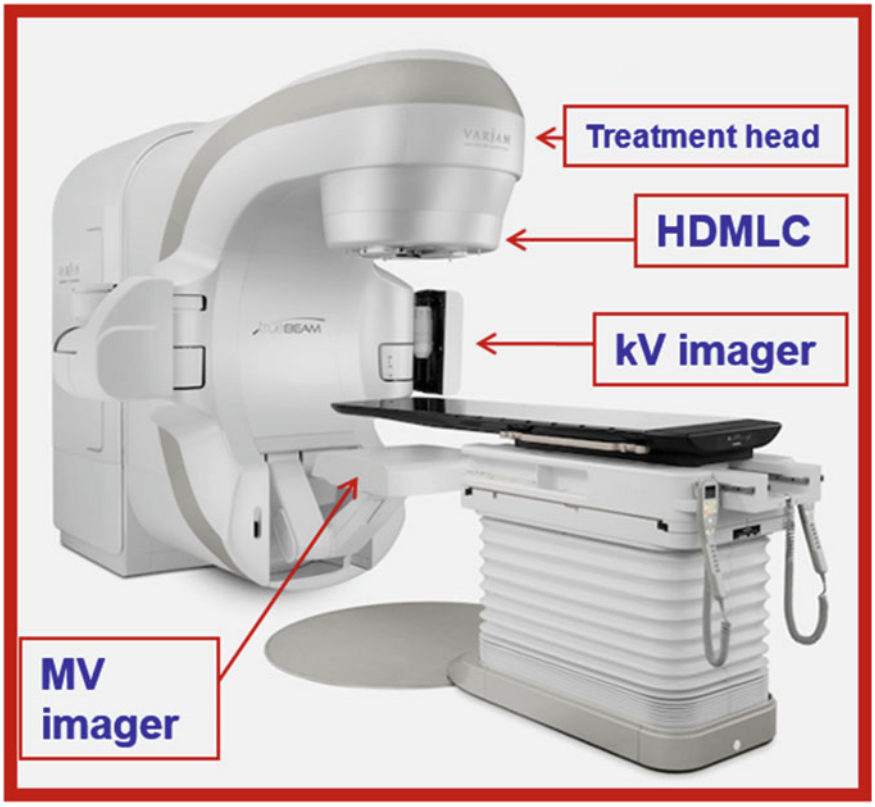

Fig. 23 Photograph of a multimodality standard medical electron linear accelerator (Courtesy: Varian Medical Systems, Mumbai, India)

except Cyber-knife is partially self-shielded and hence shielding thickness required is relatively less.

4.2 Brachytherapy Systems and Facilities

Brachytherapy had its beginnings in Europe in the late 1890s with the discovery of Radium-^{226}Ra. The early application of radium to skin lesions demonstrated the effectiveness of this new treatment technique. Since that time, many radionuclides have been developed offering a wide range of half-lives and radiation. There is also a large variety of clinical instrumentation available today for implementing numerous types of brachytherapy procedures.

Depending on the duration of treatment, brachytherapy is of two different categories, namely temporary implant and permanent implant. In a temporary implant,

the source is removed from the patient body on completion of the pre-calculated treatment duration. However, in the case of a permanent implant, the radiation source is permanently implanted to the patient body.

On the basis of placement of the source and treatment applicator with respect to the patient body, brachytherapy is classified into four different categories, namely surface mould, intracavitary, interstitial and intraluminal brachytherapy. Among these, intracavitary and interstitial brachytherapy are the most common treatment modes. Intracavitary brachytherapy is the treatment technique where radiation sources inside specialized applicators are placed into the natural body cavities (e.g. treatment of cancer of the uterine cervix) in close proximity to the tumour of the patient. In interstitial brachytherapy, radioactive sources are implanted directly into the tumour volume (e.g. breast implant, prostate implant). Intracavitary brachytherapy is always temporary and usually a fractioned approach is used now. On the other hand, interstitial brachytherapy can be temporary or permanent. Many recently developed brachytherapy techniques heavily utilize advanced technology for target localization, planning and optimization of the implant geometry, and delivery and verification of the treatment. Intravascular brachytherapy technique is used for inhibiting restenosis of both coronary and peripheral vessels employing gamma- and beta-emitting radioactive sources [22]. This form of brachytherapy is generally performed in a cardiac catheterization laboratory.

Brachytherapy with ^{226}Ra-, ^{137}Cs, ^{60}Co or ^{192}Ir sources has traditionally been given at dose rates of 0.4–0.8 Gy/h, a level referred to as low dose rate (LDR). Using these radionuclides, the early pioneers of radiation therapy developed highly successful treatment schedules for gynecologic malignancies. In the past few decades, high dose rate (HDR) brachytherapy has been developed as an alternative to LDR brachytherapy. HDR refers to a dose rate in excess of 0.5 Gy/min [23], a rate commonly administered with linear accelerators for external beam therapy. Table 1 presents the physical characteristics of photon-emitting radionuclides commonly used for brachytherapy treatments.

Both manual and remote after-loading source delivery systems are used to place the brachytherapy source at the treatment location. Hi-tech miniature sources are preferred considering patient comfort and acceptability. Miniature high dose rate

Table 1 Physical characteristics of photon-emitting radionuclides commonly used in brachytherapy treatments

Radionuclide	$T_{1/2}$	Energy (MeV)		Γ_x	Γ_k
		Gamma	Beta	$Rcm^2h^{-1}\ mCi^{-1}$	$\mu Gym^2h^{-1}\ MBq^{-1}$
^{60}Co	5.26 y	1.25	0.31	13.07	0.308
^{137}Cs	30 y	0.662	0.51–1.17	3.26	0.077
^{192}Ir	73.84 d	0.38 (0.14–1.06)	0.67	4.69	0.111
^{125}I	59.4 d	0.028	–	1.46	0.034
^{103}Pd	17 d	0.021	–	1.48	0.035

(HDR) ^{192}Ir sources are increasingly being used for different types of brachytherapy treatments [22, 23]. ^{125}I seed sources are also becoming popular for ocular as well as interstitial brachytherapy applications [24]. A few beta-emitting sources (^{106}Ru/^{106}Rh-, ^{90}Sr) are also used in brachytherapy treatments.

The quantity recently used to specify the source strength of brachytherapy sources are Reference Air Kerma Rate (RAKR). It is defined as the kerma rate to air, in air, measured at 1 m along the perpendicular bisector of the long axis of the source, corrected for air attenuation and scattering. The recommended unit is $\mu Gy \cdot h^{-1}$ (at 1 m). American Association of Physicists in Medicine (AAPM) has recommended the use of Air Kerma Strength (AKS) to specify the strength of brachytherapy sources which is given as $Sk = K_{air}(d) \times d^2$, where K_{air} is the air kerma rate in free space at a distance of d from the source, in the plane normal to and bisecting the long axis of the source. The recommended unit of AKS (S_k) is $\mu Gy\ m^2\ h^{-1}$ or $cGycm^2\ h^{-1}$. It is to be noted here that conceptually RAKR and AKS are different but numerically they are equal. Most of the brachytherapy sources used in clinical practice are cylindrical sources which can be treated as line sources. For the dosimetry of encapsulated line sources, the Sievert Integral model was widely used. However, AAPM Task Group 43 recommended formalism is now popularly used for patient dose calculations.

High dose rate (HDR) remote after-loading brachytherapy is now very popular because of its many advantages over manual after-loading techniques. The HDR brachytherapy uses a single ^{60}Co or ^{192}Ir miniature source mounted at one end of a long cable. This cable is motor-driven, and the source can be moved in steps to pre-calculated treatment positions (dwell positions). The source drive system uses a stepper motor of high linear precision to move and position the source inside the treatment applicators. A large variety of treatment applicators are available nowadays to deliver the treatment to almost all body parts. The brachytherapy treatment is thought to be inherently conformal and dose delivery is almost localized. 3D brachytherapy approaches with the help of volumetric imaging systems are now very commonly used. Intensity-modulated brachytherapy with the help of specially designed radiation sources or treatment applicators has been demonstrated and could be a choice of routine treatment in future.

5 Nuclear Medicine Therapy Systems and Facilities

Nuclear medicine therapy has been used in the management of cancer since the 1940s. Due to the ever-increasing pool of radiopharmaceuticals, radionuclide therapy has now become a rapidly expanding cancer treatment modality. It has been used to manage the various types of malignancies.

Benign thyroid disease, which is also known as hyperthyroidism or thyrotoxicosis and mostly caused by Graves' disease, has been treated successfully using ^{131}I since the 1940s. Depending on the volume of the thyroid and the condition of the patient, the prescribed activity may vary from 200 to 800 MBq. Treatment of thyroid cancer is the most common and successful application of radionuclide therapy. It is mostly

used in conjunction with thyroidectomy. Patient undergoing radioiodine therapy has to remain in isolation (usually admitted in therapy wards) until radiation levels around the patient drop to acceptable levels.

During the advanced stages of cancer, cancerous cells leave their primary sites and invade other organs including bone. These bone metastases cause severe pain, which is managed by palliative treatment. Radionuclide therapy has been used as an effective agent in bone metastase pain alleviation for a long time. ^{90}Sr and ^{153}Sm are the two most commonly used radionuclides in the management of bone metastases. Apart from this, ^{32}P, ^{186}Re, ^{117m}Sn and ^{177}Lu have also been used. Recently, ^{223}Ra has also shown promising results and is continuously gaining attraction in the oncology community.

^{90}Y radionuclide has been used in the treatment of liver cancers. ^{90}Y either embedded in small silica beads or incorporated in resin spheres is generally administered intra-arterially using an angiographic catheter under radiological supervision. Apart from it, ^{131}I and ^{188}Re have also been explored for the treatment of such lesions.

^{131}I-MIBG has been used in the management of NETs for more than two decades. The prescribed activity may vary from 3700 to 37,000 MBq. Apart from ^{131}I, ^{90}Y, ^{111}In and ^{177}Lu have been used for NET management.

Radionuclide therapy has shown superior treatment outcomes as compared to chemotherapy in the treatment of non-Hodgkin's lymphoma. Since lymphomas are inherently sensitive to radiation and express a number of antigens, they can be treated using radio-immunotherapy (RIT), ^{131}I or ^{90}Y, tagged antibodies.

Neuroblastoma is a neuroendocrine malignancy which is mostly limited to children and young people. It is also a radiosensitive malignancy, which has been treated using ^{131}I for many years. ^{177}Lu has also been used for its management.

6 Conclusion

Ionizing radiations, encompassing X-rays, gamma rays, electrons, positrons, protons, neutrons, alpha particles and heavy ions, have become integral to modern human health care. In today's healthcare landscape, ionizing radiation-based imaging and therapeutic procedures are indispensable. Medical imaging relies on kilovoltage X-rays and gamma rays from radioisotopes, utilized in diverse techniques like radiography, fluoroscopy and computed tomography (CT). Emission imaging involves radiopharmaceuticals containing radionuclides like ^{99m}Tc and ^{18}F, recorded through gamma cameras, single photon emission computed tomography (SPECT) and positron emission tomography (PET). Hybrid systems such as SPECT-CT and PET-CT enhance diagnostic capabilities. Therapeutically, radiotherapy and nuclear medicine therapy deploy sealed or unsealed sources, with external beam and brachytherapy options, featuring advanced technologies like proton and ion beam therapy. This chapter provided a concise overview of crucial medical imaging and therapy systems, elucidating the associated radiation environments in these medical facilities.

References

1. Atomic Energy Regulatory Board (AERB) (2016) Radiation safety in manufacture, supply and use of medical diagnostic X-ray equipment. Code No. AERB/RF-MED/SC-3 (Rev. 2)
2. International Electrotechnical Committee (IEC) (2013) Medical electrical equipment: Part 1–3—general requirements for basic safety and essential performance—collateral standard: radiation protection in diagnostic X-ray equipment. IEC 60601-1-3
3. International Electrotechnical Committee (IEC) (2013) Medical electrical equipment—Part 2–11: particular requirements for the basic safety and essential performance of gamma beam therapy. IEC 60601-2-11
4. Tabar L (2012) Imaging of the breast: technical aspects and clinical Implication. http://www.intechopen.com
5. Markus K, Christof HW, Stefan W, Klaus-Jurgen P, Maximilian FR, Marcus T (2007) Advances in digital radiography: physical principles and system overview. Radiographics 27:675–686
6. Impact Scan (2022) http://www.impactscan.org/cthistory.htm. Accessed 30 Dec 2022
7. Goldman LW (2007) Principles of CT and CT technology. J Nucl Med Technol 35:115–128
8. Bushberg JT, Seibert JA, Leidholdt EM, Boone JM (2012) Essential physics of medical imaging, 3rd edn. Lippincott Williams & Wilkins, Philadelphia
9. Lewis MA, Edyvean S (2005) Patient dose reduction in CT. Br J Radiol 78:880–883
10. Flohr T (2013) CT systems. CurrRadiol Rep 1:52–63. https://doi.org/10.1007/s40134-012-0005-5
11. Balter S, Hopewell JW, Miller DL, Wagner LK, Zelefsky MJ (2010) Fluoroscopically guided interventional procedures: a review of radiation effects on patients' skin and hair. Radiology 254(2):326–341
12. Gingold E, Jefferson T (2023) Modern fluoroscopy imaging systems image wisely. https://www.imagewisely.org/Imaging-Modalities/Fluoroscopy/Modern-Imaging-Systems. Accessed 19 Jan 2023
13. International Atomic Energy Agency (IAEA) (2014) Diagnostic radiology physics: a handbook for teachers and students. IAEA, Vienna
14. National Council on Radiation Protection and Measurements (NCRP) (2004) A guide to mammography and other breast imaging procedures. Report No. 149, 2004, Bethesda
15. Skaane P (2010) Digital mammography in European population based screening programs. In: Bick U, Diekmann F (eds) Digital mammography. Springer, Berlin, pp 155–173
16. Atomic Energy Regulatory Board (AERB) (2011) Radiation therapy sources, equipment and installations, Safety code no. AERB/RF-MED/SC-1 (Rev. 1)
17. International Electrotechnical Committee (IEC) (1998) Medical electrical equipment—Part 2–1: particular requirements for the safety of electron accelerators in the range 1–50 MeV. IEC 60601-2-1
18. International Electrotechnical Committee (IEC) (2002) Medical electrical equipment—Part 2–1: particular requirements for the safety of electron accelerators in the range 1–50 MeV. IEC 60601-2-1, Amendment 1
19. International Electrotechnical Committee (IEC) (2007) Medical electrical equipment—medical electron accelerators—functional performance characteristics. IEC 60676
20. International Electrotechnical Committee (IEC) (2008) Medical electrical equipment—medical electron accelerators—guidelines for functional performance characteristics. IEC 60677
21. International Electrotechnical Committee (IEC) (2004) Medical electrical equipment—Part 2–1: particular requirements for the safety of automatically-controlled brachytherapy after loading equipment. IEC 60601-2-17
22. Nath R, Amols H, Coffey C, Duggan D, Jani S, Li Z, Schell M, Soares C, Whiting J, Cole PE, Crocker I, Schwartz R (1999) Intravascular brachytherapy physics: report of the AAPM radiation therapy committee task group No. 60. Med Phys 26:119–152

23. Nath R, Anderson LL, Meli JA, Olch AJ, Stitt JA, Williamson JF (1997) Code of practice for brachytherapy physics: report of the AAPM radiation therapy committee task group No. 56. Med Phys 24(10):1557–1598
24. Nath R, Anderson LL, Luxton G, Weaver KA, Williamson JF, Meigooni AS (1995) Dosimetry of interstitial brachytherapy sources: recommendations of the AAPM radiation therapy committee task Group No. 43. Med Phys 22:209–234

Role of Bayesian Inference in TLD-Based Personnel Monitoring

Munir S. Pathan, S. M. Pradhan, and T. Palani Selvam

1 Introduction

As researchers, our endeavours revolve around the analysis and interpretation of data acquired from diverse experiments, instruments, measurements, and resources. Our primary objective is to formulate predictive models that enable the understanding of complex natural phenomena or experimental observations. This pursuit often involves an initial process of simplification, whereby complex systems are distilled to focus on salient components, while the less crucial elements are omitted. By using this simplification strategy, we create models that lean towards being statistical rather than strictly deterministic. This is because we're dealing with uncertainties in certain parts of the system, which adds a level of unpredictability to the outcomes. Within the domain of statistical modelling, the forefront is occupied by two methodologies: the Frequentist approach, recognized as classical inference, and Bayesian inference. This chapter has two main purposes: first, to explore the underlying thought processes and methodologies of the Bayesian approaches, and, second, to utilize the Bayesian approach for the prediction of actual dose in the personnel monitoring of occupational workers in the radiation fields. Particularly, the actual dose estimation for the group of occupational workers who are working at nuclear facilities and monitored for external exposure to gamma and beta radiation using thermoluminescence-based dosimeters (TLD) is discussed in this chapter.

Now, let's proceed to explore the underlying thought processes and methodologies of the Frequentist and Bayesian approaches.

The Frequentist approach rests on the concept of repeated random sampling. This approach is grounded in the notion that if an experiment could be infinitely replicated, the long-term frequencies of observed outcomes would converge towards

M. S. Pathan (✉) · S. M. Pradhan · T. Palani Selvam
Radiological Physics and Advisory Division, Bhabha Atomic Research Centre, Mumbai 400 085, India
e-mail: mspathan@barc.gov.in

D. K. Aswal (ed.), *Handbook on Radiation Environment, Volume 2*,
https://doi.org/10.1007/978-981-97-2799-5_12

the true probabilities. This concept gives rise to point estimates, where parameters are approximated using sample statistics. For reaching conclusions, hypotheses are tested through *p*-values, which helps in determining whether the results of an experiment are statistically significant. Confidence intervals also play a pivotal role, indicating the range within which the true/actual parameter value is likely to fall.

In the Bayesian framework, the initial beliefs or expectations we hold about the elements being studied are deliberately combined with the actual observed data. This integration is facilitated through Bayes' rule. This rule guides the process of incorporating prior beliefs with the newly gathered data to recalibrate our understanding. Consequently, we arrive at a fresh collection of beliefs, which are explicitly depicted in what is referred to as the "posterior distribution" [1]. This posterior distribution operates as a representation of our updated beliefs, reflecting the interplay between our initial assumptions and the insights gained from the real-world data. Significantly, this distribution serves to encompass the uncertainties and ambiguities associated with the elements we are studying. In this way, it offers a much broader and more nuanced perspective compared to making singular predictions or establishing confidence intervals. It is important to highlight that throughout this chapter, the terms 'true dose' and 'actual dose,' as well as 'reported dose' and 'measured dose,' are employed interchangeably.

The National Occupational Dose Registry System (NODRS) at the Bhabha Atomic Research Centre is responsible for maintaining records of radiation workers' occupational doses [2]. The evolution of personnel dosimetry began with the utilization of film badges, and this journey towards refinement saw the initiation of replacing these film dosimeters with Thermoluminescent Dosimeters (TLDs) in 1975. This transition was punctuated by the indigenous development of $CaSO_4$:Dy-Teflon-based TLD badges [3–5].

At present, approximately 250,000 occupational workers are monitoring for exposures incurred from external sources of ionizing radiation encompassing X-rays, and gamma and beta radiation using TLDs. The occupational doses are reported in terms of the whole-body dose (WBD) and beta-dose estimated from the total TL counts acquired during heating of TL dosimeters. The WBD, akin to the dose equivalent from photons at the surface of an individual or phantom, emerges as an estimate of the effective dose, wielding its significance in the verification of compliance with prescribed effective dose limits. These estimated doses are relayed by personnel monitoring laboratories to both the respective facilities and NODRS. The sanctity of these dose records is paramount, as they chronicle the cumulative dose of radiation workers throughout their careers.

To account for insignificant dose variations, an approach involving recording levels comes into play. In essence, this method involves setting thresholds for reporting evaluated doses; any dose falling below this threshold is considered negligible and marked as zero. In the context of whole-body dose, the prescribed recording levels in case of exposure to photons with average energy greater than 40 keV is 0.1 mSv and that for exposures to photons with average energy below 40 keV is 0.05 mSv [5]. This differentiation is rooted in the observation that at lower photon energies, there is a substantial over-response, which consequently leads to notably

elevated TL counts. It's important to note that recorded doses of "0" for a sizable group of monitored personnel doesn't necessarily mean no exposure. These readings simply indicate radiation exposure below the established minimum level for reporting. While seemingly innocuous, this practice introduces a bias in estimating the true/actual doses received by the radiation workers. Consequently, the doses which are reported by the laboratory may not represent the values of true exposures that may have occurred, primarily because of the prevalent practice of censoring. This bias, in most instances, skews towards the underestimation of actual doses, consequently amplifying the likelihood of overestimating dose–response relationships when this data is employed in epidemiological investigations. Furthermore, a layer of uncertainty envelopes the measured doses, stemming from the inherent uncertainty in the response of the TLD badge and the intricacies of the TLD personnel monitoring system employed. Given these intricacies, a thorough analysis of measured doses becomes imperative, culminating in the derivation of a dependable estimate of actual doses.

Within academic literature, scholars have examined the Bayesian approach as a means to estimate the genuine radiation exposure encountered by occupational workers. This methodology hinges on the weekly reported doses retrieved from film badges and pocket dosimeters [6, 7]. This method, rooted in the Bayesian framework, introduces a novel perspective that aims to provide a more precise understanding of individuals' radiation exposure. This chapter extends the Bayesian framework to the specific context of TLD-based occupational dosimetry. The primary objective is to explain the actual dose estimation methodology, accounting for recording levels and censoring of the dose values. By combining statistical methodology with the intricacies of the TLD personnel monitoring system as whole, this chapter strives to offer a statistical method which incorporates the uncertainties and bias in the dosimetry system for appropriate estimation of occupational dose.

2 An Overview of the TLD Personnel Monitoring System

2.1 TLD Badge and Readout System

The TLD badge comprises two essential components: a TLD card and a cassette. Inside the TLD card, three TL elements, also known as discs, are securely affixed to an aluminium holder plated with nickel [4]. Each individual TL element takes the form of a pellet (disc) with dimensions of 13.3 mm in diameter and 0.8 mm in thickness. The composition of each TL element consists of a mixture in a 1:3 weight ratio of polytetrafluoroethylene and $CaSO_4$:Dy, which acts as the TL phosphor. Significantly, the TL phosphor $CaSO_4$:Dy exhibits a noteworthy energy-dependent response. To address this energy dependence, filters are incorporated within the cassette that houses the TLD card. These filters serve as a means of mitigating energy dependence and offer an initial evaluation of the energy and type of the radiation. The first disc, also denoted

as D1, is placed between a dual-layered metal filter. The first layer has a thickness of 0.6 mm Aluminium, while the second layer is 1 mm thick Copper. The second disc, D2, is placed between a polystyrene filter with a thickness of 1.6 mm and with density thickness of 180 mg/cm^2. Subsequently, the TLD card is first enveloped by a wrapper bearing personalized user information and then encased within a transparent polyethylene pouch. The combined density thickness of the pouch and wrapper is approximately 13–14 mg/cm^2 which is present over the third disc, D3 [8, 9].

A semiautomatic TLD badge reader that uses hot N2 gas heating with a clamping temperature of 285 °C for 30 s is used to read the TLD cards [10]. The TL element's heat delivery is regulated by maintaining a pressure of 2 kg/cm^2 and a flow rate of 5 L per minute throughout the readout process. Every second, the amount of TL that is released during the heating cycle is measured and saved as TL counts.

2.2 Dose Estimation and Reporting

As the effective atomic number of $CaSO_4$:Dy is 15.3, a significant energy-dependent response is observed. Therefore, the calibration factor (i.e., TL signal/dose) varies with photon energy [11], resulting in the need for estimation of energy before dose estimation. As discussed in the above section, there are three TL elements in each TLD badge with different filters for each element; this facilitates not only the identification of the type of radiation to which the badge is exposed but also the gross estimation of photon energy. Once the range of photon energy is known, appropriate calibration corrections are applied to estimate the doses. However, reported dose values are reported as zero if they are below the Minimum Measurable Limit (MLD). At the dose below ~ 0.1 mSv, the significant inherent non-radiation-induced TL signal and its stochastic nature lead to degradation in the Signal-to-Noise Ratio (SNR), thereby enfeebling the ability to demarcate authentic radiation signatures from the ambient noise floor. This can lead to Type I errors, where noise is mistakenly seen as radiation exposure, or Type II errors which means missing a genuine exposure, i.e., considering genuine dose as a part of background noise.

3 Development of Bayesian Framework

3.1 Basic Principles

3.1.1 Conditional Probability

Conditional probabilities serve as a cornerstone in probability theory, elucidating the probability of an event transpiring provided that another event has already taken place. It's all about understanding how the likelihood of one event is influenced

by the occurrence or knowledge of another event. Mathematically, the conditional probability of Event A occurring given Event B has occurred is denoted as $P(A|B)$, and it is defined as

$$P(A|B) = \frac{P(A \cap B)}{P(B)}, \tag{1}$$

where $P(A \cap B)$ represents the probability of both events A and B occurring together, and $P(B)$ is the probability of Event B occurring.

3.1.2 Bayes' Theorem

Bayes' theorem is a foundational concept in probabilistic reasoning that provides a systematic framework for updating our beliefs in light of new evidence. It serves as a bridge between what we know beforehand (our prior beliefs) and what we learn from observed data. This theorem offers a formal method to adjust our understanding based on the interplay between prior beliefs and empirical observations.

At its core, Bayes' theorem enables us to calculate the updated probability of a hypothesis, given new information. It quantifies how our beliefs shift in response to evidence. This shift is achieved through a careful examination of two vital components: the prior probability and the likelihood of the evidence:

$$P(A|B) = \frac{P(B|A) \cdot P(A)}{P(B)}. \tag{2}$$

The notation $P(A|B)$ represents the posterior probability of Event A given Evidence B. Similarly, $P(B|A)$ denotes the likelihood of Evidence B given the occurrence of Event A. Furthermore, $P(A)$ signifies the prior probability of Event A. Lastly, $P(B)$ represents the probability of Evidence B.

Bayes' theorem can be derived from the definition of conditional probabilities. Starting with the definition of conditional probability from Eq. (1):

$$P(A|B) = \frac{P(A \cap B)}{P(B)}. \tag{3}$$

We can rearrange the terms using the definition of conditional probability in the reverse direction:

$$P(A \cap B) = P(B|A) \cdot P(A). \tag{4}$$

Substituting this into the conditional probability equation, we get the statement of Bayes' theorem.

3.1.3 Probabilistic Inference/Bayesian Inference: Prior, Likelihood, and Posterior

In the previous section, we explored the fundamental concept of Bayes' theorem, a powerful mathematical tool that allows us to update our beliefs in the face of new evidence. Now, let's delve deeper into the components that make up this theorem: the prior probability, the likelihood, and the posterior probability. Understanding these components will illuminate how Bayesian reasoning works and why it's so valuable in various fields.

Prior Probability

The prior probability, often denoted as $P(H)$, represents our initial belief in a Hypothesis H before considering any new evidence [1]. It encapsulates what we know or assume about the hypothesis based on existing information, but without taking into account the current context. The prior is a starting point for our analysis and can heavily influence our conclusions, especially when the amount of new evidence is limited.

Imagine a scenario where we're trying to predict the outcome of a medical test for a certain disease. The prior probability might reflect the general prevalence of the disease in the population. If the disease is rare, the prior probability of an individual having the disease will be low, even before we conduct any tests.

Likelihood

The likelihood, often denoted as $P(E|H)$, is a measure of how well the Evidence E supports the Hypothesis H [1]. In other words, it quantifies the probability of observing the evidence under the assumption that the hypothesis is true. This is where the specifics of the evidence come into play.

Continuing with our medical test example, the likelihood could represent how likely the test results (e.g., positive or negative) are given the true disease status of the individual. A highly accurate test will have a high likelihood of producing the correct result, while a less accurate test will have a lower likelihood.

Posterior Probability

By applying Bayes' theorem, we can combine the initial likelihood of an event (prior probability) with new evidence (likelihood) to calculate the posterior probability, denoted as $P(H|E)$. The posterior probability represents our updated belief in Hypothesis H after considering the new Evidence E. It's a refined view that takes both our initial beliefs and the strength of the evidence into account.

Back to our medical test scenario, the posterior probability would give us the probability that an individual actually has the disease given a positive test result. This is the juncture where the prior probability along with the likelihood comes into the picture. If the prior probability was low (disease is rare), a positive test result might not be as conclusive in confirming the disease, even with a high likelihood, as compared to a more common disease. Bayesian reasoning is incredibly powerful because it allows us to iteratively update our beliefs as new evidence becomes available. This

process of updating can lead to substantial shifts in our understanding of a hypothesis based on the strength and nature of the evidence.

3.2 Implementing Bayesian Approach in TLD Personnel Monitoring Data

As already discussed above, within the Bayesian framework, we combine our existing knowledge, referred to as the "prior," about dose distributions with new data, the "reported dose," to create a probability distribution for an unknown parameter. In this particular context, the documented/reported dose (y) of an occupational worker over the monitoring period, as evaluated by the TLD laboratory, is a known value. However, the precise/actual dose (x) to which the worker/TLD badge is subjected remains unknown.

In personnel monitoring, a single reported dose (y) is recorded. Although it might seem that this directly corresponds to a single actual dose value, however, it's important to acknowledge the inherent uncertainty surrounding the precise actual dose. Thus, we treat the actual dose for a given reported dose as a random variable. This variability is characterized by the probability density function $P(x|y)$.

The collective reported dose trends observed among a group of occupational workers are typically recognizable [12]. This enables us to make reasonable estimations about an individual's likely actual dose during a monitoring period even before TLD doses are measured.

The level of certainty we hold regarding the actual dose, without any knowledge of the reported dose, is encapsulated within the prior probability distribution $P(x)$. By leveraging historical data that documents recurring dose trends among occupational workers engaged in similar activities, we can derive this prior distribution. This serves as a foundation that not only reflects our prior understanding of dose patterns but also lays the groundwork for subsequent Bayesian estimations.

Further, on the arrival of the measured dose from the TLD badge, the prior information and the characteristics of the personnel monitoring system with regards to implicating uncertainties in the measured dose [13–17], we can get the estimate of the actual dose. This estimate now has better accuracy as it is not only based on the overall trend but is also supported by the measured dose. The sections to follow cover the details of the implementation of the Bayesian approach.

3.2.1 Bayesian Formulation of the TLD Dosimetry

Preceding the assessment of doses derived from TLD readouts, the measured dose possesses an element of uncertainty with regards to a given value of true dose, x, attributable to the inherent uncertainty in measurements. Thus, the measured dose is regarded as a random variable (y), and the relationship between the true dose at a

given reported/measured dose can be expressed as a conditional probability denoted as $P(y|x)$. This conditional probability, $P(y|x)$, elucidates the probability distribution of y at a given measured dose x taking into account the uncertainties involved in the TLD personnel monitoring system. By employing Bayes' theorem, we can estimate the value of x when y is known. This estimation is based on our understanding of $P(x)$ and $P(y|x)$ and represented by Eq. (5):

$$P(x|y) = C \cdot P(x)P(y|x). \tag{5}$$

Here, C signifies a constant for normalization which is responsible for upholding the condition $\sum_x P(x|y) = 1$.

After specifying $P(y|x)$ for all probable values of x, we can utilize it to define the sampling density of x across all potential y values. This defines the likelihood of x at a given y, denoted as $L(x|y)$. Hence the Eq. (5) can be written as

$$P(x|y) = C \cdot P(x)L(x|y). \tag{6}$$

3.2.2 Determining Uncertainty Distribution $P(y|x)$ and Likelihood $L(x|y)$

To comprehensively explore the uncertainty distribution $P(y|x)$ as well as the likelihood $L(x|y)$, it's essential to delve into uncertainties that envelop the measurement process. These uncertainties originate from various sources, including the inherent characteristics of the TLD badge, the intricacies of the readout system, and the complex algorithms used for dose estimation. In the journey to untangle this, we begin by focusing on a fundamental aspect—the uncertainties associated with the reported dose. As documented in prior literature [14, 18], the lognormal distribution emerges as a suitable model to elucidate the nature of uncertainties within such measurements.

The lognormal distribution emerges as a robust model to elucidate the nature of these uncertainties, given its capability to effectively represent the statistical characteristics of measurements in radiation dosimetry. To establish the foundation for our analysis, we introduce the unrounded and uncensored measured dose, which we denote as y'. In this context, $P(y'|x)$ signifies the probability distribution function governing the measured dose y' for a given true dose x. By harnessing the lognormal distribution model, we define the mean parameter as $\mu(x) = \log(x/1\ \text{mSv})$ and the standard deviation parameter as $\sigma(x)$. It is important to note that both $\mu(x)$ and $\sigma(x)$ are rendered dimensionless for the sake of maintaining consistency within the lognormal distribution framework. The expression for $P(y'|x)$ can be derived as shown in Eq. (7). The interpretation of $P(y'|x)$ lies in envisioning it as the distribution of reported doses by TLD labs (unrounded and uncensored) for a substantial number of TLD badges exposed to the same dose level. The formulated expression for $P(y'|x)$ is as follows [6]:

$$P\left(y'|x\right) = \frac{1}{x}\frac{1}{\sigma(x)\sqrt{2\pi}}\exp\left(\frac{-(\log(y') - \log(x))^2}{2\sigma(x)^2}\right). \tag{7}$$

The uncertainty in the reported/measured dose can be broken down into two distinct components, classified as Type *A* and Type *B* uncertainties [15]. Type *A* uncertainty pertains to random effects that contribute to the overall uncertainty of a measurement or observation. These effects arise due to inherent variations in the measurement process and are typically statistical in nature. In the context of TLD dose estimation, Type *A* uncertainty originates from stochastic influences, including variations in detector sensitivity due to inhomogeneity, background readings, non-radiation-induced TL signal from dosimeters, and deviations in reading parameters like reader sensitivity and background, etc. This type of uncertainty can be gauged by analysing a series of measurements of recorded doses at known actual dose levels. For the assessment of Type *A* uncertainties in this case study, we draw upon the findings of Pradhan et al. for the same system of TLD personnel monitoring. In their study, the coefficient of variation (CoV) was determined at different delivered (actual) dose levels [17].

On the other hand, Type *B* uncertainty encompasses systematic effects that contribute to the overall uncertainty of a measurement. These effects are typically non-random and arise from various sources of bias or systematic error in the measurement process. Within the context of TLD personnel monitoring, Type *B* uncertainty originated from systematic factors such as the energy-dependent response and angular dependence, non-linearity, thermal/optical fading effects, and uncertainties in system calibration. Among these factors, the influence of energy and angular response tends to be more substantial compared to others. Nonetheless, it's noteworthy that the TLD badge in our study showcases a nearly energy-independent response within the occupational field of the workers. As a result, the uncertainty related to energy response is notably reduced. Consequently, we adopt an overall Type *B* uncertainty value of 10%.

The total uncertainty is determined by applying the quadrature summation method to Type *A* and Type *B* uncertainties. Figure 1 depicts Type *A* uncertainty and the resultant combined uncertainty, presented in the form of the coefficient of variation.

The previously calculated combined uncertainty serves as a key component in establishing the relationship between the standard deviation parameter, $\sigma(x)$, of the lognormal distribution and the actual dose. A methodology akin to that employed by Mitchell et al. [6] is adopted to determine suitable values for $\sigma(x)$. For any specific actual dose, x, the approach ensures that the probability of the measured dose exceeding the upper limit (i.e., the mean plus three times the standard deviation) is less than 0.001, thus providing a robust 99.9% confidence level that the measured dose falls within the specified range. As a result, the standard deviation parameter, $\sigma(x)$, is computed for the lognormal distribution across different values of x, utilizing the values of the total coefficient of variation ($\mathrm{CoV}_{\mathrm{total}}$). Equation (8) is employed for fitting and calculating $\sigma(x)$ for any given x within the context of the lognormal distribution (Fig. 2):

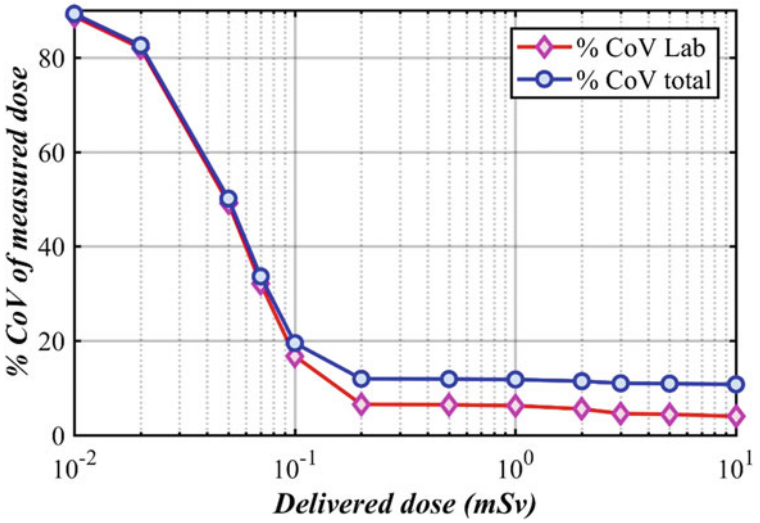

Fig. 1 Variation of the coefficient of variation in relation to delivered dose for the TLD personnel monitoring system. The red curve represents data sourced from the existing literature [17]

$$\sigma(x) = a - b \cdot \mathrm{erf}\left[\frac{(kx - c)}{(d|kx - g| + h)} + l\right] \tag{8}$$

where the x is the actual dose in mSv, erf is an error function of normal distribution, and the values of coefficients *a, b, c, d, g, h, k,* and l are determined using non-linear least squares.

Let's explore the scenario where the actual dose is 0.11 mSv. In this context, we can derive the distribution y', represented by $P(y'|x)$, utilizing the values $\mu(x) = -2.207$ and corresponding $\sigma(x)$ obtained from Eq. (8). The resulting distribution $P(y'|x)$ is depicted in Fig. 3. Notably, this distribution showcases the statistical representation of possible measured doses when the actual dose is 0.10 mSv.

When examining the distribution in Fig. 3, it's evident that the 99% confidence bounds of y' span from 0.07 to 0.19 mSv. This range signifies an asymmetric interval, which underscores the inherent asymmetry in uncertainty. The skewness of this interval is pronounced due to the lognormal nature of the uncertainty concerning the actual dose.

Furthermore, upon delving deeper into the comprehensive characterization of the confidence interval pertaining to the measured dose at any given delivered dose using the $\mathrm{CoV}_{\mathrm{total}}$ metric, we present in Fig. 4 a graphical representation of the 99% confidence interval. The obvious behaviour of uncertainty in relation to the dose is readily apparent when observing the upper and lower boundary curves. Notably, at lower dose levels, these boundaries exhibit a pronounced degree of asymmetry and considerable dispersion, whereas they progressively narrow as the dose increases. This

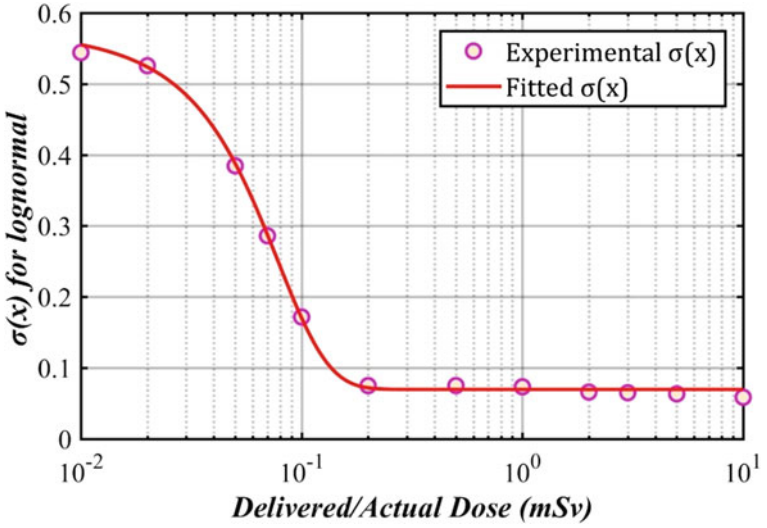

Fig. 2 Variation in $\sigma(x)$ of the corresponding lognormal distribution in relation to the delivered dose/actual dose

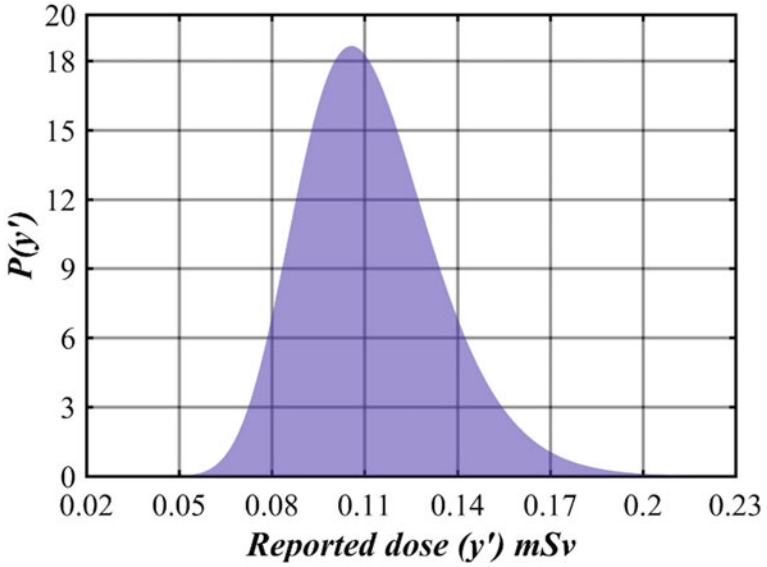

Fig. 3 The probability distribution of the measured/reported dose at the given actual dose

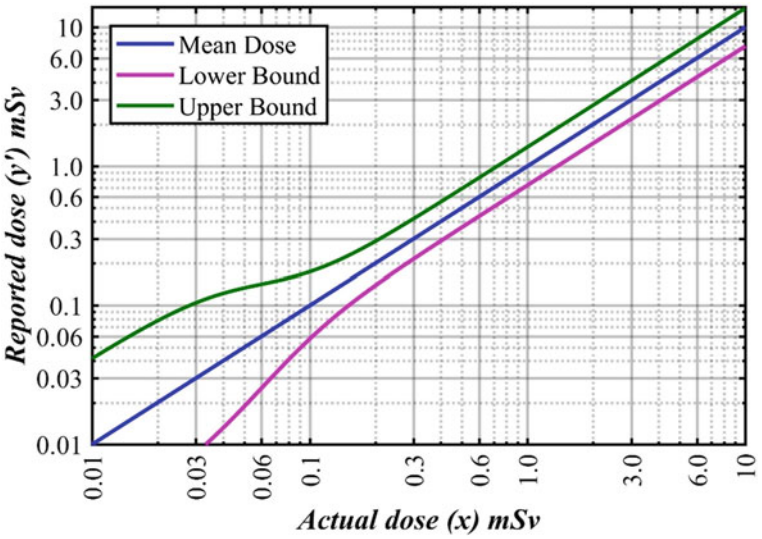

Fig. 4 Confidence bounds pertaining to 0.99 probability values of measured doses (y') at various true doses (x)

phenomenon is primarily governed by the diminishing influence of noise significance as the dose levels increase.

Using the derived probability distribution function $P(y'|x)$ across the range of possible x values, we can calculate the likelihood associated with each specific x value. This process forms the basis for determining the likelihood of a given true dose x, considering a reported dose y'.

For instance, let's take the case where the reported dose y' is 0.11 mSv. By adopting the y' as the independent variable and considering a range of possible x values, along with the associated $\sigma(x)$ parameters, we construct the likelihood distribution of x, represented as $L(x|y')$. Figure 5 presents the likelihood distribution.

However, when the dose is significantly high, i.e., in the range of few tens of mSv, the uncertainty values reduce and the probability as well as likelihood almost follow a more symmetrical shape with not much significant spread as that of lower dose levels. Figure 6 depicts the likelihood of the actual dose when the reported dose is 11.0 mSv.

In the pursuit of ascertaining the distribution of x conditioned on y, denoted as $P(x|y)$, an application of the Bayesian framework, as expounded by Eq. (2), necessitates the a priori knowledge of the distribution characterizing the actual dose for occupational workers during a specified monitoring period. For this, the lognormal probability distribution, characterized by a substantial standard deviation parameter, is invoked. This selection finds its rationale in the widely recognized notion that higher dose values correspond to diminished probabilities, thus conforming to an intrinsic pattern of dose occurrence. Furthermore, an examination of cumulative

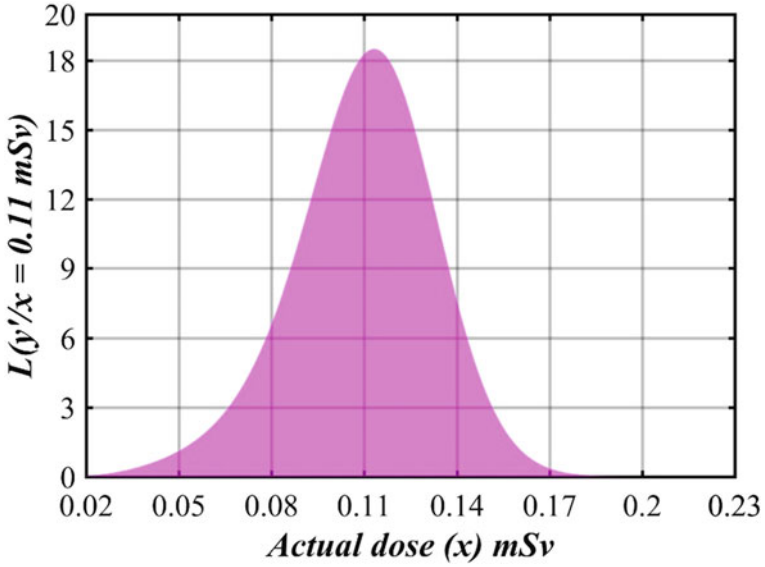

Fig. 5 The likelihood of true/actual dose at a given measured/reported dose

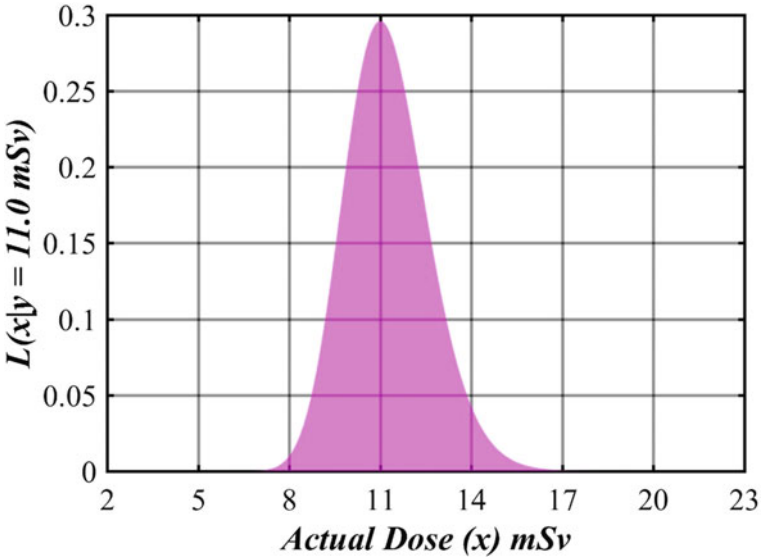

Fig. 6 The likelihood distribution of true dose at higher reported doses (example 11 mSv)

dose histograms documented in the literature reveals a distinct resemblance to distributions of exponential or lognormal nature [12]. The utilization of the lognormal distribution also yields computational coherence, enhancing the interpretability of the analysis.

In the process of determining the parameters that underlie the prior distribution, it becomes imperative to acknowledge that the selected probability distribution should encapsulate the prevalent uncertainty surrounding the actual dose prior to the acquisition of dose measurements through the readout of TLDs. A meticulous analysis of monitoring data pertaining to occupational workers unveils a characteristic trend: the median of reported dose levels converges around the threshold of 0.1 mSv, with over 95% of the recorded doses registering below 1 mSv. These empirical insights into reported doses inform our preliminary estimation of the distribution concerning the actual dose. Consequently, the parameters that define the lognormal prior distribution are computed to ensure congruence between the median of the true dose distribution and the censoring point situated at 0.1 mSv. Simultaneously, the 95th percentile aligns with the dose value of $x = 1$ mSv. Hence, the lognormal distribution is characterized by a mean of -2.303 and a standard deviation of 1.484.

Figure 7 represents the prior probability distribution encompassing the actual dose variation. An analysis of the Fig. 7. reveals that at lower dose values, the prior probability distribution will significantly influence the resulting posterior distribution of the actual dose. Conversely, as doses exceed the ~ 0.6 mSv, the prior probability distribution takes on a plateauing trajectory, signifying its diminishing influence on the resulting posterior distribution characterizing the actual dose.

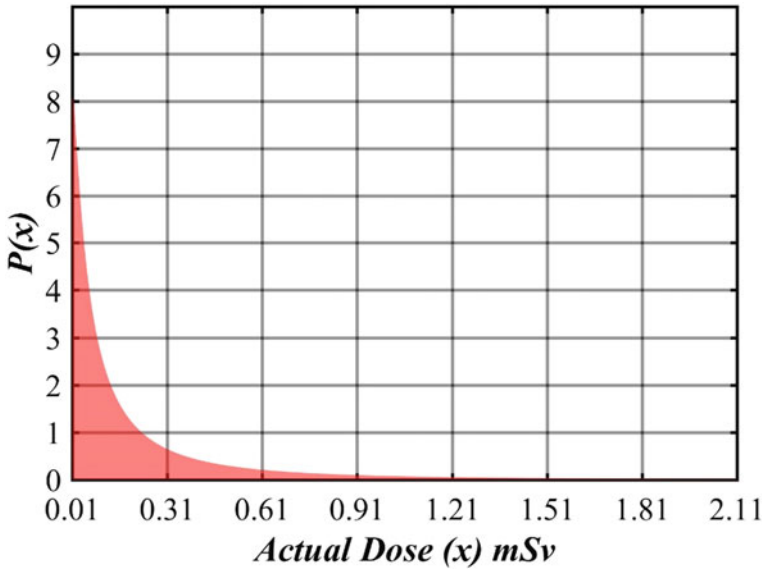

Fig. 7 Prior probability distribution for actual dose over a monitoring period

Up to this point, our focus has been on estimating the distribution of the actual dose when reported doses are provided. However, it's worth noting that in many instances, the reported doses are registered as zero. This occurrence is primarily attributed to the censoring or recording threshold set at 0.1 mSv. Consequently, there arises the need to estimate the likelihood function for the actual dose when the reported dose is zero.

3.2.3 Determination of Likelihood of the Actual Dose in Case of Zero Value of Reported Dose

In situations when the reported dose registers as zero, it is imperative to discern the likelihood of the actual dose through a comprehensive analysis. This determination can be achieved by adopting two distinct methodologies. Firstly, one can employ a likelihood function $L(x|y = \text{censoring dose})$ (Fig. 8). This function enables the establishment of a cumulative probability density function for the x at the censoring point, herein referred to as $C(x, y)$. In this context, $C(x, y)$ serves as a representation of the probability that an actual dose will be reported with a non-zero value. Consequently, the complement of this probability, $1 - C(x, y)$ [18], encapsulates the likelihood of the actual dose being reported as zero.

The second approach entails a more straightforward procedure. It involves the utilization of personnel monitoring data from cohorts. Specifically, a histogram is constructed from the TLD readings that have been reported as zero. Subsequently, an exponential function is fitted to this normalized histogram, as stipulated by Eq. (9). This exponential function can be construed as the likelihood function governing the actual dose for instances where zero doses have been reported. Figure 9 represents

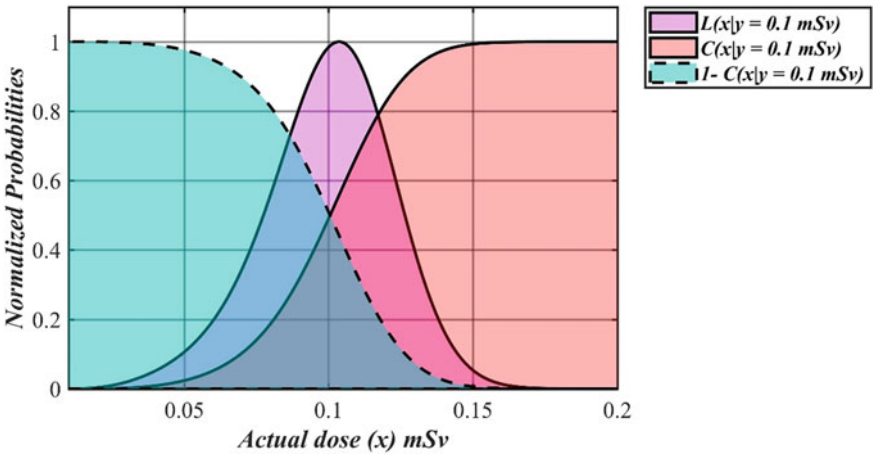

Fig. 8 Likelihood distribution of actual dose when reported dose is zero, modelled based on the likelihood of dose at the censoring level

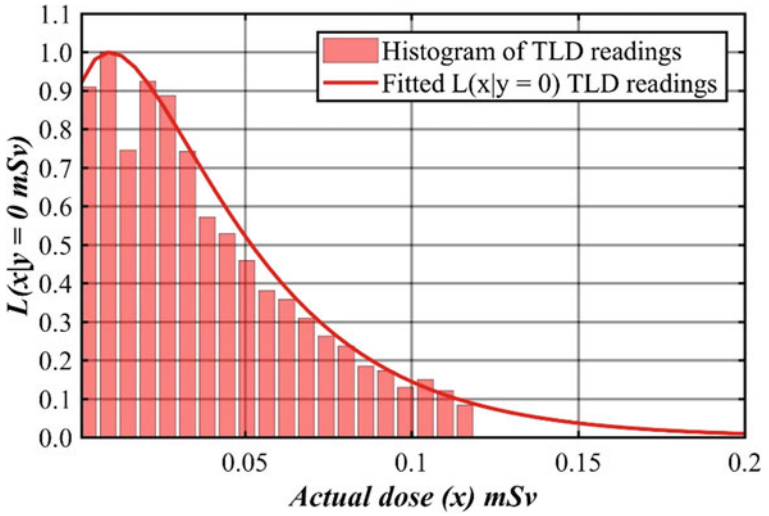

Fig. 9 Likelihood of actual dose when reported dose is zero using TL readout

the likelihood distribution for the actual dose when the reported dose equals zero based on the readout data:

$$L(x|y = 0) = C \cdot \exp(-Dx) + G \cdot \exp(-Hx) \tag{9}$$

where *C, D, G, H* are coefficients and their values are estimated using non-linear least square fitting.

Given an understanding of the potential dose a priori, the intrinsic characteristics of the dosimetry system, and the quantified reported dose value, one can employ the Bayesian paradigm to deduce the actual dose. In the subsequent sections, we will delve into specific scenarios where the reported dose is zero and proximate to the recording threshold in a single monitoring period.

4 Determining Actual Dose for Monthly Monitoring Reported Dose Data from TLD

Using a Bayesian approach, we can gain deeper insights into the process of estimating the actual dose in two specific scenarios: when reported doses are either 0 or 0.15 mSv during a monitoring period. In this framework, we start with the prior $P(x)$, representing our initial beliefs about the actual dose before incorporating new information about the measured dose. It encapsulates the possible values of the actual dose and their associated probabilities based on prior information. Simultaneously, the likelihood L($x|y$) describes how the reported dose correlates with the actual dose.

Employing Bayes' theorem, the posterior $P(x|y)$ is computed, combining the likelihood and prior distributions [18]. When the reported dose is 0 mSv, the posterior distribution accounts for our prior knowledge and the likelihood of observing zero doses.

Similarly, for a reported dose of 0.15 mSv, the posterior distribution updates our estimate of the actual dose based on this specific observation. Figure 7 visually illustrates the dynamic evolution of these prior and posterior distributions, highlighting the power of Bayesian inference in refining our understanding of actual dose estimation.

4.1 Estimation of Actual Dose in Case of Zero Reported Dose for Single Service Period

As discussed in the previous section, one can employ two different approaches for estimation of the likelihood function for zero measured dose. In the following section, we discuss the impact of both likelihoods on the posterior probability of the actual dose.

In both of the above scenarios (Fig. 10 and Fig. 11), the reported dose is zero; however, the likelihood function is derived using two different approaches. In earlier case, actual dose distribution has a significantly higher probability of doses in the proximity of the censoring level. However, in the latter case, where the likelihood is based on the TL readouts, the probability of the actual dose close to the censoring level is lesser. The readout-based likelihood can be an appropriate approach when cohorts monitored are experiencing the same amount of workload and working conditions. Because, if there is always a low level of radiation in the working area or radiation levels are very close to the background radiation level, then the readout-based likelihood function may vary accordingly.

4.2 Determination of Actual Dose in Case of Non-zero Reported Dose

When the non-zero values of the measured dose (Fig. 12) are recorded by the TL laboratory then the likelihood can be calculated considering the lognormal distribution of the measured dose for a given actual dose. It is to be noted that while computing likelihood, the parameters of the probability density function are treated as variables. Therefore at a given recorded dose, the actual dose is treated as a random variable with a finite range around the reported dose and the likelihood is computed for all possible values of the actual dose using the lognormal probability density function.

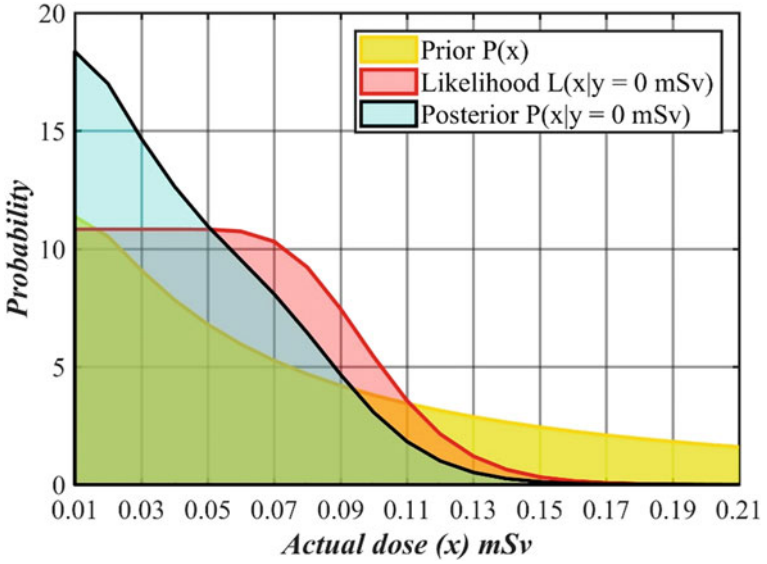

Fig. 10 Probability of actual dose at zero reported dose using likelihood based on censoring level

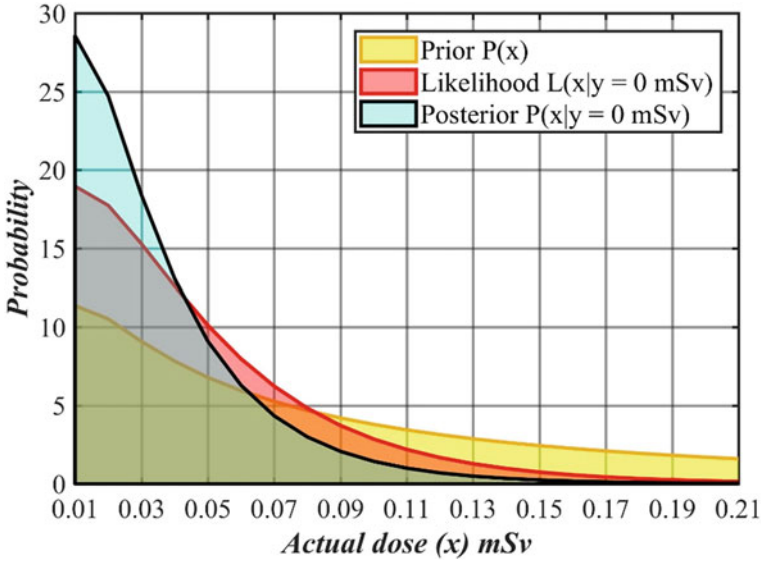

Fig. 11 Probability of actual dose at zero reported dose using likelihood based on censoring level using likelihood derived from TL readouts

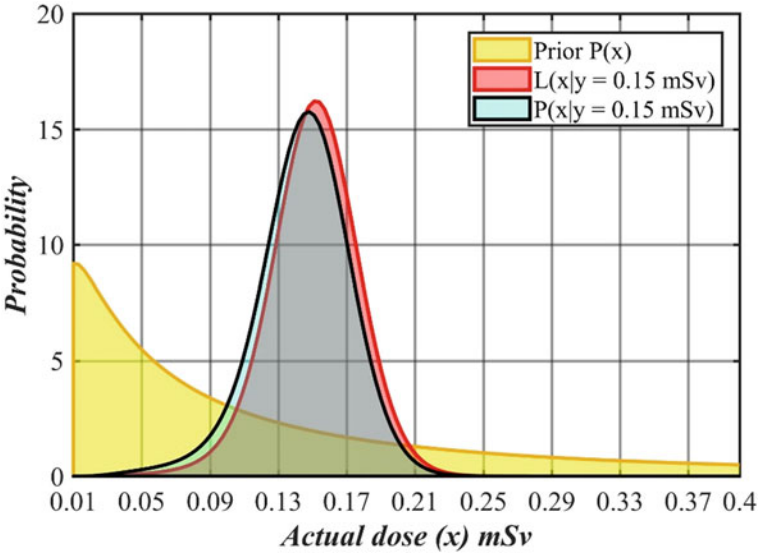

Fig. 12 Probability of actual dose when the reported dose is 0.15 mSv by using likelihood derived from TL readouts

5 Computation of Annual Doses

5.1 Combining the Monthly Posterior Probability Distributions

The annual reported dose (Y) is calculated by adding up all the reported doses from individual monitoring periods throughout the year. And it can be expressed as $Y = \sum_{i=1}^{12} y_i$, where y_i represents the reported dose for the i^{th} month. Our goal is to determine the posterior probability, denoted as $P(X|Y)$, where X represents the sum of the true doses for each corresponding month. This can be expressed as $X = \sum_{i=1}^{12} x_i$. It's important to note that the actual dose for a given month isn't a single, fixed value; instead, it is represented as a probability distribution function. Therefore, in order to arrive at an accurate estimation of the annual true dose, we need to combine or convolute each monthly actual dose probability distribution.

To illustrate this concept, consider the situation where we want to find the distribution of the sum of random variables x_1 and x_2, which represent the actual dose distributions from two consecutive months. Let's denote this sum as x (i.e., $x = x_1 + x_2$, where x, x_1, and x_2 belong to the set X, which encompasses the range of possible doses). This distribution of x can be determined through a mathematical operation known as convolution, as detailed in Eq. (10):

$$f_x(x) = \int f_{x_1}(x_1) \cdot f_{x_2}(x - x_1) \mathrm{d}x_1. \tag{10}$$

To determine f_x from f_{x_1} and f_{x_2}, the convolution is performed by taking the product of Fourier transforms and then obtaining the inverse Fourier transform of the product as shown in Eqs. (11)–(15). Hence Fourier transform of Eq. (10) can be written as

$$g_x(\varphi) = \frac{1}{\sqrt{2\pi}} \int_X f_x(x) e^{-i\varphi x} \mathrm{d}x \tag{11}$$

$$g_x(\varphi) = \frac{1}{\sqrt{2\pi}} \int_X f_{x_1}(x_1) e^{-i\varphi x_1} \mathrm{d}x_1 \cdot \int_X f_{x_2}(x_2) e^{-i\varphi x_2} \mathrm{d}x_2 \tag{12}$$

$$g_x(\varphi) = \sqrt{2\pi}\, g_{x_1}(\varphi) \cdot g_{x_2}(\varphi). \tag{13}$$

Here $g_x(\varphi)$ is a Fourier transform of the sum of probability distributions. To retrieve the probability distribution of the sum, the inverse Fourier transform of $g_x(\varphi)$ is taken as

$$f_x(x) = \frac{1}{\sqrt{2\pi}} \int_{\emptyset} g_x(\varphi) e^{i\varphi x} \mathrm{d}\varphi. \tag{14}$$

The same methodology can be employed to combine the monthly posterior probability distributions over the course of a year, enabling us to determine the posterior probability distribution for the true annual dose. Since the actual dose values are represented as discrete values, we employ a mathematical technique known as the discrete Fourier transform ($f_{\mathrm{d}x}$).

This technique allows us to perform the convolution operation efficiently in the context of discrete data. In practical terms, it helps us combine the probabilities associated with each month's dose distribution to calculate the posterior probability distribution for the actual annual dose.

The final expression for this convolution process can be articulated as follows:

$$P(X|Y) = \mathrm{inv} f_{\mathrm{d}x} \left(\prod_{i=1}^{12} [f_{\mathrm{d}x}(P(x_i|y_i))] \right) \tag{15}$$

where the $\mathrm{inv} f_{dx}$ represents inverse discrete Fourier transform.

In essence, the convolution process allows us to combine the probability distributions from individual months to obtain a probability distribution for the total annual true dose, taking into account the uncertainty associated with each monthly measurement.

To demonstrate the impact of the quantity of lower/zero monthly reported doses on the distribution of the annual actual dose, let's examine three distinct scenarios with reported annual doses of 0, 0.85, and 10 mSv [18]. The corresponding monthly reported doses are detailed in Table 1.

Table 1 Annual dose report of three test cases

Case	Annual dose (mSv)	Month											
		Jan	Feb	Mar	Apr	May	Jun	Jul	Aug	Sep	Oct	Nov	Dec
A	0.00	0.00	0.00	0.00	0.00	0.00	0.00	0.00	0.00	0.00	0.00	0.00	0.00
B	0.85	0.00	0.00	0.15	0.00	0.00	0.10	0.15	0.00	0.10	0.00	0.25	0.10
C	10.0	0.20	2.20	1.30	1.20	1.00	1.20	0.30	0.15	1.50	0.25	0.50	0.20

The posterior distribution, associated with Case A, is represented in Figs. 13 and 14. Two distinct methodologies were employed: one involving the censored zero dose likelihood, and the other by utilizing zero dose likelihood derived from TLD readings. The deliberate choice of zero dose likelihood exhibits a discernible impact on both the distribution's variability and central tendency.

In the situation where the likelihood of censored zero dose is utilized, the median estimation for the annual actual dose converges to 0.49 mSv, accompanied by 95% confidence intervals spanning from 0.31 to 0.70 mSv. Conversely, selecting the zero-dose likelihood derived from TLD readings yields a slightly lower median for the annual actual dose, approximately 0.36 mSv, with a more confined 95% confidence interval ranging from 0.22 to 0.59 mSv. Importantly, it should be noted that for Case B and Case C, the computation of the posterior probability distribution is exclusively based on the likelihood derived from TLD readings whenever zero dose was reported.

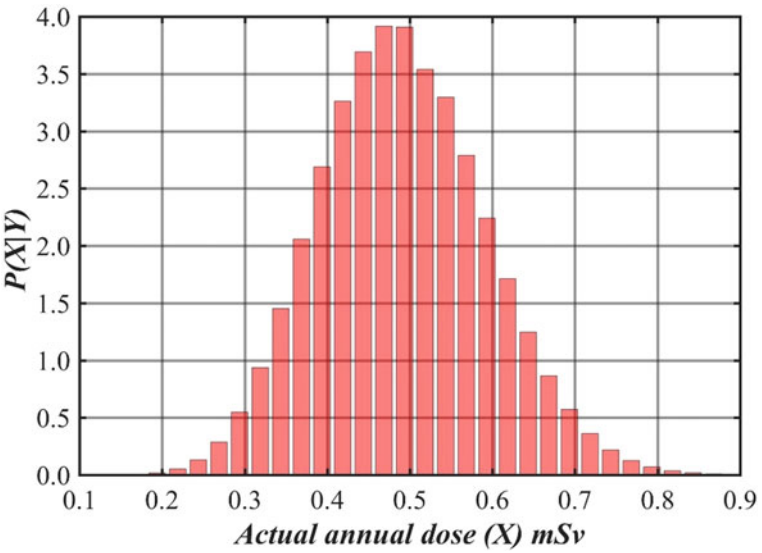

Fig. 13 Posterior of actual dose pertaining to the zero value of annual reported dose (Case A) utilizing censoring-based likelihood

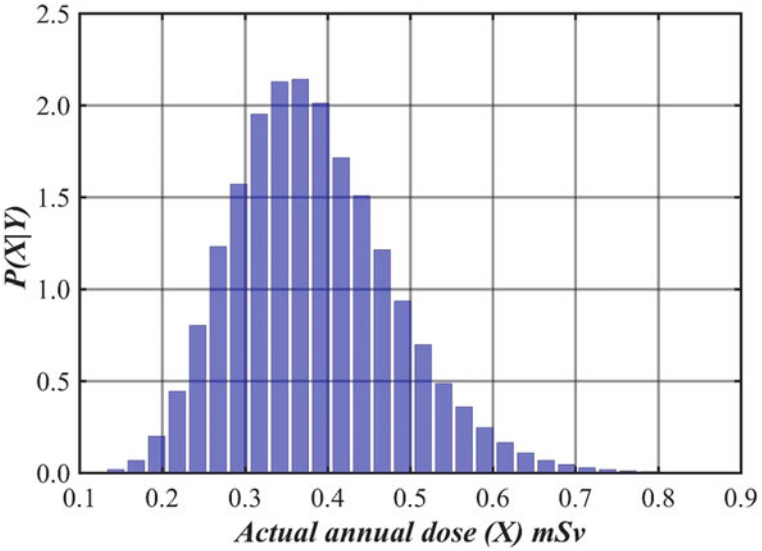

Fig. 14 Posterior of actual dose pertaining to the zero value of annual reported dose (Case A) utilizing TLD reading-based likelihood

In Figs. 13, 14, 15 and 16, the breadth of the histograms illustrates a notable increase in uncertainty in the estimated actual doses, particularly at lower dose levels. This heightened uncertainty is attributed to a higher frequency of reported zero doses within these lower ranges. In contrast, as we progress towards higher dose levels, the estimated annual actual doses exhibit reduced uncertainty, closely aligning with the reported annual doses.

This observed pattern in the uncertainty of actual dose estimates across different dose levels can be attributed to the prevalence of zero dose occurrences. Furthermore, Fig. 13 offers additional insights, indicating that for doses surpassing 0.1 mSv, the standard deviation ($\sigma(x)$) is comparatively low. As a result, with a decrease in the frequency of zero dose reports, both the level of uncertainty and the extent of underestimation in the actual dose tend to diminish.

5.2 *Utilizing the Methodology of Personnel Monitoring Datasets*

An annual dose estimation study involving approximately 500 radiation workers who share a similar work profile was reported in the literature [18], where the comprehensive comparison was carried out between the reported annual doses and the estimated annual actual doses. These cases were categorized into three distinct annual dose ranges: (i) less than or equal to 0.6 mSv, (ii) between 1 and 1.5 mSv, and (iii)

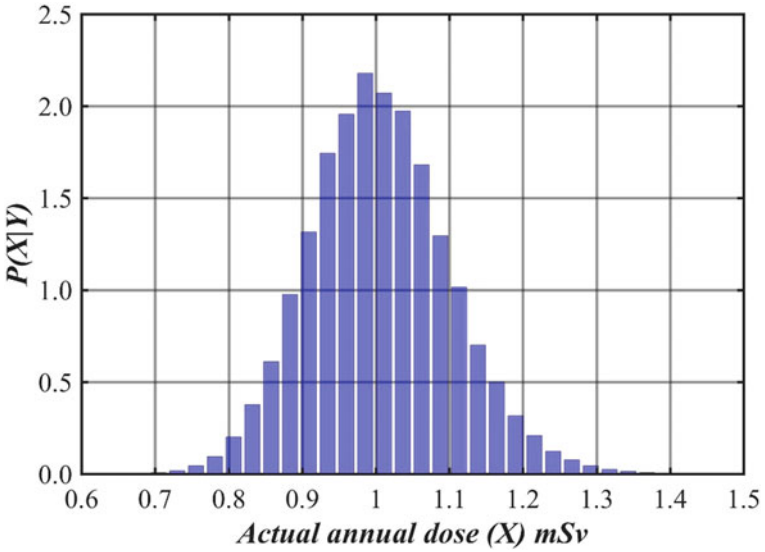

Fig. 15 Posterior of actual dose pertaining to the 0.85 mSv of annual reported dose (Case B)

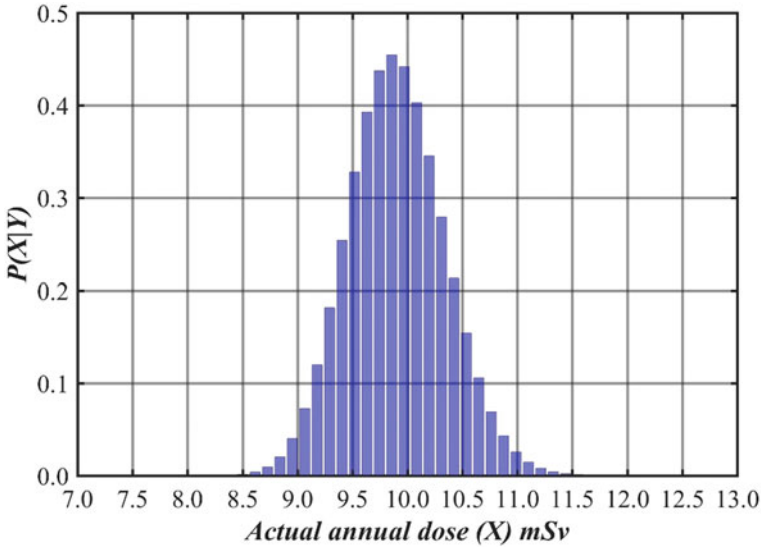

Fig. 16 Posterior of actual dose pertaining to the 10.0 mSv of annual reported dose (Case C)

between 2 and 4 mSv. To estimate $P(X|Y)$ for each individual, we utilized the TLD reading-based zero dose likelihood in combination with a fixed prior distribution, maintaining uniformity across all cases. The distribution of estimated annual actual doses, $P(X|Y)$, is visually depicted through boxplots in Figs. 13, 14, and 15 for the three aforementioned dose ranges, respectively. In these boxplots, the endpoints of each box represent the 25th and 75th percentiles, a horizontal line inside the box signifies the 50th percentile, and the whiskers extending from the box encapsulate the 5th and 95th percentiles of the annual actual dose distribution.

Figure 17, which pertains to lower annual doses and includes cases with numerous instances of zero monthly doses, clearly illustrates that a substantial portion of the annual reported doses falls below the 5th percentile of the estimated annual actual doses. This observation strongly indicates a systematic underestimation of the annual actual dose within this particular low dose range.

Figure 18 illustrates the scenario within the second dose range of 1–2 mSv, mirroring a pattern akin to that observed in the first dose range. However, in this case, the underestimation of annual actual doses is less pronounced compared to the previous scenario. This reduction in underestimation can be attributed to a decrease in the occurrence of zero reported doses as the reported values increase. Figure 19 presents a comparison for relatively high annual doses, where the reported and actual annual doses closely align. This alignment can once again be linked to the absence of, or very few instances of, monthly reported zero doses. Moreover, at higher dose levels, the level of uncertainty induced by the occurrence of rare reported zero doses becomes negligible.

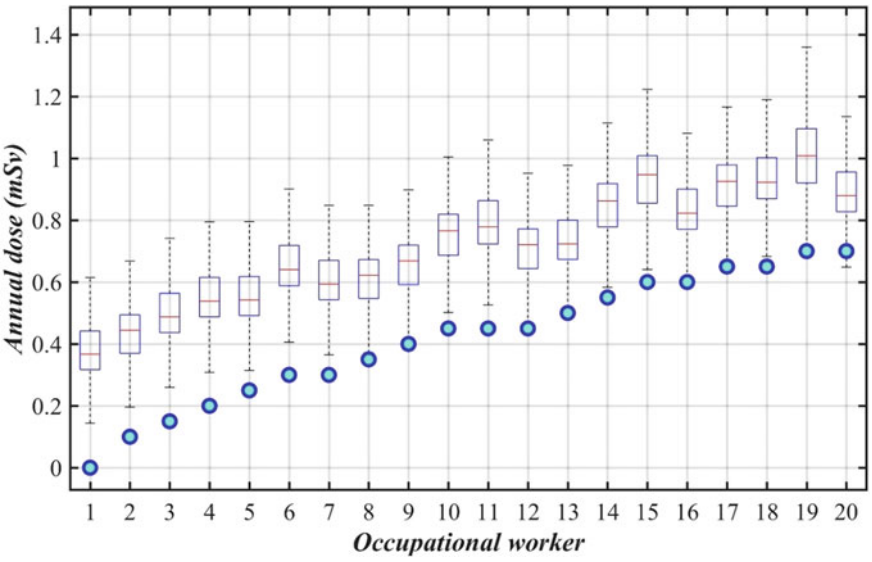

Fig. 17 Comparison of estimated actual annual dose and reported annual dose at lower dose ranges (i.e., reported annual dose less than 1 mSv)

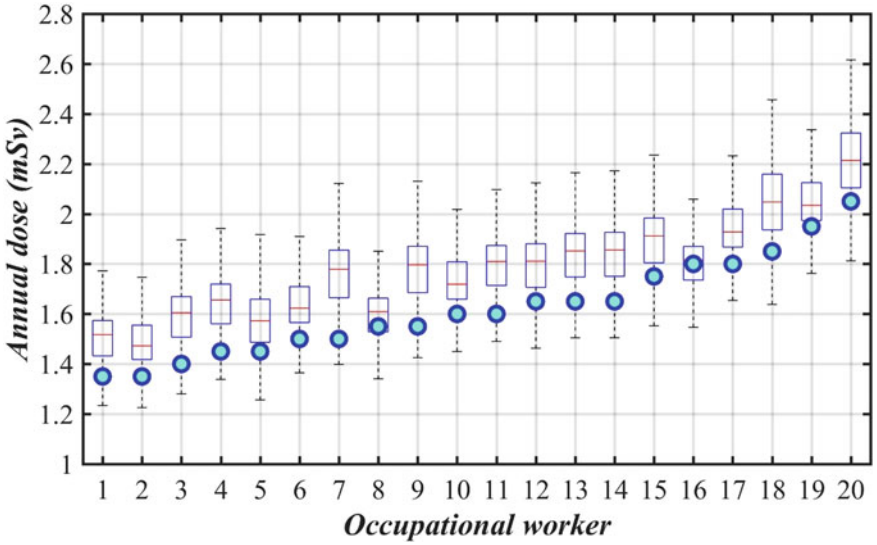

Fig. 18 Comparison of estimated actual annual dose and reported annual dose at middle dose range (i.e., reported annual dose ranging 1–2 mSv)

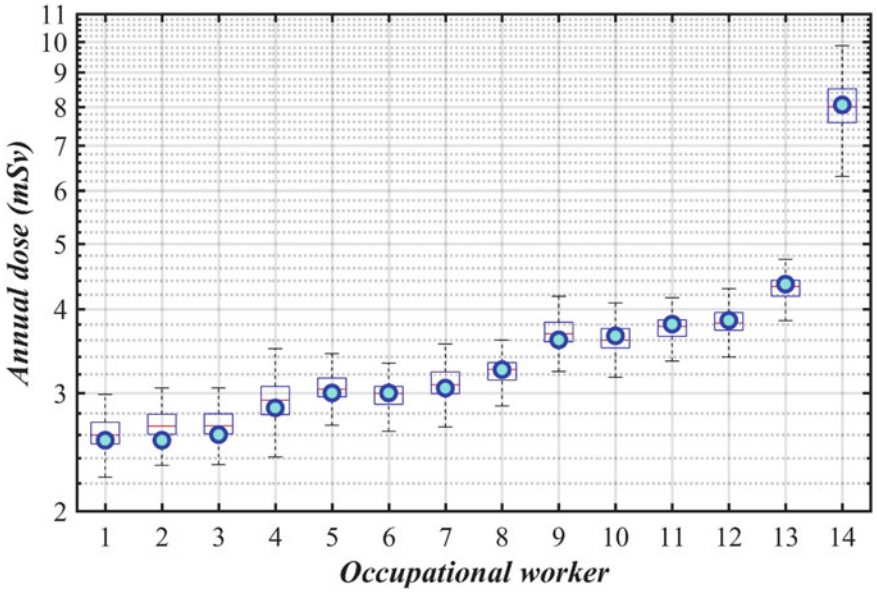

Fig. 19 Comparison of estimated actual annual dose and reported annual dose at slightly higher dose range (i.e., reported annual greater than 2.4 mSv)

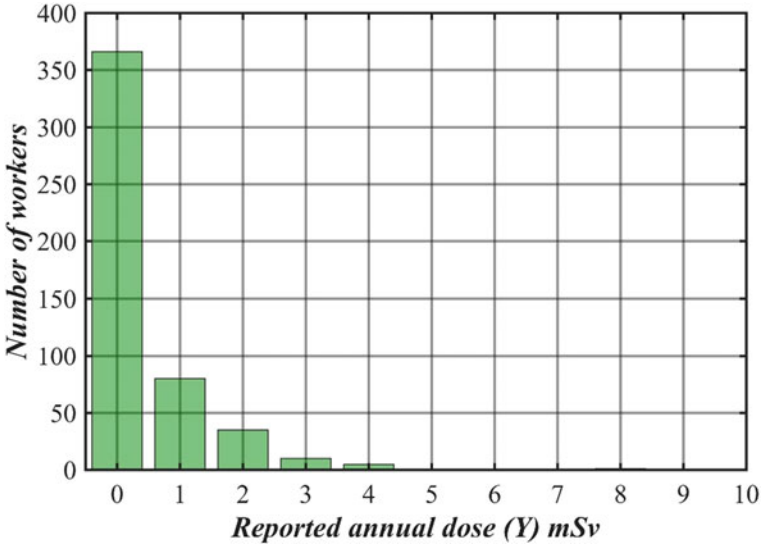

Fig. 20 Histogram of annual reported dose in a nuclear installation

Above-shown boxplots unequivocally highlight a substantial underestimation of actual doses in cases where annual reported doses fall below approximately 1 mSv. Consequently, annual reported doses below 1 mSv should not be employed in epidemiological studies.

Further, in Fig. 20, we present a histogram depicting the distribution of reported doses from a pool of 497 dose records of occupational workers. Notably, the majority of these annual reported doses, among the 497 workers, either register as zeros or are less than 1 mSv.

6 Conclusion

In this chapter, the development of a Bayesian framework aimed at estimating the actual dose received by occupational workers based on reported dose in TLD personnel monitoring was explored. The central challenge addressed is the inherent uncertainty associated with TLD dose measurements across various dose levels, coupled with historical data on dose patterns, which are harnessed to derive accurate estimates of actual doses from reported ones.

One key facet explored in this chapter is the impact of the zero-dose distribution and the method used to estimate it on the calculation of the annual actual dose. The chapter discusses the utilization of a comprehensive dataset, encompassing around 500 cohorts from nuclear installations, to scrutinize the accuracy of estimated annual actual doses, especially at lower reported annual dose levels.

The methodology and its application on the reported doses of cohorts indicate that there may be a substantial underestimation of actual doses, particularly when annual reported doses are relatively low. The primary contributing factor to this discrepancy is revealed to be the frequency of zero reported monthly doses, often occurring due to the recording threshold/censoring level of 0.1 mSv. Nevertheless, the recording threshold of 0.1 mSv is, from a radiation protection perspective, adequate and appropriate.

Although the primary focus of this chapter is not on establishing a dose–response relationship, the analysis of personnel monitoring data unmistakably indicates that using such data for epidemiological studies may introduce a bias. This bias arises from the significant underestimation of actual doses, particularly in cases involving lower radiation exposure levels.

References

1. Downey AB (2012) Think bayes: bayesian statistics made simple; version 1.0. 5. Green Tea Press.
2. Sanaye SS et al (2010) Networked national occupational dose registry system. Radiat Protect Environ 33(4):167
3. Nambi KSV, Bapat VN, Ganguly AK (1974) Thermoluminescence of $CaSO_4$ doped with rare earths. J Phys C Solid State Phys 7(23):4403–4415
4. Vohra KG et al (1980) A personnel dosimeter TLD badge based on $CaSO_4$: Dy Teflon TLD discs. Health Phys 38(2):193–197
5. Datta D et al (2018) Handbook on tld-based personnel monitoring (rev. 1–2018). In: BARC report. Bhabha Atomic Research Centre: BARC Press, Mumbai
6. Mitchell TJ et al (1993) A method for estimating occupational radiation dose to individuals, using weekly dosimetry data. Oak Ridge National Lab.(ORNL), Oak Ridge
7. Ostrouchov G, Frome EL, Kerr GD (2000) Dose estimation from daily and weekly dosimetry data. ORNL/TM-1999/282, Oak Ridge National Laboratory, Oak Ridge
8. Pradhan AS, Bhatt RC (1979) Metal filters for the compensation of photon energy dependence of the response of $CaSO_4$:Dy—Teflon TLD discs. Nucl Instr Methods 166(3):497–501
9. Lakshmanan AR, Popli KL, Kher RK (1989) Photon energy dependence of $CaSO_4$: Dy TLD under different metal filters in terms of the new ICRU quantities. Radiat Protect Dosimetry 28(4):273–276
10. Kulkarni MS, Ratna P, Kannan S (2000) A new PC based semi-automatic TLD badge reader system for personnel monitoring. In: Proceedings of international radiation protection association conference, Hiroshima
11. Vohra KG, Pradhan AS, Bhatt RC (1982) X and γ-ray response of a tld badge based on $CaSO_4$: Dy teflon TLD discs. Health Phys 43(3):391–397
12. Cardis E, Esteve J (1991) Uncertainties in recorded doses in the nuclear industry: identification, quantification and implications for epidemiology studies. Radiat Protect Dosimet 36(2–4):315–319
13. Van Dijk JWE (2006) Uncertainties in personal dosimetry for external radiation: a Monte Carlo approach. Radiat Protect Dosimet 121(1):31–38
14. Behrens R (2010) Uncertainties in external dosimetry: analytical versus Monte Carlo method. Radiat Protect Dosimet 138(4):346–352
15. Pradhan SM et al (2020) Estimation of uncertainty in measurement of dose equivalent at laboratory level using $CaSO_4$:Dy-based tld badge system in india. Radiat Protect Dosimet 188(2):135–147

16. Sadek AM (2020) Uncertainty of thermoluminescence at low dose levels: a Monte-Carlo simulation study. Radiat Protect Dosimet 192(1):14–26
17. Pradhan SM et al (2015) Development of a technique for improving coefficient of variation of $CaSO_4$: Dy teflon-based TLD personnel monitoring system in low-dose region. Radiat Protect Dosimet 167(4):429–436
18. Pathan MS, Pradhan SM, Selvam TP (2020) Estimation of actual dose based on Bayesian probabilistic approach using personnel monitoring dose records. Radiat Protect Dosimet 192(3):299–308

Retrospective Dosimetry

S. N. Menon

1 Introduction

Retrospective (originated from the Latin word *retorspectare*) generally means looking back. In the context of dosimetry, retrospective dosimetry means to estimate the absorbed dose received by the person in the past. In fact, all the dosimetry methods are retrospective in nature as one measures the dose received by the person in the past. These dosimetry methods use the signal generated in synthetic materials for measuring the dose (signal is proportional to dose). In contrast to these methods, retrospective dosimetry involves the measurement of dose when conventional dosimeters are not available and dose measurements are not planned. Terrorism involving the use of Improvised Nuclear Devices (IND), Radiological Exposure Devices (RED) and Radiolological Dispersive Devices (RDD), accidents due to mishandling of abandoned or orphaned radiological sources, large-scale nuclear power plant accidents leading to exposure of large number of people demands the use of retrospective dosimetry.

Immediately after any of the above-mentioned events, the most urgent radiological assessment requirement is to make a decision on the order of treatment of a large number of people (triage). During any nuclear or radiological accident, it is important to identify the persons who have been exposed to significant levels of radiation and are separated from the "worried well", i.e. those that are concerned that they have been exposed, but who have received no or a non-health threatening radiological dose as rapidly as possible so that treatment can be administered to those in need. Immediate treatment is needed for otherwise healthy persons who have had whole or near-total body radiation exposure exceeding 2 Gy [1]. The dose level of 2 Gy as the triage level is arrived at from the data from the Chernobyl accident. In Chernobyl,

S. N. Menon (✉)
Radiological Physics and Advisory Division, Bhabha Atomic Research Centre, Mumbai 400085, India
e-mail: snm@barc.gov.in

D. K. Aswal (ed.), *Handbook on Radiation Environment, Volume 2*,
https://doi.org/10.1007/978-981-97-2799-5_13

no fatalities were reported for people who received doses lower than 2.1 Gy. In the cases where the doses exceeded 2.1 Gy, the number of fatalities increased with the received dose [2]. The separation of exposed persons from the worried well is a major task as for every genuine person who is exposed about 100–500 worried well will request medical evaluation, leading to the wastage of precious time and resources [1]. It is thus very important to carry out this task more rapidly so that valuable medical resources can be utilized for those in need.

Also, health monitoring of the exposed population may be required for a long duration either for health care or epidemiological studies of the long-term health consequences of radiation. The target dose in this case is much lower than 2 Gy. Since the members of the public are not monitored using individual radiation monitors, innovative methods are required to assess the dose to individual, population and environment [3].

A variety of dosimetry techniques for the purpose of retrospective dosimetry have been proposed. These techniques are broadly divided into physical and biological dosimetry techniques. The realm of physical dosimetry systems encompasses luminescence-based methods, including Thermoluminescence (TL) and Optically Stimulated Luminescence (OSL), alongside Electron Spin Resonance (ESR) dosimetry and Neutron Activation Analysis (NAA). Both physical and biological dosimetry techniques have their advantages and disadvantages in estimating dose depending upon the severity and nature of radiological/nuclear accidents [4]. It is noteworthy that no universal dosimetry technique exists that can seamlessly address all situations and diverse exposed population groups. The applicability of these methods hinges on factors such as the relevant dose range and the achievable coverage of the population under investigation [5]. Depending on the circumstances, it may involve the utilization of a single technique or a combination of multiple techniques during the planning phase of dose reconstruction [4]. This chapter gives a brief introduction to physical dosimetry systems used for retrospective dosimetry.

The primary concern during emergency situations is deterministic effects caused by ionizing radiation. The concept of effective dose is not appropriate in this case as it is applicable only to stochastic effects. The radiation protection quantity Gray-equivalent defined as the absorbed dose (D) modified by the dimensionless quantity, namely, Relative Biological Effectiveness (RBE) is appropriate in this case [3]. Gray-equivalent for tissue that received dose D is given by:

$$G_{\text{rad,tissue}} = \text{RBE}_{\text{rad, tissue}} D_{\text{rad, tissue}}$$

where G is the quantity measured by biodosimetry methods. The suffix "rad" represents the type of radiation.

During an emergency, the radiation type mostly encountered has RBE = 1, thus $G = D$ expressed in Gy [3]. In case of emergency situations involving neutrons or low LET radiations, this assumption is not valid.

In the actual measurement of dose by any physical dosimeters, the measured quantity is the absorbed dose. However, for triage, the required quantity is the whole body average dose.

Therefore, conversion coefficients are required to estimate the whole body dose from the dose measured by the physical dosimeters. Many attempts have been made to evaluate these conversion coefficients to determine the organ and whole body dose from the dose measured by the dosimeters [6–9]. The generally adopted methodology is to make use of a virtual, computerized phantom and Monte Carlo methods to simulate the dose absorbed by the dosimeters and doses absorbed by different organs under various conditions of exposure [6]. It is interesting to note that in all of the above studies, the whole body dose matched well with the dose measured by the physical dosimeters when the body was exposed to isotropic radiation, which is the most realistic case during any accidents.

2 Physical Dosimetry Systems

The terminology of physical dosimetry comes from the fact that these methods are used in physical sciences. In general, the time taken to evaluate the dose from the receipt of the sample is 1–48 h [4]. The primary requirements for such dosimeters include: (1) the dose accrued over geological time periods from natural radiation (background dose) should be small, (2) negligible fading of signal during the time interval between exposure and measurement and (3) the ability to determine the cumulative dose from natural radiation sources.

2.1 Luminescence-Based Systems

The basic mechanism of the luminescence-based system is explained below. This system uses the TL or OSL from the exposed material as a measure of absorbed dose. TL is the emission of light from a previously irradiated insulator or semiconductor when it is heated. If the stimulation is carried out by a light source, the phenomenon is known as OSL. The fundamental principles that govern both TL and OSL are similar to those of all luminescence processes. The process of luminescence can be briefly explained as when radiation is incident on any material, some of its energy is reemitted as photons of lower energy (longer wavelength). The emission of light takes place at a characteristic time τ_c after the absorption of the radiation. The luminescence process can be further subdivided into fluorescence and phosphorescence depending upon the value of τ_c. Processes in which $\tau_c < 10^{-8}$ s and $\tau_c > 10^{-8}$ s are termed fluorescence and phosphorescence, respectively. Thermoluminescence and optically stimulated luminescence are phenomena where few minutes $< \tau_c < 4.6 \times 10^{-9}$ years [10].

The process of fluorescence and phosphorescence can be understood from the following simple energy level diagrams [10] (Fig. 1).

Electrons from the ground state are transferred to a higher energy level (excited state) by absorbing radiation (transition (i) in the Fig. 1). The excited electron returns

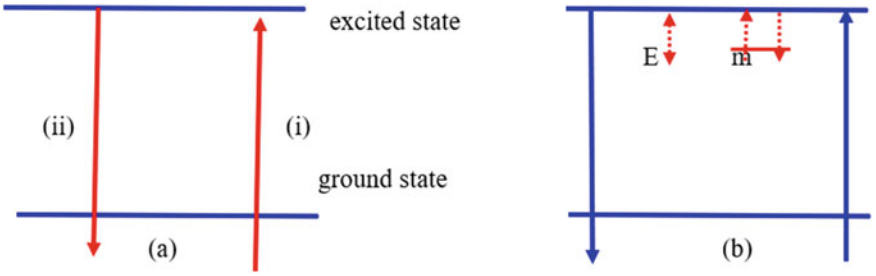

Fig. 1 Transitions showing the process of **a** fluorescence and **b** phosphorescence. *m* is the metastable level inside the forbidden gap and *E* is the trap depth of the metastable level

back to the ground state by emitting photons (transition (ii) in the Fig. 1). If this transition occurs within a time $< 10^{-8}$ s after the excitation of the electron, then it is termed fluorescence and this process is temperature-independent. However, if a metastable level is present in the forbidden gap, the electron in the excited level may get trapped in this metastable level and remain there until an energy E equivalent to trap depth (difference in energy between the excited and metastable level) is supplied so that it can go to the excited state and undergo a transition to the ground state.

The delay observed in the phosphorescence is due to the time spent by the electron at the metastable level. The mean time spent in the trap at temperature T is given as

$$\tau = s^{-1}\exp\left(\frac{E}{kT}\right) \tag{1}$$

where E is the trap depth, k is the Boltzmann constant, T is the temperature and s is a constant often called an attempt to escape frequency, i.e. it represents the number of times per second (ν) a bound electron interacts with the lattice phonons times a transition probability K. The maximum value expected for s is the lattice vibration frequency 10^{12}–10^{14} s^{-1}.

Equation 1 can be rewritten as

$$p = s\exp\left(\frac{-E}{kT}\right) \tag{2}$$

where p is the probability of the release of electron per unit time from the trap.

More appropriately, s can be identified in the following way: according to thermodynamic expressions as applied to luminescence phenomena, the rate of release of trapped electrons is given by

$$p = \nu K\exp\left(\frac{-F}{kT}\right) \tag{3}$$

where F is the Helmholtz free energy, given by $F = E - \mathrm{TS}$ where S is the entropy [9].

Thus

$$p = \nu K \exp\left(\frac{S}{k}\right)\exp\left(\frac{-E}{kT)}\right) \tag{4}$$

By comparing Eqs. 2 and 3, s can be identified with ν K exp (S/k).

In case of phosphorescence observed at room temperature, the combined values of E and s are such that the value of τ is small so that luminescence is obtained at room temperature. However, in cases where the trap depth E is such that $E > kT$, then the electron will remain trapped indefinitely. And the rate of release of trapped electrons is very small at T. In case of quartz, a natural dosimeter which is used extensively in retrospective dosimetry, typically the trap depth is ~ 1.35 eV and s ~ 10^{11} s^{-1} which gives a mean life time of electrons in the trap of ~ 2.15×10^4 years at room temperature. The electron can be released from the metastable trap by heating the sample such that $E \leq kT$. This will increase the probability of the release of electrons from the metastable level.

This theory was further developed by arguing that once the electron is freed from the trap, the probability of returning to the trap is much less than the probability of going to the ground state. The intensity of the emission at any time is proportional to the rate of recombination (transition from the excited state to the ground state). However, the recombination rate is governed by the transition of electrons from the metastable state to the excited state. Hence, the intensity of phosphorescence emission is proportional to the rate of release of electrons from the trap

$$I(t) = -C\frac{\mathrm{d}N}{\mathrm{d}T} = \frac{Cn}{\tau} \tag{5}$$

C is proportionality constant and n is the number of electrons trapped in the metastable level.

Integrating (5) gives

$$I(t) = I_0 \exp\left(\frac{-t}{\tau}\right) \tag{6}$$

where t is the time and I_0 is the intensity at time $t = 0$.

Equation (6) represents the decay of phosphorescence at a constant temperature following the end of irradiation. However, the light emission can be induced by raising the temperature. If the temperature is raised at a linear rate $\beta = \mathrm{d}T/\mathrm{d}t$, there will be a temperature at which $I(t) = n/\tau$ is large enough for the luminescence to be observed. As T increases, τ will decrease and the intensity will increase as electrons are freed from the trap and recombined at the recombination centre. As the trap gets depleted, the intensity will start to decrease and the resultant graph of intensity versus temperature is in the form of a peak known as the glow curve (Fig. 2a). This

process is termed as thermally stimulated luminescence commonly known as TL. In OSL, it is common to use a light source of constant power for stimulation, and in this case, one gets an exponentially decaying luminescence output. This is known as the shine down curve (Fig. 2b). Readers may refer to Botter Jensen et al. [11] for more insight into this phenomenon. The intensity of TL and OSL depends upon the number of trapped electrons which is proportional to the amount of energy imparted to the material. This property is utilized to measure the absorbed dose by TL and OSL. Huntley et al. [12] were the first to carry out the OSL measurements. The OSL measurements were done on quartz and feldspar.

2.2 TL and OSL in Retrospective Dosimetry

The initial application of TL was in the age determination of rocks since the intensity of TL is directly proportional to the amount of radioactivity present in the rock. This radioactivity will give rise to dose, geological dose, in the rocks. If one can determine the rate of radioactivity in the sample, and if the fading of the TL signal is negligible, the age of the rock, i.e. the length of the time the rock has been irradiated can be determined as

$$\text{Age of rock} = \text{absorbed dose}/\text{dose rate} \tag{7}$$

The proper development of TL as a tool for age determination began when natural TL was observed from samples of ancient pottery [10]. The accumulated dose in the constituents of the pottery will be lost when it is heated during the preparation of the pottery. Once the pottery is made, it will start accumulating the dose due to the irradiation from the radioactivity present in the building material of pottery and surroundings. The TL from the ingredients will be proportional to this dose and thereby to the archaeological age

$$\begin{aligned}\text{Age} = {} & (\text{archaeologically acquired TL})/[(\text{TL}/\text{unit dose of radiation} \\ & \times \text{annual dose from radioactivity in the building material and surrounding})]\end{aligned}$$

The basic principle of retrospective dosimetry using TL and OSL is similar to that of age determination. In this case, the contribution of dose is from both the external source of radiation (accident dose) as well as the radioactive materials present in the sample/surroundings and cosmic radiation which constitutes the background. It is the aim of retrospective dosimetry to obtain the accident dose as accurately as possible. In the case of an accident, materials found within the accident area like bricks, pottery, and tiles collected from local buildings can be used. In fact, the determination of the distribution of gamma dose from the atomic bombs dropped on Hiroshima and Nagasaki was carried out using TL from the roof tiles of the building [13].

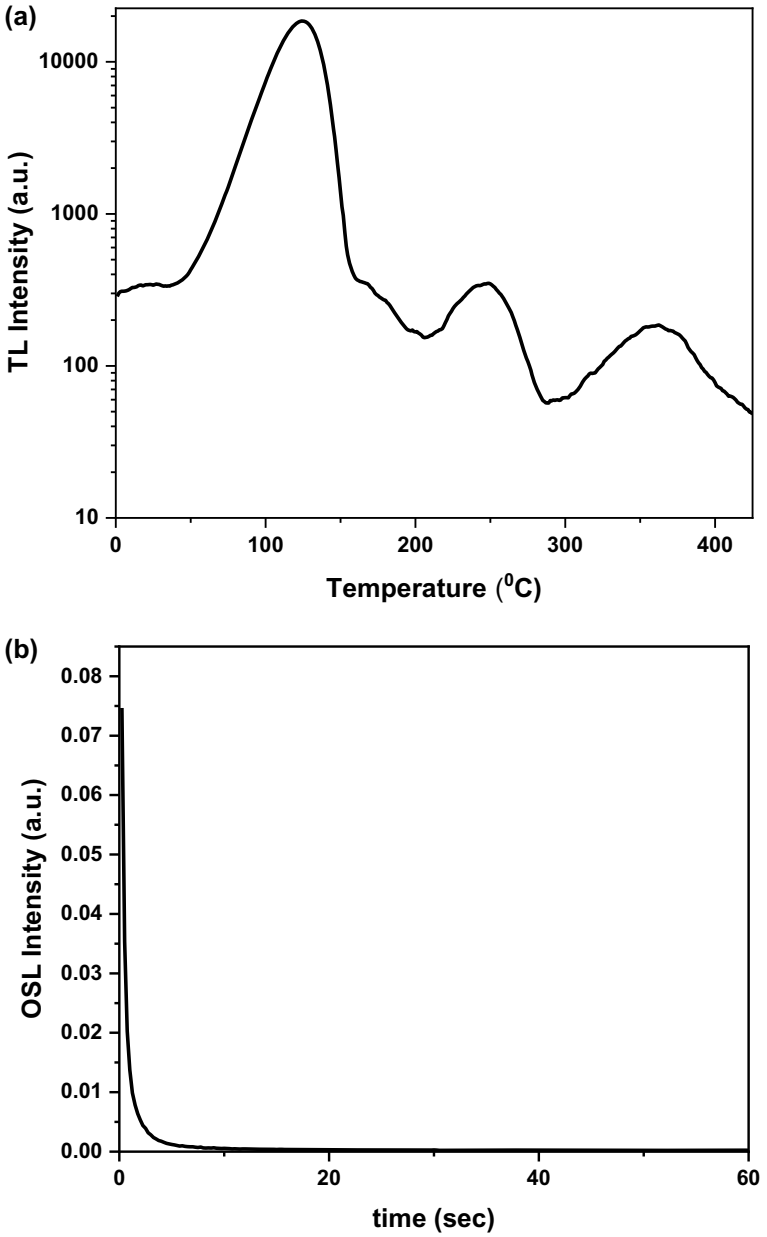

Fig. 2 **a** TL glow curve of quartz separated from a brick sample recorded at a heating rate of 50 C/s; **b** OSL decay curve (shine down curve) of the same quartz sample recorded with 480 nm light stimulation

2.3 Measurement Protocol

As mentioned previously, the estimation of accident dose involves the measurement of the background dose rate and the dose received during the accident.

2.3.1 Background Dose

The estimation of the background dose is one of the most important and time-consuming steps in retrospective dosimetry. Background dose arises from the radionuclides present in the material and surroundings as well as cosmic radiation and constitute of the dose due to alpha, beta and gamma from the terrestrial radiation and cosmic radiation

$$D_{\mathrm{BG}} = D_{\alpha} + D_{\beta} + D_{\gamma} + D_{c}$$

where D_{BG} is the background dose, D_{α}, D_{β}, D_{γ} and D_{c} are doses due to alpha, beta, gamma and cosmic radiation.

As the range of alpha particles is very low (~ 25 μm) in quartz, the contribution of alpha dose can be reduced to zero by etching the surface of the quartz by hydrofluoric acid (HF) during its separation from bricks. Therefore, in case of bricks and ceramics, the background dose in quartz/feldspar grains is due to (i) beta emitters within the brick, (ii) gamma-emitters in the surroundings and (iii) cosmic rays. In case of other materials mentioned previously, the contribution to the background dose is from external gamma and cosmic radiation.

For dosimetry purposes, both gamma and cosmic ray components are grouped together and can be measured (in uncontaminated locations) by in situ TL or OSL dosimeters [14]. Dosimeter capsules prepared by placing phosphor into tubes of sufficient thickness to absorb beta radiation from the brick are placed inside the bricks to measure the dose. By using portable gamma spectrometers or by measuring the uranium, thorium and potassium content, and by applying the published dose rate conversion table, one can estimate the gamma and beta dose [15]. Cosmic ray dose rate can be estimated using the geomagnetic latitude [16].

The internal beta dose can be determined by alpha counting, gamma spectrometry, flame photometry, atomic absorption spectrophotometry, fission track counting, neutron activation analysis and beta TL dosimetry. In the case of beta TL dosimetry, a thin layer of TL phosphor is placed under a beta thick sample for sufficient time and the TL from the phosphor is measured. The samples along with the phosphor are kept in a lead shield to prevent the background radiation. A detailed description of this method is given in Bailiff et al. [17].

2.3.2 Accident Dose

As mentioned above, the techniques to measure the accident dose are similar to those used in case of luminescence dating. For consistency with luminescence dating, the accident dose is referred to as the equivalent dose in this section. The basic procedure to measure the equivalent dose is the following: (a) measure the TL/OSL output of the sample as received and (b) use known radiation dose (laboratory dose) for calibration of the sample and determine the unknown dose. This will result in the accurate determination of the equivalent dose only if (a) the TL/ OSL response is similar during the measurement of both the natural and laboratory-induced signals and (b) the traps are stable for the relevant time periods [18]. As an example, the peak at about 110 °C in Fig. 2a has a lifetime of a few hours, therefore, the electrons in this trap will be released during this period. Hence, for the sample that has received the accident dose, this peak is not visible; however, if the TL signal is recorded after giving the laboratory dose. the peak at 110 °C will contribute to the TL signal. So it is imperative to remove this unstable peak before recording the TL signal after delivering the laboratory dose. The low-temperature peaks are removed by preheating the sample before recording the TL.

Two methods of dose evaluation are followed generally: (a) additive dose technique, and (b) regenerative dose technique. These are briefly described below. Readers may note that several other modifications or extensions of these methods are available in the literature [18].

The simplest method developed to determine the equivalent dose was the additive dose method. The main assumption in using this method is that all the grains of the sample have uniform sensitivity. This method can be used in both the cases of TL and OSL. In this method, the sample is divided into several identical fractions, which are then given incremental beta doses ranging from zero (sample which has received the accident dose) to some known dose. The luminescence yield (recorded after preheating the sample after laboratory dose, no preheat is required for the zero dose sample) when plotted against the applied dose provides the growth curve (Fig. 3), and if the mathematical expression of the growth curve is known, then the accident dose can be obtained by extrapolating back to the dose axis and the intercept will give the dose value.

The additive dose method can also be applied to OSL. In this case, the OSL is recorded after preheating the sample to remove the unstable peak as mentioned above. The disadvantage of the additive dose method is that it involves extrapolation and the obtained value of the dose depends on the mathematical expression used. This technique leads to a large error in equivalent dose estimation for samples with poor reproducibility as it is difficult to be confident of the most appropriate mathematical expression [18].

In order to circumvent the problems of the additive dose method, regenerative techniques were developed. In this method, the natural signal is read completely and the sample is given a known laboratory dose, preheated to remove the unstable peaks, and then TL/OSL is recorded. The process is repeated for several samples, each with a different radiation dose administered. The equivalent dose is obtained

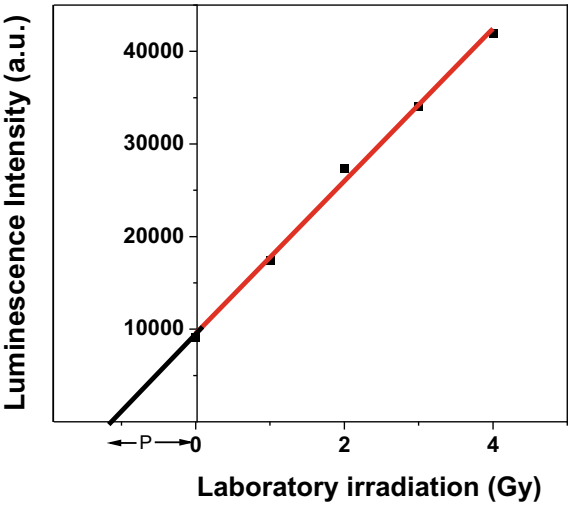

Fig. 3 A typical plot for additive dose technique. The point in y-axis corresponding to $x = 0$ is the signal corresponding to the accident dose. Other points correspond to the signal due to the additional dose given to the sample. The value of P is the accident dose

from a plot of luminescence against laboratory administered dose. Thus, the precise form of the growth curve, and the mathematical function selected, are unimportant, and an equivalent dose is obtained by interpolation. This approach will result in a higher precision for the value of the equivalent dose.

The repeated bleaching and reheating of the samples may change the luminescence characteristics of the sample leading to a mismatch of regenerated growth of luminescence with dose and the growth during antiquity. In order to address the issue of sensitivity change, an improved Single Aliquot Regenerative (SAR) protocol was suggested [19].

The SAR protocol explicitly measures and corrects for sensitivity change using the OSL response to a test dose, it is interpolative and efficiently provides multiple independent estimates of D_e. Figure 4 shows the flow chart of the SAR protocol used in the case of quartz. Appropriate preheat and cut heat temperatures may be employed for different samples depending on the location of the unstable peak. Figure 5 shows a typical plot of dose–response curve using the SAR protocol.

3 Commonly Investigated Materials

To estimate the dose, it is important to collect the samples that are not exposed to light or to remove the portion of the samples that are exposed to light to avoid the bleaching of the signal. In the laboratory, the samples are handled in dim red or orange light.

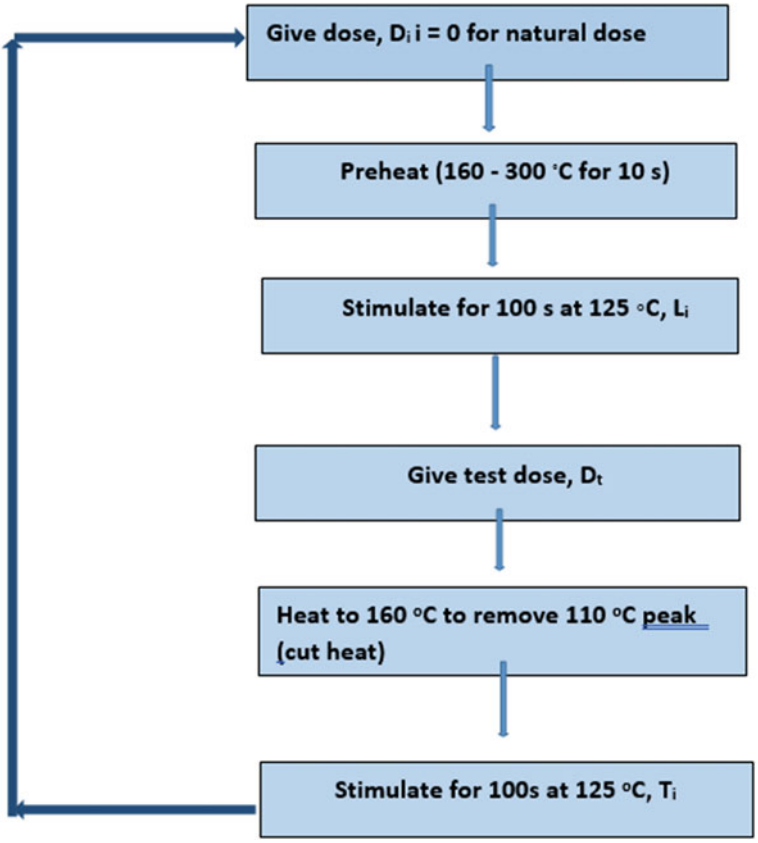

Fig. 4 Flow chart of Single Aliquot Regenerative protocol for quartz. For the natural sample, $i = 0$ and D0 = 0 Gy, Li and Ti are estimated from the initial OSL signal minus a background estimated from the last part of the shine-down curve

3.1 Ceramics

The fired materials that are suitable for retrospective dosimetry are bricks, glazed and unglazed tiles, roof tiles, interior floor tiles, sanitary wares and exterior fittings such as lamp holders and electrical power line insulators [11]. The nature of the external field and the degree of shielding within the interiors of the building can be determined by investigating these materials. Ceramic materials are the only candidates for the measurement of doses at 10 mGy level [10]. Recently, there have been reports of using cementitious material for the dose estimation. Quartz and feldspar separated from these materials are used in dose determination [20].

In case of brick the general procedure to separate quartz is to slice the brick into thin sections, crush and the grains in the size 90–100 μm are sieved These grains are then treated with hydro chloric acid (HCl) (20%) to remove the carbonate,

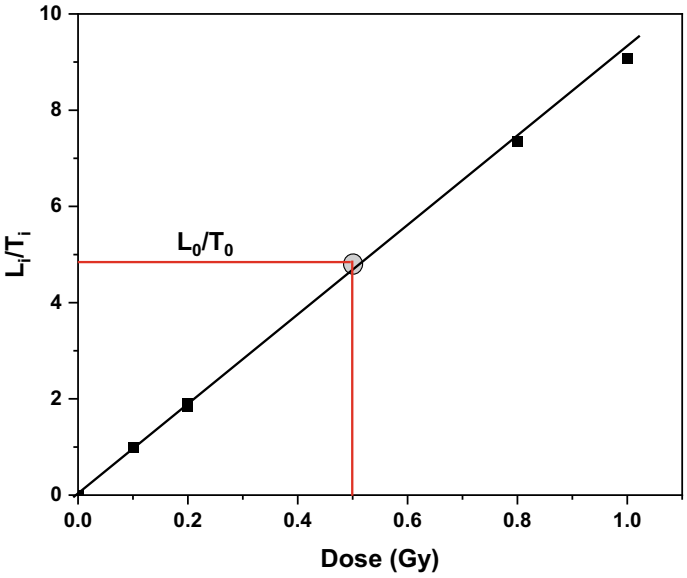

Fig. 5 A typical plot of dose–response curve using SAR protocol. The point in the dose axis corresponding to Lo/To is the unknown dose

hydrogen peroxide (H_2O_2) to remove the organic contents. The grains obtained are then separated into quartz and feldspar using a density separation technique with sodium poly tungstate solution (2.62–2.65 g/cm^3). The use of magnetic separation instead of heavy liquid separation is also reported [21]. The advantage of magnetic separation is that it can separate chert (having a density close to that of quartz), feldspars and insoluble dolomite.

The obtained quartz grains always have some deposited dose due to alpha particles and this dose contribution can be removed by etching the surface of the quartz grains with 40% HF. Treatment with HF is also efficient in dissolving feldspar as it is imperative that the quartz grains to be used for analysis should be devoid of any feldspar contamination. Soaking the HF-etched quartz grains in HCl is recommended to remove all fluorides [21]. Many variations of the above-mentioned general procedures are available in the literature [22–25]. Similar procedures are adapted to separate quartz from unheated materials like mortar and concrete.

3.2 Porcelain

Porcelain can be a useful dosimetric material in areas where there is a lack of brick-built structures. Both TL and OSL techniques are found to be useful in determining the dose. However, simpler experimental requirements for OSL techniques make it

much more attractive than TL. Two types of porcelain are prevalent, the first type is the one found mostly in electrical fuses, lamp holders, or electrical holders (type K), and the other type is usually covered with glaze and found in toilet cisterns and basins (type E and TI') [26]. The glazes have an order of magnitude higher luminescence sensitivity than that of the body due to the presence of a greater proportion of Al_2O_3. However, the use of glaze for dose determination is limited to the cases where the sample has not been exposed to any light. In cases where the sample has been exposed to any light, the surface of porcelain samples is etched using HF to remove the glaze and the outer part. Then the samples were washed, dried and crushed. Grains between 90 and 125 ~ μm were selected by sieving and further washing in acetone.

3.3 Electronic Components

Recently, with the advent of cell phones, efforts are being carried out to use the TL and/or OSL from various components of the phone to determine dose. As these phones are positioned close to the body, it gives a more accurate estimation of personal dose in case of accidents [27].

Surface mount components like resistors, capacitors, or integrated circuits from cellular phones, components from USB flash drives and cards with memory chip modules have been studied for their dosimetric properties. As the circuitry of these electronic items are in light tight conditions, the components extracted from them do not experience any light-induced fading after exposure to radiation. Hence, they are used directly for the TL/OSL studies [27–29]. It is well established that the Al_2O_3 substrates of these components are sensitive to ionizing radiation and produce TL and OSL.

3.4 Dental Enamel and Dental Ceramics

Dental ceramics and enamel are found to be radiation-sensitive materials and their dosimetry properties are being investigated. The advantage of dental enamel is that the measurement of OSL can be potentially made in situ. The first OSL measurements of dental enamel were carried out in deproteinated and non-deproteinated dental enamel with IR and green light [30]. Further OSL studies on dental enamel using better instrumentation and optics were carried out to improve the OSL sensitivity [31, 32].

Dental ceramics refers to materials including porcelain, feldspathic ceramics, glass–ceramics, alumina-based ceramics and zirconia-based ceramics. These materials are being used in the construction of crowns, restorative components of teeth and prosthetic teeth.

Dental ceramics, because of their proximity to the human body, are of interest as a dosimeter material because of their potential to provide a means of determining

exposure to external gamma radiation arising from accidents or large-scale incidents involving population groups. TL and OSL studies of various dental ceramics have been carried out [33–35].

3.5 *Other Materials*

Several other materials like common salt [36–38], medicinal tablets [39–41], desiccants [42], fabric [43], bones [44], glass [45–47], mobile phone screens [46–51], soil [52, 53], etc. are also being investigated for its application in retrospective dosimetry.

Out of all the materials discussed above, quartz extracted from fired bricks and tiles is the most sensitive luminescence material available as a natural environmental dosimeter and was used extensively to estimate the dose after nuclear accidents/incidence. Availability of sensitive TL/OSL equipment and the advancement in the measurement protocols have led to the possibility of estimating contamination-related absorbed dose at the level of only 10–20 mGy, even in the presence of a natural background dose of about 50–100 mGy [54].

Quartz separated from bricks and tiles was used for atomic bomb radiation dosimetry in Hiroshima and Nagasaki [13], fallout from Nevada atomic bomb test site [55], Chernobyl [56], radioactive contamination of the Techa river as a result of liquid radioactive waste discharges by the Mayak plutonium facility [57] and Fukushima [58]. Table 1 shows the reported minimum detectable dose using TL and OSL of some materials.

Table 1 Minimum detectable dose reported for different materials

Material	Minimum detectable dose (mGy)
Quartz	11
Porcelain	10
Electronic components from mobile phone	10
Dental enamel	4000
Dental ceramics (leucite glass-based)	4
Fabric	100
Medicines	120
Salt	0.1

4 Uncertainties

In OSL and TL, the evaluation of uncertainties follows the classical Guide to the Expression of Uncertainty in Measurement (GUM). Two major contributions to the uncertainty in dose evaluation are the uncertainties in the background signal and fading of the signal.

Several methods for estimating the uncertainty in cases where the time of the accident is known and the fading function is available are given in the literature [59]. In cases of materials where there is no or very little fading, the detection limit depends on the magnitude and uncertainty of the background signal. In the cases where the dose to be determined is in the region of the background dose, the variance in the background dose will dominate the uncertainty in the dose measurement itself. However, if the dose to be measured is greater than 100 mGy, the impact of uncertainty in the background dose will be less [59].

5 Electron Spin Resonance

Electron spin resonance (ESR) or electron paramagnetic resonance (EPR) spectroscopy is the only method to detect, identify and quantify free radicals. Quantitative measurement of radiation-induced radicals can be achieved by using the ESR technique, thereby making it an established tool for dosimetry.

5.1 Basic Principle

Consider a charged particle of charge e and mass m moving in an orbit of radius r about an axis. According to classical physics, it possesses both orbital angular momentum (due to its mass) and magnetic moment (due to the charge). The magnetic moment μ is given by

$$\mu = I \cdot A$$

where I is the current and A is the area of the loop.

$$A = \frac{e}{t}\pi r^2 \tag{8}$$

Time t is given by

$$A = \frac{ev}{t}\pi r^2 \tag{9}$$

where v is the velocity of the particle

$$\mu = \frac{evr}{2} \tag{10}$$

Angular momentum L is given by

$$L = mvr \tag{11}$$

From Eqs. (10) and (11), we get

$$\mu = \frac{e}{2m} L \tag{12}$$

The gyromagnetic ratio (γ), defined as the ratio between the magnetic moment and angular momentum, is given by

$$\gamma = \frac{e}{2m},$$

where e is the charge of the particle and m is the mass

Experimentally, it was observed that, in the case of free electrons, the gyromagnetic ratio is given by

$$\gamma_e = \frac{e}{2m_e} g_e \tag{13}$$

m_e = rest mass of the electron

The extra factor, g_e, is called as g factor. g factor for a free electron is very close to 2. The cause of this g factor is the intrinsic spin of the electron.

In quantum mechanics, the component of spin along an axis (usually taken as z-axis) is quantized and is given as

$$s_z = \frac{m_s}{2\pi} h$$

where m_s can take values $\pm$ 1/2

Substituting the above equation in (8), we get

$$\mu = g_e e \frac{h}{4\pi m} m_s \tag{14}$$

$$\mu = g_e \beta m_s \tag{15}$$

where $\frac{eh}{4\pi m}$ is known as Bohr magneton (β). It may be noted that the factor g_e in Eq. (5) is to take into account the experimental observation of the gyromagnetic ratio of the electron. When an electron of magnetic moment μ is placed in a magnetic

field B, its energy is given by

$$E = -\vec{\mu} \cdot \vec{B} \text{ or } -\vec{\mu} \cdot \vec{H} \tag{16}$$

Substituting Eq. (6) in Eq. (7) and considering the fact that $m_s = \pm ½$, one gets

$$E = \pm \frac{1}{2} g_e \beta H \tag{17}$$

Transitions between the energy levels are induced when the electrons are irradiated with electromagnetic waves of frequency ν_0 such that

$$h\nu_0 = \Delta E = g_e \beta H$$

The resonance condition can be obtained by changing either frequency or field. In magnetic resonance, it is experimentally most convenient to change the magnetic field. The resonance position is determined by the g factor.

5.2 Estimation of Dose

Once the ESR signal is acquired, it has to be converted to the absorbed dose by means of the calibration curve. There are two methods of generating the calibration curve, viz. additive dose and calibration curve method.

The additive dose method is similar to that employed for TL and OSL (Sect. 2.3.2). In this case, a tooth enamel sample is prepared and its initial ESR signal is measured. After this, the sample is subjected to additional doses, and the respective signals are measured and plotted against the delivered doses.

In the calibration method, samples of enamel are irradiated with known doses, and the signal is measured. In this case, the teeth should have a negligible intrinsic dose, and for this, young permanent teeth are normally used [60]. The calibration curve is obtained as the best fit of the radiation responses of the calibration samples. The unknown dose is estimated using this calibration curve.

6 Commonly Investigated Materials

6.1 Tooth Enamel

Retrospective dosimetry using ESR of teeth is a well-established technique. The signal from the tooth or bone is "stored" for a long period of time which aids in providing information on exposure to ionizing radiation many years after the event.

Tooth enamel has an extremely low metabolism and a stable mineral composition. The enamel once matured cannot be changed except for any chemical and physical action of its environment. The stable radiation-induced radicals formed in the hydroxyapatite ($Ca_{10}(PO_4)_6(OH)_2$) contained in bones and teeth are used for dose reconstruction. The radicals have a long-term stability of 10^9–10^{11} years. ESR signal from CO_2^- radicals formed by the absorption of ionizing radiation in the carbonate impurities attached to the hydroxyapatite crystals gives a measure of the absorbed dose [61]. The concentration of radicals increases with an absorbed dose of up to 300 Gy. A minimum detection limit of 100 mGy is reported [62]. Fattibene et al. [63] and IAEA Tecdoc [61] gives comprehensive reviews of ESR using tooth enamel.

Dose reconstruction using ESR dosimetry in tooth enamel was first carried out on atomic bomb survivors [64]. The method was subsequently applied to determine the doses of various cases of radiation accidents, such as workers in Mayak, residents in the reaches of Techa River contaminated by the radioactive wastes of the above plant, residents around Chernobyl Nuclear Power Plants, residents around the Semipalatinsk Nuclear Test Site and victims of Tokaimura criticality accident [61].

6.2 Other Potential Materials

ESR dosimetry using fingernails, chemical compounds and sugar has been studied extensively for its use in dosimetry [65, 66]. Several studies were carried out on sugar for its use as a potential ESR dosimeter in emergencies [60]. However, ESR dosimetry using tooth enamel has emerged as a standard technique for dose evaluation using ESR technique.

6.3 Limitations

The need to extract teeth from the body for analysis (in vivo ESR dosimetry may exclude this necessity).

Indistinguishability of ESR signals due to both ionizing radiation (γ, β and X-rays) and ultraviolet light.

Signal due to previously received medical doses, especially dental X-rays.

Imperfect and non-uniform removal of dentine from different tooth samples can result in significant non-uniformity of radiation sensitivity.

7 Neutron Activation Analysis

Neutron activation analysis (NAA) is an analytical technique that relies on the measurement of gamma/beta rays emitted from biological tissues such as blood, nails, or hairs, or metallic items like coins, jewellery, or belt buckles worn by the persons which were irradiated by neutrons. Activation techniques can be used during criticality accident and other situations where neutron exposure is suspected.

7.1 Basic Principle

The activation process and the subsequent decay can be expressed quantitatively. If a sample containing N_T target atoms with cross-section σ is exposed to a uniform, broad beam of monoenergetic neutrons with a fluence rate $\acute{\Phi}$, then the production rate of daughter atoms is $\acute{\Phi}\sigma N_T$. If N is the number of atoms of the daughter element and λ is the decay constant, then the rate of change in the number of daughter atoms present at any time is given by

$$\frac{\mathrm{d}N}{\mathrm{d}T} = \acute{\emptyset}\sigma N_T - \lambda N \tag{18}$$

To solve this equation, we assume that the fluence rate is constant, insignificant depletion of the original number of target atoms and no daughter atoms are present before the neutron irradiation.

The above equation can be integrated to get

$$\lambda N = \acute{\emptyset}\sigma N_T \tag{19}$$

The left-hand side gives the activity of the daughter element as a function of time and is proportional to the neutron fluence.

The total neutron kerma and the total dose can be estimated if the neutron spectrum and the gamma-to-neutron dose ratio are known [4].

7.2 Commonly Investigated Materials

Measurement of Na activation in blood [^{23}Na (n, γ) ^{24}Na, $T_{1/2}$ = 14.96 h, E_γ = 1.36 MeV (100%) and 2.75 MeV (99.85%)] has played an important role in dosimetry of criticality accidents. Measurement of gamma radiation emitted by ^{24}Na with a gamma survey meter positioned against the abdomen of the victims gives a good indication of the severity of the neutron exposure. More precise estimation of the Na activity can be carried out using whole-body counters. In addition to activated sodium, measurement of activated sulphur in hair and nails [^{32}S (n, p) ^{32}P, $T_{1/2}$

= 14.28 d, $E_{\beta max}$ = 1.71 MeV (100%)] has also been used for dose construction following accidents [4]. The activity can be measured by a Gieger-Muller counter or a liquid scintillator.

Neutron doses were re-evaluated in atomic bomb survivors by measuring the long-lived activated nuclei ^{63}Ni [^{63}Cu (n, p) ^{63}Ni] in copper samples, ^{152}Eu [^{151}Eu (n, γ) ^{152}Eu], ^{60}Co, ^{59}Ni [^{58}Ni (n, γ) ^{59}Ni], ^{41}Ca [^{40}Ca (n, γ) ^{41}Ca], ^{39}Ar [^{39} K (n, p) ^{39}Ar], ^{36}Cl[^{35}Cl (n, γ) ^{36}Cl], ^{14}C [^{14}N (n, p) ^{14}C and ^{17}O (n, α) ^{14}C], ^{10}Be [^{9}Be (n, γ) ^{10}Be and ^{10}B (n, p) ^{10}Be] in granite gravestones.

The fast neutron dose to a senior technician who was exposed due to criticality accident at the Nuclear Centre, Sarov, Russia, was determined with the rhodium (103Rh) neutron activation detector as well as activation of the aluminium filter in the IKS TLD. The dose was also estimated using the activated biological samples like the blood and hair of the victim [67]. The neutron dose to the exposed persons at the nuclear fuel processing facility of Tokaimura, Japan, was determined on the basis of ^{24}Na measurements using whole-body counters [68].

8 Conclusion

This chapter offers a concise overview of essential physical dosimetry tools utilized in the assessment of radiation doses during and after significant radiological incidents. The importance of this dose information in guiding the prioritization of medical treatment for a large population is highlighted. The methods discussed in this chapter have undergone rigorous global research, forming the bedrock of radiological dosimetry. While firmly grounded in established principles, continuous efforts are directed towards refining and augmenting these methodologies to enhance result accuracy. The chapter provides a much-needed primer on the foundational principles and diverse procedures integral to precise dose estimation.

References

1. JIWG (2005) Technology assessment and roadmap for the emergency radiation dose assessment. http://www.dhs.gov/xlibrary/assets/S_T_TechAsess_ERDAP_June05.pdf
2. Guskova AK, Barabanova AV, Baranov AY, Gruszdev GP, Pyatkin YK, Nadezhina NM, Metlyaeva NA, Selidovkin GD, Moiseev AA, Gusef IA, Dorofeeva EM, Zykova IE (1988) UNSCEAR report Appendix to Annex G "Early effects in man of high radiation doses". Acute radiation effects in victims of the Chernobyl accident
3. Bailiff IK, Sholom S, McKeever SWS (2016) Retrospective and emergency dosimetry in response to radiological incidents and nuclear mass-casualty events: a review. Radiat Meas 94:83–139
4. Ainsbury AE, Bakhanova E, Barquinero JF, Brai M, Chumak V, Correcher V, Darroudi F, Fattibene P, Gruel G, Guclu I, Horn S, Jaworska A, Kulka U, Lindholm C, Lloyd D, Longo A, Marrale M, Monteiro Gil O, Oestreicher U, Pajic J, Rakic B, Romm H, Trompier F, Veronese I, Voisin P, Vral A, Whitehouse CA, Wieser A, Woda C, Wojcik A, Rothkamm A (2011) Review

of retrospective dosimetry techniques for external ionizing radiation exposures. Radiat Prot Dosim 147:573–592
5. Chumak V. V (2013) Retrospective dosimetry of populations exposed to reactor accident: chernobyl example, lesson for Fukushima. Radiat Meas 55:3–11
6. Ulanovsky A, Wieser A, Zankl M, Jacob P (2005) Photon dose conversion coefficients for human teeth in standard irradiation geometries. Health Phys 89:645–659
7. Takahashi F, Yamaguchi Y, Iwasaki M, Miyazawa C, Hamada T (2001) Relations between tooth enamel dose and organ doses for electron spin resonance dosimetry against external photon exposure Radiat Prot Dosim 95:101–108
8. Khailov AM, Ivannikov AI, Skvortsov VF, Stepanenko VF, Orlenko SP, Flood AB, Williams BB, Swatrz HM (2015) Calculation of dose conversion factors for doses in fingernails to organ doses at external gamma irradiation in air. Radiat Meas 82:1–7
9. Eakins JS, Hager LG, Kouroukla E, Smith RW, Tanner RJ (2016) The PHE fortuitous dosimetry capability based on optically stimulated luminescence of mobile phones Radiat Prot Dosim. 10 1093/rpd/ncv520
10. Mckeever SWS (1983) Thermoluminescene of solids. Cambridge University Press
11. BotterJensen L, McKeever SWS, Wintle AG (2003) Optically stimulated dosimetry. Elsevier
12. Huntley DJ, Godfrey-Smith DI, Thewalt MLW (1985) Optical dating of sediments. Nature 313:105–107
13. Higashimura T, Ichikawa Y, Sidei T (1963) Dosimetry of atomic bomb radiation in hiroshima by thermoluminescence of roof tiles. Science 139:1284–1285
14. Aitken MJ (1985) Thermoluminescence dating. Academic press, London
15. Adamiec G, Aitken M (1998) Dose rate conversion factors: update. Ancient TL 16:37–39
16. Prescott JR, Hutton JT (1988) Cosmic ray and gamma ray dosimetry for TL and ESR. Nucl Tracks Radiat Meas 14:223–227
17. Bailff IK, Aitken MJ (1980) Use of thermoluminescence dosimetry for evaluation of internal beta dose rate in Archaeological dating. Nucl Inst Methods 173:423–429
18. Wintle AG (1997) Luminescence dating: laboratory procedures and protocols. Radiat Meas 27:769–781
19. Murray AS, Wintle AG (2000) Luminescence dating of quartz using an improved single aliquot regenerative- dose protocol. Radiat Meas 32:57–73
20. Goksu HY, Bailiff IK, Mikhailik VB (2003) New approaches to retrospective dosimetry using cementitious building materials. Radiat Meas 37:323–327
21. Porat N, Faerstein G, Medialdea A, Murray AS (2015) Re-examination of common extraction and purification methods of quartz and feldspar for luminescence dating. Ancient TL 33:22–30
22. Fujita H, Hashimoto T (2007) Usability of VTL from natural quartz grains for retrospective dosimetry. Radiat Prot Dosim 123:143–147
23. Fujita H, Jain M, Murray AS (2011) Retrospective dosimetry using Japanese brick quartz: a way forward despite an unstable fast decaying OSL signal. Radiat Meas 46:565–572
24. Campos SS, Sasaki J, Gennari RF, Souza SO (2011) Proposal for a new method to extract quartz from materials used for retrospective dosimetry and dating. Radiat Meas 46:1509–1513
25. Joshi S, Jakathamani S, Panda M, Annalakshmi O, Mathiyarasu R, Venkata Srinivas C, Venkatesan R, Venkatraman B (2021) A systematic quartz extraction method for retrospective dosimetry and dating. Microchem J 169:106555
26. Göksu HY, Wieser A, Stoneham D, Bailiff IK, Figel M (1996) EPR, OSL, TL and spectral studies of porcelain. Appl Radiat Isotopes 47:1369–13742
27. Inrig EL, Godfrey-Smith DI, Khanna S (2008) Optically stimulated luminescence of electronic components for forensic, retrospective, and accident dosimetry. Radiat Meas 43:726–730
28. Bassinet C, Trompier F, Clairand I (2010) Radiation accident dosimetry on electronic components by OSL. Health Phys 98:441
29. Jakathamani S, Annalakshmi O, Menon SN, Kadam SY, Jose MT, Venkatraman B (2019) Ceramic resistors as optically stimulated luminescent retrospective dosimeter. Radiat Phys Chem 165:108436

30. Godfrey-Smith DI, Pass B (1997) A new method of retrospective radiation dosimetry: optically stimulated luminescence in dental enamel. Health Phys 72:744–774
31. Godfrey-Smith DI (2008) Toward in vivo OSL dosimetry of human tooth enamel. Radiat Meas 43:854–858
32. Yukihara EG, Mittani J, McKeever SWS, Simon SL (2007) Optically stimulated luminescence (OSL) of dental enamel for retrospective assessment of radiation exposure. Radiat Meas 42:1256–1260
33. Bailiff K, Correcher V, Delgado A, Goksu Y, Hubner S (2002) Luminescence characteristics of dental ceramics for retrospective dosimetry: a preliminary study Radiat. Prot Dosim 101:519–524
34. Ekendahl D, Judas L, Sukupova L (2013) OSL and TL retrospective dosimetry with a fluorapatite glass-ceramic used for dental restorations. Radiat Meas 58:138–144
35. Ekendahl D, Judas L (2017) OSL and TL retrospective dosimetry with leucite glass-based dental ceramics. Radiat Meas 104:1–7
36. Bernhardsson C, Christiansson M, Mattsson S, Rääf CL (2009) Household salt as a retrospective dosemeter using optically stimulated luminescence. Radiat Environ Biophys 48:21–28
37. Spooner NA, Smith BW, Williams OM, Creighton DF, McCulloch I, Hunter PG, Questiaux DG, Prescott JR (2011) Analysis of luminescence from common salt (NaCl) for application to retrospective dosimetry. Radiat Meas 46:1856–1861
38. Singh AK, Menon SN, Kadam SY, Koul DK, Datta D (2018) OSL properties of three commonly available salt brands in India for its use in accident dosimetry. Nucl Instrum Methods Phys Res Sect B 419:38–43
39. Menon SN, Singh AK, Kadam SY, Koul DK, Datta D (2017) OSL studies of commonly available medicines for their use as retrospective dosimeters. Radiat Meas 101:7–12
40. Kazakis NA, Tsirliganis NC, Kitis G (2014) Preliminary thermoluminescence and optically stimulated luminescence investigation of commercial pharmaceutical preparations towards the drug sterilization dosimetry. Appl Radiat Isot 91:79–91
41. Sholom S, Mckeever S W S (2016) Emergency EPR and OSL dosimetry with table vitamins and minerals. Radiat Prot Dosim 172:139–144
42. Geber-Bergstrand T, Bernhardsson C, Christiansson M, Mattsson S, Rääf CL (2015) Desiccants for retrospective dosimetry using optically stimulated luminescence (OSL). Radiat Meas 78:17–22
43. Bossin L, Bailiff IK, Terry I (2017) Luminescence characteristics of some common polyester fabrics: application to emergency dosimetry. Radiat Meas 106:436–442
44. Kazakis NA, Tsirliganis NC (2019) Optically stimulated luminescence investigation of chicken bones towards their use at food post-sterilization and retrospective dosimetry. Appl Radiat Isot 154:108899
45. Şahiner E (2017) TL and OSL dose response and stability properties of various commercially glass samples obtained from Turkey for dosimetric purposes in the UV emission spectral region. Appl Radiat Isot 128:68–74
46. Moffatt JE, Spooner NA, Creighton DF, Smith BW (2012) Luminescence properties of common glasses for application to retrospective dosimetry. Radiat Meas 47:851–856
47. Bassinet C, Trompier F, Clairand I (2010) Radiation accident dosimetry on glass by TL and EPR spectrometry. Health Phys 98:400–405
48. Bassinet C, Pirault N, Baumann M, Clairand I (2014) Radiation accident dosimetry: TL properties of mobile phone screen glass. Radiat Meas 71:461–465
49. Discher M, Bortolin E, Woda C (2016) Investigations of touchscreen glasses from mobile phones for retrospective and accident dosimetry. Radiat Meas 89:44–51
50. Chandler JR, Sholom S, McKeever SWS, Hall HL (2019) Thermoluminescence and photo transferred thermoluminescence dosimetry on mobile phone protective touchscreen glass. J Appl Phys 126:074901
51. Kadam S, Menon SN, Singh AK, Dhabekar B (2022) Luminescence studies in touch screen protective glass of mobile phones for its possible application as retrospective dosimeter. J Luminesc 252:1–9

52. Fujita H (2011) Application of TL-OSL from surface soil to retrospective dosimetry. Radiat Meas 46:1870–1872
53. Menon SN, Kadam SY (2021) Thermoluminescence and optically stimulated luminescence studies of Indian soils for its application in retrospective dosimetry. Radiat Prot Environ 44:98–102
54. Ramzaeva V, Bøtter-Jensen L, Thomsen KJ, Andersson KG, Murray AS (2008) An assessment of cumulative external doses from Chernobyl fallout for a forested area in Russia using the optically stimulated luminescence from quartz inclusions. J Environ Radioact 99:1154–1164
55. Haskell EH, Bailiff IK, Kenner GH, Kaipa PL, Wrenn ME (1994) Thermoluminescence measurements of gamma-ray doses attributable to fallout from the Nevada Test Site using building bricks as natural dosimeters. Health Phys 66:380–391
56. Vischnevekii IN, Drozd IP, Koval GN, Fominych VI, Baran NP, Bartchuk VI, Bugal AA, Maksimenko VM, Baryachtar VG (1993) The use of quartz inclusion thermoluminescence for the retrospective dosimetry of the Chernobyl area. Radiat Prot Dosim 47:305–306
57. Göksu HY, Degteva MO, Bougrov NG, Meckbach R, Haskell EH, Bailiff IK, Bøtter-Jensen L, Jungner H, Jacob P (2002) First international intercomparison of luminescence techniques using samples from the Techa River valley. Health Phys 82:94–101
58. Endo S, Fujii K, Kajimoto T, Tanaka K, Stepanenko V, Kolyzhenkov T, Petukhov A, Akhmedova U, Bogacheva V (2018) Comparison of calculated beta- and gamma-ray doses after the Fukushima accident with data from single-grain luminescence retrospective dosimetry of quartz inclusions in a brick sample. J Radiat Res 59(3):286–290
59. Ainsbury EA, Samag D, Monac SD, Marral M, Bassinet C, Burbidge CI, Correcher V, Discher M, Eakins J, Fattibene P, Güçlü I, Higueras M, Lund E, Maltar-Strmecki N, McKeever S, Rääf CL, Sholom S, Veronese I, Wieser A, Woda C, Trompier F (2018) Uncertainty on radiation doses estimated by biological and retrospective physical methods. Radiat Prot Dosim178:382–404
60. Fattibene P, Duckworth TL, Desrosiers MF (1996) ESR of sugar as a personnel monitor for radiation emergencies. Appl Radiat lsot 47(1):1375–1379
61. IAEA-TECDOC-1331 (2002) Use of electron paramagnetic resonance dosimetry with tooth enamel for retrospective dose assessment
62. Kleinerman RA, Romanyukha AA, Schauer DA, Tucker JD (2006) Retrospective assessment of radiation exposure using biological dosimetry: chromosome painting, electron paramagnetic resonance and the glycophorin a mutation assay. Radiat Res 166(1):287–302
63. Fattibene P, Callens F (2010) EPR dosimetry with tooth enamel: a review. Appl Radiat Isot 68:2033–2116
64. Ikeya M, Miyajima J, Okajima S (1984) ESR dosimetry for atomic bomb survivors using shell buttons and tooth enamel. Jpn J Appl Phys 23:697–699
65. Gonzales CAB, Yasuda H, Hirota S, Miki K, Saito A, Taño JE, Nagata Y (2019) Investigation of the applicability of the ESR nail dosimetry for assessment of accidental exposure in medical facilities. Radiat Meas 124:91–97
66. Rech AB, Kinoshita A, Donatec PM, Baff O (2022) ESR dosimetry with lithium, potassium, and sodium compounds. Appl Radiat Isot 181:110105
67. International Atomic Energy Agency (2001) The criticality accident in Sarov, Vienna
68. IAEA (1999) Report on the preliminary fact finding mission following the accident at the nuclear fuel processing facility in Tokaimura, Japan

Biological Retrospective Dosimetry

Nagesh Bhat, Rajesh K. Chaurasia, and Usha Yadav

1 Introduction

Scientific investigation based on biological indicators is an indispensable part of the assessment of dose to exposed individuals. Biodosimetry is a retrospective analysis of suspected or accidental exposures. This includes regulatory requirements as in suspected over-exposures indicated by personal monitoring devices, reportable radiological incidents as in malfunction of radiation devices, and triage as in radiological emergencies involving a large number of individuals. In most of the radiation incidents, physical dosimetric information is rarely available. Besides, most of the accidental exposures are non-uniform involving either partial body or localized exposure to significant doses. In such situations, physical dosimetry does not provide reliable dose estimates. It has been realized that biological dosimetric techniques can play an important role in the assessment of absorbed dose. In recent years, a number of biological indicators of radiation have been identified. These include the kinetics of onset and persistence of prodromal syndromes (radiation sickness), cytogenetic changes in peripheral blood lymphocytes, hematological changes, biochemical indicators ESR spectroscopy of biological samples induction of gene mutations in red blood cells, cytogenetic and physiological changes in the skin, and neurophysiological changes.

Biological dosimetry methods based on cytogenetic indicators and protein markers help to assess the biological doses retrospectively, i.e., post-radiological incidents and excess exposures.

Many complex scenarios of excess exposures, including false positives due to mishandling of personnel dosimeters demand alternate and reliable methods to ascertain the genuineness of exposure and also estimate the actual dose. Besides, protracted exposure, non-uniformity in radiation fields leading to partial body exposure, internal

N. Bhat (✉) · R. K. Chaurasia · U. Yadav
Radiological Physics and Advisory Division, Bhabha Atomic Research Centre, Mumbai 400085, India
e-mail: nageshnb@barc.gov.in

D. K. Aswal (ed.), *Handbook on Radiation Environment, Volume 2*,
https://doi.org/10.1007/978-981-97-2799-5_14

exposures due to radioactive contamination, mixed radiation fields, and LET of radiation and type of radiation add to the complexities while estimating the dose. Biological dosimetry methods relying on biological signals in response to radiation exposure are helpful to address most of these challenges. Dicentric chromosome aberration (DCA) is considered as gold standard of biological dosimetry owing to its specificity and ability to detect doses as low as 100 mSv, which is of regulatory relevance. Reciprocal translocation (RT) assay based on Fluorescence in situ hybridization (FISH) is known for its long retention of signal making it suitable for retrospective and cumulative Biodosimetry [1, 2]. Mitotic fusion-induced premature chromosome condensation has demonstrated itself as a tool for estimating clinically significant doses, i.e., above 300 mSv while offering quick and reliable estimation [3]. The assay also helps estimation of high-dose and non-uniform exposures, which are limiting factors for other assays. Assays based on repair proteins such as γH2AX and 53BP1 are also being explored for quick estimation. Besides biodosimetry applications, all these assays are being explored as clinical tools for addressing challenges such as determination of radio-sensitivity, estimation of bone marrow dose, whole-body dose estimation in diagnostic and therapeutic procedures, and detection of genetic abnormalities. Deploying multiple assays for multi-parametric analysis has further helped to strengthen the analysis and dose estimation.

Ideal characteristics of biological dosimetry are:

- Should have sensitivity in a wide dose range of 20 mGy to several Gy.
- Should be a radiation-specific change.
- Should show a reproducible dose response.
- Changes must occur early but remain stable for long durations.
- Should respond to all types of radiation (low/high LET).
- Partial body irradiations must be detectable and should enable the part exposed to be identified.
- As far as possible the technique should be non-invasive.
- It should be possible to repeat the assay.
- It should be rapid and simple.
- The technique should be amenable to automation.

No single biological indicator can suffice all the requirements to meet the challenges of dose estimation owing to the complexities of exposure scenarios. Nonetheless, depending on the need, a particular assay or combination of assays helps us to address the requirements. Often it becomes necessary to adapt the multi-parametric approach to estimate exposure levels. This helps to eliminate the limitations of some assays and also to ascertain exposure levels independently by a set of assays.

In general, the dosimetric information is derived by a combination of several different methods. Although some of these indicators may be purely qualitative or semi-quantitative, they have the potential to serve as prognostic indicators. A summary of the different biological indicators and their specific usefulness under different exposure conditions is presented in Table 1. Many of these techniques are

sensitive to radiation exposure but due to their non-specificity to radiation exposure alone, their applications are limited to only either as supplementary techniques or in special scenarios.

While addressing retrospective analysis, biodosimetry procedures are usually performed for past exposures ranging from several years to decades. This is helpful for situations where exposure might have come to light after several years or even for the follow-up actions. Besides, retrospective analysis plays a major role in cumulative exposures involving radiation workers, those who might have accumulated a

Table 1 Comparison of cytogenetic techniques

Assay	Dose range (Gy)	Advantages/applications	Limitations
Dicentric chromosome aberration analysis	0.1–6	Radiation specific, very low background, amenable to automation	Labor intensive, requires skilled manpower. Not suitable for high-dose (> 6–8 Gy) localized exposures
Micronucleus assay	0.25–6	Easy to score, amenable to automation	Not possible to detect non-uniform exposure, relatively high background, inter-individual variation of response and background, and longer culture duration
Reciprocal translocations by Fluorescent in situ Hybridization (FISH)	0.25–6	Stable signal for many years, very helpful for retrospective biodosimetry, internal exposure and high LET exposure	Relatively non-specific, high background, very tedious and lengthy procedure, expensive
Drug-induced premature chromosome condensation assay (G2-PCC)/PCC-ring assay	3–25	Useful for high doses, high specificity, simple, relatively quicker than dicentric assay	Low yield, low sensitivity for low doses, large uncertainty below 3 Gy, requires 48 h of cell culture, not suitable for high-dose localized exposures
Mitotic cell fusion induced premature chromosome condensation assay (G_0-PCC)	0.3–25	Quicker results, useful for high-dose exposures where other assays may fail, most suitable for non-uniform exposures to high doses	Relatively non-specific, high background, high skill demand
γH2AX assay	0.1–> 6	Very quick results, amenable to automation, possibility of detecting doses < 0.1 Gy with blood samples available immediately after exposure, very high sensitivity, good tool as a clinical application	Signal fades very fast, needs to be performed quickly after exposure, not suitable for protracted exposures, can be only used as a supplementary technique with other assays

small number of doses over several decades and crossed doses in the range of 300–500 mSv. Such workers are usually monitored for possible hypersensitivity and also possible excess exposure beyond the control of physical monitoring. No regulatory action is applicable for such cases as the allowed lifetime dose is 1 Sv and practically no radiation worker is likely to cross such limits. Monitoring helps to keep a check on such situations and take action in advance if necessary.

Few of the cytogenetic changes have been proven to exhibit very good radiation specificity thereby qualifying them as very good indicators for biodosimetry. In particular, dicentric chromosomal aberration assay (DCA) based on the identification of dicentrics is proven to be highly specific to radiation exposure with a minimum detectable limit of about 100 mSv. DCA involves many biological processing steps. Most of these steps need aseptic conditions demanding stringent requirements of class II type biological laboratory. In BARC, we have established this technique and developed an SOP for radiation dose assessment. We have successfully handled many incidents involving both radiation workers and members of the public in suspected and accidental exposures. More than 1000 cases over the years have been referred for analysis in India and several thousand were analyzed in many part of the world facilitating biological dose estimations. Biodosimetry analysis was carried out to estimate doses to exposed individuals during many small-scale radiation accidents. In the recent past, the radiation accident, that occurred at Mayapuri, New Delhi, is one such example.

We have carried out many research studies to address the complex nature of radiation accidents such as non-uniform exposures, protracted exposures with varying dose rates, chronic exposure, lifestyle type confounding factors, and retrospective or follow-up assessments. We have established various cytogenetic techniques to address these requirements. The advantages and features of these techniques are listed in Table 1.

2 Cytogenetic Techniques in Biodosimetry

2.1 Dicentric Chromosomal Aberration (DCA) Analysis

Chromosomal aberration analysis based on the frequency of dicentric chromosomes (DCA) in cultured peripheral blood lymphocytes is so far the most reliable biological dosimetric technique. Dicentrics are formed as a result of the misrepair of two double-strand breaks leading to the crosslinking of chromosomal bodies (Fig. 1). The background dicentric frequency in unexposed blood samples is in the range of 0.0005–0.001. The frequency increases with dose linear-quadratically for low LET radiations and linearly for neutrons and high LET radiations. The frequency of dicentrics "y" varies with the dose "D" as follows:

$$y = c + \alpha D + \beta D^2 \tag{1}$$

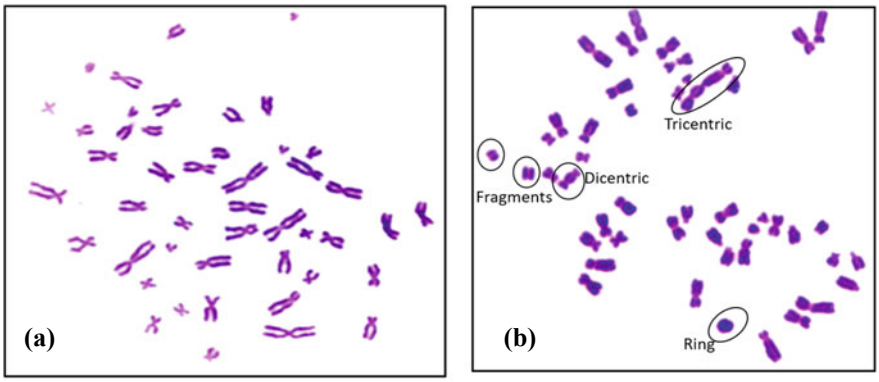

Fig. 1 **a** Chromosomes of a normal cell (left) and **b** cells with multiple dicentrics and breaks

The linear (α) and quadratic (β) coefficients are characteristic of the type of radiation. For neutrons, the response is almost linear. Generally, 500 metaphases are scored per sample and the frequency of dicentrics y is determined. Absorbed dose is assessed from the relationship

$$D = \frac{\left[-\alpha + \sqrt{\alpha^2 + 4\beta y}\right]}{2\beta} \tag{2}$$

This dose refers to the equivalent whole-body dose received acutely in an accidental exposure. The lower limit for detection is 50 mGy for X-rays, 100 mGy for γ radiation, and 10 mGy for fast fission neutrons. Different laboratories have obtained calibration curves for many different radiations. The calibration curves for different radiations are described in Fig. 2.

Doses over a wide range of 0.1–6 Gy can be detected by this technique. DCA has provided a very reliable dose estimate during the Chernobyl and Goiania accidents. Following acute radiation exposure, dicentric frequency remains unaltered for several weeks but decays to half the value in around 180 days. The subsequent reduction in the signal occurs more slowly with an approximate half-life of 3 years, as seen in the case of low dose and chronic exposures. Hence, doses from past exposures can be assessed with reasonable reliability by applying appropriate correction factors. Some individual differences in the response to the induction of CA may arise due to variations in genetic composition and DNA repair capacity. Hence, DCA can serve as a useful indicator of biological response of a specific individual.

One of the most important limitations of this technique is the requirement of a well-experienced scorer. Further, the scoring of dicentrics is not only time-consuming, but also not amenable to automation due to the complexity of the image of dicentrics to signal processing systems. Recent advances such as metaphase scanners and

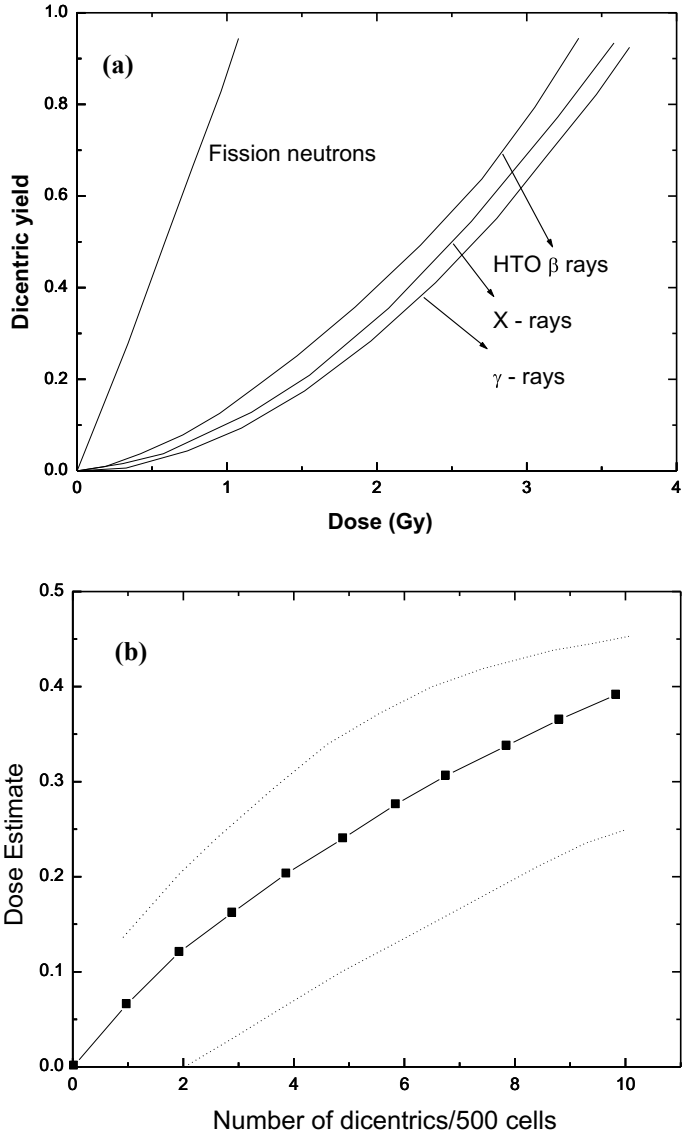

Fig. 2 **a** Calibration curves for different radiations and **b** confidence level of dose estimation using CA for low doses

centromeric painting by antikinetocore antibodies can enhance the scoring speed and reduce errors in the identification of dicentrics. In accidents involving exposures in the lethal range (3–6 Gy), suffice it to score 25–50 metaphases for providing the preliminary information required for medical management of victims. However, at higher doses, most of the severely damaged cells fail to go through the division and it

may be very difficult to find even a few metaphases. Whenever low doses of the order of a few 100s of mGy have to be detected, since only a few dicentrics are involved, the Poisson error associated with the estimates can be very large.

DCA for Non-uniform Exposures

In uniform whole-body exposures, the radiation-induced dicentric chromosomes follow a perfect Poisson distribution. However, in most accidents, the exposures are non-uniform, resulting in a fraction of lymphocytes receiving a much larger dose as compared to those in the unexposed part of the body. As a result, the total aberrations scored are concentrated in a few damaged cells, which reach the metaphase. The degree of over-dispersion can be assessed by the dispersion coefficient u.

$$u = \frac{\left[\frac{\sigma^2}{y-1}\right][N-1]}{\sqrt{s(N-1)\left(1-\frac{1}{Ny}\right)}} \tag{3}$$

where N is the total number of cells scored, y is the frequency of dicentrics, and σ^2 is its variance. A positive value of u indicates over-dispersion, a negative value is an under-dispersion, and a zero value is a perfect Poisson distribution. In accident situations, a value greater than 1.96 suggests a partial body or localized exposure.

2.2 Micronucleus Assay (MN Assay)

Micronuclei refer to small nuclei formed from chromatin material, which lag behind and do not get included in either of the daughter nuclei formed during cell division (Fig. 3). Exposure to radiation and other clastogenic agents results in a dose-dependent increase in the frequency of MN. Dividing cells are blocked at cytokinesis using cytochalasin B, in order to visualize the induced MN.

Even though there are claims that MN assay can detect absorbed doses of the order of 50 mGy, large individual variations in background frequency do not permit reliable estimates of doses less than 0.25 Gy. In accident situations involving absorbed doses in the range of 2–6 Gy, very reliable information can be obtained within 3 days after the exposure. In accidents involving exposure to a large number of people, MN assay may be particularly useful, when well-trained technicians are not available to score dicentrics. The prospects of automation are much better for MN assay as compared to DCA.

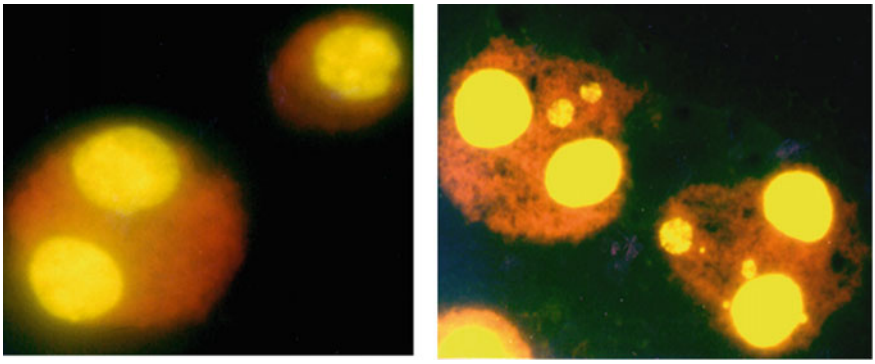

Fig. 3 Binucleated cell with single micronuclei and another cell with five micronuclei

2.3 Drug-Induced Premature Chromosome Condensation (PCC)

Cytogenetic markers/Chromosomal aberrations are the most suitable endpoints for biodosimetry, being specific to radiation and stable for months to years [4]. These can be visualized easily once chromosomes are in their condensed state. However, lymphocytes are non-dividing cells, and hence have chromosomes in the form of fibers that cannot be distinctly visualized under the microscope. Naturally, chromosome condensation occurs at its best in the metaphase stage during cell division. Conventionally, to study chromosomal aberrations in dicentric assay, lymphocytes are first stimulated to divide and then arrested at the metaphase stage. To get there, it takes a minimum of 48 h after blood withdrawal to collect sufficient cells at the desired stage. Moreover, at high-dose exposures, getting cells at metaphase becomes difficult due to cell cycle arrest at G2/M checkpoint and severe leucopenia. In such cases, to visualize aberrations, chromosome condensation is induced artificially at the interphase stage itself by methods called premature chromosome condensation or PCC.

There are two means of inducing PCC:

1. Drug-induced PCC in which some chemicals such as Calyculin-A, Okadaic Acid, and Caffeine can induce condensation efficiently in cells arrested at the G2 phase by allowing them to enter prematurely in mitosis.
2. Fusion-induced PCC in which chromosomes are condensed artificially in resting G_0-phase itself without culturing them for 48 h. In this process, chemical factors responsible for chromosome condensation are transferred into the cells by fusing them into mitotic cells.

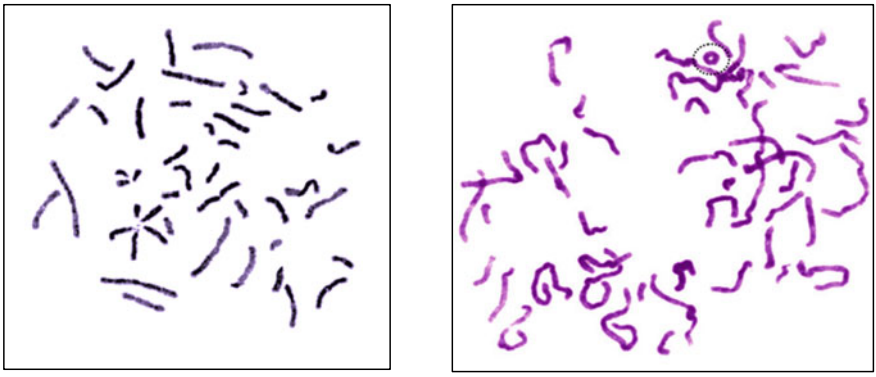

Fig. 4 Images of chromosomal spreads analyzed in PCC-ring assay with ring type of chromosomal aberration

2.4 Drug-Induced PCC-Ring Assay

Blood collected from the subject is cultured for 48 h and PCC-inducing chemical Calyculin-A (50 nM) is added for the last one hour of the culture. Processing and slide preparation are the same. Chromosomal spreads from every phase of mitosis can be seen. Hollow ring chromosomes induced by radiation are beautifully visible in this assay and the frequency of the same is used for dose estimation (Fig. 4). Radiation dose–response curve has been prepared by in vitro experimentation and it has been found to be linear in the range of 5–15 Gy.

2.5 Mitotic Cell Fusion Induced PCC: G_0-PCC

In this method, rather than waiting for $\geq$ 48 h for the cells to reach metaphase for chromosomal aberration analysis, chromosomes are prematurely condensed in G_0-phase by fusing the blood lymphocytes to cells that are preserved in metaphase. The cell fusion leads to the transfer of mitotic factors to the lymphocytes causing premature chromosome condensation. It only takes ~ 4–6 h starting from blood collection to chromosomal spread preparation on the slide. Mitotic cell fusion-induced PCC overcomes three major shortcomings of conventional gold standard assay. First, it is quick, with dose estimations duration within 24 h even with the application of FISH. Second, it works well at high doses; even beyond 15 Gy, and most importantly, it is most suitable for localized exposures among all other methods. The only limitations of this method are uncertainty at low doses and high skill demand. The various scopes of this method are given below.

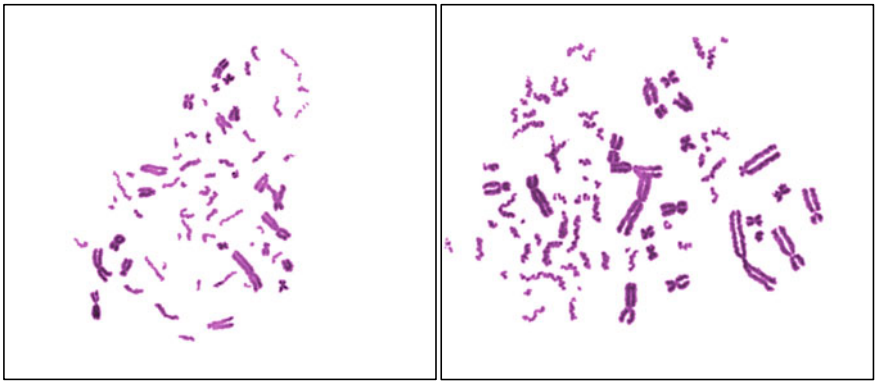

Fig. 5 Representative images of chromosomal spread after G_0-PCC stained with Geimsa captured at 6300 magnification. The spreads can be seen with the presence of two types of chromosomes one metaphase chromosome coming from mitotic cells and the other thread-like prem

2.6 Fragment Analysis

Chromosomal bodies excess to 46 are counted as fragments (Fig. 5). This is the quickest endpoint which can be observed ~ 4–6 h post PCC. For counting fragments, 10 min staining with Geimsa, an inexpensive dye, and a further 1 h scoring of ~ 50 spreads under the microscope is sufficient.

2.7 Detection in G_0-PCC with Centromere-FISH

Dicentrics in metaphase can be identified by the presence of constriction at the centromere where two sister chromatids are attached in G_0-PCC chromosomes without any constriction or presence of sister chromatids. Hence, for dicentric detection, fluorescent in situ hybridization using centromere-specific probes is performed after slide preparation on G_0-PCC spreads [5] (Fig. 6). Pan-centromere probes are applied and give fluorescence wherever the centromere is present on lymphocyte chromosomes. Chromosomes with two centromeres are counted as dicentrics and without centromeres are counted as fragments. Dicentric counting provides radiation specificity to the estimate.

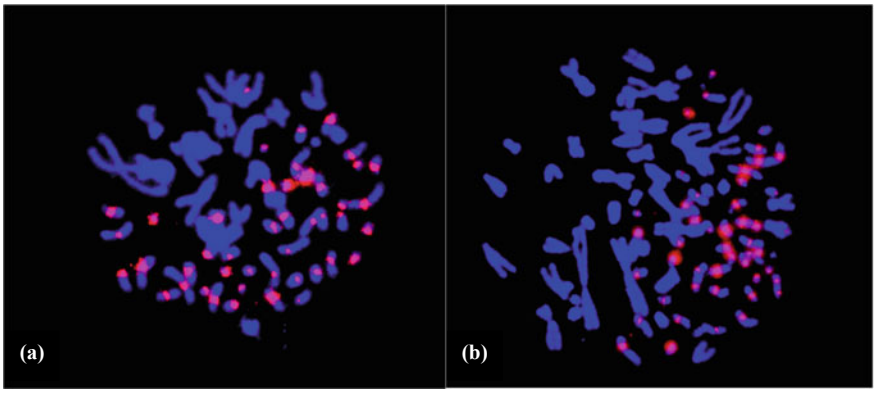

Fig. 6 G_0-PCC spreads are stained with centromere specific probes showing red fluorescence with counterstain of DAPI a blue fluorescent dye, **a** shows un-aberrated cell in terms of dicentrics as each chromosome is having only one centromere. **b** With the same staining shows a dicentric chromosome with two distinct centromeres

2.8 Translocation Detection in G_0-PCC with Whole Chromosome Painting FISH

Fluorescent in situ hybridization using whole chromosome paints provides different colors to different chromosomes (Fig. 7). This helps in visualization of exchange between two different chromosomes, i.e., translocations also chromosomal origin of a break/fragment. The frequency of fragments and translocation together follows a linear quadratic dose response and provides an excellent method for rapid dose estimation [2]. Similar to metaphases, whole chromosome painting of the desired number of chromosomes can be performed or it can be performed for all the chromosomes.

2.9 Multicolor BAND-FISH: Identifying Region-Specific Rearrangements

Multicolor band can be applied to G_0-PCC chromosomes (Fig. 8) and may be analyzed for inter as well as intrachromosomal aberrations. The latter is more useful for identifying high LET components in exposed samples. In case of high LET exposure, aberrations are high and a big proportion of aberrated cells may not reach metaphase. Hence, G_0-PCC may enhance sensitivity to detect high LET exposure to any sample compared to the conventional method.

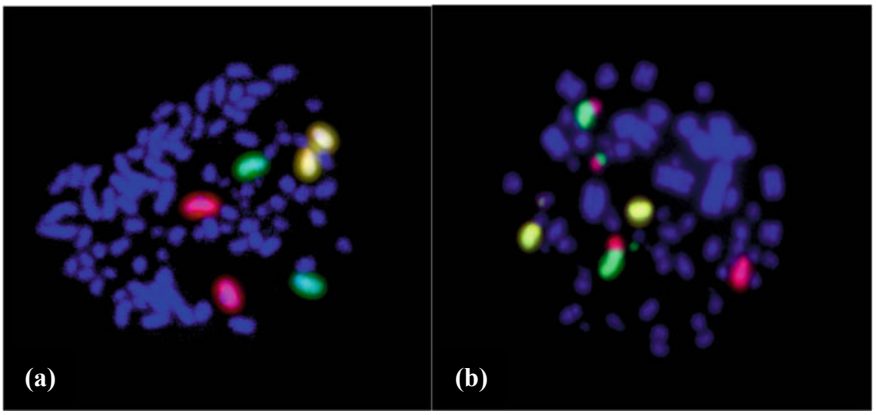

Fig. 7 Representative images of chromosomal spreads after G_0-PCC post whole chromosome painting FISH. Chromosomes 1, 2, and 4 are seen as red, green, and yellow signals, respectively. Spread from a normal cell is seen having a pair of each painted chromosome (**a**), whereas translocations between chromosomes 1 and 2, and fragment of chromosome two can be seen distinctly in a damaged cell (**b**)

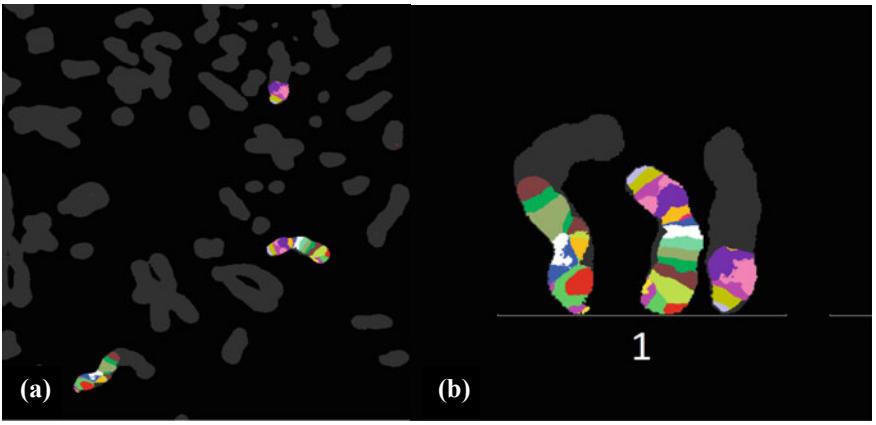

Fig. 8 A G_0-PCC spread with one intact chromosome and another homologous chromosome interchanged with a non-banded chromosome. The region of miss-joining can be identified

2.10 Exciting Progress in Fluorescence In Situ Hybridization (FISH) Assay

Radiation-induced chromosomal changes, such as dicentrics, rings, and fragments, exhibit a decay rate with a half-life ($T_{1/2}$) ranging from 1 to 3 years, represents unstable chromosomal aberrations. This characteristic decay presents a significant challenge in accurately assessing dose for past radiation exposures. To overcome this

problem, scoring stable chromosomal exchanges, such as translocations (reciprocal), has emerged as a valuable marker.

Conventionally, translocations have been scored using the banding technique, which is known for being tedious and time-consuming. Even with automation, the quality of banding preparations needs to be exceptionally high. However, recent advancements in the field have introduced whole chromosome-specific libraries, enabling the application of the fluorescence in situ hybridization (FISH) technique for painting individual chromosomes. FISH involves labeling specific DNA sequences with fluorescent probes, allowing for the visualization of chromosomal rearrangements at higher resolution.

Translocations involving exchanges between painted chromosomes and counterstained (unpainted) chromosomes can be visualized as bicolored structures using FISH. This technique not only simplifies the identification of translocations but also increases sensitivity by enabling the detection of events that may go unnoticed using conventional banding methods. FISH has shown great potential as a biological dosimeter due to its ability to accurately identify and quantify radiation-induced translocations.

In recent years, many laboratories have explored the application of the FISH assay for translocations in radiation dosimetry. Researchers have focused on optimizing the technique and developing standardized protocols to ensure reliable and reproducible results. The use of FISH as a biological dosimetry technique offers advantages such as higher sensitivity, faster analysis, and improved accuracy compared to traditional methods.

2.10.1 Interphase FISH (I-FISH)

Interphase fluorescence in situ hybridization (I-FISH) is a technique used in biodosimetry and other clinical investigations, to assess radiation-induced (or by any other agent) genetic damage/changes. It allows the visualization and quantification of chromosomal abnormalities, such as translocations, deletions, and fragmentations, in the interphase nuclei of cells (Fig. 9) [6]. Cell culturing is not required here. By labeling specific chromosomes or sequences of DNA with fluorescent probes, I-FISH enables the detection of genetic alterations, providing valuable data on radiation exposure levels. This technique is widely utilized in cancer and radiation biology, and biodosimetry research to evaluate the biological effects of radiation exposure.

2.10.2 Painting of Whole Chromosome and Centromere by FISH

Translocation detection using whole chromosome paint probes has revolutionized biodosimetry by enabling precise identification and quantification of chromosomal translocations. With advanced imaging techniques (Fig. 10), these probes can detect translocations with high sensitivity, reaching minimum detection limits in the kilobase range. By fluorescently labeling entire chromosomes, translocations

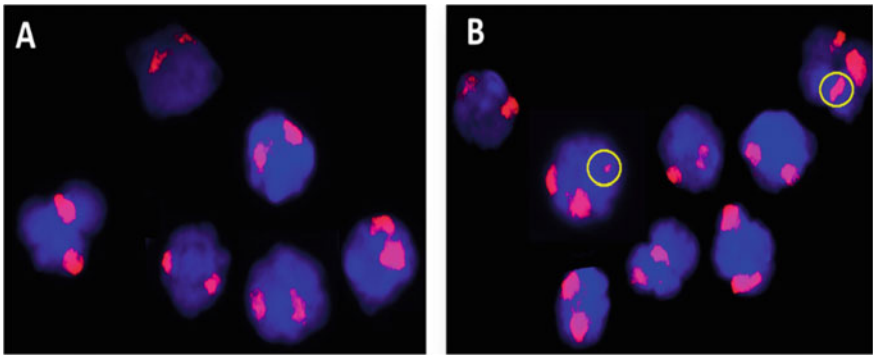

Fig. 9 Representative interphase-lymphocytes, processed with one color FISH, wherein chromosome pair-one is painted with red fluorophore. **A** Control interphase-lymphocyte with NO aberration and **B** Irradiated (4 Gy) interphase-lymphocyte with chromosomal breaks (circled in yellow)

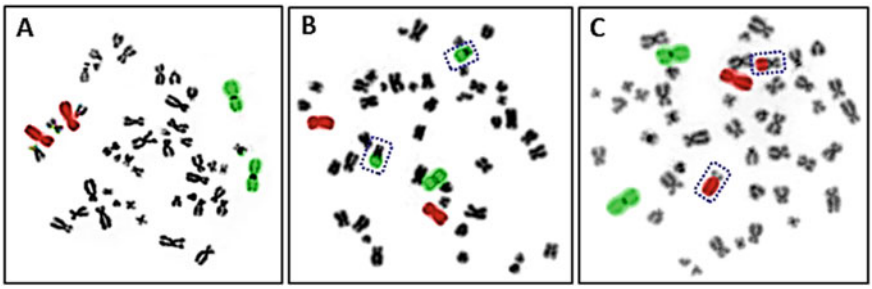

Fig. 10 Metaphase spreads, processed with two color FISH, wherein chromosome pairs 1st and 2nd are painted with green and red fluorophores respectively. **A** Control metaphases, **B** Metaphases with one inter-chromosomal translocation between green and black chromosomes and **C** Metaphases with one inter-chromosomal translocation between red and black chromosomes

involving exchanges between painted and unpainted (counter stained) chromosomes can be visualized and accurately assessed. This approach enhances our ability to quantify radiation exposure, providing valuable data for biodosimetry with improved resolution at the kilobase level.

Centromere-FISH (Fig. 11) is used for the precise detection of dicentric chromosomes. By targeting centromeric regions with fluorescent probes, centromere-FISH enhances the accuracy of dicentric identification in biodosimetry, providing valuable information about radiation exposure and genetic damage.

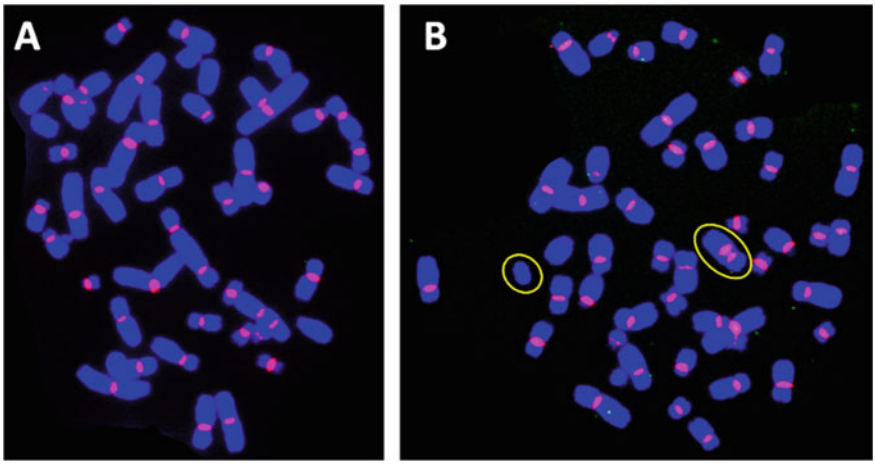

Fig. 11 Metaphase spreads, processed with pancentromere FISH, wherein the centromeres of all the chromosomes is painted with red fluorophores **A** Control metaphases with NO chromosomal aberration and **B** Metaphase with one dicentric chromosome and an acentric fragment; centromeres are closely placed in dicentric, difficult to detect by conventional Giemsa staining.

2.10.3 Multiplex FISH and Spectral Karyotyping

Multiplex fluorescence in situ hybridization (mFISH) is an advanced technique that employs a set of fluorescent probes to simultaneously hybridize with all 24 types of chromosomes (Fig. 12), each labeled with a distinct color. mFISH hybridized metaphases can be processed for spectral karyotyping (SKY) that assigns distinct colors to homologous pairs of chromosomes. This comprehensive labeling enables the detection and quantification of various types of chromosomal changes or rearrangements in one metaphase. By visually distinguishing each chromosome, mFISH offers a high-resolution view of complex genomic alterations, including translocations, deletions, duplications, and inversions. This method has been extensively validated and utilized in cytogenetics research and clinical diagnostics, providing valuable insights into genetic abnormalities. mFISH, can not detect intrachromosomal changes.

2.10.4 Multiplex BAND-FISH and Intrachromosomal Rearrangements

Multiplex BAND-FISH is an innovative technique which offers chromosome banding to detect and quantify intrachromosomal rearrangements. By using distinct colors to label different regions of the same chromosomes. mBAND-FISH (Fig. 13) enables precise visualization and identification of intrachromosomal rearrangements. These rearrangements are predominantly induced by high linear energy transfer (LET) radiation. This method has been applied successfully to study radiation-induced

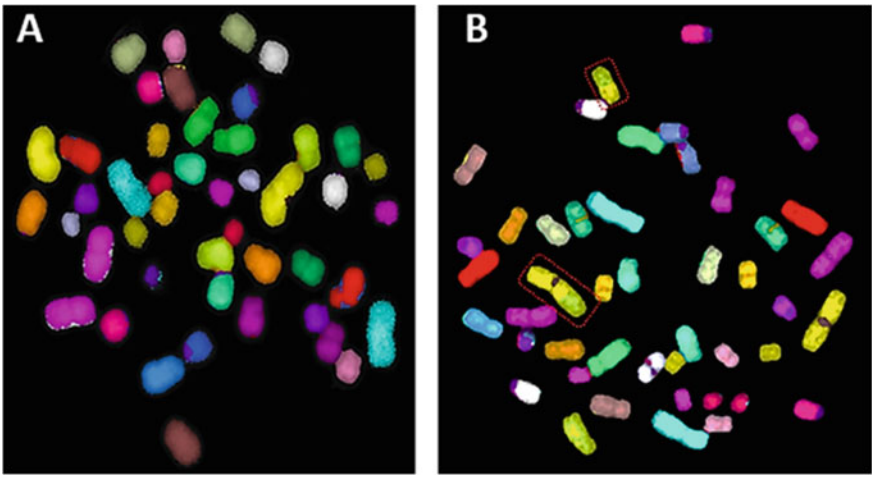

Fig. 12 Representative metaphase spreads, processed with multiplex FISH, wherein all 24 types of chromosomes are painted with different colors. **A** Control metaphases with NO chromosomal aberration and **B** metaphases with one inter-chromosomal translocation between yellow and light green chromosomes (highlighted in red dotted square)

genomic alterations and has proven valuable in biodosimetry research. It enhances our understanding of the complex molecular changes within chromosomes and provides insights into radiation-induced genomic instability.

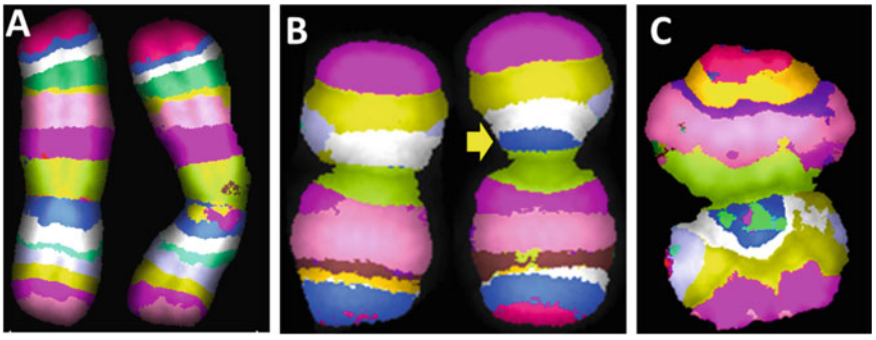

Fig. 13 Representative chromosome pairs, processed with multiplex-BAND-FISH, wherein different region of the same chromosome is painted with different colors. **A** Control chromosome pair with NO alteration in banding pattern, **B** chromosome pair with one interstitial deletion (blue-band) and **C** a chromosome with complex rearrangements (banding pattern is completely lost). These cells are exposed to Am-α

2.10.5 Phospho-γH2AX, DSB-Repair Protein-A Rapid Biodosimetry Tool

Phospho-γH2AX (phosphorylated histone H2AX) has emerged as a rapid biodosimetry tool due to its association with DNA double-strand breaks (DSBs) and its crucial role in DSB repair [7, 8]. Upon induction of DSBs, H2AX is phosphorylated at the sites of DNA damage, resulting in the formation of γH2AX foci. These foci serve as sensitive and specific markers for assessing the extent of radiation-induced DNA damage.

The detection of phospho-γH2AX foci can be achieved using various techniques, such as immunofluorescence staining followed by fluorescence microscopy or flow cytometry (Fig. 14). By quantifying the number and distribution of γH2AX foci in cells, it is possible to estimate the radiation dose received and assess the severity of the individual.

The advantages of phospho-γH2AX as a biodosimetry tool lies in its rapidity and sensitivity. It allows for the detection of DNA damage within a short timeframe after exposure, making it useful for immediate assessment. Furthermore, the sensitivity of phospho-γH2AX to low-dose radiation enables its application in scenarios involving diagnostic exposures or accidental radiation incidents with relatively low radiation doses.

Overall, phospho-γH2AX has proven to be a valuable tool in biodosimetry, providing a rapid and reliable assessment of radiation-induced DNA damage. Its continued development and optimization hold promise for enhancing our ability to accurately estimate radiation doses and evaluate potential health risks associated with radiation exposure.

With the DSB repair, γH2AX signal fades. To facilitate the transportation of blood samples to analyzing laboratories, efforts are underway to develop protocols that can arrest the biological processes soon after sample collection using various fixing methods and inhibitors. This step aims to preserve the integrity of the samples and minimize any changes that may occur during transport.

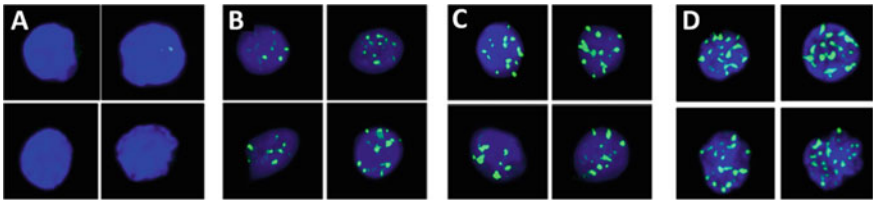

Fig. 14 Lymphocytes showing an increasing number of phospho-γH2AX foci in the nucleus with increasing doses **A** 0 Gy, **B** 0.5 Gy, **C** 1.0 Gy, and **D** 2.0 Gy, after 1 h of incubation, post irradiation)

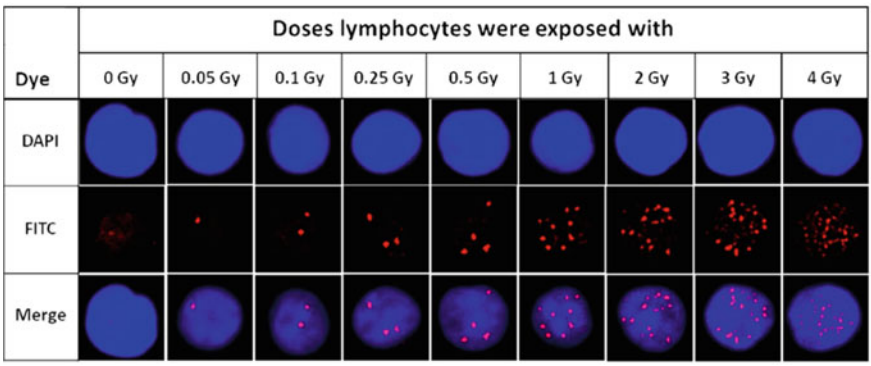

Fig. 15 Lymphocytes showing an increasing number of phospho-53BP1 foci in the nucleus with increasing doses (0.05–2.0 Gy after 1 h and 3 and 4 Gy after 4 h of incubation, post irradiation)

2.10.6 53BP1, DSB-Repair Protein-A Rapid Biodosimetry Tool

Phosphorylated-53BP1 is an additional proteomic marker, along with γH2AX, used for rapid biodosimetry as an indicator of DNA double-strand breaks (Fig. 15). Both phosphorylated histone γH2AX and p53 binding protein-1 (53BP1) are widely accepted protein markers of foci induced by ionizing radiation. When DSBs occur, histone H2AX molecules within chromatin domains containing DSBs undergo phosphorylation. Subsequently, 53BP1, a downstream protein, is recruited to the sites of induced DSBs, undergo phosphorylation and serve as a marker for DSBs.

Currently, the most sensitive and specific method for analyzing DSBs involves enumerating small foci, such as γH2AX and 53BP1, and their colocalization, that form at the locations of DSBs. These foci provide valuable information for assessing and quantifying radiation-induced damage at the molecular level.

2.10.7 Pseudo-Pelger Huët (PHA) Neutrophil—A New Permanent Radiation Biomarker

Pseudo Pelger Huet Anomaly (PHA) is a newly discovered marker that indicates radiation exposure in circulating blood neutrophils within the body [9, 10]. Unlike normal neutrophils, which have 3–4 lobed nuclei (Fig. 16), PHA is characterized by nuclei that are round, oval, bean-shaped, or symmetric bilobed, and connected by a thin mitotic bridge. The anomaly is caused by a mutation in the lamin-B receptor (LBR) gene, leading to reduced LBR expression.

PHA is specific to in vivo exposure, occurring within the bone marrow, and cannot be induced in cells outside the body (ex vivo). In a study analyzing archived blood samples from the 1958 Y-12 criticality accident in Oak Ridge, Tennessee, researchers found that the Pseudo Pelger Huet morphology appeared in the circulating blood within 12 h after radiation exposure, suggesting its potential as an indicator of acute

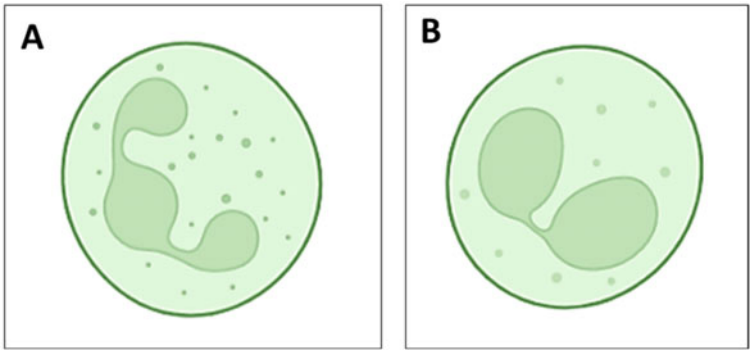

Fig. 16 **A** Illustrative representation of a normal/healthy neutrophil with a multilobed nucleus and **B** a pseudo-Pelger Huët (PHA) neutrophil with bilobed (goggle-shaped) nucleus

radiation exposure. In one case from the same accident, the PHA marker persisted for up to 16 years, serving as a stable and permanent mutation marker induced by radiation and providing retrospective dosimetry capabilities.

To establish a dose–response curve for PHA, researchers have analyzed circulating blood neutrophils from two individuals exposed to radiation. However, creating this curve is a challenging task as it requires the involvement of radiation-exposed human volunteers for in vivo exposure. Ongoing worldwide research aims to further investigate and validate PHA as a reliable biodosimeter for protracted and past radiation exposures.

3 Case Studies

Biodosimetry assays play a major role in assessing and ascertaining personnel dose for regulatory needs and triage input for medical management of radiological incidents. In total, about 1500 cases are resolved by the biodosimetry lab of BARC till 2023. Most of the cases are related to regulatory requirements where the personnel dosimetry by physical personnel dosimeter has indicated excess exposure amounting to > 100 mSv in a monitoring period. Few cases are related to internal contamination, badge contamination, and localized contaminations. These cases were resolved with inputs from both Biodosimetry and internal dosimetry. A few radiological incidents involving radiography sources were also handled.

3.1 Regulatory Needs

Biodosimetry assay can serve as an excellent indicator of radiation exposure when whole-body doses are more than 100 mSv [11]. The background incidence of dicentric is about 1 in 1000–2000 cells scored in normal unexposed individuals. It is known that environmental and lifestyle agents such as smoking, alcohol consumption, exposure to pollutants, pesticides, etc., are not affecting the dicentric frequency significantly. With aging, it is found to increase to the level of about 1 in 1000 compared to 1 in 2000 in young individuals. The only confounder is medical radiation exposure, which is again due to radiation but not due to occupational exposure. In such a situation, recording the recent history of medical radiation exposure such as fluoroscopy, multiple CT scans, etc., is needed.

In most cases, occupational excess exposures are due to mismanagement of personnel dosimeters. Lost badges in hot areas, contaminated badges, reverse loading, wearing of badges above the lead apron, improper storage of badges such as tool kits while in field use, etc., can lead to erroneous dose recording while the radiation worker has not received any dose.

3.2 Radiological Incidents—Suspected/Reportable

Many reportable incidents leading to suspicious scenarios lead to large physical uncertainties in dose estimates. Even if physical personnel dosimeters are available, their accuracy is questionable. Most of such incidents involve partial or non-uniform exposure. A narrow geometry beam of radiation field can result only in the exposure of a dosimeter or it may so happen that the dosimeter may get masked off. Exposure from the backside of the person can shield the dosimeter up to a factor of 2–3 leading to underestimation. The exact duration of exposure may not be available and the worker may not be using any personnel dosimeter. Many such scenarios pose serious challenges while estimating the dose through physical methods. In one of the incidents, a driver transporting radionuclides has reported possible mishandling by him. His personnel dosimeter has shown 63 mSv. However, since it was an incident report, biodosimetry was conducted, which revealed a dose of 480 mSv. This was further analyzed and found to be due to possible spillage or contamination which has led to large personnel dose but underestimated physical dose.

3.3 Small-Scale Radiological Incident in Public Domain

In 2010, a gamma chamber containing about 6 Ci of ^{60}Co source still active and intact in the shielded condition was sold to a scrap vendor by a university. The scrap vendors opened the device to separate out and salvage raw materials such as lead as scrap

products. In the process, a few vendors found the source pencils intact. Without proper information about the radioactive source, a few pencils were broke open, which led to the spread of radioactive dust and contamination of structural materials and personal items. One person who is suspected of ingesting some radioactive material in the process of breaking the source has succumbed due to internal injury. The autopsy has shown large patches of radiation damage in the digestive systems. The exposure has lasted for several days to weeks. Correction factors for modification of biological damage were applied to estimate inferred doses.

Biodosimetry was conducted on all personnel involved in this scenario. The doses were reported to IAEA as radiological incident. In such scenarios, biodosimetry is the only method available to report the personnel dose. The estimation has also helped the medical fraternity to prepare itself for the prognosis. All the victims except for the one with internal contamination have survived.

4 Multiparametric Approach for Biodosimetry of Complex Scenarios

No single biodosimetry assay can suffice to address many complex scenarios of radiation exposure. It becomes necessary to perform multiple assays to meet the challenges [3]. Figure 17 outlines the approach of multi-parametric analysis in various scenarios [3, 12]. Few of the assays are still in the development stage but offer themselves as excellent tools in certain scenarios.

The described assays help to conclude and ascertain the genuineness of most excess exposure scenarios. These assays are helpful in the following ways:

- To confirm or reject the findings of physical dosimeters and to distinguish between genuine and non-genuine exposures.
- To detect a suspected exposure when there is no information from physical dosimeters, such as in the case of a person who is not routinely monitored or a radiation worker not wearing a badge.
- To provide reassurance to those who are false positive on physical dosimeters which got exposed while being not worn; or maliciously irradiated.
- To detect the average dose to the body in the case of very non-uniform exposures. In such situations, the dosimeters may indicate a very high or low dose depending upon the irradiation geometry.
- To distinguish between protracted and acute exposures in accidents. DCA provides a purely biological response taking into consideration the duration of exposure and accounting for the possible repair of radiation damage.
- To detect the dose to the exposed part of the body and the fraction of the body exposed, in accidents involving inhomogeneous exposure (Partial-body, or localized). Dispersion analysis of the chromosome aberration data indicates the deviation from a Poisson distribution, which in turn is a measure of the non-uniformity of exposure.

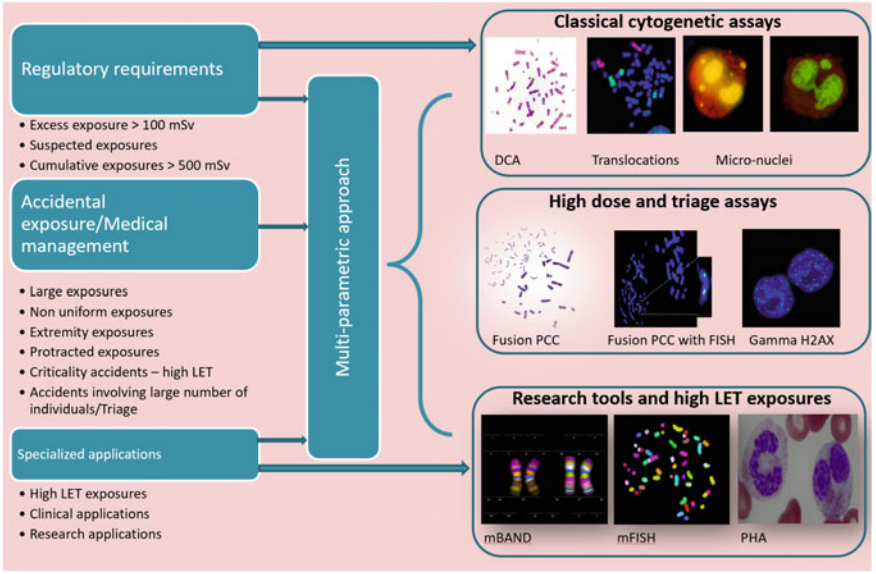

Fig. 17 Flow chart of multi-parametric approach for various scenarios of excess exposure analysis or research applications

- To assist the triage of victims in accidents involving a large number of exposed individuals. In the medical management of radiation accidents, DCA can serve as a reliable prognostic indicator.
- To address complex scenarios of excess exposure, multi-parametric approach with a combination of assays can be employed.

Besides their applications in biological dose assessment, these assays are also useful to estimate radio-sensitivity prior to treatment of cancer, plan in advance for hypersensitivity, measure bone marrow doses in past therapeutic exposures needing repeated administration of nuclear medicine and measure body burden. Such clinical applications are currently gaining importance and are expected to help individualization of treatment protocols.

5 Conclusion

Biological retrospective dosimetry, crucial in radiological emergency scenarios, is important for accurately determining and estimating radiation exposure levels. Biodosimetry assays stand as the sole methods available for discerning biological doses in cases of suspected over-exposures, playing a vital role not only in emergency response, but also in medical management and triage. The complexity of radiological emergencies demands a strategic approach to effectively allocate medical resources,

wherein biodosimetry proves indispensable. In such situations, the challenge lies in distinguishing between those requiring specialized medical attention and the larger population with either no exposure or clinically insignificant doses.

A multi-parametric approach is imperative, involving the selection of a set of biological indicators tailored to specific exposure scenarios. Advanced cytogenetic and molecular methods have significantly contributed to overcoming the challenges inherent in assessing biological doses. These sophisticated techniques enhance the precision and reliability of biodosimetry, facilitating a comprehensive understanding of radiation-induced effects at the cellular and molecular levels. By leveraging a diverse array of biological indicators, ranging from cytogenetic markers to molecular signatures, biological retrospective dosimetry empowers healthcare professionals to make informed decisions regarding medical intervention and resource allocation in radiological emergencies.

References

1. Bauchinger M, Braselmann H, Kulka U et al (1996) Detection of translocations in human chromosomes exposed to ionizing radiation using fluorescence in situ hybridization (FISH). Int J Radiat Biol 70(4):457–466
2. Bhatnagar Y, Srivastava P, Venkatachalam P et al (2019) Translocation frequency estimation from biodosimetry: a review of recent advances. Mutat Res 781:126–138
3. Yadav U, Bhat NN, Shirsath KB, Mungse US, Sapra BK (2020) Multifaceted applications of pre-mature chromosome condensation in radiation biodosimetry. Int J Radiat Biol 96(10):1274–1280. https://doi.org/10.1080/09553002.2020.1798545
4. Lloyd DC, Edwards AA, Moquet JE et al (2019) The role of cytogenetics in radiation protection: a 40-year review. Radiat Prot Dosim 183(1–2):176–184
5. Yadav U, Bhat NN, Shirsaath KB, Mungse US, Sapra BK (2021) Refined premature chromosome condensation (G_0-PCC) with cryo-preserved mitotic cells for rapid radiation biodosimetry. Sci Rep 11(1):1–11
6. Puig R, Barrios L, Caballín MR et al (2019) Fluorescence in situ hybridization (FISH) analysis of chromosome aberrations in lymphocytes for biological dosimetry: a review. Front Genet 10:382
7. Chaurasia RK, Bhat NN, Gaur N, Shirsath KB, Desai UN, Sapra BK (2021) Establishment and multiparametric-cytogenetic validation of ^{60}Co-gamma-ray induced, phospho-gamma-H2AX calibration curve for rapid biodosimetry and triage management during radiological emergencies. Mutat Res/Genet Toxicol Environ Mutagen 866:503354
8. Chaurasia RK, Shirsath KB, Desai UN, Bhat NN, Sapra BK (2022) Establishment of in vitro calibration curve for ^{60}Co-γ-rays induced phospho-53BP1 foci, rapid biodosimetry and initial triage, and comparative evaluations with γH2AX and cytogenetic assays. Front Public Health 10:845200
9. Goans RE, Iddins CJ, Christensen D, Wiley A, Dainiak N (2015) Appearance of pseudo-Pelger Huet anomaly after accidental exposure to ionizing radiation in vivo. Health Phys 108(3):303–307
10. Hayes JM, Olson JD, Chino Y, Bourland JD, Cline JM, Johnson TE (2022) Pseudo Pelger-Huët anomalies as potential biomarkers for acute exposure radiation dose in rhesus macaques (*Macaca mulatta*). Int J Radiat Biol 98(5):913–923
11. Vijayalakshmi J, Chaurasia RK, Srinivas KS, Vijayalakshmi K, Paul SF, Bhat NN, Sapra BK (2023) Establishment of ex vivo calibration curve for X-ray induced "dicentric + ring"

and micronuclei in human peripheral lymphocytes for biodosimetry during radiological emergencies, and validation with dose blinded samples. Heliyon 9(6)
12. Chaurasia RK, Shirsath KB, Sapra BK (2021) Protocol for one-step selective lysis of red blood cells and platelets with long-term preservation of white blood cells (human) at ambient temperature. STAR Protoc 2(4):100834

Internal Dosimetry

Introduction to Internal Dosimetry

Soumitra Panda, Sushanta Halder, Minal Y. Nadar, and Hemant Kumar Patni

1 Introduction

Internal dosimetry refers to dose assessment due to the internal radioactive contamination inside any living being. Since internal radiation protection and medical applications are primarily confined to human body, we will limit our scope to internal contamination of human body. Unlike external dose, caused by radiation sources present outside the body, such as X-rays, gamma, beta or neutrons emitting radionuclides, internal dose is also effective due to alpha, beta or gamma particles emitting radioactive material present inside the person's body.

External exposure can be controlled by limiting time duration of exposure, increasing distance from the radiation source and using shielding to reduce exposure as shown in Fig. 1. External exposure also ceases when the worker leaves the working area or if source is removed. It is measured using personal dosimeters like direct reading dosimeter, thermos luminescence dosimeter, optically stimulated luminescence dosimeters, etc.

In contrast to external exposure, internal exposure presents a unique challenge as radioactive sources keep on continuously irradiating tissues and organs until it is present in the body. To mitigate internal exposure risks at the workplace, several measures are commonly employed. First, strict adherence to safety protocols and procedures is followed while handling radioactive material. Sources are handled in glove boxes or in fume hoods depending upon the activity level. Workers have to wear appropriate personal protective equipment (PPE) [1] to minimize the risk of contact with radioactive material as shown in Fig. 2. Furthermore, workplaces are well-ventilated with proper containment facilities to reduce the concentration of airborne radioactive substances [2]. Additionally, workers are not allowed to eat in

S. Panda (✉) · S. Halder · M. Y. Nadar · H. K. Patni
Internal Dosimetry Section, Radiation Safety Systems Division, Health, Safety and Environment Group, Bhabha Atomic Research Centre, Trombay, Mumbai 400 085, India
e-mail: spanda_ta@barc.gov.in

D. K. Aswal (ed.), *Handbook on Radiation Environment, Volume 2*,
https://doi.org/10.1007/978-981-97-2799-5_15

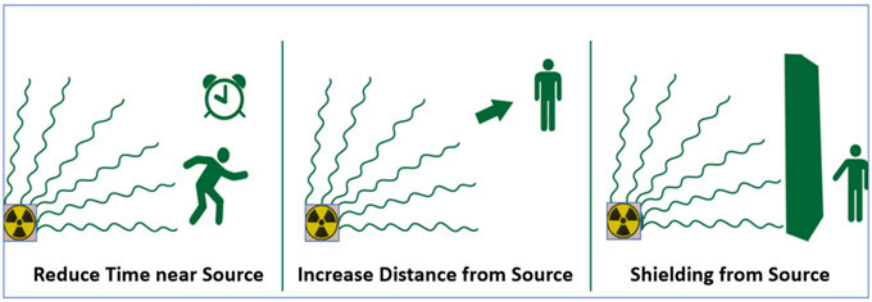

Fig. 1 Protection against external exposure using methods of time, distance and shielding

radioactive working areas. These work practices help in preventing and minimizing accidental internal contamination. Despite all these protective measures, there are still chances, when radioactivity may enter inside the body. Internal exposure can only be inferred through measurement of radioactivity in the whole body or in some specific organs, blood or through excreted activity in urine and faeces or through area monitoring. Therefore, regular workplace monitoring and personal monitoring are carried out to detect probable internal contamination of radiation workers.

Internal exposure to radioactive materials can occur in various scenarios, depending on the source of radiation and the pathway through which the radioactive substances can enter body [3]. Some common scenarios of internal exposure are shown in Fig. 3 and discussed here briefly. The most prominent places of internal contamination are nuclear power plants, research reactors or nuclear fuel processing facilities. In these nuclear industry setups, exposure can occur when radioactive particles are released during nuclear operations and other incidents and protective

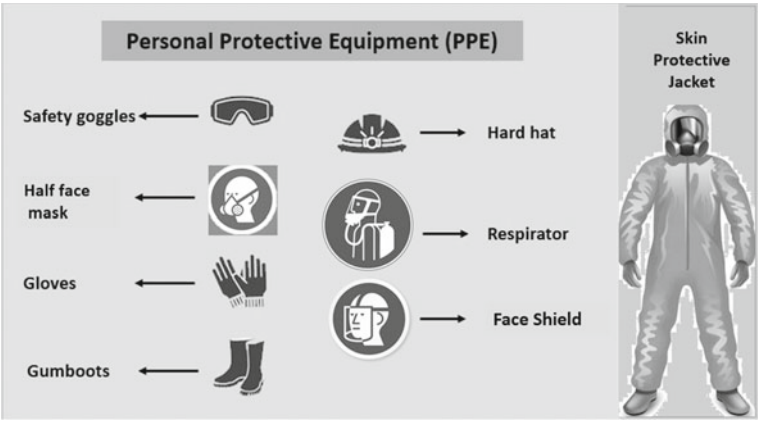

Fig. 2 Protection against internal exposure using personal protective equipment like masks and respirators

methods are not fully effective. Another internal exposure scenario is public exposure due to radiological accident [4]. In the unfortunate event of a radiological accident or nuclear incident[4], such as a nuclear reactor meltdown or a transportation accident involving radioactive materials, individuals in the vicinity may be internally exposed to radioactive particles dispersed in the air or deposited on soil, water, etc. In the context of medical procedures, healthcare workers who manage or administer radioactive isotopes, such as those employed in cancer treatments and diagnostic techniques like nuclear medicine scans [5], may be susceptible to internal exposure if they do not adhere to the necessary safety precautions. On the other hand, patients undergoing medical examinations in molecular imaging techniques and receiving treatment through nuclear medicine intentionally undergo internal exposure for their own medical benefit. Another internal exposure scenario is related to radioactive-contaminated area. Workers involved in the clean-up and remediation of sites contaminated by radioactive materials [6], such as old nuclear testing sites or decommissioned facilities, may face exposure risk if precautions are not taken. Workers in mining industries, particularly in the extraction of radioactive minerals like uranium [7, 8], can be exposed to radioactive dust or gases, leading to potential internal exposure. Radon is a naturally occurring radioactive gas that can be found in buildings, especially in underground spaces or areas with high concentrations of certain minerals [9]. Prolonged exposure to radon can lead to inhalation. Radon being inert gas does not interact with lungs but its daughter products can be absorbed from lungs leading to significant internal exposure to general public. Insignificant internal exposure for general public can also occur due to naturally occurring radionuclides like K-40, U, and Th through food and water.

To protect against internal exposure in various scenarios, strict adherence to safety protocols, proper use of PPE and appropriate training and education on radiation safety are essential. Regular monitoring and assessment of workplace conditions and individual bioassay can help detect internal exposure at an early stage and allow for prompt medical intervention if required. By implementing these mitigation strategies, workplaces can strive to maintain a safe environment and safeguard the health and well-being of their employees.

2 Routes of Intake

Radioactive source can enter through various routes into human body. Each route presents different internal contamination patterns within the human body. The quantity of radioactivity entering into body is defined as intake. There are different routes of intake, namely ingestion, inhalation, absorption and wounds. When a person consumes food or drinks that contain radioactive materials, they can be exposed internally. This is known as ingestion. Radioactive substances present in the ingested items can enter the body through the digestive system. Inhalation of radioactive materials occurs when a person breathes in air contaminated with radioactive particles or gases. These particles can enter the respiratory system and become internal sources

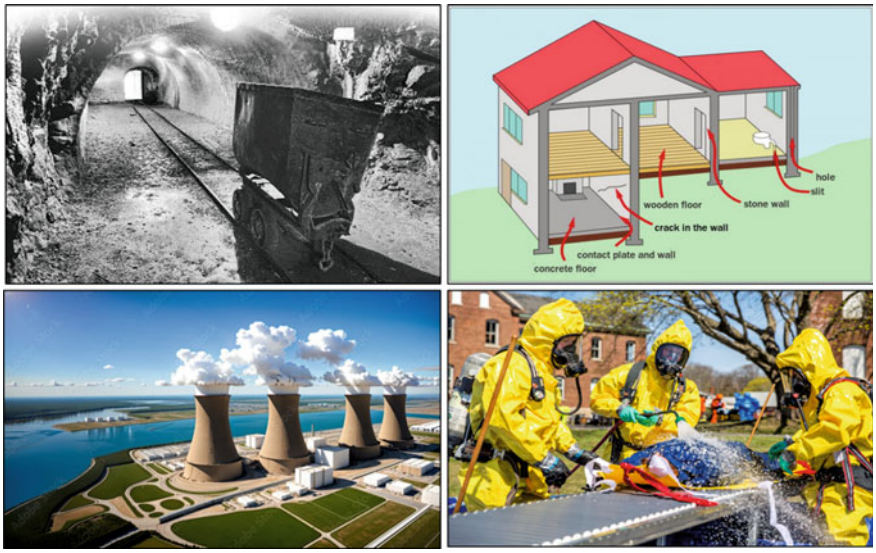

Fig. 3 Various scenarios of internal radiation exposure including mines, radon in enclosed space, decontamination and nuclear accident

of radiation. Radioactive materials can be absorbed through intact skin, a process known as absorption. If the skin comes into contact with radioactive substances, they may penetrate through the skin layers and enter the body, contributing to internal exposure. In cases where the skin is damaged, such as through wounds or punctures, radioactive materials can enter the body directly through the compromised area. This route bypasses the skin's protective barrier and allows for potential internal contamination.

Once radioactive materials enter the body, the individual remains exposed to radiation until those materials are either excreted through biological processes (such as exhalation or excreta) or naturally decayed through the radioactive decay process. Figure 4 illustrates the different routes of internal contamination within the human body, highlighting how radioactive materials can enter and distribute within various organs and tissues. Understanding these routes of internal contamination is essential for assessing and managing radiation exposure risks and implementing appropriate protective measures.

3 Biokinetic and Dosimetric Models

Once radioactive material enters into body it can remain at the site of entry, redistribute or be eliminated from body. For the purpose of dose estimation, we require the information of time for which radioactive material resides in the body and how

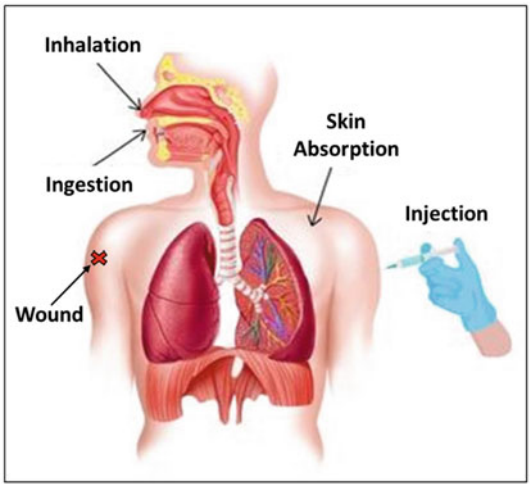

Fig. 4 Routes of intake including inhalation, ingestion, absorption through intact skin and wound

much energy deposition would occur into various parts of the body. Biokinetic and doismetric models cover both these aspects.

3.1 Biokinetic Models

Biokinetic models describe the time-dependent transport and transfer of radionuclides within the body and the excretion from the human body. This knowledge is essential for the interpretation of measurement of activity in the organ or whole body or in excreta to estimate intake and internal dose. Mathematically, biokinetic models are divided into units called compartments, where each compartment can be an organ, collection of organs or whole body. Sometimes, an organ can be represented by more than one compartment for mathematical simplicity.

In the computational scheme given by the International Commission on Radiological Protection (ICRP), the metabolic behaviour of radionuclides in the human body is described into three types of biokinetic models. The first type is a generic respiratory tract model that predicts the deposition and clearance as well as the translocation of inhaled material in the respiratory tract. The second type is a generic gastrointestinal tract model with the element-specific gastrointestinal absorption fractions (f_A value) and absorption of radionuclides from small intestine to blood. The third types are the element-specific systemic models that describe the time-dependent distribution and excretion of radioisotope of an element after its absorption or injection into blood.

The systemic models describe the behaviour of radionuclides after they have been absorbed into the blood. By this stage, the radionuclides are in chemical forms that are soluble in body fluids, and which are certainly different from the chemical forms that were inhaled or ingested. The values of parameters in the systemic models are

therefore usually assumed to depend on the element of which the radionuclide is an isotope, but not on the chemical form of the material that originally entered the body.

The systemic models are developed using some combination of four data types [8]. The data which is from the direct information in humans based on quantitative measurements of the element in human subjects is the most preferred and reliable data for model formation. The second data type is based on the behaviour of the chemically similar element in human subjects, e.g. Ca for Sr, etc. Next data is obtained from the study of behaviour of the element in non-human species, e.g. baboons, dogs, etc. The last data is based on the behaviour of chemically similar elements in non-human species.

The data used to build these models come mainly from animal experiments and/or from follow-ups of occupational exposure and patients of nuclear medicine. Their diversity allows the construction of several types of models. Some of them describe the entry of radionuclides into the body and then, after absorption, other (systemic) models describe the behaviour of radionuclides in the blood and in the organs.

These models were initially developed to describe the most common radionuclides found in the nuclear workplaces. Since the Chernobyl and other nuclear accidents, the numbers of radionuclides considered for radiation protection have considerably increased. Also, physiologically more realistic models have been developed which now describe the deposition, retention, recycling and excretion of radionuclides not only in workers but also in members of the public, including children at different ages, embryos and foetuses. The latest series of ICRP documents, dedicated to occupational intakes of radionuclides (OIR), now provides models for contamination by most elements from the periodic table, except for some noble gases [8–12]. Figure 5 shows a generalized biokinetic model including intake and excretion [4].

Figure 5 shows the respiratory tract and gastrointestinal tract, wound and skin as major entry points for radionuclides inside the body. From deposition sites, a small amount of activity gets absorbed in the blood. The activity absorbed into blood is known as uptake. Activity reaching the transfer compartment which is body fluids is known as systemic activity [1]. Transfer compartment considers the translocation of radioactive material through the blood to other organs or tissues. The activity then undergoes various complex transfers. It results in distribution in various organs and excretion of activity through sweat, urine and faeces. Some radionuclides undergo homogeneous distribution of activity in the body such as tritium, whereas some radionuclides such as ^{239}Pu and actinides get deposited in the lungs after inhalation and remain in lungs for a longer duration. The systemic models used to describe the behaviour of radionuclides absorbed into blood, range in complexity from very simple models that assume uniform whole-body distribution such as hydrogen and caesium to multicompartment recycling models that take account of movement within and between body organs and tissues such as strontium, lead, uranium and plutonium.

Urinary excretion consists of removal of material from plasma and extracellular fluid in urine. Faecal excretion has a contribution from systemic components via gastrointestinal tract and direct component of unabsorbed part through gastrointestinal tract.

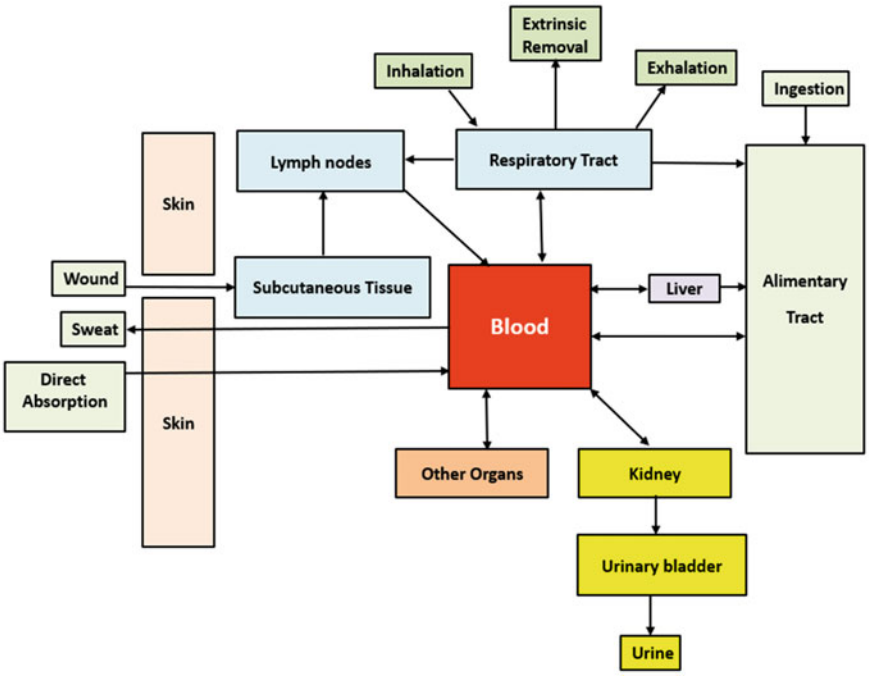

Fig. 5 A generalized biokinetic model having respiratory tract, alimentary tract, blood and including intake and excretion pathways

Biokinetic models are used to estimate the retained activity in various organs as well as excretion of activity through urine and faeces as a function of time. Activity in the organ is integrated for many years to obtain U_s, the total number of transformations of radionuclide in source organ S over a commitment time following intake. U_s is determined by solving biokinetic models of the respective radionuclide for the intake pathway.

3.2 Dosimetric Model

Dosimetric models are used to estimate the radiation doses received by specific organs and tissues due to the presence of radioactive materials. Dosimetric models [13] provide a quantitative measure of the amount of energy deposited by radiation in specific tissues, which is expressed in terms of absorbed dose (measured in gray, Gy) or equivalent dose (measured in sieverts, Sv) due to radionuclide present in another organ. Since experiments on human body are difficult, human body replicas, known as phantoms, are used for computations of dosimetric quantities. Phantoms describe geometric relationship between different tissues and organs. For dosimetric model,

we require body to be divided into organs having radionuclides (source organs) and organs where dose is to be estimated (target organs). The following subsections describe these in detail.

3.2.1 Source Organ

The source organ refers to the specific region or organ within the body that contains or accumulates a radionuclide. In the context of internal dosimetry, it is essential to identify the source organ in order to accurately assess the radiation dose delivered to organs or tissues. When a radionuclide is introduced into the body, it may distribute and accumulate in various organs or tissues depending on its chemical properties, metabolic pathways and physiological factors. Different radionuclides have different affinities for certain organs or tissues. For example, if a person is exposed to a radioactive iodine isotope (such as iodine-131), it may accumulate in the thyroid gland due to the body's natural iodine metabolism. In this case, the thyroid gland would be considered the source organ for the radionuclide iodine-131 [14, 15].

3.2.2 Target Organ

The term 'target organ' pertains to a distinct tissue or region within the body where a dose of radiation is received [16]. In radiation protection, identifying the target organ is important to evaluate the potential health effects of radiation exposure. When ionizing radiation interacts with the body, it deposits energy in the tissues it passes through. This energy deposition can cause biological damage, and the severity of the damage depends on some of the factors including the radiation type and energy, and the sensitivity of the tissues involved. The target organ is the organ or tissue region that is of primary interest when evaluating radiation effects. It may be the organ that is directly exposed to the radiation source or the organ that is particularly vulnerable to damage caused by radiation. The target organ can vary depending on the specific radiation source, exposure scenario and purpose of the assessment.

3.2.3 Specific Effective Energy

Specific Effective Energy (SEE) is a measure of the energy transferred to a target organ when a source organ undergoes a single radioactive disintegration event [17]. During this process, radiation particles like alpha or beta particles interact with tissues, depositing energy and causing biological effects. SEE quantifies this energy transfer and is calculated using a formula that considers factors like radiation type, energy and absorbed fraction. The formula helps estimate the potential impact of radiation on organs, aiding in areas like radiation protection and medical physics. SEE is crucial for assessing radiation risks and establishing safety standards. SEE ($T \leftarrow S$) is specific effective energy which is equivalent dose in target organ T per

nuclear transformation in source organ S. It is given by

$$\mathrm{SEE}(T \leftarrow S) = \sum_R \frac{Y_R E_R w_R \mathrm{AF}(T \leftarrow S)_R}{m_T(t)} \tag{1}$$

In Eq. 1, Y_R is the yield of radiation R, E_R is the energy of radiation R, W_R is the radiation weighting factor for radiation R, AF ($T \leftarrow S$) is the absorbed fraction (AF) in target organ, T, per transformation in source organ, S, for radiation R, at age t and $m_T(t)$ is the mass of the target organ at age t. A number of transformations are obtained by integrating the activity over a period of 50 years for radiation worker. These are obtained by solving the biokinetic model of the radionuclide. W_R is the dimensionless factor by which the organ or tissue absorbed dose component of a radiation type R is multiplied to reflect the relative biological effectiveness of that radiation type.

Thus, dose calculations involve the use of E_R and Y_R which are obtained from nuclear decay data as well as anthropomorphic phantoms. Data on the radiations emitted during spontaneous nuclear transformations of radionuclides can be found in ICRP [38]. The tabulation includes the yield and energy of internal conversion electrons, Auger electrons, X-rays, gamma rays, beta and positron emissions and annihilation photons. AFs are calculated using the Eq. 2:

$$\mathrm{AF}(T \leftarrow S) = \frac{\text{Energy absorbed in } T}{\text{Energy emitted in } S} \tag{2}$$

AFs depend on the anatomical model used and the type and energy of radiation. Since the evaluation of the radiation transport includes adoption of an anatomical model that specifies the mass of the target, the specific absorbed fractions (SAF) as defined in Eq. 3, are used

$$\mathrm{SAF}(T \leftarrow S) = \frac{\mathrm{AF}(T \leftarrow S)}{m_T} \tag{3}$$

where m_T is the mass of the target organ. These are evaluated using reference voxel phantoms which are based on the latest anatomical model such as given in ICRP 89.

The combination of biokinetic and dosimetric models enables experts to assess the potential health risks posed by internal exposure to radioactive materials accurately. This information is used to establish radiation protection standards, develop safety guidelines for workers in radiation-related industries and guide medical professionals in administering radiation therapies safely. These models are continuously refined and updated based on new research findings and advancements in our understanding of radiation biology and health effects.

4 Special Quantities Used in Internal Dosimetry

Dosimetric quantities like absorbed dose, equivalent dose and effective dose are used in both external and internal dosimetry, and they have been already defined elsewhere in this book. Due to long retention of radionuclides in the body, some more quantities are defined, especially in internal dosimetry. These special quantities used in internal dosimetry are described in this section. There are two operational quantities used in internal dosimetry which are also explained at the end of this section.

4.1 Biological Half-Life

Biological half-life refers to the duration it takes for half of a radionuclide content within a specific compartment of a biological system to be eliminated, assuming no additional input of the radionuclide and no radioactive decay occurring [17]. Biological half-life is inversely proportional to biological reduction rate. This proportionality constant is same as the one between radioactive half-life and radioactive decay rate.

We have already seen that after intake the radionuclide may undergo various processes such as biological elimination, metabolism, excretion or redistribution within the body. Therefore, biological half-life is determined by the physiological processes involved in the elimination or excretion of the radionuclide from that compartment. The biological half-life can vary depending on the specific radionuclide, the tissue or organ involved and the individual's physiological characteristics. Different radionuclides have different affinities for various tissues, and the elimination processes, hence biological half-life can be influenced by factors such as renal clearance, metabolism and other physiological factors. Understanding the biological half-life of a radionuclide in a specific compartment is essential for assessing the radiation dose delivered to that compartment over time. It helps in estimating the potential long-term exposure and the duration of radiation effects on the associated tissues or organs. Biological half-life is an important parameter used in dosimetry calculations, radiation protection assessments and monitoring the clearance of radionuclides from the body in medical or occupational settings.

4.2 Effective Half-Life

Overall reduction of radioactivity in an organ or compartment is dependent on both radioactive half-life and biological half-life. Since the combination of both half-lives results in an effective reduction of radioactivity is an organ/compartment, their combination is known as effective half-life. Effective half-life is inversely proportional to effective decay rate, where effective decay rate is the sum of radioactive

decay rate and biological reduction rate. In general, effective half-life is closer to the smaller of the two half-lives.

4.3 Committed Equivalent Dose [H_T]

The committed equivalent dose is a term used in radiation protection and dosimetry to quantify the dose of radiation absorbed by a specific target organ over the course of an individual's lifetime, resulting from the radioactive decay of a radionuclide in all source organs [17]. When a radioactive substance enters the body, it can be distributed throughout various organs and tissues. As the radionuclide undergoes radioactive decay, it emits radiation, exposing the surrounding tissues to radiation dose. The committed equivalent dose accounts for the cumulative radiation dose absorbed by a particular target organ throughout the entire period during which the radionuclide remains in the body, considering both the physical decay and biological elimination of the radionuclide. The committed equivalent dose is obtained from the time integral of the equivalent dose rate in a target organ or tissue T. Commitment period, τ, of 50 years is used for adults and 70 years for infants and children. Equation 4 is the mathematical expression for $H_T(\tau)$

$$H_T(\tau) = \int_{\tau_0}^{\tau_0+\tau} \dot{H}_T(t)\mathrm{d}t \tag{4}$$

The equivalent dose rate received by an individual at age t, in target organ T, due to acute intake of radionuclide at age t_0 is given in Eq. 5:

$$\dot{H}_T(t, t_0) = \sum_S U_S(t, t_0)\mathrm{SEE}(T \leftarrow S; t) \tag{5}$$

4.4 Committed Effective Dose (E)

The committed effective dose [$E(\tau)$] is a concept used in radiation protection and dosimetry to quantify the radiation dose absorbed by the whole body over a specific period of time (τ) (called committed time) after the intake of a radionuclide [18]. It represents the integrated dose rate over that time period. When a radionuclide is entered into the body through ingestion, inhalation, or absorption, it can distribute throughout the body and emit radiation. This emitted radiation contributes to the dose of radiation received by various organs and tissues. The committed effective dose takes into account the total contribution of radiation from all organs and tissues to estimate the overall radiation dose to the whole body.

The committed effective dose is obtained as the sum of weighted committed equivalent doses to organs or tissues. The tissue weighting factor takes into consideration the relative contribution of that organ or tissue to overall radiation detriment from stochastic effects. It is defined such that the sum of all tissue weighting factors is one. The SI unit for committed equivalent and effective dose is J kg^{-1} and the special name is Sievert (Sv). The use of effective dose allows the summation of internal doses due to the intake of radionuclides and from external sources. Total dose is used for comparison with dose limits and constraints. Equation 6 is the mathematical expression for $E(\tau)$

$$E(\tau) = \sum_{T} W_T * \frac{\left(H_{T,M} + H_{T,F}\right)}{2} \tag{6}$$

where $H_{T,M}$ and $H_{T,F}$ are the equivalent dose of male and female, respectively.

4.5 Dose Coefficients

Dose coefficients for radionuclide intakes are numerical values used to estimate the radiation dose a person might receive from ingesting or inhaling specific radioactive substances [17]. Dose coefficient is defined as either the committed equivalent dose in organ or tissue T per intake. The unit of dose coefficient is Sv/Bq.

Using dose coefficient, annual limit of intake (ALI) and Derived Air Concentration (DAC) are also defined by ICRP. These two are covered in the next two subsections.

4.6 Annual Limit of Intake

The Annual Limit of Intake (ALI) is a concept utilized in the field of radiation protection to specify the maximum amount of a particular radionuclide that an individual can ingest or inhale within a 1-year period without exceeding a specific dose limit [18]. The ALI is expressed in units of becquerel (Bq). It is defined as the intake of a radionuclide over 1 year that would result in a Committed Effective Dose (CED) of 20 mSv. The ALI value for a radionuclide is given by Eq. 7:

$$\text{ALI} = \frac{0.02}{e_j(50)} \tag{7}$$

where $e_j(50)$ is the dose coefficient (Sv/Bq) for the radionuclide.

4.7 Derived Air Concentration (DAC)

Derived Air Concentration (DAC) is a term used in radiation protection to indicate the airborne concentration of a specific radionuclide. It is defined as the level of radionuclide concentration in the air that, if inhaled by a reference person (typically an adult male), over a working year (approximately 2000 h) at that concentration, would result in an intake equivalent to the Annual Limit of Intake (ALI) [18]. The DAC is represented in units of Bq/m^3. The standard respiration rate assumed for the reference person is typically 1.2 cubic metres per hour (m^3/h). The DAC value is specific to each radionuclide and takes into account factors such as the radiological properties of the radionuclide, its biological behaviour in the body and the established dose limits or reference levels.

$$\mathrm{DAC} = \frac{\mathrm{ALI}}{2400}\left(\mathrm{Bq/m^3}\right) \tag{8}$$

5 Need for Monitoring of Internal Contamination and Its Applications

Whenever radioactive substance enters human body, it can irradiate various organs in the body before the substance completely decays or is eliminated from body. For such internal exposure cases, internal radioactivity measurement is carried out for various reasons [16]. Some of these reasons are discussed in the following subsections.

5.1 Occupational Safety of Radiation Workers

There is a regulatory requirement to limit occupational dose to radiation workers. For internal contamination, this regulatory requirement can be fulfilled by monitoring of internal contamination and computation of internal dose. Since workplaces involve radioactive materials or in nuclear industries, workers may be exposed to radioactive substances internally through various routes of intakes, e.g. inhalation, ingestion, wound or skin absorption.

There are various activities where there is a potential for internal contamination. Workers involved with Uranium ore milling and fuel fabrication may get internally contaminated. If workers are handling very large amounts of gaseous materials like tritium or handling large quantities of volatile substances like iodine-131, then they may get internally contaminated. In addition, workers involved with procession of plutonium and thorium are also at potential risk for internal contamination. Production of large quantities of other radionuclides for various applications is also associated with potential risk of internal contamination.

In all such cases, internal contamination and computation of internal dose helps to ensure that workers' radiation exposure remains within permissible regulatory limits. Therefore, internal contamination monitoring is necessary to ensure compliance with regulations and guidelines to protect radiation workers from excessive radiation exposure [17].

5.2 Safety of Members of Public

For safe operation of nuclear power plants, public exposure also needs to be minimized. Therefore, regulators of every country also limit the exposure to members of public. To quantify the internal exposure of members of public is a tough task due to very little releases for these power plants. These minuscule releases can be in water, ground and air. So, measurement of activity in these samples and computation of assumed intake from these can be used to estimate dose to members of public. This measurement of internal contamination for public can then be used to show compliance with regulations.

Another scenario in which public exposure can occur is in the unfortunate event of a radiological accident or a nuclear incident. In such cases, individuals may be exposed to radioactive materials internally. For these emergency exposure cases, quick measurement of internal contamination is required. Quick computation of dose to critical organs from this measured internal contamination is required. This is required for medical management of highly exposed individuals. Therefore, accurate internal dose estimation aids in assessing the severity of exposure and enables timely medical interventions to mitigate health consequences.

5.3 Optimization of Dose to Patients

Radionuclides are ingested or injected for diagnostic application of molecular imaging and therapeutic application of nuclear medicine. In both diagnostic and therapeutic applications, internal dose estimation is useful to medical professionals. In fact, measurement of internal contamination during molecular imaging is used for the development of patient-specific mathematical models. This in turn can be used for optimization of dose to patients. This ensures effective therapy while minimizing radiation exposure to healthy tissues.

5.4 Scientific Studies

Internal contamination monitoring for exposed workers provides critical data for future applications. One such application is epidemiological studies based on the

research on the health effects of internal contamination. For this, estimated internal dose provides critical data for understanding the relationship between radiation exposure and health outcomes. If an internally exposed worker is monitored for a long period, then data from such measurements can be used to improve biokinetic model of such radionuclide. This helps in correct dose estimation of that worker and improves the current understanding of biokineitc behaviour of the radionuclide as well.

Overall, internal contamination monitoring and assessment of dose, is a fundamental tool for radiation protection, safety assessment and medical applications, providing valuable information to safeguard the health and well-being of individuals and populations. In the next section, we will see how internal contamination is measured.

6 Internal Contamination Monitoring Types and Instruments

Based on the type of internal contamination scenario and purpose of monitoring different instruments can be selected. Some of these monitoring types and instruments used for monitoring of internal contamination are discussed in this section.

6.1 Radioactive Workplace Monitoring

In general, radioactive workplaces are very safe to work and do not pose any issue of internal contamination. However, in some places which were mentioned in Sect. 5.1, there can be a chance for internal exposure. In such workplaces, there is a need for special monitors to detect any increase in radioactivity level, which can internally expose workers. This can be used for initiating an individual monitoring program. Workplace monitoring can also provide important information like particle size and chemical form of the aerosols. This information can be used for dose estimation when individual monitoring is carried out. Sometime workplace monitoring works as a complementary for individual monitoring when a very small amount of intake can lead to a very high dose, e.g. for actinides.

Two very important workplace-monitoring methods are personal air sampling (PAS) and static air sampling (SAS), shown in Fig. 6a and b. In the case of SAS, workplace air sampling involves collection using particulate air sampler. The analysis of particles collected on filter paper is a representative of the working environment concentration of airborne radioactive particles. The collected samples are analysed to identify the specific radionuclides present and their activity levels. Analysis of the samples can be carried out using gamma monitoring system and GM tubes if the radionuclides are beta gamma emitters. For alpha emitters scintillator detectors are preferred for gross counting and semiconductor detectors are used if identification

Fig. 6 Personal air sampler (**a**) and static air sampler for workplace monitoring (**b**) to identify internal contamination

is also required. The only issue with SAS is that it is not a very good representative of individual exposure as the sampling is at a specific location. PAS has air sampling in the level of breathing to be worn by workers above the torso region. It is a better representative of workers' dose than SAS. Since the sampling rate in PAS is much slower than normal human breathing, some computational adjustment is required. Studies have shown that PAS data can be used for dose estimation of a group of workers rather than an individual.

The data obtained from workplace air sampling is useful in understanding the potential for inhalation exposure. It aids in the development of appropriate safety measures and minimizes the risk of internal exposure to workers. It also helps in identifying the group of workers who will require personal monitoring. Details of personal monitoring are discussed in the next section.

6.2 Personal Monitoring of Radiation Workers

Personal monitoring, also known as individual monitoring, involves the assessment of radiation doses received by individual workers who are exposed to internal contamination. The primary purpose of personal monitoring is to ensure that, workers' radiation exposure remains within permissible limits and to provide data for dose assessment and regulatory compliance. The individual measurement frequency, type of

monitoring technique and time of monitoring depends on the radionuclides involved and expected exposure levels.

Some of the monitoring types are routine, task-related, incident-related and confirmatory. People working in workplace where there is a potential for significant exposure are routinely monitored for internal contamination. Time of the next routine monitoring is selected in such a way that the underestimation in the estimated dose is not more than 3 times. If there is some internal contamination detected in routine monitoring follow-up monitoring may be carried out to ascertain probable time and quantity of intake. If some special work is carried out, where there is a potential of internal contamination, then internal contamination monitoring of involved workers is carried out after completion of the work. Similarly, if there is some incident in a workplace which can lead to internal contamination, then after the removal of any external contamination, incident-related monitoring is carried out. A small fraction of workers from a place not expected to have internal contamination are also monitored under confirmatory monitoring category. Confirmatory monitoring is carried out to demonstrate that the assumption of lack of internal contamination from the workplace was correct.

There are several methods of personal monitoring in internal dosimetry, including:

6.2.1 Direct Body Activity Measurement

This method involves directly measuring the radioactivity in the body using specialized equipment. It provides a direct estimate of the radioactive content in organs or tissues and therefore it is considered the most accurate method for monitoring of internal contamination. This monitoring method is also known as in vivo monitoring. Measuring the activity directly in the body or organs offers a rapid and convenient estimation of the content. The feasibility extends to all radionuclides, which emit radiations that can come out from the body of internally exposed person. This means body activity measurement can be applied to radionuclides that emit various types of radiation, including X- or gamma radiation, positrons (detectable through annihilation radiation), energetic beta particles (detectable through bremsstrahlung), and alpha emitters (detectable through characteristic X-rays produced during alpha decay). This encompasses the majority of fission/activation products and other potentially important actinides like Pu/Am, U, Th, etc.

The internal contaminant radionuclides which can be assessed by in vivo monitoring technique are classified as high-energy photon (HEP) and low-energy photon (LEP) emitters based on the energy of photons emitted being more or less than 100 keV, respectively. Appropriate detector and shield types required for their measurements are also given as shown in Fig. 7. Since most LEP emitters are actinides having very low ALI, detecting requirements are very stringent. The minimum detectable activity (MDA) should be lower to account for lower ALI values. Therefore, low background completely shielded monitoring systems are required for measuring LEP emitters. For HEP emitters, being fission and activation products emitters having very high ALI, even partially shielded systems can be used to achieve sufficient MDA. A

(a) (b)

Fig. 7 Actinide monitoring systems having Thin NaI (Tl) inside a completely shielded steel room (**a**) and shadow shield scanning bed having thick NaI (Tl) (**b**)

brief description of the systems used for in vivo monitoring system of LEP and HEP emitters is covered in the next two paragraphs.

To assess radiation workers' internal contamination caused by LEP emitters like actinides, various organ-monitoring techniques are employed using specialized detectors and measurement systems. The organs monitored include lungs (for inhalation of type *S* material), liver and skull (for long time after intake) and lymph nodes (for follow-up monitoring). The detectors used include a sandwich of two detector crystals (phoswich), High-Purity Germanium (HPGe) crystal arrays and thin NaI (Tl) detectors. These detectors are positioned within a standardized measurement geometry inside a fully shielded steel room as shown in Fig. 7a. These in vivo monitoring systems are calibrated using human equivalent phantoms to ensure accurate measurements of radioactivity present inside human body [19]. The efficiency calibration for measurement in lung geometry is typically performed using realistic physical or mathematical thorax phantoms that simulate the geometry and distribution of radioactive sources in the lungs. When radionuclides deposited in the lungs emit photons, these photons undergo attenuation and scattering as they interact with the lung tissue and surrounding tissues. The detection system only records the interaction of these photons within these crystals, which results in the generation of discrete numbers of charge carriers. Due to various processes and interactions, these charge carriers exhibit random fluctuations from event to event within the detector. In order to ascertain the activity attributed to a particular radionuclide within the lungs, a subtraction method is employed. The spectrum obtained from the person being monitored, showing higher counts, is compared to the spectrum obtained from an uncontaminated person. The net counts, obtained by subtracting the uncontaminated spectrum, are subsequently utilized to calculate the deposited activity within the lungs. This calculation incorporates counting efficiencies (CEs) derived from realistic thorax physical or mathematical phantoms that are specific to the assessed radionuclide. For monitoring of other organs, similar methods of calibration and measurements are carried out. By utilizing these monitoring techniques, calibration methods and calculations, the internal contamination within the lungs and other organs of radiation workers caused by actinides can be accurately assessed.

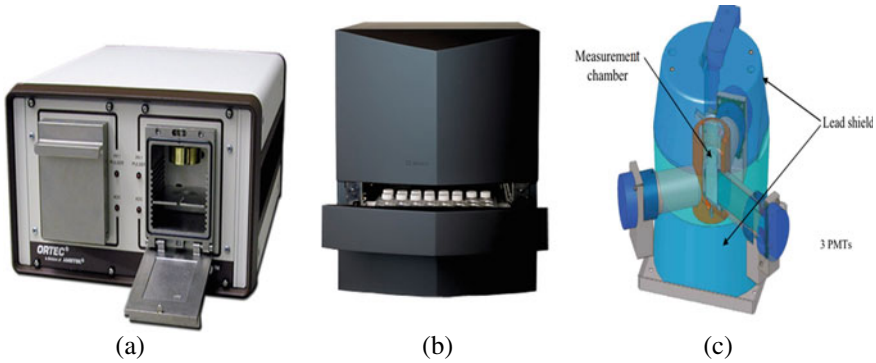

Fig. 8 Alpha spectrometry system (**a**) and liquid scintillation counter (**b** and **c**)

For HEP emitters partially shielded systems are used in in vivo monitoring. These systems have various positioning geometries, like standing, sitting and sleeping for workers being monitored. As with completely shielded systems, partial shielding is used to reduce the effects of natural ambient radiation, so that MDA is sufficiently low. The standing type system has detectors placed in shielding and a person stands in front of the shielded detector. These standing-type systems is good for quick and gross measurement of workers but are not useful to identify location of radionuclide inside body. Most simplistic sleeping-type monitoring system has detector in a shielded enclosure and the worker lying on a bed below the detector. There is a relative motion between person and detector so that the detector can scan complete body. One such system [20] where detector position is fixed and person is moving in a bed is shown on the left of Fig. 7b. This system is good for knowing the distribution of radionuclide and the most accurate but takes a larger area and time for monitoring. A third type of monitoring is carried out in a shielded chair [21] where person sits in a chair and shielded detector monitors major parts of the body. This system is quick, accurate cheaper and comfortable but does not provide distribution-related information. All of these monitoring systems are calibrated using water-filled BOMAB phantoms with uniformly distributed radioactivity in the phantom. Using the CE and person's spectrum, the radionuclide is identified and internal contamination present inside that person can be quantified.

Using in vivo monitoring systems, we get full or partial body internal contamination. This contamination-related information is valuable for radiation protection which can be used to ensure the safety of workers in environments where various radionuclides are present.

6.2.2 In Vitro Analysis

This method involves analysing samples of urine or faeces to detect and quantify radioactive contaminants. Therefore, it provides indirect information about the

internal contamination based on the excretion rates of the radionuclides. It is also known as excreta analysis. In vitro analysis is generally less accurate than body activity measurement but can still provide valuable information when in vivo technique cannot provide sufficient information [19]. In some incident-related cases nasal swabs and tissues samples are also analysed using in-vitro techniques. It generally involves radiochemical analysis and detection as per the radionuclide of interest. So, pre-knowledge of radionuclide of interest is helpful.

Since the 1940s, the analysis of urine and faecal samples has proven to be a valuable technique for evaluating the uptake of uranium and other actinide elements in individuals [22]. Over the period, a variety of radiochemical analysis methods have been developed to correctly isolate the radionuclides in these samples. The developed methods include solvent extraction, anion exchange and chromatography. In the field of identification of radionuclides in urine and faecal samples, there are developments of autoradiography, kinetic phosphorescence, fission-track analysis, high-resolution solid-state alpha spectroscopy, liquid scintillation systems, fluorimetry etc. The most recent trend growing is utilization of various mass spectroscopy techniques for the detection of trace and ultrarace levels of actinides also. These advancements have allowed for improvement in sensitivity and accuracy for measurement of various radionuclide concentrations in in vitro samples. A few of these radiochemical analysis techniques and detection system are discussed in this sub-section.

Most likely used radiochemical analysis for excreta samples includes processes such as sample preparation, chemical separations, purification, and concentration of the radionuclide of interest. Table 1 outlines the general steps involved in radiochemical analysis for separation of a particular actinide from the samples. It can also be seen from the table that unlike in-vivo measurement, in-vitro radiochemical analysis involving preparation of sample for measurement itself is a very time taking process. Radiochemical analysis is followed by specific analytical technique for identification and quantification of the radionuclide in this pre-processed sample.

Since most of the actinides are alpha-emitting radionuclides, therefore it is natural to use alpha spectroscopy technique for identification and quantification of them [22]. This method is favoured for its simplicity, relatively low equipment cost, high sensitivity due to minimal background, and strong selectivity for alpha particles compared to other types of radiation. Figure 8a shows the preferred alpha detector which is the passivated implanted planar silicon (PIPS) detector. PIPS detector offers ruggedness and good energy resolution. Achieving detection limits below 0.5 mBq/d takes around one day of counting in contamination-free alpha chambers using carefully selected

Table 1 Steps involved in in-vitro analysis for actinides

Sr. No	Steps involved in radiochemical analysis	Time required (hour)
1	Wet digestion	4–5
2	Pre-concentration	14–16
3	Ion exchange separation	7–8
4	Electrodeposition	2–3

detector geometry. However, alpha spectrometry is a time-consuming process which struggles to distinguish peaks of ^{239}Pu and ^{240}Pu due to their similar energies, leading to combined reporting of their activity concentrations. High radiochemical purity is also essential to avoid any interference, especially with natural uranium series elements in environmental and biological samples. Alpha spectrometry requires a thin counting source (electrodeposition) to prevent alpha particle self-absorption. Notably, interferences from various radionuclides like ^{241}Am, ^{228}Th, and others can occur in plutonium measurements.

On the other hand, Liquid scintillation Counting (LSC) is a standard laboratory method used for quantification of activity of α and β emitting radionuclides. A typical LSC system is shown in Fig. 8b and c. Sample preparation for LSC, involves mixing of a sample aliquot to a scintillation cocktail to obtain a homogeneous test sample [23–25]. Because every radioactive atom in prepared sample is essentially encircled by detector (scintillation cocktail) molecules, 4π geometry is achieved which facilitates β counting with reasonable CE. Radionuclides having high β energies ($\geq$ 150 keV or more) are detected with more than 95% efficiency. High CE and the absence of self-absorption are the leads that make LSC an extensively used analytical technique for detecting not only beta but alpha emitters also. Over the previous decades, significant developments have been made in nuclide separation and liquid scintillation sample preparation techniques, in the optics and electronics of detectors, and in methods of minimizing background, which has made LSC a practical tool and becoming a method of choice nowadays.

Using in vitro measurements, concentration of radionuclide in excreta sample is known. This information can further be used to compute the excretion rate in the excreta sample. This is very useful in evaluating dose and helps in radiation protection of workers.

From the earlier subsections, we know that personal monitoring provides valuable data on the internal radiation dose received by individual workers. Personal monitoring allows for the early detection of any excessive exposures and enabling appropriate actions to reduce further exposure and ensure radiation safety in the workplace. It also helps in the assessment of compliance with radiation protection regulations and guidelines.

6.3 Monitoring of Internal Contamination for Medical Applications

In case of medical application, like molecular imaging and nuclear imaging, intake for internal exposure is already known. The amount of radioactivity inside patient's body is generally very large. For such cases, direct detection of the radionuclide in the body is the preferred method. One difference from in vivo measurement of radiation worker is that not much shielding is required as the desired MDA is very

high. For this purpose, shielded scintillators like Gamma camera or pixel crystals-based detectors are used. But the aim of detection of this internal contamination in patient is not to estimate CED of the patient. The detected radioactivity in the part of body of the patient is used to either find organ dose or create the image of the body parts.

Patient's internal contamination has helped the medical professional to identify various ailments and accurately curing cancer.

6.4 Monitoring of Internal Contamination for General Public

In case of radiological or nuclear emergency members of general public may get exposed to internal contamination also. For such cases internal contamination measurement is required to quickly identify the group of people who require special attention due to large amount of internal contamination. Again, like medical application MDA requirement is not high but the number of people required to be monitored in a given time interval may be very high. For this purpose, hand held systems having scintillator or GM counter-based systems are well suited. It is better to know the possible internal contaminants beforehand and remove any trace of external contamination before carrying out any internal contamination monitoring. Based on the monitored data most contaminated people can be separated from all others. These people may be further be given special medical attention.

7 Intake Estimation, Dose Estimation and Decorporation

After detection and quantification of radioactivity inside person's body, it is required to estimate of intake and CED for radiation workers and general public. For medical application, only the absorbed dose in the organ or cancer cell is required. If the CED or some organ dose is very high then decorporation can be carried out to remove the excess activity and reduce the dose substantially. All these aspects of internal dosimetry are covered in this section.

7.1 Estimation of Intake and CED for Radiation Workers and Public

Calculating the dose of radionuclides involves estimating the radiation dose received by an individual due to exposure or intake of specific radioactive substances. This process includes various steps to determine the behaviour of radionuclides within the body and convert their activity into radiation dose. Biokinetic models describe

the movement and distribution of radionuclides in the body, while intake assessment considers the route and amount of radionuclide intake.

For occupational intakes, the ICRP biokinetic models are used to convert bioassay measurements such as whole-body or organ retention or urinary excretion rates into the intake. Intake can also be estimated by measuring radionuclide concentrations in the working environment, i.e. by air concentration. For environmental exposures, estimates of intakes are based on measurements of radionuclides in diet and air, and may involve the use of food-chain models. In many cases, a major contributor to uncertainties in dose estimates will be uncertainties on intakes. For occupational workers uncertainty in the time of intake can be a factor affecting its estimation. Intake estimation using bioassay measurement is provided in Eq. 9:

$$\text{Intake} = \frac{\text{Measured activity}}{\text{Retaintion fraction or Excretion rate}} \tag{9}$$

Dose conversion factors are utilized to convert radionuclide activity into radiation dose as provided in Eq. 10, accounting for the type and energy of radiation emitted. Dosimetry models, such as the Committee on Medical Internal Radiation Dose (MIRD) or ICRP models [10], are employed to calculate organ-specific or whole-body radiation doses based on biokinetic data and dose conversion factors. The calculated doses are then evaluated against established dose limits or reference levels to ensure compliance with radiation protection standards. Accurate radionuclide dose calculation requires expertise in radiation dosimetry, the utilization of appropriate models and tools, and adherence to ethical guidelines to ensure originality and reliability in providing effective radiation protection and risk management.

$$\text{CED} = \text{Intake} \times \text{Dose coefficient} \tag{10}$$

For public exposure in emergency situation, the time of exposure is known. For exposure to I-131, we may also need to know the dose to thyroid. To estimate an organ dose in emergency, it is better to use some ready reckoner than computing the entire dosimetric quantities. Therefore, international bodies like ICRP [17] are providing dose per content which can convert

7.2 Estimation of Organs Doses in Medical Exposure

In case of medical exposure, the dose computation is a bit simpler. By using the detection technique radioactivity is well known. Organ dose computation is carried out by using the MIRD methodology. In this methodology, product of *S*-values between a source target organs and number of disintegrations in the source organ is the total equivalent dose in the organ. These *S*-values can be pre-determined reference values or can be derived for patient for more realistic dose estimation.

7.3 Decorporation of Radionuclide

In the event of an accidental internal exposure, prompt medical intervention can be crucial. This may include administering chelation therapy to help the body eliminate certain radioactive substances. Decorporation therapy is a crucial approach to mitigate the health risks associated with the intake of radionuclides through ingestion, inhalation or injection. When radionuclides enter the body and circulate in the bloodstream or deposit in tissues and organs, they can cause systemic or local radiation effects. Decorporating agents, also known as chelating agents, are specific drugs used to facilitate the removal of radioactive materials from the body or critical tissues [26]. Decorporation therapy involves various strategies, including reducing or inhibiting the absorption of radionuclides from the gastrointestinal tract, diluting the isotopes, and employing diuretics, adsorbents, and chelating agents. These approaches aim to enhance the elimination of radionuclides through urine or faces. Monitoring the effectiveness of decorporation therapy is essential, and it can be achieved through the use of a whole-body counter or bioassay techniques. These monitoring methods enable the quantification and assessment of the reduction in radioactive material within the body. To assist healthcare professionals in selecting appropriate decorporation agents, authoritative organizations such as the National Council on Radiation Protection and Measurements (NCRP) [27] and the International Atomic Energy Agency (IAEA) [28] have provided recommendations on suitable agents for different radionuclides. Table 2 presents a list of various decorporating agents recommended for specific radionuclides, indicating their effectiveness in facilitating the removal of these radioactive materials from the body. It is important to note that the use of decorporation therapy and the selection of specific agents should be guided by medical professionals with expertise in radiation protection and appropriate training in the management of internal contamination.

Table 2 List of decorporating agents

Radionuclide	Treatment
Iodine	Potassium iodide
Caesium	Prussian blue
Tritium	Water
Strontium	Strontium therapy
Uranium	Sodium bicarbonate
Plutonium	DTPA
Americium	
Curium	

8 Mathematical Tools, Quality Assurance and International Guidelines/Standards in Internal Dosimetry

There are many mathematical techniques and computational tools used in internal dosimetry. These tools help in better internal dose estimation. Since there can be various sources of uncertainty in internal dose computation, quality assurance forms an integral part of internal dosimetry programme. In addition, various international agencies are working for standardization of internal dosimetry procedures. A few of them are discussed in this section.

8.1 Mathematical Tools Used in Internal Dosimetry

Monte Carlo simulations are used for various applications in internal dosimetry. It is used to estimate calibration factors for personal monitoring system, estimation of organ doses for medical applications and computation of dose coefficients for occupational workers and public. There are several computational phantoms like MIRD's stylized phantoms and Voxel phantoms used to represent human body. These phantoms, when applied with Monte Carlo simulations, are used to compute various dosimetric quantities like SEE, SAF etc. [29]. Additionally, Monte Carlo simulations with computational phantoms, enhance the accuracy of dose calculations with the possibility of individual anatomical and metabolic variations.

Since internal dose estimation depends on the output of biokinetic and dosimetric models therefor it can be a very tedious process. A simple solution is to have readymade tools which can convert the measured bioassay quantity into dose. A very important readymade tool available internationally includes IMBA and TAURUS [30] developed by the Health Protection Agency of the UK. It is used in internal dose estimation of occupational workers. European Radiation Dosimetry Group (EURADOS) has developed the CADORmed tool for internal dose assessment. There are separate tools like NCIDose [31] used in nuclear medicine for internal dose assessment of patients.

8.2 Quality Assurance in Internal Dosimetry

There are various sources of uncertainties in the internal dose assessment. From variation in biokinetic parameters, time of intake, measurement errors, individual variation in metabolic and anatomical parameters, these uncertainties are unavoidable. Therefore, quality management is very essential in internal dosimetry [17]. For quality assurance, a robust internal measurement and dose computation setup is required. Auditing of labs is also useful in this regard. National and international intercomparison exercises prove any laboratory's standing with respect to other labs.

8.3 Internal Dosimetry Guidelines

There are several ICRP documents, which deals with internal dosimetry. The latest ICRP OIR series 1–5 [10–12, 17, 32] has recommendations on monitoring at workplace and individual monitoring. OIR series also gives comprehensive idea on development and recommended biokinetic and dosimetric models for all possible radionuclides. Latest wound model can be found in NCRP report no. 156 [33]. For accreditation of laboratories, there are several ISO/IEC Standards on measurement of radioactivity and internal dosimetry. For assessment of intake and dose, ICRP OIR series data viewer provides recommended values of bioassay function and dose coefficients. Assessment of internal dose is also covered in ISO Standard 27048 [34] and IDEAS Guidelines by EURADOS [35]. IAEA documents on Radiation Protection and Safety of Radiation Sources: International Basic Safety Standards, General Safety Requirements, No. GSR Part 3 [36] is also meant for internal dosimetry of radiation workers and public.

In addition, based on these standards and recommendations many national regulators make their own standards and regulation. For example, in India, we have standards developed by BIS and regulations related to internal dosimetry developed by AERB [37]. Using all these standards and regulations, internal dosimetry is well-regulated and has done a great contribution to radiation protection and public/medical service.

9 Conclusion

Workplace radiation safety is essential for preventing internal exposure to radioactive materials through ingestion or inhalation, which poses prolonged risks compared to external exposure. To address these risks in industries like nuclear work and medical procedures, strict protocols, appropriate PPE use and continuous monitoring are vital. This internal exposure arises from various scenarios, including accidents and mining, requiring adherence to safety measures, thorough training and constant vigilance. Methods like biokinetic models estimate substance distribution in the body, while urine and faecal analysis assess uptake. Advanced techniques such as mass spectroscopy enhance assessment accuracy. Decorporation therapy, using chelating agents, minimizes risks by removing radionuclides. Accurate dose calculation employs dosimetry models and tools like Monte Carlo simulations. Overall, managing internal exposure risks safeguards employees, patients and general public.

References

1. Antunes-Raposo JA, França D, Lima A, Mendonça-Galaio L, Sacadura-Leite EM (2022) Evaluation of personal protective equipment use in healthcare workers exposed to ionizing radiation in a Portuguese university hospital. Rev Bras Med Trab 20(2):240–248
2. Joshi SR (1982) Airborne radioactive materials and plants: a review. Sci Total Environ 24(2):101–117
3. Kazzi Z, Buzzell J, Bertelli L, Christensen D (2014) Emergency department management of patients internally contaminated with radioactive material. Emerg Med Clin North Am 33(1):179–196
4. Bomanji JB, Novruzov F, Vinjamuri S (2014) Radiation accidents and their management: emphasis on the role of nuclear medicine professionals. Nucl Med Commun 35(10):995–1002
5. Wanwisa S et al (2022) Biological and internal dosimetry for radiation medicine: current status and future perspectives. J Radiat Res 63(2):247–254
6. Khan S, Syed A, Ahmad R, Rather TA, Ajaz M, Jan F (2010) Radioactive waste management in a hospital. Int J Health Sci 4(1):39–46
7. Karlsson BG (2009) Nuclear lives: uranium mining, indigenous peoples, and development in India. Econ Polit Weekly 44(34):43–49
8. AERB Safety guidelines on radiological safety in uranium mining and milling, guidelines no. AERB/FE-FCF/SG-2
9. Grzywa-Celińska A, Krusiński A, Mazur J, Szewczyk K, Kozak K (2020) Radon-the element of risk. Impact Radon Expos Hum Health 8(4):120
10. ICRP (2016) Occupational intakes of radionuclides: part 2. ICRP Publication 134. Ann ICRP 45(3/4):1–352
11. ICRP (2017) Occupational intakes of radionuclides: part 3. ICRP Publication 137. Ann ICRP 46(3–4)
12. ICRP (2019) Occupational intakes of radionuclides: part 4. ICRP Publication 141. Ann ICRP 48(2/3)
13. Paquet F, Harrison J (2018) ICRP task group 95: internal dose coefficients. Ann ICRP 47(3–4):63–74
14. Tae-Eun K, Yoonsun C, Wi-Ho H, Young WJ (2020) Application of the new ICRP iodine biokinetic model for internal dosimetry in case of thyroid blocking. Nucl Eng Technol 52(8):1826–1833
15. Leggett RW (2010) A physiological systems model for iodine for use in radiation protection. Radiat Res 174(4):496–516
16. ICRP (1997) Individual monitoring for internal exposure of workers. ICRP Publication 78. Ann ICRP 27(3–4)
17. ICRP (2015) Occupational intakes of radionuclides: part 1. ICRP Publication 130. Ann ICRP 44(2)
18. ICRP (1991) 1990 Recommendations of the international commission on radiological protection. ICRP Publication 60. Ann ICRP 21(1–3)
19. Bérard P, Franck D, Dubiau C, Soulié R (2000) Intercalibration of French lung monitoring systems for actinide measurements. Radiat Protect Dosimet 89(3–4):235–238
20. Boddy K, Elliott A, Robertson I, Mahaffy ME, Holloway IA (1975) High sensitivity dual-detector shadow-shield whole-body counter with an 'invariant' response for total body in vivo neutron activation analysis. Phys Med Biol 20(2):296–304
21. Singh IS, Suri MMK, Vidhani JM, Garg SP, Sharma RC (2002) Development of an automated shielded chair whole-body monitor. Radiat Protect Dosimet 102(2):145–151
22. Thakur P, Ward AL (2019) An overview of analytical methods for in vitro bioassay of actinides. Health Phys 116(5):694–714
23. Schonhofer F (1998) Use of low-level liquid scintillation spectrometry for rapid measurement and decision making. Radioact Radiochem 9:18–24
24. Horrocks DL (1974) Applications of scintillation counting. Academic Press, New York

25. Brooks FD (1979) Development of organic scintillation. Nucl Instrum Methods 162:477–505
26. Cassatt DR, Kaminski JM, Hatchett RJ, DiCarlo AL, Benjamin JM, Maidment BW (2008) Medical countermeasures against nuclear threats: radionuclide decorporation agents. Radiat Res 170(4):540–548
27. NCRP Report No. 166—Population monitoring and radionuclide decorporation following a radiological or nuclear incident (2010)
28. IAEA Safety Reports series no. 101, Medical Management of Radiation Injuries
29. Patni HK, Akar DK, Nadar MY, Ghare VP, Rao DD, Sarkar PK (2013) Estimation of specific absorbed fractions for selected organs due to photons emitted by activity deposited in the human respiratory tract using ICRP/ICRU Male Voxel Phantom in Fluka. Radiat Protect Dosimet 153(1):32–46
30. Lee HY, Yang KT, An JY et al (2022) Evaluation of workers' internal exposure because of inhalation of radioactive aerosols in a plasma melting facility by using IMBA and TAURUS codes. J Radioanal Nucl Chem 331:4397–4404
31. https://dceg.cancer.gov/tools/radiation-dosimetry-tools. Accessed 30 Oct 2023
32. ICRP (2022) Occupational intakes of radionuclides: part 5. ICRP Publication 151. Ann ICRP 51(1–2)
33. NCRP Report No. 156, development of a biokinetic model for radionuclide-contaminated wounds and procedures for their assessment, Dosimetry and Treatment
34. Henrichs K (2011) Application of ISO standard 27048: dose assessment for the monitoring of workers for internal radiation exposure. Radiat Prot Dosimet 144(1–4):43–46
35. Castellani CM, Marsh JW, Hurtgen C, Blanchardon E, Berard P, Giussani A, Lopez MA (2013) IDEAS guidelines (Version 2) for the estimation of committed doses from incorporation monitoring data
36. IAEA Safety Standards series No. GSR Part 3, Radiation protection and safety of radiation sources: international basic safety standards
37. AERB SAFETY GUIDE NO. AERB/NRF/SG/RP-1 (2019) Monitoring and assessment of occupational exposure due to intake of radionuclides

Biokinetic Models of Radionuclides

Pradeep Kumar Singh

1 Introduction

To assess the dose due to the presence of internal radioactive contamination, it is required to estimate the most likely value of intake and intake date. Monitoring methods such as in vivo and in vitro bioassay provide crucial information regarding the organ and whole body retained active material, as well as its excretion rates through urine or faeces. The most probable intake is estimated by dividing these retained and or excreted material values by reference values of retention/excretion fractions based on reference biokinetic models for the radionuclides. The reference models themselves are dependent on intake routes (inhalation, ingestion, wound/uptake or absorption through wound, etc.), physicochemical properties of the materials, age and sex of the individual [1].

The International Commission on Radiological Protection (ICRP) compiles and provides reference biokinetic models for various radionuclides in their most common physicochemical forms and routes of intake. Retention fractions (retained activity per unit of intake) and excretion fractions (excreted activity per day per unit intake) are obtained by solving these biokinetic models for reference populations of different age groups [2].

This chapter presents the fundamental principles involved in the development of reference biokinetic models for radiological protection and briefly discusses their historical development. It also highlights the latest ICRP reference biokinetic models for specific radionuclides such as Pu, Cs, I, Co and Sr. Additionally, it covers the NCRP wound model and the mathematical approach used to solve biokinetic models for a given intake scenario in order to obtain various bioassay functions.

P. K. Singh (✉)
Internal Dosimetry Section, Radiation Safety Systems Division, Bhabha Atomic Research Centre, Trombay 400085, India
e-mail: pradeepsingh@barc.gov.in

D. K. Aswal (ed.), *Handbook on Radiation Environment, Volume 2*,
https://doi.org/10.1007/978-981-97-2799-5_16

2 Pathways of Intake, Excretion and Transfer

Activity enters the body through various routes, namely inhalation, ingestion, and skin absorption or a wound. This initial deposited activity is termed intake. In any case, activity from the deposited site will dissolve into the bloodstream depending on its solubility and deposition site. The activity reaching the bloodstream (uptake) will circulate throughout the body. This circulating activity is termed as systemic activity [3]. This systemic activity undergoes intricate transfers within the body, determining how it is distributed among different organs and influencing both the route and speed of elimination. Removal of activity from the body primarily occurs through two routes: urinary excretion, which involves eliminating materials from the plasma and extracellular fluids via urine, and faecal excretion, which includes the removal of materials from the gastrointestinal tract for systemic faecal excretion, as well as direct excretion of materials through faeces.

3 Principle of Biokinetic Models

Biokinetic models are mathematical representations of the processes that radionuclides undergo within the human body. These models are built upon the principles of mass balance, compartmental analysis and our understanding of how radionuclides are transported within the body. The general structure of a biokinetic model consists of compartments that represent organs or tissues, connected by transfer rates that describe the movement of radionuclides between them. The goal of these models is to capture the complex interactions involved in the absorption, distribution, metabolism and excretion of radionuclides. A comprehensive biokinetic model for a radionuclide includes its initial deposition in various organs/tissues upon intake, the transfer of radionuclide activity within these organs/tissues, absorption into the bloodstream and subsequent transfer into other organs/tissues. While the metabolic behaviour and movement of activity within organs are complex phenomena, first-order transfer approximation is commonly used for simplicity in most cases [4, 5]. If first-order approximation is not applicable, the problem is often divided into multiple first-order transfer rates by defining different transfer rates or dividing organs into additional compartments. The results obtained from biokinetic models provide bioassay functions, denoted as $m(t)$, which represent retention and excretion fractions of the activity. These functions describe the time-dependent rates of retention within compartments and the rates of excretion through urine, faeces, etc. Bioassay functions offer a framework for assessing the amount of activity that has been incorporated into the body (intake I in Bq) at the initial time of internal exposure. Figure 1 illustrates a three-compartment model where compartment A represents intake, compartment B represents urinary excretion and compartment C represents faecal excretion. The transfer of activity between compartments A and B, as well as B and C, is depicted by the transfer rates λ_{AB} and λ_{BC}, respectively.

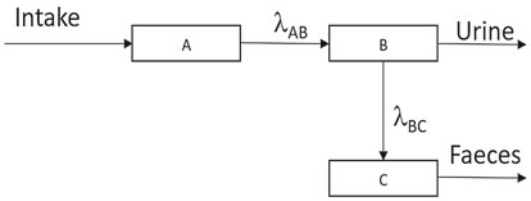

Fig. 1 Depiction of biokinetic model with three compartments and transfer rates

Even though a biokinetic model for a given radionuclide is specific in terms of its absorption, transfer or clearance from the body, ICRP publications have shown a trend to develop default models. For example, default respiratory tract models are developed which are independent of elements, rather the deposition, movement and elimination of material from lungs depends only on particle size and physiological parameters of lungs. These models further have flexibility to incorporate element-specific or subject-specific parameters based on measurements [3, 6, 7]. Similarly, to represent the movement of ingested and secreted activities, a general alimentary tract model is used with flexibility to incorporate element/material-specific gut absorption parameters [3, 6, 8, 9]. The distribution, retention and excretion patterns of radionuclide material after their absorption or administration into the bloodstream are typically addressed using element-specific systemic models. However, even in the case of systemic models, ICRP has tried to develop default models for chemically similar elements, with provision to incorporate element-specific parameters [2, 3, 10].

4 Development of Biokinetic Models

The development of a comprehensive biokinetic model for a specific radionuclide and route of intake requires extensive studies involving humans and animals such as mice, rodents and monkeys. In most cases, systemic models are created by intravascular injection of the radionuclide in a specific chemical form into animals and measuring its retention and excretion rates. The retention and excretion rates for humans are then derived using the principle of allometry, mass balance and scaling factors [9]. Furthermore, corrections are applied using in vivo and in vitro monitoring data obtained from human individuals who have accidentally been exposed to the radionuclide. Consequently, parameters for biokinetic models are primarily derived through four types of measurements:

(a) **Direct information on humans**: This involves measurements of the distribution or excretion of the radionuclide in humans, as well as quantitative data on the physiological processes that are believed to govern its biokinetics.
(b) **Direct information on animals**: This includes data on the radionuclide in laboratory animals or mammalian species. It also encompasses quantitative information on the physiological processes in laboratory animals that are presumed

to control the biokinetics of the radionuclide. In vitro data on the radionuclide or similar elements can also be considered.

(c) **Indirect information on humans**: A less or nontoxic element having chemically similar properties is used on volunteer subjects under controlled environment.

(d) **Indirect information on animals**: A less or nontoxic element having chemically similar properties is used on mammals under controlled environment.

It is essential to note that biokinetic models typically incorporate common behavioural patterns observed in collective data for the material of interest. Biokinetic models based on 'Direct information on humans' are considered more reliable and trustworthy than those relying on other three data types of equal quality and completeness. However, obtaining this kind of data is often challenging for most elements, and in such cases, it is supplemented with the other three data types. Usually, data based on mammalian species are extrapolated to obtain data for humans. Extrapolation process is based on the fact that mammals, who exhibit qualitative similarities, would show quantitatively similar behaviour of radionuclides, after accounting for differences in physiological parameters, which is not always the case [11]. Even though for most cases, chemically similar elements show similar metabolic parameters for humans (e.g. K and Rb, Cm and Am, Ra and Ba, Sr and Ca, etc.), there are exceptions to this rule, as certain chemical analogues may not necessarily be physiological analogues (e.g. Na and K). The use of indirect information from animals poses even more challenges due to the need for both interspecies and inter-element extrapolations. As a result, it is common to consider a combination of various data types to increase confidence when constructing a biokinetic model [12].

5 Evolution of Reference Biokinetic Models

When a radionuclide enters the human body, its biological and metabolic processes are influenced by its physicochemical nature and the intake pathways. As a result, the biokinetics of the same radionuclide can vary due to its material composition and their interaction with the metabolic system. Additionally, the metabolism of a specific chemical can vary from person to person. Therefore, it is not possible to assign default values for transfer rates (within organs) of radionuclides that are applicable to all individuals. However, as a first approximation, mean transfer rates can be derived from various studies for a given age and sex. In the absence of person-specific transfer rates, these mean values can be used to predict the bioassay functions. Reference values for deposition, transfer rates and other parameters have been established for various radionuclides and their chemical forms. Radionuclide intake can generally be categorized into four forms: inhalation, ingestion, injection (directly into the bloodstream) and wounds. Once the activity reaches the bloodstream due to any of these intake forms, it is assumed to behave in similar manner, regardless of the intake route. The activity within the blood is referred to as systemic activity,

and the model used to represent its further movement is known as the systemic model [2, 3].

In the case of inhalation, the initial deposition of the material in different parts of the lungs depends on the aerosol size and physiological parameters of the lungs, which are influenced by age and sex. Similarly, in the case of ingestion, the movement of the material within the various parts of the gastrointestinal tract (stomach, intestines and rectum) depends mainly on the form of the material (solid or liquid) and physiological parameters such as age and sex. Therefore, reference deposition and transfer parameters have been developed for different forms of materials and particle sizes based on human and animal studies for specific age and sex groups. The following subsections provide a brief review of the reference respiratory tract and alimentary tract models. The section also describes evolution of radionuclide-specific systemic models for Pu, Cs, I, Co, Sr. This highlights the periodic revisions of the models, along with their advantages and limitations. The discussion also covers the current default model parameters and the basis for their determination based on the Occupation Intake of Radionuclides (OIR 1–4) series of ICRP publications [2, 13–15].

5.1 Review of Respiratory Tract Model

Respiratory Tract (RT) models consist of three distinct components that describe different aspects of particle behaviour in the respiratory system. The first component deals with particle deposition, estimating where particles will settle based on individual breathing patterns, Activity Median Aerodynamic Diameter (AMAD), and physiological factors. The second component focuses on mechanical clearance, considering how deposited particles are removed from specific locations within the respiratory tract. Lastly, the third component addresses particle dissolution, considering the physicochemical properties of particles and how they may interact with the local environment of the RT [2, 3].

The first comprehensive reference RT model for occupational workers appeared in ICRP Publication 2 [16]. The model was based on studies of inhaled radionuclides in animals and workers. Soluble and insoluble forms of activity were treated differently in this model in terms of its transfer and clearance from lung tissues. In this model, the following assumptions were made: inhaled material was divided into soluble and insoluble forms. Half of the activity is assumed to be deposited in the upper RT and one-fourth in the lower RT region, while the remaining one-fourth was assumed to be exhaled out immediately. Activity from upper RT was assumed to be quickly transferred to stomach. If activity in lower RT is soluble, it immediately enters into bloodstream, while, if insoluble, half of it is swallowed to stomach (immediately) and the remaining half is cleared to environment with a half-life of 120 days [2].

ICRP Publication 10 [6] presented a slightly modified respiratory tract model, in which the slowly removed portion of insoluble activity from lower RT was assumed to be absorbed into the bloodstream rather than clearing into environment. ICRP-2 and

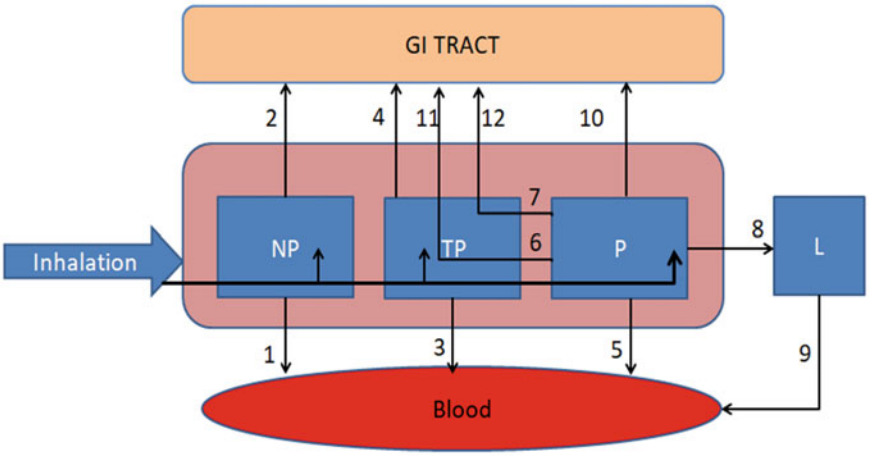

Fig. 2 ICRP-30 lung model with arrows showing clearance and transfer of material (adopted from ICRP-30, 1979)

-10 RT models had their limitations since these models assumed material depositions and clearance rates irrespective of inhaled particle size. Further, it only describes only soluble and insoluble aerosol types, clearance rate from RT was arbitrarily assumed as instantaneous and completely disregarded other material categories altogether.

Later on, ICRP Publication 30 [10] revised its RT model with a more comprehensive one, based on a substantial amount of data from human subjects regarding the deposition and clearance of inhaled substances. This information was gathered by the Task Group Lung Model (TGLM) from various sources, including measurements in human subjects, predictions based on lung anatomy and airflow patterns and studies on laboratory animals. In this RT model, lungs were divided into four main anatomical regions: nasal-pharynx (NP), tracheobronchial (TB), pulmonary (P) and lymphatic (L) (Fig. 2).

Particle size-dependent deposition was assumed, and inhaled material is deposited in the NP, TB and P regions. Materials were divided into three groups for the clearance model: D (days), W (weeks) and Y (years), representing rapid, intermediate and slow clearance, respectively. Clearance from NP and TB was assumed into bloodstream and gastrointestinal tract (stomach), and from P regions into blood, GI tract and lymph regions. Table 1 provides the biological half-times for the TGLM and deposition fractions ($D_{\text{N-P}}$, $D_{\text{T-B}}$ and D_{P}) for 1 μm AMAD.

In 1994, the TGLM was further updated by ICRP, resulting in the Human Respiratory Tract Model (HRTM-ICRP 66). This updated model incorporated a wealth of data from controlled studies of the deposition and clearance of inhaled substance in both healthy human subjects and in laboratory animals. Additionally, data from follow-up studies of occupational workers exposed to hazardous materials were also taken into account [7].

Table 1 Solubility classes D, W and Y used in the ICRP-30 lung model

Region	Path	Class					
		D		W		Y	
		T (day)	F	T (day)	F	T (day)	F
NP	1	0.01	0.5	0.01	0.1	0.01	0.01
($D_{\text{N-P}} = 0.30$)	2	0.01	0.5	0.4	0.9	0.4	0.99
TB	3	0.01	0.95	0.01	0.5	0.01	0.01
($D_{\text{T-B}} = 0.08$)	4	0.2	0.05	0.2	0.5	0.2	0.99
P	5	0.5	0.8	50	0.15	500	0.05
($D_{\text{P}} = 0.25$)	6	NA	NA	1	0.4	1	0.4
	7	NA	NA	50	0.4	500	0.4
	8	0.5	0.2	50	0.05	500	0.15
L	9	0.5	1	50	1	1000	0.9

The half-life (T) is given in days and fraction (F) is given for the default size of 1 μm of particles (adopted from ICRP-30, 1979)

In ICRP-HRTM, the respiratory tract is divided into five regions: the extra-thoracic (ET) airways, including ET_1 (anterior nasal passage) and ET_2 (posterior nasal and oral passages, pharynx and larynx) and the thoracic regions, which are bronchial (BB: trachea and bronchi), bronchiolar (bb) and alveolar-interstitial (AI: gas exchange region). Lymphatic tissue is associated with both the thoracic and extra-thoracic regions (LN_{TH}, LN_{ET}) (Fig. 3).

Deposition efficiencies in the ET regions are determined based on measured data related to aerosol size and breathing rate, and they are adjusted according to the anatomy of different sex and ethnic groups. In the thoracic airways, a theoretical model is used to calculate particle deposition in each region (BB, bb, AI) considering lung volume and breathing patterns. Particle deposition is modelled by treating the regions as a set of filters during breathing. Aerodynamic mechanism (gravitational settling, inertial impaction) and thermodynamic diffusion that act competitively were considered for the deposition and filtration efficiency of these regions. Regional deposition fractions are calculated for aerosols with lognormal particle size distributions, with the geometric standard deviation (σ_g) varying as a function of the median particle diameter.

For inhalation of radionuclides by workers, a normal breathing adult male (non-smoker) engaged in light work is considered as the reference subject. Default values recommended for occupational exposure include an AMAD of 5 μm, which is deemed more representative of the workplace environment [3]. Table 2 provides deposition fraction in each region of the RT for aerosols with a 5 μm AMAD for the reference worker. On the day of intake, about 82% of activity is deposited in lungs, while remaining 18% is cleared to environment due to nose blow, etc. Activity deposited in bronchi and bronchiolar regions are about 1.78 and 1.10%, out of which 0.33341 and 0.39748% are deposited in sequestered parts of respective regions.

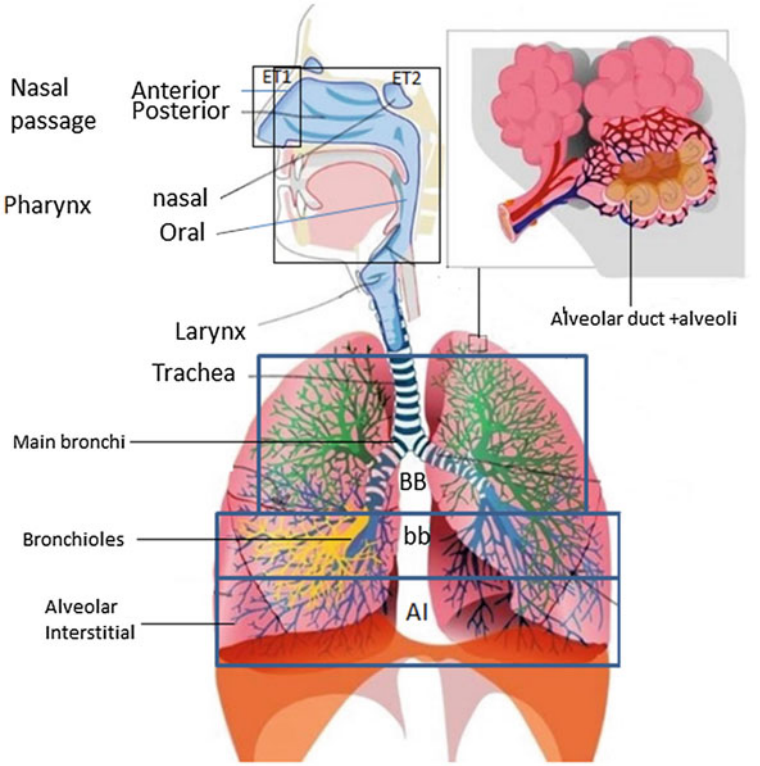

Fig. 3 Human Respiratory Tract Model (adopted from ICRP-78, 1997)

Table 2 Gross deposition of activity in lungs compartments after inhalation (adopted from ICRP-78, 1997)

Region	Deposition (%) of 5 μm AMAD
ET_1	33.85
ET_2	39.91
BB	1.78 (0.33341)
Bb	1.10 (0.39748)
AI	5.32
Total	81.96

In the model, clearance rates in each region of the RT are considered to be independent processes. The total clearance rate from a region is given as the sum of particle transport and absorption to the blood. This relationship is expressed by Eq. 1:

$$\lambda_i(t) = m_i(t) + s_i(t) = g_i(t) + l_i(t) + s_i(t) \tag{1}$$

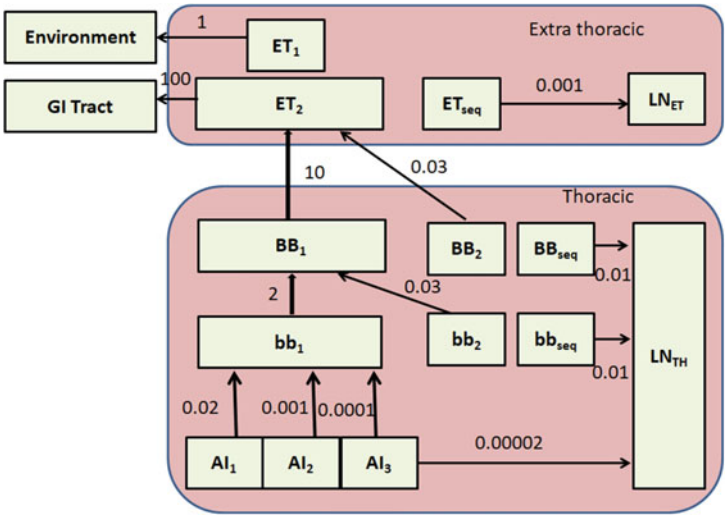

Fig. 4 Compartment model for transport from regions of RT (adopted from ICRP-78, 1997)

where $m_i(t)$ and $s_i(t)$ are rates due to transport and absorption, respectively; $g_i(t)$ and $l_i(t)$ are particle transport rates towards the GI tract and regional lymph nodes, respectively. Figure 4 shows the compartment model for time-dependent particle transport rates (transfer rates in d^{-1}) from each region of RT.

In the case of the extra-thoracic region ET_1, the material deposited is removed back to environment, due to nose-blowing, etc. For thoracic regions, the clearance process is competitive between the movement of particles towards the GI tract and lymph nodes (Fig. 5) and the absorption of material into the blood from the particles in the respiratory tract. Absorption to bloodstream is assumed to occur at same rate from all regions (except ET_1) depending on the physicochemical properties of materials.

Figure 5 shows a general view of transfer of activity from HRTM to blood and to GI tract. Activity in blood reaches from lung tissue as well as from lymph nodes.

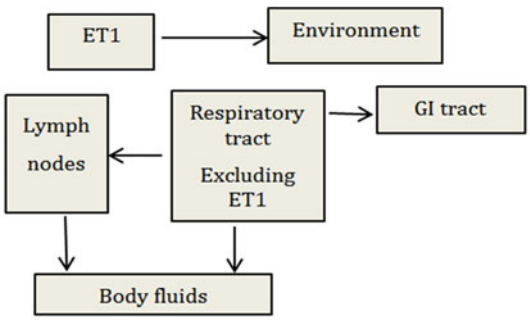

Fig. 5 Routes of clearance from respiratory tract (adopted from ICRP-78, 1997)

Table 3 Default absorption rates for type F, M and S class materials

Model parameter (d^{-1})	Type of compound		
	F (fast)	M (moderate)	S (slow)
S_p	100	10	0.1
S_{pt}	0	90	100
S_t	–	0.005	0.0001

From ET_1 all the activity cleared out into environment via nose blow or exhalation and no blood absorption occurs from this region.

The model also has provision to incorporate material-dependent blood absorption rates from lungs, for this the initial activity deposited in lungs is assumed to undergo transformations within the same regions and then activity in original and transformed forms has different absorption half-lives for clearance into bloodstream. Depending on the transformation fractions for material inside lungs, the materials are classified into three classes, namely: Fast (F), Moderate (M) and Slow (S). Table 3 shows the reference absorption half-lives for the original and transformed activities.

Figure 6 depicts a general view of transfer of activity from lungs to blood compartment. A part of activity is directly transferred to blood, while the remaining part is first chemically transformed (with rates provided in Table 3) and then transfer to blood with different transfer (absorption) rate.

In the given model, there are three types of absorption characteristics for the deposited materials:

Type F: This type represents materials that are 100% absorbed with a half-time of 10 min. It means that all the deposited materials in the respiratory tract, including BB, bb, AI and ET_2, are rapidly absorbed into the bloodstream within a short period of time.

Type M: Materials of this type have a mixed absorption pattern. Approximately 10% of the deposit in BB, bb and ET_2 are rapidly absorbed with a half-time of 10 min,

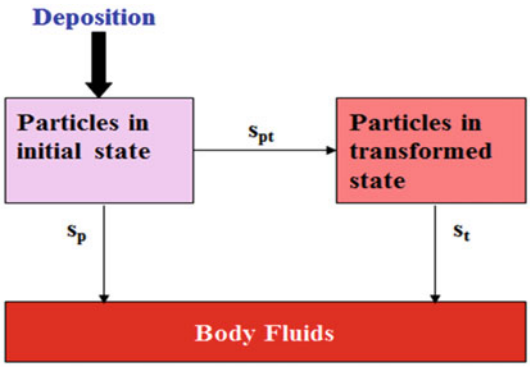

Fig. 6 Absorption of activity into blood in the initial state as well as in the transformed state

while the remaining 90% have a much slower absorption rate with a half-time of 140 days. Additionally, about 7% of the deposit in AI eventually reaches body fluids.

Type S: This type represents materials with minimal absorption. Only 0.1% of the deposit in ET, BB and bb is absorbed rapidly with a half-time of 10 min, while the remaining 99.9% have an extremely slow absorption rate with a half-time of 7000 days. However, about 10% of the deposit in AI eventually reaches body fluids.

These absorption characteristics play a significant role in determining the fate of deposited materials in the respiratory tract and their subsequent distribution throughout the body [3, 7].

5.2 ICRP-130 HRTM

An updated version of the HRTM was published in 2015 [2], by ICRP report on occupational intake of radionuclides (OIR-1). The update was prompted by new insights into the deposition and clearance of substances in different parts of the RT. Specifically, the updated information was primarily derived from various studies, including controlled experiments on the clearance of radiolabelled insoluble particles in the nasal passage under different conditions (resting or light exercise), observations of the removal of relatively large tagged particles from the bronchial region, a 15-year follow-up study of workers exposed to Co-60 particles, a controlled investigation into the lung retention of gold-195 tagged insoluble particles in volunteers over a period of approximately three years, and a 30-year follow-up study on workers who inhaled Pu-oxides during a fire incident.

Figure 7 illustrates the structure of the revised HRTM. Several key modifications have been made to the original model's [3] structure, which can be summarized as follows:

1. The region previously known as ET_2' has been redefined to consist of ET_{seq} and ET_2' compartments. The subscript 'seq' denotes sequestered material.
2. Compartment ET_2' in the revised model encompasses the posterior nasal passage, pharynx and larynx.
3. In both the bronchial (BB) and bronchiolar (bb) regions, the revised model introduces a single phase of clearance towards the throat. Previously, there were two phases of clearance in each of these regions.
4. Figure 5's compartments BB_1 and BB_2 have been replaced by compartment BB′ in Fig. 8. Similarly, compartments bb_1 and bb_2 have been substituted with compartment bb′.
5. In the alveolar-interstitial (AI) region of the respiratory tract, the revised HRTM replaces the three AI compartments from the original model with the alveolar (ALV) and interstitial (INT) compartments. Particles in the ALV compartment are cleared either to the ciliated airways or to the INT compartment. Clearance from INT to the lymph nodes occurs at a very slow rate.

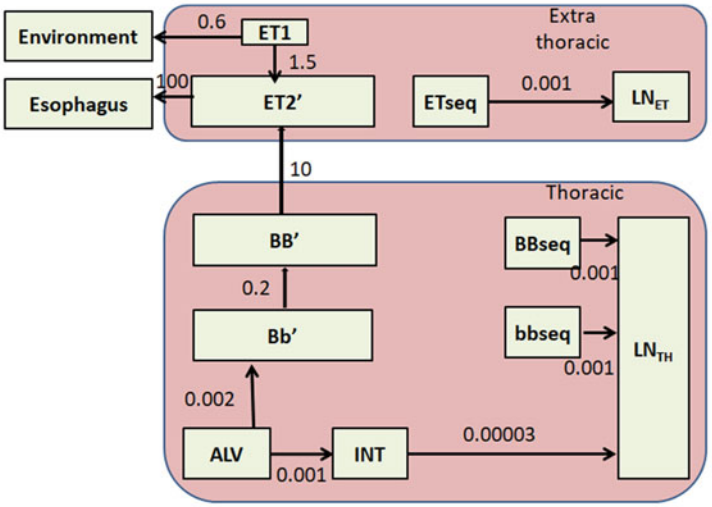

Fig. 7 Structure of the updated HRTM (adopted from ICRP-130, 2015)

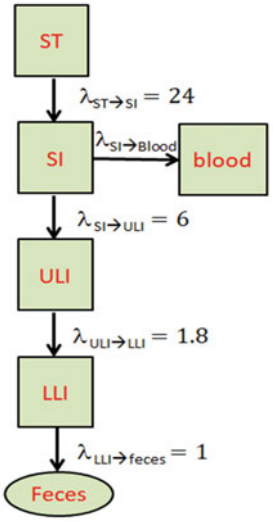

Fig. 8 Human GI tract compartment model (ST = stomach, SI = small intestine, ULI = upper large intestine, LLI = lower large intestine) (adopted from ICRP-30, 1979)

6. In the updated model, the default deposition in ET_1 and ET_2 are changed to 47.94 and 25.82% rather than 33.85 and 39.91%, respectively. The deposition in other regions remains the same as the previous model of ICRP-66. For each of the regions, 0.998 fractions of the assigned activity is assumed to be deposited in ET_1' and ET_2, BB, bb and ALV, while reaming 0.002 is assumed to be in ET_{1seq} and ET_{2seq}, BB′, bb′ and INT compartments.

7. The revised ICRP-130 HRTM has provided AMAD-dependent particle deposition fractions for various cases of breathing patterns. The parameter values in the HRTM, both in the original and revised versions serve as reference values and are intended to represent typical values for healthy, non-smoking individuals in the general population.

5.3 ICRP-30 GI Tract Model

The gastrointestinal (GI) tract model described in ICRP Publication 30 [10] is based on research conducted in the mid-1960s by Eve and Dolphin [17]. It represented the most current knowledge available at that time. Figure 8 depicts the diagram of the GI tract compartment model presented in ICRP Publication 30, along with the associated transfer rate coefficients for adults. This model comprises four compartments: the stomach (ST), small intestine (SI), upper large intestine (ULI) and lower large intestine (LLI). The model considers absorption into the circulation from the small intestine, assuming that inter-compartmental transfer rates and absorption follow first-order processes. In simpler terms, the movement of contents from one segment to the next is proportional to the amount present in the current segment. A similar principle applies to the excretion kinetics from the lower large intestine. The recommended transfer rate coefficients are derived from experimental data. The primary objective of the ICRP Publication 30 GI tract model was to establish radiation protection standards for individuals exposed to radiation in occupational environment. However, it is important to note that the model was specifically developed for adult males and did not account for variables such as gender and age in relation to GI motility. Therefore, the model did not include female individuals or different age groups such as paediatrics and the elderly.

5.4 ICRP-100 Alimentary Tract Model

A revised more comprehensive model for ingested and secreted activity was introduced in ICRP Publication 100 [8]. Unlike, an earlier model which included only four compartments, the updated model of ICRP-100, incorporated more compartments, covering the whole alimentary tract from oral cavity to rectum. Further, in this model, provisions are made for absorption of materials from tract to bloodstream not only from SI but also from all compartments (when information is available).

The updated HATM is shown in Fig. 9. In this model, the entry of radionuclide occurs in oral cavity instead of stomach in case of ingestion and in oesophagus (from ET regions of RT) in case of inhalation. The model also separates content regions from wall regions for dosimetric purposes and provides provision to incorporate blood absorption rates from walls.

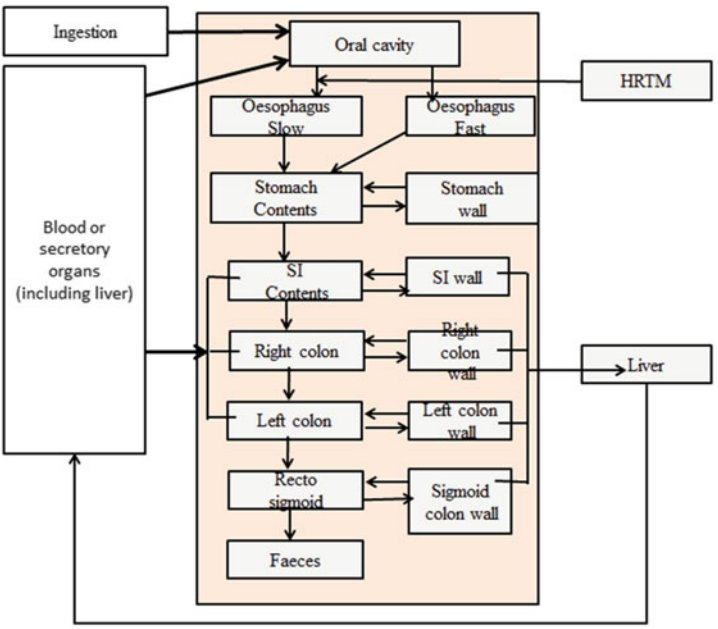

Fig. 9 Structure of the revised HATM (adopted from ICRP-100, 2006)

The ICRP-100 HATM incorporates distinct transit times for solid foods, liquids and the total diet within the mouth, oesophagus and stomach assuming first-order kinetics. Table 4 shows default alimentary tract transfer rates (day^{-1}) for adult workers.

The absorption of radionuclides into the blood is represented as a fraction of the amount entering from the alimentary tract to blood, denoted as f_A. In most cases, all absorption is assumed to occur in the small intestine as a default ($f_{SI} = f_A$).

Table 4 Default generic HATM transfer coefficients (day^{-1}) for total diet adult workers

Transfer pathway	Rate (day^{-1})
Oral cavity contents → Oesophagus fast	6480
Oral cavity contents → Oesophagus slow	720
Oesophagus fast → Stomach contents	12,343
Oesophagus slow → Stomach contents	2160
Stomach contents → Small intestine contents	20.57
Small intestine contents → Right colon contents	6
Right colon contents → Left colon contents	2
Left colon contents → Recto sigmoid contents	2
Recto sigmoid contents → Faeces	2

The extent of absorption depends on the element and its chemical forms, which can change during digestive processes [3, 8].

6 Evolution of Systemic Models

The earlier systemic models commonly employed in radiation protection tend to be simplified compartmental models that do not explicitly account for material feedback. These models typically described the retention of a radionuclide in the entire body or a specific organ using a single exponential term or the sum of a few exponential terms. The selection of these exponential terms is generally based on fitting data obtained from human studies or laboratory animal experiments. However, the biological interpretation and significance of the model formulations can vary significantly among different models. This section describes the evolution of element-specific systemic models in brief, highlighting systemic models mainly described in ICRP-30, -56, -67 and -78 models.

6.1 Systemic Model of Cobalt

The systemic model for cobalt adopted in ICRP Publication 30 was based on a study conducted by Thomas et al. [18]. The study involved daily administration of ^{60}Co in form of drinking water for rats. The results of the study showed that the retention of cobalt in the bones was lower compared to an earlier study by Hollins and McCullough [19], which claimed that cobalt had the highest retention in bones. Based on the findings of the Thomas et al. study, the ICRP-30 systemic model for cobalt assumed that half of the cobalt reaching the bloodstream would be excreted with a half-life of 0.5 days. Five per cent of the remaining half is deposited in the liver and the remaining activity is uniformly distributed among other organs. To account for translocation from the liver and other tissues, both compartments were further divided into three sub-compartments. Retention half-lives of 6, 60 and 800 days were assigned to represent 60%, 20% and 20% of the activity deposited, respectively. The retention function, obtained from a study involving two human subjects over a span of 1000 days, is assumed to be applicable to all cobalt distributed within the body [19]. This function closely resembles the one derived by Letoumeau et al. [20], although the latter was based on a shorter study period and involved more subjects.

6.2 Systemic Model of Strontium

A comprehensive systemic model for strontium was first presented by the ICRP Task Group on alkaline Earth Metabolism in Adult man [21]. This model was carefully

developed to account for different processes and to incorporate physiological information in the determination of parameter values. The retention of a radionuclide in the whole body, denoted as $R(t)$, at a given time t (in days) following injection, is given by the following expression 2:

$$R(t) = (1 - p)\mathrm{e}^{-mt} + pE^{b}(t + E)^{-b}\left[(1 - B)\mathrm{e}^{-sr\lambda t}\right] \tag{2}$$

where:

λ = the rate of apposition and resorption in compact bone.
s = the ratio of turnover rates of trabecular and compact bone.
B = the fraction of bone volume activity deposited in compact bone.
r = a factor that corrects for redeposition of activity in new bone.
b = related to diffusion of activity from bone.
E = a small time period related to the turnover of an initial pool in bone.
m = the rate constant of a small early exponential loss.
p = the fraction of R not in the early exponential loss.

6.3 Systemic Model of Caesium

In contrast to the alkaline earth model, most of the models presented in ICRP Publication 30 [10] are simpler in formulation and have weaker physiological connections. In many cases, it is assumed that radioelements are uniformly distributed throughout the body at all times. However, in some instances, multiple hypothetical compartments with uniform distribution are introduced to account for the need of multiple exponential terms in fitting the available whole-body data. This can be seen in the model for caesium, where the retention in the whole body at time t (in days) after injection is described by Eq. 3. This formulation is derived from extensive data on measurements of whole-body retention of caesium in individuals who were acutely exposed to the radionuclide:

$$R(t) = a \times \exp^{\frac{-0.693\,t}{T_1}} + (1 - a) \times \exp^{\frac{-0.693\,t}{T_2}} \tag{3}$$

where $a = 0.1$, $T_1 = 2$ d, and $T_2 = 110$ d for adult workers.

T_1 and T_2 are biological half-times for short-term and long-term components of retention, respectively. The caesium systemic model was later on updated in ICRP Publication 72 [22–24] in which parameters (a, T_1 and T_2) were extended to include pre-adult ages based on age-specific retention data for ^{137}Cs. The caesium systemic model was later on updated by Leggett [25], in which a physiological-based comprehensive model was introduced. The model predicted peak kidney content of 22 and 0.4%, respectively, following injection of stable caesium.

6.4 Systemic Model of Iodine

A simple three-compartment model (Fig. 10) was developed by Riggs [26] and used in ICRP Publications 30, 56 and 78 for estimation of dosimetric quantities. In this model, it was assumed that 30% of iodine reaching in blood is accumulated in thyroid, while the remaining 70% is excreted in urine. The retention of half-lives in blood and thyroid and other tissues of the body were taken as 0.25, 80 and 12 days, respectively. From other tissues to blood, a feedback of iodine with a half-life of 15 days is also present in model, while clearance to faecal is with a half-life of 60 days.

A detailed compartmental model for iodine based on various studies involving human subjects was first presented by Leggett et al. [27]. The ICRP recently adopted a revised model for iodine aimed at enhancing the accuracy of dose estimates for short-lived iodine isotopes encountered in nuclear facilities or nuclear medicine. Figure 11 illustrates this model, which incorporates three sub-models representing different physiological systems involved in the iodine cycle within the human body.

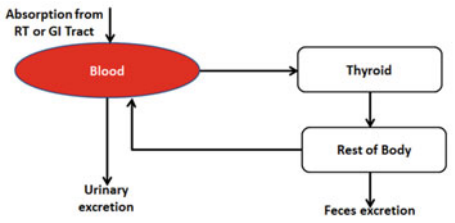

Fig. 10 Three-compartment systemic model of iodine (adopted from ICRP-78, 1997)

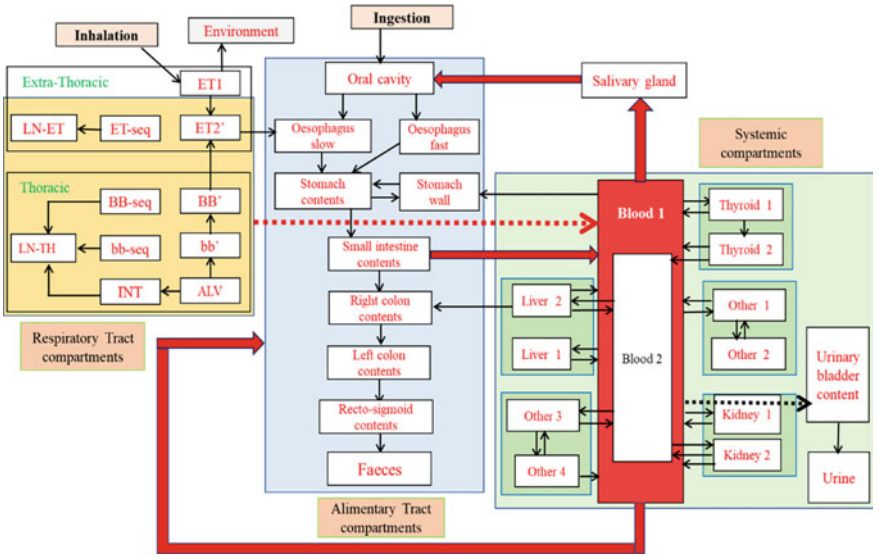

Fig. 11 A complete physiological biokinetic model for iodine (adopted from Leggett et al. 2017)

The first sub-model concentrates on extra-thyroidal inorganic iodide and includes compartments for blood, salivary glands, stomach wall, liver, kidneys and other extra-thyroidal tissues. The second sub-model describes iodine behaviour in the thyroid and consists of compartments for inorganic iodide and organic iodine. The third sub-model addresses extra-thyroidal organic iodine and encompasses compartments for blood, liver, kidneys and other extra-thyroidal tissues. The model takes into account urinary and faecal excretion as the primary pathways for iodine elimination from the body.

The transfer rate λ from compartment blood iodide to thyroid iodide depends on the ratio of dietary stable iodine intake (Y) to the thyroid's secretion rate (S). By utilizing typical reference values for Y and S, the estimation of λ is performed, resulting in transfer rates of 7.26 d^{-1} for a Y: S ratio of 2.5. However, when the ratio is lower, the transfer rate is 2.5 d^{-1} due to the challenges associated with modelling thyroid uptake in the presence of high dietary iodine levels. The model's predictions are compared to observations of iodine distribution in humans after intravenous injection.

6.5 Systemic Model of Plutonium

Most of the excretion functions for plutonium were based on studies conducted by Langham et al. [28]. These data, along with data from animal experiments, were used by Durbin [29] to develop a series of exponential functions representing urinary and faecal excretion. However, later on, it was seen that these exponential functions were inadequate to predict the long-term retention of plutonium and provided lower excretion functions than observed [30–33]. Several modified excretion functions have been proposed [34, 35] to address these discrepancies. Due to discrepancies in excretion rates obtained from different exponential functions, it was recommended that laboratories or organizations with sufficient data develop an appropriate excretion function and use it to interpret monitoring results.

Reference plutonium biokinetic model used in ICRP Publication 2 is mainly based on studies carried out by Langham et al. [16, 28]. The model considered the total body, bone, liver and kidneys as the reference organs for absorbed plutonium. The removal half-times from these organs were assumed to be 178 years, 200 years, 82 years and 88 years, respectively. The model was reviewed later in 1965 by an ICRP task group and a revised model for plutonium was published in ICRP Publication 30 (Part 1) [10], which accounted for transfer compartments, deposition on bone surfaces, liver retention, gonad retention and excretion.

As per the ICRP-30 systemic model, plutonium is primarily deposited in the liver and skeleton. However, there is significant variability in the relative deposition of plutonium in these two organs, as observed later in human autopsy studies and experimental data on animals. For example, ICRP Publication 18 recommended fractional deposition values of 0.45 for liver and bone each and the remaining fraction of 0.10 for other tissues. Biological half-lives of 100 years and 40 years were recommended

for skeleton and liver retention for Pu, respectively, based on data from human and mammalian species studies [36]. A permanent deposition of fractional plutonium in testes and ovaries was 3.5×10^{-4} and 1.1×10^{-4}, respectively, was recommended. The remaining plutonium entering the transfer compartment is assumed to be directly excreted.

In 1993, ICRP Publication 67 revised the model to reflect updated information on the long-term distribution of plutonium and recent modifications to the effective dose concept [22]. However, certain discrepancies were noted, including an underestimate of blood plutonium and faecal excretion rates at early and intermediate times after intake. To address these discrepancies, an updated model for systemic plutonium was proposed. The model structure included additional blood compartments to account for differences in urinary clearance between initially absorbed and recycled plutonium. The liver compartment was modified to reflect a gradual shift of activity from the liver to the skeleton over time. The proposed model addressed the earlier discrepancies and better aligned with the observed behaviour of plutonium [22].

7 NCRP Wound Models

The ICRP doesn't offer wound models as they're outside standard operations and represent unique situations. In the mid-1990s, NCRP and ICRP formed a committee to develop default wound models to incorporate the cases of accidental injection of activity via skin breach, etc. Radioactive materials can move from wound sites into the body. NCRP created a model for this transfer, used with element-specific biokinetic models to calculate doses to organs. It covers soluble and insoluble substances, simplifying based on the substance's form. Four retention categories for soluble radionuclides at wounds were defined: weak, moderate, strong and avid, based on rat experiments. Release from wounds happens via blood for soluble materials and lymph nodes for particles. Blood compartment links the wound model and systemic model of radionuclide (Fig. 12). Skin damage increases radioactive material's movement. Wound contamination assessment relies on expert judgement. Radionuclide transfer can be assessed from urine data. ICRP doesn't endorse dosimetric models for wound contamination, but NCRP-156 [37] does offer some in their publications, aiding equivalent and effective dose calculated based on different classes of wound modes and appropriate systemic models amalgamated to these.

8 Application of Biokinetic Models

Biokinetic models have extensive applications in various fields of radiological protection. In radiation protection, these models are used to estimate numbers of nuclear disintegrations in various source regions of the body using which; committed tissue equivalent and effective doses are established for radiation workers and the general

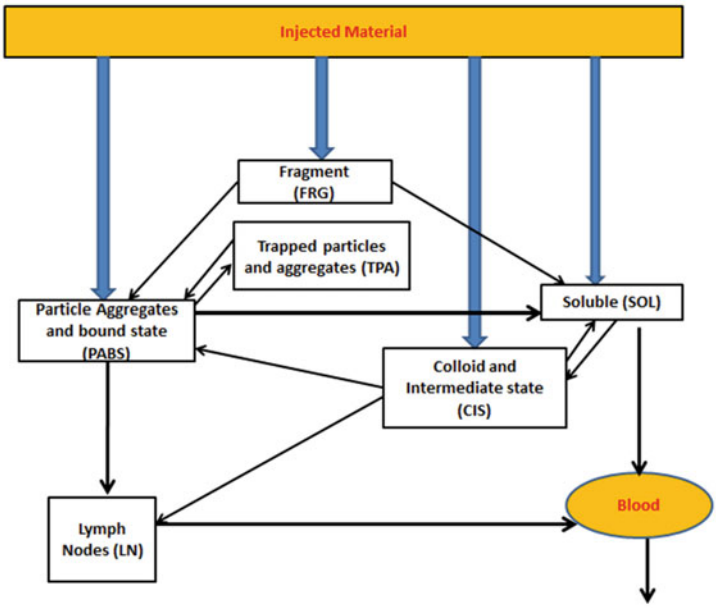

Fig. 12 Schematic representation of the NCRP wound model (adopted from NCRP-156, 2015)

public. These coefficients provide a quantitative estimate of the radiation dose resulting from radionuclide intake. In nuclear medicine, biokinetic models aid in optimizing diagnostic procedures and therapeutic treatments involving radionuclides. Additionally, these models are valuable tools for environmental risk assessment, helping to evaluate the potential impacts of radionuclide releases on ecosystems and human populations.

9 Mathematical Approach to Solve Biokinetic Models

For simplicity, it is assumed that the whole body is made of simple compartments. Each compartment represents a tissue or an organ of the body. Transfer of activity from one compartment to another follows exponential decay law over time.

Let '*i*' and '*j*' are two compartments, rate of transfer of activity from compartment '*i*' to '*j*' is λ_{ij} and vice versa. Also, λ_R is the radioactive decay rate of nuclide (Fig. 13). Let N_i and N_j be the number of nuclides in the *i*th and *j*th compartments, respectively, at any time. Then, by balancing the equation, we know.

The rate of change of material (dN_i/dt) in the *i*th compartment is given by Eq. 4:

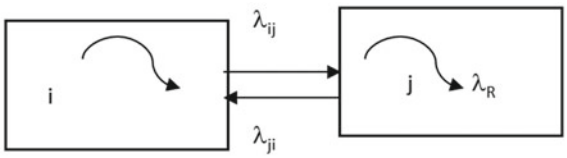

Fig. 13 Schematic of radionuclide transfer within two compartments

$$\frac{\mathrm{d}N_i}{\mathrm{d}t} = \sum_{\substack{j=1 \\ j \neq i}}^{n} \lambda_{ji} N_j - \sum_{\substack{j=1 \\ j \neq i}}^{n} \lambda_{ij} N_i - \lambda_{\mathrm{R}} N_i \tag{4}$$

Equation 4 is a matrix equation, where matrix R is a square matrix of $n \times n$ order, n being the number of compartments in body and matrix $N(t=0)$ is a column matrix of initial values of activity in those compartments. To solve these equations, we need to simplify the equations by making transformations given by Eq. 5:

$$r_{ij} = \lambda_{ji} \; and \; r_{ii} = - \sum_{\substack{j=1 \\ j \neq i}}^{n} \lambda_{ij} - \lambda_{\mathrm{R}} \tag{5}$$

Substituting these in Eq. 4, we get Eq. 6, which can be rearranged as Eq. 7:

$$\frac{\mathrm{d}N_i}{\mathrm{d}t} = \sum_{\substack{j=1 \\ j \neq i}}^{n} r_{ij} N_j + r_{ii} N_i = \sum_{i=1}^{n} r_{ij} N_i \tag{6}$$

The solution of equation is also given in Eq. 7:

$$\frac{\mathrm{d}N}{\mathrm{d}t} = RN(0) \Rightarrow N(t) = \mathrm{e}^{Rt} N(t=0). \tag{7}$$

Construction of transfer matrix is clear from the transformations given in Eq. 5. All the off-diagonal terms r_{ij} are merely the transfer rates from compartment 'j' to 'i' while diagonal terms in a particular row are negative of sum of all the off-diagonal terms in that row and radioactive decay constant.

Integrating Eq. 7, for a commitment time τ, provides total numbers of nuclear disintegrations $[U_{\mathrm{S}}(\tau)]$ in each compartment as given by Eq. 8:

$$U_{\mathrm{S}}(\tau) = \frac{\lambda_{\mathrm{decay}}}{R}\left(\mathrm{e}^{Rt} - I\right) N(t=0) \tag{8}$$

10 Conclusion

Recent trends in biokinetic model formulation within the ICRP have shown a shift towards greater biological realism. Specifically, age-dependent biokinetic models described in the ICRP publication series on age-dependent doses to the public from intake of radionuclides have incorporated physiological motivation and explicit depiction of material feedback and specific excretion pathways. These models aim to capture the main structures and processes that govern the biokinetics of the radioisotopes, allowing for a wider range of relevant information to be considered compared to earlier, simplistic approaches. These models provide a stronger foundation for extrapolating beyond observed data to other population subgroups or time periods. However, it is important to recognize the challenges in representing reality in biokinetic models. Even the most detailed physiologically motivated models are not entirely process models, as some compartments and directions of flow are empirically hypothesized. Additionally, there are many radioelements for which detailed physiologically motivated models may not be advantageous due to a lack of information about their biokinetic processes. As a result, many models in the ICRP publication series have retained the simple formulation used in ICRP Publication 30 while assigning physiological significance to the terms whenever possible.

References

1. International Atomic Energy Agency (2007) Intercomparison exercise on internal dose assessment. IAEA-TECDOC-1568. IAEA, Vienna
2. ICRP (2015) Occupational intakes of radionuclides: part 1. ICRP publication 130. Ann ICRP 44(2)
3. ICRP (1997) Individual monitoring for internal exposure of workers (preface and glossary missing). ICRP publication 78. Ann ICRP 27(3–4)
4. Leggett RW, Eckerman KF, Williams LR (1993) An elementary method for implementing complex biokinetic models. Health Phys 64(3):260–271
5. Matsumoto M, Yamanaka T, Hayakawa N, Iwai S, Sugiura N (2015) Development of a computer code to calculate the distribution of radionuclides within the human body by the biokinetic models of the ICRP. Radiat Prot Dosim 163(4):446–457
6. ICRP (1968) Report of committee IV on evaluation of radiation doses to body tissues from internal contamination due to occupational exposure. ICRP publication 10. Pergamon Press, Oxford
7. ICRP (1994) Human respiratory tract model for radiological protection. ICRP publication 66. Ann ICRP 24(1–3)
8. ICRP (2006) Human alimentary tract model for radiological protection. ICRP publication 100. Ann ICRP 36(1–2)
9. Mordenti J (1986) Man versus beast: pharmacokinetic scaling in mammals. J Pharm Sci 75(11):1028–1040
10. ICRP (1979) Limits for intakes of radionuclides by workers. ICRP publication 30 (part 1). Ann ICRP 2(3–4)
11. Brown RP, Delp MD, Lindstedt SL, Rhomberg LR, Beliles RP (1997) Physiological parameter values for physiologically based pharmacokinetic models. Toxicol Ind Health 13(4):407–484

12. Lindstedt SL, Schaeffer PJ (2002) Use of allometry in predicting anatomical and physiological parameters of mammals. Lab Anim 36(1):1–19
13. ICRP (2016) Occupational intakes of radionuclides: part 2. ICRP publication 134. Ann ICRP 45(3/4):1–352
14. ICRP (2017) Occupational intakes of radionuclides: part 3. ICRP publication 137. Ann ICRP 46(3/4)
15. ICRP (2019) Occupational intakes of radionuclides: part 4. ICRP publication 141. Ann ICRP 48(2/3)
16. ICRP (1960) Report of committee II on permissible dose for internal radiation. ICRP publication 2. Pergamon Press, London
17. Dolphin GW, Eve IS (1966) Dosimetry of the gastrointestinal tract. Health Phys 12(2):163–172
18. Thomas RG, Furchner JE, London JE, Drake GA, Wilson JS, Richmond CR (1976) Comparative metabolism of radionuclides in mammals—X. Retention of tracer-level cobalt in the mouse, rat, monkey and dog. Health Phys 31(4):323–333
19. Hollins JG, McCullough RS (1971) Radiation dosimetry of internal contamination by inorganic compounds of cobalt: an analysis of cobalt metabolism in rats. Health Phys 21(2):233–246
20. Letoumeau EG, Jack GC, McCullough RS, Hollins JG (1972) The metabolism of cobalt by the normal human male: whole body retention and radiation dosimetry. Health Phys 22:451–459
21. ICRP (1973) Alkaline earth metabolism in adult man. ICRP publication 20. Pergamon Press, Oxford
22. ICRP (1993) Age-dependent doses to members of the public from intake of radionuclides—part 2 ingestion dose coefficients. ICRP publication 67. Ann ICRP 23(3–4)
23. ICRP (1990) Age-dependent doses to members of the public from intake of radionuclides—part 1. ICRP publication 56. Ann ICRP 20(2)
24. ICRP (1995) Age-dependent doses to members of the public from intake of radionuclides—part 3 ingestion dose coefficients. ICRP publication 69. Ann ICRP 25(1)
25. Leggett RW (2013) Biokinetic models for radiocaesium and its progeny. J Radiol Prot 33(1):123–140. https://doi.org/10.1088/0952-4746/33/1/123. Epub 7 Jan 2013
26. Riggs DS (1952) Quantitative aspects of iodine metabolism in man. Pharmacol Rev 4(3):284–370
27. Leggett RW (2010) A physiological systems model for iodine for use in radiation protection. Radiat Res 174(4):496–516
28. Langham WH, Carter RE, Bassett SH, Harris PS (1950) Distribution and excretion of plutonium administered intravenously to man. United States
29. Durbin PW (1972) Plutonium in man: a new look at the old data
30. Heid KR (1983) A comparison of systemic burdens at autopsy to estimates based on health physics data for selected plutonium workers. Health Phys 44(Suppl 1):477–483
31. Ohlenschlaeger L, Schieferdecker H, Schmidt-Martin W (1984) Systemic burden and body burden of Pu in man: comparison of results from bioassay and autopsy. Health Phys 46(4):833–838
32. Voelz GL, Hempelmann LH, Lawrence JNP, Moss WD (1979) A 32-year medical follow-up of Manhattan Project plutonium workers. Health Phys 37(4):445–485
33. Ide HM, Moss WD, Gautier MA (1985) Rapid screening methods for the analysis of Pu or Am in urine. Health Phys 49(5):970–976
34. Jones SR (1985) Derivation and validation of a urinary excretion function for plutonium applicable over tens of years post uptake. Radiat Prot Dosim 11(1):19–27
35. Parkinson WW Jr, Henley LC (1981) A proposed long-term excretion equation for plutonium. Health Phys 40(3):327–331
36. ICRP (1972) The metabolism of compounds of plutonium and other actinides. ICRP publication 19. Pergamon Press, Oxford
37. Poudel D, Guilmette RA, Klumpp JA, Bertelli L, Walters TL (2017) Application of NCRP 156 wound models for the analysis of bioassay data from plutonium wound cases. Health Phys 113(3):209–219

Monte Carlo in Internal Dosimetry

Hemant Kumar Patni and Deepak Kumar Akar

1 Introduction

The Monte Carlo technique gets its name from the Monte Carlo Casino in Monaco city, a city famous for its luxurious casinos [1]. From casinos, one can guess about the inherent randomness expected in this technique. If randomness can be thought of as a part of the problem, this technique can be thought of as providing a solution, which has a statistical convergence to the *actual* solution. The randomness is introduced by probability-based definitions used in the mathematical construction of the problem. The simulations in this technique are like performing experiments on a computer using random numbers. The technique becomes particularly useful when the problems become multidimensional, and taking care of each dimension during solving it becomes too complicated by analytical methods.

Informal use of this method can be found in eighteenth-century experiments by Buffon for the computation of the value of π [2]. The name Monte Carlo technique was coined by Stanislaw Ulam and Nicholas Metropolis [3] while working on the Manhattan Project. Neumann and Ulam with their team used the technique for neutron transport through shielding and weapon related calculations during this project [4]. This application is assumed to be the first application of this technique in its present form and later it has been extended for application in more complicated radiation transport problems. The technique has been considered so powerful that nowadays it is being used in diverse fields to study and predict complex behaviors in their respective domains. Some of the fields where this technique is applied are science, medicine, gaming, finance, energy industry, and many more [5].

H. K. Patni (✉) · D. K. Akar
Internal Dosimetry Section, Radiation Safety Systems Division, Health, Safety and Environment Group, Bhabha Atomic Research Centre, Trombay, Mumbai 400 085, India
e-mail: patnihk@barc.gov.in

D. K. Akar
Homi Bhabha National Institute, Anushakti Nagar, Mumbai 400094, India

D. K. Aswal (ed.), *Handbook on Radiation Environment, Volume 2*,
https://doi.org/10.1007/978-981-97-2799-5_17

2 Basic Mathematics for Monte Carlo Simulations

In Monte Carlo simulations, a probabilistic model for the problem is created using all necessary aspects of the system for solution [6, 7]. Random sampling, with these models and random numbers, is used to simulate the system's behavior. A quantity that can itself be taken as the solution or as an indicator of the solution of the problem is identified and scored in the simulation. The simulations are repeated many times and the mean value of the scored quantity is a representative of the solution for the problem. This means, often known as the sample mean approaches solution or the true value and statistical uncertainty in simulated results decreases following the law of large number and central limit theorem, respectively. The convergence to true results depends on several factors including the description of the physical system by functions to define involved probabilities, coverage of various aspects by random sampling, and computational speeds.

In the case of internal dosimetry, one of the problems under consideration is the computation of energy deposition in the detector or organs of the body. For such problems, the system definition includes the geometry of the system, material composition and distribution, interactions and their probabilities, source distribution, radiation emissions and their probabilities, scoring regions, etc. The random sampling is used for source point generation, emissions, interactions, energy depositions, etc. Total energy deposition in the scoring region for each simulation is scored and its mean is computed. This mean of energy deposition is used for dose computations.

The major components of Monte Carlo methods are described in the next subsections.

2.1 Probability Density and Cumulative Distribution Functions

The first step in solving a problem using the Monte Carlo method is to define it mathematically. One way of thinking it is like creating an experiment to solve a problem. The first step is to identify the areas which are static and the areas where random sampling is possible. The problem itself may have a probability associated with it such as in rolling of a dice the number displayed is probabilistic or the definition introduces probability tactfully, such as the calculation of the area of a circle using the ratio of points falling in a circle when they were generated uniformly in a concentric square. The functions may be discrete or continuous depending on the variable of interest.

For example, in radiation transport the geometries, composition, overall source regions, emission and interaction probabilities, and scoring regions are constant throughout the simulations. However, the initial source point (in a source region or regions), emissions in each decay, and interaction in individual steps are different and must be randomly sampled using a probability model often known as probability

density function (pdf) or cumulative distribution function (cdf). Here the interaction type may take discrete values such as for photon it may be photoelectric or Compton scattering, etc., whereas the path covered before interaction can take continuous values.

Mathematically, let X be a continuous variable such that $x \in (a, b)$. If the probability of x taking a value in a very small region Δx, about x, is $f(x)\ \Delta x$ then $f(x)$ is defined as its pdf. Its cdf is defined as

$$F(x) = \int_a^x f(t)\mathrm{d}t \tag{1}$$

If $x = b$, integration is over the full range and the cdf, $F(x) = 1$, and pdf is said to be normalized. For Monte Carlo simulations pdf must be normalized. If $f(t)$ is not normalized ($F(x) \neq 1$) it can be converted to pdf, by dividing it with $F(x)$.

In the case of discrete variables, the word probability density is replaced by probability (mass functions). The set of values X can take values from set $\{x_i : 0 < i < n\}$, with probabilities $\{f(x_i) : 0 < i < n\}$. Cumulative probabilities can be created as

$$F(x_i) = \sum_{k=1}^{i} f(x_k) \tag{2}$$

$F(x) = 1$ if $i = n$. The set of all possible values of x is known as its sample space (Ω).

Figure 1a shows pdf and cdf for an arbitrary continuous distribution. Figure 1b shows probabilities and their cumulative values for an arbitrary discrete case.

For example, in the continuous case, path length before interaction, for a photon, follows an exponential distribution, $f(t) = \mu e^{-\mu t}$, where μ is the linear attenuation coefficient of the medium and t is the distance traversed before interaction. Then,

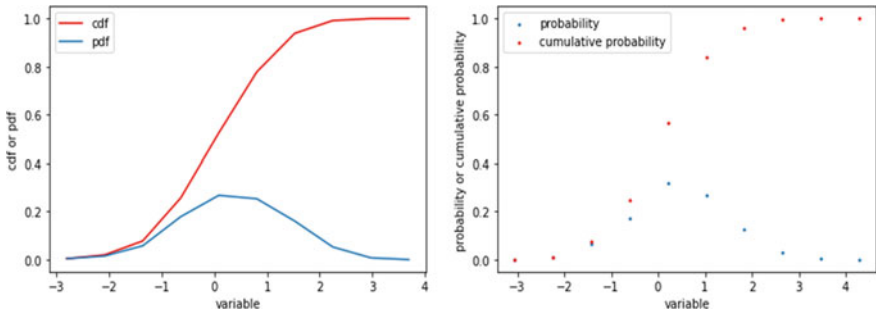

(a) (b)

Fig. 1 **a** Probability density and cumulative distribution functions for continuous variable and **b** probability and cumulative probability for discrete case

cumulative probability or probability of no interaction up to distance x is given by

$$F(x) = \int_0^x \mu e^{-\mu t} \mathrm{d}t = 1 - e^{-\mu x} \tag{3}$$

In the case of photon transport, possible interactions are photoelectric absorption (PA), Compton scattering (CS), and pair production (PP). Then sample space for interactions is taken as [PA, CS, PP]. If linear attenuation coefficients for PA, CS, and PP are μ (PA), μ (CS), and μ (PP) respectively, then the total attenuation coefficient is

$$\mu = \mu(\mathrm{PA}) + \mu(\mathrm{CS}) + \mu(\mathrm{PP}) \tag{4}$$

In case of an interaction, the probability of the interaction to be PA, CS, or PP are

$$f(\mathrm{PA}) = \frac{\mu(\mathrm{PA})}{\mu}, \quad f(\mathrm{CS}) = \frac{\mu(\mathrm{CS})}{\mu}, \quad f(\mathrm{PP}) = \frac{\mu(\mathrm{PP})}{\mu} \tag{5}$$

Cumulative probability of PA (F(PA)) and PA with CS (F(PA+CS)) are

$$F(\mathrm{PA}) = f(\mathrm{PA}) \tag{6a}$$

$$F(\mathrm{PA} + \mathrm{CS}) = f(\mathrm{PA}) + f(\mathrm{CS}) \tag{6b}$$

Cumulative probability including PP is 1 which means interaction has taken place.

Random Numbers

An important feature of the Monte Carlo technique is the use of random numbers for solving problems. They are necessary to cover the sample space as per the probability distribution of the variable involved so that the results obtained using sample space converge to those expected from the population.

Random numbers are sequences of numbers where the next number is independent of previous numbers. Random events such as noise and radioactive decay can be used to get an infinite sequence of random numbers. But these sequences are in general not reproducible and a large memory is required to store them. In simulations, one requires sequences that are reproducible for quality checks and that can be used to study the effect of variation in simulation parameters. These sequences are generated using mathematical algorithms. These algorithms are known as Pseudo-random number generators or random number generators (RNG). They provide sequences of uniformly distributed random numbers, which are real numbers and belong to [0, 1). The sequence of these numbers repeats after a long period (ideally the sequence

never repeats) and passes several tests of randomness related to the uniform distribution and independence of these numbers before their application in Monte Carlo simulations.

The properties of random numbers are as follows:

1. R is a random number which is uniformly distributed between 0 and 1.
2. Probability density $p(R) = 1$ in the range [0, 1), zero otherwise.
3. The cumulative distribution function $P(R)$ is given by,

$$P(R) = \int_0^R p\left(R'\right)\mathrm{d}R' = R. \tag{7}$$

4. They pass several tests devised to check for their independence.

Figure 2 shows pdf and cdf for uniformly distributed random numbers.

The range of random numbers can be expanded to L by multiplying the random numbers with L. The initial and final number can be translated from 0 to the lower bound or 1 to the upper bound of the required range by addition/subtraction. So, if numbers are required in the range $[a, b)$, the lower bound will be **a**, the upper bound will be **b** and the modified range is $(b - a)$. The random number ξ in this $[a, b)$ will be given by

$$\xi = a + (b - a)R \tag{8}$$

In the following sections R will be used for random numbers but in practice, it is converted to ξ before use with probabilities.

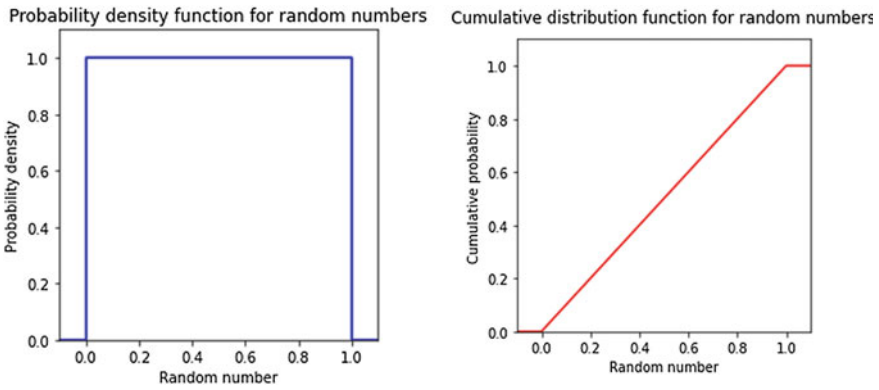

Fig. 2 Probability density and cumulative distribution functions for uniformly distributed random numbers

Random Sampling Techniques

Once pdfs and random numbers are available, they have to be combined so that sample space can be mapped to the solution space. The techniques used for this purpose are known as random sampling techniques. Random variables are used for random sampling of the variables defined by pdfs. These are functions to establish a relation between the sample space and the random (real) numbers. In other words, during sampling, a random number is generated using RNG, and then a random variable uses this number to select a point from the sample space.

The sample space can be sampled adequately only if the random numbers are unbiased, else some parts may be over or under sampled to give erroneous results. The idea is to redistribute the uniformly distributed random numbers as per the pdf. The fundamental techniques for this conversion are inversion and rejection techniques.

Inversion Technique: In this technique cumulative distribution function is used to derive the sample point using random numbers. The steps are as follows:

(i) Create the cumulative distribution function, $F(x)$
(ii) Generate a random number R.
(iii) $x = F^{-1}(R)$.
(iv) Repeat steps (ii) and (iii) to generate multiple histories.

This technique is suitable when the cumulative distribution function is invertible. Here, all the random numbers are used to get values of the variable, so its efficiency is 100%. However, sometimes the inversion is complicated/not possible or time consuming. In such cases rejection technique defined later is used.

Examples:

Discrete case:

Interaction probabilities for photon case are sampled using random number R by following steps,

if $R \leq F(\text{PA})$ interaction is PA.
if $F(P) \leq R < F(\text{PA} + \text{CS})$ interaction is CS.
if $R > F(\text{PC})$ interaction is PP.

Continuous case:

Path length for photon interaction is sampled as

$$R = 1 - e^{-\mu x} \tag{9a}$$

$$x = -\ln \frac{1 - R}{\mu} = -\ln \frac{R}{\mu} \tag{9b}$$

where R is a uniformly distributed random number in range [0, 1). In the last step, R has replaced $1 - R$ using the fact that $1 - R$ also has the same probability of being sampled as R.

Rejection technique: This technique is used to sample from a pdf which may not be easy or feasible to sample from. In such cases, sampling from an approximately

similar function is done using the inversion technique. In the next step, those samples are accepted or rejected based on a comparison with the required distribution.

The steps used in the rejection sampling technique are as follows:

(i) Sample from an approximate distribution to sample from a space that includes the required sample space.
(ii) A constant or equation or function is defined which is used to accept or reject the points sampled in Eq. 1.

Here is an example to illustrate the rejection sampling technique.

Suppose, points in an ellipse having semi-axes as **a** and **b** are to be sampled and this ellipse is centered at the origin. It can be sampled by sampling points in a rectangle with sides 2**a** and 2**b** as Eq. 10, followed by acceptance of points satisfying the Eq. (11) and rejecting other points as follows.

Using Eq. 8, points in a rectangle centered at (0, 0) and sides $2a$, $2b$ are sampled as a combination of x in range $(-a, a)$ and y in range $(-b, b)$ as

$$x = -a + \{a - (-a)\} * R_1 = -a + 2aR_1 \tag{10a}$$

$$y = -b + 2bR_2 \tag{10b}$$

Out of these points, those falling in ellipses will satisfy the following equation:

$$\frac{x^2}{a^2} + \frac{y^2}{b^2} \leq 1 \tag{11}$$

Rejection sampling is a powerful technique for functions that are not invertible or the inversion process is difficult. These are generally not as efficient as inversion, especially if the approximate distribution to the required distribution is very much different. There may be situations where a combination of such techniques is useful. In fact, each rejection sampling uses inversion technique as its first approximation.

The efficiency dependence of the rejection technique on the approximate function can be seen in the following example of sampling points in an ellipse using a rectangle. The equations used for sampling are 10 and 11. The red points are accepted as falling in the area of interest whereas those in green are rejected.

For points in an ellipse of semi-axes length 4 and 3 units can be sampled using a rectangle of sides 8 and 6 units by Eq. 10 and the efficiency is more than 78% as some points fall outside the region of interest Fig. 3a. If the same rectangle is used to sample a circle of radius 3 cm (ellipse with equal semi-axes of length 3 units) the efficiency reduces to less than 59%. The fraction of points falling outside the circle is more as can be seen in Fig. 3b. But if a square (rectangle of all equal sides) of side 6 cm is used for a circle of radius 3 cm the efficiency again reaches about 79%. It has been shown in Fig. 3c. (Although the better way of sampling points in a circle is by inversion technique using polar coordinates results in 100% efficiency.) An approximate function closer to the simulated function gives better results.

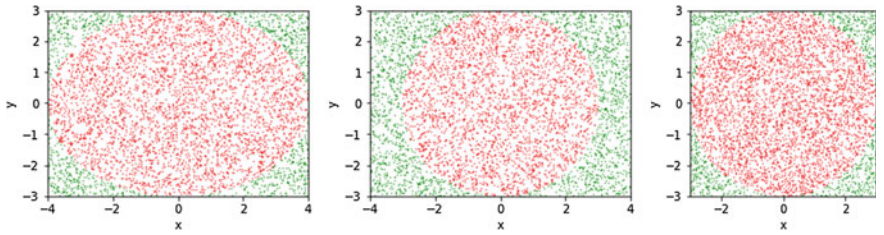

Fig. 3 Rejection sampling of points in **a** ellipse using rectangle as approximate function, **b** circle using rectangle as approximate function, **c** circle using square as approximate function

Law of Large Numbers and Central Limit Theorem

In Monte Carlo simulations, simulations are carried out to estimate a quantity using the sample size much smaller than the population size. Moreover, the problems solved here are multidimensional and involve a number of random variables which follow different distributions. The outcome of the simulations is another random variable whose distribution depends on all the random variables involved in the problem.

The mean of a random variable is an estimator of the population mean

$$E(X) = \overline{X} = \frac{1}{n}\sum_{i=1}^{n} x_i \tag{12}$$

Sample variance, an estimate of the dispersion in values of X about its sample mean, is given by

$$V = \text{var}(X) = s^2 = \frac{1}{(n-1)}\sum_{i=1}^{n}\left(x_i - \overline{X}\right)^2 \tag{13}$$

It can be proved that s is an estimate of standard deviation σ (which can otherwise be estimated by the same formula with n in place of $n-1$ if the true mean is known).

Due to the law of large numbers when several random variables with finite expected values are combined to get the value of a random variable, the mean of this resultant variable tends to be the true value of the variable with an increase in the number of simulations.

For any $\varepsilon > 0$

$$\lim_{n\to\infty} P(\overline{x} - \mu \geq \varepsilon) = 0 \tag{14}$$

Due to the central limit theorem, the resultant distribution is a normal distribution, provided involved functions have finite means and variances. Further, the variance of the resulting estimate of the mean is $\frac{1}{n}$ times the variance of the population

$$\mathrm{Var}(\overline{x}) = \frac{\mathrm{Var}(x)}{n} \tag{15}$$

The square root of this quantity is the variance of the mean which decreases as $\frac{1}{\sqrt{n}}$, n being the number of histories, the number of times simulations were repeated.

Variation Reduction Techniques

The convergence to a mean value requires the standard deviation of the mean to be small. In Monte Carlo simulations the standard deviation of the mean decreases by $\frac{1}{\sqrt{n}}$, whereas the time in simulations increases as *n*. Reduction in standard deviation of mean by a factor of 10 requires time to be increased by 100 times. This slow convergence is a drawback of the Monte Carlo technique. The improvement of efficiency is a major challenge during simulations.

There are several techniques used to improve convergence, which is known as variance reduction techniques. These rely on the prior information about the expected behavior of the simulations. Most important of these are biased sampling such as importance sampling, stratified sampling, and splitting with the use of Russian roulette.

3 Radiation Transport and Estimators

Radiation Transport

In the case of internal dosimetry, energy deposition in different parts of the human body or detector is solved using Monte Carlo simulations. The estimation is done using radiation transport [8] which uses the following steps:

I. Inputs about the system required for the simulation:
   1. The geometry of the system: The definition of the physical system such as the structure and composition of the human body, shielding, and detector the first step in the estimation of required quantities.
   2. Source description: This includes the distribution of radioactive sources in the geometry such as the human body or organs, description of radiations emitted by the source.
   3. Description of transport parameters: This includes types of definition of interactions for the radiation emitted from the source or generated during interactions, their probabilities, cross sections, cut-off energies, etc. for all the material in the geometry.

II. Simulation of emissions and interactions:
   1. Initiate a history by selecting a source point (randomly if an extended source is simulated).

2. Assign the radiation, energy, and direction to the emission as per the source description.
3. Determine the interaction path length, type of interaction, energy deposition, new direction, and secondary particles generated during interaction, using cross sections and random numbers.
4. Record the quantities of interest such as energy deposition in different regions at each interaction.
5. Continue the transport of particles in history until the particle energy falls below the cut-off or it escapes the region of interest.

III. Scoring the response

1. The quantities recorded in history are averaged to get their mean values.
2. The simulations are continued for a large number of histories for convergence of the mean value as per the law of large numbers.
3. The standard deviation of the mean (indicator of simulation error) reduces as $\frac{1}{\sqrt{n}}$ where n is the number of histories as per the central limit theorem.

Estimators

In Monte Carlo transport, particles are tracked through the problem geometry as expected by physical processes. In such simulations, detector scoring is done separately after storing event data from the particle random walk. However, with advances in computer technology and available algorithms, detector scoring estimations are now performed simultaneously with the random walk calculation using estimators. In radiation transport, these mathematical techniques are used to score quantities such as flux, dose, reaction rates, and other important parameters.

Here are a few commonly used estimators [8] in radiation transport:

1. Track-Length Estimator: This estimator records the total track length of particle tracks within a specified region of interest. The number of tracks with volume and interaction cross section can be used to estimate flux, collision rates, and energy deposition in a region.
2. Collision Estimator: This estimator counts the number of particle collisions within a specific region of interest. It can be used for interaction rates between particles and material.
3. Energy Deposition Estimator: This estimator is used to compute energy deposited at different points.
4. Flux Estimator: The flux estimator can be used to find the number of particles crossing between different surfaces.
5. Angular Distribution Estimator: This estimator is used for the angular distribution of particles.
6. Reaction Rate Estimators: These can be used to estimate interaction probabilities in different parts of the system.

Many other estimators can be devised to compute different quantities during radiation transport simulations. More than one estimator can be used to get the same quantity, it depends on the user how he wants to approach the problem.

4 Monte Carlo Transport Codes

Many Monte Carlo codes are readily available for users to apply their radiation transport problems. Many man-hours have been invested to make them efficient and produce accurate results. These codes use different estimators in an optimized manner so that the user gets results with the required precision in a smaller amount of time. Most of them have provisions to implement the variance reduction techniques to further increase the efficiency of the simulations. The codes try to use the latest cross-sectional data available at a point in time. Each of these codes was initiated for some set of problems but now they are versatile enough to solve the problems of different domains. Over time they have developed their user communities which help the users to solve their problems in different steps of radiation transport. Most of the codes have been used for internal dosimetry problems also. A selected number of codes most wildly used as listed below.

Monte Carlo codes such as FLUKA [9–12], Geant4 [13], MCNP [14], PenEasy [15], TRIPOLI-4 [16], etc. have been utilized for estimating S-values, absorbed dose calculations, efficiency estimation of monitoring systems and in various other applications. All these codes allow for energy deposition studies for monoenergetic single-particle transport. Apart from those emissions by different radionuclides such as ^{18}F, ^{89}Zr, ^{153}Sm, ^{177}Lu, and ^{125}I can also be simulated. Most of the codes can simulate complete decay chains of the radionuclide in a simulation. Advanced users of the codes can simulate a mix of particles, radionuclide, and their emissions. They can be used with different types of phantoms having different types of geometrical distributions and compositions. The measurements of these values are not directly possible through experimental measurements. In such cases, Monte Carlo simulations provide researchers and practitioners with fast, precise, and user-friendly solutions applicable in diverse fields such as radiation protection, environmental releases, and medicine.

EGSnrc

EGSnrc [17] released in 2000 was a complete overhaul of the Electron Gamma Shower (EGS) software package originally developed at the Stanford Linear Accelerator Center (SLAC) in the 1970s. It models the propagation of photons, electrons, and positrons with kinetic energies between 1 keV and 10 GeV, in homogeneous materials. EGSnrc provides user-friendly interfaces for dosimetric applications, such as BEAMnrc (for external beams) and DOSXYZnrc (for treatment scenarios both beam and brachytherapy), which simplify the setup and execution of simulations for specific applications.

FLUKA

FLUKA code [9–12], developed in INFN and CERN collaboration is useful for radiation transport in applications ranging from accelerator shielding to radiotherapy. It can simulate over 60 particles, including photons, electrons, neutrinos, muons, hadrons, and heavy ions, covering a wide energy range. It uses the EPDL97 library for cross sections. It can handle complex geometries and supports polarized and optical photons in different fields. Flair is its user-friendly interface to run the simulations, visualization, and debugging. It can also be used for different internal and external source distributions including voxel geometries.

Geant4

Geant4 or GEometry ANd Tracking code [13] is a toolkit for the simulation of the passage of particles through matter. Its areas of application include high energy, nuclear and accelerator physics, as well as studies in medical and space science. It requires basic knowledge of C++ to implement different physical models complex geometries and user-specific parameters. Geant4 uses cross-sectional libraries, which are based on evaluated nuclear data files obtained from external sources such as Evaluated Nuclear Data File/B (ENDF/B), Japanese Evaluated Nuclear Data Library (JENDL), and others. Usage of Geant4 requires comprehensive training for optimum utilization of its capabilities. Nowadays scripting in Python is also supported for the code. Its interface with ROOT can be used to store the data generated during simulations for solutions afterward. Based on it following two codes were developed for medical applications. These are listed below.

4.1 GATE

Geant4 Application for Tomographic Emission (GATE) [18] is an advanced open-source software based on Geant4, developed by the international OpenGate collaboration for numerical simulations in medical imaging and radiotherapy such as Emission Tomography (**P**ositron **E**mission **T**omography and **S**ingle **P**hoton **E**mission **C**omputed **T**omography), Computed Tomography (CT), Optical Imaging (Bioluminescence and Fluorescence) and radiotherapy experiments. It has an easy-to-learn macro mechanism to make experimental settings due to which it is used for designing new imaging devices, optimization of acquisition protocols, and development of image reconstruction algorithms.

4.2 GAMOS

GAMOS (GEANT4-based Architecture for Medicine-Oriented Simulations) [19] is also GEANT4-based framework but it is easy-to-use and flexible for modifications.

The plug-in technology together with a careful modular design, detailed documentation, and a set of examples and tutorials that explain in detail how to extend the framework in different directions allows to exploit the full flexibility of GEANT4, by creating new user code or by reusing any piece of GEANT4 code and mixing it seamlessly with the existing GAMOS components. Due to its flexibility 2500 GAMOS users work in other fields than medical physics.

MCNP

The MCNP (Monte Carlo N-Particle) [14] code is a powerful tool for simulating the transport and interaction of particles, including neutrons, photons, electrons, ions, etc. It employs a three-dimensional representation of materials in a constructive solid geometry, utilizing user-defined surfaces to define boundaries. Tabulated nuclear and atomic data or physics models are used to simulate the physics during particle transport, accounting for various reaction channels and secondary-particle production mechanisms. Mcplib84 cross-sectional data is used for simulations. Different particle types, such as neutrons, photons, electrons/positrons, and ions, have specific models for scattering, absorption, and secondary-particle production. Pseudo-random numbers are used to sample pdfs, ensuring independent and statistically significant results. The code offers a wide range of tallies for tracking events, including flux, heating, radiography, and perturbation/sensitivity. MCNP is widely used in radiation protection, dosimetry, shielding, medical physics, and many other applications. It supports various operating systems and parallel execution and provides extensive cross-sectional data.

PenEasy

PenEasy [15] based on Penelope code performs Monte Carlo simulations of coupled electron-photon transport in different materials for a few hundred eV to about 1 GeV energies. Photon transport is simulated by means of the standard, detailed simulation scheme.

Tripoli-4

Tripoli-4 [16], code was developed by the Radiation Safety Information Computational Center (RSICC) at Oak Ridge National Laboratory. It has been used for radiation transport calculations in different scenarios including in the field of internal dosimetry calculations by voxel phantoms. The code uses the ENDL-97 library for cross sections.

5 Computational Phantoms

Computational phantoms are mathematical representations of the human body. These phantoms are also known as virtual human models. They are an integral part of computational dosimetry. These phantoms are used for calculations that are particularly challenging to determine directly from experimental data or measurements.

By employing computational phantoms, researchers can simulate the interaction of radiation with the human body's tissues and organs, allowing for accurate estimation of dose distribution. They are used as a computational tool in external and internal dosimetry. Additionally, computational phantoms can be customized to account for specific scenarios or populations of interest. For example, phantoms representing pregnant women and developing fetuses allow for the assessment of radiation exposure and associated risks during pregnancy. These specialized phantoms incorporate anatomical changes and physiological considerations unique to the population, facilitating more accurate dose estimations and informed decision-making. In internal dosimetry, sources of radiation are situated within the human body, making it impractical and ethically unfeasible to measure doses directly. Here, computational phantoms serve as valuable substitutes. There are three variations of computational phantoms, which are described in the following subsections.

Stylized Phantoms

The development of stylized phantoms by Oak Ridge National Laboratory (ORNL) was initially driven by the need for accurate estimations of internal radiation doses within the Medical Internal Radiation Dose (MIRD) Committee of the Society of Nuclear Medicine. Therefore, stylized phantoms are also known as MIRD phantoms. These phantoms serve as representations of the human body's organs, albeit in an idealized manner, allowing for precise calculations and analyses. Mathematical expressions were ingeniously utilized to portray a range of shapes, including cylinders, cones, ellipsoids, and spheres, providing a versatile framework for modeling different organ structures and geometries [20]. The structure of the MIRD phantom in Geant4 is as shown in Fig. 4. The pioneering adult-stylized phantom served as the foundation for subsequent advancements, leading to the development of several pediatric phantoms tailored to represent infants and children across various age groups [21]. Recognizing the significance of encompassing the unique physiological characteristics of pregnant females and their developing fetuses, the ICRP also incorporated specialized models developed at ORNL into their studies [22]. These models facilitate a more accurate estimation of radiation doses during pregnancy, accounting for the dynamic changes and considerations specific to this population.

Although these phantoms may exhibit noticeable dissimilarities compared to real human beings, they offer distinct advantages for their intended purposes. Notably, they are gender-neutral, eliminating the need for separate male and female models. Additionally, they are designed based on the organ masses and volumes specified in the Reference Man publication by the International Commission on Radiological Protection [23], ensuring consistency and standardization in dose calculations.

Overall, the stylized phantoms developed by ORNL and utilized by the ICRP represent a substantial advancement in radiation dosimetry. Through their mathematical representation of organs and their adaptability to various age groups and pregnancy scenarios, these phantoms play a crucial role in providing reliable and standardized data for assessing radiation risks and implementing effective protection strategies.

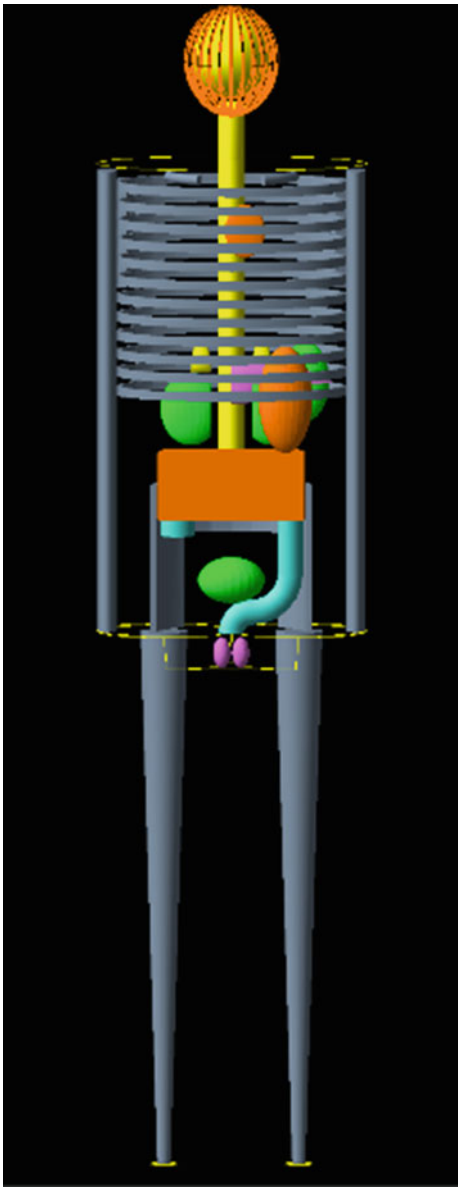

Fig. 4 MIRD phantom as seen in Geant4

Voxel Phantoms

Voxel phantoms are developed from CT/MRI scan data and digital photographs of real human body. Utilizing the picture elements (pixels) with the thickness of the scan, the volume elements (Voxels) are developed. The identification of each voxel with an organ is known as segmentation. A medical team helps in the process of

segmentation. Finally, a voxel phantom may have millions of voxels with each voxel belonging to an organ. There are several voxel phantoms being used around the globe. Out of them, the one adopted by ICRP [24] is the reference adult male and female models which were developed using voxel phantoms created at Helmholtz Zentrum [25, 26]. In order to minimize the need for modifications, individuals with dimensions as close as possible to the reference [27] were chosen as the basis for these models. The voxel-based approach resulted in a significant level of detail, with the male model utilizing approximately 2 million voxels and the female model using around 4 million. Despite the very good resolution, these models still have limitations in adequately delineating all-important tissues for various applications. The rightmost picture in Fig. 5 is the ICRP reference adult male voxel phantom as seen in FLUKA.

Like the adult phantoms, the reference pediatric phantoms [28] were developed using medical imaging data from actual individuals, which were carefully modified to align with the established reference parameters. However, instead of directly representing the organs and tissues with voxel data, the digital information was utilized to create surfaces that incorporated as much intricate detail as possible, drawing from anatomical knowledge. These models were then voxelized at an exceptionally high resolution, considering the age-dependent variations in total skin thickness, in order to preserve the richness of anatomical detail. With the advancements in computer hardware and powerful computational codes available today, these high-resolution

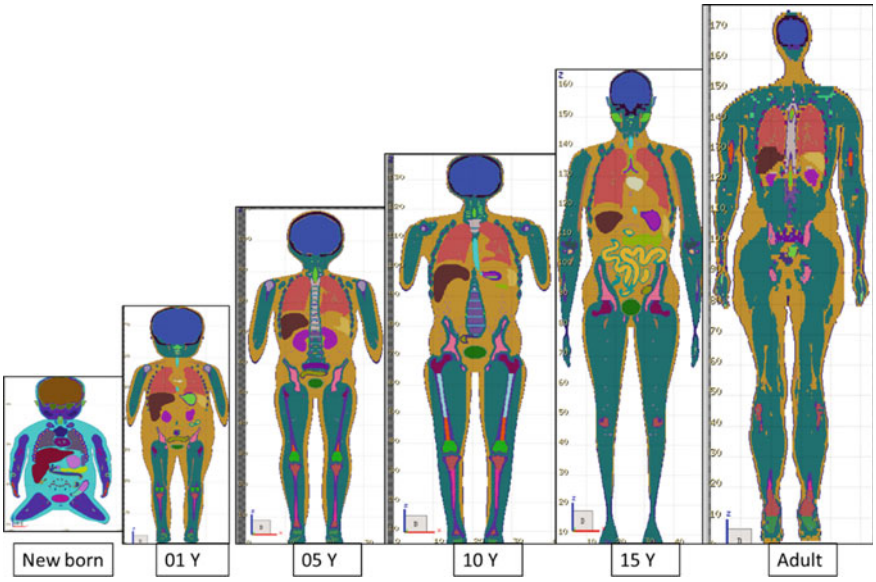

Fig. 5 ICRP pediatric and adult male voxel phantoms incorporated in FLUKA and visualized from flair

voxel phantoms have become practical for calculating doses and other quantities. ICRP reference pediatric computational phantoms are shown in Fig. 5.

Mesh Phantoms

Compared to the older stylized phantoms, the voxel phantoms offer improved anatomical realism regarding internal anatomy. However, they do have limitations primarily related to voxel resolution, particularly when it comes to small tissue structures and very thin tissue layers. To address these limitations mesh phantoms were developed [29]. In mesh phantom, the human body is represented by polygon mesh/tetrahedron mesh of varying sizes. These phantoms encompass all the necessary regions of the human body, including even the micrometer-thick regions within respiratory and alimentary tract organs, skin, and urinary bladder. ICRP adopted the adult mesh-type reference computational phantoms (MRCPs). The MRCPs enable seamless implementation into Monte Carlo particle transport for dose calculations, maintaining the advantages of mesh geometry without the need for voxelization. ICRP reference mesh-type computational phantoms with polygon mesh viewed using Freecad [30] are shown in Fig. 6. Figure also shows its internal organs as drawn in Geant4.

These phantoms can be modified into customized (non-reference) phantoms. These customized phantoms can be used to calculate person-specific dose coefficients and other radiation protection quantities. These calculations allow for estimating organ doses in the event of accidental exposure among workers as well as the public, considering the body size of the exposed individual. Furthermore, the mesh phantoms can be transformed into phantoms representing different postures, including walking, sitting, bending, kneeling, and squatting. These transformed phantoms can be employed to assess variations in various radiation protection quantities compared to the traditional upright standing position.

Comparison of Computational Phantoms

Each phantom has its own advantages, suitability, and complications depending on the specific requirements of the simulation study. The stylized phantom offers simplicity and efficiency, while voxel and mesh phantoms provide more accurate anatomical representations at the expense of increased computational complexity. Researchers should consider the trade-offs between required accuracy, available computational resources, and simulation time while choosing phantom for their applications. Table 1 compares all the above-mentioned phantom categories for their characteristics and applications.

Random sampling in these phantoms requires different schemes. Random sampling of radiation in an organ/tissue of MIRD or stylized phantom requires sampling within some mathematical shapes. Either inversion or rejection technique can be used for this purpose. Random sampling within an organ or tissue of a voxel phantom is a bit more complex. Due to the irregular shape of the organs in voxel phantoms, it requires the selection of voxels of an organ first. After that, it is as simple as sampling in a cuboid. The rejection technique of sampling within a regular mathematical shape and only the selection of points belonging to an organ voxel point can

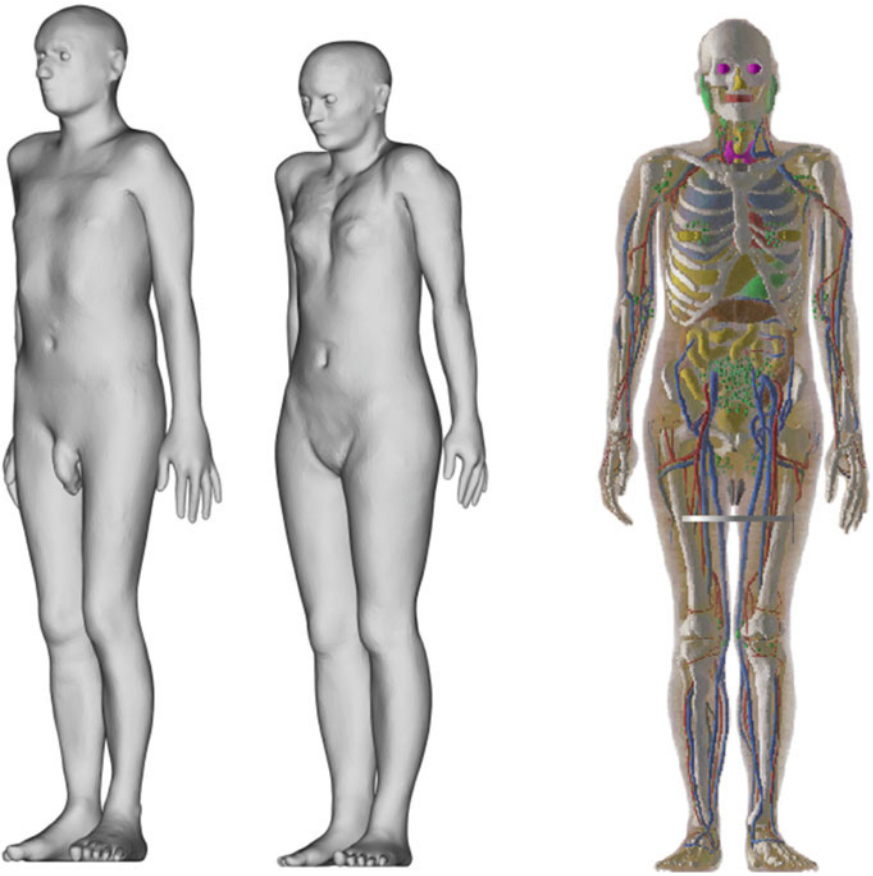

Fig. 6 ICRP Mesh type reference computational male and female phantoms viewed using Freecad and Geant4

Table 1 Comparison of computational phantoms

Phantom category	Characteristics	Applications
Stylized phantom	Assumes homogeneous distributions within organs Simplifies simulation process Limited anatomical detail	Efficient for simpler simulations Suitable for dose estimation studies
Voxel phantom	Represents anatomy using three-dimensional grids (voxels) Captures anatomical heterogeneity More accurate geometry representation	Accurate dose calculation in complex anatomies Radiation therapy planning
Mesh phantom	Utilizes surface-based representation with interconnected triangles or polygons Balances between accuracy and computational efficiency	Detailed anatomical modeling Radiation transport studies Image-based simulations

also be used as a sampling technique in voxel phantoms. For random sampling in mesh phantom, tetrahedron or polygon mesh elements belonging to an organ can be utilized. Due to the very large number of mesh elements, internal organ simulations are very computationally intensive and require workstations for simulations.

6 Applications of Monte Carlo in Radiation Protection of Internal Dosimetry

Radiation protection in internal dosimetry deals with the protection of workers from ionizing radiation emitting radionuclides going into worker's body. Since for radiation protection in internal dosimetry, we need to quantify radioactivity present in the human body and dose to various human organs, they require human body representation. For utilization of the Monte Carlo method, computational phantoms are used as a representation of the human body. Monte Carlo simulations are used to estimate the counting efficiency (CE) of various in-vivo monitoring systems [31]. They are also used to estimate various dosimetric quantities like absorbed dose, *S*-values, etc. [32]. Intercomparison exercises involving computation phantoms are also carried out internationally [33]. There are applications of Monte Carlo simulation to estimate uncertainties in biokinetic and dosimetric quantities which may not require computational phantoms [34]. All these applications of Monte Carlo for radiation protection of internal dosimetry are provided in the following subsections.

Estimating CE of In-Vivo Monitors

In-vivo or direct monitoring systems are used to identify and quantify the amount of radioactivity present in a person's body. They employ photon detectors/spectrometers and detect the photon emission from the human body. To quantify radioactivity present in the human body computational phantoms are used. Monte Carlo simulations to estimate the CE of these monitors involve source sampling in computational phantoms. In addition to this, the geometry of in-vivo monitoring system is also simulated. The monitoring system and phantom are simulated to match with actual monitoring geometry. Some monitoring systems involve the movement of a person or detector. This relative movement can be simulated by averaging the response of the detector at many static positions. Using Monte Carlo simulations CE can be estimated for various radioactive isotopes concentrated in different organs or distributed in the entire body. Researches have done assessments of radionuclides like ^{131}I in the thyroid, ^{241}Am in the skull, enriched U in the lungs, whole-body distribution of ^{137}Cs, etc. [35–41]. Figure 7 shows experimental and simulated spectra for ^{137}Cs in the BOMAB phantom [35].

Any validated Monte Carlo study offers a very effective and cost-efficient approach to derive CE for specific scenarios. Generally, validation of Monte Carlo

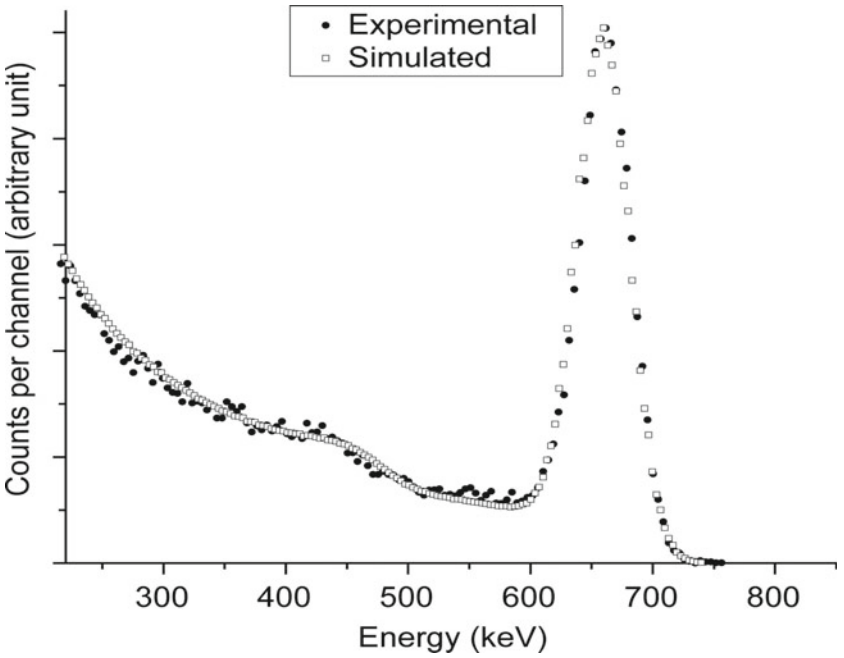

Fig. 7 Experimental and simulated spectra for ^{137}Cs in BOMAB phantom (reproduced from [35] © 2013 Oxford University Press, with permission from Oxford University)

simulation for CE estimation involves using a mathematical form of physical phantoms. Researchers have used the mathematical form of BOMAB and LLNL phantoms to do validation of their simulation with experiments in their labs using the same phantom and monitoring system geometry. Once validated, it can be used for other geometries and radionuclides. Since these simulations completely replicate actual experiments, they are very effective in estimating CE. This method of CE calculation is not only highly accurate but also economical. They remove the need for creating physical phantoms having various radionuclides other than standards. Researchers have also used simulations to represent non-standard biokinetic distributions, which are not possible/very costly with physical phantoms. Figure 8 shows the CE vs photon energy of shadow shield whole-body monitor for source uniformly distributed in adult male voxel phantom. The monitoring systems used in figure incorporate 5-inch diameter and 3-inch thick NaI (Tl) detector. Validation for simulation of this system was done with the experiments carried out in the same system with Indian reference BOMAB phantom.

Simulations enable radiation safety personnel to obtain reliable and trustworthy results when assessing and monitoring radioisotopes in specific organs or conducting whole-body measurements. By ensuring that CE is properly accounted for, the monitoring system can provide accurate data regarding the presence and concentration of radioactive isotopes. This leads to enhanced radiation management practice.

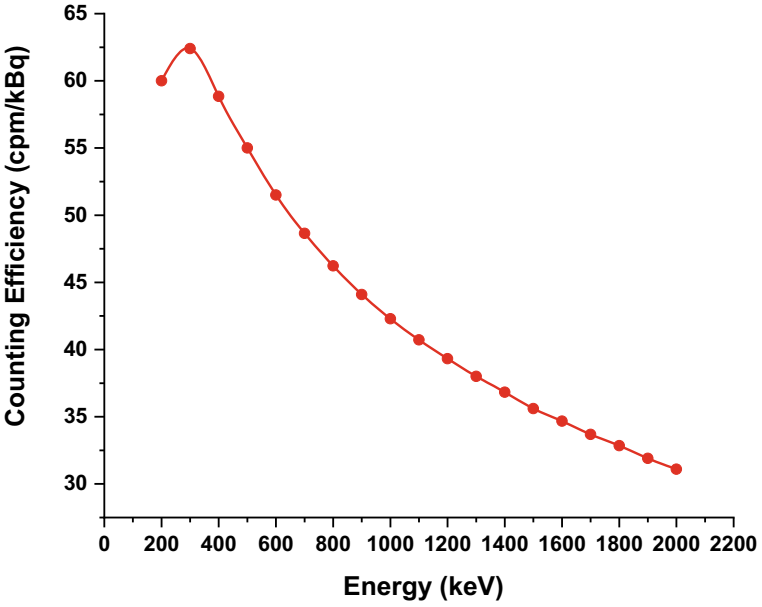

Fig. 8 CE versus photon energy of shadow shield whole-body monitor (5-inch diameter and 3-inch thick NaI(Tl) detector) for source uniformly distributed in adult male voxel phantom

Computation of Dosimetric Quantities

Estimating the radiation dosimetry quantities like absorbed dose, S-values (which represent the absorbed dose per unit activity in different target tissues), etc. is not possible without Monte Carlo simulations. For estimating these quantities due to internal contamination, radiation sources are sampled inside organs/tissues of computational phantoms. After that radiation transport from sources up to other organs is carried out. Energy deposited in the organs or particle fluence is used to then compute the required dosimetric quantities. For example, to compute the absorbed dose in an organ, the energy deposited is divided by the mass of the organ. For dose estimation in skeletal tissues due to photons and neutrons in voxel phantoms, fluence in conjunction with some pre-estimated response functions are used.

Dosimetric quantities can be estimated for monoenergetic radiations including photons, electrons, neutrons, etc. and a variety of radiopharmaceuticals such as $^{223}RaCl_2$ [42], ^{18}F-FDG, and ^{131}I, etc. [32]. Computational phantoms, with their ability to replicate individualized anatomical features, facilitate the calculation of organ-specific dosimetric quantities. Since dosimetric quantities form the basis for radiation protection, Monte Carlo simulations play a very important role here. Figure 9 shows the *S*-values for various target organs due to uniform distribution of ^{131}I in the liver of ICRP reference male voxel phantoms [28] for pediatric age groups of newborn, 1, 5, 10, and 15 years.

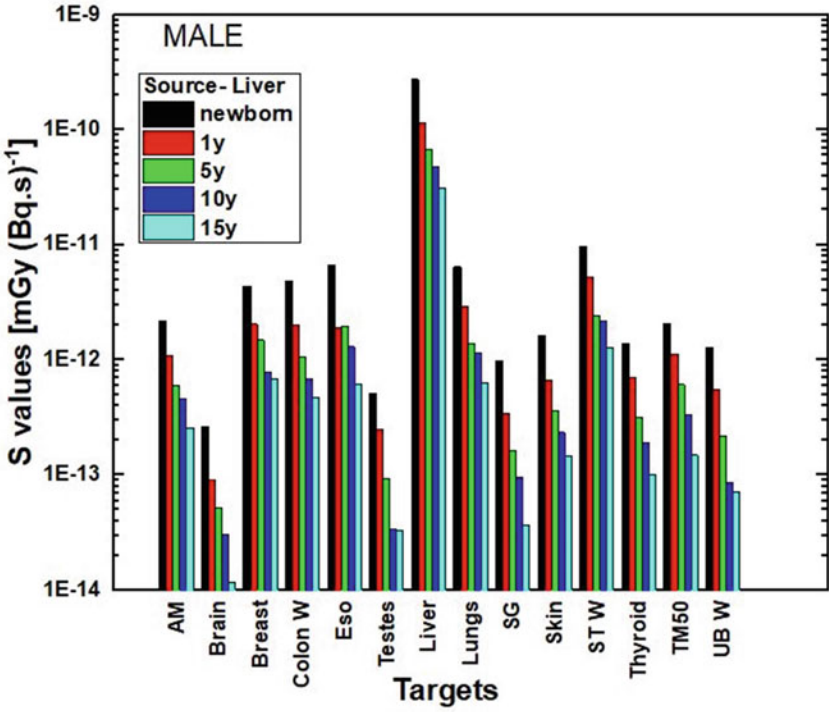

Fig. 9 *S*-values for various target organs due to uniform distribution of ^{131}I in the liver of ICRP reference male voxel phantoms for pediatric age groups of newborn, 1, 5, 10, and 15 years

Intercomparison Exercise

We have seen that dosimetric quantities and CE are two categories of quantities, estimated using Monte Carlo simulation application in radiation protection of internal dosimetry. Intercomparison exercises provide a valuable platform for evaluating and improving the accuracy of various radiation dosimetry parameters. Therefore, intercomparison exercises are carried out for quality assurance of these. By comparing the results obtained from different laboratories, these exercises help to identify any discrepancies and improve the overall consistency and reliability.

The research work published recently has utilized ICRP voxel phantoms as a common practice in these exercises. In one specific exercise, the activities of ^{241}Am in three different skull phantoms were investigated. This exercise aimed to evaluate the accuracy of measuring and quantifying the ^{241}Am activities in these specific anatomical structures. The results obtained from this exercise contribute to the improvement of calibration procedures and measurement techniques for skull phantoms [43], enhancing the reliability of dose assessments in this region of the body. Another collection of work was on the application of ICRP voxel phantoms to estimate SAF values for monoenergetic photons and electrons [44]. It also included the

estimation of *S*-values for ^{99m}Tc and ^{18}F for various source-target pairs. This exercise also tested the labs for their specific method used for the estimation of skeletal doses. Users have used various Monte Carlo codes like EGSnrc [17], FLUKA [9–12], Geant4 [13], MCNP [14], etc. for carrying out their simulations. Standardizing organ dose estimation can help in both the correct incorporation of these phantoms and the correct computation of dosimetric quantities.

Overall, the intercomparison exercises serve as an essential tool for quality assurance in radiation dosimetry. By participating in these exercises, laboratories can identify areas for improvement, enhance their computational techniques, and ensure the accuracy and traceability of their dose estimations. This continuous quality assurance process ultimately leads to improved radiation protection practices and a higher level of confidence in radiation dose assessments.

Uncertainty Analysis

Uncertainties in internal dose arise from several sources, including variations in the biokinetic models used to describe the intake and uptake, distribution, and elimination of these radionuclides within the body. Additionally, uncertainties in the *S*-values can significantly affect the accuracy of internal dose calculations. One crucial aspect of addressing these uncertainties is to identify the parameters that have a substantial influence on the internal dose estimates. Sensitivity analysis plays a vital role in this process by determining the parameters that have the greatest impact on the calculated doses. By identifying these sensitive parameters, researchers can focus their efforts on reducing the associated uncertainties and improving the accuracy of the dose assessments.

Recently published works have estimated uncertainty in doses resulting from exposure to radionuclides such as ^{141}Ce, ^{144}Ce, ^{131}I, etc. [34, 45–48]. The observed variations in the geometric standard deviation (GSD) ranging from 1.1 to 3.9 in one such study highlight the importance of considering anatomical variability in internal dose calculations. Accounting for this variability is crucial to capture the individual anatomical characteristics and improve the accuracy of internal dose calculations. By identifying the sensitive parameters and incorporating anatomical variability, researchers can enhance our understanding of the radiation dose received by specific tissues or organs, contributing to improved radiation safety practices and better-informed decision-making in radiation protection.

7 Medical Applications of Monte Carlo Simulations for Internal Dosimetry

Since internal sources are used a lot for diagnostic and therapeutic purposes, so Monte Carlo is also applied in medical applications. This branch of medicine is known as nuclear medicine. Medical application is related to the protection of patients. Unlike

radiation protection, where the linear no threshold (LNT) hypothesis is used to minimize stochastic effects, patient protection has different concerns. Here identification of life-threatening tumors is the diagnostic purpose. The purpose of therapy is to maximize the dose to the tumor and minimize doses in other organs. Internal radiation protection is for cases where there is a chance of internal contamination of low radioactivity. Medical applications use internal contamination deliberately with very high radioactivity. Another difference from radiation protection is the level of dose accuracy required is much more in medical applications, as it is not based on some hypothesis and judgment. The prime concern is patient safety in medical applications. The best tool in such situations is very accurate simulations with can represent the patient itself. In many situations, specific organs are to be targeted, so instead of using radionuclides, they are tagged with pharmaceuticals. These radiopharmaceuticals form the backbone of nuclear medicine. This section will describe the application of Monte Carlo simulations for patient-specific dosimetry and radioembolization. Since dose estimates are quickly required, so lot of tools are used in patient dosimetry. This section also includes a discussion on these tools and applications of artificial intelligence (AI) in patient dosimetry.

Monte Carlo as Gold Standard for Patient-Specific Dosimetry

Monte Carlo simulations have emerged as the gold standard in nuclear medicine for accurately estimating radiation doses to patients [49]. These simulations utilize sophisticated mathematical models to simulate the interactions between radiation and human tissues, providing detailed insights into the distribution and deposition of radiation within the body. As an initial step, state-of-the-art imaging technologies such as SPECT/CT (Single Photon Emission Computed Tomography/Computed Tomography) using radiotracers like ^{99m}Tc, and PET/CT (Positron Emission Tomography/Computed Tomography) using radiotracers like ^{18}F, physicians can obtain comprehensive anatomical and functional information about patients. These imaging techniques enhance the accuracy of dose estimation by creating person-specific phantoms from these imaging techniques. These imaging techniques also allow for the precise localization of radiopharmaceuticals within specific organs, tissues, and tumors. By integrating patient-specific data, such as organ size, shape, and uptake of the radiotracer, into the phantom, the simulations can generate personalized dose calculations. These phantoms are based on individual patient characteristics and information about the biodistribution of radiopharmaceuticals inside that individual is also incorporated. Figure 10 (a) axial, (b) sagittal, and (c) coronal projections of the fusion of a CT slice and ^{18}F-Choline PET image. (d) Axial, (e) sagittal, and (f) coronal projections of the absorbed dose rate map as resulting from MC simulations [50].

Isotopes like ^{90}Y, ^{131}I [51], ^{177}Lu [52], etc. are utilized for their specific radiobiological properties and ability to deliver targeted radiation therapy. By incorporating these isotopes into the Monte Carlo simulations, researchers can accurately assess the radiation doses delivered to the cancerous tissues. This provides valuable information for treatment planning and optimizing therapeutic outcomes. This integration of imaging data, Monte Carlo simulations, and person-specific phantoms has revolutionized the field of nuclear medicine by enabling more precise and personalized

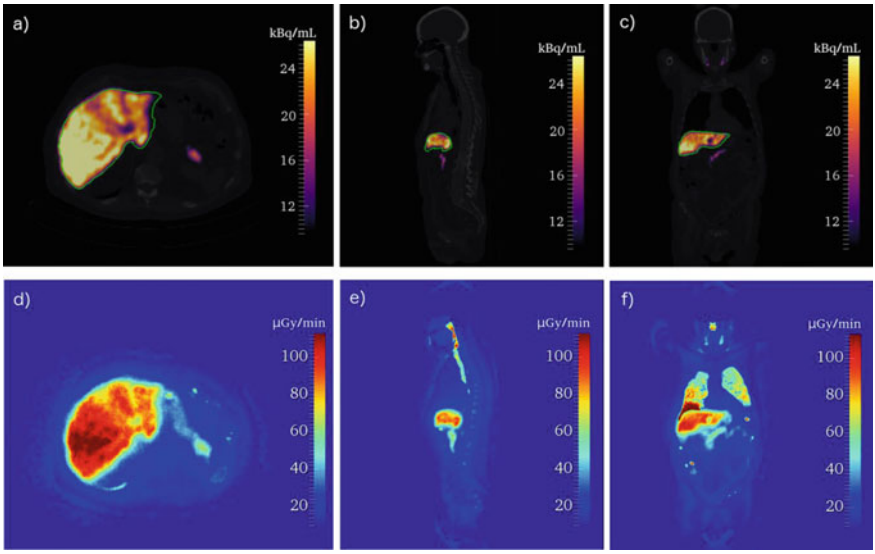

Fig. 10 **a** Axial, **b** sagittal, and **c** coronal projections of the fusion of a CT slice and 18F-Choline PET image. **d** Axial, **e** sagittal, and **f** coronal projections of the absorbed dose rate map as resulting from MC simulations (reproduced from [50] under the terms of Creative Commons Attribution 3.0 licence)

dose estimation. This approach enhances patient safety by ensuring that radiation doses are tailored to individual characteristics, minimizing potential side effects, and optimizing therapeutic efficacy. Through ongoing research and quality assurance exercises, the accuracy and reliability of these techniques are continuously improved.

Radioembolization

Embolization is a process of stopping the flow of blood to tumor cell by using particles. Embolization of liver tumors employs ^{90}Y microspheres. Because of the radioactive nature of ^{90}Y, this process is known as radio-embolization. Radioembolization is the preferred technique for the treatment of otherwise incurable liver cancers. A lot of research work is going on for the upgradation of radio-embolization [53]. This technique involves delivering tiny radioactive spheres directly into the blood vessels supplying the tumor, thereby selectively irradiating the tumor while minimizing damage to healthy tissues. To optimize the treatment, various software are utilized to incorporate tomographic images of the patient's liver into Monte Carlo simulations. By accurately modeling the patient-specific anatomy and dosimetry, these simulations enable the optimization of radiation dose delivery to the liver tumor and surrounding tissues, ensuring effective treatment while minimizing the potential for adverse effects. This integration of advanced imaging and Monte Carlo simulation techniques offers a precise and personalized approach to liver tumor embolization therapy.

Development and Validation of Tools

Researchers have been actively involved in the development and validation of various tools [54] for patient-specific dose estimation. These tools, such as DOSIS [55], RAPID [56], MCID [57], irtGPUMCD [58], etc., play a crucial role in accurately estimating dose values in medicine. These tools incorporate advanced algorithms and techniques to calculate Specific absorbed fractions (SAF) and/or *S*-values, allowing for precise estimations of radiation doses to specific organs and tissues. To ensure the reliability and accuracy of these tools, extensive validation is conducted using standard software like OLINDA or reference values [59]. The aim is to establish their consistency with established benchmarks and validate their performance in real-world scenarios. Most of these standards are based on Monte Carlo simulations. These tools are designed to be fast, precise, and user-friendly, enabling practitioners to efficiently estimate patient-specific doses for a wide range of applications. These tools make it easy for operators to compute patient organ doses without much knowledge of image processing. The application of tools validated with Monte Carlo simulations is making patient dosimetry easier, efficient, and simpler.

AI Applications

AI tools have revolutionized the field of dosimetry by providing advanced solutions for accurate and efficient dose estimation [60]. One prominent development is the utilization of convolutional neural network (CNN) based dosimetry methods [61], which leverage deep learning algorithms to analyze SPECT/CT or PET/CT scans of previous patients. These AI models are trained on large datasets, enabling them to learn complex patterns and relationships between imaging features and radiation doses. By extracting relevant information from the scans, the models can predict radiation doses in specific organs with remarkable precision. To optimize the computational performance of these AI models, Graphics processing unit (GPU) acceleration techniques are employed. GPUs are highly parallel processors that significantly speed up the training and inference processes, allowing for rapid dose calculations. This acceleration enables real-time or near-real-time dose estimations, which is particularly valuable in clinical settings where timely decision-making is crucial.

To validate the accuracy of the AI-based dosimetry approach, experimental studies are conducted using water phantoms. These validation studies have demonstrated that the AI models can accurately estimate radiation doses, providing results comparable to direct Monte Carlo simulations while requiring significantly less computational resources. One of the key advantages of AI-based dosimetry is its ability to enable person-specific dose calculations. By incorporating patient-specific anatomical and physiological information into the AI models, such as voxel-based phantoms and biodistribution data, personalized dose estimations can be achieved. This personalized approach enhances the precision and safety of radiation treatments by accounting for individual variations in organ sizes, shapes, and biodistribution of radiopharmaceuticals. It has paved the way for more efficient and accurate radiation dose estimations in nuclear medicine, enabling improved treatment planning and personalized patient care.

8 Conclusion

Monte Carlo simulations are the application of random numbers to represent probability densities. Due to its statistical nature, it converges to the quantity required if large samples are used or some biasing techniques are utilized. For application in internal dosimetry various codes and computational phantoms are used. The application of Monte Carlo for internal dosimetry can be primely divided into two categories. They are applied in radiation protection and application in nuclear medicine. In radiation protection, Monte Carlo is used to estimate the CE of in-vivo monitoring systems, various dosimetric quantities, uncertainty analysis, and intercomparison exercise. Monte Carlo is an effective and economical radiation protection tool for internal dosimetry. In nuclear medicine applications, Monte Carlo simulation using patient-specific imaging is considered as gold standard. Monte Carlo is also used for validation in radioembolization. Various computational tools are developed and validated for nuclear medical applications. Nowadays AI tools validated with Monte Carlo simulation are also utilized for effective and easy methods of patient dose evolution. With the brighter future of computational methods, Monte Carlo simulation will find more utilization for internal dosimetry applications.

References

1. Harrison RL, Granja C, Leroy C (2010) Introduction to Monte Carlo simulation, pp 17–21
2. de Buffon C (1977) Essai d'Arithmétique morale, Supplément à l'Histoire Naturelle. H. Champion, Paris
3. Rhodes R (1986) The making of the atomic bomb. Simon & Schuster, New York
4. Metropolis N (1987) The beginning of the Monte Carlo method. Los Alamos Sci 15:125–130
5. Kroese DP, Brereton T, Taimre T, Botev ZI (2014) Why the Monte Carlo method is so important today. WIREs Comput Stat 6:386–392. https://doi.org/10.1002/wics.1314
6. Rubinstein RY, Kroese DP (2016) Simulation and the Monte Carlo method. Wiley, Hoboken
7. Murthy KPN (2001) Monte Carlo: basics
8. Dupree SA, Fraley SK (2004) A Monte Carlo primer. Springer, Boston
9. Ferrari A, Sala PR, Fasso A, Ranft J (2005) FLUKA: a multi-particle transport code
10. Battistoni G, Boehlen T, Cerutti F et al (2015) Overview of the FLUKA code. Ann Nucl Energy 82:10–18. https://doi.org/10.1016/j.anucene.2014.11.007
11. Ahdida C, Bozzato D, Calzolari D et al (2022) New capabilities of the FLUKA multi-purpose code. Front Phys 9:253. https://doi.org/10.3389/fphy.2021.788253
12. Böhlen TT, Cerutti F, Chin MPW et al (2014) The FLUKA code: developments and challenges for high energy and medical applications. Nucl Data Sheets 120:211–214. https://doi.org/10.1016/j.nds.2014.07.049
13. Agostinelli S, Allison J, Amako K et al (2003) Geant4—a simulation toolkit. Nucl Instrum Methods Phys Res A 506:250–303. https://doi.org/10.1016/S0168-9002(03)01368-8
14. Kulesza JA, Adams TR, Armstrong J et al (2022) MCNP® code version 6.3.0 theory and user manual
15. Sempau J, Badal A, Brualla L (2011) A PENELOPE-based system for the automated Monte Carlo simulation of clinacs and voxelized geometries-application to far-from-axis fields. Med Phys 38:5887–5895. https://doi.org/10.1118/1.3643029

16. Brun E, Damian F, Diop CM et al (2015) TRIPOLI-4®, CEA, EDF and AREVA reference Monte Carlo code. Ann Nucl Energy 82:151–160. https://doi.org/10.1016/j.anucene.2014.07.053
17. Kawrakow I, Mainegra-Hing E, Rogers DWO et al (2023) The EGSnrc code system: Monte Carlo simulation of electron and photon transport
18. Jan S, Santin G, Strul D et al (2004) GATE: a simulation toolkit for PET and SPECT. Phys Med Biol 49:4543–4561. https://doi.org/10.1088/0031-9155/49/19/007
19. Arce P, Rato P, Canadas M, Lagares JI (2008) GAMOS: a Geant4-based easy and flexible framework for nuclear medicine applications. In: Proceedings of the 2008 IEEE nuclear science symposium conference record. IEEE, pp 3162–3168
20. Snyder WS, Fisher HL, Ford MR, Warner GG (1969) Estimates of absorbed fractions for monoenergetic photon sources uniformly distributed in various organs of a heterogeneous phantom. J Nucl Med Suppl 3:7–52
21. Cristy M, Eckerman KF (1987) Specific absorbed fractions of energy at various ages from internal photon sources: methods. Oak Ridge
22. Stabin MG, Watson EE, Cristy M et al (1995) Mathematical models and specific absorbed fractions of photon energy in the nonpregnant adult female and at the end of each trimester of pregnancy. Oak Ridge, TN
23. (1979) Report of the task group on reference man. Ann ICRP 3:iii. https://doi.org/10.1016/0146-6453(79)90123-4
24. (2009) Realistic reference phantoms: an ICRP/ICRU joint effort. Ann ICRP 39:3–5. https://doi.org/10.1016/j.icrp.2009.09.001
25. Zankl M, Wittmann A (2001) The adult male voxel model "Golem" segmented from whole-body CT patient data. Radiat Environ Biophys 40:153–162. https://doi.org/10.1007/s004110100094
26. Zankl M, Becker J, Fill U et al (2005) GSF male and female adult voxel models representing ICRP reference man-the present status
27. Valentin J (2002) Basic anatomical and physiological data for use in radiological protection: reference values. Ann ICRP 32:1–277. https://doi.org/10.1016/S0146-6453(03)00002-2
28. Bolch WE, Eckerman K, Endo A et al (2020) ICRP publication 143: paediatric reference computational phantoms. Ann ICRP 49:5–297. https://doi.org/10.1177/0146645320915031
29. Kim CH, Yeom YS, Petoussi-Henss N et al (2020) ICRP publication 145: adult mesh-type reference computational phantoms. Ann ICRP 49:13–201. https://doi.org/10.1177/0146645319893605
30. Freecad. https://www.freecad.org/. Accessed 9 Jul 2023
31. Park M, Kwon T-E, Ha W-H et al (2019) Counting efficiencies determined by Monte Carlo methods for in vivo measurement of 131I activity in thyroid. Health Phys 117:388–395. https://doi.org/10.1097/HP.0000000000001070
32. Patni HK, Akar DK, Nadar MY et al (2013) Estimation of specific absorbed fractions for selected organs due to photons emitted by activity deposited in the human respiratory tract using ICRP/ICRU male voxel phantom in fluka. Radiat Prot Dosim 153:87. https://doi.org/10.1093/rpd/ncs087
33. Zankl M, Gómez Ros J-M, Moraleda M et al (2021) Monte Carlo calculation of organ dose coefficients for internal dosimetry: results of an international intercomparison exercise. Radiat Meas 148:106661. https://doi.org/10.1016/j.radmeas.2021.106661
34. Spielmann V, Li WB, Zankl M et al (2020) Uncertainty analysis in internal dose calculations for cerium considering the uncertainties of biokinetic parameters and S values. Radiat Environ Biophys 59:663–682. https://doi.org/10.1007/s00411-020-00872-9
35. Akar DK, Patni HK, Nadar MY et al (2013) Monte Carlo simulation of NaI(TL) detector in a shadow-shield scanning bed whole-body monitor for uniform and axial cavity activity distribution in a bomab phantom. Radiat Prot Dosim 155:12. https://doi.org/10.1093/rpd/nct012
36. Ghare VP, Patni HK, Akar DK, Rao DD (2014) Counting efficiency of whole-body monitoring system using BOMAB and ANSI/IAEA thyroid phantom due to internal contamination of ^{131}i. Radiat Prot Dosim 162:269. https://doi.org/10.1093/rpd/nct269

37. Bhati S, Patni HK, Ghare VP et al (2012) Monte carlo calculations for efficiency calibration of a whole-body monitor using BOMAB phantoms of different sizes. Radiat Prot Dosim 148:203. https://doi.org/10.1093/rpd/ncr203
38. Nadar MY, Patni HK, Akar DK et al (2013) Monte carlo simulation of embedded ^{241}am activity in injured palm. Radiat Prot Dosim 154:165. https://doi.org/10.1093/rpd/ncs165
39. Nadar MY, Akar DK, Patni HK et al (2014) Monte carlo simulation of skull and knee voxel phantoms for the assessment of skeletal burden of low-energy photon emitters. Radiat Prot Dosim 162:367. https://doi.org/10.1093/rpd/nct367
40. Nadar MY, Akar DK, Mishra L et al (2021) Monte Carlo simulation of enriched uranium in the lungs of thorax voxel phantom for assessment of enrichment and its effect on dose. Appl Radiat Isotopes 173:9721. https://doi.org/10.1016/j.apradiso.2021.109721
41. Nadar MY, Akar DK, Rao DD et al (2016) Methodology for the assessment of ingested actinides from Monte Carlo simulation of voxel phantom. Radiat Prot Dosim 93:ncw015. https://doi.org/10.1093/rpd/ncw015
42. Silva CCO, da Silva AX, Braz D et al (2022) S-values for radium-223 and absorbed doses estimates for 223RACL2 using three computational phantoms. Appl Radiat Isotopes 189:110387. https://doi.org/10.1016/j.apradiso.2022.110387
43. López MA, Nogueira P, Vrba T et al (2019) Measurements and Monte Carlo simulations of 241Am activities in three skull phantoms: EURADOS-USTUR collaboration. Health Phys 117:193–201. https://doi.org/10.1097/HP.0000000000001080
44. Zankl M, Gómez Ros J-M, Moraleda M et al (2021) Monte Carlo calculation of organ dose coefficients for internal dosimetry: results of an international intercomparison exercise. Radiat Meas 148:6661. https://doi.org/10.1016/j.radmeas.2021.106661
45. Kwon T-E, Chung Y, Yoo J et al (2020) Uncertainty quantification of bioassay functions for the internal dosimetry of radioiodine. J Radiat Res 61:860–870. https://doi.org/10.1093/jrr/rraa081
46. Bhati S, Patni HK (2009) Monte-Carlo simulation of uncertainty in the estimation of ^{125} I in the thyroid. Radiat Prot Dosim 136:143. https://doi.org/10.1093/rpd/ncp143
47. Nadar MY, Akar DK, Rao DD et al (2017) Evaluation of uncertainties in lung measurement of actinides due to non-uniform distribution of activity in lungs. Appl Radiat Isotopes 127:109–115. https://doi.org/10.1016/j.apradiso.2017.05.019
48. Nadar MY, Akar DK, Rao DD et al (2015) Assessment of uncertainties in the lung activity measurement of low-energy photon emitters using Monte Carlo simulation of ICRP male thorax voxel phantom. Radiat Prot Dosim 167:461–471. https://doi.org/10.1093/rpd/ncu349
49. Karimipourfard M, Sina S, Alavi MS (2022) Toward three-dimensional patient-specific internal dosimetry using GATE Monte Carlo technique. Radiat Phys Chem 195:110046. https://doi.org/10.1016/j.radphyschem.2022.110046
50. Amato E, Auditore L, Italiano A et al (2020) Full Monte Carlo internal dosimetry in nuclear medicine by means of GAMOS. J Phys Conf Ser 1561:012002. https://doi.org/10.1088/1742-6596/1561/1/012002
51. Asl RG, Sabbaghi R, Ahangari HT et al (2021) Prediction of absorbed dose to normal organs with endocrine tumors for I-131 by use of 99mTC single photon emission computed tomography/computed tomography and Geant4 application for tomographic emission simulation. Indian J Nucl Med 36:273–281. https://doi.org/10.4103/ijnm.ijnm_6_21
52. Ligonnet T, Pistone D, Auditore L et al (2021) Simplified patient-specific renal dosimetry in 177Lu therapy: a proof of concept. Phys Med 92:75–85. https://doi.org/10.1016/j.ejmp.2021.11.007
53. Botta F, Ferrari M, Chiesa C et al (2018) Impact of missing attenuation and scatter corrections on ^{99m} Tc-MAA SPECT 3D dosimetry for liver radioembolization using the patient relative calibration methodology: a retrospective investigation on clinical images. Med Phys 45:1684–1698. https://doi.org/10.1002/mp.12774
54. Danieli R, Milano A, Gallo S et al (2022) Personalized dosimetry in targeted radiation therapy: a look to methods, tools and critical aspects. J Pers Med 12:205. https://doi.org/10.3390/jpm12020205

55. Pérez P, Valente M (2019) DOSIS: An integrated computational tool for patient-specific dosimetry in nuclear medicine by Monte Carlo and dose point kernel approaches. Appl Radiat Isot 150:135–140. https://doi.org/10.1016/j.apradiso.2019.05.031
56. Besemer AE, Yang YM, Grudzinski JJ et al (2018) Development and validation of RAPID: a patient-specific Monte Carlo three-dimensional internal dosimetry platform. Cancer Biother Radiopharm 33:155–165. https://doi.org/10.1089/cbr.2018.2451
57. Milano A, Gil AV, Fabrizi E et al (2021) In silico validation of MCID platform for Monte Carlo-based voxel dosimetry applied to 90Y-radioembolization of liver malignancies. Appl Sci 11:1939. https://doi.org/10.3390/app11041939
58. Frezza A, Joachim-Paquet C, Chauvin M, Després P (2020) Validation of irtGPUMCD, a GPU-based Monte Carlo internal dosimetry framework for radionuclide therapy. Phys Med 73:95–104. https://doi.org/10.1016/j.ejmp.2020.04.010
59. Mostafa MYA, Zakaly HMH, Tekin HO et al (2021) Assessment of absorbed dose for Zr-89, Sm-153 and Lu-177 medical radioisotopes: IDAC-Dose2.1 and OLINDA experience. Appl Radiat Isot 176:109841. https://doi.org/10.1016/j.apradiso.2021.109841
60. Kim KM, Lee MS, Suh MS et al (2023) Voxel-based internal dosimetry for 177Lu-labeled radiopharmaceutical therapy using deep residual learning. Nucl Med Mol Imag 57:94–102. https://doi.org/10.1007/s13139-022-00769-z
61. Lee MS, Hwang D, Kim JH, Lee JS (2019) Deep-dose: a voxel dose estimation method using deep convolutional neural network for personalized internal dosimetry. Sci Rep 9:10308. https://doi.org/10.1038/s41598-019-46620-y

Internal Dose Evaluation, Quality Assurance and Uncertainty Analysis

Rahul Roy, Sushanta Halder, and Pradeep Kumar Singh

1 Internal Dose Evaluation

Internal contamination of occupational workers due to exposure to radionuclides is a critical concern in nuclear industries, radiography, or medical procedures using radioactive materials. Radionuclides, when inhaled, ingested, or absorbed, can become lodged within the body and emit harmful ionizing radiation, potentially causing long-term health risks, including cancer. To mitigate this risk, meticulous monitoring of internal contamination is imperative. Workers are routinely subjected to radiation exposure assessments through methods like whole-body counting, lung counting, urine analysis, and bioassays. These assessments help quantify the presence and concentration of radionuclides in the body, enabling the implementation of safety measures, such as enhanced shielding, worker rotation, and stricter safety protocols. By rigorously monitoring internal contamination, organizations can ensure the health and safety of their employees and maintain compliance with strict regulatory standards governing radiation protection. In contrast, external contamination involves the presence of hazardous substances on the surface of the worker's body or clothing. This contamination occurs when workers come into contact with substances on their skin, hair, or clothing during their work. Monitoring external contamination typically involves using instruments like Geiger-Muller counters or chemical detectors to identify and measure the presence of contaminants on the body or clothing. The primary goal is to prevent the further spread of contaminants and ensure that they are safely removed through decontamination procedures. In summary, internal contamination involves hazardous substances within the body, requiring internal monitoring methods, while external contamination involves substances on the body's surface and necessitates external monitoring and decontamination measures. Both types of

R. Roy (✉) · S. Halder · P. K. Singh
Internal Dosimetry Section, Radiation Safety Systems Division, Bhabha Atomic Research Centre, Trombay 400085, India
e-mail: rroy@barc.gov.in

D. K. Aswal (ed.), *Handbook on Radiation Environment, Volume 2*,
https://doi.org/10.1007/978-981-97-2799-5_18

contamination are critical concerns in occupational safety and require strict protocols to protect the health and well-being of workers.

The main pathways of human exposure leading to internal irradiation are inhalation and ingestion of radionuclides and in certain instances, through intact or injured skin as described later. Further, in medical procedures involving diagnosis and treatment, radiopharmaceuticals are commonly administered through intravenous injection. Intake is the cumulative quantity of radioactive material that enters the body. This section covers the fundamental aspects of the methods used for estimating internal doses and describes the implementation of these methods in occupational workers. Figure 1 shows the flow chart of various steps involved in the evaluation of committed effective dose (CED) in the realm of internal dosimetry.

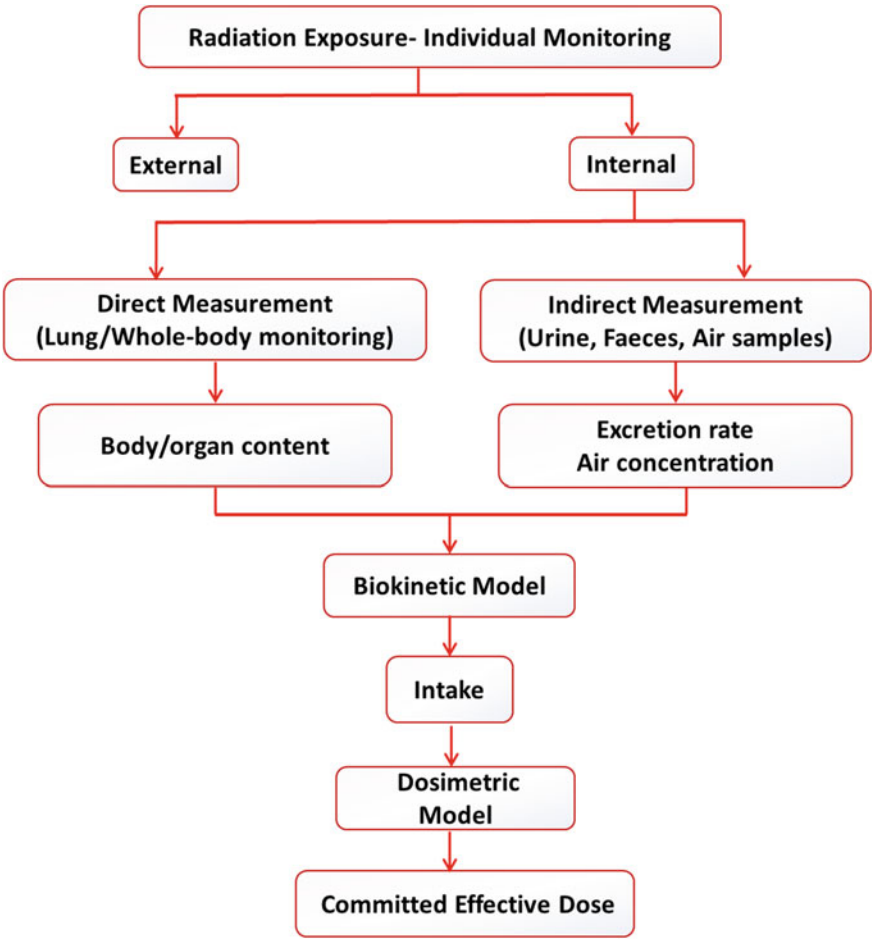

Fig. 1 CED evaluation in internal dosimetry

1.1 General Methods for Internal Dose Calculations

The methods used for internal dose calculation are typically categorized into two groups: biokinetic and dosimetric models. Additionally, the biokinetic model has two parts: the intake models and systemic models. Intake models describe how activity is taken in through different pathways, such as inhalation, ingestion, and contaminated wounds. The intake of activity through different pathways, initial deposition of activity at the intake site, and the proportion of intake that is absorbed into bodily fluids are also taken into account. The systemic model explains the time-dependent distribution of activity in different organs and tissues, and its excretion in urine and feces. Dosimetric models are employed to compute the equivalent doses to various target organs due to radioactive disintegrations occurring in source organs.

1.1.1 Biokinetic Models

Intake Models: Intake of radionuclides refers to the process by which radionuclide enters the respiratory tract or gastrointestinal tract from the environment. Radionuclide intake typically occurs through following routes:

i. **Inhalation**: Inhalation is one of the most common routes of radionuclide intake. Workers in industries involving radioactive materials can breathe in airborne particles or gases that contain radioactive isotopes. These isotopes can become deposited in the lungs and may irradiate surrounding tissues.
ii. **Ingestion**: Ingestion occurs when radionuclides are swallowed or consumed. This can happen if contaminated food, water, or beverages are ingested. The radionuclides then enter the gastrointestinal tract and may be absorbed into the bloodstream, potentially irradiating internal organs.
iii. **Absorption through the Skin**: Radionuclides can also enter the body through the skin. If a person comes into direct contact with radioactive materials or contaminated surfaces, especially if they have open wounds or cuts, some of the radionuclides may be absorbed through the skin.
iv. **Injection**: In some medical procedures, radionuclides are intentionally injected into the body for diagnostic or therapeutic purposes.
v. **Wounds and Injuries**: If an individual sustains an injury or wound in an environment containing radioactive materials, radionuclides may enter the body through the open wound, especially if proper wound care and decontamination measures are not taken promptly.
vi. **Intravenous Administration**: Similar to injection, radionuclides can enter the body through intravenous administration during certain medical procedures or treatments.

Intake models find extensive application in occupational and environmental settings, where exposures primarily occur through inhalation and ingestion, and in some instances, through absorption via intact or injured skin. The respiratory tract model

developed by ICRP provides an overview of the deposition, translocation, and absorption of various inhaled substances [1]. ICRP has also developed the gastrointestinal (GI) tract model, which explains the behavior of swallowed materials within the GI tract. This model, along with element-specific absorption fractions (f_1 values), determines the rate and extent of absorption of materials from the GI tract into the bloodstream [2]. These ICRP respiratory and GI tract models represent the actual movement of radionuclides inside the human body, but the biological realism of these biokinetic models is element specific. Additionally, the NCRP has published a model that describes the intake and subsequent uptake (an activity that enters blood stream from the respiratory or alimentary tract or through the skin) of radioactive materials through wounds or damaged skin [3].

Systemic Models: After entering the bloodstream, the biokinetic distribution of radioactive material in various organs relies on the body's metabolic processes specific to each element. For instance, radium has a tendency to accumulate in the bone matrix, whereas iodine is predominantly deposited in the thyroid. These elements can be deposited in one organ, remain there temporarily, re-enter the bloodstream, get absorbed by another organ, and continue this pattern before eventually being eliminated. ICRP has developed comprehensive biokinetic models for almost all chemical elements. These models describe the movement of elements within the body. Some models are primarily based on empirical data, providing detailed information on the specific routes taken by elements. In contrast, other models consist of simplified mathematical expressions that provide a reasonable estimation of the overall activity deposited within major repositories of the body.

Systemic models are commonly employed in occupational and environmental exposures, but their usage is less prevalent in medical exposures. In medical scenarios, where the focus is often on predicting the time-integrated concentration of radiopharmaceuticals in specific organs, measurements of activity in the organ of interest are frequently taken over a series of time points. The primary outputs of systemic models are time-dependent activities of radioactive materials in various organs of interest. Additionally, estimations of urinary and fecal excretions are also provided by these models.

1.1.2 Dosimetric Models

Dosimetric models are utilized to determine the doses to specific organs of interest, known as target organs. These models rely on calculating the fraction of energy deposited in the target organs due to radioactive emissions from all organs involved, known as source organs. These models calculate the absorbed doses by quantifying the energy deposited in the target organs relative to the total energy emitted by a radionuclide deposited in the source organs. This allows a more comprehensive understanding of radiation exposure and its potential effects on the human body.

The main objective of all internal dose calculations is to determine the absorbed or equivalent dose received by specific organs or tissues over a designated time period following the intake. This computed dose is known as the committed dose. Different

time periods are used for these calculations, such as 1 year for annual doses, 50 years for committed doses in workers, up to 70 years for committed doses in members of the public, or an infinite time period where radionuclides have a short effective half-life as compared to the human lifespan. Typically, the committed dose is computed by integrating time-dependent dose rate over the specified time period. It's important to note that all internal doses mentioned in this context are specifically referring to committed doses.

There are two widely used systems for internal dose calculations:

i. **MIRD system:** This system is primarily employed for internal dose assessments in medical exposures, particularly those involving radiopharmaceuticals and diagnostic or therapeutic procedures. The MIRD system provides specific models and methodologies tailored to the unique characteristics of medical applications.
ii. **ICRP system:** This system is primarily utilized for internal dose calculations in occupational and environmental exposures. The ICRP system offers comprehensive guidelines, models, and reference data for assessing internal radiation doses in various scenarios encountered in workplaces and environmental settings.

Both the MIRD and ICRP systems serve as valuable frameworks for estimating internal radiation doses, with each system focusing on different applications and contexts. Both systems share similarities but differ in their terminologies and symbols used. The MIRD system focuses on predicting absorbed doses. On the other hand, the ICRP system utilizes equivalent doses and effective doses as endpoints, where absorbed doses and their uncertainties are the primary endpoints, except for a few exceptions. In the descriptions that follow, it is assumed that the distributions of activities in the organs of the body have been either measured or estimated. The organs that emit radiations are referred to as source organs and the organs for which the absorbed dose (D) is calculated are known as the target organs. The absorbed dose to a given target organ is defined as the average energy deposited per unit mass of that target tissue.

i. MIRD System of Internal Dose Calculations

Although initially developed for medical exposures, the equations utilized in the MIRD system can also be applied to occupational and environmental exposures. The essential elements of radionuclide dosimetry are described below [4–7].

Mean absorbed – dose rate: The time-dependent absorbed-dose rate $\dot{D}(r_T, t)$ which gives a dose delivered to the target tissue r_T, due to uniformly distributed activity within source tissue r_S within a patient from a radiopharmaceutical at time 't' post-administration is given as

$$\dot{D}(r_T, t) = \sum_{r_S} A(r_S, t) S(r_T \leftarrow r_S, t) \tag{1}$$

The S values exhibit distinct characteristics based on the radionuclide involved and the specific anatomical model selected to represent the targeted tissue or patient,

taking into account their age and gender. These S values are regarded as time-dependent due to potential alterations in the geometric arrangement between the source and target tissues over time. For instance, S values may fluctuate over time if there is tumor reduction following medical treatment in the field of nuclear medicine, or if a long-lasting radionuclide remains strongly within the body after being consumed at a young age.

$A(r_S, t)$	time-dependent activity of the radioactive material in the source tissue r_S obtained from biokinetic modeling or direct imaging quantification
$S(r_T \leftarrow r_S, t)$	mean absorbed-dose rate to target tissue r_T per unit activity present in source tissue r_S at time t post-administration as obtained from a dosimetric anatomic model of the patient

S values can be derived from preconstructed computational models of the entire body that represent reference individuals with specific characteristics such as sex, age, standing height, and total body mass [8, 9]. This model can also be built using segmented images of the individual's anatomy obtained from magnetic resonance imaging (MRI) or computed tomography (CT) [10]. Additionally, the source and target regions, denoted as r_S and r_T, respectively, are defined within the anatomical model and can encompass various configurations such as complete organs, sub-organs, voxels extracted from tumors, medical images, cell components, individual cells, or cell clusters [11–13].

Mean absorbed dose – Time-dependent formulation: The mean absorbed dose $D(r_T, T_D)$ to target tissue r_T over a specified period T_D (dose-integration period) after administering the radioactive material to the subject is given as

$$D(r_T, T_D) = \int_0^{T_D} \dot{\mathrm{D}}(r_T, t)\mathrm{d}t = \sum_{r_S} \int_0^{T_D} A(r_S, t) S(r_T \leftarrow r_S, t)\mathrm{d}t \tag{2}$$

where T_D is typically considered to be infinity, since radionuclides commonly used in nuclear medicine have relatively short half-lives. The absorbed dose is expressed in joule per kilogram (J kg^{-1}) and is commonly referred to as Gray (Gy).

If $A(r_S, t)$ is normalized to a unit-administered activity A_0 and represented as $a(r_S, t)$, the absorbed-dose coefficient $d(r_T, T_D)$ in target tissue r_T can be expressed as

$$d(r_T, T_D) = \sum_{r_S} \int_0^{T_D} a(r_S, t) S(r_T \leftarrow r_S, t)\mathrm{d}t \tag{3}$$

where $a(r_S, t) =$ fraction of the activity administered in the source tissues r_S at time 't' post-administration.

Both the ICRP and MIRD systems utilize numerical methods to obtain the time-dependent activity in various compartments representing source tissues. This is

accomplished by solving a set of first-order coupled differential equations that are defined by compartment models for all relevant organs and sub-organ tissues. Another approach to obtain the time-dependent activity in source tissues of the patient is through quantitative imaging or by collecting tissue samples such as biopsy, blood or urine collection, etc.

The S value is unique to the radionuclide being considered and the computational phantom that defines the spatial arrangements and tissue compositions of r_S and r_T, as well as the tissues in between, within the reference individual or tissue model. The S value is expressed as

$$S(r_T \leftarrow r_S, t) = \sum_i E_i Y_i \frac{\phi(r_T \leftarrow r_S, E_i, t)}{M(r_T, t)} = \sum_i \Delta_i \frac{\phi(r_T \leftarrow r_S, E_i, t)}{M(r_T, t)} \quad (4)$$

where

E_i and Y_i	mean energy and yield of radiation type 'i' emitted by the radionuclide [14]
Δ_i	product of E_i and Y_i
$\phi(r_T \leftarrow r_S, E_i, t)$	absorbed fraction (fraction of energy deposited in the target tissue r_T due to radioactive emissions E_i in source tissue r_S at time 't'
$M(r_T, t)$	target tissue mass r_T in the reference individual at time 't'

The range of beta particles in tissue is small as compared to the size of the target tissue. In such case, the absorbed fraction is taken to be unity and E_i is considered to be the average value of the energy spectrum. However, if there are significant variations in absorbed fraction across the range of emission energies, then the summation in the above equation is replaced by an integral over the entire beta energy spectra. This situation is described by the quotient of the absorbed fraction to the target mass:

$$\Phi(r_T \leftarrow r_S, E_i, t) = \frac{\phi(r_T \leftarrow r_S, E_i, t)}{M(r_T, t)} \quad (5)$$

such that:

$$S(r_T \leftarrow r_S, t) = \sum_i \Delta_i \Phi(r_T \leftarrow r_S, E_i, t) \quad (6)$$

Mean absorbed dose – Time independent formulation: The assessment of certain scenarios requires the preservation of the time dependency of the S value. These situations include:

- Estimating the absorbed dose in tumor regions that experience changes in mass (either increasing or decreasing) during the irradiation period; and
- Determining the 50-year mean organ doses in individuals who were exposed to long-lived radionuclides during their childhood.

In most of the cases, when the source and target masses remain constant throughout the irradiation period, the time dependency of the S value may be neglected. In such situations, Eq. 6 can be simplified to the following time-independent form:

$$D(r_T, T_D) = \sum_{r_S} \tilde{A}(r_S, T_D) S(r_T \leftarrow r_S) \tag{7}$$

where $\tilde{A}(r_S, T_D)$ is the total number of radioactive transformations occurring in the source region r_S over the specified period T_D such that – $\tilde{A}(r_S, T_D) = \int_0^{T_D} A(r_S, t)\mathrm{d}t$.

The absorbed-dose coefficient $d(r_T, T_D)$, which represents the absorbed dose in the target tissue r_T per unit activity administered, is expressed as

$$d(r_T, T_D) = \sum_{r_S} \tilde{a}(r_S, T_D) S(r_T \leftarrow r_S) \tag{8}$$

where

$$\tilde{a}(r_S, T_D) = \int_0^{T_D} a(r_S, t)\mathrm{d}t = \frac{1}{A_0} \int_0^{T_D} A(r_S, t)\mathrm{d}t \tag{9}$$

and $\tilde{a}(r_S, T_D)$ is the time-integrated activity coefficient. In previous versions of the MIRD schema, $\tilde{a}$ was referred to as the residence time τ and was assigned the units of time (seconds). Here, $\tilde{a}(r_S, T_D)$ corresponds to the cumulative number of radioactive transformations (Becquerel-second) that occur in source tissue r_S over the specified period T_D per unit-administered activity A_0 (Becquerel).

ii. **ICRP System of Internal Dose Calculations**

The ICRP system of internal dose calculations quantifies the activities deposited in the source organs to dose limits, that are defined as equivalent and effective doses. The ICRP system is primarily employed for regulatory purposes in the assessment of doses resulting from occupational and environmental exposures. The dose-integration period for adults is standardized at 50 years, assuming a reference age of 20 years at the time of exposure. For individuals exposed as infants, children, or adolescents, the time is variable and extends up to 70 years [15]. Figure 2 shows the steps in the ICRP schema of internal dose calculations.

Taking the example of occupational exposures, the dose equivalent in sievert (Sv) is calculated for 50 years after intake by means of the following equation, developed by [16]:

$$H_{50,T} = 1.6 \times 10^{-10} \sum_S \left[U_S \left(\sum_i \mathrm{SEE}(T \leftarrow S)_i \right) \right]_j \tag{10}$$

$$\mathrm{SEE}(T \leftarrow S)_i = \frac{W_i Y_i E_i \phi(T \leftarrow S)}{M_T} \tag{11}$$

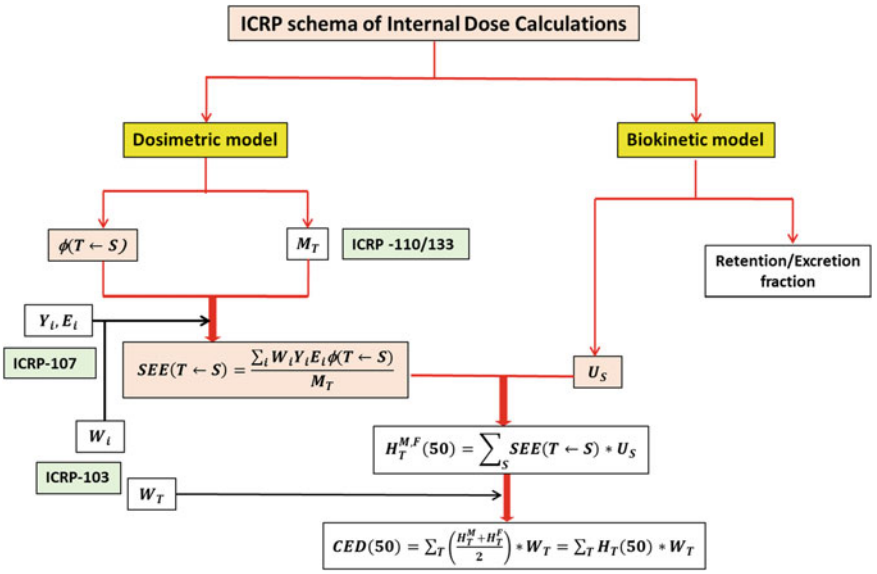

Fig. 2 ICRP schema of internal dose calculations

where

$H_{50,T}$	dose equivalent to tissue T in 50 years after intake of radionuclide j
U_S	total number of radioactive transformations occurring in source tissue S in 50 years following intake of radionuclide j
$\text{SEE}(T \leftarrow S)_i$	specific effective energy of radiation type 'i' absorbed in target tissue T per transformation of radionuclide j in source organ S (MeV kg^{-1})
Y_i	yield of radiation type 'i' per nuclear transformation
E_i	energy of radiation type 'i' (MeV)
W_i	radiation weighting factor for radiation type 'i'
$\phi(T \leftarrow S)$	absorbed fraction (kg^{-1})
M_T	mass of target organ T (kg)

Originally, the simplifying assumption is made that all emitted charged particle radiation is absorbed solely in the source tissue, and no absorption occurs in other target tissues. However, more recent dosimetric models consider the contributions of charged particle radiations when the source and target tissues are different. For photons, absorbed fractions are computed from mathematical phantoms representing a stylized anatomy of the human body. These phantoms allow for Monte Carlo calculations to be made of how much-emitted photon energy is deposited in the source and target tissues, taking into account the energy of photons [17]. By summing over all radiations i, the specific effective energy of radionuclide j is given by

$$\text{SEE}(T \leftarrow S)_j = \sum_i \text{SEE}(T \leftarrow S)_i \tag{12}$$

Finally, the effective dose equivalent (H_E) is estimated by taking the product of the committed organ dose equivalent to different tissues and tissue weighting factor (w_T), and summing over all target tissues:

$$H_E = \sum_T w_T H_{50,T} \tag{13}$$

The tissue weighting factors are used to quantify the relative detriments of radiation to different tissues, taking into account the varying sensitivities of various internal organs to the development of stochastic effects caused by radiation exposure. Occupational dose limits still rely on this system [18] and require that for all radionuclide intakes in a single year:

$$H_{50,T} \leq 0.05\ \text{Sv} \tag{14}$$

to prevent deterministic effects and:

$$\sum_T w_T H_{50,T} \leq 0.05\ \text{Sv} \tag{15}$$

to prevent stochastic effects.

In early 1990s, ICRP published revised guidance [19] and introduced a different nomenclature for internal dose parameters. The absorbed dose in a tissue T resulting from exposure to a specific radiation R is represented by $D_{T,R}$. Radiation-specific quality factors were replaced with radiation weighting factors (w_R) and the equivalent dose ($H_{T,R}$) to a given target tissue T is given by

$$H_{T,R} \leq w_R D_{T,R} \tag{16}$$

to limit stochastic risk to a specified level.

The total equivalent dose, when the absorbed dose is due to different radiations with different radiation weighting factors is given by

$$H_T = \sum_R w_R D_{T,R} \tag{17}$$

Finally, the effective dose E is calculated by taking the product of tissue weighting factors (w_T) and the equivalent doses summed over all organs T:

$$E = \sum_T w_T H_T \tag{18}$$

According to the ICRP guidance [19], the limit for occupational effective dose is set at $\leq$ 20 mSv per year, with a 5-year rolling average time period. There is an additional provision that the occupational effective dose does not exceed 50 mSv in

any 1 year. While ICRP [15] published new recommended values for the radiation weighting factors for protons and neutrons and a revised set of tissue weighting factors, the 1990 dose limits are unchanged [15].

ICRP recommended values of effective doses per unit intake:

- Publication 30 [16, 18, 20] and Publication 68 [21] for workers;
- Publication 53 [22], Publication 62 [23], Publication 80 [24], and Publication 106 [25] for patients;
- Publication 56 [26], Publication 67 [23], Publication 69 [27], Publication 71 [28], and Publication 72 [29], for members of the general public;
- Publication 88 [30] for the embryo and fetus from intakes of radionuclides by the mother; and
- Publication 95 [31] for infants following ingestion of radionuclides from mothers' milk.

Several organizations have released values for derived quantities useful in occupational radiation protection. These quantities include the annual limit of intake (ALI) and the derived air concentration (DAC). ALI is defined as the intake of a specific radionuclide by a particular pathway that corresponds to an effective dose equivalent to the regulatory limit. DAC is defined as that concentration of radionuclide in air that, if an occupational worker were to breathe it at gender-averaged breathing rates for a full work year (2000 h), would lead to intake equivalent to 1 ALI for inhalation. The product of DAC and exposure time, in units of DAC-h, can be used to estimate inhalation intake, since by definition, 1 ALI = 2000 DAC-h.

1.2 Dose Computation

The dose to an occupational worker is computed using the methodology described in Fig. 3. The calibration factors (cpm/kBq) for a given whole-body monitor (WBM)/lung counting (LC) or alpha spectrometry system is derived using suitable phantoms and sources. For WBM's, Bottle Mannequin Absorption (BOMAB) phantom and for LC's Lawrence Livermore National Laboratory (LLNL) or Japan Atomic Energy Research institute (JAERI) phantoms are used for calibration purposes. Planchette sources of Pu/Am are used for calibrating the alpha spectrometry system. These calibration factors are used to quantify the measured count rate in a worker to measure activity. Then, the intake of radionuclides is estimated by dividing the measured activity with the retention/excretion fraction of radionuclides at the time '*t*'. In a routine monitoring scenario, '*t*' is taken as 180 days, and in a special monitoring scenario, the time of intake is known. Finally, the dose to the occupational worker for a given radionuclide is estimated by taking the product of intake calculated from the previous step, and the dose coefficient is estimated by solving the dosimetric model.

The dose for a given radionuclide is computed from intake and dose coefficient that depends upon various parameters such as mode of intake, physical and chemical form

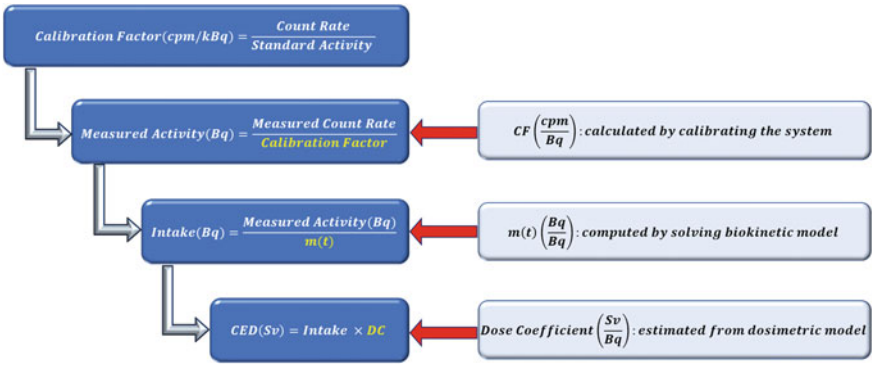

Fig. 3 Dose computation methodology

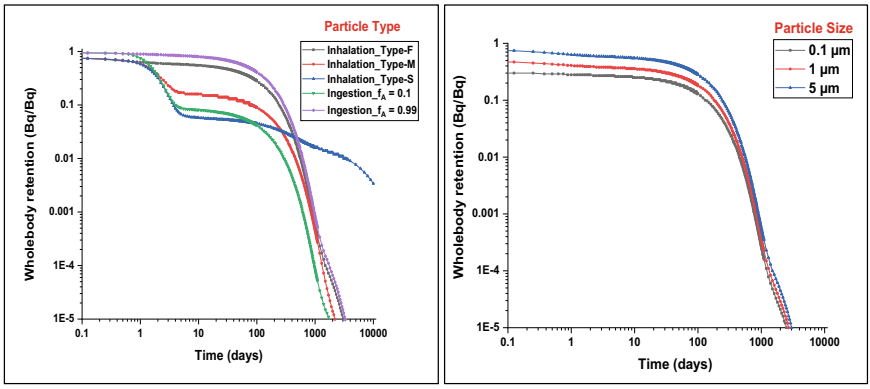

Fig. 4 Variation in whole-body retention of Cs-137 with particle type and size

of the radionuclide, particle size of the aerosol deposited in lung compartments, and its absorption type (Type-F, M, S), gut absorption factor (f_A) of soluble and insoluble materials, etc. Figure 4 shows the variation in whole-body retention of Cs-137 with particle type and its size.

2 Quality Assurance

2.1 Intercomparison Exercise

An intercomparison exercise in the field of internal dosimetry is a controlled and systematic comparison of the methods and practices used by different laboratories or organizations to assess the radiation doses received by individuals due to

the internal intake of radioactive materials. It involves the evaluation of measurement techniques, instrumentation, and procedures to ensure accuracy, consistency, and compliance with regulatory standards. These exercises are essential for quality assurance, standardization, and improving the reliability of internal radiation dose assessments.

1. **Objective:** The primary objective of intercomparison exercises in the field of internal dosimetry is to evaluate and improve the accuracy and reliability of methods used to assess radiation doses received by individuals due to the intake of radioactive materials. These exercises are conducted to ensure the quality and consistency of internal dosimetry practices and to enhance radiation protection for workers, especially in industries where there is potential exposure to radioactive substances.
2. **Quality Assurance and Validation**: Intercomparison exercises help validate the accuracy of internal dosimetry measurements and calculations. By comparing results from different laboratories or institutions, it is possible to identify potential sources of error and improve measurement techniques.
3. **Standardization**: These exercises promote the standardization of dosimetry procedures and methodologies across different organizations and laboratories. Standardized practices ensure that dose assessments are consistent and reliable, regardless of where they are conducted.
4. **Training and Education**: Intercomparison exercises provide valuable opportunities for training and educating personnel involved in internal dosimetry. Participants can learn from one another and gain experience in handling various aspects of dosimetry, from sample collection to analysis.
5. **Method Development and Optimization**: Through intercomparisons, researchers and practitioners can identify areas where dosimetry methods can be refined or optimized. This can lead to the development of improved techniques for assessing internal radiation exposure.
6. **Benchmarking**: Intercomparisons serve as benchmarks for evaluating the performance of laboratories and dosimetry systems. Laboratories can assess their proficiency in accurately measuring and quantifying radioactive materials in biological samples.
7. **Quality Control**: These exercises help ensure that laboratories maintain high standards of quality control and quality assurance in their dosimetry practices. It encourages the ongoing monitoring and improvement of measurement accuracy.
8. **Regulatory Compliance**: Compliance with regulatory requirements is a critical objective. Many regulatory authorities mandate that organizations involved in handling radioactive materials participate in intercomparison exercises to demonstrate compliance with safety standards and dose limits.
9. **Emergency Preparedness**: Intercomparisons can assess the preparedness of dosimetry laboratories to respond to emergencies, such as nuclear accidents or radiological incidents. It helps ensure that accurate dose assessments can be made rapidly during crisis situations.

10. **Confidence Building**: By demonstrating the accuracy and reliability of internal dosimetry practices, intercomparisons build confidence among workers and the public regarding the safety measures in place to protect against radiation exposure.

Overall, intercomparison exercises in the field of internal dosimetry play a crucial role in maintaining the highest standards of radiation protection, improving measurement techniques, and ensuring that workers and the public are adequately safeguarded against the potential hazards of internal radiation exposure.

2.2 Intercomparison Exercise on Internal Dose Assessment

Numerous intercomparison exercises have been conducted at both national and global scales to assess occupational exposure resulting from radionuclide intakes. These exercises have highlighted substantial variations in assumptions, methods, approaches, and as a result, the outcomes achieved by different practitioners involved. Recognizing the importance of this issue for internal dosimetrists, the International Atomic Energy Agency (IAEA) has coordinated a fresh intercomparison exercise in collaboration with the IDEAS project. Under the 5th EU Framework Program (EU Contract No. FIKR-CT2001-00160), the IDEAS project has developed comprehensive guidelines known as "Guidelines for the Evaluation of Incorporation Monitoring Data". The objective of this collaborative effort is to address the challenges associated with harmonizing evaluation practices and promoting consistency in the assessment of incorporation monitoring data.

With the primary focus on assessing the impact of the harmonization guidelines in the field of internal dosimetry, this recent intercomparison exercise aimed to accomplish the following objectives:

- Participating laboratories were given the opportunity to assess the effectiveness of their internal dose assessment methods by implementing the most recent recommendations from ICRP, which included the latest respiratory tract model.
- Comparative analysis of various approaches used to interpret monitoring data related to internal contamination.
- Quantify the disparities in internal dose evaluations that arise from implementing the latest guidelines in comparison to other established methodologies.
- Offer insights on the impact of input parameters on monitoring outcomes by presenting relevant figures.
- Establish a broad forum for the exchange of information among participating entities, facilitating discussions and knowledge sharing.

By addressing these aspects, the intercomparison exercise sought to enhance the understanding and consistency of internal dose assessments and promote the application of harmonized guidelines in internal dosimetry.

2.3 IAEA/IDEAS Intercomparison Exercise

For harmonizing the methods of assessing the committed effective dose to workers after an intake of radionuclides using these guidelines, a joint IDEAS/IAEA intercomparison exercise viz." Intercomparison exercise on assessment of occupational exposure" was organized. Internal Dosimetry Section (IDS) laboratory, RSSD, BARC, Mumbai has participated in this exercise, which consisted of six cases covering wide and complex exposure scenarios. The cases given were (i) acute intake of HTO, (ii) acute inhalation of fission products ^{137}Cs and ^{90}Sr, (iii) acute inhalation of ^{60}Co, (iv) chronic intake of ^{131}I, (v) enriched uranium intake, and (vi) intake of Pu and Am. The cases were solved using LUDEP, MONDAL/MONDES, and IMBA dose evaluation software, and the results were submitted to IAEA. Eighty-one participants from 42 countries submitted the results to the IAEA. Out of these, only thirty-five participants had solved all the cases. Our laboratory was one of them. IAEA statistically analyzed the results reported by the participating laboratories, using Log-Normal distribution for Geometric Mean (GM) and Geometric Standard Deviation (GSD) for a better graphical representation of the data. Our results were found to be in good agreement with the IAEA results. Table 1 shows the Intakes and CED values estimated by our laboratory and the results compiled by IAEA for the six cases given in the intercomparison exercise.

This table includes only a brief description of the exposure cases. The CED values given by the IAEA are the GM of all the values reported by the participating laboratories. These values are given in this table along with their GSD. The detailed results of the participating laboratories for Case No. 6 (b) as reported by IAEA are given in Fig. 5. The results of our laboratory are shown by a red arrow. It is seen that the results have excellent agreement with mean values.

2.4 Development of the General Guidelines

The IDEAS project primarily focused on formulating comprehensive guidelines. The project partners collaborated in order to formulate a unified approach for evaluating monitoring data. Through an online workshop hosted on the website http://www.ideas-workshop.de/, they created and discussed the general guidelines with internal dosimetry experts. This collaborative discussion strengthened the shared strategy and facilitated the finalization of the draft guidelines. Several contractors involved in the IDEAS project were also active members of the ICRP party working on the interpretation of Bioassay data. Their participation was instrumental in the development of an ICRP Supporting Guidance Document that deals with Bioassay Data Interpretation. The goal of this document is to supplement the forthcoming Occupational Intakes of Radionuclides (OIR) document, which is set to replace ICRP Publications 30, 54, 68, and 78.

Table 1 Our reported values of Intake and CED for various cases and the compiled results of IAEA

Case No	Cases	Reported results		IAEA compilation of the results	
		Intake (kBq)	CED (mSv)	Intake (kBq)	CED (GM ± GSD) (mSv)
1	Acute Intake of HTO: urinary excretion data of 0–274 days was given. CED is estimated using the direct method of dose estimation given in the guidelines	–	23.36	–	25.7 ± 1.4
2 (a)	Acute inhalation of fission products ^{90}Sr and ^{137}Cs: Whole-body counting data for ^{137}Cs and urinary and fecal excretion data from 0 to 634 days for ^{90}Sr were given ^{137}Cs results	118	0.789	103.2	0.666 ± 0.1
2 (b)	^{90}Sr and ^{90}Y results	60.8	4.68	106.57	8.97 ± 6.61
3	Acute inhalation of ^{60}Co: Whole-body counting data and urinary excretion data from 10 to 1010 days were given	404	5	396	5.2 ± 1.7
4	Repeated intake of ^{131}I: thyroid monitoring data for 0–8 days has been given following repeated intake of ^{131}I	118	2.33	169.66	2.58 ± 0.17
5	Acute intake of enriched U: Lung monitoring data and urinary excretion data were given	3.368	23	9.719	39 ± 33
6 (a)	Single intake of Pu isotopes and ^{241}Am: ^{241}Am chest, lung, liver, bone measurement data & urinary and fecal excretion data were given. ^{241}Am results	4.59	34.7	4.3	69.5 ± 62.2
6 (b)	Single intake of Pu isotopes and ^{241}Am: ^{239}Pu urinary and fecal excretion data were given. ^{239}Pu results	13.8	114	14.2	155 ± 78

The Guidance Document shares the same goals as that of the IDEAS project. Therefore, both documents have been developed in close coordination to ensure consistency between the ICRP Guidance Document and the IDEAS guidelines. However, there exist disparities in terms of scope. In particular, the ICRP Guidance Document will be focused on the upcoming ICRP Recommendations and the revised biokinetic and dosimetric models employed in the OIR document such as the

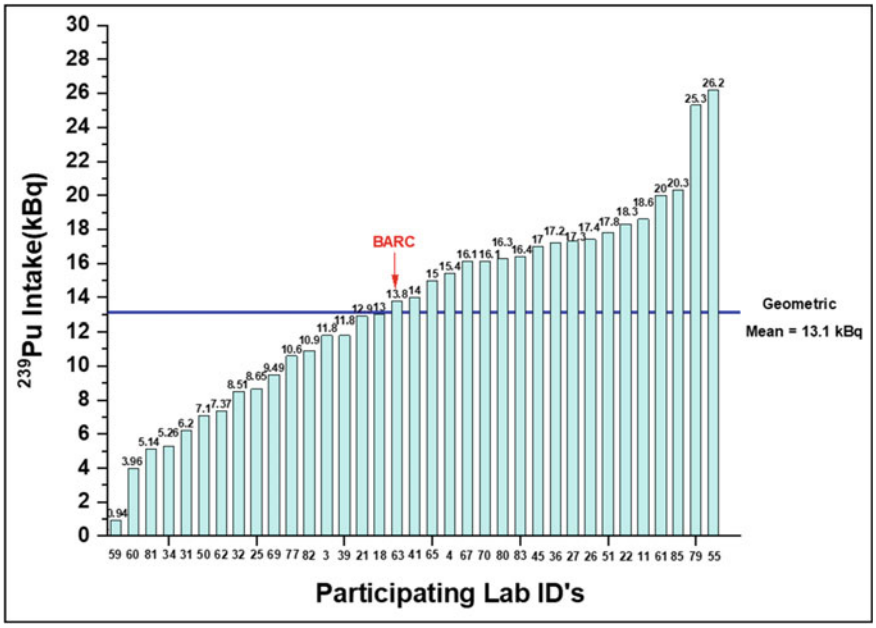

Fig. 5 Results of the individual participants as reported by IAEA for ^{239}Pu. The results of our laboratory are shown by red arrow

Human Alimentary Tract Model (HATM). On the other hand, the IDEAS Guidelines are applicable to the existing models in use.

Nevertheless, the draft ICRP Guidance Document shares common principles and incorporates systematic assessment approach that draws inspiration from the IDEAS Guidelines.

2.5 Evaluation of Monitoring Data Based on the IDEAS Guidelines

2.5.1 Introduction

While using monitoring data for evaluating internal committed doses, various factors are assumed where required information is not available. These factors include the intake pattern and material properties.

When multiple measurements are accessible, the relative significance assigned to each set of data can significantly impact the outcome of the assessment. Intercomparison exercises conducted recently have demonstrated significant discrepancies in doses derived from the same dataset, primarily attributable to different choices made

for these factors. As a result, there is a pressing need for guidance to ensure consistent evaluations and harmonize the results.

The guidelines put forth a set of procedures that are based on these principles:

- Harmonization: from a given data set, the doses estimated by any two assessors should be the same when adhered to the procedures.
- Accuracy: the available dataset should be utilized to obtain the most accurate estimate of dose.
- Proportionality: the level of effort involved in the evaluation should be proportional to the dose being assessed. As the dose decreases, the process should be simplified accordingly.

2.5.2 Harmonization

The guidelines recognize the importance of having a well-defined procedure, and therefore, the process is primarily described through a series of flowcharts. The aim is to make the procedure widely applicable, without assuming the availability of sophisticated bioassay interpretation software.

It is relatively straightforward to establish a procedure in the case of routine monitoring scenarios as only one measurement is available for each potential intake. However, in special monitoring scenarios, multiple measurements and potentially different types of measurements (such as urine, feces, etc.) are involved. In such cases, even when using the same parameter values, model, and software, the doses evaluated are different as various options for data handling are involved.

When it becomes suitable to consider alternative parameter values rather than solely relying on the ICRP defaults, additional possibilities and opportunities for different evaluated doses emerge. In order to ensure consistency and standardization in the evaluation process, the guidelines propose a systematic approach to dose assessment in all these scenarios. They offer proposals to address these situations to provide a framework for maintaining consistency and standardization throughout the evaluation process.

2.5.3 Accuracy

The significant uncertainties related to assessed internal doses, particularly for actinides, which are difficult to detect within the body and have relatively high dose coefficients ($SvBq^{-1}$), are acknowledged. In situations, when the initial dose estimates surpass 1 mSv, there is a possibility that a considerably higher dose, such as 6 mSv, cannot be ruled out easily. In such situations, it becomes crucial to maximize the utilization of available information in order to obtain the most accurate assessment It can be achieved by modifying parameter values from the ICRP default, taking into account the specific circumstances. Therefore, guidance is required to determine

which parameter values can reasonably be adjusted based on the available information. This ensures that the evaluation process takes into consideration all relevant factors and maximizes the utility of the available data.

2.5.4 Proportionality

The level of effort invested in evaluating monitoring data should be proportional to the anticipated exposure level and the complexity of the particular case. In scenarios where the anticipated exposure is significantly lower than the dose limits, it is permissible to employ simpler procedures for dose evaluation with a higher level of uncertainty. However, more advanced evaluation procedures are employed, if the monitoring values are approaching or exceeding the dose limits.

These advanced procedures consider any case-specific information that is available, aiming to minimize both the uncertainty and bias in the best estimate. The goal is to achieve the lowest reasonable level of uncertainty and bias by taking into account all relevant factors and utilizing the available information effectively. This ensures a more accurate assessment of the incorporation of monitoring data, particularly in cases where the exposure is significant or approaching the dose limits.

2.5.5 Level of Task

The suggested framework of "Levels of Task" is proposed in the context of operational radiation protection. This structure fundamentally draws from routine monitoring scenarios but can also be extended to encompass other scenarios.

i. **Level 0:** If the annual dose is less than 0.1 mSv in the accounting year, dose evaluation is not necessary.
ii. **Level 1:** A straightforward "reference" evaluation is conducted utilizing ICRP default parameter values. However, if there is better prior information available, such as particle size distribution for inhalation intakes, it is taken into account. The typical dose range for evaluations at this level is 0.1 to 1 mSv.
iii. **Level 2:** An advanced evaluation is performed, incorporating supplemental information to assess the dose which is more realistic. This level is commonly employed for special assessments of accidental intakes. Model predictions are compared with the available data ("the fit") for selecting the most suitable parameter values or determining the optimal values post-evaluation. At this level, adjustments are made to parameters related to material, such as absorption type and AMAD for inhalation intakes. Additionally, adjustments may be made for the parameters associated with the unknown time of intake. The dose range for evaluations at this level is typically 1 to 6 mSv.
iv. **Level 3:** An even more advanced evaluation is conducted in cases where comprehensive data are available, such as after an accident. This level extends the evaluation process from Level 2, focusing on parameters related to the subject

(e.g., particle transport rates in the Human Respiratory Tract Model for inhalation intakes). The fundamental approach at this level is to systematically adjust model parameter values in a specific order using a "step-by-step" approach until an acceptable level of goodness of fit is achieved. Evaluations at this level generally involve doses exceeding 6 mSv.

3 Uncertainty Analysis

Mathematical models are used to assess radiation doses resulting from exposure to internally distributed radionuclides, but these models often rely on limited or inconsistent data. Since the scope of behavior of radionuclides inside the human body is limited, it is crucial to evaluate uncertainties when estimating internal doses. Uncertainties in dose calculations can have significant implications, such as influencing the outcomes of epidemiological studies, impacting the remediation of contaminated areas, affecting compensation programs for atomic veterans and nuclear workers, as well as influencing radiation-based diagnosis and treatment plans for patients. Communicating the uncertainties alongside the assessment results can enhance the credibility of the findings when they are shared with interested parties.

The degree of uncertainty varies depending on the quantity and quality of data regarding the given exposure scenario, as well as the specific objective of the assessment. While calculating internal doses and their associated uncertainties by utilizing the established biokinetic and dosimetric models, it is crucial to comprehend the origins of uncertainty as well as the various types and categories it encompasses. Figure 6 shows the primary sources of uncertainties in internal dosimetry, including uncertainties associated with the measurement process, characteristics of intake, etc.

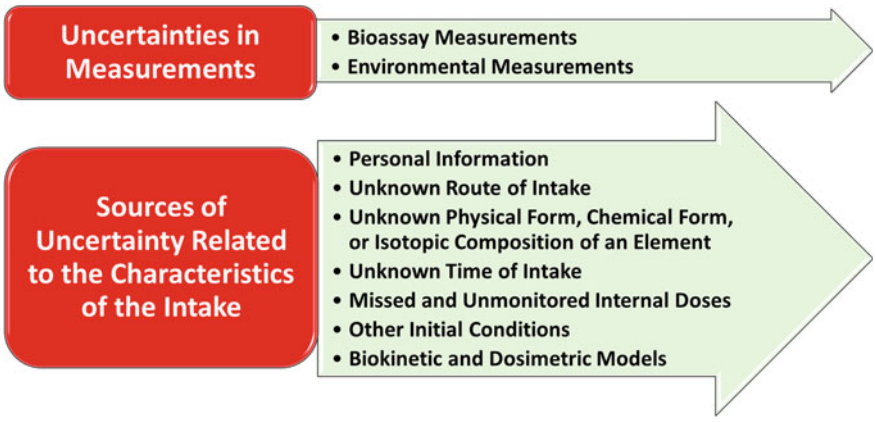

Fig. 6 Sources of uncertainties in the field of internal dosimetry

3.1 Uncertainties in Measurements

3.1.1 Bioassay Measurements

NCRP (1987) has provided guidance on utilizing bioassay measurements for retrospective internal dosimetry, but the focus on uncertainties in these measurements has only gained significant attention in recent years [32]. Uncertainties associated with bioassay measurements encompass radiation detection uncertainties and data normalization uncertainties. Radiation detection uncertainties often arise from counting statistics, although certain measurements utilize more complex techniques such as mass spectrometry. The uncertainty in data normalization for bioassay measurements depends on the specific type of measurement employed.

In in-vivo measurements, which include partial-body, whole-body, and wound counting, uncertainties in normalization involve variations in subject position, variations in body dimensions, and activity distribution inside the body. However, in vitro measurements involve uncertainties stemming from the natural variability observed when the same type of measurement is repeated multiple times for a single individual, as well as uncertainties associated with adapting or standardizing a bioassay measurement. An example of the latter is inferring the activity excreted in a 24-h period based on a measurement of activity from a single-voiding urine sample.

The recent report of the European IDEAS Project [32] provides a comprehensive account of uncertainty in radiation detection and data normalization, including their magnitudes. In this report, errors that follow a Poisson distribution, such as counting errors, are categorized as Type A errors, and uncertainties in other components are labeled as Type B errors. Additionally, uncertainties stem from the interpretation of bioassay data in relation to biokinetic models or the exposure scenario. These uncertainties arise because bioassay measurements need to be compared to expected excretion or retention quantities, which themselves are uncertain due to the unknown parameters of the biokinetic model.

3.1.2 Environmental Measurements

In cases where bioassay data are unavailable or of questionable quality, activity is measured in the environmental media such as food, soil, air, water, or material found in a wound to estimate the radionuclide intake within the body. Alternatively, predictions obtained from environmental transport models can be utilized. However, the measurement of environmental samples introduces sources of uncertainties. Uncertainties related to environmental measurements include the natural variability of activity in the media, errors arising from sampling techniques (such as insufficient sample size or inadequate geographical or temporal distribution of samples), and errors that occur during radiation detection (such as variations in the number of counts, calibration, efficiency, and background noise). Similar to bioassay data, the interpretation of environmental measurements introduces another important source

of uncertainty. For instance, determining whether the measured activity in air, water, soil, or food is relevant to the individual for whom dose reconstructions are being conducted can be a source of uncertainty.

When environmental measurements are lacking for a certain period, location, or type of environmental media, the intake of a radionuclide is determined through interpolation or extrapolation of available data. For example, at a given location, the radionuclide concentration in the air can be estimated using interpolation measurements from surrounding locations. Environmental transport models may also be employed for intake estimation. However, the process of interpolation/extrapolation or the use of environmental models introduces uncertainties that can significantly impact the uncertainties in intake and, consequently, internal dose calculations. In cases where environmental models are utilized to quantify activities in environmental media, it is preferable to perform an uncertainty analysis. However, often environmental model inputs are assigned with the expectation of resulting in a conservative overestimate of media concentrations. Consequently, point estimates of environmental media concentrations, without associated uncertainties, are used to estimate intake rates and doses. As these point estimates are believed to be overestimates, reported internal doses should be accompanied by statements acknowledging that an overestimate of radionuclide intake rate was assumed because of the absence of environmental data, regardless of whether the uncertainty is evaluated or not.

3.2 Sources of Uncertainty Related to the Characteristics of the Intake

Bioassay and environmental measurements, as discussed in the previous subsection, play crucial roles in determining the intake of a radionuclide and assessing the internal dose. This subsection will cover additional quantities and aspects that are necessary for a comprehensive characterization of radionuclide intake in the human body.

3.2.1 Uncertainties Related to Personal Information

The quantity of activity entering the body is influenced by various factors specific to the individual being exposed. In cases of inhalation exposure, factors such as breathing rates, occupancy factors (the fraction of time spent indoors), and filtration efficiency affect the intake. In cases of ingestion, factors such as consumption rates of different food items, the time delay between contamination and consumption, the fraction of contaminated food, and activity loss during culinary preparation (culinary factors) impact the intake. When specific information about individuals is not available, these factors can be set equal to average or best estimate values for representative subgroups of the population. The uncertainty associated with these factors should reflect the variability within the respective population group. For example, ingestion

rates for adult males may have a different range of potential values compared to adult females or children between the ages of 1 and 5.

Exposure information for specific individuals is often collected through personal interviews, aiming to gather details about the location and types of activities during the exposure period (for occupational settings) or ingestion rates, food sources, and residence history (for environmental settings). However, this information is subject to biases and uncertainties because it relies on recollections of events that may have occurred a long time before the interview. Additionally, interviewees may struggle to accurately define certain physical quantities. For example, individuals may have difficulty recalling their long-term average milk consumption rate but can remember specific instances when they consumed three to four glasses of milk.

3.2.2 Uncertainties Related to an Unknown Route of Intake

In certain occupational or environmental scenarios, there are situations where the route of intake of a radionuclide cannot be readily determined due to a lack of conclusive information from existing bioassay data, environmental measurements, or health physics records. For example, there are instances where it remains uncertain whether the intake occurred solely through inhalation, ingestion, or through a combination of both. Even when it is established that both inhalation and ingestion occurred, accurately determining the precise fraction of activity that was inhaled and ingested poses a challenge.

3.2.3 Uncertainties Related to an Unknown Physical Form, Chemical Form, or Isotopic Composition of an Element

The physical and chemical forms of radionuclides in intakes can have a significant impact on internal doses. In certain exposure situations, uncertainties in the physical and chemical forms of radionuclides can directly impact dose estimates, leading to increased uncertainties in the calculated doses. In medical applications, the forms of active material are typically known. Radioactive compounds with specific chemical forms are intentionally designed to serve a particular medical purpose, and therefore, their biokinetics are specialized and usually well understood. It is also possible to have radioactive compounds with similar biokinetics but containing different radionuclides.

In occupational or environmental settings, the form (physical/chemical) of active materials is often unknown. For instance, radionuclides can be attached to particles of unknown sizes or distributed to an unknown extent within the volume of insoluble material that enters the body. These factors can have a significant impact on internal doses, not only in cases of inhalation but also in cases of ingestion or wound contamination. The chemical form of a radionuclide plays a crucial role in its transit and systemic absorption within the human body. Different chemical forms of the same radionuclide can coexist in the environment, and changes in chemical form can occur

during the transport of the radionuclide from the release point to the exposed individual. The form (physical/chemical) of a radionuclide that enters the human body can greatly influence the magnitude of the internal dose. Therefore, uncertainties in the physical and chemical form of the radionuclide can lead to significant uncertainties in the estimated internal dose. Consideration of uncertainties is important, as they can impact the accuracy and reliability of dose assessments in occupational or environmental exposure scenarios.

In addition to the influence of physical and chemical forms, uncertainties in internal doses can also arise from the unknown level of enrichment of an element. For instance, when conducting chest counting of uranium, the measurements may be based on emissions specifically from ^{235}U. However, it may be uncertain whether a worker was exposed to, natural U, enriched U (5 or 95%), or depleted U (DU). In such situations, accurately translating the quantity of 235 U in the lungs into total uranium becomes challenging. In many cases, the uncertainties associated with interpreting bioassay data can be even greater than the uncertainties in the actual measurements themselves.

3.2.4 Uncertainties Associated with an Unknown Time of Intake

Uncertainty in the estimated internal doses can arise from the unknown timing of events that led to the intake of a radionuclide. The extent to which this uncertainty impacts the estimated dose can vary depending upon the particular circumstances. In environmental settings, for instance, the uncertainty in the date of a change in residence (such as moving in or out of an affected area) may have little to no effect on the uncertainty in the internal dose if the change occurred before the arrival of the radioactive material in the affected area. However, if the change in residence occurred around or shortly after the radionuclide reached the affected area, the uncertainty in the timing of the event will have a substantial influence on the uncertainty in the dose estimated. It is crucial to take into account and quantitatively assess the uncertainty associated with the unknown timing of intake events when estimating internal doses. Understanding the potential impact of this uncertainty can help in interpreting dose estimates more accurately and assessing the overall uncertainty in radiation exposure scenarios.

In occupational settings the intake dates or periods normally available from health physics records could represent one of the following cases:

i. intake date is known precisely because there was a well-documented incident;
ii. facility had a default procedure for assigning an intake date for regulatory purposes (e.g., the midpoint of the time since the last routine bioassay measurement, or a uniform intake rate since the last measurement);
iii. air monitoring suggests a certain pattern of intake during the period since the last measurement;

iv. work records indicate that there was potential intake only during a certain time period (e.g., because at other times the worker was on sick leave or vacation or only worked in clean areas).

In Case A, the intake date is known precisely and there is no uncertainty related to the date of intake. This means that the dose estimate can be calculated accurately without any additional uncertainties or biases. In Case B, where there is great uncertainty in the intake date, it can result in large uncertainties or biases in the dose estimate. Since the exact timing of the intake is unknown, the dose estimate may have a wide range of possible values, making it less precise and reliable. Case C represents a scenario where the uncertainties in the intake date are reduced compared to Case B, but significant uncertainties may still remain. While there is some information available from air monitoring data, it may not provide a precise intake date. Therefore, the dose estimate may still have sizable uncertainties associated with it. In Case D, the impact of the uncertainty in the intake date on the dose estimate can vary. If the urinary excretion pattern is fairly flat around the estimated exposure period, the dose estimate may be less sensitive to the uncertainty in the intake date. However, if the urinary excretion curve declines rapidly during the suspected exposure period, the uncertainty in the exposure date can have a significant effect on the estimated dose. Overall, uncertainty in the date of intake can introduce varying degrees of uncertainty or sensitivity in the estimated internal dose, depending on the specific circumstances and the relationship between the timing of intake and the biological excretion or retention of the radionuclide.

In routine monitoring scenarios, when only one measurement data is available at the conclusion of the monitoring interval and the timing of a single intake during that interval remains unknown, various methods can be employed for intake or dose estimation. The ICRP recommended midpoint method assumes that intake had occurred at the midpoint of the time interval since the previous bioassay sample. This method provides a simple estimate, but it has the tendency to overestimate the true intake. To mitigate this bias, the monitoring interval is recommended to be chosen in such a way that, the bias in estimated intake is less than a factor of three. The U.S. Department of Energy (DOE) standards suggest dividing monitoring intervals into equal intervals and reporting the average of the representative intakes from each interval. The purpose of the midpoint method is to offer a more precise estimation of the average intake during the monitoring interval. In contrast, the constant-chronic method proposed by Puncher et al. [33] assumes a constant intake rate throughout the entire monitoring interval. This method aims to provide a more accurate estimate of the average intake during the monitoring interval.

Alternatively, Monte Carlo or Bayesian methods can be employed to estimate the intake or dose and their uncertainties while considering both the measurement error and the significant uncertainties associated with the excretion or retention functions. These methods account for the uncertainty propagation and can provide more comprehensive and probabilistic estimates of the intake or dose. The selection of the method depends on several factors, including the availability of information, the

accuracy of the measurement and biological data, and the desired level of detail and uncertainty characterization.

3.2.5 Missed and Unmonitored Internal Doses

Estimation of intake and dose when bioassay data points are below the limit of detection (LOD), especially when reported as zero, can pose a significant problem in internal dosimetry. When data points are below the LOD, it is possible that a portion of the intake and dose is missed, leading to an underestimation of the actual dose received. In routine monitoring scenarios, a worker may experience chronic low-level intakes that result in bioassay samples consistently below the LOD. As a result, no internal dose would be assigned, even though some level of dose has been incurred over time. This can result in an underestimation of the cumulative dose for the worker. Similarly, for an acute intake of a radionuclide which is eliminated rapidly from the body, the bioassay samples taken at the beginning and end of the monitoring period may both be below the LOD, suggesting no irradiation. However, this does not accurately reflect the actual dose received during the interval of the acute intake. Dealing with bioassay data points below the LOD requires careful consideration. Various statistical methods and techniques, such as statistical imputation or maximum likelihood estimation, can be employed to address this issue. These methods aim to estimate the true values that lie below the LOD based on statistical models, measurement uncertainties, and other available information. By incorporating these techniques, more accurate estimates of intake and dose can be obtained, even in cases where bioassay data points fall below the LOD. It is crucial to acknowledge the limitations and potential biases associated with handling data points below the LOD and to implement appropriate statistical approaches to minimize the underestimation of intake and dose in such situations.

Bioassay data less than the LOD can lead to biases in the assessed doses in various ways:

- underestimated if the potential for a missed dose is not recognized;
- underestimated if data less than LOD are set to zero;
- overestimated if data less than LOD are set equal to the LOD;
- overestimated if data less than LOD are ignored and only data greater than LOD are used;
- biased by an uncertain amount if the data less than LOD are set to an arbitrary fraction of the LOD.

The biases in doses due to bioassay data less than LOD can be reduced or eliminated if the underlying error distribution of the measurement is known or reasonably estimated [34, 35]. Maximum likelihood or Bayesian methods can be employed, where the likelihood function for data points below the LOD is substituted by the probability that the true value lies between zero and the LOD. This probability can be obtained by calculating the area under the measurement error probability curve.

In cases where certain workers with low potential for exposure were not monitored, there is still a possibility that they could have been exposed and received a dose. In such situations, dose reconstruction can be performed by analyzing possible exposure pathways, similar to environmental dose reconstructions. Another category of workers includes those who should have been monitored, but their bioassay data were not recorded, compromised, or lost. In these cases, unmonitored internal doses can still be assessed by analyzing possible exposure pathways. Alternatively, numerical fits to bioassay results from similarly exposed co-workers can be used to estimate doses, incorporating appropriate biokinetic models. However, using co-worker data introduces uncertainties due to the variability of bioassay data among co-workers and the potential differences in relevance to the individual with incomplete or no bioassay data. Overall, in situations where bioassay data is missing or below the LOD, efforts should be made to reconstruct doses by considering available information, employing statistical methods, and analyzing exposure pathways. These approaches help mitigate biases and uncertainties associated with unmonitored doses or incomplete bioassay data.

3.2.6 Uncertainties in Other Initial Conditions

The assessment of intakes and doses can be impacted by the presence of unsuspected previous exposures. For instance, when a worker begins activities in an area that requires bioassay monitoring, their bioassay samples may indicate elevated activity levels. This could be attributed to unintentional or unmonitored intakes of the same radionuclide prior to their current activities. Mathematically, this situation can be considered as an unknown initial condition. In other words, the compartments of the biokinetic model are not empty at the designated starting time but already contain some unknown amount of the radionuclide from a previous exposure. This unknown initial condition influences bioassay data interpretation and introduces uncertainties in dose estimation. It is important to recognize the potential impact of previous exposures on the assessment of doses and to account for this factor when interpreting bioassay data and estimating internal doses accurately. By acknowledging the existence of unknown initial conditions, the uncertainties associated with dose estimates can be better understood and managed.

3.2.7 Uncertainties in Biokinetic and Dosimetric Models

Biokinetic models are developed to predict the movement and deposition of radionuclides in different organs, and dosimetric models are used for the computation of dose received by target organs due to radioactive transformations occurring in source organs of the body. These models are based usually on limited experimental data, and on a constantly evolving understanding of the real processes occurring in the human body.

i. **Uncertainties in Biokinetic Models**

The general framework of a biokinetic model is a simplified illustration of known processes, as certain processes are excluded from the model and the formulation of the model relies on mathematical ease instead of a comprehensive understanding of the processes involved [36]. The structure of the model dictates how data is extrapolated and reduced beyond the observed region. Different model structures can be devised for the same radionuclide, and updated data can result in significant modifications to the model structure [37, 38]. The uncertainty stemming from the model structure can be assessed by employing various model structures to estimate doses in the same exposure scenario.

The anticipated accumulation of a radionuclide and the computed doses resulting from internally deposited radionuclides are influenced by uncertainties in model parameters, which arise from a lack of precise knowledge (such as an insufficient number of relevant data) or the stochastic variability of parameter values or temporal variability due to metabolic and physiological factors. The data sources employed in the construction of biokinetic models are categorized into four groups based on their relevance [36, 39, 40]:

H1: direct measurement in humans (i.e., quantitative measurements of the element in humans);
H2: observations of the behavior of chemically-similar elements in humans;
A1: observations of the behavior of the element in nonhuman species;
A2: observation of the behavior of chemically-similar elements in nonhuman species.

The primary data source, H1, is preferred, while data from H2, A1, and A2 are utilized as substitutes for H1. Although H1 data are considered the most relevant, there exists uncertainty regarding the standard or quality of a given data set. The limitations associated with H1 data can include:

- Small study groups;
- Short observation periods;
- Usage of small tissue samples, which are potentially non-representative;
- Inaccurate techniques used for measurement;
- Uncertainties surrounding the pattern or quantity of element intake;
- Study conditions that deviate from the norm;
- Inconsistencies in reported values.

H1 data may not always be entirely applicable. Data collected from individuals with illnesses that can alter the biokinetics of the element may not be relevant for healthy individuals. Additionally, data obtained from adult males may only be partially relevant for females or children. When dealing with data from individuals affected by a disease or health condition, there are three potential approaches:

1. Consider the data as unaffected by the disease or health condition and use them without any modifications.

2. Acknowledge that the data are influenced by the disease and apply corrections using adjustment factors, which may introduce uncertainty.
3. Regard the data as not relevant and exclude them from usage.

H1 data may include personal interview information that can be used to adjust biokinetic parameters. Factors such as smoking history, pre-existing health conditions, and certain habits can affect these parameters. However, personal interview data may be affected by recall bias and uncertainty, leading to uncertainties in biokinetic parameters and internal doses. Alternatively, the use of H2 or A2 data assumes, elements that are chemically similar exhibit similar physiological behavior.

Chemical analogs such as radium and barium, calcium, and strontium, and americium and curium exhibit close physiological similarities. Similarities are also observed to a lesser extent for potassium and rubidium, zirconium and hafnium, germanium and silicon, gallium and indium, or promethium and samarium [36]. However, there are exceptions to the assumption that chemical similarity implies physiological similarity. For instance, potassium and sodium, demonstrate opposite behaviors in the body, despite having similar physical and chemical properties as alkali metals. Potassium is predominantly found in intracellular space, whereas sodium is primarily located in the extracellular compartment [41].

An example involving potassium and cesium highlights that these elements have similar physiological behavior qualitatively in the body. However, there can be significant variations in the quantitative aspect, with cesium being retained three to four times more than potassium in healthy adults during the early stages after intake [16, 18]. When applying animal data to humans (A1, A2), it is based on the assumption that there are general regularities across different species in terms of cellular or organ structure, and biochemistry. However, this extrapolation process is uncertain. The similarities observed across species are primarily qualitative rather than quantitative. Two species may exhibit different kinetics of a radionuclide, even if they handle it in a qualitatively similar manner [36].

In addition to the issue of relevancy, the uncertainty introduced by H2, A1, and A2 data types is dependent upon the quality of data collection, study design, and interpretation difficulties associated with using data collected for purposes other than building a biokinetic model. Inter-subject variability and variability of repeated measurements on the same subject contribute to the sources of uncertainty in data collection and interpretation. Accounting for these uncertainties is important when assessing the reliability of predictions made using biokinetic models. In addition to H1, H2, A1, and A2 data, supplementary information and constraints are employed to enhance the biokinetic modeling process. These include physiological information, mass balance considerations, theoretical models based on fundamental principles, experimental data from anatomically realistic physical models, and in vitro data related to compound dissolution in simulated lung fluids.

The level of uncertainty introduced by the additional types of information depends on the relevance and quality of the available data. A biokinetic model, along with its parameters, designed for occupational and environmental settings can be further modified to account for specific characteristics of a dose assessment problem. Default

parameters in the model are often adjusted by analyzing bioassay data from exposed workers or considering other specific exposure information, such as the chemical form of a radionuclide. For instance, the absorption fraction of 137 Cs from the alimentary tract is typically set close to one, assuming soluble forms of cesium. However, if an individual ingests insoluble forms of cesium, as found in nuclear weapons fallout, the absorption fraction needs to be lowered. Moreover, highly specialized chemical forms of certain radionuclides used in medical applications may require different biokinetic models and parameters, which may carry smaller degrees of uncertainty compared to models used in occupational or environmental settings.

ii. **Uncertainties in Dosimetric Models**

Estimation of doses using dosimetric models is based on the energy emitted by radionuclides within tissues. Uncertainty arises in identifying target cells for dose calculations and determining the location of cells at risk. The debate continues among pathologists regarding the specific cells from which cancer may arise in thoracic tissues. Similarly, the risk of lymphoma is estimated based on doses received by active bone marrow, but indications suggest that mature lymphocytes throughout the lymphatic system may also be at risk. Average values are used for epithelial thickness and cell nucleus depth, despite their variability across the epithelial region and among individuals. In GI tract dosimetry, contributions from radioactive disintegrations in the tract's contents are significant due to energy deposition by alpha particles and low-energy electrons.

Recently, ICRP adopted the Human Alimentary Tract Model (HATM) [2] which acknowledges the fact that the depth of cells at risk extends beyond the range of low-energy electrons or alpha particles. Consequently, doses from radioactive contents are considered zero for these particles. However, HATM recognizes an exchange of radioactive material between contents and the tract's wall, resulting in the presence of radionuclides in the wall and potentially higher doses for certain emitters like ^{210}Po. Even when target cells and their location are known, uncertainties arise from simplified target tissue geometry assumptions, different methods of solving radiation transport equations, uncertainties in cross-section data, and statistical variations in Monte Carlo calculations.

Another source contributing to uncertainty in dose assessments is the variability in mass of organs and tissues among individuals, influenced by factors such as age, sex, body size, and overall health. In most cases, organ mass is not directly measured for dose assessment subjects, except in situations where advanced imaging techniques provide such information. It is important to note that, energy deposition in an organ can be correlated to its mass. Larger organs tend to receive more energy from their own activity as compared to smaller organs because the escape probability of penetrating radiation in the case of the former is relatively less. Additionally, larger organs present larger targets and receive more energy from neighboring source organs. Accounting for these correlations in dose calculations reduces the uncertainty compared to ignoring them. Organ mass can also be correlated with the fractional uptake of radionuclides by that organ. For instance, a person with a larger organ, such

as the thyroid gland, may have a higher fractional uptake than someone with a smaller organ if physiological requirements necessitate similar element concentrations in that organ.

4 Conclusion

The chapter discusses the importance of dose evaluation methods, quality assurance practices, and uncertainty analysis in assessing internal radiation exposure. It focuses on the different pathways of human exposure to internal irradiation and highlights the use of intake, systemic, and dosimetric models for dose calculations, including specific models developed by the ICRP. It also introduces the MIRD and ICRP systems as widely used approaches for internal dose calculations. It emphasizes the significance of quality assurance through intercomparison exercises and guidelines, emphasizing harmonization and accuracy. Additionally, this chapter highlights the importance of uncertainty analysis in measurements and intake characteristics, emphasizing the need for understanding and evaluating these uncertainties for accurate dose estimation and reliable communication of results.

References

1. ICRP (1994) International commission of radiological protection. Human respiratory tract model for radiological protection, ICRP Publication 66. Ann ICRP 24(1–3) (Elsevier, New York)
2. ICRP (2006) International commission of radiological protection. Human alimentary tract model for radiological protection, ICRP Publication 100. Ann. ICRP 36(1–2) (Elsevier, New York)
3. NCRP (2007) National council on radiation protection and measurements. Development of a biokinetic model for radionuclide contaminated wounds and procedures for their assessment, dosimetry and treatment. NCRP report no 156, Bethesda, Maryland
4. Bolch WE, Eckerman KF, Sgouros G, Thomas SR (2009) MIRD Pamphlet No. 21—a generalized schema for radiopharmaceutical dosimetry: standardization of nomenclature. J Nucl Med 50(3):477–484
5. Loevinger R, Berman M (1968) A formalism for calculation of absorbed dose from radionuclides. Phys Med Biol 13(2):205–217
6. Loevinger R, Berman M (1976) A revised schema for absorbed-dose calculations for biologically distributed radionuclides, MIRD Pamphlet 1, rev. Society of Nuclear Medicine, New York
7. Loevinger R, Budinger TF, Watson EE (1991) MIRD primer for absorbed dose calculations, Revised. Society of Nuclear Medicine, New York
8. Snyder WS, Ford MR, Warner GG, Watson SB (1974) A tabulation of dose equivalent per microcurie-day for source and target organs of an adult for various radionuclides, ORNL/TM-5000. National Technical Information Service, Springfield, Virginia
9. Snyder WS, Ford MR, Warner GG, Watson SB (1975) MIRD Pamphlet No. 11, 'S,' absorbed dose per unit cumulated activity for selected radionuclides and organs. Society of Nuclear Medicine, Reston, Virginia. http://interactive.snm.org/docs/MIRD%20Pamphlet%2011.1-69.pdf. Accessed 13 Aug 2010

10. Zaidi H, Xu XG (2007) Computational anthropomorphic models of the human anatomy: the path to realistic Monte Carlo modeling in radiological sciences. Ann Rev Biomed Eng 9:471–500
11. Bolch WE, Bouchet LG, Robertson JS, Wessels BW, Siegel JA, Howell RW, Erdi AK, Aydogan B, Costes S, Watson EE, Brill AB (1999) MIRD Pamphlet No. 17: the dosimetry of nonuniform activity distributions—radionuclide S values at the voxel level. J Nucl Med 40(1):11–36
12. Howell RW, Bouchet LG, Bolch WE, Rao DV, Goddu SM (1997) MIRD cellular S values: self-absorbed dose per unit cumulated activity for selected radionuclides and monoenergetic electron and alpha particle emitters incorporated into different cell compartments. Society of Nuclear Medicine, Reston, Virginia
13. Howell RW, Wessels BW, Loevinger R (1999) The MIRD perspective 1999. J Nucl Med 40(1):3S-10S
14. Eckerman KF, Endo A (2008) MIRD: radionuclide data and decay schemes, 1st edn. Society of Nuclear Medicine, Reston, Virginia
15. ICRP (2007) International commission of radiological protection. The 2007 recommendations of the international commission on radiological protection, ICRP Publication 103. Ann ICRP 37(2–4) (Elsevier, New York)
16. ICRP (1979) International commission on radiological protection. Limits for intakes of radionuclides by workers, ICRP Publication 30, Part 1. Ann ICRP 2(3–4) (Elsevier, New York)
17. Cristy M, Eckerman KF (1987) Specific absorbed fractions of energy at various ages from internal photon sources, ORNL/TM-8381/V1. Oak Ridge National Laboratory, Oak Ridge, Tennessee. http://ordose.ornl.gov/documents. Accessed 13 Aug 2010
18. ICRP (1980) International commission of radiological protection. Statement and recommendations of the 1980 Brighton Meeting of the ICRP, limits for intakes of radionuclides by workers, ICRP Publication 30, Part 2. Ann ICRP 4(3/4) (Elsevier, New York)
19. ICRP (1991) International commission on radiological protection. 1990 Recommendations of the international commission on radiological protection, ICRP Publication 60. Ann ICRP 21(1–3) (Elsevier, New York)
20. ICRP (1981) International commission on radiological protection. Limits for intakes by workers, ICRP Publication 30, Part 3. Ann ICRP 6(2/3) (Elsevier, New York)
21. ICRP (1994) International commission on radiological protection. Dose coefficients for intakes of radionuclides by workers.
22. ICRP (1987) International commission on radiological protection. Radiation dose to patients from radiopharmaceuticals, ICRP Publication 53. Ann ICRP 18(1–4) (Elsevier, New York)
23. ICRP (1993) International commission on radiological protection. Age-dependent doses to members of the public from intake of radionuclides: part 2, ingestion dose coefficients, ICRP Publication 67. Ann ICRP 23(3–4) (Elsevier, New York)
24. ICRP (1998) International commission on radiological protection. Radiation dose to patients from radiopharmaceuticals, ICRP Publication 80. Ann ICRP 28(3) (Elsevier, New York)
25. ICRP (2008) International commission on radiological protection. Radiation dose to patients from radiopharmaceuticals, ICRP Publication 106. Ann ICRP 38(1–2) (Elsevier, New York)
26. ICRP (1989) International commission on radiological protection. Age-dependent doses to members of the public from intake of radionuclides, part 1, ICRP Publication 56. Ann ICRP 20(2) (Elsevier, New York)
27. ICRP (1995) International commission on radiological protection. Age-dependent doses to members of the public from intake of radionuclides: part 3, ingestion dose coefficients, ICRP Publication 69. Ann ICRP 25(1) (Elsevier, New York)
28. ICRP (1995) International commission on radiological protection. Age-dependent doses to members of the public from intake of radionuclides: part 4, inhalation dose coefficients, ICRP Publication 71. Ann ICRP 25(3–4) (Elsevier, New York)
29. ICRP (1996) International commission on radiological protection. Age-dependent doses to members of the public from intake of radionuclides: part 5, compilation of ingestion and inhalation dose coefficients, ICRP Publication 72. Ann ICRP 26(1) (Elsevier, New York)

30. ICRP (2001) International commission on radiological protection. Doses to the embryo and fetus from intakes of radionuclides by the mother, ICRP Publication 88. Ann ICRP 31(1–3) (Elsevier, New York)
31. ICRP (2004) International commission on radiological protection. Doses to infants from ingestion of radionuclides in mothers' milk, ICRP Publication 95. Ann ICRP 34(3–4) (Elsevier, New York)
32. Doerfel H, Andrasi A, Bailey M, Berkovski V, Blanchardon E, Castellani CM, Hurtgen C, Leguen B, Malatova I, Marsh J, Stather J (2006) General guidelines for the estimation of committed effective dose from incorporation of monitoring data, Project IDEAS report FZKA 7243. Karlsruhe Institute of Technology, Germany
33. Puncher M, Marsh JW, Birchall A (2006) Obtaining an unbiased estimate of intake in routine monitoring when the time of intake is unknown. Radiat Prot Dosim 118(3):280–289
34. James AC, Marsh JW, Birchall A, Jarvis NS, Puncher M, Davis K, King D (2004) User manual for IMBA expert™ OCAS-edition (version 3.2); Appendix A: technical basis. ACJ and Associates, Inc., Richland, Washington
35. Riddell AE, Britcher AR (1994) Pluto—a software package using the maximum likelihood method to fit plutonium in urine data to an excretion function. Radiat Prot Dosim 53(1–4):199–201
36. Leggett RW (2001) Reliability of the ICRP's dose coefficients for members of the public. 1. Sources of uncertainty in the biokinetic models. Radiat Prot Dosim 95(3):199–213
37. Leggett RW (2003) Reliability of the ICRP's dose coefficients for members of the public: U.S. government III. Plutonium as a case study of uncertainties in the systemic biokinetics of radionuclides. Radiat Prot Dosim 106(2):103–120
38. Leggett RW, Eckerman KF (1994) Evolution of the ICRP's biokinetic models. Radiat Prot Dosim 53(1):147–155
39. Leggett RW, Bouville A, Eckerman KF (1998) Reliability of the ICRP's systemic biokinetic models. Radiat Prot Dosim 79(1):335–342
40. NCRP (1998) National council on radiation protection and measurements. Evaluating the reliability of biokinetic and dosimetric models and parameters used to assess individual doses for risk assessment purposes, NCRP commentary No. 15. National Council on Radiation Protection and Measurements, Bethesda, Maryland
41. Guyton AC, Hall JE (1997) Human physiology and mechanisms of disease, 6th edn. W.B. Saunders Company, Philadelphia

Direct Monitoring Method to Detect Internal Radioactive Contamination

Minal Y. Nadar, Lokpati Mishra, and I. S. Singh

1 Introduction

In case of internal radioactive contamination, the source/sources will keep on irradiating the nearby tissues as long as they are inside the body [1, 2]. Also, activity in whole body or organ will always evolve due to biokinetic behaviour resulting in transfer to various organs, radioactive decay and excretion from the body [1, 2]. The objective of internal dosimetry is to estimate the dose received by a radiation worker due to intake [3]. The doses received by radiation workers serves as an input to verify the presence of sufficient shielding or adequate exposure control mechanisms of plant. They also help in design of facilities in case of shortcomings. Internal dose assessment also provides inputs for protective or remedial measures such as wound excision or decorporation in case of accidents. It is also useful in metabolic and tracer studies used in medical applications for understanding many complex processes occurring in the human body.

In direct or in vivo monitoring method, external detectors are placed close to the body or organ in which internal radioactive contamination has to be measured [2] as shown in Fig. 1. It is basically a gamma ray spectrometry method and radiation should reach the detector so that internal activity can be measured. Therefore, direct monitoring can be carried out for those radionuclides which emit gamma rays of sufficient energy and yield as well as for high energy beta emitters. This method is dependent upon standardised geometry used for detection of internal activity. Calibration of the detector system needs to be carried out in that geometry using anthropomorphic or anthropometric phantoms and required source distribution [4]. If calibrated properly using required phantoms and used in the calibrated standard geometry, then this method is fastest and most accurate [4].

M. Y. Nadar (✉) · L. Mishra · I. S. Singh
Radiation Safety Systems Division, Bhabha Atomic Research Centre, Mumbai 400085, India
e-mail: minalyn@barc.gov.in

D. K. Aswal (ed.), *Handbook on Radiation Environment, Volume 2*,
https://doi.org/10.1007/978-981-97-2799-5_19

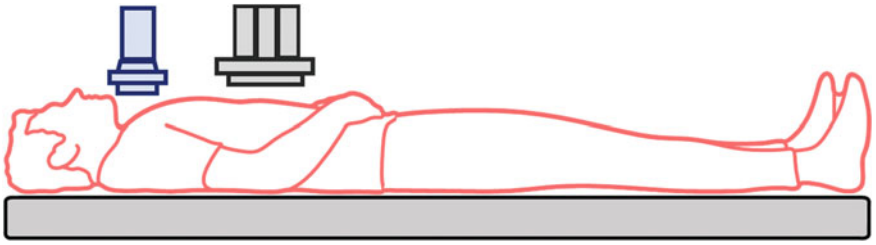

Fig. 1 Direct method of organ/whole body activity measurement

Internal contamination occurs when activity goes inside the person's body [1, 2]. Inhalation intake is the most common and important pathway [2, 5]. Activity can also enter inside the body through wounds in case of accidents [1, 2, 6]. Ingestion of contaminated food or water is the common pathway for general public when activity becomes airborne in case of nuclear accidents or releases into the atmosphere [3, 7]. Some radionuclides such as iodine and tritium can also be absorbed through skin, although it serves as a strong barrier for other radionuclides [1]. In case of diagnostic and therapeutic applications of nuclear medicine, a specific radioactivity tagged with pharmaceutical is injected or ingested by patients, which is also quantified using direct monitoring technique.

2 Historical Perspective

Direct measurement of internal contamination using external detectors [8] started in 1925 for luminous dial workers, majority of whom were young females. The female workers were tipping their brushes with tongue to keep them pointed which resulted in ingestion of radium [9]. They were also exposed by absorption through skin and inhalation of radioactive dust, but major pathway was chronic ingestion of small amounts of radium [8, 9]. Most of the amount was excreted, but small amount was deposited in bones, which got built up over a period of time and replaced the calcium in bones [10]. Lots of workers started showing osteomyelitis (Inflammation) of the jaw, radium necrosis, bone tumors and bone changes, spontaneous fractures and anemia after working for ~ 1 to 4 years in the luminous dial industry [9–11]. This resulted in an effort in the quantification of internal contamination.

Initially, to show the presence of radium in the body, measurements were carried out using Wulf type electrometer by Martland et al. in 1925 [10, 11].

First serious in vivo measurements on luminous dial workers were carried out by Schlundt et al. in 1929, by Wulf-Hess quartz fibre electrometer [12]. It was kept on a table behind the middle of the back of the subject who was seated in a chair [8, 13]. Calibration of the chamber was based on body content of radium of a subject who died later. Based on chemical analysis of bones and other body parts, activity in the body was determined and used for calibration purpose. The limit of detection was 2.5

μg of ^{226}Ra free of ^{228}Ra. They also determined the radium present in the body by measuring radon exhaled from the aspired air. The total activity was the combined activity obtained though radon measurement and direct whole body measurement [13].

The drawback of the methodology was its inability to differentiate ^{226}Ra from short-lived ^{228}Ra [13] and it was assumed that both have same emanating power. But in reality, once embedded in bone, only 1% of ^{220}Ra (emitted in decay chain of ^{228}Ra) is exhaled in the breath compared to 60–70% of ^{222}Ra (emitted in decay chain of ^{226}Ra).

The researchers recommended special precautions to reduce the background in direct monitoring of internal activity. They gave importance to bathing, changing over fresh clothes and removing the jewellery wore by the subjects before measurement. These recommendations are still followed up in the direct monitoring laboratories [8, 13].

3 Evolution of Detectors in Direct Measurement of Internal Contamination

3.1 Initial Measurements with G.M. Counters

In 1937, measurements of luminous dial workers were carried out with Geiger-Muller (GM) tube by Evans et al. in MIT [13, 14]. Evans replaced the electroscope by a GM tube with a direct reading counting-rate meter. Patient was placed on a wooden bed in an arc geometry of 1 m in radius. Detector was kept at the center of the curvature of the midline of the patient. Two measurements were carried out, one in supine and other in prone geometry [14]. Third measurement was carried out to correct for self-absorption by positioning three radium sources of equal activities at three locations, i.e., shoulders, hips and thighs. Thus, the detection system doesn't require a phantom for calibration but activity was estimated using these three measurements. Limit of detection was 0.2 μg. The system had a drawback as that of Schlundt et al. that it could not differentiate between ^{226} and ^{228}Ra activities [13].

3.2 Measurements with Ionisation Chamber

In 1947, Hess and McNiff carried out measurements on luminous dial workers with Ionization chamber [15]. The quantification of radium in vivo was possible at a substantially lower level of 0.11 μg of radium using the chamber. It is of 40.6 cm hight and 20.3 cm in diameter with a volume of 13 L, and 2.5-mm thick brass wall and filled with dry nitrogen at atmospheric pressure. Subject was sitting upright from the vertical axis of chamber at a distance of 35 cm. The subject was monitored

in supine and prone geometry simultaneously. They used water filled tank in the shape of human thorax for calibration purpose. Sources of radium was placed at 57 different positions in the water tank. Hess and Mcniff also built the first shadow shield to reduce the local background. It is of 10.5 cm thick iron wall, 110 cm in height and 82 cm in width and positioned behind the subject's chair [15]. They also described the method of measurement of radon in breath samples.

3.3 Measurements with High Pressure Ionisation Chamber

In 1951, measurements to determine radium content were carried out with high pressure ionization chamber by Sievert [8]. He used ten cylindrical high pressure ionisation chambers with 4π geometry around subject. The detection system was further shielded with concrete and tanks filled with water. The detection level of 0.015 μg of radium was possible. The chambers were 0.22 m in diameter, 1.25 m long and filled with Nitrogen at 2.45 MPa around a ring 0.5 m in diameter as shown schematically in Fig. 2. In this ring, the subject lies on a curved aluminium plate.

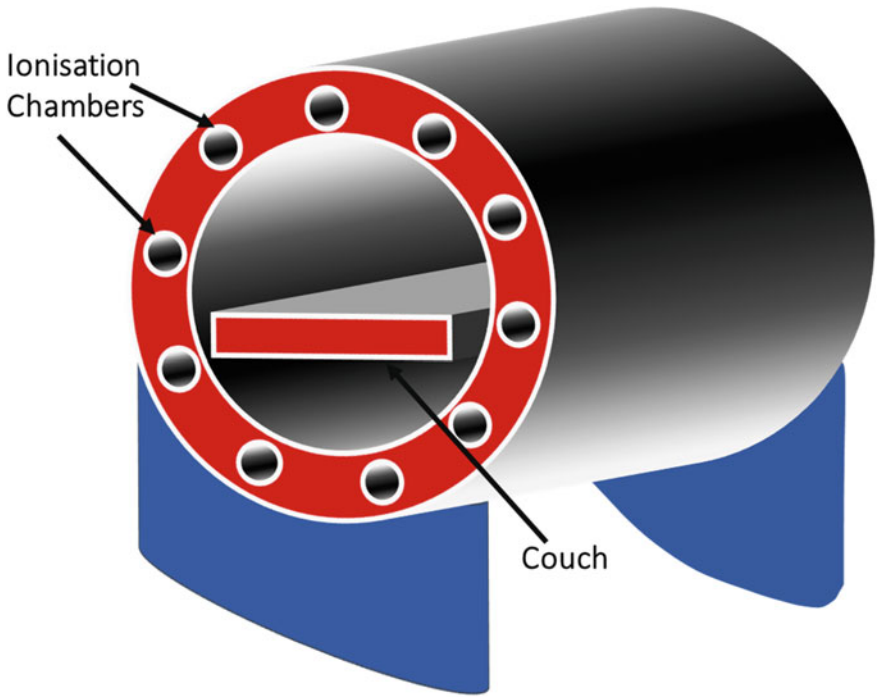

Fig. 2 Schematic of ten high pressure ionisation chambers used for body activity measurements (adopted from [8])

Later, he installed similar equipment in an underground laboratory which was 50 m below the ground and shielded in all directions by 1 m thick layer of water. His research paved the way for designing shielded laboratories for direct measurement of internal contamination.

Burch and spiers used four high pressure ionisation chambers to determine body radioactivity measurements [8, 16]. Ionisation chambers were steel cylinders 198.12 cm long and 29.2 cm dia. with 0.635 cm thick wall. The subject used to lie on a couch beneath them. Water shielding was around the apparatus which reduces the total background by 50%. Another set of seven ionisation chambers were used to compensate for variation of cosmic ray background. The differential ionisation current was measured to estimate ^{40}K as well as additional radioactivity present in the body.

3.4 Measurements Using Liquid Scintillation Detectors

In Los Alamos, Reines et al. [17] developed apparatus to determine radioactivity in total body. The apparatus was constructed for neutrino measurement, but it was found that with person it was showing higher background. This observation led to the use of the counter for whole body activity measurement. They used large volume liquid scintillator in an annular cylinder of 0.76 m high, 0.76 m outer dia. and a thickness of 0.13 m. It was viewed by 45 photomultipliers. The equipment was shielded on all sides by 1.27 m thick Pb, except at the top [8]. The subject was measured in foetal position in 0.5 m aperture with the top position kept open. As human body was in the detector, 4π geometry was partially approximated.

This apparatus inspired researchers in developing other systems with 2π and 4π geometries incorporating liquid scintillators. One of the systems was Geneva walk in counter [18]. It had 2π geometry with 265 L of triethyl benzene, six 41 cm dia. PMTs and 8 cm Pb shielding. There was also a human counter situated at Los Alamos [18]. It had 4π geometry with 530 L of scintillation fluid which was viewed by 108 PMTs. Annular tank can slide into the 20-ton Pb shield of 12.7 cm thick. The subject lies on the bed which can slide in the annular ring of the detector.

The disadvantage of liquid scintillator systems was their poor energy resolution, low stopping power, hazard due to fire, explosion and toxicity.

3.5 Measurements Using NaI(Tl) Detectors

In 1950, development of solid NaI(Tl) crystals lead to their incorporation in whole body counters. In 1955, Marinelli et al. used NaI(Tl) for the first time in whole body counting [19–21]. They measured radioactivity present in the human body such as ^{40}K, radium and other radionuclides by NaI(Tl) detector. Initially, they used NaI(Tl) crystal with minimum shielding in a meter arc geometry. Then, measurements were

carried out in tilted chair geometry which is a modified arc geometry. Later, to improve the efficiency the detector was kept close to the body at ~ 0.5 or 0.1 m [13].

In tilting-chair geometry, the patient used to sit with ~ 90° angle between the trunk and thighs and between the thighs and lower legs. A NaI(TI) crystal was positioned in front of the patient. For homogeneous distribution of activity, an accuracy of ± 5% was possible independent of the subject's body weight which can be between 50 and 90 kg. The chair geometry has also been used in several clinical tracer studies. For example, for measuring the retention of gamma emitting isotopes in tracer amounts. A subject was positioned in chair geometry for a measurement of gamma rays emitted from the internal contaminant present in the body [18, 21]. The patient reclines on a metal chair beneath the cylindrical NaI(Tl) detector after wearing clean clothes supplied by the laboratory.

3.6 Measurements Using Proportional Counters

Initially developed NaI(Tl) crystal has certain limitations due to the difficulties in making thin crystals, high cost, and high background, also they were easily breakable. Therefore, researchers tried other detector systems for whole body counting such as gas filled proportional counters. These were especially useful for low energy measurement of actinides. To increase the area, multiwire proportional counters were used by Taylor et al. in 1969 [22]. They had superior energy resolution than NaI(Tl) detector and efficiency similar to NaI in low energy regions. But with the development of Phoswich detector, their use in low energy photon measurement was stopped.

3.7 Measurements Using Phoswich Detectors

Phoswich is a sandwich of two phosphors [23]. It was developed by Lam et al. in 1965 [24]. To detect lung burdens of actinides, Phoswich was first used by Laurer and others in 1968 and onwards [25–28]. Initial Phoswich had thin CsI(Tl) and thick NaI(Tl) phosphors. Later Phoswich with thin NaI(Tl) and thick CsI(Tl) were developed. It has been irreplaceable in lung monitoring laboratories all over the world since then.

The two crystals of different thicknesses used in Phoswich detector have different rise time properties [23–25]. Low energy photons (LEPs) will deposit maximum energy in lowermost detector having low thickness whereas high energy photons (HEPs) will interact in both the crystals but deposit maximum energy in bigger and thicker detector. The first thin crystal is called as primary detector and the thick crystal is called as secondary crystal. It acts as an anti-coincidence shield for thin crystal. Figure 3a shows the schematic of Phoswich detector. The LEPs will be interacting in thin crystal; HEPs are partially depositing energy in it and maximum in thicker

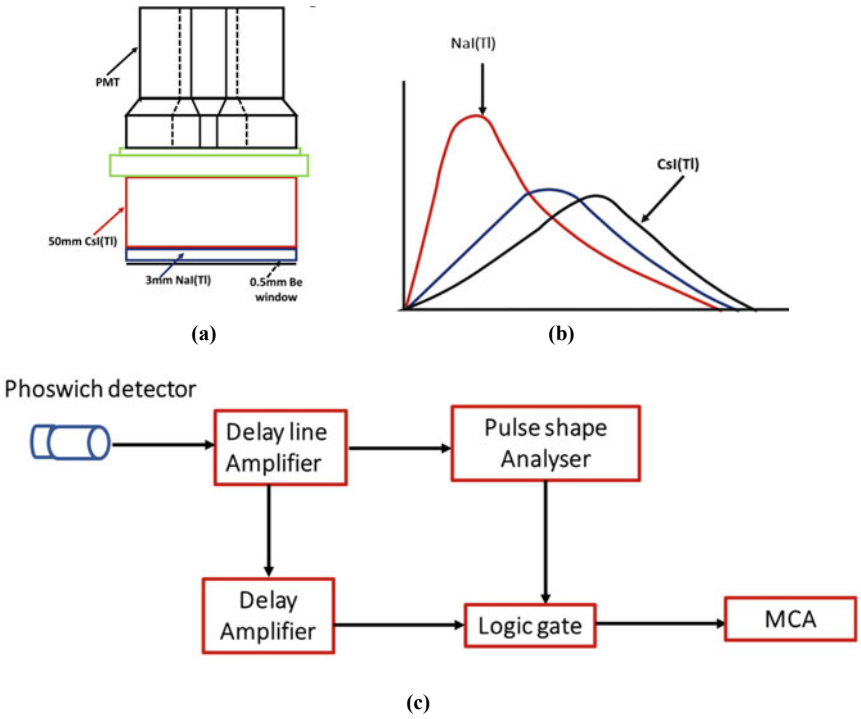

Fig. 3 **(a)** Phoswich detector schematics, **(b)** The rise time properties of two crystals and **(c)** PSD system

crystal. HEPs emitted due to background sources can enter the detector from any side and can deposit energy in both the crystals.

Due to different rise time properties of selected crystals, photons after interacting in the detector form pulses of different rise times as shown in Fig. 3b. Then using pulse shape discrimination (PSD) technique [29, 30], the required pulses either of low energy or high energy can be selected. Figure 3c shows the schematics of PSD system. Thus, by selecting low energy pulses, it can be used for monitoring LEP emitters, i.e. actinides [31, 32]. The pulses due to interactions in both the crystals as well as in thicker crystal will be rejected. Figure 4a shows ^{241}Am source spectrum and Fig. 4b shows ^{137}Cs source spectrum observed with the Phoswich detector. Only LEPs of 32 keV of ^{137}Cs are visible as HEP pulses are rejected by PSD.

3.8 Measurements Using HPGe Detectors

With the advent of better crystal development methods, hyperpure germanium (HPGe) solid state detectors were made available with impurity concentration of

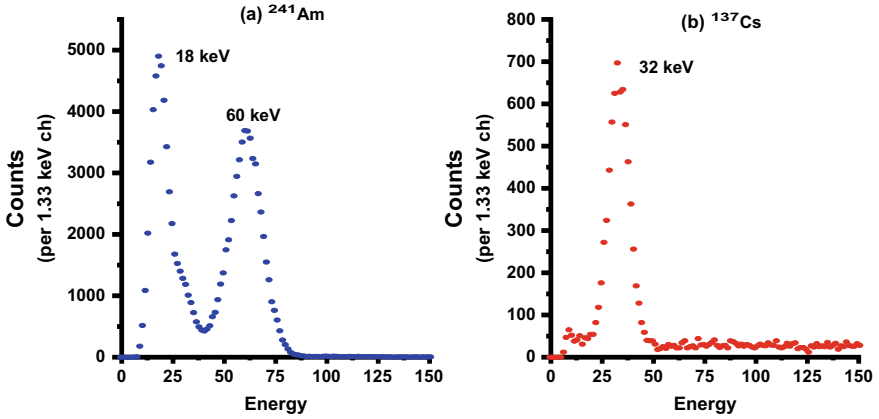

Fig. 4 **(a)** ^{241}Am source spectrum and **(b)** ^{137}Cs source spectrum with Phoswich detector using PSD for LEPs

10^{10} atoms/cm^3 [33]. These are p–n junction detectors, one of them is very thin and heavily doped so that depletion region covers the other whole region and when operated in reverse bias, it acts as a detector. Researchers started using them for in-vivo measurement since 1978 [34–36].

HPGe detectors have advantage of high resolution due to their low energy bandgap which results in large number of charge carriers. A very high resolution of about 1.1% is obtained with HPGe detection system compared to 20% of the phoswich detector at 60 keV of ^{241}Am and 0.3% (~ 2 keV) at 662 keV compared to 7% of NaI(Tl). Figure 5a and b shows whole body counter with HPGe detectors used for measurement of actinides and HEP emitters in the body. These detectors are required to be cooled to liquid nitrogen temperature 77 K during use to reduce the leakage current due to thermal generation of charge carriers [33].

A sensitive actinide lung monitor consisting an array of three HPGe detectors has been in use at IDS, BARC Hospital for measurement of internally deposited

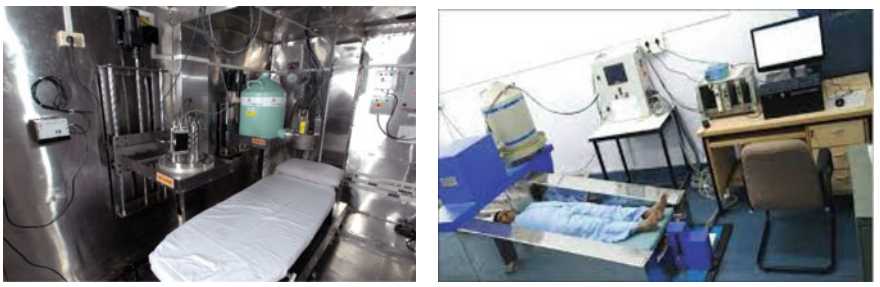

(a) **(b)**

Fig. 5 **(a)** HPGe array for lung monitoring of actinides and **(b)** HPGe detector in scanning WBC

radionuclides in lungs and other organs of the radiation workers since 2006 [37, 38]. It is very helpful in measurement of mixture of radionuclides. In an array, there are three HPGe detectors, each of 70 mm dia. and 25 mm thickness positioned at 120 degrees with respect to each other. An array has a single 30 L Dewar, a separate preamplifier and power supply with each detector. An array has 0.8 mm thick carbon entrance window which can transmit photons above 10 keV. The signal from each detector can be analyzed separately using three separate MCAs as well as summed with respect to energy. The spectrum of individual detector is used to obtain information about the distribution of the contaminant in the lungs. The MDA values obtained with HPGe detector are similar to the Phoswich detector. Still the identification and quantification of LEP emitters is possible [37] at MDA level due to its better resolution and lower background.

The interesting fact about the development of in vivo detection system is that the limit of detection decreases with time from 1929 to 1960 with a half-life of 3 years. Combining the development and use of phoswich detector since 1965 and use of HPGe detectors since 1980's, the same trend is continued with the saturation observed at the end.

4 Evolution of Shielding in Direct Monitoring for Detection of Internal Contamination

Background radiation is omnipresent due to cosmic rays, terrestrial radiation as well as airborne radionuclides [33]. To measure the low level of activities, present inside the body of the worker with precision, it is very important that background radiation should be minimized. Therefore, appropriate shielding of detection systems is required [39]. Shielding can be partial such as in shadow shielded bed or shielded chair whole body counters or complete such as totally shielded steel room.

Shielding for protection of operators was started in 1913 with 2 mm Pb shielding for X-rays by German radiological society. Till then shielding was at the discretion of the practitioner [40]. Since 1920s, studies were carried out to provide protection to operators and workers from gamma and neutrons in the reactors.

4.1 Selection of Shielding Materials

Two important parameters which characterize shielding are background index and background reduction factor [2]. The former is the count rate per unit detector volume, cpm per cm^3, measured inside the enclosure over energy range 100 keV to 2 MeV [2]. The latter is the ratio of count rates measured in the same energy range outside and inside the enclosure. A good shielding produces background reduction factor of 100 [2].

Main mechanism of photon interaction in the shield is Compton interaction which reduces the photon energy subsequently. As mass attenuation coefficient is independent of material, any material of proper thickness can be used as a shielding material [2]. The only requirement will be that it should be dense and available in large quantities. Lead, steel, concrete, and water have been used by the researchers for shielding.

4.2 Totally Shielded Room Concept

Totally shielded room concept was used by Miller et al. in 1955 for in vivo measurement of Radium in luminous dial workers [41]. This was the aftermath of the in vivo studies carried out by Sievert et al. in underground laboratories where apparatus was further shielded with water containers. Miller et al. used NaI (1.5 × 1 in., 4.2 × 1.5 in.), CsI (1.5 × 1 in.) crystals, and a large plastic scintillator (6″ × 5″) in 2.4 m × 2.1 m × 1.9 m room, shielded by 8″ Iron.

15 cm steel with 1 cm Pb and 0.2 cm steel has background reduction factor of 100 [2] in low energy regions of 150 keV to 2 MeV. The 20 cm steel is sufficient to absorb more than 99% of all incoming photons predominantly with Compton scattering. The Compton scattered photons have energy less than 500 keV. The photoelectric interaction with high Z element can absorb incoming photon flux from steel. Several installations made use of silica sand of ~ 70 cm for outer shield and 10 cm inner shield of iron which also has an additional graded Z lining [2].

Graded Z lining is an arrangement of shielding in descending order of atomic number, where photoelectric effect is utilised for absorption of 150–200 keV photons coming out of large steel shield. It is typically made of 3 mm Pb ($Z = 82$), 2 mm Cd ($Z = 48$) or Sn ($Z = 50$) and 0.5 mm Cu ($Z = 29$). Pb absorbs the 150–200 keV photons by photoelectric effect, during which it emits characteristic X-rays of ~ 72–74 keV. These are absorbed by Cd or Tin (Sn) which also emits characteristic X-rays of ~ 23 keV. These are absorbed by Cu which emits characteristic X-rays of ~ 8 keV and does not contribute in the region of interest for measuring LEPs of energy greater than 13 keV emitted by Pu. Instead of Cd/Cu, steel layer is also used due to toxicity hazard of Cd. Also, other metals can be used having similar Z. An additional layer of plastic can be used for further attenuation of low energies. Figure 6 shows the reduction in gamma background due to the use of shield [42].

For measurement of LEPs emitted by actinides in radiation workers, 20 cm thick steel room with graded Z lining of 3 mm Pb, 2 mm Cd and 0.5 mm Cu is used at most of in-vivo laboratories and at BARC [43].

There was also an emphasis for low background materials in shield and detector, and avoiding unnecessary materials in the counting room [2, 8] which increase the scattering in the detector increasing the background. These factors are taken into consideration in the design of direct monitoring laboratories.

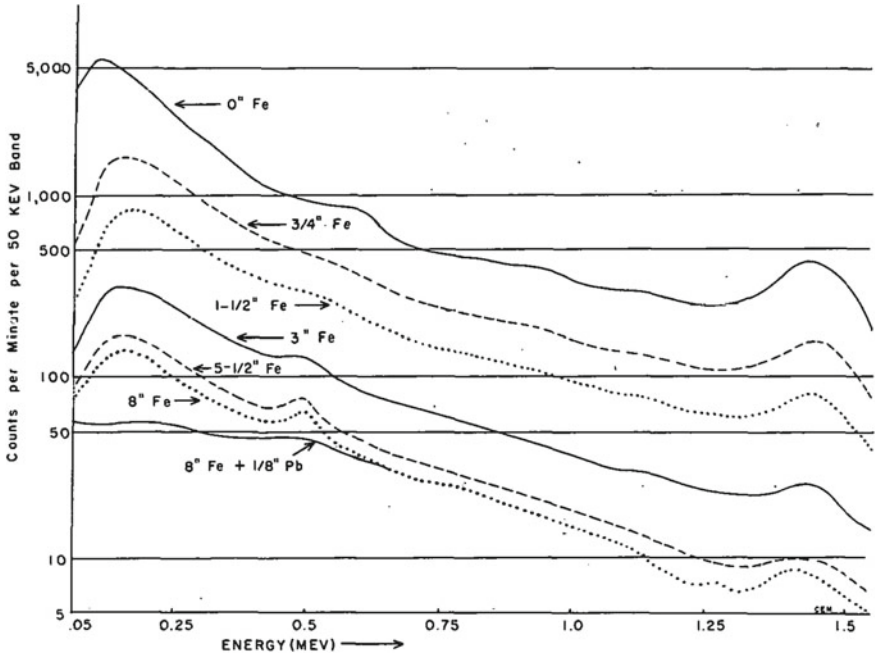

Fig. 6 Reduction in gamma ray background of an 8″ × 4″ NaI(Tl) crystal for various thicknesses of shield of internal dimension 2.4 × 2.2 × 1.9 m [42] (reproduced with permission from Elsevier)

4.3 Partially Shielded Concept

There was a need to monitor a subject with an economical, transportable whole-body counter which will be auxiliary to expensive totally shielded steel room [42, 44]. Also, being transportable, it could be taken to work areas or to places of accidents. Therefore, partially shielded concept was studied in 1957 by Hine and Rasmussen in MIT [44]. It resulted in the development of shielded chair and shadow shield bed whole body counters [44].

4.3.1 Shadow Shield Bed Whole Body Counter

The shield consisting of lead bricks can easily be assembled and dissembled into shadow shield counter [45]. Subject was shielded from below and all four sides and NaI detector shielded on all side except the one facing the subject. As the shield casts a shadow on the detector [44–46] it is called as shadow shield and the photons reaching the detector directly, are only from the subject's body. Researchers also studied various shielding materials for detector and subject such as steel and Pb. No significant difference is observed in the background spectra of steel room and shadow shield above 0.3 MeV [44]. Thus, it suitable for measurement of HEP emitters

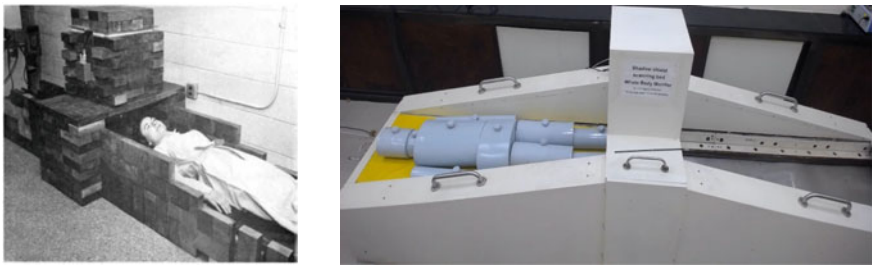

(a) **(b)**

Fig. 7 **(a)** Portable Shadow shield counter in the laboratory (reproduced with permission from Elsevier) [42] and **(b)** Shadow shield bed counter with NaI(Tl) detector at IDS, BARC

above 300 keV. It is also used to study profile scan of the subject to evaluate activity distribution.

Due to portable nature of these counters, they are also used to monitor people at distant places to study their internal contamination. Figure 7a shows the portable shadow shield counter situated in the laboratory for monitoring of radiation workers [45]. It was also used in the field of Alaska for monitoring people to detect their internal contamination. The presently available shadow shield counter is shown in Fig. 7b. They are made up of ~ 6 tons of mild steel with 3 mm of Pb lining [46].

4.3.2 Shielded Chair Whole Body Counter

Earlier chair was used in the shielded room for measurement of whole-body activity. Later, economical, transportable shielded chair was developed for quantifying whole-body activity. At BARC, a shielded chair whole-body monitor has been in use since late 1960s and is shown in Fig. 8. It is now automated, computer controlled, walk-in type of whole-body counter [3, 47]. The chair is shielded by 15 cm thick mild steel from all sides except at the front and the top. A $4'' \times 3''$ thick NaI(Tl) detector shielded with 5 cm lead from all sides except the face views the body from head to knees. The shield weighs ~ 3 tonnes. The counting time normally used is ~ 10 min. The steel and lead for chair and detector shielding respectively are used for the background reduction.

4.3.3 Portable Whole-Body Counter

These are low-cost portable systems mainly used for screening of personnel in remote areas from the laboratory [48]. As inhaled activity is deposited in the lungs and some fraction will be transferred to GI tract, detector was collimated to view thorax region. Pb shielding of 1.9 cm was provided to the $3'' \times 3''$ NaI(Tl) detector. The subject was shielded by 1.27 cm Pb positioned in back and side of chair and under the seat. The

Fig. 8 Chair geometry used for whole body monitoring [3] (Courtesy: BARC Newsletter)

effect of shielding thickness was studied and 1.27 cm Pb was used as the optimum thickness of shield in portable counter with total shield of ~ 0.3 tons [48].

At present, systems such as Quickscan [49] whole body monitors are available for monitoring the large number of subjects to detect internal contamination due to fission and activation products during nuclear accidents or emergency scenarios. Person has to stand in these counters for few minutes for monitoring.

5 Evolution of Measurement Geometry

Measurement geometry is the arrangement of detector and subject [2]. It is selected based on various parameters such as physical characteristics of radionuclide incorporated in the body, anatomical characteristics of the organ to be measured, biokinetic behaviour of the radionuclide and available infrastructure and workload.

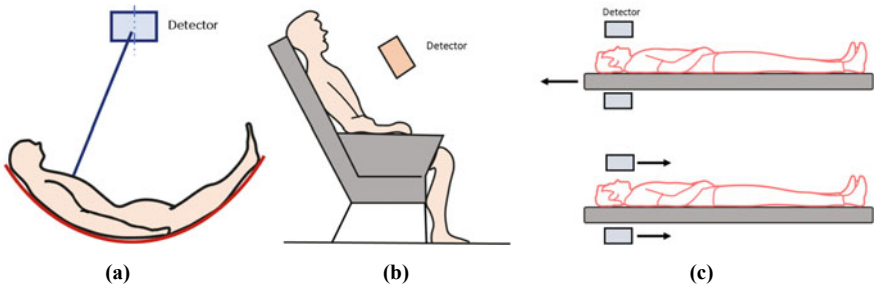

Fig. 9 Various geometries used for whole body counting **(a)** arc geometry, (**b)** chair geometry and **(c)** bed geometry (adopted from [50])

5.1 Various Measurement Geometries

The first geometry which was used for the measurement of radium in luminous dial workers was an arc geometry developed by Evans [13] (see Fig. 9a). This geometry has the advantage that response of the detector is independent of source distribution in the body which is the main objective of whole body counting. The next geometry developed was a chair geometry which is a modified arc, inside totally shielded steel room as shown in Fig. 9b.

Later, bed geometry is evolved by placing subject on the bed and viewed by detector. It is commonly used for monitoring with one or more detectors kept above or below the bed [50]. In the scanning geometry, either subject moves or detector moves. The schematics of these geometries are shown in Fig. 9c. Bed geometry with partial shield incorporating NaI and HPGe detector are shown in Figs. 5b and 7b. The modified chair geometry where the chair was shielded from all the sides and detector was collimated and shielded to reduce the background is shown in Fig. 8.

Comparison of various geometries used in the whole-body counting is given in Table 1. It can be seen from the table that totally shielded steel room with either static or scanning bed geometry gives good response, source distribution information and has high sensitivity. Shadow shield chair gives the poor response and no information about distribution of source. It also has low sensitivity.

5.2 Lung Measurement Geometry for Actinides

Lung measurement is carried out to detect internal contamination due to actinides using Phoswich, thin NaI(Tl) or HPGe detectors. In lung measurement geometry, one end of the Phoswich detector or HPGe array is kept tangential to the sternal notch of the radiation worker and detector center is kept on the midline of the person's body [6, 50]. In the same geometry, phantom measurements were carried out to estimate calibration factors for various radionuclides. Figure 10 shows the Phoswich detector

Table 1 Characteristics of various geometries used in the whole body counting

Geometry	Shield	Mechanical arrangement	Uniformity of response	Distribution information	Sensitivity
Arc	Steel room	Fixed	Very Good	No	Low
Tilting chair	Steel room	Fixed	Poor	No	Medium
Static array	Steel room	Fixed	Good	Yes	High
Scanning	Steel room	Moving detector	Good	Yes	High
Shadow shield bed	Partial	Moving bed	Good	Yes	Medium
Shadow shield chair	Partial	Fixed	Poor	No	Low
Standing	Partial	Fixed	Poor	No	Medium

positioned over the JAERI phantom in standard lung measurement geometry. Lung measurements of the all the radiation workers were carried out in this geometry to minimize the positional errors [51].

Fig. 10 Phoswich detector over JAERI phantom in standard lung measurement geometry

5.3 Wound Monitor for Measurement of Embedded Activity of Pu/^{241}Am

To estimate the embedded activity of Pu/^{241}Am in the wound, wound is kept at 10 cm below the HPGe array as shown in Fig. 11a. HPGe array is calibrated in this geometry to estimate wound activity. LEPs emitted by ^{241}Am such as 13.9 (13.03%), 17.6 (18.86%), 20.82 (4.81%), 26.3 (2.4%) and 59.5 (35.78%) keV having different yields, attenuate differently in the overlying tissue of wound [52]. This property is used to estimate the depth of a wound and embedded activity [52–55]. ^{241}Am source spectrum is shown in Fig. 11b for a point source without attenuation and a source kept under a 3 mm Perspex [53]. Attenuation of 13.9, 17.6 and 20.82 keV photons is visible in the spectrum.

Ratio of counts in 17.6 and 59.5 keV energy regions or ratio of counts of 26 and 59.5 keV energy regions are used to estimate the depth. Embedded activity is estimated using calibration factor at that depth. Figure 12a gives variation of calibration factor with depth. Variation of ratios of counts of 17.6 and 59.5 keV as ratio1 and ratio of counts of 26 and 59.5 keV as ratio2 are given in Fig. 12b [54]. The influence of attenuating material such as soft tissue and Lucite is also given in Figs. It can be seen that at 59.5 and 26 keV, there is not much difference between the two materials at lower depths, but as depth increases, the variation increases. At 17.6 keV, the variation in attenuation is observed at lower depths which increases with depth [54].

5.4 Skeleton Measurement Geometries

In case of internal contamination of long-lived actinides by inhalation or injection pathway, a major portion of activity will be deposited in the skeleton over a period of time as they are bone seekers [1, 56]. As actinides are LEP emitters, first the skull or knee activity is estimated [2] which is then converted into skeletal activity using fractional bone mass of those sites.

Earlier detectors used for in vivo knee or skull measurements were calibrated using physical knee or skull phantoms [3]. Later knee and skull voxel phantoms are derived from ICRP reference voxel phantom [56]. These were used for calibrating Phoswich and HPGe array detectors. The skull and knee voxel phantoms are shown in Fig. 13a and b. The combined bone masses of the skull and a single knee phantom were found to be 10 and 9.3% of the total skeletal mass of 10.45 kg. Using fractional skeletal mass, the total skeletal activity can be estimated from measured skull or knee activity.

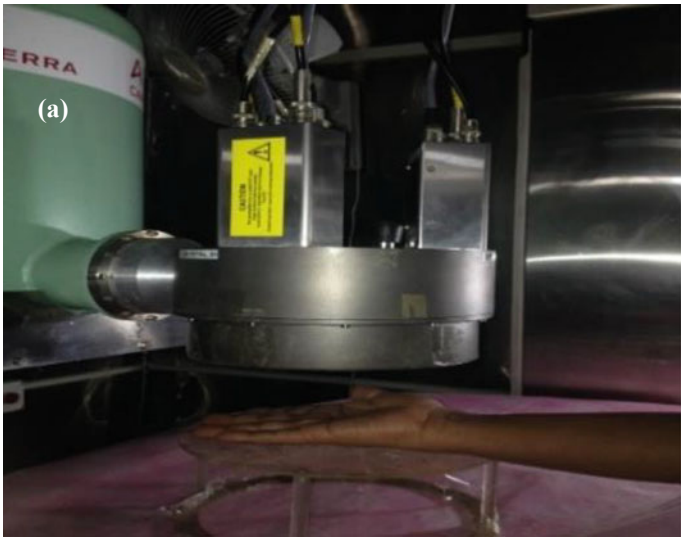

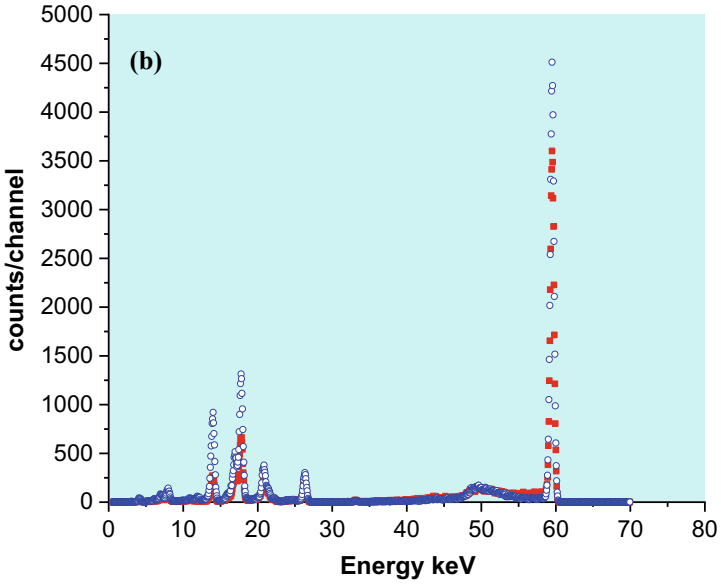

Fig. 11 **(a)** Wound at 10 cm below the HPGe array and **(b)** ^{241}Am source spectrum with HPGe detector

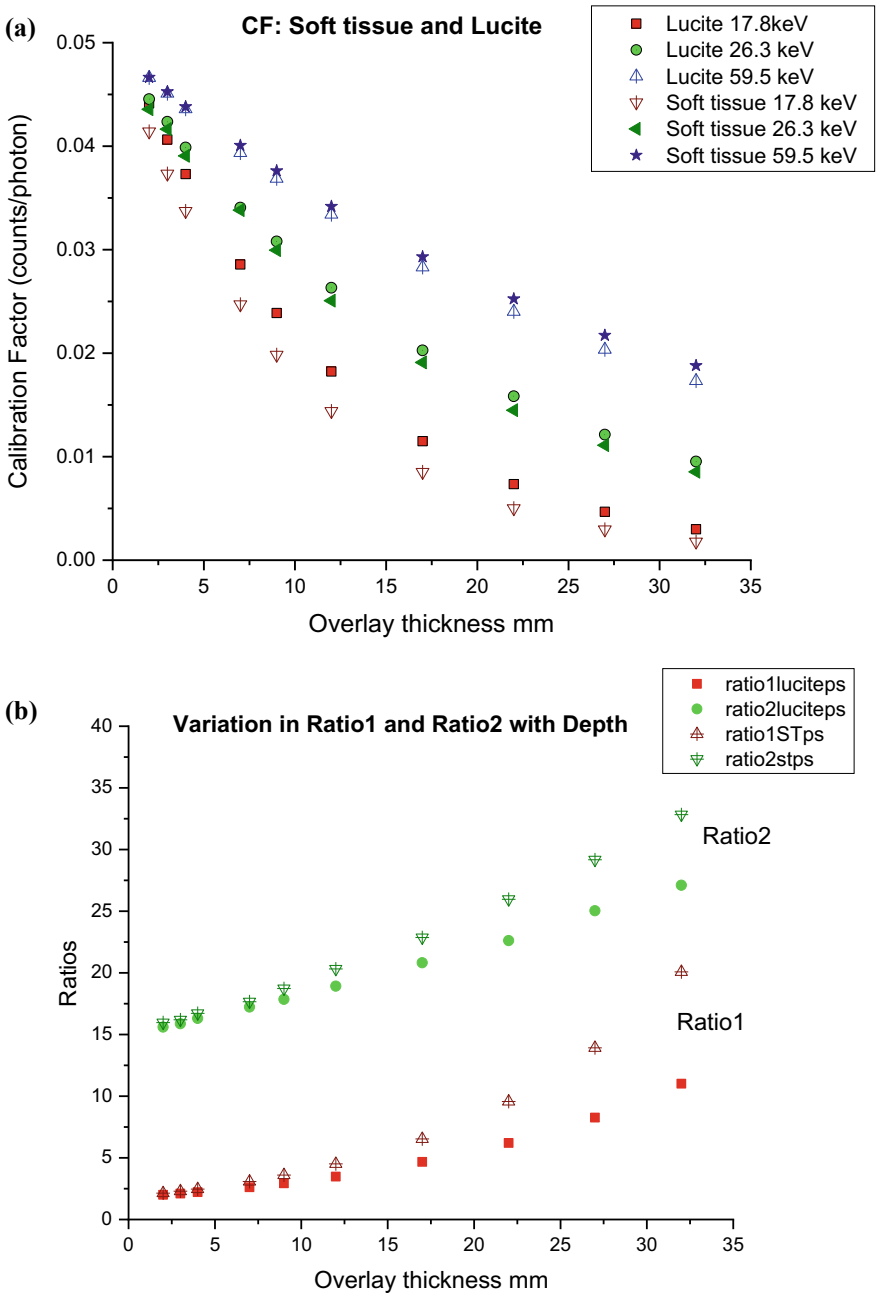

Fig. 12 Variation of **(a)** calibration factor with depth and **(b)** Ratio1 and Ratio2 with depth (reproduced from [54] with permission from Oxford University Press)

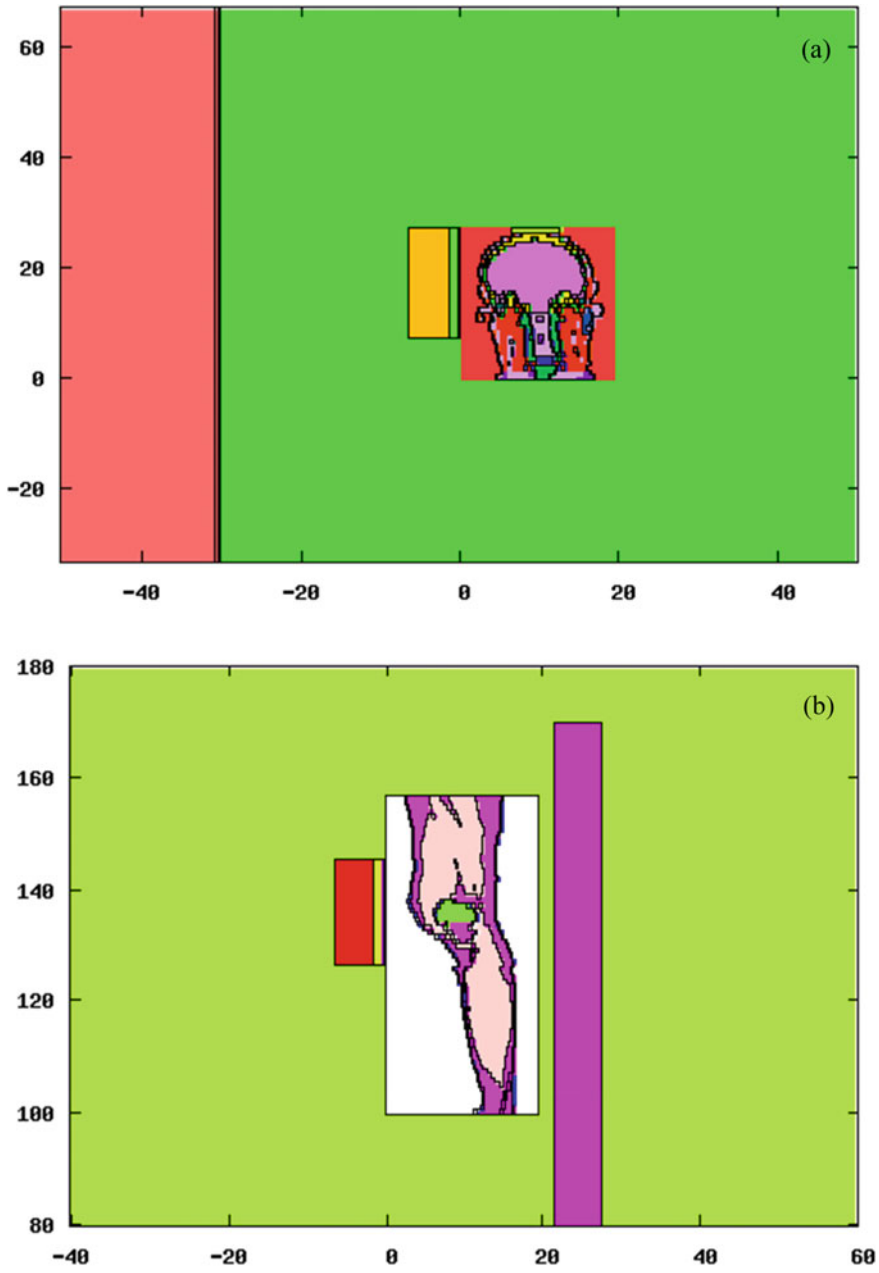

Fig. 13 **(a)** Skull voxel phantom and **(b)** knee voxel phantom (reproduced from [56] with permission from Oxford University Press)

5.5 Liver Measurement Geometry for Actinides

Pu/^{241}Am gets accumulated in the liver [1], also activity in the liver can contribute in the response of detectors to lung measurement [2]. To measure liver activity, the detector is placed close to the body with one end near to sternum end and other end tangential to the midline of the body [57, 58].

5.6 Whole Body Measurement Geometry for Fission and Activation Products

Internal contamination due to fission and activation products in whole body is obtained by using large volume NaI(Tl) or HPGe detector incorporated in steel room or shadow shield bed or chair type of whole-body counters. The worker is scanned from head to toe in scanning bed system of whole-body counters [3]. In chair geometry, subject sits on a shielded chair and whole body activity is determined by shielded and collimated detector which views upper thorax region [2]. In a standing type of whole body counter, subject stands in front of the detector inside shielded enclosure and measurements were carried out [49].

5.7 Thyroid Measurement Geometry for ^{125}I, ^{131}I

Due to the volatile nature of Iodine, it may be released in the atmosphere in case of leakages or fuel clad failure, which may lead to intakes of radiation workers as well as public by inhalation or ingestion pathway. Thyroid produces T4 and T3 hormones, with Iodine as one of the constituents, thus, Iodine gets accumulated in thyroid gland [59]. It leaves thyroid with a biological half-life of ~ 90 to 120 days [59]. Therefore, Iodine intakes are determined by thyroid monitoring [2]. The system used at Trombay, Mumbai for ^{131}I and ^{125}I measurements is shown in Fig. 14. To determine the thyroid activity with minimal interference from other organs, the detector is collimated and shielded [60]. The chair is also provided with shielding to reduce the background.

6 Evolution of Calibration Methods and Phantoms

The calibration methods used in internal dosimetry has undergone significant advancements over the years [2]. Efficiency calibration involves establishing the correlation between the measured count rate, and radioactivity present in the person's body for a particular radionuclide and for a particular measurement geometry [2, 50]. It is a crucial that source distribution as expected in person should be simulated in

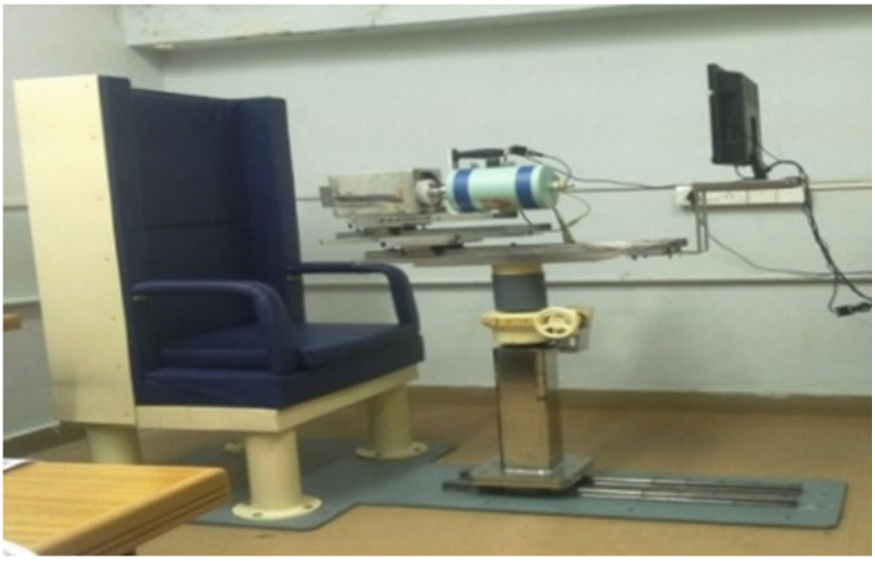

Fig. 14 Thyroid monitoring system at Trombay, Mumbai

realistic way for accurate organ activity measurement. In 1930s, calibration of the in vivo detection system for measurement of radium was carried out by distributing 11 radon sources in the cadaver [12]. Then in 1950, researchers started using tank in the shape of human thorax filled with water and radium sources at different positions [15]. Half skeleton of the cadaver of dead luminous dial worker was also used for calibration purpose. The efficiency of the in vivo detection systems for assessment of internal contamination can be evaluated either by absolute method or by relative method [2].

Absolute calibration method requires the knowledge of measurement geometry, overlying tissue composition and source distribution in the organ or body [2]. It is rarely used as it is difficult to approximate source distribution and absorbing material configuration.

Relative efficiency evaluation method requires phantoms or human surrogates with source distribution similar to the one expected in the humans [2, 50]. The phantoms can be anthropometric, having same measurement characteristic as a human but not exactly look like human. Anthropomorphic phantoms have same measurement characteristic and they also look like human. Phantoms have various tissue substitutes. Different phantoms are used for LEPs and HEPs measurement. Relative calibration of direct measurements can be carried out by three methods, in vivo calibration for LEP emitters, physical phantoms and computational phantoms.

6.1 Tissue Substitutes

Tissue substituent is a material which simulates transmission properties of the various tissues [2]. Important tissues in the human body are muscle, soft tissue, adipose tissue, lungs and bones. Mass attenuation coefficient, μ/ρ, of all these tissues becomes similar above 100 keV. Also, μ/ρ of soft tissue is similar to water, therefore, water is used in phantoms as soft tissue and all the other tissue substituent for efficiency evaluation of detection systems used for measurement of HEPs emitters such as fission and activation products.

At low energies less than 100 keV, attenuation depends upon tissue thickness as well as tissue composition. Therefore, realistic phantoms having realistic tissue substitutes for each tissue are required for efficiency calibration. Polyurethane plastic with varying amounts of $CaCO_3$ is used to simulate various tissues [4]. Foamed polyurethane is used for creating lung tissue substitute having similar density and attenuation characteristics [4].

6.2 In-Vivo Method for Efficiency Evaluation

In vivo calibrations were especially carried out to estimate efficiency of lung monitoring detection systems for LEP emitters, especially Plutonium [43]. In this method, a simulant (single or a combination of radionuclides) with similar emission characteristics as of Pu, is administered to the volunteers [43]. The principle used was that simulant radionuclide will emit X-rays similar to U L X-rays of Pu and it will also be quantified by other method such as whole body counting by measuring HEPs emitted by it [43].

The labelled aerosol with both low and high energy gamma emitter tracer is generated and is inhaled by a human volunteer [61]. It is required that the distribution should be similar to the radionuclide of interest, the simulant should be non-toxic, it should have low effective half-life to reduce dose to the volunteers and the volunteers should have the physique which is a representative of the radiation workers [43]. Pu-simulant also called as mock Pu, was inhaled by volunteers ensuring very low dose to the lungs. Examples of mock Pu are ^{103}Pd and ^{51}Cr, ^{92m}Nb.

^{103}Pd undergoes electron capture and emits low-energy X-rays of ~ 20 keV (67%), has a half-life of approximately 17 days [61]. It is tagged with ^{51}Cr which also undergoes electron capture and emits γ-rays of ~ 330 keV and has a relatively long half-life of about 27.7 days [62, 63]. IAEA carried out Intercomparison with volunteers who inhaled ^{103}Pd/^{51}Cr aerosols between 14 US and European laboratories [4, 62, 63]. Intercomparison was also carried out between Trombay and Harwell laboratories on volunteers who inhaled ^{103}Pd [63].

Similarly, ^{92m}Nb is used as a Pu simulant, it emits both low energy and HEPs. It has been adjudged as a better 'mock Pu' than ^{103}Pd as there is less uncertainty in its determination which can be carried out by both lung monitoring and whole body

counting. It is mainly used to validate LLNL phantom by comparing the detection efficiencies obtained using LLNL phantom with the lung set containing uniformly distributed ^{92m}Nb and volunteers with known amount of ^{92m}Nb in their lungs [64].

6.3 Phantom Calibrations

Phantom calibration can further be categorized in two subcategories (i) experimental calibration with realistic physical phantoms, and (ii) calibration with computational/mathematical phantoms using Monte Carlo simulations [43].

An important requirement for accurate estimation of organ or whole-body activity is realistic phantom. It should have source distribution similar to the one expected in the radiation worker of internally deposited radionuclides, should be made up of tissue equivalent materials and it should be rugged.

Based on the photon energy emitted by radionuclides deposited in the organ or whole body, specification of the phantom changes. For estimating fission and activation products which emits HEPs, BOMAB phantoms are used [2] for efficiency calibration.

Realistic phantoms are required when LEPs from the radionuclides of interest are severely attenuated by body tissues. LEPs of energy less than 100 keV are totally attenuated within the first few centimetres of the body. Therefore, the detector is positioned close to the human subject to achieve higher efficiency, it results in a large solid angle. When detectors are placed close to the body, their response becomes highly dependent on source distribution. Hence, realistic phantom becomes a necessity to simulate exact source distribution [2, 4]. Different phantoms are available to estimate activity in various organs such as lung, liver, knee, skull, thyroid, whole body [2]. They are based on ICRP reference man [65]. The realistic composition is achieved using tissue equivalent material like polyurethane, to simulate muscles, fat, bones and other tissues [4]. Examples of these phantoms are LLNL [64, 66] and JAERI [67] phantoms. There are other phantoms such as REMAB and REMCAL which are used for whole body calibration and nuclear medicine studies. REMAB (radiation equivalent manikin absorption) phantom consists of a plastic shell with a full skeleton. It is filled with water or tissue equivalent solution [50]. REMCAL (radiation equivalent manikin calibration) phantom consists of a plastic shell with cavities for major organs such lungs, thyroid, heart, kidneys, spleen, pancreas, stomach, bladder and lower intestinal tract. Phantom and organs are filled with water or tissue equivalent and radioactive solutions [50].

The emergence of computational modelling and Monte Carlo simulation techniques further revolutionized calibration methods in internal dosimetry [43]. These methods involve creating virtual models of the human body and simulating the transport of radiation within these models based on known anatomical and physiological data [68]. The first computational MIRD phantom consists of a set of mathematical equations and geometric representations of various organs and tissues in the body [68]. In recent years voxel phantoms [69] have replaced MIRD phantoms.

6.3.1 Physical Phantoms

A. LLNL Phantom

The LLNL (Lawrence Livermore National Laboratory) Phantom is used for calibration of detection systems for LEP emitters. It is a realistic anthropomorphic phantom. It is based on Caucasian man with weight of 75 kg and height of 177 cm [66]. It consists of thorax region that includes simulated rib cage and removable lungs, heart, liver and major trachea bronchial lymph nodes. It also has various chest overlay plates corresponding to different chest wall thicknesses. Lung sets uniformly distributed with ^{239}Pu, ^{241}Am, natural Uranium and enriched Uranium sources are available for calibration of detection systems. LLNL phantom has been validated with the inhalation experiments with ^{103}Pd–^{51}Cr and ^{92m}Nb, using human volunteers during IAEA intercomparison exercises [64].

This phantom is made up of a tissue-equivalent material polyurethane and calcium carbonate [4] that closely resembles soft tissue and bone respectively in terms of its radiation interaction properties. Foamed polyurethane is used to achieve the low density of the lungs [50]. The realistic thorax physical LLNL phantom and detection efficiencies estimated for various chest wall thicknesses is shown in Fig. 15a and b respectively.

LLNL phantom simulates a human male torso without head and arms. The torso and organ molds are based on a male cadaver of 1.77 m height and 75 kg weight [66]. In initial phantom, rib cage from cadaver was used in the phantom. It was first cleaned to remove soft tissue, further cleaned with beetles to remove traces of soft tissues. The rib cage cavities then filled with mix D tissue simulant. In later versions, artificial rib cage was used. Uniform source distribution was simulated in various organs by labelling the tissue equivalent organ with the appropriate radioactive materials. Thus, phantom is available with ^{239}Pu, ^{241}Am, natural Uranium, enriched U lung sets, lymph node and liver with uniform source distribution with ^{241}Am. Chest overlays of thicknesses from 1.7 to 4.2 are available so that detection efficiencies can be evaluated for various chest wall thicknesses (CWTs) covering radiation workers of different physiques.

B. JAERI Phantom

It is developed by Japan Atomic Energy Research Institute (JAERI) [67]. It represents a reference Asian man of weight 63.5 kg and height 168 cm. The torso is based on solid plaster cast of an average Japanese adult male. It also has artificial rib cage and different body organs such as lungs, liver, heart, and kidneys. It has solid and sliced lungs and different muscle equivalent chest overlays to simulate different chest wall thickness. In this phantom, polyurethane and epoxy resins are used as a base material for soft tissue substitutes and bones respectively. It has 6 different lung sets uniformly distributed with ^{239}Pu, ^{241}Am, natural Uranium, enriched Uranium (3%), ^{232}Th and blank lung set. The phantom has basic overlay containing rib bones. Using the lung set of radionuclides of interest, the detection efficiency can be evaluated as a function of CWT for that radionuclide. JAERI phantom is shown in Fig. 16.

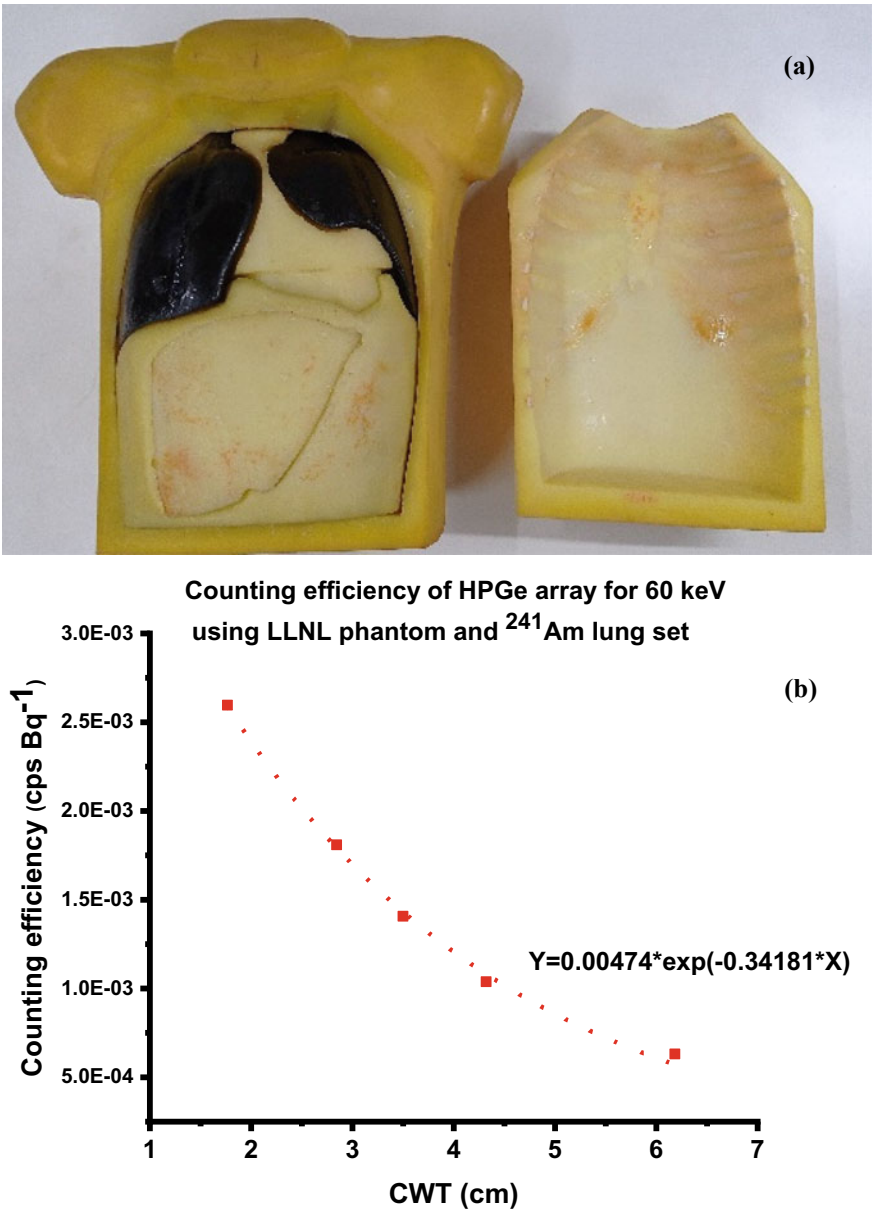

Fig. 15 **(a)** LLNL phantom and **(b)** detection efficiencies estimated using LLNL phantom for various chest wall thicknesses

Fig. 16 JAERI Phantom with lungs, heart, and chest overlay with rib bones

One of the drawbacks of the physical phantoms is that they represent reference man and are not available for varying anatomies. Most of them have arrangements for uniform distribution of activity for few radionuclides but it is difficult to get different activity distributions of various radionuclides in them. Also, the composition, shape and size variations are difficult to incorporate in them. The cost of these phantoms is very high. Theoretical methods which make use of mathematical phantoms and Monte Carlo photon transport techniques are useful in addressing these issues.

C. **BOMAB phantoms**

The Bottle Mannequin Absorber (BOMAB) phantom is a standard anthropometric phantom used for calibration of detection systems used for detection of HEP emitters such as ^{60}Co, ^{137}Cs, etc.

It consists of ten cylindrical polyethylene bottles which can be filled with water and other liquid based tissue substitutes that mimics the human body tissue in terms of radiation interactions [50]. The complete phantom consists of torso, pelvis, head and neck, arms and legs. Indian reference BOMAB phantom and family of BOMAB phantoms were developed by Mehta et al. [70]. Family of BOMAB phantoms is developed to perform efficiency calibration for different age groups. Figure 17 shows the family of BOMAB phantoms [49].

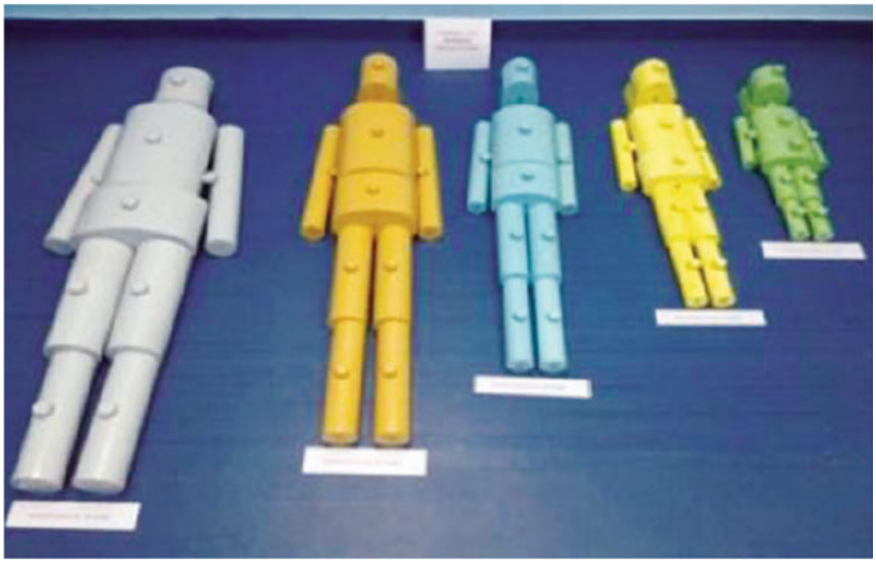

Fig. 17 The family of BOMAB phantoms (Courtesy: BARC newsletter [49])

By placing known quantities of radioactive sources within the various parts of the phantom according to weight fraction of each organ, uniform source distribution is achieved. Detection efficiencies for HEP emitters were evaluated for shadow shield bed and chair whole-body counting systems as well as Quickscan monitoring systems using these phantoms.

6.3.2 Computational/Mathematical Phantoms

Theoretical calibration of detection systems can be carried out using mathematical or computational phantoms and radiation transport codes. Using this method, efficiencies and other dosimetric parameters can be calculated for any photon energy, source distribution, shape and size of the organ, detector and detection geometry as well as the physique of the radiation workers [3]. Earlier, MIRD phantoms were used for the efficiency calibration of the detection systems as well as for evaluating important dosimetric parameters such as absorption fraction, dose conversion coefficients; recently voxel phantoms and mesh phantoms are being used.

A. **MIRD Phantom**

The MIRD (Medical Internal Radiation Dose) phantom is a standardized mathematical model. The principal internal organs are defined by simple geometric shapes such as ellipsoids, elliptical cylinders, and cones, or portions of these shapes [68]. These simple shapes were chosen to facilitate the computer calculations. This phantom was later adopted by the MIRD Committee of the Society of Nuclear Medicine for

evaluation of doses to patients from nuclear medicine diagnosis studies. They are known as MIRD phantom [71].

It consists of a set of mathematical equations and geometric representations of various organs and tissues in the body. It divides the body into a series of compartments or regions, each representing a specific organ or tissue. The size, shape, and composition of each compartment are based on average anatomical data [71].

MIRD phantom has been used in internal dosimetry to estimate dosimetric parameters such as absorption fraction, specific absorption fraction using Monte Carlo radiation transport and anatomical data of reference man [65, 68, 71]. The phantom was further used to estimate detection efficiencies for different types of source distributions in the different organs such as lungs, skull and whole body [3].

Over the years, there have been significant advancements in the phantoms used in the internal dosimetry computations, and one notable development has been the evolution of voxel phantoms.

B. **Voxel Phantoms**

Voxel phantom is a computational anthropomorphic phantom based on medical tomographic images of a single individual, having external dimensions similar to ICRP reference man [69]. It consists of large number of small three-dimensional volume elements (voxels), each assigned a specific number corresponding to the organ or tissue to which they belong [69] by a segmentation process. The specific number contains information of the position of that voxel as well as information regarding composition, density of the tissue to which it belongs.

Voxel phantoms revolutionized internal dosimetry by providing a more accurate and realistic representation of human anatomy. Monte Carlo simulation techniques, which use random sampling to model radiation interactions within the body, were coupled with voxel phantoms to estimate radiation doses to specific organs and tissues for both internal, external, medical and occupational exposure scenarios. The adult reference male and female voxel phantoms are provided in ICRP 110 [69]. Flair [72], an advanced user interface of the FLUKA code [73, 74], has been used for the creation of the input file and the visualisation of the geometry using voxel phantom, at BARC.

ICRP reference male and female voxel phantoms have ~ 2 million and 4 million voxels with in-plane resolution of 2.137 mm and 1.775 mm and slice thickness of 8 mm and 4.84 mm respectively. ICRP reference male voxel phantom corresponds to reference man of height 176 cm and weight 73 kg. ICRP reference female voxel phantom corresponds to reference female of height 163 cm and weight 60 kg.

ICRP reference voxel phantoms are used to calculate equivalent and effective dose coefficients for internal, external and medical exposures using ICRP 103 methodology [75]. At present, a series of reference paediatric phantoms representing different age groups and anatomical characteristics were developed.

These phantoms were used to estimate dosimetric parameters [76, 77], to estimate detection efficiencies [56, 78] as well to estimate uncertainties of monitoring systems for organ or whole body activity determination [51, 79, 80]. These reference

phantoms were also used to estimate organ doses and dose coefficients for occupational, medical, internal and external exposure scenarios as part of EURADOS intercomparison exercise [81, 82].

6.3.3 Mesh Phantoms

Voxel phantoms though realistic have in-plane resolution and voxel thickness of few mm. Therefore, dose evaluation of few micrometer thick target layers of the alimentary tract and respiratory tracts as well as lens of eye and skin regions was not possible [83, 84]. To overcome this, most advanced, 'Mesh' phantoms were constructed by converting voxel phantoms provided in ICRP 110 to a high-quality mesh format to include thin target and source regions. These phantoms will be used in future to estimate radiation doses to different organs and tissues within the human body as well as to estimate dosimetric parameters [83].

Mesh phantoms employs polygon mesh or tetrahedral mesh geometry to describe the human anatomy. They have an advantage that they can be implemented directly into Monte Carlo codes without voxelisation process [83, 85]. Mesh phantoms offer greater flexibility in representing complex anatomical structures of few micrometer thick such as eye lenses, and cell layers of respiratory and alimentary tract, skin, urinary bladder, lymph nodes, etc. They provide effective dose coefficients similar to voxel phantoms for penetrating radiations and more accurate results for weekly penetrating radiations. Mesh phantoms have an additional advantage of deformation [83]. Thus, it is possible to create phantoms of various body sizes and postures [83, 85, 86].

7 Estimation of Whole Body/Lungs/Wound/Skeleton Activity from Direct Monitoring Method

The efficiency calibration of the detection systems is carried out using relevant anthropometric or anthropomorphic phantoms for quantification of HEP or LEP emitters present in the whole body or lungs or wound or skeleton. The calibration is carried out for the range of photon energies for the radionuclides of interest. Efficiency response function is generated for 10–300 keV [4] for estimation of LEP emitters and for 300–2600 keV [4] for estimation of HEP emitters. Prior to efficiency calibration, energy calibration is carried out using reference ^{241}Am, ^{57}Co, ^{137}Cs, ^{60}Co point sources in standard geometry. In this geometry, point source is kept at a 10 cm from the detector.

7.1 Lung Activity Estimation

When measuring LEP emitters incorporated into lungs, emitting less than 200 keV, it is usually necessary to correct for the thickness of the overlying tissue. It is carried out by using proper chest wall thickness (CWT). The effects of overlying tissues are the change in distance between the radioactive source in the organ and detector and the absorption of the low-energy photons by the overlying tissues.

CWT is defined as the exponential average of tissue thickness from the surface of lungs to the points in the intercostals space in between the ribs [87]. CWT depends upon linear attenuation coefficient, μ. Tissue overlying lungs consists of muscle and adipose which have different μ. To remove this discrepancy, the concept of MEQ-CWT has been established. The MEQ-CWT is the thickness of muscle-equivalent absorber that reduces the photon flux from the lungs by the same amount as the actual combination of muscle and adipose tissue in the chest [4]. It is estimated from CWT using following equation

$$\text{MEQ-CWT} = \frac{X}{\mu_M}[\mu_A A + \mu_M(1 - A)] \tag{1}$$

where A is the fractional content of adipose tissue, $(1 - A)$ is the fractional content of muscle, μ_A is the linear attenuation coefficient for adipose tissue (cm^{-1}), μ_M is the linear attenuation coefficient for muscle tissue (cm^{-1}), and X is the measured chest wall thickness. Using this equation, MEQ-CWT was evaluated for ~ 70 radiation workers using ultra-sonography, at BARC.

An empirical equation is generated by correlating MEQ-CWT data of these workers with their physically measurable parameters [87]. One such equation derived at IDS, BARC is given by following equation

$$\text{MEQ-CWT} = 1.427 * \left(\frac{W}{H}\right) + 0.014 * (\text{Ch}) + 0.0025 * (Y) - 0.156 \tag{2}$$

where, *W/H* is weight to height ratio, Ch is chest circumference in cm and Y is age in years.

Calibration for LEP emitters is carried out using realistic thorax phantom, LLNL or JAERI, with various overlying tissue substitute plates corresponding to various MEQ-CWTs and ^{241}Am, Nat. U., Enr. U. and ^{238}Pu lung sets containing uniform distribution of activity [4]. The efficiency as a function of MEQ-CWT is then evaluated from the measurements of the realistic phantom. It can also be evaluated with computational voxel phantoms using Monte Carlo simulations.

7.2 Whole Body/Organ/Wound/Skeleton/Liver Activity Estimation

Whole body/organ/wound/skeleton/liver activity can be estimated using the net counts in the required energy region and counting efficiencies of detection systems in that energy region for that calibrated geometry. Net counts are obtained by subtracting the background of an uncontaminated person having similar physical characteristics from the gross counts of the monitored subject.

8 Conclusion

Direct monitoring methods, are commonly used for measuring internal radioactive contamination using external detectors. Calibrated direct monitoring system using suitable phantom in a standard geometry with suitable radionuclides is the fastest and most accurate method for measuring body radioactivity.

Historically, measurements of internal contamination began in the 1920s for luminous dial workers who ingested radium. Various detectors such as electrometers, ionization chambers, GM counters, proportional counters and inorganic scintillators were used for the in-vivo measurements. The development of inorganic scintillators in 1950s and HPGe detectors in 1970s revolutionized the field of direct monitoring technique. These developments have resulted in accurate identification and quantification of internally deposited radionuclides in the person. These developments also helped in the nuclear medicine applications for the effective diagnosis and treatment.

Shielding materials such as lead, steel, concrete and water were used to reduce background radiation in detection systems. Different measurement geometries, including arc, chair, bed, and scanning geometries, have been developed based on radionuclide characteristics and anatomical considerations.

Efficiency calibration is a crucial aspect of internal dosimetry and involves establishing the relationship between measured count rate and radioactivity for accurate estimation of organ activity. Calibration techniques have evolved from using radon sources in cadaver to employ realistic anthropomorphic phantoms and computational models based on anatomical and physiological data. Phantoms such as LLNL, JAERI, BOMAB and voxel are used for calibration. Voxel phantoms based on CT scan data of individual provide a more accurate representation of human anatomy. Mesh phantoms offer greater flexibility and accuracy in thin target regions.

Overall, advancements in detectors, calibration methods and the use of realistic and computational phantoms have significantly improved the accuracy of body activity measurements, enabling better understanding and management of internal contamination.

References

1. International Commission on Radiological Protection (1997) Individual monitoring for internal exposure of workers. ICRP Publication 78. Ann ICRP 27
2. Griffith R, Bergmann H, Fry FA et al (2003) Direct determination of the body content of radionuclides, ICRU Report 69. J Int Commission Radiat Units Meas 3(1):1–120
3. Pendharkar KA, Bhati S, Singh IS et al (2008) Upgradation of internal dosimetry facilities at BARC Trombay. BARC Newslett 296:9–23
4. International Atomic Energy Agency (2003) Intercalibration of in vivo counting systems using an Asian phantom. IAEA TECDOC-1334, Vienna
5. International Commission on Radiological Protection (1994) Human respiratory tract model for radiological protection. ICRP Publication 66. Ann ICRP 24
6. Surendran T, Haridasan TK, Sharma RC et al (1995) Experiences at Trombay in monitoring actinide intakes by occupational workers by direct external counting. Radiat Prot Dosim 59(1):15–24
7. International Commission on Radiological Protection (1979) Limits for intakes of radionuclides by workers. ICRP Publication 30. Part 1. Ann ICRP 3–4
8. Rundo J (1993) History of the determination of radium in man since 1915. Environ Int 19(5):425–438
9. Rowland RE (1994) Radium in humans—a review of U.S. studies. ANL/ER-3. UC-408
10. Martland HS (1931) the occurrence of malignancy in radio-active persons: a general review of data gathered in the study of the radium dial painters, with special reference to the occurrence of osteogenic sarcoma and the inter-relationship of certain blood diseases. Am J Cancer
11. Coursey BM (2021) The National Bureau of Standards and the radium dial painters. J Res Nat Inst Stand Technol 126:126051
12. Schlundt H, Failla G (1931) The detection and estimation of radium in living persons. III. The normal elimination of radium. Am J Roentgenol Rad Therap xxvi:265–271
13. Hickman DP (1994) In vivo measurements. Chapter 17. In: Internal radiation dosimetry (1994 HPS SS). Medical Physics Publishing
14. Evans R (1937) Radium poisoning II the quantitative determination of the radium content and radium elimination rate of living persons. Am J Roentgenol Radium Therapy 37:368–378
15. Hess VF, Mcniff WT (1947) Quantitative determination of the radium content of the human body and of the radon content of breath samples for the prevention and control of radium poisoning in persons employed in the radium industry. Am J Roentgenol Radium Therapy 57(1):91–102
16. Burch PRJ, Spiers FW (1953) Measurement of the γ-radiation from the human body. Nature 172(4377):519–521
17. Reines F, Schuch RL, Cowan CL et al (1953) Determination of total body radioactivity using liquid scintillation detectors. Nature 172(4377):521–523
18. Woodburn JH, Lengemann FW (2015) Whole body counters. Ebook-49641. https://www.gutenberg.org/files/49641/49641-h/49641-h.htm
19. Marinelli LD, Miller CE, Gustafson PF et al (1955) The quantitative determination of gamma-ray emitting elements in living persons. Am J Roentgenol Radium Therapy Nuclear Med 73
20. Marinelli LD, Miller CE, Rowland RE et al (1955) Measurement in vivo of radium gamma-ray activities lower than ^{40}K levels existing in the human body. Radiology 64(1):116–116
21. Miller CE, Marinelli LD, May HA (1956) NaI(Tl) in chair geometry inside iron room at Argonne National Lab., USA. Argonne National Lab., Lemont, IL
22. Taylor BT (1969) A proportional counter for low-level measurement of plutonium-239 in lungs. Health Phys 17(1):59–69
23. Wilkinson DH (1952) The Phoswich—a multiple phosphor. Rev Sci Instrum 23(8):414–417
24. Lam CF, Wainerdi RE (1965) Pulse-shape discrimination technique for dual-crystal Compton reduction detector. Trans Am Nucl Soc 8:340

25. Laurer GR (1968) In vivo measurement of lung burdens of nuclides emitting soft, penetrating radiations In: Proceedings of the first international congress of radiation protection. Elsevier, p 745
26. Kornberg HA, Norwood WD (1968) Diagnosis and treatment of deposited radionuclides. Excerpta Medica Foundation, Amsterdam
27. Shapiro EG, Anderson AL (1974) Dual energy analysis using Phoswich scintillation detectors for low-level in-vivo counting. IEEE Trans Nucl Sci 21(1):201–209
28. Laurer GR, Eisenbud M (1977) A multicrystal detection system for localization and measurement of photon emitters without external collimation. Nucl Instrum Methods 140(3):481–487
29. Brooks FD, Pringle RW, Funt BL (1960) Pulse shape discrimination in a plastic scintillator. IRE Trans Nucl Sci 7(2/3):35–38
30. Brooks FD (1959) A scintillation counter with neutron and gamma-ray discriminators. Nucl Instrum Methods 4(3):151–163
31. Sharma RC, Krishnamachari G, Haridasan TK et al (1975) A large-area phoswich detector for measurement of low levels of low-energy photon emitters. Nucl Instrum Methods 130(1):305–311
32. Nadar MY, Singh IS, Kalyane GN et al (2008) Estimation of internal contamination due to actinides in the presence of ^{137}Cs using a Phoswich detector. Radiat Prot Environ 31(1–4):393–395
33. Knoll GF (2000) Radiation detection and measurement, 3rd edn. Wiley Publishing, New Delhi
34. Falk RB, Tyree WH, Wood CB et al (1978) System of high-purity germanium detectors for the detection and measurement of inhaled radionuclides. United States, p 21
35. Graham SG, Kirkham SJ (1983) Identification of ^{241}Am in the axillary lymph nodes with an intrinsic germanium detector. Health Phys 44:343–352
36. Palmer HE, Rieksts G (1984) The use of planar high-purity Ge detectors for in vivo measurement of low-energy photon emitters. Health Phys 47(4):569–578
37. Singh IS, Nadar MY, Kalyane GN et al (2008) A sensitive steel room whole body counter with three LOAX HPGE detectors for in vivo monitoring of personnel for actinides. Radiat Prot Environ 31(1–4):379–381
38. Singh IS, Nadar MY, Mishra L et al (2018) Experience with HPGe detector based actinide lung monitoring system. In: Proceedings of 33rd IARPIC-2018, p 224
39. Lynch TP (2007) A historically significant shield for in vivo measurements. Health Phys 93(2):S119–S123
40. Shultis JK, Faw RE (2005) Radiation shielding technology. Health Phys 88(4):297–322
41. Miller CE, May HA, Marinelli LD (1956) The use of low level scintillation spectroscopy in the evaluation of radioactive contamination of the human body. AECU 4156:1956
42. Andrews GA, Gibbs WD, Morris AC et al (1973) Whole-body counting. Semin Nucl Med 3(4):367–388
43. Sharma RC, Surendran T, Haridasan TK et al (1989) In-vivo measurements of low-energy Photon (LEP) emitters. Bull Rad Protect 12(4):41–56
44. Palmer HE, Roesch WC (1965) A shadow shield whole-body counter. Health Phys 11(11):1213–1220
45. Boddy K (1967) The development and performance of a prototype shadow-shield whole body monitor. Phys Med Biol 12(1):43–50
46. Singh IS, Sankhla R, Rao D et al (2016) Development and performance evaluation of HPGe detector-based shadow shield bed whole body counter. Radiat Prot Environ 39(2):68–74
47. Singh IS, Suri MMK, Vidhani JM et al (2002) Development of an automated shielded chair whole-body monitor. Radiat Prot Dosim 102(2):145–151
48. Parker D, Anderson JI (1967) A portable whole-body counter. Health Phys 13(2):141–148
49. Sankhla R, Singh IS, Rao DD et al (2015) Development of quick scan whole body monitor for in-vivo monitoring of radiation workers and general public. BARC Newslett 2015:13–19
50. International Atomic Energy Agency (1996) Direct methods for measuring radionuclides in the human body. IAEA Safety Series, Vienna, p 114

51. Nadar MY, Akar DK, Rao DD et al (2015) Assessment of uncertainties in the lung activity measurement of low-energy photon emitters using Monte Carlo simulation of ICRP male thorax voxel phantom. Radiat Prot Dosim 167(4):461–471
52. Nadar MY, Singh IS, Bhati S (2010) Assessment of ^{241}Am embedded in tissue using Phoswich and an array of HPGe detectors. Radiat Prot Environ 33(4):213
53. Singh IS, Nadar MY, Mishra L et al (2011) Measurement of plutonium in contaminated wound of worker using an array of HPGE detector. In: Proceedings of DAE-BRNS symposium on nuclear and radiochemistry, vol 2
54. Nadar MY, Patni HK, Akar DK et al (2013) Monte Carlo simulation of embedded ^{241}Am activity in injured palm. Radiat Prot Dosim 154(2):148–156
55. Singh IS, Mishra L, Yadav JR et al (2015) Applying a low energy HPGe detector gamma ray spectrometric technique for the evaluation of Pu/Am ratio in biological samples. Appl Radiat Isot 104:49–54
56. Nadar MY, Akar DK, Patni HK et al (2014) Monte Carlo simulation of skull and knee voxel phantoms for the assessment of skeletal burden of low-energy photon emitters. Radiat Prot Dosim 162(4):469–477
57. Mishra L, Singh IS, Patni HK et al (2018) Comparing lungs, liver and knee measurement geometries at various times post inhalation of ^{239}Pu and ^{241}Am. Radiat Prot Dosim 181:168–177
58. Mishra L, Singh IS, Nadar M et al (2014) In-vivo measurement of Pu/Am activity in liver using phoswich detector. In: Proceedings of the thirty first IARP national conference on advances in radiation measurement systems and techniques, p 120
59. Leggett RW (2010) A physiological systems model for iodine for use in radiation protection. Radiat Res 174(4):496–516
60. Sankhla R, Rao DD (2018) Development of portable thyroid monitor for thyroidal ^{131}I measurement during nuclear emergency situations. In: Proceedings of 33rd IARPIC-2018, p 55
61. Newton D, Taylor BT, Anderson AL (1978) X-ray counting efficiencies for plutonium in lungs, derived from studies with inhaled palladium-103. Health Phys 34(6):573–585
62. Toohey RE (1987) Intercalibration experiments with inhaled "mock plutonium". United States, pp 279–291
63. Somasundaram S, Sharma RC, Surendran T et al (1981) X-ray detection efficiencies for ^{103}Pd in lungs: synthesis of data from two laboratories. Health Phys 41(4):619–628
64. Newton D, Wells AC, Mizushita S et al (1985) The livermore phantom as a calibration standard in the assessment of plutonium in lungs. Assessment of radioactive contamination in man. IAEA, Vienna, pp 183–199
65. International Commission on Radiological Protection (2002) Basic anatomical and physiological data for use in radiological protection: reference values: ICRP Publication 89. Ann ICRP 32(3–4)
66. Griffith RV, Anderson AL, Sundbeck CW et al (1983) Fabrication of a set of realistic torso phantoms for calibration of transuranic nuclide lung counting facilities. Lawrence Livermore National Lab., CA; Humanoid Systems, Carson, CA
67. Shirotani T (1988) Realistic Torso phantom for calibration of *in-vivo* transuranic-nuclide counting facilities. J Nucl Sci Technol 25(11):875–883
68. Snyder WS, Fisher HL, Ford MR et al (1969) Estimates of absorbed fractions for monoenergetic photon sources uniformly distributed in various organs of a heterogeneous phantom. J Nucl Med 3:7–52
69. International Commission on Radiological Protection (2009) Adult reference computational phantoms. ICRP Publication 110. Ann ICRP 39(2)
70. Mehta DJ, Singh IS, Sharma RC (2003) A family of phantoms representative of male Indian population for calibration of whole body counters. Radiat Prot Environ 26(1–2, pt 2):327–332
71. Cristy M (1985) Mathematical phantoms for use in reassessment of radiation doses to Japanese atomic-bomb survivors. United States, p 55
72. Vlachoudis (2009) FLAIR: a powerful but user friendly graphical interface for fluka

73. Battistoni G, Cerutti F, Fassò A et al (2007) The FLUKA code: description and benchmarking. In: AIP conference proceedings, vol 896, pp 31–49
74. Ferrari A, Sala PR, Fasso A et al (2005) FLUKA: a multi-particle transport code. SLAC-R-773, p 877507
75. International Commission on Radiological Protection (2007) The 2007 recommendations of the international commission on radiological protection. ICRP Publication 103. Ann ICRP 37(2–4)
76. Patni HK, Nadar MY, Akar DK et al (2011) Selected organ dose conversion coefficients for external photons calculated using ICRP adult voxel phantoms and Monte Carlo code FLUKA. Radiat Prot Dosim 147(3):406–416
77. Patni HK, Akar DK, Nadar MY et al (2013) Estimation of specific absorbed fractions for selected organs due to photons emitted by activity deposited in the human respiratory tract using ICRP/ICRU male voxel phantom in FLUKA. Radiat Prot Dosim 153(1):32–46
78. Nadar MY, Akar DK, Mishra L et al (2021) Monte Carlo simulation of enriched uranium in the lungs of thorax voxel phantom for assessment of enrichment and its effect on dose. Appl Radiat Isot 173:109721
79. Nadar MY, Akar DK, Singh IS et al (2019) Evaluation of uncertainties in lung measurements of actinides due to counting statistics. Appl Radiat Isot 143:67–71
80. Nadar MY, Akar DK, Rao DD et al (2017) Evaluation of uncertainties in lung measurement of actinides due to non-uniform distribution of activity in lungs. Appl Radiat Isot 127:109–115
81. Zankl M, Gómez Ros J-M, Moraleda M et al (2021) Monte Carlo calculation of organ dose coefficients for internal dosimetry: Results of an international intercomparison exercise. Radiat Meas 148:106661
82. Huet C, Eakins J, Zankl M et al (2022) Monte Carlo calculation of organ and effective doses due to photon and neutron point sources and typical X-ray examinations: Results of an international intercomparison exercise. Radiat Meas 150:106695
83. Yeom YS, Han MC, Kim CH et al (2013) Conversion of ICRP male reference phantom to polygon-surface phantom. Phys Med Biol 58(19):6985–7007
84. International Commission on Radiological Protection (2020) Adult mesh-type reference computational phantoms. ICRP Publication 145. Ann ICRP 49(3)
85. Yeom YS, Jeong JH, Han MC et al (2014) Tetrahedral-mesh-based computational human phantom for fast Monte Carlo dose calculations. Phys Med Biol 59(12):3173–3185
86. Lee H, Yeom YS, Nguyen TT et al (2019) Percentile-specific computational phantoms constructed from ICRP mesh-type reference computational phantoms (MRCPs). Phys Med Biol 64(4):045005
87. Nadar MY, Singh IS, Chaubey A et al (2009) Ultrasonic measurements of chest wall thickness for the assessment of internal contamination due to actinides in Indian radiation workers. Recent trends in radiation physics research. Proc NSRP 18:284–285

In-Vitro Monitoring Techniques

Supreetha Prabhu, Prakash Mandal, and Nanda Raveendran

1 Introduction

In-vitro monitoring is an important technique used for the measurement and analysis of radionuclides in biological samples. This method is particularly useful for assessing internal exposure to radionuclides that cannot be detected by in-vivo monitoring, typically because they emit α or β radiation and lack sufficient gamma energy.

The contents of chapter start from type of samples collected and analysed for in-vitro monitoring which includes urine, feces, breath, blood, nasal swab, tissue samples, etc. The biological sample most commonly used for the estimation of intake. The biological sample most commonly used for the estimation of intake is urine as it provides systemic excretion of radionuclides and also due to ease of sample collection. Other biological samples such as feces, breath, blood or other samples are analysed in special cases. It also includes analysis of filter papers collected from static and/or personal air samplers, surface swipes, etc. After, sample collection, the radionuclides present in the samples are separated using various radiochemical methods. The most commonly used separation methods include precipitation, solvent extraction, ion exchange, and extraction chromatography. Further, the quantification of radionuclide content is carried out by using various analytical techniques. This includes alpha spectrometry, beta counting, liquid scintillation counting, gamma spectrometry, mass spectrometry, fission track analysis, etc. In addition recent advancements and innovations in the field of in-vitro monitoring is also described. This includes application of novel technologies such as nanomaterials and automation of sample preparation and analysis. The latest advances include development of Radioisotope Identification Systems (RIS), combining automated radionuclide separation with subsequent

S. Prabhu (✉) · P. Mandal · N. Raveendran
Radiation Safety Systems Division, Bhabha Atomic Research Centre, Trombay, Mumbai 400085, India
e-mail: spprabhu@barc.gov.in

D. K. Aswal (ed.), *Handbook on Radiation Environment, Volume 2*,
https://doi.org/10.1007/978-981-97-2799-5_20

identification and quantification of the separated radionuclides. Radioisotope Identification Systems are crucial tools in the field of actinide bioassay. They improve the efficiency, accuracy, and speed of analysis while maintaining high precision.

By addressing these four main areas, the chapter provides a comprehensive overview of in-vitro monitoring for radionuclide assessment, covering sample collection, separation techniques, analytical methods, and recent advancements.

2 Type of Samples

When selecting a bioassay sample for assessing internal radiation exposure, various factors need to be considered beyond the major excretion route dictated by the biokinetic model for the element and the physico-chemical form of the intake. Other important factors are ease of sample collection, ease of analysis and result interpretation [1]. Assessment of internal contamination by in-vitro monitoring requires collection of various biological samples such as urine, feces, breath, blood, nasal swab, tissue samples, etc. It also includes physical samples such as filter papers collected from static/personal air samplers, surface wipes, etc.

2.1 Urine

Urine samples are preferred for in vitro monitoring of radionuclides as it provides valuable information about the systemic excretion of radionuclides from the body. Also, due to the ease of sample collection and result interpretation, urine samples are preferred for in vitro monitoring [2]. The sample size required for in-vitro radiobioassay is variable and can range from a spot sample for ^{3}H to total 24 h samples for actinides (Pu, U, Am, etc.). Ideally, 24 h urine samples are preferred for assessment of radionuclide intake and dose, because the biokinetic models used for bioassay analysis are mainly based on daily excretion rates. However, 24 h urine samples are often neither practical nor convenient, and for routine monitoring usually overnight urine sample is collected which is normalized to 24 h urine result. Normalizing to 24 h is done using by: Sampling interval, e.g. 12 h sample result would be normalized by applying correction factor $= 24 \div 12$; Sample volume, e.g. Reference excretion of 1.6 (adult male) or 1.2 L d^{-1} (adult female) [3], sample result is adjusted using the ratio of sample volume to reference volume; Normalizing sample result using creatinine or specific gravity has been also suggested in earlier studies [4–6]. The methodology for collection of urine samples is thoroughly described in AERB safety guide [2].

2.2 Feces

Fecal analysis is useful when a radionuclide is preferentially excreted via feaces or to assess clearance of type-S material from the respiratory tract. Reference value of fecal excretion for an adult male and an adult female are 150 g d^{-1} and 120 g d^{-1} respectively [3]. Typically, the collection of a single bowel movement is construed as a representation of 24-h excretion. Normalization to reference values is recommended in cases of low sample mass. Normalizing to 24 h is done using sample mass to the reference mass [7]. The methodology for collection of fecal samples is thoroughly described in AERB safety guide [2].

2.3 Blood

Blood samples offer ~~a~~ direct means of gauging ongoing internal contamination. However, the majority of radionuclides are cleared rapidly from the bloodstream, coupled with recirculation in the body, can lead to blood activity measurements that might not accurately reflect the complete systemic presence of radionuclides. There are a few exceptional circumstances where blood samples may be useful for monitoring systemic activity. Examples include ^{51}Cr labelled erythrocytes (red blood cells), tritiated water (HTO)~~,~~ and radionuclide complexes attached to carriers in the blood. Blood samples are not normally used due to medical constraints on the sampling procedure; they should be collected only by qualified medical personnel within meticulously controlled hygienic settings.

2.4 Nasal Swabs

The nasal swab sampling is a semi-quantitative monitoring technique used in situations where an inhalation incident is suspected. It involves collecting a sample from the nasal cavity, and it is important to collect the sample soon after the suspected exposure [8]. A positive result from the nasal swab measurement (above the detection limit), suggests an unexpected exposure may have occurred. Further measurements, such as excreta (urine or feces) analysis or in vivo monitoring, should be carried out to confirm the intake and to provide a more accurate quantitative assessment of the exposure. Sawant et al. has reported the procedure for collection of nasal swabs [9].

2.5 Tissue Specimens

Analysis of tissue extracted from a radionuclide-contaminated wound, or the material removed during wound debridement, enables the identification and quantification of the radionuclides present. This information is important for evaluating the total intake of the radionuclide through the wound pathway [9]. The wound excision is carried out by a surgeon when the wound is contaminated with an isotope that has a very long half-life, such as plutonium.

2.6 Breath Analysis

For few radionuclides breath is the significant route of excretion, examples include gaseous decay products (radon, thoron) or metabolized to gases (CO_2). Breath analysis needs the worker to breathe into a breath collecting apparatus for a period up to 30 min depending upon the sample volume required [2].

2.7 Other Biological Samples

Other biological materials removed from the body, encompassing saliva, teeth, hair, nails, etc. can be used as indicators of radionuclide intake. Quantifying body burdens using these in-vitro techniques is generally not possible since biokinetic models for these techniques have not been developed. However, they may be useful as an indicator of exposure. For example, facial and scalp hair analyses have been useful in detecting exposures from radon and thoron. Fingernails are also integrators of exposure for some radionuclides like U, Th, etc. Analysis of saliva and perspiration samples may reflect systemic body burdens [10].

2.8 Filter Papers

Filter papers from personal/static air sampler and surface swipes are analyzed to estimate the type of radionuclide inhaled and its isotopic composition. Such information is important for assessing the total intake by inhalation pathway. Assessment of internal exposure based on activity in these physical samples is rarely done due to large variability in working conditions and potential intakes by workers.

3 Radiochemical Separation Methods

Radiochemical separation of radionuclides in bioassay samples involves isolation and purification of radioactive elements from biological samples followed by quantification of the radionuclide content. The method of radiochemical separation depends primarily on the type of emissions. Separation from matrix is necessary for radionuclides with α/β emissions or if the yield/energies of photon emissions are very low. For radionuclides emitting penetrating photons, radionuclide content can be quantified in bulk samples. Examples of various analytical techniques obtained from literature to determine few selected γ-emitting radionuclides is given in Table 1.

For beta (β) emitting radionuclides, liquid scintillation counting technique is commonly adopted after radiochemical separation of the radionuclide from the bulk sample.

This chapter mainly focuses on radiochemical separation of α-emitters (actinides) from bioassay samples followed by analysis using various analytical techniques. The radiochemical separation techniques are designed to remove interfering substances

Table 1 Analytical methods used to determine γ-emitting radionuclides (^{131}I and ^{137}Cs) in biological samples

Sample	Separation	Measurement method	References
Radionuclide: Iodine			
Urine	Collect and measure urine	γ-spectrometry	[11]
NS	Collect and measure nasal swab	γ-spectrometry	[11]
Radionuclide: Cesium			
Urine	Method 1: Sample is acidified, Cs separated using molybdate precipitate followed by dissolution in NaOH solution for radioactive measurements Method 2: The above NaOH solution is passed through cation IX column, Cs was later precipitated as cesium perchlorate	γ-spectrometry β-counting	[12]
Urine	Sample is acidified and concentrated on a KCFC column	γ-spectrometry	[13]
Urine	Direct counting of sample after transferring to Marinelli beaker	γ-spectrometry	[14]
Urine	Direct counting of sample after transferring to Marinelli beaker	γ-spectrometry	[15]
Feces	Direct counting	γ-spectrometry	[16]
Urine	Direct counting of acidified urine	γ-spectrometry	[17]
Urine	Direct counting of sample after transferring to Marinelli beaker	γ-spectrometry	[18]
Feces	Ashing in electric furnace for 10 h at 550°C followed by dissolution in 6 M HCl for radioactive measurements	γ-spectrometry	[18]

and concentrate the radionuclides of interest. Following is a general overview of the radiochemical separation process:

(1) Sample pre-treatment: The bioassay sample, such as urine, feces, tissue, or air filter, is collected and prepared for analysis. Sample pre-treatment, such as digestion or ashing is carried out to break down the biological matrix and for release of the radionuclides.
(2) Sample preconcetration: Biological samples like urine and feces contain large amounts of dissolved organic matters and inorganic salts, which can lead to notable sensitivity reduction during analysis, even after appropriate dilution. Hence prior to any quantitative analysis sample preconcentration is carried out.
(3) Chemical Separation: After sample pre-treatment various radiochemical separation techniques are employed to selectively separate and purify the radionuclides from the sample matrix. The specific method used depends on the radionuclide to be analyzed and the characteristics of the sample.

3.1 Sample Pre-treatment

Urine sample: Wet digestion of urine sample is carried out by transferring it into a beaker, addition of conc. HNO_3, H_2O_2 keeping it on hot plate (Fig. 1) [19].

Fecal sample: Fecal samples are subjected to dry ashing within a muffle furnace set at a temperature of 450°C [20]. Fecal samples contain silicates and refractory components. Hence, hydrofluoric acid digestion step is required, to bring analytes present in sample in solution form. For this, fecal sample is treated using either hydrofluoric acid in combination with mineral acids (Acid leaching) or by fusion with various fluxes, e.g. Na_2CO_3 and alkali borates (Alkali fusion) is also carried out [20].

For nasal swab, tissue samples and filter paper samples, wet digestion is carried out using conc. HNO_3, H_2O_2 [21, 22].

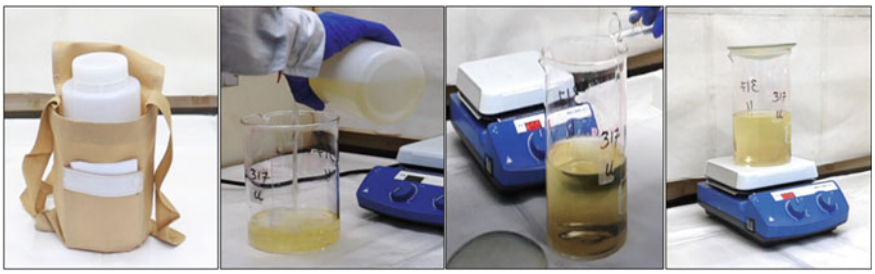

Fig. 1 Wet digestion of urine sample

3.2 Sample Preconcentration

The most commonly used preconcentration techniques used in urine bioassay are evaporation and coprecipitation [23, 24]. Coprecipitation using Ca phosphate is normally adopted for preconcentration of actinides and strontium from urine and fecal samples [25–30]. Other reagents adopted for coprecipitation are: bismuth phosphate ($BiPO_4$) [31–35], calcium oxalate (CaC_2O_4) [36, 37], etc. Recently use of HTiO has been reported to preconcentrate actinides present in urine samples [38, 39].

3.3 Chemical Separation Techniques

For radionuclide bioassay, various separation techniques are employed to isolate and quantify radioactive elements present in biological samples. These techniques include: precipitation, solvent or liquid–liquid extraction, ion exchange, and extraction chromatography. The utilization of these techniques in context of radionuclide bioassay is elaborated upon in the subsequent sections.

3.3.1 Precipitation

Precipitation: Precipitation techniques have been used since the early days of radionuclide analysis. They involve the addition of a reagent to the sample, which forms an insoluble precipitate with the target radionuclide. The precipitate can then be separated from the sample matrix through filtration or centrifugation. Separation methods based on precipitation were mainly developed for fission products, some of them are still used (Table 2).

Table 2 Radionuclide separation by precipitation or coprecipitation [12, 40–42]

Radionuclide	Precipitation or Coprecipitation	Separation
$^{89,90}Sr$	Nitrate precipitation using HNO_3	Separation of Sr from Ca
	$Ba(Ra)CrO_4$ precipitation	Separation of Sr from Ba, Ra
	Carbonate precipitation	Removal of interfering components from Sr
	$Y_2(CrO_4)_3$ precipitation	Separation of Y from Sr
	SO_4^{2-} precipitation	Separation of Sr
^{137}Cs	Coprecipitation using $(NH_4)_3PMo_{12}O_{40}{\cdot}3H_2O$	Separation of Cs
^{32}P	Precipitation using $(NH_4)_3PMo_{12}O_{40}{\cdot}3H_2O$	Separation of P
^{131}I	Precipitation using AgI	Separation of I

The principle behind precipitation is the formation of insoluble compounds containing the radionuclides by adding specific reagents. In order for precipitation to occur, the solubility product (K_{sp}) of the compound must be exceeded. The solubility product of a compound A_xB_y is determined by using Eq. 1:

$$K_{sp} = [A]^x[B]^y \tag{1}$$

where

$[A]$ is concentration cation and $[B]$ is concentration of anion in the solution;
x and y are respective charges on the cation and anion.

Radionuclides concentration in bioassay samples are present in trace or ultra-trace levels. Due to these extremely low concentrations, it is rare for the solubility product to be exceeded without the addition of a carrier. Therefore, in radionuclide separation by precipitation, an isotopic carrier is added. The carrier has the same chemical form as the radionuclide of interest. In cases where an isotopic carrier is not available for a particular radionuclide, a non-isotopic carrier can be added for precipitation. This process is known as coprecipitation. The carrier serves to enhance the precipitation by providing additional atoms or ions that can form insoluble compounds along with the radionuclide, aiding in their separation from the solution.

By using carriers in precipitation-based separation methods, the solubility product can be exceeded, allowing for efficient precipitation and subsequent separation of radionuclides from bioassay samples. This technique enables the concentration and analysis of radionuclides present in extremely low concentrations.

Use of precipitation/co-precipitation technique for radionuclide separation

Use of precipitation/co-precipitation method for radiochemical separation of ^{89,90}Sr, ^{137}Cs, ^{131}I, ^{32}P from urine samples has been reported in earlier works [12, 40–42] and is given in Table 2. Radiochemical separation by precipitation method for ^{32}P from urine samples is shown in Fig. 2 [41].

3.3.2 Solvent or Liquid–Liquid Extraction

Solvent extraction is a separation technique that exploits the unequal distribution of a solute (such as a radionuclide) between two immiscible solvents, typically water (aqueous phase) and an organic liquid (organic phase). This technique is commonly used for the separation of radionuclides, including Sr, Pu, U, Am, and Th, from bioassay samples.

The principle behind solvent extraction is that the radionuclide, often in the form of a metal, is selectively extracted from the aqueous phase into the organic phase, while interfering elements remain in the aqueous phase. Solvent extraction enables the separation and concentration of specific radionuclides from complex bioassay samples.

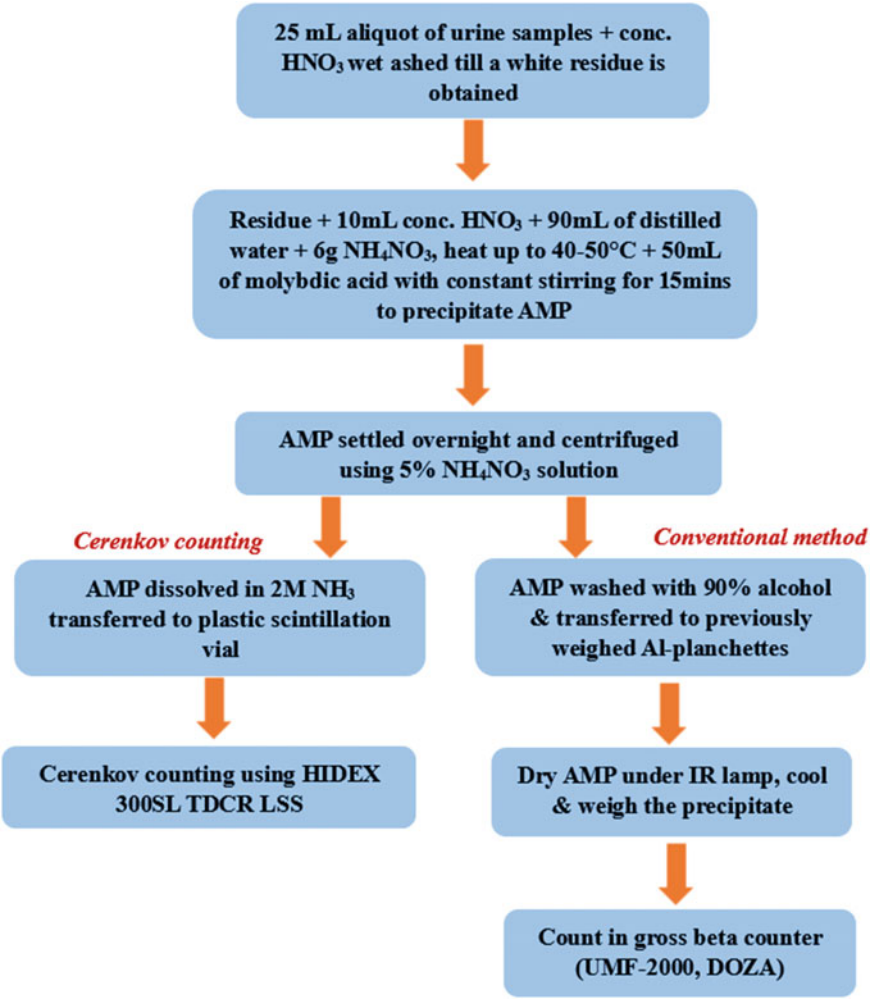

Fig. 2 Flow chart for the estimation of phosphorus-32 in bioassay samples [41]

The choice of appropriate organic solvents for solvent extraction depends on the specific radionuclide of interest (Table 3), e.g. for the extraction of Sr, solvents containing crown ethers or phosphonic acid derivatives are commonly used. These solvents have a high affinity for Sr and facilitate its transfer from the aqueous phase to the organic phase. For the extraction of Pu, U, Am, and Th, organic solvents such as tributyl phosphate (TBP) or di(2-ethylhexyl) phosphoric acid (D2EHPA) are frequently employed. These solvents exhibit strong affinity for these actinide elements, allowing for their efficient extraction into the organic phase.

Various steps involved in solvent extraction are

Table 3 Radionuclide separation by solvent or liquid–liquid extraction

Sample	Radionuclide	Extractant	References
Urine	Pu	Cupferron in chloroform	[43]
Bone, urine	Pu	Primene J-MT	[44]
Urine	^{237}Np	TTA	[45]
Urine	U, Np, Pu	Tri-iso-octyl amine	[46]
Urine	U, Np, Pu	Alamine 336	[47]
Biological samples	Am, Cm, Cf	TOMAC dissolved in toluene containing scintillators p-terphenyl and POPOP[a]	[48]
Biological samples	U, Pu, Th	25% TLA in xylene	[49]
Bone	U, Pu, Th	20%TLA in xylene	[50]
Urine	U	Calixarene	[51]
Urine	Pu	HTTA in xylene	[27]
Urine, Hair	U	TBP in xylene	[52]
Nasal swab	Pu, Am	HDEHP	[21]

[a]Extractive scintillator

- *Extraction Step*: The bioassay sample is mixed with the selected organic solvent in an extraction vessel or centrifuge tube. The solvent forms two immiscible phases with the sample, with the radionuclides partitioning preferentially into the organic solvent phase due to their affinity for the solvent. The extraction step allows the transfer of the radionuclides from the aqueous sample phase to the organic solvent phase.
- *Separation Step*: After extraction, the organic solvent phase containing the extracted radionuclides is separated from the aqueous phase by either centrifugation or decantation.
- *Stripping Step*: The next step is to selectively strip the radionuclides from the organic solvent phase into a new aqueous phase. This is done by mixing the organic solvent with a suitable stripping solution that has a higher affinity for the radionuclides than the organic solvent. The radionuclides transfer from the organic phase to the aqueous phase during this step.
- *Collection and Analysis*: The aqueous phase containing the separated radionuclides is collected, and the radionuclides can be further analyzed using techniques such as gamma spectroscopy, alpha spectrometry, or liquid scintillation counting. These methods allow for the quantification and identification of the radionuclides in the bioassay sample.

Use of solvent extraction technique for radiochemical separations

Radiochemical separation of Sr, Pu, U, Am, and Th from urine samples using solvent extraction has been reported in earlier works and is mentioned in Table 3. Radiochemical separation of Pu and Am from nasal swab sample by solvent extraction is given in Fig. 3.

There are several limitations of solvent extraction techniques, such as the requirement for large amounts of solvents, multiple steps for quantitative separation, moderate selectivity, and the labour-intensive nature of the process. However, advances have indeed been made to address these challenges and improve the preconcentration ability in liquid–liquid extraction.

One such advancement is the development of dispersive liquid–liquid microextraction (DLLME) as an analytical technique. DLLME was first introduced in 2006 and has gained popularity due to its simplicity, speed, and the use of only a small volume of organic solvents.

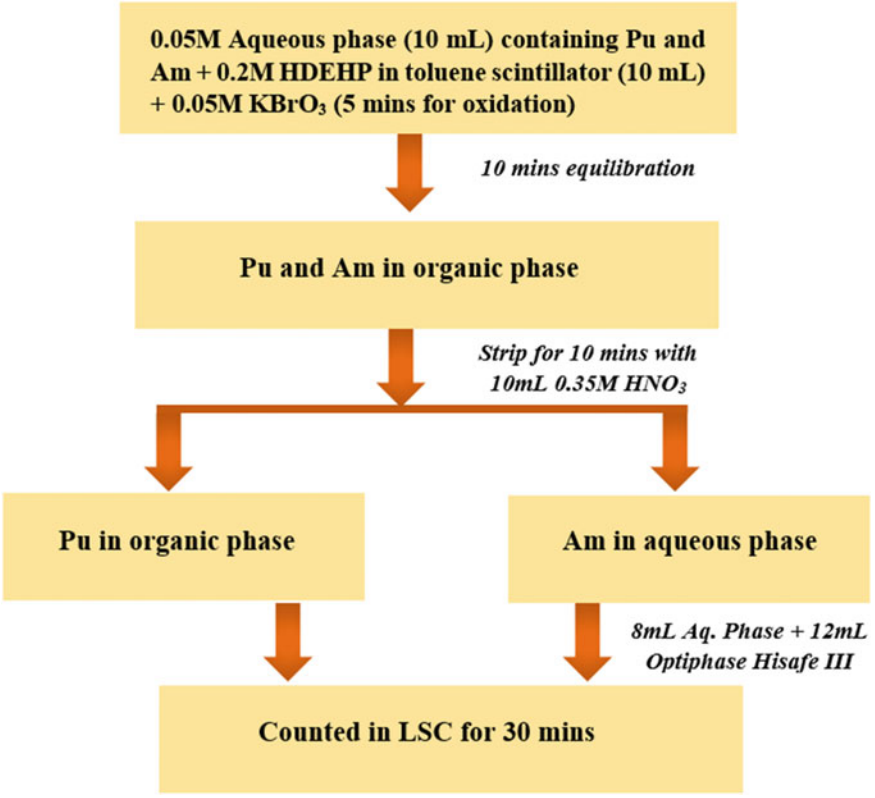

Fig. 3 Schematic flowchart for efficient separation of Pu and Am in nasal swab using HDEHP based extractive scintillator (reproduced from [21] © 2022 Elsevier Ltd., with permission from Elsevier)

Table 4 Radionuclide separation by DLLME

Sample	Radionuclide	Dispersion solvent	Extraction solvent	References
Urine	Pu	Methanol	HDEHP in tetrachloroethylene	[53]
Urine	^{226}Ra	Acetonitrile	Mixture of hexafluoroacetylacetone and dibenzo-21-crown-7 in toluene	[54]

Dispersive liquid–liquid microextraction (DLLME)

DLLME is based on ternary component solvent systems, typically consisting of an aqueous phase, an organic extraction solvent, and a dispersing solvent. The aqueous and organic phases are immiscible, while the dispersing solvent aids in the formation of fine microdroplets of the extraction solvent in the sample solution.

In the DLLME process, the mixture of the extraction solvent and the dispersing solvent is injected into the sample solution. This leads to the rapid dispersion of microdroplets of the extraction solvent throughout the aqueous sample, resulting in the formation of a cloudy solution. This cloudy solution provides a large interfacial area between the extraction solvent and the aqueous sample, facilitating the efficient transfer of analytes of interest from the aqueous phase to the extraction phase.

After the dispersion step, the mixture is typically separated by centrifugation, which causes the microdroplets to coalesce and separate from the aqueous phase. The extraction solvent, now containing the extracted analytes of interest, is collected using a microsyringe. This is followed by the identification of analytes in the extraction solvent, which can be performed using analytical instrument. The DLLME method offers several advantages, including simplicity, rapidity, and reduced solvent consumption compared to traditional solvent extraction techniques. Radiochemical separation of Pu, Ra from urine samples using DLLME method is given in Table 4.

3.3.3 Ion Exchange Chromatography

Ion-exchange chromatography operates on the principle of reversible exchange of metal ions between a liquid phase and a solid ionic resin of opposite charge. Resin is a polymer matrix (polystyrene cross linked divinylbenzene) with charge bearing functional group which acts as a stationary phase. These functional groups are permanently bonded ionic groups and have a counter ion of opposite charge which is labile. Ion exchange resins are of two types based on the exchangeable or labile ion, i.e. cation exchange resin and anion exchange resin (Fig. 4). The common functional groups for the two types of resins are given in Table 5.

Cation exchangers generally allow separation of metals with valence states + 1, + 2 and + 3. The cation exchangers rely on pH adjustment for separation and the pH required to retain a cation on the exchanger decreases as the charge of the

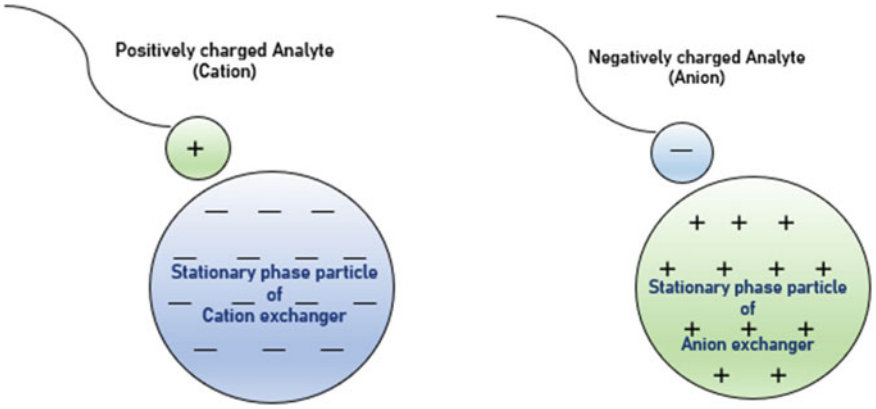

Fig. 4 Ion-exchange process

Table 5 Common functional groups in ion exchange resins

Resin type	Functional group	Functional range
Cation resin (strongly acidic)	Sulphonate-SO_3^-	Function as cation exchangers over entire pH range
Cation resin (weakly acidic)	Carboxylate-CO_2^-	Function as cation exchangers in neutral and basic conditions
Anion resin (strongly basic)	Quaternary ammonium ion-$N(CH_3)_3^+$	Function as anion exchangers over entire pH range
Anion resin (weakly basic)	Tertiary amino-$N(CH_3)_2$	Function as anion exchangers in neutral and acidic conditions

cation increases. As a result of these limitations, cation exchangers are not widely used in radioanalytical separations, particularly for the separation of metals with similar valence states. On the other hand, anion exchangers are commonly used in radiochemical separations, including the separation of actinides. Actinides form strong anionic complexes in acidic media, and these complexes are retained on anion exchangers based on their charge. The higher the charge of the anionic complex, the stronger its retention on the anion exchanger. The commonly used acids for the formation of anionic complexes in radioanalytical separations are HNO_3 (nitric acid) and HCl (hydrochloric acid). The resulting complexes are typically nitrate and chloride complexes, respectively.

Overall, anion exchangers are preferred over cation exchangers in radioanalytical separations due to their effectiveness in separating anionic complexes, particularly for actinides. The use of appropriate acids and anion exchangers allows for the selective retention and subsequent analysis of these anionic complexes, aiding in the accurate determination of actinides in bioassay samples.

There are also ion exchangers in which functional group is a chelating group, such as amino phosphate ($–CH_2–NH–PO_2^{2-}$). The functional group can form a chelate (complex) with the metal ion.

The ion exchange techniques, particularly anion exchange, play a vital role in the radiochemical separation of actinides from bioassay samples. The choice of specific resins and eluents depends on the target actinides and the analytical requirements.

Various steps involved in ion exchange separation

Column Preparation: A column is packed with the selected ion exchange resin. The resin is typically loaded into a glass or plastic column to form a stationary phase. The column is conditioned with suitable solvents or solutions to ensure optimal performance and remove any impurities.

Sample Loading: The bioassay sample is carefully loaded onto the ion exchange column. The target radionuclides selectively bind to the ion exchange resin while other ions or compounds pass through or are retained less strongly.

Washing: After the sample is loaded, a series of washing steps are performed to remove unwanted impurities or interfering substances that may have bound to the resin. This helps to improve the purity of the target radionuclides. Washing steps involve the use of appropriate solvents or solutions, ensuring efficient removal of contaminants.

Elution: The elution step involves selectively releasing the target radionuclides from the ion exchange resin. This is achieved by passing a suitable eluent through the column that disrupts the binding between the radionuclides and the resin. The eluent may be a solution containing specific complexing agents, pH modifiers, or other eluting agents that can desorb the radionuclides.

Collection and Analysis: The eluate, containing the separated radionuclides, is collected and subjected to analysis using suitable techniques such as gamma spectroscopy, liquid scintillation counting, or alpha spectrometry for quantification and identification of the radionuclides in the bioassay sample.

Use of ion exchange chromatography technique for radiochemical separations

Table 6 gives examples of ion exchangers used for radiochemical separation in bioassay samples. Figure 5 exemplifies the radiochemical separation of uranium (U) from a urine sample using anion exchange resin (AG 1 × 8).

High radiochemical recoveries using anion exchange methods is the main advantage of this technique. However, its disadvantages include laborious separation procedure and the need for substantial quantities of acidic reagents to achieve the separation.

3.3.4 Extraction Chromatography

Extraction chromatography technique have been developed for radiochemical separations only a few decades ago and is now being widely used. Extraction chromatography combines the principles of solvent extraction and chromatography, utilizing a

Table 6 Ion-exchangers used for radiochemical separation

Sample	Radionuclide	Ion exchanger	References
Urine	^{238}U	Dowex anion exchange	[55]
Urine	^{237}Np	Anion-exchange (AG-MP1)	[56]
Urine	Pu, U, Am	Dowex 50 × 8 and Dowex 1 × 8	[57]
Urine	$^{239+240}$Pu	Dowex 1 × 8	[58]
Urine	$^{239+240}$Pu	Dowex 1 × 8	[59]
Urine	Pu	Dowex 50 × 8 and Dowex 1 × 8	[35]
Urine	U	Dowex 1 × 8	[60]
Urine	^{231}Pa	Dowex 1 × 8 anion exchange	[61]
Urine	^{90}Sr	1 × 8 anion exchange	[62]
Faeces	Pu	Amberlite 1 × 8 anion exchange	[20]
Urine	^{239}Pu	AG1 × 2	[63]
Urine	Pu	Dowex 1 × 8 anion exchange	[64]
Urine	^{239}Pu	AG1 × 2	[65]
Urine	U(nat.)	Dowex 1 × 8 anion exchange	[26]
Urine	Pu	AGMP-1M	[38]
Urine	Pu, Np	AG MP-1M anion exchange	[66]
Urine	U	Biorad 4 × anion exchange	[67]

chromatography column with a stationary phase composed of extractants sorbed on a porous support material.

The extractants used in extraction chromatography resins, such as HDEHP, TBP, TOPO, CMPO, TTA, and TNOA, have high affinity and selectivity for actinides and lanthanides. These resins offer advantages such as faster exchange kinetics, simpler operational procedures, and generation of less liquid radioactive waste compared to anion exchange and solvent extraction methods.

In bioassay samples, extraction chromatography resins are commonly employed for the separation of Pu, U, Am, Sr, and Th.

Further advancements in extraction chromatography include the use of vacuum boxes, which have demonstrated faster separation times compared to gravitational-based extraction chromatography techniques. These improvements contribute to reduced analysis time for separation of radionuclides using solid-phase extraction chromatography.

Table 7 gives details of some extraction chromatography resins and resins designed for specific radionuclides that are available from Eichrom Technologies and Triskem International. Figure 6 gives the extractant present in the extraction chromatography resins [68].

Use of various extraction chromatography resins in radionuclide separation

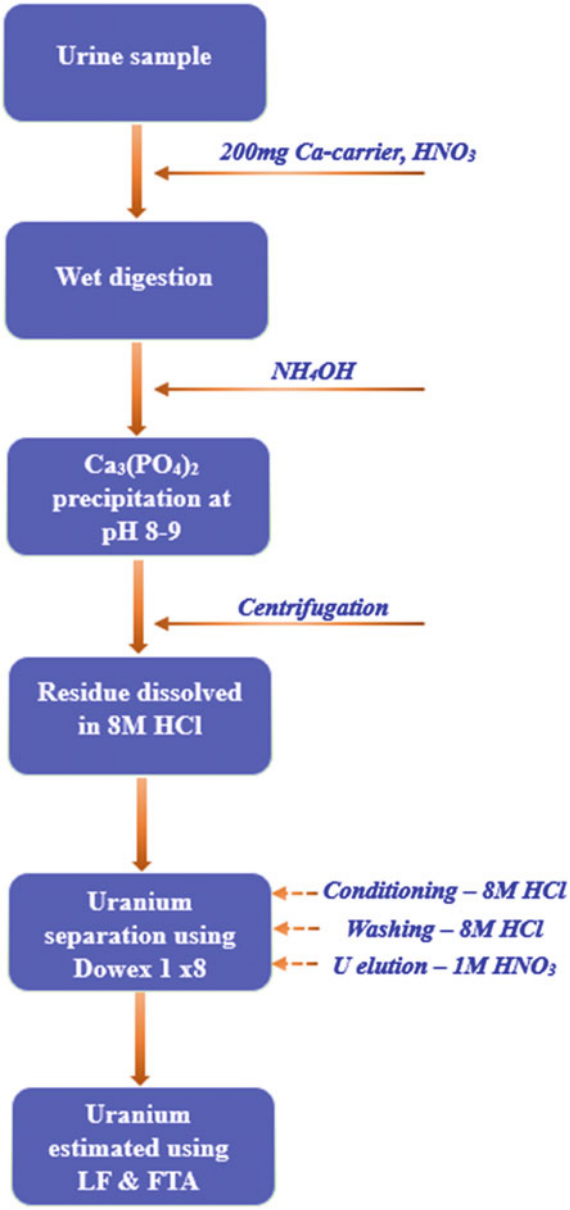

Fig. 5 Flow chart of separation of uranium from urine samples using Dowex 1 × 8 [26]

Table 7 List of extraction chromatography resins commercially available

Resin	Extractant	Application
Actinide-resin	P-P′-di(2ethylhexyl) methane diphosphonic acid	Group actinide separations/gross alpha measurements
DGA resin	N,N,N′,N′-tetra-n-octyldiglycolamide	Y, Lu, Tb, Am, Cm, Ac, U
Sr-Resin	bis-4,4′(5′)-tertbutylcyclohexano-18-crown-6	Sr, Pb
TEVA-Resin	Tri-n-octylmethylammonium chloride (Aliquat 336)	Tc, Th, Np, Pu, Am/ lanthanides
TRU-Resin	octylphenyl-N,N-di-isobutyl carbamoylphosphine oxide (CMPO)	Fe, Th, Pa, U, Np, Pu, Am, Cm
UTEVA Resin	diamyl amylphosphonate (DAAP)	Th, U, Np, Pu

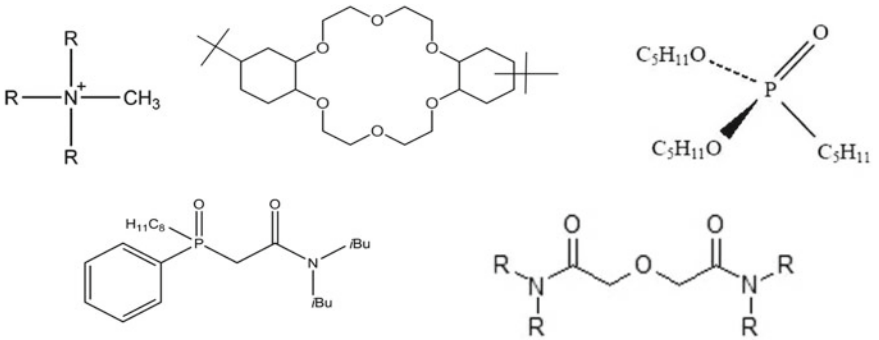

Fig. 6 **a** Quaternary amine salt within TEVA resin, **b** 18-crown-6 within Sr-resin, **c** dipentyl-pentylphosphonate within UTEVA resin, **d** mixture of TBP and CMPO within Sr resin and **e** N, N,N′,N tetraoctyldiglycolamid in DGA resin

- TEVA resin, based on aliquot-336, exhibits high retention for plutonium (Pu) and neptunium, with improved performance compared to conventional anion exchange resins. It is widely used for separation of Pu and Np, from bioassay samples [29].
- TRU resin, functionalized with TBP, is widely used for the separation of transuranic elements such as Pu, U, and Am [40, 69]. TRU resin has a strong affinity for these radionuclides, allowing for their efficient extraction and separation.
- UTEVA resin, functionalized with D2EHPA, is commonly employed for the separation of U and other tetravalent actinides, including Th [70, 71]. UTEVA resin has excellent selectivity and separation efficiency for these radionuclides.
- DGA resin, functionalized with diglycolamide (DGA) ligands, is utilized for the separation of trivalent actinides, such as americium (Am) [72, 73]. It exhibits a high affinity and selectivity for trivalent actinides, enabling their effective separation.

- Sr resin, specialized for the separation of strontium (Sr), typically contains a crown ether ligand, such as dicyclohexano-18-crown-6 (DCH18C6), immobilized on a support material. Sr resin demonstrates a strong affinity for strontium, allowing for its efficient extraction and separation [40].

These resins are used alone for radionuclide separation or in combination with other extraction chromatography resins for determination of radionuclides in bioassay samples [74–76].

Table 8 gives examples of various extraction chromatography resins used for radiochemical separation in bioassay samples. Figure 7 gives an example for the radiochemical separation of Sr from a urine sample using Sr-spec resin.

In literature use of various combination of ion exchange resins and SEC resins have also been reported for radiochemical separation of bioassay samples (Table 9).

4 Radioanalytical Techniques/Determination Methods

4.1 Alpha Spectrometry

Alpha spectrometry is a highly sensitive technique used for the identification and quantification of alpha-emitting radionuclides present in a biological sample.

Principle

Alpha spectrometry is a technique used to detect and analyse alpha particles emitted by radioactive materials. It involves several key steps like sample preparation, alpha particle detection, energy loss, electrical signal generation, signal amplification and processing, alpha spectrum analysis, radionuclide identification and quantification. The sample containing alpha-emitting radionuclides is prepared by chemically separating the analyte of interest from the sample matrix. This purification step is crucial to obtain a clean alpha spectrum. The source preparation of purified radionuclide is carried out either by electrodeposition or micro-precipitation (Fig. 8). For counting, the electro-deposited planchet is placed inside the detector, typically a solid-state silicon or semiconductor detector. When an alpha particle enters the detector material, it interacts with the atoms of the material, losing energy through ionization and excitation processes. This energy loss causes the alpha particle to slow down and eventually stop within the detector. As the alpha particle loses energy, it produces electrical signals in the detector. These signals are generated by the ionization of atoms in the detector material. The signals are typically in the form of electrical pulses which are amplified and processed by specialized electronics. This amplification step helps to increase the detectable signal level and improve the signal-to-noise ratio. The processed signals are then converted into digital form for further analysis. The resulting signals are analysed using software and algorithms to construct an alpha spectrum. The alpha spectrum displays the number of detected alpha particles as a function of their energy (Fig. 8). The block diagram of alpha spectrometry

Table 8 Radiochemical separation by extraction chromatography

Sample	Radionuclide	Resin	References
Urine	Pu	TRU	[77]
Urine	U	TRU	[78]
Urine	U, Th, Np, Pu, Am	TRU	[79]
Urine	Pu	TEVA	[25]
Urine	Pu	TEVA	[80]
Urine	Pu	TRU	[81]
Urine	U	UTEVA	[82]
Urine	Pu	TEVA	[83]
Synthetic fecal	^{239}Pu	TEVA	[84]
Urine	U	TRU	[85]
Urine	Th, U, Np, Pu, Am	TEVA, TRU	[86]
Urine	Np, Pu, Am, U	TEVA, TRU, DGA	[87]
Fecal	Pu, Am, U	TEVA, TRU, DGA	[88]
Urine	U	TRU or UTEVA	[89]
Urine	Np	TEVA	[90]
Urine	Pu, Np	TEVA	[91]
Urine	^{90}Sr	TRU, Sr-resin (vacuum box)	[92]
Urine	Sr	SR-resin	[40]
Urine	Am, Cm	TEVA, DGA	[39]
Urine	Pu, U, Am, Th	DGA	[93]
Urine	^{237}Np, ^{241}Am, Th, Pu and U	TEVA, TRU	[76]
Biological sample	^{90}Sr	Crown ether on teflon powder	[94]
Urine	Pu	TEVA, UTEVA, DGA	[74]
Feces	^{238}Pu, ^{240}Pu, ^{241}Am, and natural U	TEVA, TRU, DGA (vacuum manifold)	[95]
Urine	Pu, Th, Am, U, ^{90}Sr	TEVA, TRU, Sr-resin cartridges	[96]
Urine	^{210}Po, natural uranium, Th	TEVA, UTEVA (vacuum manifold)	[97]
Urine	^{226}Ra, U	UTEVA	[71]
Urine	^{90}Sr	(vacuum system)	[98]
Urine	Pu	TEVA	[99]
Urine	U	TRU	[69]
Urine	^{90}Sr	Sr-resin (vacuum box)	[100]
Urine	Pu, U, Am, Sr	TRU, Sr-spec	[101]
Brain tissue	Pu, U, Am	TEVA, UTEVA, DGA	[75]

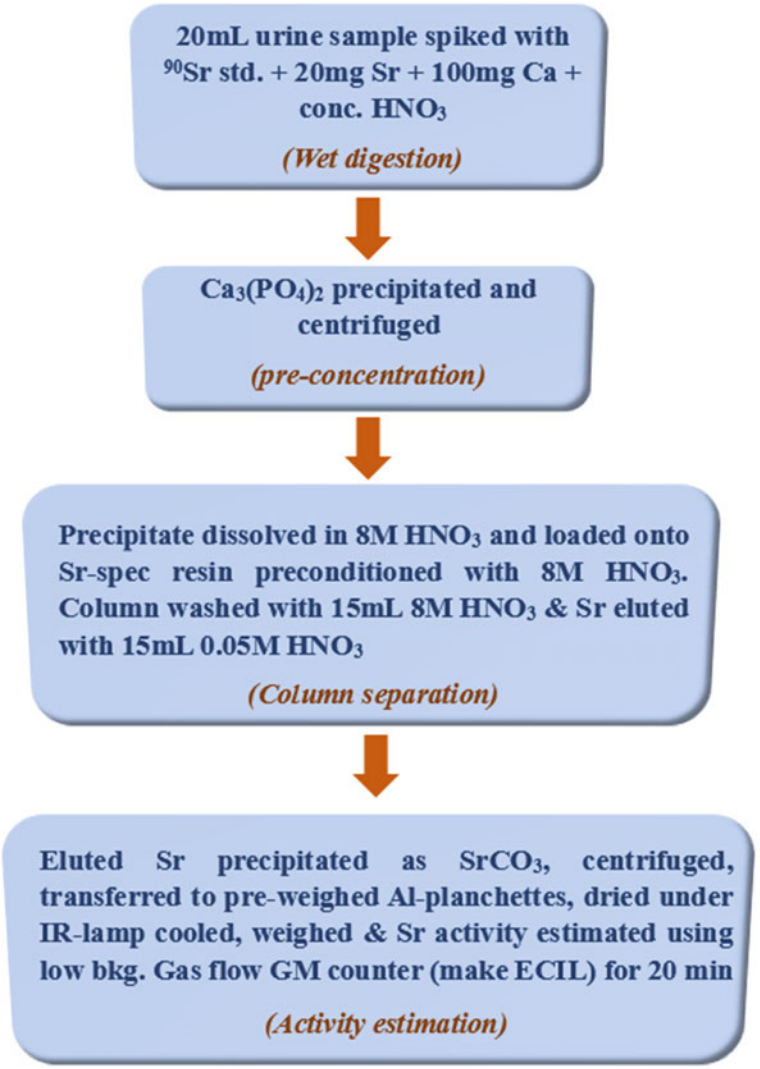

Fig. 7 Flow chart of separation of Sr from urine samples using Sr-spec [40]

Table 9 Radiochemical separation using combination of ion-exchange and extraction chromatography techniques

Sample	Radionuclide	Ion exchanger	References
Urine	Np, Pu	TRU, Chelex	[102]
Synthetic fecal	Am, Cm	AGMP-1, UTEVA, DGA	[103]
Urine	^{239}Pu	TEVA, Dowex 1 × 4	[104]
Urine	^{90}Sr	Diphonix, Sr-spec	[105]

system including the primary components is shown in Fig. 9. The alpha spectrum contains distinct peaks corresponding to specific alpha energies emitted by different radionuclides present in the sample. The identification and quantification of radionuclides in a sample are achieved by comparing the energies and intensities of the peaks observed in the alpha spectrum with those from known reference standards.

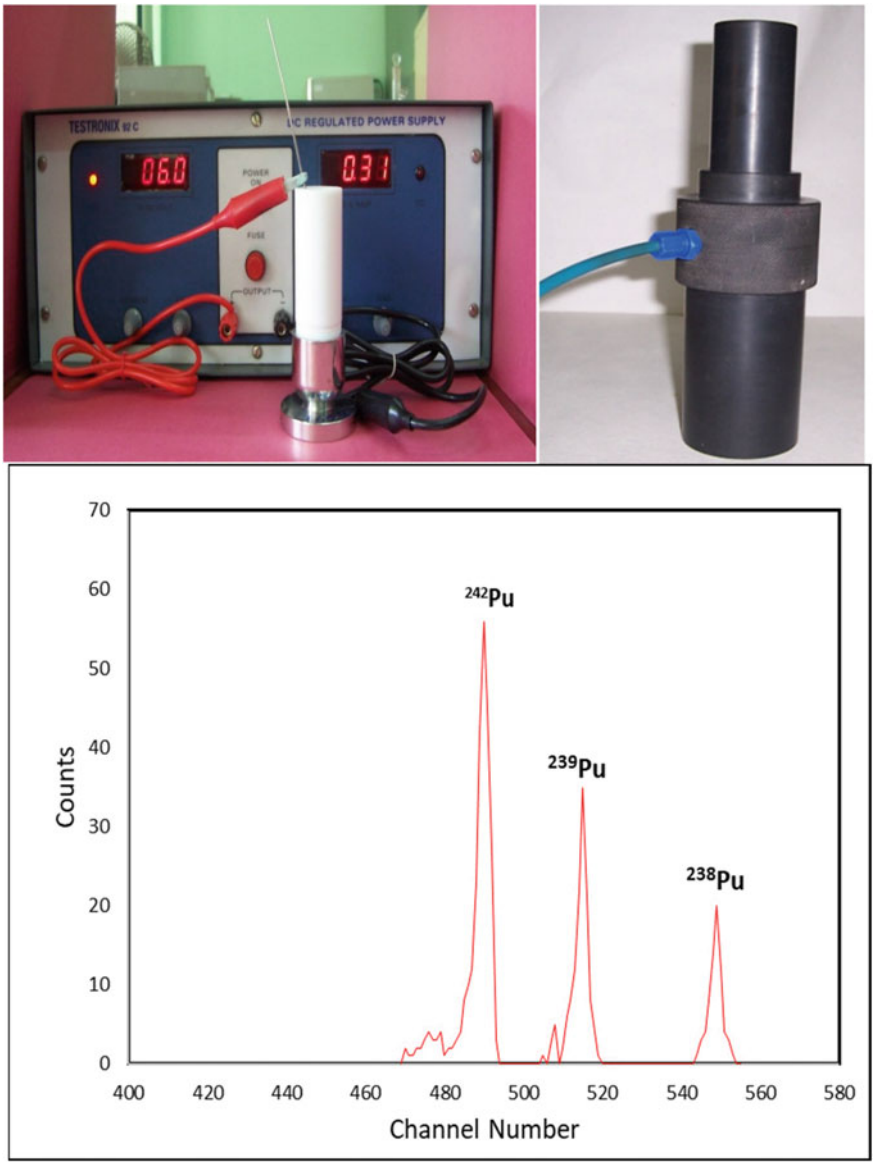

Fig. 8 Source preparation for alpha spectrometry and observed alpha spectrum for Pu isotopes

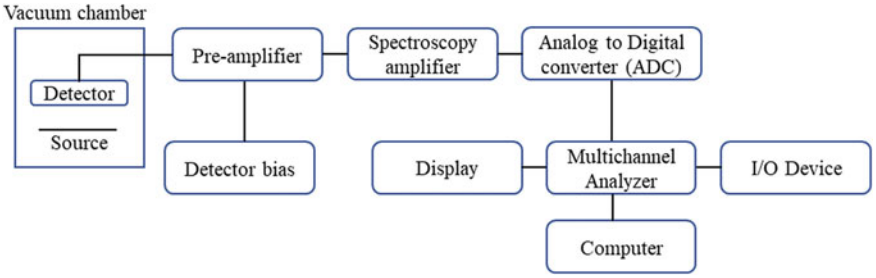

Fig. 9 Block diagram of alpha spectrometry system

Advantages

Alpha spectrometry offers several advantages as a radioanalytical technique for the detection and estimation of alpha emitters in terms of selectivity, sensitivity, energy resolution, wide radionuclide range, reliability and stability, cost-effectiveness, etc. Alpha spectrometry is highly selective for alpha-emitting radionuclides. This selectivity allows for specific identification and estimation of actinides in complex sample matrices. Alpha spectrometry is known for its exceptional sensitivity, capable of detecting very low amounts of alpha-emitting radionuclides. The minimum detectable amount (MDA) in alpha spectrometry can range from femtograms to picograms, depending on various factors including the type of detector used, the efficiency of the setup, and the characteristics of the radionuclide being analysed. This high sensitivity makes it suitable for trace-level analysis of alpha emitting radionuclides in biological samples. Alpha spectrometry provides excellent energy resolution. It can detect and analyze a variety of alpha-emitting radionuclides, including isotopes of U, Pu, Ra, Th, Am, etc. Alpha spectrometry technique is particularly useful for measuring radionuclides with short half-lives such as plutonium isotopes (^{238}Pu). Compared to other analytical techniques, alpha spectrometry is relatively cost-effective. The equipment required for alpha spectrometry, such as detectors and electronics, is readily available and can be more affordable compared to specialized equipment used in other analytical methods. Its reliability, stability, and cost-effectiveness make it a valuable tool in various fields involving the analysis and monitoring of alpha radiation.

Disadvantages

While alpha spectrometry has numerous advantages, there are also some limitations and disadvantages associated with this technique. Sample preparation for alpha spectrometry can be complex and time-consuming. Achieving a clean and pure sample matrix can be challenging, especially in complex biological samples with multiple radionuclides and matrix interferences. Any impurities or contaminants in the sample can interfere with the analysis, causing overlapping peaks or background noise. Achieving high radiochemical purity can be difficult and may require additional separation techniques. Due to high ionization power, large mass and short range in matter

not all emitted alpha particles from the radionuclides in the sample are detected and registered by the detector. Because of that the counting efficiency of alpha spectrometry is relatively low compared to other techniques. This lower counting efficiency may require longer counting times to achieve desirable statistical precision, especially for samples with low activity levels. Although alpha spectrometry can provide accurate identification and quantification of known alpha-emitting radionuclides, it may face challenges in identifying unknown or unexpected radionuclides present in the sample. Despite these disadvantages, alpha spectrometry remains a valuable technique for the detection and estimation of alpha-emitters in biological samples.

Applications

Alpha spectrometry is a widely used radioanalytical technique for determining the activity concentration of actinides in biological samples, particularly for monitoring of radiation workers [86, 106, 107]. Detection limit of alpha spectrometry technique can be achieved up to 0.5 mBq for 24 h counting time however below this level this technique is not much sensitive particularly for ultra-trace level estimation of Pu and Np in urine sample [108]. Using alpha spectrometry technique ^{239}Pu, ^{241}Am in urine samples were determined by Alvarez and Navarro [109]. Radiochemical recovery of ~ 85% for ^{239}Pu with MDA of 0.5 mBq for 24 h counting time was achieved. MDA of 0.2–04 mBq L^{-1} was obtained in urine samples for uranium isotopes [110].

Traditional alpha spectrometry methods can be relatively slow due to the time required for sample preparation, instrument setup, and counting. However, there have been efforts to develop faster and more streamlined alpha spectrometry techniques, particularly for specific applications like bioassay analysis of urine samples. Maxwell and colleagues developed such methods, achieving a sample turnaround time of less than 8 h in their reported procedures [86, 107, 111].

4.2 LED Fluorimetry

LED Fluorimetry technique is widely used mainly for estimation of ultra-trace level of uranium present in biological samples. Principle of an LED fluorimeter is based on the phenomenon of fluorescence, which is the emission of light by a substance after it absorbs light of a shorter wavelength. LED fluorimeters utilize light-emitting diodes (LEDs) as the light source to excite the sample and measure the emitted fluorescence as shown in Fig. 10. The LED emits light at a specific wavelength, typically in the ultraviolet (UV) or visible range. The emitted light passes through a filter that selects the desired excitation wavelength, which matches the absorption characteristics of the fluorophore or fluorescent substance present in the sample. The emitted light from the LED excites the fluorophore present in the sample. The fluorophore absorbs the excitation light and moves to a higher energy state, known as the excited state. As the excited fluorophore returns to its ground state, it emits light of a longer wavelength than the excitation light. This emitted light is referred to as fluorescence. The emitted fluorescence passes through another filter that selects the desired

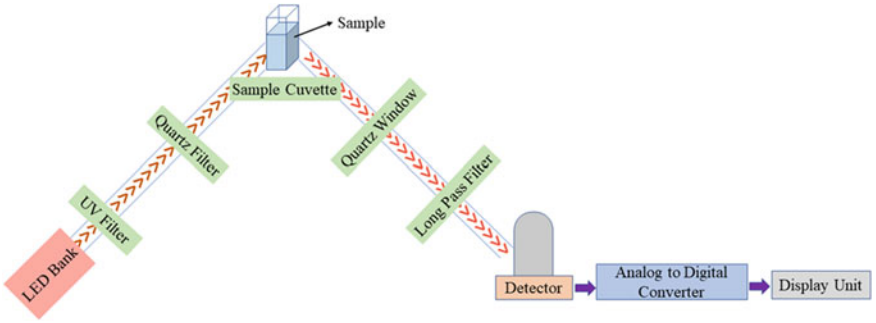

Fig. 10 Schematic diagram of LED Fluorimeter

emission wavelength, blocking any remaining excitation light and other unwanted background signals. A photodetector, such as a photomultiplier tube (PMT) or a solid-state detector, detects and measures the intensity of the emitted fluorescence. The photodetector converts the incoming light into an electrical signal, which is then amplified and processed to provide a measurable output. The measured fluorescence signal can be analyzed and quantified to provide information about the sample. This may involve comparing the fluorescence intensity to known standards or using calibration curves to determine the concentration of the fluorescent substance in the sample. LED fluorimeters offer several advantages, such as their compact size, durability, long operational life, low power consumption, and the ability to emit light at specific wavelengths.

LED based fluorescence spectroscopy is a sensitive, selective, and versatile technique, especially for trace-level analysis of uranium in various fields [112–116]. Uranium is indeed a strong fluorophore with well-defined absorption and emission spectra. It absorbs light in the UV range (260–350 nm) and emits strongly in the visible range (450–600 nm) with a high quantum yield. However, complications arise when dealing with real-life samples due to presence of various quenching species in the analyte solution [117, 118]. Effect of quenching in uranium analysis by some of the important ions such as Cl^-, Na^+, SO_4^{2-}, Mg^{2+}, Ca^{2+}, K^+, HCO_3^-, Br^-, etc. were studied by Sanjukta et al. [112]. They have achieved a detection limit of approximately 3 ng mL^{-1} in the environmental samples without prior separation of matrix. Uranium phosphate species exhibit high fluorescence quantum efficiencies, making them suitable for studying uranium at low concentrations. Phosphate containing chemicals such as sodium pyrophosphate, penta-sodium tri-poly phosphate, sodium hexameta phosphate, ammonium dihydrogen phosphate, phosphoric acid, etc. are quite established uranium fluorescence enhancing reagents [114–116, 119]. Advantage of using fluorimetric technique is the simple analytical procedure, rapid counting and capable of estimating 0.1–0.2 ppb uranium in complex matrices like urine. Disadvantage of this method is that it is applicable to limited number of radionuclides commonly used for uranium and also this method cannot provide isotopic information of the radionuclide present in the sample.

4.3 Adsorptive Stripping Voltammetry

Adsorptive stripping voltammetry (ASV) is utilized for the estimation of heavy metals such as uranium concentrations in samples. The technique involves the preconcentration of uranium ions onto an electrode surface through adsorption, followed by the stripping of the adsorbed ions and subsequent measurement of the resulting current. Here is a general outline of the steps involved in utilizing ASV for uranium estimation. Select an appropriate working electrode material, such as mercury, glassy carbon, or gold, which can facilitate the adsorption of uranium ions. The electrode is typically polished and cleaned prior to use. Immerse the working electrode into the sample solution containing uranium ions. Apply a suitable potential to the electrode to induce the adsorption of uranium ions onto the electrode surface. The adsorption time and potential may need optimization to achieve maximum adsorption efficiency. After the preconcentration step, initiate the stripping process by applying a specific potential waveform or potential scan. This causes the desorption of the accumulated uranium ions from the electrode surface. Measure the resulting current response during the stripping step using an appropriate electrochemical technique, such as square wave voltammetry or differential pulse voltammetry. The current response is proportional to the concentration of uranium ions in the sample. Calibration and Analysis: Construct a calibration curve using standard solutions of known uranium concentrations. The obtained current responses from the unknown samples can be compared to the calibration curve to determine the uranium concentration in the original sample. It's important to note that the specific experimental conditions and parameters for uranium estimation using ASV may vary based on factors such as the choice of electrode material, supporting electrolyte, pH, and the presence of interfering species.

For the estimation of trace level uranium by Adsorptive Stripping Voltammetry, L-3-(3, 4-dihydroxy phenyl) alanine (LDOPA) was used as a selective complexing agent [120]. Spectrophotometric study shows the formation of ML_2 complex of uranium with the ligand LDOPA in solution. Minimum detection limit of 0.27 ng mL^{-1} for uranium measurement was achieved by adsorption of the uranium-LDOPA complex at hanging mercury drop electrode. The promising behavior of this reagent in relation to uranium analysis holds significant potential for bioassay monitoring.

4.4 Neutron Activation Analysis (NAA)

Neutron Activation Analysis (NAA) is a powerful analytical technique used to determine the elemental composition and concentrations of a wide range of elements in various samples. It involves the irradiation of a sample with neutrons, which induces nuclear reactions resulting in the production of radioactive isotopes. The emitted radiation from these isotopes is then measured to quantify the elemental composition of the sample. Basic steps involved in Neutron Activation Analysis are sample

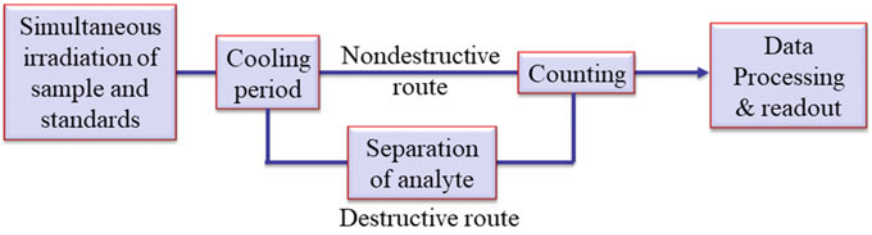

Fig. 11 Flow diagram of two types of Neutron Activation Methods

preparation, irradiation, decay, radiation measurement and data analysis (Fig. 11). The sample of interest is collected and prepared in a suitable form for analysis. The sample may need to be dried, ground, or homogenized depending on its nature and the desired analysis. The prepared sample is exposed to a neutron source, typically in a research reactor or a neutron generator. Neutrons bombard the sample, resulting in nuclear reactions where stable isotopes in the sample capture neutrons, becoming radioactive isotopes. After the irradiation, the sample is allowed to undergo a period of radioactive decay. During this time, the radioactive isotopes formed during irradiation undergo radioactive decay and emit characteristic radiation. The emitted radiation from the radioactive isotopes is measured using suitable detection techniques. This can involve gamma-ray spectrometry, beta particle counting, or other relevant methods depending on the type of radiation emitted by the isotopes. The measured radiation spectra are analyzed to identify the specific radioactive isotopes present and their respective activities. The activities are used to determine the elemental concentrations in the original sample based on known cross-section data and decay properties of the isotopes. Neutron Activation Analysis is known for its high sensitivity and accuracy in elemental analysis, particularly for trace elements.

NAA has proven to be a valuable method for the accurate determination of thorium (Th) and U at ppb (parts per billion) or even lower levels in various scientific fields, including material sciences, geo- and cosmo-sciences, environmental sciences, and bio-sciences [121–123]. NAA is particularly effective for trace element determination due to its ability to achieve virtually blank-free and matrix-insensitive measurements. This makes it suitable for accurate low-level determinations of trace elements such as Th and U. A radiochemical NAA method developed by Byrne and Benedik [121] was successfully used to study ultra-trace levels of uranium in blood, hair, and urine samples from occupationally exposed individuals and a control group without known uranium exposure. In this method, 24-h urine samples were collected in clean polythene bottles and stabilized with concentrated nitric acid. Subsamples were immediately taken from a single voiding and frozen until analysis. After irradiation in a TRIGA MK II reactor, the samples were wet-ashed, and uranium was extracted using tri-n-butyl phosphate (TBP) in toluene. The extracted uranium was then measured using a high-purity germanium (HPGe) detector and a multichannel analyzer system for gamma spectrometry. The isotopic tracer technique used in this

method allowed for the calculation of the chemical yield based on the relative activities of ^{239}U in the sample and a standard. The minimum detectable limit achieved for uranium in urine samples was approximately 1–2 pg mL^{-1} using this method [124]. NAA offers the advantage of being highly sensitive and capable of providing accurate low-level determinations of Th and U. It has been successfully applied in various research areas where precise measurements of these elements at trace levels are required.

4.5 Inductively Coupled Plasma Mass Spectrometry (ICP-MS)

ICP-MS (Inductively Coupled Plasma Mass Spectrometry) is an analytical technique used for the quantitative and qualitative analysis of elements in a wide range of samples. It combines two powerful methods: ICP (Inductively Coupled Plasma) and mass spectrometry. Primary components of ICP-MS system include sample introduction system, ICP torch, Mass Spectrometer, ion optics, detector, data system and software, vacuum System and cooling system (Fig. 12). Inductively Coupled Plasma (ICP) is the ionization source in ICP-MS. It is generated by introducing a sample into a plasma torch, which is a high-temperature ionized gas (typically argon) sustained by radiofrequency (RF) energy. The plasma reaches temperatures of 6000–10,000 K, causing the sample to atomize and ionize. In the ICP, the high temperature causes the sample elements to convert into ions. The sample atoms are stripped of their electrons and form positively charged ions. The ions are then excited to higher energy states by collisions with other ions and electrons in the plasma. The ions generated in the plasma are extracted and introduced into the mass spectrometer. Inside the mass spectrometer, the ions are separated based on their mass-to-charge ratio (m/z). This separation is achieved using various methods, such as quadrupole, magnetic sector, or time-of-flight analyzers, depending on the instrument design. Once the ions are separated according to their mass-to-charge ratio, they are detected by a suitable detector, typically a Faraday cup or an electron multiplier. The detector generates an electrical signal proportional to the abundance of the ions reaching it. This signal is then amplified and processed by the instrument's data acquisition system. The signal obtained from the detector is processed and analyzed to determine the concentration of various elements in the sample. Calibration curves are typically constructed using standard solutions of known element concentrations. The unknown sample concentrations are then quantified based on the response obtained from the calibration curve. ICP-MS offers excellent sensitivity, allowing the detection and quantification of trace elements down to parts per trillion (ppt) levels. It's important to note that proper sample preparation techniques and calibration methods should be employed for accurate results. Interferences from isobaric interferences and polyatomic species can be addressed through the use of various correction techniques and isotopic measurements.

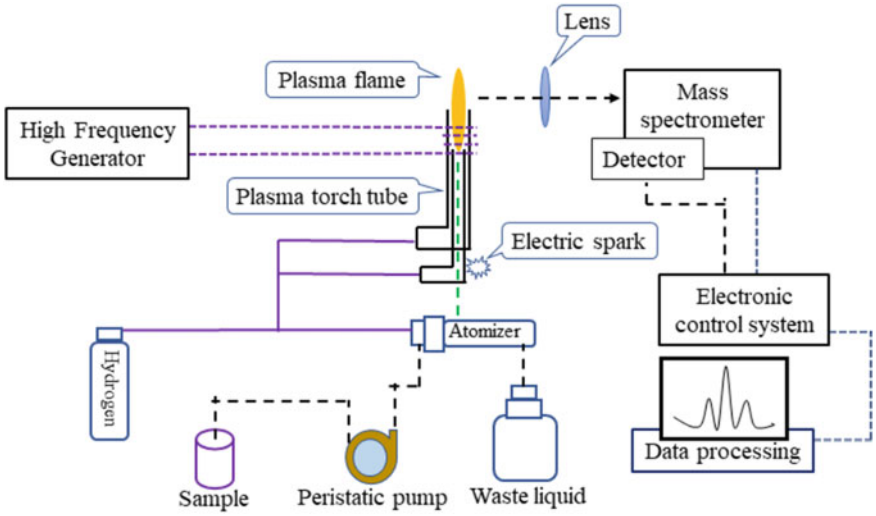

Fig. 12 Schematic diagram of ICP-MS

Application of ICP-MS in the scientific world particularly in analytical chemistry has opened a new era in modern research as it provides much faster and sensitive analysis of a wide range of analytes in various sample matrices. It is capable of detecting femtogram quantities of radionuclides having half-lives more than 10^4 years, present in urine or faecal samples [80, 125]. Many literatures are reported for successful application of ICP-MS for the determination of uranium, plutonium, neptunium, thorium, etc. in urine samples with detection limit ranging from picogram to femtogram level [77, 102, 126–128]. Use of solid phase extraction chromatography resins (UTEVA, TRU, TEVA, etc.) for radiochemical separation followed by quantification by ICP-MS showed better sensitivity for U and Pu isotopes in urine samples [80, 89, 129–132]. These studies highlight various methods and approaches for the determination of uranium and plutonium in urine samples using ICP-MS, employing different separation techniques and sample introduction systems to achieve low detection limits and accurate measurements.

4.5.1 Direct Urine Analysis by ICPMS

Often urine samples are analyzed directly for actinides like U and Th using ICP-MS without extensive sample pre-treatment. One popular direct analysis technique is dilute and shoot method where the sample is treated with nitric acid for dilution followed by actinide quantification by ICP-MS [133, 134]. Such methods although slightly compromised to the detection limits (0.05–10 ng L^{-1}) but much faster due to simple analytical method for sample preparation [134–137]. Depleted uranium, its isotopic ratio in urine was determined using magnetic sector ICP-MS [80, 138, 139].

Such rapid analysis with significant sensitivity could be a useful technique during emergency exposure situations. Studies without sample pre-treatment achieved a detection limit for ^{239}Pu 230 pg L^{-1} whereas with sample digestion the detection limit obtained was 4.7 pg L^{-1} [140]. In emergency situations where there is a need to quickly evaluate elevated levels of ^{239}Pu due to exposure, the speed of analysis becomes crucial. In such cases, direct analysis of urine without sample digestion or extensive chemical separation steps are preferred.

4.5.2 Thermal Ionization Mass Spectrometry (TIMS)

Thermal Ionization Mass Spectrometry (TIMS) is an analytical technique used for the precise measurement of isotopic ratios and elemental concentrations of various elements, particularly those with stable isotopes. It involves the ionization of atoms in a solid or liquid sample using thermal energy, followed by mass spectrometric analysis.

Principle of TIMS

Sample Preparation: The sample of interest is typically prepared in the form of a solid metal or oxide. It is loaded onto a metal filament or a graphite rod, which serves as the ion source.

Ionization: The sample-loaded filament or rod is heated to a high temperature in a vacuum. The thermal energy causes the atoms in the sample to vaporize and ionize. The ions formed are typically positive ions (cations).

Mass Separation: The ion beam generated from the ion source is then introduced into a mass spectrometer. TIMS usually employs a magnetic sector mass spectrometer, which separates ions based on their mass-to-charge ratio (m/z). The magnetic field bends the ions according to their m/z values, allowing their separation.

Ion Detection: As the ions pass through the mass spectrometer, they are detected by ion detectors such as Faraday cups or electron multipliers. The detectors generate electrical signals proportional to the number of ions reaching them, allowing for the quantification of the isotopes of interest.

Key Components of TIMS

Ion Source: The ion source consists of a filament or a rod made of a refractory metal or graphite. The sample is loaded onto the ion source and heated to release the ions. The ion source temperature is carefully controlled to ensure reproducible ionization.

Mass Spectrometer: TIMS employs a magnetic sector mass spectrometer. It consists of a magnet that creates a magnetic field perpendicular to the ion beam path. This magnetic field causes the ions to be deflected based on their mass-to-charge ratios, enabling their separation.

Ion Detectors: The mass spectrometer includes ion detectors positioned at specific locations along the ion beam path. Common detectors used in TIMS are Faraday cups and electron multipliers. Faraday cups measure the ion beam current, while electron multipliers provide higher sensitivity for low ion beam currents.

Vacuum System: TIMS requires a high vacuum environment to minimize gas-phase interferences and preserve the ion beam integrity. The vacuum system typically includes pumps, valves, and pressure gauges to establish and maintain the desired vacuum conditions.

Data System and Software: The data system records and processes the ion beam currents measured by the detectors. The software facilitates instrument control, data acquisition, and data analysis, allowing for the determination of isotopic ratios and elemental concentrations.

TIMS is known for its high precision and accuracy in isotopic ratio measurements, making it valuable in bioassay applications.

This technique is preferred for analysis of accurate isotope ratio but it involves extensive sample preparation which make this technique quite slower as compared to ICP-MS [141]. Using this technique, a minimum detectable activity of ~ 5 mBq L^{-1} and ~ 20 mBq L^{-1} was achieved in urine for ^{239}Pu and ^{240}Pu respectively [34, 142].

Comparative studies for different analytical techniques, in synthetic biological samples using different isotopic ratios of uranium, showed lowest MDA for total uranium by quadrupole ICP-MS (0.1 pg g^{-1}) as compared to other techniques such as sector-field ICP-MS, TIMS, NAA, etc. [143].

Accelerator mass spectrometry (AMS) is also a rapid analytical technique used for trace level estimation of actinides in biological samples with detection limits of ~ 6 mBq L^{-1} for ^{239}Pu and ~ 15 mBq L^{-1} for ^{240}Pu [144].

4.6 Kinetic Phosphorescence Analyzer (KPA)

Kinetic Phosphorescence Analyzer (KPA) is a sensitive analytical instrument used for the detection and estimation of uranium in various samples [145, 146]. This technique is particularly useful for detecting trace amounts of uranium in environmental samples, such as water or soil, as well as in industrial and nuclear-related applications. The first step involves preparing the sample for analysis. Sample may need to be dissolved or extracted to obtain the uranium in a suitable form for measurement. In the next step, the sample is exposed to a specific wavelength of light, typically UV light, which excites the uranium atoms in the sample to higher energy states. After the photoexcitation, the uranium atoms return to their ground state by emitting characteristic phosphorescent light. The emitted light has a longer decay time than the fluorescence, allowing for better differentiation from background fluorescence and other interfering signals. The emitted phosphorescent light is detected using a sensitive PMT or other light detectors. The signal is then amplified and processed, and the decay time of the phosphorescence is measured. The measured decay time is related to the concentration of uranium in the sample through calibration curves or standard reference materials. This allows for the accurate quantification of uranium content in the original sample. Advantages of kinetic phosphorescence analysis for uranium include its high sensitivity, ability to detect trace levels of uranium, and

relatively fast analysis times compared to other traditional methods like alpha spectroscopy or mass spectrometry. However, in general, KPA instruments are known for their high sensitivity, allowing for the detection of trace levels of uranium. The MDA for uranium using KPA is typically in the range of picograms (10^{-12} g) to femtograms (10^{-15} g) of uranium per sample.

4.7 Fission Track Analysis (FTA)

Fission Track Analysis (FTA) technique is used for estimation of fissile materials in biological and environmental samples [147–149]. It relies on the natural process of nuclear fission, which occurs in certain isotopes of uranium and plutonium.

In FTA, the analyte is deposited on a suitable planchette, which is covered with polycarbonate solid-state nuclear detector. It is then bombarded with neutrons in a nuclear reactor. During fission, two energetic fission fragments are released in opposite directions. One of these fragments impinges on the detector and create a highly localized track, which are counted under an optical microscope after chemical etching. This method is used for the assessment of Pu in biological samples [147–149] due to high sensitivity and lower detection limits. FTA has also been standardized in India, for estimation of μBq levels of actinides in biological and environmental samples [35]. However, the limitation of FTA technique is that it cannot differentiate between tracks formed by unlike fissile nuclides (Fig. 13). ^{235}U generally present as trace levels in biological samples which make troubles during estimation of low concentration of Pu in biological samples. Hence, extensive separation methods need to be adopted to estimate trace level ^{239}Pu in biological samples. These separation procedures are described in the work by Sawant et al. [35].

4.8 Solid State Nuclear Track Detectors (SSNTDs)

Solid State Nuclear Track Detectors (SSNTDs), particularly CR-39 detectors, are widely used for the detection of ionizing particles, including alpha particles, protons, and other heavy charged particles [150–152].

When charged particles pass through the material of the detector, they create spatially correlated zones of damage known as latent tracks. These latent tracks are then visualised by chemical etching using solutions like NaOH or KOH. The chemical reaction during the etching process, is more pronounced along the latent tracks as compared to the surrounding bulk material. This etching process is referred to as detector etching or track visualization, and the resulting effect is known as the track effect. The etched tracks become visible under a standard optical microscope [153–157].

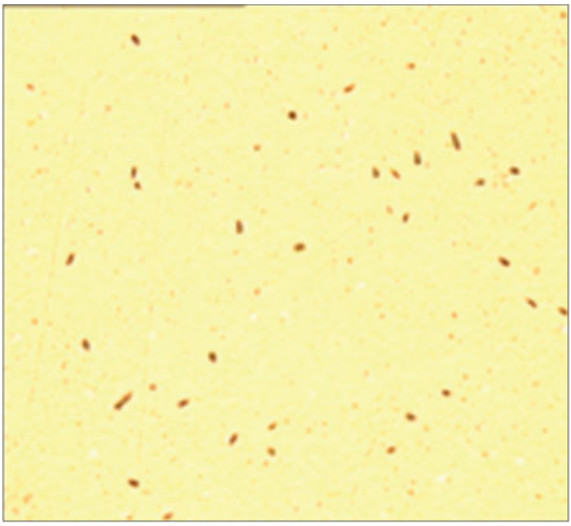

Fig. 13 Fission tracks per field (1.91×10^{-3} cm^2) observed under 400 × due to ^{239}Pu

Mass, charge and energy of the incident particles plays a vital role on the size of the visible tracks [158–163]. Track size also depends on the properties of the detector material, etching solution, etching time, temperature, etc.

The alpha track registration technique utilizing CR-39 detectors has been standardized for the estimation of plutonium in bioassay samples, as developed by Sawant [59]. This technique allows for the detection and quantification of alpha particles emitted by plutonium isotopes in urine samples. The CR-39 detector's ability to record and visualize these alpha tracks provides a reliable method for plutonium assessment in bioassay samples.

4.9 Gross Alpha and Beta Measurement Technique Using LSC

Alpha and beta emitting radionuclides mainly actinides, fission products and activation products present in environmental and biological samples are assessed by gross alpha–beta measurement technique. It involves the determination of the combined intensity of all alpha or beta-emitting radioactive isotopes present in the sample.

The process of gross alpha and beta analysis typically involves the following: Collection of the biological (urine, nasal swab, etc.) followed by sample preparation either by direct addition (e.g. urine) into the scintillator or after processing like separation or pre-concentration techniques. Further measurement for gross alpha and beta in these samples is carried out using liquid scintillation counting (LSC) [164].

4.10 Gross Beta Measurement Using GM Counter

Gross beta measurement is also carried out using Geiger-Muller (GM) counter [165] mainly for samples in solid form. A GM counter consists of a tube filled with a gas, typically a low-pressure inert gas such as argon or helium, with a small amount of a quenching agent. The tube contains an anode and a cathode, and when radiation enters the tube, it ionizes the gas, creating an electrical current. When a beta particle enters the GM counter tube, it ionizes the gas along its path. The resulting ion pairs (positive ions and free electrons) create an electrical pulse. The high voltage applied between the electrodes causes the free electrons to accelerate, creating more ion pairs and amplifying the signal. The electrical pulses generated by the ionization events are detected and counted by the GM counter's electronics. The pulses typically correspond to individual alpha or beta particle interactions. To determine the activity or intensity of beta radiation, the GM counter must be calibrated using known beta radiation sources with known activities. By comparing the counts obtained from the sample to the calibration data, the approximate activity or intensity of the beta radiation can be estimated.

The gross beta measurement technique is easy and rapid but this technique cannot provide the isotopic composition of the sample it only measures the gross activity.

4.11 Solid State Scintillator

A solid-state scintillator is a type of scintillator material that is in a solid state rather than a liquid or crystal form. It is used in radiation detection and measurement systems to convert ionizing radiation into detectable light signals. Solid-state scintillators offer several advantages over traditional liquid or crystal scintillators, including improved stability, ruggedness, and ease of handling. They can be easily fabricated into various shapes and sizes, making them suitable for a wide range of applications.

The basic principle of solid-state scintillators

Absorption of Radiation: When ionizing radiation, such as gamma rays or beta particles, interacts with the solid-state scintillator, it deposits energy into the material. This energy excites the atoms or molecules within the scintillator.

Light Emission: The excited atoms or molecules in the solid-state scintillator subsequently return to their ground state, releasing the excess energy as visible or near-visible light photons. The wavelength and intensity of the emitted light depend on the specific properties of the scintillator material.

Light Detection: The emitted light photons are then detected using a suitable light sensor, such as a PMT or a solid-state photodetector, such as a photodiode or a silicon photomultiplier (SiPM). These detectors convert the detected light into electrical signals that can be further processed and analyzed.

The choice of solid-state scintillator material depends on the specific requirements of the application. Common examples of solid-state scintillator materials include:

Organic scintillators: These are based on organic compounds or plastics, such as polyvinyltoluene (PVT) or polystyrene. Organic scintillators offer good energy resolution and can be easily moulded into various shapes.

Plastic scintillation is indeed an increasingly valuable technique for radionuclide analysis, offering several advantages along with some limitations. One of the primary advantages of plastic scintillation is its capability for alpha/beta discrimination based on pulse shape analysis [166]. By analyzing the shape of the scintillation pulses generated by the detected particles, it becomes possible to distinguish between alpha and beta particles, providing additional information about the type of radiation present in the sample.

However, there are certain limitations associated with plastic scintillation. One significant limitation is the low detection efficiency for low-energy beta emitters. Low-energy beta particles may not generate sufficient scintillation light in the plastic scintillator, leading to reduced sensitivity in detecting these radionuclides. This can be a drawback when analyzing samples that contain predominantly low-energy beta emitters.

Inorganic scintillators include NaI(Tl), CsI(Tl), ZnS(Ag). The ZnS(Ag) is solely used for the detection of alpha particles (Fig. 14). ZnS(Ag) has a high radiation conversion efficiency ~ 20%. The main drawback is ZnS is available only as polycrystalline powder, due to which it cannot be used spectrometric measurements. A thin layer of 20–30 mg/cm^2 thickness is used because thicker layer of ZnS becomes opaque to the incident light. NaI(Tl) and CsI(Tl) detectors are primarily used for γ-spectrometry.

5 Recent Advancements in Radiochemical Separations

Recent advancements in radiochemical separation of bioassay samples have focused on improving separation efficiency, reducing analysis time, enhancing sensitivity and reducing manual handling. Here are a few notable advancements:

5.1 Development of Novel Separation Media

The development of novel separation media, including advanced resins and sorbents, has contributed to improved separation performance. These media offer enhanced selectivity, increased capacity, and faster kinetics. For example, functionalized silica materials or composite sorbents with specific ligands or nanoparticles embedded within them have shown improved radionuclide separation capabilities. The related literature is enlisted in Table 10.

Fig. 14 ZnS(Ag) detector

5.2 Automation in Radiochemical Separation

Automated separation of radionuclides from bioassay samples involves the use of automated systems or instruments that streamline the separation process, reducing manual handling and improving efficiency.

Automatic separation systems based on ion-exchange/extraction chromatography: Automated extraction separation systems utilize robotic arms or automated platforms to perform the various steps involved in the separation process. These systems often include column containing ion-exchange resins or pre-packed columns with specific resins for targeted radionuclide separation. The automated process controls sample loading, washing, elution, and collection of the eluate. The related work obtained

Table 10 Radiochemical separation using molecular sorbents and nanoparticles

Sample	Radionuclide	Separation media	References
Urine	^{210}Po, ^{226}Ra, ^{233}U, ^{241}Am	Fe_3O_4 and a composite nanoparticle (Mn-Fe–O)	[167]
Urine	U	Fe_3O_4 and Mn-doped Fe_3O_4 (MNPs)	[168]
Urine	^{239}Pu, ^{241}Am, ^{90}Sr	AnaLig Pu-02, AnaLig Sr-01, DGA Resin	[169]
Urine	Pu, U	Polymeric sorbents	[170]
Urine, blood serum	U	Magnetic iron oxide nanoparticles (MIONPs) modified by sodium dodecyl sulfate (SDS)	[171]
Urine	^{90}Sr	molecularly imprinted polymer (MIP) comprising dicyclohexano-18-crown-6	[172]

Table 11 Radiochemical separation using automation system

Sample	Radionuclide	Automated separation system	References
Urine	^{90}Sr	Prep*Fast* pre-analytical system (Elemental Scientific, Inc)	[173]
Urine	^{90}Sr, ^{241}Am, Pu	Automated ion chromatographic (IC) system	[174]
Urine	U, Th, Am, Pu, Sr	Automated separation based on FIA	[25]
Urine	Pu, U, Am	Automated separation based on ion-exchange	[175]

from literature is enlisted in Table 11 and Fig. 15 shows photo of automation system using ion-exchange at Bioassay Lab., BARC, Trombay.

These automated systems and instruments play a significant role in improving the efficiency, accuracy, and throughput of radionuclide separation in bioassay samples. They minimize manual handling, reduce operator exposure to radiation, and enhance the reliability of the analysis process.

5.3 Radioisotope Identification Systems (RIS)

RIS combines automated radionuclide separation with subsequent identification and quantification of the separated radionuclides. For this automated or rapid or simplified separation methods are coupled with ICP-MS systems. These systems show improved turnaround time and efficiency, high accuracy and precision, minimum cross contamination risk, reduced sample and reagent requirements and improved detection limits. These parameters are very much crucial in bioassay analysis of radionuclides. This method also minimizes human error and human exposure to

Fig. 15 Photo of automation system for radiochemical separation of actinides based on ion-exchange

radioactive samples and improves reproducibility and worker safety through operation of the automation platform. The related work on RIS obtained from literature is enlisted in Table 12.

Table 12 Application of RIS in in vitro monitoring

Sample	Radionuclide	Separation	Analytical technique	References
Urine	^{241}Am, ^{239}Pu, ^{237}Np, ^{232}Th, and ^{238}U	In-Line Extraction Chromatography	EC-ICP-MS	[176]
Urine	^{239}Pu	1-probe prepFAST MC-4	SF-ICP-MS	[130]
Urine	Pu, U, Am and Sr	Flow injection, EXC	Triple quadrupole ICP-MS/MS	[177]

6 Conclusion

This chapter presents an all-encompassing layout of the in-vitro analysis, exploring its different features. From sample collection to separation strategies, radiochemical procedures, and measurements, the portion incorporates the full range of this basic approach. This chapter also offers a brief look into the state-of-the-art improvements reforming the field of bioassays. Novel advances, for example, nanomaterials and automation of sample preparation and analysis envoy another time in proficiency and accuracy. A recent development is the Radioisotope Identification System (RIS), a unique advantage in actinide bioassay. As innovation develops and information extends, in-vitro monitoring stands ready to proceed with its innovative procedures in the field of radiological evaluation.

References

1. IAEA (2018) Medical management of persons internally contaminated with radionuclides in a nuclear or radiological emergency, emergency preparedness and response. IAEA, Vienna
2. AERB (2019) Monitoring and assessment of occupational exposure due to intake of radionuclides. AERB/NRF/SG/RP-1
3. ICRP (2002) Basic anatomical and physiological data for use in radiological protection reference values. ICRP Publication 89. Ann ICRP 32(3–4):1–277
4. NCRP (1987) Use of dioassay procedures for assessment of internal radionucelide deposition. NCRP Wo.87, Hethesda, Maryland
5. Duke K (1998) Use of the urinary excretion of creatinine in Plutonium in urine bioassay. Radiat Prot Dosimetry 79(1–4):125–128
6. Karpas Z, Lorber A, Elish P, Marcus P, Roiz J, Marko R, Kol R, Brikner D, Halicz L (1998) Uranium in urine-normalization to creatinine. Health Phys 74(1):86–90
7. NCRP (2008) Management of persons contaminated with radionuclides. NCRP Report 161
8. Smith JRH, Etherington G, Youngman MJ (2012) An investigation of monitoring by nose blow sampling. HPA-CRCE-030
9. Sawant PD, Prabhu SP, Rath DP, Gopalakrishnan RK, Rao DD (2015) Nasal swab reference levels for plutonium based on aerosol characteristics & breathing pattern of individuals. Radiat Prot Environ 38:115–119
10. Technical Basis Document for Internal Dosimetry at Sandia National Laboratories (2014) Revision 3. SAND2014-17442R
11. Lendoiro N, Cabitto M, Puerta Yepes N, Vázquez M (2020) Proposed guideline for dose assessment after exposure to I-131 in an accidental situation. IRPA15, COEX, Seoul, Korea
12. Izawa M, Hiroyuki T (1962) Concentration in human urine and estimation of cesium-137 body burden due to world-wide fallout. J Radiat Res 3–2:120–129
13. Boni AL (1966) Rapid ion exchange analysis of radiocesium in milk, urine, sea water, and environmental samples. Anal Chem 38(1):89–92
14. Cahill DF, Wheeler JK (1968) The biological half-life of cesium-137 in children determined by urinary assay. Health Phys 14:293–297
15. Gautier MA (1983) Manual of analytical methods for radiobioassay. LA-9763-M manual. Los Alamos National Laboratory, Los Alamos, NM
16. Lipsztein JL, Bertilli L, Melo DR, Azeredo AM, Julião L, Santos MS (1991) Application of in-vitro bioassay for ^{137}Cs during the emergency phase of the Goiânia accident. Health Phys 60:43–49

17. Peekhunthod D, Bangvirunrak J, Sansakon S, Nukultham A, Pukkhaw T (2017) Baseline quantity of ^{131}I, ^{137}Cs, ^{134}Cs and ^{40}K in urinary excretions from Thai people and internal exposure dose. J Phys Conf Ser 860:012038
18. Yoo J, Park S, Yoon S, Ha WH, Lee SS, Kim KP (2016) Radiobioassay performance evaluation of urine and faeces samples for radiation emergency preparedness. J Nucl Sci Technol 53(11):1742–1748
19. Kumar R, Rao DD, Dubla R, Yadav JR (2017) A rapid method for estimation of Pu-isotopes in urine samples using high volume centrifuge. Appl Radiat Isot 125:176–179
20. Raveendran N, Rao DD, Baburajan A, Yadav JR (2015) Evaluation of alkali fusion and acid leaching methods for the determination of insoluble plutonium and Americium in fecal samples. Radiat Prot Envt 38(1):39–44
21. Panda S, Reddy PJ, Yadav JR, Sawant PD, Kulkarni MS (2022) Development of a rapid technique for sequential separation of plutonium/americium in nasal swab using solvent extraction and liquid scintillation spectrometry. Appl Radiat Isot 186:110297
22. Sawant PD, Prabhu SP, Rath DP, Rao DD, Pradeepkumar KS (2014) Estimation of Pu and its contribution to internal dose, vol 137. IARPNC-2014
23. Campbell EE, Milligan MF, Moss WD, Schulte HD (1972) History of the plutoniumbioassay program at the Los Alamos Scientific Laboratory, 1944–1972. Los Alamos National Laboratory, Los Alamos, NM (Report LA-5008)
24. Efurd DW, Steiner RE, LaMont SP, Lewis D (2008) History of the plutonium bioassay program at the Los Alamos National Laboratory, 1944–2006. J Radioanal Nucl Chem 276:499–504
25. Zoriy P, Flucht R, Burow M, Ostapczuk P, Lennartz R, Zoriy M (2010) Development of a relatively cheap and simple automated separation system for a routine separation procedure based on extraction chromatography. J Radioanal Nucl Chem 286(1):211–216
26. Suja A, Prabhu SP, Sawant PD, Tiwari AK, Sharma R, Sarkar PK (2012) Estimation of uranium in bioassay samples of occupational workers by laser fluorimetry. J Radioanal Nucl Chem 294(3):439–442
27. Prabhu SP, Sawant PD, Reddy PJ, Rao DD (2011) Estimation of ^{241}Pu in bioassay samples by liquid scintillation spectrometry. NUCAR 2011:529–530
28. Thakkar A (2001) Rapid sequential separation of actinides using Eichrom's extraction chromatographic material. J Radioanal Nucl Chem 252:215–218
29. Maxwell SL, Culligan BK, Jones VD, Nichols ST, Noyes GW, Bernard MA (2011) Rapid determination of ^{237}Np and plutonium isotopes in urine by inductively coupled plasma mass spectrometry and alpha spectrometry. Health Phys 101:180–186
30. Kumar R, Dubla R, Yadav JR, Rao DD (2014) Quality assurance exercise for estimating radiochemical recovery and low-levels of alpha emitters in urine samples: performance of Health Physics Laboratory, Tarapur. In: Proceedings of DAE-BRNS biennial symposium on emerging trend in separation science and technology. SESTEC-2014
31. Hölgye Z (1985) Separation of plutonium from feces and urine by coprecipitation with bismuth phosphate. Anal Chem 320:181–182. https://doi.org/10.1007/BF00488686
32. Holgye Z (1998) Separation of neptunium from urine by coprecipitation with $BiPO_4$. J Radioanal Nucl Chem 227:127–128
33. Hölgye Z (2007) Coprecipitation of polonium with bismuth phosphate. J Radioanal Nucl Chem 274(3):647–649
34. Elliot NL, Bickel GA, Linauskas SH, Paterson LM (2006) Determination of femtogram quantities of ^{239}Pu and ^{240}Pu in bioassay samples by thermal ionization mass spectrometry. J Radioanal Nucl Chem 267:637–650
35. Sawant PD, Prabhu SP, Kalsi PC, Pendharkar KA (2009) Estimation of trace levels of plutonium in urine samples by fission track technique. J Radioanal Nucl Chem 279(1):179–183
36. Kressin IK (1981) Separation of plutonium in urine without sample ashing for determination by alpha-spectrometry. Anal Chem 53:1270–1274
37. Larson RP, Urnezis PW, Meechan PJ, Walkup RE, Oldham RD (1978) Application of calcium oxalate precipitation to the separation and determination of the actinide elements in biological materials. In: Program and abstracts of 24th annual conference on bioassay, environmental and analytical chemistry. Annapolis, MD

38. Dai X, Christ M, Kramer-Tremblay S, Synal HA (2012) Ultra-trace determination of plutonium in urine samples using a compact accelerator mass spectrometry system operating at 300 kV. J Anal At Spectrom 27:126–130
39. Dai X, Christ M, Kramer-Tremblay S, Synal HA (2016) Determination of atto- to femtogram levels of americium and curium isotopes in large-volume urine samples by compact accelerator mass spectrometry. J Anal Chem 88:2832–2837
40. Wankhede S, Sawant PD, Rao DD, Pradeepkumar KS (2014) A rapid radiobioassay method for strontium estimation in nuclear/radiological emergencies. Radiat Prot Environ 37(2):95–100
41. Wankhede SM, Sawant PD, Yadav RB, Rao DD (2016) Methodology for estimation of phosphorus-32 in bioassay samples by Cerenkov counting. Radiat Prot Environ 39:149–154
42. Chaudhary S, Gondane S, Sawant PD, Rao DD (2017) A simple method for estimation of phosphorus in urine. Radiat Prot Environ 40(1):44–47
43. Langham WH, Murray A III, Perley AM, Mattison RW (1945) Monitoring of certain personnel for internal plutonium contamination. Los Alamos Scientific Laboratory, Los Alamos, NM (LASLReport LA-349)
44. Bruenger FW, Stover BJ, Atherton DR (1963) Determination of plutonium in biological materials by solvent extraction with primary amine. Anal Chem 35:1671–1673
45. Miller JA, Biggerstaff GE (1964) Determination of neptunium-237 in human urine, report. Kentucky. https://digital.library.unt.edu/ark:/67531/metadc865245/. Accessed 6 July 2023
46. Butler FE (1968) Rapid bioassay methods for plutonium, neptunium, and uranium. Health Phys 15:19–24
47. Veselsky JC, Kirl PC, Sezginer N (1974) The determination of U, Np and Pu in urine by sequential extraction with alamine-336 from hydrochloric acid medium. J Radioanal Nucl Chem 21:97–106
48. Miglio JJ (1978) The determination of americium, curium and californium in biological samples by combined solvent extraction-liquid scintillation counting. Appl Radiat Isot 29(9–10):581–584
49. Singh NA, Ibrahim SA, Cohen N, Wrenn ME (1979) Simultaneous determination of alpha-emitting radionuclides of thorium and plutonium in human tissues including bone. Anal Chem 51:1978–1981
50. Singh NP, Zimmerman CJ, Lewis LL, Wrenn ME (1984) Quantitative determination of environmental levels of uranium, thorium and plutonium in bone by solvent extraction and alpha spectrometry. Nucl Instrum Methods Phys Res 223(2–3):558–562
51. Baglan N, Dinse C, Cossonnet C, Abidi R, Asfari Z, Leroy M, Vicens J (1997) Investigation of U(VI) extraction with calixarene: application to analysis of urine sample. J Radioanal Nucl Chem 226(1–2):261–265
52. Israelsson A, Pettersson H (2014) Measurements of ^{234}U and ^{238}U in hair, urine, and drinking water among drilled bedrock well water users for the evaluation of hair as a biomonitor of uranium intake. Health Phys 107(2):143–149
53. Raymond K (2016) Determination of radionuclides in biological samples by liquid and solid phase extraction. https://repository.library.carleton.ca/concern/etds/j6731460j
54. Sadi BB, Li C, Kramer GH (2011) An emergency radiobioassay method for ^{226}Ra in human urine samples. Radiat Prot Dosimetry 151(1):10–16
55. Dang HS, Pullat VR, Pillai KC (1992) Determining the normal concentration of uranium in urine and application of the data to its biokinetics. Health Phys 62(6):562–566
56. Lee SC, Robin Hutchinson JM, Inn K, Thein N (1995) An intercomparison study of ^{237}Np determination in artificial urine samples. Health Phys 68:350–358
57. Sawant PD, Jaiswal DD, Mehta DJ, Sharma RC (2003) Quality assurance exercise for estimating low-levels of alpha emitters in urine samples: performance of Trombay's Bioassay Laboratory. Radiat Prot Environ 26(1–2):134–138
58. Giardina I, Andreocci L, Bazzarri S,Mancini L, Battisti P (2006) A comparison of different radiochemical methods applicable for the determination of plutonium isotopes in urine via alpha spectrometry. Czech J Phys 56:D265–D270

59. Sawant PD, Prabhu SP, Kalsi PC (2008) Application of alpha track registration technique for plutonium estimation in bioassay samples. Appl Radiat Isot 66(12):1945–1947
60. Sawant PD, Prabhu SP, Kalsi PC (2011) Application of fission track technique in solution media for analysis of uranium in bioassay samples. Radiat Prot Environ 34(1):74–76
61. Prabhu SP, Sawant PD, Bhati S (2010) Standardization of radiochemical procedure for the estimation of protactinum in bioassay samples. Radiat Prot Environ 33(3):137–139
62. Sadi BB, Li C, Bahraini N, Lai EPC, Kramer GH (2010) Selectivity of ^{90}Sr urine bioassay technique over ^{241}Am, $^{238/239}$Pu, ^{210}Po, ^{137}Cs and ^{60}Co. Radiat Prot Dosimetry 141(2):205–209
63. Hernandez MH, Chamizo E, Yllera A, Garcia LM, Delgado A (2010) A highly sensitive method for the reassessment and quantification of Pu-239 in urine samples based on a MV accelerator mass spectrometry system. J Anal At Spectrom 25:1410–1415
64. Santhanakrishnan V, Sreedevi KR, Rajaram S, Ravi PM (2011) Radioanalytical determination of plutonium and americium using ion exchange and extraction chromatography technique in urine. Radiat Prot Environ 34:157–158
65. HernandezMH CE, Delgado A, GarcıaLM YA (2011) Comparison of methods and application of alpha spectrometry and mass spectrometry techniques for ^{239}Pu determination in biological samples. J Anal At Spectrom 26:1509–1513
66. Yang G, Zheng J, Kim E, Zhang S, Seno H, Kowatari M, Aono T, Kurihara O (2021) Rapid analysis of ^{237}Np and Pu isotopes in small volume urine by SF-ICP-MS and ICP-MS/MS. Anal Chimica Acta 1158 (art. no. 338431)
67. Xarchoulakos DC, Kallihtrakas-Kontos NG (2022) Uranium analysis in urine after membrane complexation and alpha spectrometry counting. J Radioanal Nucl Chem 331(1):283–288
68. https://www.triskem-in ernational.com/scripts/files/6454d4deef8fc4.36986672 /techdoc_all_resins_0423_website.pdf. Accessed on 13 July 2023
69. Reinhard AA, Inglis JD, Steiner RE, LaMont SP, Cardon AR, Wende AM, Lopez DL, RoachJL (2020) An improved method for uranium separation from urine for rapid bioassay by inductively coupled plasma mass spectrometry. J Radioanal Nucl Chem 326(1):611–619
70. Horwitz EP, Dietz ML, Chiarizia R, Diamond H, Essling AM, Graczyk D (1992) Separation and preconcentration of uranium from acidic media by extraction chromatography. Anal Chim Acta 266:25–37
71. Žunic ZS, Benedik L, Kritsananuwat R, Veselinovic N, Tokonami S, Arae H, Stojanovska Z, Sahoo SK (2019) Measurement of uranium in urine, hair and nails in subjects of niska banja town, a high natural background radiation area of Serbia. Radiat Prot Dosimetry 184(3–4):319–323
72. Raveendran N, Dubla R, Kumar R, Suja A, Yadav JR, Sawant PD (2023) Sequential separation of plutonium & Americium in urine using DGA resin. In: 6th Asian and oceanic congress for radiation protection (AOCRP6), p S197
73. Horwitz EP, McAlister DR, Bond AH, Barrans RE (2005) Novel extraction of chromatographic resins based on tetraalkyldiglycolamides: characterization and potential applications. Sol Extr Ion Exch 23:319–344
74. Ni Y, Zheng J, Guo Q, Men W, Tagami K, Uchida S (2018) Rapid determination of ultra-trace plutonium isotopes (^{239}Pu, ^{240}Pu and ^{241}Pu) in small-volume human urine bioassay using sector-field inductively coupled plasma mass spectrometry. Anal Chim Acta 1000:85–92
75. Arbova DL, Tolmachev SY, Brockman JD (2022) ICP-MS analysis of actinides in brain tissue of an occupationally exposed individual. J Radioanal Nucl Chem 331(12):5147–5151
76. Vasile M, Jacobs K, Bruggeman M, Van HK, Dobney A, Verrezen F (2018) On the sequential separation and quantification of ^{237}Np, ^{241}Am, thorium, plutonium, and uranium isotopes in environmental and urine samples. Appl Radiat Isot 134:455–460
77. Kuwabara J, Noguchi H (2002) Development of rapid bioassay method for plutonium. J Radioanal Nucl Chem 252:273–276
78. Pappas RS, Ting BG, Jarrett JM, Paschal DC, Samuel P, Caudill SP, Miller DT (2002) Determination of uranium-235, uranium-238 and thorium-232 in urine by magnetic sector inductively coupled plasma mass spectrometry. J Anal At Spectrom 17:131–134

79. Hang W, Zhu L, Zhong W, Mahan C (2004) Separation of actinides at ultra-trace level from urine matrix using extraction chromatography-inductively coupled plasma mass spectrometry. J Anal At Spectrom 19:966–972
80. Pappas RS, Ting BG, Paschal DC (2004) Rapid analysis for plutonium-239 in 1 mL of urine by magnetic sector inductively coupled plasma mass spectrometry with a desolvating introduction system. J Anal At Spectrom 19:762–766
81. Epov VN, Benkhedda K, Cornett RJ, Evans RD (2005) Rapid determination of plutonium in urine using flow injection on-line preconcentration and inductively coupled plasma mass spectrometry. J Anal At Spectrom 20:424–430
82. Parrish RR, Thirlwall MF, Pickford C, Horstwood M, Gerdes A,Anderson J, Coggan D (2006) Determination of $^{238}U/^{235}U$,$^{236}U/^{238}U$ and uranium concentration in urine using SF-ICP-MS and MC-ICP-MS: an interlaboratory comparison. Health Phys 90:127–138
83. Lariviere D, Cumming T, Kiser S, Li C, Cornett R (2008) Automated flow injection system using extraction chromatography for the determination of plutonium in urine by inductively coupledplasma mass spectrometry. J Anal At Spectrom rom 23:352–360
84. Li C, Lariviere D, Kiser S, Moodie G, Falcomer R, Elliott N, Burchart L, Patterson L, Epov V, Evans D, Smith J, Cornette J (2008) Method intercomparison for the analysis of 239/240Pu in human urine. J Anal At Spectrom 23:521–526
85. Godoy MLDP, Juliao LMQC, Godoy JM (2009) Uranium isotopic ratio determination in urine using flow-injection ICP-MS: a tool for emergency monitoring. Radiat Prot Dosim 133:234–239
86. Maxwell SL, Culligan BK (2009) New column separation method for emergency urine samples. J Radioanal Nucl Chem 279:105–111
87. Maxwell SL, Jones VD (2009) Rapid determination of actinides in urine by inductively coupled plasma mass spectrometry and alpha spectrometry: a hybrid approach. Talanta 80:143–150
88. Maxwell SL, Culligan BK, Hutchison JB, Spencer RB (2013) Rapid fusion method for determination of actinides in fecal samples. J Radioanal Nucl Chem 298:1533–1542
89. Arnason JG, Pellegri CN, Parsons PJ (2013) Determination of uranium isotope ratios in human urine by sector field inductively coupled plasma mass spectrometry for use in occupational and biomonitoring studies. J Anal At Spectrom 28:1410–1419
90. Qiao J, Hou X, Roos P (2013) Method for determination of neptunium in large-sized urine samples using manganese dioxide coprecipitation and ^{242}Pu as yield tracer. Anal Chem 85:1889–1895
91. Qiao J, Hou X, Roos P, Lachner J, Christl M, Xu Y (2013) Sequential injection approach for simultaneous determination of ultra-trace plutonium and neptunium in urine with accelerator mass spectrometry. Anal Chem 85:8826–8833
92. Dai X, Cui Y, Kramer-Tremblay S (2013) A rapid method for determining strontium-90 in urine samples. J Radioanal Nucl Chem 296:363–368
93. Zagyvai M (2017) Assay of actinides in human urine by rapid method. J Radioanal Nucl Chem 314(1):49
94. Kong X, Dang L, Shao X, Yin L, Ji Y (2018) Rapid method for determination of ^{90}Sr in biological samples by liquid scintillation counting after separation on synthesized column. J Environ Radioact 193–194:15–19
95. Yoon S, Ha WH, Park S, Jin YW, Kim JM (2018) Improved procedure for Pu/Am, and U isotope analysis in fecal samples. J Radioanal Nucl Chem 316(3):1151–1155
96. González C, Sierra BI (2019) Rapid procedure for actinides and 90Sr analysis in emergency urine spot samples applied in the GHSI-RNWG emergency intercomparison exercise. Appl Radiat Isot 144:19–23
97. Yoon S, Kim Y, Ha WH, Jo MK, Park S, Kim JM (2019) Improved urine analysis for polonium, natural uranium, and thorium isotopes and background survey in collected samples of normal people. J Radioanal Nucl Chem 322(3):1871–1875
98. Jumpei T, Erina T (2019) Rapid analytical method of ^{90}Sr in urine sample: Rapid separation of Sr by phosphate co-precipitation and extraction chromatography, followed by determination

by triple quadrupole inductively coupled plasma mass spectrometry (ICP-MS). Appl Radiat Isot 150:103–109
99. Xiao G, Liu Y, Jones RL (2020) Determination of ^{237}Np and ^{239}Pu in urine using sector field inductively coupled plasma mass spectrometry (SF-ICP-MS). J Radioanal Nucl Chem 324(2):887–896
100. Piraner O, Jones RL (2021) The effect of Sr resin cartridge age on stable Sr recovery methods used in Sr-90 analysis. J Radioanal Nucl Chem 328:369–375
101. Dubla R, Kumar R, Yadav JR, Sawant PD (2021) Sequential separation of actinides and Sr in urine sample using TRU and Sr-spec resin in tandem. Bhabha Atomic Research Centre, India
102. Wyse EJ, Fisher DR (1994) Radionuclide bioassay by inductively coupled plasma mass spectrometry (ICP/MS). Radiat Protect Dosim 55:199–206
103. Gagné A, Surette J, Tremblay SK, Dai X, Didychuk C, Larivière D (2013) A bioassay method for americium and curium in feces. J Radioanal Nucl Chem 295:477–482
104. LaMont SP, Shick CR, Cable-Dunlap P, Fauth DJ, LaBone TR (2005) Plutonium determination in bioassay samples using radiochemical thermal ionization mass spectrometry. J Radioanal Nucl Chem 263:477–481
105. Kaminski M, Sandi G, Dietz, M, Park A (2019) Optimization of a tandem ion exchange—extraction chromatographic scheme for the recovery of strontium from raw urine. Separation Sci Technol 1–10
106. Lee YK, Bakhtiar SN, Akbarzadeh M, Lee JS (2000) Sequential isotopic determination of strontium, thorium, plutonium, uranium, and americium in bioassay samples. J Radioanal Nucl Chem 243:525–533
107. Maxwell SL, Culligan BK (2009) Rapid separation method for emergency water and urine samples. J Radioanal Nucl Chem 279:901–907
108. Thakur P (2005) Radiochemical methods/food and environmental applications. In: Worsfold P, Townshend A, Poole C (eds) Encyclopedia of analytical science, 2nd edn. Elsevier, Atlanta, GA, pp 79–86
109. Alvarez A, Navarro N (1996) Method for actinides and Sr-90 determination in urine samples. Appl Radiat Isot 47:869–873
110. Dai X (2011) Isotopic uranium analysis in urine samples by alpha spectrometry. J Radioanal Nucl Chem 289:595–600
111. Maxwell SL (2008) Rapid analysis of emergency urine and water samples. J Radioanal Nucl Chem 275:497–502
112. Sanjukta AK, Niyoti SS, Shailaja P, Suvarna S, Venkateswaran G (2008) Direct determination of uranium in seawater by laser fluorimetry. Talanta 77(1):422–426
113. Rathore DPS, Talanta MK (2004) Analytical applications of a differential technique in laser-induced fluorimetry: accurate and precise determination of uranium in concentrates and for designing microchemielectronic devices for on-line determination in processing industries. Talanta 62:343
114. Veselsky JC, Kwlecinsk B, Wehrstein E, Suschny O (1988) Determination of uranium in minerals by laser fluorimetry. Analyst 113:451–455
115. Rani A, Singh S (2006) Analysis of uranium in drinking water samples using laser induced fluorimetry. Health Phys 91:101
116. Premadas A, Srivastava PK (1999) Rapid laser fluorometric method for the determination of uranium in soil, ultrabasic rock, plant ash, coal fly ash and red mud samples. J Radioanal Nuclear Chem. 242:23
117. Lakowicz JR (1991) Topics in fluorescence spectroscopy-principles, vol 2. New York
118. Matsui T, Fujimori H, Suzuki K (1988) Effects of coexisting ions upon UO_2^{2+} fluorescence in fuel reprocessing solutions. J Nucl Sci Tech 25:868
119. Maji S, Sundararajan K, Viswanathan KS (2000) Correction for quenching in fluorimetric determinations using steady state fluorescence. Spectrochimica Acta Part A 56:1251–1256
120. Abbasi S, Sohrabi A, Naghipour A, Gholivand MB, Ahmadi F (2008) Determination of ultra trace amounts of uranium (VI) by adsorptive stripping voltammetry using L-3-(3, 4-dihydroxy phenyl) alanine as a selective complexing agent. Anal Lett 41(7):1128–1143

121. Byrne AR, Benedik L (1991) Uranium content of blood, urine and hair of exposed and non-exposed persons determined by radiochemical neutron activation analysis, with emphasis on quality control. Sci Total Environ 107:143–157
122. Dang HS, Pullat VR (1993) Passage of uranium through human cerebral microvascular endothelial cells: influence of time exposure in mono- and co-culture in vitro models. Health Phys 65(3):303–305
123. Kikawada JY, Honda T, Oi T, Ossaka T, Kakihana H (1991) Determination of Th and U at ppt levels in a neutral hot spring water by neutron activation analysis. J Radioanal Nucl Chem Lett 153:357–364
124. Jaiswal DD, Sawant PD, Nair MG, Nair S (2006) Application of neutron activation analysis in estimation of thorium and uranium in biological samples. In: Proceedings of DAE BRNS discussion meet on current trends and future perspective of neutron activation analysis, pp 144–145
125. Ejnik et al (2005) Uranium analysis in urine by inductively coupled plasma dynamic reaction cell mass spectrometry. Anal Bioanal Chem 382:73–79
126. Nguyen SN, Miller PE, Wild JF, Hickman DP (1996) Simultaneous determination of ^{237}Np, ^{232}Th, and U isotopes in urine samples using extraction chromatography, ICP-MS and gamma-ray spectroscopy. Radioact Radiochem 7:16–22
127. Truscott JB, Jones P, Fairman BE, Evans EH (2001) Determination of actinides in environmental and biological samples using high performance chelation ion chromatography coupled to sector-field inductively coupled plasma mass spectrometry. J Chromatogr A 928:91–98
128. ASTM (1997) Standard test method for analysis of urine for uranium-235 and uranium-238 isotopes by inductively coupled plasma-mass spectrometry. ASTM International, West Conshohocken, PA (ASTM C1379-97)
129. Gerdes A (2004) Precise detection of long-lived radionuclides at the mBq to nBq level. In: Oeh U, Roth P, Paretzke HG (eds) Proceedings of the 9th international conference on the health effects of incorporated radionuclides. Neuherberg, Germany, pp 279–285
130. Xiao G, Jones RL (2021) Determination of ^{239}Pu in urine by sector field inductively coupled plasma mass spectrometry (SF-ICP-MS) using an automated offline sample preparation technique. J Radioanal Nucl Chem 328(1):277–287
131. Shi Y, Dai X, Collins R, Kramer-Tremblay S (2011) Rapid determination of uranium isotopes in urine by inductively coupled plasma mass spectrometry. Health Phys 101:148–153
132. Zoriy MV, Pickhardt C, Ostapezuk P, Hille R, Becker JS (2004) Determination of Pu in urine at ultratrace level by sector field inductively coupled plasma mass spectrometry. Int J Mass Spectrom 232:217–224
133. Karpas Z, Halicz L, Roiz J, Marko R, Katorza E, Lorber A, Goldbart Z (1996) Inductively coupled plasma mass spectrometry as a simple, rapid, and inexpensive method for determination of uranium in urine and fresh water: comparison with LIF. Health Phys 71:879–885
134. Hernandez MH, Conde E, Fernandez M, Yllera A (2013) Quantification of the uranium concentration in human urine by inductively coupled plasma-sector field mass spectrometry (ICP-SFMS). Quim Nova 36:865–869
135. Kinman et al (2009) A rapid isotope dilution inductively coupled plasma mass spectrometry procedure for uranium bioassay. J Radioanal Nucl Chem 282:1027–1030
136. Haldimann M, Baduraux M, Eastgate A, Froidevaux P, O'Donovan S, Von Gunten D, Zoller O (2001) Determining picogram quantities of uranium in urine by isotope dilution inductively coupled plasma mass spectrometry. Comparison with aspectrometry. J Anal At Spectrom 16:1364–1369
137. Ting BG, Daniel C, Paschal, Kathleen LC (1996) Determination of thorium and uranium in urine with inductively coupled argon plasma mass spectrometry. J Anal At Spectrom 11:339–342
138. Gwiazda RH, Squibb K, Mc Diarmid M, Smith D (2004) Detection of depleted uranium in urine of veterans from the 1991 Gulf War. Health Phys 86:12–18

139. Ting et al (2003) Rapid analysis for plutonium-239 in urine by magnetic sector inductively coupled plasma-mass spectrometry using Aridus desolvation introduction system. J Anal At Spectrom 18:795–797
140. Baglan N, Bérard P, Trompier F, Cossonnet C, Le BG (1998) How to reduce the uncertainties of committed dose derived from urinary uranium measurements: investigation of new protocols using ICP-MS. Radiat Prot Dosimetry 79(1–4):477–480
141. US Environmental Protection Agency (2004) Multi-agency radiological laboratory analytical protocols manual (MARLAP). Volume II: chapters 10–17 and Appendix F. US EPA, Washington DC (EPA 402-B-04-001A)
142. McCurdy D, Lin Z, Inn KG, Bell R III, Wagner S, Efurd DW, Steiner R, Duffy C, Hamilton TF, Brown TA, Marchetti AA (2005) Second interlaboratory comparison study for the analysis of ^{239}Pu in synthetic urine at the microBq (~100 aCi) level by mass spectrometry. J Radioanal Nucl Chem 263:447–455
143. D'Agostino PA, Ough EA, Glover SE, Vallerand AL (2002) Determination of natural and depleted uranium in urine at the ppt level: an interlaboratory analytical exercise. Los Alamos National Laboratory, . Los Alamos, MN (Report LA-UR-02-5973)
144. Hamilton TF, Brown TA, Hickman DP, Marchetti AA, Martinelli RE, Kehl SR (2004) Low-level plutonium bioassay measurements at the Lawrence Livermore National Laboratory. LLNL, Livermore, CA (UCRL-MI207082)
145. Hedaya MA, Birkenfeld HP, Kathren RL (1997) A sensitive method for the determination of uranium in biological samples utilizing kinetic phosphorescence analysis (KPA). J Pharm Biomed Anal 15(8):1157–1165
146. Paquet F, Houpert P, Blanchardon E, Delissen O, Maubert C, Dhieux B, Moreels AM, Frelon S, Gourmelon P (2006) Accumulation and distribution of uranium in rats after chronic exposure by ingestion. Health Phys 90(2):139–147
147. Moorthy, Schopfer CJ, Banerjee S (1988) Plutonium from atmospheric weapons testing: fission track analysis of urine samples. Anal Chem 60(14): 857A
148. Wrenn ME, Singh NP, Xue YH (1994) Urinary excretion of ^{239}Pu by the general population: measurement technique and results. Radiat Prot Dosim 53:81–84
149. Johansson L, Holm E (1996) Determination of trace-amounts ^{239}Pu using fission track analysis. Nucl Instrum Methods Phys Res Sect A 376(2):242–247
150. Abumurad KM, Ismail AM, Abu-Safia H (2005) A photometry method for measuring tracks density on SSNTDs. Radiat Meas 40:303–306
151. Somogyi G, Grabisch K, Scherzer R, Enge W (1976) Revision of the concept of registration threshold plastic track detectors. Nucl Instrum Methods 109:129–141
152. Ball CJ (1971) An introduction to the theory of diffraction. Pergamon Press, New York
153. Fleischer RL, Price PB, Walker RM (1975) Nuclear tracks in solids. University of California Press, Berkley
154. Durrani SA, Bull RK (1987) Solid state nuclear track detection. principles. Methods and applications. Pergamon Press
155. Nikezic D, Yu KN (2004) Formation and growth of tracks in nuclear track materials. Mater Sci Eng R 46:51–123
156. Yu KN, Nikezic D, Ng FMF, Leung JKC (2005) Long-term measurements of radon progeny concentrations with solid-state nuclear track detectors. Radiat Meas 40:560–568
157. Yu KN, Ng FMF, Nikezic D (2005) Measuring depths of sub-micron tracks in a CR-39 detector from replicas using atomic force microscopy. Radiat Meas 40:380–383
158. Jeong TW, Singh PK, Scullion C, Ahmed H, Hadjisolomou P, Jeon C, Yun H, Kakolee KF, Borghesi M, Ter-Avetisyan S (2017) CR-39 track detector for multi MeV ion spectroscopy. Sci Rep 7(1):2152
159. Malinowska A, Jasko´la M, Korman A, Szydlowski A, Kuk M (2014) Characterization of solid-state nuclear track detectors of the polyallyl-diglycolcarbonate (CR-39/PM-355) type for light charged particle spectroscopy. Rev Sci Instrum 85:123505
160. Zhang Y, Wang HW, Ma YG, Liu LX, Cao XG, Fan GT, Zhang GQ, Fang DQ (2019) Energy calibration of a CR-39 nuclear-track detector irradiated by charged particles. Nucl Sci Tech 30:87

161. Hermsdorf D (2012) Influence of external and internal conditions of detector sample treatment on the particle registration sensitivity of Solid State Nuclear Track Detectors of type CR-39. Radiat Meas 47:518–529
162. Janik M, Hasan MM, Bossew P, Kavasi N (2021) Effects of storage time and preetching treatment of CR-39 detectors on their response to alpha radiation exposure. Int J Environ Res Publ Health 18(16):8346
163. Oliveira CS, Malheiros B, Pires KCC, Assunção, M, Guedes S, Corrêa JN, Paschuk SA (2021) Low energy alpha particle tracks in CR-39 nuclear track detectors: chemical etching studies. Nucl Instrum Methods A 995:165130
164. Piraner O, Jones RL (2021) Urine gross alpha/beta bioassay method development using liquid scintillation counting techniques. J Radioannal Nucl Chem 327(1):513–523
165. Sivasailanathan V, Kumar P, Sagadevan S (2017) Calibration and estimation of efficiency of Geiger Muller counter using a standard radioactive source. Int J Phys Sci 12(1):8–12
166. Tarancón A, Bagán H, García JF (2017) Plastic scintillators and related analytical procedures for radionuclide analysis. J Radioanal Nucl Chem 314:555–572
167. O'Hara MJ, Carter JC, MacLellan JA, Warner CL, Warner MG, Addleman RS (2011) Investigation of magnetic nanoparticles for the rapid extraction and assay of alpha-emitting radionuclides from urine: demonstration of a novel radiobioassay method. Health Phys 101(2):196–208
168. Mandal P, Sawant PD, Bhattacharyya K (2023) A rationale for the rapid extraction of ultra-low-level uranyl ions in simulated bioassays regulated by Mn-dopants over magnetic nanoparticles. RSC Adv 13:15783–15804
169. Dulanská S, Bilohuščin J, Remenec B (2015) Determination of ^{239}Pu, ^{241}Am and ^{90}Sr in urine using pre-filter material and combined sorbents AnaLig® Pu-02, AnaLig® Sr-01, DGA® Resin. J Radioanal Nucl Chem 304:127–132
170. Paul S, Pandey AK, Shah RV, Bhushana KS, Aggarwal SK (2016) Polymer based sorbent materials for thermal ionization mass spectrometric determination of uranium(vi) and plutonium(iv) ions. J Anal At Spectrom 31:985–993
171. Khayatian G, Hassanpoor S, Azar ARJ, Mohebbi S (2013) Spectrophotometric determination of trace amounts of uranium(VI) using modified magnetic iron oxide nanoparticles in environmental and biological samples. J Braz Chem Soc 24(11):1808–1817
172. Negar B, Edward PCL, Li C, Sadi BB, Kramer GH (2011) Molecularly imprinted polymers for 90Sr urine bioassay. Health Phys 101(2):128–135
173. Piraner O, Jones RL (2021) Urine strontium-90 (Sr-90) manual and automated pre-analytical separation followed by liquid scintillation counting. J Radioanal Nucl Chem 329(1):383–390
174. Sadi BB, Rinaldo C, Spencer N, Li C (2018) An ion chromatographic separation method for the sequential determination of 90Sr, 241Am and Pu isotopes in a urine sample. J Radioanal Nucl Chem 316(1):179–189
175. Sawant PD, Prabhu SP, Raj SS, Bhati S, Sarkar PK, Kushwaha HS, Rajendran S, Dey C, Das AP, Shiwalkar V, Singh M (2010) Conceptual design for comprehensive automation in radiochemical analysis of bioassay samples. Radiat Prot Environ 33:219–221
176. Liu Y, Xiao G, Jones RL (2022) High-throughput determination of ultratrace actinides in urine by in-line extraction chromatography combined with quadrupole inductively coupled plasma mass spectrometry (EC-ICP-MS). Anal Chem 94(51):18042–18049
177. Wang W, Evans RD, Evans HE (2021) A rapid, automated system for the separation, preconcentration and measurement of 90Sr, and U, Am and Pu isotopes. Talanta 233 (art. no. 122507)

Radon Inhalation Dose Monitoring

Bijay Kumar Sahoo, Rosaline Mishra, Arshad Khan, and B. K. Sapra

1 Introduction

Radon isotopes, namely ^{222}Rn and ^{220}Rn, are inherent components of the air we breathe, constituting the predominant share (~ 55%) of the natural background radiation dose (~ 2.4 mSv/y) through inhalation [1]. These isotopes raise significant radiological health concerns both in public spaces and occupational settings like uranium mining and thorium processing industries. Prolonged exposure to elevated concentrations of these gases and their decay byproducts heightens the risk of lung cancer [1–3], a fact underscored by numerous global epidemiological studies [4–7].

Monitoring radon inhalation dose aligns with several national and international imperatives:

1. Raising public awareness about natural background radiation exposure.
2. Establishing foundational radon-thoron data for future nuclear facilities, contributing to background radiation mapping.
3. Facilitating national low-dose epidemiological inquiries into radon exposure and its health ramifications.
4. Identifying regions prone to radon and proposing preemptive measures for public safety.
5. Contributing to international initiatives by renowned organizations such as UNSCEAR, IAEA, and WHO.

Radon emanation from the Earth's crust stands as the foremost contributor to indoor radon. Other sources encompass radon release from building materials and radon dissolution in groundwater. Stemming from the decay of radium trapped in soil grains, radon atoms migrate to soil pore spaces due to nuclear recoil, a process known

B. K. Sahoo (✉) · R. Mishra · A. Khan · B. K. Sapra
Radiological Physics and Advisory Division, Health, Safety and Environment Group, Bhabha Atomic Research Centre, Trombay, Mumbai 400094, India
e-mail: bijay@barc.gov.in

D. K. Aswal (ed.), *Handbook on Radiation Environment, Volume 2*,
https://doi.org/10.1007/978-981-97-2799-5_21

as radon emanation. Subsequently, radon diffuses and moves through soil pores, a phenomenon termed radon exhalation [8, 9]. Upon entering the atmosphere, radon accumulates indoors due to inadequate ventilation. Within enclosed spaces, radon decays to form Po, Bi, and Pb decay products, which adhere to aerosol particles, leading to a size distribution categorized into fine/unattached and coarse/attached fractions. Accurate inhalation dose assessment necessitates measuring both size modes.

While earlier studies primarily focused on ^{222}Rn and overlooked the shorter-lived ^{220}Rn due to its rapid decay, it's crucial to reconsider this stance. The inhalation dose from ^{220}Rn progeny surpasses that from ^{222}Rn progeny by fourfold [1], warranting attention, particularly in high natural background radiation areas (HNBRAs) rich in thorium and in occupational settings involving thorium and Naturally Occurring Radioactive Materials (NORMs) [10–12]. Emerging interest in ^{220}Rn and its decay products measurement pertains to both residential and occupational environments [13–15].

Various techniques exist for measuring radon, thoron, and decay products, each with distinct merits and demerits. Indoor concentrations vary due to building materials, ventilation patterns, and temporal fluctuations, necessitating monitoring for at least three months, preferably a full year, for accurate annual averages. Standardized protocols are paramount for harmonizing techniques in large-scale surveys, ensuring accuracy and comparability across studies.

This chapter aims to provide researchers in universities and R&D institutes with information, recommendations, and technological insights for radon, thoron, and decay product measurements.

2 Special Quantities and Units for Radon Monitoring

Various specialized metrics are employed to quantify the presence of ^{222}Rn, ^{220}Rn, and their respective decay products, as outlined in the following section [16].

Potential Alpha Energy (PAE)

The Potential Alpha Energy (PAE) of an atom within the ^{222}Rn/^{220}Rn decay chain is the cumulative sum of alpha energies (in MeV) released during its decay through the chain to the stable radionuclide ^{210}Pb for ^{222}Rn or ^{208}Pb for ^{220}Rn.

Potential Alpha Energy Concentration in Air (PAEC)

The Potential Alpha Energy Concentration (PAEC) characterizes the collective alpha energy potentially emitted by all radon and thoron decay product atoms within a given volume of air. Traditionally expressed in Working Level (WL), its International System of Units (SI) equivalent is J m^{-3}. One Working Level (WL) corresponds to 2.08×10^{-5} J m^{-3}, originating from 100 pCi l^{-1} (3700 Bq m^{-3}) of ^{222}Rn gas in equilibrium with its decay products. Table 1 illustrates a representative calculation of

potential alpha concentration from 3.7 Bq l^{-1} (100 pCi l^{-1}) of each progeny nuclide related to ^{222}Rn, as shown.

Equilibrium Equivalent Concentration (EEC)

The Equilibrium Equivalent Concentration (EEC) for radon represents the concentration at which radon is in a state of secular equilibrium with its decay products, thereby leading to an equivalent Potential Alpha Energy Concentration (PAEC) for the decay products present in the air. The mathematical representation of EEC is as follows:

$$\mathrm{EEC} = \frac{0.136C_\mathrm{a} + 0.660C_\mathrm{b} + 0.488C_\mathrm{c}}{1.284} = 0.106C_\mathrm{a} + 0.514C_\mathrm{b} + 0.380C_\mathrm{c}$$

where C_a, C_b, and C_c denote the concentrations (Bq l^{-1}) of ^{218}Po, ^{214}Pb, and ^{214}Bi, respectively.

Notably, one Working Level (WL) corresponds to an EEC of 3700 Bq/m^3 for radon and 275 Bq/m^3 for thoron.

Equilibrium Factor (*F*)

A streamlined approach to estimate EEC involves measuring the concentration of radon gas and utilizing an equilibrium factor tailored to the particular environment. The Equilibrium Factor (F) denotes the relationship between the EEC and the radon concentration present in the environment. While this factor does exhibit variability contingent upon environmental circumstances, it remains relatively consistent for typical indoor locations such as houses. The global average for radon Equilibrium Factor is approximately 0.4. However, when it comes to thoron, due to its brief half-life and wide-ranging concentration distribution, it is not advisable to estimate EEC through the thoron gas concentration and equilibrium factor approach.

Table 1 Potential Alpha Energy Concentration (PAEC)

Daughter nuclide	Half-life (s)	N_i	PAE E_i (MeV)	N_iE_i ($\times 10^5$ MeV)
^{218}Po	183	976	13.69	0.136
^{214}Pb	1608	8583	7.69	0.660
^{214}Bi	1194	6374	7.69	0.488
^{214}Po	0.0002	0.001	7.69	< 0.001
Total				1.284

Assuming 3.7 Bq l^{-1} for each ^{222}Rn daughter
N_i = number of atoms per liter of ith daughter
E_i = alpha-particle energy released for ith daughter

Working Level Month (WLM)

Exposure to the concentration of radon and thoron decay products is measured in terms of Working Level Months (WLM), which corresponds to an equivalent exposure of 1 Working Level (WL) over the course of one month (equivalent to 170 h of work).

In summary, these specialized metrics play a pivotal role in enhancing our understanding and evaluation of radon, thoron, and their respective decay products across diverse environments.

3 Radon Generation and Transport

Radon and thoron emerge predominantly from the soil due to the presence of minerals containing ^{238}U and ^{232}Th. Similarly, building materials housing these minerals also serve as sources. Technological processes, like mining and industrial treatment of sands and ores, can further elevate radon/thoron production. Radon or thoron in the earth's crust or porous materials can migrate only by infiltrating pores or capillaries. The migration of radon to indoor air occurs via emanation and exhalation processes (see Fig. 1). Emanation involves nuclear recoil, where ^{222}Rn atoms generated within solid mineral grains escape into air-filled pores within the soil matrix. On the other hand, exhalation is the transfer of ^{222}Rn gas from these air-filled pores to the atmosphere. This process hinges on the mechanisms of diffusion and advection. Various factors like rainfall, snowfall, freezing, and atmospheric pressure changes can impact diffusivity, thereby influencing exhalation rates.

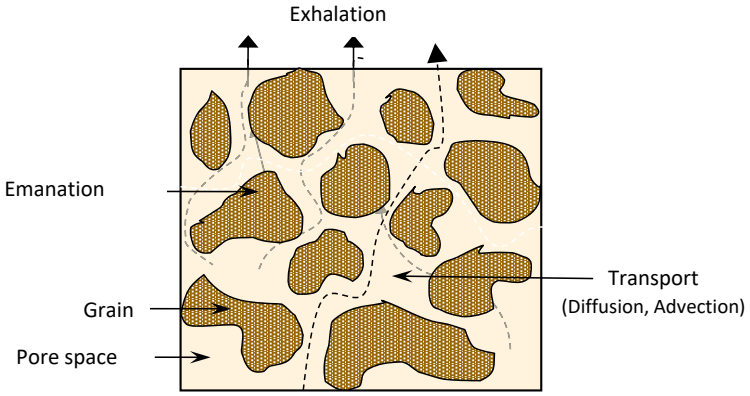

Fig. 1 Processes of radon emanation and exhalation to the environment [16]

3.1 Formulation of the Radon Diffusion Equation for Soil Matrix

Consider a soil matrix where radon continuously emanates into the pore space. Let's denote by S the radon activity released per unit of time into the unit volume of the pore. C_p represents the radon concentration in the pore space at any given point and time. Radon is transported within pores with a local flux density F_p, indicating the radon activity transported per unit pore area per unit time. The governing transport equation emerges from the time rate of change of radon activity within an infinitesimal pore volume. This change arises from the difference between the generation rate and the loss rate due to transport and radioactive decay (with decay constant λ) [17]:

$$\frac{\partial C_p}{\partial t} = S - \nabla \cdot F_p - \lambda C_p \tag{1}$$

In general, F_p comprises two components: (i) pressure-driven advective flux and (ii) gradient-driven diffusive flux. Typically, the pressure difference between the pore space and the atmosphere is negligible and can be disregarded. In a one-dimensional (1-D) system, applying Fick's law of diffusion, the diffusion flux is related to the concentration gradient [18]:

$$F_p = -D\frac{\partial C_p}{\partial z} \tag{2}$$

where, D is the radon diffusion coefficient in the pore space in the soil matrix.

Substitution Eq. (2) in Eq. (1) yields the following diffusion equation:

$$\frac{\partial C_p}{\partial t} = S + D\frac{\partial^2 C_p}{\partial z^2} - \lambda C_p \tag{3}$$

The source term, S can be expressed in terms of soil parameters as follows:

$$S = \frac{\lambda R \rho E}{n_T} \tag{4}$$

where

R is the radium content of the soil (Bq/kg),
ρ is the bulk density of the matrix (kg/m^3),
E is the emanation coefficient of radon from soil grain to pore volume and
n_T is the total porosity of the matrix.
Using Eq. (4), Eq. (3) can be simplified to

$$\frac{\partial C_p}{\partial t} = D\frac{\partial^2 C_p}{\partial z^2} - \lambda C_p + \frac{\lambda R \rho_B E}{n_T} \tag{5}$$

The exhalation rate at the soil surface encompasses the overall area, which comprises both the pore area and the area occupied by solid grains. If we assume that the fractional pore area at the surface is equivalent to the fractional pore volume within the entire soil matrix, the radon surface exhalation rate (flux density) can be connected to the concentration within the pore space as depicted in the following manner [18]:

$$F = -n_{\mathrm{T}} D \frac{\partial C_{\mathrm{p}}}{\partial z} \tag{6}$$

In general, pore space may be partly filled with air and partly with water. It is the correct approach to recast the diffusion equation in terms of radon concentration in pore air. If C_{w} and C_{a}, denote radon concentration in water and in air respectively and n_{w}, n_{a} denote air-filled and water-filled porosity respectively, then the conservation law demands that:

$$n_{\mathrm{T}} C_{\mathrm{p}} = n_{\mathrm{a}} C_{\mathrm{a}} + n_{\mathrm{w}} C_{\mathrm{w}} \tag{7}$$

C_{w} can be related to C_{a} using law of equilibrium partitioning as follows:

$$C_{\mathrm{w}} = K \cdot C_{\mathrm{a}} \tag{8}$$

where K denotes the water-to-air radon partition coefficient.

Combining Eqs. (7) and (8), one can arrive at

$$n_{\mathrm{T}} C_{\mathrm{p}} = C_{\mathrm{a}}(n_{\mathrm{a}} + K n_{\mathrm{w}}) = n_{\mathrm{e}} \cdot C_{\mathrm{a}} \tag{9}$$

where,

$$n_{\mathrm{e}} = (n_{\mathrm{a}} + K n_{\mathrm{w}}) \tag{10}$$

n_{e} represents the partition-corrected effective porosity. It may be expressed in terms of the volumetric moisture saturation (m), defined as $m = n_{\mathrm{w}}/n_{\mathrm{T}}$, as follows:

$$n_{\mathrm{e}} = n_{\mathrm{T}}[1 - (1 - K)m] \tag{11}$$

With this, Eq. (5) may be formulated in terms of C_{a} as follows:

$$\frac{\partial C_{\mathrm{a}}}{\partial t} = D \frac{\partial^2 C_{\mathrm{a}}}{\partial z^2} - \lambda C_{\mathrm{a}} + \frac{\lambda R \rho E}{n_{\mathrm{e}}} \tag{12}$$

For steady-state conditions, Eq. (12) becomes

$$D \frac{\partial^2 C_{\mathrm{a}}}{\partial z^2} - \lambda C_{\mathrm{a}} + \frac{\lambda R \rho E}{n_{\mathrm{e}}} = 0 \tag{13}$$

And the corresponding expression for radon surface exhalation rate can be written as

$$F = -n_e D \frac{\partial C_a}{\partial z} \tag{14}$$

3.2 Analytical Models

Analytical models grounded in diffusion theory are extensively employed to assess the potential radon exhalation from both soil and building materials. The rate of radon surface exhalation holds crucial significance as an input parameter for concentration dispersion models, facilitating the prediction of radon activity distribution in the atmosphere and indoor settings. Presented here are two exhalation models tailored for soil matrices and building walls.

3.2.1 Model for Radon Exhalation from Soil Matrices

Consider a soil matrix where radon diffusion transpires in a one-dimensional vertical direction following emanation from soil grains to the pore space (refer to Fig. 2). In this context, soil characteristics like porosity, diffusion coefficient, and radium content are presumed to remain consistent throughout the matrix.

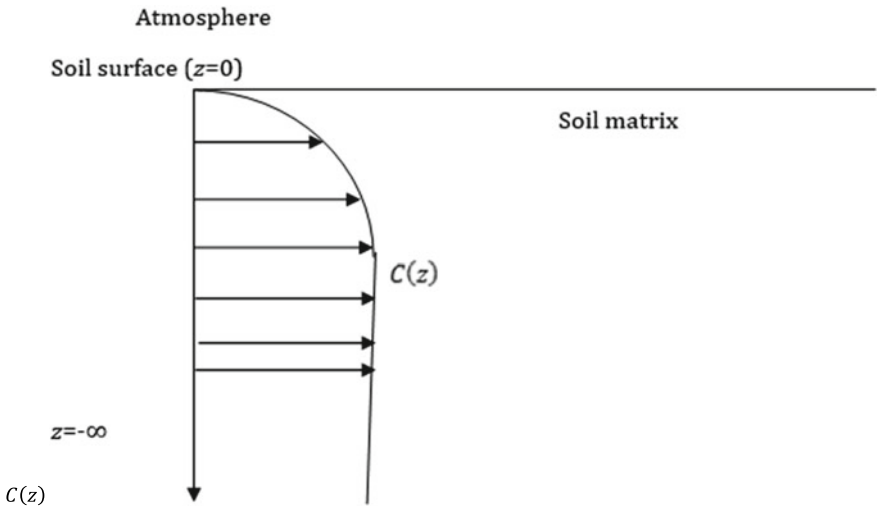

Fig. 2 Depth profile of radon in soil [16]

Under a steady state condition, the concentration profile of radon $C(z)$ will satisfy the following mass balance equation:

$$D_s \frac{\partial^2 C}{\partial z^2} - \lambda C + \lambda \frac{R\rho E}{n} = 0; \tag{15}$$

where,

D_s is the diffusion coefficient of radon in the soil matrix ($m^2\ s^{-1}$),
λ is the radon decay constant (s^{-1}),
R is ^{226}Ra content (Bq kg^{-1}) in the soil,
ρ is the dry bulk density (kg m^{-3}) of soil,
E is the radon emanation factor and λ is the radon decay constant (s^{-1}),
n is the porosity of the soil matrix.

Once the radon atom reaches the atmosphere, it immediately get diluted and radon concentration becomes negligible in comparison to the concentration in soil pores. With this, boundary conditions of the problem may be formulated as:

$$C(z = 0) = 0 \tag{16}$$

$$C(z = -\infty) = R\rho E/n = C_\infty \tag{17}$$

Using these Boundary Conditions, the solution to this equation may be derived to get the expression of the concentration profile of radon in the soil matrix as:

$$C(z) = C_\infty\{1 - \exp(z/l_s)\} \tag{18}$$

where l_s is the radon diffusion length defined as $l_s = \sqrt{D_s/\lambda}$.

Using Eq. (18), the radon surface exhalation rate at the soil surface (F_s) may be derived as:

$$F_s = -nD_s \left.\frac{dC(z)}{dz}\right|_{z=0} = \frac{nD_s}{l_s} C_\infty = \lambda l_s R\rho E \tag{19}$$

Equation (19) demonstrates how the radon exhalation flux from the soil surface can be evaluated based on various soil properties such as radium content, radon diffusion length in soil, radon emanation factor, and bulk density. This equation can be restructured to include the radon mass exhalation rate as the primary input parameter. The mass exhalation rate of radon (denoted as J_m in Bq kg^{-1} h^{-1}) is traditionally defined as the radon activity released per unit time from a unit mass of the soil matrix. Mathematically, this can be represented as:

$$J_m = RE\lambda \tag{20}$$

With this, the expression for radon surface exhalation rate given in Eq. (19) may be simplified to

$$F_s = J_m \rho l_s \tag{21}$$

Equation (21) indicates that the radon surface exhalation rate at the soil surface can be readily computed by knowing just two primary parameters: the mass exhalation rate (J_m) and the radon diffusion length in soil (l_s).

3.2.2 Model for Radon Exhalation from Building Walls

Radon exhalation from a wall transpires through two faces of the wall, resulting in a symmetric concentration profile, with zero flux at the wall's center. The radon diffusion process follows a one-dimensional pattern as depicted in Fig. 3. The steady-state equation for radon concentration ($C(z)$) in the pore space of the wall matrix can be formulated as [9]:

$$D_w \frac{\partial^2 C(z)}{\partial z^2} - \lambda (C(z) - C_\infty) = 0 \tag{22}$$

where the notations correspond to parameters for the building material instead of soil as defined in the previous problem.

The boundary conditions of the problem may be written as:

$$C(z = \pm t) = 0 \tag{23}$$

$$n D_w \left. \frac{\partial C}{\partial z} \right|_{z=0} = 0 \tag{24}$$

Using these BCs, the solution to Eq. (22) may be derived as:

$$C(z) = C_\infty \left[1 - \frac{\cosh(z/l_w)}{\cosh(t/l_w)} \right] \tag{25}$$

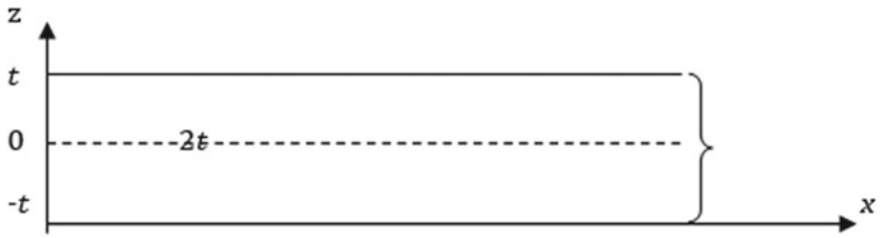

Fig. 3 Coordinate system for radon diffusion in the building wall [16]

Applying Fick's law of diffusion, the radon flux at the surface of the building wall (F_w) can be expressed as:

$$F_w = -nD_w \left.\frac{dC(z)}{dz}\right|_{z=t} = \lambda l_w R\rho E \tanh \frac{t}{l_w} \tag{26}$$

In terms of mass exhalation rate of radon in building materials, Eq. (26) may be simplified to

$$F_w = J_m \rho l_w \tanh \frac{t}{l_w} \tag{27}$$

3.2.3 Indoor Radon Concentration Model

Armed with the data regarding radon exhalation rates from both walls and floors, it becomes feasible to anticipate the radon concentration within a standard room through the consideration of ventilation rates. Such a model is commonly referred to as a concentration dilution model. Under conditions of steady-state equilibrium, the speed at which the radon is generated from wall exhalation will match the pace at which it is eliminated through ventilation and radioactive decay.

I.e.,

$$\sum F_{wi} A_i = CV(\lambda + \lambda_v) \tag{28}$$

where

F_{wi} refers to radon exhalation flux from the ith building wall (Bq m^{-2} s^{-1}),
A_i is the surface area of the ith building wall (m^2),
C is the radon concentration in the room (Bq m^{-3}),
V is the volume of the room (m^3),
λ is the radon decay constant (s^{-1}) and
λ_v is the ventilation rate (s^{-1}).

Combining the aforementioned elements, the ultimate model to foresee radon concentration within a standard room takes the form:

$$C = \frac{\sum F_{wi} A_i}{V(\lambda + \lambda_v)} \tag{29}$$

This model serves as an invaluable tool during the building's design phase for projecting the average radon concentration within a room. It utilizes measured radon exhalation data from both soil and building materials. Subsequently, this estimated concentration can be harnessed to predict the anticipated inhalation dose for an individual by leveraging the standard dose conversion factor.

4 Radon and Thoron Gas Monitoring

The field of radon/thoron measurement has witnessed significant advancement. Numerous instruments and techniques are now accessible for assessing radon, thoron, and their decay products. These measurement techniques rely on detecting independent or combined alpha, beta, or gamma-ray radiations emitted by these substances. These instruments can be categorized into three groups based on their sampling methods: grab (or instantaneous), integrating, and continuous types. They further fall into either active or passive categories. This section outlines some of the popular measurement methods.

4.1 Scintillation Cell Method

A prevalent method for spot measurement of radon in air involves the use of a scintillation cell (commonly referred to as LUCAS cell) for air sample collection. This cell, with an approximate volume capacity of 150 cc, incorporates a particulate filter. The interior surfaces of the scintillation cell are coated with a zinc sulfide phosphor layer. The cell is hermetically sealed and features a transparent glass window at one end. This window is connected to a photomultiplier tube that registers light pulses (scintillations) arising from the interaction of alpha particles with the ZnS: Ag scintillator due to the disintegration process of radon and its decay products within the cell's volume.

The quantity of registered alpha pulses is directly proportional to the radon activity concentration within the cell. The alpha counting takes place after a delay period of approximately 3 h following sampling. This delay ensures the establishment of radioactive secular equilibrium between the short-lived radon decay products and the radon gas.

The ^{222}Rn activity concentration (C_R) can be estimated from the counts using the following relation:

$$C_R\left(\mathrm{Bq\,m^{-3}}\right) = \frac{X}{3\eta\, V\, \exp(-\lambda T)} \tag{30}$$

where:

X—is the net count rate, CPS (s^{-1}) after subtracting the background
η—is the counting efficiency (~ 75%)
V—is the volume of the sampler (m^3)
λ—is the decay constant of radon (s^{-1})
T—is the time delay post-sampling (s).
Factor 3 accounts for contribution from three alphas (^{222}Rn, ^{218}Po and ^{214}Po).

4.2 Double Filter Method

In this approach, an air sample is drawn through a cylinder equipped with high-efficiency particulate filters positioned at both ends to capture decay products. The cylinder's volume typically falls within the range of 0.5–1000 L, and the sampling duration spans about 5–30 min, depending on the desired radon concentration level. The inlet filter serves to exclude short-lived decay products from the sampled air, while the exit filter collects progeny formed inside the cylinder during its transit from one end to the other. Analyzing the activity accumulated on the exit filter provides insights into the radon or thoron concentration. The radon decay product activity recorded on the second filter is directly proportional to the radon concentration within the sampled air. If C_{Rn} represents the radon concentration in the air (measured in Bq m^{-3}), X signifies the counts measured between t_1 and t_2, which are determined from the end of sampling over time T, and f denotes the fraction of radon progeny reaching the exit filter, with V representing the volume of the cylinder between the filters, then:

$$C_{\mathrm{Rn}}\left(\mathrm{Bq\,m^{-3}}\right) = \frac{X}{EVf\,Z(t_1, t_2)} \tag{31}$$

where:

E—is the counting efficiency of the setup used

Z—is the theoretical count depending on the radioactive build-up in the cylinder.

Larger cylinder volumes, with a sensitivity of approximately 0.7 Bq m^{-3}, can be effectively employed for environmental sampling. To establish accurate correction factors in this method, it's essential to draw samples at various humidity and temperature levels. Calibration exercises should encompass diverse flow rates and sampling durations to validate adherence to acceptable limits.

4.3 Ionization Chamber-Based Radon Monitor

The ionization chamber-based technique stands as the most sensitive approach for radon detection, serving as a primary method in this field. In this methodology, radon gas within the atmospheric air diffuses into the ionization chamber via a particulate filter. Inside the chamber volume (Fig. 4), the disintegration process of radon and its decay products yields alpha particles that generate ion bursts. These ions are gathered at the central electrode, translating into electrical pulses corresponding to each disintegration event. Subsequently, these pulses undergo processing and amplification by the monitor's electronics. They are then converted into radon activity concentration through the utilization of calibration factors embedded in the monitor's microcontroller.

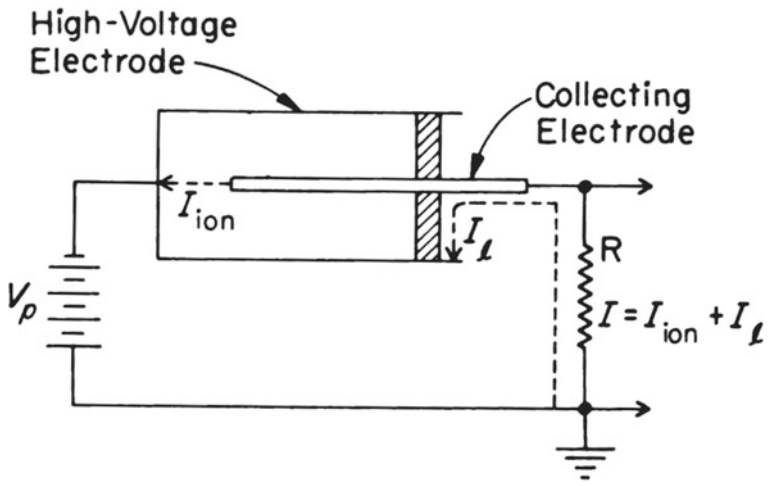

Fig. 4 Schematic of ionization chamber-based radon detection system [16]

4.4 Semiconductor-Based Radon Monitor

Among the notable online radon monitors, the RAD7 and RTM-2200 stand out for their utilization of semiconductor detectors. Figure 5 illustrates a schematic of this particular type of radon monitor. Within this approach, a solid-state silicon detector is harnessed to perform spectroscopic differentiation of the alpha particles emitted during radon decay. The detection process commences by pumping ambient air into the detection chamber through a particulate filter. As radon undergoes decay within the chamber, charged polonium atoms (radon's decay products) are captured onto the detector surface via an electric field.

Subsequently, alpha particles emitted by these polonium atoms are spectroscopically identified and subsequently transformed into radon concentration using established calibration factors. This detector type facilitates the differentiation between radon and thoron. Notably, this technology boasts lower background counts, thereby mitigating measurement errors. However, it's important to note that these detectors are susceptible to interference from humidity and trace gases present in the surrounding air.

4.5 Scintillation-Based Radon Monitor

This variant of online radon monitor employs a scintillation chamber coated with ZnS: Ag scintillator to detect radon and thoron. The Smart Radon Thoron Monitor (RnDuo) is a widely adopted portable instrument that relies on this technology.

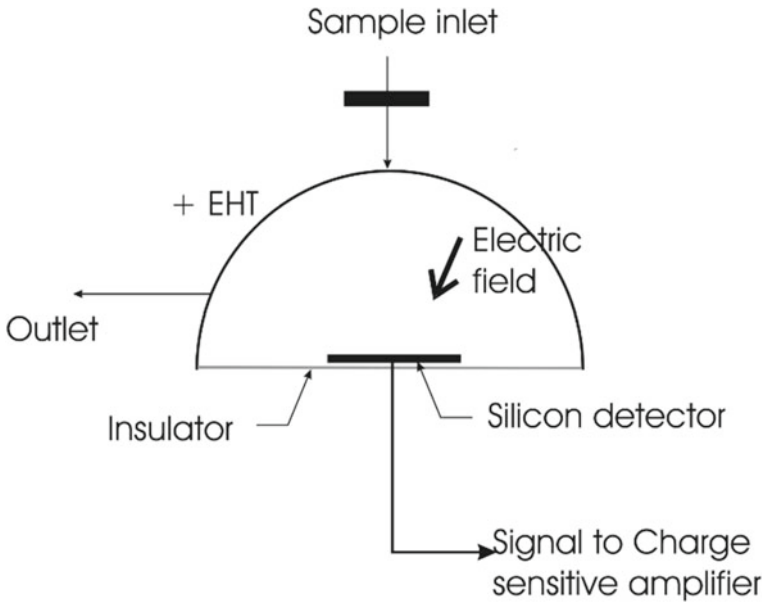

Fig. 5 Schematic of silicon detector-based radon monitoring system [16]

Figure 6a illustrates the schematic of the microprocessor-based RnDuo, while its photograph is depicted in Fig. 6b.

For radon measurements, ambient air traverses through a "progeny filter" and a "thoron discriminator," both of which eliminate radon/thoron progenies and thoron gas. The design of the thoron discriminator hinges on a "diffusion-time delay" concept. This approach ensures that almost all of the thoron ^{220}Rn (with a half-life of 55.6 s) undergoes substantial decay during the air's diffusion from the exterior to the scintillation cell. However, this setup allows nearly 99% of the exterior radon gas to pass through. Within the system, alpha particles generated during the decay processes of radon and thoron are detected by the ZnS: Ag scintillation cell coupled with a photomultiplier. A sophisticated algorithm, embedded within the microcontroller, serves to compensate for the contributions arising from decay products formed by radon gas at the conclusion of each cycle. This algorithm plays a pivotal role in enabling the continuous measurement of radon concentration. The algorithm operates based on the theoretical decay and growth patterns of radon's decay products during the ongoing measurement cycle, as well as historical radon concentration data. The alpha counts acquired are subjected to this algorithmic processing, leading to the presentation of radon concentration.

In the realm of thoron monitoring, ambient air is drawn into the scintillation cell (150 cc) through the integrated pump of the monitor. The inlet particulate filter serves to exclude progenies while permitting gas that might encompass both thoron and

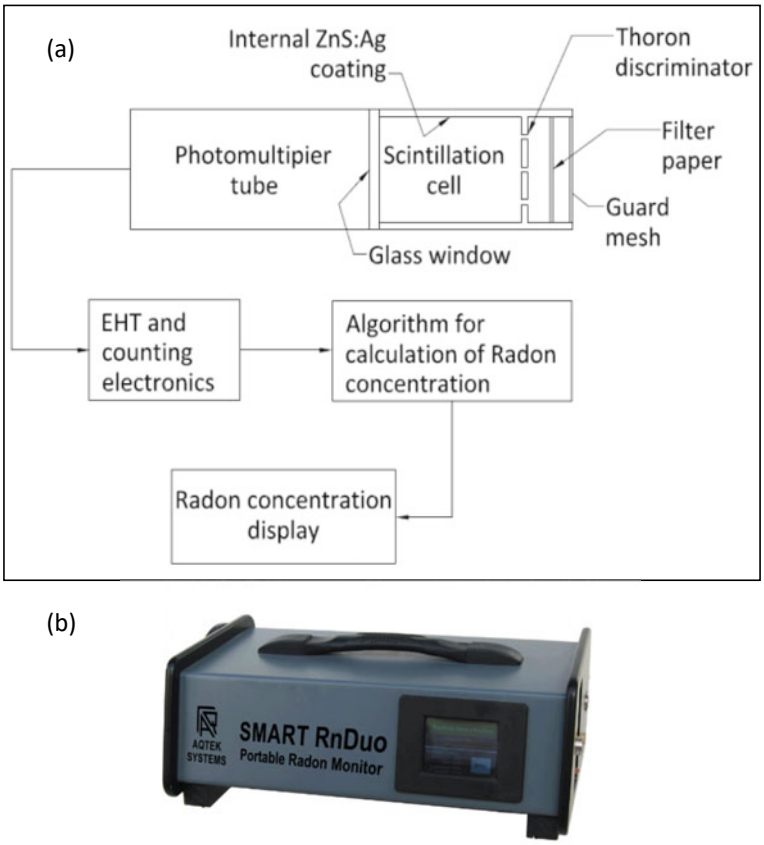

Fig. 6 **a** Schematic of the radon measurement process in RnDuo [16]. **b** Photograph of the Smart Radon-Thoron Monitor (RnDuo) [16]

radon. During the initial phase of each measurement cycle, the sampled gas undergoes total alpha counts, encompassing contributions from radon, thoron, and their long-lived decay products (background activity with a half-life of several minutes). As the cycle progresses, the sampling pump is automatically deactivated by the microcontroller. This pause, lasting 5 min, enables nearly complete decay of thoron (over 5 half-lives) while in the remaining activity, a combination of radon and background activity, is quantified after the delay period. Upon cycle completion, the thoron concentration is deduced by calculating the difference between the two counts and applying an appropriate calibration factor.

This method, utilizing a scintillation-based monitor, exhibits heightened sensitivity to radon compared to semiconductor detector-based monitoring systems due to its larger detector size. Notably, the radon and thoron monitoring facilitated by the scintillation-based monitor remains immune to fluctuations in humidity and trace

gas concentrations within the ambient air. This versatile technique finds application across various domains, including (i) radon/thoron measurements in air, water, and soil, (ii) indoor radon surveys encompassing dwellings, caves, and office spaces, (iii) functioning as a reference monitor for calibrating passive detector systems, (iv) workplace monitoring within contexts such as uranium mines and NORM facilities, (v) uranium exploration studies, and (vi) earthquake precursory investigations.

4.6 Solid State Nuclear Track Detectors (SSNTDs)

Solid State Nuclear Track Detectors (SSNTDs) have found extensive application in surveys involving radon and thoron within residential environments, owing to a range of compelling advantages they offer. These advantages encompass cost-effectiveness, the elimination of power supply requirements, easy portability, and straightforward deployment. Notably, these detectors employ cellulose nitrate (LR-115) and allyl diglycol carbonate (CR-39) as their primary materials.

Specifically, LR-115 film features a red-dyed cellulose nitrate emulsion, with a thickness of 12 μm, coated onto an inert cellulose acetate substrate measuring 100 μm in thickness. The chemical etchant commonly used for LR-115 is sodium hydroxide (NaOH). The exposure to alpha radiation induces damage within the SSNTD film, resulting in the formation of tracks that become visible through subsequent chemical etching. The quantification of these registered tracks on the film serves as an indicator of radon and thoron exposure. Nevertheless, achieving accurate assessments of radon and thoron concentrations, as well as the corresponding inhalation doses, requires careful consideration when selecting the appropriate exposure mode. Furthermore, a meticulously defined protocol for etching and track counting is imperative to ensure dependable and trustworthy outcomes in these measurements.

4.6.1 Twin Cup Dosimeter

To ensure accurate measurements of radon gas utilizing Solid State Nuclear Track Detectors (SSNTDs), the selection of an appropriate exposure mode is paramount. Historically, the bare mode of SSNTD exposure was prevalent. However, the interpretation of results in the bare mode encountered complexities arising from responses to decay products and thoron. To surmount this limitation, the cup mode of exposure, often referred to as the diffusion chamber, has been devised. A notable contribution in this realm is the 'twin cup dosimeter,' pioneered by BARC, which has proven highly effective for extensive and long-term radon and thoron measurements within dwellings. This dosimeter employs two compartments, each characterized by a length of 4.5 cm and a radius of 3.1 cm (as illustrated in Fig. 7).

In these compartments, glass fiber particulate filters and latex membrane filters are strategically positioned. The disparate permeabilities of these filters facilitate the selective diffusion of radon and thoron gases into their respective compartments. Each

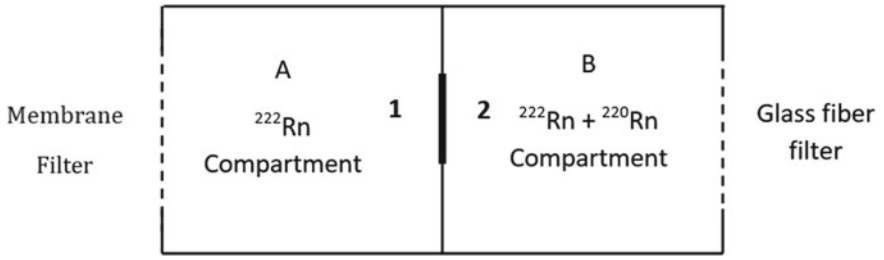

Fig. 7 Schematic diagram of twin cup dosimeter [16]

compartment accommodates a type II LR-115 film (12 μm thick, Kodak cellulose nitrate). The film within the membrane-filter compartment records tracks attributed solely to radon gas, while the one in the glass fiber filter compartment registers tracks resulting from both radon and thoron gases.

After an exposure period of approximately 90 days, the films are retrieved and treated with a 10% NaOH solution for about one hour at 60 °C while maintaining continuous stirring. The resulting etched films are then meticulously scanned using a spark counter to enumerate the tracks that have developed. Subsequently, these tracks are converted into radon and thoron concentrations by applying appropriate calibration factors.

However, this particular dosimeter is designed with two distinct entry points that are positioned opposite each other. Both entry points utilize glass fiber filters to prevent the entry of decay products. One of these entrances incorporates a cellophane membrane that selectively blocks the transmission of ^{220}Rn, allowing only ^{222}Rn to enter the designated 'radon' chamber. The second entrance is designed to admit both ^{222}Rn and ^{220}Rn into the 'radon + thoron' chamber. To determine the thoron concentration, a subtraction technique is employed to eliminate the radon contribution from the tracks recorded in the 'radon + thoron' chamber.

However, in some instances, it has been observed that the track densities of the Solid State Nuclear Track Detector (SSNTD) within the 'radon' chamber surpass those within the 'radon + thoron' chamber. This unexpected outcome leads to a seemingly implausible negative ^{220}Rn concentration. One possible explanation for this inconsistency is linked to variations in the entry rates of ^{222}Rn through the two entrances of the dosimeter, potentially stemming from differences in airflow direction. To address this uncertainty, an innovative approach has been developed: the "pin-holes based twin cup dosimeter." This novel design features a single-entry face that accommodates both ^{222}Rn and ^{220}Rn gases from the surrounding environment. Further exploration of this advancement is detailed in the subsequent discussion.

4.6.2 Innovative Pinhole-Based Dosimeter System

The breakthrough pinhole-type dosimeter system introduces a pioneering approach to radon and thoron measurements, as depicted in Fig. 8. This dosimeter system ingeniously integrates a single entrance mechanism to streamline the entry of gas into its two distinct chambers, namely the "radon + thoron" chamber and the "radon" chamber. The gas ingress occurs via a glass fiber filter paper (with a porosity of 0.56 μm), setting off a series of diffusion processes. Notably, the diffusion from the "radon + thoron" chamber to the "radon" chamber is mediated through precisely crafted pinholes, strategically excluding the entry of ^{220}Rn into the latter chamber. The design philosophy behind this dosimeter is illustrated in the following schematic.

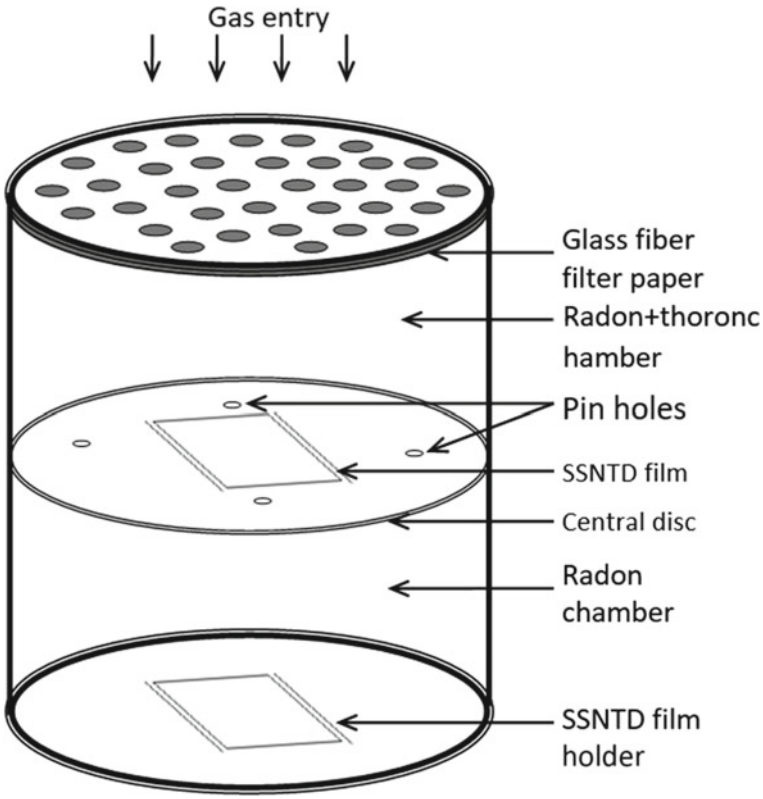

Fig. 8 Schematic diagram of the pin holes-based radon thoron dosimeter [19]

5 Monitoring Radon Progeny

Radon progeny, arising from ^{222}Rn and ^{220}Rn, are solid particles that, upon inhalation, deposit in the respiratory tract and subsequently irradiate nearby tissues due to their radioactive decay. Their contribution to the dose surpasses that of their parent radon isotopes, accounting for over 95% of the total inhalation dose. This emphasizes the significance of progeny measurements for accurate dose assessment.

Both active and passive techniques are employed for progeny monitoring. Among the active techniques are instantaneous filter-paper sampling and continuous monitors. Short-term samplings lack representativeness due to diurnal fluctuations, while employing continuous monitors for extended periods is impractical. Hence, a prevalent approach involves deriving progeny concentration (EECR—Equilibrium Equivalent Concentration of Radon) from measured ^{222}Rn concentration (C_0) using the Equilibrium factor (F) [20], given by:

$$F = \frac{\text{EECR}}{C_0} \tag{32}$$

It's important to note that progeny activity concentration never equals that of the parent gas due to factors like radioactive decay, ventilation, and deposition onto surfaces. EECR reflects the activity concentration of Radon in equilibrium with its short-lived progeny, mirroring the potential energy alpha concentration of the actual non-equilibrium mixture [21].

Conventionally, F for Radon is assumed to be 0.4 [1, 21], but research reveals its dependence on environmental parameters like aerosol concentration, attachment rate, ventilation rate, and humidity [12, 22–27]. Observations underscore that F varies with these parameters, leading to the introduction of the "reduced equilibrium factor" to enhance F's accuracy in dose estimation [25]. The present study endeavors to explore the frequency distributions and variability of F in an indoor environment by considering lognormal distributions for these parameters.

A comprehensive understanding of F's behavior is essential. Mishra et al. [28] established that F varies linearly with deposition flux, revealing a weak correlation with dose. This suggests that the deposition flux, not F, offers a superior measure of true dose [29]. Consequently, deposition-based progeny measurement using direct sensors emerges as a more accurate approach for inhalation dose assessment [30, 31].

Radon progeny, being solid particles, exhibit a deposition characteristic when exposed to surfaces [32]. This principle underpins their measurement. Air is drawn through a predetermined filter-paper rate, causing progeny particles to deposit on the paper. Subsequent decay is then detected using an appropriate detector.

These methods can be grouped based on collection techniques into three categories [33]:

(a) Active Grab/Instantaneous
(b) Active Continuous
(c) Passive Time-Integrated.

Furthermore, instrumentation is categorized based on sampling devices into two groups:

(a) Active (requiring power for sample collection)
(b) Passive (relying on natural diffusion, devoid of power supply).

5.1 Grab/Instantaneous for Radon Progeny

This is an active sampling technique in which air is sampled at a fixed flow rate for a specified time and the progeny atoms deposited on the filter paper are counted during and after sampling at different counting regimes [33].

As per the counting regimes, there can be a 1-count method, 2-count method, or 3-count method.

5.1.1 One-Count Method

$$\text{PAEC} = \frac{N/t_c}{\eta V t_s K} \tag{33}$$

where N/t_c is the count rate, η is the alpha counting efficiency of the counter, t_s is the duration of sampling, V is the air volume sampled per unit of time, and K is the factor (based on the sampling and counting durations).

Air is sampled for 5 min and then after a delay time of 40 min the gross alpha activity on the filter is counted, usually by a scintillation detector [33, 34].

5.1.2 Two-Counts Method

These methods give an estimate of PAEC in a shorter period and with lower uncertainty than the 1 count method. This Markov method is the oldest where the two counting regimes are taken as one between 1 and 3 min and the other between 7 and 10 min.

5.1.3 Three-Counts Method

This method allows the exact determination of radon daughter concentrations. C_i is the concentration of the three daughters ^{218}Po, ^{214}Pb, and ^{214}Bi are calculated from three N_j counts by the following formula [35]:

$$C_i = \frac{1}{\eta V} \sum_{j=1}^{3} K_{ij} N_j \tag{34}$$

^{214}Po is always in equilibrium with ^{214}Bi activity concentration owing to its short half-life. So, only 3 counts are sufficient for an exact determination of Radon progeny.

5.1.4 Counting Factor-Based Approach (*Z*-Factor)

This method is based on *Z*-factors which are based on sampling time, and initial and final counting times [32].

In the case of Thoron progeny, a delay time of ~ 5 h is given after sampling to allow the complete decay of the radon progeny. Then Thoron progeny atoms deposited per unit time (Φ_T) are obtained from the counts (X) by alpha-counting of the filter paper, using η (alpha-counter efficiency) and Z_T (counting factor) using the equation:

$$\Phi_T = \frac{X}{\eta Z_T} \tag{35}$$

Thoron progeny (^{212}Pb) activity concentration C_2 in the room is calculated using the flow rate (q) as:

$$C_2 = \frac{\Phi_T \lambda_2}{q} \tag{36}$$

In the case of Radon progeny, ^{218}Po, ^{214}Pb, and ^{214}Bi atoms deposited per unit time of exposure are denoted by Φ_1, Φ_2, and Φ_3 respectively, and can be obtained by multiple regression analysis of D (disintegrations per unit time) against the counting factors [32].

The total atom concentration of ^{218}Po, ^{214}Pb, and ^{214}Bi can be calculated as the ratio of the total atoms deposited per unit sampling time to the flow rate (q), using the following formulation:

$$N = \frac{\varphi_1 + \varphi_2 + \varphi_3}{q} \tag{37}$$

In an indoor environment, the sampling should be carried out preferably in the center of the room at least 30 cm away from any surface. The sampler should face the center of the room. The flow rate should not vary significantly during the sampling period. The initial and final flow rate, time of sampling, delay time, and counting time should be carefully monitored.

5.2 Continuous Monitoring

Continuous monitoring offers real-time activity concentration measurement of progeny through active sampling and simultaneous counting. This method employs

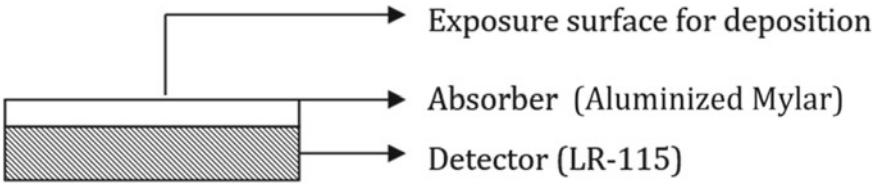

Fig. 9 Schematic diagram of the detector element [36]

filter-paper sampling at a fixed flow rate, with an anion-implanted solid-state detector placed facing the filter-paper [33]. As progeny atoms decay on the deposited filter paper, the emitted alpha particles are detected by the solid-state detector. The resulting quantity of electrons across the semiconductor diode junction is proportional to the alpha particle energy, which is further categorized by a multichannel analyzer based on emitted energy.

5.3 Integrated Monitoring

Integrated monitoring provides long-term measurements, integrating data to offer an average value over the monitoring period [35].

5.3.1 Direct Radon/Thoron Progeny Sensors (DRPS/DTPS)

DRPS and DTPS are time-integrated, passive measurement techniques for ^{222}Rn and ^{220}Rn progeny. These sensors comprise LR115 (cellulose nitrate-based) solid-state nuclear track detectors mounted with aluminized-mylar absorbers (Fig. 9). The absorber thickness is selected to reduce emitted progeny alpha particle energy to < 4 MeV. Progeny atoms deposited on the absorber film decay, and the alpha particle energies are selectively detected by LR115 film. Sensitivity factors, derived from track-registration efficiency and deposition velocities, convert track density into progeny activity concentration. These passive detectors offer direct progeny concentration measurement and are suitable for long-term surveys, ensuring accurate and interference-free results.

5.3.2 Direct Radon/Thoron Progeny Sensors Based Integrated Sampler

The integrated sampler features a sampling head and pump. A wire-mesh and filter paper arrangement, coupled with DRPS/DTPS sensors, captures unattached and attached fractions of progeny atoms. Unattached fractions are captured by the wire mesh, while attached fractions deposit on the filter paper. Subsequent decay of deposited progeny atoms emits alpha particles detected by DRPS/DTPS sensors.

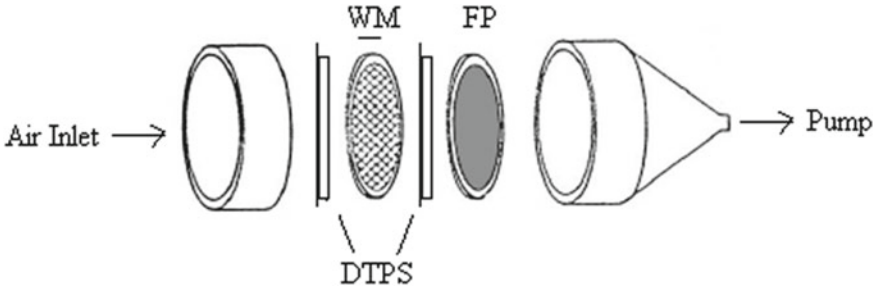

Fig. 10 Schematic diagram of the integrated sampler with WM (wire-mesh) and FP (filter-paper) arranged in an array each facing the detector surface [38]

Track density converts to unattached and attached activity concentrations using sensitivity factors, providing accurate measurements for both radon and thoron progeny [37].

5.3.3 Direct Radon/Thoron Progeny Sensors Capped with Wire-Mesh

In extreme conditions with high ventilation rates, sensitivity factors of DRPS/DTPS may vary due to unattached fractions. To address this, wire-mesh capped DTPS/DRPS detectors are employed. These detectors consist of DRPS/DTPS sensors capped with a wire mesh (Figs. 10 and 11), rendering them solely attached fraction detectors. Sensitivity factors of wire-mesh capped DTPS and DRPS are determined, offering robust measurements under challenging environmental conditions.

These integrated monitoring methods provide valuable insights into the behavior of radon and thoron progeny, allowing for accurate and interference-free assessments of potential health risks associated with their inhalation.

6 Calibration Procedures

The calibration factor serves as the pivotal value for converting the observed track densities into the activity concentration of the specific species under examination. If T represents the track densities observed on a Solid-State Nuclear Track Detector (SSNTD) resulting from exposure to a concentration C of a particular species for a duration of time t, the relationship is defined as follows:

$$T = k \cdot C \cdot t \tag{38}$$

where,

k = Calibration factor (tracks cm^{-2} per Bq d m^{-3})

t = time in the day

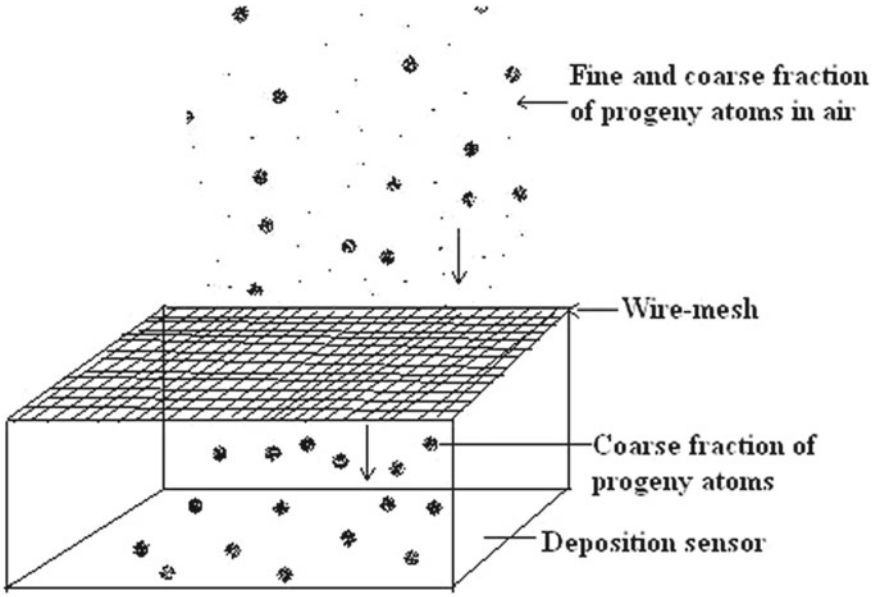

Fig. 11 Schematic diagram of the operation of the capped DRPS/DTPS [39]

C = concentration in Bq m^{-3}
T = tracks cm^{-2}.

The calibration factor, denoted as k, is contingent upon several parameters. These include the dimensions of pinholes and characteristics of the progeny filter, along with the energy of the alpha particles during cup mode exposure. Additionally, factors related to the etching process, characteristics of spark counting, and other relevant aspects play a role in determining the calibration factor.

6.1 Calibration of Pinhole-Based Twin Cup Dosimeter

The recently developed dosimeter, featuring side-entry pinholes, necessitates exposure within a calibration chamber with a volume exceeding 0.5 m^3 to ascertain the calibration factor. To introduce ^{222}Rn gas into the chamber, utilize the designated inlets in conjunction with a standardized ^{222}Rn source. Initiate the experiment by activating fans for approximately 5 min to achieve uniform spatial distribution of the ^{222}Rn concentration. Employ a continuous ^{222}Rn monitoring device, such as the RnDuo, for precise measurements. Suspend the dosimeters within the chamber by affixing them to the arms of the central rod approximately 3 h after the initial gas infusion. Refer to Fig. 12 for a depiction of the typical experimental arrangement employed in determining the ^{222}Rn calibration factor. For this calibration process,

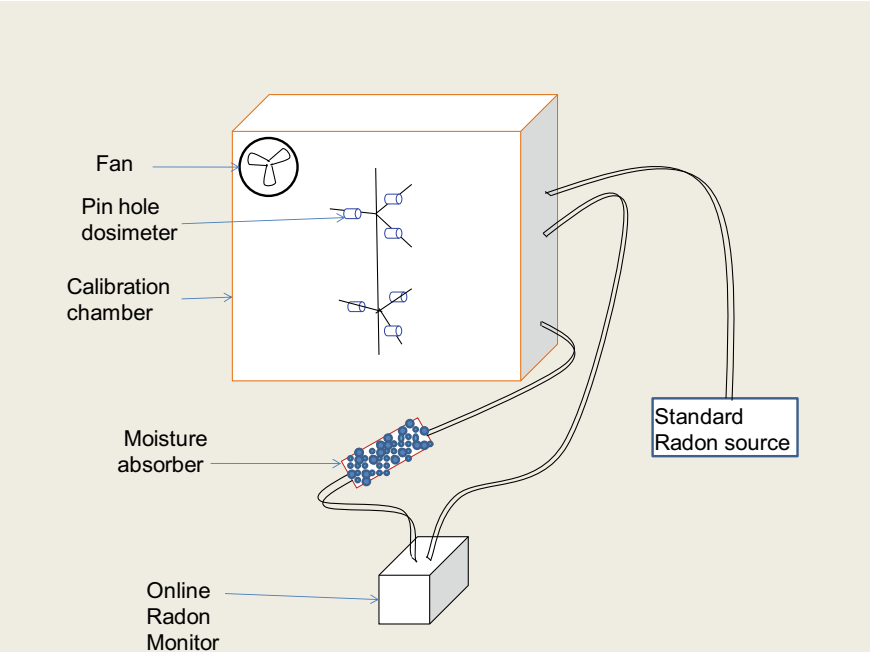

Fig. 12 A typical experimental setup for calibration of pin-hole based twin cup dosimeter [16]

expose around 10 dosimeters to a chamber environment with a ^{222}Rn concentration of roughly 1000 Bq m^{-3} for a period exceeding 7 days. Upon completion of exposure, extract all dosimeters from the chamber and allow them to sit in an open environment for approximately one day, ensuring the LR-115 film remains intact on the dosimeters.

Subsequently, remove the films and subject them to etching using the established standard procedure, involving a 2.5 N NaOH solution for 90 min at a temperature of 60 °C, without agitation. Consistently assess the etching parameters to confirm the removal of 4 mm thickness from the film during the etching process. Following etching, meticulously rinse the films with distilled water before setting them aside to dry. Once dry, detach the base from the films and tally the recorded tracks using a spark counter.

The track densities measured as tracks cm^{-2}, duly adjusted using a spark counter's relative factor, serve as the basis for establishing the calibration factor. This process is achieved by applying the subsequent two equations:

$$k_{\mathrm{R},1} = \frac{T_{\mathrm{R},1}}{tC_{\mathrm{R}}} \tag{39}$$

$$k_{\mathrm{R},2} = \frac{T_{\mathrm{R},2}}{tC_{\mathrm{R}}} \tag{40}$$

where, $k_{R,1}$ and $k_{R,2}$ are the calibration factors, $T_{R,1}$ and $T_{R,2}$ are the track densities in the first and second compartment of the pin holes dosimeter, respectively. C_R is the average ^{222}Rn concentration and t is the exposure period.

While the exposure chamber typically utilized for ^{222}Rn exposure is unsuitable for ^{220}Rn exposure due to significant differences in decay rates, the calibration chamber boasts a larger volume (around 0.5 m^3). Given the short-lived nature of ^{220}Rn, it rapidly decays, posing challenges in maintaining a consistent concentration within the chamber. The potential for ^{220}Rn to exhibit a non-uniform distribution within the chamber should also be considered. To mitigate this concern, chamber design should prioritize uniform thoron (^{220}Rn) concentration throughout the volume. Care must be taken to minimize turbulence to ensure gas diffusion is the primary mechanism for dosimeter entry.

The subsequent steps for exposure, etching, and counting remain analogous to the procedure outlined for radon exposure. The derived track densities can be harnessed to ascertain the ^{220}Rn calibration factor through the following equations:

$$k_{T,1} = \frac{T_{T,1}}{tC_R} \tag{41}$$

$$k_{T,2} = \frac{T_{T,2}}{tC_R} \tag{42}$$

where $k_{T,1}$ and $k_{T,2}$ is the calibration factor, $T_{T,1}$ and $T_{T,2}$ is the track densities in the first and second compartments respectively. C_T is the average ^{220}Rn concentration and t is the exposure period.

6.2 Calibration of DRPS/DTPS

The DTPS (Direct Thoron Progeny Sensor) and DRPS (Direct Radon Progeny Sensor) function as passive detectors designed to directly measure the integrated concentration of progeny (EEC) over time. The Sensitivity factor (S) establishes a relationship between the alpha-track density registered per unit exposure time due to progeny (T) and the progeny activity concentration (EEC), as defined by the following equation [29, 36, 37]:

$$\mathrm{EEC}\left(\mathrm{Bq\,m^{-3}}\right) = \frac{T\left(\mathrm{Tracks\,cm^{-2}\,d^{-1}}\right)}{S\left(\mathrm{Tracks\,cm^{-2}\,d^{-1}}\right)/\mathrm{EEC}\left(\mathrm{Bq\,m^{-3}}\right)} \tag{43}$$

The sensitivity factors for DTPS and DRPS are composed of two essential elements: the geometric parameter referred to as "Track Registration Efficiency," intrinsic to the detector itself, and the "Deposition Velocity" of progeny atoms, which is influenced by environmental factors.

To determine track registration efficiencies, a known amount of radon and thoron decay product activities should be electrodeposited onto DRPS and DTPS respectively. This is followed by chemical etching and subsequent alpha track counting. The ratio of alpha track density to the deposited atom density provides the track registration efficiency. The deposition velocity can be estimated by calculating the ratio of deposited atom flux to atom concentration present in the environment. The deposited atom flux can be assessed by exposing DTPS and DRPS in controlled indoor settings. Meanwhile, atom concentrations can be directly measured through filter-paper sampling and subsequent alpha counting within the mentioned environments during the exposure period of DRPS and DTPS.

Determining sensitivity factors for DRPS and DTPS requires both controlled laboratory conditions and real indoor environments. In a calibration chamber with a known progeny activity concentration, DTPS and DRPS should undergo exposure for a defined duration. After exposure, subject the detectors to chemical etching and track counting to determine the track density per unit exposure time. The sensitivity factor can then be calculated by dividing the track density per unit exposure time by the initial progeny concentration in the chamber.

For real indoor environmental conditions, approximately 50 DTPSs/DRPSs can be placed in a naturally ventilated room environment for around 3 months. Throughout this period, consistent filter paper sampling and alpha counting efforts should be carried out to assess the atom concentration in the room. Commercially available working-level monitors can also be used to measure progeny concentration. Following the 3-month exposure, process the detectors chemically and perform alpha track counting using established protocols. The resulting ratio of track density per unit exposure time to progeny concentration provides the sensitivity factor specific to that environment.

7 Assessment of Inhalation Dose

The estimation of Annual Inhalation Doses (mSv y^{-1}) for radon (AIDR) and thoron (AIDT), considering both gas and progeny concentrations, can be determined using the measured gas and progeny concentrations through the following equations [40, 41]:

For radon:

$$\mathrm{AID_R} = [(C_\mathrm{R} \times 0.17) + (\mathrm{EEC_R} \times 9)] \times 8760 \times 0.8 \times 10^{-6} \tag{44}$$

For thoron:

$$\mathrm{AID_T} = [(C_\mathrm{T} \times 0.11) + (\mathrm{EEC_T} \times 40)] \times 8760 \times 0.8 \times 10^{-6} \tag{45}$$

Here, the dose conversion factor (DCF) values are 0.17 and 9 nSv Bq^{-1} h^{-1} m^3 for radon gas and radon progeny, respectively. Similarly, the dose conversion factor

(DCF) values are 0.11 and 40 nSv Bq^{-1} h^{-1} m^3 for thoron gas and thoron progeny, respectively [1]. The occupancy factor (OF) is assumed to be 0.8 for a typical dwelling.

8 Radon Monitoring: World Scenario

National radon mapping initiatives across various continents have been instrumental in understanding the spatial distribution of radon gas and its potential health implications. These mapping efforts provide crucial insights into radon exposure levels, enabling governments, researchers, and policymakers to formulate effective strategies for radon mitigation and public health protection. Here is an overview of national radon mapping initiatives across different continents:

North America

Countries in North America, including the United States and Canada, have implemented comprehensive radon mapping programs. These initiatives involve extensive radon measurements in residential and occupational settings, contributing to the creation of detailed radon potential maps. These maps offer insights into regions with high radon concentrations, guiding the development of targeted radon mitigation strategies. In the United States, for instance, the Environmental Protection Agency (EPA) offers a Radon Potential Map that classifies areas into zones based on radon potential.

Europe

Many European countries have embarked on extensive radon mapping projects, often collaborating at regional and international levels. The European Atlas of Natural Radiation provides detailed information on radon distribution across Europe. National agencies and research institutions in countries such as the United Kingdom, Germany, and France have conducted large-scale radon measurement campaigns, leading to the creation of radon hazard maps. These maps enable governments to prioritize areas for radon prevention measures.

Asia

Several Asian countries have initiated radon mapping programs to assess the potential health risks associated with elevated radon levels. Japan, for example, has conducted radon surveys to understand indoor and outdoor radon concentrations. India has also been active in radon research and mapping due to the presence of uranium and monazite deposit and elevated radon risk in some regions. These mapping efforts aim to provide valuable data for public awareness and health protection.

Australia

In Australia, where radon levels can vary significantly due to geological factors, comprehensive radon mapping projects have been carried out. These initiatives help

identify areas of higher radon potential, which is crucial for designing building codes and regulations. The Australian Radiation Protection and Nuclear Safety Agency (ARPANSA) provides radon maps and information to the public and policymakers.

South America

Countries in South America, such as Brazil and Argentina, have recognized the importance of radon mapping to safeguard public health. These countries have conducted radon surveys in residential and occupational environments to assess the risk of exposure. Collaborative efforts between governments, research institutions, and international organizations contribute to a better understanding of radon distribution and exposure patterns.

Africa

While radon mapping initiatives in Africa are relatively limited compared to other continents, there is a growing awareness of the need to assess radon exposure risks. Some African countries have conducted radon measurements and surveys, particularly in areas with known uranium deposits. These efforts contribute to building a comprehensive understanding of radon distribution across the continent.

National radon mapping initiatives across different continents have significantly advanced our understanding of radon distribution, exposure risks, and potential health impacts. These mapping efforts provide essential data for the formulation of effective radon mitigation strategies, building codes, and public awareness campaigns. Continued collaboration between governments, researchers, and international organizations will play a pivotal role in enhancing radon mapping accuracy and protecting public health globally.

9 Conclusion

Accurately assessing the inhalation dose stemming from Radon, Thoron, and their progeny holds utmost significance due to their profound radiological implications. Within occupational environments like Uranium mines and Thorium plants, the precise measurement of individual inhalation doses and comprehensive area monitoring are imperative. This chapter serves as a comprehensive exploration of the latest developments in Radon research, with a particular focus on monitoring techniques, the transport and distribution of Radon, Thoron, and their progeny.

The chapter systematically examines Radon transport mechanisms and the associated analytical models, delivering a comprehensive grasp of this intricate subject. It endeavours to stand as an essential technical resource catering to researchers and industry professionals, compiling the cutting-edge progressions and insights within the realm of Radon research. Introducing the concept of Pin-hole dosimeters, a notable advancement over the conventional Twin-cup dosimeter system is outlined. By managing turbulence effects through a singular entry for both Radon and Thoron gases, the dosimeter's performance is notably enhanced. Furthermore, the adoption

of a single glass fiber filter paper in lieu of polypropylene film significantly bolsters the detector's response time. In terms of continuous monitoring of Radon and Thoron gases in mining areas, a scintillation-based Radon and Thoron gas monitor has been developed and is elaborated upon within the chapter. This monitor proves to be particularly advantageous for comprehensive area monitoring purposes.

The chapter extensively delves into the innovative technique of Direct Radon and Thoron progeny sensors, elucidating their operation within both passive and active sampling modes. These sensors offer a direct assessment of progeny activity concentration, enabling accurate inhalation dose calculations. Given the significant contribution of progeny to inhalation doses, the adoption of direct progeny sensors obviates the need to assume an equilibrium factor, thereby enhancing the precision of dose estimation.

This chapter serves as a thorough compendium, encapsulating the forefront advancements in the realm of Radon research. Its comprehensive coverage addresses various dimensions of the field, providing a valuable resource for researchers, professionals, and anyone seeking a nuanced understanding of this critical subject.

References

1. UNSCEAR (2000) Sources and effects of ionizing radiation: UNSCEAR 2000 report to the general assembly with scientific annexes. United Nations Publication, New York
2. World Health Organization (2009) WHO handbook on indoor radon—a public health perspective. World Health Organization, Geneva
3. UNSCEAR (2010) Annex B: exposures of the public and workers from various sources of radiation. In: Sources and effects of ionizing radiation. UNSCEAR 2008 report to the general assembly with scientific annexes. United Nations Publication, New York, pp 223–463
4. National Research Council (1999) Health effects of exposure to radon: BEIR VI. Washington, DC
5. Darby S, Hill D, Auvinen A, Barros-Dios JM, Baysson H, Bochicchio F, Deo H, Falk R, Forastiere F, Hakama M, Heid I, Kreienbrock L, Kreuzer M, Lagarde F, Mäkeläinen I, Muirhead C, Oberaigner W, Pershagen G, Ruano-Ravina A, Ruosteenoja E, Rosario AS, Tirmarche M, Tomásek L, Whitley E, Wichmann H-E, Doll R (2005) Radon in homes and risk of lung cancer: collaborative analysis of individual data from 13 European case-control studies. BMJ 330:223. https://doi.org/10.1136/bmj.38308.477650.63
6. Krewski D, Lubin JH, Zielinski JM, Alavanja M, Catalan VS, William Field R, Klotz JB, Létourneau EG, Lynch CF, Lyon JL et al (2006) A combined analysis of North American case-control studies of residential radon and lung cancer. J Toxicol Environ Health Part A 69:533–597
7. Lecomte JF, Solomon S, Takala J, Jung T, Strand P, Murith C, Kiselev S, Zhuo W, Shannoun F, Janssens A (2014) ICRP publication 126: radiological protection against radon exposure. Ann ICRP 43:5–73. https://doi.org/10.1177/0146645314542212
8. Nazaroff WW (1992) Radon transport from soil to air. Rev Geophys 30:137–160
9. Sahoo BK, Sapra BK, Gaware JJ, Kanse SD, Mayya YS (2011) A model to predict radon exhalation from walls to indoor air based on the exhalation from building material samples. Sci Total Environ 409:2635–2641. https://doi.org/10.1016/j.scitotenv.2011.03.031
10. Sahoo BK, Kumara KS, Karunakara N, Gaware JJ, Sapra BK, Mayya YS (2017) Thoron mitigation system based on charcoal bed for applications in thorium fuel cycle facilities (part 1):

development of theoretical models for design considerations. J Environ Radioact 172:237–248. https://doi.org/10.1016/j.jenvrad.2017.03.015
11. Kanse SD, Sahoo BK, Gaware JJ, Prajith R, Sapra BK (2016) A study of thoron exhalation from monazite-rich beach sands of high background radiation areas of Kerala and Odisha, India. Environ Earth Sci 75:1–10. https://doi.org/10.1007/s12665-016-6279-9
12. Ramola RC, Rautela BS, Gusain GS, Prasad G, Sahoo SK, Tokonami S (2013) Measurements of radon and thoron concentrations in high radiation background area using pin-hole dosimeter. Radiat Meas 53–54:71–73. https://doi.org/10.1016/j.radmeas.2013.04.008
13. Wang J, Meisenberg O, Chen Y, Karg E, Tschiersch J (2011) Mitigation of radon and thoron decay products by filtration. Sci Total Environ 409:3613–3619. https://doi.org/10.1016/j.scitotenv.2011.06.030
14. Semwal P, Agarwal TK, Singh K, Joshi M, Gusain GS, Sahoo BK, Ramola RC (2018) Indoor inhalation dose assessment for thoron-rich regions of Indian Himalayan belt. Environ Sci Pollut Res. https://doi.org/10.1007/s11356-018-3891-0
15. Tokonami S (2010) Why is ^{220}Rn (thoron) measurement important? Radiat Prot Dosim 141:335–339
16. Radiological Physics and Advisory Division (2016) Handbook on radon transport models and measurement methods. Radiological Physics and Advisory Division, Bhabha Atomic Research Centre, Mumbai
17. Ishimori Y, Lange K, Martin P, Mayya YS, Phaneuf M (2013) Measurement and calculation of radon releases from NORM residues. IAEA Publications, Vienna
18. Sahoo BK, Mayya YS (2010) Two dimensional diffusion theory of trace gas emission into soil chambers for flux measurements. Agric For Meteorol 150:1211–1224. https://doi.org/10.1016/j.agrformet.2010.05.009
19. Sahoo BK, Sapra BK, Kanse SD, Gaware JJ, Mayya YS (2013) A new pin-hole discriminated ^{222}Rn/^{220}Rn passive measurement device with single entry face. Radiat Meas 58. https://doi.org/10.1016/j.radmeas.2013.08.003
20. Porstendörfer J, Reineking A (1999) Radon: characteristics in air and dose conversion factors. Health Phys 76:300–305. https://doi.org/10.1097/00004032-199903000-00011
21. Porstendörfer J (1994) Properties and behaviour of radon and thoron and their decay products in the air. J Aerosol Sci 25:219–263
22. Rout RP, Mishra R, Prajith R, Jalaluddin S, Sapra BK (2014) Measurement of ^{222}Rn and ^{220}Rn decay product deposition velocities using SSNTD based passive detectors. J Radioanal Nucl Chem 302:1495–1499. https://doi.org/10.1007/s10967-014-3610-3
23. Porstendörfer J (1984) Behaviour of radon daughter products in indoor air. Radiat Prot Dosim 7:107–113
24. Chu T-C, Liu H-L (1996) Simulated equilibrium factor studies in radon chamber. Appl Radiat Isot 47:543–550
25. Amgarou K, Font L, Baixeras C (2003) A novel approach for long-term determination of indoor ^{222}Rn progeny equilibrium factor using nuclear track detectors. Nucl Instrum Methods Phys Res Sect A Accel Spectrometers Detect Assoc Equip 506:186–198
26. Shaikh AN, Muraleedharan TS, Ramachandran TV, Ramu MCS (1992) Estimation of ventilation rates in dwellings. Sci Total Environ 121:67–76
27. Mishra R, Sapra BK, Mayya YS (2014) Multi-parametric approach towards the assessment of radon and thoron progeny exposures. Rev Sci Instrum 85:22105
28. Mishra R, Prajith R, Rout RP, Sriamirullah J, Sapra BK (2020) Effect of air velocity on inhalation doses due to radon and thoron progeny in a test chamber. Radiat Prot Dosim 189:401–405. https://doi.org/10.1093/rpd/ncaa054
29. Mayya YS, Mishra R, Prajith R, Gole AC, Sapra BK, Chougaonkar MP, Nair RRK, Ramola RC, Karunakara N, Koya PKM, Physics R, Division A, Atomic B, Centre RC, Garhwal T, Biology R, Division HS, Atomic B (2012) Deposition-based passive monitors for assigning radon, thoron inhalation doses for epidemiological studies. Radiat Prot Dosim 152:18–24. https://doi.org/10.1093/rpd/ncs196

30. Mishra R, Prajith R, Sapra BK, Mayya YS (2010) An integrated approach for the assessment of the thoron progeny exposures using direct thoron progeny sensors. Radiat Prot Dosim 141:363–366. https://doi.org/10.1093/rpd/ncq236
31. Meisenberg O, Mishra R, Joshi M, Gierl S, Rout R, Guo L, Agarwal T, Kanse S, Irlinger J, Sapra BK, Tschiersch J (2017) Radon and thoron inhalation doses in dwellings with earthen architecture: comparison of measurement methods. Sci Total Environ 579. https://doi.org/10.1016/j.scitotenv.2016.11.170
32. Mishra R, Mayya YS, Kushwaha HS (2009) Measurement of ^{220}Rn/^{222}Rn progeny deposition velocities on surfaces and their comparison with theoretical models. J Aerosol Sci 40. https://doi.org/10.1016/j.jaerosci.2008.08.001
33. George AC (1990) An overview of instrumentation for measuring environmental radon and radon progeny. IEEE Trans Nucl Sci 37:892–901
34. Porstendörfer J (1997) Radon: measurements related to dose. Environ Int 22. https://doi.org/10.1016/S0160-4120(96)00158-4
35. Tommasino L (1998) Passive sampling and monitoring of radon and other gases. Radiat Prot Dosim 78:55–58. https://doi.org/10.1093/oxfordjournals.rpd.a032333
36. Mishra R, Mayya YS (2008) Study of a deposition-based direct thoron progeny sensor (DTPS) technique for estimating equilibrium equivalent thoron concentration (EETC) in indoor environment. Radiat Meas 43:1408–1416. https://doi.org/10.1016/j.radmeas.2008.03.002
37. Mishra R, Sapra BK, Prajith R, Rout RP, Jalaluddin S, Mayya YS (2015) Inhalation exposures due to radon and thoron (^{222}Rn and ^{220}Rn): do they differ in high and normal background radiation areas in India? J Environ Radioact 147:125–129. https://doi.org/10.1016/j.jenvrad.2015.05.028
38. Mishra R, Sapra BK, Mayya YS (2009) Development of an integrated sampler based on direct ^{222}Rn/^{220}Rn progeny sensors in flow-mode for estimating unattached/attached progeny concentration. Nucl Instrum Methods Phys Res Sect B Beam Interact Mater Atoms 267:3574–3579. https://doi.org/10.1016/j.nimb.2009.08.021
39. Mayya YS, Mishra R, Prajith R, Sapra BK, Kushwaha HS (2010) Wire-mesh capped deposition sensors: novel passive tool for coarse fraction flux estimation of radon thoron progeny in indoor environments. Sci Total Environ 409:378–383. https://doi.org/10.1016/j.scitotenv.2010.10.007
40. Mayya YSS, Eappen KPP, Nambi KSVSVV (1998) Methodology for mixed field inhalation dosimetry in monazite areas using a twin-cup dosemeter with three track detectors. Radiat Prot Dosim 77:177–184. https://doi.org/10.1093/oxfordjournals.rpd.a032308
41. Chougaonkar MP, Eappen KP, Ramachandran TV, Shetty PG, Mayya YS, Sadasivan S, Venkat Raj V (2004) Profiles of doses to the population living in the high background radiation areas in Kerala, India. J Environ Radioact 71:275–297. https://doi.org/10.1016/S0265-931X(03)00174-7

Liquid Scintillation Based In-Vitro Analysis of Various Radionuclides in Bioassay Samples

Sonali P. D. Bhade and Priyanka J. Reddy

1 Introduction

Liquid Scintillation Counting (LSC) is a standard laboratory method generally employed for activity estimation of alpha (α) and beta (β) radionuclides. Sample preparation for LSC, involves mixing of a sample aliquot to a scintillation cocktail to obtain a homogeneous test sample. Because every radioactive atom in the prepared sample is essentially encircled by detector (scintillation cocktail) molecules, 4π geometry is achieved which facilitates β counting with reasonable counting efficiency. Radionuclides having maximum β energies $\geq$ 150 keV or more are detected with more than 95% efficiency. High counting efficiency and the absence of self-absorption are the leads that make LSC an extensively used analytical technique for detecting not only β but α emitters also. Over the previous decades, significant developments have been made in nuclide separation and liquid scintillation sample preparation techniques, in the optics and electronics of detectors, and in methods of minimizing background, made α LSC a practical tool and becoming a method of choice nowadays.

LSC technique has been established in 1950s and since then, for more than 70 years, it is employed as an efficient detection technique for β emitters. LS instrumentation was launched commercially in 1953 with introduction of Packard Tri-Carb series LSCs. By 1980s, almost all the modern LSCs used the coincidence detection along with pulse summation techniques, which facilitate its use for measurement of low energy β emitters. Also, during this period, one of the most prominent features, analysis of pulse height energy spectrum was introduced in the LSCs. With the introduction of this technology, windowless counting was enabled with pulse height distribution that ranged from 0 to 2000 keV [1]. In a new generation LSCs, various

S. P. D. Bhade (✉) · P. J. Reddy
Radiation Safety Systems Division, Bhabha Atomic Research Centre, Trombay, Mumbai 400085, India
e-mail: sonali@barc.gov.in

D. K. Aswal (ed.), *Handbook on Radiation Environment, Volume 2*,
https://doi.org/10.1007/978-981-97-2799-5_22

background reduction features were incorporated which enable them to measure much lower activities that were earlier feasible. Besides, the assimilation of Multichannel Analysers (MCAs) and Pulse Shape Analysis (PSA) technique into modern LSCs has enhanced their data handling capability. These key features make LSC, a prominent analytical tool for analyses of α and β nuclides in various fields.

The competence of LSC to measure α activity concentration has been documented in the past few years. Much of the prime innovative work on PSA based α/β discrimination was carried out by several researchers [2–4]. Enduring progress in LSC instrumentation from gross counting to α spectrometry permits the deconvolution and detection of different α spectral peaks [5]. Ultra-low background and simultaneous quantification of α/β events are the major features of PSA technique and facilitate determination of actinides even at low concentrations. In Modern LSCs, α events can be discriminated efficiently as interference from β/γ pulses is entirely (> 99.95%) rejected [6]. Application of PSA technique in numerous fields such as biomedical [7], environmental [8–12], geological [13], food sample testing [14, 15] and to assess nuclear waste [16, 17] is reported earlier. Its extensive use for measurement of α activity in effluent waters, urine samples and other matrices, made LSC an adaptable and popular technique. LSC has emerged as a prevalent technique for assessment of various radionuclides due to several significant advantages such as high counting efficiencies, simple and rapid sample preparation procedures, automatic sample loading and spectral data processing capabilities [18]. Generally, LSC is used for β quantitative assay, but doesn't have the capability of energy identification. Nevertheless, improvements in instrumentation, scintillators, and sample preparation techniques have proved that liquid scintillation is a prominent option for α assay also. Nuclide identification with LSC can be brought into reality using deconvolution technique [19, 20].

1.1 Principle of Liquid Scintillation Counting

The traditional method used for estimation of tritium in the biological matrix is LSC. A liquid scintillator is made up of solvent and phosphor which is added into the liquid sample hence allowing close contact between the isotope atoms and the scintillator [21]. Energy from the radionuclide is absorbed by the solvent which is transmitted to the solute. The solute converts the energy to photons. The released photons are detected by the Photo Multiplier Tube (PMT) as shown in Fig. 1.

2 Estimation of Tritium (^{3}H) in Urine

Tritium is a pure β emitter [E_{max}:18.6 keV, E_{av}: 5.6 keV] with a half-life of 12.3 years [22]. Anthropogenic ^{3}H is produced in Nuclear Power Plants (NPP's) due to activation of deuterons or as a fission product. Heavy water exposure to thermal neutrons

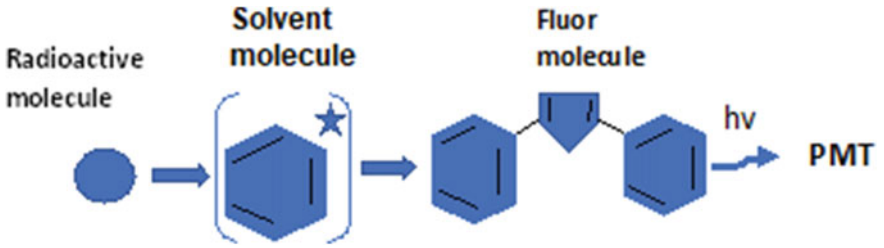

Fig. 1 Principle of liquid scintillation counting

determines the rate of production of ^{3}H. It is present in the plant environment through leakage, maintenance, etc. resulting in an important occupational exposure to radiation workers. ^{3}H contributes to about 20–30% of the annual radiation dose to the radiation workers [23]. It is also encountered in the nuclear decommissioning [24]. The maximum range of ^{3}H is approximately 6 mm in human tissues. Hence, inhalation and ingestion are the source of exposure to ^{3}H and primarily exist in the form of tritiated water (HTO) in the moderator and coolant of heavy water reactor NPPs. ^{3}H exposure pathways are as follows:

(i) Inhalation through the nose and mouth
(ii) Skin absorption
(iii) Ingestion through food and drink.

2.1 Tritium Concentration in the Body

97% of HTO rapidly passes in the bloodstream and mixes with body water. Hence, biokinetics of body water is followed by ^{3}H retention in the body. Few hours of post-exposure ^{3}H activity in urine is expected to be the similar as in other body fluids. Biological half-life of ^{3}H is approximately 10 days [25, 26]. Organically Bound Tritium (OBT) is present in the body as a result of exchange of ^{3}H atoms with hydrogen atoms in organic compounds such as proteins and carbohydrates. The short-term component has biological half-life of about 40 days and the long-term component follows one year half-life. Figure 2 depicts the exposure pathways and metabolism of HTO incorporated into according to UNSCEAR and ICRP [25, 27].

Urine sample analysis is usually performed to determine internal exposure of radiation workers due to ^{3}H. Urine is one of the most universally used matrices for internal contamination assessment due to its non-invasive sample collection, easy availability and adequate sensitivity to meet the requirements [28].

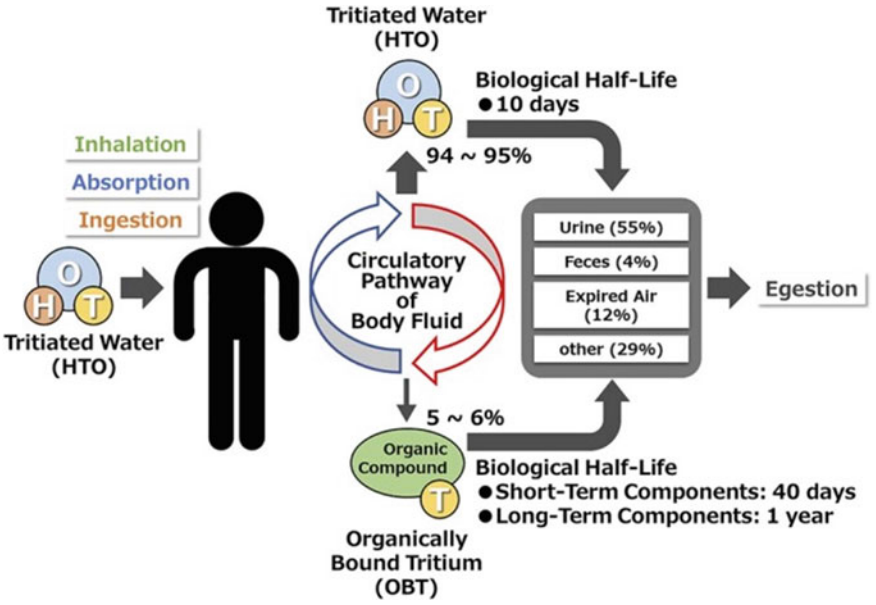

Fig. 2 HTO metabolism in the human body [29]

2.2 *Urine Sampling Frequency for HTO*

HTO rapidly distributes all over the blood stream and within 60–120 min, all over water in the body. After equilibrium, the ^{3}H activity in blood, sputum and urine are found to be the same. In case of bioassay, urine is the common matrix for estimating ^{3}H activity in body water. Exposed workers are required to submit urine samples for the bioassay periodically. Depending on the potential for substantial exposure, sampling duration may vary viz., daily, biweekly, or longer. The worker must empty the bladder 60–120 min later after probable exposure. A representative of the body water concentration is obtained for the sample collected after the bladder is emptied. However, the sample collected earlier to this might be an useful indication of the potential exposure.

2.3 *Methodologies for Sample Preparation*

Sample preparation for urine is affected by various metabolites present in it. Chemiluminescence and quenching are the main interferences in the measurement of ^{3}H in urine and it is necessary to remove these interferences prior analysis. Distillation is the conventional method for purification of the samples. A distinct distillation apparatus is suggested by Coops et al. and Nogawa et al. for urine sample purification [30,

31]. In order to achieve low detection limit, azeotropic distillation has been proposed [32]. For separating aqueous and non-volatile organic fractions, vacuum distillation has been used [33]. Distillation and ion chromatography combined methods were reported by Ishii et al. [34]. Urine samples can be decolorized using activated carbon prior LSC as suggested by Momoshima et al. [35–38]. Mingote et al. proposed low-cost and quick substitute in place of distillation of urine using active carbon [38]. According to the authors, active carbon adsorbs quenching and also controls luminescence. The authors proposed addition of 2 g of the powdered active carbon to 20 mL of urine. Recently, Watanabe and Kuwabara proposed ultraviolet photolysis to suppress colour quenching [39]. Butler reported addition of 1 mL urine sample to 15 mL scintillation cocktail [40]. According to Shen et al. 10 g of potassium persulfate is to be added to the distillation apparatus containing 50 mL urine sample followed by 30 min oxidation. 20 mL of the distillate is collected prior analysis [41]. Four mL of the distilled sample was added to 14 mL of scintillation cocktail for analysis [42].

Pedehontaa-Hiaa et al. studied conditions to obtain a quench free sample [43]. Also, a two-stage procedure involving filtration on activated charcoal to remove organic molecules [38, 44] and distillation to avoid the inorganic content [44, 45] was developed by Pedehontaa-Hiaa et al. 2.5 g activated charcoal at a concentration of 50 g L^{-1} was added to 50 mL urine. In order to remove the colour of sample followed by rapid filtration, the amount of charcoal was optimized. The mixture was shaken vigorously for 2–6 min until the white foam ceased. Charcoal and absorbed organic matter were removed by filtration. Following filtration, 45 mL aliquot was collected for distillation. 10 mL of the distilled sample was added to 10 mL of scintillation cocktail and 10 mL was used for ^{3}H measurement.

2.4 Quench Correction Methods

Urine sample when mixed with scintillation cocktail gives rise to a different chemical and colour quench because of its variation in chemical composition and particulate matter. Hence, variation in detection efficiencies is observed in urine samples under measurement. Such variability in sample composition is accounted for while calibrating LSC.

2.4.1 Internal Standard Method

An internal ^{3}H standard technique was proposed by Okita et al. for the determination of counting efficiency of each sample [46]. In the said method, net count rate of the sample (N_{sample}) is determined. A known standard of the same radionuclide under measurement is added to the sample. The sample is recounted under same conditions ($N_{std+sample}$). Increase in count rate due to the internal standard (N_{std}) is obtained by subtraction. Counting efficiency for the internal standard is found using the following

equation.

$$\text{Efficiency} = \frac{N_{\text{std+sample}} - N_{\text{sample}}}{\text{dpm}_{\text{std}}} \tag{1}$$

Addition of an internal standard does not change the quench level and therefore, the counting efficiency determined using this technique is applicable for the original sample.

2.4.2 Spectral Index of the Sample (SIS)

SIS uses the sample isotope spectrum to monitor the quench of the sample. Calculation of SIS is given by the following formula:

$$\text{SIS} = K * \frac{\sum_{x=0}^{u} x * n(x)}{\sum_{x=0}^{u} n(x)} \tag{2}$$

where $n(x)$ is the number of counts with pulse heights between X and $X + \Delta X$

$x =$ pulse height

$u =$ upper level of pulse height distribution.

2.4.3 External Standard Method

Transformed Spectral Index of the External Standard (tSIE) is a quench indicating parameter to determine the counting efficiency corresponding to the quench present in the sample. It is calculated from the Compton spectrum induced in the scintillation cocktail by ^{133}Ba gamma as an external source. From mathematical transformation of this spectrum, tSIE value is generated. For most quenched samples, tSIE is 0 and for the unquenched sample its value is 1000.

Series of quenched standards is prepared by adding ^{3}H standard in the vials containing the scintillation cocktail. Activity per vial is constant with increasing amount of quench. The standards are then counted in LSC and the variation in the count rate and quench as shown in Fig. 3 is obtained. Counting efficiency is calculated corresponding to each tSIE and a plot of tSIE versus counting efficiency is generated. Yellow food dye was used as the colour quenching agent to prepare quench curves by L'Annunziata et al. due to its color near to that of urine [47].

Priyanka et al. [48] adopted Zero Detection Threshold technique to quantify the activity of ^{3}H in urine samples. An unquenched ^{3}H standard was used as a tracer to determine the zero-detection threshold of Packard Tri-Carb 2900TR LSC. Zero detection threshold of LSC was determined by counting unquenched ^{3}H standard different counting regions and plotting count rates corresponding to the lower levels of the counting regions. A similar procedure was adopted for urine samples and

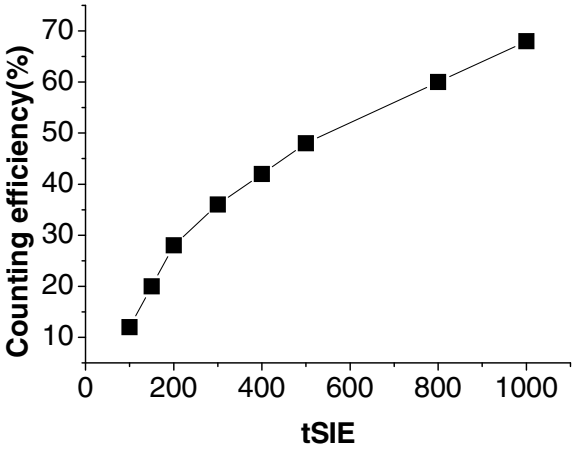

Fig. 3 Calibration curve of tSIE verses counting efficiency (%) for ^{3}H

the activity was obtained by extrapolating the integral pulse-height spectra to the determined detection threshold of LSC.

2.5 Dose Control

^{3}H activity in urine is classified under 'CAUTION' category (2 M Bq L^{-1}) and 'REMOVAL' category (4 M Bq L^{-1}) respectively to control internal ^{3}H contamination in NPP's [49]. In case urine samples exceed 4 M Bq L^{-1}, occupational workers are not allowed to do radioactive jobs till his/her urine sample shows less than 1 M Bq L^{-1} of ^{3}H.

Procedure for Calculation of Dose

(a) ^{3}H activity in urine for a given period for a given worker is collected date-wise.
(b) The method of average is used to calculate the dose for the interval between successive samples which is 10 days or less.
(c) When the sampling interval between successive samples is more than 10 days then the period is divided into 2 parts. The first part of the period is the exact multiple of 10 days, and the second part is the remaining period. Dose for the first part is calculated by the method of exponential decay. For the second part it is the method of average.
(d) Thus, an internal dose for an individual up to a particular day will be the summation of the dose calculated by either the average method or by the exponential method based on his/her urine sample frequency and committed dose due to the last sample submitted. When he/she submits the next sample, the committed dose of the earlier sample is suitably adjusted.

(e) Dose for a particular month is calculated by truncating the uptake at the last day of the month. The calculated uptake is carried forward to the first day of the following month for subsequent dose calculation.

2.5.1 Principle of Dose Calculation

The equivalent dose (D mSv) due to average ^{3}H activity in urine (Q M Bq L^{-1}) for a period of t (days) will be:

$$D = \left[Q * 10^6\right] * [0.0057] * \left[1.6 * 10^{-13}\right] * [86{,}400] * [1.11] * \left[\frac{2}{3}\right] * \left[10^3\right] * [t]$$

(mSv) (Bq/1) (Mev/dis) (J/Mev) (Sec/d) (Remark 1 and 2) (mSv/Sv) (d)

$$= 0.0583 * Q * t \text{ (mSv)} \tag{3}$$

Remark 1: According to ICRP 78, 97% of ^{3}H activity in the form of HTO equilibrates with body water and follows biological half-life of 10 days for a standard man [50]. However, 3% activity which forms OBT follows biological half-life of 40 days. Thus, the total dose due to both components is 11% higher than the dose calculated by body water activity calculation.

Remark 2: While calculating the dose using the ^{3}H activity in body water, it is assumed that 60% of body weight receives dose i.e., only the water component. However, all tissues containing water receive the dose. Thus, except bones all soft tissues in the body receive the dose. The soft tissues comprise 90% of the body weight. Therefore, 0.90 * W is the mass of the organ that receives the dose whereas 0.60 * W mass of the organs was assumed to receive the dose. Hence, the multiplication factor of 2/3 is introduced to arrive at the correct dose to the body.

(i) **Method of Average**: Method of average is used for chronic exposure cases where samples are submitted regularly at the prescribed frequency

$$D = 0.0583 * Q * t \text{ (mSv)} \tag{4}$$

where, D is the dose in mSv during the interval of t days and Q is

$$(Q_1 + Q_2) * 0.5$$

Q_1 is tritium activity in urine (M Bq L^{-1}) on day t_1 and
Q_2 is tritium activity in urine (M Bq L^{-1}) on day t_2 and $t = t_2 - t_1$.

(ii) **Method of Exponential Decay**: This is used in cases where the period between two successive samples is more than 10 days.

$$D = 0.0583 Q_1 \int_{t_1}^{t_2} \mathrm{e}^{\frac{-0.693t}{T_b}} \mathrm{d}t \tag{5}$$

(iii) **Committed Dose**: Committed dose is calculated for acute exposure cases where no successive samples are submitted.

$$D = 0.0583 Q_1 \int_{0}^{\infty} \mathrm{e}^{\frac{-0.693t}{T_b}} \mathrm{d}t \tag{6}$$

2.6 Medical Intervention for ^3H

Medical intervention need not be considered for ^{3}H intake less than 1 ALI as it is allowed for normal operation of the facility. Annual effective dose (internal and external as well) in the calendar year is the deciding criteria to exceed up to 1.5 ALI. In case worker's dose history is close to the regulatory dose limits, individuals may be advised for short period diuretics. Short-term treatment may be considered for maximum Committed Effective Dose (CED) reduction with ^{3}H intake in the range of 1–10 ALI (20–200 mSv). Special treatment of kidney dialysis or 0.5% NaCl solution may be advised for a long time for ^{3}H intake > 10 ALI, however, if the estimated intake is $\geq$ 100 ALI, prolonged strong therapeutic or medical intervention may be advised in view of the severity of exposure reduction under constant medical administration.

Diuretics like, water, coffee, tea, beer or wine can be used to lower ^{3}H concentration of the body for low/intermediate uptakes. The excretion rate can be increased by water, coffee, tea, beer or wine to reduce dose resulting into the regulatory dose limit for corresponding to 1.0–1.5 ALI. Chemical diuretics under medical supervision to keep suitable vital contents in the body are administered in case of acute ^{3}H intake. A peritoneal or kidney dialysis machine may reduce ^{3}H half-life up to 4–13 h in the event of life-threatening situation [51].

3 Estimation of High Energy Beta Emitters in Urine

3.1 Strontium-90 (^{90}Sr)

^{90}Sr is an anthropogenic radionuclide that can be released into the environment, during any nuclear or radiological emergency scenario. It is produced in nuclear fission (yield: 4.5%) in Nuclear Power Plants and is a probable source of exposure in radiation dispersal devices [52]. ^{90}Sr is radiotoxic due to its moderately long physical

(28.6 y) and biological (49.3 y) half-lives. It decays to ^{90}Y which emits high energy β (E_{max} = 2.27 MeV) particle. Since ^{90}Sr is chemically analogous with calcium, it amasses chiefly in bone tissues.

In radiological and nuclear emergency incidents, rapid bioassay techniques for detection and quantification of ^{90}Sr in urine samples are desirable for estimation of internal dose due to radio-strontium [53–56]. Several well-known techniques are employed for the separation and quantification of ^{90}Sr such as gravimetry, ion-exchange and extraction chromatography, and gas flow proportional counting [57]. Although these techniques offer reliable results and high sensitivity, the major shortcomings of these methods are requirement for large sample volume, low sample throughput, and substantial losses during radiochemical separation leading to small strontium recovery. Liquid scintillation spectrometry stands out contrarily as it offers high counting efficiency, minimum sample preparation steps, and high sample output.

To cater to any nuclear or radiological emergency involving ^{90}Sr, it is crucial to monitor a large number of people for internal contamination and hence a rapid extractive liquid scintillation spectrometric technique was developed to estimate ^{90}Sr in spot urine samples. A technique that has been developed by Ritika et al. is a fusion of solvent extraction and LSC employing Sr-selective crown ethers as the extracting agent [58]. Interference of various metal ions like calcium, potassium and lead was also taken into account in the extraction of strontium by crown ethers. Repeatability of the method and reusability of the extracting agent for subsequent analysis have been reported.

Use of Sr-spec resin in the estimation of radio-strontium, is the most significant advancement which offers incomparable separation of Sr from Y. The size selective extraction of Sr^{2+} by crown ethers relies on two important factors viz.: crown size of the extractant and the ionic size of Sr^{2+} ion. The cavity of 4,4′, (5″)-di tertbutyl cyclo-hexano 18-crown-6 (DCE) has a radius of 1.3–1.6 Å which captures Sr^{2+} ions (hydrated ionic radius 1.32–1.40 Å) precisely. Sr-spec resin effectively retain Sr, and thus gets separated from Yttrium (eluted from the column) as reported by Visser et al. and Wankhede et al. [59, 60]. Kramer separated low level ^{90}Sr/^{90}Y from wet ashed urine using co-precipitation and solvent extraction techniques [61]. The extracting agent used was di (2-ethylhexyl) Phosphoric Acid (HDEHP: 1.5 mol L^{-1}) in n-heptane and radionuclides were separated by a series of extractions. A rapid technique for estimation of ^{90}Sr in urine samples was developed by Dai et al. [55]. The method comprises column separation of Sr from 20 mL urine using Eichrom TRU and Sr resin followed by LSC measurement using a Hidex TDCR LSC. A detection limit of 10 Bq L^{-1} was reported for 10 min counting time. Due to its simplicity, Cerenkov Counting technique can also be used as a rapid screening technique for estimation of ^{90}Sr in urine samples [62].

3.2 Phosphorus-32 (^{32}P)

Phosphorus-32 is an extensively used radio-labelled compound in radiopharmaceuticals and tracer studies. ^{32}P is employed to lower the pain in bones in terminal cancer patients in several hospitals. To meet the cumulative demand, production and synthesis of ^{32}P, has increased throughout the years.

^{32}P is a pure β emitting radionuclide (E_{max} = 1.709 MeV) with a half-life of 14.3 days. Following inhalation, ^{32}P gets deposited in the respiratory tract and then is cleared from lungs into the body fluids depending on its solubility. From the plasma, it is then removed with a biological half-life of 0.5 days and dispersed to cell fluids, soft tissue, bone, and excreta. Therefore, internal contamination of ^{32}P is monitored rapidly after the possible intake to confirm a measurable signal. A rapid bioassay method for ^{32}P in urine samples would be desirable to evaluate the internal dose [63, 64].

Yang has developed a simple and rapid screening technique for ^{32}P measurement in urine samples and also established an empirical correlation between TDCR parameter and Cerenkov efficiency [64]. To reduce the interference from colour quenching and chemiluminescence, he adopted simple processes like acidification and oxidization. Minimum Detection Activity (MDA) of 11 Bq L^{-1} was obtained for urine sample (15 mL) with 30 min counting time. Moreover, he suggested that with selection of a shorter monitoring interval (7 days) and a long counting duration (2 h), the method would offer an adequately lower detection limit so as the sensitivity requirement for ^{32}P in urine samples corresponding to 0.1 mSv (annual committed effective dose for routine bioassay) can be met.

Wankhede et al. explored the viability of Cerenkov counting technique for detection of ^{32}P in bioassay samples, and the results obtained were validated with the routine gross beta technique. The detection limit reported is ~ 10 Bq day^{-1} using Hidex 300 SL LSC [65].

Even though Cerenkov counting generally offers lower counting efficiency than LSC, it has several advantages over LSC such as (1) insensitive to α and low energy β/γ nuclides, (2) non-destructive in nature and (3) free of chemical quenching.

4 Estimation of Electron Capture Radionuclides in Urine Using LSC Technique

4.1 Iodine-125 (^{125}I)

^{125}I is usually used in clinical medicine for radio-labelling and tracer studies [66]. It decays by electron capture with a half-life of 60.1 d. ^{125}I emits γ (35.5 keV) and *K* X-rays (27.4 keV) along with auger electrons. Workers handling radio-iodine are monitored routinely for internal contamination. This is to ensure workplace controls

and for timely estimation of intakes [67, 68]. Due to low energy emissions by ^{125}I, common survey meters are unable to detect contamination due to ^{125}I. Therefore, bioassay monitoring is the solitary technique for estimation of ^{125}I intake. Bioassays are conducted for radioactive workers handling unsealed radio-iodine sources to evaluate whether any intake has occurred. This practice is beneficial for (1) estimation of internal doses, (2) determination of airborne radioactive particles which contribute to dose and (3) evaluation of work conducts and integrity of safety designs of plants.

Jimenez et al. described the development of a methodology for estimation of airborne ^{131}I using activated charcoal canisters followed by the measurement by liquid scintillation spectrometry [68]. Reported MDA value for estimation of ^{131}I using this technique was 140 m Bq m^{-3}. The author revealed the benefits of using LSC in comparison to gamma spectrometry are simple and rapid sample processing and better sensitivity.

Generally, in-vivo monitoring of ^{125}I is carried out using a thin NaI (Tl)-based Thyroid Monitoring System [69]. LSC based methodology is reported for quantification of ^{125}I in urine samples, as an alternate technique to thyroid monitoring. The proposed technique doesn't require any chemical separation and further it was revealed that the technique is sensitive to detect CED < 1 mSv within 3 days of incidental exposures [70].

4.2 Iron-55 (^{55}Fe)

Radiation workers get internally contaminated with ^{55}Fe, due to particles of corroded steel in the form of iron oxide. Iron is one of the major components in structural material in nuclear reactors. In these structural components, ^{55}Fe is produced by neutron activation of stable iron isotopes, ^{56}Fe and ^{54}Fe with natural abundance of 5.845% and 91.754% respectively. ^{55}Fe ($t_{1/2} = 1001.0 \pm 2.3$ d) decays via electron capture with the emission of Auger electrons (4.95–6.49, 60%) and low energy X-rays (5.89 keV, 24.9%) to stable ^{55}Mn [71].

In the bioassay, urine being collected with an ease, is an ideal sample matrix for assessment of dose over feces or blood. Reported values of Fe excreted out of the body by various routes is ~ 0.6 mg d^{-1} [feces (60%), skin (30%) and urine (10%)] [72]. Subsequently, urinary excretion rate of Fe is 0.07 mg L^{-1} [73].

Usually, ^{55}Fe is measured by X-ray spectrometry and gas flow proportional counting techniques, with counting efficiencies < 5% [74]. However, the advantage of measurement of ^{55}Fe by LSC technique is lack of self-absorption and nearly 40% counting efficiency. In case of pure β emitting radionuclides, Triple-to-Double Coincidence Ratio (TDCR) is directly proportional to the overall efficiency within ± 15% [75]. However, in case of ^{55}Fe, it was observed that TDCR deviated largely from the experimentally derived CE depending upon the sample quench [76]. For standardization of TDCR based LSC technique for ^{55}Fe measurements, an empirical Correction Factor (CF) (ratio of TDCR/CE), was derived for various sets of quenched

standards. A consistent value of CF (0.5) was obtained for TDCR ranging from 0.40 to 0.15.

Guerin has discussed a methodology for determination of ^{55}Fe in urine samples by LSC [73]. In NPP, other components of steel, such as Ni, Cr, Mo, Mn, Co, and Zn apart from Iron, are also getting neuron activated and therefore interfere in the measurement of ^{55}Fe using LSC. To remove these interferences, chemical separation techniques such as NH_4OH co-precipitations [77], solvent extractions [78], ion-exchange [73] and extraction chromatography [79] were employed previously. Two analytical techniques such as solvent extraction using isopropyl ether and Tri-n-Octylamine (TOA) chromatography were discussed by Cregan et al. for ^{55}Fe bioassay [78].

Reported recovery and MDA values for estimation of ^{55}Fe in urine samples using LSC are 90 ± 10% and 0.18 Bq L^{-1} respectively [73]. The developed methodology is useful for assessment of the internal dose received by radiation workers following an inadvertent intake of ^{55}Fe.

5 Rapid Screening Method Based on LSC Measurements for Estimation of Gross α/β Activities in Urine

5.1 Basis of α/β Discrimination

Photon intensity generated from a scintillation event is a function of time and displays prompt (fast) and delayed (slow) components. The prompt component decays in few nanoseconds, while the slow component decays in around 200–300 ns. The respective light component in the prompt and delayed constituents is a function of specific ionization and hence the type of particle instigating it [80]. Alpha particles give rise to longer pulses due to the higher specific ionization. This phenomenon provides the basis of Pulse Shape Analysis (PSA) for particle recognition and subsequent discrimination of α particles from β.

Alpha radionuclides emanate high energy particles in the range 4–7 MeV. Alpha being a highly ionizing (high Linear Energy Transfer (LET)) radiation, produces fewer photons upon interaction with the liquid scintillation media. Their light yield is 10 times lower than β. Regardless of being monoenergetic, α particles, exhibit wider pulse height distribution peaks as compared to β particles. Accordingly, the poor light yield, short range and higher specific ionization in case of α, eventually results in deficient energy resolution (200–300 keV). Pulse height spectral peak of 5 MeV α particle will occur at 500 keV on the LSC pulse height scale. Thus, pulse height spectra of α and β nuclides overlay despite the fact that energy of the α nuclide is ~ 10 times higher than the β nuclide. Hence, it is challenging to quantify actinides in the presence of β radionuclides in LSC.

5.2 Radio-Analytical Technique Based on LSC for Quantification of Actinides and β Emitters

In bioassay laboratories, conventional methods for the quantification of actinides and beta emitters (^{90}Sr) in urine samples involve radiochemical separation processes and long counting time to obtain lower MDA values. Though these adopted techniques are accurate and highly sensitive, the major shortcoming with the radiochemical separation method is the longer turnaround time (nearly 1–2 weeks). Consequently, small number of samples can be analysed in a given time interval, and hence these time-consuming separation methods cannot to be employed in an emergency scenario [81, 82]. It is essential that in-vitro laboratories should develop alternate rapid methods which can be implemented efficiently and adequately in radiological emergency situations.

By employing LSC and PSA techniques, potential interference from β emitters in the determination of actinides in urine samples, can be removed entirely without the need of tedious and time-consuming radiochemical separation procedures. Alpha LSC in combination with specific solvent extraction technique provides a viable alternate for the determination of actinides without any intervention in urine samples. Incentives of α LSC include insignificant quenching effects, nearly 100% counting efficiencies, and lower background which results in an improved MDA.

In LSC, quenching is the detrimental feature that hinders the yield of light photons. In LSC technique, three different quenching types are encountered viz.: physical, chemical and colour quenching. These interfering processes are compensated through careful sample preparation, use of quench calibration plots and data correction. Viable results using LSC will be obtained only when the impact of quench in the sample matrix will be taken into account. In LSC, various factors such as quenching, type of sample and scintillation cocktail used and the sample preparation techniques affect the counting efficiencies [18]. Users need to optimize these parameters for efficient determination of gross alpha/beta activities in urine samples.

Chemical conformation of urine can diverge for each person and even varies for the same person from day to day. For this reason, chemical and colour quench vary extensively from sample to sample. Therefore, initially impurity/quench associated with each individual sample is quantified and quench parameter was obtained from the LSC system. This primary measurement, in conjunction with a quench calibration plot, allows calculation of the counting efficiency in consequence to a sample's quench level. To obtain optimal discrimination of α and β emitters, PSA has to be set for each sample, vial type and scintillation cocktail used.

Generally, to calibrate the LSC system and for optimization of the PSA setting, it is a usual practice to scan a pure α (^{214}Am) and a pure β standard (^{36}Cl or ^{90}Sr/^{90}Y) at various PSA levels and then depending on the minimum misclassification of α events in β and vice versa, PSA level is selected subsequent to a particular quench level [20].

Nowadays there is an increasing trend of utilizing extractive reagents that are miscible with liquid scintillation cocktails for the separation and analysis of actinides

in urine samples. Development of extractive scintillators that facilitate minimum quenching and improved α energy resolution has proven to be the key element in practical LS spectrometry [83]. Alpha spectral resolution and sample quenching rely on the type of extractant and the amount used to prepare the extractive cocktail [84].

Reese in his report in 2007, explained the detailed procedure for optimization of various counting parameters for efficient and simultaneous alpha beta discrimination in urine samples [85]. For radioactivity characterization of urine samples using LSC as a screening technique in an emergency scenario, he suggested a novel concept of 'typical urine'. He employed Tri-Carb 2500TR LSC for measurement. Quench is measured in this LSC, using a standard scale known as the transformed spectral index of an external standard or tSIE. Quench value encountered for typical urine samples was determined through a study of historic samples. Corresponding to a quench parameter value of typical urine further counting parameters such as optimized PSA, blank count rate, counting and spillover efficiencies and MDA values were determined. These parameters can be used for quick and accurate measurement of gross alpha and beta activities in urine samples in case of emergency scenarios using LSC technique.

Sas, in 2017, discussed the direct addition of untreated urine sample to the scintillation cocktail for determination of gross activities in urine sample [86]. The author optimized various counting parameters based on Pulse Length Index (PLI) for efficient discrimination of α and β radionuclides in the urine sample. He also studied the dependence of the sample volume on the measurement efficiency. It was exhibited that LSC proved to be a rapid and precise technique for the determination of gross α and β activity in the urine matrix. Further various benefits of using LSC, such as easy sample preparation, small counting time, high efficiency and measurement sensitivity were highlighted in the study. Another advantage he emphasized while employing TDCR instrument is that it corrects for probable chemical and optical quenching which is crucial for activity quantification of β radionuclides.

5.3 Application of LSC Technique for In-Vitro Analysis in Emergency Scenario

In radiological or nuclear emergency incident, valued evidence could be gained by using LSC technique as it offers fast screening of urine samples collected from probably contaminated persons. Recently Piraner et al. described the optimization of LSC parameters for Tri-Carb and Quantulus GCT systems for rapid screening of urine samples in an emergency scenario [87].

During emergency, valuable information could be gained using LSC technique by rapidly screening urine samples of the affected inhabitants. For receiving timely information, various methods have been examined, such as (1) usage of portable and field-deployable LSC for the preliminary analysis of radionuclide concentrations in

nasal swabs and urine samples [52], (2) gross α and β counting using LSC technique for preliminary screening of bioassay samples [88, 89].

In view of this, various studies were carried out to investigate and optimize different LSC parameters such as sample volume, counting time, quenching and discriminator settings [90]. Optimization of time discriminator setting is a crucial factor in LSC to identify and quantify individual radionuclides present in mixed α/β sample. In modern LSCs, PSA or PLI software are provided. This adaptable α/β discriminator offers simultaneous measurement of α and β nuclides in a single sample without using time consuming, tedious radiochemical separation procedures. Using this valuable feature, various researchers have employed LSC successfully as a screening tool for rapid assessment of gross α and β activities in bioassay samples [91–93].

In LSC, quenching poses major challenge in the assessment of the radiological characterization of the sample. Particularly, in case of urine samples, varying amount of chemical and colour constituents largely affect the counting efficiencies as well as discriminator settings. In view of this, quench correction is mandatory for the quantification of gross α and β activities in urine samples. These strategies assist the researchers to determine optimum analysis time so as to hasten the decision for rapid medical intervention, in case of radiation emergency [94, 95].

5.4 Rapid Determination of ^{226}Ra in Urine Samples

^{226}Ra is a long-lived radionuclide ($t_{1/2}$—1600 years) which emits α particles with energies of 4.60 MeV (5.9%) and 4.784 MeV (94.0%) to its daughter ^{222}Rn. This decay process is also accompanied by a γ emission of 186.2 keV (3.5%). The radiological impact of radium on human health is not only due to radium isotopes themselves but also due to exposure to their daughters in decay series.

US Environmental Protection Agency signifies ^{226}Ra as a class A carcinogen, as it amasses in bones and due to the agility of its gaseous daughter, ^{222}Rn [96]. Also, as per the USNRC document, ^{226}Ra is the precarious radionuclide in emergency scenarios, such as a nuclear accident or Radiological Dispersal Device (RDD) detonation [52].

For determination of radium, commonly employed techniques are α spectrometry [97], γ spectrometry [98], Inductively Coupled Plasma Mass spectrometry [99], Cerenkov [100] and LSC [101, 102]. Among all these techniques, α spectrometry is the most sensitive technique that facilitates isotopic analysis of radionuclides, however it involves a complex sample preparation procedure for the separation of radium from other alkaline earth metals [103]. Whereas in case of γ spectrometry, γ rays emitted from ^{235}U (185.7 keV) interfere with ^{226}Ra gamma (186.1 keV). Therefore, sample matrix effects (self-attenuation) and paired coincidence decays need to be taken into account when analysing samples by γ spectrometry [104]. LSC, instead, is proved to be rapid and precise technique for determination of radium and radon in water samples due to its simplicity and promising results.

Subsequent to the proposed medical intervention dose of 0.1 Sv (CED), for quantification of ^{226}Ra in urine matrix, an action level of 2.0 Bq L^{-1} is obtained [88]. Accordingly, MDA of 0.2 Bq L^{-1} is desirable for ^{226}Ra in emergency urine samples. As mandatory in emergency scenarios, high sample throughput and rapid analysis time are prerequisites in cases involving ^{226}Ra exposure [105]. The method proposed by Sadi et al. was based on organic removal and urine decolourisation by a polymeric sorbent material. While extraction and pre-concentration of ^{226}Ra was achieved using a dispersive liquid–liquid micro extraction technique and was done using LSC technique. The MDA reported was 0.15 Bq L^{-1} which is lower than the required sensitivity of 0.2 Bq L^{-1} for ^{226}Ra in human urine samples.

5.5 Plutonium/Americium Estimation in Nasal Swab Samples

Fuel reprocessing and fuel fabrication plants, come across different compounds of Plutonium/Americium (Pu/Am). The predominant route of internal contamination for radiation workers in these facilities is the airborne Pu/Am. It undergoes dissolution and reaches the circulatory system generally in a monomeric and soluble form following inhalation/injection/wounds and/or ingestion [106] and gets deposited on the bone surface, liver, gonads etc. with biological half-life of 50 y, 20 y and 10 y, respectively [107]. Quick decisions concerning medical intervention and dose estimation need to be taken in the event of incident related and/or emergency situation. Nasal swab (NS) analysis for Pu/Am activity using LSC is the best indicator of possible internal contamination by inhalation which provides isotopic composition of the inhaled radionuclide a crucial input for CED.

However, additionally lung monitoring and bioassay analysis is carried out for further confirmation. Overnight or 24 h collected urine sample is analysed to determine internal exposure. Analytical techniques like HR-ICPMS [108] or α spectrometry [109] are adopted for the estimation of Pu/Am activity in bioassay samples. Nevertheless, pre-concentration of actinides followed by ion exchange to separate Pu/Am from the sample matrix is a pre-requisite prior measurement. A single sample takes about 4–5 working days for complete analysis. Solvent extraction technique coupled with LSC with α/β discrimination is a rapid method due to rapid measurement and simple sample preparation for sequential isolation and determination of Pu and Am activity in NS.

McDowell et al. studied the possibility of detecting and identifying α emitters in low count-rate samples using LSC techniques [110]. Techniques to control quenching in extractive scintillators for α emitting nuclides have been developed by McDowell and Coleman [111]. Quenching effects of 7 extractants were studied in detail and it was observed that tributyl phosphate offers the least quenching. Quick and simple nuclide specific determination of α emitters is possible with the application of LSC

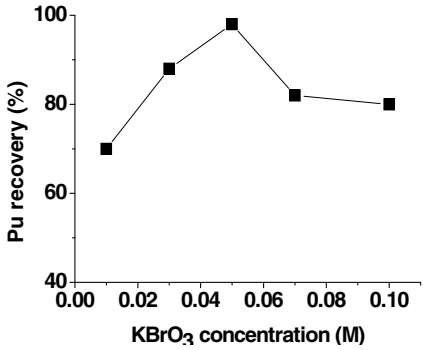

Fig. 4 Pu recovery with various concentrations of $KBrO_3$

coupled with selective extracting agents. Rapid determination of Pu activity on filters and smears using α LSC was developed by Shaw [112].

Yang et al. [113–115] studied the interference of β and γ radionuclides in the estimation of α emitters using extractive LSC. Panda et al. developed a rapid solvent extraction technique coupled with LSC for sequential separation and estimation of Pu/Am in NS samples [116]. HDEHP was used as an extracting agent in the Toluene based scintillator. Various parameters for optimum extraction of Pu and Am were standardized. Pu was converted into Pu(IV) state using $KBrO_3$ as an oxidizing agent. The authors obtained 96% Pu recovery at 0.05 M conc. of HNO_3 and $KBrO_3$ as shown in Fig. 4.

About 95% Am was stripped into the aqueous phase using 0.35 M HNO_3. 12 mL of Optiphase HiSafe III cocktail was used to count 8 mL of extracted Am fraction in LSC. Estimation of ^{241}Pu is a very significant input parameter for CED computation and in in-situ build-up of ^{241}Am in lungs due to its decay as well.

6 C-14 Urea Breath Test for the Detection of *H. pylori* Infection in Patients Using LSC

Helicobacter pylori is a large family of related spiral shaped bacteria which are present in the stomach of vertebrates for the whole life span of the host [117]. Studies suggest that all human beings carry some or other closely related bacteria of *H. pylori* family in their stomach. As per the studies these bacteria enter the human body during childhood and carried by the host for the whole life span. It can be transferred from human to human through body secretion and excretions such as saliva, vomit or faeces [118].

H. pylori present in the stomach may cause cellular infiltration in the gastric mucosa, known as chronic gastritis. Most people may not show any symptom, while some may have increased risk of developing peptic ulcer, adenocarcinoma in the antrum and body of the stomach. Researches also suggest an increased risk of non-Hodgkin's lymphoma of stomach (MALToma) in people who carry *H. pylori*. The

cases of peptic ulcer and the gastric cancers of the antrum and body of the stomach are declining in many countries where lesser cases of *H. pylori* colonisation in the human stomach are reported. Elimination of *H. pylori* with antimicrobial drugs heals the ulcers and further reduces the risk of development of gastric cancers [118].

6.1 Urea Breath Test (UBT)

UBT is considered to be the gold standard technique to detect *H. pylori* worldwide. It is based on the presence of an enzyme Urease in human body. The presence of Urease enzyme in the body indicates the presence of some microbes. The most common microbe which is urease positive that could be present in human stomach is *H. pylori*. Urease enzyme hydrolyses the urea to ammonia and carbamate, which is later converted to soluble carbon dioxide [119]. Hence introducing 'Urea' labelled with either non-radioactive or radioactive carbon isotope to human stomach can be to ammonia and labelled carbon dioxide, in the presence of *H. pylori*. This labelled carbon dioxide will enter the blood stream and will be released through exhalation. Thus, by collecting the breath samples of the patient in a specific medium and analysing it with an appropriate technique can detect the presence of *H. pylori* [120].

6.2 UBT Labelled with ^{14}C

^{14}C is a radioactive isotope of carbon which emits low energy beta of 156 $keV_{(max)}$ and 49 $keV_{(mean)}$ energy. In ^{14}C labelled UBT, the urea labelled with this radioactive carbon isotope is prepared as a capsule which the patient takes orally after a fasting period of 6 h. The radioactivity content is normally very low as 37 k Bq. After 10 min of ingestion of the capsule breath sample of the patient is collected in a specific trapping solution. The samples are further measured using Liquid scintillation technique. In case of *H. pylori* positive patients, an increase in $^{14}CO_2$ happens due to hydrolysis of ^{14}C-urea by the urease enzyme from *H. pylori*. The ^{14}C-urea will remain unhydrolyzed in the absence of *H. pylori*, which will be absorbed in the stomach and will enter the bloodstream. This will be further excreted through urine.

Studies on application of ^{14}C UBT for detection of *H. pylori* is widely carried out internationally by researchers while the studies and published data of the ^{14}C labelled UBT are limited in India. A few Indian researchers have published the data on detection of *H. pylori* using ^{14}C labelled urea breath test [121–123]. Tiwari et al. in their study explains that the test is not so widely used in the country due to limited availability of ^{14}C labelled urea capsules. Board of Radiation and Isotope Technology (BRIT) is the only institution authorised for the production and supply of these capsules in India. Import of these capsules is very expensive. BRIT has produced 37 k Bq ^{14}C labelled urea gelatin capsules absorbed in non pareil seeds in dry form. Efficacy of these capsules is studied by Tiwari et al. They have also

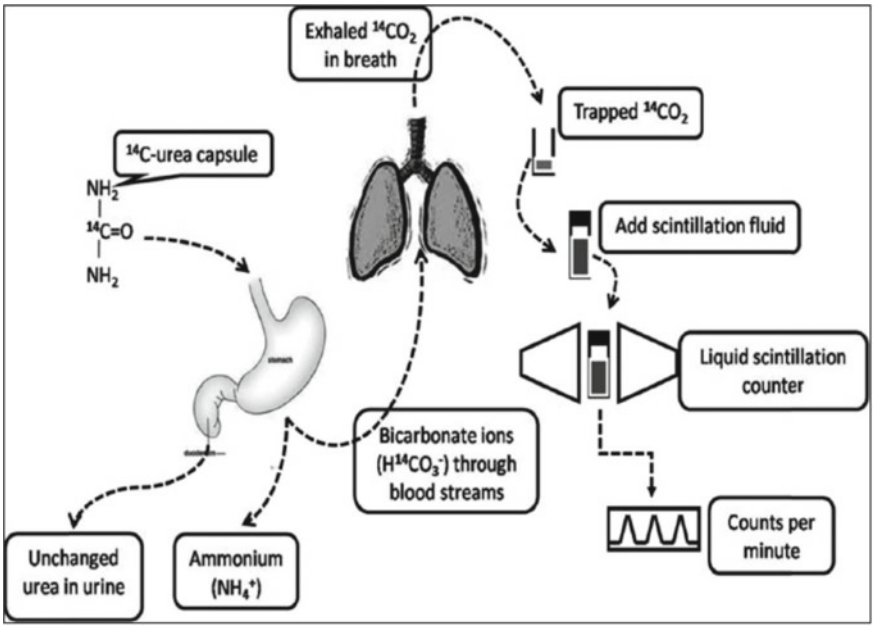

Fig. 5 Schematic diagram of ^{14}C labelled urea breath test [123]

studied the modified direct trapping of exhaled air into a trapping solution to replace the previously used method of collecting the breath samples in a balloon and then transferring it to a trapping medium. Tiwari et al. had set 3.3 Bq as cut off for trapped breath sample being positive and value less than 3.3 Bq is negative for *H. pylori* detection. The authors studied the use of ^{14}C UBT in the breath samples collected from the patients from a hospital in Mumbai [121]. Figure 5 shows the schematic diagram of ^{14}C labelled urea breath test.

The exhaled breath samples from the patients suspected with *H. pylori* is collected before (blank) and after administration of ^{14}C labelled urea capsules. The patient is asked to ingest labelled urea capsule with an activity of 37 k Bq prepared indigenously by BRIT.

The patient blows into the precisely titrated solution of Hyamine hydroxide with thymolphthalein blue indicator (2 mL) till the solution turns colourless. This trapping solution changes its colour once a definite volume of CO_2 is solubilized (normally 1 or 2 mmol of CO_2). The amount of CO_2 exhaled will vary from person to person, hence the colour changing property of the medium helps in collecting a fixed amount of CO_2 from all patients. When sufficient CO_2 is exhaled into the solution it becomes acidic and turns colourless. The medium with dissolved exhaled breath is the sample for the analysis and detection of *H. pylori*. A selected scintillator solution (10 mL of scintillator to 2 mL sample or as optimised) is added to this and it is counted in Ultra Low Level Liquid Scintillation Counter (Quantulus 1220) for 300 min (5 h). The MDA of the system for this measurement is 45 m Bq. The net counts of the

samples are converted to activity by using the standard radioactivity calculation. If the sample has any ^{14}C activity the subject is considered to be positive.

7 Conclusion

LSC has emerged as one of the major radio-analytical techniques for assessment of various α and β radionuclides due to several substantial advantages such as utmost ~ 100% counting efficiencies for high energy β and α emitters, simple and rapid sample preparation procedures, and spectral data processing capabilities. LSC is widely employed for estimation of low (^{3}H and ^{14}C) as well as high energy (^{90}Sr and ^{32}P) β emitters in urine samples. A rapid extractive liquid scintillation spectrometric technique using various extracting agents such as Sr-selective crown ethers, HDEHP is developed and used extensively for the interference free estimation of ^{90}Sr in spot urine samples. Cerenkov counting technique is also used as a rapid screening technique for estimation of ^{90}Sr and ^{32}P in urine samples. The detection limit reported is ~ 10 Bq day^{-1} using Hidex 300 SL LSC for these high energy β emitters. LSC is also used for estimation of electron capture radionuclides such as ^{125}I and ^{55}Fe. The developed methodologies are useful for assessment of the internal dose received by radiation workers following an inadvertent intake of ^{125}I and ^{55}Fe. Ultra-low background and simultaneous quantification of α and β events are the key features of PSA based LSC technique which facilitate determination of actinides at reasonably low concentrations. A screening method for rapid estimation of gross-α and gross-β activities in urine samples using LSC technique is advantageous for high throughput screening of large number of individuals following a radiation emergency. Quick decisions concerning medical intervention and dose estimation need to be taken in the event of incident related and/or emergency situation. Nasal swab analysis for Pu/Am activity using LSC is the best indicator of possible internal contamination and also provides isotopic composition of inhaled radionuclide which is a crucial input for CED. Development of LSC based rapid methods for analysis of various α and β radionuclides, provide feasible alternative and can be implemented efficiently and adequately in radiological emergency situations.

References

1. Schonhofer F (1998) Use of low-level liquid scintillation spectrometry for rapid measurement and decision making. Radioact Radiochem 9:18–24
2. Horrocks DL (1974) Applications of scintillation counting. Academic Press, New York
3. Brooks FD (1979) Development of organic scintillation. Nucl Instrum Methods 162:477
4. McKlveen JW, McDowell WJ (1984) Liquid scintillation alpha spectrometry techniques. Nucl Instrum Methods Phys Res 223(2–3):372–376
5. Mirashi NN, Keshav C, Aggarwal SK (2000) Liquid scintillation counting techniques for the determination of some alpha emitting actinides: a review. BARC report

6. Dacheux N, Aupiais J (1997) Determination of uranium, thorium, plutonium, americium and curium ultra-traces by photon electron rejecting α liquid scintillation. Anal Chem 69(13):2275–2282
7. Cherry SR, Sorenson JA, Phelps ME (2012) Radiation detectors. In: Cherry SR, Sorenson JA, Phelps ME (eds) Physics in nuclear medicine, 4th edn. W.B. Saunders, pp 87–106
8. Tinker RA, Smith JD, Cooper MB (1997) Determination of strontium-90 in environmental samples containing thorium. Analyst 122:1313–1318
9. Oh JS, Warwick PE, Croudace IW, Lee SH (2013) Rapid measurement of ^{241}Pu activity at environment level using low-level liquid scintillation analysis. J Radioanal Nucl Chem 298:353–359
10. Cakal GO, Guven R, Yucel H (2015) An application of LSC method for the measurement of gross alpha and beta activities in spiked water and drinking water samples. Nukleonika 60(3):637–642
11. Nikolov J, Stojkovic I, Todorovic N, Tenjovic B, Vukovic S, Knezevic J (2018) Evaluation of different LSC methods for ^{222}Rn determination in waters. Appl Radiat Isot 142:56–63
12. Abbasi A (2018) A review of the analytical methodology to determine radium-226 and radium-228 in drinking waters. Radiochim Acta 106(10):819–829
13. Blanco P, Lozano JC, Gomez Escobar V, Vera Tome F (2004) A simple method for ^{210}Pb determination in geological samples by liquid scintillation counting. Appl Radiat Isot 60(1):83–88
14. Maxwell SL, Culligan BK, Kelsey-Wall A, Shaw PJ (2012) Rapid determination of actinides in emergency food samples. J Radioanal Nucl Chem 292:339–347
15. Lin Z, Healey S, Wu Z (2016) Rapid and simultaneous detection of α/β radioactivity in food by solid phase extraction liquid scintillation counting. J Radioanal Nucl Chem 307:1987–1994
16. Cooper EL, Cox JM, Workman WJ (1998) Analysis of Sr-90 and α-particle emitters on air filters and swipe samples using a liquid scintillation counter with α/β discrimination. Radioact Radiochem 9:25–40
17. Diodati JM, Sartori FM (2007) ^{239}Np as a tracer of ^{237}Np in effluent samples and low-level nuclear waste. J Radioanal Nucl Chem 272(1):11–15
18. L'Annunziata MF, Kessler MJ (2012) Liquid scintillation analysis: principles and practice. In: L'Annunziata MF (ed) Handbook of radioactivity analysis, 3rd edn. Elsevier, Amsterdam
19. Aupiais J (2004) Deconvolution of alpha liquid scintillation spectra for quantitative analysis of actinide elements in water samples. Radiochim Acta 92(3):125–132
20. Stamoulis KC, Loannides KG, Karamanis D (2010) Deconvolution of liquid scintillation alpha spectra of mixtures of uranium and radium isotopes. Anal Chim Acta 657(2):108–115
21. Pujol L, Sanchez-Cabeza JA (1999) Optimisation of liquid scintillation counting condition for rapid tritium determination in aqueous sample. J Radioanal Nucl Chem 242(2):391–398
22. Lucas LL, Unterweger MP (2000) Comprehensive review and critical evaluation of the half-life of tritium. J Res Natl Inst Stand Technol 105:541–549
23. ISOE Annual Report (2018) Organization for Economic Co-operation and Development
24. Choppin G, Liljenzin JO, Rydberg J (1995) Radiochemistry and nuclear chemistry, 2nd edn. Butterworth-Heinemann, Oxford, p 70
25. UNSCEAR Report (2017) Sources, effects and risks of ionizing radiation. In: Annex C—biological effects of selected internal emitters—tritium. United Nations, New York
26. ICRP 78 (1997) Individual monitoring for internal exposure of workers, vol 27, no 3/4
27. ICRP (2002) Basic anatomical and physiological data for use in radiological protection reference values. ICRP publication 89. Ann ICRP 32:3–4
28. International Atomic Energy Agency (2018) Occupational radiation protection. IAEA safety standards series no. GSG-7
29. Hideki M, Yoshiya S, Asako JN, Noriko U, Mitsuaki O, Shizuko K, Mikio S, Masaaki S, Ryoichi H, Hiroshi T (2021) Health effects triggered by tritium: how do we get public understanding based on scientifically supported evidence? J Radiat Res 62(4):557–563
30. Coops AJ, Van der Jagt PJ, Duijsings JH, Beentjes LB (1985) A multivial distillation apparatus for routine tritium urine analysis. Int J Appl Radiat Isot 36:408–411

31. Nogawa N, Makide Y (1999) A sub-boiling distillation method for the preparation of low carbon content water from urine samples for tritium measurement by liquid scintillation counting. Appl Radiat Isot 50:985–988
32. Wood MJ, McElroy RGC, Surette RA, Brown RM (1993) Tritium sampling and measurement. Health Phys 65(6):610–627
33. Strom DJ, Bohner KR (1989) An inexpensive and practical ambient-temperature vacuum still for bioassays. Health Phys 56(3):355–359
34. Ishii K, Yoshino K (1980) Background radio activities in urine using a quick analyzing technique. Denryoku Chuo Kenkyusho Houkoku (No. 280013)
35. Eakin JD, Hutchison WP, Lally AE (1975) The radiological hazard of tritium sorbed on metal surfaces. Health Phys 28(3):213–224
36. Momoshima N, Nagasato Y, Takashima Y (1986) A sensitive method for the determination of tritium in urine. J Radioanal Nucl Chem 107(6):353–359
37. Stencel JR, Gilbert JD, Griesbach OA, Greco JM (1988) TFTR health physics tritium measurements following D–D operation. Fusion Technol 14(2):1047–1053
38. Mingote RM, Barbeira PJS, Rocha Z (2006) Methodology for rapid tritium determination in urine. J Radioanal Nucl Chem 269(2):475–479
39. Watanabe Y, Kuwabara J (2006) Ultraviolet photolysis of urine for suppression of color quenching prior to liquid scintillation counting of tritium. Anal Bioanal Chem 384(2):547–550
40. Butler FE (1961) Determination of tritium in water and urine. Anal Chem 33(3):409–414
41. Chinese Standards (1997) Analytical determination of tritium in urine, EJ/T 1047–1997. China National Nuclear Corporation, Beijing
42. Bao MS, Yan QJ, Qing T, Xiang ZS, Liang LY, Su X (2015) Determination of total tritium in urine from residents living in the vicinity of nuclear power plants in Qinshan, China. J Environ Res Public Health 12(1):888–894
43. Pedehontaa-Hiaa G, Holstein H, Mattsson S, Raaf CL, Stenstrom KE (2020) Tritium in urine from members of the general public and occupationally exposed workers in Lund, Sweden, prior to operation of the European Spallation Source. J Environ Radioact 213:106141
44. Hou X (2011) Analysis of urine for pure beta emitters: methods and application. Health Phys 101(2):159–169
45. Yoon S, Ha W-H, Seun SL (2013) Tritium analysis of urine samples from the general Korean public. Appl Radiat Isot 81:276–278
46. Okita GT, Spratt J, Le Roy GV (1956) Liquid-scintillation counting for assay of tritium in urine. Nucleonics 14:76–79
47. L'Annunziata MF, Kessler MJ (eds) (1998) Handbook of radioactivity analysis. Academic Press, San Diego
48. Reddy P, Wankhede SM, Mandal P, Sawant PD (2021) Intra-laboratory inter-comparison exercise for tritium measurement using zero detection threshold technique. In: 34th IARPNC-2020 virtual conference, p 75
49. Radiation protection for nuclear facilities (2005) AERB/NF/SM/O-2, Rev-4
50. International Commission on Radiological Protection (1978) The principles and general procedures for handling emergency and accidental exposures of workers. Publication 28. Pergamon Press, Oxford and New York
51. Foy JM, Schnieden H (1960) Estimation of total water (virtual tritium space) in the rat, cat, rabbit, guinea-pig and man, and the biological half-life of tritium in man. J Physiol 154:169–176
52. U.S. Department of Energy/U.S. Nuclear Regulatory Commission (DOE/NRC) (2003) Radiological dispersive devices
53. Li C, Sadi BB, Moodie G, Daka JN, Lai EPC, Kramer GH (2009) Field deployable technique for ^{90}Sr emergency bioassay. Radiat Prot Dosim 136(2):82–86
54. Sadi BB, Li C, Jodayree S, Lai EP, Kochermin V, Kramer GH (2010) A rapid bioassay method for the determination of ^{90}Sr in human urine sample. Radiat Prot Dosim 140(1):41–48
55. Dai X, Cui Y, Kramer TS (2013) A rapid method for determining strontium-90 in urine samples. J Radioanal Nucl Chem 296:363–368

56. Plionis A, Gonzales ER, Landsberger S, Peterson D (2009) Evaluation of flow scintillation analysis for the determination of Sr-90 in bioassay samples. Appl Radiat Isot 67:14–20
57. Grahek Z, Dulanska S, Karanovic G, Coha I, Tucakovic I, Nodilo M, Matel Ľ (2018) Comparison of different methodologies for the ^{90}Sr determination in environmental samples. J Environ Radioact 181:18–31
58. Ritika D, Sawant PD, Bhade SPD, Kulkarni MS (2020) Development of extractive liquid scintillation spectrometry for the determination of Sr-90 in urine samples for emergency bioassay. In: Proceedings of 34th IARPNC-2020, p 222
59. Visser G (2016) The application of Sr-spec resin in the analysis of ^{90}Sr in effluent and environmental samples at KNPS. Cape Peninsula University of Technology, Peninsula. http://hdl.handle.net/20.500.11838/2327
60. Wankhede SM, Sawant PD, Rao DD, Pradeep Kumar KS (2014) A rapid bioassay method for strontium estimation in nuclear/radiological emergencies. Radiat Prot Environ 37(2):95–100
61. Kramer GH, Davies JM (1982) Isolation of strontium-90, yttrium-90, promethium-147, and cerium-144 from wet ashed urine by calcium oxalate coprecipitation and sequential solvent extraction. Anal Chem 54(8):1428–1431
62. Tsroya S, German U, Pelled O, Katorza E, Alfassi ZB (2013) Determination of ^{90}Sr–^{90}Y activity in urine samples by using Cherenkov counting. Appl Radiat Isot 73:12–16
63. Yoon S, Pak MJ, Park S, Yoo J, Ha WH, Jang HK, Kim JK (2014) ^{32}P measurement of urine samples and internal dose assessment for radiation workers in life science laboratories. J Radiol Prot 34(4):775–785
64. Yang Y, Ma Y, Wang Y, Dai X (2020) A rapid screening method for ^{32}P in urine samples by TDCR Cerenkov measurement. J Radioanal Nucl Chem. https://doi.org/10.1007/s10967-020-07304-4
65. Wankhede SM, Sawant PD, Yadav RB, Rao DD (2016) Methodology for estimation of phosphorus-32 in bioassay samples by Cerenkov counting. Radiat Prot Environ 39:149–154
66. Preedy VR (2009) Comprehensive handbook of iodine. Academic Press, Elsevier Publication
67. Ching YC, Robert YLC (1990) Bioassay for iodine-125. J Nucl Med Technol 18(2):98–101
68. Jimenez F, Deban L, Pardo R, García-Talavera P (2012) Combination of liquid scintillation counting and passive sampling strategy for the determination of ^{131}I in air and application to estimate the inhalation dose to the staff of a nuclear medicine service. J Environ Sci Health A Tox Hazard Subst Environ Eng 47(12):1843–1848
69. Sankhla R, Singh IS, Rao DD (2015) Development of thyroid monitoring system for measurement of iodine 125. In: Proceedings of NUCAR 2015, pp 648–649
70. Bhade SPD, Sankhla R (2023) Standardization of a liquid scintillation counting based methodology for quantification of ^{125}I in urine sample. In: Book of abstracts, 6th Asian and oceanic congress for radiation protection (AOCRP-6), pp S186–S187
71. Eckert & Ziegler (2010) Recommended nuclear decay data: ^{55}Fe. Nuclitec GmbH
72. ICRP Publication 69 (1995) Age-dependent doses to members of the public from intake of radionuclides: part 3 ingestion dose coefficients. Pergamon, Oxford
73. Guerin N, Dai X (2015) Determination of ^{55}Fe in urine by liquid scintillation counting. J Radioanal Nucl Chem 304:1059–1069
74. Hou X (2018) Liquid scintillation counting for determination of radionuclides in environmental and nuclear application. J Radioanal Nucl Chem 318:1597
75. Application note, HIDEX 300SL 453 TM, DOC 413-001 version 1.0
76. Bhade SPD, Kulkarni DB, Sankhla R, Sawant PD (2021) Development of methodology to estimate ^{55}Fe in aqueous samples using LSC technique. In: Proceedings of 15th biennial DAE-BRNS symposium on nuclear and radiochemistry (NUCAR-2021), p 189
77. Skwarzec B, Holm E, Struminska D (2001) Radioanalytical determination of ^{55}Fe and ^{63}Ni in the environmental samples. Chem Anal (Warsaw) 46:23
78. Cregan SP, Leon JW, Linauskas SH (1993) Bioassay techniques for ^{55}Fe in urine samples. CA9500471, AECL-10778, COG-92-398
79. Warwick PE, Croudace IW (2006) Isolation and quantification of ^{55}Fe and ^{63}Ni in reactor effluents using extraction chromatography and liquid scintillation analysis. Anal Chim Acta 567:277–285

80. Knoll GF (2010) Radiation detection and measurement, 4th edn. ISBN: 978-0-470-13148-0
81. Gonzalez CH, Bercedo IS (2019) Rapid procedure for actinides and ^{90}Sr analysis in emergency urine spot samples applied in the GHSI-RNWG emergency intercomparison exercise. Appl Radiat Isot 144:19–23
82. Prabhu SP, Reddy PJ, Wankhede SM, Panda S, Raveendran N, Sawant PD, Chaudhury P, Kulkarni MS (2023) Emergency radiobioassay methodologies for first responders & public approach. BARC Newsl (387). ISSN: 0976-2108
83. Bhade SPD, Ajay K, Reddy PJ, Kolekar RV, Rajvir S, Pradeepkumar KS (2015) Comparison of radiometric and non-radiometric methods for uranium determination in groundwater of Punjab, India. J Radioanal Nucl Chem 307(1):395–405
84. Bhade SPD, Reddy PJ, Anil Kumar S, Kolekar RV, Singhal RK, Singh R (2017) Study of liquid scintillation α spectral properties. Appl Radiat Isot 122:121–126
85. Reese RP, Shanks ST, Preston RT (2007) Optimization of screening for radioactivity in urine by liquid scintillation. Sandia report, SAND2007-5312
86. Sas D, Janda J (2017) Rapid determination of gross alpha/beta activity in urine with LSC. J Radioanal Nucl Chem 311(1):23–27
87. Piraner O, Jones R (2021) Urine gross alpha/beta bioassay method development using liquid scintillation counting techniques. J Radioanal Nucl Chem 327(1):513–523
88. Li C, Vlahovich S, Dai X, Richardson RB, Daka JN, Kramer GH (2010) Requirements for radiation emergency urine bioassay techniques for the public and first responders. Health Phys 99(5):702–707
89. Li CI (2011) International workshop on emergency radiobioassay: considerations, gaps and recommendations. Health Phys 101(2):107–111
90. Bhade SPD, Reddy PJ, Narayanan A, Narayan KK, Babu DAR, Sharma DN (2010) Standardization of calibration procedures for quantification of gross alpha and gross beta activities using liquid scintillation counter. J Radioanal Nucl Chem 84:367–375
91. Shoji M, Kondo T, Honoki H, Nakajima T (2007) Investigation of monitoring for internal exposure by urine bioassay in a biomedical research facility. Radiat Prot Dosim 127(1–5):456–460
92. Piraner O, Jones RL (2009) Urine gross alpha/beta analysis by liquid scintillation counting for terrorism preparedness. In: Eikenberg J, Jaggi M, Beer H, Baehrle H (eds) Advances in liquid scintillation spectrometry, 2008. Radiocarbon Publishers, University of Arizona, Tucson, pp 41–46
93. Yoon S, Ha WH, Yoo J, Lee SS (2014) Screening of alpha- and beta-emitting radionuclides using liquid scintillation counting and monitoring procedures in radiation emergencies. Health Phys 107(5):382–387
94. Yoon S, Kim Y, Ha WH, Jin YW (2018) Screening criteria for the general public in radiation emergencies from liquid scintillation urinalysis. Health Phys 114(1):27–31
95. Piraner O, Jones R (2020) The effect of quench agent on urine bioassay for various radionuclides using Quantulus™1220 and Tri-Carb™3110. J Radioanal Nucl Chem 326(1):657–663
96. United States Environmental Protection Agency (USEPA) (1991) Part 2. CFR parts 141, 142, national primary drinking water regulations; radionuclides; proposed rule. Fed Reg 56(138):33072
97. Garcia-Torano E (2006) Current status of alpha-particle spectrometry. Appl Radiat Isot 64(10–11):1273–1280
98. Herranz M, Idoeta R, Abelairas A, Legarda F (2006) Radon fixation for determination of ^{224}Ra, ^{226}Ra and ^{228}Ra via gamma-ray spectrometry. Radiat Meas 41(4):486–491
99. Copia L, Nisi S, Plastino W (2015) Low-level ^{226}Ra determination in groundwater by SF-ICP-MS: optimization of separation and pre-concentration methods. J Anal Sci Technol 6:22
100. Blackburn R, Al-Masri MS (1993) Determination of radon-222 and radium-226 in water samples by Cerenkov counting. Analyst 118:873–876
101. Ariffin NAN, Mahmood Z, Mohamed R (2011) Application of in-house method for determination of radium isotopes in environmental samples using the liquid scintillation counting technique. J Anal Sci Methods Instrum 1:1–8

102. Bhade SPD, Reddy PJ, Anil Kumar S, Singhal RK, Rao DD (2018) Calibration and optimization of α/β separation procedures for determination of radium/radon in single- and two-phase liquid scintillation systems. J Radioanal Nucl Chem 315:13–20
103. Kim G, Burnett W, Dulai H, Swarzenski P, Moore W (2002) Measurement of ^{224}Ra and ^{226}Ra activities in natural waters using a radon-in-air monitor. Environ Sci Technol 35:4680–4683
104. Dowdall M, Selenaes OG, Gwynn JP, Davids C (2004) Simultaneous determination of ^{226}Ra and ^{238}U in soil and environmental materials by gamma-spectrometry in the absence of radon progeny equilibrium. J Radioanal Nucl Chem 261:513–521
105. Sadi BB, Li C, Kramer GH (2012) An emergency radio-bioassay method for ^{226}Ra in human urine samples. Radiat Prot Dosim 151(1):10–16
106. International Commission on Radiological Protection (1986) The metabolism of plutonium and related elements. ICRP publication 48. Ann ICRP 16:2–3
107. International Commission on Radiological Protection (1993) Age-dependent doses to members of the public from intake of radionuclides—part 2 ingestion dose coefficients. ICRP publication 67. Ann ICRP 23:3–4
108. Helal AI, Zahran NF, Amr MA, Abd El-Lateef AM, Bashter II, Mohsen HT, Abbas Y (2004) Ultra-trace and isotope ratios analyses of some radionuclides by ICP-MS. Radiochim Acta 92:369–374
109. Arginelli D, Berton G, Bortoluzzi S, Canuto G, Montalto M, Nocente M, Ridone S, Vegro M (2008) Purification and separation of $^{239+240}$Pu and ^{241}Am in biological samples by anion-exchange and extraction chromatography for high resolution alpha-spectrometry analyses. J Radioanal Nucl Chem 277:65–71
110. McDowell WJ, Henley LC (1972) An evaluation of the possibility of identifying alpha emitters in low-count-rate samples using some new liquid scintillation counting techniques, ORNL-TM-3676, p 13
111. McDowell WJ, Coleman CF (1973) Some methods of controlling quenching in extractive scintillators for liquid scintillation counting of alpha-emitting nuclides. Anal Lett 6(9):795–799
112. Shaw PG (1989) International conference on new trends in liquid scintillation counting and organic scintillators. Gatlinburg, TN
113. Yang D, Zhu Y, Möbius S, Keller C (1991) Rapid method for alpha counting with extractive scintillator and pulse shape analysis. J Radioanal Nucl Chem Lett 144(1):63
114. Yang D, Zhu Y (1991) International topical conference on methods and applications of radioanalytical chemistry II (MARC-2). In: Abstracts: American nuclear society, 16. RN: CONF-910422, Kona, HI
115. Yang D, Zhu Y, Jiao R (1994) Determination of Np, Pu and Am in high level radioactive waste with extraction liquid scintillation counting. J Radioanal Nucl Chem 183(2):245–260
116. Panda S, Reddy PJ, Yadav JR, Sawant PD, Kulkarni MS (2022) Development of a rapid technique for sequential separation of plutonium/americium in nasal swab using solvent extraction and liquid scintillation spectrometry. Appl Radiat Isot 186:110297
117. Diaconu S, Predescu A, Moldoveanu A, Pop CS, Fierbinţeanu-Braticevici C (2017) *Helicobacter pylori* infection: old and new. J Med Life 10(2):112–117
118. Blaser MJ (1998) *Helicobacter pylori* and gastric diseases. BMJ 316:1507–1510
119. Kusters JG, van Vilet AHM, Kuipers EJ (2006) Pathogenesis of *Helicobacter pylori* infection. Clin Microbiol Rev 19(3):449–490
120. Savarino V, Vigneri S, Celle G (1999) The ^{13}C urea breath test in the diagnosis of *Helicobacter pylori* infection. Gut 45:118–122
121. Tiwari BP, Nistala S, Patil SP, Kalgutkar DP, Jayachandran N, Chander H, Basu S (2014) Evaluation of the ^{14}C-urea breath test using indigenously produced ^{14}C-urea capsules and a modified technique for trapping exhaled breath: a pilot study. Nucl Med Commun 35:325–330
122. Swaroop K, Jayachandran, Patil SL, Somashekarappa HM (2011) A study of *Helicobacter pylori* infection using the ^{14}C UBT method. Radiat Prot Environ 34(3):206–209
123. Kolekar RV, Gadgil A, Bhade SPD, Reddy PJ, Bhandarkar P, Roy N, Patil SP, Singh R (2016) Study on urea breath test a tool for *Helicobacter pylori* infection. Radiat Prot Environ 39(3):146–148

Radiation Dose Assessment in Nuclear Medicine

Kamaldeep

1 Introduction

Nuclear Medicine is a branch of clinical medicine where unsealed radioactive sources (radiotracers or radiopharmaceuticals) are used for diagnosis and/or treatment of various diseases. Radiotracers or radiopharmaceuticals are the chemical compounds which consist of a target specific molecule, labeled with a radioactive substance, and used to deliver the radioactive substance to specific parts of the body. These radiotracers or radiopharmaceuticals, are administered to the patients via intravenous or oral route. The distribution of a radiotracer and its temporal changes in the body are traced by using external measurement of emitted penetrating radiations for obtaining diagnostic information of various diseased states. During the treatment of various disease states by using radiopharmaceuticals, higher amount of radioactivity is administered to the patients with the intent of exploiting the ability of radiations emitted from the radiopharmaceuticals, to kill the cancerous/diseased cells at the target site [1]. In nuclear medicine it is desirable to assess the benefits and risks from a particular nuclear medicine procedure, and assure that the benefits accrued from the procedure outweigh the radiation related risks [2]. This assessment can only be performed provided one knows the radiation dose delivered to the patient for the given nuclear medicine procedure. In nuclear medicine it is difficult to estimate the radiation absorbed dose directly using some radiation detector system. Instead, dose is estimated with the help of standardized phantoms or mathematical models using physical and biological data of the patients [3]. In diagnostic nuclear medicine procedures, absorbed dose estimates from standardized phantom or models may be appropriate as the amount of radioactivity administered is less, hence absorbed dose levels are far less. In case of therapeutic nuclear medicine, more individualized dose estimations are preferred. Several studies published in the

Kamaldeep (✉)
Health Physics Division, Bhabha Atomic Research Center, Mumbai 400085, India
e-mail: kdeep@barc.gov.in

D. K. Aswal (ed.), *Handbook on Radiation Environment, Volume 2*,
https://doi.org/10.1007/978-981-97-2799-5_23

literature [4–9] suggested that individualized dose estimates can prevent unwanted therapies, improve therapeutic efficacy, and provide the platform for advancement in the field of radionuclide therapies. In nuclear medicine procedures, the absorbed dose to an organ/tissue is governed by radiopharmaceutical uptake, its retention and clearance from the organ/tissue along with radioisotope physical half-life. Nuclear medicine community currently does not have adequate resources for collection of useful biokinetic or dosimetric data for radionuclide therapy procedures.

Currently, radionuclides therapies are conducted with the 'one-size-fits-all' protocol where all the patients are injected with similar amount of the radiopharmaceutical compound [5]. Consequently, a large inter-patient variability in dose to organ at risk and the tumor target, which is far from optimal, were observed and reported in literature [6, 7]. The empiric, fixed dose regimen adopted widely may result in suboptimal treatment with a low dose to the tumor in patients, particularly those having high tumor burden. In view of this, there is need of patient-specific dosimetry in patients undergoing radionuclide therapy. The administered activity may be tailored for each individual patient such that the highest possible absorbed dose may be delivered to the tumor while restricting the absorbed dose to critical organs/tissues below the threshold dose to limit the onset of any deterministic effect to these organs. This chapter describes the method for calculating the absorbed doses to the tumor and normal organs from radionuclides administered for cancer treatment.

2 Nuclear Medicine Radiation Dosimetry

For successful therapy, dosimetry has been considered as a useful tool, and this would allow maximizing the therapeutically administered radioactivity in patients with low risk for toxicity thus reducing the administered radioactivity in patients with high risk for toxicity. In principle, a personalized dosimetric approach based on patient specific measurements can ensure the administration of a minimal effective radiopharmaceutical compound, thereby minimizing the potential for long-term risk to the patients. The fixed dosage administration protocols result in the delivery of a very wide range of absorbed doses to the target organs [10]. In 1946, Seidlin et al. [11] had calculated the cumulative absorbed doses to the metastases and later many studies published in literature [12, 13] have used a blood absorbed dose of 2 Gy as a surrogate biomarker for bone marrow toxicity, 300 Gy to ablate thyroid remanent tissue, and 80 Gy to eradicate lymph node metastases.

The professional bodies which have immensely contributed in the development of radiation dosimetry in nuclear medicine are the *International Commission on Radiological Protection (ICRP)* and the *Medical Internal Radiation Dose (MIRD)* Committee of the American Society of Nuclear Medicine [14, 15]. However, the objective of both professional bodies is somewhat different. ICRP mission is to emphasize the radiological protection of the worker who is occupationally (knowingly or accidentally) exposed to ionizing radiation. On the other hand, the MIRD Committee provides guidelines, reports, and methods of absorbed dose estimation

exclusively for the nuclear medicine patient. Since 1968, the MIRD schema has provided a broad framework for the assessment of the absorbed dose to the organs (as a whole), subregions in the tissue, voxelized tissue structures, and individualized cellular compartments from internally deposited radionuclides for use in both diagnostic and therapeutic nuclear medicine [16, 17]. At the same time ICRP also formulated an almost identical dosimetry schema that includes physical quantities such as absorbed dose, in addition, it has defined the radiation protection quantities; equivalent dose and effective dose, to take account of relative biological effectiveness (RBE) of all types of emitted radiations from the radiation sources and the radiosensitivity of the individual organs to radiation induced stochastic effects (cancer induction due to mutation of somatic cells or heritable effects due to mutations of germ cells) [18, 19]. ICRP has also come out with a series of publications on radiation absorbed dose profiles of many radiopharmaceuticals used in nuclear medicine and give recommendations on medical radiation exposure safety [20–24]. Both professional bodies i.e., ICRP and MIRD committee have developed parallel algorithms for internal dose estimation, and these algorithms developed by both these professional bodies are virtually identical as each uses the concepts of the source region where the radiopharmaceutical is concentrated, and the target region where the absorbed dose to be estimated, absorbed fraction in the target region, specific absorbed fraction in the target region, reference computational phantoms for dosimetry and compartmental models for dosimetry describing biokinetic distributions of activity in the human body. These two-dosimetry schema differs in nomenclature of fundamental quantities and target application. To bridge this gap MIRD committee has published a pamphlet Number 21 [15]. In this pamphlet; (1) the MIRD Committee restates the MIRD schema for absorbed dose estimation in a manner consistent with the needs of both the radiation protection and nuclear medicine communities using a standardized nomenclature, (2) adoption of equivalent dose and effective dose by MIRD committee for carrying out comparative evaluation of radiation-induced risks of stochastic effects in patients who had undergone nuclear medicine procedures, and (3) committee also advocates the need of dosimetry quantities for addressing the deterministic effects (due to cell death or impairment of organ function after high absorbed doses and dose rates) associated with radionuclide therapy.

2.1 The International Commission on Radiological Protection Method

The ICRP internal dosimetry model is almost identical to that of the MIRD committee [25]. Since ICRP mainly focuses on radiological protection of radiation workers, hence, in ICRP method, the committed equivalent dose is calculated rather than the absorbed dose. The committed equivalent dose is the total equivalent dose received by the target region T in a period of 50 years following uptake of a radionuclide. As per ICRP Publication 30 [25], its expression is,

$$H_{50,r_T} = k \sum_{r_S} U_{r_s} \mathrm{SEE}(r_T \leftarrow r_S) \tag{1}$$

where, k is a constant ($k = 1.6 \times 10^{-13}$ Gy kg/Bq s) for the matching of units (the committed effective dose has units of sieverts), U_{r_s} is the total number of transformations in source region r_S over a period of 50 years following intake of the radionuclide (cumulated activity in the source region r_S) (Bq s) and $\mathrm{SEE}(r_T \leftarrow r_S)$ is the specific effective energy, equivalent to the modified MIRD S-factor with the radiation weighting factor w_R, its unit is Sv/(Bq s). In this equation, r_T represents a target region and r_S represents a source region.

$$\mathrm{SEE}(r_T \leftarrow r_S; t) = \frac{\sum_i w_R E_i Y_i \mathrm{AF}(r_T \leftarrow r_S; E_i; t)}{m(r_T, t)} \tag{2}$$

where, w_R is the radiation weighting factor, E_i is the energy in MeV of radiation i, Y_i is the yield of radiation i of energy E, $\mathrm{AF}(r_T \leftarrow r_S; E_i; t)$ is the absorbed fraction i.e. fraction of radiation energy E_i absorbed in the target region r_T per emission of radiation i within the source region r_S at time t, and $m(r_T, t)$ is the time-dependent mass of the target region r_T in the reference individual.

For decades, ICRP has developed dose coefficients and other guidance related to calculating doses to patients undergoing nuclear medicine procedures using radiopharmaceuticals. The dose coefficients presented in ICRP publications 106 (ICRP, 2008) [23], 128 (ICRP, 2015a) [24], 53 (ICRP, 1987) [20] and 80 (ICRP, 1998) [22] are intended for diagnostic nuclear medicine and not for therapeutic applications. Recently, ICRP in its publication ICRP 140 [26], provided a framework to perform individual dosimetry to plan therapeutic procedures and to verify the absorbed dose delivered to various organs and to the tumors.

2.2 *Medical Internal Radiation Dose (MIRD) Schema*

The MIRD schema was primarily developed for estimating the radiation doses received by patients who were administered with radiopharmaceuticals. This scheme is not intended to be applied to a system of dose limitation for workers. In 1968, MIRD Committee provided its first set of instructions on nuclear medicine dosimetry calculations [27]. Since then, the MIRD schema has evolved to accommodate modern anatomical views by computed tomography (CT) or magnetic resonance imaging (MRI), voxel-level activity distributions, Monte Carlo energy transport codes, pharmacokinetic compartment models, and radiobiological response parameters. In recent years, nuclear medicine dosimetry has become a well-known field and it provides a measure of the absorbed dose (i.e., the integral of the absorbed dose rate) to a target region due to a temporally varying amount of activity in a source region (Fig. 1). The source region and target region may be the same region, in fact in radionuclide therapy the most important contributor to the radiation absorbed dose is

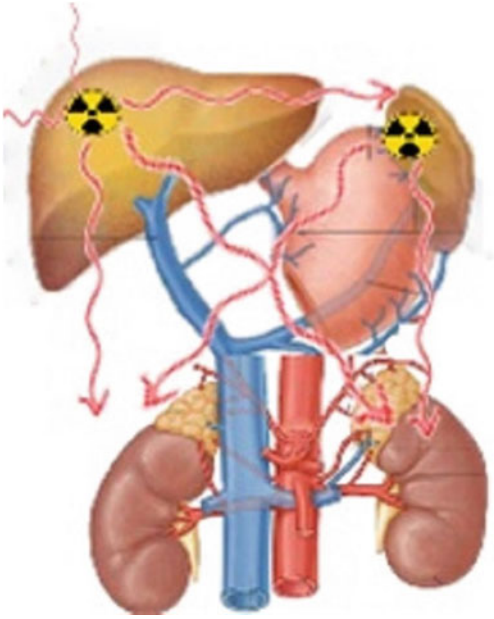

Fig. 1 Absorbed dose delivered to a target region from one or more source region containing radioactivity. Adapted from gray's anatomy for students [28]

cumulative activity present in the target region itself. The estimation of the radiation absorbed dose to the target region from the radioactivity present in the source organ is a three-step process [17]; (1) Quantification of amount of radioactivity and the duration of time for which the radioactivity is present in the source region, (2) Calculation of total amount of radiation energy emitted by the time integrated activity present in the source region, (3) Determination of fraction of radiation energy emitted from the source region that is absorbed by the target region. The separate absorbed dose contributions to the target region are summed over the various source regions and the result provides the total absorbed dose to the target region.

2.2.1 Time Integrated Activity

Time integrated activity (MIRD pamphlet 21, 2019 [15]), previously known as cumulative activity (MIRD Primer, 1991 [29]) is defined as the product of amount of radioactivity and the duration of time for which the radioactivity is present in the source region. It is denoted by $\tilde{A}_{r_S}$. Its SI unit is becquerel-second (Bq s) and the traditional unit is μCi h (1 μCi h $= 1.332 \times 10^8$ Bq s). It gives the total number of disintegrations occurring during the time-period when radioactivity is present in the source region. It has a direct relationship with the absorbed dose to the target region; higher the cumulative activity present in the source region, higher will be the absorbed dose to the target region. In case of nuclear medicine procedures, each radiopharmaceutical has its own biodistribution pattern in the body depending upon

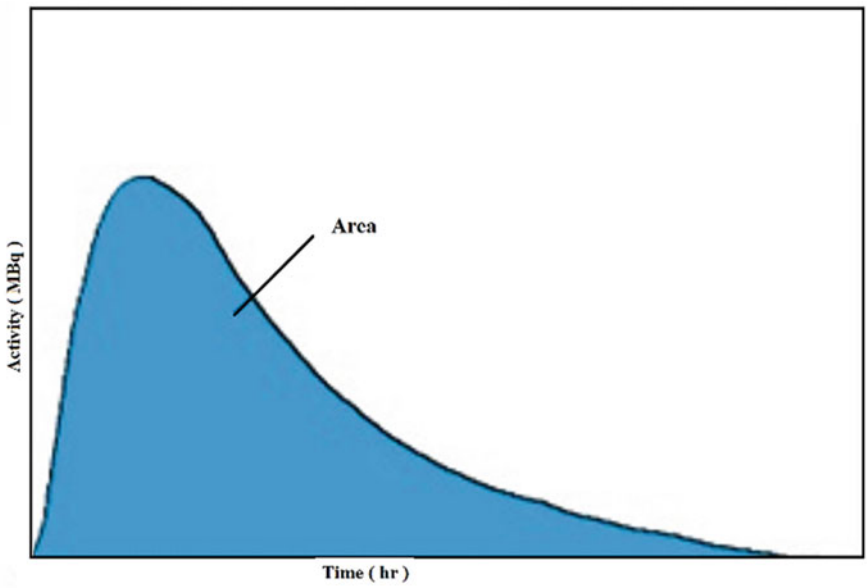

Fig. 2 Time activity curve for a radiopharmaceutical in a source region

the uptake of the radiopharmaceutical in the organ/tissue, its metabolism, biological clearance and excretion from the source region, and the physical decay of the radionuclide labeled in the radiopharmaceutical. Therefore, the amount of radioactivity present in a source region changes with time. If the time-activity curves of a given radiopharmaceutical, for a particular-source region is known, then cumulative activity in the source region can be obtained by calculating the area under the curve (Fig. 2).

Mathematically, cumulative activity is expressed as:

$$\tilde{A}_{r_S} = \int_{t}^{\infty} A(t)\mathrm{d}t \tag{3}$$

It is assumed that the radiopharmaceutical is administered to the patient at time $t = 0$ and is measured for complete clearance from the source region ($t = \infty$).

$$\tilde{A}_{r_S} = 1.44\, T_{\mathrm{eff}} A_0 \tag{4}$$

where, $A(t)$ is the radioactivity present in the source region r_S at a given time $= t$; A_0 is the administered activity at $t = 0$; T_{eff} is the effective half-life of the radionuclide in the source region.

$$T_{\text{eff}} = \frac{T_{\text{P}} T_{\text{B}}}{(T_{\text{P}} + T_{\text{B}})} \tag{5}$$

where, T_{P} is the physical half-life of the radionuclide; T_{B} is the biological half-life of the radionuclide in the source region or it is the time-period in which radioactivity from the source region is cleared to half of its original value by biological means.

2.2.2 Equilibrium Dose Constant

It is defined as the average energy emitted per nuclear transformation in the source region. It is denoted by Δ. Its SI unit is Gy kg/Bq s and traditional unit is rad g/μCi h. Equilibrium dose constant mainly depends on the energy of the radionuclide emissions and their frequency of emissions.

Consider a radionuclide which emits only one type of radiation of energy E (MeV) per decay.

1 Bq of this radionuclide will, thus, emit energy at a rate of

$$\Delta = 1 \times E \ \frac{\text{MeV}}{\text{Bq s}} \tag{6}$$

$$\Delta = 1.6 \times 10^{-13} \times E \ \frac{\text{J}}{\text{Bq s}} \tag{7}$$

$$\Delta = 1.6 \times 10^{-13} \times E \ \frac{\text{Gy kg}}{\text{Bq s}} \tag{8}$$

where, 1 MeV $= 1.6 \times 10^{-13}$ J and 1 J = 1 Gy kg.

If a radionuclide emits more than one radiation then

$$\Delta_i = 1.6 \times 10^{-13} \sum_{i}^{n} Y_i E_i \ \frac{\text{Gy kg}}{\text{Bq s}} \tag{9}$$

where, E_i is the energy emitted by the ith radiation and Y_i = yield of the ith radiation.

In traditional unit:

$$\Delta_i = 2.13 \sum_{i}^{n} Y_i E_i \ \frac{\text{rads g}}{\mu\text{Ci h}} \tag{10}$$

2.2.3 Absorbed Fraction

Absorbed fraction is defined as the ratio of the energy absorbed by the target region r_{T} from the ith radiation to the energy emitted from the source region r_{S} by the ith

radiation. In other words, it is the absorbed dose in the target region per nuclear disintegration in the source region.

It is denoted by $\phi_{i_{(r_T \leftarrow r_S)}}$. It is a unitless quantity and is given by:

$$\phi_{i_{(r_T \leftarrow r_S)}} = \frac{\text{Energy absorbed in the target organ per nuclear transformation}}{\text{Energy released in the source organ per nuclear tranformation}} \tag{11}$$

The absorbed fraction depends on the size, shape and geometry of the target and source organs, and on the characteristics of radiation.

In case of non-penetrating radiations

When source organ and target organ are same; $\phi_{i_{(r_T \leftarrow r_S)}} = 1$.
When source organ and target organ are different; $\phi_{i_{(r_T \leftarrow r_S)}} = 0$.

The absorbed fraction for the penetrating radiation varies from 0 to 1 depending on the size and shape of the source and target organs, and the distance between the source and target organs and energy of the radiation.

In a dosimetry calculation, a value of ϕ must be determined for each type of emission from the radionuclide and for each source–target pair in the calculation. The values of the absorbed fractions are calculated based on the Monte Carlo nuclear transport code that accounts for individual geometry, tissue compositions, and absorber densities. These values are tabulated in many MIRD pamphlets and MIRD primers for different types and energies of emissions from the radionuclide and different source–target pairs.

The total energy absorbed by a specific target organ is given as

$$\text{Total energy absorbed (Gy kg)} = \tilde{A}_{r_S} \sum_i \phi_{i_{(r_T \leftarrow r_S)}} \Delta_i \tag{12}$$

2.2.4 Mean Absorbed Dose

The total energy absorbed by a specific target organ divided by the target organ mass, M_{r_T} gives the mean absorbed dose ($D_{(r_T \leftarrow r_S)}$) to the target region from the time integrated activity in the source organs.

$$D_{(r_T \leftarrow r_S)} = \frac{\tilde{A}_{r_S}}{M_{r_T}} \sum_{i=1}^{n} \Delta_i \phi_{i_{(r_T \leftarrow r_S)}} \tag{13}$$

This equation is also called as general absorbed dose equations in the MIRD schema which apply to all types of radiations and targets. The simplified form of the general absorbed dose equation is:

$$D = \tilde{A}_{r_S} \cdot S_{(r_T \leftarrow r_S)} \tag{14}$$

The value of S is given as

$$S_{(r_T \leftarrow r_{S,T})} = \frac{\sum_{i=1}^{n} \Delta_i \phi_{i(r_T \leftarrow r_S)}}{M_{r_T}} \tag{15}$$

S is the mean absorbed dose per unit cumulated activity, commonly referred to as the S-value (sometimes also known as the dose factor, DF). It has SI units of Gy/Bq s and traditional unit of rad/μCi h. MIRD has complied 'S' factors for more than 110 radionuclides' and 20 source target combinations [2]. Now a days, many dosimetry software are commercially available, which have built-in S values and the weight of the organs of human phantoms, in these software, where the users enter the total number of disintegrations in the source regions and the absorbed dose to the target organs can be computed.

2.2.5 Specific Absorbed Fraction and Dose Reciprocity Theorem

The absorbed fraction per unit mass of the target organ is known as the specific absorbed fraction

$$\Phi_{i(r_T \leftarrow r_S)} = \frac{\phi_{i(r_T \leftarrow r_S)}}{M_{r_T}} \tag{16}$$

In other words, it is defined as the fraction of radiation emitted in the source region that is absorbed per unit mass of the target region.

According to dose reciprocity theorem for a given pair of source and target regions the specific absorbed fraction is the same, regardless of which region is the source or target;

$$\Phi_{i(r_T \leftarrow r_S)} = \Phi_{i(r_S \leftarrow r_T)} \tag{17}$$

3 Radiation Dosimetry Softwares

Carrying out radiation dosimetry by using manual calculations for different source and target combinations is a daunting and time-consuming proposition. Alternatively, a software presents a practical means of calculating the absorbed dose to the target region from different source regions. There are many software developed for radiation dosimetry and some of them are in current use. Few examples of available software are MIRDOSE (MIRDOSE 1, MIRDOSE 2 and MIRDOSE 3), OLINDA/EXM (OLINDA 1.0, OLINDA 1.1, OLINDA 2.0, OLINDA 2.1, OLINDA 2.2), IDAC-Dose 2.1, DOSIsoft and many others based on the Monte Carlo code (OEDIPE,

MABDOSE, MINERVA) [30]. In literature, the OLINDA/EXM software is extensively used in many dosimetric studies in nuclear medicine therapeutic procedures and details of this software are given below.

OLINDA/EXM

OLINDA/EXM, short for Organ Level Internal Dose Assessment/Exponential Modeling, is a computer program created in 2004 to compute radiation absorbed doses and kinetic modeling for radiopharmaceuticals [31]. This software determines the radiation doses absorbed by various organs, tissues, or tumors of individuals receiving systemically administered radiopharmaceuticals. It also conducts regression analysis on biokinetics data provided by users to facilitate calculations for nuclear medicine drugs.

These computations play a vital role in assessing the risk-versus-benefit ratio of both established and newly developed pharmaceuticals for diagnostic and therapeutic purposes in nuclear medicine. They involve the utilization of various standard body models designed for adults, children, pregnant women, and other specific demographics, widely recognized and employed within the internal dose community. OLINDA version 1 adopted largely similar calculation methodologies as MIRDOSE, with several updates. These include the incorporation of nearly 600 additional radionuclides, encompassing alpha emitters, introduction of new organ phantoms, refinement of the bone model, implementation of a code for analyzing biokinetic data kinetics, and the capability to adjust organ masses to patient-specific values.

OLINDA version 2 introduces several significant enhancements [32], including:

- Incorporation of over 1000 radionuclides, encompassing alpha emitters.
- Introduction of next-generation, voxel-based realistic phantoms representing both male and female subjects across six different age groups: newborn, 1 year, 5 years, 10 years, 15 years, and adult, including pregnant women at 3, 6, and 9 months of gestation.
- Integration of voxel-based realistic phantoms for 3 mouse, 5 rat, and 2 dog models, enabling more precise animal dosimetry assessments.
- Adoption of a new set of decay data based on ICRP 107 standards, ensuring updated and accurate data for dosimetry calculations.
- Inclusion of an option to incorporate radionuclide decay series, allowing for more comprehensive dosimetry analyses.
- Incorporation of new tissue weighting factors based on ICRP 103 guidelines, improving the accuracy of dose calculations.
- Implementation of a code for kinetic analysis of biokinetic data, facilitating more detailed analysis of radionuclide kinetics.
- Capability to adjust organ masses to patient-specific values, enhancing individualized dosimetry assessments.
- Ability to assign activity to the walls of hollow organs, providing more accurate dosimetry calculations for these structures.

4 Challenges in Radiation Dose Assessment

Accurately assessing radiation doses in nuclear medicine procedures poses a significant challenge, primarily due to the need for precise determination of the biokinetics of radiopharmaceuticals within normal organs and tumors. This involves understanding the uptake time, retention time, and clearance of radiopharmaceuticals from these regions. Biokinetics are typically determined through direct measurements, such as nuclear medicine imaging, as well as direct bioassays involving blood, excreta, and tissue biopsy counting. Direct measurements using imaging techniques must consider various factors to ensure accuracy. These include the geometry and density of the source organ or tumor, its size and mass, potential overlap by surrounding tissues or organs, the distance between the tissue or organ and the detector, and the spatial distribution of activity within the tissue or organ. Additionally, factors such as detector background, detector dead time, and photon attenuation and scatter can influence the accuracy of direct counting when measuring the correct amount of time-integrated activity.

In nuclear medicine, organ activity measurements are often conducted using calibrated nuclear imaging systems, which include planar gamma cameras (anterior/posterior imaging), SPECT, PET, and single crystal photon detectors (such as sodium iodide or other scintillators). When precise quantification of radiopharmaceuticals in tumors or organs isn't feasible, estimates of radioisotope quantity can be derived using biokinetic modeling for those organs. The accuracy of this assessment relies heavily on the validity of the biokinetic model employed. Dosimetric modeling can be valuable in situations where data are scarce, but these models are typically not customized for individual patients. Therefore, potential inaccuracies introduced by such models should be taken into account when interpreting the results.

5 Conclusion

The growing application of radiopharmaceuticals in cancer treatment holds promise for offering new therapeutic avenues to patients. A key challenge in all radionuclide therapies is to transition from a "one-size-fits-all" approach to a personalized dosing regimen. The goal is to optimize the efficacy of radiopharmaceuticals in treating cancer while minimizing the potential side effects and complications in normal tissues, aiming to maximize the therapeutic benefit.

In radionuclide therapy, the amount of radiation absorbed by an organ or tissue is influenced by individual patient biokinetics, including uptake, retention, and clearance, which can vary significantly from one patient to another. Therefore, measuring the biokinetics of radiopharmaceuticals is crucial for accurately assessing the internal radiation dose in patients undergoing radionuclide therapy. Given the variations in biokinetics among patients, personalized dosimetry must be conducted for each individual.

In essence, a fully personalized dose strategy based on patient-specific measurements can ensure that radionuclide therapy is administered at an appropriate radioactivity level without surpassing toxicity thresholds in normal organs and tissues.

References

1. Volkert WA, Hoffman TJ (1999) Therapeutic radiopharmaceuticals. Chem Rev 99(9):2269–2292
2. Cherry SR, Sorenson JA, Phelps ME (2012) Physics in nuclear medicine, 4th edn. ISBN: 978-1-4160-5198-5
3. Chandra R (2004) Nuclear medicine physics: the basics, 6th edn. ISBN: 978-0-7847-4753-0
4. Stabin MA, Flux GD (2012) The use of dosimetry in the planning of patient therapy. In: Baum RP (ed) Therapeutic nuclear medicine, medical radiology. Radiation oncology. Springer-Verlag Berlin Heidelberg, Berlin. https://doi.org/10.1007/174_2012_739
5. Stabin MG (2008) Fundamentals of nuclear medicine dosimetry. ISBN: 978-0-387-74578-7
6. Jonsson H, Mattsson S (2004) Excess radiation absorbed doses from non-optimised radioiodine treatment of hyperthyroidism. Radiat Prot Dosim 108:107–111
7. Sisson JC, Avram AM, Rubello D et al (2007) Radioiodine treatment of hyperthyroidism: fixed or calculated doses; intelligent design or science? Eur J Nucl Med Mol Imaging 34:1129–1130
8. Strigari L et al (2014) The evidence base for the use of internal dosimetry in the clinical practice of molecular radiotherapy. Eur J Nucl Med Mol Imaging 41(10):1976–1988. https://doi.org/10.1007/s00259-014-2824-5
9. Chiesa C, Castellani MR, Vellani C, Orunesu E, Negri A, Azzeroni R, Botta F, Maccauro M, Aliberti G, Seregni E, Lassmann M, Bombardieri E (2009) Individualized dosimetry in the management of metastatic differentiated thyroid cancer. Q J Nucl Med Mol Imaging 53(5):546–61. PMID: 19910908
10. Flux GD, Haq M, Chittenden SJ et al (2010) A dose–effect correlation for radioiodine ablation in differentiated thyroid cancer. Eur J Nucl Med Mol Imaging 37:270–275
11. Seidlin SM, Marinelli LD, Oshry E (1946) Radioactive iodine therapy; effect on functioning metastases of adenocarcinoma of the thyroid. JAMA 132:838–847
12. Benua RS, Cicale NR, Sonenberg M et al (1962) The relation of radioiodine dosimetry to results and complications in the treatment of metastatic thyroid cancer. Am J Roentgenol Radium Ther Nucl Med 87:171–182
13. Maxon HR 3rd, Englaro EE, Thomas SR et al (1992) Radioiodine-131 therapy for well differentiated thyroid cancer—a quantitative radiation dosimetric approach: outcome and validation in 85 patients. J Nucl Med 33:1132–1136
14. Parland BJM (2010) Nuclear medicine radiation dosimetry. In: Advanced theoretical principles, vol XXXII. Springer-Verlag, London, p 610
15. Bolch WE, Eckerman KF, Sgouros G, Thomas SR (2009) MIRD pamphlet No. 21: a generalized schema for radiopharmaceutical dosimetry—standardization of nomenclature. J Nucl Med Off Publ Soc Nucl Med 50(3):477–484
16. Bolch WE, Bouchet LG, Robertson JS et al (1999) MIRD pamphlet no. 17: the dosimetry of nonuniform activity distributions: radionuclide S values at the voxel level. J Nucl Med 40(suppl):11S–36S
17. Howell RW, Wessels BW, Loevinger R, Watson EE, Bolch WE, Brill AB, Charkes ND, Fisher DR, Hays MT, Robertson JS et al (1999) The MIRD perspective 1999. Medical Internal Radiation Dose Committee. J Nucl Med Off Publ Soc Nucl Med 40(1):3s–10s
18. International Commission on Radiological Protection (2007) The 2007 recommendations of the international commission on radiological protection. ICRP publication 103. Ann ICRP 37(2–4)

19. International Commission on Radiological Protection (1990) 1990 recommendations of the international commission on radiological protection. ICRP publication 60. Ann ICRP 21(1–3)
20. International Commission on Radiological Protection (1987) Radiation dose to patients from radiopharmaceuticals. ICRP publication 53. Ann ICRP 18(1–4)
21. International Commission on Radiological Protection (1991) Radiation dose to patients from radiopharmaceuticals: addendum 1 to ICRP publication 53. ICRP publication 62. Ann ICRP 22(3)
22. International Commission on Radiological Protection (1998) Radiation dose to patients from radiopharmaceuticals: addendum 2 to ICRP publication 53. ICRP publication 80. Ann ICRP 28(3)
23. International Commission on Radiological Protection (2008) Radiation dose to patients from radiopharmaceuticals: addendum 3 to ICRP publication 53. ICRP publication 106. Ann ICRP 38(1/2)
24. International Commission on Radiological Protection (2015) Radiation dose to patients from radiopharmaceuticals: a compendium of current information related to frequently used substances. ICRP publication 128. Ann ICRP 44
25. International Commission on Radiological Protection (1979) Limits for intakes of radionuclides by workers. ICRP publication 30. Ann ICRP 2(3–4)
26. International Commission on Radiological Protection (2019) Recommendations of the international commission on radiological protection. ICRP publication 140. Ann ICRP 40(1)
27. Loevinger R, Berman M (1968) A schema for absorbed-dose calculations for biologically-distributed radionuclides. MIRD pamphlet no. 1. J Nucl Med 9(suppl 1):7–14
28. Richard LD, Wayne AV, Adam WMM (2015) Gray's anatomy for students, 3rd edn. ISBN: 978-0-7020-5131-9
29. Loevinger R, Budinger TF, Watson EE (1991) MIRD primer for absorbed dose calculations, Revised. The Society of Nuclear Medicine, New York, NY
30. McParland BJ (2010) Nuclear medicine dosimetry. In: McParland BJ (ed) Nuclear medicine radiation dosimetry: advanced theoretical principles. Springer London, London, pp 455–477
31. Stabin MG, Sparks RB, Crowe E (2005) OLINDA/EXM: the second-generation personal computer software for internal dose assessment in nuclear medicine. J Nucl Med Off Publ Soc Nucl Med 46(6):1023–1027
32. Stabin MG, Siegel JA (2018) RADAR dose estimate report: a compendium of radiopharmaceutical dose estimates based on OLINDA/EXM version 2.0. J Nucl Med Off Publ Soc Nucl Med 59(1):154–160

Internal Radioactive Contamination Monitoring During Off-Normal Situations

Rajesh Sankhla, Prathibha Pradosh, and Rahul Roy

1 Introduction

Hazards related to the radiation emergencies are due to the energy released from a nuclear chain reaction or from the daughter products or radiation exposure from a source.

The radiation emergencies can be classified as nuclear emergencies or radiological emergencies.

Nuclear Emergency

Nuclear emergencies involve the release of energy from a nuclear chain reaction or decay of the products from a chain reaction [1]. Nuclear Emergency may occur due to accidents at nuclear reactors (e.g., Chernobyl, Three Mile Island and Fukushima accidents), nuclear explosions/nuclear attack, sabotage of a nuclear facility (with fissile chain reaction initiated), detonation of Improvised Nuclear Device (IND), etc.

Radiological Emergency

Radiological emergencies are situations involving a radiation exposure from a radioactive source. It can involve a non-fissile radioactive material undergoing spillage, spread (e.g., Goiania) or due to accidents involving medical or industrial radiation sources, transport accident involving consignment of radioactive material, radioactive dispersal device (RDD)/Radiological exposure device, fire incidents involving radiation sources etc. When referring to an emergency situation regardless of its type, "radiation emergency" term is often used [1].

Radiation emergency is a major concern as it can impact human health and the environment considerably. The intensity of the impact will be dependent on the scale

R. Sankhla (✉) · P. Pradosh · R. Roy
Radiation Safety Systems Division, Bhabha Atomic Research Centre, Trombay, Mumbai 400094, India
e-mail: rsankhla@barc.gov.in

D. K. Aswal (ed.), *Handbook on Radiation Environment, Volume 2*,
https://doi.org/10.1007/978-981-97-2799-5_24

of emergency, type of radiation and exposure pathways, duration and the individual factors (age, gender, health condition) of the exposed individual. During a radiation emergency, people may get exposed to very low radiation doses which may not cause any clinical manifestations or to high doses which can cause radiation injuries and can even be fatal [1]. During a radiation emergency, there should be an immediate response from authorities, regulatory bodies, etc. for urgent protective actions to ensure that the damages caused by such a situation is minimum. Emergency preparedness and response strategies play a significant role in nuclear safety and security.

1.1 Scale of Nuclear and Radiological Emergencies

The International Nuclear and Radiological Event Scale (INES) was introduced in 1990 [2] by IAEA and the OECD Nuclear Energy Agency (OECD/NEA). The scale designed is used for prompt communication to the public about the safety significance of events. The nuclear events are classified into seven categories. Levels "1–3" are classified as incidents and Level "4–7" are classified as accidents. Events without nuclear safety relevance are classified as "Below scale/Level 0". In order of increasing severity, the distinct phrases have been attributed to each level of INES.

1.2 Scenarios Under Which Internal Contaminations Can Occur

A nuclear and radiological emergency can lead to radioactive contamination of the environment as well as human subjects. The radioactive contamination could be external or internal depending on the severity of the incident/accident. Different off-normal situations that may lead to internal radioactive contamination can be listed as

(i) Use of radiological dispersal device (RDD)
(ii) Sealed radioactive source incidents
(iii) Incidents involving contamination of food or water supplies
(iv) Transport accidents involving radioactive materials
(v) Improvised nuclear device
(vi) Nuclear reactor accidents
(vii) Incidents at other nuclear facilities.

Radiological Dispersal Device

A radiological dispersal device (RDD), which is commonly referred to as a "dirty bomb", uses either conventional explosives or some other mechanism to spread radioactive contamination [3]. A radioactive material can be incorporated into an

explosive device, detonation of which may lead to an explosion causing the spread of radioactive materials over a large area. Such an explosion can lead to high levels of external contamination as well as internal contamination of general public either by inhalation and ingestion or injection of radioactive materials through the wound. The commonly encountered radionuclides in such an emergency include ^{60}Co, ^{137}Cs, ^{192}Ir.

Sealed Radioactive Source Incidents

There are many incidents reported as a lost radioactive source that have resulted in human injury [4]. The radiological hazard associated with a sealed radioactive source depends on many factors such as the activity, the type of radiation emitted, distance from the source, and time of exposure. Most of the sealed sources may contain many terabecquerel of activity and an intact source will not cause radioactive contamination. But any accidental release from a physically damaged source can cause large-scale contamination to the environment and can also result in internal contamination of the public. The accidental exposures happened in Goiânia, Brazil [5] and accidental melting of a radioactive source at the Acerinox Facility in Los Barrios, Spain in 1998 [6] are examples of such incidents. The contamination due to Goiânia incident caused four deaths. Most of the sealed radioactive sources in use are ^{137}Cs or ^{60}Co.

Contamination of Food or Water Supplies

Food and water supplies may become contaminated following an accident involving radioactive materials or by introducing radioactive materials to food or water supply deliberately and surreptitiously.

Improvised Nuclear Device

An improvised nuclear device (IND) is a nuclear weapon and it refers to any type of explosive device designed to cause a nuclear explosion [3]. Such a nuclear explosion can cause a mass casualty as well as extensive radioactive contamination. The radioactive contamination due to a nuclear detonation will include a number of radioactive fission products such as radioisotopes of iodine, cesium, strontium, etc.

Nuclear Reactor Accident

An accident at a nuclear reactor facility can cause a widespread radioactive contamination in and around the site. A large-scale contamination incident at a nuclear power plant will have fission and activation products. It may lead to the contamination of workers and residents. Two nuclear power plant accidents that were of heavy impact are Chernobyl and Fukushima NPP accidents. The major radionuclides of concern during these two accidents are presented in Table 1.

Large-Scale Fires and Incidents

Many nuclear facilities have experienced large-scale fire incidents and such an incident can cause accidental spread of radioactive materials. A fire incident or explosion

Table 1 Major radionuclides released to the environment due to Chernobyl and Fukushima Daiichi NPS accidents

Radionuclide	Radioactivity (PBq)	
	Chernobyl NPS[a]	Fukushima Daiichi NPS[b]
Xe-133	6500	11,000
I-131	1760	160
Cs-134	47	18
Cs-137	85	15
Sr-90	10	0.14
Pu-239	1.3E−2	3.2E−6

[a] Reference [7]
[b] Report of Japanese Govt to the IAEA ministerial conference on nuclear safety (June 2011)

will initially lead to have the radioactive material to be airborne with varying particle sizes, resulting in external and internal contamination.

2 Radiation Emergency Preparedness

The growing global concern of nuclear and radiological accidents/incidences has intensified the planning and preparedness for effective response to deal with such kind of emergencies worldwide. For successful implementation of emergency management program, the practical goals of emergency response plan should be established. To achieve these goals, the inputs required should be specified and quantified.

The establishment of criteria for planning, preparedness, and response for nuclear and radiological emergency as recommended by IAEA takes into account the projected dose, averted dose, and residual dose during an emergency [8, 9].

2.1 Reference Levels

In emergency exposure situations, the reference levels are defined as the levels of doses or risks, above which it is judged to be inappropriate to plan to allow exposures to occur and for which protective actions should be planned and optimized. The establishment of reference levels helps in the decision-making by nodal authorities and regulators not only during emergency situations but also during post-emergency recovery phases of nuclear or radiological accident. As recommended by IAEA [8] and AERB [9], the reference level for protection of public during emergency situation is set within an effective dose (in terms of residual dose from all exposure pathways) range of 20–100 mSv, where the residual dose is defined as the dose expected to be incurred in the future after protective actions have been terminated (or a decision has been taken not to implement protective actions).

The 1–20 mSv per year; reference-level band is recommended for existing exposure situations which include the post-accident recovery phase. Actions during this phase include decontamination of environment, waste management and the return of the population following an evacuation or long-term relocation.

The overall aim of protection strategy followed during an emergency scenario is the reduction of the exposure below the reference level. Protective and other actions carried out during emergency is based on generic and operational criteria to ensure that the exposure does not exceed the reference level.

2.2 Operational Criteria for Deciding Reference Levels

The operational criteria are based on the generic criteria. Operational criteria include (a) Emergency Action Levels (EAL)—a specific, predetermined, observable criterion used to detect, recognize, and determine the emergency class, i.e., abnormal facility condition, (b) Operational Intervention Levels (OILs)—a set of a measurable quantity that corresponds to a generic criterion. OILs [10] are typically expressed in terms of dose rates or activity of radioactive materials released like time integrated air concentrations, ground or surface concentrations, or activity concentrations of radionuclides in environmental, food or water samples, i.e., field and laboratory measurements and (c) Observables—condition on the scene (by operator or first responders); for decision-making on emergency categorization and initiating the protective actions. Operational criteria are established in advance by using the generic criteria and these are normally the observables (control room indications, radiation and contamination levels in public domain etc.).

2.3 Basis for Decorporation Decisions

The radionuclides that enter the human body will be deposited based on intake pathway and chemical behavior of the radionuclide. When high intake of radioactive substance happens, as in case of a radiation emergency scenario, the natural removal mechanism of the body will not be sufficient for the fast excretion of these contaminants from the body. The natural excretion processes need to be accelerated by the use of some specific drugs or chemical agents to impede the deposition of radionuclides in organs or tissues, thereby avoiding accumulation and retention of radionuclides in the body. The process of enhancing the biological removal mechanism of the body by chemical or biological agents is known as decorporation [11]. The decorporation includes the procedures for reduction in absorption, prevention of incorporation and internal deposition of radionuclides within organs, and promotion of elimination or excretion of absorbed nuclides. The decorporation is achieved by methods such as blocking and isotopic dilution, displacement, use of ion exchange resins, mobilization, and chelation.

Table 2 Generic criteria for decorporation in emergency exposure situations [11]

Risk	Value (%)	Actions
Risk of development of sever deterministic effect	> 0.5	Reasonable decorporation action is expected to be undertaken as early as possible
Risk of development of radiation induced cancer	≥ 1	Reasonable decorporation action is required to minimize lifespan risk of radiation induced cancer
Risk of development of radiation induced cancer	< 1	No decorporation required

The decorporation mechanism and therapies may also have its own side effects. Hence, decorporation therapy should be carried out based on the risk identification. Sometimes an immediate decorporation therapy may be required based on the strength of evidence, preliminary or early assessments and/or clinical judgment. Long-term decorporation procedure should be followed only after proper assessment of intake. If there is a severe risk of deterministic effect, reasonable decorporation actions are expected to be carried out [11], promptly. Table 2 gives the generic criteria for decorporation. If risk of stochastic effects is identified, decorporation should be carried out in accordance with the appropriate operational intervention level (OIL).

2.4 Basis for the Use of OILs for Decorporation

IAEA Safety Standards Series No. GSR Part 7 [8], defines an OIL as "A set level of a measurable quantity that corresponds to a generic criterion" or "A calculated level, measured by instruments or determined by laboratory analysis, that corresponds to an intervention level or action level [12]. An OIL is a type of action level that is used immediately and directly (without further assessment) to determine the appropriate protective actions on the basis of an environmental measurement." Table 3 presents the list of some radionuclides with reference level of intake (RLI). These values correspond to the generic criteria for use of decorporation treatment [11].

Table 3 Minimum values of reference level of intake (RLI) for important high energy photon emitters corresponding to the generic criteria [11]

Radionuclide	RLI (Bq)	Radionuclide	RLI (Bq)
H-3	2.6E9	Ru-106	1.7E7
Mn-54	6.3E7	Ag-110m	8.2E6
Co-58	4.7E7	Sb-125	2.2E7
Co-60	3.7E6	I-131	4.5E6
Rb-86	2.8E7	Cs-134	7.2E6
Zr-95	1.8E7	Cs-137	9.9E6

The intake of radioactive material by an individual can be quantified by measurement of radionuclides distributed in whole body or retained in an organ or tissues or from the excretion rates of radionuclides from the body (using biokinetic models). OILs for decorporation are based on this relationship. In-vivo bioassays and invitro bioassays can be used for internal dose assessment and for calculation of and establishment of OILs. OILs are calculated quantities that can be measured by instruments, either directly or after analyses in a radiochemical laboratory followed by measurement. These values correspond to Reference Level of Intake for the decision on decorporation to avoid severe deterministic effect or future occurrence of stochastic effects.

The OIL is the radionuclide specific, time (t) dependent function of corresponding RLI:

$$\mathrm{OILR}(t) = \mathrm{RLI} * f_{\mathrm{T,R}}(t)$$

where $f_{\mathrm{T,R}}(t)$ is the time dependant radionuclide specific retention function for in vivo monitoring or the radionuclide specific excretion function for in-vitro bioassay monitoring. To limit harmful effects of decorporation, the decorporation therapy need not be used for intake less than one tenth of the minimum value of RLI [11].

3 Importance of Internal Contamination Monitoring During Radiation Emergency Situation

The reactor accidents like Chernobyl, Fukushima have demonstrated that environmental radioactive contamination due to nuclear accident cannot be completely eliminated in spite of strict regulations. Similarly, accidents involving medical or industrial radiation sources, transport of radioactive materials, misuse of orphan sources etc., can also lead to radiological emergencies causing exposure to the public. In such radiation emergency situation, radioactive release may cause contamination at on-site/or off-site and may require rapid response to assess contamination and mitigate potential exposure to workers at nuclear facility and the general public.

In the management of radiation emergency, it is essential to assess the radiation exposures to the people in the affected areas. Hence, an essential component in the emergency management program is the monitoring of internal contamination [13]. In such circumstances, the existing fixed set-ups or installations may be of limited use because they may be located far from the affected site and also it is difficult to ferry large number of contaminated (external + internal) individual public to such facilities. However, some of the affected public may be referred to such facilities after initial screening of radioactive contamination for precise measurements.

During the assessment and remedial actions taken following the Chernobyl, Fukushima, and Goiania accidents, the experience showed that there is an acute need

of Internal Contamination Monitoring Units (ICMU) for conducting large-scale individual monitoring of internally contaminated people using simple, readily available systems/equipments and improvised techniques. It is necessary to arrange required suitable portable monitoring systems, which can be easily assembled, transported and used for long duration even during power outages. Such systems must be able to acquire useful data in a reasonably short time so that monitoring of a large group of contaminated people can be carried out.

In a nuclear accident, the gamma emitters such as ^{131}I, ^{132}Te,–^{132}I, ^{137}Cs, ^{134}Cs, and ^{103}Ru are the main contributors [14] to the radiation dose to human body mainly entering through inhalation. Therefore, following a nuclear accident, whole body and thyroid monitoring are essentially required for a correct dose assessment of the individual.

For whole body and thyroid measurement, the system mostly consists of one or more spectrometry instruments (for identifying and quantifying different gamma emitters in mixture of radionuclides) and handheld NaI(Tl) instruments (both unshielded and shielded). For internal contamination monitoring, different radio nuclides incorporated in the body give rise to different doses as each radionuclide follow specific biokinetic and dosimerty behavior result in different doses. Therefore, it is necessary to use spectrometry systems for identification and quantification of individual radionuclide incorporated in the body.

4 Guidelines for Internal Contamination Monitoring

4.1 Monitoring Program: Objective and Design

The International Commission on Radiological Protection (ICRP) has formulated basic principles for planning urgent actions following major radiation accidents and these are reflected in the IAEA's Safety Series documents [3]. In establishing the need for certain counter measures and judging their effectiveness, assessments of internal radioactive contamination are required on a large scale. The aim is to identify those at risk who could benefit from early medical intervention and those whose lower levels of contamination may justify a recorded assessment of committed dose [13].

In this situation, nodal agency must plan to set up, independent internal contamination monitoring units using equipment which has either been developed/acquired specially for emergency preparedness plan or which can be brought from other facilities in short notice. The nodal agency should also formulate a plan for monitoring which makes the best use of resources to get the required information as quickly as possible.

During the primary screening procedure, people are categorized [13] into three groups according to predetermined levels of estimated internal contamination after screening/triage.

Group I People with internal contamination below action level A. The group is not of particular concern. They may be monitored at a future stage for statistical or epidemiological purposes (with more sensitive equipment).

Group II People with internal contamination between action levels A and B. After the initial survey they would be directed to separate facilities for more thorough evaluation, may require gamma ray spectrometry measurements.

Group III People with internal contamination above action level B. They are referred to specialists for prompt and accurate assessment with gamma ray spectrometers suited to investigate high levels of contamination. If required appropriate medical treatment to be considered for the group.

IAEA has provided a general guideline [13] for setting up the decision levels for A and B, depending on the emergency scenarios such as number of persons to be screened, available monitoring systems/equipments, measurement range and capacity for more rigorous monitoring, etc. IAEA TECDOC-746 mentions an example for this as, CED values of 0.5 and 50 mSv may be considered as appropriate decision levels and the equivalent internal contamination levels as action level (A and B). The document clearly mentions that the action levels are to be established by the authorities such as, the decision-making nodal agency and regulatory board. The authorities should select appropriate action levels in terms of Committed Effective Dose (CED) based on the prevailing situations.

Internal contamination monitoring during emergency scenario includes in-vivo (direct monitoring) and in-vitro bioassay (indirect monitoring). Figure 1 presents the procedure followed during internal contamination monitoring during emergency situations.

5 Important Considerations of In-Vivo Monitoring Systems for Field Deployment During Emergency Monitoring

5.1 Location of Internal Contamination Monitoring System

The field deployable in-vivo monitoring units or monitoring systems should be deployed where the levels of natural background radiation are not unusually high and the place where the minimum contamination from the incident is present. The preliminary screening and segregation should be carried out in an area appropriate to the potential demand. It should be spacious enough for adequate separation between (i) people awaiting initial monitoring, (ii) those being monitored, (iii) those awaiting transfer for further assessment, and (iv) there should be enough place for temporary collection of contaminated clothing [13].

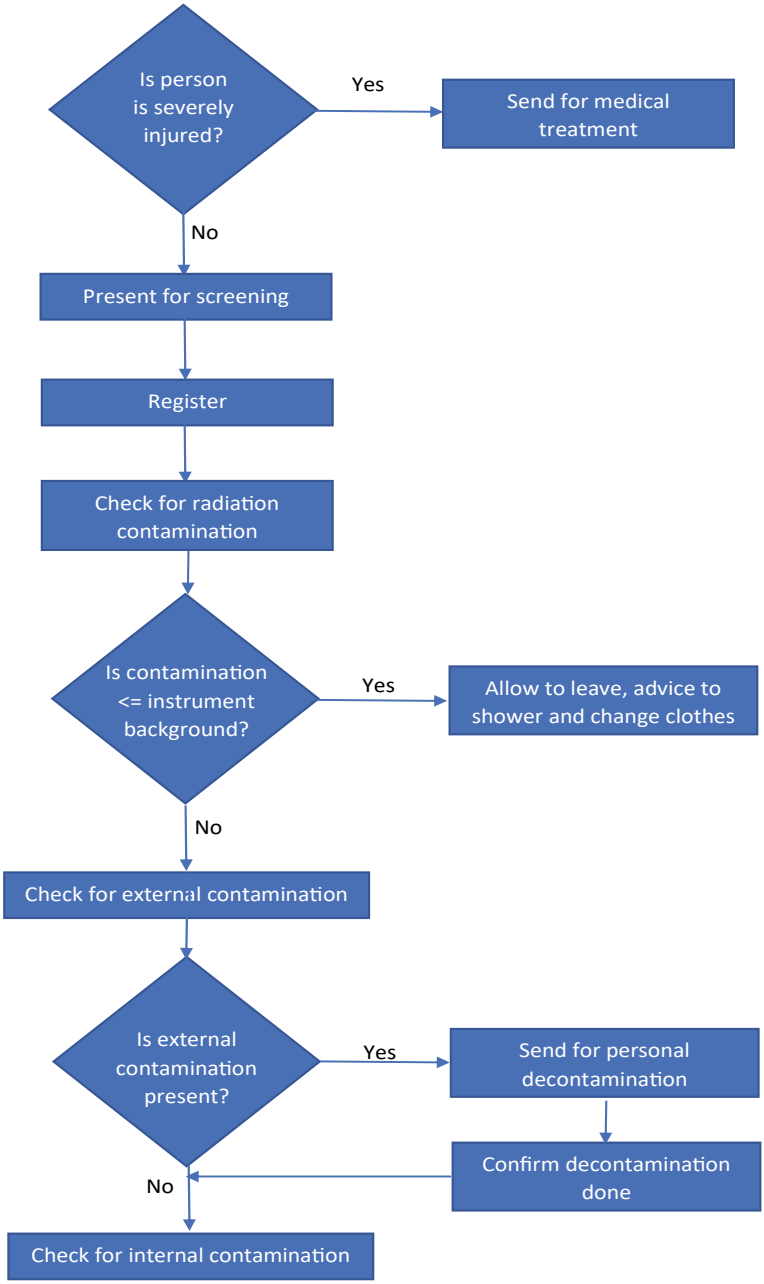

Fig. 1 Flowchart for recommended procedures of internal contamination monitoring during radiation emergency [13]

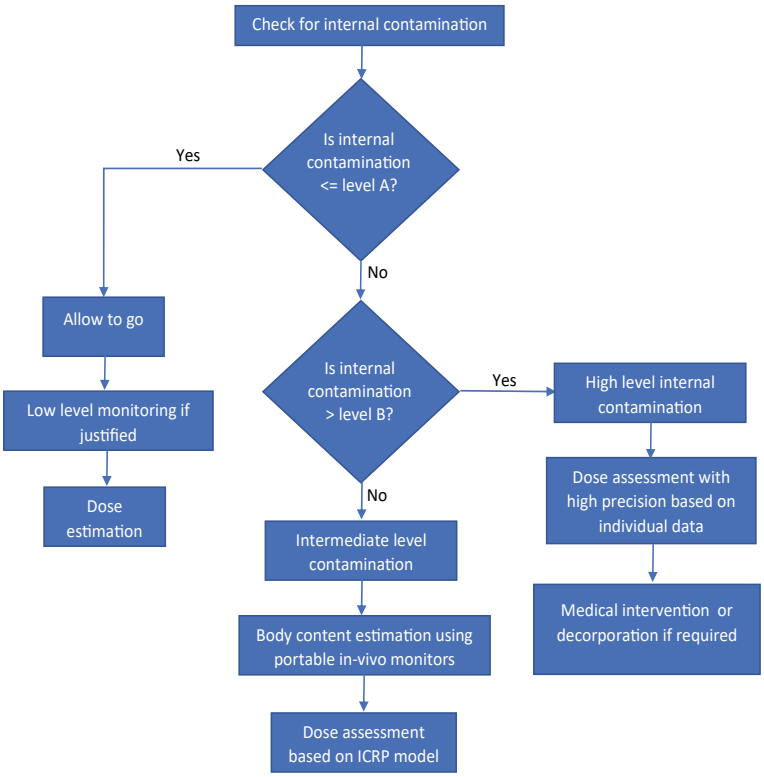

Fig. 1 (continued)

5.2 Control on External or Surface Contamination on the Subject

During the initial screening, there is a possibility of spurious assessments as the subjects may have loose surface contamination on their clothing and/or on the body. A screening should be carried out for external contamination on persons involved in a radionuclide contamination incident and if external contamination is observed the person should be sent for decontamination. Care should be taken to avoid the contamination of monitoring probe and the staff handling the survey instruments should wear Personal Protective Equipment (PPE). For subjects showing levels > A (level A decided by the nodal agency/the regulatory board), then the subjects should be instructed to take bath/shower, change of clothing and to be checked for external loose contamination if any before re-monitoring which should be undertaken preferably with other internal contamination monitoring unit (duplicated facility). Sometimes the external decontamination may be incomplete or may not be practical as it can damage the skin. Studies report that ~ 80–90% of contamination is eliminated if outer clothing of the contaminated individual is changed [11]. There is always

a possibility of persistent external contamination which needs to be considered. Any difference between anterior or posterior survey results can be considered as an indicator of external contamination due to gamma-emitting radionuclides.

In case of field deployable monitoring units, the effects of fluctuating airborne contamination may be difficult to be avoided. So, in such scenario, it is advisable to check the background response of the systems as frequently as possible. This may also help to identify if is there any system contamination.

Once the issues associated with external contamination are sorted out, the persons should be screened for internal contamination. It should be ensured that medical care is not delayed irrespective of screening for external or internal contamination.

5.3 Systems Required for Internal Contamination Monitoring

The basic requirements for the instruments being used for screening are adequate sensitivity, portability, ease of handling, durability for long operation in the field and also the system should have malfunction indicator. The system should be sensitive enough to detect the lower level "A" of the action level (CED).

The instruments that will be used for internal contamination monitoring should be calibrated for whole body (or organ) content, both while measuring in contact or at an increasing distance. If, the radionuclides that are expected to be present is widely dispersed or uniformly distributed in the body then the measurement at abdomen region is the suggested choice.

Initial measurements are to be carried out by keeping the detector probe in contact with the subject's abdomen. If a positive response is obtained, then the probe should be moved to larger distance for which both (i) a statistically adequate response could be recorded and (ii) efficiency calibration is available. Measurements at increasing distances are particularly important when the survey monitor is a GM detector to exclude the possibility of overloading effects. Survey monitors incorporating scintillation detectors are preferable than a Geiger–Muller (GM) detector due to the lower detection level and capability to identify contaminants.

The background response of the instrument should be recorded periodically during the daily monitoring program. For a more detailed monitoring of the subjects, spectrometry-based field deployable or laboratory-based whole body monitors, thyroid monitors, lung monitors and wound monitors, etc. should be used. A more detailed description of the systems is given in Sect. 8.

5.4 Calibration and Testing of the System

The systems that will be deployed for internal contamination monitoring at the site should be calibrated, and the response of the systems should be evaluated with radioactive sources of known activities (i) over the required range of energies, (ii)

for a series of locations in contact with the chosen region of the body (thyroid and thorax part of the body), and (iii) at distances from the body.

5.5 Shielding and Other Requirements

The shielding approach adopted depends on several factors such as detectors, the distribution of the radionuclides in the body, requirement to accommodate injured or sick people and availability of shielding materials. Applications of shielded systems are required to achieve statistically reliable results in shorter counting time while carrying out the measurement at the lower range of activity. General guideline is the lead shield of 50 mm thickness [13] or its equivalent material. The weight limitation should be considered while selecting the shielding material. For thyroid monitoring for radioiodine, small size detector [15] with collimation is sufficient.

5.6 Identification of Radionuclide(s) Involved

Most of the beta, gamma emitters can be identified and quantified by portable gamma spectrometry instruments incorporated with solid state detectors like HPGe and scintillation detectors such as NaI(Tl), $LaBr_3$. The presence of alpha contamination can be detected using ZnS(Ag) scintillation counter but identification and quantification of alpha emitters can be carried out with bioassay monitoring in a radiochemical laboratory. Most of the survey instruments are also equipped to display dose rate, usually in units of $\mu Gy\ h^{-1}$ or $\mu R\ h^{-1}$.

It is observed that in radiological incident, most of the emitted radionuclides were having gamma energy > 0.1 MeV. This facilitates the direct internal contamination monitoring of persons using suitable whole body/partial body monitors. In other situations when in-vitro monitoring is required and the logistics and analytical requirement will be different. The possible strategy to identify the group that may need a detailed internal contamination monitoring is to segregate people into groups based on the possibility of contamination as per the inputs followed by screening a few from each group.

Dose computation and assessment can be carried out by in-vivo measurement of retained activity in the whole body or organ like Whole Body Retention (WBRt), Lung Retention (LRt) and Thyroidal Retention (TRt), and invitro measurement of excretion of radioactive content (Bq/d) such as Daily Urinary excretion (UEx) and Daily fecal excretion (FEx). The effective dose can be computed using the biokinetic models proposed by ICRP for each radionuclide. In-vivo measurements are the most rapid measurement methods that can be adopted for total activity of the radionuclide in whole body or organ during an emergency scenario. The measurement methods for individual monitoring applicable to some selected radionuclides are presented in Table 4.

Table 4 Measurement methods for individual monitoring of some selected radionuclides

Radionuclide	Absorption type	In-vivo measurement			In-vitro measurement	
		Whole body counting	Lung/organ monitoring	Thyroid	Urine	Fecal
H-3	F				•	
Fe-59	M	•	•		•	
Co-57	S	•	•		•	•
Co-58	S	•	•		•	•
Co-60	M, S	•	•		•	•
Sr-89	F, S				•	
Sr-90	F, S				•	
Ru-106	F, M, S	•	•		•	
I-125	F			•	•	
I-131	F			•	•	
I-133	F			•	•	
Cs-134	F	•	•		•	
Cs-137	F	•	•		•	
Ra-226	M	•	•		•	
Ra-228	M	•	•		•	
Th-228	M, S	•	•		•	•
Th-232	M, S	•	•		•	•
U-234	F, M, S				•	•
U-235	F, M, S		•		•	•
U-238	F, M, S		•		•	•
Pu-238[a]	M, S				•	•
Pu-239[a]	M, S				•	•
Pu-240[a]	M, S				•	•
Am-241	M		•		•	•

F fast, *M* moderate, *S* slow

[a] In-vivo lung/organ monitoring using Am-241 as a tracer

5.7 Acceptable Level of Accuracy in the Measurement

An estimated accuracy factor of 2 or better is adequate for CED computation, in case of intermediate level of activity (Level between A and B, measured in the site/field) [13]. For the high level of activity that is equal or more than level B, the in-vivo monitoring systems with high precision are required. The in-vivo monitoring systems with adequate statistical precision for short-term counting are scintillation or HPGe detectors. In case of heavily contaminated subjects, multiple or series of assessments with an accuracy of 20% or better are used to determine the committed

effective dose. These computations will be based on the individual metabolism for the selected radionuclide and its relevant physical characteristics rather than based on the parameters as per ICRP models. The final computation of dose will be in conjunction with the results of in-vitro monitoring and information on the effectiveness of decorporation therapy, if administered.

6 Monitoring of Internal Contamination

6.1 Initial Survey

The main purpose of initial screening with a field survey equipment is to identify and group people according to their internal contamination levels, which can be helpful in further actions.

The basic instrument required for the initial screening should be of adequate sensitivity, easy to handle, suitable for long hours of continuous operation and it should have indicators if any malfunctioning of the system happens. The system should be sensitive enough to detect activity at the lower level of committed effective dose (Level A).

Survey monitors with scintillation detectors are the preferred choice for initial screening, than a GM survey meter. But if the GM detector-based survey meter is the only option available, the operator should be aware that a zero response may result from overloading in a high radiation field from the subject.

The initial survey should be carried out with due regard to the possibility of external contamination and if it is observed then follow the decontamination procedure and return back to internal contamination survey. The background response of the system should be recorded prior to the measurement as well as before and after the measurement. The general procedures mentioned here are for contamination which is widely spread on the body, the required modifications are to be made for organ-specific contamination, e.g., thyroid monitoring for radioiodine contamination.

(1) over the relevant range of energies the survey meter should be carried out over the relevant range of energies, (2) for a series of locations in contact with the chosen region of the body, (3) at distances up to several meters from the body, and (4) with radioactive sources whose activities are known. In case of radionuclides that could be widely dispersed in the body measurement at abdomen is the suitable choice. Initial measurements should be done by detector kept on contact with the subject's abdomen and if the response is positive the detector should be moved to a larger distance which has an established calibration factor and a statistically adequate response could be recordable. As a check of localized surface contamination, a rapid scanning of the most likely regions (head, feet, hands) may be appropriate.

6.2 Investigation of Internal Contamination at Intermediate Levels (Level Between A and B)

Subjects with internal contamination in the activity range A–B during initial assessment should be referred for more rigorous assessment by appropriate methods. The setting of the action levels A and B decides the range of intermediate activity. IAEA TECDOC-746 gives an example by assuming the body contents in the range 10^4–10^7 Bq as intermediate level (this value may vary as per the actual scenario), and that there is abundant gamma radiation at energies > 0.1 MeV. For intermediate level of monitoring, highly sensitive detectors are not required. An extensive shielding can be used if contamination is present in the local environment. If the gamma ray fluxes are well outside this range, alternative arrangements may be required like high level monitoring procedures or referral to an established laboratory that can handle the measurements at low levels of whole-body content for precise quantification of the activity for dose computation.

The requirements of instruments at intermediate level monitoring are (1) transportability; (2) flexible mechanical arrangements for individual monitoring (e.g., whole body or specific regions); (3) rapid processing of monitoring for subjects in succession; (4) prompt data evaluation. When a mixture of radionuclides could be present, gamma spectrometry instruments to be used to achieve proper identification and quantification of specific radionuclide composition. The accuracy should be at least within a factor of 2 [13].

Any suitable gamma spectrometric system with appropriate shielding and portability with scintillation spectrometers or semi-conductor detectors can be used for monitoring purpose. The system should be flexible to allow (i) adjustment of the detector-subject position in optimizing count rate and accuracy and (ii) fitting collimators for measurement of activity in specific organs.

Various geometries for whole body monitoring include standing geometry, arc geometry, simpler arrangements with subject lying down on a bed below the detector arrangement, chair geometry, etc. The approach opted will depend on factors like availability of detector, probable distribution of radionuclides in the body and availability of proper shielding, etc. At the lower end of the activity range under consideration (10^4–10^7 Bq) to achieve adequate statistical reliability in a short counting time, partial shielding would be required. Shielding of the subject, on all sides except that exposed to the detector, is recommended. Weight limitation is the practical difficulty that may affect the effectiveness of shielding.

The system should be calibrated for the large energy range of interested radionuclides. Procedures are also required to establish the linearity of response with respect to activity up to the highest count rates. The calibration should be performed with suitable phantoms. For a measurement accuracy of a factor of 2, the phantom need not be closely realistic, but roughly it should simulate the relevant conditions of attenuation and scattering. An improvised array of point sources in stacks of polyethylene plates may be used to simulate a localized deposit. For measurement of thyroid activity, a neck phantom with standardized solution in appropriately shaped chamber

is sufficient. For widely spread radionuclides, BOMAB-type phantoms may be used to simulate subjects of various sizes. Calibration factors for gamma rays that cover the range can be used for unrepresented radionuclides. The system performance and calibration should be checked daily using appropriate point source. The continued validation of an adopted calibration should be carried out daily by measuring a designated reference point source, in a fixed and reproducible geometry.

Regular background checks should be carried out to limit the possibility of measurements in high background or contamination in the shielded area and check for any background variation is present due to weather conditions. When organ-specific measurements are required, the system should be fitted with a shielded collimator. In specific applications like thyroid monitoring, it is advisable to use collimated small detectors. Whenever body parts have irremovable surface contamination those parts to be shielded with appropriate shielding to avoid spurious assessment of internal contamination. If extensive contamination of the body has happened where application of shielding is not possible bioassay analysis will be required to provide a basis for the assessment of committed effective dose.

A computer-based data processing system for data acquisition, storage, spectrum analysis should be used. An estimated accuracy of a factor of 2 or better is adequate for the purposes of calculating the CED for the individual, based on the standard metabolic models provided in ICRP Publications [13].

6.3 Investigation of Internal Contamination at High Levels (> B)

The monitoring systems or equipments required to assess internal contamination in subjects whose level of activity is > B are decided from preliminary screening results or following re-evaluation from "intermediate" level monitoring results. The basic requirement for high level monitoring system (gamma ray spectrometer) should be a detector that can be positioned at sufficient distance from the body. The count rate should be at an acceptable level in the presence of high activity in the person's body. A systematic error of up to 20% is acceptable [13]. When relative activity estimates from sequential measurements are made to establish a retention pattern, a much better precision is required. For continuity in measurement program for retention studies, the range of measurable activity by the instrument should overlap with intermediate level of activity.

The efficiency calibration techniques using phantoms are to be carried out for the in-vivo monitoring systems used to assess whole body radioactivity or organ activity as the case may be. These can provide accuracy within 10% or better, depending on photon energy.

The computation of committed effective dose is carried out from the results of a series of measurements/assessments in heavily contaminated subjects, with an absolute accuracy of 20% or better. The determination will be based on the actual

Table 5 A typical format for internal contamination monitoring records during radiation emergency

Registration No				Date		
Personal details						
Name		Date of birth		Sex	M/F/T	
Identification No		Contact No		Email		
Address						
Radiological data sheet						
Contamination survey						
External contamination present			Yes		No	
If yes, specify location						
Recommendation						
Decontamination is required			Yes		No	
External decontamination procedure performed			Yes		No	
Internal contamination measurement			Date		Time	
Instrument type			Serial No			
Lower action level (kBq)		Upper action level (kBq)			Background reading	
Measurement data sheet						
Date and time	Geometry and distance	Reading with subject	Background reading	Net reading	Calibration factor	Activity
CED (mSv)						
Recommendation						
Name of analyst			Signature			

metabolism rate in the individual rather than the values used in ICRP models. The results should be in conjunction with excreta analyses and decorporation therapies used. The format for monitoring records is provided in Table 5.

7 Indirect (In Vitro) Determination of Internal Contamination

Indirect (in vitro) measurement of internally-deposited radionuclides are carried out by analyzing the material removed or excreted from the body. These include radiochemical processing and further analyses of nasal swabs, urine and fecal samples. Blood samples are not used for monitoring of internal contamination, routinely and as part of screening for a radionuclide exposure. The concentration of a radionuclide

of concern in circulation will be too small for detection by field survey instruments and also by typical radiochemical methods, at any point of time. Nasal swabs can be an indicator of a possible internal contamination, urine samples are helpful to demonstrate systemic uptake and fecal samples provide a direct evidence of internal contamination. Nasal swabs are crude indicators of intake and should be considered qualitative and not quantitative with regard to dose intervention measurement.

Urine and fecal samples are the most common part of an in-vitro bioassay monitoring to assess intake and dose. The indirect method needs to be carried out by properly trained staff of radiochemical laboratory and sensitive instrumentation and difficult to have prompt analysis for large population. The preferred method for rapid screening by indirect bioassay in an emergency situation is collection of a single void (50–100 mL sample) of urine. The samples are to be collected in clean, tightly sealed containers with proper care to avoid cross-contamination or external contamination. Samples should be labeled properly to identify the person and sample collection date. The results of the samples taken before 4–6 h post-exposure should be interpreted carefully as the metabolism and transfer to urine may be insufficient to provide a valid indication of intake.

On dealing with a large population with potential exposure, the collection and analysis of fecal samples renders them relatively ineffective as rapid screening tools. Fecal samples cannot be taken as smears or swabs and total voiding is required for radio analysis and dose assessments.

Fecal samples can be considered to be a useful tool post-crisis dosimetry investigation or a long-term registry program for individual monitoring when inhalation of radionuclides in a relatively-insoluble form has happened.

8 Systems Required for Internal Contamination Monitoring (for High Energy Photons E_γ > 200 keV)

8.1 Basic Requirements for the Choice of Contamination Monitoring Equipment

1. The system should be sensitive to the type of radiations.
2. Results of survey of external contamination should be reported in units of Bq or cpm.
3. Results of surveys for external radiation exposure rates should be reported in mGy h^{-1} or mR h^{-1}.

Instrument Checks and Measurement

Several checks are required before using any radiation survey instrument to ensure that the instrument is operational. The following checks should be performed,

a. Calibrated for the radionuclide(s) of interest.

b. Cable connectivity and power supply/batteries should be checked.
c. Set zero on survey meter if required.
d. Use a check source to confirm that the instrument detects radiation.
e. Turn "On" the instrument and check for the usable reading. This reading is the background for the system.
f. Hold the detector ~ 1 cm from the person to be surveyed.
g. When surveying people, spot-check the mouth, nose, chest, hands, fingers, knees, and feet. Scan other areas as per the situation.
h. Specific location (e.g., the nose or fingertips), should be surveyed at least for 10 s.
i. While surveying large areas, the detector should be moved slowly [~ 3–5 cm s^{-1}].
j. Note the highest count rate (in counts per minute above background levels) and record.

Most widely used instruments for radiation/contamination survey during an emergency are presented in Table 6.

The internal contamination monitoring systems required for field application for rapid screening of the public during radiation emergency situations are as follows.

Field Application Non-spectrometry Systems

1. Hand-held radiation survey monitors—NaI(Tl) detector-based, GM-based and plastic Scintillator detector-based systems.

Field Application Spectrometry Systems

Table 6 Widely used radiation monitors for personnel contamination survey during radiation emergency

Monitor type	Detection probe	Output	Applications
General survey	Thin window GM pancake	Counts per minute (CPM)	Beta gamma contamination
	ZnS(Ag) scintillator	CPM	Alpha contamination
	Plastic scintillator	CPM	Alpha beta contamination
	Energy compensated GM	μGy h^{-1}, CPM	Dose rate and contamination
	Na(Tl) scintillator	μGy h^{-1}, CPM (variable range)	Dose rate (gamma)
	Ionization chamber	μGy h^{-1}	Dose rate
Hand and foot monitor	Thin window GM pancake, plastic scintillator	CPM	Beta gamma contamination on hand and feet
Handheld identifinder Gamma spectrometry	Na(Tl) detector	Radionuclide identification, CPM	Qualitative and quantitative estimation of gamma emitters

1. Portable thyroid monitor with collimator—for thyroidal radioiodine measurements.
2. Portable whole body monitor—for HEPs measurement in the body.

Laboratory-Based System for Rapid Screening of Public

1. Quick Scan Whole Body Monitor (QS-WBM).

Laboratory-Based System for Detailed Investigation

1. HPGe/NaI(Tl) detector based Shadow Shield Bed Whole Body Monitor (SSBWBM).
2. Scanning bed WBC inside totally shielded steel room.

8.2 Handheld Radiation Survey Meters (Non-spectrometry Systems for Field Measurement)

Handheld radiation monitors can be used for measurement of internal contamination in public. To carry out this work typically 25 mm dia × 25 mm thick NaI(Tl)-based radiation monitor, proportional counter (10 nSv/h–100 mSv/h), GM counter-based ambient dose equivalent rate meter (0.01 μSv/h–0.1 Sv/h), etc. can be used. Calibration of the system can be carried out using respective phantoms depending on the purpose of use. Figure 2 shows a handheld radiation survey monitor used during emergency monitoring.

GM Survey Meter is commonly used for detection of external radioactive contamination on personnel and work surfaces. It is relatively inexpensive and sensitive to most beta/gamma radiation. The detector contains a thin window with a surface area that varies from a pancake model (typically 15 cm^2) to a standard end window probe (6 cm^2). The pancake-type GM detector-based survey monitor is shown in Fig. 3. The housing is provided with cap for Beta/Gamma selection and typically measures the dose rate range ~ 0–200 mR/h and also measures contamination in cpm mode.

Another survey monitor widely used is a built-in ~ 25 mm × 25 mm NaI(Tl) scintillator detector coupled with 25 mm dia PMT with a typical measurement range from 0 to 5000 μR/h with adjustable range knob.

8.3 Thyroid Monitoring System

Thyroid monitoring is very important to evaluate the influence of short-lived radionuclides such as ^{132}I ($T_{1/2}$ = 2.295 h) and ^{133}I ($T_{1/2}$ = 20.8 h) present in the thyroid along with ^{131}I, after a nuclear accident. Both non-spectrometry-based and spectrometry-based systems are used for thyroid monitoring purpose.

Following a nuclear or radiological accident, the devices that are used in environmental surveys, which can operate in dose rate mode, may be used to measure

Fig. 2 Handheld radiation survey monitor used in radiation emergency monitoring

Fig. 3 Pancake-type GM contamination/survey monitor

thyroid contamination. They are calibrated in ambient dose equivalent rate H*(10). Study suggested that the use of surface contamination monitors that are mainly GM detector based is to be avoided [14]. Various studies suggest that while using non-spectrometry systems for thyroid measurements, we have to take into account the contribution not only of ^{131}I alone but also for short-lived radioiodine isotopes (^{132}Te/^{132}I, ^{133}I, ^{134}I and ^{135}I) present in the thyroid. It is recommended to perform thyroid monitoring 2 days after the supposed time of intake [16]. NaI(Tl) detector-based spectrometry systems are used worldwide for environmental monitoring and are also useful for thyroid monitoring after a nuclear accident [17]. Additionally, gamma ray spectrometry systems using $LaBr_3$, $CeBr_3$, or SrI_2(Eu) detectors, which are having mid-level energy resolution and efficiency is also now available.

Thyroid Monitor or Thyroid-Uptake Probe would be a preferred method for measuring specifically ^{131}I in the thyroid of subjects who had been exposed to ^{131}I during an incident. A typical portable thyroid monitoring system that can be used during emergency thyroid monitoring is given as Fig. 4. A 51 mm dia × 51 mm thick or a 76 mm dia × 76 mm thick NaI(Tl) detector-based system with a shielded collimator can be used for monitoring of thyroid for ^{131}I isotope which is of a major concern during radiation emergency [18]. The thyroidal content can be measured on contact or adjustable detector collimation (1–15 cm as required) for different measurement geometries. The detector shield top can also be used as chin rest to minimize the positional errors in the measurement of thyroidal content. A known amount of ^{133}Ba (^{131}I simulant) source distributed in IAEA standard thyroid phantom can be used for the calibration purpose. It is easy to transport and install, simple to operate, has lower counting time and compatibility for measurement of thyroidal content in child to adult. Typical MDA of 100 Bq is achievable by the system for ^{131}I in thyroid measurement.

8.4 Portable Whole-Body Monitor

The Portable Whole-Body Monitor (PWBM) can be used to measure the internal contamination due to high energy gamma ($E > 200$ keV) emitters incorporated in human body. A typical PWBM is given in Fig. 5. It is a 76 mm dia × 76 mm thick NaI(Tl) detector with proper shielding to reduce the background during the measurement of the subject [19]. The system is flexible for the sitting height of the subject (child to adult).

The calibration of the system should be carried out with known activity of ^{133}Ba, ^{137}Cs, and ^{60}Co radioactivity uniformly distributed in water filled BOMAB phantom for sitting/chair geometry. The typical Minimum Detection Activity (MDA) for PWBM for counting time of 10 min at 20 cm distance is 1500 Bq for ^{137}Cs and 1000 Bq for ^{60}Co. The system can measure doses less than 1 mSv and can play an important role in monitoring/screening the public during and/or after emergency situations.

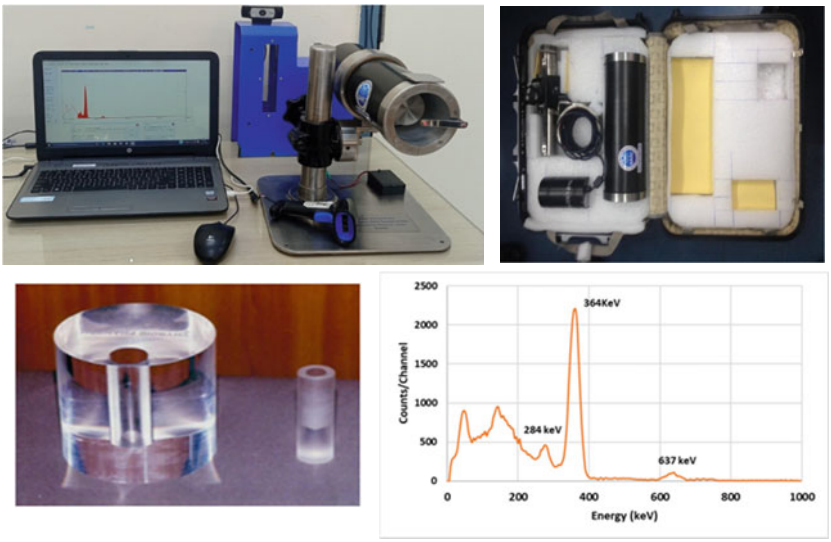

Fig. 4 Portable thyroid monitoring system along with a typical ^{131}I spectrum and IAEA/ANSI neck phantom

Fig. 5 Portable whole body monitor for measurement of internal contamination due to high energy photon emitters

8.5 Laboratory-Based Whole-Body Counters

Whole-body counters are used to detect and quantify internally-deposited radionuclides that emit photons with energies in excess of ~ 200 keV. They are equipped with scintillation detector (e.g., NaI(Tl)) gamma scintillation or semiconductor (e.g., germanium) based detectors in a low-background environment achieved through proper shielding. Counting configurations require subjects to stand, sit in a constant

geometry chair, or recline on a fixed or moving bed. A standing geometry can be used for a shorter time period of counting than a sitting geometry. Hence, the standing geometry monitors are good option for the large population monitoring. Shadow shield whole body monitoring systems present in typical internal dosimetry laboratories comprises shield with mild steel and lead lining, a moving bed and Detector (102 mm diameter and 76.2 mm thick NaI(Tl) detector) and associated electronics [20]. The system gives almost uniform response to activity distributed in any part of human body. Profile scan of whole body is also possible for localization of the contamination. A chair geometry of the whole body monitoring system has tilted shielded chair and static geometry scintillation detector (102 mm diameter and 76.2 mm thick NaI(Tl) detector) [21]. A typical counting time of 10–20 min is used in these types of monitors. These systems are less applicable in a field-based monitoring during emergency and more widely used as lab-based system.

8.6 Laboratory-Based Quick Scan Whole Body Monitor (QS-WBM)

A Quick Scan Whole Body Monitor (QS-WBM) can be used for quick and efficient whole-body monitoring of the radiation workers for internal contamination due to gamma emitting radio nuclides like fission and activation products during emergency [22]. The system has a sensitivity comparable with conventional WBM for 1 min counting time. The QS-WBM is calibrated using Bottle Mannequin Absorption (BOMAB) type phantom. Figure 6 is the photographic representation of QSWBM. This is a walk-in and walk-out type of system, useful during radiological and nuclear emergency situations, for monitoring a large number of radiation workers as well as members of public. The shield is constructed using 50 mm thick lead bricks of different sizes in a laminar fashion and has interlocking arrangement. The QS-WBM is incorporated with two rectangle shape NaI(Tl) detectors each of dimension 406 mm (L) $\times$ 127 mm (W) $\times$ 76 mm (D). The two detectors are configured vertically in a linear array on a common vertical axis, one below other.

9 In-Vivo Monitoring System for Low-Level Photon Emitters

In case alpha emitters specially designed shielding facility is required for monitoring of low energy gamma or X-rays emitted by these nuclides. Lung monitors equipped with gamma spectrometry systems need heavy shielding and long-term counting which makes not a preferable choice for population monitoring. Detectors used for the systems are phoswich detectors, thin NaI(Tl) detectors or HPGe array-based spectrometry systems. The measurement is carried out in fully shielded steel rooms.

Fig. 6 Standing type whole body monitor for rapid screening of individuals for in-vivo monitoring of high energy gamma emitters and BOMAB phantom

The typical Phoswich detector is a sandwich of two detectors viz. 202.4 mm dia × 3 mm thick NaI(Tl) as primary crystal and 51 mm thick CsI(Tl) as secondary crystal with a Pulse Shape Discriminator. The HPGe-based monitoring system consists of an array of three 70 mm dia HPGe detector and associated electronics placed inside a totally shielded steel room. It provides better resolution compared to Phoswich detector. The systems are used for the measurement of internally deposited low energy photon emitting radionuclides such as ^{239}Pu (17 keV), ^{241}Am (60 keV), ^{238}U (63 and 93 keV), etc. in lungs/liver/skeleton/stomach/wound etc. of workers.

10 Measurement of Radioactivity in Environmental and Biological Samples

Apart from individual monitoring systems, there is a requirement of rapid monitoring of environmental or food samples during an emergency scenario. Portable monitoring systems which can be shifted to the site or selected near by monitoring centers will be highly useful for this purpose. Vehicle Mountable Detection System (VMDS) is a complete transportable system for quickly determining whether raw or processed food has become contaminated with gamma emitting radionuclides during any nuclear and/or radiological event [23]. It incorporates 76 mm × 76 mm NaI(Tl)

Fig. 7 Vehicle mountable detection system for in-situ measurement of environmental and food samples with containers representing various sample geometries

detector, laptop and shield (51 mm lead rings, 2 mm tin and 1 mm copper lining) mounted on a SS trolley with brakes. Radioactivity in milk, meat, fish, grain, fruit, grass and vegetables, as well as air swipes, soil samples, and other materials can be assessed in a few quick steps. VMDS should be calibrated for a wide range of sample geometries. Depending on the sampling time and the isotope, the detection limit is approximately 20–100 Bq L^{-1} and can easily identify concentrations of ^{131}I, ^{134}Cs, and ^{137}Cs. It has enhanced the capability for rapid screening of foodstuffs/biological/environmental samples for gamma-emitting radionuclides released during any radiological and nuclear emergency situations. Figure 7 presents a vehicle mountable monitoring system and different geometries for which measurements can be carried out.

11 Conclusion

In this chapter, an overview of the present strategies of emergency preparedness and response during an off-normal situation of radiation emergency are reviewed. Details of the methodologies followed during monitoring of large number of individuals, guidelines for internal contamination monitoring during emergency situations, important monitoring parameter considerations are discussed in the present chapter. Also, the field procedure/considerations for screening of the people after nuclear or radiological accident, large-scale individual thyroid and whole body monitoring, etc. by means of spectrometric and non-spectrometric equipment are discussed. Application of instruments such as deployable in-vivo monitoring systems Portable Whole Body Monitor (PWBM), Portable Thyroid Monitors (PTM), Vehicle Mountable

Detection Systems, etc. that are the important for internal contamination monitoring during radiation emergency situations are also discussed.

References

1. https://www.who.int/health-topics/radiation-emergencies. Accessed 12/10/2023
2. The international nuclear and radiological event scale user's manual (2008)
3. NCRP (2005) Key elements of preparing emergency responders for nuclear and radiological terrorism. NCRP commentary no. 19
4. IAEA (2003) Categorization of radioactive sources (revision of IAEA TECDOC-1191)
5. IAEA (1988) The radiological accident in Goiania. ST1/PUB/815
6. Population monitoring and radionuclide decorporation following a radiological or nuclear incident. NCRP report no. 166
7. Sources and effects of ionizing radiations. UNSCEAR report 2000
8. IAEA (2015) General safety requirements no. GSR part 7. In: IAEA safety standards preparedness and response for a nuclear or radiological emergency
9. Criteria for planning, preparedness and response for nuclear or radiological emergency. AERB safety guideline AERB/NRF/SG/EP-5 (Rev. 1)
10. International Atomic Energy Agency (2017) Operational intervention levels for reactor emergencies. IAEA, Vienna
11. IAEA-EPR-Internal Contamination (2018) Medical management of persons internally contaminated with radionuclides in a nuclear or radiological emergency
12. IAEA (2011) Criteria for use in preparedness and response for a nuclear or radiological emergency. IAEA safety standards series no. GSG-2. IAEA, Vienna
13. IAEA (1994) Rapid monitoring of large groups of internally contaminated people following a radiation accident IAEA-TECDOC-746. IAEA, Vienna
14. Vilardi I et al (2018) Large-scale individual thyroid monitoring following nuclear accidents by means of non-spectrometric devices. J Radiol Prot 38:1454–1468
15. Etherington G (2017) CAThyMARA report: technical guidelines for radio-iodine in thyroid monitoring. In: OPERRA deliverable D5.31 seventh framework programme OPERRA D5.31
16. ISO (2010) Radiation protection—performance criteria for radiobioassay ISO 28218. International Organization for Standardization, Geneva
17. Balonov M, Kaidanovsky G, Zvonova I, Kovtun A, Bouville A, Luckyanov N, Voillequé P (2003) Contributions of short-lived radioiodines to thyroid doses received by evacuees from the Chernobyl area estimated using early in vivo activity measurements. Radiat Protect Dosim 105:593–599
18. Sankhla R, Rao DD (2018) Development of portable thyroid monitor for thyroidal ^{131}I measurement during nuclear emergency situations. In: Book of abstracts 33rd IARP international conference (IARPIC-2018), p 55
19. Sankhla R, Sawant PD, Kulkarni MS (2020) Development of portable whole body monitor for measurement of internal contamination during emergency situation. Paper presented in virtual national conference IARPNC2020, 21–23 Jan 2021, p 125
20. Singh IS, Sankhla R, Patni HK, Akar DK, Ghare VP, Hans RP, Rao DD, Pradeepkumar KS (2014) Development of new shadow shield bed whole body radioactivity monitor. Published in health physics professional meet held at AERB, Mumbai, 20 Nov 2014
21. Singh IS, Suri MMK, Vidhani JM, Garg SP, Sharma RC (2002) Development of an automated shielded chair whole body monitor. Radiat Prot Dosim 102(2):145–152
22. Sankhla R, Singh IS, Rao DD, Pradeepkumar KS (2015) Development of quick scan whole body monitor for in-vivo monitoring of radiation workers and general public. In: BARC newsletter, July–Aug 2015, pp 13–19

23. Sankhla R, Nair S, Sawant PD, Kulkarni MS (2023) Development of vehicle mountable detection system for measurement of gamma emitters in biological/environmental samples during radiological/nuclear emergencies. In: Proceedings of 6th Asian and oceanic congress for radiation protection (AOCRP6) conference, Mumbai, 07–11 Feb 2023, p S433

Decorporation of Radionuclides

Vijayakriti Mishra and Suma Nair

1 Introduction

Various processes in nuclear fuel cycle (such as mining, processing, fuel fabrication, reactor operation and maintenance, decommissioning, reprocessing, waste management) as well as activities in other industries might lead to accidental emissions of radioactive substances, even with safety measures and radiation safeguards in place. Major nuclear accidents, inappropriate practices for management and disposal of radioactive waste, nuclear weapon tests, and incidents involving radionuclides at nuclear facilities or other user establishments such as hospitals, research and industrial facilities are considered as probable sources of external and internal contamination. Intentional malicious actions, such as terrorist acts in medical facilities, research centers, public spaces, or the natural surroundings, can also lead to the discharge of radioactive substances.

Internal contamination occurs when radioactive substances enter the body via inhalation, ingestion or absorption through the skin. The primary routes of internal contamination are inhalation and absorption through wounds. While ingestion as a pathway for contamination is rare in work-place, it could become significant for the general population following the release of radioactive materials into the air or water, or intentional contamination of food/water sources [1]. Irrespective of the route of entry, once inside the body, these radioactive particles are taken up by the bloodstream, and carried to specific organs (e.g. bone, kidney, liver, etc.) where they accumulate before eventually being eliminated through urine and feces. The rate of elimination varies depending on the type of radionuclides and their physical and biological half-lives [2, 3].

V. Mishra (✉) · S. Nair
Internal Dosimetry Section, Radiation Safety Systems Division, Health, Safety and Environment Group, Bhabha Atomic Research Centre, Mumbai 400085, India
e-mail: vijayakm@barc.gov.in

D. K. Aswal (ed.), *Handbook on Radiation Environment, Volume 2*,
https://doi.org/10.1007/978-981-97-2799-5_25

Till these radioactive pollutants persist within the body, they irradiate specific organs, which can potentially lead to long-term stochastic health consequences. To quantify internal exposure, the concept of "committed effective dose" is commonly used. This term refers to the cumulative effective dose resulting from the integration of the radioactive element over a span of 50 years for occupational workers (or 70 years for public).

Major goal after the internalization of radionuclides is to reduce the committed effective dose by removal of internalized radionuclide. In case of high internal contamination, the natural excretion rate cannot ensure fast removal of radionuclides from the body and hence needs to be accelerated. The biological removal processes are enhanced by employing specific drugs or chemical agents and this is known as decorporation. As per IAEA glossary [4], "*decorporation is the action of the biological processes by means of which incorporated radionuclides are removed from the human body. It may be promoted by chemical or biological agents.*"

In contrast to unaltered exposure through external radiation, doses stemming from accumulated radioactive substances due to internal contamination can be reduced. The goal of reducing dose after intake is achieved by decorporation. Although post-exposure intervention usually falls within the realm of medicine, it's important to engage the internal dosimetry program to effectively address the situation [5].

The measurement and analysis of internal contamination's extent and nature are conducted using bioassay methods. These techniques involve either direct measurements within the body (in vivo) or indirect measurements outside the body (in vitro). This process encompasses identifying the specific radionuclide(s) present, activity measurements, evaluation of intake and computation of dose using dosimetric/biokinetic models. These methodologies are discussed in detail in previous chapters. The present chapter deals with various decorporation strategies employed for removal of internalized radionuclides, current practices and research developments in this field.

2 Decorporation: Goals and Factors Affecting Treatment

The primary goal of decorporation is to minimize the internal dose, consequently lowering the potential health risks. The immediate goals of decorporation treatment can be summarized as [6]:

- Reducing the absorption of the radionuclide into the bloodstream and its subsequent accumulation in specific organs or tissues;
- Accelerating the radionuclides removal rates from the body;
- Minimizing the absorbed dose by utilizing the most efficient technique.

The primary objective of the decorporation therapy is to decrease the likelihood of radiation-induced cancer over the long term. These goals can be achieved by decreasing absorption, halting the incorporation and internal accumulation of

radionuclides within organs, and encouraging the elimination or removal of absorbed particles. This approach is most effective when initiated promptly [7].

The first and foremost consideration while deciding on decorporation treatment is route of entry, i.e. intake pathway. There are four potential pathways through which radionuclides can be internalized. These encompasses inhalation of radioactive particles or gases, consumption of radioactive dust, contaminated food, or water, absorption through open wounds or unbroken skin, and injection of radioactive materials into the body. After a radionuclide enters the body, it undergoes a sequence of physiological changes. How radioactive material is held in or discharged from organs and tissues hinges on factors like its physical and chemical forms, the route of entry, and physiological circumstances [2, 3].

Choosing a preferable decorporation strategy depends on several factors [6] such as:

- Physical properties of the radioactive contaminant (decay mode, half-life, etc.);
- Biokinetics of the radionuclide (solubility classification);
- Radiosensitivity of target organ or tissue;
- Route of intake and its amount (activity);
- Effectiveness of the treatment and potential therapy-related adverse effects;
- Age and concurrent health conditions of the affected individual.

The efficacy of treatment using chelating agents can be influenced by several factors. These include the route of entry, the amount and physico-chemical characteristics of the incorporated radionuclide, its interactions with biological molecules at the entry site, during blood absorption, and at the deposition site. Additionally, the kinetics of radionuclide absorption into the blood, the treatment method, treatment duration, and the ratio of radionuclide to chelating agent also affect therapy effectiveness.

Clinically approved chelating agents are ideally best assessed after accidental human exposure. However, this can be challenging for certain radionuclides, particularly actinides, due to uncertainties about their physico-chemical form, intake pattern, and intake assessment. Furthermore, the administration method of the chelating agent might not align with the most suitable route or protocol.

Many physicians prefer slow intravenous injection or infusion, as they believe chelation is most effective when the radionuclide is in the bloodstream. On the contrary, research on animals has demonstrated that chelating agents are most potent for biologically soluble radionuclide forms when these substances are at the deposition site such as the lungs or a wound. In such cases, applying the chelate locally is the optimal choice. However, if systemic absorption occurs over a prolonged period, intravenous infusion either directly or as a result of oral administration—might be the most effective strategy. For biologically insoluble materials inhaled into the lungs, broncho-pulmonary lavage might be the only viable treatment method.

3 Decision on Decorporation Treatment

After the intake of radioactive substances, the evaluation of internal dose and the subsequent strategy for treatment will be contingent upon various factors. These factors encompass the physical and biological attributes of the radionuclide, including its radioactive half-life, particle size, chemical form, solubility, and biokinetics. Internal dose assessment program comprises of radionuclide or set of radionuclide identification, assessment of quantities (excretion values, retention values, etc.) with the aid of bioassay procedures, evaluation of intake and assigning internal dose for workers/individuals. Samples such as blood, urine, feces, nasal swabs, filter paper, etc. should be collected for analysis [1, 6]. The selection of a bioassay sample to be collected will be influenced not solely by the primary excretion pathway, which is identified through the physical and chemical characteristics of the intake and the biokinetic model for the element(s) in question but also by considerations such as the simplicity of collection, analysis, and interpretation.

After assessment of internal contamination, based on estimated internal dose, decorporation therapy may be initiated by medical doctor in consultation with health physicist. Treatment is not considered if the estimated internal doses are below Medical Reference Level (MRL) value of 20 mSv [8]. When the internal dose is likely to be between 20 and 200 mSv, medical doctor in consultation with health physicist should decide the treatment for decorporation. If the calculated dose surpasses 200 mSv, extended or prolonged treatment should be employed, contingent upon the severity of the radiation-induced injury or effects. Decorporation treatment should be initiated for children and pregnant ladies at one-fifth of the adult value [1]. It's important to recognize that the implementation of interventional methods to accelerate the natural elimination rate of a substance or potentially impede the absorption of a radionuclide in specific tissue can potentially undermine the applicability of standard ICRP model methodologies for estimating intake and dose. Moreover, any decorporation therapy itself is not completely risk free and can incur some side effects in long run [1].

The implementation of decorporation therapy needs to be carefully weighed against the potential toxicological hazards associated with the drugs employed. For instance, while chelating agents are highly proficient at binding radioactive isotopes, they can also bind stable isotopes. Decorporation procedures involving chelating agents and similar substances typically involve a sequence of administrations spread out over days, weeks, and occasionally months.

If these compounds are administered for long time, close monitoring of electrolytes and essential trace elements is also needed [9]. On the other hand, if there's a potential risk for severe deterministic effects, it's advised to initiate decorporation treatments as early as possible. Decorporation is predominantly employed in situations where substantial doses are anticipated. Tailored decorporation therapies for specific radionuclides are employed to avoid deterministic effects, reduce stochastic risk and prevent deaths [10]. In the majority of instances, the objective of treating internal contamination is to mitigate the potential for long-term effects

rather than addressing an acute radiation-related injury [6]. Historical radiological incidents suggest that the internalization of radionuclides generally doesn't lead to acute radiation sickness [11].

In case of emergency scenarios, the determination of whether to proceed with decorporation treatment relies on Operational Intervention Levels (OILs). OILs are predefined action levels employed promptly and directly without additional evaluation to establish suitable protective measures, guided by measurements. In case of internal exposure, OIL values for decorporation are based on the retention values of radionuclides in in particular organs or tissues, along with excretion rates. These values correspond to reference level of intake for the decision on decorporation to avoid severe deterministic effect or future occurrence of stochastic effects [12].

Internal decontamination (decorporation) should be carried out by medical staff to reduce the amounts of radionuclides in wounds and body of affected workers/individuals by considering their individual factors into account. Several factors must be taken into account, including potential trauma resulting from the incident, overall health condition, age, pregnancy status, emotional well-being, intake route, time elapsed since intake, and the biochemical and physical characteristics of the radionuclide causing internal contamination, along with its deposition site within the body. Considering the incident itself, the number of individuals contaminated holds significance due to logistical constraints and the availability of resources, including medication. Physicians might rely on chest or whole-body counts, activity measurements in bodily excretions, or nasal swabs for assessments.

4 When to Start Decorporation Treatment?

Another key issue is when to start the decorporation treatment. The question arises whether treatment should be postponed to await internal dosimetry results or if it should be initiated promptly. Treating early subsequent to internal contamination improves efficacy of employed decorporation therapy. However, concerns arise regarding potentially subjecting workers or individuals to the side effects of chelating agents or drugs when the internalized activity is turned out to be irrelevant. Furthermore, the inventory of drugs used for decorporation may be very limited due to their infrequent use and low demand which might lead to shortages afterwards if administered indiscriminately shortly after an accident or incident [11]. Stochastic health effects resulting from internal contamination are assessed through the absorbed effective dose. Therefore, basing the decision for decorporation treatment on the committed effective dose, following established radiological protection guidelines, seems reasonable. This approach aligns with the recommendations of various authors and agencies and is known as the "precautionary approach" in decorporation treatment [13]. Indication of treatment depends on the committed effective dose, for < 20 mSv: no treatment is indicated, for 20–200 mSv: case by case decision is made and for > 200 mSv: indication for treatment.

However, the assessment of committed effective dose involves identifying the radionuclide(s) internalized, measuring radioactivity in the body through whole-body counting or excretion measurements in urine or feces (depending on the radionuclide(s)), and calculations based on appropriate biokinetic and dosimetric models. These procedures are time consuming and, are feasible in case of incidents in nuclear facilities for a small number of individuals exposed. Depending on the location and number of individuals, obtaining results can take days or even weeks. For cases when intake is substantial, this delay can result in substantial drop in efficacy of decorporation treatment. While there isn't a standard protocol that specifies when treatment is warranted, experience has shown that detailed dose assessments are often not possible in a timely manner, making the decision to treat a subjective judgment [14].

5 Decorporation Methods

After the internal contamination of radionuclides, interventions are primarily aimed at expediting the removal of the radionuclide(s). Chemical compounds, drugs are employed for assisting elimination of the radionuclides but their basis of mechanism varies. The decorporating agents can be clubbed in groups based on mechanism of action. General decorporation methods [1, 6, 7, 14] are discussed in detail below.

5.1 Reduction of Uptake

There are overarching methods designed to prevent or decrease the absorption of radionuclides from the gastrointestinal (GI) or respiratory tracts, as well as from skin and wounds. These strategies encompass rinsing the nose, mouth, pharynx, and wounds. To minimize gastrointestinal absorption, procedures like gastric lavage and the use of mild emetics and purgatives can be employed to hasten the elimination of radioactive isotopes. Especially in the immediate aftermath of intake, these straightforward actions should not be overlooked. Any reduction in the duration that radioactivity remains in the GI tract will subsequently lower the absorbed dose.

Lung lavage, although it could be considered as a part of "general procedures," however due to its particularities is distinct in its nature and will be addressed separately. E.g.: the administration of magnesium sulfate as a laxative can diminish the time radioactive materials reside in the lower segment of the large intestine. Additional approaches involve using activated charcoal, Prussian blue (for cesium) (Fig. 1), antacids (for strontium), and barium sulfate to absorb radioactive substances.

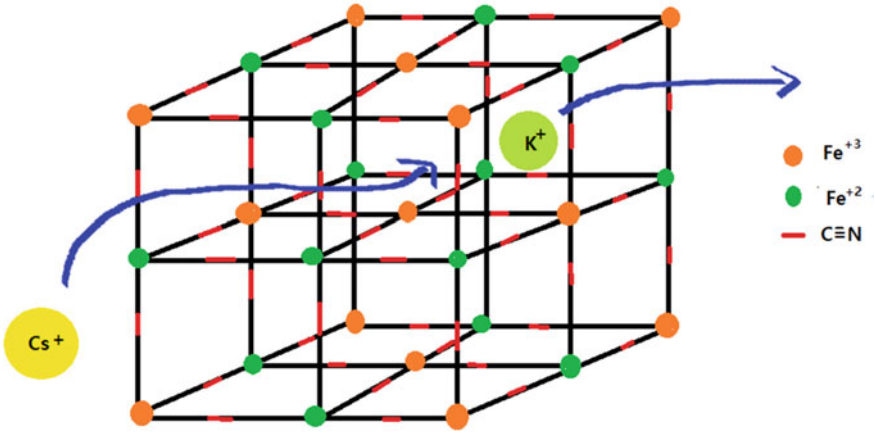

Fig. 1 Ion exchange mechanism of Prussian blue for cesium decorporation

5.2 Blocking

Blocking agents function by saturating the metabolic pathways of a particular tissue or organ with a stable isotope, thereby diminishing the body's absorption of a radionuclide. E.g.: stable potassium iodide (KI) is administered to hinder the uptake of radioiodine in the thyroid. This method is particularly effective when taken shortly before or promptly after internal contamination transpires.

5.3 Isotopic Dilution

The method of treating involves administering significant amounts of a stable isotope of the radionuclide in question. This large quantity of stable element serves to dilute the smaller quantity of the radioactive isotope, thereby expediting the elimination process of the radionuclide. E.g.: enhanced fluid intake for tritium contamination reduces the biological half-life of tritium (radioactive hydrogen) within the body. This is achieved through the dilution effect and the accelerated turnover time of water.

5.4 Displacement

This approach operates on the same principle as blocking and dilution therapies but it involves the use of non-radioactive elements with distinct atomic numbers. In this treatment, the non-radioactive element competes effectively for the uptake sites,

displacing the radioisotope from the receptors. E.g.: calcium gluconate competes with radio-strontium for bone deposition, while stable iodine is employed to displace ^{99m}Tc.

5.5 *Mobilization*

This pertains to treatment involving compounds referred to as mobilizing agents. These agents stimulate the body's natural turnover processes, thereby trigger the release of radionuclides from body tissues and augmenting the rate of elimination. E.g.: when administered orally, ammonium chloride leads to blood acidification and elevates the elimination of internalized radiostrontium. Diuretics are used for sodium, chlorides, potassium, and tritium, further enhancing elimination.

5.6 *Chelation*

Several organic or inorganic compounds have been identified for their ability to facilitate the removal of metals from the body through chelation. Chelation involves the binding of chelating agents with metal ions (Fig. 2) to create a relatively stable non-ionized ring complex, known as chelates. This soluble complex can be easily excreted by the kidneys. This topic is discussed in detail in Sect. 9.1. E.g.: Ca-DTPA for transuranics.

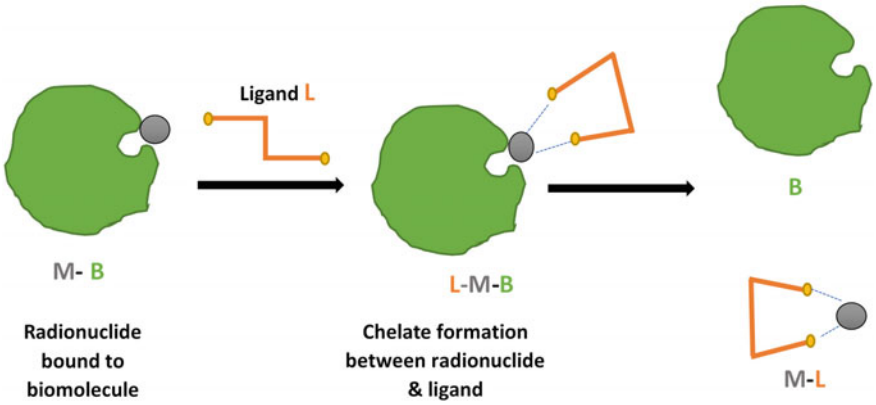

Fig. 2 Schematics for decorporation of radionuclide by chelation

5.7 Excision

Wound debridement and excision may be employed to eliminate fixed contamination. Surgical exploration and the removal of contaminated tissue or foreign substances might be necessary in cases where such actions are warranted.

The procedure demands a thorough evaluation by specialized experts and surgical procedure should be performed with assistance of health physicist monitoring through a wound probe. The excision is performed primarily to remove long-lived alpha contaminants.

5.8 Lung Lavage

This is an invasive procedure that is seldom employed and is typically reserved for cases involving a significant accumulation of insoluble inhaled particles within the lungs. The deposition of radioactive particles in the lungs is the most prevalent form of internal contamination by radionuclides. When insoluble particles are deposited in the lungs, they dissolve slowly, and their uptake into the bloodstream, followed by transport to other targeted organs, takes place over many months to years.

Lavage of the tracheobronchial tree is a treatment technique suited for individuals who have inhaled substantial amounts of insoluble radionuclides. This process involves inserting an endotracheal tube into the trachea and major bronchi while the individual is under general anesthesia. The lungs are then washed with isotonic saline. Before resorting to this treatment, a comprehensive medical and dosimetric evaluation is crucial. Parameters such as clinical status, worker's age, existing health conditions, the radiotoxicity of the internalized radionuclides, the burden of contamination, and dose assessments should all be taken into consideration. This procedure should be considered only in cases of high exposure where a dose reduction could potentially avert deterministic effects such as radiation Pneumonitis or Fibrosis.

A summary of common decorporation strategies for treatment of internalized radionuclides is given in Table 1.

6 Decorporation Therapy Recommendations

Table 2 summarizes some important decorporating agents recommended by agencies like NCRP, IAEA, etc. [1, 6, 14]. Element-specific procedures are given in the last section of this chapter.

Table 1 Decorporation strategies for internal contamination

Decorporation method	Mechanism of action	Examples
GI uptake reduction	Reduction of radionuclide adsorption in GI tract by physical absorption, by reduction in transit time (laxative), by forming insoluble compounds	Activated charcoal, sulfate salts, Prussian blue, alginate, aluminum phosphate, magnesium sulfate
Blocking or dilution	Saturation of the target organ with a stable isotope or similar element to prevent the uptake of the radionuclide	Stable potassium iodide Stable strontium or calcium salts
Mobilization	Enhance turnover and natural elimination rate	Diuretics Ammonium chloride
Chelation	Forming soluble complexes thereby enhancing elimination from body	Ca-DTPA, Zn-DTPA

Table 2 Recommended decorporating agents for radionuclides of concern

Radionuclides	Treatment
Iodine	KI
Rare earths, yttrium, plutonium, transplutonics, cobalt, thorium	DTPA[a]
Polonium, arsenic, mercury, gold	BAL[b]
Uranium	Bicarbonate
Cesium, rubidium, thallium	Prussian blue
Strontium, radium	Aluminum hydroxide
Tritium	Water
Calcium, barium	$BaSO_4$, sodium alginate
Copper, gold, lead, polonium, gallium	D-penicillamine
Sodium, potassium	Diuretics
Bismuth, mercury	DMPS[c]
Carbon	Consider hydration and stable carbon
Iron, neptunium	DFOA[d]
Lead, mercury	DMSA[e]
Phosphorus	Hydration, oral sodium or potassium phosphate
Sulfur	Sodium thiosulfate
Fluorine	Aluminum hydroxide
Nickel	DDTC[f], BAL

[a] *DTPA* Diethylenetriaminepentaacidic acid
[b] *BAL* British Anti-Lewisite (2,3-dimercapto-l-propanol)
[c] *DMPS* Dimercaptopropansulphonate
[d] *DFOA* Deferoxamine
[e] *DMSA* Dimercaptosuccinic acid
[f] *DDTC* Diethyldithiocarbamate

7 Adverse Effects of the Decorporating Agents

Very less side health risks are associated with decorporation therapy in humans. The potential side effects of decorporation therapy should never be overlooked; however, their necessity must be weighed to accurately assess the risk-to-benefit ratio of the treatment. Adsorptive agents like activated charcoal can lead to abdominal discomfort, frequent nausea, vomiting, and constipation. Laxatives may cause stomach cramps, dehydration, and electrolyte imbalance, especially with excessive dosing. Overall, assuming short-term treatment and no contraindications, the use of adsorptive agents and laxatives is relatively safe [11].

Allergic reactions must be considered when employing any treatment method. Allergic reactions associated with iodide, such as skin irritation, rash, and gastrointestinal distress, are commonly encountered in surgical patients. The use of potassium iodide in Poland after the Chernobyl accident provided valuable safety information, with only allergic reactions reported in adults [14]. Another potentially life-threatening reaction to iodide treatment, particularly at the dosage used for radioiodine prophylaxis, is thyrotoxicosis, involving inappropriately high levels of circulating thyroid hormones. Patients with a history of thyroid gland issues should be assessed before potassium iodide administration to identify those at risk [11].

Prussian Blue, known to cause constipation, was observed in some patients in the aftermath of the Goiânia radiation accident. High doses over an extended period may cause slight obstipation. In addition, the patient will observe blue stool, which may be a psychological consideration [11, 14]. No toxic symptoms were observed in adults treated with various doses of Prussian Blue [13]. The theoretical concern of cyanide ion release due to its chemical structure was extensively studied and dismissed.

BAL, a potent chelating agent, especially for arsenic and mercury poisoning, may lead to various serious side effects. These include nausea, vomiting, lip and throat burning, salivation, abdominal pain, anxiety, weakness, and neurological effects like headache and tingling. Cardiovascular effects and other miscellaneous symptoms may also occur.

Repeated Ca-DTPA doses can deplete essential trace metals like zinc and manganese, interfering with crucial cellular processes over time. Small side effects such as nausea, vomiting, diarrhea, chills, fever, and muscle cramps may occur within the first 24 h of treatment. Serious complications have been rare in humans following administrations of Ca-DTPA and Zn-DTPA at recommended dosages. Severe toxicity was mainly observed in animal studies with high doses compared to clinical human doses. Ca-DTPA is more effective than Zn-DTPA for initial transuranic chelation, while Zn-DTPA is preferred for protracted therapy due to its comparable efficacy and lower toxicity [14].

In cases of internal contamination with a mixture of radionuclides, potential redistribution phenomena with adverse health effects should be considered when making therapeutic decisions.

8 Research Related to Decorporation Strategies

This section focuses on new decorporation strategies and chelating agents currently being investigated or have been investigated in past for efficient removal of radionuclides from body. Extensive research has been conducted in the past and is ongoing, particularly focused on designing ligands with appropriate structural and coordination properties for radionuclides, particularly with a primary emphasis on actinides. The cornerstone of developing successful sequestering agents for radionuclides lies in gaining a deeper comprehension of their behavior within living organisms.

Actinides can bind with many biological ligands present in biological fluids like saliva, gastric juice, blood, etc. The majority of studies investigating actinide biochemistry center around blood, as the overall characteristics of radionuclides are influenced by how long they remain within this compartment. In blood, most of the An ions tend to associate with plasma proteins like human serum albumin (HSA), globulin and serum transferrin (sTf). Pu(IV), Th(IV), Cm(III), Np(IV), and Np(V) have found to bind to transferrin [15–18]. Binding of Uranyl ion has been investigated with HAS [19, 20]. However, in all An cases, a fraction of An complexes with ligands of low molecular weight ions (e.g. carbonate, phosphate and citrate) is also present. Among plasma proteins, HSA (most abundant) and sTf (presence of iron-binding sites) serve as major metal transport carriers. In case of actinides, chelation mechanism is used for enhancing the radionuclide excretion.

8.1 Chelation Therapy

Chelation therapy is a medical procedure involving the introduction of chelating agents into the body to eliminate heavy metals or other toxic substances. A chelating agent, also known as a chelant, is a complex ion or compound composed of a ligand attached (coordinated) to a metal atom or ion through two or more nonmetal atoms. This arrangement forms a cyclic structure known as a chelation complex or chelate. The term "chelate" originates from the Greek word "chela," meaning the large claw of a lobster. Ligands, which form these chelation complexes, can consist of inorganic ions like Cl, F, or carbonate, or organic compounds containing two, four, or six functional groups with atoms such as S, N, O, or P [14, 21].

Chelating agents can possess varying levels of complexity based on the number of atoms capable of forming complexes with a metal atom simultaneously. They can be bidentate (two atoms), tridentate (three atoms), tetradentate (four atoms), and so forth. In thermodynamic terms, chelates tend to be more stable than regular metal complexes where complexing agents feature only a single electron donor atom. This enhanced stability is reflected in significantly higher equilibrium constants for chelates compared to standard metal complexes.

Chelation plays a significant role in the field of medicine. Chelation therapy, a notable application, has primarily been employed for treating heavy metal poisoning,

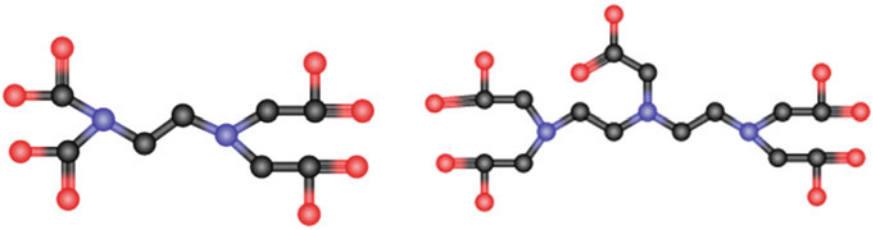

Fig. 3 General chemical structures of **a** EDTA and **b** DTPA

including lead, mercury, or arsenic toxicity. One important medical application of chelation is the removal of radionuclides from the human body, i.e. decorporation.

8.1.1 Polyaminopolycarboxylic Acids

Ethylene Diamine Tetra-Acetic Acid (EDTA)

First synthesized in 1935, EDTA (ethylenediaminetetraacetic acid) initially found application as a calcium-sequestering agent in the textile industry. However, by the mid-1940s, EDTA garnered significant attention and underwent intense investigation. It became recognized as a prominent analytical agent for assessing calcium and various metal ions. EDTA is capable of creating stable complexes (Fig. 3) with lanthanide and actinide elements, which could be excreted from the body. It is the first chelating agent proposed as decorporating agent in 1949. However, M-EDTA complexes such as Na_4-EDTA and Ca_2-EDTA were found renally toxic and responsible for depletion of vital divalent trace metals (e.g. Zinc) [22].

Diethylene Triamine Penta-Acetic Acid (DTPA)

Over time, it became evident that the development of new ligands with higher affinities than EDTA for multivalent cations and lower affinities for divalent metals was essential. DTPA (diethylenetriaminepentaacetic acid) emerged as a superior agent compared to EDTA for removing many toxic metals. The enhanced effectiveness of DTPA over EDTA, particularly with polyvalent cations like lanthanides and actinides, arises from DTPA's octadentate nature in contrast to EDTA's hexadentate structure.

H_5-DTPA was patented as a decorporating agent in 1955. Although H_5-DTPA and Na_5-DTPA displayed acute toxicity, this adverse effect could be mitigated by using the Ca chelate. $CaNa_3$-DTPA, while being as renally toxic as $CaNa_2$-EDTA, demonstrated efficacy as a decorporating agent due to its significantly higher log KML stability constant values for chelates with lanthanide and actinide ions compared to

EDTA. $CaNa_3$-DTPA proved effective but required very low doses (clinically acceptable levels). In some species, frequent injections of $CaNa_3$-DTPA led to toxicity due to the depletion of essential divalent metals.

Substituting Zn for Ca in $ZnNa_3$-DTPA reduced the overall effectiveness for Pu decorporation but lowered toxicity, allowing for daily treatment over a prolonged period. In 2004, the U.S. Food and Drug Administration (FDA) approved two forms of DTPA, $CaNa_3$-DTPA and $ZnNa_3$-DTPA, to accelerate the excretion of Pu, Am, and Cm after internal contamination [23].

Shortcomings

Conventional DTPA therapy, despite its capacity to chelate soluble trivalent actinides and Pu(IV) in bodily fluids, faces certain limitations. The stability constant of Pu(IV)-DTPA is insufficient to effectively suppress the solubilization of plutonium hydroxides at physiological pH. Consequently, while DTPA can eliminate soluble actinide complexes in bodily fluids, its efficacy diminishes significantly for removing lanthanides or actinides after the hydrolysis of metals and the subsequent formation of colloids or polymers. DTPA lacks specificity for metals with high ionic charges, and the less potent Ca or Zn chelates must be used to avoid depleting essential divalent metal ions such as Ca, Zn, Co, Cu, and Mn [14, 24].

Hydrophilic $CaNa_3$-DTPA and $ZnNa_3$-DTPA are limited to distribution within extracellular water and cannot penetrate cells, making them ineffective against intracellular actinides. Once Pu is bound in tissues and bones, DTPA has minimal impact on its mobilization and does not compete with actinides already incorporated into bone. These factors understandably restrict decorporation's effectiveness if the chelating agent is not administered immediately following radionuclide intake [10]. The current FDA-approved drugs, $CaNa_3$-DTPA or $ZnNa_3$-DTPA, are not orally effective at recommended clinical doses and are typically administered through injection or inhalation. Oral bioavailability would be a highly desirable attribute for an actinide sequestering agent, particularly if repeated doses or widespread treatment are necessary. Furthermore, DTPA is ineffective for certain other actinides like Th(IV), Np(IV), or U(VI), which could pose challenges in cases of multiple metal contaminations or uncertainties about the contaminant [25]. This may be an issue if more than one metal is present in an accident or if there are questions about the contaminant.

Efforts to explore alternative solutions have led to the synthesis and testing of other Polyaminocarboxylic acids (PACAs) with longer central bridges and additional carboxylic acid groups. However, the affinities of these ligands for trivalent lanthanides and Ca were not more favorable than those of DTPA. None of these alternatives proved more effective than $CaNa_3$-DTPA; in fact, some were even less effective, leading to the discontinuation of these investigations. Certain PACAs with various alkyl chain lengths were found to reduce orally administered Am deposits, but the differences in bone Pu were negligible. Some compounds are still being studied for potential applications [22].

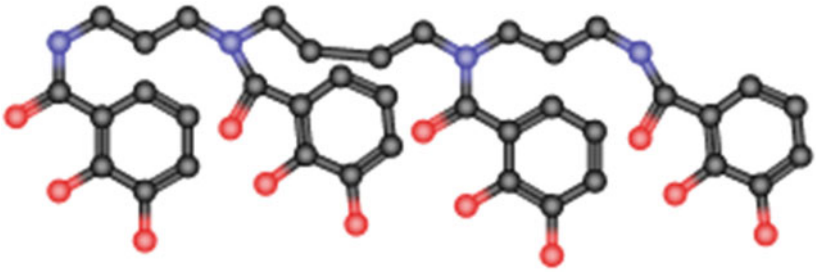

Fig. 4 General chemical structure of 3,4,3-LICAM

8.1.2 Siderophores

Chelating agents analogous to siderophores, the natural agents produced by microorganisms to sequester iron are quite efficient for selective decorporation of actinides. Siderophores are microbial iron-binding compounds widely recognized as effective agents for controlling biological processes, detecting substances, remediation, and chelation, primarily due to their exceptionally strong attraction to Fe(III). When competing with Fe(III) for binding, siderophores can also capture protons and other metal ions with two or three positive charges. These encompass not only Ln(III) ions but also An ions in various oxidation states. The robust inclination of siderophores to form bonds with these highly charged metal ions is attributed to the robust oxygen-donating atoms present within their distinct structures.

The binding components that exist in siderophores, such as catecholates, catecholamides, amino carboxylic acids, hydroxamates, or hydroxypyrimidonates (HOPOs), exhibit a notably specific affinity for Fe^{3+} and similar radioactive analogs. In the pursuit of designing synthetic compounds with properties akin to siderophores, a biomimetic approach was adopted. This strategy involved crafting octadentate ligands, resembling siderophores, that incorporate hydroxamate and catecholate functionalities. These ligands were developed for the purpose of efficiently sequestering Ln/An elements.

Catecholates (LICAMS)

Highly promising linear catechol ligands have been formulated for application in therapeutic treatments aimed at removing toxic metals from the body. Notable among these ligands are 3,4,3-LICAM (Fig. 4) and its derivatives containing sulfonate and carboxylate groups, namely 3,4,3-LICAM(S) and 3,4,3-LICAM(C). These ligands have been specifically designed for their effectiveness in chelating Pu(IV) ions. A comprehensive investigation revealed that among these compounds, 3,4,3-LICAMS exhibited the highest efficacy as a chelating agent for incorporated plutonium [26].

When addressing the potential contamination of inhaled transuranic elements, which represents a primary concern in workplace settings, it was found that DTPA

(Diethylenetriaminepentaacetic acid) outperformed 3,4,3-LICAMS as a chelating agent. It's important to note that this observation contrasts with studies involving injected transuranics. In the context of inhaled transuranics, which pose a significant risk due to their mode of exposure, DTPA demonstrated a higher level of effectiveness in comparison to 3,4,3-LICAMS. Both chelating agents, however, displayed equal efficiency in terms of eliminating circulating radionuclides from the bloodstream [14].

The ineffectiveness of LICAMS could be later explained by chemical investigations. These investigations revealed that, at a pH of 7, only three out of the eight phenolic oxygens available in LICAMS could undergo deprotonation for the purpose of engaging in ion binding. This finding suggests that in order to achieve effective in vivo chelation, the incorporation of functionalities possessing greater acidity than catechol would be necessary [22].

Hydroxyl Pyrimidonates (HOPOs)

Bidentate hydroxypyridinone chelators have proven to be highly effective in forming complexes and aiding in the excretion of trivalent iron from the body. When in an ionized state, these isomers of HOPO (hydroxypyridinone) are isoelectronic to catechol, the bidentate functional group found in hexadentate enterobactin—a naturally occurring potent iron chelator [22, 26]. These HOPO isomers hold structural and electronic resemblances to both hydroxamic acids and catechol. Similar to hydroxamic acids, hydroxypyridinones are monoprotic acids that establish binding with metal ions through two oxygen atoms. The bonding within metal-hydroxypyridinonate complexes displays substantial delocalization. These factors collectively position HOPOs as effective chelators for hard metal ions, particularly lanthanides and actinides. The cyclic HOPOs exhibit greater acidity compared to aliphatic hydroxamic acids.

The 1,2-HOPO group becomes ionized at pH levels above 5, indicating that ligands containing this group would act rapidly at pH 7, while forming complexes that remain stable across the physiological pH range of 5–8. The monoprotic HOPO groups experience ionization under physiological pH conditions. Within this range, they display a specific high affinity for ferric and other metal ions with charge-to-radius ratios similar to that of Pu(IV). Due to this unique combination of attributes, HOPOs are particularly well-suited for the development of agents aimed at sequestering actinides. Furthermore, the formation constants of Fe(III)-HOPO complexes are significantly higher (by 4–9 orders of magnitude) than those formed with biologically essential divalent cations.

From an array of more than 60 evaluated ligands, two leading candidates have emerged: 3,4,3-LI(1,2-HOPO), an octadentate ligand, and 5-LIO(Me-3,2-HOPO), a tetradentate ligand (Figs. 5 and 6). These candidates have demonstrated considerable potential in actinide sequestration efforts [22, 27].

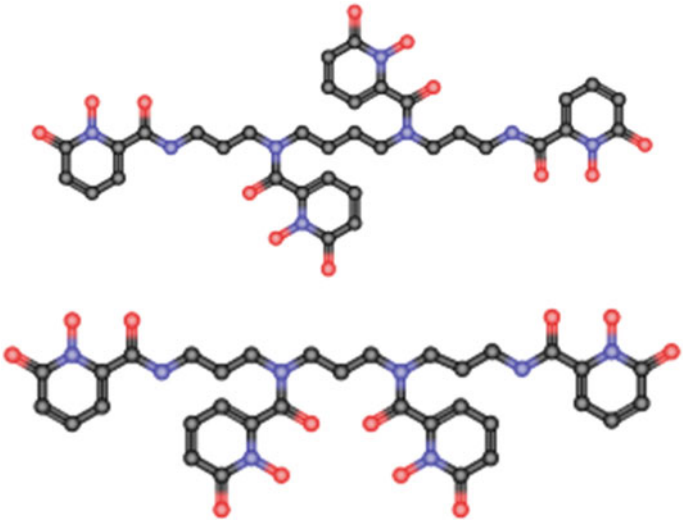

Fig. 5 General chemical structures of **a** 3,4,3-LI(1,2-HOPO) and **b** 3,3,3-LI(1,2-HOPO)

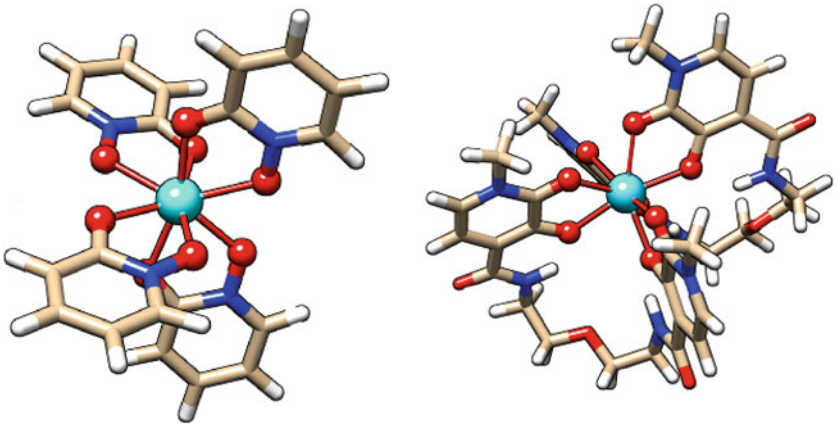

Fig. 6 Molecular structure of Pu bound to 1,2-HOPO and 3,2-HOPO, respectively

The significance of amino carboxylic acids, 1,2-HOPOs, and 3,2-HOPOs having pKa values that fall below or near physiological pH lies in their exceptional effectiveness under physiological circumstances. Many experimental and theoretical studies on HOPO-based ligands have been carried out till now, these studies include studies based upon synthesis of ligands based on HOPOs, their preclinical studies, in vivo administration on rats to compare efficiency of hexadentate ligands over bidentate HOPO-based ligands for Pu decorporation [28–31]. In vivo evaluations were conducted on hydroxypyridonate ligands that drew inspiration from siderophores.

These ligands, available in tetradentate, hexadentate, and octadentate forms, were meticulously assessed for their selectivity and effectiveness in chelating iron or actinide elements. The evaluations encompassed various procedures for both loading metals onto the ligands and assessing their performance. Radioactive tracers, such as ^{59}Fe,^{238}Pu, and ^{241}Am, were employed to facilitate these investigations. These tracers served as markers to track and understand the behavior of the ligands in the presence of these specific metal ions within living systems.

Many improved efficient HOPO-based ligands have been designed and tested. A novel chelating agent called as the mixed chelate, octadentate ligand, 3,4,3-LI (1,2-Me-3,2-HOPO), was specifically developed, synthesized, and subsequently evaluated for its potential to chelate plutonium (Pu) in vivo. This unique ligand was designed to include both 1,2-HOPO and Me-3,2-HOPO metal-binding units. Notably, the Me-3,2-HOPO unit is known to exhibit a higher affinity for actinide ions, including Pu, in comparison to the 1,2-HOPO unit under physiological pH conditions. This ligand was then tested for its effectiveness in sequestering Pu in a mouse model, aiming to assess its ability to efficiently bind and mitigate the presence of this radioactive element within the body.

The administration of the mixed chelate, octadentate ligand, 3,4,3-LI (1,2-Me-3,2-HOPO), yielded significant reductions in body plutonium (Pu) levels compared to control groups when orally administered to mice after injecting Pu intravenously. The effectiveness of HOPOs was evident even at low dosages, and these compounds exhibited oral activity while maintaining low toxicity levels at effective injected dosages. The pharmacological characteristics of HOPOs are highly favorable for in vivo Pu chelation. They possess properties such as the ability to penetrate extracellular water, maintaining a useful presence within the circulation, undergoing substantial hepato-biliary excretion, demonstrating low yet useful gastrointestinal absorption, and temporary residence within the kidneys. This combination of attributes underscores their potential as effective agents for sequestering Pu within living organisms [28].

The chemical syntheses of both potential compounds have been refined for scalability, ensuring that they can be produced in larger quantities as needed. Additionally, foundational preparation techniques and analytical methods suitable for manufacturing substantial quantities have been developed. Importantly, no toxicity was observed in vitro when these compounds were introduced to cells derived from three distinct human tissue sources, even at high ligand concentrations of up to 1 mM. Furthermore, in animal studies, both candidate ligands were administered orally to rats on a daily basis at high doses exceeding 100 μmol kg^{-1} day^{-1} for a duration of 28 days, following the guidelines of good laboratory practice (GLP). These studies demonstrated that both ligands were well-tolerated by the rats, indicating their potential safety for use in vivo. Given these favorable findings, both compounds are currently undergoing an accelerated development pathway towards potential clinical application. The research and development efforts are focused on advancing these compounds for therapeutic use, leveraging their promising characteristics and the significant progress made in terms of synthesis, scalability, safety, and efficacy assessments [30].

The compound 3,4,3-LI(1,2-HOPO) has demonstrated remarkable efficacy characterized by high potency and minimal toxicity when administered through both parenteral and oral routes. These attributes align well with the desired qualities in drug development. Extensive tests have established its effectiveness and safety across multiple animal models, a necessary step to meet the criteria outlined in the FDA's Animal Efficacy Rule. This approach becomes necessary because conducting efficacy trials directly on human subjects would be ethically unfeasible.

Given its promising performance as a potential treatment for internal radionuclide contamination, 3,4,3-LI(1,2-HOPO) was granted an investigational new drug (IND) designation by the FDA in August 2014. Particularly noteworthy is its exceptional prophylactic efficacy, where the compound demonstrated significant preventive capabilities when administered as early as 48 h before exposure to plutonium. These findings further reinforce the compound's potential value as a viable candidate for addressing internal radionuclide contamination concerns [32].

8.1.3 Biomaterials—Chitosan

Chitin is a long chain natural biopolymer of an amide derivative of glucose, N-acetylglucosamine. It is one of the most abundant polysaccharides present in nature, second only to cellulose. Chitin and its derivatives are non-toxic and renewable in nature. Among these derivatives, chitosan stands out as a significant compound. It has been subject to testing as a potential agent for decorporation, aiming to remove harmful radioactive substances from the body. This includes elements like strontium, radium, cobalt, americium, plutonium, uranium, and potentially other radionuclides. Furthermore, the chemical structure of chitosan can be easily modified to enhance its suitability as a decorporating agent for various other metals, including cesium. Researchers, including Nishimura and colleagues, have conducted studies showcasing chitosan's effectiveness. They found that oral administration of chitosan significantly reduced the whole-body retention of strontium in rats [33]. Additionally, chitosan was observed to have a positive impact on hematopoiesis, likely due to its ability to scavenge free radicals [34]. This multifaceted potential, combined with the non-toxic and renewable nature of chitin and its derivatives, makes them appealing candidates for addressing concerns related to the presence of radioactive materials within the body.

8.2 Development of Improved Formulations

8.2.1 Oral Administration

While Ca-DTPA and Zn-DTPA have received approval for the removal of internalized transuranic radionuclides, their administration through intravenous injection or nebulization poses limitations in radiological emergency scenarios. Consequently,

there is a need for an improved DTPA formulation that is more suitable for mass casualty situations like radiological emergency scenarios. Ongoing efforts are focused on enhancing the oral bioavailability of Ca/Zn DTPA and other actinide decorporation agents [25]. It is important to highlight that significant advancements in the efficacy of DTPA for soluble forms of plutonium (Pu) and americium (Am) could be achieved if the absorption through the intestinal wall could be notably increased. DTPA is a synthetic polyamino carboxylic acid equipped with eight binding sites for complexing metal ions. However, due to the presence of five carboxylic acid groups and three nitrogen atoms, DTPA is highly ionic and hydrophilic. This characteristic results in compounds with high solubility but low permeability. The current administration profile of intravenously delivered DTPA does not align well with the biokinetic profile of transuranic radionuclides. This discrepancy leads to a period during which DTPA plasma concentrations fall below the required effective concentration for chelating radionuclides within the systemic circulation. Consequently, this mismatch could potentially limit the effectiveness of existing parenteral DTPA treatments. The ongoing efforts to develop more suitable formulations aim to address these challenges and improve the overall efficacy and availability of DTPA treatments for radiological emergencies.

Research involving lipophilic derivatives of the PACAs (Polyaminocarboxylic acids) has shown promising results. In particular, oral administration of one such chelator was found to be equally effective as injected Zn-DTPA in removing plutonium (Pu) and americium (Am) from rats. Amphiphilic PACA chelators, which are structurally akin to DTPA and based on triethylenetetramine-hexaacetic acid (TT), have also been studied. These TT compounds can be administered orally and, if necessary, can be modified to favor uptake into specific tissues for targeted excretion through either the biliary (more lipophilic) or urinary (more hydrophobic) systems. This adaptability suggests that the more lipophilic agents can be particularly efficient in removing metals that have accumulated in the liver, potentially reducing renal toxicity as well. Compared to DTPA, these compounds feature an additional binding moiety, which appears to result in a wider range of binding affinities for heavy metals. These metals include thorium, samarium, plutonium, americium, uranium, strontium, cobalt, and others. Notably, the decorporation effectiveness of TT was directly linked to its lipophilicity. However, despite this positive aspect, orally administered TT compounds did not perform as well as parenterally administered Zn-DTPA. In addition to Pu and Am, preliminary data from rat studies suggest that TT also holds potential for effectively removing uranium and cobalt. The ongoing exploration of these lipophilic derivatives and amphiphilic chelators offers a promising avenue for improving the removal of heavy metals from the body through oral administration [35].

8.2.2 Transdermal Application

Zhang et al. [36] have proposed a different approach, i.e. use of a transdermal formulation to deliver chelating agents into the systemic circulation, presenting

an effective and mass-casualty-ready solution for radionuclide contamination. This method focuses on achieving systemic delivery of a radionuclide decorporation agent, allowing for a sustained release pharmacokinetic profile that matches the biokinetic profile of internally accumulated actinides.

DTPA, due to its hydrophilic nature, is not inherently suitable for transdermal delivery. However, Zhang et al. addressed this limitation by esterifying the five carboxylic groups on DTPA, leading to the creation of lipophilic compounds that possess favorable physicochemical properties for transdermal administration. Specifically, they synthesized the penta-ethyl ester of DTPA, referred to as C2E5, and successfully incorporated it into a nonaqueous gel formulation. Through their study, they assessed the transdermal absorption and excretion of C2E5 nonaqueous gels and evaluated the radionuclide decorporation efficacy of these gels at various dosage levels. The effectiveness of the approach was substantiated by observing enhanced total body decorporation and reduced liver and skeletal burden of americium (Am) following a single topical application of the C2E5 gel, administered 24 h after contamination. The sustained enhancement in Am elimination for at least 3 days post-application indicated that the C2E5 nonaqueous gels provided continuous delivery of metabolites capable of chelating Am. Importantly, no signs of skin irritation or skin abnormalities were observed throughout the study period, indicating the safety and tolerability of the C2E5 nonaqueous gel formulation. This innovative transdermal approach presents a potential avenue for effective radionuclide decorporation, especially in scenarios requiring mass-casualty treatments.

9 Decorporation Therapy for Selected Radionuclides

When radionuclides are accidentally ingested or inhaled, blood circulation or tissue/organ deposition of the radionuclides causes systemic or local radiation effects. In such cases, decorporation therapy is used to reduce the health risks due to their intake by accelerating the rates of elimination through urine. Decorporation therapy includes reduction and/or inhibition of absorption from the gastrointestinal tract, isotopic dilution, and the use of diuretics, adsorbents, and chelating agents. The authorities, such as the National Council on Radiation Protection and Measurements and International Atomic Energy Agency have reported recommended decorporation agents for some important radionuclides [1].

9.1 Transuranics

9.1.1 Indication and Usage

Ca-DTPA is the recommended treatment for individuals who are known or suspected to have internal contamination with plutonium and americium [37]. Ca-DTPA is

a calcium complex of DTPA (Diethylenetriamine pentaacetate). This compound has the ability to bind to radioactive plutonium, americium, and curium. A similar compound called Zn-DTPA is also available, with zinc replacing calcium.

These DTPA-based compounds have found extensive use as chelating agents for plutonium and other transuranic elements in both the United States and Europe. DTPA is a synthetic poly-amino polycarboxylic acid that creates stable complexes (metal chelates) with a wide array of metal ions. Administering these chelating agents to individuals internally contaminated with radioactive substances can enhance the excretion of these elements through urine and feces. The use of DTPA aids in reducing the time it takes for radioactive plutonium, americium, and curium to be eliminated from the body [1, 38].

9.1.2 Dosage and Administration

For the treatment of internal contamination, it is recommended to administer the initial dose of Ca-DTPA within the first 24 h. During this time frame, Ca-DTPA has been shown to be more effective than Zn-DTPA. If Ca-DTPA is not accessible, then Zn-DTPA can be used as the initial therapeutic option.

If additional chelation therapy is deemed necessary on the following day, daily treatment with Zn-DTPA should be initiated. In cases where Zn-DTPA is not available, the chelation therapy can be continued using Ca-DTPA, along with concurrent mineral supplements containing zinc. It's important to note that only one dose should be administered per 24 h period [1, 39].

9.1.3 Dose

For adults and adolescents, a single initial dose of Ca-DTPA amounting to 1.0 g should be administered intravenously. However, for children under the age of 12, a single initial dose of Ca-DTPA is recommended at 14 mg per kilogram of body weight, administered intravenously. It's important to ensure that the dose for children does not exceed 1.0 g of Ca-DTPA [1].

9.1.4 General Information

The optimal effectiveness of chelation treatment occurs when it is administered within the initial 24 h after internal contamination. It is recommended to initiate chelation treatment promptly upon suspicion or confirmation of internal contamination. In situations where immediate treatment is not feasible, chelation therapy should be administered as soon as it becomes accessible.

It's important to note that the efficacy of chelation treatment remains significant even if some time has passed since the internal contamination incident. The chelating properties of Ca-DTPA are most potent when radioactive contaminants are

still actively circulating or present in interstitial fluids. As time progresses following internal contamination, the effectiveness of chelation diminishes, particularly as the radioactive contaminants become sequestered within the liver and bones [1].

9.1.5 Methods of Administration

In cases where the route of internal contamination is uncertain or there is a likelihood of multiple contamination routes, the intravenous administration of Ca-DTPA is recommended. The Ca-DTPA solution, containing 1 g in 5 mL, can be administered using two different methods [1, 39]:

Slow Intravenous Push: The Ca-DTPA solution can be administered through a slow intravenous push, taking around 3–4 min to complete.
Intravenous Infusion: Alternatively, the Ca-DTPA solution can be diluted in 100–250 mL of compatible fluids such as 5% dextrose in water (D5W), Ringer's Lactate, or Normal Saline, and then administered as an intravenous infusion [1].

For individuals who have experienced internal contamination solely through inhalation within the past 24 h, an alternative route of administration is possible. Ca-DTPA can be administered through nebulized inhalation. To prepare for nebulization, Ca-DTPA should be diluted at a 1:1 ratio with sterile water or saline. After nebulization, patients should be advised not to swallow any of the expectorant that may be produced. It's worth noting that some individuals may encounter respiratory adverse effects following inhalation therapy.

However, it's important to acknowledge that the use of nebulized Ca-DTPA in the pediatric population has not yet been established for safety and effectiveness [1].

9.1.6 Treatment for Contaminated Wounds

The irrigation treatment of wounds using DTPA has shown effectiveness for certain radionuclides like lanthanides and actinides [40]. In these cases, either Ca-DTPA or Zn-DTPA can be employed. Early application of DTPA can enhance the efficacy of the treatment process, thereby reducing the uptake of metals into tissues. This is achieved by forming stable complexes that allow for urinary excretion.

For effective irrigation treatment, a solution containing 1 g of Ca- or Zn-DTPA and 10 mL of 2% lidocaine, mixed in 100 mL of 5% glucose solution or sterile isotonic saline, can be used. This solution is administered for irrigation [41].

In addition to irrigation, other routes of administration can be employed concurrently. Intravenous (IV) administration and inhalation therapy with DTPA are also potential approaches. However, it's important to exercise caution to prevent overdosing with DTPA, as the activity of radionuclides absorbed by wound tissues cannot be accurately measured.

9.1.7 Use in Pregnancy and Nursing Mothers

Ca-DTPA is categorized as a Pregnancy Category C drug, while Zn-DTPA falls under Pregnancy Category B [42]. When it comes to chelation treatment for pregnant women, it's advised to initiate and maintain treatment using Zn-DTPA. It's important to note that while animal reproduction studies may not always accurately predict human responses, if the use of the drug is deemed necessary during pregnancy, it should be used. The decision to administer Zn-DTPA should consider the balance between the potential risk of toxicity arising from untreated internal radioactive depositions and the risk associated with Zn-DTPA treatment itself. Regarding $CaNa_3$-DTPA, its distribution in extracellular water may extend to breast milk. To determine if Zn-DTPA is excreted in breast milk, appropriate studies should be conducted. The safety and potential impact of these drugs on pregnancy and breastfeeding should be carefully considered in consultation with healthcare professionals.

Due to the fact that numerous radionuclides are known to be excreted to varying extents in breast milk, it is strongly recommended that women with confirmed or suspected internal depositions of radionuclides avoid breastfeeding. This guideline applies regardless of whether they are undergoing chelation therapy or not. The potential for radionuclide transmission to the infant through breast milk poses a risk that should be avoided to ensure the infant's safety and well-being.

9.1.8 Renally Impaired Patients

Dosage adjustments are not generally recommended for patients with renal impairment when using DTPA-based chelation treatment. However, it's important to note that renal impairment can potentially slow down the removal rate of radionuclides from the body through chelation therapy.

In cases where patients with significant contamination are also experiencing renal impairment, the rate of elimination may be enhanced during dialysis. To effectively remove radionuclides from the body in such situations, high-efficiency and high-flux dialysis methods are suggested for patients with renal impairment.

It's crucial to take necessary precautions to ensure safety when undergoing dialysis for these purposes. Since the dialysis fluid can become radioactive due to the chelated radionuclides, appropriate measures should be taken to safeguard healthcare personnel, other patients, and the general public from potential radiation exposure [1].

9.1.9 Duration of Treatment

The duration of chelation treatment is determined by two key factors: the quantity of radionuclide that has been internally deposited in the body and the individual's response to the chelation treatment. Both of these factors play a significant role in guiding how long the treatment should be continued.

The amount of radionuclide present in the body influences the extent of contamination and the time required to effectively remove it through chelation. Additionally, individual responses to the treatment can vary based on factors such as metabolism, overall health, and the specific radionuclide involved [1].

9.1.10 Monitoring

Before initiating treatment with Ca-DTPA, it is crucial to establish a baseline for the individual's health status and internal radioactive contamination [39]. This involves recording baseline measurements of various parameters, including:

Complete blood count (CBC)
Serum creatinine
BUN (blood urea nitrogen)
Electrolytes
Urinalysis
Blood and urine radio-assays.

These baseline measurements serve as reference points for comparison during and after the treatment.

Throughout the treatment process, careful monitoring of serum zinc levels and complete blood counts is necessary due to the potential impact of Ca-DTPA on zinc levels. When appropriate, the administration of vitamin or mineral supplements containing zinc can be considered.

To better understand the treatment's effectiveness and the elimination of radioactive substances, it's advisable to establish an elimination curve. This involves obtaining a quantitative baseline estimation of the total internalized transuranium element(s). Methods for assessing elimination include whole-body counting, bioassay (such as bio-dosimetry), and analysis of fecal/urine samples whenever feasible. By adhering to these monitoring practices and baseline measurements, the treatment can be tailored to the individual's needs and any potential adverse effects can be promptly addressed. This process ensures the safety and efficacy of the treatment and should be overseen by healthcare professionals.

9.1.11 During Treatment

To effectively manage and monitor the treatment with Ca-DTPA, the following steps are recommended [1]:

Radioactivity Measurements: Regularly measure the radioactivity levels in blood, urine, and fecal samples on a weekly basis. This monitoring helps assess the rate at which radioactive contaminants are being eliminated from the body.
Laboratory Tests: Conduct comprehensive laboratory tests, including.

Complete Blood Count (CBC) with Differential: This provides insights into blood cell counts and helps detect any potential abnormalities.
BUN (Blood Urea Nitrogen) and Serum Creatinine: These tests assess kidney function and can help identify any kidney-related issues.
Electrolytes: Monitor levels of electrolytes (such as sodium, potassium, chloride) to ensure electrolyte balance is maintained.
Urinalysis: Regular urinalysis helps detect any changes in urine composition and can provide valuable information about kidney function.

Depending on the results of these tests and the number of Ca-DTPA doses administered, consider appropriate mineral supplementation.

Adverse Event Recording: Keep a record of any adverse events experienced by the individual undergoing Ca-DTPA treatment. This information is crucial for assessing the overall impact of the treatment and ensuring patient safety.

Monitoring these aspects ensures that the treatment is both effective and safe. Regular evaluation helps adjust the treatment plan if needed and ensures timely intervention in case of any complications. This monitoring process should be carried out under the supervision of healthcare professionals.

9.1.12 Action Plan for Inhalation Incidents

In the case of inhalation incidents (Fig. 7), Ca-DTPA can be administered at a personal decontamination center through the use of aerosol generators or nebulizers [39]. For adults, the initial dose involves inhaling 1.0 g of Ca-DTPA (diluted in 5 mL) with an equal amount of sterile water or saline solution. This inhalation process should last for 15–20 min.

Subsequent to this, depending on the levels of radioactive activity, the following methods of administration are recommended:

Slow Intravenous Infusion: A dose of 1 g of Ca-DTPA, diluted with isotonic 0.9% NaCl or 5% Glucose solution, should be administered over a half-hour period.
Slow IV Push: Alternatively, undiluted Ca-DTPA solution (5 mL:1 g) can be administered through slow intravenous push over a duration of 3–4 min.

It's important to note that intravenous administration should not be extended for more than 2 h. These administration methods are designed to effectively deliver Ca-DTPA in response to inhalation exposure, and should be carried out under medical supervision.

In the first 24 h following internal contamination, Ca-DTPA is more effective than Zn-DTPA. If prolonged use of DTPA is being considered, the recommended approach involves administering one dose of Ca-DTPA initially and then switching to Zn-DTPA for subsequent doses.

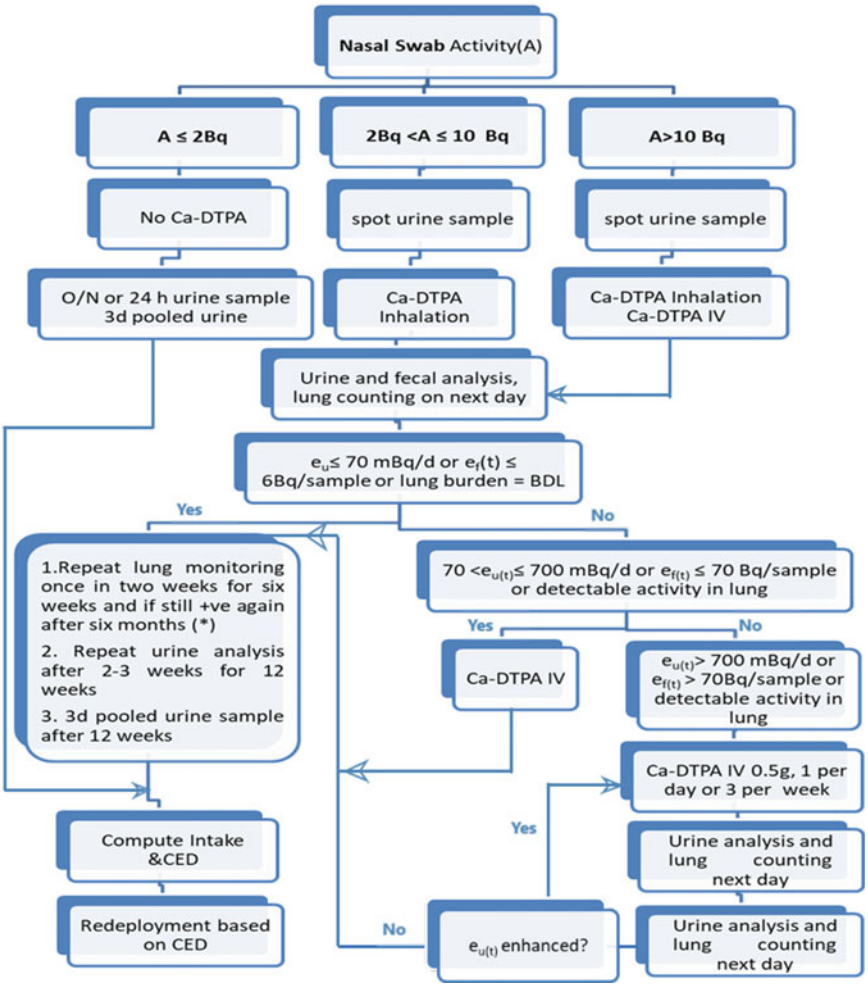

Fig. 7 Flowchart of action plan for Pu/Am (Type M) inhalation incident [39]

In cases where Ca-DTPA is not available, Zn-DTPA can be used as the initial therapy. On the following day, if additional chelation therapy is needed, daily treatment can commence with Zn-DTPA. If Zn-DTPA is unavailable, Ca-DTPA can be continued along with Zn supplements.

It's important to adhere to the principle of not administering more than one dose within a 24 h period. The decision to continue treatment with Ca-DTPA or Zn-DTPA should be guided by the results of urine and fecal analysis. The daily dose of DTPA should not exceed 1 g for any extended treatment period.

The administration schedule for Ca-DTPA is in accordance with guidelines provided by the International Atomic Energy Agency (IAEA) [43] (Table 3), and

Table 3 IAEA guidelines for the administration of Ca-DTPA

Time following the incident	Dose	Pathway	Frequency
As soon as possible	1 g	IV injection or inhalation	
First week	0.5 g	IV injection or inhalation	One per day or three per week
First month or first two months	0.25 g or 0.5 g	IV injection or inhalation	Two per week
Following month	No treatment		
Subsequently	0.25 g or 0.5 g	IV injection or inhalation	One or two per week for the first month, alternating with pauses of 2 or 3 weeks until no further enhancement is observed in urinary excretion of plutonium (refer to D-3)

you may refer to those guidelines for more detailed information on the treatment regimen.

9.1.13 Children Less Than 12 Years of Age

The initial treatment with Ca-DTPA involves administering a single dose of 14 mg per kilogram of body weight intravenously. However, this initial dose should not exceed 1.0 g in total [1, 38].

For the ongoing maintenance phase, the recommended dosage is also 14 mg per kilogram of body weight, administered intravenously once daily. The maintenance dose should not exceed 1.0 g per day.

These dosages are in accordance with established guidelines and should be closely followed under the supervision of medical professionals.

9.2 Chelation Therapy for Other Important Radionuclides

If there is a suspicion of internal contamination with radionuclides other than plutonium, americium, or curium, or if the specific radio-contaminants are unknown, additional therapies may be necessary. For instance, treatments like Prussian blue and potassium iodide might be considered in such cases. The choice of additional therapies would depend on the nature of the contamination, the involved radionuclides, and the medical evaluation of the situation. It's important to tailor the treatment approach to the specific contaminants and their potential health effects.

9.2.1 Prussian Blue Insoluble Treatment for Cs

Cesium-137 stands out as a commonly occurring fission product resulting from the nuclear fission of ^{235}U and other fissionable isotopes within the nuclear industry. It's also frequently found in sealed sources utilized in radiation oncology. Additional isotopes like ^{134}Cs are observed in various industrial or laboratory settings. The radioactive ^{131}Cs is employed as an implantable seed to treat prostate cancer. To eliminate radioactive cesium from the body, the most effective method involves orally administering ferric ferrocyanide, commonly known as Prussian blue. Prussian blue, with its chemical formula Fe_4 $[Fe(CN)_6]_3$, is taken as a medication by mouth and promotes the removal of cesium and thallium isotopes from the body through ion exchange. This treatment is particularly effective against cesium that's been ingested, as opposed to inhaled. Prussian blue has a lengthy and successful history in addressing internal deposits of radiocesium and has been endorsed for years by national and international radiation protection organizations. According to FDA guidelines, a recommended treatment regimen involves taking Prussian blue at a dose of 3 g three times a day for a minimum of 30 days to address internal contamination [38].

Modes of Treatment

The recommended dosage for adults and adolescents is three grams orally, to be taken three times a day. For children aged between 2 and 12 years, the recommended dosage is one gram orally, also three times a day. For children below 2 years of age, there is no specific dosage recommended by the FDA due to limited clinical experience [5]. However, a scaled dose could be considered based on the individual situation and consultation with a healthcare professional.

To assess the effectiveness of the treatment, bioassay monitoring of urine and fecal samples can be employed. This monitoring helps in tracking the excretion of the radioactive substances from the body and gauging the response to the treatment. As always, it's important to follow medical guidelines, consider individual circumstances and involve medical professionals when making decisions about treatment dosages and monitoring procedures [38].

Precautions

Patients should be made aware that their stool may turn blue following the administration of Prussian blue. In cases where liver function is impaired, the effectiveness of Prussian blue may be reduced due to decreased cesium excretion in bile. Consequently, close monitoring of serum electrolytes is necessary during insoluble Prussian blue treatment. Special caution should be exercised for patients who have pre-existing cardiac arrhythmias or electrolyte imbalances.

It's worth noting that the administration of Prussian blue can potentially lead to constipation. To address this, it's advisable to consider co-administering a stool

softener or a mild laxative during the course of treatment. As always, patients should follow medical guidance closely, and healthcare professionals should be consulted for any concerns or specific needs related to treatment [38].

Efficacy

Prussian blue operates by inhibiting the process of enterohepatic recirculation within the gastrointestinal tract. This action results in a reduction of the cesium dose by a factor of two to three. It's important to note that Prussian blue's effectiveness is likely to be higher in incidents involving ingestion of radioactive cesium as compared to incidents involving inhalation. This distinction underscores the varying degrees of effectiveness based on the route of exposure [38].

Clinical Experience

The main clinical experience in utilizing Prussian blue as a chelating agent stems from the Goiânia incident in Brazil in 1987 [44–46]. This incident provided valuable insights into the application of Prussian blue in cases involving radiation exposure. It's noteworthy that the clinical experience with Prussian blue has primarily been in incidents where ingestion of radioactive materials occurred. This underlines that the main body of evidence comes from situations where individuals ingested radioactive substances.

Prussian blue insoluble capsules comprise insoluble ferric hexacyanoferrate (II), with an empirical formula of Fe_4 $[Fe(CN)_6]_3$.

9.2.2 Summary of Treatment Recommendations for Cobalt (^{59}Co, ^{60}Co)

The recommended drug for the de-corporation of Cobalt (^{59}Co, ^{60}Co) is DTPA (Diethylenetriaminepentaacetic acid), albeit it's considered an off-label use [1]. The recommended dosage for DTPA is 1g administered intravenously. However, if DTPA is not available, there are alternative drugs to consider:

DMSA (Dimercaptosuccinic acid)
EDTA (Ethylenediaminetetraacetic acid)
NAC (N-Acetylcysteine).

The dosages for these alternative drugs would be similar to those described for DTPA.

In situations of mass casualty, a single intravenous dose of DTPA is recommended. To determine the appropriate course of treatment, the excretion kinetics of the drug can be assessed by analyzing the results of whole-body counting. This assessment helps guide decisions regarding further treatment. It's crucial to follow medical guidelines and recommendations closely in such situations.

Clinical Experience

While there is no published clinical experience available for the use of DTPA in adults following inhalation or ingestion of cobalt, there is a limited case of pediatric cobalt poisoning described in the literature. In that particular case, EDTA was administered at a dose of 50 mg per kg per day for a period of 5 days. This treatment facilitated the enhanced renal elimination of cobalt, leading to the resolution of the patient's metabolic acidosis and cardiac dysfunction.

Animal studies have provided insights into the effectiveness of both DTPA and EDTA in reducing tissue concentrations of cobalt after intraperitoneal or parenteral injection. Furthermore, N-acetyl cysteine has shown the ability to increase cobalt excretion in animals and could be considered as an alternative approach [47].

Although clinical data might be limited, these findings from animal studies and the single pediatric case offer valuable information regarding potential treatments for cobalt poisoning. Nonetheless, any treatment decisions should be based on careful consideration of individual patient circumstances and consultation with medical professionals.

9.2.3 Medical Treatment for Iodine Radionuclides

Summary of FDA Treatment Recommendations for Iodine (^{125}I, ^{131}I)

Potassium iodide (KI) is an FDA-approved thyroid-blocking agent that can be obtained without a prescription. Its use is geared towards preventing the uptake of radioactive iodine by the thyroid. For adults, the traditional thyroid-blocking regimen involves orally administering 130 mg of KI as early as possible following exposure. Subsequently, one tablet is taken daily for a period of 7–14 days. KI is most effective when administered before or shortly after exposure to radioactive iodine. KI blocks or reduces the accumulation of radioactive iodine in the thyroid [47].

Both tablet and liquid forms of KI have received FDA approval. The administration of KI should commence immediately after an incident and can be effective up to 4 h post-exposure. Even if exposure is ongoing, stable iodine, such as KI, can still be about 50% effective even 5–6 h after contamination with radioiodine [1, 47].

Certain individuals, such as those intolerant to protective doses of KI, neonates, pregnant and lactating women (with safety concerns for repeated administration of KI), should be given priority for alternative protective measures like sheltering, evacuation, and food supply control.

For individuals over 40 years of age, the use of KI is typically reserved for cases where a substantial internal radiation dose to the thyroid of more than 5 Gy (500 rad) is projected, to prevent hypothyroidism [48]. As long as there's ongoing exposure to radioiodine, KI should be taken daily. If an extended stay in contaminated areas is necessary (lasting over 1 day), the dosing schedule should be determined by a physician's discretion.

Alternative Therapy Modes

An alternative convenient method for delivering stable iodide is by adding around five to six drops of a saturated solution of potassium iodide (SSKI) with a concentration of 1 g/mL to juices. This provides an easy way to take stable iodide [1].

Anti-thyroid agents like propylthiouracil or methimazole, which are typically used to treat hyperthyroidism, can be employed as well. These medications work by inhibiting the synthesis of thyroid hormones. In the context of radioactive iodine contamination, these drugs should be taken early, before radioiodine becomes organified in the thyroid. It's important to note that these drugs can have potential toxicity, so the balance between benefits and risks should be carefully considered before their use.

Potassium iodate (KIO_3) is another compound used to block thyroid uptake of radioactive iodine. However, it's worth mentioning that KIO_3 is not FDA approved for this purpose in the United States. Nonetheless, it's utilized in certain countries as a thyroid-blocking agent [1].

9.2.4 Medical Treatment for Strontium Radionuclides

Modes of Treatment

The recommended agent for decorporation is Aluminum hydroxide [1], which should be taken promptly after an incident to prevent the intestinal absorption of radio-strontium. This can be achieved through oral administration. The standard dose is as follows:

Adults: 10 mL (equivalent to 1200 mg)
Pediatric: 50 mg per kg of body weight, not exceeding the adult dose.

To achieve a reduction in intestinal absorption, the dose range is set at 60–100 mL. These regimens, when administered after exposure, effectively inhibit the intestinal absorption of radio-strontium. The action of this drug also involves competitive inhibition of absorption.

In situations involving mass casualties, a single administration is recommended for a given regimen. However, it's important to note that hypersensitivity reactions to the drug might lead to constipation. Additionally, prolonged use of aluminum hydroxide could potentially result in hypophosphatemia.

Given that strontium tends to accumulate in bones, monitoring of blood counts should be conducted to detect pancytopenia, a condition characterized by low levels of all blood cell types. This caution is especially relevant due to strontium's affinity for bone tissue.

Alternate Regimens

Alginate, an over-the-counter ion-exchange resin, is effective in the gastrointestinal tract and can bind to strontium and other radionuclides [1]. Alginate is found as an inactive ingredient in products like Gaviscon. The recommended dosage of alginate is around 200 mg per tablet or per tablespoon, and it's important not to exceed the dose indicated on the label.

A suggested dosing regimen for alginate involves:

Initial dose: 5 g taken twice daily for 1 day
Followed by: 1 g taken four times daily (qid).

Additionally, it's advised to take Calcium phosphate at a dosage of 10 g orally once.

This approach is aimed at utilizing the binding properties of alginate to help remove strontium and other radionuclides from the body through the gastrointestinal system. Always follow the recommended doses and guidelines as provided on the product label or by a healthcare professional.

9.2.5 Medical Treatment for Decorporation of Tritium (^{3}H)

Tritium represents the sole radioactive variation of hydrogen, undergoing decay to form ^{3}He by emitting Beta rays with a maximum energy output of 18.6 keV. Tritiated water (HTO) can be readily introduced into the body through inhalation, ingestion, or absorption via the skin. Once inside the body, the absorption of ^{3}H is swift and complete, immediately blending with bodily water. Therefore, the primary concern in managing internal tritium contamination lies in its impact on total body water. Addressing tritium intake from a medical standpoint predominantly involves enhancing the turnover of body water.

In situations involving single instances of contamination, the approach to treatment centers around increasing oral fluid consumption. This approach serves a dual purpose: it dilutes the presence of tritium and boosts its excretion through natural physiological mechanisms [1].

Modes of Treatment

Raising the intake of oral fluids to a range of 3–4 L per day results in a halving to a third of the biological half-life of tritium, consequently leading to a proportional reduction in the total body dose. In situations of severe internal deposition, the recommended liquid intake can be further elevated to a range of 6–10 L per day, unless there are clinical reasons to avoid this approach. This increased fluid consumption regimen is advised to be followed for a period of 5 days [1].

By maintaining an elevated fluid intake up to the limits of personal tolerance, the biological half-life of tritium can be decreased significantly, ranging from half to an

eighth of its normal value. This adjustment directly correlates with a corresponding reduction in the overall radiation dose.

Contraindications

It's important to exercise caution when applying these fluid intake recommendations, especially for patients who might be at risk of fluid overload, such as individuals with congestive heart failure.

9.2.6 Medical Treatment for Uranium Isotopes ^{234}U, ^{235}U, ^{238}U, and Depleted Uranium (DU)

Modes of Treatment

The recommended choice of medication to counteract uranium contamination is Isotonic sodium bicarbonate [1]. For adults, the suggested dosage is 250 mL (equivalent to 1–2 mEq per kg of body weight) administered through a slow intravenous infusion. Alternatively, two bicarbonate tablets can be taken orally every 4 h until the urine pH reaches a range of eight to nine. It's important to closely monitor urine pH on an hourly basis for a duration of 3 days. In cases where there is suspicion of a high level of uranium intake, the following dosing strategies should be considered:

Renal dialysis may be appropriate.
Etidronate (Didronel) can be taken orally at a dosage of 400 mg daily.
Diamox (Acetazolamide) can be taken orally at a dosage of 500 mg twice daily.

These interventions should be continued for a span of 3 days.

Precautions

In cases of uranium contamination, the preferred treatment method involves administering oral doses or infusions of sodium bicarbonate. The goal of these treatments is to maintain an alkaline urine pH, which should be closely monitored through frequent pH measurements. By achieving an alkaline urine environment, the formation of non-toxic uranium carbonate complexes is significantly enhanced, increasing their concentration by several orders of magnitude. This, in turn, facilitates efficient excretion of uranium from the body [1].

10 Conclusion

This chapter explores the concept of decorporation, which involves removing internally absorbed radionuclides from the body to reduce long-term health risks. The primary goal is to decrease the committed effective dose by expediting radionuclide

elimination. The chapter covers decorporation goals, factors influencing treatment, and the decision-making process for initiating treatment. It discusses the timing of decorporation therapy and various methods, including reducing uptake, blocking, chelation, and more. The recommended decorporating agents for different radionuclides are summarized, and potential adverse effects of treatment are briefly outlined. The chapter delves into research on decorporation strategies, focusing on chelating agents, formulations, and applications. The use of decorporation therapy for specific radionuclides is also addressed, emphasizing individualized treatment under medical supervision. Overall, this chapter serves as a comprehensive guide for understanding and implementing decorporation strategies in cases of internal contamination, providing valuable insights into treatment goals, methods, and considerations.

References

1. NCRP Report 161 (2008) Management of persons contaminated with radionuclides: handbook. Bethesda, MD
2. ICRP (1994) Dose coefficients for intake of radionuclides by workers. ICRP Publication 68. Ann ICRP 24(4)
3. ICRP (1997) Individual monitoring for internal exposure of workers. ICRP Publication 78. Ann ICRP 27
4. IAEA (2018) IAEA glossary
5. U.S. Department of Energy (2008) DOE standard: internal dosimetry. DOE-STD-1121-2008. U.S. Department of Energy, Washington, DC
6. EPR-Internal Contamination (2018) Medical management of persons internally contaminated with radionuclides in a nuclear or radiological emergency. EPR-Internal Contamination, Vienna
7. International Atomic Energy Agency, World Health Organization (1998) Diagnosis and treatment of radiation injuries. Safety reports series no. 2. IAEA, Vienna
8. AERB (2019) Monitoring and assessment of occupational exposure due to intake of radionuclides. In: AERB safety guide. AERB/NRF/SG/RP-1
9. Bodin L, Menetrier F (2021) Treatment of radiological contamination: a review. J Radiol Prot 41(4)
10. Dainiak N, Albanese J (2022) Assessment and clinical management of internal contamination. J Radiol Prot 42(4):041001
11. Rump A et al (2016) Reconsidering current decorporation strategies after incorporation of radionuclides. Health Phys 111(2):204–211
12. IAEA (2015) General safety requirements no. GSR part 7. In: IAEA safety standards preparedness and response for a nuclear or radiological emergency. IAEA
13. Wood R, Sharp C, Gourmelon P, Le Guen B, Stradling GN, Taylor DM, Heng-Napoli M-H (2000) Decorporation treatment—medical overview. Radiat Prot Dosim 87:51–57
14. Waller E, Stodilka SZ, Leach K, Prud'homme-Lalonde L (2002) Literature survey on decorporation of radionuclides from the human body. Technical memorandum DRDC Ottawa TM 2002-042. Defence R&D Canada—Ottawa, Ottawa
15. Ansoborlo E et al (2006) Actinide speciation in relation to biological processes. Biochimie 88(11):1605–1618
16. Vincent JB, Love S (2012) The binding and transport of alternative metals by transferrin. Biochim Biophys Acta 1820(3):362–378
17. Mishra L et al (2019) Binding of Cm(III) and Th(IV) with human transferrin at serum pH: combined QM and MD investigations. J Phys Chem B 123(13):2729–2744

18. Mishra L, Sundararajan M, Bandyopadhyay T (2020) Molecular dynamics simulations of plutonium binding and its decorporation from the binding-cleft of human serum transferrin. J Biol Inorg Chem 25(2):213–231
19. Ali M et al (2016) The interaction of human serum albumin with selected lanthanide and actinide ions: binding affinities, protein unfolding and conformational changes. Biochimie 123:117–129
20. Mishra V, Pathak AK, Bandyopadhyay T (2022) Binding of human serum albumin with uranyl ion at various pH: an all atom molecular dynamics study. J Biomol Struct Dyn 1–11
21. Multi-agency radiological laboratory analytical protocols manual (MARLAP) (2004) 1
22. Gorden AE et al (2003) Rational design of sequestering agents for plutonium and other actinides. Chem Rev 103(11):4207–4282
23. U.S. Food and Drug Administration (2004) Guidance for industry calcium DTPA and zinc DTPA drug products.Submitting a new drug application. U.S. Food and Drug Administration
24. Tominaga T et al (2021) Effects of the chelating agent DTPA on naturally accumulating metals in the body. Toxicol Lett 350:283–291
25. Cassatt DR et al (2008) Medical countermeasures against nuclear threats: radionuclide decorporation agents. Radiat Res 170(4):540–548
26. Götzke L et al (2019) Coordination chemistry of f-block metal ions with ligands bearing bio-relevant functional groups. Coord Chem Rev 386:267–309
27. Durbin PW, Lauriston S (2008) Taylor lecture: the quest for therapeutic actinide chelators. Health Phys 95(5):465–492
28. Durbin PW et al (2003) Octadentate hydroxypyridinonate (HOPO) ligands for plutonium (IV): pharmacokinetics and oral efficacy. Radiat Prot Dosim 105(1–4):503–508
29. Durbin PW et al (1998) ^{237}Np: oxidation state in vivo and chelation by multidentate catecholate and hydroxypyridinonate ligands. Health Phys 75(1):34–50
30. Abergel RJ et al (2010) Biomimetic actinide chelators: an update on the preclinical development of the orally active hydroxypyridonate decorporation agents 3,4,3-LI(1,2-HOPO) and 5-LIO(Me-3,2-HOPO). Health Phys 99(3):401–407
31. Sadhu B, Mishra V (2018) The coordination chemistry of lanthanide and actinide metal ions with hydroxypyridinone-based decorporation agents: orbital and density based analyses. Dalton Trans 47(46):16603–16615
32. An DD et al (2017) From early prophylaxis to delayed treatment: establishing the plutonium decorporation activity window of hydroxypyridinonate chelating agents. Chem Biol Interact 267:80–88
33. Nishimura Y, Kakuta I, Takeda H, Inaba J, Imai K, Watari K, Matsusaka N (1994) Effect of natural chelating agents on the intestinal absorption of radiostrontium in rats. Radiat Prot Dosim 53:331–334
34. Nishimura Y, Kim HS, Ikota N, Arima H, Bom HS, Kim YH, Watanabe Y, Yukawa M, Ozawa T (2003) Radioprotective effect of chitosan in sub-lethally X-ray irradiated mice. J Radiat Res 44:53–58
35. Taylor DM, Hodgson SA, Stradling N (2007) Treatment of human contamination with plutonium and americium: would orally administered Ca- or Zn-DTPA be effective? Radiat Prot Dosim 127(1–4):469–471
36. Zhang Y, Sadgrove MP, Mumper RJ, Jay M (2013) Radionuclide decorporation: matching the biokinetics of actinides by transdermal delivery of pro-chelators. AAPS J 15(4):1180–1188
37. Zasshi Y (2015) Decorporation agents for internal radioactive contamination. Yakugaku Zasshi: Journal of the Pharmaceutical Society of Japan 135(4):557–563
38. FDA (2009) The food code is a model for safeguarding public health and ensuring food is unadulterated and honestly presented when offered to the consumer
39. AERB (2013) Action plan for intake of Pu/Am by occupational workers through various root of intakes. In: AERB safety guide, 2013. BARC/2013/1/015
40. NCRP (2006) Development of a biokinetic model for radionuclide-contaminated wounds for their assessment, dosimetry and treatment. Report no. 156

41. NCRP (1980) Management of persons accidentally contaminated with radionuclides. NCRP report no. 65
42. Meadows L, Morse J (2001) Constructing evidence within the qualitative project. In: The nature of qualitative evidence, vol 1. Sage, Thousand Oaks, pp 188–202
43. IAEA. Radiation protection in the design of radiotherapy facilities. IAEA safety series no. 47. STI/PUB/1223 92-0-100505-9
44. IAEA (1988) Principles for the exemption of radiation sources and practices from regulatory control. Safety series no. 89
45. IAEA (1998) Annual report for 1998
46. CDC (2008) Guideline for disinfection and sterilization in healthcare facilities
47. FDA (2001) Recommendations of the United States public health service. Food and Drug Administration
48. Stifter E, König F, Lang T, Bauer P (2004) Reliability of a standardized reading chart system: variance component analysis, test-retest and inter-chart reliability. NAS/NRC. Springer

Glossary

Absorbed Fraction Ratio of the energy absorbed by the target region from the *i*th radiation to the energy emitted from the source region by the *i*th radiation.

Activity Concentration Activity of a radionuclide per unit volume of a sample and is expressed in units of Bq m^{-3}.

Activity of Radioactive Source The expectation value of number of nuclear transformations occurring per unit time and is expressed in unit of Bq. 1 Bq = 1 disintegration/s.

Activity Median Aerodynamic Diameter (AMAD) The aerodynamic diameter of aerosol particles above which 50% of activity is associated. Used when deposition is primarily governed by inertial impaction and sedimentation.

Activity Median Thoracic Diameter (AMTD) The aerodynamic diameter of aerosol particles above which 50% activity is associated. Used when deposition is primarily governed by diffusion.

Alveolar Tiny air sacs in the lungs where gas exchange between oxygen and carbon dioxide takes place.

Alpha Spectrometry A technique used for detecting and quantifying alpha-emitting radionuclides during the decaying process.

Anodic Stripping Voltammetry (ASV) An electroanalytical technique is used to quantify the concentration of trace metals in a solution. This method is particularly effective for measuring metals that form reversible redox reactions and can be deposited onto an electrode surface. ASV is employed for estimation of uranium in biological/environmental samples.

Accident Dose Refers to the amount of radiation exposure an individual receives due to an unexpected event or accident involving radioactive materials or radiation sources.

Active Dosimeter A dosimeter (electronic pocket dosimeter, ionization chamber, proportional counter, etc.) that produces signal in real time when exposed to ionizing radiation, which can be measured in real time using an associated electronics system.

D. K. Aswal (ed.), *Handbook on Radiation Environment, Volume 2*,
https://doi.org/10.1007/978-981-97-2799-5

Antiparticle A subatomic particle has the same mass as a given particle but opposite electric or magnetic properties. Every kind of subatomic particle has a corresponding antiparticle, e.g. the positron has the same mass as the electron but an equal and opposite charge.

Annual Limit of Intake (ALI) Maximum amount of a particular radionuclide that an individual can ingest or inhale within a 1-year period without exceeding a specific dose limit.

Area Monitoring Assessment/measurement of radiation levels at various locations around the work place of radiation facilities.

Bayesian Statistics Bayesian statistics is a branch of statistics that deals with the updating of probabilities based on new evidence. It relies on Bayes' theorem to calculate the probability of hypotheses given observed data.

Bioassay Sample A biological sample is excreted or otherwise removed from the body in order to assess the presence of radionuclides.

Biodosimetry Measurement of radiation dose based on biological changes or signals in response to the damage created by ionizing radiation.

Biokinetic Models Mathematical representations that describe the movement, distribution, and transformation of substances within living organisms over time. Used to understand the fate of substances in biological systems.

Biological Half-life Biological half-life refers to the time required for half of the radionuclide content within a compartment of a biological system to undergo elimination.

Bone Resorption The process by which bone tissue is broken down, and its minerals, such as calcium, are released into the bloodstream. Crucial for maintaining calcium balance in the body and for the repair and renewal of bone tissue.

Brachytherapy Cancer treatment modality that involves the strategic placement of sealed radioactive sources directly within or adjacent to the targeted tumor, facilitated either through direct insertion or catheters.

Bronchi The large and main air passages in the respiratory system branch off from the trachea and extend into the lungs. Crucial for conducting air to and from the lungs and simulating respiratory tract deposition in biokinetic models.

Bronchiole A small, thin-walled air passage in the respiratory system branching off from the bronchi. Involved in regulating airflow within the lungs.

Bubble Detector Bubble detector consists of a clear plastic tube filled with a superheated polymer gel which produces bubbles on interacting with fast neutrons. It is used to determine personal dose equivalent.

Calibration of Personal Dosimeters The process to establish the relationships between values indicated by a measuring instrument/measuring system, and the corresponding known values of a measurand under specified conditions.

Čeronkov Radiation Emission of electromagnetic radiation (bluish in color) when a charged particle traverses in a dielectric medium with a speed greater than the speed of light in vacuum.

Chest Wall Thickness The exponential average of tissue thickness from the surface of lungs to the points in the intercostal space in between the ribs.

Chromatography A process in which components of a mixture are separated by differential distribution between a mobile phase and a stationary phase.

Creatinine A substance produced in muscle tissue by the metabolism of creatinine phosphate, which is taken in the diet primarily in meats, is filtered by the kidneys and eliminated in urine. The reference value of urinary excretion of creatinine for adult male is 1.7 g d^{-1}, and for adult female is 1.0 g d^{-1}.

Collision Stopping Power Energy is transferred to orbital electrons of an absorber per unit length when a charged particle traverses in the absorber.

Committed Effective Dose Radiation dose absorbed by the whole body over a specific period of time (50 years, called committed time) after the intake of a radionuclide.

Committed Equivalent Dose The committed equivalent dose is radiation absorbed by a specific target organ over the course of an individual's lifetime, resulting from the radioactive decay of a radionuclide in all source organs.

Compton Effect An interaction of X-ray or gamma photon with a free electron in which the photon is scattered at a reduced energy and the electron is ejected from the atom.

Computed Tomography A volumetric X-ray imaging technique that provides computer-calculated cross-sectional images of the body.

Contamination Presence of radioactive material on the human body or other surrounding materials in excess of quantities as specified by the competent authority.

Continuous Slowing Down Approximation In this approximation, a charged particle is considered to be losing its kinetic energy gradually and continuously while traversing in a medium.

Conversion Coefficients The coefficients which relate operational and protection quantities to physical quantities.

Criticality The "stage" or "state" of a fissile material system where a self-sustained nuclear chain reaction is just maintained.

Criticality Accident Accidental production of a self-sustaining or divergent chain reaction of fissionable material.

Criticality Accident Dosimetry A procedure for the measurement of dose due to criticality accident using a combination of neutron activation foils and other passive detectors.

Cyclotron An apparatus in which charged atomic and subatomic particles are accelerated by an alternating electric field while following an outward spiral or circular path in a magnetic field.

Cytogenetics Studies based on chromosomes or part of it, which can be microscopically analyzed.

Decorporation The therapeutic processes by which radioactive materials are mobilized from tissues/organs and removed from the body by enhanced material excretion.

Defense in Depth Provision of multiple levels of protection for ensuring the safety of workers, the public, or the environment.

Derived Air Concentration (DAC) The level of radionuclide concentration in the air that, if inhaled by a reference person over a working year (approximately 2000 h) at that concentration, would result in an intake equivalent to the Annual Limit of Intake (ALI).

Deterministic effect Definitive health effects caused by excessive cell killing at high doses of radiation (> 0.7–1 Gy).

Direct Monitoring Method A gamma ray spectrometry method in which external detectors are placed close to the body or organ in which internal radioactive contamination has to be measured.

Dose Limit The value of the effective dose or the equivalent dose to individuals from planned exposure situations shall not be exceeded.

Dose and Dose Rate Effectiveness Factor (DDREF) A correction factor for stochastic risk at low dose (< 200 mGy) or low dose rate (100 mGy/h).

Dosimeter A device used to measure the dose of any radiation worker wearing it.

Dosimetry Dosimetry is the science and practice which deals with measurement, calculation, and assessment of the absorbed dose.

Early versus late effects of radiation Effects appearing within hrs to months post radiation exposure versus effects appearing years to decades after exposure.

Efficiency Calibration Response of the detection system for known amount of activity distributed in phantom and similar measurement geometry as that of worker.

Elastic Scattering A scattering process in which two or more particles collide and the total kinetic energy and momentum of the system are always conserved.

Electro Chemical Etching It is a process in which a material (such as insulating material) is etched chemically at high temperature in an etchant solution in the presence of high electric field (few kV/mm).

Electrodeposition The deposition of a substance on an electrode by passing electric current through an electrolyte. It is used as a source preparation method for alpha spectrometry.

Electron Spin Resonance A spectroscopic technique used to study materials with unpaired electrons.

Equilibrium Dose Constant Average energy emitted per nuclear transformation in the source region.

Equilibrium Equivalent Concentration The Equilibrium Equivalent Concentration of radon is the radon concentration that is in secular equilibrium with its decay products, providing an equivalent PAEC for the progeny nuclides actually present in the atmosphere.

External beam therapy A cancer treatment technique by means of delivering the collimated beams of ionizing radiation to the delineated tumo volume.

Fluoroscopy A real-time medical X-ray imaging procedure that provides the video of the movements inside a part of the body.

Gamma Camera A nuclear medicine imaging device that detects radiation emitted from the patient body and enables the acquisition of dynamic as well as static images of the area of interest.

Genetic abnormality Deviation from normal genome leads to certain disorders or appearance.

Genetic Effect Effects transferrable through generation due to one or both parental radiation exposure.

Glow Curve A plot of thermoluminescence intensity versus temperature or time.

Hematological Parameters Blood-related factors such as blood cell counts.

High LET Radiation Ionizing radiations such as protons, neutrons, alpha particles, and other heavy ions having LET values ≥ 10 keV/μm.

Human Phantom Human surrogates with source distribution similar to the one expected in humans with tissue substitutes similar to human tissue in Z, density and scattering, and attenuation characteristics.

Immuno-fluorescence Obtaining fluorescence signal using immunological methods through antibodies specific to certain cellular expressions.

Individual Monitoring Periodic measurement of individual doses due to occupational exposure to ionizing radiation in order to monitor and control the associated radiation hazard.

Industrial Radiography A nondestructive technique to identify any possible defects in products and assemblies that are used in industries by utilizing ionizing radiation sources such as X-rays, gamma rays, and radionuclides.

Inelastic Scattering A scattering process in which the momentum is conserved, but the kinetic energy of the system is not conserved.

In-situ Hybridization Bonding of chromosome-specific or region-specific sites by probes using the sequence of the chromosome.

Intake The process of bringing a substance into the body. In biokinetic models, it refers to the entry of a substance into an organism through inhalation, ingestion, or skin absorption.

Internal Contamination Radioactive contamination of organs or tissues of human subject or any organism due to intakes of radionuclides mainly by inhalation, ingestion, or injection.

Internal Dose Evaluation The process of assessing the amount of radioactive or hazardous substances absorbed, distributed, and retained within the body following exposure.

Interphase Stage of cell cycles where cell is preparing for and synthesizing genetic material. This includes G0, G1, S, and G2 phases.

In-utero Effect Biological effects in embryo/fetus/person after exposure during embryonic or fetal stage.

Investigation level The level of measured radiation quantity, above which the cause or the implications of the result are examined.

In-vitro Monitoring Measurements to determine the presence of, or to measure the amount of, radioactive material in the excreta or in other biological materials removed from the body.

Ion-exchange Chromatography Ion-exchange chromatography is a form of chromatography that separates ions or charged molecules based on their affinity to the ion exchanger.

Ionizing Radiation Electromagnetic radiation that has sufficient energy to ionize the medium directly or indirectly.

Latent Period Dormant non-symptomatic period between exposure and disease manifestation.

LED Fluorimetry Refers to the use of light-emitting diodes (LEDs) as the light source in fluorimetric analysis. Fluorimetry itself is a technique that involves measuring the fluorescence emitted by a substance when it absorbs light. LED fluorimetry technique is used for estimation of trace levels of uranium present in biological/environmental samples.

Likelihood Likelihood in probability statistics is the measure expressing how well a given statistical model explains observed data, indicating the relative plausibility of different parameter values.

Linear Accelerator A type of particle accelerator that imparts a series of relatively small increases in energy to subatomic particles as they pass through a sequence of alternating electric fields set up in a linear structure.

Linear Energy Transfer An average linear rate of energy loss of charged particle radiation in a medium, i.e., the radiation energy lost per unit length of path traversed through a material.

Liquid Scintillation Counting A radio-analytical technique is used to quantify the radioactivity of alpha/beta isotopes and involves the conversion of energy of a radioactive decay event into photons of light.

Lognormal Distribution A probability distribution of a random variable whose logarithm is normally distributed. It is characterized by two parameters the mean (μ) and standard deviation (σ) of the natural logarithm of the variable.

Low LET Radiation Ionizing radiations such as photons, electrons and muons having LET values $\leq$ 10 keV/μm.

Lymph Nodes Small, bean-shaped structures that are part of the lymphatic system, filtering lymphatic fluid and playing a crucial role in immune response. Relevant in biokinetic models for the distribution and clearance of substances.

Mammography An X-ray imaging procedure to examine the internal structure of the breast.

Mass Spectrometry Mass spectrometry is an analytical tool for measuring the mass-to-charge ratio (m/z) of one or more molecules present in a sample.

Medical Cyclotron A particle accelerator which is used to produce radioisotopes for diagnostic and therapeutic applications in nuclear medicine.

Micro-precipitation A type of co-precipitation that uses a soluble component combined with a non-isotopic carrier to form a precipitate. Microprecipitation is another source preparation method for alpha spectrometry.

Minimum Detectable Activity (MDA) The minimum activity from the source, which can be measurable by 95% probability where false negative and false positive rate is ensured to be no longer than 5%.

Monitoring Period The time period between dosimeter exchanges in routine monitoring.

Multi-parametric Based on multiple parameters or signals or methods.

Neutron Activation Analysis A nuclear analytical technique used for the quantitative and qualitative determination of elements in a wide variety of materials.

Neutron Dosimetry A procedure that encompasses the detection and evaluation of neutron dose by a suitable neutron detector.

Nuclear Emulsion Plate A photographic plate coated with a thicker photographic emulsion of gelatine containing a higher concentration of very fine silver halide grains to detect charged particles.

Nuclear Fission Heavy nucleus after absorbing an additional neutron splits into two parts with a release of about 200 MeV per fission and emission of about 2.5 neutrons/fission.

Nuclear Fuel Cycle All operations associated with production of nuclear energy, including mining, milling, processing and enrichment of uranium or processing of thorium, manufacture of nuclear fuel, operation of nuclear reactors, reprocessing of irradiated nuclear fuel, decommissioning, and any activity for radioactive waste management and research or development activity related to any of the foregoing.

Nuclear Fuel Reprocessing Plant A nuclear chemical plant together with all the associated structures, systems, components and equipment necessary for safe separation of Uranium and Plutonium from fission products.

Nuclear or Radiation Emergency They are emergencies in which there is or perceived to be, a hazard due to: (i) The energy resulting from a nuclear chain reaction or from the decay of the products of a chain reaction; or (ii) Radiation exposure.

Nuclear Medicine Nuclear Medicine is a branch of clinical medicine, where unsealed radioisotopes are used for various diagnostic and therapeutic applications.

Nucleonic Gauges An equipment that consists of radiation source and detector to measure various process control and quality control parameters in industries.

Occupational exposure Radiation exposure acquired by workers in the course of their work, with the exception of: (1) excluded exposures and exposures from exempt activities involving radiation or exempt sources; (2) any medical exposure; and (3) the normal local natural background radiation.

Operation All activities following commissioning and before decommissioning were performed to achieve, in a safe manner, the purpose for which a nuclear/radiation facility was constructed, including maintenance.

Operational Interventional Level (OIL) It is an operational criterion. It is a set level of a measurable quantity that corresponds to a generic criterion. OILs are typically expressed in terms of dose rates or of activity of radioactive material released, time integrated air concentrations, ground or surface concentrations, or activity concentrations of radionuclides in environmental, food or water samples.

Operational Quantities Practically realizable quantities are defined for estimation of radiation protection quantities.

Optically Stimulated Luminescence A process in which a pre-irradiated (exposed to ionizing radiation) material when subjected to an appropriate optical stimulation, emits a light signal proportional to the absorbed dose.

Organically Bound Tritium The buried non-exchangeable tritium bound to organic matter, resulting from tritium being incorporated in various organic compounds during the synthesis process of living matter.

Pair Production Production of an electron–positron pair in the field of nucleus of the absorbing atom when the incident X-ray or gamma photon of energy is greater than 1.022 MeV.

Passive Dosimeter A dosimeter (TLD, films, solid state nuclear track detector, etc.) does not produce signal in real time when exposed to ionizing radiation. Post irradiation, the radiation-induced response is collected by processing the dosimeter separately using a dedicated system.

Path length The actual path is traversed by a charged particle in a medium due to extensive multiple scattering with atomic nuclei and atomic electrons of the medium.

Personnel Dosimetry Monitoring of radiation dose of radiation workers during routine occupational exposure.

Phantom A model for substitute of human body or body part which is used for calibration of personal dosimeters.

Phoswich Detector A sandwich of two phosphors (Scintillators).

Photoelectric Effect An interaction of X-ray or gamma photon with an orbital electron in which the photon is absorbed and an electron is ejected from the atom.

Physical Quantities The quantities used in radiation metrology whose units are directly obtained through primary standards at national standards laboratories.

Posterior Distribution The distribution of possible values for a parameter after observing data. It is a key result in Bayesian analysis and encapsulates uncertainty about the parameter.

Posterior Probability The updated probability of a hypothesis after incorporating observed data. It is calculated using Bayes' theorem and is proportional to the product of the prior and likelihood.

Potential Exposure Exposure that is not expected to be delivered with certainty but that may result from an accident at a source or owing to an event or sequence of events of a probabilistic nature, including equipment failures and operating errors.

Potential Alpha Energy (PAE) The potential alpha energy (in MeV) of an atom in the decay chain of ^{222}Rn/^{220}Rn is the total alpha energy emitted during the decay of this atom through the decay chain to ^{210}Pb in the case of radon or ^{208}Pb in the case of thoron.

Potential Alpha Energy Concentration in Air (PAEC) This concentration refers to the total potential alpha energy of any mixture of short-lived radon or thoron decay products per unit volume of air. The historical unit for this quantity is the Working Level (WL), while the SI unit is J m^{-3}.

Precipitation/Co-precipitation Precipitation and co-precipitation are processes used in chemistry to separate or isolate substances from a solution based on their solubility characteristics.

Prior Probability The initial probability is assigned to a hypothesis before considering new evidence. It represents the belief or knowledge about the hypothesis before data is observed.

Protection Quantities The risk-related quantities used for expressing the radiation dose limits.

Quality Assurance (QA) A systematic process is implemented to ensure that a set of procedures, protocols, and standards are followed consistently to achieve desired outcomes. In the context of internal dose evaluation, QA involves establishing and maintaining high standards in data collection, analysis, and reporting to ensure the reliability and accuracy of results.

Quality Factor The factor characterizing the biological effectiveness of a radiation, based on the ionization density along the tracks of charged particles in tissue.

Quenching An interference in the energy transfer process reduces the number of photons reaching the photomultiplier tubes.

Radiation Accident An unplanned event resulting in (or having the potential to result in) personnel injury or damage to equipment which may or may not cause the release of unacceptable quantities of radioactive material or toxic/hazardous chemicals.

Radiation Detriment A concept used to quantify the harmful health effects of radiation exposure in different parts of the body.

Radiation Processing A technology that uses ionizing radiations such as gamma rays, X-rays and electron beam for irradiation of food and allied products (cross-linking of wires, cables and rubbers, coloration of diamonds and precious stones etc.) and sterilization of medical products.

Radiation Protection The protection of occupational workers, general public and environment from the effects of exposure to ionizing radiation, and the means for achieving this.

Radiative Stopping Power Energy lost by a light-charged particle through radiative collisions with the nuclei of an absorber per unit length that it traversed in the absorber.

Radiopharmaceuticals Radiopharmaceuticals are the target-specific molecule (pharmaceutical), labeled with a radioactive element and are of adequate purity and safety for administration in human being.

Radiophotoluminescence Emission of light from the certain substances after irradiation to ionizing radiations.

Radiotracer Technique A technique that utilizes radioisotopes for detecting blockage and leak detection in pipelines, flow rate measurement, measuring fluid dynamics parameters, and troubleshooting investigations.

Radon Emanation Factor The fraction of radon produced in the grains of a porous matrix that is released to the pore space of the matrix and available for further transport. Also known as the radon emanation coefficient or radon emanating power.

Radon Mass Exhalation Rate The rate of radon exhalation per unit mass of the sample expressed in units of Bq kg^{-1} s^{-1}. It is typically used to assess the radon exhalation potential of powdered samples such as soil and cement.

Radon Flux The rate of radon emission per unit area of the surface of a porous matrix like soil or walls expressed in units of Bq m^{-2} s^{-1}. This quantity serves

as a measure of the source term for radon in the environment and is valuable for predicting radon concentrations through dispersion and dilution models.

Radon Surface Exhalation Rate Refers to the rate of radon exhalation per unit surface area of the sample expressed in units of Bq m^{-2} s^{-1}. It is generally used to assess the radon exhalation potential of samples with regular geometries, like bricks, tiles, and concrete blocks.

Range Straight distance that a charged particle traverses in a medium before its energy becomes negligible or zero.

Recording Level A level of effective or equivalent dose above which a result from a monitoring program is included in a dose record.

Reference Level It is the action level, intervention level, investigation level or recording level established for any of the quantities determined in the practice of radiation protection.

Relative Biological Effectiveness Ratio of doses of a reference radiation versus test radiation to produce certain biological effect.

Residual Dose The dose expected to be incurred in the future after protective actions have been terminated or a decision has been taken not to implement protective actions during an emergency exposure situation or existing exposure situation.

Retention/Excretion Functions Mathematical expressions in biokinetic models describe how a substance is retained or eliminated within the body over time. Depict accumulation and removal processes for activity.

Retrospective Dosimetry Estimation of absorbed dose received by the person in past when conventional dosimeters are not available and dose measurements are not planned.

Single Photon Emission Computed Tomography (SPECT) A nuclear medicine imaging device which acquires 2D images at different views around the patient and provides an estimate of the 3D radioactivity distribution through image reconstructions from multiple projections.

Scintillators Materials which convert the energy of the incident radiation in to light.

Solid State Nuclear Track Detector A detector (photographic emulsion, crystal, glass or plastic) produces damage in the form of a track when exposed to nuclear radiation and is examined microscopically after etching.

Solvent Extraction A method to separate compounds or metal complexes, based on their relative solubilities in two different immiscible liquids, usually water (polar) and an organic solvent (non-polar).

Source Organ Refers to the specific region or organ within the body that contains or accumulates radionuclide.

Specific Absorbed Fraction Fraction of radiation emitted in the source region that is absorbed per unit mass of the target region.

Specific Effective Energy Specific Effective Energy (SEE) is a measure of the energy transferred to a target organ when a source organ undergoes a single radioactive disintegration event.

Specific Radioactivity Refers to the amount of radioactivity per unit mass of the radioactive material and is expressed in units of Bq kg^{-1}.

Stochastic Effect Radiation health effects caused by mutations, probabilistic in occurrence without a threshold.

Stopping Power Energy lost by a charged particle in a medium per unit length through radiative and electronic collisions.

***S*-Value** Mean absorbed dose to the target organ per unit time integrated activity in the source region.

Synchrotron radiation The electromagnetic radiation emitted when charged particles travel in curved paths.

Systemic Activity Refers to the distribution and behavior of a substance throughout the entire body, typically after absorption into the bloodstream. Crucial in understanding the overall fate of a substance in the body.

Target Organ Pertains to a distinct tissue or region within the body where a dose of radiation is received.

Thermoluminescence Emission of light from the materials upon heating which are previously exposed to ionizing radiation. TLDs utilize this property to quantify radiation exposure.

Time Integrated Activity Time Integrated Activity is the product of amount of radioactivity and the duration of time for which the radioactivity is present in the source region.

Tissue Free Water Tritium Exchangeable fraction of tritium that represents the free-water cellular tritium. The part of tritium in living organisms that remains as HTO.

TLD Badge A wearable dosimeter that contains TLDs and is worn by individuals working with ionizing radiation. It is used for monitoring radiation exposure in occupational settings.

TLD Badge Reader An equipment that applies pre-programmed heating cycle to the thermoluminescence dosimeter, detects the dosimeter's instantaneous light and displays the total integrated light in counts.

Triage The sorting of and allocation of treatment to individuals exposed to ionizing radiation to maximize the number of survivors.

Tritium Filled Sources Sealed glass tubes filled with tritium gas for night-illumination of various military gadgets, and commercial/industrial buildings as warning signs.

Uptake Quantity of a radionuclide taken up by the systemic circulation (e.g., by injection into the blood, by absorption from compartments in the respiratory or GI tracts, or by absorption through the skin or through wounds in the skin).

Uranium Milling Uranium milling is a series of mechanical and chemical processes that process extracted uranium ore and produce dry powder-form material consisting of natural uranium called "yellowcake" (chemically U_3O_8).

Uranium Mining Uranium mining is the process of extraction of uranium ore from the earth.

Water Radiolysis Lysis of water into radicals, ions, and other reactive oxygen species induced by ionizing radiation.

X-ray radiography A medical X-ray imaging technique provides two-dimensional image of the internal structures of the human body.